Analysis and Design of Energy Geostructures

Theoretical Essentials and Practical Application

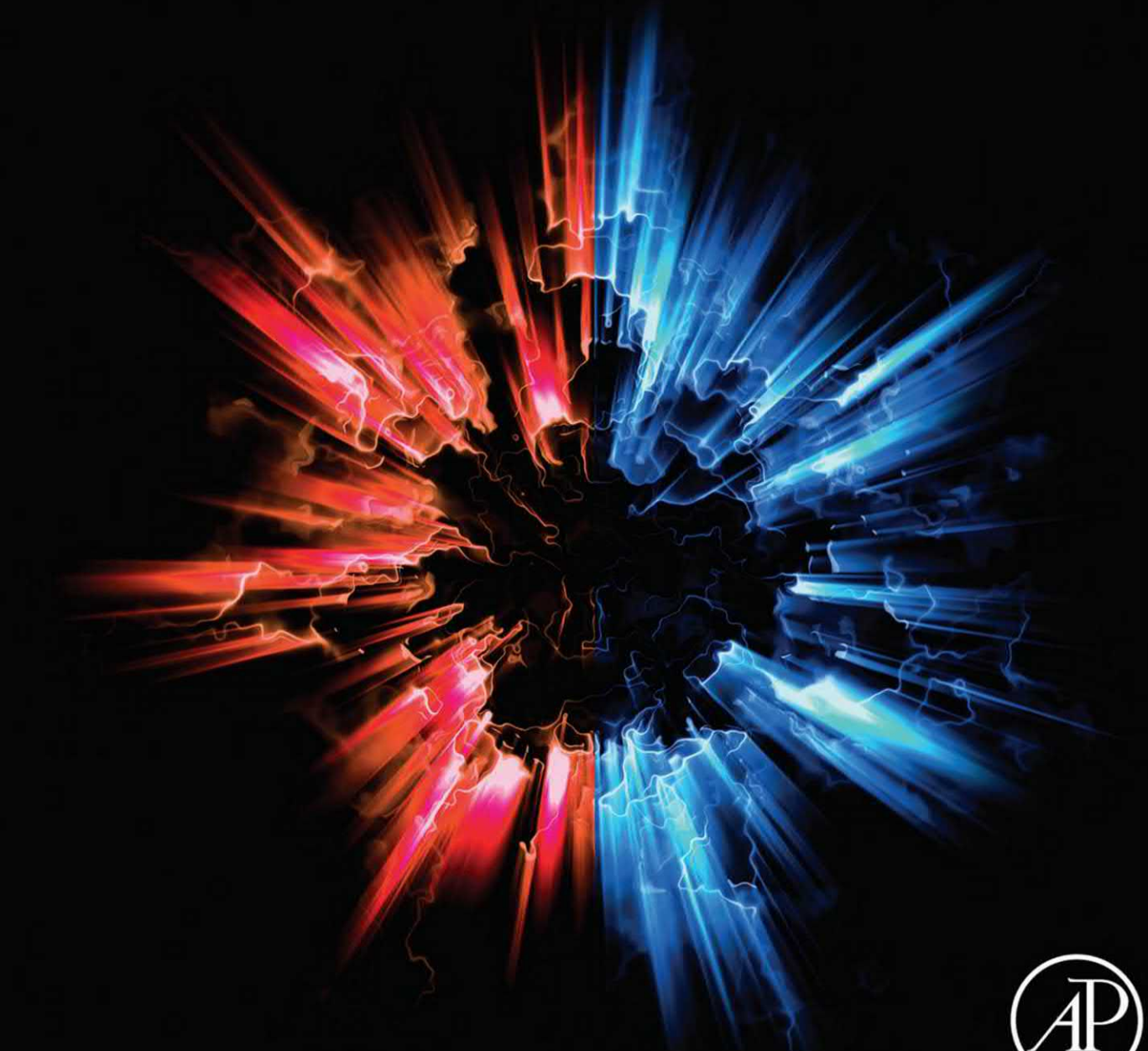

Lyesse Laloui and Alessandro F. Rotta Loria

Analysis and Design of Energy Geostructures

Analysis and Design of Energy Geostructures

Theoretical Essentials and Practical Application

LYESSE LALOUI
Soil Mechanics Laboratory, Swiss Federal Institute of Technology, Lausanne, Switzerland

ALESSANDRO F. ROTTA LORIA
Mechanics and Energy Laboratory, Northwestern University, Evanston, IL, United States

ACADEMIC PRESS
An imprint of Elsevier

Academic Press is an imprint of Elsevier
125 London Wall, London EC2Y 5AS, United Kingdom
525 B Street, Suite 1650, San Diego, CA 92101, United States
50 Hampshire Street, 5th Floor, Cambridge, MA 02139, United States
The Boulevard, Langford Lane, Kidlington, Oxford OX5 1GB, United Kingdom

Notices

Knowledge and best practice in this field are constantly changing. As new research and experience broaden our understanding, changes in research methods, professional practices, or medical treatment may become necessary.

Practitioners and researchers must always rely on their own experience and knowledge in evaluating and using any information, methods, compounds, or experiments described herein. In using such information or methods they should be mindful of their own safety and the safety of others, including parties for whom they have a professional responsibility.

To the fullest extent of the law, neither the Publisher nor the authors, contributors, or editors, assume any liability for any injury and/or damage to persons or property as a matter of products liability, negligence or otherwise, or from any use or operation of any methods, products, instructions, or ideas contained in the material herein.

British Library Cataloguing-in-Publication Data
A catalogue record for this book is available from the British Library

Library of Congress Cataloging-in-Publication Data
A catalog record for this book is available from the Library of Congress

ISBN: 978-0-12-820623-2

Publisher: Brain Romer
Acquisition Editor: Raquel Zanol
Editorial Project Manager: Carlos Rodriguez
Production Project Manager: Vijayaraj Purushothaman
Cover Designer: Miles Hitchen

Typeset by MPS Limited, Chennai, India

Contents

Preface

Urban systems present an enormous demand for innovative solutions to meet human activity needs. In many situations, these needs require built environments and are associated with substantial amounts of energy requirements. While it is a critical challenge to develop buildings and infrastructures whose energy requirements are supplied with a limited impact on the environment, employing renewable energy sources is essential for this purpose. So-called *energy geostructures* represent a breakthrough multifunctional technology for the sustainable development of present and future urban systems.

A substantial amount of renewable geothermal energy is readily available in the ground. Geostructures, including foundations and general earth-contact structures, are essential means for the structural support of built environments through the ground. By leveraging the previous concepts, energy geostructures represent integrated earth-contact structures and thermal energy carriers for all built environments. Energy geostructures particularly explicate a multifunctional role for buildings and infrastructures: reinforce soils and rocks for their structural support and, at the same time, extract or store thermal energy from or in the subsurface for the supply of their heating and cooling energy requirements.

An extraordinary interest has risen over the past 20 years in both the scientific and practitioner communities about energy geostructures. The capabilities of this technology are unique in serving the structural support and renewable energy supply of built environments. However, the analysis and design of energy geostructures can be daunting, inappropriate or even unsuccessful without a sound understanding of their behaviour and performance by means of the relevant *theoretical essentials* and the appropriate *practical application*.

Many and complex are the phenomena associated with the multifunctional operation of energy geostructures that need to be considered in analysis and design (e.g., energy, geotechnical and structural). The competence required for such purpose is strongly multidisciplinary, gathering theoretical essentials that govern heat and mass transfers, and the mechanics of geomaterials and structures, as well as practical knowledge about performance-based design and detailing. Some competence on the previous subjects may be acquired through educational paths that include energy engineering, civil and environmental engineering, mechanical engineering and architecture. More advanced yet fragmented competence addressing unique features that characterise energy geostructures may be acquired through the scientific literature. However, at the present time, the competence required to develop the analysis and

design of energy geostructures is not available in a unified framework. This book resolves such a challenge for the first time, by gathering the available theoretical and experimental competence to develop the analysis and design of energy geostructures.

Structured in 5 parts and 16 chapters, this book provides the broad training that is required to understand, model and predict the behaviour and performance of energy geostructures, as well as to carry out the related analysis and design from energy, geotechnical and structural perspectives. Part A presents an introduction to the scope of energy geostructures. Part B summarises the theoretical essentials allowing the understanding of the phenomena governing the behaviour of energy geostructures. Part C provides experimental evidence about the referenced behaviour. Part D covers analytical and numerical approaches to analyse the behaviour of energy geostructures. Part E provides elements to design energy geostructures and assess the related performance. At the end of each chapter, theoretical questions and practical application exercises are proposed.

The book has been designed with civil engineers in mind, but targets energy engineers, environmental engineers, geologists, architects and urban project managers as well. By covering theoretical and practical aspects as homogeneously and comprehensively as its scope permits, the book targets readers who have no experience with energy geostructures as well as audiences who have already been involved in the analysis or design of energy geostructures. Particularly useful for university students at the graduate level, this book aims to inspire and prepare current and future generations of scientists and practitioners to positively revolutionise urban environments.

A substantial amount of the content of this book is based on research and development activities carried out over the past 20 years at the Swiss Federal Institute of Technology in Lausanne (EPFL). Various theoretical frameworks and results proposed by colleagues in the scientific and technical literature are also included in an effort to make this treatise as comprehensive as possible. While the scientific community is acknowledged for making available relevant knowledge that helped to broaden the scope of this book, a particular vote of thanks is devoted to current and past collaborators of the authors for their valuable contributions to this treatise.

The following collaborators are acknowledged for revising some chapters, preparing a number of figures and tables, developing some exercise solutions and sharing fruitful discussions during the preparation of this book: Margaux Peltier, Benoît Cousin, Elena Ravera, Jose Antonio Bosch Llufriu, Jacopo Zannin, Eleonora Crisci, Niccolò Batini, Louise Copigneaux, Christopher Gautschi, Aldo Madaschi, Chao Li, Simon Caldi, Laurette Rohrbach, Francesco Di Bari, Etienne Cassini, Alberto Minardi, Patrick Dubey, Francesco Parisio, Patrycja Baryla, Roba Houhou and Carlo Gaffoglio. The following colleagues are thankfully acknowledged for sharing photographs of construction sites of energy geostructures that enriched the content of the introductory part of the book: Tony Amis, Sebastian Homuth and Stefan Wehinger.

The following colleagues and collaborators are acknowledged for contributing to this book by means of the work and discussions developed across generations of research projects at the graduate and undergraduate levels, PhD theses and postdoctoral research: Alice Di Donna, Thomas Mimouni, Hervé Péron, Christoph Knellwolf, Mathieu Nuth, Bertrand François, Cane Cekerevac, Alessio Ferrari, Laurent Vuillet, Melis Sütman, Fabrice Dupray, Aurélien Vadrot, Matteo Bocco, Cristiano Garbellini, Hani Taha, Pia Hartmann, Lea Kaufmann, Aymen Achich, Thibaut Duparc, Etienne Dominguez, Perrine Ratouis, Qazim Llabjani, Samuel Kivell, Stefano Cingari, Alain Kazangba, Marianna Adinolfi, Dimitrios Terzis, Claire Silvani, Sarah Dornberger, Matteo Moreni, Gilbert Steinmann, Gangqiang Kong, Gunter Siddiqi, Tomasz Hueckel and Gilbert Gruaz.

Last, but not least, the continued and special support provided by Claire, Sinan and Inès to the first author as well as by Giorgia to the second author are gratefully acknowledged.

Lyesse Laloui[1] **and Alessandro F. Rotta Loria**[2]
[1]Soil Mechanics Laboratory, Swiss Federal Institute of Technology, Lausanne, Switzerland;
[2]Mechanics and Energy Laboratory, Northwestern University, Evanston, IL, United States
April 2019

List of symbols

Roman symbols

Symbol	Variable name	Unit measure
A	Cross-sectional area	m^2
A_b	Cross-sectional area of pile base	m^2
A_c	Cross-sectional area of concrete	m^2
$A_{c,eff}$	Effective area of concrete in tension	m^2
A_{ct}	Cross-sectional area of concrete in tension	m^2
A_{eq}	Equivalent cross-sectional area	m^2
A_{exc}	Plan area in which the thermal strain potential of soil is in excess of that of piles	m^2
A_{EP}	Cross-sectional area of piles	m^2
A_f	Skempton pore water pressure coefficient	–
A_g	Plan area of pile group	m^2
$A_{g,s}$	Area of the block shaft	m^2
A_{inf}	Plan area of involved soil volume	m^2
A_L	Constant	–
A_p	Cross-sectional area of pipe	m^2
A_r	Cross-sectional area of reinforcement	m^2
A_{rl}	Cross-sectional area of tensile reinforcement	m^2
A_{rw}	Cross-sectional area of shear reinforcement	m^2
$A_{r,min}$	Minimum longitudinal reinforcement	m^2
A'_r	Cross-sectional area of reinforcement working in tension	m^2
A_s	Area of pile shaft	m^2
A_{si}	Area of body immersed in the fluid; interstitial surface area	m^2
A_{soil}	Plan area of soil delimiting the shape of the pile group	m^2
$A_{t,EP}$	Total cross-sectional area of piles	m^2
$A_{th,soil}$	Plan area of soil influenced by the heat exchange	m^2
A_{ZH}	Material parameter	–
$\overline{AA'}$	Distance	m
AR	Aspect ratio of pile group	–
$\tilde{A}$	Actual contact area	m^2
A^*	Calibration factor	Pa
a	Shape function	–
a_d	Design value of geometrical data of the structure	Variable
a_{exp}	Material constant	1/°C
a_L	Material parameter	–
a_M	Empirical constant	–
a_r	Material parameter	–
a_v	Compressibility index	1/Pa
B_L	Constant value	–
B_r	Breadth of foundation	m
B_{slab}	Breadth of slab/strip foundation	m
B_{ZH}	Material parameter	–
Bi	Biot number	–
B^*	Calibration factor	Pa
b	Shape function	–

Roman symbols

Symbol	Variable name	Unit measure
b_{exp}	Material constant	1/°C
b_i	Body forces vector	N/m^3
b_L	Material parameter	–
b_M	Empirical constant	–
b_r	Material parameter	–
C_A	Consolidation ratio	–
C_c	Compression index	–
C_d	Limiting design value for the serviceability criterion	Variable
C_E	Manufacturer constant	1/A
C_h	Horizontal consolidation coefficient	m^2/s
C_{ijkl}	Stiffness tensor	Pa
C^{ep}_{ijkl}	Elastoplastic stiffness tensor	Pa
C^{e}_{ijkl}	Elastic stiffness tensor	Pa
C_L	Constant	–
C_r	Recompression index	–
C_S	Hazen equation coefficient	–
C_s	Swelling index	–
C_{sp}	Specific heat storage capacity	J/°C
C_t	Lumped thermal capacitance of the solid	J/°C
C_{ud}	Uniformity coefficient	–
C_1	Fitting coefficient	–
C_α	Secondary compression index	–
$C_{\alpha\varepsilon}$	Secondary compression ratio	–
C^*	Calibration factor	Pa/°C
COP	Coefficient of performance of the heat pump	–
CR	Compression ratio	–
c	Cohesion	Pa
$c_{a,cv}$	Adhesion under constant volume conditions	Pa
$\overline{c}_a$	Pile–soil interface adhesion	Pa
c_c	Concrete cover	m
$\tilde{c}_c$	Comprehensive correction coefficient	–
c_{DB}	Dittus and Boelter factor	–
c_{exp}	Material constant	1/°C
$c_{E,w}$	World final energy consumption	toe
$c_{E,w,\%}$	Proportion of world final energy consumption	%
c_p	Specific heat	J/(kg °C)
$c_{p,EP}$	Specific heat of pile	J/(kg °C)
$c_{p,f}$	Specific heat of fluid	J/(kg °C)
$c_{p,s}$	Specific heat of solid particles	J/(kg °C)
$c_{p,soil}$	Specific heat of soil	J/(kg °C)
$c_{p,w}$	Specific heat of the water	J/(kg °C)
c_r	Material parameter	–
c_u	Undrained soil cohesion	Pa
c_v	Primary consolidation coefficient	m^2/s
c'	Effective cohesion	Pa
c_0	Kozeny coefficient	–
c_1	Dimension of cross section perpendicular to the axis of bending	m
c_2	Dimension of cross section parallel to the axis of bending	m
$c_{\%}$	Percentage of clay mineral in the soil	%

Roman symbols

Symbol	Variable name	Unit measure
cty	Country	–
D	Diameter of pile	m
D_b	Bending rigidity per unit area	N/m
D_{eq}	Equivalent diameter	m
D_{exc}	Excess diameter	m
D_f	Fractal dimension	–
D_{ijkl}	Elastic stiffness tensor	Pa
D_L	Constant	–
D_{max}	Diameter of the biggest aggregate characterising the mix design of the filling material	m
D_p	Effective hydraulic diameter	m
D_r	Displacement ratio	–
D_R	Relative density	%
D_{10}; D_{50}	Grain size diameter	m
DOF	Degree of freedom	–
d_e	Hydraulic equivalent rock joint opening	m
d_{exp}	Material constant	1/°C
d_p; $d_{p,in}$	Inner diameter of pipe	m
$d_{p,out}$	Outer diameter of pipe	m
d_q; d_c; d_γ	Bearing factors	–
d_r	Material parameter	–
d_{rj}	Rock joint opening	m
d'	Depth at which the compression reinforcement is placed from the most compressed fibre of the cross section	m
E	Young's modulus	Pa
E_c	Young's modulus of concrete	Pa
E_C	Cooling energy	Wh
E_{cm}	Mean secant Young's modulus	Pa
E_d	Design value of action or action effect	Variable
E_{eq}	Equivalent Young's modulus	Pa
E_{EP}	Young's modulus of pile	Pa
E_H	Heating energy	Wh
$E_{H,C}$	Total thermal energy	Wh
E_L	Constant	–
E_M	Menard pressuremeter modulus	Pa
E_{oed}	Oedometric modulus	Pa
E_r	Young's modulus of reinforcement	Pa
E_{slab}	Young's modulus of slab	Pa
E_{soil}	Young's modulus of soil	Pa
$E_{soil,b}$	Young's modulus of soil at the level of pile base	Pa
$E_{soil,m}$	Young's modulus of soil mass	Pa
$E_{soil,s}$	Young's modulus of soil around the pile shaft	Pa
$\overline{E}_{soil}$	Average value of Young's modulus of soil	Pa
E_1	Exponential integral	–
e	Void ratio	–
de	Incremental change of void ratio	
e_c	Critical void ratio	–
$e_{E,w}$	World energy-related greenhouse gas emissions	t_{CO2eq}
$e_{E,w,s}$	World energy-related CO_2 emissions by sector and region	kg

Roman symbols

Symbol	Variable name	Unit measure
e_{E,w,CO_2}	Proportion of world energy-related CO_2 emissions	%
$e_{E,w,\%}$	Proportion of world energy-related greenhouse gas emissions	%
e_i	Void ratio at loading step i	–
e_{ij}	Deviatoric strain tensor	–
e_0	Initial void ratio	–
Δe^e	Elastic change of void ratio	–
de^e	Incremental change of elastic void ratio	–
$\hat{e}_x, \hat{e}_y, \hat{e}_z$	Standard unit vectors in Cartesian coordinates	–
F	Resonant frequency of wire at actual time	Hz
F_a	Weighting factor for pores filled with air	–
F_b	Correction factor indicating the effect of bearing stratum	–
F_c	Forces given by the compressed concrete portion	N
$F_{c;d}$	Design value of axial load	N
F_d	Design value of a mechanical load acting on a single pile or a group of piles	N
F_h	Run fraction of the GSHP during the design month	–
F_k	Characteristic value of the considered action	N
F_L	Constant	–
F_n	Applied normal force	N
F_r	Forces given by the traction steel cross section	N
F_{rep}	Representative value of the considered action	N
F_s	Weighting factor for soil particles	–
F_0	Resonant frequency of wire at initial time	Hz
Fo	Fourier number	–
f	Yield function	Pa
f_{cd}	Design value of compressive strength of concrete	Pa
f_{ck}	Characteristic compressive cylinder strength of concrete	Pa
$f_{ck,cube}$	Characteristic compressive cube strength of concrete	Pa
f_{ct}	Axial tensile strength of concrete	Pa
f_{ctd}	Design value of axial tensile strength of concrete	Pa
$f_{ct,eff}$	Mean value of the tensile strength of the concrete after crack formation	Pa
$f_{ctk,0.05}$	Characteristic (inferior) axial tensile strength	Pa
f_{cm}	Peak stress of concrete	Pa
f_{ctm}	Mean value of axial tensile strength of concrete	Pa
f_{dev}	Deviatoric yield limit	–
f_D	Darcy friction factor	–
f_{iso}	Isotropic yield surface	–
f_l	Vector containing f_{iso} and f_{dev}	–
f_t	Tensile strength of steel	Pa
f_y	Compressive strength of steel	Pa
f_{yd}	Design value of steel compressive strength	Pa
f_{yk}	Characteristic values of yield strength of steel	Pa
f_{ywd}	Design value of yield strength of the shear reinforcement	Pa
f_M	Moody (or Darcy) friction factor	–
$f_{0.2k}$	0.2% proof-stress	Pa
$\overline{f}$	Average stress acting on the compression zone	Pa
G	Shear modulus	Pa
G_f	Time-dependent part of the thermal resistance	°C/W
G_k	Permanent load	N

Roman symbols

Symbol	Variable name	Unit measure
G_{ref}	Shear modulus at a reference point	Pa
G_{soil}	Shear modulus of soil	Pa
$G_{soil,b}$	Shear modulus of soil at the level of pile base	Pa
$G_{soil,s}$	Shear modulus of soil around pile shaft	Pa
G'_f	Time-dependent part of the thermal resistance per unit of length	°C/(W m)
G''_f	Time-dependent part of the thermal resistance per unit of surface	°C/(W m^2)
G_0	Soil shear modulus at small strains	Pa
g	Plastic potential function	–
g_a	Shape factor	–
g_c	Shape factor	–
g_{dev}	Deviatoric plastic potential function	–
g_i	Gravity vector	m/s^2
g_{iso}	Isotropic plastic potential function	–
g_l	Vector containing g_{iso} and g_{dev}	–
H	Total head	m
H_i	Specimen height at loading step i	m
H_0	Initial specimen height	m
$\tilde{h}$	Hardening variable	Variable
h_c	Local convection heat transfer coefficient; contact conductance	W/(m^2 °C)
$h_{c,ef}$	Reinforcement depth	m
$h_{c,fd}$	Convection heat transfer coefficient in fully developed region	W/(m^2 °C)
$h_{c,in}$	Inner convection heat transfer coefficient	W/(m^2 °C)
$h_{c,out}$	Outer convection heat transfer coefficient	W/(m^2 °C)
$h_{c,n}$	Portion of convection coefficient associated to natural convection	W/(m^2 °C)
$h_{c,f}$	Portion of convection coefficient associated to forced convection	W/(m^2 °C)
$h_{c,ent}$	Convection heat transfer coefficient in thermal entrance region	W/(m^2 °C)
$\overline{h}_{c,ent}$	Mean convection heat transfer coefficient in thermal entrance region	W/(m^2 °C)
$\tilde{h}_i$	Vector of hardening variables	Variable
h_{in}	Convective heat transfer coefficient	W/(m °C)
h_K	Kozeny constant	–
h_L	Head losses	m
h_l	Model depth	m
h_p	Pressure head	m
h_r	Radiation heat transfer coefficient	W/(m °C)
h_v	Velocity head	m
h_z	Elevation head	m
h_1	Apex water	–
h_0	Water adsorbed as a film around the soil particles	–
I_p	Plasticity index	–
I_r	Rigidity index	–
I_R	Relative dilatancy index	–
I_1	First invariant of the deviatoric stress tensor	Pa
I_2	Second invariant of the deviatoric stress tensor	Pa
I_3	Third invariant of the deviatoric tensor	Pa
i	Lu parameter	–
J	Second moment of area of the section	
$J_{B,0}$	First kind Bessel function of the first order	–
$J_{B,1}$	First kind Bessel function of the second order	–
$J_{B,n}$	First kind Bessel function of n order	–

Roman symbols

Symbol	Variable name	Unit measure
$J_1;J_2;J_3$	Invariants of the deviatoric stress tensor	Pa
$\overline{K}$	Average value of the relevant coefficient of lateral pressure	–
K_b	Slope of loading/unloading elastic branch of base load-displacement function	Pa/m
K_{EP}	Pile stiffness	Pa/m
K_g	Gauge factor	$1/Hz^2$
K_h	Head stiffness of superstructure or connected structural element	Pa/m
K_{int}	Far-field normal stiffness	Pa/m
K_L	Coefficient of local losses	–
K_p	Passive earth pressure coefficient	–
K_{ref}	Bulk modulus at a reference point	Pa
K_s	Slope of loading/unloading elastic branch of shaft load-displacement function	Pa/m
K_{slab}	Stiffness of slab	Pa/m
K_{ss}	Slab–soil stiffness ratio	–
K_0	Coefficient of earth pressure at rest	–
k	Hydraulic conductivity	m/s
k_{AR}	Aspect ratio coefficient	–
k_B	Thermal constant	–
k_h	Horizontal hydraulic conductivity	m/s
k_{sl}	Slope of straight line	°C
k_t	Factor depending on the duration of the load	–
k_{sr}	Shape factor	–
k_1	Coefficient associated to the design problem of shear	–
$k_{0.85}$	Hydraulic conductivity for a void ratio of 0.85	m/s
k_ε	Factor of the internal nonuniform self-equilibrating stresses	–
k^i	Intrinsic permeability	m^2
L	Length of pile	m
L'	Length of pile after the application of temperature variation	m
L_{eff}	Effective length of pile	m
L_g	Width of pile group	m
L_p	Pipe length	m
L_{tot}	Total required thermally active length of energy piles	m
L_{seg}	Length of segment	m
L_{slab}	Length of slab	m
l_i	Length of the ground layer	m
l_{OF}	Length of optical fibre	m
M	Moment	Nm
M_c	Critical state parameter	–
M_{Ed}	Design value of acting moment	Nm
M_{ijkl}	General constitutive tensor of the material	Pa
M_i	Mass i	kg
M_{lim}	Limiting design moment	Nm
M_{Rd}	Design value of resisting moment	Nm
M_s	Kozeny coefficient	–
m_{sl}	Intercept constant	°C
m_t	Coefficient	1/Pa
m_v	Compressibility coefficient	1/Pa

Roman symbols

Symbol	Variable name	Unit measure
$m_{\%}$	Actual percentage of specific mineral	%
$\dot{m}$	Mass flow rate	kg/s
N	Normal force (e.g., axial)	N
$N^m_{b,k}$; $N^m_{m,k}$; $N^m_{h,k}$	Axial force at base, middle and head of each pile element	N
N_c, N_q, N_γ	Bearing capacity factors	–
N_c	Proportion of sectional axial force received by concrete	N
N_{cr}	Axial force needed to crack the concrete	N
$N_{cr,c}$	Axial force mobilised by the concrete upon cracking	N
$N_{cr,d}$	Design value of axial force mobilised by the concrete upon cracking	N
$N_{cr,r}$	Axial force mobilised by the concrete upon cracking	N
N_{cyc}	Cycle number	–
N_d	Design values of axial cross-sectional load	N
$N_{E,d}$	Design value of acting axial force	N
N_{Gd}	Design permanent load	N
N_{Gk}	Characteristic permanent load	N
N_{h_l}	Correction factor for effect of finite layer depth	–
N_{Qd}	Design variable load	N
N_{Qk}	Characteristic variable load	N
N_R	Resisting axial force	N
$N_{R,d}$	Design value of resisting axial force	N
N_r	Proportion of sectional axial force received by reinforcement	N
Nu_d	Nusselt number related to a pipe	–
$Nu_{d,T}$	Nusselt number influenced by the temperature	–
Nu_{turb}	Nusselt number under turbulent flow conditions	–
N_ν	Correction factor for effect of Poisson's ratio	–
n	Porosity	–
n_{HC}	Empirical coefficient	–
n_e	Material parameter	–
n_{EP}	Number of energy piles	–
$\tilde{n}_{EP}$	Number of piles along a row or a column of the pile group in plan view	–
n_i	Normal vector	–
n_{LP}	Number of loaded piles	–
n_L	Material parameter	–
$n_{p,EP}$	Number of energy pile projects	–
$\tilde{n}_p$	Number of projects	–
n_p	Number of pipes	–
n_{rc}	Steel to concrete stiffness ratio	–
n_ϕ	Number of reinforcement bars	–
n_1	Normal to the contact surface	–
o_1; o_2	Material parameters	–
P_b	Vertical or axial mechanical load applied at pile base	N
P_d	Design value of vertical or axial mechanical load	N
$\overline{P}_{daily}$	Response of the semiinfinite medium to daily periods	s
$P_{E,w}$	World primary energy supply	toe
$P_{E,w,\%}$	Proportion of world primary energy supply	%
P_p	Wetted perimeter of pipe cross section	m
P_{ref}	Reference value of vertical mechanical load	N
Pr	Prandtl number	–
$\overline{P}_{yearly}$	Response of the semiinfinite medium to yearly periods	s

Roman symbols

Symbol	Variable name	Unit measure
p	Mean stress	Pa
p'	Mean effective stress	Pa
$\overline{p}'$	Constant mean effective stress	Pa
p_a	Atmospheric pressure	Pa
p'_c	Isotropic effective preconsolidation stress	Pa
p'_{c0}	Isotropic preconsolidation stress at reference temperature	Pa
p'_{cr}	Critical effective stress	Pa
p'_{cool}	Preconsolidation pressure at the end of the cooling phase	Pa
p'_e	Equivalent effective pressure	Pa
p_f	Fluid pressure	Pa
p_i	Contact forces	Pa
p'_{ref}	Mean effective stress at reference point	Pa
p_w	Pore water pressure	Pa
pop	World population	–
Q_b	Base capacity	N
$Q_{b,d}$	Design value of base capacity	N
$Q_{b,mob}$	Mobilised base capacity	N
$Q^m_{b,mob}$	Mechanical contribution of mobilised base capacity	N
$Q^{th}_{b,mob}$	Thermal contribution of mobilised base capacity	N
Q_k	Variable load	N; °C
$Q_{k,1}$	Dominant variable action or action effect	N; °C
Q_R	Energy required from the piles	J
Q_{rep}	Single variable mechanical load	N
Q_s	Shaft capacity	N
Q_S	Energy supplied by the heat pump	J
$Q_{s,d}$	Design value of shaft capacity	N
$Q_{s,eq}$	Equivalent shaft capacity	N
$Q_{s,mob}$	Mobilised shaft capacity	N
$Q_{s,mob,down}$	Mobilised shaft capacity below the null point	N
$Q_{s,mob,up}$	Mobilised shaft capacity above the null point	N
$Q^m_{s,mob}$	Mechanical contribution of mobilised shaft capacity	N
$Q^{th}_{s,mob}$	Thermal contribution of mobilised shaft capacity	N
$Q^{th}_{s,mob,down}$	Thermal contribution of mobilised shaft capacity below null point of shear stress	N
$Q^{th}_{s,mob,up}$	Thermal contribution of mobilised shaft capacity above null point of shear stress	N
Q_h	Design ground source heat pump system heating capacity	W
Q_h	Head action	N
Q_u	Ultimate capacity	N
$Q_{u,d}$	Design value of ultimate capacity	N
$Q_{u,b}$	Block capacity of a pile group	N
$Q_{u,eq}$	Equivalent base capacity	N
$Q_{u,exp}$	Experimentally determined pile axial capacity	N
$\dot{Q}$	Thermal power	W
$\dot{Q}_{conv}$	Thermal power by convection	W
$\dot{Q}_{inst}$	Installed power	W
$\dot{Q}_R$	Required thermal power	W

Roman symbols

Symbol	Variable name	Unit measure
$\dot{Q}_S$	Nominal heating power	W
q	Deviatoric stress	Pa
q_b	Base resistance	Pa
$q_{b,mob}$	Mobilised base resistance	Pa
$q_{b,g}$	Base resistance for block failure of pile group	Pa
$q_{b,eq}$	Base resistance of equivalent pier	Pa
q_c	Cone resistance	Pa
q_s	Ultimate shaft resistance	Pa
$q_{s,mob}$	Mobilised shaft resistance	Pa
$q_{s,g}$	Shaft resistance for block failure of pile group	Pa
$q_{s,eq}$	Shaft resistance of equivalent pier	Pa
$\dot{q}_{D,i}$	Mass flux density	m/s
$\dot{q}_{D,x}$	Mass flux density in the flow direction	m/s
$\dot{q}_n$	Hydraulic power	W/m
$\dot{q}_{i,\ cond}$	Heat flux density generated by conduction	W/(m^2 s)
$\dot{q}_{i,\ conv}$	Heat flux density generated by convection	W/(m^2 s)
$\dot{q}_l$	Heat flux per unit length	W/m
$\dot{q}_i$	Heat flux density/heat flux per unit of surface	W/m^2
$\dot{q}_p$	Heat flux per unit length exchanged through the pipe	W/m
$\dot{q}_r$	Radial heat flux	W/m^2
$\dot{q}_{red,\ e}$	Heat flux density generated by radiation	W/(m^2 s)
$\dot{q}_{red,\ a}$	Heat flux density generated by irradiation	W/(m^2 s)
$\dot{q}_{red,\ i}$	Neat heat flux density	W/(m^2 s)
$\dot{q}_s$	Heat flux at the pipe surface	W/m^2
$\dot{q}_v$	Heat generation by unit of volume	W/m^3
$\dot{q}_x$	Heat flux per unit of surface	W/m^2
r	Radial coordinate	m
r_{in}	Inner radius of the infinite cylinder	m
r_{out}	Outer radius of the infinite cylinder	m
r_{soil}	Radius of the soil volume associated to one energy pile	m
r_g	Grain radius	m
r_m	Magical radius	m
r_p	Radius of pipe	m
$r_{p,in}$	Inner radius of pipe	m
$r_{p,out}$	Outer radius of pipe	m
r_{iso}	Degree of mobilisation of plasticity of the isotropic mechanism	–
r_{iso}^{el}	Initial value of r_{iso}	–
r_{iso}^{cyc}	Material parameter	–
r_{dev}	Degree of mobilisation of plasticity of the deviatoric mechanism	–
r_{dev}^{el}	Initial value of r_{dev}	–
r_c	Compression factor	–
r_χ	Curvature radius	m
r_{cr}	Critical radius	m
r_e	Expansion factor	–
R	Radius of pile/cavity/sphere	m
R_{cr}	Critical value of roughness	–
R_d	Design value of resistance	Variable
$R_{c;d}$	Design value of ground resisting load	N

Roman symbols

Symbol	Variable name	Unit measure
$R_{c;k}$	Characteristic resisting load	N
$R_{s;k}$	Characteristic shaft load	N
$R_{b;k}$	Characteristic base load	N
$R_{c;m}$	Measured resistance load	N
R_{exc}	Excess radius	m
R_s	Settlement ratio	–
R_1	First characteristic distance in Mindlin's solution	m
R_2	Second characteristic distance in Mindlin's solution	m
R_k	Material or product characteristic resistance	Variable
$Re; Re_x$	Reynolds number	–
Re_c	Critical Reynolds number	–
R_{eff}	Effective radius of the heat exchanger	m
R_{ghe}	Time-independent thermal resistance	°C/W
R_{max}	Maximum vertical distance between the highest and lowest peaks of a structure asperities	m
R_n	Normalised roughness	–
R'_c	Thermal resistance of the grouting material	m °C/W
R'_p	Thermal resistance of the pipe	m °C/W
R'_{ghe}	Time-independent thermal resistance of geothermal heat exchanger per unit length	m °C/W
R''_{ghe}	Time-independent thermal resistance of geothermal heat exchanger per unit surface	m^2 °C/W
R'_{conv}	Convection time-independent thermal resistance per unit length	m °C/W
$R'_{conv,p}$	Convection time-independent thermal resistance of pipe per unit length	m °C/W
R''_{conv}	Convection time-independent thermal resistance per unit surface	m^2 °C/W
$R'_{cond,p}$	Conduction time-independent thermal resistance of pipe per unit length	m °C/W
$R'_{cond,c}$	Conduction time-independent thermal resistance of concrete per unit length	m °C/W
R''_{cond}	Conduction time-independent thermal resistance of geothermal heat exchanger per unit surface	m^2 °C/W
R'_{rad}	Radiation time-independent thermal resistance per unit length	m °C/W
R''_{rad}	Radiation time-independent thermal resistance per unit surface	m^2 °C/W
R'_i	*i*-th thermal resistance of the circuit per unit length	m °C/W
R''_i	*i*-th thermal resistance of the circuit per unit surface	m^2 °C/W
R'_{soil}	Thermal resistance of the soil per unit length	m °C/W
R_T	Total thermal resistance	°C/W
R'_T	Total thermal resistance per unit of length	m °C/W
R''_C	Contact resistance	m^2 °C/W
R''_T	Total thermal resistance per unit of surface	m^2 °C/W
R^*	Body force in *r* direction	N/m^3
$\tilde{R}^*$	Dimensionless distance	–
$\tilde{\tilde{R}}^*$	Dimensionless distance	–
RR	Recompression ratio	–
s	Spacing	m
s_R	Pipe absolute surface roughness	m
$s_{r,max}$	Maximum crack spacing	m
$s_q; s_c; s_\gamma$	Shape factor	–
s_i	Distance from the tunnel intrados	m

Roman symbols

Symbol	Variable name	Unit measure
s_t	Transition distance	m
s_{ij}	Deviatoric stress tensor	Pa
S	Surface	m^2
S_c	Shape factor	–
S_r	Degree of saturation	%
S_k; S_f	Solid skeleton parameters	–
SFP	Seasonal factor of performance	–
SR	Swelling ratio	–
t	Time	s
t_b	Normal stress developed at pile toe	Pa
t_h	Normal stress developed at pile head	Pa
t_i	Contact forces vector	Pa
t_s	Soil shear strength	Pa
t_p	Residence time of the fluid circulating in the pipes	s
t_{ghe}	Characteristic time of the geothermal heat exchanger	s
t_g	Characteristic time of the heat transfer in the ground	s
t_{95}	Time at 95% of primary consolidation	s
t_{slab}	Thickness of slab	m
t_w	Thickness of wall	m
$t_{w,r}$	Half of the plane wall thickness	m
t_l	Thickness of lining	m
t_0	Initial time; reference time	s
t_{CO2}	Tons of CO_2	ton
t^*	Reference time	s
$\overline{t}_i^n$	Average value of normal stress acting on a surface	Pa
T	Actual value of temperature	°C
T_a	Air temperature	°C
$T_{m,L}$	Bulk temperature	°C
T_0	Reference temperature	°C
T_s	Surface temperature of the pipes	°C
T_{s-p}	Uniform temperature at the surface of the soil–pile interface	°C
$T_{s,in}$	Fluid temperature adjoining the inner surface of the pipe	°C
$T_{s,out}$	Fluid temperature adjoining the outer surface of the pipe	°C
T_{ext}	Temperature at outer pipe side	°C
T_f	Actual value of fluid temperature	°C
T_k	Characteristic value of temperature	°C
T_{EP}	Actual value of temperature of pile	°C
T_{in}	Inflow fluid temperature	°C
T_{out}	Outflow fluid temperature	°C
T_{soil}	Actual value of temperature of soil	°C
$\overline{T}$	Average value of temperature	°C
$\overline{T}_{in}$	Average value of inflow fluid temperature	°C
$\overline{T}_{out}$	Average value of outflow fluid temperature	°C
$\overline{T}_{soil}$	Average value of soil temperature	°C
$\overline{T}_{s-p}$	Average value of temperature at the pile–soil interface	°C
$\overline{T}_f$	Average value of the fluid temperature	°C
$\overline{T}_{in}$	Average value of the inlet fluid temperature	°C
$\overline{T}_{out}$	Average value of the outlet fluid temperature	°C
T_R	Actual temperature at pile radius	°C

Roman symbols

Symbol	Variable name	Unit measure
T_0	Initial temperature	°C
T_∞	Temperature at far field	°C
$T_{\infty,in}$	Internal undisturbed temperature	°C
$T_{\infty,out}$	External undisturbed temperature	°C
$\tilde{T}$	Temperature at which plasticity occurs	°C
T_{lm}	Log mean temperature	°C
u	Horizontal/radial displacement	m
u_i	Peculiar length of the control perimeter	m
$u_{out,ef}$	Control perimeter	m
$\overline{U}$	Average value of overall heat transfer coefficient	W/(m^2 °C)
U	Overall heat transfer coefficient	W/(m^2 °C)
UA	Heat transfer capacity	W/°C
U_r	Normalised velocity of the moving medium	m/s
v	Horizontal displacement	m
v_f	Fluid velocity in relevant direction of pipe (e.g., axial)	m/s
v_{Ed}	Design value of maximum acting punching shear stress	Pa
v_{Rd}	Design value of maximum resisting punching shear stress	Pa
v_w	Fluid velocity on a streamline	m/s
$v_{w,c}$	Critical water fluid velocity	m/s
v_∞	Characteristic fluid velocity	m/s
v_i	Fluid velocity vector	m/s
$\overline{v}_{in}$	Average value of inlet fluid velocity	m/s
$\overline{v}_f$	Average value of fluid velocity in relevant direction of pipes or tubes	m/s
$\overline{v}_{tf,i}$	Average fluid velocity vector	m/s
$\overline{v}_{nw,i}$	Average water velocity vector	m/s
$\overline{v}_{ra}$	Average airflow velocity	m/s
$v_{x,0}$	Inlet uniform fluid velocity	m/s
$v_{x,c}$	Fluid velocity in the core	m/s
$\overline{v}_x$	Average fluid velocity component along x direction	m/s
v_x	Fluid velocity component along x direction	m/s
v'_x	Velocity along the laminar zone	m/s
$V; V_i$	Volume of the considered body	m^3
V_a	Volume of the air	m^3
V_{Ed}	Design value for acting shear force	N
V_s	Volume of solid	m^3
V_w	Volume of pore water	m^3
V_{dr}	Volume of outflowing water	m^3
V_{de}	Thermal expansion of drainage system	m^3
V_w	Thermal expansion of pore water	m^3
V_s	Thermal expansion of solid skeleton	m^3
$\dot{V}$	Volumetric flow rate	m^3/s
w	Vertical displacement	m
w^m	Vertical displacement caused by a mechanical load	m
w^{th}	Vertical displacement caused by a thermal load	m
w^{m+th}	Vertical displacement caused by mechanical and thermal loads	m
$\overline{w}$	Average value of vertical displacement	m
w_b	Vertical displacement of pile toe	m
w_h	Vertical displacement of pile head	m
w_s	Pile shaft displacement	m

Roman symbols

Symbol	Variable name	Unit measure
w_i	Vertical head displacement of the receiver pile in a pair	m
w_j	Vertical head displacement of a single isolated pile	m
w^*	Vertical displacement of a single source pile in a group	m
w^1	Unitary vertical displacement	m
$w^{1,m}$	Unitary vertical displacement caused by a mechanical load	m
$w^{1,th}$	Unitary vertical displacement caused by a thermal load	m
w_f^{th}	Vertical displacement under free thermal expansion conditions	m
$w_{q_b/2}$	Vertical base displacement mobilised for $q_b/2$	m
$w_{q_s/2}$	Vertical shaft displacement mobilised for $q_s/2$	m
w_k	Crack width	m
w_n	Water content	%
$W; W_i$	Weight of the considered body	N
W_s	Weight of solid	N
W_w	Weight of water	N
W_1	Shear distribution	m
x	Coordinate (e.g., horizontal)	m
x_H	Material parameter	–
x_p	Pipe length	m
$\tilde{x}^*$	Normalised distance	–
x_t	Integral variable with the dimension of time	m
$x_{fd,th}$	Thermal entry length	m
$x_{fd,h}$	Hydrodynamic entry length	m
x_H	Haigh equation parameter	–
$X_{d,i}$	Material or product design properties	
$X_{k,i}$	Material or product characteristic properties	
X	Soil–pile thermal expansion coefficient ratio	–
X^*	Body forces in the x direction	N/m^3
$\overline{X}$	Component of the prescribed stress vector in the x direction	Pa
y	Horizontal coordinate	m
$Y_{B,0}$	Second kind Bessel function of first order	–
$Y_{B,1}$	Second kind Bessel function of second order	–
$Y_{B,n}$	Second kind Bessel function of order n	–
Y^*	Body forces in the y direction	N/m^3
$\overline{Y}$	Component of prescribed stress vector in the y direction	Pa
z	Vertical coordinate or depth	m
z_G	Shape function	–
z_M	Empirical constant	–
z_{tc}	Distance of thermocouples	m
z_{min}	Minimum depth	m
z_{max}	Maximum depth	m
$\tilde{z}$	Specific vertical coordinate; inner level arm	m
$z_{NP,w}$	Depth of null point of vertical displacement	m
$z_{NP,\tau}$	Depth of null point of shear stress	m
Z^*	Body forces in the z direction	N/m^3
$\overline{Z}$	Component of prescribed stress vector in the z direction	Pa

Greek symbols

Symbol	Variable name	Unit measure
α	Linear thermal expansion coefficient	1/°C; με/°C
α_c	Thermal expansion coefficient of concrete	1/°C; με/°C
α_{cc}	Coefficient considering long-term effects on the compressive strength of concrete	–
α_{ct}	Coefficient considering long-term effects on the tensile strength of concrete	–
α_d	Thermal diffusivity	m^2/s
$\alpha_{d,f}$	Thermal diffusivity of the fluid	m^2/s
$\alpha_{d,soil}$	Thermal diffusivity of the soil	m^2/s
$\alpha_{d,EP}$	Thermal diffusivity of the energy pile	m^2/s
α_{eq}	Equivalent linear thermal expansion coefficient	1/°C; με/°C
α_r	Rheological coefficient	–
α_{soil}	Linear thermal expansion coefficient of soil	1/°C; με/°C
$\alpha_{soil,b}$	Linear thermal expansion coefficient of soil at the level of pile base	1/°C; με/°C
$\alpha_{soil,s}$	Linear thermal expansion coefficient of soil around the pile shaft	1/°C; με/°C
α_{wire}	Linear thermal expansion coefficient of wire	1/°C; με/°C
α_E	Modular ratio	–
α_{EP}	Linear thermal expansion coefficient of pile	1/°C; με/°C
α_h	Dilatancy rule parameter	–
α_{irr}	Surface absorptivity	–
α_0;α_1; α_2	Material constants	1/°C
a^f	Adhesion factor	–
β_0; β_1	Empirical constants	–
β_H	Material parameter	–
β_p	Plastic rigidity	–
β_{kl}	Thermal expansion coefficient vector	1/°C; με/°C
β; β_j	Volumetric thermal expansion coefficient	1/°C; με/°C
β_w	Volumetric thermal expansion coefficient of water	1/°C; με/°C
$\beta_{\gamma\gamma}$	Angle between plastic strain increment vector and normal to the yield surface	degrees
$\tilde{\beta}$	Ratio of the distance of the centre of compression from the compression face to the neutral axis depth	–
$\approx{\beta}$	Shear factor	–
β^f	Beta factor	–
γ	Unit weight	kN/m^3
ς_1; ς_2	Material parameters	–
ς_i	Factors for unfavourable permanent actions	–
γ'	Buoyant unit weight	N/m^3
γ_{sat}	Saturated unit weight	N/m^3
γ_d	Dry unit weight	N/m^3
γ_s	Unit weight of solid particles	N/m^3
γ_{Sd}	Partial factor for design action effect	–
γ_b;γ_s;γ_t;$\gamma_{s,t}$	Partial resistance factors	–
γ_{kl}	Engineering shear strains	–
γ_w	Unit weight of water	–
γ_r	Partial factor for steel	–
γ_E	Partial factor for effect of actions; Euler constant	–
γ_F	Partial factor for actions	–
γ_G	Partial factor for permanent action or permanent action effects	–

Greek symbols

Symbol	Variable name	Unit measure
γ_P	Partial factor for precompression	–
γ_Q	Partial factor for variable action or variable action effect	–
$\gamma_{Q,1}$	Partial factor of the dominant variable action or action effect	–
$\gamma_{Q,i}$	Partial factors of the *i* th variable actions or action effects	–
γ_R	Partial factor for resistance	–
γ_{Rd}	Partial factor for design resistance	–
γ_T	Material parameter	–
$\gamma_{\varphi'}; \gamma_{c'}; \gamma_{cu}; \gamma_{UCS}; \gamma_\gamma$	Partial factors for ground parameters	–
γ_i	Partial factor *i*	–
δ, δ'	Pile–soil interface angle of shear strength	degrees
δ_{cv}	Soil–structure interface angle of shear strength under constant volume conditions	degrees
δ_p	Thermal penetration depth	m
δ_n	Normal displacement	m
δ_h	Horizontal displacement	m
δ_{ij}	Kroenecher's delta	
$\lambda; \lambda_i$	Thermal conductivity	W/(m °C)
λ_a	Thermal conductivity of air	W/(m °C)
λ_c	Thermal conductivity of concrete	W/(m °C)
λ_e	Function representing the influence of the degree of saturation	–
λ_{eq}	Equivalent thermal conductivity	W/(m °C)
λ_f	Thermal conductivity of fluid	W/(m °C)
λ_{lt}	Load-transfer coefficient	–
λ_p	Thermal conductivity of pipe	W/(m °C)
λ_c	Thermal conductivity of concrete	W/(m °C)
λ_s	Thermal conductivity of solid particles	W/(m °C)
λ_{sb}	Effective height factor	–
λ_{soil}	Thermal conductivity of soil	W/(m °C)
λ_w	Thermal conductivity of water	W/(m °C)
λ_{EP}	Thermal conductivity of pile	W/(m °C)
λ_{EW}	Thermal conductivity of energy wall	W/(m °C)
$\lambda_{n,i}$	Haigh equation parameters	–
λ^p	Plastic multiplier	–
λ^p_{iso}	Plastic multiplier of the isotropic mechanism	–
λ^p_{dev}	Plastic multiplier of the deviatoric mechanism	–
λ^p_l	Vector containing λ^p_{iso} and λ^p_{dev}	–
λ^f	Factors depending on the pile length	–
λ_p	Thermal conductivity of pipe	W/(m °C)
λ_*	Eigen value	Pa
$\lambda_{(0)}$	Thermal conductivity at a temperature of 0°C	W/(m °C)
$\tilde{\lambda}$	Normal consolidation line parameter; compression index	–
Γ	Critical state line parameter	–
Γ_{in}	Interconnectivity parameter	–
Λ	Pile–soil stiffness ratio	–
μ	Dynamic viscosity of fluid	Pa s
μ_E	Ratio between Young's moduli	–
ε	Total strain	–; με
ε_a	Axial strain	–; με
ε_c	Concrete strain	–; με

Greek symbols

Symbol	Variable name	Unit measure
ε_{cm}	Mean strain in the concrete between cracks	−; με
ε_{cu1}	Nominal ultimate concrete strain	−; με
ε_{c1}	Concrete strain at peak stress	−; με
ε_G	Strain at centre of gravity	−; με
ε_r	Radial strain; nominal strain in reinforcement	−; με
ε_{rr}; $\varepsilon_{r\theta}$; ε_{rz}; ε_{zz}; $\varepsilon_{z\theta}$; $\varepsilon_{\theta\theta}$	Strains in cylindrical coordinates (r, θ, z)	−; με
ε_{rm}	Mean strain in the reinforcement under the relevant combination of loads	−; με
ε_x	Horizontal strain in the x direction	−; με
ε_y	Horizontal strain in the y direction	−; με
ε_z	Vertical strain	−; με
ε_i	Strain vector	−; με
ε_i^e	Elastic strain vector	−; με
ε_i^p	Plastic strain vector	−; με
ε_{kl}; ε_{ij}	Strain tensor	−; με
ε_{kl}^e; ε_{ij}^e	Elastic component of the strain tensor	−; με
ε_{kl}^p; ε_{ij}^p	Plastic component of the strain tensor	−; με
$d\varepsilon_{ij}$	Increment of strain	−; με
$d\varepsilon_{kl}^e$; $d\varepsilon_{ij}^e$	Increment of elastic strain	−; με
$d\varepsilon_{kl}^p$; $d\varepsilon_{ij}^p$	Increment of plastic strain	−; με
ε_b^{th}	Strain under blocked thermal expansion conditions	−; με
ε_f^{th}	Strain under free thermal expansion conditions	−; με
$\varepsilon_{f,EP}^{th}$	Strain under free thermal expansion conditions of pile	−; με
$\varepsilon_{f,soil}^{th}$	Strain under free thermal expansion conditions of soil	−; με
ε_o^{th}	Observed thermally induced strain	−; με
$\overline{\varepsilon}_f^{th}$	Average strain under free thermal expansion conditions	−; με
$\overline{\varepsilon}_r$	Average value of radial strain	−; με
$\overline{\varepsilon}_z$	Average value of vertical strain	−; με
$\overline{\varepsilon}_o^{th}$	Average observed thermally induced strain	−; με
ε_v	Volumetric strain	−; με
$d\varepsilon_v$	Incremental change of volumetric strain	−; με
ε_v^e	Elastic volumetric strain	−; με
$d\varepsilon_v^e$	Incremental change of elastic volumetric strain	−; με
ε_v^p	Plastic volumetric strain	−; με
$d\varepsilon_v^p$	Incremental change of plastic volumetric strain	−; με
ε_q	Deviatoric strain	−; με
$d\varepsilon_q$	Incremental change of deviatoric strain	−; με
ε_q^e	Elastic deviatoric strain	−; με
$d\varepsilon_q^e$	Incremental change of elastic deviatoric strain	−; με
ε_q^p	Plastic deviatoric strain	−; με
$d\varepsilon_q^p$	Incremental change of plastic deviatoric strain	−; με
$\varepsilon_v^{p,iso}$	Volumetric plastic deformation developed with the isotropic mechanism	−; με
$\varepsilon_v^{p,iso,cyc}$	Volumetric plastic deformation developed with the isotropic mechanism starting from the last reheating	−; με
ε_{uc}	Compressive ultimate strain of concrete	−; με
ε_{ud}	Design strain at maximum load	−; με

Greek symbols

Symbol	Variable name	Unit measure
ε_{uk}	Characteristic strain at maximum load	−; με
ε_{yd}	Yield steel deformation	−; με
ϵ_{ghe}	Effectiveness of the heat pump	−
$\overline{\varepsilon}$	Time lag	s
ϵ	Surface emissivity	−
$\tilde{\kappa}$	Elastic compressibility	−
$\kappa_1; \kappa_2$	Empirical parameters	−
$\tilde{\kappa}$	Swelling index	−
θ	Angular coordinate	m
θ_w	Volumetric water content	%
θ_l	Lode's angle	degrees
$\tilde{\theta}$	Angle between the concrete compression strut and the beam axis perpendicular to the shear force	degrees
$\tilde{\tilde{\theta}}; \tilde{\tilde{\theta}}_i$	Temperature at reached at a time t	°C
$\theta_{EP}; \theta_g$	Dimensionless temperature	−
θ^*	Body forces in the θ direction	N/m^3
$\tilde{\theta}^*$	Normalised temperature	°C
η_{UTES}	Energy efficiency of underground thermal energy storage systems (UTES)	−
$\eta_{UTES,tot}$	Total system energy efficiency of UTES	−
$\eta_{UTES,int}$	Internal system energy efficiency of UTES	−
η_{pq}	Ratio of deviatoric stress over mean effective stress	−
η_f	Kinematic viscosity of the fluid	m^2/s
η_{sb}	Effective strength factor	−
η_i	Partial safety factors for volume or scale effect	−
$\overline{\eta}_B$	Factor	−
η_ε	Normalised strain factor	−
η^*	Integration variable	−
$\aleph$	Equivalent property of a composite material	Variable
$\aleph_i$	Equivalent effective property of a composite material	Variable
ρ	Bulk density	kg/m^3
ρ_a	Density of air	kg/m^3
ρ_d	Dry density	kg/m^3
$\rho_{ly}; \rho_{lz}$	Reinforcement ratios in the y and z directions	−
ρ_{sat}	Saturated density	kg/m^3
ρ_f	Density of fluid	kg/m^3
ρ_w	Density of the water	kg/m^3
$\rho_{p,eff}$	Normalised area	−
ρ_r	Reinforcement ratio	−
ρ_{eff}	Effective longitudinal reinforcement ratio	−
$\rho_{r,eff}$	Effective reinforcement ratio	−
$\rho_{r,min}$	Minimum reinforcement ratio	−
ρ_s	Density of solid particles	kg/m^3
ρ_{soil}	Bulk density of soil	kg/m^3
ρ_{EP}	Bulk density of pile	kg/m^3
ϱ	Material parameter	−
$\sigma; \sigma_z; \sigma_{zz}$	Total vertical stress	Pa
σ_{cp}	Average longitudinal stress	Pa

Greek symbols

Symbol	Variable name	Unit measure
σ_{cy}; σ_{cz}	Normal concrete stresses in the y and z directions	Pa
σ_i	Vertical stress vector	Pa
σ_{kk}	Normal stresses	Pa
σ_{kl}	Shear stresses	Pa
σ_r	Maximum stress permitted in the reinforcement after the formation of cracks	Pa
σ'_i	Vertical effective stress vector	Pa
σ_1; σ_2; σ_3	Principal normal stresses	Pa
σ'_1; σ'_2; σ'_3	Principal effective normal stresses	Pa
σ_{zb}	Total vertical stress at the level of pile base	Pa
σ_b^{th}	Value of thermally induced stress under blocked conditions	Pa
σ_{ij}	Total stress tensor	Pa
σ'_{ij}	Effective stress tensor	Pa
σ_o^{th}	Observed value of thermally induced stress	Pa
σ'_{zb}	Vertical effective stress at the level of pile base	Pa
$\overline{\sigma}'_z$	Average value of vertical effective stress	Pa
$\overline{\sigma}_z$	Average value of total vertical stress	Pa
$\overline{\sigma}_o^{th}$	Average observed thermally induced stress	Pa
σ_n	Normal stress	Pa
σ'_n	Normal effective stress	Pa
σ'_{n0}	Initial normal effective stress	Pa
$\overline{\sigma'_n}$	Average effective normal stress at the pile–soil interface after pile installation	Pa
σ'_p	Effective preconsolidation stress/pressure	Pa
σ_{SB}	Stefan–Boltzmann constant	–
τ; τ_z; τ_{rz}	Shear stress	Pa
τ_s	Shear stress at the surface	Pa
τ_t	Thermal time constant	s
τ_{cv}	Shear strength at constant volume	Pa
τ_D	Shear strength due to soil dilatancy	Pa
$\overline{\tau}$	Average shear stress	Pa
ζ	Stiffness reduction factor	–
μ_f	Dynamic viscosity of the fluid	Pa/s
$\overline{\mu}_f$	Fluid dynamic viscosity at the mean temperature	Pa/s
μ_s	Fluid dynamic viscosity at the surface	Pa/s
ν	Poisson's ratio	–
ν_{slab}	Poisson's ratio of slab	–
ν_{soil}	Poisson's ratio of soil	–
$\nu_{soil,b}$	Poisson's ratio of soil at the level of pile base	–
$\nu_{soil,s}$	Poisson's ratio of soil around pile shaft	–
ν_{EP}	Poisson's ratio of pile	–
ν_e	Specific volume	–
$d\nu_e$	Incremental change of specific volume	–
$\Delta\nu_e^e$	Elastic change of specific volume	–
$\Delta\nu_e^p$	Plastic change of specific volume	–
ψ	Dilatancy angle	degrees
ψ	Factor for combination value of a variable action	–
ψ_0	Factor for combination value of a variable action	–

Greek symbols

Symbol	Variable name	Unit measure
ψ_1	Factor for frequent value of a variable action	–
ψ_2	Factor for quasipermanent value of a variable action	–
ψ_H	Haigh equation parameter	–
ψ_n	Bessel function	–
φ_n	Bessel function	–
φ'	Angle of shear strength	degrees
φ'_c	Angle of shear strength in compression	degrees
φ'_e	Angle of shear strength in expansion	degrees
φ'_{cv}	Angle of shear strength at critical state	degrees
φ^*	Body forces in the φ direction	N/m^3
ϕ	Angle	degrees
$\varnothing$	Steel bar diameter	m
ϖ	Integration variable	degrees
ω	Angular frequency	rad/s
Ω	Displacement interaction factor; pile–soil–pile interaction factor; corrected interaction factor	–
Ω^m	Displacement interaction factor for piles subjected to mechanical loads	–
Ω^{th}	Displacement interaction factor for piles subjected to thermal loads	–
$\tilde{\Omega}$	Pile–soil interaction factor; approximate interaction factor	–
$\Omega_{h_l/L\to\infty}$	Displacement interaction factor for $h_l/L \to \infty$	–
$\Omega_{s/D}$	Interaction factor between two piles	–
$\Omega_{\nu_{soil}=0.3}$	Displacement interaction factor for $\nu_{soil} = 0.3$	–
ξ	Integration limit	–
$\xi_1; \xi_2; \xi_3; \xi_4$	Correlation factor	–
ξ_H	Haigh equation parameter	–
$\chi; \chi_i$	Volume fractions	–
χ_a	Volume fraction of air	–
χ_s	Volume fraction of soil particles	–
χ_w	Volume fraction of water	–
χ_ϵ	Curvature of cross section	1/m
$\mathcal{F}_i$	Vector containing prescribed displacement functions	m
$\mathcal{H}$	Point of bounding surface	–

Operators, functions and counters

Symbol	Name
$d()$	Increment operator
$erfc()$	Complementary Gaussian error function
∂	Derivative
Δ	Difference operator
$\sum$	Sum
$\ln()$	Natural logarithm
∇	Gradient operator
$\nabla \cdot ()$	Divergence operator
i, j, k, l, m, n	Counters

PART A

Introduction

CHAPTER 1

Energy and geotechnologies

1.1 Introduction

Since the 18th century energy consumption and supply have contributed to a marked increase in environmental pollution. Many are the ways and frameworks that can be accounted for restraining environmental pollution, but a development that meets human activity needs and progress goals with a limited impact on the environment can undoubtedly contribute to such a challenge.

In the construction sector, national and international policies, directives and regulations are increasingly requiring, or promoting, the use of so-called "environmentally friendly" technologies that involve a limited impact on the environment. This result can be achieved, for example through technologies that supply buildings and infrastructures with energy drawn from sources that can renew themselves at a sufficient rate in human time frames and cause low environmental pollution. In a growing number of countries, new buildings must be constructed with such technologies.

This chapter expands on energy sources and technologies that can sustain human activity needs with a limited impact on the environment. Among the various energy sources and technologies available, attention is devoted to geothermal energy (from the Greek roots *geo*, meaning earth and *thermos*, meaning heat) and geotechnologies because of their unique features for addressing the previously mentioned challenge.

With this aim, *world anthropogenic development* and the *energy question* are first expanded: in this context the goal is to describe the interplay between the trend in the world's population and the exploitation of energy sources, the related effect on the environment, and the perspectives that need to be considered in the building sector to contribute to a development of low environmental impact. Next *geothermal energy* is addressed: the objective of this part is to discuss the origin and the features of the considered energy source as well as to establish acquaintance with the principles that govern the operation of geotechnologies (and associated technological systems) harvesting this energy source. Then *geothermal systems* are discussed: in this context the purpose is to provide a classification of geothermal systems, to describe their features and uses, and to highlight the technology of *energy geostructures*. Finally *questions and problems* are proposed: the purpose of this part is to fix and test the understanding of the subjects covered in this chapter by addressing a number of exercises.

Analysis and Design of Energy Geostructures
DOI: https://doi.org/10.1016/B978-0-12-816223-1.00001-1

1.2 Anthropogenic development and the energy question

1.2.1 World population

The world population has continued to markedly grow since the 20th century. It currently numbers 7.6 billion living human individuals and is expected to continue to grow in the next decades (cf. Fig. 1.1). Different scenarios of world population increase can be considered for the future, but the median trend currently predicted approximately accounts for up to 9.8 billion living human individuals by 2050 and 11.2 billion living human individuals by 2100 (United Nations, 2017).

1.2.2 Energy forms and classification of energy sources

Energy, which can be appreciated in various forms, represents a key source to meeting human activity and development, and can be quantified with different unit measures (cf. Table 1.1). One typical classification of energy sources is based on their availability in nature. This classification includes *primary energy sources* and *secondary energy sources*. Primary energy sources, such as fossil fuels, mineral fuels, solar energy, geothermal energy, wind energy, tidal energy and biomass sources, represent an energy form that has not been subjected to any conversion and is available in nature. Secondary energy sources or energy carriers, such as electrical energy, refined fuels and synthetic fuels, represent an energy form that has been transformed from primary energy sources and is not available in nature.

Depending on whether primary energy sources can renew themselves at a sufficient rate in human time frames or cannot, one further classification can be employed. This

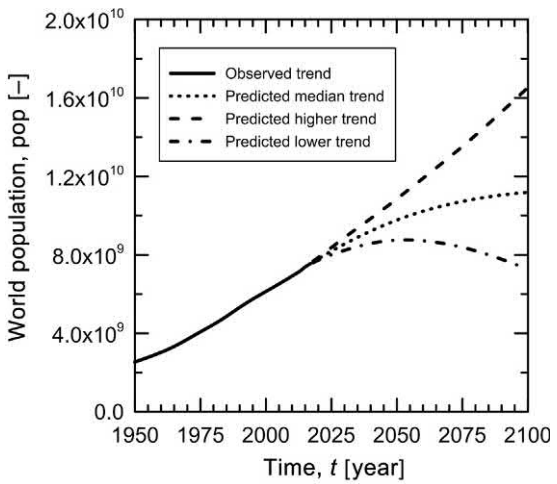

Figure 1.1 World population trend. *Data from United Nations, U. N., 2017. World Population Prospects: The 2017 Revision. Department of Economic and Social Affairs, P. D., United Nations, New York.*

Table 1.1 Some energy-related unit measures.

Name	Symbol	Description
Joule	J	1 Joule is equal to the energy transferred to an object when a force of 1 Newton acts on that object in the direction of its motion through a distance of 1 m (1 J = 1 Nm) Basic energy unit of the metric system (SI)
Calorie	cal	1 calorie is the amount of heat required to raise the temperature of 1 gram of water by 1°C, from 14.5°C to 15.5°C The calorie can be defined in terms of the Joule (thermochemical calorie: 1 cal = 4.184 J)
Watt-hour	Wh	The standard unit of electricity production and consumption (1 Wh = 3.6×10^3 J)
Tonne of oil equivalent	toe	1 toe is the amount of energy released by burning one ton of crude oil (1 toe = 41.868 GJ), that is an energy equivalence for oil
Watt	W or J/s	A derived unit of power that expresses 1 Joule per second and can be used to quantify the rate of energy transfer

classification includes *renewable energy sources* and *nonrenewable energy sources*. Renewable energy sources, such as solar energy, geothermal energy, wind energy, hydropower energy, tidal energy and biomass sources, can renew themselves at a sufficient rate in human time frames. Nonrenewable energy sources, such as fossil fuels (e.g. oil, coal and natural gas) and mineral fuels (e.g. natural uranium), cannot renew themselves at a sufficient rate in human time frames.

1.2.3 World energy consumption and supply

Various are the uses of energy by human civilisation and associated with these uses there is always an energy supply. Depending on the stage of the utilisation or production of energy, three different definitions can be employed to characterise the use of energy (as well as the energy itself), that is *primary energy consumption*, *final energy consumption* and *net energy consumption*, and one definition to characterise the supply of energy, that is *primary energy supply* (cf. Fig. 1.2). Primary energy consumption refers to the direct use or supply at the source of energy that has not been subjected to any conversion or transformation process. This energy is often termed primary energy or crude energy as well. In most cases, however, energy cannot be used without conversion or transformation processes and for this reason it is refined in the so-called final energy. The final energy consumption represents the total energy consumed by end users (e.g. the building sector, the industry sector, etc.), excluding the energy that is used by the energy sector itself. In the context of constructions, this term is usually associated with the amount of energy supplied that is necessary to run the generator of

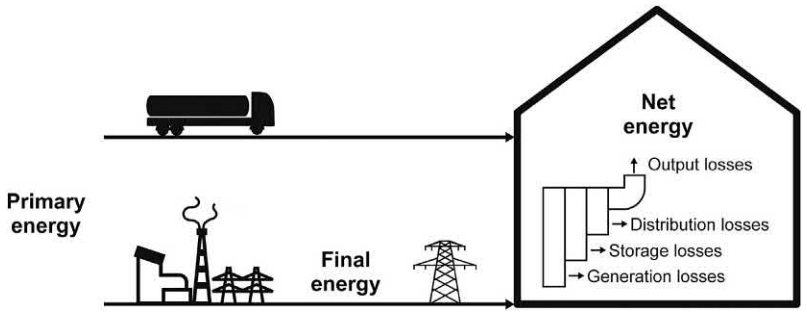

Figure 1.2 Energy definitions and pathway of supply and consumption.

cold and heat. From the final energy to the net or effective energy that is eventually used, however, there are in many instances various losses associated with the use of devices for further refining, storing, or delivering energy. These losses comprise (1) generation losses, (2) storage losses, (3) distribution losses and (4) output losses and characterise the so-called net energy. The net energy consumption represents the consumption of energy in its desired form, usually drawn from a consuming device. In the context of constructions this term is usually associated with the thermal energy to be delivered to, or extracted from, a conditioned space by a heating or cooling system to maintain the set-point temperature during a given period of time for the comfort of the occupants.

Often the consumption of final energy is termed, although inappropriately, energy demand. In reality, energy consumption and demand are two related, yet different, variables. The former refers to the quantity of energy added to or removed from a space, whereas the latter is the immediate rate of that consumption, that is the power at a particular instant in time. For this reason, final energy consumption is measured in kilowatt-hours, whereas the energy demand, that is the rate of that consumption, is measured in kilowatts.

In the European Union and in developed countries such as the United States, three dominant end users have characterised the final energy consumption over recent decades: the building sector, the industry sector and the transportation sector. In 2015 these three sectors contributed to the total final energy consumption of the European Union by 25.4%, 25.3% and 33.1%, respectively (cf. Fig. 1.3) (Eurostat, 2017). In Switzerland, as in many other developed countries, approximately 60%–85% of the final energy consumption associated with the building sector is used for space conditioning and the production of domestic hot water (Kemmler et al., 2013) (cf. Fig. 1.4).

Along with the aforementioned statistics, the world final energy consumption and primary energy supply continue to rise to meet the increase in world population and the expansion of economies (cf. Figs 1.5 and 1.6) (International Energy Agency, 2016c).

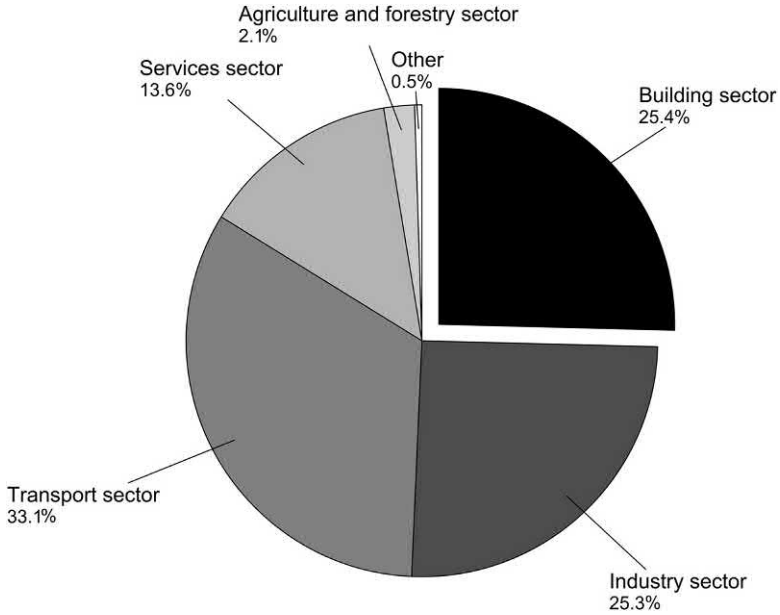

Figure 1.3 Final energy consumption shares by end users in the European Union in 2015. *Data from Eurostat, 2017, Europe in Figures—Eurostat Yearbook. Office for Official Publications.*

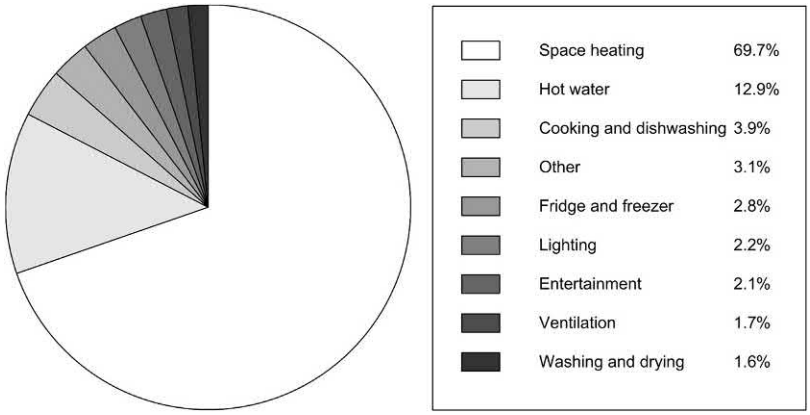

Figure 1.4 Final energy consumption in the Swiss building sector in 2012. *Data from Kemmler, A., Piégsa, A., Ley, A., Keller, M., Jakob, M., Catenazzi, G., 2013. Analysis of the Swiss Energy Consumption According to the End Use. Swiss Federal Office of Energy, Bern.*

Historically, the global energy market has been, and is still, dominated by the combustion of fossil fuels, that is nonrenewable primary energy sources. In recent years (since the mid-20th century), fossil fuels have met at least 60% of the final energy consumption and at least 80% of the primary energy supply (cf. Figs 1.5 and 1.6).

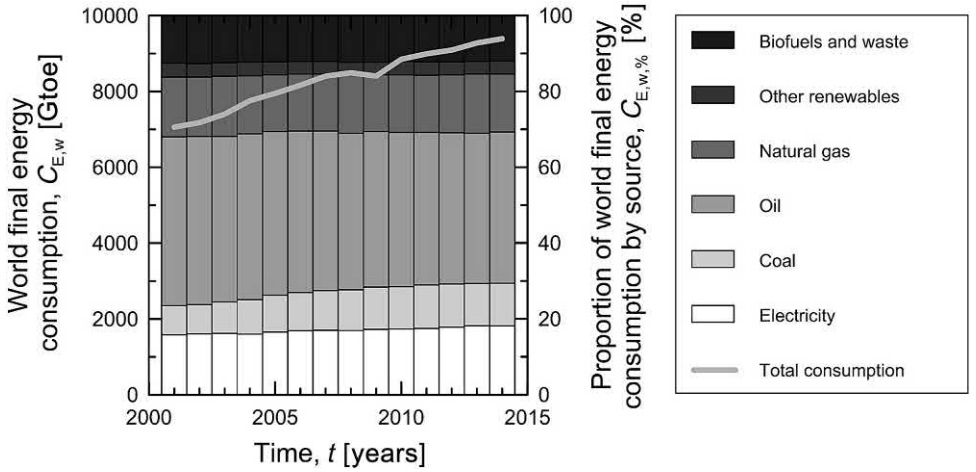

Figure 1.5 World final energy consumption from 2000 to 2014. *Data from International Energy Agency, I. E. A., 2016c. Key World Energy Statistics. International Energy Agency, Paris.*

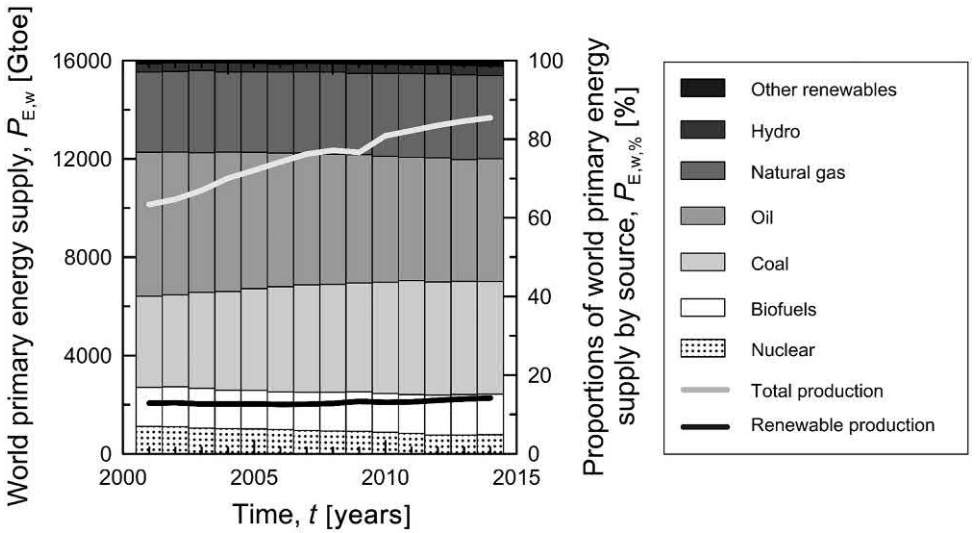

Figure 1.6 World primary energy supply from 2000 to 2014. *Data from International Energy Agency, I. E. A., 2016c. Key World Energy Statistics. International Energy Agency, Paris.*

1.2.4 Consequences

The historical use of nonrenewable energy sources, often unregulated, poorly regulated, inefficient, or overexploited, in contrast to renewable energy sources, has caused, without being limited to, two consequences: (1) the increase in greenhouse gas emissions and (2) the depletion of nonrenewable energy sources.

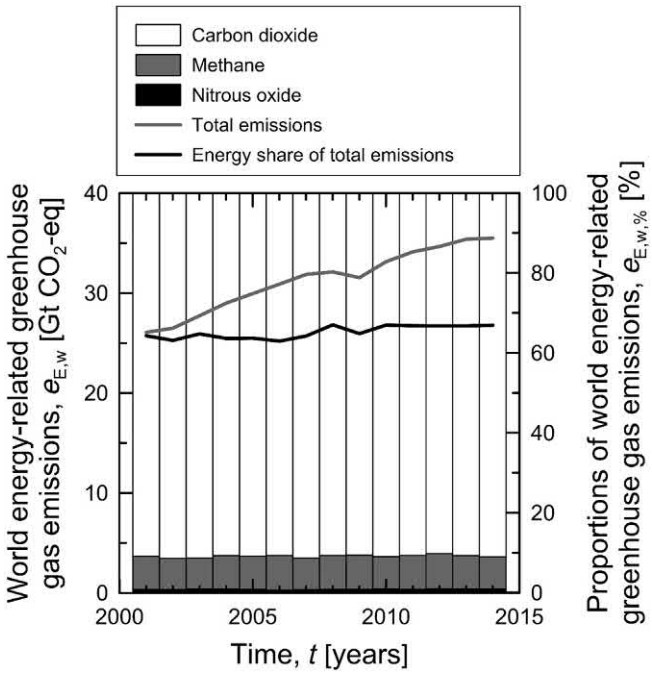

Figure 1.7 World anthropogenic energy-related greenhouse gas emissions by type. *Data from International Energy Agency, I. E. A., 2015. Energy and Climate Change. International Energy Agency, Paris.*

Greenhouse gas emissions are caused to a substantial amount by the combustion of fossil fuels. Global dependence on fossil fuels has led to the release of over 1100 Gt of carbon dioxide (CO_2) into the atmosphere since the mid-19th century to 2007 (Sims et al., 2007), an amount that continued to increase up to a first stabilisation in 2014 (International Energy Agency, 2016a). Over 90% of energy-related emissions are CO_2 from fossil fuel combustion (cf. Fig. 1.7), of which approximately 10% is associated with the building sector, both in developed and developing countries (International Energy Agency, 2015) (cf. Fig. 1.8).

Two problems associated with fossil fuel combustion and greenhouse gas emissions are that they represent the most important source of air (and environment) pollutant emissions deriving from anthropogenic development (International Energy Agency, 2016b) and are considered to be the dominant cause of the observed climate change and global warming since the mid-20th century (IPCC, 2013). One problem associated with the depletion of nonrenewable energy sources is that, within approximately a century, resorting to these sources will no longer be technically and economically convenient in many cases (IPCC, 2013).

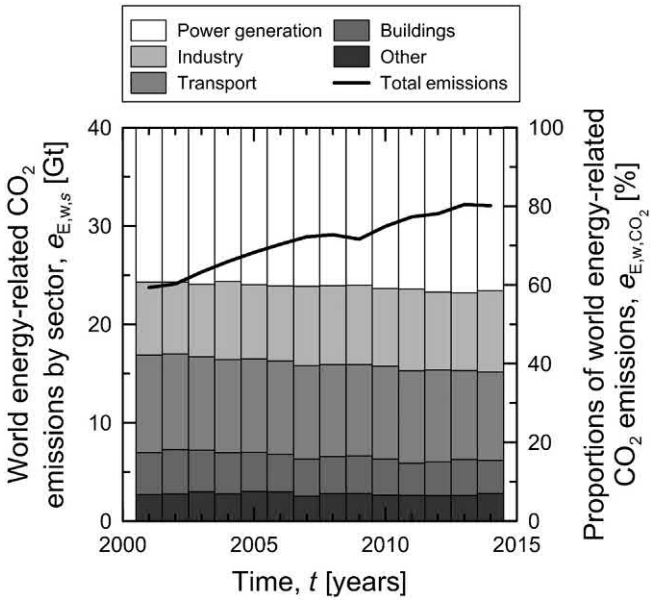

Figure 1.8 World energy-related carbon dioxide (CO_2) emissions by sector. *Data from International Energy Agency, I. E. A., 2015. Energy and Climate Change. International Energy Agency, Paris.*

All of the aforementioned problems have a profound impact on society, the economy, politics and the environment. Resorting to renewable energy sources is an essential and effective solution to these problems.

1.2.5 Perspectives

Many are the initiatives, policies, regulations and agreements at the national and international levels that are being promoted and established to target *sustainable development*, that is a development that sustains human needs and progress goals with a limited impact on the environment (see, e.g. Magee et al., 2013). Undoubtedly, because of the noteworthy influence of the building sector on energy consumption, nonrenewable energy exploitation and greenhouse gas emissions, developing buildings and infrastructures characterised by (1) integrated passive design strategies (i.e. approaches employing technologies that use ambient energy sources such as daylighting, natural ventilation and solar energy, instead of purchased energy sources like electricity or natural gas); (2) high-performance building envelopes and energy efficient heating, ventilation and air-conditioning (HVAC) systems, as well as lighting and appliances; and (3) technologies harvesting on-site renewable energy sources can represent a major contribution to sustainable development. An environment characterised by the aforementioned features (1)−(3) is usually termed a "low-carbon built environment".

The Energy Performance of Buildings Directives (Energy Performance of Buildings Directive, 2002, 2010), the Carbon Neutral Design Project and the ASHRAE Vision 2020 represent examples of key directives and initiatives for the development of a low-carbon built environment. The goal of the referenced directives and initiatives is to require (or to foster) the design and construction of so-called "nearly zero-energy buildings (NZEB)", "carbon neutral buildings", and "net zero energy buildings", respectively, in the years to come.

For example the Energy Performance of Buildings Directives required all new *public* buildings constructed in the European Union to be nearly zero-energy from 2018, while all new *general* buildings are to be nearly zero-energy by the end of 2020. A NZEB is defined as "a building with very high energy performance", where "the nearly zero or very low amount of energy required should be extensively covered by renewable sources produced on-site or nearby" (Energy Performance of Buildings Directive, 2010). The purpose to develop NZEB is to achieve constructions with significantly reduced energy consumption combined with the increased use of low-carbon energy sources to meet this consumption. The broad definition of "NZEB" has been adapted in various Member States of the European Union while considering the feasibility of implementing such a concept in their national contexts (Buildings Performance Institute Europe, 2015). In Italy, for example the definition of NZEB proposed by the Energy Performance of Buildings Directive (2010) has been adopted and implemented in the construction sector by the national law 90/2013. In France this definition has been extended to "positive energy building" and will be adopted and implemented in the construction sector from 2020 by the technical document RT2020. The concept of positive energy building advances the concept of energy consumption being close to zero that characterises NZEB by referring to a building that produces more energy, for example from renewable energy sources available on-site, than it consumes during a reference period of time (e.g. 1 year).

Based on the aforementioned aspects, it appears abundantly clear that the conceptual development, analysis, design and application of environment-friendly technologies harvesting on-site renewable energy sources for targeting the supply of heating and cooling energy to the built environment [i.e. aspect (3)] represent crucial contributions to a sustainable development.

1.3 Geothermal energy

1.3.1 General

Geothermal energy is the natural thermal energy contained in the Earth's subsurface, which can be divided into the crust, the mantle (subdivided into the upper and lower mantle), and the core (comprising the outer and inner core). This natural heat

results from (1) the formation of the planet, (2) the radioactive decay of minerals and (3) the solar energy absorbed at the surface. It is contained in approximately 1.084×10^{21} cubic metres of rocks and metallic alloys located in the Earth subsurface (Lee et al., 2007). Ninety-nine percent of this volume is characterised by a temperature higher than 1000°C, while only 0.1% is characterised by a temperature lower than 100°C (Barbier, 2002).

1.3.2 Geothermal gradient

The temperature field in the shallow subsurface typically exhibits a noteworthy sensitivity to atmospheric conditions within the first 4–6 m (cf. Fig. 1.9), being usually strongly influenced by daily (day–night) temperature fluctuations and more or less markedly by seasonal temperature fluctuations. Below this region, the temperature remains relatively stable throughout the year, that is between 10°C and 25°C depending on the latitude, and is approximately equal to the mean annual outside air temperature. Therefore the ground tends to be warmer than the atmosphere during winter and cooler during summer for most locations around the world regardless of geology (Narsilio et al., 2014). From the aforementioned values the temperature increases with depth in the Earth crust (Barbier, 2002). An average geothermal gradient of approximately 3°C per 100 m of depth characterises the Earth's subsurface down to the upper mantle. This gradient can vary depending on the location from values of 1°C per 100 m in ancient continental zones of the Earth's crust to values of 10°C per 100 m in areas of active volcanism. At greater depths this temperature gradient decreases to

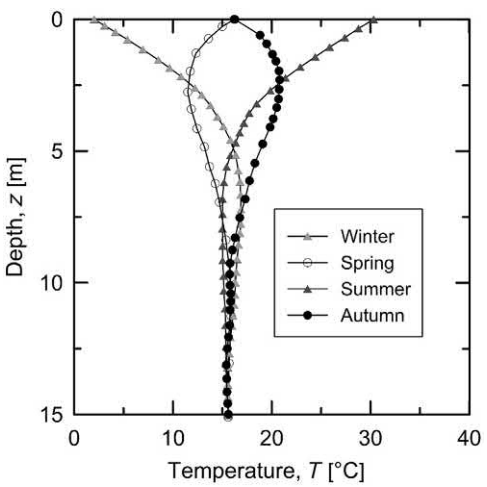

Figure 1.9 Sketch of typical temperature evolution with depth in the shallow subsurface throughout the year for a temperate climatic zone.

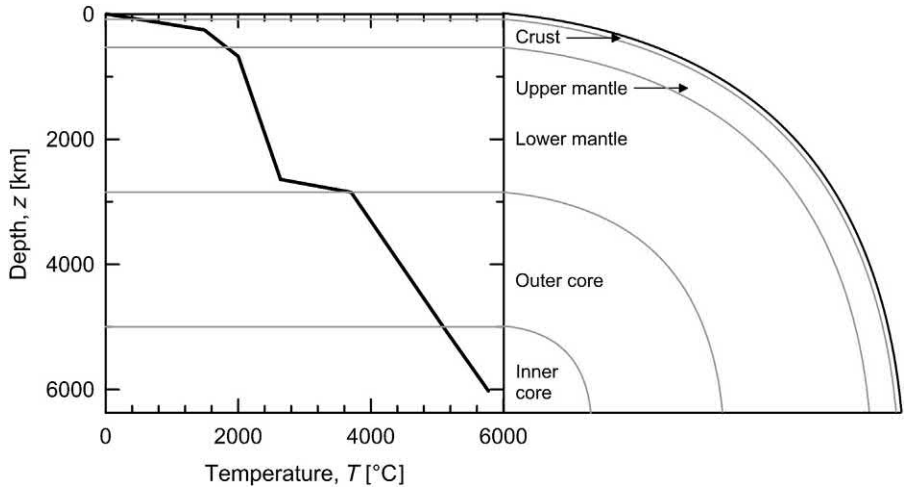

Figure 1.10 Sketch of typical temperature evolution with depth in the Earth's subsurface. *Redrawn after Boehler, R., 1996. Melting temperature of the Earth's mantle and core: Earth's thermal structure. Annu. Rev. Earth Planet. Sci. 24 (1), 15–40.*

approximately 0.1°C per 100 m of depth (cf. Fig. 1.10). These temperature levels can be used in geothermal applications to meet human activity needs in the built environment.

1.3.3 Features of geothermal energy

Geothermal energy represents the second most abundant source of primary energy on Earth, after solar energy (Lee et al., 2007). It is classified as both renewable and sustainable (Lund, 2009), and represents one of the energy sources that can be used in the construction sector for the development of low-carbon buildings (in several countries, also resorting to the support of government grants and incentives). Geothermal energy can be considered as a clean and environment-friendly energy source as it generates no (or minimal) greenhouse gas emissions because the conversion and utilisation processes do not involve any chemical reactions (e.g. combustion) (Lee et al., 2007). This energy source is also available continuously, regardless of the weather conditions and everywhere on Earth, which makes it attractive in contrast to other renewable energy sources such as solar and wind energy. Among other various positive attributes (Lee et al., 2007), geothermal energy reduces the current dependence on nonrenewable energy sources and it can be used for various purposes from a local to a relatively large scale. Because geothermal energy is available almost everywhere, the consequent reduction of energy imports means a reduced dependence on external economic or political situations (Brandl, 2006). Geothermal energy ensures the security of supply.

1.4 Geothermal systems

1.4.1 Classification of geothermal systems

Geothermal systems are technological systems that harvest geothermal energy. Various classifications of geothermal systems can be made, but one classification that is often employed relies on the exploitation depth of the thermal energy present in the subsurface. Depending on whether a lower or greater depth than 400 m (by governmental definition in several countries) is considered, geothermal systems can be classified as *shallow geothermal systems* or *deep geothermal systems*, respectively. Shallow geothermal systems deal with low temperature and enthalpy. Deep geothermal systems deal with medium to high temperature and enthalpy.

1.4.2 Features and use of geothermal systems

Geothermal systems are made up of three main components: a *heat source*, a *heat sink* and a *heat exchanger*. Typically the heat source is the ground while the heat sink is a built environment (in general, a structure). However, the opposite can also occur, that is the heat source is a built environment while the heat sink is the ground. The heat exchanger is generally constituted by one or more elements containing a fluid that transfers the heat between the heat source and the heat sink.

Employing the ground as a heat reservoir, that is a heat source or sink, is a result of long historical developments that can often be addressed only on the basis of indirect considerations (Cataldi, 1999). Some early development examples of their type are listed hereafter. In early Sumerian and Akkadian times, the ground was employed as a heat sink to store ice (and food) in so-called "ice houses" constructed partly or completely underground (e.g. Dalley, 2002), based on the limited affection of these environments to the surface thermal conditions. In palaeolithic and ancient Roman times, the ground was used as a heat source for bathing and space heating (e.g. Armstead, 1973), based on the presence of sources of hot water in the subsurface (e.g. thermal springs). In 1904 the ground was used as a heat source for electrical power production via the construction of the first geothermal power plant by Prince Piero Ginori Conti in Italy (e.g. Lungonelli, 2003).

One key feature of geothermal systems is the way the thermal energy that is harvested from the ground is used via such systems. In shallow geothermal systems, an indirect use of geothermal energy is typically made. Machines or devices that modify (enhance or lower) the energy input transferred between the ground and the target environment, in addition to machines or devices that force a heat carrier fluid to flow (exchanging heat) between them, are employed in such cases. In deep geothermal systems a direct use of geothermal energy can be made when an indirect use is not targeted. In contrast to the previous case, machines that modify the energy input transferred between the ground and the target environment can be avoided in this

circumstance and only machines that force a heat carrier fluid to flow between the ground and the target environment are required.

Shallow geothermal systems can be used to provide heating, cooling and hot water, using temperatures available underground of less than 25°C. These systems are suitable for small-scale and domestic use in almost any geographical location. Deep geothermal systems can be used to provide heating and hot water as well as electrical power, using temperatures available underground greater than 25°C and up to 200°C [the temperatures required for electrical power generation being generally greater than 175°C (Narsilio et al., 2014)]. These systems are suitable for medium- to large-scale uses, but can be applied in more particular locations than shallow geothermal systems.

In addition to the previously proposed classification of geothermal systems, one additional criterion is often employed to characterise these systems and is related to the presence of closed- or open-loops in the heat exchanger. Based on this criterion, geothermal systems can be classified in most cases as either *closed-loop* or *open-loop systems*. Closed-loop systems use a water-based mixture circulating through sealed pipes to transfer the heat from the ground to the superstructure or vice versa. Open-loop systems directly use groundwater extracted from or injected into aquifers through wells in the considered heat exchange process.

The crucial difference between closed- and open-loop systems is that in the latter systems mass exchange occurs, in contrast to the former, and heat transfer is more favourable. However, although providing the highest energy yield, open-loop systems require a greater financial input and pose technical risks related to, for example underground pollution (Boënnec, 2008). Because there is no mass exchange with the ground, closed-loop systems minimise environmental risks and mineral precipitation issues, and do not require the need to obtain extractive licensing (Narsilio et al., 2014). Shallow geothermal systems can be either open- or closed-loop. Deep geothermal systems are open-loop.

Fig. 1.11 presents typical examples of shallow and deep geothermal systems. Typical shallow geothermal systems are horizontal geothermal boreholes, geothermal baskets, groundwater capture systems, vertical geothermal boreholes and *energy geostructures*. Typical deep geothermal systems are thermal springs, hydrothermal systems and petrothermal systems.

Horizontal geothermal boreholes are the shallowest type of geothermal systems. These systems typically consist of closed polyethylene pipes ploughed or dug down horizontally in the ground next to buildings at a few metres of depth (from a depth of $z = 2-5$ m). In the pipes a circulating heat carrier fluid allows the exchange of the heat present in the ground (predominantly as a consequence of solar radiation), especially for heating purposes in residential, agricultural, or aquaculture applications. However, storage purposes can also be achieved in those situations in which the boreholes are placed under buildings.

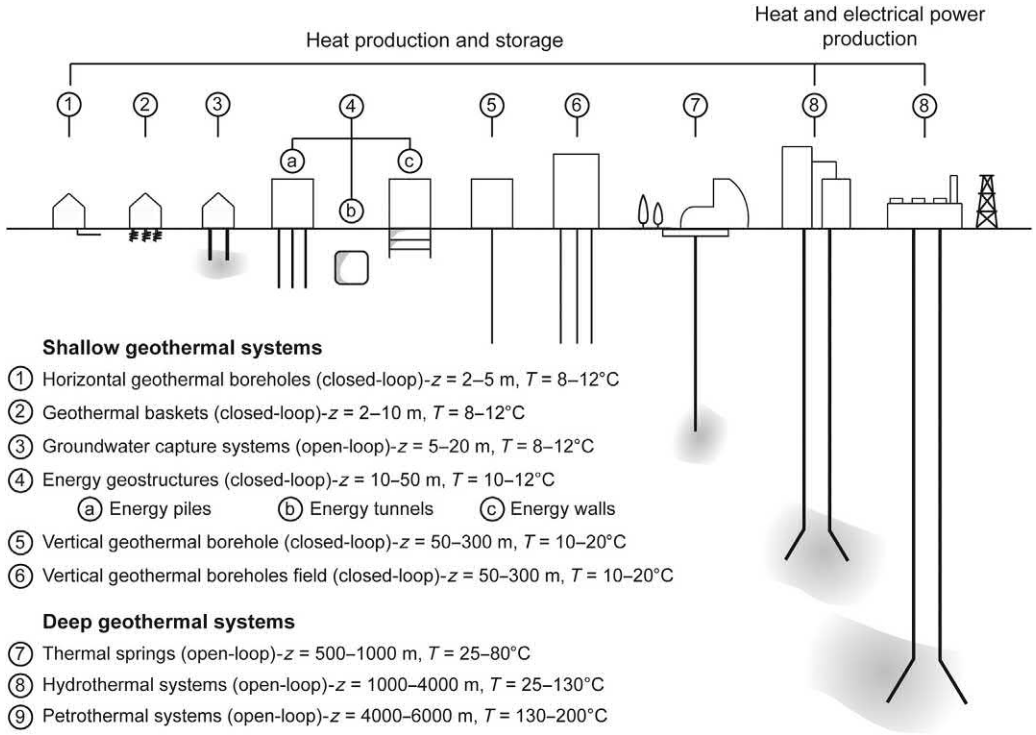

Figure 1.11 Classification of geothermal systems. *Modified after Geothermie Schweiz.*

Geothermal baskets represent a more compact system than horizontal geothermal boreholes and can be used for similar purposes. These systems are typically buried in the ground at a few metres of depth (from a depth of $z = 2-10$ m) and consist of closed polyethylene pipes fixed in a spiral geometry in which a heat carrier fluid flows. Applications where spiral coils are located in surface water reservoirs next to buildings are also possible, provided that such reservoirs are located deep enough to avoid problematic conditions for the system operation, for example freezing of the reservoir water and thus of the circulating heat carrier fluid in the pipes.

Groundwater capture systems employ open wells surrounded by groundwater reservoirs located at shallow depths (from a depth of $z = 5-20$ m). These systems can be applied when no hydrological, geological and environmental constraints are present. They are typically used for heating purposes by extracting the thermal energy present in the subsurface water. For small constructions, single wells may be used. Larger constructions usually require doublet wells. Extraction and injection wells may be employed to ensure a balanced underground thermal field, which is essential for performance and, in some cases, environmental concerns.

Vertical geothermal boreholes consist of closed polyethylene pipes that are embedded vertically in the ground below or next to buildings at deeper depths than the previous applications (from a depth of $z = 50-300$ m). A filling material (e.g. bentonite) is usually placed in the borehole to enhance the heat exchange between the ground and the pipes. A heat carrier fluid circulating in the pipes allows exchanging heat for heating, cooling, storage and hot water production purposes in the most diverse construction types. Single boreholes can supply small residential constructions. Borehole fields are required when aiming to supply with thermal energy larger constructions. Higher energy inputs than those transferred through shallower geothermal systems can be achieved through vertical geothermal boreholes because of the higher temperature levels characterising the ground at the considered depths.

Energy geostructures are novel geothermal systems that couple (from a depth of $z = 10-50$ m) the structural support role of any structure in contact with the ground with the heat exchanger role of shallow geothermal systems with comparable and even more favourable outcomes than the previously described systems.

Thermal springs may generally be classified as deep geothermal systems, although they can also be found at depths characteristic of shallow geothermal systems. These systems employ open wells surrounded by hot groundwater reservoirs that are located relatively deep in the subsurface (from a depth of $z = 500-1000$ m). They are typically used for bathing and medical purposes by extracting the thermal energy present in the subsurface water.

Hydrothermal systems extract groundwater through open wells from depths that allow the temperature and thermal energy present to be sufficiently high for realising large-scale heating applications (from a depth of $z = 1000-4000$ m). Typical uses of

these systems are for district heating, but heating of large industrial or agricultural constructions can also be conveniently achieved.

Petrothermal systems also extract groundwater through open wells, but from deeper depths than hydrothermal systems (from a depth of $z = 4000-6000$ m). The temperature and thermal energy present in the water at these depths can be used for large-scale electrical power production and supply.

References

Armstead, H.C.H., 1973. Geothermal energy. Review of Research and Development. UNESCO, Chambéry.

Barbier, E., 2002. Geothermal energy technology and current status: an overview. Renew. Sustain. Energy Rev. 6 (1), 3–65.

Boehler, R., 1996. Melting temperature of the Earth's mantle and core: Earth's thermal structure. Annu. Rev. Earth Planet. Sci. 24 (1), 15–40.

Boënnec, O., 2008. Shallow ground energy systems. Proc. ICE Energy 161 (2), 57–61.

Brandl, H., 2006. Energy foundations and other thermo-active ground structures. Geotechnique 56 (2), 81–122.

Buildings Performance Institute Europe, B. P. I. E., 2015. Nearly Zero Energy Buildings Definitions Across Europe. Buildings Performance Institute Europe, Brussels, p. 8.

Cataldi, R., 1999. The Year Zero of Geothermics. Association, G. R. C. I. G, Sacramento, CA, pp. 7–17.

Dalley, S., 2002. Mari and Karana: Two Old Babylonian Cities. Gorgias Press LLC.

Energy Performance of Buildings Directive, E. P. B. D., 2002. Directive 2002/91/EC of the European Parliament and of the Council of 16 December 2002 on the Energy Performance of Buildings. Off. J. Eur. Union 1, 65–71.

Energy Performance of Buildings Directive, E. P. B. D., 2010. Directive 2010/31/EU of the European Parliament and of the Council of 19 May 2010 on the energy performance of buildings (recast). Off. J. Eur. Union 153, 13–35.

Eurostat, 2017. Europe in Figures—Eurostat Yearbook. Office for Official Publications.

International Energy Agency, I. E. A. (2015) Energy and Climate Change. International Energy Agency, Paris.

International Energy Agency, I. E. A. (2016a) CO_2 Emissions from Fuel Combustion. International Energy Agency, Paris.

International Energy Agency, I. E. A. (2016b) Energy and Air Pollution. International Energy Agency, Paris.

International Energy Agency, I. E. A. (2016c) Key World Energy Statistics. International Energy Agency, Paris.

IPCC, 2013. Climate change 2013: the physical science basis. Contribution of Working Group I to the Fifth Assessment Report of the Intergovernmental Panel on Climate Change. Cambridge University Press, Cambridge.

Kemmler, A., Piégsa, A., Ley, A., Keller, M., Jakob, M., Catenazzi, G., 2013. Analysis of the Swiss Energy Consumption According to the End Use. Swiss Federal Office of Energy, Bern.

Lee, S., Speight, J.G., Loyalka, S.K., 2007. Handbook of Alternative Fuel Technologies. CRC Press.

Lund, J.W., 2009. Utilisation of geothermal resources. Proc. ICE Energy 162 (1), 3–12.

Lungonelli, M., 2003. Piero Ginori Conti: scienza, cultura e innovazione industriale nella Toscana del Novecento. Laterza, Bari.

Magee, L., Scerri, A., James, P., Thom, J.A., Padgham, L., Hickmott, S., et al., 2013. Reframing social sustainability reporting: towards an engaged approach. Environ. Dev. Sustain. 15 (1), 225–243.

Narsilio, G.A., Bidarmaghz, A., Colls, S., 2014. Geothermal energy: introducing an emerging technology. In: Proceedings of International Conference on Advances in Civil Engineering for Sustainable Development, pp. 141–154.

Sims, R.E.H., Schock, R.N., Adegbululgbe, A., Fenhann, J., Konstantinaviciute, I., Moomaw, W., et al., 2007. Energy supply. In: Metz, B., Davidson, O.R., Bosch, P.R., Dave, R., Meyer, L.A. (Eds.), Climate Change 2007: Mitigation. Contribution of Working Group III to the Fourth Assessment Report of the Intergovernmental Panel on Climate Change. Cambridge University Press, Cambridge.

United Nations, U. N, 2017. World Population Prospects: The 2017 Revision. Department of Economic and Social Affairs, P. D., United Nations, New York.

Questions and problems

Statements

a. Classify the energy sources based on their availability in nature and further expand on the classification of one type of these sources detailing their capability to renew themselves at a sufficient rate in human time frames. Which type of energy source is geothermal energy?

b. Primary energy sources are:
- **i.** Renewable at human time frames
- **ii.** Nonrenewable at human time frames
- **iii.** Renewable or nonrenewable, it depends on the energy sources
- **iv.** None of the above

c. Recall the principal unit measures of energy forms.

d. The basic energy unit of the metric system (SI) is:
- **i.** Joule, J
- **ii.** Watt, W
- **iii.** Calorie, Cal
- **iv.** Watt-hour, Wh

e. The Watt is defined as:
- **i.** $J \cdot s$
- **ii.** J
- **iii.** J/s
- **iv.** s/J

f. What is intended with the definition of primary energy, final energy and net energy?

g. What is the difference between final energy consumption and demand?

h. Can you state what are the three main end users that have more pronouncedly contributed in recent years in the final energy consumption of developed countries?

i. What have been two noteworthy consequences of the historical use of nonrenewable energy sources, often unregulated, poorly regulated, inefficient, or overexploited, in contrast to renewable energy sources? Summarise remarkable problems associated with these consequences.

j. Define low-carbon buildings and expand on their importance for sustaining human activity with a limited impact on the environment.

k. In which country/countries has the definition of NZEB been extended to positive energy building?
- **i.** Switzerland
- **ii.** France and United Kingdom
- **iii.** Italy and France
- **iv.** France

l. What are the three main components of geothermal energy? How does the geothermal gradient vary in the shallow subsurface and which temperature values are usually observed in temperate areas?

m. The temperature field in the subsurface, in the worst case, is sensitive to a variation of the atmospheric conditions within the first:
- **i.** 4–6 m
- **ii.** 25–30 m
- **iii.** 40–50 m
- **iv.** 80–100 m

n. In general, shallow geothermal systems can be exploited:
- **i.** To produce heat and electrical power
- **ii.** To produce power
- **iii.** To produce heat
- **iv.** None of the above

Solutions

a. Energy sources can be classified based on their availability in nature as primary and secondary energy sources. *Primary energy sources* represent an energy form that has not been subjected to any conversion and is available in nature, for example fossil fuels, mineral fuels, solar energy, geothermal energy, wind energy, tidal energy and biomass sources. *Secondary energy sources* represent an energy form that has been transformed from primary energy sources and is not available in nature, for example electrical energy, refined fuels and synthetic fuels.

Primary energy sources can be further classified depending on whether they can renew themselves at a sufficient rate in human time frames. *Renewable energy sources*, such as solar energy, geothermal energy, wind energy, tidal energy and biomass, can renew themselves at a sufficient rate in human time frames. *Nonrenewable energy sources*, such as fossil fuels and mineral fuels, cannot renew themselves at a sufficient rate in human time frames. Based on the classification described above geothermal energy is a renewable primary energy source.

b. Primary energy sources are:
- **i.** Renewable at human time frames
- **ii.** Nonrenewable at human time frames
- **iii. Renewable or nonrenewable, it depends on the energy sources**
- **iv.** None of the above

c. Joule [J], Calorie [cal], Watt-hour [Wh] and Tonne of oil equivalent [toe].

d. The basic energy unit of the metric system (SI) is:
  i. Joule, J
  ii. Watt, W
  iii. Calorie, Cal
  iv. Watt-hour, Wh

e. The Watt is defined as:
  i. J · s
  ii. J
  iii. J/s
  iv. s/J

f. Primary energy, final energy and net energy consumption are three different definitions usually employed to characterise the use of energy.

Primary energy consumption is the characterisation of the (use of) energy that has not been subjected to any conversion or transformation processes. It refers to the direct use or supply of the source of energy. Final energy consumption represents the total energy consumed by end users, excluding the energy that is used by the energy sector itself. The net energy consumption is the energy in its final desired form usually drawn from a consuming device, obtained from the final energy considering the losses associated with the use of devices for further refining, storing, or delivering energy.

g. Energy consumption refers to the quantity of energy added to or removed from a space. Energy demand refers to the immediate rate of energy added to or removed from a space, that is the power at a particular instant in time.

h. The three main end users that have more pronouncedly contributed over recent years in the final energy consumption of developed countries are the building sector, the industry sector and the transportation sector.

i. The main consequences of the historical use of nonrenewable energy sources are the increase in greenhouse gas emission and the depletion of nonrenewable energy sources.

Problems associated with fossil fuel combustion and greenhouse gas emissions are that they represent the most important sources of air pollutant emissions and are considered to be the dominant cause of the observed climate change and global warming. Concerning the depletion of nonrenewable energy sources, one problem is that, within approximately a century, resorting to these sources will no longer be technically and economically convenient anymore.

j. Low-carbon buildings are characterised by the use of integrated passive design strategies, high-performance building envelopes and energy efficient heating, ventilation and air-conditioning systems, as well as lighting

and appliances, and technologies harvesting on-site renewable energy sources. The main purpose for the design of such constructions is to develop buildings with significantly reduced energy consumption combined with the increased use of low-carbon energy sources to meet this consumption.

k. In which country/countries has the definition of NZEB been extended to positive energy building?
- **i.** Switzerland
- **ii.** France and United Kingdom
- **iii.** Italy and France
- **iv.** **France**

l. **Geothermal energy is the natural thermal energy contained in the Earth's surface. It results from the formation of the planet, the radioactive decay of minerals, and the solar energy absorbed at the surface**.

Excluding a shallow layer typically sensitive to atmospheric conditions, the temperature increases with depth in the Earth's crust. The average geothermal gradient is of approximately 3°C per 100 m of depth to the upper mantle. This value depends on the location and can be assessed as 1°C per 100 m in ancient continental zones. At greater depths, this temperature gradient decreases to approximately 0.1°C per 100 m of depth.

m. The temperature field in the subsurface, in the worst case, is sensitive to a variation of the atmospheric conditions within the first:
- **i.** **4–6 m**
- **ii.** 25–30 m
- **iii.** 40–50 m
- **iv.** 80–100 m

n. In general, shallow geothermal systems can be exploited:
- **i.** To produce heat and electrical power
- **ii.** To produce power
- **iii.** **To produce heat**
- **iv.** None of the above

CHAPTER 2

Energy geostructures

2.1 Introduction

Along with the ancient use of soils and rocks as heat reservoirs, the employment of geostructures (e.g. piles, walls and tunnels) as structural supports represents an effective historical means to meet human activity needs. Energy geostructures are an innovative technology that couples the structural support role of conventional geostructures to the heat exchanger role of shallow geothermal systems for any type of built environment.

This chapter addresses the technology of energy geostructures as a breakthrough means for contributing to the sustainability of human activity needs via the establishment of low-carbon buildings and infrastructures. Features, uses and capabilities of energy geostructures are addressed, examples of applications worldwide are presented, and an overview of the phenomena governing the behaviour of this technology is proposed.

To this aim, the *energy geostructure technology* is described first: in this context the purpose is to highlight the roles of energy geostructures, the materials involved and other relevant features of this technology. Next *energy geostructure operation modes* are presented: the purpose of this part is to illustrate possible uses of energy geostructures for heat exchange and storage purposes. Then so-called *ground source heat pump systems* and *underground thermal energy storage systems* are described: in this framework the aim is to propose relevant aspects related to the composition and operation of such systems. Afterward the *application and development of energy geostructures* are discussed: the aim of this part is to propose typical features characterising applications of such technology and expand on three energy geostructure projects that involve an energy pile foundation, energy tunnel linings and energy walls. Later *physical phenomena and approaches to analysis and design* are expanded: in this section the aim is to highlight key physical phenomena that characterise energy geostructures and to propose approaches for describing such phenomena in analysis and design. Finally *questions and problems* are proposed: the purpose of this part is to fix and test the understanding of the subjects covered in this chapter by addressing a number of exercises.

Analysis and Design of Energy Geostructures
DOI: https://doi.org/10.1016/B978-0-12-816223-1.00002-3

2.2 The energy geostructure technology

2.2.1 Roles of energy geostructures

Energy geostructures, more properly defined from a theoretical perspective as thermo-active geostructures, are an innovative, multifunctional technology that can be used for energy transfer applications as well as for providing structural support to any type of built environment. This technology includes all ground-embedded structures that can be used as structural supports while exchanging heat with the ground. Similar to other shallow geothermal systems, energy geostructures deal with low enthalpy and take advantage of the relatively constant temperature field in the shallow subsurface throughout the year for their heat exchanger role (Batini et al., 2015).

Energy geostructures can involve deep foundations (e.g. piles, piers and barrettes), earth retaining structures (e.g. diaphragm walls and sheet pile walls), shallow foundations (e.g. footings, base slabs), tunnel linings and anchors. Deep foundations enable massive constructions to be supported with a limited use of subsurface, such an aspect representing a great advantage in dense urban areas compared, for example, to shallow foundations. Earth retaining structures can be used to generate useful space for human activity below the underground. Tunnels are typically used to contribute to transportation in the underground. In this framework, the geostructures resulting from coupled energy transfer and structural support purposes are so-called energy piles, energy walls, energy slabs, energy tunnels, etc. (cf. Fig. 2.1).

There are various purposes of the heat exchange that can be established with energy geostructures. These purposes can consist of (1) heating and cooling superstructures to reach comfort levels in the built environment, (2) contributing to the production of hot water for anthropogenic, agricultural or tank-farming uses, (3) providing heat to prevent the icing of pavements and decks of structures and infrastructures such as roads, bridges, station platforms and airport runways and (4) storing heat in the subsurface for a successive use.

The use of energy geostructures for heating and cooling superstructures to reach comfort levels in the built environment can be achieved with the broadest range of energy geostructures, such as energy piles, energy walls, energy slabs and energy tunnels (the latter located close – e.g. within 400–600 m – to the superstructure they supply with thermal energy).

The use of energy geostructures for contributing to the production of hot water for anthropogenic purposes can nowadays be achieved via the lower temperature levels needed for this aim (e.g. 45°C–55°C) compared to those needed in constructions built during the 20th century to a few decades ago (e.g. 75°C–85°C). Typical energy geostructures that can be employed for this purpose, as well as for contributing to the production of hot water for agricultural or tank-farming purposes, are energy piles and energy walls, but also energy tunnels located in the vicinity of agricultural or

Figure 2.1 Examples of (A) energy piles, (B) energy slabs, (C) energy tunnels and (D) energy walls. *Courtesy (B) GI-Energy US, (C) Züblin Spezialtiefbau and (D) ENERCRET.*

tank-farming activities. The reason for this is that significant amounts of heat can be exchanged with the tunnel environment and the surrounding ground. This heat exchange can be particularly favourable especially when tunnels are characterised by a significant length or high traffic, and when they are constructed at significant depths or in locations where noteworthy geothermal gradients are present. The use of energy

geostructures for providing heat to prevent the icing of pavements and decks of infrastructures such as roads, bridges, station platforms and airport runways can be typically achieved via energy piles supporting bridge piers, energy slabs and energy pavements. The use of energy geostructures for storing heat in the subsurface for subsequent use can also be achieved via energy piles, energy walls, energy slabs and energy tunnels.

2.2.2 Materials and technology

Energy geostructures are typically made of reinforced concrete. From a technological perspective, they differ from conventional geostructures only because pipes are fixed along their reinforcing cage or are placed within the filling material (cf. Fig. 2.2). Placing the pipes along the reinforcing cage on the groundside is common when dealing with energy walls or tunnels and there is the need to avoid potential issues due to maintenance of the geostructure or the adjacent environment (e.g. fixing supports to the geostructure that may pierce the pipes embedded within the reinforced concrete). Embedding the pipes within the concrete is otherwise preferable to ensure adequate concrete cover on the reinforcing cage.

Fixing the pipes to the reinforcing cage of energy geostructures can be performed either in a plant or on site. The latter is more common (Brandl, 2006), whereby the piping is delivered to site on reels and a special working area is used. At the inflow and outflow of the pipework of each energy geostructure a locking valve and a manometer are fixed (Brandl, 2006). These instruments allow the pipe circuit to be pressurised within a range of 5–8 bar for integrity check. In most applications the locking valves and manometers are also used upon concreting to resist the head of the wet concrete without collapsing. Pressure testing for 24 hours after concreting is good practice. The pressure in the pipes is again applied before the working phase involving the construction of the superstructure starts (Brandl, 2006).

Inside the pipes a fluid is pumped via electrically driven machines and is used as a thermal energy carrier for the operation of the energy geostructures in most shallow, closed-loop geothermal systems. The pipes of energy geostructures are usually made of high-density polyethylene and are characterised by a diameter of 10–40 mm with a wall thickness of 2–4 mm (cf. Fig. 2.3). Thermal insulation of the pipes can be considered for the first meters of the inlet and outlet to limit the influence of the climatic condition on the heat exchange process, aiming at optimising the energy efficiency (Gao et al., 2008; Batini et al., 2015).

The heat carrier fluid (i.e. the heat transfer medium) circulating in the pipes usually consists of water, water with antifreeze or a saline solution. Water–antifreeze mixtures containing additives to prevent corrosion are also a well-performing and durable solution. Antifreezes are employed to lower the freezing point of water-based mixtures that may be characterised by freezing otherwise. The usual antifreeze additives

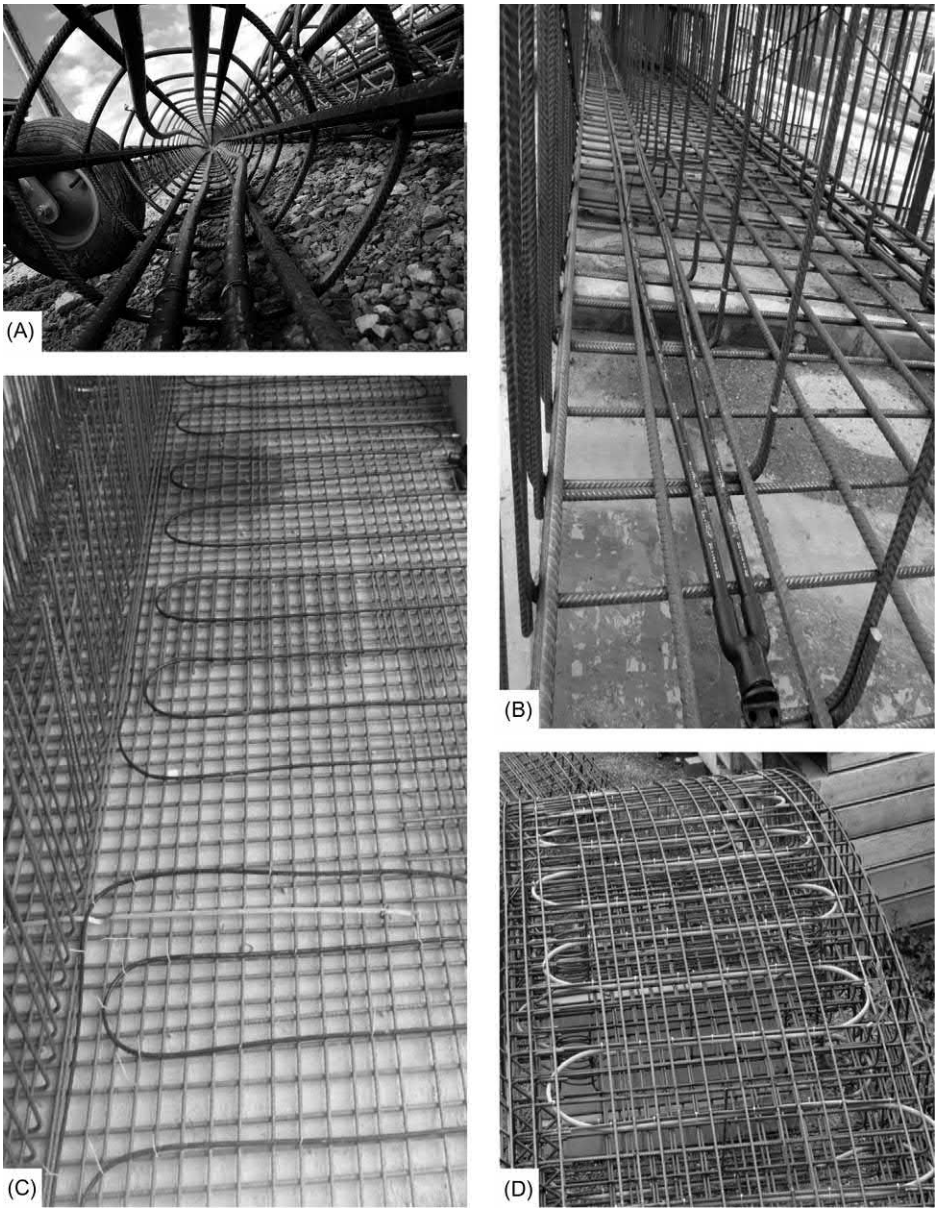

Figure 2.2 Pipes mounted along the reinforcing cage of (A) an energy pile, (B) an energy diaphragm wall, (C) an energy slab and (D) an energy tunnel segmental lining. *Courtesy (B) BG Ingénieurs Conseils, (C) BG Ingénieurs Conseils and (D) Züblin Spezialtiefbau.*

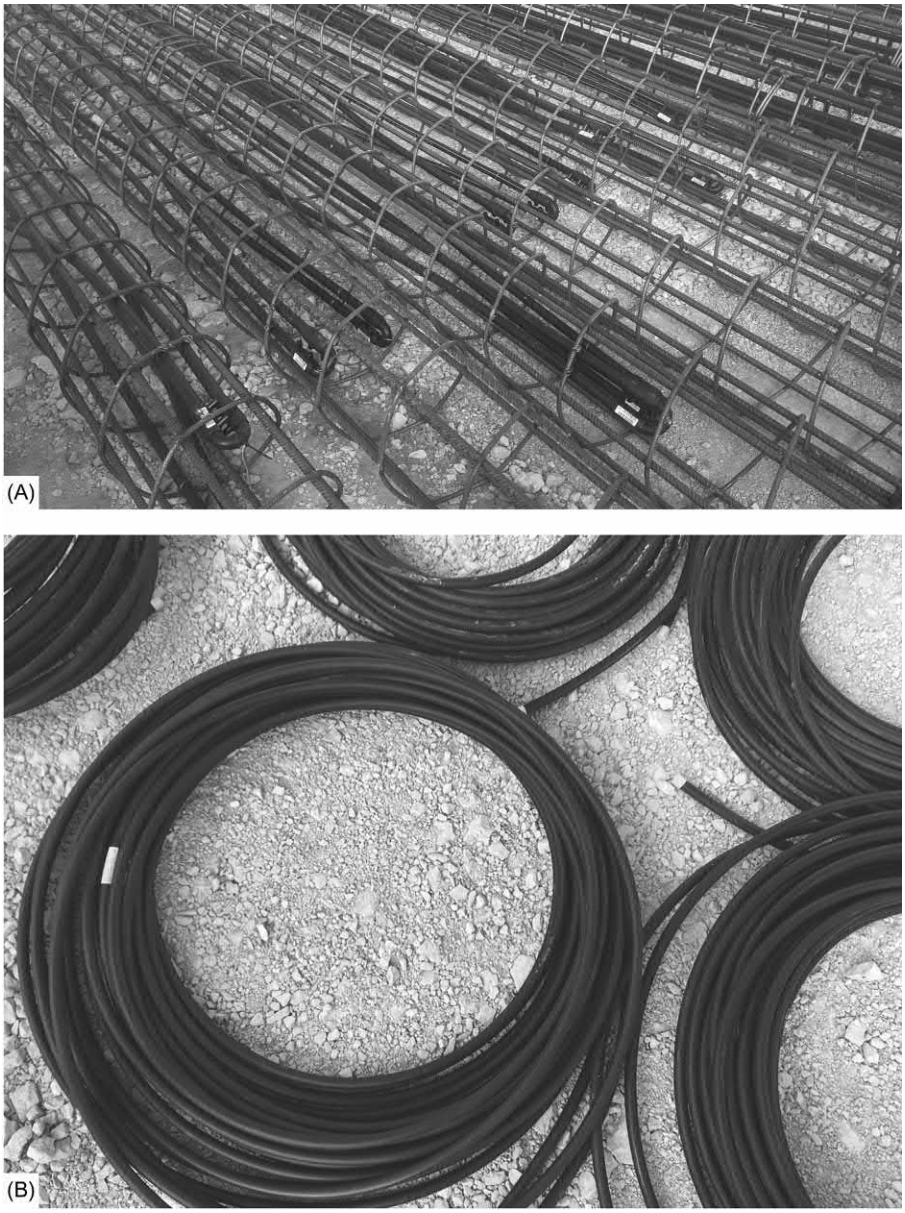

Figure 2.3 Typical pipes characterising energy geostructures: (A) example of connection between pipe edges in energy piles and (B) storage of pipes in a construction site.

employed for such a purpose are ethylene glycol and propylene glycol. Ethylene glycol is poisonous to humans and animals, and should be handled carefully and disposed of properly. Propylene glycol is considerably less toxic than ethylene glycol and may be preferred in some cases.

2.2.3 Pipe configurations

Many different pipe configurations can be foreseen for energy geostructures. This design variable influences the installation, the operation and the operating costs of the energy system (cost resulting from the ease and speed of installation as well as from the installed pipe length).

Examples of pipe configurations for energy piles include the single U-shaped, bent U-shaped, parallel double U-shaped, series double U-shaped, multi U-shaped, indirect double, W-shaped, spiral (or helix) and coaxial pipe configurations (cf. Fig. 2.4). In many practical circumstances, the spiral pipe configuration is not employed despite its marked heat transfer potential because of the difficulties associated with its installation, especially in small diameter piles. The multi U-shaped pipe configuration is often used for large diameter piles.

When dealing with energy tunnels, configurations involving pipes oriented perpendicular or parallel to the axial direction of the tunnel can be foreseen (cf. Fig. 2.5). Such design solutions need to be envisaged considering the position of the header pipes, which often represents a more significant restraint for the pipe layout of tunnels compared to that of piles.

Various pipe configurations can also be foreseen for energy walls and energy slabs (cf. Fig. 2.6). In designing the pipe layout for energy tunnels, energy walls and other energy geostructures characterised by a significant heat exchange surface, a key aspect is to obtain the largest heat exchange surface for the selected energy geostructure portion at the lowest pressure drop and investment.

2.2.4 Pipe locations

Energy tunnels, walls and slabs can be characterised by both air–solid and solid–solid interfaces. Therefore these energy geostructures can exchange heat with both the air and the ground. Such a feature can have major implications on the overall efficiency of the energy system if not properly considered. Depending on the situation, one may target to foster or limit the heat exchange between the air– or solid–solid interfaces by choosing an appropriate pipe location, or sometimes to prevent heat exchange even by insulating one side of the geostructure (e.g. cold tunnel equipped as a geothermal heat exchanger for heating purposes). An example of these solutions is shown in Fig. 2.7. To minimise fire risk and prevent accidental damage, the pipes should be placed at least 200 mm from the geostructure intrados (Nicholson et al., 2014).

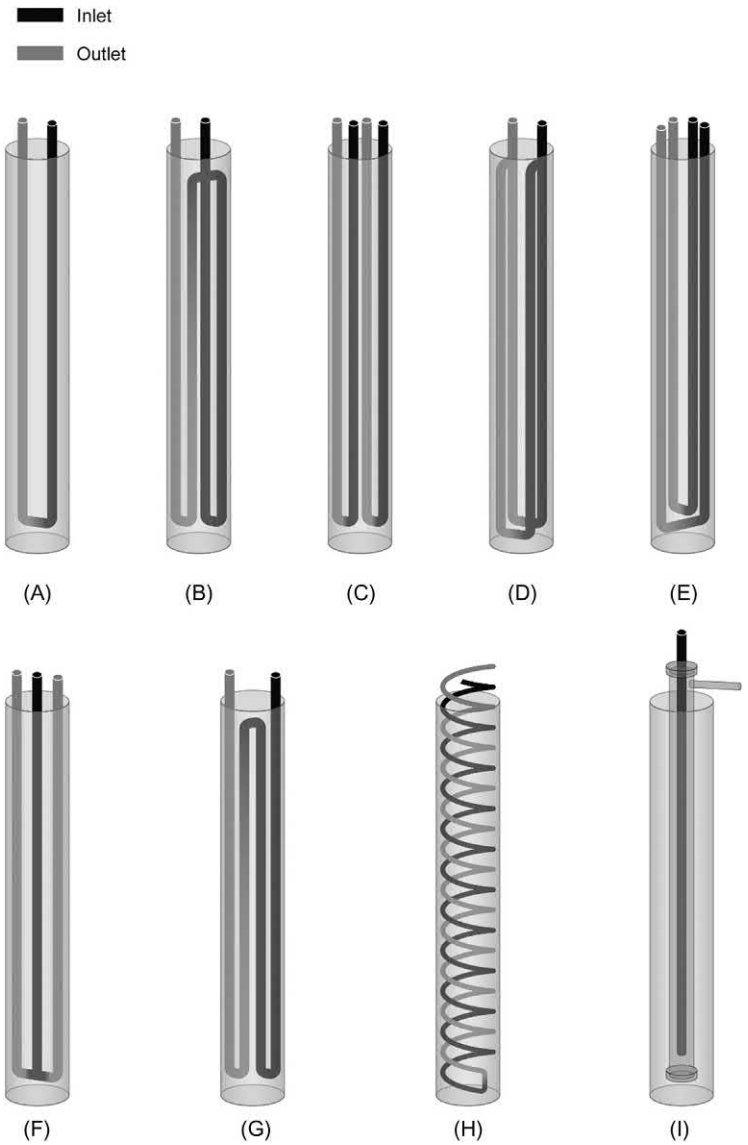

Figure 2.4 Examples of pipe configurations for energy piles: (A) U-shaped pipe, (B) bent U-shaped pipe, (C) parallel double U-shaped pipe, (D) series double U-shaped pipe, (E) multi U-shaped pipe, (F) indirect double pipe, (G) W-shaped pipe, (H) spiral (or helix) pipe and (I) coaxial pipe configurations. *Fadejev, J., Simson, R., Kurnitski, J., Haghighat, F., 2017. A review on energy piles design, sizing and modelling. Energy 122, 390−407.*

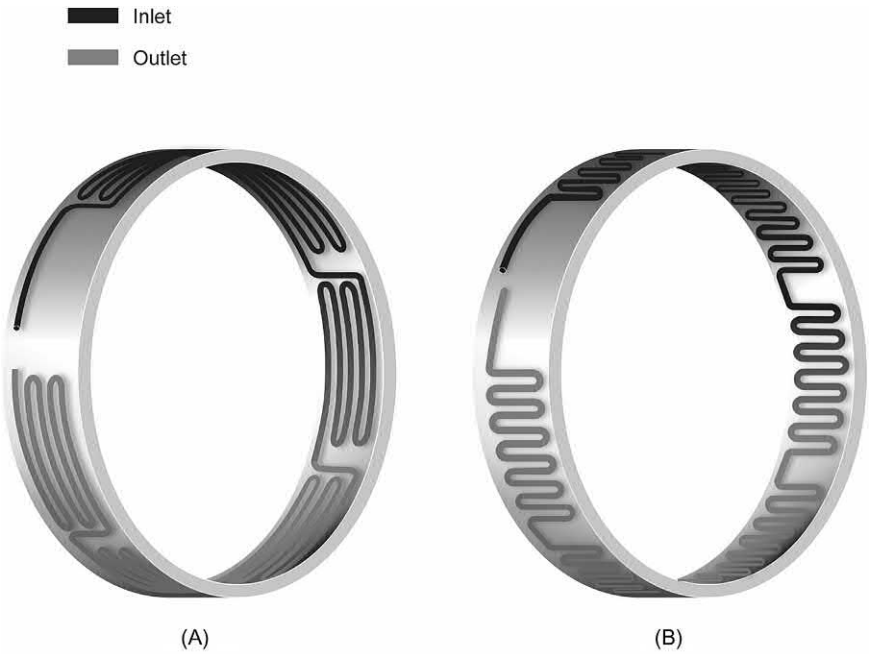

Figure 2.5 Examples of pipe configurations running (A) perpendicular and (B) parallel to the axis of energy tunnels.

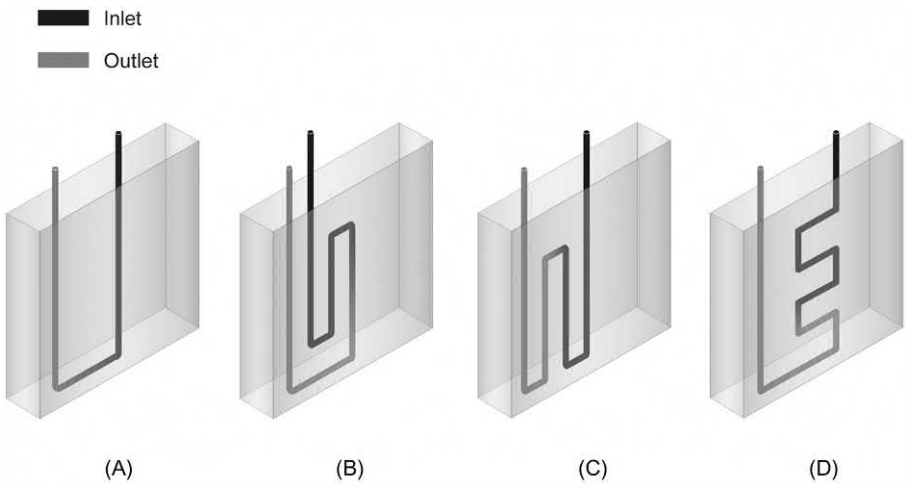

Figure 2.6 Examples of pipe configurations for energy walls: (A) U-shaped pipe, (B) bent U-shaped pipe, (C) W-shaped pipe and (D) repeatedly bent pipe. *Sterpi, D., Coletto, A., Mauri, L., 2017. Investigation on the behaviour of a thermo-active diaphragm wall by thermo-mechanical analyses. Geomech. Energy Environ. 9, 1–20.*

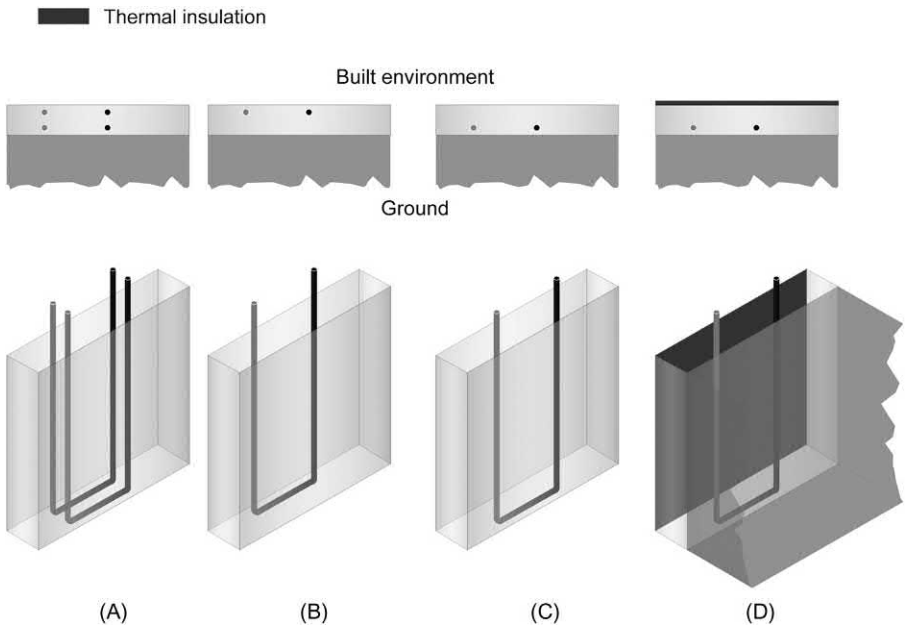

Figure 2.7 Possible pipe locations in energy tunnels, walls and slabs, considering a U-shaped pipe configuration located: (A) close to both sides, (B) close to the airside, (C) close to the groundside and (D) close to the groundside with an insulated airside.

2.2.5 Advantages involved with energy geostructures

Similar to other technologies harvesting renewable energy, such as conventional geothermal systems, energy geostructures are an environment-friendly technology that reduces the need of fossil energy sources and hence the greenhouse gas emissions. For this reason the use of energy geostructures promotes and complies with national and international initiatives, policies, regulations and agreements. Furthermore, energy geostructures may be applied with other technologies harvesting renewable energies to form highly efficient systems.

In contrast to conventional shallow geothermal systems, the earth-contact elements that characterise energy geostructures and serve as heat exchangers are already required for structural reasons and need not to be constructed separately (Brandl, 2006). This fact involves savings related to the construction process that should be undertaken in a separate realisation of geostructures and geothermal heat exchangers.

Another key difference between energy geostructures and other conventional closed-loop geothermal systems is that concrete typically has more favourable thermal properties than the filling materials (e.g. bentonite) of the other geothermal technologies. This feature makes the heat exchange more favourable in the former case

compared to the latter. One final difference is that usually the bending radius of the pipes in energy geostructures is greater compared to that characterising the pipes in conventional geothermal heat exchangers. This fact involves a lower flow resistance of the fluid circulating in the pipes, which results in a lower pumping power and thus in a lower operation cost.

With reference to the purposes of the heat exchange that can be established with energy geostructures various are the advantages compared to other technological systems. The use of energy geostructures for heating and cooling superstructures to reach comfort levels in the built environment reduces the environmental impact of any construction and can be exploited to get incentives for the design project and construction of the superstructure. The use of energy geostructures for contributing to the production of hot water for anthropogenic purposes reduces the costs compared to systems entirely resorting to more conventional technologies and is again characterised by a reduced environmental impact. When energy geostructures are employed for contributing to the production of hot water for agricultural or tank-farming uses, cost savings can be achieved via lower operational costs and environmental impacts. The use of energy geostructures for providing heat to prevent the icing of pavements and decks of infrastructures such as roads, bridges, station platforms and airport runways involves reducing the environmental and structural impacts of these applications because the use of salts or grits is not necessary and hence chemical and mechanical degradation phenomena that would otherwise be enhanced do not occur. The use of energy geostructures for storing heat in the subsurface allows harvesting at a later time waste heat that would be lost otherwise as well as establishing particularly effective and efficient energy systems.

2.3 Energy geostructure operation modes

2.3.1 Possible operations

Two operation modes of energy geostructures involving a markedly different conceptual purpose can be employed: the heat exchange operation and the heat storage operation. Depending on whether energy geostructures are used for heat exchange or storage purposes through the respective operations, so-called ground source heat pump systems (GSHPS) and underground thermal energy storage systems (UTES) are employed, respectively.

2.3.2 Heat exchange operation

In the heat exchange operation, the primary purpose of energy geostructures is to use the ground as a heat reservoir. The heat present in the ground is typically extracted and transferred to the superstructure in cool climates or cold seasons. In contrast the

heat is typically extracted from the superstructure and injected into the ground in warm climates or during hot seasons.

Two possible uses of the energy geostructures are possible for the heat exchange operation mode:

1. *Heating and/or cooling only* can be employed when the natural thermal recharge occurring in the ground during nonoperating periods of the energy geostructure system is sufficiently high to keep the shallow temperature field in the subsurface undisturbed (except for the influence of climatic conditions) over time. This situation generally characterises energy geostructures in permeable soil with significant groundwater flow.
2. *Heating and/or cooling combined with heat storage* has to be employed when the natural thermal recharge occurring in the ground during nonoperating periods of the energy geostructure system is insufficient to keep the shallow temperature field in the subsurface undisturbed (except for the influence of climatic conditions) over time. This situation generally characterises energy geostructures in low permeable soil with negligible groundwater flow.

2.3.3 Heat storage operation

In the heat storage operation the primary purpose of energy geostructures is to use the ground as a storage medium. Waste heat and solar heat is typically injected into the ground. While solar heat is usually injected in warm climates during hot seasons for subsequent heating use in cold seasons, waste heat (involving elevated or low temperatures) can be stored for subsequent use in the ground for both heating and cooling purposes in cool climates or cold seasons and in warm climates or hot seasons, respectively. Heat storage is often required when heating or cooling needs do not match the heating or cooling productions.

2.4 Ground source heat pump systems

2.4.1 General

Ground source heat pump systems comprise a primary and a secondary circuit that allow the heat to be exchanged between the ground and any considered built environment via energy geostructures. The primary circuit includes the ground heat exchanger system. The secondary circuit characterises the built environment to be heated or cooled.

In the primary circuit heat is exchanged between the ground and the geostructure, and is collected to be transferred to the built environment. In the secondary circuit heat is transferred to the built environment for heating or cooling purposes. In between these two circuits electrically driven machines such as heat pumps or reversed

heat pumps can be employed. These machines are not present in all applications and when heating or cooling functional modes are targeted without them, the resulting energy geostructure operations are called 'free heating' or 'free cooling' (or geocooling), respectively. The need to use heat pumps or reversed heat pumps depends on the significance of the temperature difference between the primary circuit (i.e. the ground) and the secondary circuit (i.e. the built environment). In fact the temperature difference between the two circuits makes the heat exchange between them more or less favourable.

The operation of ground source heat pump systems can involve sufficiently high and low temperature levels for the heating and cooling of built environments, respectively, but also insufficient temperature levels for the same purposes. When the temperature level in the ground is sufficient for the aforementioned purposes, heat pumps or reversed heat pumps are not needed and 'free' operations can be achieved. Otherwise, heat pumps or reversed heat pumps are employed to increase and decrease the temperature level (and associated energy input), respectively, in those cases in which the heat originally exchanged with the ground may not be sufficient for heating or cooling purposes. In other words heat pumps or reversed heat pumps allow overcoming the apparent restriction involved with the use of a cooler ground to heat built environments or a warmer ground to cool built environments, respectively. The reason for this is that the quoted situations defy the second law of thermodynamics, for which heat flows from hot to cold, if left to itself (Narsilio et al., 2014). Typically heat pumps are employed to raise the temperature level from 10°C–15°C to 40°C–45°C for the heating of superstructures.

It is worth noting that, even though the term free is used for operations that do not employ heat pumps or reversed heat pumps, pumping machines using electrical energy are required to transfer the thermal energy from the ground to the superstructure or the opposite. Fig. 2.8 presents a schematic of a typical ground source heat pump system for the heating of a superstructure.

2.4.2 The primary circuit

Heat exchange between the ground and energy geostructures occurs via the heat carrier fluid circulating in the pipes embedded in such geostructures (i.e. the ground heat exchangers) and allows exploiting the large thermal storage capabilities of the ground for heating and cooling purposes.

One or more header and manifold blocks are generally present to collect all the pipes arising from the energy geostructure(s). Resilience of these systems is fundamental. Hence, submanifolds are generally employed to affect only a minor portion of the energy geostructure system if there are any problems related to the installation or

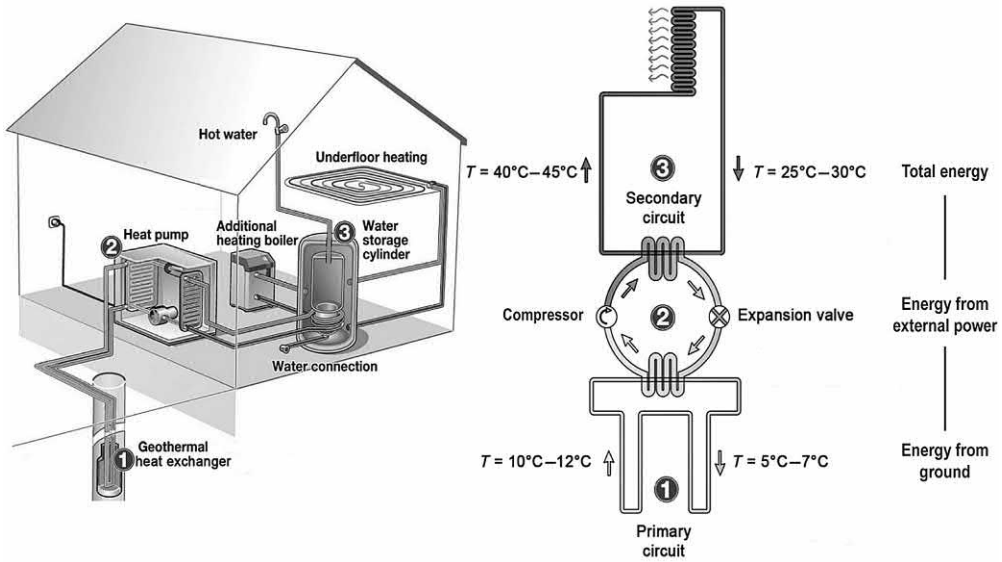

Figure 2.8 Typical composition of a ground source heat pump system and associated operation for the heating of a superstructure. *Modified after Agentur für Erneuerbare Energien.*

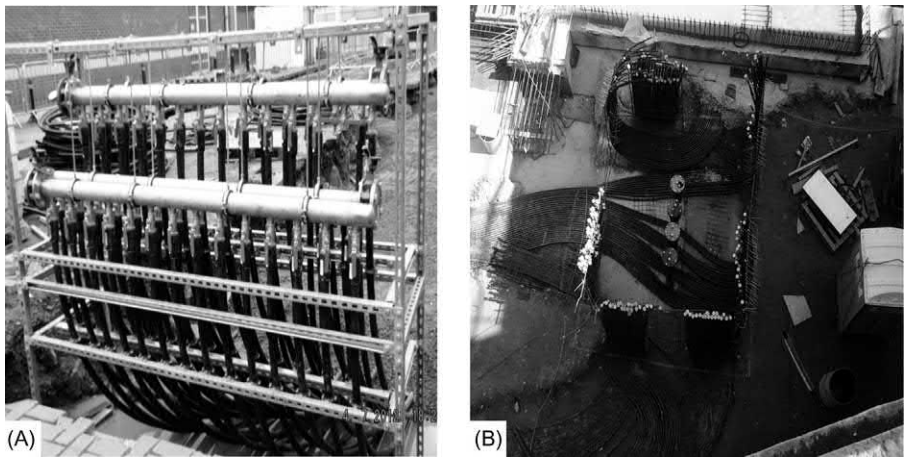

Figure 2.9 Examples of (A) pipes collection from energy geostructures in submanifolds and (B) lay-out of pipes beneath a building. *Courtesy (A) GI-Energy US and (B) ENERCRET.*

operation of the energy geostructures (cf. Fig. 2.9A). These elements, together with the runout proportion of the pipes that characterise the energy geostructure(s), often lie within the blinding beneath the base slab and constitute the primary circuit together with all of the aforementioned elements (cf. Fig. 2.9B).

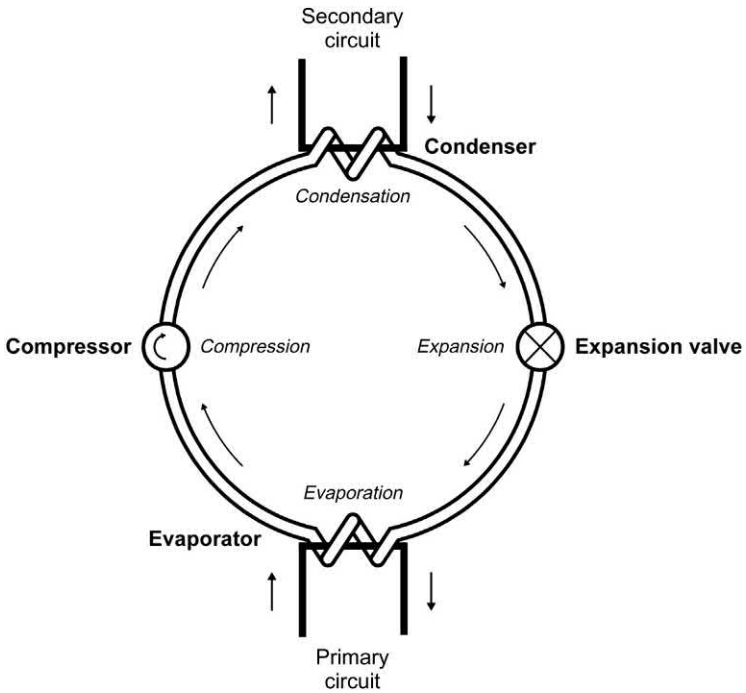

Figure 2.10 Schematic of a heat pump.

2.4.3 The heat pump or reversed heat pump

Heat pumps are thermal devices that convert mechanical work into heat. The thermodynamic principle behind heat pumps is that fluids become warmer when they are compressed into a smaller volume. The opposite is true for reversed heat pumps, that is fluids become cooler when they are expanded. This fact indicates that heat pumps and reversed heat pumps are characterised by the same operating principle (Yunus and Michael, 2006).

Simple heat pumps (e.g. compression heat pumps) comprise four main devices: the evaporator, the compressor, the condenser and the expansion valve (cf. Fig. 2.10). Heat pumps work with a refrigerant, which is a special fluid that (1) circulates in a closed circuit in the heat pump, (2) undergoes phase transitions from a liquid to a gas and back again and (3) evaporates at low temperatures.

In the evaporator the refrigerant is put in its liquid form in contact with the heat carrier fluid circulating in the pipes of the energy geostructures in the primary circuit and is evaporated to a gas, with its temperature being lower than that of the heat carrier fluid and its boiling point (at relatively low pressure) below the entering heat carrier fluid temperature. The phase change from liquid to gas of the refrigerant fluid decreases the temperature of the heat carrier fluid, which is then reinjected into the

ground via the pipes of the energy geostructures to warm up again. The refrigerant gas, at low pressure and relatively low temperature, then passes to the compressor.

In the compressor, this gas is compressed by using external energy (e.g. electrical power) to a higher temperature. The refrigerant gas, now at a relatively high pressure and temperature, afterward passes to the condenser.

In the condenser the resulting hot gas supplies the gained heat to a heat carrier fluid circulating in the secondary circuit by condensing (at a much higher temperature than at which it boiled). Eventually the hot liquid refrigerant at high pressure passes through an expansion valve that returns the pressure and temperature of the liquid to its original conditions prior to reentering the evaporator where it starts a new cycle.

The aforementioned process is reversed when reversed heat pumps are used, the refrigerant condensation heating the heat carrier fluid circulating in the primary circuit, which is reinjected in the ground to cool down again.

Water-to-water heat pumps used in energy geostructures applications are available in numerous sizes for different possible uses. Depending on the use the heat pump must be supplied with a constant water flow coming from the source. The required water flow can range from a couple of cubic metres per hour for relatively small heat pumps characterised by a peak power of 4–6 kW up to 60 cubic metres per hour for 300 kW heat pumps. The optimal required source water flow is usually provided in the heat pumps' technical information. The considered water flow corresponds to that of the header pipe collecting the several pipes included in the various subsystems that constitute the energy geostructure(s) (e.g. piles and tunnel rings), the manifold(s) and other connections.

2.4.4 The secondary circuit

Heat exchange in the built environment is typically achieved in the secondary circuit through heat exchangers such as radiant heating floors or ceilings, radiators, fan coil units, etc. Temperature values that are adequate to reach comfort levels in living spaces and advantageous for engineering applications (e.g. deicing of infrastructures) can be achieved through energy geostructures with a highly efficient use of primary energy (Batini et al., 2015).

The distribution schemes employed for the secondary circuit are typically the same as conventional systems and details of these may be found in standard heating, ventilation and air-conditioning references (see, e.g. ASHRAE, 2011). However, one must note that ground source heat pump systems may deliver hot air or water at temperatures marginally lower than that of other conventional heating, ventilation and air-conditioning systems (Narsilio et al., 2014): hence due consideration should be taken for the design of ducting and piping in the secondary circuit.

The heating and cooling consumption of a building can also be determined by well-established procedures found in standard heating, ventilation and air-conditioning references (see, e.g. ASHRAE, 2009). The heating and cooling consumptions of superstructures are a function of many factors, including the climate, construction forms and orientations, materials used for the construction, the effects of sun and shade, ventilation, lights and appliances, people's presence and activity, and building use and purpose (Narsilio et al., 2014).

For new constructions some of the previous factors may be designed in such a way that heating and cooling consumptions are reduced and, if possible, balanced, so that the ground source heat pump systems become more economical to install and operate (Narsilio et al., 2014).

2.4.5 The coefficient of performance

The amount of external energy input to be supplied to heat pumps has to be kept as low as possible to make the heat pump ecologically and economically desirable, the heat pump efficiency becoming a crucial design parameter. The efficiency of heat pumps can be characterised using the coefficient of performance, *COP*, which is a device parameter that defines how many units of heat can be obtained using one unit of electricity. The *COP* is defined as

$$COP = \frac{\text{Energy output after heat pump operation [kW]}}{\text{Energy input for heat pump operation [kW]}} \tag{2.1}$$

The higher the *COP*, the lower the external energy input compared to the energy output (e.g. useful heat). For example a *COP* of 4 means that from one unit of electrical energy and three units of thermal energy (supplied, e.g. by the ground heat exchanger), four units of usable energy are derived. Usually, geothermal heat pumps have a *COP* in the range of 3.5−4. For economic reasons a value of $COP \geq 4$ may preferably be achieved (Brandl, 2006).

The efficiency of a heat pump is strongly influenced by intrinsic machine features such as efficiency of internal heat exchangers and thermal losses, as well as by the difference between extracted and actually used temperature. A high user temperature (inflow temperature to the heating system of the secondary circuit) and a low extraction temperature (due to a too low return-flow temperature) in the heat exchanger (primary circuit) reduces its efficiency. To have a good efficiency the usable temperature in the building should not exceed 35°C−45°C and the extraction temperature in the pipes should not fall below 0°C−5°C (Brandl, 2006). Besides, thermal properties of the ground might vary considerably in freezing conditions and it is recommended that excessive heat extraction causing ground freezing should be avoided (SIA-D0190, 2005).

2.4.6 The seasonal factor of performance

The efficiency of ground source heat pump systems along seasons can be characterised through the seasonal factor of performance, *SFP*. This factor includes not only the energy of the heat pump but also that of other energy-consuming elements (e.g. circulation pumps) (Brandl, 2006). The *SFP* is defined as

$$SFP = \frac{\text{Energy output usable from the energy system [kWh]}}{\text{Energy input of the energy system [kWh]}} \tag{2.2}$$

Values of *SFP* of 3.8–4.3 can be achieved with standard electric heat pumps, with an increase of 10%–15% when special devices with direct vaporisation are used (Brandl, 2006). The seasonal performance of ground source heat pump systems is generally represented in a Sankey diagram that graphically indicates the energy budget of a system with the internal and external energy fluxes.

2.4.7 Possible applications of ground source heat pump systems

Two main types of application of ground source heat pump systems can be foreseen depending on the features of the given location and project, and the number of energy geostructures required:

1. *Monovalent systems* relying only on energy geostructures to provide the entire amount of heating and cooling needs. This type of system is rare but achievable under certain conditions (i.e. significant groundwater flow and favourable conditioning loads). In these systems at least 70% of the extracted energy may be injected when encountering minimum groundwater flow, although injecting more than 90% of the extracted energy may compromise the long-term efficiency of free cooling (SIA-D0190, 2005). An example of such a system is the industrial building Lidwil at Altendorf, Switzerland. The system uses 120 spun energy piles out of 155 spun piles constituting the entire building foundation that are equipped with two U-shaped pipes per pile (embedded within a gravel layer characterised by a groundwater velocity between 100 and 150 m/day), and provides 160 kW of heating using three heat pumps of 18 kW each with a *COP* of 2.9–3 (SIA-D0190, 2005).
2. *Bivalent systems* using energy geostructures to provide only a proportion of the heating and cooling needs, the rest being satisfied using conventional heat sources. An example of such a system is the Dock Midfield at Zürich airport, Zürich, Switzerland. The system uses more than 300 energy piles out of 440 piles to provide 65% of the heating needs and 70% of the cooling needs. The remaining proportions come from district heating for heating and from a cooling tower for cooling, respectively (Pahud and Hubbuch, 2007a).

2.5 Underground thermal energy storage systems

2.5.1 General

Underground thermal energy storage systems allow the heat collected from solar thermal panels or in excess from built environments to be exchanged for storage purposes in the ground. Different storage strategies can be achieved depending on the technology or approach used for this storage, resulting in so-called (1) hot water energy storage; (2) gravel–water thermal energy storage; (3) aquifer thermal energy storage; (4) borehole thermal energy storage; and (5) energy geostructure storage. The latter systems are of particular interest herein and involve the heat exchange between any considered built environment and the ground via energy geostructures.

The storage can be targeted on a daily or seasonal basis, the coupling between these solutions being characterised by showing the highest promise. In fact since seasonal storage might have slow charging or discharging rates, coupling seasonal storage with diurnal storage might bridge this gap (Lanahan and Tabares-Velasco, 2017).

In ground source heat pump systems the heat exchange between energy geostructures and the surrounding ground should be maximised. In contrast in underground thermal energy storage systems the heat exchange between energy geostructures and the surrounding ground should be minimised to preserve heat storage. Underground thermal energy storage systems are often considered to hold little promise if applied via a limited number of energy geostructures such as piles (Ingersoll et al., 1954). However, where the site conditions are favourable and significant amounts of heat can be stored via substantial (or multiple) energy geostructures, underground thermal energy storage systems can represent an advantageous solution. The ground occupation of these systems is limited and, among different storage technologies, they can be characterised by approximately 100% round trip efficiency of thermal energy storage and recovery, compared to the 80% efficiency batteries possess (Denholm et al., 2012, 2015; Evans et al., 2012).

Underground thermal energy storage systems established via energy geostructures can be particularly effective as compared to other storage systems achieved via aquifers or gravel–water systems, because they are not limited to specific formations as per the former solutions (Dincer and Rosen, 2002; Rad et al., 2013; Kalaiselvam and Parameshwaran, 2014; Xu et al., 2014; Rad and Fung, 2016). However, as reported by Lanahan and Tabares-Velasco (2017), limitations of underground thermal energy storage systems applied with elements such as energy piles include the comparatively large amount of heat loss compared to insulated water tank or gravel tank systems (Schmidt and Mangold, 2006; Rad and Fung, 2016).

2.5.2 Efficiency of underground thermal energy storage systems

Underground thermal energy storage systems can be coupled to ground source heat pump systems and can be realised with or without heat pumps or reversed heat pumps. There are many ways to measure the performance of such systems (Lanahan and Tabares-Velasco, 2017).

When heat pumps or reversed heat pumps are used in underground thermal energy storage systems coupled with ground source heat pump systems and are the primary driver for such technological systems, the *COP* of the pumps can be used for this purpose. This approach is particularly favourable when the goal of the installation is to improve heat pump performance by raising evaporator temperatures (Rad et al., 2013; Nam et al., 2015; Omer, 2008; Wang and Qi, 2008).

In general, however, the performance of underground thermal energy storage systems is defined in terms of the efficiency

$$\eta_{\mathrm{UTES}} = \frac{\text{Total amount of heat extracted from the energy system [kWh]}}{\text{Total amount of heat injected into the storage [kWh]}} \tag{2.3}$$

When underground thermal energy storage systems employ solar thermal panels to inject heat into the ground, two particular definitions of efficiency become useful and these are the total system efficiency, defined as (Sweet and McLeskey, 2012):

$$\eta_{\mathrm{UTES,tot}} = \frac{\text{Total amount of heat provided to the energy system [kWh]}}{\text{Total amount of incident solar radiation on solar collectors [kWh]}} \tag{2.4}$$

and the internal system efficiency, defined as (Sweet and McLeskey, 2012):

$$\eta_{\mathrm{UTES,int}} = \frac{\text{Total amount of heat provided to the energy system [kWh]}}{\text{Total amount of heat provided by solar collectors [kWh]}} \tag{2.5}$$

While the efficiency provides a better understanding of required energy storage size, the total system efficiency characterises the overall performance of the system and the internal system efficiency provides a better understanding of how well the system meets an energy goal (Lanahan and Tabares-Velasco, 2017).

2.6 Application and development of energy geostructures

2.6.1 Historical facts

Energy geostructures have been increasingly applied worldwide since the 1980s (Brandl, 2006). To date the highest number of energy geostructure applications involves energy piles, whereas fewer projects involve energy walls, energy slabs and energy tunnels. Only the advent of the 'Grand Paris Express' project in France, which

may be considered to contribute to the most significant modern urban renovation of the city of Paris following that introduced by Haussmann during the mid-19th century, has caused a major increase in the designs for future applications of energy walls and energy tunnels.

2.6.2 Application and development examples based on a literature survey

In the following a state of the art of the application and development of energy geostructures worldwide is presented. This review does not claim to be comprehensive of all the actual applications and features of energy geostructures worldwide. However, it is considered to be useful to assess remarkable features of energy geostructure projects constructed around the world.

The presented review is based on the results of (1) a survey targeting international practitioner companies involved with the construction of energy geostructures (2) data obtained from a literature review about the number of applications and features of constructed energy geostructures for operational purposes and (3) complementary results published by Di Donna et al. (2017) while the previous activities were carried out. The survey was carried out through a questionnaire sent between September 2016 and July 2017 to the following companies (listed in alphabetical order): Amstein et Walthert SA (Switzerland), Borel Energy Consulting (Switzerland), Bilfinger Berger (Germany), Caverion (Finland), Cementation Skanska (United Kingdom), Enercret (Austria), GI-Energy (United States), Géothermie Professionnelle (France), Ruukki (Finland), Sacyr Industrial (Spain), Soletanche Bachy (France) and Tecnoservice Eng. (Switzerland). The questionnaire was divided into two parts of increasing detail and was written in English and French. A summary of the English version of this questionnaire is presented in Appendix A.

Based on the integration of the previous information, the considered state of the art includes a dataset about the following energy geostructure projects (latest update June 2018):

- 157 projects of energy piles;
- 17 projects of energy walls;
- 7 projects of energy slabs; and
- 11 projects of energy tunnels.

In the following, some of the results of the discussed state of the art are proposed. Additional data can be found in the work of Di Donna et al. (2017).

Fig. 2.11A presents the cumulative number of energy geostructure projects constructed around the world. The construction of energy geostructures is increasing remarkably, with a predominant application of energy piles that is followed by applications of energy walls and energy tunnels. Fig. 2.11B shows the carbon dioxide (CO_2) savings associated with the available projects constructed worldwide. The significance

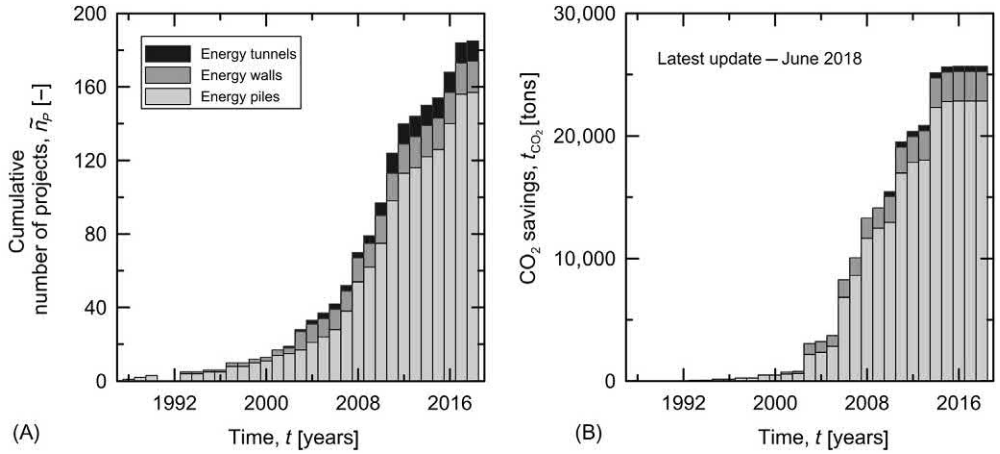

Figure 2.11 Cumulative number of (A) energy geostructure projects around the world and (B) carbon dioxide (CO_2) savings around the world. *Data obtained through a survey addressed to practitioners, a literature review and complementary results presented by Di Donna, A., Marco, B., Tony, A., 2017. Energy geostructures: analysis from research and systems installed around the world. In: Proceedings of 42nd DFI Conference.*

of CO_2 savings depending on the type of energy geostructure applications consistently reflects the data presented in Fig. 2.11A, with a dominant amount of CO_2 savings related to energy pile applications, followed by the savings associated with energy wall and energy tunnel applications.

Fig. 2.12 presents the installed thermal power by country, based on the same survey. Leading countries in the installed power through energy piles currently are Austria, United Kingdom and China, although in the latter case it is not known if those projects are actually operational.

Fig. 2.13 presents the number and average length of energy piles installed by country. Leading countries in the application of energy piles currently appear to be the United Kingdom, Austria and Switzerland. The average length of the constructed energy piles is approximately 18 m.

2.6.3 The energy pile foundation of the Dock Midfield at the Zürich Airport

Terminal E of Zürich Airport, Dock Midfield, in Switzerland, is a particularly successful application of energy piles (cf. Fig. 2.14). The Dock Midfield is a building of 500 m by 30 m that was constructed from 1999 to 2003. It is characterised by a volume of 200,000 m^3 to be heated and cooled (with 18 daily estimated hours of cooling) and serves 26 aircrafts. Four hundred and forty piles structurally support the building,

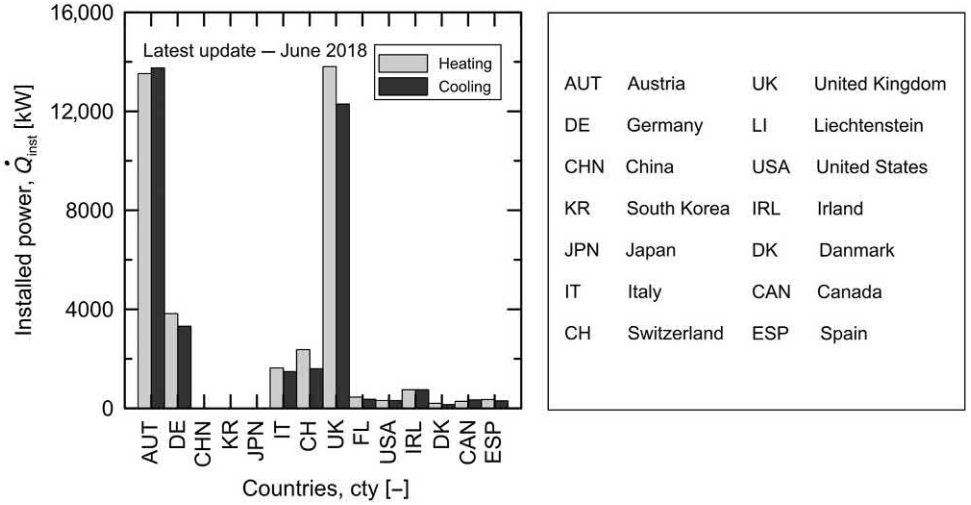

Figure 2.12 Installed thermal power by country. *Data obtained through a survey addressed to practitioners, a literature review and the complementary results presented by Di Donna, A., Marco, B., Tony, A., 2017. Energy geostructures: analysis from research and systems installed around the world. In: Proceedings of 42nd DFI Conference.*

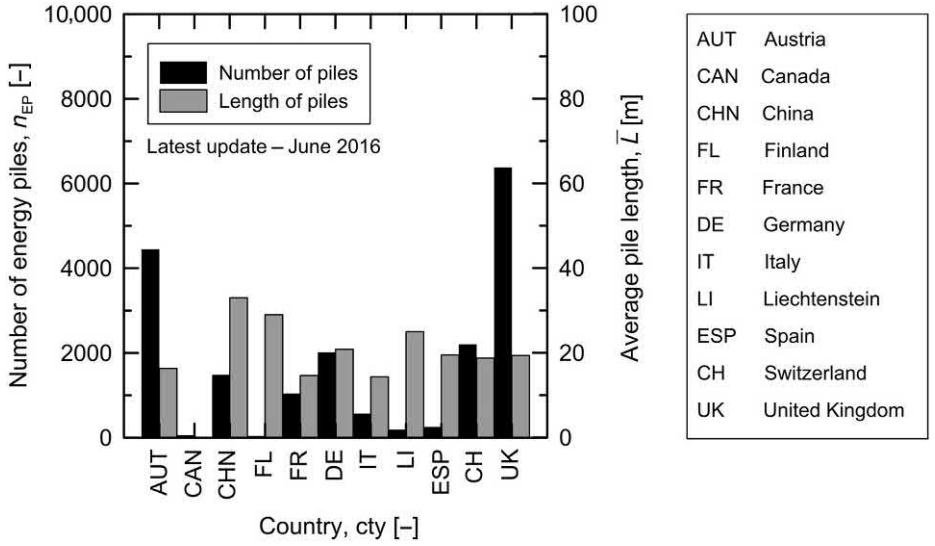

Figure 2.13 Number and average length of energy piles by country. *Data obtained through a survey addressed to practitioners and a literature review.*

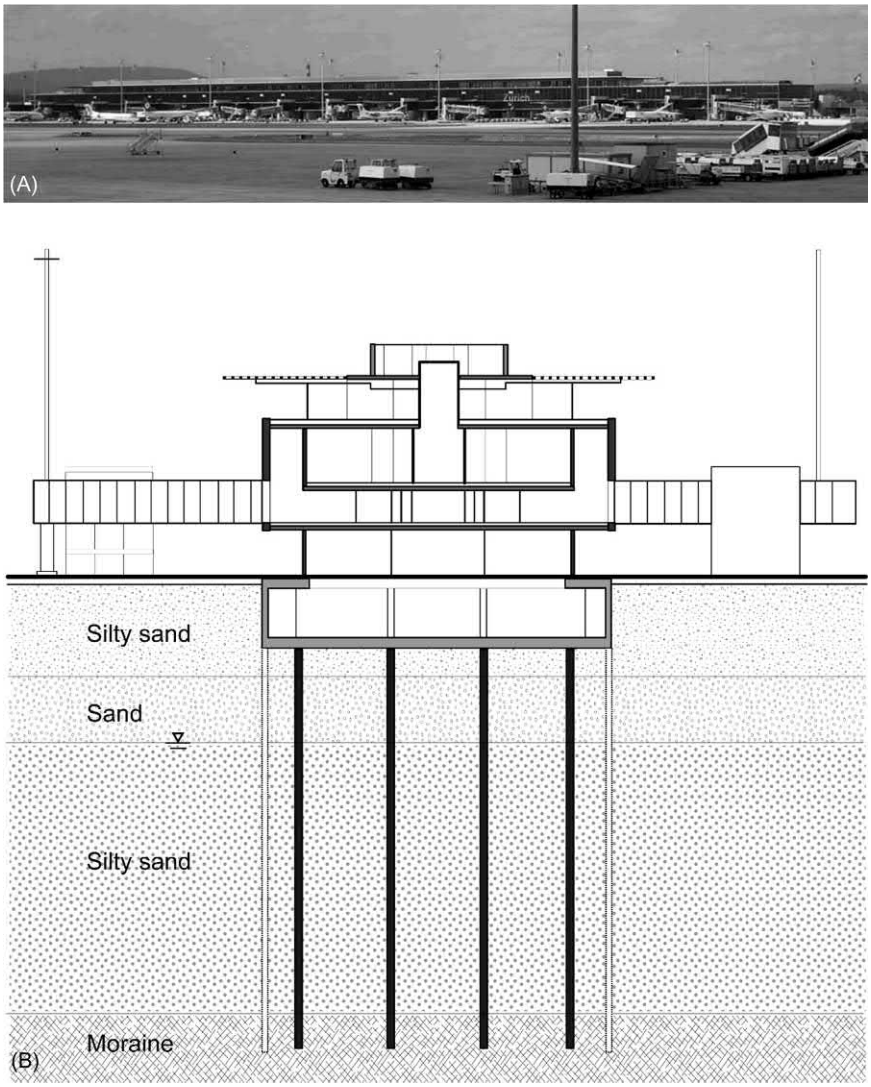

Figure 2.14 (A) Photograph and (B) sketch of a relevant vertical cross section of the Zürich Airport, Dock Midfield, in Switzerland. *(A) Modified after Pahud, D., Hubbuch, M., 2007a. Measured thermal performances of the energy pile system of the dock midfield at Zürich Airport. In: Proceedings of European Geothermal Congress. Bundesverband Geothermie and (B) redrawn after Pahud, D., Fromentin, A., Hubbuch, M., 1999. Heat Exchanger Pile System of the Dock Midfield at the Zürich Airport, Office fédéral de l'énergie, Lausanne, Suisse, p. 49.*

and these are socketed in soft soil and rest on a moraine (e.g. a stiff sandstone) layer at approximately 30 m of depth. Three hundred and six of the 440 piles were equipped with five U-pipes fixed on their metallic reinforcement and operate as energy piles (Pahud and Hubbuch, 2007b). The energy piles are made of reinforced concrete and

are cast in place. They are characterised by an average length of 26.5 m and a diameter varying between 0.9 and 1.5 m. Their total length is 8300 m (Pahud and Hubbuch, 2007b). The piles can be characterised as predominantly end-bearing piles because they rest on a moraine layer.

The energy design process of the energy piles began early in the project: it was iterative and went hand in hand with the structural design of piles, which changed in number and sizes with the increasing accuracy and availability of the data typical of the later phase of a project. The energy piles were monitored over 2 years of operation (2004–06). The main project contractor was also the direct user and responsible for system maintenance.

The energy pile system was designed to contribute to both the heating and cooling supply throughout three successive design stages. In the final stage the heating energy consumption of the building was estimated to be 2720 MWh/year (Pahud and Hubbuch, 2007a). A ground source heat pump system was designed to deliver 630 kW (Pahud et al., 1999) and to cover 2312 MWh/year (85%) of the heating energy consumption (Pahud and Hubbuch, 2007a). The remaining portion of approximately 408 MWh/year (15%) was intended to be supplied by district heating (Pahud and Hubbuch, 2007a). The cooling energy consumption of the building was estimated to be of 1240 MWh/year (Pahud et al., 1999). A cooling distribution network was designed to deliver 690 MWh/year (56%) through the ground source heat pump system when the cooling needs might have been simultaneous to the heating needs, 470 MWh/year (38%) by geocooling (i.e. free cooling without heat pump) and 80 MWh/year (6%) by the heat pump used as a cooling machine (i.e. reversed heat pump) (Pahud et al., 1999).

Ventilation of the building was intended to be achieved with conventional cooling machines, which supply 510 MWh/year (Pahud and Hubbuch, 2007a). The heat pump was designed to prevent the fluid temperature dropping under 0°C or exceeding 40°C–45°C (Pahud and Hubbuch, 2007a). The overall system operation mode was controlled by valves and was monitored by the building automation system every 5 minutes.

Fig. 2.15 presents the monthly energy of the ground source heat pump system, from October 2005 to September 2006 (Pahud and Hubbuch, 2007a). According to Pahud and Hubbuch (2007a), the annual heating energy was measured to be 3020 MWh. The heating energy delivered by the ground source heat pump system was measured to be 2210 MWh (73%) and the district heating contribution was 810 MWh (27%). The annual coefficient of performance of the heat pump was estimated to be 3.9, including the electrical energy for the circulation pumps.

Fig. 2.16 presents the monthly energy of the cooling distribution networks, from October 2005 to September 2006 (Pahud and Hubbuch, 2007a). According to Pahud and Hubbuch (2007a), the annual cooling energy was measured to be 1170 MWh.

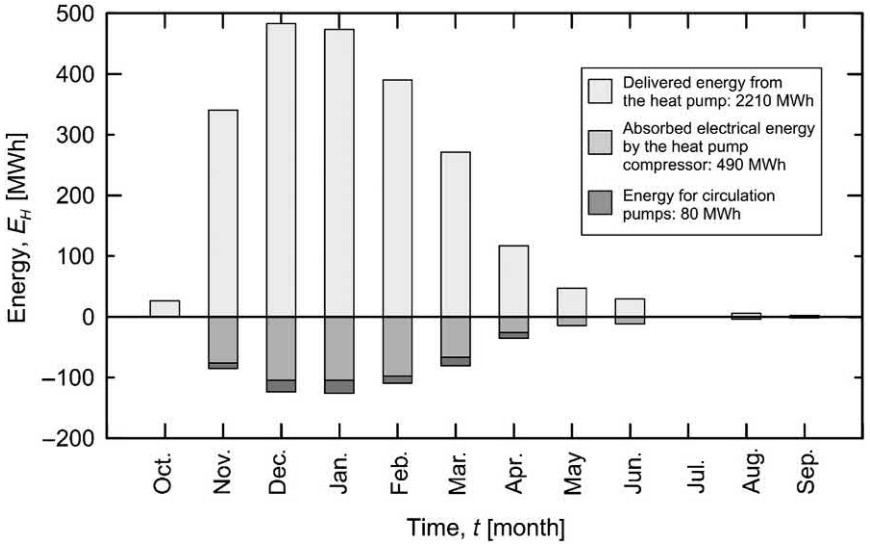

Figure 2.15 Monthly energy of the ground source heat pump system at Zürich Airport. *Redrawn after Pahud, D., Hubbuch, M., 2007a. Measured thermal performances of the energy pile system of the dock midfield at Zürich Airport. In: Proceedings of European Geothermal Congress. Bundesverband Geothermie.*

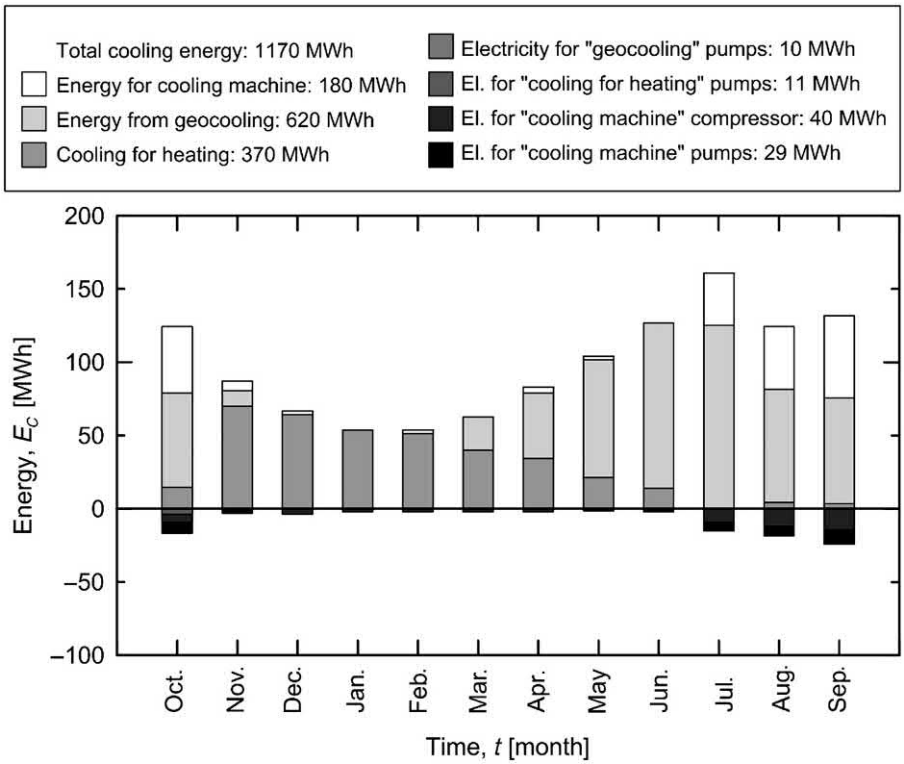

Figure 2.16 Monthly energy of the cooling distribution network at Zürich Airport. *Redrawn after Pahud, D., Hubbuch, M., 2007a. Measured thermal performances of the energy pile system of the dock midfield at Zürich Airport. In: Proceedings of European Geothermal Congress. Bundesverband Geothermie.*

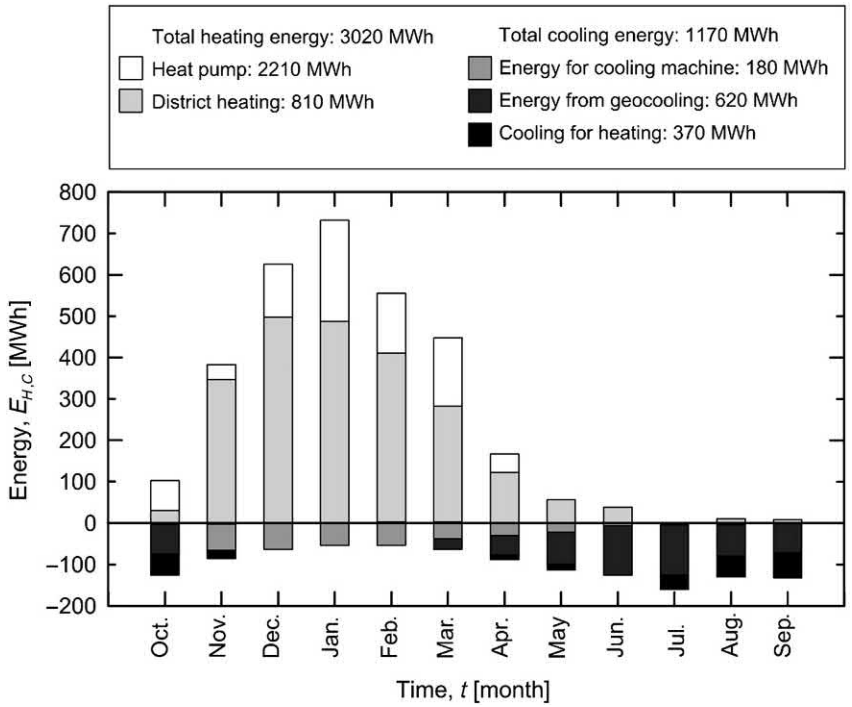

Figure 2.17 Monthly energy balance for the energy pile system at Zürich Airport. *Redrawn after Pahud, D., Hubbuch, M., 2007b. Performances mesurées des pieux énergétiques. Bull. Soc. Suisse Géotherm. 42(17), 13–14.*

This amount of energy was covered by simultaneous heating requirements (370 MWh, 32%), geocooling (620 MWh, 53%) and by the heat pump used as a cooling machine (180 MWh, 15%). The electrical energy for the circulation pumps and the cooling machine was measured to be 90 MWh. The annual geocooling efficiency, that is the ratio between the injected energy in the piles and the electrical energy used to transfer the cooling energy from the distribution system to the piles, was 61. The annual cooling machine efficiency, that is the ratio between the cooling energy extracted at the evaporator and the electrical energy absorbed by the compressor, was measured to be 2.7. This value was decreased by the electric consumption of the circulation pumps. The overall cooling efficiency, that is the ratio between the delivered cooling energy and the electrical energy used to operate the system for the cooling production, was estimated to be of 13.

Fig. 2.17 summarises the monthly energy balance for heating and cooling based on the previously presented results, from October 2005 to September 2006. Fig. 2.18 shows the monthly extracted and injected energy as well as the inflow and outflow temperatures associated with energy extraction and injection for the energy pile

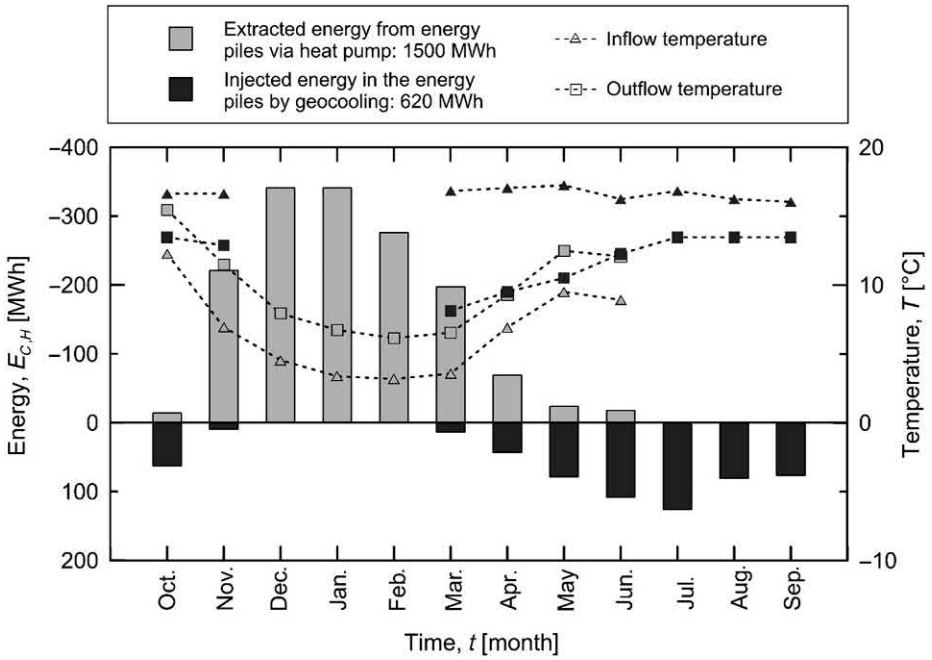

Figure 2.18 Monthly extracted and injected energy as well as inflow and outflow temperature associated with the energy extraction and injection for the energy pile system at Zürich Airport. *Redrawn after Pahud, D., Hubbuch, M., 2007a. Measured thermal performances of the energy pile system of the dock midfield at Zürich Airport. In: Proceedings of European Geothermal Congress. Bundesverband Geothermie.*

system, from October 2005 to September 2006. According to Pahud and Hubbuch (2007a), the injected energy corresponds to the geocooling production of 620 MWh. This production represents 41% of the 1500 MWh extracted by the Ground Source Heat Pump System. The measured maximum and average thermal powers extracted from the energy piles are of −72 and −45 W/m, respectively. The annual heating energy extracted from the energy piles is −183 kWh/m. The measured maximum and average thermal powers injected in the energy piles are 33 and 16 W/m, respectively. The annual cooling energy injected in the energy piles is 74 kWh/m. The overall system efficiency, that is the ratio between the thermal energy delivered by the system (for heating and cooling) and the total electric energy required to run it (all the circulation pumps, the heat pump and the reversed heat pump), was estimated to be 5.1 (Pahud and Hubbuch, 2007a). This efficiency could be improved to 5.7 by lowering the delivered cooling energy in the cooling distribution (thus using geocooling only) and the electric consumption of the pump (Pahud and Hubbuch, 2007a).

In this project the design values were close to the measured ones (Pahud and Hubbuch, 2007a). This fact, in conjunction with the success of the energy pile

Table 2.1 Economic comparison between the energy pile system with a conventional system (Pahud and Hubbuch, 2007a).

Heating/cooling system		Energy piles	Conventional	Difference
Investment		670,000 €	80,000 €	590,000 €
Annual cost	Capital	46,170 €	5450 €	+40,720 €
	Maintenance	10,070 €	3170 €	+6900 €
	Energy	71,660 €	156,180 €	−84,520 €
Total annual cost		127,900 €	164,800 €	−36,900 €
Thermal energy cost		0.04 €/kWh	0.05 €/kWh	

installation, highlights the need for detailed considerations regarding the application of energy geostructures from the early stages of the design process.

Table 2.1 shows an economic analysis of the considered energy pile system, with respect to other conventional heating/cooling systems. The analysis shows that the energy pile system is economically more convenient than a conventional heating/cooling system. The cost of the investment is paid back in 8 years without taking into account interest (Pahud and Hubbuch, 2007a).

2.6.4 The Stuttgart-Fasanenhof and the Jenbach energy tunnels

The Stuttgart-Fasanenhof tunnel in Germany and the Jenbach tunnel in Austria are among the first energy tunnels constructed around the world (cf. Fig. 2.19).

The Stuttgart-Fasanenhof tunnel is a suburban, double-tracked, 380-m-long metro tunnel, with a 20-m-long thermoactive section (Buhmann et al., 2016). This section was installed inside the tunnel in 2011. The tunnel ceiling is situated approximately 10 m below the surface throughout its length and is surrounded by marlstone and mudstone (Buhmann et al., 2016). The tunnel contains two detached thermoactive sections and is directly connected to a station where a heat pump, an electrical heater, a heat exchanger for cooling purposes and a main pump for the circulation of heat exchanger fluid are located and were employed over a 4-year period from 2011 to 2015 (this tunnel operated purely as a test plant) (Berga et al., 2017).

The Jenbach tunnel (which is a part of the Brenner Base tunnel) is a double-tracked, 3740-m-long railway tunnel, with a 54-m-long thermoactive section (Frodl et al., 2010). This section was installed inside the tunnel in 2008. The tunnel overburden depth is approximately 27 m and is surrounded by gravel (Franzius and Pralle, 2011). This section supplies the Jenbach municipal town council building heating needs (this tunnel is in real operation). The tunnel owner is responsible for the maintenance of the absorber and pipe system inside the main tunnel while the town council is responsible for the whole heat pump system.

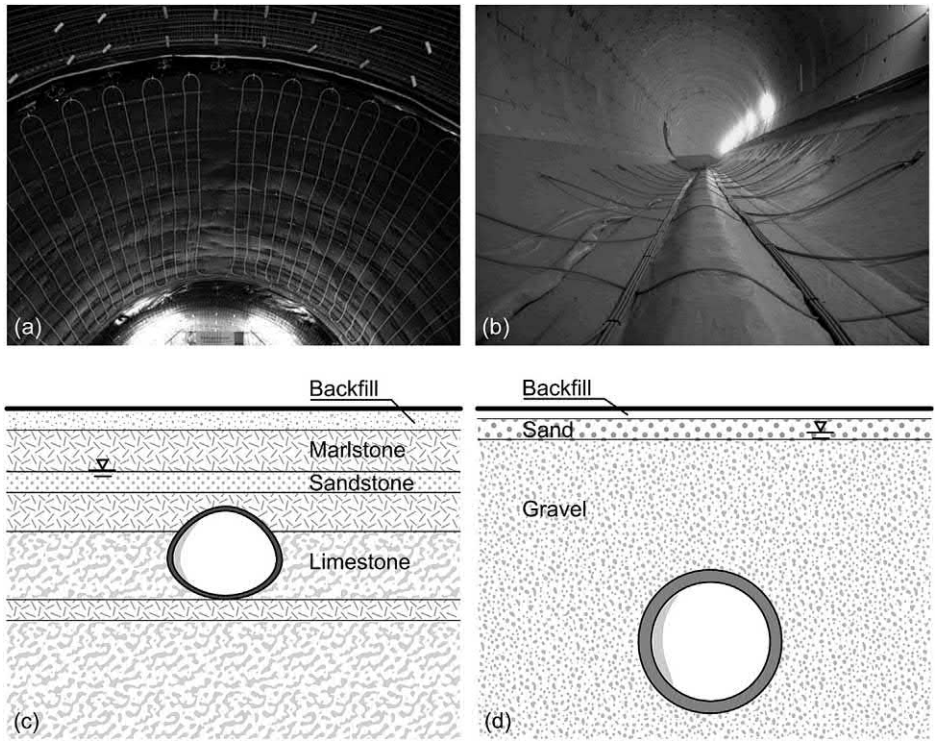

Figure 2.19 (A) The Stuttgart-Fasanenhof energy tunnel, (B) the Jenbach energy tunnel, (C) sketch of a relevant vertical cross section of the Stuttgart-Fasanenhof energy tunnel and (D) sketch of a relevant vertical cross section of the Jenbach energy tunnel. *(A) Courtesy Züblin Spezialtiefbau, (B) courtesy Züblin Spezialtiefbau, (C) redrawn after Buhmann, P., Moormann, C., Westrich, B., Pralle, N., Friedemann, W., 2016. Tunnel geothermics—a German experience with renewable energy concepts in tunnel projects. Geomech. Energy Environ. 8, 1–7 and (D) personal communication of Dr Sebastian Homuth, Züblin Spezialtiefbau GmbH.*

The Stuttgart-Fasanenhof tunnel was equipped with a length of approximately 800 m running pipes, which were installed in loops. The thermoactive area of tunnel lining was approximately of 360 m^2 and high-pressure polyethylene pipes with a diameter of $d_p = 25$ mm were used (Buhmann et al., 2016).

The Jenbach tunnel was equipped with a length of approximately 4700 m of running pipes, which were installed in loops. The thermoactive area of tunnel lining was approximately 2200 m^2 and high-pressure polyethylene pipes with a diameter of $d_p = 25$ mm were used (Buhmann et al., 2016).

The first stationary measurements in the Stuttgart-Fasanenhof energy tunnel with fixed inlet temperatures in the pipes showed variations between 5 and 37 W/m^2 of thermal power per heat exchange area (Berga et al., 2017). The Jenbach tunnel was designed to supply approximately 15 kW of thermal power to the municipal town

council building (Frodl et al., 2010). Preliminary field tests indicated thermal powers between 10 and 20 W/m^2 (Franzius and Pralle, 2011).

2.6.5 The energy walls of the Taborstraße station

The U2/2 metro line in Vienna, Austria, represents the first worldwide full-scale application of energy geostructures to this type of transportation system (Brandl, 2006). An extension of the U2 metro line offered the possibility to equip four stations with approximately 103 km of absorber pipes installed in walls, slabs and tunnel linings. The Taborstraße station was the first station to be equipped among the four (Brandl, 2006). It was opened in 2008 and included energy geostructures to supply the metro stations with both heating and cooling energy (cf. Fig. 2.20). The system was primarily designed to inject in the ground a large amount of heat produced in the underground. The metro line was surrounded by a soil deposit mostly composed of sand and silt. The U-bahn Company is the main owner and user of the energy. In a preliminary phase of the design project, it was necessary to prove that the geothermal system did not affect the soil and groundwater surrounding the station.

The Taborstraße station was equipped with a total of 1865 m^2 of energy diaphragm walls and 1640 m^2 of energy slabs (Brandl, 2006). The absorber pipes were characterised by a diameter of $d_p = 25$ mm. A total fluid volume of 10 m^3 circulates in the absorber system and provides a maximum cooling capacity of 81 kW. The surplus energy not used for heating is designed to be transferred into the soil via the absorber system, thus avoiding noisy or unsightly outdoor cooling towers (Brandl, 2006). Absorber pipes were attached to the reinforcements of structural elements and connected via manifolds to the service rooms. The U2/2 station hosts a total of two heat pumps and one cooling machine. For safety reasons no gas was used but only an electric refrigeration system. According to Brandl et al. (2010), the design of the energy geostructure system included a total thermal power installed for heating and cooling of 185 and 114 kW, respectively. According to Brandl (2006), the maximum power for heating and cooling was 95 and 67 kW, respectively. The average energy extracted and injected for heating and cooling was 175 and 437 MWh/year, respectively.

Fig. 2.21 shows the simulation diagram of monthly cooling and heating energy characterising the year 2009 (Widerin, 2011). It is worth noting that the energy consumption data of the cooling machine in winter are measurement errors. The circulation pump energy consumption is constant over the year. In heating mode the efficiency ratio is 3.34 against 1.25 in cooling mode.

Fig. 2.22 presents the cooling capacity histogram and the seasonal fluid temperature in the absorber pipes over the same year (Brandl, 2006). According to Brandl (2006), sufficient heat can be transferred into the ground to achieve the yearly cooling of the entire metro station.

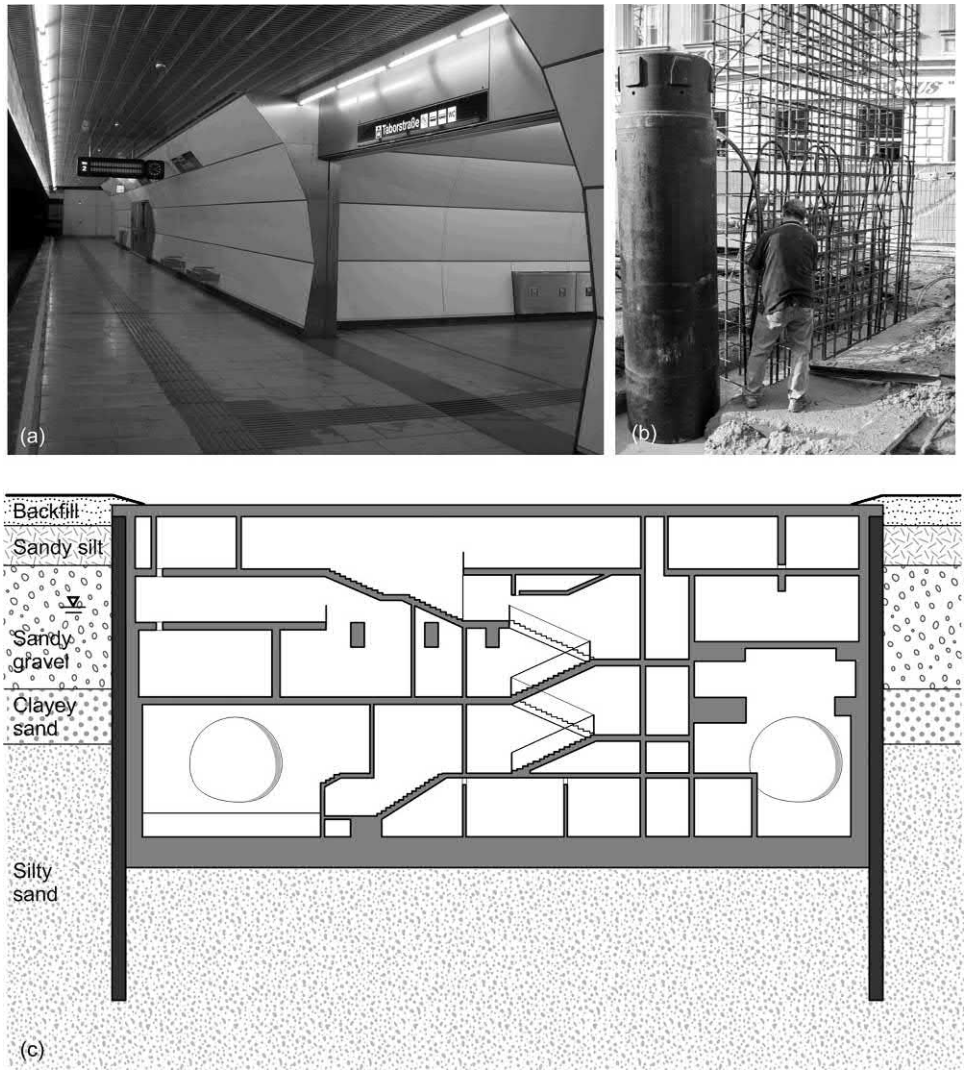

Figure 2.20 (A) Photograph of the Taborstraße energy station, (B) construction phase of an energy wall and (C) sketch of vertical cross section of the station. *(A) Courtesy IGT Geotechnik und Tunnelbau, (B) courtesy IGT Geotechnik und Tunnelbau, (C) redrawn after Brandl, H., 2006. Energy foundations and other thermo-active ground structures. Geotechnique 56(2), 81–122.*

2.7 Physical phenomena and approaches to analysis and design

2.7.1 General

The analysis and design of energy geostructures rely on an appropriate understanding, modelling and prediction of the phenomena that govern the behaviour and performance of the considered technology. Three key physical phenomena characterise energy geostructures: (1) heat transfer, (2) mass transfer and (3) deformation. Heat

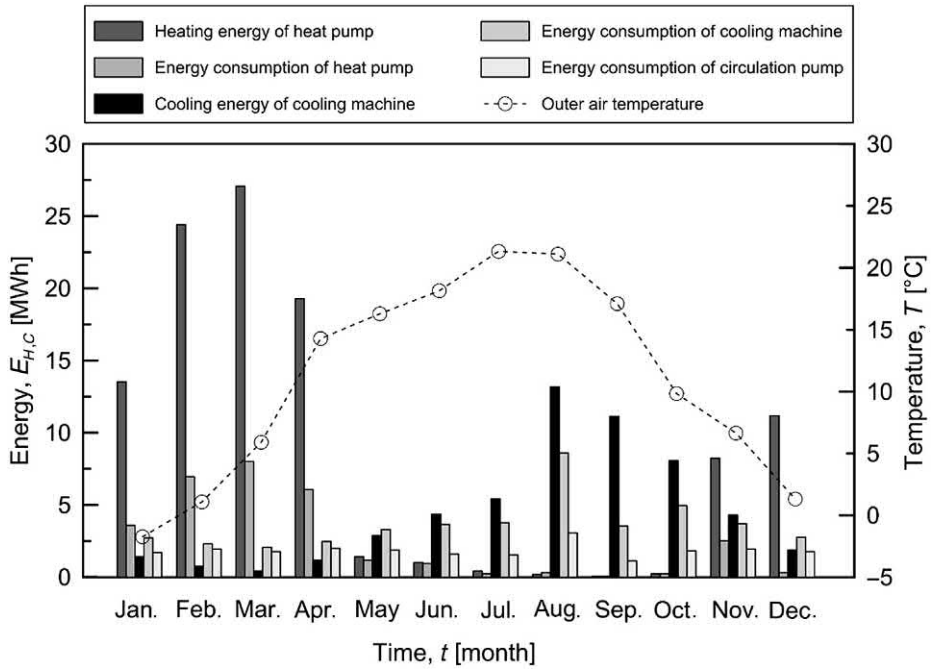

Figure 2.21 Monthly energy and outside temperature associated with the energy operation at the Taborstraße station. *Redrawn after Widerin, B., 2011. Thermiche Nutzung von Verkehrsbauwerken, p. 16.*

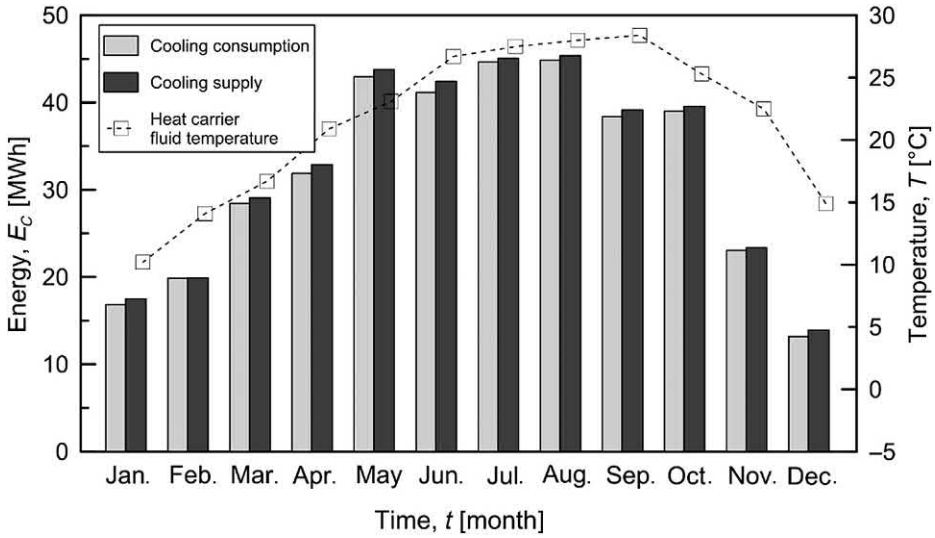

Figure 2.22 Monthly energy and fluid temperature associated with the cooling operation at the Taborstraße station. *Redrawn after Brandl, H., 2006. Energy foundations and other thermo-active ground structures. Geotechnique 56(2), 81–122.*

transfer occurs, for example, in the subsurface between the heat carrier fluid circulating in the pipes, the pipes, the energy geostructure and the ground. Mass transfer characterises the flow of the heat carrier fluid circulating in the pipes embedded in the energy geostructures, the flow of air in underground built environments potentially adjacent to the considered structures (e.g. metro tunnels adjacent to energy tunnels and walls), and the possible flow of groundwater in the subsurface. Deformation affects energy geostructures because of the influence of loadings applied to these structures.

The understanding, modelling and prediction of the aforementioned phenomena rely on the determination of laws that govern such physical evidence as well as to relations between variables involved in these evidences. These (balance) laws and relations are typically termed *governing equations* and *constitutive equations*, respectively. Only when these laws and relations are used to define determined problems can these and all general phenomena be addressed.

2.7.2 Governing and constitutive equations

Governing equations explicate general physical principles that are valid for all materials (solid, fluid and gaseous) and characterise physical phenomena. Constitutive equations are mathematical expressions that relate two physical quantities for describing the behaviour of materials (solid, fluid and gaseous) and characterising physical phenomena. These latter equations are included in the governing equations to complete the description of phenomena of interest with reference to the materials involved, while leaving the governing equations valid a priori.

The relevant physical principles for addressing heat transfer, mass transfer and deformation phenomena through relevant governing equations are the *conservation of energy*, the *conservation of mass* and the *conservation of linear* and *angular momentum*, respectively.

- The principle of conservation of energy states that the time rate of change of the kinetic energy and internal energy for a fixed part of material is equal to the sum of the rate of work done by the surface and body forces and the heat energy entering the boundary surface.
- The global principle of conservation of mass states that the total mass of a fixed part of material should remain constant at all times.
- The global principle of linear momentum states that the total force acting on any fixed part of material is equal to the rate of change of the linear momentum of the part.
- The global principle of moment of momentum states that the total moment about a fixed point of surface and body forces on a fixed part of material is equal to the time rate of change of total moment of momentum of the part about the same point.

Associated with the previous principles are the energy conservation equation, the mass conservation equation and the momentum conservation equations. In some (simple) situations, the energy, mass and momentum conservation equations can be individually solved to address thermal problems involving heat transfer, hydraulic problems involving mass transfer and mechanical problems involving deformation. In general, however, the coupled solution of more than one among the energy, mass and momentum conservation equations may be required for a rigorous treatment of heat transfer, mass transfer and deformation. The reason for this is that heat transfer, mass transfer and deformation are coupled phenomena (i.e. the dependent variables governing them can influence each other to a more or less pronounced extent) and result in couplings in the material behaviour as well.

2.7.3 Modelling approaches serving the analysis and design of energy geostructures

The coupled analysis of heat transfer, mass transfer and deformation and the resulting thermohydromechanical behaviour of materials have been addressed in detail, for example, by Lewis and Schrefler (1987) and Lewis et al. (1996), and relies on a so-called thermohydromechanical modelling approach. While the referenced approach may be considered to be the most accurate for addressing the considered phenomena in the scope of energy geostructures, separate yet coupled analyses of heat transfer and mass transfer as well as of deformation and heat transfer phenomena can be employed. This modelling approach may be particularly effective when the use of a single conservation equation to address the relevant variable governing heat transfer, mass transfer or deformation prevents the analysis of the considered phenomena, and the simultaneous solution of the energy, mass and momentum conservation equations is impractical. In this context thermohydraulic modelling may be employed to address essential aspects of heat and mass transfers, while thermomechanical modelling may be employed to address deformation and heat transfer. These possibilities should be accounted for the analysis and design of energy geostructures.

2.7.4 Problems of interest

In the analysis and design of energy geostructures, two classes of problems may conveniently be distinguished: (1) problems related to heat and mass transfers (and deformation) that occur in the pipes embedded within energy geostructures or in the underground built environments potentially adjacent to such structures (e.g. metro tunnels and railway stations); and (2) problems related to heat and mass transfers, and deformations that characterise the geomaterials constituting energy geostructures and the surrounding ground. Despite relying on the same governing equations, the phenomena involved in the former class of problems are typically addressed from

a *fluid mechanics perspective*, while those involved in the latter class of problems are usually addressed from a *geomechanics and structural mechanics perspective*. The referenced approach involves the mathematical relations employed for investigating the considered aspects being expressed differently for convenience, and using the same formulations may thus hinder their comprehension.

References

ASHRAE, 2009. ASHRAE Handbook: Fundamentals. ASHRAE, Atlanta.

ASHRAE, 2011. ASHRAE Handbook: HVAC Applications. ASHRAE, Atlanta.

Batini, N., Rotta Loria, A.F., Conti, P., Testi, D., Grassi, W., Laloui, L., 2015. Energy and geotechnical behaviour of energy piles for different design solutions. Appl. Therm. Eng. 86 (1), 199–213.

Berga, A., Grimma, M., Stergiaropoulos, K., 2017. Geothermal usage in inner city tunnels – a study of the Fasanenhof subway tunnel in Stuttgart Germany. In: Proceedings of 12th IEA Heat Pump Conference, vol. P.2.7.4.

Brandl, H., 2006. Energy foundations and other thermo-active ground structures. Geotechnique 56 (2), 81–122.

Brandl, H., Adam, D., Markiewicz, R., Unterberger, W., Hofinger, H., 2010. Concrete absorber technology for earth-coupled concrete structures using geothermal energy for the Vienna Underground line U2. Oesterreichische Ingenieur-und Architekten-Zeitschrift 155 (7–12), 193–199.

Buhmann, P., Moormann, C., Westrich, B., Pralle, N., Friedemann, W., 2016. Tunnel geothermics—a German experience with renewable energy concepts in tunnel projects. Geomech. Energy Environ. 8, 1–7.

Denholm, P., Ong, S., Booten, C., 2012. Using utility load data to estimate demand for space cooling and potential for shiftable loads. NREL Technical Report 6A20-54509.

Denholm, P., Jorgenson, J., Miller, M., Zhou, E., Wang, C., 2015. Methods for Analyzing the Economic Value of Concentrating Solar Power with Thermal Energy Storage. National Renewable Energy Lab.(NREL), Golden.

Di Donna, A., Barla, M., Amis, T., 2017. Energy geostructures: analysis from research and systems installed around the world. In: Proceedings of 42nd DFI Conference.

Dincer, I., Rosen, M., 2002. Thermal Energy Storage: Systems and Applications. John Wiley & Sons.

Evans, A., Strezov, V., Evans, T.J., 2012. Assessment of utility energy storage options for increased renewable energy penetration. Renew. Sustain. Energy Rev. 16 (6), 4141–4147.

Fadejev, J., Simson, R., Kurnitski, J., Haghighat, F., 2017. A review on energy piles design, sizing and modelling. Energy 122 (2017), 390–407.

Franzius, J.N., Pralle, N., 2011. Turning segmental tunnels into sources of renewable energy. Proc. Inst. Civ. Eng. Civ. Eng. 164 (1), 35–40.

Frodl, S., Franzius, J.N., Bartl, T., 2010. Design and construction of the tunnel geothermal system in Jenbach/Planung und Bau der Tunnel-Geothermieanlage in Jenbach. Geomech. Tunn. 3 (5), 658–668.

Gao, J., Zhang, X., Liu, J., Li, K.S., Yang, J., 2008. Thermal performance and ground temperature of vertical pile-foundation heat exchangers: a case study. Appl. Therm. Eng. 28 (17–18), 2295–2304.

Ingersoll, L.R., Zabel, O.J., Ingersoll, A.C., 1954. Heat Conduction with Engineering, Geological, and Other Applications. Mc-Graw Hill, New York.

Kalaiselvam, S., Parameshwaran, R., 2014. Thermal Energy Storage Technologies for Sustainability: Systems Design, Assessment and Applications. Elsevier.

Lanahan, M., Tabares-Velasco, P.C., 2017. Seasonal thermal-energy storage: a critical review on BTES systems, modeling, and system design for higher system efficiency. Energies 10 (6), 743.

Lewis, R., Schrefler, B., 1987. The Finite Element Method in the Deformation and Consolidation of Porous Media. John Wiley and Sons.

Lewis, R.W., Morgan, K., Thomas, H., Seetharamu, K., 1996. The Finite Element Method in Heat Transfer Analysis. Wiley.
Nam, Y.J., Gao, X.Y., Yoon, S.H., Lee, K.H., 2015. Study on the performance of a ground source heat pump system assisted by solar thermal storage. Energies 8 (12), 13378–13394.
Narsilio, G.A., Bidarmaghz, A., Colls, S., 2014. Geothermal energy: introducing an emerging technology. In: Proceedings of International Conference on Advances in Civil Engineering for Sustainable Development, pp. 141–154.
Nicholson, D.P., Chen, Q., de Silva, M., Winter, A., Winterling, R., 2014. The design of thermal tunnel energy segments for Crossrail, UK. Proc. Inst. Civ. Eng. Eng. Sustain. 167, 118–134.
Omer, A.M., 2008. Ground-source heat pumps systems and applications. Renew. Sustain. Energy Rev. 12 (2), 344–371.
Pahud, D., Hubbuch, M., 2007a. Measured thermal performances of the energy pile system of the dock midfield at Zürich Airport. In: Proceedings of European Geothermal Congress. Bundesverband Geothermie.
Pahud, D., Hubbuch, M., 2007b. Performances mesurées des pieux énergétiques. Bull. Soc. Suisse Géotherm. 42 (17), 13–14.
Pahud, D., Fromentin, A., Hubbuch, M., 1999. Heat Exchanger Pile System of the Dock Midfield at the Zürich Airport. Office fédéral de l'énergie, Lausanne, Suisse, p. 49.
Rad, F.M., Fung, A.S., 2016. Solar community heating and cooling system with borehole thermal energy storage—review of systems. Renew. Sustain. Energy Rev. 60, 1550–1561.
Rad, F.M., Fung, A.S., Leong, W.H., 2013. Feasibility of combined solar thermal and ground source heat pump systems in cold climate, Canada. Energy Build. 61, 224–232.
Schmidt, T., Mangold, D., 2006. New steps in seasonal thermal energy storage in Germany. In: Proceedings of Ecostock.
SIA-D0190, 2005. Utilisation de la Chaleur du Sol par des Ouvrages de Fondation et de Soutènement en Béton. Guide pour la Conception, la Realisation et la Maintenance. Zurich, Switzerland.
Sterpi, D., Coletto, A., Mauri, L., 2017. Investigation on the behaviour of a thermo-active diaphragm wall by thermo-mechanical analyses. Geomech. Energy Environ. 9, 1–20.
Sweet, M.L., McLeskey, J.T., 2012. Numerical simulation of underground Seasonal Solar Thermal Energy Storage (SSTES) for a single family dwelling using TRNSYS. Sol. Energy 86 (1), 289–300.
Wang, H., Qi, C., 2008. Performance study of underground thermal storage in a solar-ground coupled heat pump system for residential buildings. Energy Build. 40 (7), 1278–1286.
Widerin, B., 2011. Thermiche Nutzung von Verkehrsbauwerken, pp. 16.
Xu, J., Wang, R., Li, Y., 2014. A review of available technologies for seasonal thermal energy storage. Sol. Energy 103, 610–638.
Yunus, A.C., Michael, A.B., 2006. Thermodynamics: An Engineering Approach. McGraw-Hill, New York.

Questions and problems

Statements

a. What are the two fundamental roles of energy geostructures? What is the main difference between energy and conventional geostructures?
b. What are the purposes of the heat exchange that can be established with energy geostructures?
c. Describe the technology of energy geostructures.
d. List typical pipe layouts for energy piles.
e. What is a key difference between pipe layouts applicable to energy tunnels?
f. In designing the pipe layout for energy tunnels, energy walls and other energy geostructures characterised by a significant heat exchange surface, a key aspect is to obtain the lowest heat exchange surface for the selected energy geostructure portion at the highest pressure drop and investment:
  i. True
  ii. False
g. Thermal insulation layers can be foreseen in energy tunnel, wall and slab applications to prevent heat exchange with either the airside or the groundside:
  i. True
  ii. False
h. What are the purposes of the heat exchange that can be established with energy geostructures?
  i. Heating and cooling of superstructures
  ii. Prevent the icing of pavements and decks
  iii. Production of hot water
  iv. Production of electricity
i. List and describe the purpose of two possible applications of energy piles.
j. Describe the components of ground source heat pump systems.
k. How many circuits characterise the ground source heat pump system? To which circuit do energy geostructures belong?
  i. Two circuits. The primary
  ii. Three circuits. The primary
  iii. Two circuits. The secondary
l. The purpose of using a heat pump to heat a built environment through energy geostructures is:
  i. To enhance the heat input that can be extracted from the ground
  ii. To diminish the heat input that can be extracted from the ground
  iii. To equilibrate the heat input that can be extracted from the ground
  iv. None of the above

m. When an energy geostructure is cooled as a consequence of its geothermal operation, the building is:
  - **i.** Cooled
  - **ii.** Heated
  - **iii.** Heated and cooled
  - **iv.** None of the above

n. Describe the rationale of using heat pumps or reversed heat pumps, and the components of basic heat pumps.

o. Define mathematically the coefficient of performance and specify the meaning and unit measure of each factor involved in this definition. What does the coefficient of performance physically represent?

p. How is the seasonal factor of performance defined and in which situations may its use be more convenient than resorting to the coefficient of performance?

Solutions

a. To couple the role of the structural support with that of the geothermal heat exchanger. Conventional geostructures serve only for the former role.

b. The purposes of the heat exchange that can be established with energy geostructure consists of (i) heating and cooling superstructures to reach comfort levels in the built environment; (ii) contributing to the production of hot water for anthropogenic, agricultural or tank-farming uses; (iii) providing heat to prevent the icing of pavements and decks of infrastructures such as roads, bridges, station platforms and airport runways; and (iv) storing the heat in the subsurface for a successive use.

c. Energy geostructures are typically made of reinforced concrete. Pipes are fixed along their reinforcing cage or are placed within the filling material. Pipes are usually made of high-density polyethylene and characterised by a diameter of 20−40 mm with a wall thickness of 2−4 mm. Two or more pipe loops can be installed in series or in parallel and fluid is used as a thermal energy carrier. The heat carrier fluid usually consists of water, water with antifreeze (glycol) or a saline solution.

d. Examples of pipe configurations for energy piles include the single U-shaped, bent U-shaped, parallel double U-shaped, series double U-shaped, multi U-shaped, indirect double, W-shaped, spiral (or helix) and coaxial pipe configurations.

e. When dealing with energy tunnels, configurations involving pipes oriented perpendicular or parallel to the axial direction of the tunnel can be foreseen.

f. In designing the pipe layout for energy tunnels, energy walls and other energy geostructures characterised by a significant heat exchange surface, a key aspect is to obtain the lowest heat exchange surface for the selected energy geostructure portion at the highest pressure drop and investment:

i. True

ii. False

g. Thermal insulation layers can be foreseen in energy tunnel, wall and slab applications to prevent heat exchange with either the airside or the groundside:

i. True

ii. False

h. What are the purposes of the heat exchange that can be established with energy geostructures?

i. Heating and cooling of superstructures

ii. Prevent the icing of pavements and decks

iii. Production of hot water

iv. Production of electricity

i. Heat extraction: heat is extracted from the ground in the cool season to heat the built environment, cooling the energy geostructure;

Heat injection: heat is injected in the ground in the warm season to cool the built environment, heating the energy geostructure;

Heat extraction and heat injection: heat is extracted in the cool season to heat the built environment and injected in the warm season to cool the built environment, cooling and heating the energy geostructure, respectively;

Heat injection for storage purposes: heat (usually arising from thermal solar panels) is injected in the ground (usually during the warm period) for a successive use of the superstructure (usually during the cool period), heating the energy geostructure.

j. Ground source heat pump systems comprise a primary and a secondary circuit. The primary circuit includes the ground heat exchanger while the secondary circuit characterises the built environment to be heated or cooled. In between these two circuits, electrically driven machines such as a heat pump or reversed heat pump can be employed.

k. How many circuits characterise the ground source heat pump system? To which circuit do energy geostructures belong?

i. Two circuits. The primary

ii. Three circuits. The primary

iii. Two circuits. The secondary

l. The purpose of using a heat pump to heat a built environment through energy geostructures is:
  i. To enhance the heat input that can be extracted from the ground
  ii. To diminish the heat input that can be extracted from the ground
  iii. To equilibrate the heat input that can be extracted from the ground
  iv. None of the above

m. When an energy geostructure is cooled as a consequence of its geothermal operation, the building is:
  i. Cooled
  ii. Heated
  iii. Heated and cooled
  iv. None of the above

n. The rationale of using heat pumps is based on the thermodynamic principle that fluids become warmer when they are compressed into a smaller volume. The opposite is true for reversed heat pumps – fluids become cooler when they are expanded.

Simple heat pumps consist of four main devices: the evaporator, the compressor, the condenser and the expansion valve.

o. The coefficient of performance, *COP*, is defined as

$$COP = \frac{\text{Energy output after heat pump operation [kW]}}{\text{Energy input for heat pump operation [kW]}}$$

The *COP* is a device parameter that defines how many units of heat can be obtained using one unit of electricity.

p. The seasonal factor of performance is defined as a ratio between the energy output usable from the energy system and the energy input of the energy system. Compared to the coefficient of performance, this factor includes not only the energy of the heat pump but also that of other energy-consuming elements.

PART B

Fundamentals

CHAPTER 3

Heat and mass transfers in the context of energy geostructures

3.1 Introduction

Heat and mass transfer phenomena arise because of the gradient of variables and may be considered independently from each other. Heat transfer characterises the thermal behaviour of materials and is often associated with the influence of thermal loads. Mass transfer characterises the hydraulic behaviour of materials and is often associated with the influence of hydraulic loads. However, heat and mass transfers are coupled phenomena: one phenomenon (i.e. the flow) can be triggered by the gradient of the variable typically associated with the other phenomenon. That is heat transfer can trigger mass transfer and the opposite is true.

Heat and mass transfer phenomena crucially characterise energy geostructures through the thermohydraulic response of the materials involved. Understanding the physical principles governing heat and mass transfers, and accounting in a suitable way for the coupling between these phenomena in the analysis and design of energy geostructures is crucial.

This chapter presents a theoretical treatment of heat and mass transfers in the context of energy geostructures. The topic is addressed by focusing on the features of heat and mass transfers that may be considered for the characterisation of the thermohydraulic behaviour of materials and the related analysis and design of energy geostructures. Comments on the coupling between heat and mass transfers are also provided.

To this aim, *idealisations and assumptions* are presented first: in this context, the objective is to propose a summary of the conceptual descriptions and hypotheses that are employed for describing heat and mass transfer phenomena. Second, *principles of heat transfer* are described: the purpose of this part is to characterise the physical phenomenon of heat transfer in the context of the analysis and design of energy geostructures. Third, *conduction, convection* and *radiation* are addressed: the purpose of this part is to discuss salient features of the considered modes of heat transfer. Next, the *energy conservation equation* and the associated *initial and boundary conditions* are presented: in this framework, the aim is to propose mathematical expressions that allow the modelling of any given heat transfer problem together with the use of initial and boundary conditions. The *principles of mass transfer* are subsequently discussed: the purpose of this section is to describe the fundamentals of the considered physical phenomenon.

Analysis and Design of Energy Geostructures
DOI: https://doi.org/10.1016/B978-0-12-816223-1.00003-5

Later, *laminar and turbulent flows* and the problem of *seepage flow* are addressed: the purpose of this part is to expand on the regimes that govern mass transfer as well as on the phenomenon of groundwater flow. Then, the *mass conservation equation* and the associated *initial and boundary conditions* are presented: the goal of this digression is to progress with the understanding and mathematical modelling of mass transfer. Next, *boundary layers in flow problems* are discussed: the aim in this context is to characterise the considered subjects in view of their influence on the operation of energy geostructures. Afterward, the *momentum conservation equation* is considered: the aim of this section is to complete the mathematical description of mass transfer phenomena for situations in which the equilibrium of the moving fluid is accounted for. Finally, *questions and problems* are proposed: the purpose of this part is to fix and test the understanding of the subjects covered in this chapter by addressing a number of exercises.

3.2 Idealisations and assumptions

Different materials characterise energy geostructure applications. These materials include, for example (1) the soil or rock surrounding energy geostructures, (2) the concrete constituting energy geostructures, (3) the steel reinforcing energy geostructures, (4) the plastic material constituting the pipes embedded in energy geostructures, (5) the heat carrier fluid circulating in the pipes and (6) the air in a built environment adjacent to energy geostructures.

In principle all of the aforementioned materials can be characterised by different constituents and are heterogeneous at all scales, that is characterised by properties that vary in space. Geomaterials such as soil, rock and concrete contain solid particles and pores typically filled with water and air, with the solid particles consisting of different solid components that may differ, for example in size, shape, mineralogy and behaviour. Reinforcing steel and plastic pipes are characterised by impurities in the form of pores filled with air. The heat carrier fluid circulating in the pipes of energy geostructures and the air flowing in an adjacent built environment can be characterised by impurities in the form of solid particles.

In practice, heterogeneous materials can be modelled via the *continuum medium idealisation* as if they were *homogeneous*, that is characterised by properties that do not vary in space. The main advantage of this approach is that governing equations and constitutive equations can be applied to describe the behaviour and phenomena characterising such materials from a continuum perspective, with reference to an elementary volume (see, e.g. Timoshenko and Goodier, 1951; Lai et al., 2009).

An approach for describing the behaviour and phenomena characterising materials from a continuum perspective, without being influenced by their actual heterogeneities, relies on the concept and the definition of a so-called '*Representative Elementary Volume*' (REV). The REV concept, originally proposed by Lorentz (1952), is defined

in such a way: (1) it assumes evenly distributed material constituents in space; (2) it representatively describes the material characteristics via homogeneous *effective properties* associated with all points of the medium; and (3) it neglects heterogeneity at smaller scales. Typically, the linear scale characterising the REV needs to be much smaller than the scale of the global problem considered and much greater than the scale of the motion of the particles that compose the material. The previous requirements ensure that the size selected for the REV removes the effect of inhomogeneity at smaller scales (e.g. microscopic) without eliminating the potential inhomogeneity at greater scales (e.g. macroscopic) (see, e.g. Vulliet et al., 2016). This fact includes that as far as the REV is independent of time and location within the medium, the different equations established are independent of the geometry of the REV. In the following, the REV concept is employed to describe materials in their solid, liquid, or gaseous state.

When dealing with the analysis of geomaterials, the REV concept is often applied in conjunction with the concept of volume fraction, which represents the essence of the theory of porous media expanded by Bedford and Drumheller (1983) and De Boer and Ehlers (1988). In this context, the REV is composed of the sum of the volumes of any different subregions constituting it according to their volume fraction. In the following the volume fraction concept is employed to describe geomaterials.

Based on the above, reference is made in the following to continuous and homogeneous materials that are characterised by at least one phase. Soil, rock and concrete are assumed as multiphase materials characterised by one solid phase constituted by the material particles and one fluid phase constituted by water or air (cf. Fig. 3.1); in other words, partially saturated geomaterials are not considered, while materials fully saturated with a fluid are accounted for. Steel and plastic are assumed to be materials characterised by a unique solid phase. The fluid circulating in the pipes of energy geostructures is assumed in the simplest case to be characterised by a unique liquid phase constituted by water, but more generally by a liquid mixture constituted by water and an antifreeze liquid. The fluid flowing in built environments adjacent to energy geostructures is characterised by one gaseous phase constituted of air.

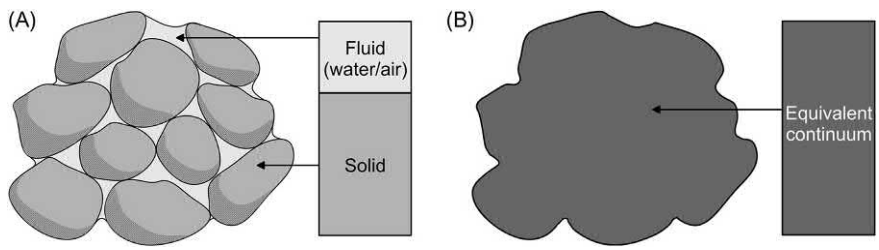

Figure 3.1 (A) Typical multiphase representation of a coarse-grained matrix of geomaterial and (B) equivalent continuum homogenisation.

The hypothesis for geomaterials to be characterised by only one fluid phase of water or air, which involves completely dry or fully saturated conditions with water, may be approximate to describe practical problems. While theories and modelling approaches are available to address this problem (see, e.g. Fredlund et al., 1993), they currently remain out of the scope of this book. Table 3.1 reports a summary of so-called index properties that relate the phases, masses M_i (or weights W_i) and volumes V_i of geomaterials.

In addition to the previous hypotheses, unless otherwise specified, reference is made in the following to materials that are *isotropic*, that is characterised by properties that are the same in all directions in space. When dealing with soil, rock and concrete, the hypothesis of isotropy may be approximate in some cases. However, when applied with judgement, the considered assumption has been largely proven to be effective in modelling the behaviour of materials and the related physical phenomena, and for this reason it is employed in the following.

Once effective properties are defined for continua, interest may lie in determining equivalent properties of composite materials, such as reinforced concrete. In those situations it is assumed that the equivalent property $\aleph$ of a composite material can be determined from the average of the effective properties $\aleph_i$ of the single materials i over representative dimensions x_i (lengths, surfaces, volumes) characterising the composite material of interest with reference to the total reference dimension x. This approach involves

$$\aleph = \sum_i \frac{\aleph_i x_i}{x} \tag{3.1}$$

3.3 Principles of heat transfer

Heat transfer is the physical phenomenon for which energy is transferred between any two particles of matter that are at different temperatures. There are three *modes of heat transfer* considered in the following: *conduction*, *convection* and *radiation*. Additional heat transfer phenomena caused, for example by latent processes that result from phase variations of material constituents exist. However, from an engineering perspective, latent heat transfer processes are considered negligible for the analysis and design of energy geostructures.

Heat transfer phenomena can be quantified and analysed in terms of suitable *rate equations*. These equations express the amount of thermal energy transferred per unit time. Heat transfer cannot be measured directly. However, its occurrence can be quantified through a measurable scalar quantity, that is the temperature, T. Temperature is the variable governing heat transfer. Knowledge of the temperature distribution within a region allows calculating the heat flow within this region (Hermansson et al., 2009). The analysis of the heat transfer in any medium is therefore strictly related to the determination of the temperature distribution within the medium that is subjected to certain boundary and initial conditions.

Table 3.1 Typical parameters relating phases, masses and volumes.

Fundamental variable	Unit measure	Mathematical formulation	Meaning of involved terms
Unit bulk weight (or weight per unit volume), γ	N/m^3	$\gamma = \frac{W}{V}$	W is the total weight of the material V is the total volume of the material
Bulk density, ρ	g/m^3	$\rho = \frac{M}{V} \equiv \frac{\gamma}{g}$	M is the total mass of the material g is the acceleration of gravity (9.81 m/s^2, often considered as 10 m/s^2)
Water content, w_n	%	$w_n = \frac{W_w}{W_s}$	W_w is the weight of the water W_s is the weight of the solid particles
Unit weight of solid particles, γ_s	N/m^3	$\gamma_s = \frac{W_s}{V_s}$	V_s is the volume of the solid particles
Density of solid particles, ρ_s	g/m^3	$\rho_s = \frac{M_s}{V_s} \equiv \frac{\gamma_s}{g}$	M_s is the mass of the solid particles
Unit weight of water, γ_w	N/m^3	$\gamma_w = \frac{W_w}{V_w}$	V_w is the volume of the water
Density of water, ρ_w	g/m^3	$\rho_w = \frac{M_w}{V_w} \equiv \frac{\gamma_w}{g}$	M_w is the mass of the water
Derived variable	**Unit measure**	**Mathematical formulation**	**Meaning of involved terms**
Dry unit weight, γ_d	N/m^3	$\gamma_d = \frac{W_s}{V} \equiv \frac{\gamma}{1+w_n} \equiv \frac{\gamma_s}{1+e}$	e is the void ratio
Dry density, ρ_d	g/m^3	$\rho_d = \frac{M_s}{V} \equiv \frac{\rho}{1+w_n} \equiv \frac{\rho_s}{1+e}$	
Porosity, n	–	$n = \frac{V_a+V_w}{V} = 1 - \frac{\gamma_d}{\gamma_s} = \frac{e}{1+e}$	V_a is the volume of the air
Void ratio, e	–	$e = \frac{V_a+V_w}{V_s} = \frac{\gamma_s}{\gamma_d} - 1 = \frac{n}{1-n} = \frac{w_n\gamma_s}{\gamma_w S_r}$	S_r is the degree of water saturation
Degree of saturation, S_r	%	$S_r = \frac{V_w}{V_a+V_w} = \frac{w_n\gamma_d}{\gamma_w n} = \frac{\gamma_s w_n}{\gamma_w e}$	
Saturated unit weight, γ_{sat}	N/m^3	$\gamma_{sat} = n\gamma_w + (1-n)\gamma_s = n\gamma_w + \gamma_d = \frac{\gamma_s + e\gamma_w}{1+e}$	
Saturated density, ρ_{sat}	g/m^3	$\rho_{sat} = n\rho_w + (1-n)\rho_s = \frac{\rho_s + e\rho_w}{1+e}$	
Buoyant unit weight, γ'	N/m^3	$\gamma' = \gamma_{sat} - \gamma_w$	

3.4 Conduction

3.4.1 Physical phenomenon and governing equation

Conduction is the mode of heat transfer that occurs at the molecular and atomic levels between particles of a solid or a fluid that are at different temperatures. This mode of heat transfer is generally associated with a macroscopically invisible motion of the particles that constitute the medium and is related to the mechanism of energy *diffusion*.

The physical phenomenon of conduction can be explained, for example with reference to the motion of molecules characterising a medium bounded by two surfaces, which at a meaningful scale can be considered plane walls at different temperatures. This problem is represented in Fig. 3.2 considering a conduction phenomenon that can characterise, for example an energy pile. The continuous collision of molecules involves a transfer of energy from the more energetic regions of the system (at higher temperature) to the less energetic regions of the system (at lower temperature) according to thermodynamics. The motion of molecules through the surfaces allows establishing a net transfer of energy in the system, which is associated with conduction. In gases the molecules involved in the molecular interactions are less closely spaced than in liquids and are characterised by less frequent and lower interactions. In solids atomic activity in the form of lattice vibrations governs conduction. The previous facts indicate that conduction heat transfer is more pronounced in solids than in fluids.

The rate equation governing conduction is *Fourier's law*. According to this law, the heat flux density (i.e. the rate of heat energy, Q, transferred through a given surface, A, per unit time, t) generated by conduction, $\dot{q}_{cond,i}$, for a medium that possesses homogeneity and isotropy with respect to the heat conduction phenomenon, is

$$\dot{q}_{cond,i} = \frac{Q}{At} = \frac{\dot{Q}}{A} = -\lambda \nabla T = -\lambda \left(\frac{\partial T}{\partial x}\hat{e}_x + \frac{\partial T}{\partial y}\hat{e}_y + \frac{\partial T}{\partial z}\hat{e}_z \right) \tag{3.2}$$

where λ is the thermal conductivity of the medium (the parameter, i.e. a positive scalar quantity, that governs heat conduction), ∇ is the vector differential operator (gradient) and $\hat{e}_x$, $\hat{e}_y$ and $\hat{e}_z$ are the standard unit vectors in Cartesian (also termed

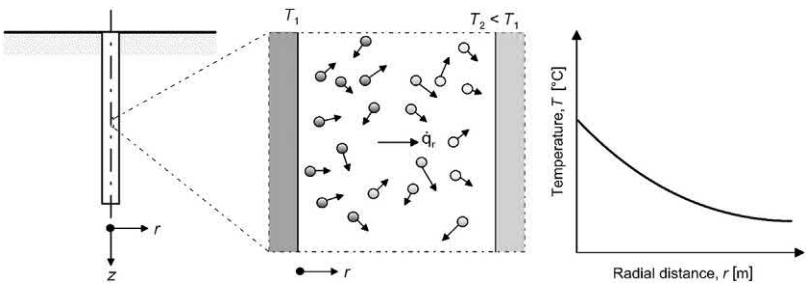

Figure 3.2 Heat transfer by conduction in an energy pile.

rectangular) coordinates. The assumption of homogeneity and isotropy indicates that the thermal conductivity is independent of direction and position and for this reason appears outside the argument of the gradient.

In Eq. (3.2), the minus sign makes the heat flux density a positive quantity as a consequence of its direction towards decreasing temperature. The law expressed in Eq. (3.2) was first stated based on experimental evidence by Fourier (1822) but may be derived from the principles of irreversible thermodynamics as well (Boley and Weiner, 1997).

Fourier's law expresses that thermal equilibrium can only be achieved when no temperature gradient occurs. In other words, heat flows as far as there is a temperature gradient.

Fourier's law can be markedly simplified for problems involving plane geometries under steady-state conditions. These situations may characterise, for example energy walls (cf. Fig. 3.3). In this case, the temperature distribution across the wall is linear and the heat flux in the direction of heat transfer, x, reads

$$\dot{q}_x = -\lambda \frac{dT}{dx} = -\lambda \frac{(T_2 - T_1)}{t_w} = \frac{\lambda(T_1 - T_2)}{t_w} \tag{3.3}$$

where T_2 and T_1 are the temperatures of the inner and outer surface of the wall and t_w is the wall thickness. It is worth noting that Eq. (3.3) provides the heat flux, that is the rate of heat transfer per unit area of wall, A. The heat rate (or thermal power) may be calculated at any time by multiplying $\dot{q}_x$ by the area of wall perpendicular to the direction of heat transfer as $\dot{Q}_x = \dot{q}_x A$.

3.4.2 Thermal conductivity values

The thermal conductivity of materials is strongly characterised by the chemical composition of the material constituents as well as by physical factors that influence the

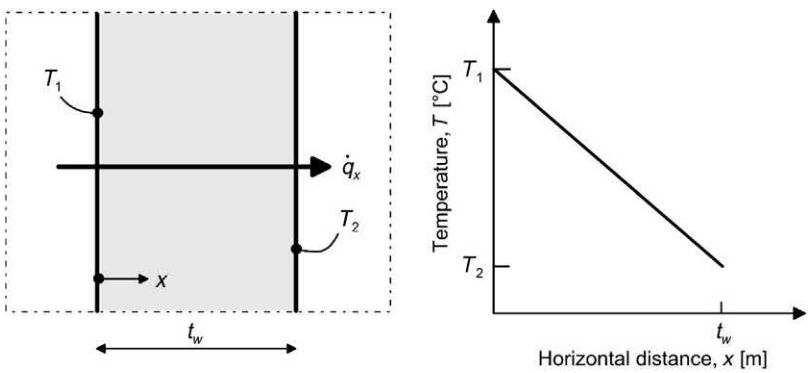

Figure 3.3 Conduction heat transfer across a plane energy wall.

material density. For soils the thermal conductivity markedly depends on (1) mineralogy, (2) dry density, (3) water content and (4) gradation (see, e.g. Brandon and Mitchell, 1989; Alrtimi et al., 2016; Vulliet et al., 2016). For concrete the thermal conductivity markedly depends on (1) aggregate types and sources (and thus mineralogy), (2) dry density, (3) water content and (4) mix proportioning (see, e.g. Morabito, 1989; Lanciani et al., 1989; Neville, 1995; Kim et al., 2003). Mineralogy is representative of the origin and chemical composition of the material. Dry density is representative of the compaction state of the material. Water content yields information on the wetting of the medium. Gradation is a feature typically related to the granulometric curve of soils representing their particle size distribution (the shape of particles being complementary information to gradation for characterising the morphology of the material). Mix proportioning represents the proportions of the ingredients used in the mix design of concrete.

The significance of the aforementioned factors in the estimation of the thermal conductivity of geomaterials, such as soil, rock and concrete, can be shown by referring to Table 3.2, which presents values of thermal conductivity, λ_i, summarised by Loveridge (2012) for common constituents i of geomaterials:

1. Among the considered minerals, Quartz can have a thermal conductivity of up to approximately five times that of the others. For this reason, soils, rocks and concretes characterised by different mineralogy can have markedly different values of thermal conductivity.

Table 3.2 Thermal conductivity of geomaterials constituents.

Material	Thermal conductivity, λ_i [W/(m °C)]
Air	0.024
Water	0.6
Feldspar	1.4–2.5
Plagioclase	1.5–2.0
Mica	1.6–3.5
Amphibole	2.8–4.8
Garnet	3.1–5.5
Olivine	3.2–5.0
Pyroxene	3.5–5.7
Calcite	3.6
Chlorite	5.2
Quartz	7.7

Source: Data from Banks, D., 2012. An Introduction to Thermogeology: Ground Source Heating and Cooling. John Wiley & Sons, Côté, J., Konrad, J.-M., 2005. A generalized thermal conductivity model for soils and construction materials. Can. Geotech. J. 42 (2), 443–458 and Midttømme, K., Banks, D., Kalskin Ramstad, R., Sæther, O.M., Skarphagen, H., 2008. Ground-source heat pumps and underground thermal energy storage: energy for the future. NGU Spec. Publ. 11, 93–98, after Loveridge, F., 2012. The Thermal Performance of Foundation Piles Used as Heat Exchangers in Ground Energy Systems (Ph.D. Thesis). University of Southampton.

Table 3.3 Typical values of soil porosity.

Soil type		Porosity range, n [−]
Uniform materials	Equal spheres (theoretical values)	$0.26 < n < 0.48$
	Standard Ottawa sand	$0.33 < n < 0.44$
	Clean, uniform sand (fine or medium)	$0.29 < n < 0.50$
	Uniform, inorganic silt	$0.29 < n < 0.52$
Well-graded materials	Silty sand	$0.23 < n < 0.47$
	Clean, fine to coarse sand	$0.17 < n < 0.49$
	Micaceous sand	$0.29 < n < 0.55$
	Silty sand and gravel	$0.12 < n < 0.46$
Mixed soils	Sandy or silty clay	$0.20 < n < 0.64$
	Skip-graded silty clay with stones or rock fragments	$0.17 < n < 0.50$
	Well-graded gravel, sand, silt and clay mixture	$0.11 < n < 0.41$
Clay soils	Clay (30%−50% clay sizes)	$0.33 < n < 0.71$
	Colloidal clay (0.002 mm > 50%)	$0.37 < n < 0.92$
Organic soils	Organic silt	$0.35 < n < 0.75$
	Organic clay (30%−50% clay sizes)	$0.41 < n < 0.81$

Source: Modified after Rees, S., Adjali, M., Zhou, Z., Davies, M. & Thomas, H., 2000. Ground heat transfer effects on the thermal performance of earth-contact structures. Renew. Sustain. Energy Rev. 4 (3), 213−265.

2. In general, the denser the soil, rock, or concrete is, the smaller the pores and the greater the contact points between solid grains are [typical values of porosity, n, which are intrinsically related to dry density, ρ_d, are reported for soils in Table 3.3 with reference to the work of Rees et al. (2000)]. The thermal conductivity of minerals is greater than that of water and air. For this reason, the greater the dry density of geomaterials is for the same fluid filling the pores, the higher the overall effective thermal conductivity of the medium will be.
3. Since water has a higher thermal conductivity than air, a geomaterial with pores filled with water is characterised by a higher thermal conductivity than the same material with the pores filled with air. The different magnitude between the thermal conductivity of minerals, water and air also indicates that conduction heat transfer primarily occurs between the solid particles rather than through the fluid phase(s) (cf. Fig. 3.4). This phenomenon is particularly pronounced when a porous material is completely dry and heat flows mainly through the contact points between the grains instead of through the air-filled pores because of the greater thermal conductivity of the grains compared to that of the air. This phenomenon still characterises porous materials with increasing water content, although the presence of water layers of increasing thickness that cover the solid particles until the pores are completely filled with water indicates a more significant proportion of heat flowing in the water-filled pores compared to a dry case. A typical relationship

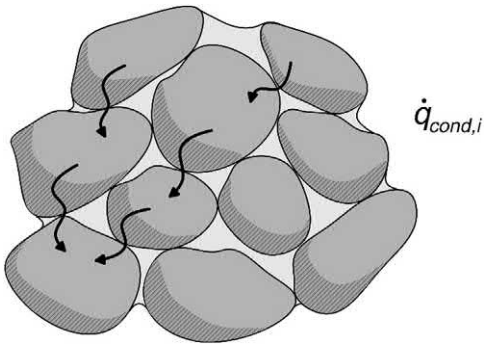

Figure 3.4 Sketch of the typical, primary component of conduction heat transfer in a geomaterial.

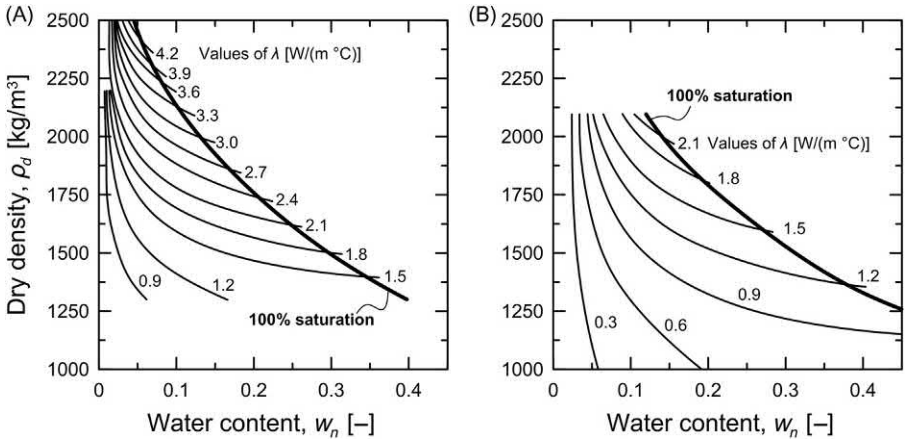

Figure 3.5 Typical relationship for an unfrozen (A) coarse-grained soil and (B) fine-grained soil. *Redrawn after Brandl, H., 2006. Energy foundations and other thermo-active ground structures. Geotechnique 56 (2), 81–122.*

between dry density and water content for coarse- and fine-grained soils is presented in Fig. 3.5 with reference to the data presented by Brandl (2006).

4. In addition to the influence of dry density on the number of small pores and contact points, the gradation of a soil (e.g. coarse-grained soil) plays also a major role in the variation of thermal conductivity. In fact the number of small pores and contact points between grains increases with the more diverse granulometric composition of the soil. Therefore the more well-graded soils are, the higher the thermal conductivity is. This phenomenon finds a comparable influence with respect to the features of the mix design proportioning in concrete.

The influence of all of the aforementioned variables should be considered when estimating the thermal conductivity of soil, rock and concrete in the analysis

and design of energy geostructures. In addition to the previous variables, a dependence of thermal conductivity of soil, rock and concrete on time (through the so-called phenomenon of ageing) and temperature can be highlighted. In fact a variation of these variables leads to a change in the size of the material pores (via, e.g. cementation and thermal expansion of the solid grains because of the former and latter variable, respectively), which can modify the effective value of thermal conductivity of the material. In principle the thermal conductivity of soils can increase as a consequence of ageing (Brandon and Mitchell, 1989) and an increase in temperature (Hiraiwa and Kasubuchi, 2000), whereas that of concrete does not sensibly vary (Kim et al., 2003) or decreases (Shin et al., 2002) as a consequence of ageing and an increase in temperature, respectively. In practice the effect of ageing can be significant only in specific applications and the effect of temperature can be significant for temperature variations that do not characterise energy geostructure applications (e.g. greater than 80°C−100°C). Based on the previous comments, the influence of ageing and temperature on the variation of the thermal conductivity of geomaterials may be neglected for the analysis and design of energy geostructures.

Typical values of thermal conductivity for relevant materials are reported in Table 3.4. The thermal conductivity of soils typically varies between 0.2 and 3 W/(m °C) and can achieve values of 3.5 W/(m °C). The thermal conductivity of rocks can achieve values greater than 5 W/(m °C). Steel has a much greater thermal conductivity than soils, rocks and concrete, while the polyethylene characterising the pipes embedded in energy geostructures usually has a lower thermal conductivity than the previous materials.

In many instances, the effective thermal conductivity of porous materials, such as soils, rocks and concrete, assumed to be isotropic and with pores fully filled with a fluid, can be evaluated as

$$\lambda = \lambda_f n + \lambda_s(1 - n) \tag{3.4}$$

where λ_f is the thermal conductivity of the general fluid filling the pores of the material and λ_s is the thermal conductivity of the solid particles. For materials with pores fully saturated with water, λ_f is replaced by the thermal conductivity of the water λ_w. The same approach may be applied to materials with pores fully saturated with air by using the thermal conductivity of the air λ_a. When a dry material is however characterised by relatively low values of porosity, for example $n \leq 0.2$, the contribution of the thermal conductivity of air in the calculation of the effective thermal conductivity is often neglected because it plays a limited role in the final result. A number of mathematical expressions for the estimation of the effective thermal conductivity of geomaterials are reported in Table 3.5.

Table 3.4 Thermal conductivity of materials characterising energy geostructures.

Material	Thermal conductivity, λ [W/(m °C)]	
	Dry	Saturated
Clay	0.4–1.0	0.9–2.3
Silt	0.4–1.0	0.9–2.3
Sand	0.3–0.8	1.7–5.0
Gravel	0.4–0.5	1.8
Peat	0.2–0.7	
Claystone/siltstone	1.1–3.5	
Sandstone	1.3–5.1	
Quartzite	3.6–6.6	
Marl	1.5–3.5	
Limestone	2.5–4.0	
Argillaceous schists	1.5–2.1	
Micaschists	1.5–3.1	
Metaquartzite	5.8	
Marble	1.3–3.1	
Gneiss	1.9–4.0	
Rhyolithe	3.1–3.4	
Peridotite	3.8–5.3	
Granite	2.1–4.1	
Gabbro	1.7–2.5	
Diorite	2.0–2.9	
Basalt	1.3–2.3	
Concrete	0.9–2.0	
Steel	14–60	
Polyethylene (low-density)	0.39	

Source: Data from Pahud, D., 2002. Geothermal Energy and Heat Storage. Laboratorio di Energia, Ecologia ed Economia, Canobbio.

3.4.3 Remarks about conduction

Conduction dominates heat transfer in materials that are characterised by potential pore sizes negligibly small in relation to the considered solid volume. Based on this consideration:

- Heat transfer in reinforced concrete is generally dominated by conduction for the features of the concrete mix design and the steel that are likely to characterise energy geostructures. Conduction also governs the heat exchange across the thickness of the pipes embedded in energy geostructures.
- Heat transfer in soils is often dominated by conduction. However, considering the specific features of any considered site is essential to verify the validity of the previous statement. For example these features include the size of the solid particles and

Table 3.5 Examples of mathematical expressions available to define the thermal conductivity of materials characterising energy geostructures.

Reference	Material	Expression	Comments
Rees et al. (2000)	General soil	$\lambda = \chi_1 \lambda_1 + \chi_2 \lambda_2$	This expression is valid for the thermal conductivity of a soil where soil constituents have a distribution parallel to the direction of heat flow. It represents the 'weighted arithmetic mean' of the thermal conductivity of a soil characterised by (1) a solid phase and (2) a fluid phase, respectively, and can results in an overestimate of this parameter. In the expression, λ_1 and λ_2 are the thermal conductivities of phases 1 and 2, respectively; χ_1 and χ_2 are the volume fractions of phases 1 and 2, respectively, with (for a geomaterial fully saturated with a fluid) $\chi_1 = 1 - n$ the solid fraction and $\chi_2 = n$ the fluid fraction, where n is the porosity.
	General soil	$\lambda = \frac{\lambda_1 \lambda_2}{\chi_1 \lambda_2 + \chi_2 \lambda_1}$	This expression is valid for the thermal conductivity of a soil where soil constituents have a distribution perpendicular to the direction of heat flow. It represents the 'weighted harmonic mean' of the thermal conductivity and can result in an underestimate of this parameter.
Woodside and Messmer (1961)	General soil	$\lambda = \lambda_1^{\chi_1} \lambda_2^{\chi_2}$	This expression is known as the 'weighted geometric mean' and gives an intermediate result between the arithmetic mean and the harmonic mean.
Hamilton and Crosser (1962)	General soil	$\lambda = \frac{\chi_1 \lambda_1 + \beta_H \chi_2 \lambda_2}{\chi_1 + \beta_H \chi_2}$	In the expression, λ_1 and λ_2 are thermal conductivities of each two phases, respectively; χ_1 and χ_2 are the volume fractions of each two phases respectively, with $\chi_1 + \chi_2 = 1$; and β_H is a parameter defined as $\beta_H = \frac{n_{HC}\lambda_1}{(n_{HC}-1)\lambda_1 + \lambda_2}$ where n_{HC} is the Hamilton–Crosser model coefficient and depends on the phase distribution geometry which has to be determined experimentally. This expression is valid for any generic material constituted by two phases.
Kersten (1949)	Unfrozen sandy soil	$\lambda = \left[0.101 \log w_n + 0.0577\right] \times 10^{0.000624 \rho_d}$	This model can be applied to sandy soils with water content higher than 1% and for soils consisting of silt and clay with water content higher than 7%. The model is valid and recommended for soils with low clay and loam content (20%) (Rerak, 2017). It is particularly applicable to soils primarily consisting of quartz (Farouki, 1986). It may be applied to frozen soils with a maximum water content of 90% (Rerak, 2017).
	Unfrozen loam and clayey soils	$\lambda = \left[0.13 \log w_n - 0.0288\right] \times 10^{0.000624 \rho_d}$	
	Frozen sandy soil	$\lambda = 0.011 \times 10^{0.000812 \rho_d} + 0.00462 \times 10^{0.000911 \rho_d} w_n$	In the expressions, w_n is the soil water content in % and ρ_d is the soil dry density in kg/m^3.
	Frozen loam and clayey soil	$\lambda = 0.00144 \times 10^{0.00137 \rho_d} + 0.0123 \times 10^{0.000499 \rho_d} w_n$	

(*Continued*)

Table 3.5 (Continued)

Reference	Material	Expression	Comments
Gemant (1952)	Fine- and coarse-grained soils	$\frac{1}{\lambda}=\frac{\left[\frac{(1-a)}{a}\right]^{\frac{1}{3}}\tan^{-1}\left[\frac{(\lambda_s-\lambda_w)}{\lambda_w}\right]^{\frac{1}{2}}}{\left(\frac{h_1}{2}\right)^{\frac{1}{3}}[\lambda_w(\lambda_s-\lambda_w)]^{\frac{1}{2}}}+\frac{(1-z_G)}{\lambda_s a}f\left\{\frac{b^2}{a}\right\}$	This is an expression for a general moist soil, with water surrounding the soil particles and forming thermal bridges. In the expression, h_1 is the 'apex' water (water collected around the contact points) that can be calculated as $h_1=9.988\times10^{-3}\rho_d w_n-h_0$ where h_0 [−] is the water absorbed as a film around the soil particles, ρ_d is the dry density of the soil expressed in g/cm^3 and w_n is the water content expressed in %. The adsorbed water is a function of temperature and should be recorded from the appropriate diagram. For the temperature of $T=20°C$, it is found $h_0=0.01$. a, b, z_G are shape functions, with: $a=4.869\rho_d^{1/2}$ $b^2=\left(\frac{a}{1-a}\right)^{2/3}\left(\frac{h_1}{2}\right)^{2/3}$ $z_G=\left(\frac{1-a}{a}\right)^{2/3}\left(\frac{h_1}{2}\right)^{1/3}$ The dimensionless function $f\left\{\frac{b^2}{a}\right\}$ can be approximated as (Różański and Stefaniuk, 2016) $f\left\{\frac{b^2}{a}\right\}=\frac{1}{0.976+0.2355\ln\left(\frac{b^2}{a}\right)}$ λ_w and λ_s are the thermal conductivities of the water and the soil particles, respectively.
Makowski and Mochlinski (1956)	General soil	$\lambda=(a_M\log w_n+b_M)10^{z_M}$	This is an empirical expression for a general sand-clay mixture, for which $a_M=0.142408-0.000465c_{\%}$ $b_M=0.04192-0.000313c_{\%}$ $z_M=6.24\rho_d\cdot10^{-4}$ where a_M, b_M and z_M are empirical constants, $c_{\%}$ is the percentage of the clay mineral in the soil and ρ_d is the dry density of the soil expressed in kg/m^3.
Woodside and Messmer (1961)	General soil	$\lambda=(n-0.03)\lambda_w+(1-n+0.03)\left[\frac{1-n}{\lambda_s(1-n+0.03)}+\frac{0.03}{\lambda_w(1-n+0.03)}\right]^{-1}$	This model is based on the so-called three-resistor model.
De Vries (1963)	General soil	$\lambda=\frac{\lambda_w\chi_w+F_a\lambda_a\chi_a+F_s\lambda_s\chi_s}{\chi_w+F_a\chi_a+F_s\chi_s}$	This is a general expression for the thermal conductivity of a soil characterised by three phases: one solid phase (s), one fluid phase constituted by water (w) and one fluid phase constituted by air (a). In the expression, λ_a is the thermal conductivity of the air, χ_w, χ_a, χ_s are the volume fractions of water, air and soil particles, respectively, and F_s and F_a are weighting factors depending on the shape and orientation of the soil particles and the pores filled with air, respectively. These latter factors can be calculated as $F_s=\frac{1}{3}\left(\frac{2}{1+0.125\left(\frac{\lambda_s}{\lambda_w}-1\right)}+\frac{1}{1+0.75\left(\frac{\lambda_s}{\lambda_w}-1\right)}\right)$ $F_a=\frac{1}{3}\left(\frac{2}{1+g_a\left(\frac{\lambda_s}{\lambda_w}-1\right)}+\frac{1}{1+g_c\left(\frac{\lambda_s}{\lambda_w}-1\right)}\right)$ where g_a, g_c are shape factors defined as $g_a=\begin{cases}0.333-\frac{\chi_a}{n}(0.333-0.035)\text{for } 0.09\le\chi_w\le n\\ 0.013+0.944\chi_w \text{ for } 0\le\chi_w\le0.09\end{cases}$ $g_c=1-2g_a$ In this model, the effective thermal conductivity of the air λ_a varies linearly with that of the water λ_w due to humidity $\lambda_a=0.0615+1.9\lambda_w$

Johansen (1977)	General soil	$\lambda = (\lambda_{sat} - \lambda_d)\lambda_e + \lambda_d$	This equation is suitable for both coarse and fine-grained soils in frozen and unfrozen states but is valid only for saturation degrees greater than 5% (preferably greater than 20%). Below this level, it can predict negative thermal conductivities (Haigh, 2012). In the expression, λ_d and λ_{sat} are the dry and saturated thermal conductivities of the soil, respectively, when evaluated at the same dry density expressed in kg/m^3: $\lambda_d = \frac{0.135\rho_d + 64.7}{2700 - 0.94\rho_d} \pm 20$ $\lambda_{sat} = \lambda_s^{1-n}\lambda_w^n$ λ_e is a function representing the influence of the degree of saturation S_r on the thermal conductivity as: $\lambda_e = \begin{cases} 0 \text{ (for a dry soil)} \\ 1 \text{ (for a fully saturated soil)} \\ 0.7\log S_r + 1 \text{ when } S_r > 0.05 \text{ (for coarse unfrozen soils)} \\ \log S_r + 1 \text{ when } S_r > 0.1 \text{ (for fine unfrozen soil)} \end{cases}$
Donazzi et al. (1979)	Sandy soil	$\lambda = \lambda_w^n \lambda_s^{1-n} \exp[-3.08n(1-S_r)^2]$	
Gangadhara Rao and Singh (1999)	Sandy soil	$\lambda = 10^{0.01\gamma - 1}(1.07\log w_n + 0.715)$	This equation predicts thermal conductivities reasonably well for saturation degrees below 0.3, while above this level it significantly underpredicts thermal conductivity (Haigh, 2012). In the expression, γ is the unit weight of the soil expressed in lb/ft^3.
Côté and Konrad (2005)	Sandy soil	$\lambda = \left(\lambda_w^n \lambda_s^{1-n} - \varsigma_1 10^{-\varsigma_2 n}\right)\left[\frac{\varrho S_r}{1 + (\varrho - 1)S_r}\right] + \varsigma_1 10^{-\varsigma_2 n}$	This is a modification of the Johansen's model to eliminate the logarithmic reliance on the saturation degree that distorted predictions of the thermal conductivity at low saturation degrees. In the expression, ς_1 and ς_2 account for particle shape effects, and ϱ accounts for soil texture effect. For fine sand, the authors suggest $\varrho = 3.55$, $\varsigma_1 = 1.7$ W/(m °C) and $\varsigma_2 = 1.8$.
Lu et al. (2007)	Sandy soil	$\lambda = \left[\lambda_w^n \lambda_s^{1-n} - (o_2 - o_1 n)\right]\exp\left[\iota\left(1 - S_r^{\iota - 1.33}\right)\right] + (o_2 - o_1 n)$	This is a further modification of the Johansen's model, for which o_1, o_2 and ι are empirical parameters. For sandy soils, $o_1 = 0.56$, $o_2 = 0.51$, $\iota = 0.96$.
Chen (2008)	Sandy soil	$\lambda = \lambda_w^n \lambda_s^{1-n}[(1-\kappa_1)S_r + \kappa_1]^{\kappa_2 n}$	This is an empirical equation based on 80 needle-probe experimental tests on four types of sandy soils with different degrees of saturation at different porosities. In the expression, κ_1 and κ_2 are empirical parameters obtained from fitting of the measured data. Their suggested values are of $\kappa_1 = 0.0022$ and $\kappa_2 = 0.78$.
Haigh (2012)	Sandy soil	$\frac{\lambda}{\lambda_s} = 2(1+\xi_H)^2\left[\frac{\lambda_{n,w}}{(1-\lambda_{n,w})^2}\ln\frac{(1+\xi_H) + (\lambda_{n,w} - 1)}{\xi_H + \lambda_{n,w}} + \frac{\lambda_{n,a}}{1-\lambda_{n,a}}\ln\frac{(1+\xi_H)}{(1+\xi_H) + (\lambda_{n,a} - 1)x_H}\right] + \frac{2(1+\xi_H)}{(1-\lambda_{n,w})(1-\lambda_{n,a})}\left[(\lambda_{n,w} - \lambda_{n,a})x_H - (1-\lambda_{n,a})\lambda_{n,w}\right]$	This is a model for unidirectional heat flow through a three-phase soil element. The factors ξ_H, $\lambda_{n,i}$ and x_H are given by: $\xi_H = \frac{2e-1}{3}$ $\lambda_{n,w} = \frac{\lambda_w}{\lambda_s}$ $\lambda_{n,a} = \frac{\lambda_a}{\lambda_s}$ $x_H = \frac{(1+\xi_H)}{2}\left(1 + \cos\psi_H - \sqrt{3}\sin\psi_H\right)$ where ψ_H is given by $\cos 3\psi_H = \frac{2(1+3\xi_H)(1-S_r) - (1+\xi_H)^3}{(1+\xi_H)^3}$ and e is the void ratio.

(*Continued*)

Table 3.5 (Continued)

Reference	Material	Expression	Comments
Alrtimi et al. (2016)	Sandy soil	$\lambda = (1-n)\ln\theta_w - 7.75n + 6.83$ $\lambda = 1.025\rho_d - 1.065$	This model is proposed to provide close agreement at dry or nearly dry conditions as well as at high saturations for a sandy soil tested in the referenced study. In the expression, $\theta_w = V_w/V$ is the volumetric water content, where V_w is the volume of water and V is the total volume of the soil. Under dry conditions, the second linear equation of the thermal conductivity shall be used, in which ρ_d is expressed in g/cm^3.
Zoth and Haenel (1988)	Rocks	$\lambda(T) = A_{ZH} + \frac{B_{ZH}}{350+T}$	In the expression, T is the temperature in °C, while A_{ZH} and B_{ZH} are parameters determined from a least-squares fit (Zoth and Haenel, 1988).

Rock type	T [°C]	A [W/(m °C)]	B [W/m]
Rock salt	−20–400	−2.11	2960
Limestones	0–500	0.13	1073
Metamorphic rocks	0–1200	0.75	705
Acid rocks	0–1400	0.64	807
Basic rocks	50–1100	1.18	474
Ultrabasic rocks	20–1400	0.73	1293

Reference	Material	Expression	Comments
Robertson (1988)	Mafic and felsic igneous rocks, sandstone	$\lambda = \lambda_f + (1-n)^2\left[(\lambda_s + m_{\%}S_c) - \lambda_f\right]$	In the expression, λ_f is the pore fluid thermal conductivity, λ_s is the solid rock intercept at $(1-n)^2 = 1$ for zero percent specific mineral content, $m_{\%}$ is the actual percentage of the specific mineral and S_C is a slope constant equal to the change of λ with specific mineral content determined from intercept values obtained from experimental data at $(1-n)^2 = 1$. For mafic igneous rocks:

Solidity, $1-n$ [–]	Pore fluid	Olivine content, $m_{\%}$ [%]	Thermal conductivity, λ [W/(m °C)]	Slope constant, S_C [W/(m °C · %)]
0	Air	0	$\lambda_f = 0.188$	
1	Air	0	$\lambda_s = 1.51$	
1	Air	30	$\lambda_s = 1.96$	0.015
0	Water	0	$\lambda_f = 0.75$	
1	Water	0	$\lambda_s = 1.84$	
1	Water	30	$\lambda_s = 2.60$	0.025

Sass et al. (1992)	Rocks	$\lambda(T) = \frac{\lambda(0)}{1.007 + T\left(3.6 \times 10^{-3} - \frac{7.2 \times 10^{-3}}{\lambda(0)}\right)}$	For felsic igneous rocks: **Solidity, $1 - n$ [–] / Pore fluid / Quartz content $m_{\%}$ [%] / Thermal conductivity, λ [W/(m °C)] / Slope constant, S_C [W/(m °C · %)]** 0 / Air / 0 / $\lambda_f = 0.026$ / 1 / Air / 0 / $\lambda_s = 1.47$ / 1 / Air / 100 / $\lambda_s = 5.23$ / 0.038 For sandstone: **Solidity, $1 - n$ [–] / Pore fluid / Quartz content $m_{\%}$ [%] / Thermal conductivity, λ [W/(m °C)] / Slope constant, S_C [W/(m °C · %)]** 0 / Air / 0 / $\lambda_f = 0.026$ / 1 / Air / 0 / $\lambda_s = 1.47$ / 1 / Air / 100 / $\lambda_s = 5.23$ / 0.038 0 / Water / 0 / $\lambda_f = 0.62$ / 1 / Water / 0 / $\lambda_s = 1.52$ / 1 / Water / 100 / $\lambda_s = 8.10$ / 0.066 In the expression, $\lambda(0)$ is the thermal conductivity at the temperature of 0°C and is given by: $\lambda(0) = \lambda(25)\left[1.007 + 25\left(3.7 \times 10^{-3} - \frac{7.4 \times 10^{-3}}{\lambda(25)}\right)\right]$ where $\lambda(25)$ is the measured room-temperature conductivity.

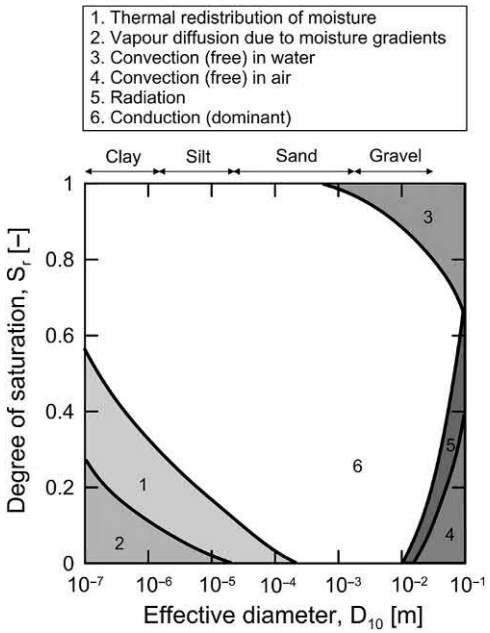

Figure 3.6 Heat transfer modes in soils depending on effective particle diameter, D_{10}, and saturation degree, S_r. *Redrawn after Farouki, O.T., 1986. Thermal Properties of Soils. Series on Rock and Soil Mechanics, vol. 11. Trans Tech Publications, Clausthal-Zellerfeld.*

pores constituting the soil, the type of fluid filling the pores, the degree of saturation of the material and the presence of fluid flow through the pores. An example of the influence of the effective particle diameter, D_{10} (i.e. the size of a sieve through which the 10% of the grains pass), and the water saturation degree, S_r, on the dominant modes of heat transfer characterising soils is reported in Fig. 3.6 with reference to the data reported by Farouki (1986).

3.5 Convection

3.5.1 Physical phenomenon and governing equation

Convection is the mode of heat transfer that characterises fluids in motion with a temperature gradient. This mode of heat transfer is associated with the *superposition* of *two mechanisms*: energy transport by a *diffusion* motion and by a *bulk* motion of the fluid. The former mechanism is the same that characterises conduction and it is the result of an invisible microscopic random movement of molecules. The latter mechanism is associated with the so-called *advection* phenomenon and it is the result of a visible macroscopic movement of fluid molecules as aggregates or a whole. The visible macroscopic movement of a fluid is often called convection mass transfer.

The motion of fluids, which involves a movement of the particles bringing their thermal energy in proximity to each other, is the result of a force. When the force that causes the motion of the fluid is due entirely to density variations caused by a nonuniform temperature distribution, that is a temperature gradient, the convection phenomenon is called *free* or *natural convection*. When the force that causes the motion of the fluid is due to any other cause, the convection phenomenon is termed *forced convection*. Free convection is an example of the coupling between heat and mass transfers.

In the analysis of motion of fluids, it is relevant to distinguish problems of *internal flow*, *external flow* and *seepage flow*. In internal flow problems, the fluid in motion is completely bounded by a surface (e.g. a heat carrier fluid circulating in a pipe or air flowing in an underground built environment). In external flow problems, the fluid in motion is not completely bounded by a surface (e.g. surface air flowing over the ground). In seepage flow problems, the fluid is in motion across a permeable material medium (e.g. groundwater flowing within soils).

The physical phenomenon of convection heat transfer can be explained, for example with reference to a fluid in motion relative to a bounding surface at a different temperature, which at a meaningful scale can be considered as a plane wall. This problem is represented in Fig. 3.7 considering a convection phenomenon that can characterise, for example an energy tunnel. The temperature varies from a value T_s at the surface (e.g. $y = 0$) to a temperature $T_\infty < T_s$ in the fluid bulk. In this case, heat transfer occurs from the wall to the bulk of the fluid. The opposite is true for $T_s < T_\infty$. At the surface wall, convection heat transfer occurs because of the sole molecular diffusion mechanism, as the velocity of the fluid is equal to zero. Beyond the surface and until $T_s \neq T_\infty$, the mechanism of bulk motion contributes to the overall convection heat transfer phenomenon.

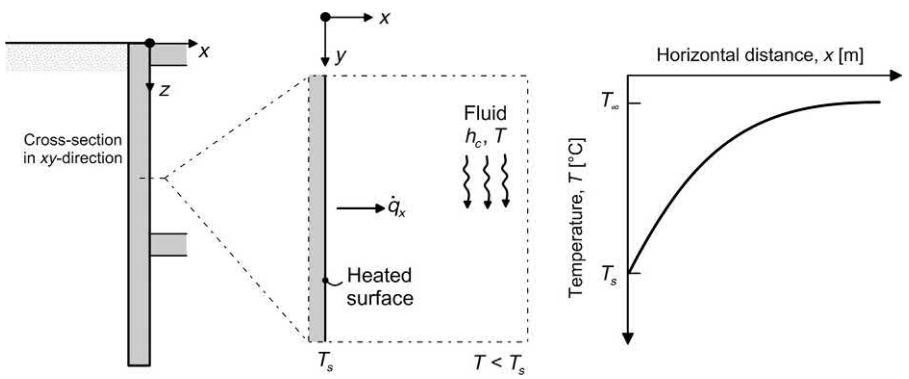

Figure 3.7 Heat transfer by convection at the surface of an energy tunnel.

The rate equation governing convection is *Newton's law of cooling*. According to this law, the heat flux density generated by convection, $\dot{q}_{conv}$, reads

$$\dot{q}_{conv} = h_c(T_s - T_\infty) \tag{3.5}$$

where h_c is the convection heat transfer coefficient (also termed boundary or film conductance), T_s is the surface temperature and T_∞ is the fluid temperature. In this case it is assumed that the convection heat flux is positive if heat is transferred from the surface ($T_s > T_\infty$) and negative if heat is transferred to the surface ($T_s < T_\infty$). However, the heat flux may also be expressed as $\dot{q}_{conv} = h_c(T_\infty - T_s)$.

Eq. (3.5) is typically employed in the context of the analysis of internal and external flows. In the context of the analysis of seepage flows, Newton's law of cooling is expressed as

$$\dot{q}_{conv,i} = \rho_f c_{p,f} \overline{v}_{rf,i}(T_s - T_\infty) \tag{3.6}$$

where $c_{p,f}$ and ρ_f are the specific heat and density of the fluid, respectively, and $\overline{v}_{rf,i}$ is the average relative velocity vector of the fluid with respect to the solid skeleton. Eq. (3.6) is employed in the analysis of groundwater seepage to characterise the heat transported by water motion with reference to the specific heat and density of the water, c_{pw} and ρ_w, respectively, and the average relative velocity of water with respect to the solid skeleton, $\overline{v}_{rw}$ (cf. Fig. 3.8). A similar equation can be obtained for an air-filled medium by replacing the material parameters of the considered gas as well as its relative velocity with respect of the solid skeleton, $\overline{v}_{ra}$.

The density of fluids, similar to the density of solid materials, varies with temperature (Bergman et al., 2011). Because density variations can influence convection mass transfer, the considered feature represents an example of the coupling between heat and mass transfers. Such a feature may be considered in the analysis and design of energy geostructures.

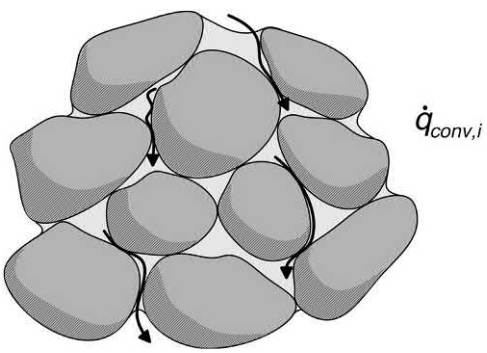

Figure 3.8 Sketch of the convection heat transfer in a geomaterial.

3.5.2 Convection heat transfer coefficient values

In the analysis of internal and external flows, the convection heat transfer coefficient, h_c, is typically used to express with the relevant temperature variation, ΔT, the heat flux density. In the analysis of seepage flows, the separate terms $\rho_f c_{pf} \overline{v}_{tf}$ are used to equivalently express the convection heat transfer coefficient. Accordingly, the convection heat transfer coefficient depends on (1) the fluid thermophysical properties and (2) the fluid velocity. These factors should be considered in the analysis and design of energy geostructures.

The convection heat transfer coefficient may be broken down for convenience into two components as

$$h_c = h_{c,n} + h_{c,f} \tag{3.7}$$

where $h_{c,n}$ is the portion of convection coefficient accounting for the natural convection phenomenon, whereas $h_{c,f}$ is the portion accounting for the forced convection phenomenon.

A large number of expressions are available for estimating the natural convection coefficient with reference to airflow over surfaces (Khalifa, 2001a; Khalifa, 2001b). Bourne-Webb et al. (2016) report values of $h_{c,n}$ for heat flow from vertical external surfaces in the range of 1–3 W/(m^2 °C) (Khalifa, 2001a) and values for enclosed vertical surfaces in the range of 2–4 W/(m^2 °C) (Khalifa, 2001b). EN ISO 6946 (2007) suggests a value of 2.5 W/(m^2 °C) for horizontal heat from internal surfaces. Various expressions are also available for estimating the forced convection coefficient with reference to airflow over surfaces. A power law theoretically relates the forced convection coefficient $h_{c,f}$ to the airflow velocity $\overline{v}_{ra}$. However, Bourne-Webb et al. (2016) suggest that a simple linear relationship is sufficiently accurate for airflows characterised by a velocity lower than approximately $\overline{v}_{ra} = 5$ m/s. Fig. 3.9 highlights the previous fact by reporting correlations for flows over concrete between the forced convection coefficient $h_{c,f}$ and the airflow velocity $\overline{v}_{ra}$. A correlation proposed by Palyvos (2008), additional correlations that describe a comparable relationship between the considered variables (EN ISO 6946, 2007; Lee et al., 2009; ASHRAE, 2012) and experimental data provided by Lee et al. (2009) as well as by Guo et al. (2011) are considered.

Different thermophysical properties should be considered for the diverse fluids that characterise convection heat transfer phenomena associated with energy geostructures. The fluid that characterises internal flow problems in pipes is water in the simplest case, but may be a mixture of water and other constituents. The fluid that characterises internal flow problems over a surface of an energy geostructure or external flow problems associated with convection at the ground surface is air. The fluid that characterises seepage flow problems occurring underground is water.

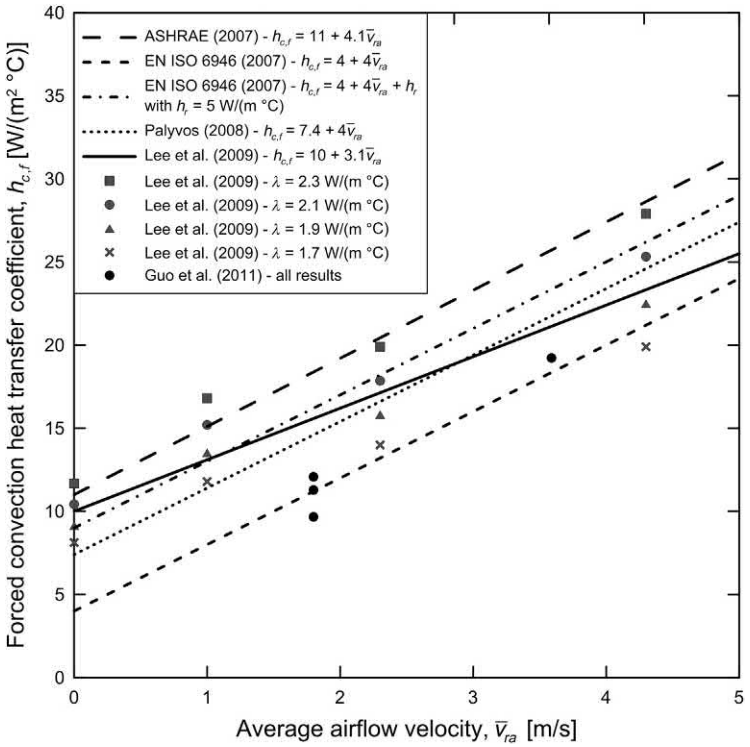

Figure 3.9 Comparison of correlations for forced convective heat transfer coefficient with data from Lee, Y., Choi, M.-S., Yi, S.-T., Kim, J.-K., 2009. Experimental study on the convective heat transfer coefficient of early-age concrete. Cem. Concr. Compos. 31 (1), 6071. and Guo, L., Guo, L., Zhong, L., Zhu, Y., 2011. Thermal conductivity and heat transfer coefficient of concrete. J. Wuhan Univ. Technol. —Mat. Sci. Ed. 26 (4), 791796. *Redrawn after Bourne-Webb, P., Freitas, T.B., da Costa Gonçalves, R., 2016. Thermal and mechanical aspects of the response of embedded retaining walls used as shallow geothermal heat exchangers. Energy Build. 125, 130–141.*

Examples of thermophysical properties as a function of temperature for pure water as well as for a heat carried fluid composed by a mixture of water and 25% and 50% of monoethylene glycol (MEG 25 and MEG 50, respectively) are reported in Tables 3.6, 3.7 and 3.8, respectively.

3.5.3 Remarks about convection

Convection dominates heat transfer when a significant fluid flow is present. Based on this consideration:

- Either free or forced convection can characterise heat and mass transfer *within* geomaterials and reinforced concrete. Convection can generally be neglected in concrete. However, it can be significant in geomaterials. Water can be considered to be the fluid responsible for a significant heat transfer in geomaterials via its mass flow.

Table 3.6 Some thermophysical properties of water.

Water				
Reference temperature, T [°C]	**Density, ρ_f [kg/m^3]**	**Specific heat, $c_{p,f}$ [J/(kg °C)]**	**Thermal conductivity, λ_f [W/(m °C)]**	**Dynamic viscosity, μ_f [Pa s]**
1	1000	4226	0.569	1.655×10^{-3}
5	1000	4216	0.576	1.484×10^{-3}
10	1000	4206	0.584	1.302×10^{-3}
15	999	4198	0.592	1.150×10^{-3}
20	998	4191	0.599	1.021×10^{-3}
30	996	4182	0.613	0.820×10^{-3}
40	992	4178	0.626	0.671×10^{-3}

Table 3.7 Some thermophysical properties of MEG 25.

MEG 25				
Reference temperature, T [°C]	**Density, ρ_f [kg/m^3]**	**Specific heat, $c_{p,f}$ [J/(kg °C)]**	**Thermal conductivity, λ_f[W/(m °C)]**	**Dynamic viscosity, μ_f [Pa s]**
-10	1048	3713	0.477	3.186×10^{-3}
-5	1046	3719	0.481	2.704×10^{-3}
0	1045	3726	0.485	2.314×10^{-3}
5	1044	3734	0.489	1.995×10^{-3}
10	1042	3742	0.493	1.733×10^{-3}
15	1040	3751	0.496	1.516×10^{-3}
20	1038	3760	0.499	1.334×10^{-3}
30	1034	3780	0.504	1.053×10^{-3}
40	1030	3801	0.509	0.849×10^{-3}

Table 3.8 Some thermophysical properties of MEG 50.

MEG 50				
Reference temperature, T [°C]	**Density, ρ_f [kg/m^3]**	**Specific heat, $c_{p,f}$ [J/(kg °C)]**	**Thermal conductivity, λ_f [W/(m °C)]**	**Dynamic viscosity, μ_f [Pa s]**
-10	1094	3201	0.413	5.316×10^{-3}
-5	1092	3221	0.412	4.428×10^{-3}
0	1090	3240	0.411	3.723×10^{-3}
5	1087	3260	0.410	3.157×10^{-3}
10	1084	3280	0.408	2.700×10^{-3}
15	1082	3301	0.407	2.326×10^{-3}
20	1079	3321	0.406	2.019×10^{-3}
30	1073	3361	0.403	1.552×10^{-3}
40	1067	3402	0.400	1.223×10^{-3}

Forced convection dominates heat transfer in geomaterials when significant groundwater flow occurs, such a condition typically characterising coarse-grained soils (i.e. highly permeable materials, such as sands or gravels) and rarely fine-grained soils (i.e. low permeable materials, such as clays). For energy pile applications, values of groundwater flow velocities in the range of $\overline{v}_{rw} = 0.5-1$ m/day have been suggested to distinguish cases in which the role of convection can be considered negligible (for lower velocities) or relevant (for greater velocities) in the global heat transfer problem (Chiasson et al., 2000; SIA, 2005). However, these values need to be considered with caution.

Free convection typically occurs in soils characterised by a pore size diameter of several millimetres (Farouki, 1986). Furthermore, it may be considered significant for temperature levels greater than 30°C or temperature gradients greater than or equal to 1°C/cm (Martynov, 1963).

- Either free or forced convection can characterise heat and mass transfer *over* geomaterials and reinforced concrete. These phenomena may typically characterise the ground surface or the interface between energy geostructures and adjacent built environments. In this context, air is the fluid responsible for the heat transfer via its mass flow. Forced convection characterises the heat carrier fluid flowing in the pipes of energy geostructures. In this context, water or the general heat carrier fluid is the fluid responsible for the heat transfer via its mass flow.

3.6 Radiation

3.6.1 Physical phenomenon and governing equation

Radiation (e.g. electromagnetic radiation) is the mode of heat transfer emitted by matter at nonzero (absolute) temperature solely on account of this variable. This mode of heat transfer involves a motion of thermal energy through waves of the electromagnetic field propagating in a medium (or a vacuum). When the material medium is a solid or a liquid, the amount of heat transferred by radiation is usually negligible compared to when the medium is a gas. The emission of thermal energy is attributed to variations in the electron configurations of the atoms and molecules constituting any medium (Bergman et al., 2011).

The physical phenomenon of radiation can be explained by considering the interaction of a medium at a given temperature with a much larger bounding surface at a different temperature. This problem is represented in Fig. 3.10 considering the interaction between the ground surface at a temperature, T_s, and a much larger surface theoretically bounding a relevant portion of the atmosphere at a different constant temperature, T_∞.

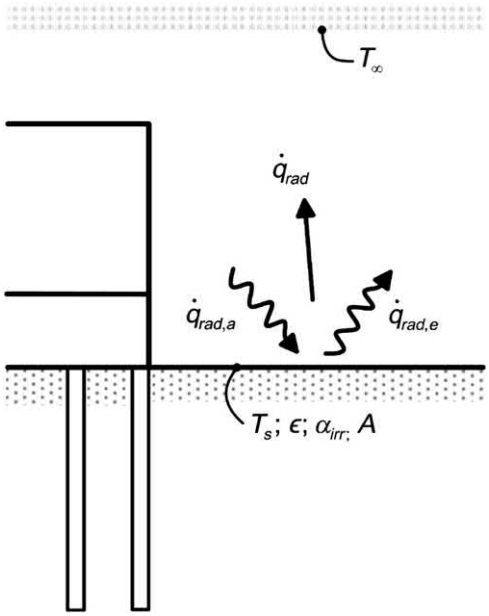

Figure 3.10 Heat transfer by radiation at the ground surface.

The rate equation governing radiation is the *Stefan–Boltzmann law*. According to this law the heat flux density *emission* radiated by a surface (i.e. a heat source), $\dot{q}_{rad,e}$, as a consequence of the thermal energy of the matter bounded by the surface reads

$$\dot{q}_{rad,e} = \epsilon \sigma_{SB} T_s^4 \tag{3.8}$$

where ϵ is the surface emissivity and σ_{SB} is the Stefan–Boltzmann constant (5.67×10^{-8} W/(m^2 K^4)). The surface emissivity is a measure of the emissive radiation efficiency of the surface. It is equal to 1 for a so-called 'black body', that is a body that (1) emits radiation independent of direction, (2) absorbs all incoming radiation and (3) is the source of highest emission at any given wavelength and temperature. Surface emissivity is typically of 0.9 for most construction materials, depending on surface material and finish (ASHRAE, 2012).

Radiation may also be absorbed by a surface as a consequence of the presence of other heat sources in the surroundings. In this case a portion or the entire rate of thermal energy that would incident the surface unit area by irradiation may be absorbed, that is

$$\dot{q}_{rad,a} = \alpha_{irr} \sigma_{SB} T_\infty^4 \tag{3.9}$$

where α_{irr} is the surface absorptivity. The surface absorptivity is a measure of the absorbed radiation efficiency of the surface. It is equal to 1 for a black body while typically lower than 1 for most construction materials, depending on the nature of the irradiation, surface material and finish.

Assuming that the surface of interest is part of a 'grey body', that is a body that emits radiation in constant proportion to the corresponding black body radiation, it results that $\epsilon = \alpha_{irr}$. In this case, the net heat flux density exchanged from the surface, expressing the difference between the thermal energy released due to radiation and absorbed due to irradiation, reads

$$\dot{q}_{rad} = \epsilon \sigma_{SB} (T_s^4 - T_\infty^4) \tag{3.10}$$

In many cases it is convenient to express Eq. (3.10) in a linear form as follows (Bergman et al., 2011)

$$\dot{q}_{rad} = h_r (T_s - T_\infty) \tag{3.11}$$

where h_r is the radiation heat transfer coefficient that can be calculated as

$$h_r = \epsilon \sigma_{SB} (T_s + T_\infty)(T_s^2 + T_\infty^2) \tag{3.12}$$

From Eq. (3.12) it can be noted that the radiation heat transfer coefficient, h_r, strongly depends on temperature, in contrast to the weak dependence of the convection heat transfer coefficient, h_c.

3.6.2 Radiation heat transfer coefficient values

The radiation heat transfer coefficient can be calculated as (EN ISO 6946, 2007)

$$h_r = \epsilon \left(4 \sigma_{SB} \overline{T}\right)^3 \tag{3.13}$$

where $\overline{T}$ is the mean between the surface and air temperatures.

3.6.3 Remarks about radiation

Radiation can markedly characterise heat transfer through fluids in the presence of significant temperature variations. Based on this consideration:

- Radiation can significantly characterise heat transfer between built environments and adjacent energy geostructures when significant sources of thermal energy are present. Otherwise the contribution of radiation in the global heat transfer may generally be considered lower than that of convection and neglected.
- Radiation can contribute up to 10%–20% of the global heat transfer in dry coarse-grained soils (Hermansson et al., 2009). However, the contribution of radiation is generally less than 1% in coarse-grained soils and becomes even smaller in moist

fine-grained soils (Rees et al., 2000). In view of this latter evidence, radiation is usually neglected in the analysis of heat transfer characterising geomaterials.

- The contribution of radiation can be considered negligible with respect of that of convection for the heat carrier fluid flowing in the pipes.

3.7 Energy conservation equation

3.7.1 General

The energy conservation equation expresses the principle of conservation of energy. This governing equation is also often termed the *energy equation*.

3.7.2 Fourier heat conduction equation

The equation that governs the conservation of energy in the context of the analysis of heat transfer only characterised by conduction is typically termed Fourier heat conduction equation. This equation can be derived by considering Fourier's law of heat conduction expressed in Eq. (3.2) for a representative volume subjected to arbitrary thermal conditions on its surfaces with internal volumetric heat generation $\dot{q}_v$ per unit time and neglecting any conversion of mechanical energy into heat (cf. Fig. 3.11). The energy balance for the elementary volume reads

$$\left[\begin{array}{c}\text{Rate of heat entering through}\\ \text{the bounding surfaces of a volume}\end{array}\right]+\left[\begin{array}{c}\text{Rate of heat}\\ \text{generation in a volume}\end{array}\right]=\left[\begin{array}{c}\text{Rate of energy}\\ \text{storage in a volume}\end{array}\right]$$

Accordingly, the generalised Fourier heat conduction equation reads

$$\nabla\cdot(\lambda\nabla T)+\dot{q}_v=\rho c_p\frac{\partial T}{\partial t} \tag{3.14}$$

where ρ and c_p are the density and the specific heat of the considered medium, respectively, and t is the time. The term on the right-hand side of the equation represents the variation of internal energy in the medium over time.

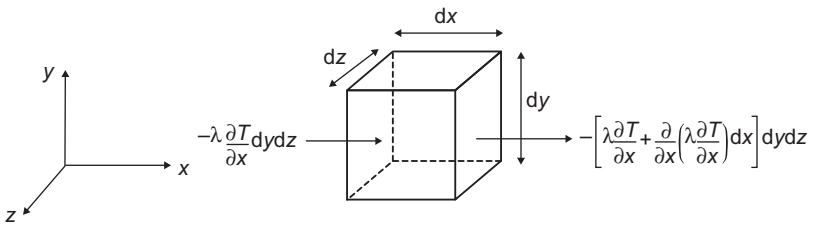

Figure 3.11 Balance of variables over the representative volume.

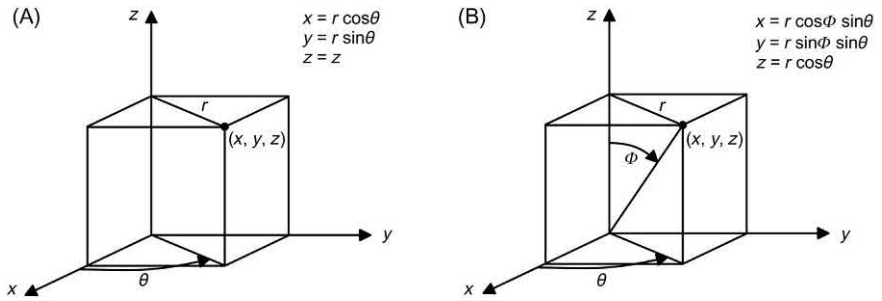

Figure 3.12 (A) Cylindrical and (B) spherical coordinate systems.

Eq. (3.14) presents a unique unknown: the temperature, T. Conduction heat transfer problems can thus be fully addressed by solving Eq. (3.14).

Because the solution of Eq. (3.14) is in general difficult to obtain, it is often assumed that the thermal conductivity of the medium is constant throughout it so that the equation reduces to

$$\lambda \nabla^2 T + \dot{q}_v = \rho c_p \frac{\partial T}{\partial t} \tag{3.15}$$

where ∇^2 is the Laplace operator. The quantity $\nabla^2 T$ is as follows in various coordinate systems.

- Cartesian coordinates x, y, z:

$$\nabla^2 T = \frac{\partial^2 T}{\partial x^2} + \frac{\partial^2 T}{\partial y^2} + \frac{\partial^2 T}{\partial z^2} \tag{3.16}$$

- Cylindrical coordinates r, θ, z (cf. Fig. 3.12A):

$$\nabla^2 T = \frac{\partial^2 T}{\partial r^2} + \frac{1}{r}\frac{\partial T}{\partial r} + \frac{1}{r^2}\frac{\partial^2 T}{\partial \theta^2} + \frac{\partial^2 T}{\partial z^2} \tag{3.17}$$

- Spherical coordinates r, θ, ϕ (cf. Fig. 3.12B):

$$\nabla^2 T = \frac{\partial^2 T}{\partial r^2} + \frac{2}{r}\frac{\partial T}{\partial r} + \frac{1}{r^2 \sin\theta}\frac{\partial}{\partial \theta}\left(\sin\theta \frac{\partial T}{\partial \theta}\right) + \frac{1}{r^2 \sin^2\theta}\frac{\partial^2 T}{\partial \phi^2} \tag{3.18}$$

3.7.3 Fourier heat conduction equation for no volumetric thermal energy generation

If no heat is generated within the medium, Eq. (3.15) reduces to

$$\alpha_d \nabla^2 T = \frac{\partial T}{\partial t} \tag{3.19}$$

where α_d is the thermal diffusivity of the medium given by

$$\alpha_d = \frac{\lambda}{\rho c_p} \tag{3.20}$$

where ρc_p is the volumetric heat capacity. The thermal diffusivity measures the ability of a material to conduct thermal energy relative to its ability to store thermal energy (Hermansson et al., 2009). Materials of large α_d will respond quickly to variations in their thermal environment, while materials of small α_d will respond more slowly. The thermal diffusivity of a medium is indicative of the propagation speed of the heat into the body during temperature variations. The higher the value of α_d is, the faster propagation of heat within the medium is.

3.7.4 Laplace's equation

The particular case in which the temperature distribution is independent of time and no heat sources are present can be of interest, and involves the Laplace's equation (e.g. for the temperature field)

$$\nabla^2 T = 0 \tag{3.21}$$

Eq. (3.21) is associated with steady-state conditions and often represents the basis for analysis and design considerations.

3.7.5 Energy conservation equation

When convection and conduction characterise the heat transfer, the energy conservation equation reads

$$\lambda \nabla^2 T + \dot{q}_v = \rho c_p \frac{\partial T}{\partial t} + \rho_f c_{p,f} \overline{v}_{rf,i} \cdot \nabla T \tag{3.22}$$

where $\overline{v}_{rf,i}$ is the fluid velocity vector.

The expression of the energy conservation reported in Eq. (3.22) presents two unknowns: the temperature field, T, and the displacement field of the moving fluid, $u_{f,i}$ (included in the term $\overline{v}_{rf,i} = \partial u_{f,i}/\partial t$). Therefore the only Eq. (3.22) makes the solution of conduction–convection related problems undetermined. Conduction–convection heat transfer problems can be addressed by solving Eq. (3.22) and the mass conservation equation, under the assumption of negligible influences of the phenomena involved in the equilibrium of the moving fluid (i.e. incompressible inviscid flow). The previous aspect explicates the essence of the thermohydraulic coupling between heat transfer and mass transfer that takes place as soon as convection is considered.

3.7.6 Typical values of volumetric heat capacity

Typical values of volumetric heat capacity for different materials involved in energy geostructures applications are provided in Table 3.9. Distinct values of specific heat and bulk density are reported in Table 3.10. The typical evolution of volumetric heat capacity with water content for soils (e.g. unfrozen) is presented in Fig. 3.13.

The estimation of the volumetric heat capacity of materials is usually simpler than that of the thermal conductivity. In such cases, in contrast to the estimation of the effective thermal conductivity, a linear function of the capacities and volume ratios of the phases characterising the material is sufficient to have a representative estimate of

Table 3.9 Volumetric heat capacity of materials characterising energy geostructures.

Material	Volumetric heat capacity, ρc_p [MJ/(m^3 °C)]	
	Dry	Saturated
Clay	1.5–1.6	1.6–3.4
Silt	1.5–1.6	1.6–3.4
Sand	1.3–1.6	2.2–2.9
Gravel	1.4–1.6	2.4
Peat	0.5–3.8	
Claystone/Siltstone	2.1–2.4	
Sandstone	1.6–2.8	
Quartzite	2.1–2.2	
Marl	2.2–2.3	
Limestone	2.1–2.4	
Argillaceous schists	2.2–2.5	
Micaschists	2.2	
Metaquartzite	2.1	
Marble	2.0	
Gneiss	1.8–2.4	
Rhyolithe	2.1	
Peridotite	2.7	
Granite	2.1–3.0	
Gabbro	2.6	
Diorite	2.9	
Basalt	2.3–2.6	
Concrete	1.8–2.0	
Steel	3.12	
Water	4.186	
Air	0.0012	

Source: Data from Pahud, D., 2002. Geothermal Energy and Heat Storage. Laboratorio di Energia, Ecologia ed Economia, Canobbio.

Table 3.10 Specific heat and bulk density of selected materials.

Material	Specific heat, c_p [J/(kg °C)]	Bulk density, ρ [kg/m^3]
Quartz	799	2650
Kaolin	937	2600
Calcium carbonate	870	2710
$CaSO_4$	816	2450
Fe_2O_3	690	5240
Al_2O_3	908	3700
$Fe(OH)_3$	946	3600
Orthoclase	812	2560
Oligaclase	858	2640
Potash mica	870	2900
Magnesia mica	862	2900
Hornblende	816	3200
Apatite	766	3200
Dolomite	929	2900
Talc	874	2700
Granite	803	2600
Syenite	833	2700
Diorite	812	2900
Andesite	833	2400
Basalt	891	3000

Source: Modified after Rees, S., Adjali, M., Zhou, Z., Davies, M. & Thomas, H., 2000. Ground heat transfer effects on the thermal performance of earth-contact structures. Renew. Sustain. Energy Rev. 4 (3), 213–265. and Clark, S.P., 1966. Handbook of Physical Constants. Geological Society of America.

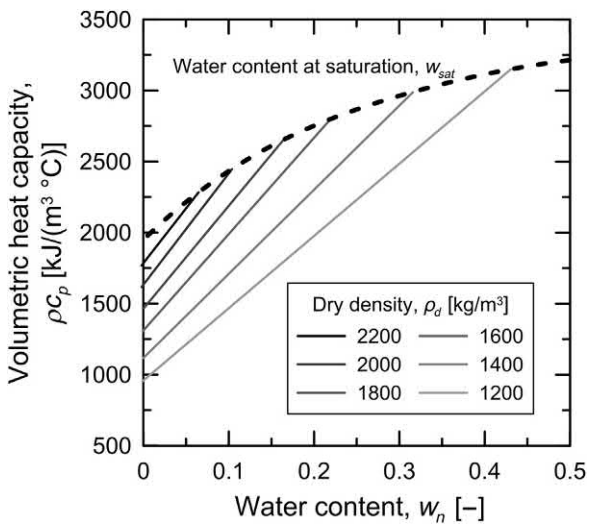

Figure 3.13 Typical evolution of volumetric heat capacity with water content for unfrozen soils. *Redrawn after Dysli, M., 1991. Le gel et son action sur les sols et les fondations. PPUR presses polytechniques.*

its effective volumetric heat capacity. In this context the effective volumetric heat capacity of porous materials fully saturated with a fluid can be calculated as

$$\rho c_p = \rho_f c_{p,f} n + \rho_s c_{p,s}(1 - n) \tag{3.23}$$

where $\rho_f c_{p,f}$ is the volumetric heat capacity of the general fluid filling the pores of the material and $\rho_s c_{p,s}$ is the volumetric heat capacity of the solid particles. For soils fully saturated with water, $\rho_f c_{p,f}$ is replaced by the volumetric heat capacity of the water $\rho_w c_{p,w}$. The same approach may be applied to calculate the volumetric heat capacity of fully dry soils by using the volumetric heat capacity of the air $\rho_a c_{p,a}$. In most cases, however, the contribution of the air volumetric heat capacity is neglected in the calculation of the effective volumetric heat capacity of the soil because of its small influence on the result unless for relatively high porosities.

3.8 Initial and boundary conditions for energy conservation

3.8.1 Rationale of initial and boundary conditions

The full mathematical description of the heat transfer problem for any medium needs initial and boundary conditions to be solved. These conditions describe a state at some initial time and at the boundaries of the medium over time. They allow obtaining the temperature distribution in the medium through the solution of the relevant formulation of the energy conservation equation. The unique case in which no initial conditions are needed is the steady-state problem governed by Eq. (3.21), that is a problem independent of time.

According to Bergman et al. (2011), because the heat equation is second order in the spatial coordinates, two boundary conditions must be expressed for each coordinate needed to describe the system. However, because the equation is first order in time, only one initial condition must be specified.

In most problems the typical initial condition employed is to assume a constant initial temperature for any portion of the bounding surface of a considered medium, that is $T_0 = \text{const}$. In contrast, there are five typical conditions that are used (in any combination) in the mathematical theory of heat transfer as idealisations for any portion of the bounding surface of a considered medium.

3.8.2 Prescribed surface temperature

The so-called Dirichlet's boundary condition or boundary condition of the first kind allows fixing the temperature of any surface as

$$T(\mathcal{H},t) = f(\mathcal{H},t) \tag{3.24}$$

where $\mathcal{H}$ is a point on the considered surface and $f(\mathcal{H},t)$ is a prescribed function. The special case where $T(\mathcal{H},t) = 0$ is called homogeneous boundary condition of the first kind.

For an energy wall considered as a one-dimensional system (cf. Fig. 3.14), heat transfer may be assumed to occur in the positive x-direction with the temperature distribution and to depend on time as $T(x, t)$. For this wall the initial temperature may be assumed to be equal to T_0. The boundary condition may consist of assuming an instantaneous increase of the temperature of the wall surface that would evolve over time according to the prescribed function $T(\mathcal{H},t) = f(\mathcal{H},t) = T_s$.

3.8.3 Prescribed heat input

The so-called Neumann's boundary condition or boundary condition of the second kind allows the fixing of a heat input. Based on Fourier's law this boundary condition takes the form

$$-\lambda \frac{\partial T}{\partial n_i}(\mathcal{H},t) = \dot{q}(\mathcal{H}, t) \tag{3.25}$$

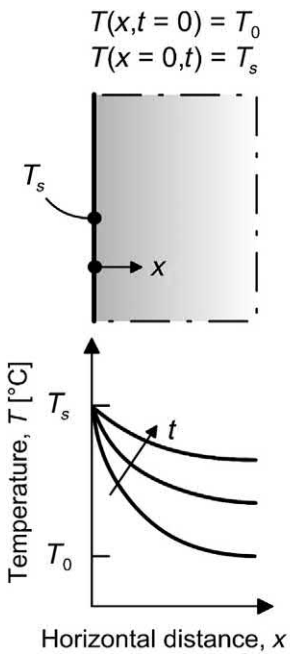

Figure 3.14 Example of an initial and a Dirichlet's boundary condition for an energy wall.

where n_i is the normal to the surface at the point $\mathcal{H}$. The special case where $\lambda \frac{\partial T}{\partial n_i}(\mathcal{H},t) = 0$ is called the homogeneous boundary condition of the second kind. It refers to a perfectly insulated surface across which no heat flux can occur.

For an energy wall considered as a one-dimensional system (cf. Fig. 3.15), the boundary condition may consist of assuming a fixed (e.g. constant) heat flux at the surface

$$-\lambda\left(\partial T/\partial x\right)_{x=0} = \dot{q}_s.$$

3.8.4 Convection boundary condition

The so-called Cauchy's boundary condition, mixed Neumann's boundary condition or boundary condition of the third kind allows prescribing a convection boundary condition. In many problems the heat flux across a bounding surface may be taken as being proportional to the difference between the surface temperature, $T(\mathcal{H}, t)$, and the known temperature, T_∞, of the surrounding medium. In this case Eq. (3.25) takes the form

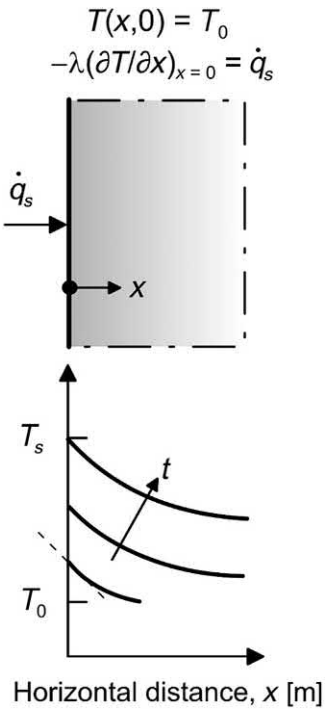

Figure 3.15 Example of an initial and a Neumann's boundary condition for an energy wall.

$$-\lambda\frac{\partial T}{\partial n_i}(\mathcal{H},t) = h_c[T_\infty - T(\mathcal{H},t)] \tag{3.26}$$

The special case where $T(\mathcal{H},t) = 0$ and thus $\lambda\frac{\partial T}{\partial n_i}(\mathcal{H},t) = h_c T_\infty$ is called the homogeneous boundary condition of the third kind. It represents convection for a medium at zero temperature.

For an energy wall considered as a one-dimensional system (cf. Fig. 3.16), the boundary condition may consist of assuming a fixed (e.g. constant) convection heat flux at the surface

$$-\lambda\left(\frac{\partial T}{\partial x}\right)_{x=0} = h_c[T_\infty - T(0,t)].$$

3.8.5 Radiation boundary condition

The Cauchy's boundary condition also allows prescribing a radiation boundary condition for conduction problems. If the surface of a body is exposed to a high-temperature source, it will receive heat by radiation according to Eq. (3.10). In this case Eq. (3.25) takes the form

$$-\lambda\frac{\partial T}{\partial n_i}(\mathcal{H},t) = \epsilon\sigma_{SB}(T_\infty^4(t) - T^4(\mathcal{H},t)) \tag{3.27}$$

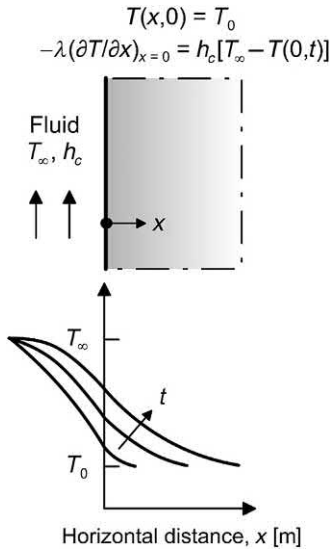

Figure 3.16 Example of an initial and a mixed Neumann's boundary condition for an energy wall.

where $T_\infty(t)$ and $T(\mathcal{H},t)$ are the temperature of the source and surface, respectively. This boundary condition renders the analytical solution of the problem extremely difficult so that two simplifications are often used (Boley and Weiner, 1997) to reduce Eq. (3.27) to Eq. (3.26), provided that $T_\infty(t)$ is very high compared to $T(H,t)$ during the period of interest or neither temperature varies over too wide a range.

3.8.6 Interface boundary condition

If two solid bodies are in perfect thermal contact (cf. Fig. 3.17A), their temperature at the surface contact must be the same. Moreover the heat flux leaving one body through the contact surface must be equal to that entering the other body. In this case, for a point $\mathcal{H}$ on the contact surface

$$T_1(\mathcal{H},t) = T_2(\mathcal{H},t) \tag{3.28}$$

$$\lambda_1 \frac{\partial T_1}{\partial n_i}(\mathcal{H},t) = \lambda_2 \frac{\partial T_2}{\partial n_i}(\mathcal{H},t) \tag{3.29}$$

where 1 and 2 are the labels for the two bodies and n_i is the common normal to the contact surface at $\mathcal{H}$.

If two solid bodies are not in perfect thermal contact (cf. Fig. 3.17B), the concept of contact resistance, R_c'' (or contact conductance $h_c = 1/R_c''$), is often used. The equality of heat fluxes must still be enforced but a difference between the two surface temperatures, proportional to the heat flux, will now exist (Boley and Weiner, 1997). The appropriate boundary conditions are in this case

$$\lambda_1 \frac{\partial T_1}{\partial n_1}(\mathcal{H},t) = \frac{1}{R_c''}\left[T_2(\mathcal{H},t) - T_1(\mathcal{H},t)\right] \tag{3.30}$$

$$\lambda_1 \frac{\partial T_1}{\partial n_1}(\mathcal{H},t) = \lambda_2 \frac{\partial T_2}{\partial n_1}(\mathcal{H},t) \tag{3.31}$$

where n_1 is the normal to the contact surface at $\mathcal{H}$ referred to body 1.

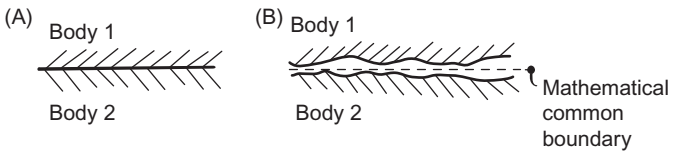

Figure 3.17 Schematic representation of two solid bodies (A) in perfect contact and (B) not in perfect contact.

3.9 Principles of mass transfer

Mass transfer is the physical phenomenon for which a net movement of generic particles is observed from one location to another. One mode of mass transfer is considered in the following: *convection*. Additional mass transfer phenomena caused, for example by diffusive processes exist. However, from an engineering perspective, diffusive mass transfer processes are considered negligible for the analysis and design of energy geostructures.

Mass is transferred by convection between any two regions of a continuous system that are characterised by different hydraulic heads. Hydraulic heads are the potential variable governing convection mass transfer. The gradient of these variables governs mass transfer in the same way a temperature gradient characterises heat transfer. The global hydraulic potential that describes mass transfer is the total head, H. This potential is made of three contributions that characterise fluids at each point: (1) the elevation head, h_z, due to the weight of the fluid; (2) the pressure head, h_p, due to the static pressure; and (3) the velocity head, h_v, due to the bulk motion of the fluid. The expression of the total head reads

$$H = h_z + h_p + h_v = z + \frac{p_f}{\gamma_f} + \frac{v_f^2}{2g} \tag{3.32}$$

where z is the elevation of a considered fluid particle above a reference plane, p_f is the fluid pressure, γ_f is the unit weight of the fluid, v_f is the velocity of the fluid at a point on a streamline and g is the gravitational acceleration.

Depending on whether mass transfer of ideal fluids, that is inviscid, or real fluids, that is viscid, is considered, a variation of the total head can be observed. When reference is made to ideal fluids in steady (or streamline) flow, the total head remains constant along the streamlines of a fluid particle in motion according to *Bernoulli's theorem*. In other words, Bernoulli's theorem expresses the principle of conservation of energy, which can also be interpreted via geometric considerations (cf. Fig. 3.18A).

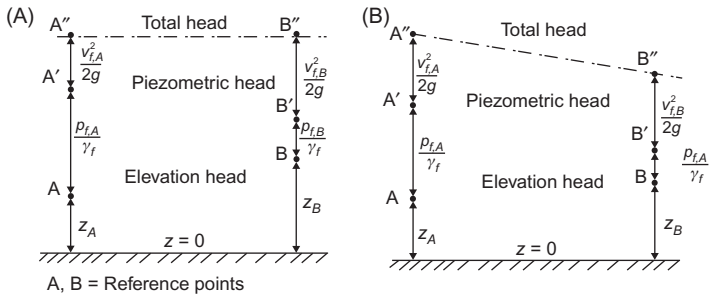

Figure 3.18 Evolution of hydraulic heads for (A) an ideal fluid and (B) real fluid.

When reference is made to real fluids, viscosity causes the insurgence of shear forces against the direction of the motion, involving the conversion of mechanical energy into heat and a consequent variation of the total head (cf. Fig. 3.18B).

An essential component in the description of mass transfer problems is the relationship between the total head and the characteristic velocity of the fluid that gives rise to the flow of mass. This characteristic velocity is the *mean macroscopic relative velocity* of the fluid and is defined with reference to a relevant volume. This volume coincides with the REV and allows simplifying the local velocity field characterising every point of the fluid in motion that may be too complex to be analysed rigorously, especially in the context of seepage flows (Vulliet et al., 2016).

3.10 Laminar and turbulent flows

A critical feature of convection mass transfer phenomena is the flow regime (or flow condition). There are two fundamental convection mass transfer regimes: *laminar flow* and *turbulent flow*. Laminar flow is a type of mass transfer in which the trajectories of the single particles constituting the fluid in motion coincide with the effective trajectories of the average fluid motion. Turbulent flow is a type of mass transfer in which the trajectories of the single particles constituting the fluid in motion are random and no more coincident with the effective trajectories of the average fluid motion.

The distinction between laminar and turbulent flows is usually based on the knowledge of the Reynolds number. The Reynolds number is a dimensionless number that can be determined as

$$Re_x = \frac{\rho_f v_\infty x}{\mu_f} \tag{3.33}$$

where v_∞ is the characteristic velocity of the fluid (i.e. typically the mean relative velocity), x is the characteristic length of the considered problem (i.e. typically the hydraulic diameter for a flow within a circular pipe) and μ_f is the dynamic viscosity of the fluid. The Reynolds number represents the ratio of the inertia to viscous forces: if the Reynolds number is relatively small, inertia forces are insignificant relative to viscous forces and the flow is laminar; the opposite is true if the Reynolds number is significant, that is viscous forces are negligible relative to inertia forces and the flow is turbulent.

In many flow processes both laminar and turbulent conditions occur, with laminar conditions preceding turbulent conditions. In between these conditions a transition zone is evidenced, in which a conversion from laminar flow conditions to turbulent flow conditions occurs. A critical Reynolds number is often employed to delimit the transition zone between laminar and turbulent flow conditions. For lower values of

this critical number the flow is stable and any potential perturbation triggered tends to vanish. In contrast, for higher values than the critical number the flow is unstable and any perturbation triggered (even if minimal) can degenerate in a turbulent mechanism.

For flows over plane surfaces, such as the surface of an energy wall, the critical value of the Reynolds number lies in the range $10^5 \leq Re_c \leq 3 \times 10^6$ (Bergman et al., 2011). For flows within pipes the critical value of the Reynolds number is approximately $Re_c \approx 2000$ (Bergman et al., 2011). For seepage flows within soils, the critical value of the Reynolds number lies in the range $2000 \leq Re_c \leq 3000$, although Khalifa et al. (2002) report this value to lie in the range $1 \leq Re_c \leq 10$. The reason for the different aforementioned values is a consequence of the characteristic length that is considered to describe the analysed problem and may vary in different situations.

A noteworthy simplification involved with laminar flows is that the contribution of velocity head can be neglected with respect to the contribution of the elevation and pressure heads, that is $h_v \ll h_z + h_p$, and Eq. (3.32) reduces to

$$H = h_z + h_p = z + \frac{p_w}{\gamma_w} = h \tag{3.34}$$

where h is the piezometric head. The previous simplification cannot be employed when dealing with problems of turbulent flow because the contribution of the velocity head significantly characterises the flow process.

The flow of the heat carrier fluid circulating in the pipes of energy geostructures can be laminar or turbulent. The flow of air in underground built environments adjacent to energy geostructures such as energy walls and energy tunnels may also occur in laminar or turbulent conditions. In contrast, the seepage flow of groundwater in soils typically occurs under laminar conditions. Turbulent conditions may arise in highly permeable soils or through fractured rocks.

An example of the negligible magnitude of the velocity head h_v, in contrast to the piezometric head $h = h_z + h_p$, for seepage flows in laminar conditions can be reported following the considerations of Vulliet et al. (2016). For a coarse-grained soil fully saturated with water characterised by pore size diameters at maximum equal to 5 mm as is usually encountered in practice, the assumption of a critical Reynolds number of $Re_c = 2000$ leads to the critical water velocity $v_{w,c} = 0.56$ m/s at which a transition between laminar and turbulent flow conditions occurs (reference is made to the usual values of water properties at a temperature of $T = 20°C$). The velocity head associated with this critical velocity reads $h_v = v_{w,c}^2/2g \approx 16$ mm. Therefore as the typical values of piezometric head h in the analysis of groundwater flow are of the order of metres, the velocity head can be considered negligible under laminar conditions.

3.11 Seepage flow

3.11.1 Physical phenomenon and governing equation

In the context of the analysis of problems involving groundwater seepage under laminar conditions, *Darcy's law* allows the expression of a relation between the hydraulic gradient and the mean flow velocity under steady conditions. Considering the flow of groundwater across a geomaterial that possesses homogeneity and isotropy with respect to the mass transfer phenomenon, Darcy's law reads

$$\overline{v}_{rw,i} = -k\nabla h = -k\nabla\left(z + \frac{p_w}{\gamma_w}\right) \tag{3.35}$$

where k is the hydraulic conductivity of the geomaterial, p_w is the pore water pressure and γ_w is the unit weight of water. The assumption of homogeneity and isotropy indicates that the hydraulic conductivity is independent of direction and position and for this reason appears outside the argument of the gradient.

In Eq. (3.35) the minus sign makes the mass flux density a positive quantity as a consequence of its direction towards decreasing piezometric head. The law expressed in Eq. (3.35) was first stated based on experimental evidence by Darcy (1856). It represents a particular expression of the Navier–Stokes equations (Whitaker, 1986) (cf. Section 3.15).

Some modifications of Darcy's law are needed for the analysis of turbulent flow conditions in porous geomaterials (Khalifa et al., 2002), as well as for the analysis of flows in unsaturated soils (Mitchell and Soga, 2005) and in fissured rocks (Vulliet et al., 2016). These problems are not treated herein.

If, instead of establishing a relationship between the apparent flow velocity, $\overline{v}_{rw,i}$, and the hydraulic gradient, ∇h, via the hydraulic conductivity, k, a relationship between the mass flux density $\dot{q}_{D,i}$ (i.e. the rate of fluid volume, V, transferred through a given surface, A, per unit time, t) and the hydraulic gradient is considered, it is found that the *rate equation* describing mass transfer in the considered case is

$$\dot{q}_{D,i} = -k\nabla h \tag{3.36}$$

Eq. (3.36) is analogous to Eqs (3.2), (3.5) and (3.11).

Darcy's law can be markedly simplified for the situation of a plane geometry in steady-state conditions. In this case the hydraulic head distribution across a surface is linear and the mass flux in the direction of the flow, x, reads

$$\dot{q}_{D,x} = -k\frac{dh}{dx} \tag{3.37}$$

3.11.2 Typical values of hydraulic conductivity and forced convection coefficient

The hydraulic conductivity of materials depends on the characteristics of the medium across which the fluid flows as well as on the physical properties of the flowing fluid itself. For soils this parameter depends on (1) granulometry, (2) soil fabric, (3) dry density and (4) temperature (Vulliet et al., 2016). For rock masses hydraulic conductivity depends on the characteristics of the fractures network (Vulliet et al., 2016).

The hydraulic conductivity is the variable characterised by the largest range of variation in energy geostructure applications. Typical values of hydraulic conductivity are reported in Table 3.11.

The dependence of the hydraulic conductivity on granulometry, soil fabric, dry density (i.e. aspects (1)−(3)) for soils and on the characteristics of the fractures network for rocks can be considered via a number of mathematical expressions. A usual reference for the derivation of such expressions is the Poiseuille's law (Poiseuille, 1844) for flow through a round capillary, which gives the mean flow velocity

$$\overline{v}_{nw,i} = -k\nabla h = -\frac{gD_p^2}{32\eta_f}\nabla h \tag{3.38}$$

where D_p is the effective hydraulic diameter and η_f is the kinematic viscosity of the fluid. For soils the effective diameter may be chosen depending on the material gradation and compaction state. For rocks the effective diameter corresponds to a representative dimension of the problem, for example the effective diameter of the pores and joints in the rock mass. Table 3.12 summarises a number of mathematical expressions for the estimation of the hydraulic conductivity of soils and rocks.

The dependence of the hydraulic conductivity on temperature (i.e. aspect (4)) can be appreciated by expressing this variable as

$$k = \frac{k^i \rho_f g}{\mu_f} = \frac{k^i g}{\eta_f} \tag{3.39}$$

where k^i is the intrinsic (or geometric) permeability, that is a property of the porous material only (not of the fluid). The term η_f summarises the dependence of the hydraulic conductivity on the fluid type. Because the viscosity and density of fluids depend on temperature, the hydraulic conductivity also depends on temperature.

For water the dependency of the dynamic viscosity on temperature can be considered via the expression (Thomas and King, 1994):

$$\mu_w = 0.6612(T-229)^{-1.562} \tag{3.40}$$

Table 3.11 Hydraulic conductivity of materials characterising energy geostructures.

Material type	Material	Hydraulic conductivity, k [m/s]
Soils	Gravel	10^{-1}–10^{-3}
	Cleaned sands (coarse grained)	10^{-2}–10^{-4}
	Sand (mixed)	10^{-4}–$5 \cdot 10^{-5}$
	Fine sand	5×10^{-4} to 10^{-5}
	Silty sand	2×10^{-5}–10^{-6}
	Silt	10^{-5}–10^{-8}
	Clay	10^{-8}–10^{-10}
Rock (laboratory testing)	Sandstone	10^{-10}–10^{-12}
	Siltstone	10^{-10}–10^{-11}
	Granite	5×10^{-13}–2×10^{-12}
	Slate	7×10^{-13}–1.6×10^{-12}
	Brèche	7×10^{-13}–4.6×10^{-12}
	Calcite	7×10^{-12}–9.3×10^{-10}
	Limestone	7×10^{-12}–1.2×10^{-9}
	Dolomite	4.6×10^{-11}–1.2×10^{-10}
	Sandstone	1.6×10^{-9}–1.2×10^{-7}
	Strong argillite	6×10^{-9}–2×10^{-8}
	Black schist (fissured)	6×10^{-6}–3×10^{-6}
	Fine sandstone	2×10^{-9}
	Olithique rock	1.3×10^{-8}
	Bradford sandstone	2.2×10^{-7}–6×10^{-9}
	Glenrose sandstone	1.5×10^{-5}–1.3×10^{-6}
	Altered sandstone	0.6×10^{-7}–1.5×10^{-7}
Rock mass (in situ)	Migmatite	3.3×10^{-6}
	Gneiss and clayey schist	0.7×10^{-7}
	Gneiss	1.2×10^{-5}–1.9×10^{-5}
	Pegmatoïde granite	1.2×10^{-5}–0.6×10^{-5}
	Lignite	1.7×10^{-4}–23.9×10^{-4}
	Sandstone	1.7×10^{-4}–23.9×10^{-4}
	Argillite	1.7×10^{-4}–23.9×10^{-4}
	Eocene limestone	1.7×10^{-4}–23.9×10^{-4}
	Impermeable rock with 0.1 mm discontinuities at 1 m intervals	8×10^{-6}
Concrete	Concrete	10^{-9}–10^{-12}

Source: Data from Vulliet, L., Laloui, L., Zhao, J., 2016. Mécanique des sols et des roches (TGC volume 18): avec écoulements souterrains et transferts de chaleur. PPUR Presses polytechniques, after Silin-Bekchurin, A., 1958. Dynamics of Underground Water. Moscow Izdat, Moscow University, Moscow.

where T is the absolute temperature expressed in Kelvin. As the dynamic viscosity of water decreases for an increase in temperature, the hydraulic conductivity of soils increases for increasing temperature values (Burghignoli et al., 2000; Towhata et al., 1993). This phenomenon yields to higher flow velocities and greater groundwater

Table 3.12 Examples of mathematical expressions available to define the hydraulic conductivity of materials characterising energy geostructures.

Reference	Material	Expression	Comments
Poiseuille (1844)	Capillary tube	$k = \frac{g}{32\eta_f} D_p^2$	This is the basic hydraulic conductivity formulation derived for a flow of kinematic viscosity η in a capillary tube of diameter D_p, which has been extended in various form for soils and rocks accounting for suitable values of the parameter D_p. In the expression, g is the gravitational acceleration.
Krumbein and Monk (1943)	Sand	$k = \frac{S_k S_f^2 \rho_f g}{\mu_f}$	In the expression, S_k and S_f are solid skeleton parameters, S_k is a nondimensional parameter and express the solid form. The value of $S_k = 6.17 \times 10^{-4}$ is proposed in the referenced work. S_f has the dimension of a length and is a size factor (depending on the size of the grains), ρ_f is the fluid density and μ_f is the fluid dynamic viscosity.
Krumbein and Monk (1943)	Sand	$k = 7.5 \times 10^{-4} D_{50}^2 e^{-1.31\sigma_d} \frac{\rho_f g}{\mu_f}$	This is an expression for sand packs characterised by a constant porosity of $n = 0.4$ for specified size and sorting ranges, which is however valuable for samples characterised by a porosity ranging from $n = 0.23$ to $n = 0.43$ (Beard and Weyl, 1973). In the expression, D_{50} is the median of the grain size distribution and σ_d is the standard deviation of the frequency distribution, approximated by the sorting of a grain size distribution. The model requires sorting values to be lower than or equal to 0.7, that is for moderately well sorted soil or better (Folk and Ward, 1957).
Hazen (1892)	Sand	$k = C_1 {D_{10}}^2$	This is a formula developed for sands with uniform grain size distribution (with uniformity coefficient $C_{ud} = D_{60}/D_{10} < 2$ where D_{60} and D_{10} are the grain diameters corresponding to a 60% and 10% passing on the particle size distribution, respectively). C_1 is a fitting coefficient varying from 25 [cm/s] for 15 mm grain diameter to 100–150 [cm/s] for 0.1–0.3 mm grain diameter. The presence of little quantities of silt or clay in the medium modifies considerably the hydraulic conductivity and limits the applicability of this formula. However, this expression represents a quick and cost-effective approach to evaluate hydraulic conductivity at a given site from soil samples.
Casagrande (1937)	Sand	$k = 1.4 k_{0.85} e^2$	This is a similar expression to the previous one, considering as the governing variable the void ratio e instead of the grain size diameter D_{10}. In the expression, $k_{0.85}$ is the hydraulic conductivity for a void ratio of $e = 0.85$
Hazen (1892)	Sand	$k = C_S \frac{g}{\eta_f} \frac{n^3}{(1-n)^2} {D_{10}}^2$	In the expression C_S is a coefficient depending of the interstices shape. For uniform sands with $U = D_{60}/D_{10} < 5$, the factor $C_S g$ can be taken equal to 2×10^{-7} [$m^5/(J\ s^2)$].
Carman (1937)	Sand	$k = \frac{g}{\eta_f} \frac{n^3}{(1-n)^2} \frac{1}{h_K S_p^2}$	This expression, usually termed Kozeny–Carman equation, has been developed by Carman (1937) by using the Poiseuille (1844) formula in the model proposed by Kozeny (1927). In the expression, S_p is the specific surface of the grains and h_K is the Kozeny constant, which depends on the shape of the solid particles and the porosity of the material.
Henderson et al. (2010)	Sand	$k = c_0 \frac{n^3}{(1-n)^2 M_s^2}$	This is an additional formulation of the Kozeny–Carman equation, where c_0 and M_s are the Kozeny coefficient and the specific surface per unit volume of solid material, respectively. The term M_s can be defined as $M_s = \frac{A_s}{V_s}$ where A_s and V_s are interstitial surface area and the volume of solids, respectively. Carman (1937) used this equation with $c_0 = 1/5$ to obtain the Kozeny–Carman equation.
Tang et al. (2011)	Clay	$k_h = \gamma_w RR \frac{C_h}{2.3\sigma'_{v0}}$	This is an expression based on CPTU testing. In the expression, k_h is the horizontal hydraulic conductivity, γ_w is the unit weight of water, σ'_{v0} is the effective stress of overlying soil and RR is the recompression coefficient that is expressed as a function of the plasticity index, I_P, as follows:

Plasticity index, I_p [–]	14–20	33	33–50
Recompression coefficient, RR [–]	0.031	0.032	0.025

(*Continued*)

Table 3.12 (Continued)

<table>
<tr><th>Reference</th><th>Material</th><th>Expression</th><th>Comments</th></tr>
<tr><td></td><td></td><td></td><td>C_h is the horizontal consolidation coefficient given by $C_h = T_{50} r_0^2 / t_{50}$, where T_{50} is the time factor of 50% degree of consolidation, r_0 is the radius of probe ($r_0 = 1.785$ cm for a CPTU test), t_{50} is the dissipating time of 50% degree of consolidation. Tables to determine T_{50} based on rigidity index I_r and Skempton pore water pressure coefficient A_f are given below (with S_t the soil sensitivity and OCR the soil overconsolidation ratio):
<table>
<tr><td>A_f, [−]</td><td colspan="4">1/3</td><td colspan="4">2/3</td><td colspan="4">1</td><td colspan="4">4/3</td></tr>
<tr><td>I_r, [−]</td><td>10</td><td>50</td><td>100</td><td>200</td><td>10</td><td>50</td><td>100</td><td>200</td><td>10</td><td>50</td><td>100</td><td>200</td><td>10</td><td>50</td><td>100</td><td>200</td></tr>
<tr><td>T_{50} [−]</td><td>1.145</td><td>2.487</td><td>3.524</td><td>5.025</td><td>1.593</td><td>3.346</td><td>4.761</td><td>6.838</td><td>2.095</td><td>4.504</td><td>6.447</td><td>9.292</td><td>2.622</td><td>5.931</td><td>8.629</td><td>12.79</td></tr>
</table>
<table>
<tr><th>I_p, [%]</th><th>S_t, [−]</th><th>OCR, [−]</th><th>I_r, [−]</th></tr>
<tr><td>30</td><td>3−4</td><td>1</td><td>205</td></tr>
<tr><td>22</td><td>2−3</td><td>1</td><td>290</td></tr>
<tr><td>17</td><td>5−6</td><td>1.5</td><td>365</td></tr>
</table>
<table>
<tr><th>Skempton pore water pressure coefficient the saturated clayey soil</th><th>High sensitivity</th><th>Normal consolidation</th><th>Slight over-consolidation</th><th>General overconsolidation</th></tr>
<tr><td>A_f, [−]</td><td>1.0−1.5</td><td>0.5−1.0</td><td>0.2−0.5</td><td>0−0.2</td></tr>
</table></td></tr>
<tr><td>Tang et al. (2011)</td><td>General soil</td><td>$k = \frac{\gamma_w r_0^2 n \tilde{c}_c}{\int_0^{t100} \Delta p_w(t) dt}$</td><td>This is another expression based on CPTU testing. In the expression, $\tilde{c}_c$ is the comprehensive correction coefficient, t_{100} is the dissipating time of 100% degree of consolidation, $\Delta p_w(t)$ is the value of excess pore pressure measured by a CPTU probe and t is the time.</td></tr>
<tr><td>Serafim and Campo (1965)</td><td>General rock</td><td>$k = \frac{g}{12\eta_f} d_{rj}^2$</td><td>This is a formula developed from fluid flow theory in two parallel planes. The fluid flow theory in two parallel planes is valid for smooth rock joints with laminar flow, which are rare conditions in practice. In the expression, g is the gravitational acceleration and d_{rj} is the rock joint opening.</td></tr>
<tr><td>Serafim and Campo (1965)</td><td></td><td>$k = \frac{g}{12\eta_f} {d_e}^2$</td><td>This is an expression in which a corrective parameter is introduced in the Serafim and Campo (1965) equation to take into account the roughness of the rock joint. This is done by replacing d_{rj} by d_e, where the latter term is the hydraulic equivalent rock joint opening that can be calculated as $d_e = f_o d_{rj}$, where f_o is factor which decreases the opening as a function of the joint surface geometry (it is equal to 0 for no fluid flow and to 1 for totally smooth rock joints).</td></tr>
<tr><td>Pape et al. (2000)</td><td>Sandstone</td><td>$k = \frac{n r_g^2}{8 \Gamma_{in}^2} \left(\frac{2n}{3\Gamma^2(1-n)} \right)^{\frac{1}{D_f - 1}}$</td><td>This is an expression coming from generalised Kozeny−Carman relation in the fractal concept theory. In the expression, r_g is the grain radius, D_f is a fractal dimension and Γ_{in} is the interconnectivity parameter.</td></tr>
</table>

flow gradients for higher temperatures. This is another feature characterising the coupling between the thermal and hydraulic behaviours of materials.

3.12 Mass conservation equation

3.12.1 General

The mass conservation equation expresses the principle of conservation of mass. Such an expression, in particular, establishes a relation between the kinematic characteristics of a fluid's motion and the density of the fluid. This conservation equation is also termed the *continuity equation*.

3.12.2 Mass conservation equation

The mass conservation equation can be derived for a representative volume in which mass flows in and out, subjected to arbitrary hydraulic conditions on its surfaces with internal volumetric mass generation $\dot{q}_v$ per unit time (cf. Fig. 3.19). The balance for the elementary volume, as performed for the energy conservation equation, reads

$$\begin{bmatrix}\text{Rate of mass entering through}\\ \text{the bounding surfaces of a volume}\end{bmatrix}+\begin{bmatrix}\text{Rate of mass}\\ \text{generation in a volume}\end{bmatrix}=\begin{bmatrix}\text{Rate of mass}\\ \text{storage in a volume}\end{bmatrix}$$

Accordingly, the mass conservation equation reads

$$-\nabla\cdot\left(\rho_f\overline{v}_{rf,i}\right)+\dot{q}_v=\frac{\partial\rho_f}{\partial t} \tag{3.41}$$

In many practical cases, no volumetric mass generation is considered. Often the fluid is also assumed incompressible. The hypothesis of incompressibility indicates that the density of the fluid remains constant in space and over time. Based on the above, Eq. (3.41) can be rewritten as

$$\nabla\cdot\overline{v}_{rf,i}=0 \tag{3.42}$$

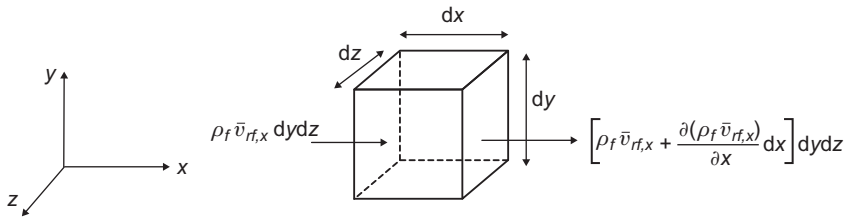

Figure 3.19 Balance of variables over the representative volume.

The above indicates that the velocity field for an incompressible fluid is a solenoidal field, that is a field in which the divergence of the considered variable is equal to zero at all points in space.

3.12.3 Laplace's equation

Recalling that Darcy's law expresses a relationship between the seepage velocity and the hydraulic gradient, Eq. (3.42) can be rewritten as

$$\nabla \cdot (k \nabla h) = 0 \tag{3.43}$$

Assuming the medium to be isotropic allows the writing of the following form of Laplace's equation (e.g. for the piezometric head)

$$\nabla^2 h = 0 \tag{3.44}$$

The quantity $\nabla^2 h$ is as follows in various coordinate systems.

- Cartesian coordinates x, y, z:

$$\nabla^2 h = \frac{\partial^2 h}{\partial x^2} + \frac{\partial^2 h}{\partial y^2} + \frac{\partial^2 h}{\partial z^2} \tag{3.45}$$

- Cylindrical coordinates r, θ, z:

$$\nabla^2 h = \frac{\partial^2 h}{\partial r^2} + \frac{1}{r}\frac{\partial h}{\partial r} + \frac{1}{r^2}\frac{\partial^2 h}{\partial \theta^2} + \frac{\partial^2 h}{\partial z^2} \tag{3.46}$$

- Spherical coordinates r, θ, ϕ:

$$\nabla^2 h = \frac{\partial^2 h}{\partial r^2} + \frac{2}{r}\frac{\partial h}{\partial r} + \frac{1}{r^2 \sin\theta}\frac{\partial}{\partial \theta}\left(\sin\theta \frac{\partial h}{\partial \theta}\right) + \frac{1}{r^2 \sin^2\theta}\frac{\partial^2 h}{\partial \phi^2} \tag{3.47}$$

Eq. (3.44) is associated with steady-state conditions and often represents the basis for analysis and design considerations.

3.13 Initial and boundary conditions for mass conservation

Analogous considerations to those presented for characterising heat transfer problems hold for describing mass transfer problems with reference to the initial and boundary conditions. In this case, the boundary conditions are generally expressed either as a function of a hydraulic head, $\overline{H}$ (Dirichlet's condition) or a flux, $\partial H / \partial n_i$ (Neumann's condition).

3.14 Boundary layers in flow problems

An essential feature of convection phenomena is the development of so-called *boundary layers*. Addressing two particular boundary layers is paramount for the analysis and design of energy geostructures, with particular reference to problems of internal and external flows: the *velocity boundary layer* and the *thermal boundary layer*.

The presence of boundary layers results in two distinct regions in convection phenomena. In one region, located relatively close to a bounding surface, significant gradients of the characteristic variable of the flow occur. In another region, located relatively far from a bounding surface, negligible gradients of the characteristic variable of the flow occur.

The velocity boundary layer develops as a consequence of the viscosity of the moving fluid, which generates shear stresses close to the surface wall (cf. Fig. 3.20A). Due to the presence of such shear stresses, the fluid velocity is equal to zero at the surface wall in the boundary layer. The velocity increases within the boundary layer as a consequence of the decreasing influence of the shear stresses acting on the fluid particles and remains constant at a velocity (different from zero) outside the boundary layer that is usually termed the free stream velocity, v_∞. The thickness of the velocity boundary layer, δ_h, is usually considered to correspond to a fluid velocity of $v_\delta = 0.99 v_\infty$. The significance of the velocity boundary layer thus depends on the

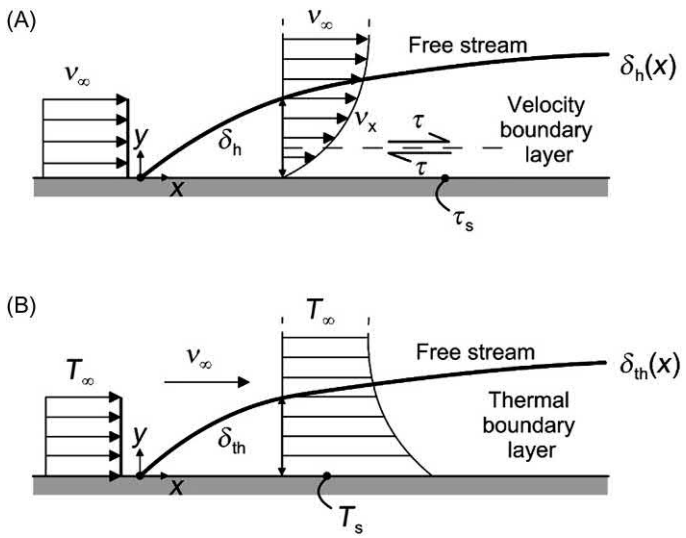

Figure 3.20 The development of velocity and thermal boundary layers. *Redrawn after Bergman, T., Incropera, F., Lavine, A., DeWitt, D., 2011. Fundamentals of Heat and Mass Transfer. Wiley, Hoboken, NJ.*

magnitude of the shear stresses at the surface wall, τ_s. This relationship is usually expressed through the local friction coefficient of the surface:

$$C_f \equiv \frac{\tau_s}{\frac{\rho_f v_\infty}{2}} \tag{3.48}$$

For Newtonian fluids, that is fluids for which the viscous stresses arising from their flow are linearly proportional to the local strain rate at every point, the surface shear stress can be determined through Newton's law as

$$\tau = \mu_f \frac{d\overline{v}_{rf,i}}{dn_i} \tag{3.49}$$

With regards to the problem depicted in Fig. 3.20A, the surface shear stress can thus be determined as

$$\tau_s = \mu_f \frac{dv_x}{dy}\Big|_{y=0} \tag{3.50}$$

The development of the thermal boundary layer is a consequence of the presence of a temperature difference between the surface and the free stream (cf. Fig. 3.20B). Due to the presence of such a temperature difference, the fluid temperature is equal to the surface temperature at the wall in the boundary layer, varies within the boundary layer and remains constant at a temperature outside the boundary layer that is usually termed the free stream temperature, T_∞. The thickness of the thermal boundary layer, δ_{th}, is usually considered to correspond to a fluid temperature of $T_\delta = (T_s - T)/(T_s - T_\infty) = 0.99$. The significance of the thermal boundary layer thus depends on the magnitude of difference between the temperature at the surface wall, T_s, and the temperature of the free stream, T_∞. This relationship is usually expressed through the *local* convection heat transfer coefficient, h_c, which can be determined by considering that at the surface wall heat transfer occurs by conduction only (i.e. Fourier's law can be applied to the fluid) and convection governs heat transfer in the fluid in motion (i.e. Newton's law of cooling can be used). With regards to the problem depicted in Fig. 3.20B, Fourier's law reads

$$\dot{q}_{cond} = -\lambda \frac{\partial T}{\partial y}\Big|_{y=0} \tag{3.51}$$

and can be substituted into Newton's law of cooling to yield the convection heat transfer coefficient

$$h_c = \frac{-\lambda \frac{\partial T}{\partial y}\Big|_{y=0}}{T_s - T_\infty} \tag{3.52}$$

The variation of the heat transfer coefficient as a consequence of the development of the boundary layers has noteworthy consequences for heat transfer analyses. Varying heat transfer coefficients are associated with different heat transfer rates by convection. In the context of energy geostructures, relevant heat transfer rates by convection can take place, for instance, between the surface of the energy geostructure, such as energy walls and tunnels, and adjacent underground built environments, as well as between the heat carrier fluid circulating in the pipes embedded in energy geostructures and the surroundings.

3.15 Momentum conservation equation

3.15.1 General

The momentum conservation equation expresses the principle of balance of linear momentum. This conservation equation is also termed *Cauchy's first law of motion* or the *Cauchy momentum equation*. When applied to the analysis of problems of internal and external flows in which due account is made of the equilibrium of the moving fluid, the momentum conservation equation is typically expressed in the form of the Navier–Stokes equations.

3.15.2 Navier–Stokes equations

The Navier–Stokes equations can be derived in a similar fashion to the conservation of mass (see for further details, e.g. Lewis et al. (1996)). For a viscous incompressible flow they read

$$\frac{d\rho_f \overline{v}_{rf,i}}{dt} = -\nabla p_f + \mu_f \nabla^2 \overline{v}_{rf,i} + \rho_f b_i \tag{3.53}$$

where b_i is the vector of body forces. In indicial form

$$\rho_f \left(\frac{\partial \overline{v}_{rf,k}}{\partial t} + \overline{v}_{rf,j} \frac{\partial \overline{v}_{rf,k}}{\partial x_j} \right) = -\frac{\partial p_f}{\partial x_k} + \mu_f \frac{\partial^2 \overline{v}_{rf,k}}{\partial x_k^2} + \rho_f b_i \tag{3.54}$$

The Navier–Stokes equations can be simplified to yield the Euler equations for describing inviscid flows. Together with the mass conservation equation, the Navier–Stokes equations allow the describing of internal and external flow problems in which due account of the equilibrium of the fluid in motion is made under isothermal conditions. Under nonisothermal conditions, the energy conservation equation must be added to the previous equations to solve the problem addressed.

References

ASHRAE, 2012. American Society of Heating Refrigeration and Air-Conditioning Engineers Handbook. ASHRAE, Atlanta, GA.

Alrtimi, A., Rouainia, M., Haigh, S., 2016. Thermal conductivity of a sandy soil. Appl. Therm. Eng. 106, 551–560.

Banks, D., 2012. An Introduction to Thermogeology: Ground Source Heating and Cooling. John Wiley & Sons.

Beard, D., Weyl, P., 1973. Influence of texture on porosity and permeability of unconsolidated sand. AAPG Bull. 57 (2), 349–369.

Bedford, A., Drumheller, D.S., 1983. Theories of immiscible and structured mixtures. Int. J. Eng. Sci. 21 (8), 863–960.

Bergman, T., Incropera, F., Lavine, A., DeWitt, D., 2011. Fundamentals of Heat and Mass Transfer. Wiley, Hoboken, NJ.

Boley, B.A., Weiner, J.H., 1997. Theory of Thermal Stresses. Dover Publications, Mineola, NY.

Bourne-Webb, P., Freitas, T.B., da Costa Gonçalves, R., 2016. Thermal and mechanical aspects of the response of embedded retaining walls used as shallow geothermal heat exchangers. EnergyBuild. 125, 130–141.

Brandl, H., 2006. Energy foundations and other thermo-active ground structures. Geotechnique 56 (2), 81–122.

Brandon, T., Mitchell, J., 1989. Factors influencing thermal resistivity of sands. J. Geotech. Eng. 115 (12), 1683–1698.

Burghignoli, A., Desideri, A., Miliziano, S., 2000. A laboratory study on the thermomechanical behavior of clayey soils. Can. Geotech. J. 37 (4), 764–780.

Carman, P.C., 1937. Fluid flow through granular beds. Trans. -Inst. Chem. Eng. 15, 150–166.

Casagrande, A., 1937. Seepage through dams. Water Works Assoc. L1 (2), 131–172.

Chen, S.X., 2008. Thermal conductivity of sands. Heat Mass Transf. 44 (10), 1241.

Chiasson, A.D., Rees, S.J., Spitler, J.D., 2000. A preliminary assessment of the effects of groundwater flow on closed-loop ground source heat pump systems. ASHRAE Trans. 106 (1), 380–393.

Clark, S.P., 1966. Handbook of Physical Constants. Geological Society of America.

Côté, J., Konrad, J.-M., 2005. A generalized thermal conductivity model for soils and construction materials. Can. Geotech. J. 42 (2), 443–458.

Darcy, H., 1856. Les fontaines publiques de la ville de Dijon: exposition et application. Victor Dalmont.

De Boer, R., Ehlers, W., 1988. A historical review of the formulation of porous media theories. Acta Mech. 74 (1-4), 1–8.

De Vries, D.A., 1963. Thermal properties of soils. In: Physics of Plant Environment. Wiley, New York.

Donazzi, F., Occhini, E., Seppi, A., 1979. Soil thermal and hydrological characteristics in designing underground cables. In: Proceedings of the Institution of Electrical Engineers. IET, vol. 126, pp. 506–516.

Dysli, M., 1991. Le gel et son action sur les sols et les fondations. PPUR presses polytechniques.

EN ISO 6946, 2007. BS EN ISO 6946: 2007 Building components and building elements—Thermal resistance and thermal transmittance—Calculation method. International Organization for Standardization.

Farouki, O.T., 1986. Thermal Properties of Soils. Series on Rock and Soil Mechanics, vol. 11. Trans Tech Publications, Clausthal-Zellerfeld.

Folk, R.L., Ward, W.C., 1957. Brazos River bar: a study in the significance of grain size parameters. J. Sediment. Res. 27 (1), 3–26.

Fourier, J., 1822. Theorie analytique de la chaleur. Chez Firmin Didot, père et fils.

Fredlund, D.G., Rahardjo, H., Rahardjo, H., 1993. Soil Mechanics for Unsaturated Soils. John Wiley & Sons.

Gangadhara Rao, M., Singh, D., 1999. A generalized relationship to estimate thermal resistivity of soils. Can. Geotech. J. 36 (4), 767–773.

Gemant, A., 1952. How to compute thermal soil conductivities. Heat. Pip. Air Cond. 24 (1), 122–123.

Guo, L., Guo, L., Zhong, L., Zhu, Y., 2011. Thermal conductivity and heat transfer coefficient of concrete. J. Wuhan Univ. Technol. —Mat. Sci. Ed. 26 (4), 791–796.
Haigh, S., 2012. Thermal conductivity of sands. Geotechnique 62 (7), 617.
Hamilton, R., Crosser, O., 1962. Thermal conductivity of heterogeneous two-component systems. Ind. Eng. Chem. Fundam. 1 (3), 187–191.
Hazen, A., 1892. Some physical properties of sands and gravels: with special reference to their use in filtration. In: 24th Annual Report. Massachusetts State Board of Health, pp. 539–556.
Henderson, N., Brêttas, J.C., Sacco, W.F., 2010. A three-parameter Kozeny–Carman generalized equation for fractal porous media. Chem. Eng. Sci. 65 (15), 4432–4442.
Hermansson, Å., Charlier, R., Collin, F., Erlingsson, S., Laloui, L., Sršen Sr, M., 2009. Heat transfer in soils. Water in Road Structures. Springer, pp. 69–79.
Hiraiwa, Y., Kasubuchi, T., 2000. Temperature dependence of thermal conductivity of soil over a wide range of temperature (5–75°C). Eur. J. Soil Sci. 51 (2), 211–218.
Johansen, O., 1977. Thermal Conductivity of Soils (Ph.D. Thesis). U.S. Army, Cold Regions Research and Engineering Laboratory.
Kersten, M.S., 1949. Thermal properties of soils. Bull. Univ. Minn. Inst. Technol. 52, 1–225.
Khalifa, A.-J.N., 2001a. Natural convective heat transfer coefficient—a review: I. Isolated vertical and horizontal surfaces. Energy Convers. Manag. 42 (4), 491–504.
Khalifa, A.-J.N., 2001b. Natural convective heat transfer coefficient–a review: II. Surfaces in two-and three-dimensional enclosures. Energy Convers. Manag. 42 (4), 505–517.
Khalifa, M.-O.A., Wahyudi, I., Thomas, P., 2002. New extension of Darcy's law to unsteady flows. Soils Found. 42 (6), 53–63.
Kim, K.-H., Jeon, S.-E., Kim, J.-K., Yang, S., 2003. An experimental study on thermal conductivity of concrete. Cem. Concr. Res. 33 (3), 363–371.
Kozeny, J., 1927. Uber kapillare leitung der wasser in boden. R. Acad. Sci. Vienna Proc. Class I 136, 271–306.
Krumbein, W., Monk, G., 1943. Permeability as a function of the size parameters of unconsolidated sand. Trans. AIME 151 (01), 153–163.
Lai, W.M., Rubin, D.H., Krempl, E., Rubin, D., 2009. Introduction to Continuum Mechanics. Butterworth-Heinemann.
Lanciani, A., Morabito, P., Rossi, P., Barberis, F., Berti, R., Capelli, A., et al., 1989. Measurements of the thermophysical properties of structural materials in laboratory and in situ: methods and instrumentation. High Temp. High Press. 21 (4), 391–400.
Lee, Y., Choi, M.-S., Yi, S.-T., Kim, J.-K., 2009. Experimental study on the convective heat transfer coefficient of early-age concrete. Cem. Concr. Compos. 31 (1), 60–71.
Lewis, R.W., Morgan, K., Thomas, H., Seetharamu, K., 1996. The Finite Element Method in Heat Transfer Analysis. Wiley.
Lorentz, H., 1952. Theory of Electrons. Dover Publications, New York.
Loveridge, F., 2012. The Thermal Performance of Foundation Piles Used as Heat Exchangers in Ground Energy Systems. (Ph.D. Thesis). University of Southampton
Lu, S., Ren, T., Gong, Y., Horton, R., 2007. An improved model for predicting soil thermal conductivity from water content at room temperature. Soil Sci. Soc. Am. J. 71 (1), 8–14.
Makowski, M.W., Mochlinski, K., 1956. An evaluation of two rapid methods of assessing the thermal resistivity of soil. Proc. IEE Part A Power Eng. 103 (11), 453–470.
Martynov, G.A. (1963) Heat and Moisture Transfer in Freezing and Thawing Soils. National Research Council of Canada Technical Translation, 56 pp.
Midttømme, K., Banks, D., Kalskin Ramstad, R., Sæther, O.M., Skarphagen, H., 2008. Ground-source heat pumps and underground thermal energy storage: energy for the future. NGU Spec. Publ. 11, 93–98.
Mitchell, J.K., Soga, K., 2005. Fundamentals of Soil Behavior. Wiley, New York.
Morabito, P., 1989. Measurement of the thermal properties of different concretes. High Temp. High Press. 21 (1), 51–59.
Neville, A.M., 1995. Properties of Concrete. Longman, London.

Pahud, D., 2002. Geothermal Energy and Heat Storage. Laboratorio di Energia, Ecologia ed Economia, Canobbio.
Palyvos, J., 2008. A survey of wind convection coefficient correlations for building envelope energy systems' modeling. Appl. Therm. Eng. 28 (8), 801–808.
Pape, H., Clauser, C., Iffland, J., 2000. Variation of permeability with porosity in sandstone diagenesis interpreted with a fractal pore space model. Pure Appl. Geophys. 157 (4), 603–620.
Poiseuille, J.L., 1844. Recherches expérimentales sur le mouvement des liquides dans les tubes de très-petits diamètres. Imprimerie Royale.
Rees, S., Adjali, M., Zhou, Z., Davies, M., Thomas, H., 2000. Ground heat transfer effects on the thermal performance of earth-contact structures. Renew. Sustain. Energy Rev. 4 (3), 213–265.
Rerak, M., 2017. Selected soil thermal conductivity models. In: E3S Web of Conferences. EDP Sciences, vol. 13, p. 02003.
Robertson, E.C., 1988. Thermal properties of rocks. Open-File Report 2331-1258.
Różański, A., Stefaniuk, D., 2016. On the prediction of the thermal conductivity of saturated clayey soils: effect of the specific surface area. Acta Geodyn. Geomater. 13 (4), 339–349.
Sass, J., Lachenbruch, A.H., Moses, T., Morgan, P., 1992. Heat flow from a scientific research well at Cajon Pass, California. J. Geophys. Res.: Solid Earth 97 (B4), 5017–5030.
Serafim, J.L., Campo, A., 1965. Interstitial pressures on rock foundations of dams. J. Soil Mech. Found. Div 91 (SM5), 65–85.
Shin, K.-Y., Kim, S.-B., Kim, J.-H., Chung, M., Jung, P.-S., 2002. Thermo-physical properties and transient heat transfer of concrete at elevated temperatures. Nuclear Eng. Des. 212 (1), 233–241.
SIA-D0190, 0190. Utilisation de la Chaleur du Sol par des Ouvrages de Fondation et de Soutènement en Béton. Guide pour la Conception, la Realisation et la Maintenance, Zurich, Switzerland.
Silin-Bekchurin, A., 1958. Dynamics of Underground Water. Moscow Izdat, Moscow University, Moscow.
Tang, Y.C., Meng, G.T., Mao, Q.F., 2011. Study on soil permeability coefficient on CPTU Model Test, Advanced Materials Research, 261. Trans Tech Publications, pp. 1401–1405.
Thomas, H., King, S., 1994. A non-linear, two-dimensional, potential-based analysis of coupled heat and mass transfer in a porous medium. Int. J. Numer. Methods Eng. 37 (21), 3707–3722.
Timoshenko, S., Goodier, J., 1951. Theory of Elasticity. McGraw-Hill.
Towhata, I., Kuntiwattanaul, P., Seko, I., Ohishi, K., 1993. Volume change of clays induced by heating as observed in consolidation tests. Soil Found. 33 (4), 170–183.
Vulliet, L., Laloui, L., Zhao, J., 2016. Mécanique des sols et des roches: avec écoulements souterrains et transferts de chaleur. PPUR Presses polytechniques.
Whitaker, S., 1986. Flow in porous media I: A theoretical derivation of Darcy's law. Transp. Porous Media 1 (1), 3–25.
Woodside, W., Messmer, J., 1961. Thermal conductivity of porous media. I. Unconsolidated sands. J. Appl. Phys. 32 (9), 1688–1699.
Zoth, G., Haenel, R., 1988. Appendix. In: Haenel, R., Stegena, L., Rybach, L. (Eds.), Handbook of Terrestrial Heat-Flow Density Determination: With Guidelines and Recommendations of the International Heat Flow Commission. Kluwer Academic Publisher, Dordrecht, p. 485.

Questions and problems

Statements

a. What is an isotropic material?

b. List the three fundamental modes of heat transfer.

c. Discuss the physical mechanisms associated with heat transfer by conduction, convection and radiation.

d. The driving cause of heat transfer by conduction is generally considered to be:

i. The motion of a fluid

ii. An invisible motion of the particles that constitute a medium

iii. Waves of the electromagnetic field propagating at the speed of light

e. Define Fourier's law.

f. Write the general mathematical formulation of Fourier's law in steady-state conditions. What are the vector and scalar quantities? Why is there a minus sign on the right-hand side of the equation?

g. Define the temperature gradient. What are its units?

h. Write the different forms that Fourier's law takes for each of the orthogonal directions of Cartesian, cylindrical and spherical coordinate systems.

i. Write Fourier's law from memory with respect to the case of a plane energy wall in a steady state represented in the following picture.

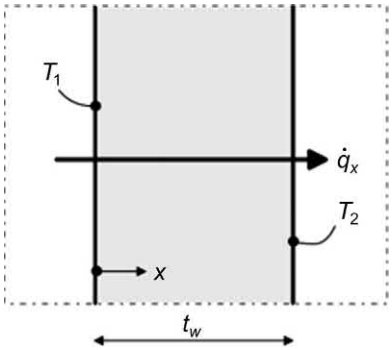

j. Define thermal conductivity. What are its units? What role does it play in heat transfer?

k. The thermal conductivity of a solid is generally larger than that of a liquid. Why? Then, why is the thermal conductivity of a liquid larger than that of a gas?

l. Is the thermal conductivity of a saturated soil greater or smaller than that of the same dry soil? Justify your answer.

m. Calculate the effective thermal conductivity, λ, of a dry sand at the temperature level of 15°C characterised by a porosity $n = 0.42$ and a value of thermal conductivity of solid particles $\lambda_s = 0.41$ W/(m °C). Repeat the calculation for the same

sand, assuming it is fully saturated with water. Comment on the results and on the impact of the different values of λ on the heat exchange characterising an adjacent energy pile.

n. Calculate the effective thermal conductivity, λ, of a saturated clay characterised by a porosity $n = 0.42$ and a value of thermal conductivity of solid particles $\lambda_s = 0.15$ W/(m °C). Compare the value of thermal conductivity with that calculated above for the saturated sand. In which condition is heat exchange favourable for an adjacent energy geostructure?

o. Which is the typical range of values of thermal conductivity for concrete?

p. Describe the two mechanisms characterising the convection heat transfer mode.

q. Discuss the difference between forced and natural convection.

r. What is radiation and which are its units?

s. What is the emissivity?

t. Which is the principal heat transfer mode that characterises the heat exchange in the pipes of energy geostructures?

u. Which is the principal heat transfer mode that characterises the heat exchange between the pipes and the reinforced concrete of energy geostructures?

v. Consider the case of an energy pile socketed in a uniform soil deposit characterised by negligible groundwater flow. What are the main heat transfer modes that occur when the pile is in function, neglecting the phenomena that may occur at the ground surface?

w. Consider an energy pile socketed in a given soil deposit and connected to a reinforced concrete base slab of underground car parking. Assume that no thermal insulation has been foreseen for the slab. Describe the heat transfer phenomena occurring in the problem.

x. Consider a generic energy pile. Why are the first metres of pipes beyond the surface thermally insulated? Which are the main effects of radiation on this kind of system and, in general, of the seasonal weather changes?

y. Consider a dry sandy soil deposit. Which are the main heat transfer modes that occur? What about a saturated soil layer with significant groundwater flow?

z. An underground metro station energy wall is thermally insulated from the surrounding soil fully saturated with water, so that the heat exchange characterising the wall predominantly occurs between the pipes embedded in the geostructure, the grouting material and the metro station environment. Describe the heat transfer phenomena occurring in the problem. What happens if no insulation may be foreseen between the wall and the soil?

aa. Consider the following form of the Fourier heat conduction equation:

$$\lambda \nabla^2 T + \dot{q}_v = \rho c_p \frac{\partial T}{\partial t}$$

Define all of the involved terms, their unit measures and their physical meaning. Write the equation for the cases where there is no internal heat generation, temperature is independent of time, or both conditions occur. Specify the meaning of an internal heat generation and when temperature can be assumed to be independent of time.

bb. Generically, to solve the Fourier heat conduction equation uniquely there is the need to specify initial and boundary conditions for the specific problem. Can you detail the role of both initial and boundary conditions in the heat transfer problem? Are initial conditions always necessary for the resolution?

cc. Boundary conditions must be given at the boundaries of any medium to solve the energy conservation equation, obtaining the temperature distribution in the medium. Summarise the boundary conditions commonly encountered in heat transfer problems.

dd. How is the contact thermal resistance defined for an interface of a unit area and what are its units?

ee. Discuss how the contact thermal contact resistance is affected by the roughness of two adjacent surfaces.

ff. Write the formulation of the energy conservation equation for an isotropic slab considering conduction, convection with a fluid and radiation from a surrounding environment with no heat generation.

gg. How is the thermal diffusivity defined and what are its units?

hh. Soils of large thermal diffusivity respond:

- **i.** Quickly to variations in their thermal environment
- **ii.** Slowly to variations in their thermal environment
- **iii.** Irrespectively of the variations of their thermal environment
- **iv.** Depending on the thermal conductivity

ii. The thermal diffusivity α_d is the controlling transport property for transient conduction. Using appropriate values of λ, ρ and c_p, calculate α_d for the following materials at the temperature level of 15°C and complete the table presented below.

Material	Thermal conductivity, λ [W/(m °C)]		Volumetric heat capacity, ρc_p [MJ/(m^3 °C)]		Thermal diffusivity, α_d [m^2/s]	
	Dry	Saturated	Dry	Saturated	Dry	Saturated
Clay	0.2–0.3	1.1–1.6	0.3–0.6	2.1–3.2		
Silt	0.2–0.3	1.2–2.5	0.6–1.0	2.1–2.4		
Sand	0.3–0.4	1.7–3.2	1.0–1.3	2.2–2.4		
Gravel	0.3–0.4	1.8–3.3	1.2–1.6	2.2–2.4		
Concrete	0.9–2.0		1.8–2.0			
Water	0.57		4.186			
Air	0.025		0.0012			

jj. In general, can you neglect the different values of thermal diffusivity of the different materials involved with energy geostructures? Why?

kk. It has been observed that the potential variable characterising heat transfer is the temperature. What is the potential variable characterising mass transfer?

ll. Can you mathematically define the total head, expressing the physical meaning of each constituting term?

mm. In which conditions can the total head be reduced to the piezometric head?

nn. Define mathematically the Reynolds number.

oo. What does the Reynolds number physically represent?

pp. A fluid flows turbulently in z-direction, at a rate of $\dot{V} = 3.5\ \mathrm{m}^3/\mathrm{s}$, through a cylindrical pipe. The pipe has a cross-sectional area of $0.5\ \mathrm{m}^2$ and the fluid has a viscosity of $1.2\ \mathrm{N}/(\mathrm{s\ m}^2)$ and a Reynolds number of 6283. What is the density of the fluid (expressed in kg/m^3)? Assume the fluid is incompressible and the flow is at the steady state.

qq. Write Darcy's law and discuss its validity depending on the flow regime.

rr. Which is the fundamental parameter that allows understanding if convection plays a major role in heat transfer in soils? To which law is this parameter related?

ss. What are the units of the hydraulic conductivity? How this variable is related to the intrinsic permeability?

tt. What is the threshold value (or range of values) of groundwater flow velocity that may be accounted for considering or neglecting convection in practical analyses and designs of energy geostructures?

uu. Write the mathematical expression of the mass conservation equation and discuss its terms.

vv. Is it reasonable to foresee thermal energy storage through energy geostructures for a site that is characterised by significant groundwater flow? Why?

ww. Consider an energy pile located below a very large raft of a building and operating as a geothermal heat exchanger. Assume that a very thick thermal insulation layer is placed at the uppermost surface of the slab, so that no influence of the ambient conditions is experienced in the subsurface. Consider that the soil is saturated and that no groundwater flow occurs. Which is/are the main mode/s of heat transfer occurring in the soil?

Solutions

a. Isotropic means having identical values of a certain property in all directions in space.

b. Conduction, convection and radiation.

c. Heat transfer generally occurs in the form of general thermal energy propagating because of a spatial temperature difference. When a temperature gradient exists in a medium, which can be a solid or a fluid, the term conduction is used to refer to the heat transfer that occurs across the medium. In contrast, the term convection refers to the heat transfer that occurs between a surface and a moving fluid when they are at different temperatures. Finally, the term radiation is used to refer to the heat transfer characterising all surfaces of finite temperature that emit energy in the form of electromagnetic waves, even in the absence of an intervening medium.

d. The driving cause of heat transfer by conduction is generally considered to be:

i. The motion of a fluid

ii. An invisible motion of the particles that constitute a medium

iii. Waves of the electromagnetic field propagating at the speed of light

e. Fourier's law is an empirical relationship between the conduction rate in a material and the temperature gradient in the direction of energy flow, first formulated by Fourier in 1822 who concluded that 'the heat flux resulting from thermal conduction is proportional to the magnitude of the temperature gradient and opposite to it in sign'.

f. The general formulation of Fourier's law is

$$\dot{q}_i = -\lambda \nabla T$$

where $\dot{q}_i$ [W/m^2] is the heat flux (i.e. the flow of thermal energy per unit of area per unit of time), λ [W/(m °C)] is the thermal conductivity of the medium, ∇ represents the gradient and T [°C] is the temperature of the medium.

λ

g. A temperature gradient is a physical quantity that describes in which direction and at what rate the temperature variations around a particular location. The temperature gradient is a dimensional quantity expressed in units of degrees (on a particular temperature scale) per unit length. The metric SI unit is K/m, or equivalently °C/m.

h. For the Cartesian coordinates x,y,z, the general form of Fourier's law is $\dot{q} = -\lambda\left(\frac{\partial T}{\partial x}\hat{e}_x + \frac{\partial T}{\partial y}\hat{e}_y + \frac{\partial T}{\partial z}\hat{e}_z\right)$, where $\dot{q}$ [W/m^2] is the heat transfer rate in space per unit area perpendicular to the direction of transfer,

λ [W/(m °C)] is the thermal conductivity, T [°C] is the temperature and $\hat{e}_x$, $\hat{e}_y$ and $\hat{e}_z$ are the standard unit vectors in Cartesian coordinates.

For the cylindrical coordinates r,θ,z, the general form of Fourier's law is $\dot{q} = -\lambda\left(\frac{\partial T}{\partial r}\hat{e}_r + \frac{1}{r}\frac{\partial T}{\partial \theta}\hat{e}_\theta + \frac{\partial T}{\partial z}\hat{e}_z\right)$, where $\hat{e}_r$, $\hat{e}_\theta$ and $\hat{e}_z$ are the standard unit vectors in cylindrical coordinates.

For the spherical coordinate system r,θ,ϕ, the general form of Fourier's law is $\dot{q} = -\lambda\left(\frac{\partial T}{\partial r}\hat{e}_r + \frac{1}{r}\frac{\partial T}{\partial \theta}\hat{e}_\theta + \frac{1}{r\,sin\theta}\frac{\partial T}{\partial \phi}\hat{e}_\phi\right)$, where $\hat{e}_r$, $\hat{e}_\theta$ and $\hat{e}_\phi$ are the standard unit vectors in spherical coordinates.

i. $\dot{q}_x = -\lambda\frac{dT}{dx} = -\lambda\frac{(T_2 - T_1)}{t_w} = \frac{\lambda(T_1 - T_2)}{t_w}$ where $\dot{q}_x$ [W/m^2] is the heat flux, λ [W/(m °C)] is the thermal conductivity of the medium, T [°C] is the temperature of the medium and t_w [m] is the wall thickness.

j. The thermal conductivity is a property that provides an indication of the rate at which energy is transferred by the diffusion process characteristic of conduction and depends on the physical structure of matter and its state. Based on Fourier's law, the thermal conductivity associated with conduction in the x-direction of a Cartesian coordinate system is defined as

$$\lambda_x \equiv -\frac{\dot{q}_x}{\left(\frac{\partial T}{\partial x}\right)}[\mathrm{W/(m^\circ C)}]$$

where $\dot{q}_x$ [W/m^2] is the heat flux (i.e. the flow of thermal energy per unit of area per unit of time), T [°C] is the temperature of the medium and x is the Cartesian coordinate representing the direction of the heat flux vector. Heat transfer occurs at a lower rate across materials of low thermal conductivity than across materials of high thermal conductivity.

k. As the intermolecular spacing is much larger and the motion of the molecules is more random for the fluid state than for the solid state, thermal energy transport is less effective. The thermal conductivity of gases and liquids is therefore generally smaller than that of solids and, for the same reason, in the specific the thermal conductivity of gases is smaller than liquids.

l. The thermal conductivity of a saturated geomaterial is greater than that of the same dry geomaterial because of the higher magnitude of the thermal conductivity of water with respect to that the air filling the geomaterial pores in the saturated and dry case, respectively ($\lambda_w = 0.57$ W/(m°C) while $\lambda_a = 0.025$ W/(m°C) at a temperature of $T = 15$°C).

m. Thermal conductivity of air at ambient temperature is $\lambda_a = 0.025$ W/(m°C). Therefore the effective thermal conductivity calculated as a weighted arithmetic mean of the thermal conductivities of its components reads

$$\lambda = n\lambda_a + (1-n)\lambda_s = 0.25\ \mathrm{W/(m^{\circ}C)}$$

The thermal conductivity of water at ambient temperature is $\lambda_w = 0.58\ \mathrm{W/(m^{\circ}C)}$. Hence, for the case in which the sand is saturated with water the effective thermal conductivity reads

$$\lambda_{sat} = n\lambda_w + (1-n)\lambda_s = 0.48\ \mathrm{W/(m^{\circ}C)}$$

The above explains why a thermal conductor present in soil pores, such as water, strongly increases the heat exchange between, for example an energy pile and the surrounding soil, in contrast to what happens with a thermal insulator like air.

n. The effective thermal conductivity can be defined as

$$\lambda = n\lambda_a + (1-n)\lambda_s$$

The thermal conductivity of air at ambient temperature is $\lambda_a = 0.025\ \mathrm{W/(m\ ^{\circ}C)}$, hence $\lambda = n\lambda_a + (1-n)\lambda_s = 0.1\ \mathrm{W/(m\ ^{\circ}C)}$, which is five times less than the value obtained for the saturated sand. Therefore in general, the heat exchange is less favourable for an energy geostructure adjacent to a saturated clayey deposit than to a saturated sandy deposit.

o. Thermal conductivity for concrete goes from about 0.15 to about 2 W/(m °C), depending, for example on its structure and mix design.

p. Energy is transferred by the macroscopic motion of the fluid, in addition to energy transfer due to random molecular motion (diffusion). The fluid motion is associated with the fact that large numbers of molecules are moving collectively or as aggregates. This motion, in the presence of a temperature gradient, contributes to heat transfer. Since the molecules in the aggregate retain their random motion, the total heat transfer is then due to a superposition of energy transport by the random motion of the molecules and by the bulk motion of the fluid. The term convection is usually used when referring to this cumulative transport, and the term advection usually refers to transport due to bulk fluid motion.

q. Convection heat transfer can be classified according to the nature of the flow. Forced convection characterises heat flows caused by external means, such as a pump, a fan or atmospheric winds. In contrast, free (or natural) convection characterises heat flows induced by buoyancy forces, which are due to density differences caused by temperature variations in the fluid.

r. Thermal radiation is energy emitted by matter that is at a nonzero temperature. Radiation that is emitted by the surface originates from the thermal energy of matter bounded by the surface and the rate at which

energy is released per unit area [W/m^2] is termed the 'surface emissive power'.

s. The emissivity of a surface ϵ [−], with values in the range $0 \leq \epsilon \leq 1$, provides a measure of how efficiently a surface emits energy by radiation relative to a blackbody. It strongly depends on the surface material and finish.

t. The main heat transfer mode within the pipes of energy geostructures is forced convection associated with the pumping of the heat carrier fluid circulating in the pipes.

u. Conduction governs the heat exchange between the walls of the pipe and the concrete. Within the pipes, forced convection governs the heat exchange.

v. In these conditions forced convection occurs within the pipes of the energy pile, whereas conduction occurs between the pipes, the concrete constituting the energy pile and the soil. The contact resistance between the outer surface of the energy pile and the soil deposit may play an important role in the heat transfer phenomenon.

w. In these conditions forced convection occurs within the pipes of the energy pile, whereas conduction occurs between the pipes, the concrete constituting the energy pile and the soil. Since there is no thermal insulation between the slab and the soil, the system can be affected by surrounding environmental variations, for example related to convection heat transfer with the surface. However, if the underground car parking were to be characterised by an almost constant temperature field throughout the year, the influence of environmental variations, for example by convection should not be significant.

x. The first metres of pipes beyond the surface are thermally insulated because the soil temperature field in the first metres below the surface is not stable throughout the year: radiation and convection phenomena caused by the sun or by external air temperature flows can significantly affect the thermohydraulic behaviour of the energy pile. The interplay between these phenomena with rainfalls and other climatic events can also significantly influence the thermal properties of the soil with a noteworthy impact on the thermohydraulic behaviour of the energy pile. Thermally insulating the pipes in this soil region allows the limiting of the influence of the aforementioned phenomena on the thermohydraulic behaviour of the energy pile.

y. In a dry sandy soil deposit the main heat transfer mode is conduction. If the soil would be fully saturated with water and characterised by a

significant groundwater flow, the main heat transfer mode would be convection.

z. In these conditions, forced convection occurs within the pipes embedded in the energy wall, conduction characterises the heat exchange between the pipes and the surrounding reinforced concrete constituting the energy wall, and natural and/or forced convection can typically govern the heat exchange between the concrete wall and the adjacent metro station environment. If no thermal insulation may be foreseen between the wall and the soil, conduction or conduction and convection may also characterise heat transfer between the wall and the soil, depending on the significance of groundwater flow.

aa. In this form of the Fourier heat conduction equation, λ [W/(m °C)] is the thermal conductivity of the medium, ∇^2 is the Laplace operator of the temperature of the medium T [°C], $\dot{q}_v$ [W/m^3] is the internal volumetric heat generation, ρ [kg/m^3] is the density of the medium, c_p [J/(kg °C)] the specific heat of the medium and t [s] is the time. The term on the right-hand side of the equation represents the variation of internal energy in the medium over time.

Defining the thermal diffusivity as $\alpha_d = \lambda/(\rho c_p)$ [m^2/s], in case of no internal heat generation the equation is

$$\alpha_d \nabla^2 T = \frac{\partial T}{\partial t}$$

while in case of time-independent temperature the equation is

$$\lambda \nabla^2 T + \dot{q}_v = 0$$

and if both conditions occur the equation is

$$\nabla^2 T = 0$$

which is also called the Laplace equation.

In general, internal heat generation is applied to a part that will either act as a heat source or heat sink throughout the analysis, such as an energy geostructure.

Temperature distribution can be assumed to be independent of time when the system is at steady-state conditions. Hence, the Laplace equation often represents the basis for analysis and design considerations of energy geostructures. However, the large heat capacity of soils delays the effects of external variations in temperature, often requiring a transient analysis.

bb. To determine the temperature distribution in a medium, it is necessary to solve the appropriate form of the energy conservation equation. However, such a solution depends on the physical conditions existing at the boundaries of the medium and, if the situation is time dependent, on conditions existing in the medium at some initial time. With regard to the boundary conditions, there are several common possibilities that are simply expressed in mathematical form. Because the heat equation is second order in the spatial coordinates, two boundary conditions must be expressed for each coordinate needed to describe the system. Because the equation is first order in time, however, only one condition, termed the initial condition, must be specified. If in steady-state conditions, no initial condition is needed.

cc. Usually, three types of boundary conditions are prescribed in heat transfer.

The so-called Dirichlet's boundary condition or boundary condition of the first kind allows fixing the temperature of any surface as

$$T(\mathcal{H}, t) = f(\mathcal{H}, t)$$

where $\mathcal{H}$ is a point on the considered surface, $f(\mathcal{H},t)$ [°C] is a prescribed function and t [s] is the time.

The so-called Neumann's boundary condition or boundary condition of the second kind allows fixing a heat input. Based on Fourier's law, this boundary condition takes the form

$$-\lambda \frac{\partial T}{\partial n_i}(\mathcal{H}, t) = \dot{q}(\mathcal{H}, t)$$

where λ [W/(m °C)] is the thermal conductivity, T [°C] is the temperature, n_i is the normal to the surface at the point $\mathcal{H}$ and $\dot{q}$ [W/m^2] is the heat flux.

The so-called Cauchy's boundary condition, mixed Neumann's boundary condition or boundary condition of the third kind allows prescribing a convection boundary condition for conduction problems. In this case the considered condition takes the form

$$-\lambda \frac{\partial T}{\partial n_i}(\mathcal{H}, t) = h_c[T_\infty - T(\mathcal{H}, t)]$$

where h_c [W/(m^2 °C)] is the convection heat transfer coefficient and $T_\infty(t)$ [°C] and $T(\mathcal{H},t)$ [°C] are the temperature of the source and surface, respectively.

The Cauchy's boundary condition also allows prescribing a radiation boundary condition for conduction problems. In this case, the considered condition takes the form

$$-\lambda\frac{\partial T}{\partial n_i}(\mathcal{H},t)=\epsilon\sigma_{SB}(T_{\infty}^{4}(t)-T^{4}(\mathcal{H},t))$$

where the term on the left side of the equation represents the heat flux vector [W/m^2] in n_i direction, $T_{\infty}(t)$ [°C] and $T(\mathcal{H},t)$ [°C] are the temperatures of the source and surface, respectively, σ_{SB} is the Stefan–Boltzmann constant [W/(m^2 °C^4)] and ϵ [–] is the surface emissivity.

dd. The temperature drop across the interface between materials can be appreciable: this phenomenon is attributed to the presence of a thermal contact resistance. The existence of a finite contact resistance is due principally to surface roughness effects, where the contact spots are separated by gaps filled with a fluid. When these gaps are filled with a gas, heat transfer is due to conduction across the actual contact area and to conduction and/or radiation across the gaps. When the gaps are filled with a liquid, heat transfer is due to conduction across the actual contact area and to conduction and/or convection across the gaps.

For a unit area of a considered interface, the thermal contact resistance is defined as:

$$R_c''=\frac{T_A-T_B}{\dot{q}_x}\left[\frac{\mathrm{m}^{2\circ}\mathrm{C}}{\mathrm{W}}\right].$$

where T_A and T_B [°C] are the temperature of the surfaces separated by the gap and $\dot{q}_x$ [W/m^2] is the heat flux in x-direction.

ee. As it can be observed in the cases where a contact resistance is present, the contact area is typically small, and, particularly for rough surfaces, the main contribution to the resistance is due to the gaps. The contact resistance can be reduced by increasing the area of the contact spots in the case of solids with a thermal conductivity exceeding that of the interfacial fluids. This increase is affected by increasing the joint pressure and/or by reducing the roughness of the mating surfaces. Selecting an interfacial fluid of large thermal conductivity can also reduce the contact resistance. With respect to this, no fluid (an evacuated interface) eliminates conduction across the gap, increasing the contact resistance.

ff. The energy conservation equation reads in this case:

$$\dot{q}_{cond} - \dot{q}_{conv} - \dot{q}_{rad} = 0$$

where $\dot{q}_{cond} = -\lambda \frac{\Delta T}{t_{slab}}$ is the conductive heat flux [W/m^2], with λ the thermal conductivity of the medium [W/(m °C)], ΔT the temperature difference through the slab [°C] and t_{slab} is the slab thickness [m];

$\dot{q}_{conv} = h_c(T_s - T_\infty)$ is the convective heat flux [W/m^2], with h_c the convective heat transfer coefficient [W/(m^2 °C)], T_s the temperature of the surface exposed to the fluid and T_∞ the bulk temperature, both expressed in [°C]; and

$\dot{q}_{rad} = \epsilon \sigma_{SB}(T_s^4 - T_{sur}^4)$ is the radiative heat flux [W/m^2], with ϵ the emissivity of the body [−], σ_{SB} is the Stefan−Boltzmann constant [W/(m^2 °C^4)] and T_{sur} is the surrounding environment temperature [°C].

gg. In heat transfer analysis the ratio of the thermal conductivity λ [W/(m °C)] to the volumetric heat capacity ρc_p [J/(m^3 °C)] is termed the thermal diffusivity α_d [m^2/s] and reads

$$\alpha_d = \frac{\lambda}{\rho c_p}$$

hh. Soils of large thermal diffusivity respond:

i. Quickly to variations in their thermal environment

ii. Slowly to variations in their thermal environment

iii. Irrespectively of the variations of their thermal environment

iv. Depending on the thermal conductivity

ii. The thermal diffusivity is defined as $\alpha_d = \lambda/(\rho c_p)$ [m^2/s].

Material	Thermal conductivity, λ [W/(m °C)]		Volumetric heat capacity, ρc_p [MJ/(m^3 °C)]		Thermal diffusivity, α_d [m^2/s]	
	Dry	Saturated	Dry	Saturated	Dry	Saturated
Clay	0.2−0.3	1.1−1.6	0.3−0.6	2.1−3.2	**0.5−0.67**	**0.5−0.52**
Silt	0.2−0.3	1.2−2.5	0.6−1.0	2.1−2.4	**0.3−0.33**	**0.57−1.04**
Sand	0.3−0.4	1.7−3.2	1.0−1.3	2.2−2.4	**0.3−0.31**	**0.77−1.33**
Gravel	0.3−0.4	1.8−3.3	1.2−1.6	2.2−2.4	**0.25**	**0.82−1.375**
Concrete	0.9−2.0		1.8−2.0		**0.5−1**	
Water	0.57		4.186		**0.14**	
Air	0.025		0.0012		**20.83**	

jj. In general, the different values of thermal diffusivity for different materials cannot be neglected: differences in thermal conductivity, density and specific heat are observed between the different materials and affect the heat transfer.

kk. **In analogy with the heat transfer, where the potential variable is the temperature, total head, H [m], characterises mass transfer.**

ll. **The expression of the total head, for a fluid such as water, reads**

$$H = h_z + h_p + h_v = z + \frac{p_w}{\gamma_w} + \frac{v_w^2}{2g}$$

where z is the elevation of a considered fluid particle above a reference plane [m], p_w is the fluid pressure [Pa], γ_w is the unit weight of the fluid [N/m^3], v_w is the velocity of the fluid at a point on a streamline [m/s] and g is the gravitational acceleration [m/s^2].

mm. **When the contribution of the velocity head can be neglected with respect to the contribution of the elevation and velocity heads (i.e. laminar flow) the total head can be reduced to the piezometric head as**

$$H = h_z + h_p = z + \frac{p_w}{\gamma_w} = h$$

where z [m] is the elevation of a considered fluid particle above a reference plane, p_w [Pa] is the fluid pressure, γ_w [N/m^3] is the unit weight of the fluid and h [m] is the piezometric head.

nn. **The Reynolds number can be mathematically expressed as**

$$Re_x = \frac{\rho_f v_\infty x}{\mu_f}$$

where ρ_f [kg/m^3] is the density of the fluid, v_∞ [m/s] is the characteristic velocity of the fluid, x [m] is the characteristic length of the problem and μ_f [Pa · s] the dynamic viscosity of the fluid.

oo. **The Reynolds number represents the ratio of the inertia to viscous forces. If the Reynolds number is small, inertia forces are insignificant relative to viscous forces. The disturbances are then dissipated, and the flow remains laminar. For a large Reynolds number, however, the inertia forces can be sufficient to amplify the triggering mechanisms, and a transition to turbulence occurs.**

pp. **Knowing that the volumetric flow rate can be expressed as $\dot{V} = A\bar{v}_z$ [m^3/s], the velocity in z-direction can be calculated as**

$$\bar{v}_z = \frac{\dot{V}}{A} = \frac{3.5}{0.5} = 7 \text{ m/s}$$

From the formula of a circle cross-sectional area $A = \pi d_p^2/4$ [m^2], the diameter of the pipe can be calculated as

$$d_p = \sqrt{4A/\pi} = 0.8 \text{ m}$$

Reynolds number is $Re = \rho_f \bar{v}_z d_p / \mu_f$, hence the density of the fluid is

$$\rho_f = \frac{\mu_f}{\bar{v}_z d_p} Re = \frac{1.2}{7 \times 0.8} \times 6283 = 1346 \text{ kg/m}^3$$

qq. Under laminar conditions, Darcy's law allows expressing a relation between the hydraulic gradient and the mean seepage flow velocity under steady conditions. For a porous geomaterial fully saturated with water, which possesses homogeneity and isotropy with respect to the mass flow process, Darcy's law reads

$$\bar{v}_{rw,i} = -k\nabla h = -k\nabla\left(z + \frac{p_w}{\gamma_w}\right)$$

where $\bar{v}_{rw,i}$ [m/s] is the mean flow velocity, k [m/s] is the hydraulic conductivity of the geomaterial, ∇ represents the gradient, z [m] is the elevation of a considered fluid particle above a reference plane, p_w [Pa] is the fluid pressure, γ_w [N/m^3] is the unit weight of the fluid and h [m] is the piezometric head.

The assumption of homogeneity and isotropy indicates that the thermal conductivity is independent of direction and position and for this reason appears outside the argument of the gradient. In Darcy's law, as above expressed, the minus sign makes the mass flux density a positive quantity as a consequence of its direction towards decreasing piezometric head. Some modifications of Darcy's law are needed for the analysis of turbulent flow conditions in porous geomaterials, as well as for the analysis of flows in unsaturated soils.

rr. The parameter governing this aspect is the hydraulic conductivity, k, which characterises the definition of the fluid velocity with respect to the solid particles $\bar{v}_{rw,i}$ in the Darcy's law.

ss. The hydraulic conductivity of the geomaterial has the dimensions of a length per unit of time [m/s]. It is a function of both the fluid type and geomaterial structure. The dependence of the hydraulic conductivity on the intrinsic permeability can be typically appreciated by expressing this variable as

$$k = \frac{k^i \rho_f g}{\mu_f} = \frac{k^i g}{\eta_f}$$

where k^i [m^2] is the intrinsic (or geometric) permeability, that is a portion of the hydraulic conductivity and property of the porous material only (not of the fluid), η_f [m^2/s] is the kinematic viscosity of the fluid and g [m/s^2] is the gravitational acceleration.

tt. Threshold values of groundwater flow velocities that may be accounted for considering or neglecting convection in the ground for analyses and designs of energy geostructures are in the range of $\bar{v}_{rw} = 0.5 - 1$ m/day.

uu. The mass conservation equation reads

$$-\nabla \cdot \left(\rho \bar{v}_{rf,i}\right) = \frac{\partial \rho}{\partial t}$$

where $\nabla\cdot$represents the divergence operator, ρ [kg/m^3] and $\bar{v}_{rf,i}$ [m/s] are the bulk density and velocity of the fluid, while t is the time [s].

vv. No, it is not. The stored heat would be transferred away because of the groundwater flow.

ww. Conduction.

CHAPTER 4

Deformation in the context of energy geostructures

4.1 Introduction

Deformation and heat transfer phenomena arise because of the gradient of physical variables and may be considered independently from each other. Deformation characterises the mechanical behaviour of materials and is often associated with the influence of mechanical loads. Heat transfer characterises the thermal behaviour of materials and is often associated with the influence of thermal loads. However, deformation and heat transfer are coupled phenomena, similar to heat transfer and mass transfer. That is heat transfer can influence the deformation of materials and the opposite is true. This fact implies that the thermal and mechanical behaviours of materials are coupled.

Deformation phenomena under nonisothermal conditions characterise energy geostructures through the thermomechanical response of the materials involved. Understanding the physical principles governing deformation phenomena under nonisothermal conditions and accounting in a suitable way for these phenomena in the analysis and design of energy geostructures is paramount.

This chapter presents a theoretical analysis of deformation phenomena that can occur under nonisothermal conditions associated with heat transfer processes in the context of energy geostructures. The topic is addressed by focusing on the essentials of the theories of thermoelasticity, plasticity and thermoplasticity that may be considered for the characterisation of the thermomechanical behaviour of materials and the related analysis and design of energy geostructures. Comments on the coupling between deformation and heat transfer are also provided.

To this aim, *idealisations and assumptions* are presented first: in this context, the objective is to propose a summary of the conceptual descriptions and hypotheses that are employed for describing deformation phenomena under nonisothermal conditions. Second, the concepts of *strain, compatibility* and *stress* are addressed: the purpose of this part is to expand on fundamental variables and principles governing the description of the mechanical response of materials. Third, the *momentum equilibrium equation* and *boundary conditions* are presented: the purpose of this part is to define the equations governing the equilibrium of materials under loading. Next, *generalities about stress–strain relations* are introduced: the goal of this section is to elaborate on mathematical expressions relating strains to stresses and the opposite. Later, *thermoelasticity* is

Analysis and Design of Energy Geostructures
DOI: https://doi.org/10.1016/B978-0-12-816223-1.00004-7

addressed: in this context, the aim is to characterise the reversible mechanical behaviour of materials through the essentials of the theory of thermoelasticity. Afterward, *plasticity and thermoplasticity* are addressed: in this part, the objective is to characterise the irreversible mechanical behaviour of materials through the essentials of the theories of plasticity and thermoplasticity. Finally, *questions and problems* are proposed: the purpose of this part is to fix and test the understanding of the subjects covered in this chapter by addressing a number of exercises.

4.2 Idealisations and assumptions

As highlighted in Chapter 3, Heat and mass transfers in the context of energy geostructures, the materials constituting energy geostructures, soils and rocks are discrete in nature. However, mathematical models based on the continuum medium idealisation and the concept of Representative Elementary Volume (REV) allow describing, predicting and analysing key aspects of the behaviour of materials (discrete in particular). In the following, the continuum idealisation and the REV concept are employed to model the mechanical behaviour of materials, by further assuming that they are isotropic and homogeneous unless otherwise specified (cf. Fig. 4.1A). According to the continuum medium idealisation, the heterogeneous nature of geomaterials is neglected, and, in the simplest case, the presence of at least one fluid phase in addition to the solid phase constituting the structure of materials is also neglected. The consideration of at least one fluid phase in addition to the solid phase in the structural characterisation of materials involves challenges in the analysis of deformation phenomena. These challenges are discussed in Appendix B for both isothermal and nonisothermal conditions while providing the essentials of a framework for the hydromechanical and thermohydromechanical modelling of geomaterials.

Among the various theories that may be considered for describing the mechanical behaviour of materials (and general structural systems) subjected to perturbations (e.g. loads) under nonisothermal conditions, the theories of thermoelasticity, (isothermal) plasticity and thermoplasticity are addressed in the following because of their relevance for the analysis and design of energy geostructures. The mathematical formalisation of the theory of thermoelasticity has been developed by Duhamel (1835), based on the classical (or isothermal) theory of elasticity (see, e.g. Hooke, 1678; Navier, 1821; Cauchy, 1823; Lamé and Clapeyron, 1831; Saint Venant, 1870). In a similar way, the theory of thermoplasticity has been expanded by Prager (1958), based on the unified framework characterising the theory of isothermal plasticity (see, e.g. Prager, 1949; Drucker and Prager, 1952).

The theories of elasticity and thermoelasticity address a *reversible* mechanical behaviour of materials (and general structural systems) by neglecting and considering sensitivity to temperature variations for this behaviour, respectively. In the former

framework, the modelled subject is characterised by an *elastic behaviour*. In the latter framework, the modelled subject is characterised by a *thermoelastic behaviour*. A reversible mechanical behaviour is associated with the property of elasticity, which is common to many materials (and general structural systems) whose deformation is caused by loads that combined do not exceed a certain limit. Under these conditions, the loading of any subject (e.g. through a mechanical load, P) produces strains that are entirely recovered once the loading is removed (cf. Fig. 4.1B), and the combined effect of several loads (e.g. a mechanical load, P, and a thermal load resulting in a temperature variation, ΔT) acting simultaneously is equal to the algebraic sum of the effect of each load acting individually based on the superposition principle (cf. Fig. 4.1C). Situations in which the behaviour of materials or general systems is reversible (under both isothermal and nonisothermal conditions) are typically associated with small deformations caused by loading (e.g. of the order of 0.001). These situations characterise energy geostructures in most applications.

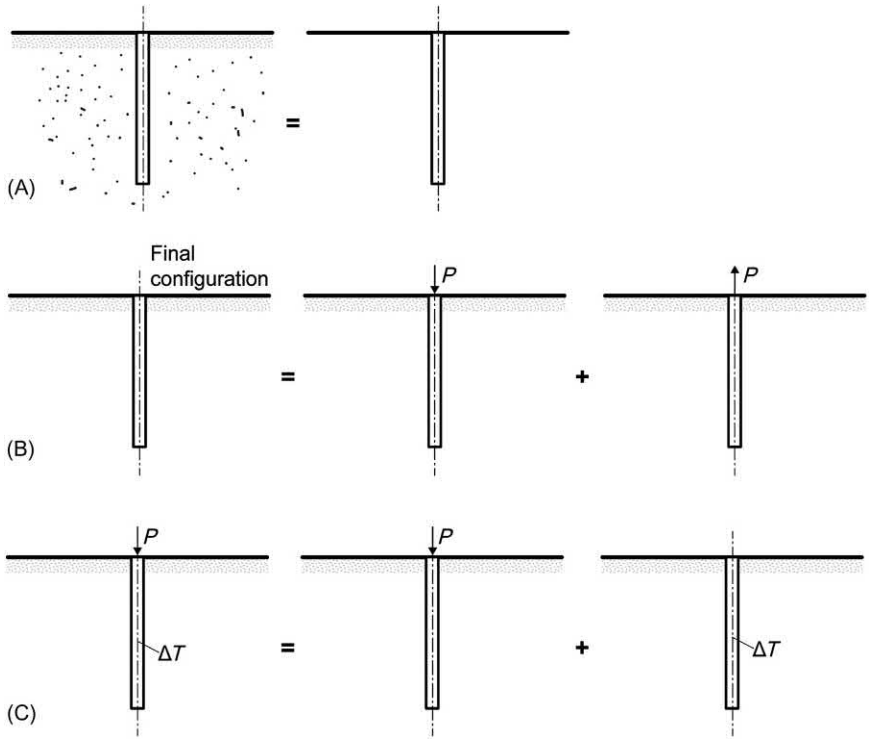

Figure 4.1 (A) Application of the continuum idealisation of the materials to an energy pile; (B) concept of reversible mechanical behaviour applied to an energy pile and (C) principle of superposition applied to the thermomechanical problem of an energy pile.

The theories of plasticity and thermoplasticity address an *irreversible* mechanical behaviour of materials (and general structural systems). An irreversible mechanical behaviour is associated with the property of plasticity, which is common to many materials (and general structural systems) whose deformation is caused by loads that do exceed a certain limit (typically termed *yield limit*). In practice, it is unlikely for the mechanical behaviour to be directly plastic due to loading (in those particular cases, reference is made to a rigid, plastic behaviour). In contrast, plasticity typically follows (e.g. progressively) elasticity. This phenomenon is common to materials such as soils, whose reversible and irreversible mechanical behaviour are mathematically distinguished through the yield limit represented by the *preconsolidation pressure*.

When plasticity is addressed in the context of nonisothermal conditions while accounting for preliminary elasticity, two main approaches can be considered. The first approach resorts to the theory of thermoelasticity to account for the influence of temperature variations on the reversible mechanical behaviour of the material, and to the theory of isothermal plasticity to model the irreversible mechanical behaviour of the material. The second approach resorts to the theory of thermoelasticity to model the influence of temperature variations on the reversible mechanical behaviour of the material and to the theory of thermoplasticity to model the irreversible mechanical behaviour of the material while considering a dependence of the yield limit on temperature. In the former framework, the modelled material (or general structural system) is characterised by a *thermoelastic, plastic behaviour*. In the latter framework, the modelled material (or general structural system) is characterised by a *thermoelastic, thermoplastic behaviour*. Situations in which the behaviour of materials is irreversible are typically associated with significant deformation levels caused by loading. These situations can characterise energy geostructures in some applications.

In the following, the sign convention adopted is the typical one of soil and rock mechanics. Contractive strains, downward displacements, compressive stresses and increases in angles in the anticlockwise direction are considered to be positive. The opposite is true, that is expansive strains, upward displacements, tensile stresses and angles in the clockwise direction are considered to be negative. The Einstein's sum convention (Einstein, 1916) is used when advantageous for the presented mathematical developments.

4.3 Strain

4.3.1 Concepts of deformation and strain

Materials subjected to loading exhibit variations of configuration. These variations of configuration can be appreciated considering the displacement of each material point before and after loading. Typical variations of configurations include a variation in size, a variation in shape or a rigid-body displacement (cf. Fig. 4.2). The former two

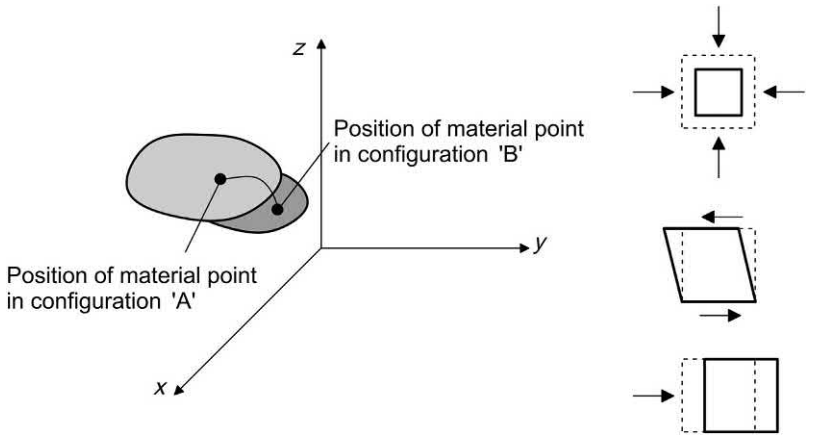

Figure 4.2 Typical variations of configurations.

phenomena describe deformations and involve a relative variation in the position of the material points. The latter phenomenon describes a rigid-body motion because there is no variation in the relative position of the material points. *Deformations* of materials are called *strains* when they are interpreted on a unit basis.

Strains can be analysed in terms of geometrical configuration as well as in analytical terms independently from the causes that produce them [for the full development, see, e.g. Timoshenko and Goodier (1970)]. In general, they are related to the spatial derivative of the displacement. Displacements are the fundamental kinematic variable of most problems involved in mechanics (Carpinteri, 1995). In continuum mechanics, this function is often considered with reference to the initial coordinates and time through a so-called Lagrangian description. The same approach is considered here.

4.3.2 Strain–displacement relations

Strains can be described through a finite or infinitesimal approach through the strain–displacement relations. Strains are defined infinitesimal if the components of displacement and the gradient of displacement are quantities of the first order. The above assumption involves considering displacements that do not to vary too abruptly from point to point, so that considering only first-order quantitates is appropriate. While simplifying the mathematical description of the problem, this assumption can be widely accepted for problems involving energy geostructures. Strain–displacement relations ensure geometrical consistency for the material.

The strain of an infinitesimal material element can be expressed through the strain tensor, ε_{ij}, which is a symmetric second-order tensor (i and j take integral values 1, 2 and 3). The infinitesimal strain tensor is characterised by nine components that in rectangular Cartesian coordinates read

$$\varepsilon_{ij} = \begin{bmatrix} \varepsilon_{xx} & \varepsilon_{xy} & \varepsilon_{xz} \\ \varepsilon_{yx} & \varepsilon_{yy} & \varepsilon_{yz} \\ \varepsilon_{zx} & \varepsilon_{zy} & \varepsilon_{zz} \end{bmatrix} \tag{4.1}$$

The diagonal components, ε_{kk}, of the infinitesimal strain tensor expressed in Eq. (4.1) are called *normal strains* and represent stretching of an element (i.e. in one dimension, this stretching expresses the fractional shortening or lengthening of a line element with respect to its initial length). The off-diagonal components, ε_{kl}, are called infinitesimal *shear strains* and measure angular distortion (i.e. in one dimension, this angular distortion expresses the half variation in angle between two segments that are parallel to the coordinate axes in the reference state). The infinitesimal shear strains are one half of the engineering shear strains, γ_{kl}, that is $\varepsilon_{kl} = 1/2\gamma_{kl}$.

The components of the strain tensor are as follows in relevant coordinate systems.

- Cartesian coordinates x, y, z:

$$\begin{aligned} \varepsilon_{xx} &= -\frac{\partial u}{\partial x} \varepsilon_{yy} = -\frac{\partial v}{\partial y} \varepsilon_{zz} = -\frac{\partial w}{\partial z} \\ \varepsilon_{xy} &= \frac{1}{2}\gamma_{xy} = -\frac{1}{2}\left(\frac{\partial u}{\partial y} + \frac{\partial v}{\partial x}\right) \\ \varepsilon_{yz} &= \frac{1}{2}\gamma_{yz} = -\frac{1}{2}\left(\frac{\partial v}{\partial z} + \frac{\partial w}{\partial y}\right) \\ \varepsilon_{xz} &= \frac{1}{2}\gamma_{xz} = -\frac{1}{2}\left(\frac{\partial w}{\partial x} + \frac{\partial u}{\partial z}\right) \end{aligned} \tag{4.2}$$

  where u, v and w are the components of the displacement vector, u_i, in the x, y and z directions, respectively.

- Cylindrical coordinates r, θ, z:

$$\begin{aligned} &\varepsilon_{rr} = -\frac{\partial u}{\partial r} \quad \varepsilon_{zz} = -\frac{\partial w}{\partial z} \quad \varepsilon_{\theta\theta} = -\left(\frac{u}{r} + \frac{1}{r}\frac{\partial v}{\partial \theta}\right) \\ &\varepsilon_{r\theta} = -\frac{1}{2}\left(\frac{1}{r}\frac{\partial u}{\partial \theta} + \frac{\partial v}{\partial r} - \frac{v}{r}\right) \\ &\varepsilon_{rz} = -\frac{1}{2}\left(\frac{\partial u}{\partial z} + \frac{\partial w}{\partial r}\right) \\ &\varepsilon_{z\theta} = -\frac{1}{2}\left(\frac{\partial v}{\partial z} + \frac{\partial w}{\partial \theta}\right) \end{aligned} \tag{4.3}$$

where u, v and w represent here the components of the displacement vector in the r, θ and z directions, respectively.

- Spherical coordinates r, θ, ϕ:

$$\begin{aligned}
&\varepsilon_{rr} = -\frac{\partial u}{\partial r} \quad \varepsilon_{\theta\theta} = -\left(\frac{u}{r} + \frac{1}{r}\frac{\partial v}{\partial \theta}\right) \quad \varepsilon_{\phi\phi} = -\left(\frac{u}{r} + \frac{v}{r}\cot\theta + \frac{1}{r\sin\theta}\frac{\partial w}{\partial \phi}\right) \\
&\varepsilon_{r\theta} = -\frac{1}{2}\left(\frac{1}{r}\frac{\partial u}{\partial \theta} + \frac{\partial v}{\partial r} - \frac{v}{r}\right) \\
&\varepsilon_{r\phi} = -\frac{1}{2}\left(\frac{1}{r\sin\theta}\frac{\partial u}{\partial \phi} + \frac{\partial w}{\partial r} - \frac{w}{r}\right) \\
&\varepsilon_{\theta\phi} = -\frac{1}{2}\left(\frac{1}{r}\frac{\partial w}{\partial \theta} - \frac{\cot\theta}{r}w + \frac{1}{r\sin\theta}\frac{\partial v}{\partial \phi}\right)
\end{aligned} \tag{4.4}$$

where u, v and w represent here the components of the displacement vector in the r, θ and ϕ directions respectively.

Fig. 4.3 expresses in graphical form and with reference to a two-dimensional case in Cartesian coordinates the geometrical meaning of infinitesimal strains.

4.3.3 Volumetric and deviatoric strains

In many cases, it is useful to decompose the strain tensor in a volumetric (i.e. spherical) part and a deviatoric (i.e. distortional) part. The above can be mathematically expressed as

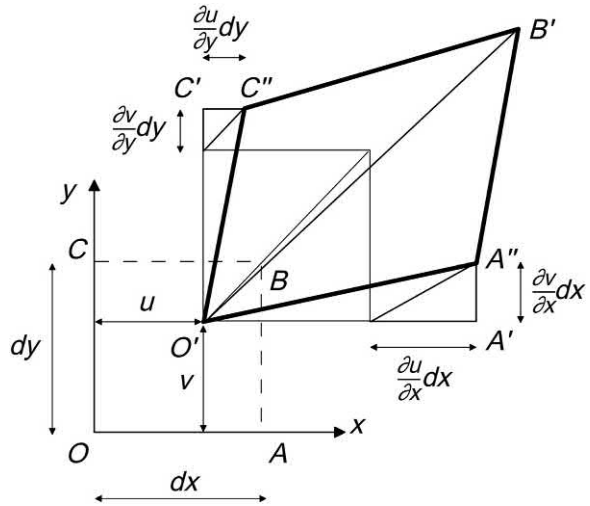

Figure 4.3 Two-dimensional representation of infinitesimal strains in a rectangular Cartesian coordinate systems. *Redrawn after Lancellotta, R., 2008. Geotechnical Engineering. CRC Press.*

$$\varepsilon_{ij} = \frac{1}{3}\varepsilon_v \delta_{ij} + e_{ij} \tag{4.5}$$

where ε_v is a scalar quantity called volumetric strain, δ_{ij} is the Kronecker delta (which is equal to 1 if $i = j$ and to 0 otherwise) and e_{ij} is a tensor characterised by zero trace called deviatoric strain tensor (or strain deviator). The volumetric strain can be written in rectangular Cartesian coordinates as

$$\varepsilon_v = \varepsilon_{kk} = \mathrm{tr}(\varepsilon_{ij}) = (\varepsilon_{xx} + \varepsilon_{yy} + \varepsilon_{zz}) \tag{4.6}$$

The deviatoric strain tensor in rectangular Cartesian coordinates reads

$$e_{ij} = \begin{bmatrix} e_{xx} & \varepsilon_{xy} & \varepsilon_{xz} \\ \varepsilon_{yx} & e_{yy} & \varepsilon_{yz} \\ \varepsilon_{zx} & \varepsilon_{zy} & e_{zz} \end{bmatrix} \tag{4.7}$$

where $e_{ii} = \varepsilon_{ii} - \varepsilon_v/3$.

Eq. (4.1) can therefore be rewritten in matrix form as

$$\begin{bmatrix} \varepsilon_{xx} & \varepsilon_{xy} & \varepsilon_{xz} \\ \varepsilon_{yx} & \varepsilon_{yy} & \varepsilon_{yz} \\ \varepsilon_{zx} & \varepsilon_{zy} & \varepsilon_{zz} \end{bmatrix} = \frac{1}{3}\begin{bmatrix} \varepsilon_v & 0 & 0 \\ 0 & \varepsilon_v & 0 \\ 0 & 0 & \varepsilon_v \end{bmatrix} + \begin{bmatrix} e_{xx} & \varepsilon_{xy} & \varepsilon_{xz} \\ \varepsilon_{yx} & e_{yy} & \varepsilon_{yz} \\ \varepsilon_{zx} & \varepsilon_{zy} & e_{zz} \end{bmatrix} \tag{4.8}$$

4.3.4 Principal strains

A feature of the strain tensor, similar to any symmetric tensor, is that at every material point of any coordinate system there exist three mutually perpendicular planes, called principal planes, along which zero shear strains are observed. The normal strains on these planes are called principal strains. The principal strains and the associated principal directions can be written as the eigenvalues and the eigenvectors of the strain tensor, respectively. Invariants can be defined for the strain tensor.

4.4 Compatibility equations

The concept of strain compatibility refers to the physical concept that when deformation occurs in a continuum material it happens without material gaps or overlaps. This means that the relation between material points before and after the variation of configuration remains the same (cf. Fig. 4.4). When displacements are known, strains can be calculated according to expressions (4.2)–(4.4) by computing partial derivatives. However, the inverse problem of determining displacements from strains, which is usually encountered in stress-based formulations, is overdetermined because either of expressions (4.2), (4.3) or (4.4) contains six equations and only three unknowns. In

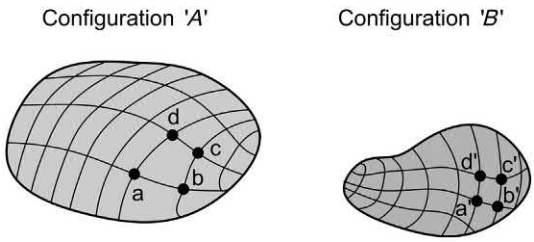

Figure 4.4 Concept of compatibility. *Modified after Davis, R.O., Selvadurai, A.P., 1996. Elasticity and Geomechanics. Cambridge University Press.*

the latter case, this implies that additional conditions, known as Saint Venant's compatibility equations (Saint Venant, 1870), need to be defined. Compatibility equations are six differential equations that are both necessary and sufficient conditions to guarantee the existence of a single-valued displacement field [for the full development, see, e.g. Davis and Selvadurai (1996)]. In rectangular Cartesian coordinates they read

$$
\begin{aligned}
2\frac{\partial^2\varepsilon_{xy}}{\partial x\partial y} &= \frac{\partial^2\varepsilon_{xx}}{\partial^2 y} + \frac{\partial^2\varepsilon_{yy}}{\partial^2 x} \\
2\frac{\partial^2\varepsilon_{yz}}{\partial y\partial z} &= \frac{\partial^2\varepsilon_{yy}}{\partial^2 z} + \frac{\partial^2\varepsilon_{zz}}{\partial^2 y} \\
2\frac{\partial^2\varepsilon_{zx}}{\partial z\partial x} &= \frac{\partial^2\varepsilon_{zz}}{\partial^2 x} + \frac{\partial^2\varepsilon_{xx}}{\partial^2 z} \\
\frac{\partial^2\varepsilon_{xx}}{\partial y\partial z} &= \frac{\partial}{\partial x}\left(-\frac{\partial\varepsilon_{yz}}{\partial x} + \frac{\partial\varepsilon_{zx}}{\partial y} + \frac{\partial\varepsilon_{xy}}{\partial z}\right) \\
\frac{\partial^2\varepsilon_{yy}}{\partial z\partial x} &= \frac{\partial}{\partial y}\left(\frac{\partial\varepsilon_{yz}}{\partial x} - \frac{\partial\varepsilon_{zx}}{\partial y} + \frac{\partial\varepsilon_{xy}}{\partial z}\right) \\
\frac{\partial^2\varepsilon_{zz}}{\partial x\partial y} &= \frac{\partial}{\partial z}\left(\frac{\partial\varepsilon_{yz}}{\partial x} + \frac{\partial\varepsilon_{zx}}{\partial y} - \frac{\partial\varepsilon_{xy}}{\partial z}\right)
\end{aligned}
\tag{4.9}
$$

4.5 Stress

4.5.1 Concepts of strength and stress

The *strength* of materials is associated with the influence of forces and the interpretation of the deformations caused by such forces. Two kinds of forces can be distinguished to act on any portion S of a continuum material C: body forces, herein associated with

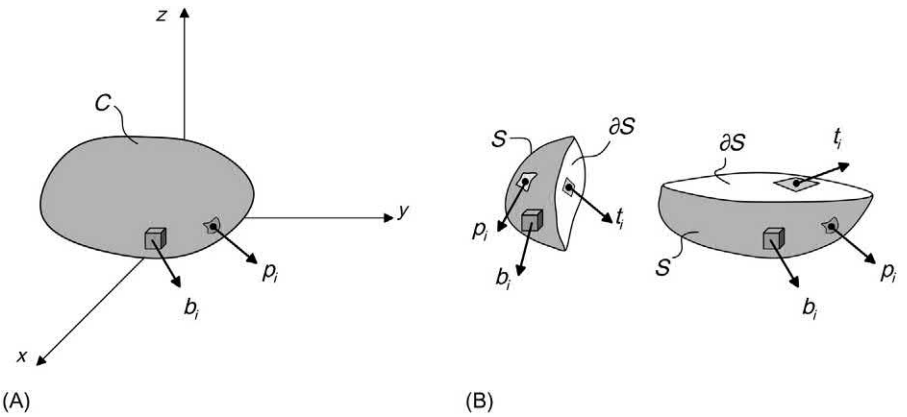

Figure 4.5 Typical force fields applied to a material: (A) continuum and (B) sectional representation.

the vector b_i, which act on volumes of the material; and contact forces, herein associated with the vectors t_i and p_i, which act on surfaces of the material (cf. Fig. 4.5A). Forces acting on materials are called *stresses* when appropriately defined on a unit basis.

Body forces result from influences from the outside of the material, that is they act on S from the exterior of C. These forces include, for example, mass forces. Contact forces result from influences from the inside of the material in the case of the functions t_i, that is they act on the boundary ∂S of the portion S from the interior of C, while they result from influences from the outside of the material in the case of the functions p_i, that is they act on the boundary ∂S of the portion S from the exterior of C. These forces include, for example, forces caused by the application of a uniform or nonuniform temperature variation to a material whose deformation is partly or entirely restrained, as well as forces caused by the application of a nonuniform temperature variation [different than a temperature field varying linearly with a set of rectangular Cartesian coordinates (Boley and Weiner, 1997)] to a material that is free to deform.

The system of internal forces t_i applied at a given point $\mathcal{H}$ on any cross-sectional surface π_i, which passes through $\mathcal{H}$ and describes a portion of a continuum material subjected to a given force field, ensures equilibrium of the considered portion of material. This equilibrium against the considered force field applied to the material would not be satisfied if these forces were not present (cf. Fig. 4.5B). This system of forces is associated with the specific surface that is chosen at any given point of the material and, as this surface tends to zero, it constitutes the components of the so-called stress vector t_i (cf. Fig. 4.6).

The stress vector depends on the orientation of surface according to the following linear mapping (Cauchy, 1823)

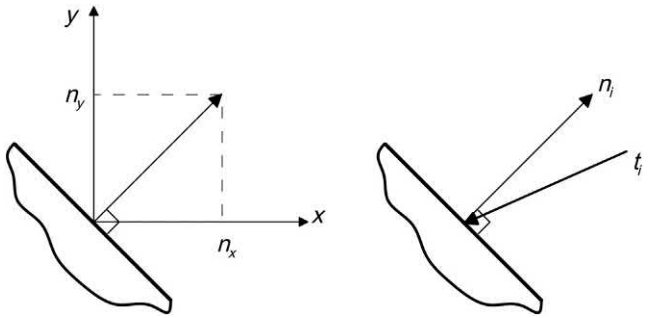

Figure 4.6 Normal vector n_i and stress vector t_i acting on a surface in a two-dimensional Cartesian coordinate system. *Modified after Jaeger, J.C., Cook, N.G., Zimmerman, R., 2009. Fundamentals of Rock Mechanics. John Wiley & Sons (Jaeger et al., 2009).*

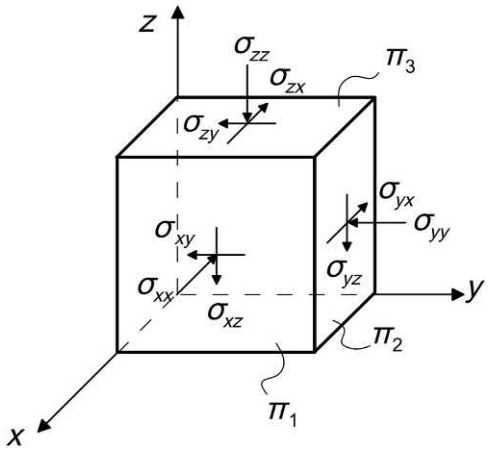

Figure 4.7 Stress components.

$$t_i^n = \sigma_{ji} n_i \tag{4.10}$$

where n_i is the outward unit normal of the surface π_i and σ_{ij} is a symmetric second-order tensor. The tensor σ_{ij} is generally known as the stress tensor and describes the stress state of any infinitesimal three-dimensional element of a considered material subjected to loading (cf. Fig. 4.7). The stress tensor is characterised by nine stress components that in rectangular Cartesian coordinates read

$$\sigma_{ij} = \begin{bmatrix} \sigma_{xx} & \sigma_{xy} & \sigma_{xz} \\ \sigma_{yx} & \sigma_{yy} & \sigma_{yz} \\ \sigma_{zx} & \sigma_{zy} & \sigma_{zz} \end{bmatrix} = \begin{bmatrix} \sigma_x & \tau_{xy} & \tau_{xz} \\ \tau_{yx} & \sigma_y & \tau_{yz} \\ \tau_{zx} & \tau_{zy} & \sigma_z \end{bmatrix} \tag{4.11}$$

The diagonal components, σ_{kk}, of the stress tensor expressed in Eq. (4.11) act normal to the coordinate planes and are called *normal stresses*. The off-diagonal

components, σ_{kl}, act tangential to the coordinate planes and are called *shear stresses*. More generally, when considering each component of the stress tensor, the first subscript indicates the coordinate plane on which the stress component acts and the second subscript identifies the direction along which it acts.

The symmetric character of the stress tensor can be proven considering the principle of balance of angular momentum (cf. Section 4.5.3). As a result, the complementary components of the shear stress are equal

$$\sigma_{xy} = \sigma_{yx} \quad \sigma_{yz} = \sigma_{zy} \quad \sigma_{zx} = \sigma_{xz} \tag{4.12}$$

The above implies that there are only six independent stress components: three normal stresses $\sigma_{xx}, \sigma_{yy}, \sigma_{zz}$ and three shear stresses $\sigma_{xy}, \sigma_{yz}, \sigma_{xz}$.

Relation (4.10) expresses that when the components σ_{ij} acting on any three mutually perpendicular planes through a point $\mathcal{H}$ are known, the stress vector on any plane through $\mathcal{H}$ can be determined. This fact is formalised by the Cauchy's theorem (Cauchy, 1823) [for the full development, see, e.g. Lancellotta (2008)].

4.5.2 Volumetric and deviatoric stresses

In many cases, it is useful to decompose the stress tensor in a volumetric (i.e. spherical) part and a deviatoric (i.e. distortional) part. The above can be mathematically expressed as

$$\sigma_{ij} = p\delta_{ij} + s_{ij} \tag{4.13}$$

where p is a scalar quantity called mean stress and s_{ij} is a tensor characterised by zero trace called deviatoric stress tensor (or stress deviator). The mean stress can be written in rectangular Cartesian coordinates as

$$p = \frac{1}{3}\sigma_{kk} = \frac{1}{3}\mathrm{tr}\left(\sigma_{ij}\right) = \frac{1}{3}\left(\sigma_{xx} + \sigma_{yy} + \sigma_{zz}\right) \tag{4.14}$$

The deviatoric stress tensor in rectangular Cartesian coordinates reads

$$s_{ij} = \begin{bmatrix} s_{xx} & \sigma_{xy} & \sigma_{xz} \\ \sigma_{yx} & s_{yy} & \sigma_{yz} \\ \sigma_{zx} & \sigma_{zy} & s_{zz} \end{bmatrix} \tag{4.15}$$

where $s_{ii} = \sigma_{ii} - p$.

Eq. (4.13) can therefore be rewritten in matrix form as

$$\begin{bmatrix} \sigma_{xx} & \sigma_{xy} & \sigma_{xz} \\ \sigma_{yx} & \sigma_{yy} & \sigma_{yz} \\ \sigma_{zx} & \sigma_{zy} & \sigma_{zz} \end{bmatrix} = \begin{bmatrix} p & 0 & 0 \\ 0 & p & 0 \\ 0 & 0 & p \end{bmatrix} + \begin{bmatrix} s_{xx} & \sigma_{xy} & \sigma_{xz} \\ \sigma_{yx} & s_{yy} & \sigma_{yz} \\ \sigma_{zx} & \sigma_{zy} & s_{zz} \end{bmatrix} \tag{4.16}$$

It can be noted that by definition the shear stresses are not influenced by adding a volumetric component in the stress tensor formulation (4.13).

4.5.3 Principal stresses

A feature of the stress tensor, similar to the strain tensor, is that at every material point of any coordinate system there exist three mutually perpendicular planes, called principal planes, along which zero shear stresses are observed. The normal stresses on these planes are called principal stresses.

The stress vector acting on a principal plane is characterised by only the normal component. Therefore considering Eq. (4.10) and by indicating with n_i the unit vector of a principal plane characterised by direction cosines n_x, n_y and n_z in a rectangular Cartesian coordinate system x, y, z, and with λ_* the modulus of the corresponding component, the stress vector can be expressed as

$$\sigma_{ji} n_j = \lambda_* n_i \tag{4.17}$$

Eq. (4.17) is equivalent to the following eigenvalue problem

$$\left(\sigma_{ij} - \lambda_* \delta_{ij}\right) n_j = 0 \tag{4.18}$$

that in extended form reads

$$\begin{cases} (\sigma_{xx} - \lambda_*) n_x + \sigma_{xy} n_y + \sigma_{xz} n_z = 0 \\ \sigma_{xy} n_x + (\sigma_{yy} - \lambda_*) n_y + \sigma_{yz} n_z = 0 \\ \sigma_{xz} n_x + \sigma_{zy} n_y + (\sigma_{zz} - \lambda_*) n_z = 0 \end{cases} \tag{4.19}$$

with

$$n_x^2 + n_y^2 + n_z^2 = 1 \tag{4.20}$$

Eqs (4.19) and (4.20) lead to a nontrivial solution for the direction cosines only if the determinant of the coefficients is zero. This condition leads to the characteristic cubic equation (also called characteristic polynomial)

$$\lambda_*{}^3 - I_1 \lambda_*{}^2 + I_2 \lambda_* - I_3 = 0 \tag{4.21}$$

where I_1, I_2 and I_3 are three coefficients that do not change for different coordinate transformations, that is they are invariants. Any linear combination of invariants still is an invariant.

The solution of the above equation is found for three real eigenvalues $\lambda_{*1} = \sigma_1, \lambda_{*2} = \sigma_2$ and $\lambda_{*3} = \sigma_3$ that represent the principal stresses. Differently to the components of the stress tensor that change for different coordinate systems taken

with reference to the same point, the three principal stresses are invariants under coordinate transformation. The substitution of each of the three eigenvalues in Eq. (4.19) allows computing the eigenvectors n_1, n_2 and n_3 that represent the principal directions.

The three invariant coefficients expressed in Eq. (4.21) are the first, second and third stress invariants (or invariants of the stress tensor) and are given by

$$\begin{cases} I_1 = \mathrm{tr}(\sigma_{ij}) = \sigma_{ii} = \sigma_{xx} + \sigma_{yy} + \sigma_{zz} \\ I_2 = \dfrac{1}{2}\left(\sigma_{ii}\sigma_{jj} - \sigma_{ij}\sigma_{ij}\right) = \sigma_{xx}\sigma_{yy} + \sigma_{yy}\sigma_{zz} + \sigma_{zz}\sigma_{xx} - \sigma_{xy}^2 - \sigma_{yz}^2 - \sigma_{zx}^2 \\ I_3 = \det \sigma_{ij} = \sigma_{xx}\sigma_{yy}\sigma_{zz} + 2\sigma_{xy}\sigma_{yz}\sigma_{zx} - \sigma_{xx}\sigma_{yz}^2 - \sigma_{yy}\sigma_{zx}^2 - \sigma_{zz}\sigma_{xy}^2 \end{cases} \tag{4.22}$$

By setting equal to zero the off-diagonal components of the stress tensor in Eq. (4.22), the relations between the invariants and the principal stresses can be found.

Alternative formulations of the stress invariants can be derived from the stress tensor itself instead from the characteristic polynomial and read

$$\begin{cases} I_{1*} = \mathrm{tr}(\sigma_{ij}) = \sigma_{ii} = I_1 \\ I_{2*} = \dfrac{1}{2}\sigma_{ij}\sigma_{ij} = \dfrac{1}{2}I_1^2 - I_2 \\ I_{3*} = \dfrac{1}{3}\sigma_{ik}\sigma_{km}\sigma_{mi} = \dfrac{1}{3}I_1^3 - I_1 I_2 + I_3 \end{cases} \tag{4.23}$$

Invariants can also be expressed in similar forms for the deviatoric stress tensor, for example, as

$$\begin{cases} J_1 = \mathrm{tr}(s_{ij}) = s_{ii} = \sigma_{ii} - \sigma_{nn} = 0 \\ J_2 = \dfrac{1}{2}s_{ij}s_{ij} = \dfrac{1}{2}\left[(\sigma_{xx}-p)^2 + (\sigma_{yy}-p)^2 + (\sigma_{zz}-p)^2 + 2s_{xy}^2 + 2s_{yz}^2 + 2s_{xz}^2\right] \\ \qquad\qquad = I_{2*} - \dfrac{I_{1*}^2}{6} \\ J_3 = \dfrac{1}{3}s_{ik}s_{km}s_{mi} = I_{3*} - \dfrac{2}{3}I_{1*}I_{2*} + \dfrac{2}{27}I_{1*}^3 \end{cases} \tag{4.24}$$

When a coordinate system is chosen such that the directions are parallel to the principal directions, the stress tensor reduces to

$$\sigma_{ij} = \begin{bmatrix} \sigma_1 & 0 & 0 \\ 0 & \sigma_2 & 0 \\ 0 & 0 & \sigma_3 \end{bmatrix} \tag{4.25}$$

It is often convenient to number the principal stresses (without mandatorily referring to the position of the stress components in the stress tensor reported in Eq. 4.26) so that

$$\sigma_1 \geq \sigma_2 \geq \sigma_3 \tag{4.26}$$

The principal directions are mutually orthogonal because the eigenvectors of a symmetric tensor, such as the stress tensor, are mutually orthogonal. Eqs (4.17)–(4.26) written thus far for the stress tensor can also be written for the strain tensor.

In two dimensions, analogous results can be obtained with Eq. (4.21) that reduces to

$$\lambda_*{}^2 - \left(\sigma_{xx} + \sigma_{yy}\right)\lambda_* + \left(\sigma_{xx}\sigma_{yy} - \sigma_{xy}^2\right) = 0 \tag{4.27}$$

The two principal stresses in the plane may then be written explicitly as

$$\lambda_* = \sigma_{1,2} = \frac{\sigma_{xx} + \sigma_{yy}}{2} \pm \sqrt{\left(\frac{\sigma_{xx} - \sigma_{yy}}{2}\right)^2 + \sigma_{xy}^2} \tag{4.28}$$

with the principal directions that make an angle φ_x with the x-axis of

$$\tan\varphi_x = \frac{n_y}{n_x} = \frac{\sigma_{xy}}{\sigma_{xx} - \lambda_*} \tag{4.29}$$

In two dimensions, the coordinate points $(\sigma_1; 0)$ and $(\sigma_2; 0)$ represent peculiar points of the so-called Mohr circle of stress [for further details, see, e.g. Timoshenko (1953)], which is given by the following equation

$$\sigma_{x_1y_1}^2 + \left(\sigma_{x_1x_1} - \frac{\sigma_{xx} + \sigma_{yy}}{2}\right)^2 = \sigma_{xy}^2 + \frac{1}{4}\left(\sigma_{xx} - \sigma_{yy}\right)^2 \tag{4.30}$$

where $\sigma_{x_1x_1}$ and $\sigma_{x_1y_1}$ are the normal and shear stress components acting in any direction x_1, y_1, where the x_1 axis makes an angle α_{x_1} with the x axis (positive in the anticlockwise direction).

The Mohr circle of stress represents the setting of all possible stress states acting on a point along different planes (cf. Fig. 4.8). The formulas for the stress components derived from the Mohr circle of stress are

$$\begin{cases} \sigma_{x_1x_1} = \dfrac{\left(\sigma_{xx} + \sigma_{yy}\right)}{2} + \dfrac{\left(\sigma_{xx} - \sigma_{yy}\right)}{2}\cos 2\alpha_{x_1} + \sigma_{xy}\sin 2\alpha_{x_1} \\ \sigma_{y_1y_1} = \dfrac{\left(\sigma_{xx} + \sigma_{yy}\right)}{2} - \dfrac{\left(\sigma_{xx} - \sigma_{yy}\right)}{2}\cos 2\alpha_{x_1} - \sigma_{xy}\sin 2\alpha_{x_1} \\ \sigma_{x_1y_1} = -\dfrac{\left(\sigma_{xx} - \sigma_{yy}\right)}{2}\sin 2\alpha_{x_1} + \sigma_{xy}\cos 2\alpha_{x_1} \end{cases} \tag{4.31}$$

The use of invariants defined in Eqs (4.22)–(4.24) is often practical for a number of considerations related to constitutive modelling of geomaterials and their interaction with geostructures. In particular, invariants of physical interest especially in the framework of plasticity theory are I_1, J_2 and J_3. Physically, I_1 represents the magnitude of the mean stress, J_2 represents the magnitude of the deviatoric stress and J_3 determines the direction of the deviatoric stress (Yu, 2006). The aforementioned concepts can be analysed graphically in the Haigh–Westergaard space, that is the three-dimensional space where the principal directions of stresses are selected as coordinate axes (cf. Fig. 4.9). The value of I_1 provides a measure of the distance along the space diagonal ($\sigma_1 = \sigma_2 = \sigma_3 = I_1/3$) from the origin to the current spherical plane, also called octahedral plane, defined as

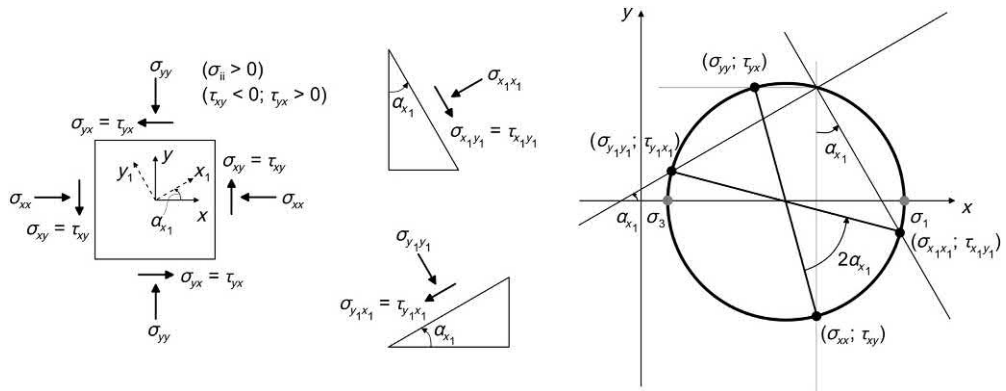

Figure 4.8 A typical Mohr circle.

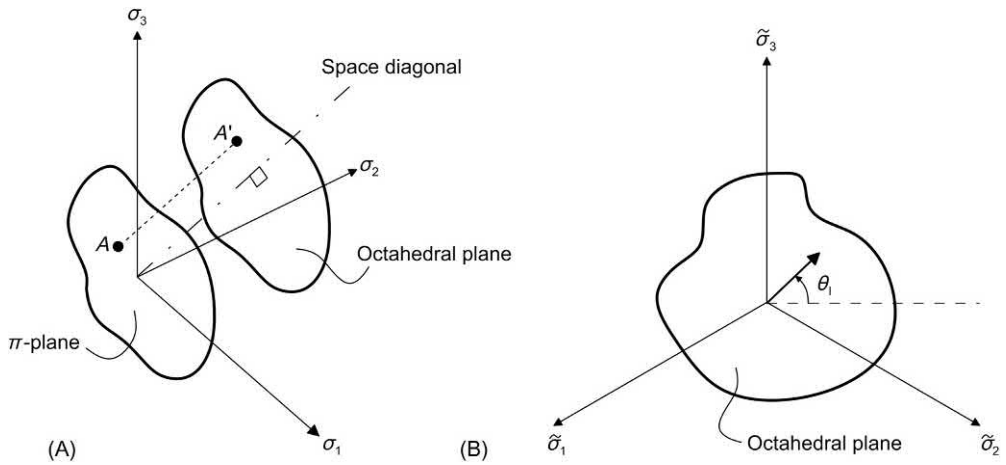

Figure 4.9 Representations in the Haigh–Westergaard space: definition of key variables in (A) the π-plane and octahedral plane and (B) the octahedral plane only.

$$\sigma_1 + \sigma_2 + \sigma_3 = I_1 = 3p \tag{4.32}$$

This distance reads

$$\overline{AA'} = \frac{(\sigma_1 + \sigma_2 + \sigma_3)}{\sqrt{3}} = \frac{\sqrt{3}}{3} I_1 = \sqrt{3}p \tag{4.33}$$

The special plane for which the mean stress p is zero is called the π-plane and reads

$$\sigma_1 + \sigma_2 + \sigma_3 = 0 \tag{4.34}$$

The second invariant of the deviatoric stress tensor J_2 is a measure of the distance from the space diagonal to the current stress state in the spherical plane. The combination of J_2 and J_3 through the formulation of the Lode's angle defines the orientation of the stress state within this plane and reads

$$\theta_l = -\frac{1}{3}\sin^{-1}\left(\frac{3\sqrt{3}}{2}\frac{J_3}{J_2^3}\right) \tag{4.35}$$

The second invariant of the deviatoric stress tensor J_2 is also related to the deviatoric stress as (Roscoe and Burland, 1968; Wood, 1990)

$$q = \sqrt{3J_2} \tag{4.36}$$

that in terms of principal stresses can also be written as

$$q = \frac{1}{6}\left[(\sigma_1 - \sigma_2)^2 + (\sigma_2 - \sigma_3)^2 + (\sigma_1 - \sigma_3)^2\right] \tag{4.37}$$

In Fig. 4.9, the principal stresses $\tilde{\sigma}_1$, $\tilde{\sigma}_2$ and $\tilde{\sigma}_3$ are the projections in space of the principal stresses σ_1, σ_2 and σ_3.

4.6 Momentum conservation equation

4.6.1 General

In all cases where inertial forces acting on a material can be neglected or are absent (i.e. the so-called quasi-static conditions hold), the so-called Cauchy's first law of motion reduces to the *indefinite equilibrium equations*.

4.6.2 Indefinite equilibrium equations

The indefinite equilibrium equations can be derived considering that the stress components are continuous functions of the point coordinates and analysing the stress components acting on the faces of an element opposite to those highlighted in Fig. 4.7.

The indefinite equilibrium equations imply that if an element is in equilibrium, when introducing body forces the sum of the forces in each direction must be zero. In compact form, this reads

$$\nabla \cdot \sigma_{ij} + \rho b_i = 0 \tag{4.38}$$

where $\nabla\cdot$ is the divergence operator, σ_{ij} is the total stress tensor, ρ is the density of the material and b_i is the vector of the body forces (per unit mass). At the surface, surface forces substitute body forces and the corresponding equations are indicated as boundary conditions (or boundary equilibrium equations, cf. Section 4.7).

Eq. (4.38) is as follows in relevant coordinate systems.

- Cartesian coordinates x, y, z:

$$\begin{aligned}
\frac{\partial \sigma_{xx}}{\partial x} + \frac{\partial \sigma_{xy}}{\partial y} + \frac{\partial \sigma_{xz}}{\partial z} + \rho X^* = 0 \\
\frac{\partial \sigma_{yx}}{\partial x} + \frac{\partial \sigma_{yy}}{\partial y} + \frac{\partial \sigma_{yz}}{\partial z} + \rho Y^* = 0 \\
\frac{\partial \sigma_{zx}}{\partial x} + \frac{\partial \sigma_{zy}}{\partial y} + \frac{\partial \sigma_{zz}}{\partial z} + \rho Z^* = 0
\end{aligned} \tag{4.39}$$

  where X^*, Y^* and Z^* are the components of the body forces in the x, y and z directions, respectively.

- Cylindrical coordinates r, θ, z:

$$\begin{aligned}
\frac{\partial \sigma_{rr}}{\partial r} + \frac{1}{r}\frac{\partial \sigma_{r\theta}}{\partial \theta} + \frac{\partial \sigma_{rz}}{\partial z} + \frac{\sigma_{rr} - \sigma_{\theta\theta}}{r} + \rho R^* = 0 \\
\frac{\partial \sigma_{rz}}{\partial r} + \frac{1}{r}\frac{\partial \sigma_{\theta z}}{\partial \theta} + \frac{\partial \sigma_{zz}}{\partial z} + \frac{\sigma_{rz}}{r} + \rho Z^* = 0 \\
\frac{\partial \sigma_{r\theta}}{\partial r} + \frac{1}{r}\frac{\partial \sigma_{\theta\theta}}{\partial \theta} + \frac{\partial \sigma_{\theta z}}{\partial z} + \frac{2\sigma_{r\theta}}{r} + \rho \Theta^* = 0
\end{aligned} \tag{4.40}$$

  where the body force components in the r, z and θ directions are denoted by R^*, Z^* and Θ^*.

- Spherical coordinates r, θ, ϕ:

$$\begin{aligned}
\frac{\partial \sigma_{rr}}{\partial r} + \frac{1}{r}\frac{\partial \sigma_{r\theta}}{\partial \theta} + \frac{1}{r\sin\theta}\frac{\partial \sigma_{r\phi}}{\partial \phi} + \frac{1}{r}[2\sigma_{rr} - \sigma_{\theta\theta} - \sigma_{\phi\phi} + \sigma_{r\theta}\cot\theta] + \rho R^* = 0 \\
\frac{\partial \sigma_{r\theta}}{\partial r} + \frac{1}{r}\frac{\partial \sigma_{\theta\theta}}{\partial \theta} + \frac{1}{r\sin\theta}\frac{\partial \sigma_{\theta\phi}}{\partial \phi} + \frac{1}{r}[(2\sigma_{\theta\theta} - \sigma_{\phi\phi})\cot\theta + 3\sigma_{r\theta}] + \rho \Theta^* = 0 \\
\frac{\partial \sigma_{r\phi}}{\partial r} + \frac{1}{r}\frac{\partial \sigma_{\theta\phi}}{\partial \theta} + \frac{1}{r\sin\theta}\frac{\partial \sigma_{\phi\phi}}{\partial \phi} + \frac{1}{r}[3\sigma_{r\phi} + 2\sigma_{\theta\phi}\cot\theta] + \rho \Phi^* = 0
\end{aligned} \tag{4.41}$$

where the body force components in the r, θ and ϕ directions are denoted by R^*, Θ^* and Φ^*.

Very often, the following formulation of the indefinite equilibrium Eq. (4.38) is found

$$\nabla \cdot \sigma_{ij} + \rho g_i = 0 \tag{4.42}$$

where g_i is the gravitational acceleration vector, representing a particular type of body forces. In elastic problems, it is often possible to omit body forces because their effect can be superimposed based on the principle of superposition.

Together with Eq. (4.38), for an element of a material in equilibrium, the principle of balance of angular momentum needs to be verified. Working with the mathematical formulation of the balance of angular momentum and that of linear momentum yields to Eq. (4.12). When Eqs (4.12) and (4.38) are satisfied at all points of the material, together with the equilibrium equations written for the boundary of the material, the required conditions of equilibrium of the material as a whole are fulfilled, with the resultant of the contact forces balancing the resultant of the body forces.

4.7 Boundary conditions

4.7.1 General

Boundary conditions, or boundary equilibrium equations, need to be defined to ensure equilibrium between the resultant of the internal forces and the condition (in terms of stresses or displacements) at the boundary of a material (cf. Fig. 4.10). In most problems, it is possible to consider one of the following particular boundary conditions.

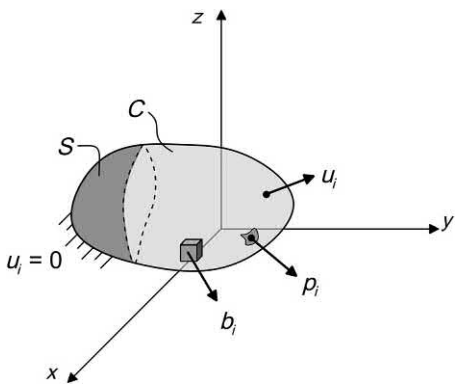

Figure 4.10 Typical force fields and boundary conditions applied to a material.

4.7.2 Traction boundary conditions

The boundary conditions for this case are expressed in terms of the stress components in compact form as

$$t_i^n = \sigma_{ji} n_i = p_i \tag{4.43}$$

where p_i is the vector of the prescribed stress components. Eq. (4.43) is equivalent to the following equations written in extended form that need to be satisfied at every point of the bounding surface:

$$\begin{cases} \sigma_{xx} n_x + \sigma_{xy} n_y + \sigma_{xz} n_z = \overline{X} \\ \sigma_{yx} n_x + \sigma_{yy} n_y + \sigma_{yz} n_z = \overline{Y} \\ \sigma_{zx} n_x + \sigma_{zy} n_y + \sigma_{zz} n_z = \overline{Z} \end{cases} \tag{4.44}$$

where $\overline{X}$, $\overline{Y}$ and $\overline{Z}$ are the components of the prescribed stress vector in the x, y, z directions, respectively, and n_x, n_y and n_z are the direction cosines of the outward surface normal. These formulas also give the components of the stress vector across any interior surface.

4.7.3 Displacement boundary conditions

The boundary conditions for this case are expressed in compact form as

$$u_i = \mathcal{F}_i(\mathcal{H}) \tag{4.45}$$

where u_i is the displacement vector, $\mathcal{F}_i$ is a vector containing prescribed displacement functions and $\mathcal{H}$ is each of the points of the bounding surface at which Eq. (4.45) needs to be satisfied. Eq. (4.45) is equivalent to the following equations in extended form:

$$\begin{cases} u = \mathcal{F}_1(\mathcal{H}) \\ v = \mathcal{F}_2(\mathcal{H}) \\ w = \mathcal{F}_3(\mathcal{H}) \end{cases} \tag{4.46}$$

where $\mathcal{F}_1, \mathcal{F}_2$ and $\mathcal{F}_3$ are prescribed functions.

In some cases, more complicated boundary conditions, which are generally defined as mixed boundary conditions, may be encountered. For example the boundary condition expressed in Eq. (4.44) may be specified over a portion of the bounding surface while that expressed in Eq. (4.46) over the remainder of the surface (Boley and Weiner, 1997). Another possible boundary condition may describe a support, in which a functional relation exists between some of the displacement and some of the stress vector components, as in the case of two materials in contact. The difficulties arising

in such problems are found in both isothermal and nonisothermal conditions (Boley and Weiner, 1997).

4.8 Generalities about stress–strain relations

The definitions of the strain and stress tensors, the equations of compatibility and equilibrium, as well as the boundary conditions alone are not sufficient to characterise the actual mechanical behaviour of materials. The characterisation of the mechanical behaviour of any material is supplied by so-called stress–strain relations (often termed constitutive equations), that is mathematical expressions that relate stresses to strains. These relations complement the description of the mechanical behaviour of materials with the elements of continuum mechanics proposed in the previous sections.

The general mathematical expression that relates stresses and strains reads

$$d\sigma_{ij} = M_{ijkl} d\varepsilon_{kl} \tag{4.47}$$

where σ_{ij} is the *relevant stress tensor*, M_{ijkl} is the general constitutive tensor of the material and ε_{kl} is the total strain tensor. Eq. (4.47) is written in incremental form to describe both linear and nonlinear relations. Linear stress–strain relations can be expressed without resorting to incremental formulations. A multitude of stress–strain relations can be formulated.

Modelling stress–strain relations of continuous materials may be made by means of the *total stress tensor* in Eq. (4.47). Modelling stress–strain relations of porous materials should be made by means of the *effective stress tensor* in Eq. (4.47). When variations in pore fluid pressures are zero, that is when (fully or partially) *drained conditions* are ensured during loading, the effective stress coincide with the total stress and analyses disregarding the influence of the pore fluid on the mechanical response of the modelled material(s) may be carried out. When pore fluid pressures vary, that is when *undrained conditions* occur during loading, the above does not hold.

4.9 Thermoelasticity

4.9.1 Perfect thermoelasticity

The concept of perfect thermoelasticity is associated with a mechanical behaviour of materials that is governed by a linear relation between stresses and strains under nonisothermal conditions. This concept derives from the one of perfect elasticity for isothermal conditions (cf. Fig. 4.11). Materials characterised by a linear stress–strain relation under nonisothermal conditions are said to follow a linear thermoelastic behaviour.

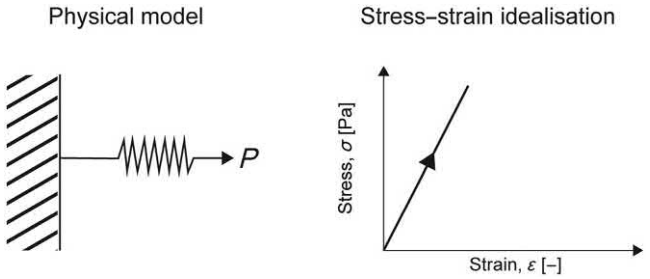

Figure 4.11 Concept of perfect elasticity.

In many situations, the reversible mechanical behaviour of materials is associated with linear stress–strain relations, while their irreversible behaviour (typically achieved when the applied loads exceed the aforementioned limit) with nonlinear stress–strain relations. However, the reversibility of the mechanical behaviour of materials does not imply linearity and various materials are characterised by a reversible behaviour following nonlinear stress–strain relations, especially at small strain levels. Elasticity can be linear or nonlinear. In the following, reference is made to a linear thermoelastic behaviour of materials.

4.9.2 Thermoelastic stress–strain relations

The total strain at each point of a material characterised by a thermoelastic behaviour is generally given by the *sum* of two contributions. The first contribution comprises the strains induced by the application of a force (or displacement) field that is required to maintain the continuity of the material by means of the generalised Hooke's law. The second contribution comprises the strains induced by the application of a temperature change to the material.

The previous considerations can be mathematically expressed in compact form as

$$\varepsilon_{ij} = C_{ijkl}\sigma_{kl} - \beta_{kl}(T - T_0) \tag{4.48}$$

where C_{ijkl} is the elastic compliance matrix (i.e. inverse of the elastic stiffness tensor, D_{ijkl}), β_{kl} is a vector that comprises the linear thermal expansion coefficient of the material, α, and $T - T_0 = \Delta T$ is the applied temperature variation. Strains induced by thermal loads are proportional to the applied temperature variation, ΔT, and to the linear thermal expansion coefficient of the material, α. Table 4.1 summarises the values of linear thermal expansion coefficient for many materials of practical interest in the context of energy geostructures. The temperature variations associated with the geothermal operation of energy geostructures should range, at worst, between

Table 4.1 Typical values of linear thermal expansion coefficient at a temperature level ranging from 20°C to 25°C.

Material	Value of linear thermal expansion coefficient, α [$\mu\varepsilon/^{\circ}C$]	Material	Value of linear thermal expansion coefficient, α [$\mu\varepsilon/^{\circ}C$]
Limestone	8	Pyrophyllite	12.2
Marble	5.5–14.1	Talc	3.7
Mica	3	Chlorine	11.1
α-Quartz	8–14	Calcite	3.8
Rock salt	40.4	Haematite	23.8
Granite	7.9–8.4	Dolomite	22.8
Sandstone	11.6	Hornblende	23.8
Graphite	7.8	Feldspars	15
Steatite	8.5–10	Gneiss	3
Mullite	4	Basalt	5
Cordierite	4–5	Gabbro	3
Muscovite	35	Portland stone	3
Phlogopite	14	Nevada sand	16
Kaolinite	5.2	Argillite	10
Dickite	5.9	Water	69
Halloysite	6	Concrete	8–12
Serpentine	6.9	Steel	11–13

Source: Data from Robertson, E.C., 1988. Thermal Properties of Rocks (Robertson, 1988). Report 2331–1258, Huotari, T., Kukkonen, I., 2004. Thermal expansion properties of rocks: literature survey and estimation of thermal expansion coefficient for Olkiluoto mica gneiss. Posiva Oy, Olkiluoto, Working Report 4, p. 62 (Huotari and Kukkonen, 2004), McKinstry, H.A., 1965. Thermal expansion of clay minerals. Am. Mineral. 50 (1–2), 212–222 (McKinstry, 1965) and Farouki, 1981. Thermal properties of soils. Cold Regions Science and Technology 5 (1), 67–75 (Farouki, 1981).

$-15^{\circ}C$ and $+30^{\circ}C$, although they may generally be limited to $-10^{\circ}C$ and $+15^{\circ}C$ (Rotta Loria, 2019).

In matrix form, Eq. (4.48) reads

$$\begin{bmatrix} \varepsilon_{xx} \\ \varepsilon_{yy} \\ \varepsilon_{zz} \\ \varepsilon_{xy} \\ \varepsilon_{yz} \\ \varepsilon_{zx} \end{bmatrix} = \begin{bmatrix} 1/E & -\nu/E & -\nu/E & 0 & 0 & 0 \\ -\nu/E & 1/E & -\nu/E & 0 & 0 & 0 \\ -\nu/E & -\nu/E & 1/E & 0 & 0 & 0 \\ 0 & 0 & 0 & 1/(2G) & 0 & 0 \\ 0 & 0 & 0 & 0 & 1/(2G) & 0 \\ 0 & 0 & 0 & 0 & 0 & 1/(2G) \end{bmatrix} \begin{bmatrix} \sigma_{xx} \\ \sigma_{yy} \\ \sigma_{zz} \\ \sigma_{xy} \\ \sigma_{yz} \\ \sigma_{zx} \end{bmatrix} - \begin{bmatrix} \alpha \\ \alpha \\ \alpha \\ 0 \\ 0 \\ 0 \end{bmatrix} (T - T_0) \tag{4.49}$$

where ν, E and G are the Poisson's ratio, the Young's modulus and the shear modulus of the material (i.e. examples of elastic properties).

In extended notation, Eq. (4.48) reads

$$\begin{aligned}
\varepsilon_{xx} &= \frac{1}{E}\left[\sigma_{xx} - \nu\left(\sigma_{yy} + \sigma_{zz}\right)\right] - \alpha(T - T_0) \\
\varepsilon_{yy} &= \frac{1}{E}\left[\sigma_{yy} - \nu(\sigma_{zz} + \sigma_{xx})\right] - \alpha(T - T_0) \\
\varepsilon_{zz} &= \frac{1}{E}\left[\sigma_{zz} - \nu\left(\sigma_{xx} + \sigma_{yy}\right)\right] - \alpha(T - T_0) \\
\varepsilon_{xy} &= \frac{1}{2G}\sigma_{xy} \\
\varepsilon_{yz} &= \frac{1}{2G}\sigma_{yz} \\
\varepsilon_{zx} &= \frac{1}{2G}\sigma_{zx}
\end{aligned} \tag{4.50}$$

Based on Eq. (4.50), it can be remarked that strains caused by mechanical loads can induce both a variation in size and a variation in shape of a material, while strains caused by thermal loads can only cause a change in size. From Eq. (4.50) it can also be obtained an expression that links the volumetric strain $\varepsilon_v = \varepsilon_{kk} = \varepsilon_{xx} + \varepsilon_{yy} + \varepsilon_{zz}$ to the sum of the normal stresses $\sigma_{kk} = \sigma_{xx} + \sigma_{yy} + \sigma_{zz} = 3p$. This formulation reads

$$\varepsilon_v = \frac{p}{K} - 3\alpha(T - T_0) \tag{4.51}$$

where K is the bulk modulus of the material.

The expressions of the stress–strain relations written thus far can be formulated in many other equivalent forms depending on the employed combination of the elastic properties of the material. Table 4.2 presents typical relationships between the elastic properties employed herein.

Table 4.2 Relationships between some elastic constants.

	Parameter to define			
Parameters available	**Shear modulus, *G***	**Young's modulus, *E***	**Poisson's ratio, *ν***	**Bulk modulus, *K***
G*, *E			$\frac{E-2G}{2G}$	$\frac{GE}{3(3G-E)}$
G*, *ν		$2G(1+\nu)$		$\frac{2G(1+\nu)}{3(1-2\nu)}$
G*, *K		$\frac{9KG}{3K+G}$	$\frac{3K-2G}{2(3K+G)}$	
E*, *ν	$\frac{E}{2(1+\nu)}$			$\frac{E}{3(1-2\nu)}$
E*, *K	$\frac{3KE}{9K-E}$		$\frac{3K-E}{6K}$	
ν*, *K	$\frac{3K(1-2\nu)}{2(1+\nu)}$	$3K(1-2\nu)$		

In general, it is convenient to explicitly express stresses in terms of the strains. In compact form, this reads

$$\sigma_{ij} = D_{ijkl}\left[\varepsilon_{kl} + \beta_{kl}(T - T_0)\right] \tag{4.52}$$

In matrix form, Eq. (4.52) reads

$$\begin{bmatrix} \sigma_{xx} \\ \sigma_{yy} \\ \sigma_{zz} \\ \sigma_{xy} \\ \sigma_{yz} \\ \sigma_{zx} \end{bmatrix} = E_0 \begin{bmatrix} (1-\nu) & \nu & \nu & 0 & 0 & 0 \\ \nu & (1-\nu) & \nu & 0 & 0 & 0 \\ \nu & \nu & (1-\nu) & 0 & 0 & 0 \\ 0 & 0 & 0 & (1-2\nu) & 0 & 0 \\ 0 & 0 & 0 & 0 & (1-2\nu) & 0 \\ 0 & 0 & 0 & 0 & 0 & (1-2\nu) \end{bmatrix} \left\{ \begin{bmatrix} \varepsilon_{xx} \\ \varepsilon_{yy} \\ \varepsilon_{zz} \\ \varepsilon_{xy} \\ \varepsilon_{yz} \\ \varepsilon_{zx} \end{bmatrix} + \begin{bmatrix} \alpha \\ \alpha \\ \alpha \\ 0 \\ 0 \\ 0 \end{bmatrix} (T - T_0) \right\} \tag{4.53}$$

where $E_0 = E/[(1+\nu)(1-2\nu)]$.

In extended form, Eq. (4.52) reads

$$\begin{aligned} \sigma_{xx} &= 2G\varepsilon_{xx} + \frac{\nu E}{(1+\nu)(1-2\nu)}\left(\varepsilon_{xx} + \varepsilon_{yy} + \varepsilon_{zz}\right) + 3K\alpha(T - T_0) \\ \sigma_{yy} &= 2G\varepsilon_{yy} + \frac{\nu E}{(1+\nu)(1-2\nu)}\left(\varepsilon_{xx} + \varepsilon_{yy} + \varepsilon_{zz}\right) + 3K\alpha(T - T_0) \\ \sigma_{zz} &= 2G\varepsilon_{zz} + \frac{\nu E}{(1+\nu)(1-2\nu)}\left(\varepsilon_{xx} + \varepsilon_{yy} + \varepsilon_{zz}\right) + 3K\alpha(T - T_0) \\ \sigma_{xy} &= 2G\varepsilon_{xy} \\ \sigma_{yz} &= 2G\varepsilon_{yz} \\ \sigma_{zx} &= 2G\varepsilon_{zx} \end{aligned} \tag{4.54}$$

4.9.3 Separation of stresses caused by mechanical and thermal loads

Eq. (4.52) expresses that *stresses can arise in materials characterised by a thermoelastic behaviour because of two causes*: mechanical loads and thermal loads (cf. Fig. 4.12). Stresses arise in a material because of the application of force fields or the prescription of displacements to ensure equilibrium and continuity of the material. Stresses arise in a material

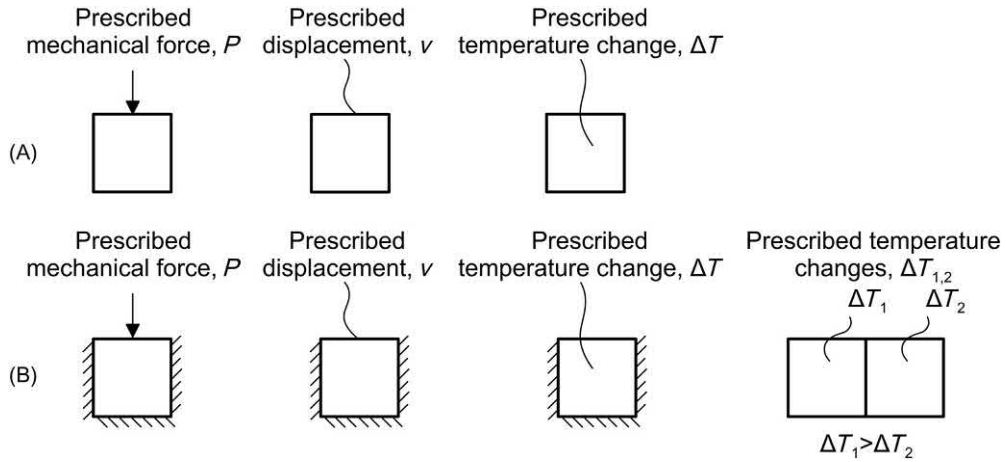

Figure 4.12 Configurations where (A) no stress arises and (B) stress arises.

because of the application of temperature variations as a result of the presence of a restraint, of a nonuniform temperature distribution or of a combination of these causes. In the context of energy geostructures, the combination of the previous causes is more common.

Thermally induced stress arises in a material subjected to a uniform or nonuniform temperature variation because, in the presence of a restraint, the development of the strain induced by the applied temperature variation is prevented with respect to a case in which free thermal deformation would occur. Thermally induced stress arises in a material subjected to a nonuniform temperature variation [different than a temperature field varying linearly with a set of rectangular Cartesian coordinates (Boley and Weiner, 1997)] also in the case in which free deformation can occur because of the differential thermal deformation of the infinitesimal elements that characterise the considered material. This differential thermally induced deformation, together with the fact that the material must remain continuous, indicates that each element restrains the distortions of its neighbours and causes stress.

4.9.4 Three-dimensional thermoelastic modelling

The three-dimensional modelling of thermoelastic problems consists in the determination of 15 functions, assuming for simplicity the temperature distribution to be known. In rectangular Cartesian coordinates, these functions are:

- six strain components $\varepsilon_{xx}, \varepsilon_{yy}, \varepsilon_{zz}, \varepsilon_{xy}, \varepsilon_{yz}, \varepsilon_{zx}$;
- three displacement components u, v, w; and
- six stress components $\sigma_{xx}, \sigma_{yy}, \sigma_{zz}, \sigma_{xy}, \sigma_{yz}, \sigma_{zx}$.

Therefore to solve this problem, the following fifteen equations need to be satisfied throughout the material:

- six strain–displacement relations;
- six stress–strain relations;
- three equilibrium equations; and
- boundary conditions.

When the problem is formulated in this way and appropriate continuity restrictions are set, the solution is unique [for the full development, see, e.g. Boley and Weiner (1997)]. This means that there exists at most one set of 12 stress and strain components, and one set of 3 displacement components [except possibly for rigid-body motions, see, e.g. Boley and Weiner (1997)], which satisfies the above equations and boundary conditions.

The three-dimensional modelling of thermoelastic problems usually resorts to numerical methods such as the finite element and difference methods to be carried out. Simplified approaches to model three-dimensional thermoelastic problems are presented hereafter. These approaches may be considered for the analysis of energy geostructures.

4.9.5 Two-dimensional thermoelastic modelling

Two-dimensional analyses of thermoelastic problems may be of interest in some cases. Such analysis approaches are proposed in the following by assuming that a temperature distribution of the form $T = T(x, y)$ is known.

There exist two simplified approaches to model three-dimensional thermoelastic problems as if they were two-dimensional. These approaches assume three-dimensional problems to be characterised by *plane strain* and *plane stress conditions*.

A plane strain problem refers to circumstances in which all the strains and the displacements associated to one coordinate direction can be considered to be zero. Plane strain conditions refer to geometries of bodies characterised by one dimension much larger than the other two. The geometry of the considered bodies may be associated to that of long prisms subjected to a uniform and perpendicular distribution of loads along their principal direction (cf. Fig. 4.13A–C). Relatively small yet long cylindrical bodies loaded orthogonally to their circular cross section may also be considered in plane strain conditions. The mathematical formulation corresponding to plane strain conditions involves

$$\varepsilon_{zz} = \varepsilon_{xz} = \varepsilon_{yz} = 0 \tag{4.55}$$

A plane stress problem refers to circumstances in which all stresses associated to one coordinate direction can be considered to be zero. Plane stress conditions refer to geometries of bodies characterised by one dimension much smaller than the other two. The geometry of the considered bodies may be associated to that of thin plates subjected to a uniform and perpendicular distribution of loads along the cross section

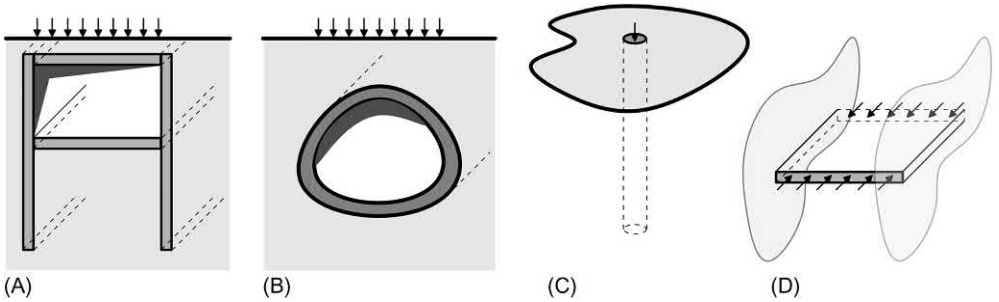

Figure 4.13 Typical configuration for (A)–(C) plane strain and (D) plane stress problems.

of their thickness (cf. Fig. 4.13D). The mathematical formulation corresponding to plane stress conditions involves

$$\sigma_{zz} = \sigma_{xz} = \sigma_{yz} = 0 \tag{4.56}$$

Especially the plane strain formulation has been widely used to analyse conventional problems involving geostructures such as walls, tunnels, slabs and piles. However, this formulation can only be used for preliminary analyses of energy geostructures such as energy walls, energy tunnels, energy slabs and energy piles. The reason for this is that the effect of temperature on the deformation of the geostructure that would conventionally be neglected in the third direction plays in this case a remarkable role for the understanding of its mechanical behaviour.

The eight quantities $\sigma_{xx}, \sigma_{yy}, \sigma_{xy}, \varepsilon_{xx}, \varepsilon_{yy}, \varepsilon_{xy}, u, v$ satisfy in either case the following eight equations:

1. *Two equilibrium equations (for the case of no body forces)*

$$\begin{cases} \dfrac{\partial \sigma_{xx}}{\partial x} + \dfrac{\partial \sigma_{xy}}{\partial y} = 0 \\ \dfrac{\partial \sigma_{xy}}{\partial x} + \dfrac{\partial \sigma_{yy}}{\partial y} = 0 \end{cases} \tag{4.57}$$

2. *Three stress–strain relations*

$$\begin{cases} \varepsilon_{xx} = \dfrac{1}{E}\left(\sigma_{xx} - \nu\sigma_{yy}\right) - \alpha(T - T_0) \\ \varepsilon_{yy} = \dfrac{1}{E}\left(\sigma_{yy} - \nu\sigma_{xx}\right) - \alpha(T - T_0) \\ \varepsilon_{xy} = \dfrac{\sigma_{xy}}{2G} \end{cases} \tag{4.58}$$

For the case of plane strain, the stresses and strains highlighted in expressions (4.57) and (4.58) are accompanied by a stress component σ_{zz} given by

$$\sigma_{zz} = \nu\left(\sigma_{xx} + \sigma_{yy}\right) + \alpha E(T - T_0) \tag{4.59}$$

For the case of plane stress, the stresses and strains highlighted above are accompanied by a strain component ε_{zz} given by

$$\varepsilon_{zz} = -\frac{\nu}{E}\left(\sigma_{xx} + \sigma_{yy}\right) - \alpha(T - T_0) \tag{4.60}$$

3. *Three strain–displacement relations*

$$\begin{aligned} \varepsilon_{xx} &= -\frac{\partial u}{\partial x} \\ \varepsilon_{yy} &= -\frac{\partial v}{\partial y} \\ \varepsilon_{xy} &= -\frac{1}{2}\left(\frac{\partial u}{\partial y} + \frac{\partial v}{\partial x}\right) \end{aligned} \tag{4.61}$$

4. *Boundary conditions*

In the two-dimensional case, traction boundary conditions, considering the surface of the body as traction-free, take the following form

$$\begin{cases} \sigma_{xx} n_x + \sigma_{xy} n_y = 0 \\ \sigma_{xy} n_x + \sigma_{yy} n_y = 0 \end{cases} \tag{4.62}$$

For displacement boundary conditions

$$\begin{cases} u = \mathcal{F}_1(\mathcal{H}) \\ v = \mathcal{F}_2(\mathcal{H}) \end{cases} \tag{4.63}$$

where $\mathcal{H}$ is a generic point of the bounding curve C_0. Mixed boundary conditions may of course arise. It may be shown that the solution of the two-dimensional problem formulated here is unique.

In addition to the previous two simplified approaches to model three-dimensional thermoelastic problems, there is one rigorous approach allowing to model three-dimensional problems with reference to two-dimensional conditions. This approach assumes that three-dimensional problems are characterised by *axisymmetric conditions*. Axisymmetric conditions refer to situations in which three-dimensional geometries, loads and boundary conditions can be described by the revolution around an axis of symmetry of a two-dimensional geometry, loads and boundary conditions. Mathematical

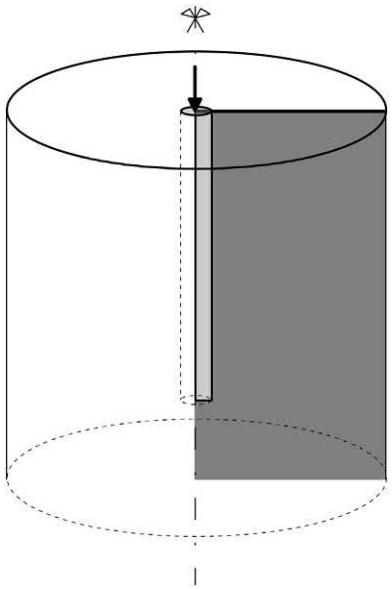

Figure 4.14 An example of axisymmetric problem.

formulations referring to axisymmetric conditions are very useful to analyse problems involving, for example, single energy piles (cf. Fig. 4.14).

In situations where an axisymmetric formulation can be used, by symmetry the two components of the displacement in any plane section along the axis of symmetry completely define the state of strain and hence the state of stress (Zienkiewicz and Taylor, 2005). In particular, considering a cylindrical coordinate system, any displacement along the radial direction causes a strain in the circumferential direction that will be associated to a stress different from zero. The need of considering four strain and stress components in axisymmetric problems instead of the three involved in plane strain and plane stress problems represents one crucial difference between the considered alternative formulations of the thermoelastic problem. One additional difference is that, while the axisymmetric formulation of the thermoelastic problem leads to an equivalent yet simpler analysis of the associated three-dimensional problem, plane strain and plane stress formulations of the thermoelastic problem lead to an approximate (simplified) analysis of the associated three-dimensional problem.

The 10 quantities $\sigma_{rr}, \sigma_{zz}, \sigma_{\theta\theta}, \sigma_{rz}, \varepsilon_{rr}, \varepsilon_{zz}, \varepsilon_{\theta\theta}, \varepsilon_{rz}, u, w$ satisfy in either case the following 10 equations:

1. *Two equilibrium equations (for the case of no body forces)*

$$\begin{cases} \dfrac{\partial \sigma_{rr}}{\partial r} + \dfrac{\partial \sigma_{rz}}{\partial z} - \dfrac{\sigma_{\theta\theta}}{r} = 0 \\ \dfrac{\partial \sigma_{rz}}{\partial r} + \dfrac{\partial \sigma_{zz}}{\partial z} + \dfrac{\sigma_{rz}}{r} = 0 \end{cases} \tag{4.64}$$

2. *Four stress–strain relations*

$$\begin{cases} \varepsilon_{rr} = \dfrac{1}{E}[\sigma_{rr} - \nu(\sigma_{zz} + \sigma_{\theta\theta})] - \alpha(T - T_0) \\ \varepsilon_{zz} = \dfrac{1}{E}[\sigma_{zz} - \nu(\sigma_{rr} + \sigma_{\theta\theta})] - \alpha(T - T_0) \\ \varepsilon_{\theta\theta} = \dfrac{1}{E}[\sigma_{zz} - \nu(\sigma_{rr} + \sigma_{zz})] - \alpha(T - T_0) \\ \varepsilon_{rz} = \dfrac{\sigma_{rz}}{2G} \end{cases} \tag{4.65}$$

3. *Four strain–displacement relations*

$$\begin{aligned} \varepsilon_{rr} &= -\frac{\partial u}{\partial r} \\ \varepsilon_{zz} &= -\frac{\partial w}{\partial z} \\ \varepsilon_{\theta\theta} &= -\frac{u}{r} \\ \varepsilon_{rz} &= -\frac{1}{2}\left(\frac{\partial u}{\partial z} + \frac{\partial w}{\partial x}\right) \end{aligned} \tag{4.66}$$

4. *Boundary conditions*

In the two-dimensional case, traction boundary conditions, considering the surface of the body as traction-free, take the following form

$$\begin{cases} \sigma_{rr} n_r + \sigma_{rz} n_z = 0 \\ \sigma_{rz} n_r + \sigma_{zz} n_z = 0 \end{cases} \tag{4.67}$$

For displacement boundary conditions

$$\begin{cases} u = \mathcal{F}_1(\mathcal{H}) \\ w = \mathcal{F}_2(\mathcal{H}) \end{cases} \tag{4.68}$$

4.9.6 One-dimensional thermoelastic modelling

Modelling thermoelastic problems with reference to one-dimensional conditions may be of interest in some situations. A one-dimensional analysis approach is proposed in the following by assuming that a temperature distribution of the form $T = T(z)$ is known.

The mathematical formulation of the considered problem is particularly simple because one normal stress, one normal strain and one relevant displacement, such as $\sigma_{zz}, \varepsilon_{zz}, w$, need to satisfy in either case the following three equations:

1. *One equilibrium equation (for the case of no body forces)*

$$\frac{\partial \sigma_{zz}}{\partial z} = 0 \tag{4.69}$$

2. *One stress–strain relation*

$$\varepsilon_{zz} = \frac{1}{E}\sigma_{zz} - \alpha(T - T_0) \tag{4.70}$$

3. *One strain–displacement relation*

$$\varepsilon_{zz} = -\frac{\partial w}{\partial z} \tag{4.71}$$

4. *Boundary conditions*

In the one-dimensional case, traction boundary conditions, considering the surface of the body as traction-free, take the following form

$$\sigma_{zz} n_z = 0 \tag{4.72}$$

For displacement boundary conditions

$$w = \mathcal{F}_3(\mathcal{H}) \tag{4.73}$$

The first one-dimensional modelling of problems involving energy geostructures has been proposed by Laloui et al. (2003), with reference to single energy piles of length L and linear thermal expansion coefficient α subjected to a temperature variation ΔT. The same problem is considered in the following for its relevance in the analysis and design of energy piles.

If an energy pile can deform freely, it is characterised by a thermally induced strain

$$\varepsilon_f^{th} = -\alpha \Delta T \tag{4.74}$$

This thermally induced strain leads to a variation in length of the energy pile of

$$\Delta L = L' - L = -L\varepsilon_f^{th} = L\alpha\Delta T \tag{4.75}$$

where L' is the energy pile length after the application of the temperature variation (cf. Fig. 4.15).

When the thermally induced deformation is completely blocked

$$\varepsilon_b^{th} = -\varepsilon_f^{th} = \alpha\Delta T \tag{4.76}$$

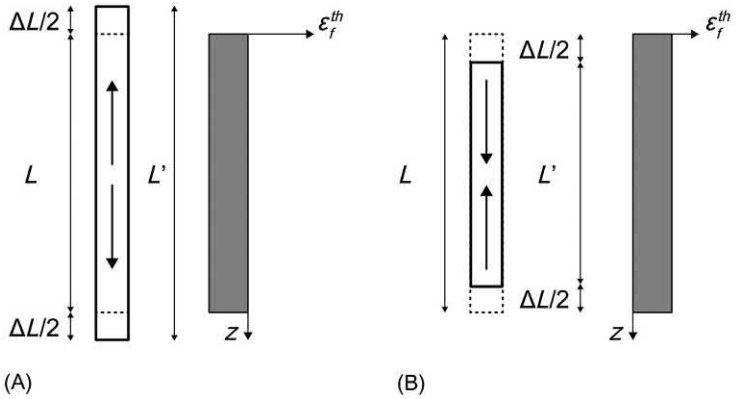

Figure 4.15 Thermally induced strain caused by (A) heating and (B) cooling of an energy pile under free expansion conditions.

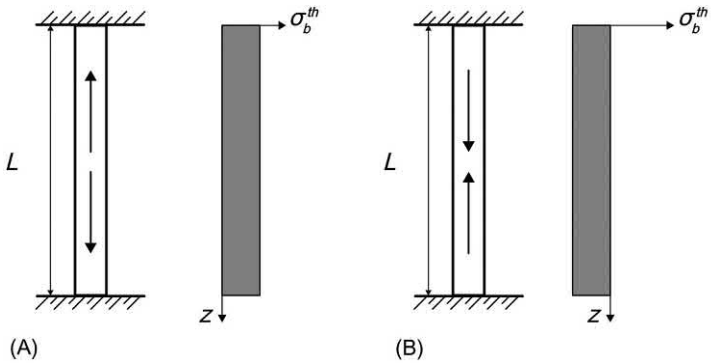

Figure 4.16 Thermally induced stress caused by (A) heating and (B) cooling of an energy pile under completely restrained conditions.

the observed strain is

$$\varepsilon_o^{th} = 0 \tag{4.77}$$

Therefore a thermally induced stress

$$\sigma_b^{th} = E\varepsilon_b^{th} = E\alpha\Delta T \tag{4.78}$$

arises in the energy pile (cf. Fig. 4.16).

In reality, energy piles do not deform freely because of the presence of the surrounding ground and superstructure. Therefore the observed thermally induced strain is generally

$$\varepsilon_o^{th} \leq \varepsilon_f^{th} \tag{4.79}$$

Eq. (4.79) implies that only a proportion of the strain is blocked, that is

$$\varepsilon_b^{th} = \varepsilon_o^{th} - \varepsilon_f^{th} \tag{4.80}$$

In other words, the response of the energy pile is governed by a certain degree of freedom, defined as (Laloui et al., 2003)

$$DOF = \frac{\varepsilon_o^{th}}{\varepsilon_f^{th}} \text{ with } 0 \leq DOF \leq 1 \tag{4.81}$$

The blocked thermally induced strain induces an observed thermally induced stress that can be calculated as

$$\sigma_o^{th} = E\varepsilon_b^{th} = E\left(\varepsilon_o^{th} - \varepsilon_f^{th}\right) = E\left(\varepsilon_o^{th} + \alpha\Delta T\right) = E\alpha\Delta T(1 - DOF) \tag{4.82}$$

Eq. (4.82) is the simplified one-dimensional formulation of the generalised thermo-elastic stress–strain relation expressed in Eq. (4.52). Fig. 4.17 shows the impact of the degree of freedom of the energy pile on the development of the average thermally induced deformation, $\overline{\varepsilon}_o^{th}$, and stress, $\overline{\sigma}_o^{th}$. The higher the restraint provided by the presence of the surrounding ground and the superstructure, the greater the thermally induced stress and the lower the thermally induced strain. The opposite is true for the lower pile restraint.

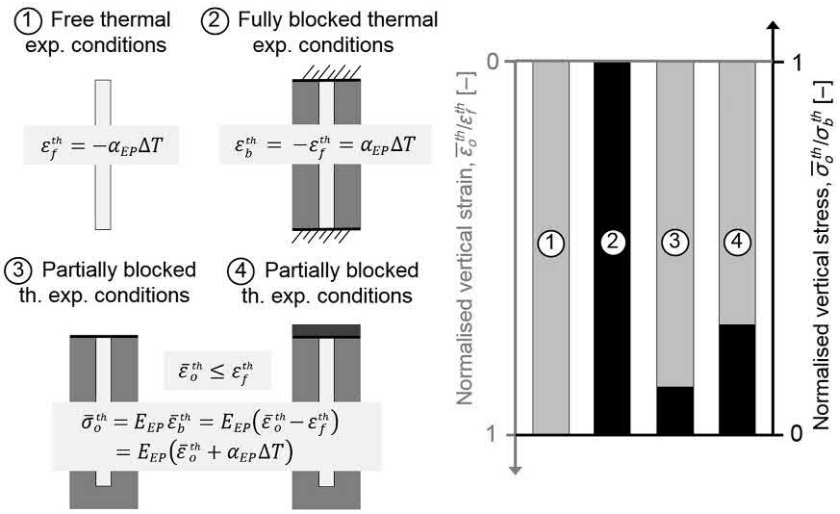

Figure 4.17 Impact of the system restraint on the thermally induced strain and stress in energy piles. *Modified after Rotta Loria, A.F., 2019. Performance-based design of energy pile foundations. DFI J. 12 (2), 94–107.*

The term $\bar{\varepsilon}_o^{th}$ is generally not known a priori but needs to be estimated based on the results of similar case studies or preferably to be calculated. During preliminary analysis and design stages where the term $\bar{\varepsilon}_o^{th}$ would not be known yet, the aforementioned formulations are still powerful tools to get acquainted with the orders of magnitude of the thermally induced strain and stress that may characterise the energy pile under free or completely restrained conditions, respectively. Orders of magnitude are given, for example, by Bourne-Webb et al. (2016b).

The previously proposed framework implicitly refers to energy piles embedded in typical soil deposits for which the soil-pile thermal expansion coefficient ratio $X = \alpha_{soil}/\alpha_{EP} \leq 1$, where α_{soil} is the linear thermal expansion coefficient of the soil. In rare cases where $X = \alpha_{soil}/\alpha_{EP} > 1$, typically at successive stages of geothermal operations, the temperature variation applied to an energy pile and its thermal expansion coefficient do not satisfy inequality (4.79), that is

$$\varepsilon_o^{th} > \varepsilon_f^{th} \tag{4.83}$$

The above occurs because when the linear thermal expansion coefficient of the soil is greater than that of the energy pile, the thermally induced deformation of energy piles is dominated by that of the soil rather than by the deformation of the piles. This phenomenon becomes more pronounced as wider soil regions are affected by temperature variations (Bourne-Webb et al., 2016a; Rotta Loria and Laloui, 2017).

For example inequality (4.83) indicates that heating thermal loads applied to energy piles can induce tensile stress. This phenomenon has been confirmed by full-scale experimental evidence and numerical analyses (Rotta Loria and Laloui, 2017, 2018).

4.10 Plasticity and thermoplasticity

4.10.1 Yield criterion

The condition that defines the limit of elasticity and the onset of plasticity through the concept of yield limit is known as the yield condition or *yield criterion*. The yield criterion defines all of the possible stress states that are associated with a reversible mechanical behaviour of the material as well as those that are associated with an irreversible mechanical behaviour of the material (depending on the loading situation).

The graphical representation of a yield criterion assumes different forms depending on the dimensions considered for any given problem (Yu, 2006). In one dimension, the yield criterion is represented by a point. In two dimensions, the yield criterion is represented by a curve. In three dimensions, the yield criterion is represented by a surface. The most comprehensive representation of a yield criterion is through a surface represented in stress space, which is generally termed as *yield surface*.

The limit of the elastic domain characterising the mechanical behaviour of a material can be expressed mathematically through the following general yield surface (or yield function)

$$f = 0 \tag{4.84}$$

4.10.2 Elastic and plastic strains

The existence of a yield criterion indicates that increments of stress that lie within the yield surface produce elastic deformation, while those that lie on the yield surface produce plastic deformation for further loading. In this context, the total strain of any material can be decomposed in an elastic ε_{kl}^{e} and a plastic ε_{kl}^{p} portion:

$$d\varepsilon_{kl} = d\varepsilon_{kl}^{e} + d\varepsilon_{kl}^{p} \tag{4.85}$$

The elastic part of the strain produced by a given load is recoverable when the load is removed, while the plastic part of the strain is irrecoverable when the load is removed. In this sense, the work done by the plastic strain must be positive and this corresponds to the condition of irreversibility postulated by Prager (1949). Decomposing the total strain with an elastic and a plastic component represents the first essential step for deriving a complete stress–strain relation for materials characterised by plasticity, irrespective of whether isothermal or nonisothermal conditions are considered.

4.10.3 Flow rule

A key aspect when addressing plasticity is to determine plastic strains, which are induced by the phenomenon of plastic flow (Yu, 2006). The increments of plastic strain can be expressed as (von Mises, 1928; Melan, 1938)

$$d\varepsilon_{ij}^{p} = d\lambda^{p} \frac{\partial g}{\partial \sigma_{ij}} \tag{4.86}$$

Eq. (4.86) is often referred to as *flow rule*. In this equation, $d\lambda^{p}$ is a positive scalar called *plastic multiplier*, which represents the magnitude of plastic strain, and g is termed *plastic potential function*, which defines the direction of plastic strain vectors. Eq. (4.86) defines ratios of the components of plastic strain rate. In particular, $\partial g/\partial \sigma_{ij}$ gives the components of normal vector to g in the stress space. In other words, the potential function defines the direction of plastic strains (and to which incremental plastic strain vectors are orthogonal).

Eq. (4.86) also indicates that only one plastic mechanism is considered. However, several plastic mechanisms may be considered, each one referring to a relevant plastic

potential function. According to Yu (2006), if the unit normal to the plastic potential approaches a finite number of linearly independent limiting values as the stress point approaches the singular point in question, the following generalised flow rule initially proposed by Koiter (1953) can be considered

$$d\varepsilon_{ij}^{p} = \sum_{k=1}^{N} d\lambda_{k}^{p} \frac{\partial g_{k}}{\partial \sigma_{ij}} \tag{4.87}$$

where $d\lambda_{k}^{p}$ are nonnegative and $\partial g_{k}/\partial \sigma_{ij}$ are the linearly independent gradients.

In general, the plastic potential function may or may not be the same as the yield function. If the plastic potential is assumed to be the same as the yield function (i.e. $f = g$), the plastic flow rule is called *associated (or normality) flow rule*. In contrast, if the potential is assumed to differ compared to the yield function (i.e. $f \neq g$), the plastic flow rule is called *nonassociated flow rule* (cf. Fig. 4.18). In the latter case, plastic potential function usually has a mathematical expression similar to yield function and the difference might be in some coefficients that are related to material properties.

Employing an associated flow rule involves assuming that the principal axes of the plastic strain tensor coincide with those of the stress tensor. This means that directions of ε_{ij}^{p} and σ_{ij} in Eq. (4.86) are the same. Employing a nonassociated flow rule involves assuming that the principal axes of the plastic strain tensor do not coincide with those of the stress tensor. This means that directions of ε_{ij}^{p} and σ_{ij} in Eq. (4.86) are not the same. A graphical representation of this concept is shown in Fig. 4.18. Plastic flow rules based on nonassociated flow may typically be more suitable to achieve a

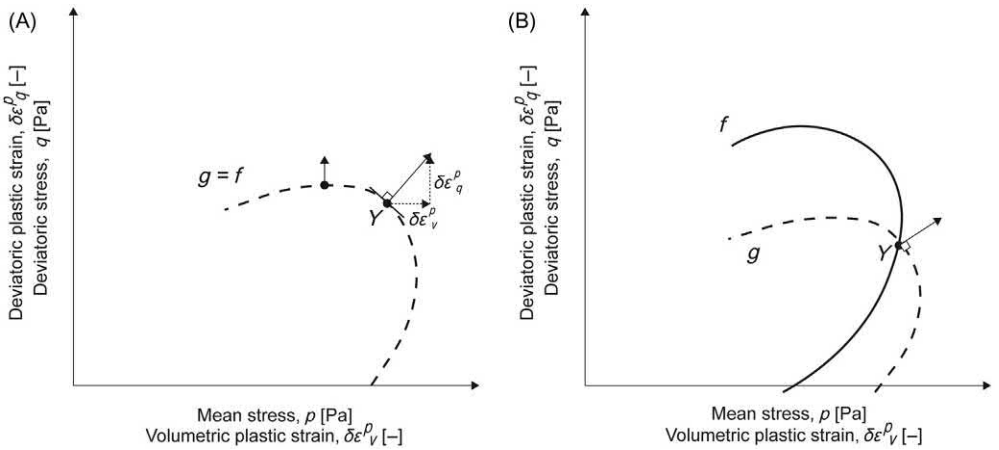

Figure 4.18 Potential function and plastic strain increments for an (A) associated flow rule and a (B) nonassociated flow rule.

thorough modelling of the mechanical behaviour of geomaterials, although flow rules based on associated flow are typically employed for simplicity.

4.10.4 Perfect plasticity

The concept of perfect plasticity is associated with the mechanical behaviour of materials that while yielding do not present a further increase of stress for an increase in strain (i.e. a *plateau* is observed in two dimensions, cf. Fig. 4.19). The concept of perfect plasticity has been initially used to solve geotechnical stability problems involving geomaterials by Coulomb (1773) and Rankine (1857), and has been successively applied to the analysis of other materials such as metals by Saint Venant (1870) and Lévy (1870), for example.

Materials behaving according to the theory of perfect plasticity are characterised by the same size and shape of the yield surface under the development of plastic deformations. In these situations, the yield function is only a function of the stress state. In the other words, the elastic domain characterising the mechanical behaviour of perfectly plastic materials is always the same.

The simplest mathematical expression of the yield surface for a perfectly plastic material reads

$$f = f\left(\sigma_{ij}\right) = 0 \tag{4.88}$$

where σ_{ij} is the relevant stress (i.e. total or effective stress). The stress conditions characterising the reversible and irreversible response of materials with a thermoelastic (or elastic), perfectly plastic behaviour are as follows

$$\text{Reversible behaviour} \qquad f\left(\sigma_{ij}\right) < 0 \ \text{ or } \ df < 0 \tag{4.89}$$

$$\text{Irreversible behaviour} \qquad f\left(\sigma_{ij}\right) = 0 \ \text{ and } \ df = 0 \tag{4.90}$$

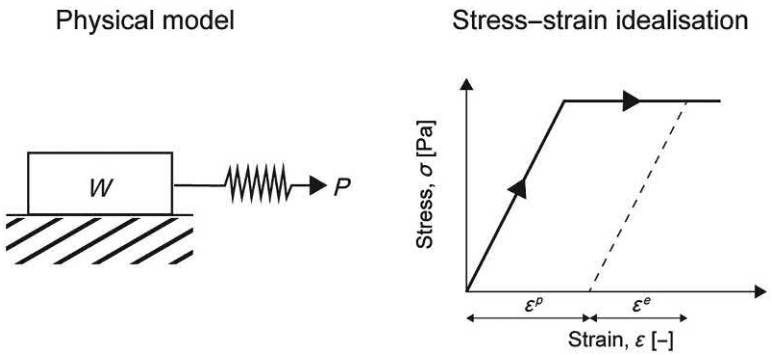

Figure 4.19 Concept of perfect plasticity.

Eq. (4.89) expresses that elastic deformation arises as long as the stress state is *inside* the yield surface. Eq. (4.90) expresses that plastic deformation arises as long as the stress state *lies or travels* on the yield surface.

According to Prager (1949), when loading of a material characterised by a plastic behaviour happens, the stress state must stay on the yield surface. This is the so-called *condition of consistency* that should be satisfied to ensure an appropriate description of the physical process involved in plastic deformation. The condition of consistency requires that a yield criterion is satisfied as long as the material is in a plastic state.

The condition of consistency for the yield function of a material characterised by perfect plasticity reads

$$df = \frac{\partial f}{\partial \sigma_{ij}} d\sigma_{ij} = 0 \tag{4.91}$$

Classical examples of perfectly plastic yield criteria are those that have been presented, for example, by Coulomb (1773), Tresca (1864), von Mises (1928), Drucker and Prager (1952), Lade and Duncan (1975), Matsuoka and Nakai (1974), Matsuoka (1982) and Hoek and Brown (1980). Especially the Mohr–Coulomb yield criterion, which is based on the work of Coulomb (1773), may be used in a relatively straightforward way in the analysis and design of energy geostructures to address key features of the mechanical behaviour of geomaterials such as soils and rocks.

4.10.5 Hardening plasticity

The concept of hardening plasticity is associated with the mechanical behaviour of materials that while yielding present a further variation (e.g. increase) in stress for an increase in strain (cf. Fig. 4.20). The concept of hardening plasticity has been applied

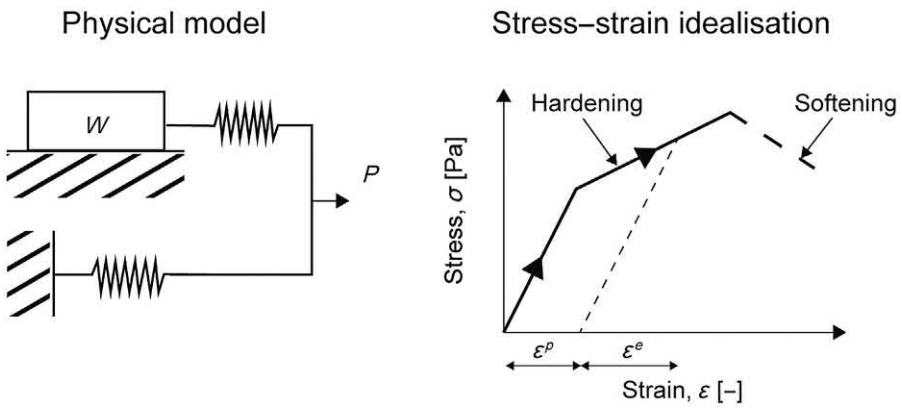

Figure 4.20 Concept of hardening (and softening) plasticity.

in early studies by Melan (1938) and Prager (1949), and it has been employed for the analysis of geomaterials such as soils by Drucker et al. (1957), for example.

Materials behaving according to the theory of hardening plasticity are characterised by a size, location or shape of the yield surface that may change under the development of plastic deformations. In these situations, the yield function depends on the stress state *and* the stress history, and may explicitly depend also on temperature.

Materials characterised by hardening and an elastic limit that is assumed to be insensitive to temperature (isothermal yield surface) are characterised by the following yield function

$$f = f\left(\sigma_{ij}, \tilde{h}_i\right) = 0 \tag{4.92}$$

where σ_{ij} is the relevant stress and $\tilde{h}_i$ are the internal variables that define the hardening. Materials characterised by hardening and an elastic limit that is considered to be sensitive to temperature are characterised by the following yield function

$$f = f\left(\sigma_{ij}, \tilde{h}_i, T\right) = 0 \tag{4.93}$$

The hardening rule defines the modification of a yield surface during the process of plastic flow. In most situations, it is assumed that the shape of the yield surface remains unchanged while this surface can change in size, location or both. Reference is made to *isotropic hardening* when upon the development of plastic strains changes in size of the yield surface occur but the centre and orientation of the yield surface in the stress space remain the same. Reference is made to *kinematic hardening* when upon the development of plastic strains the size of the yield surface remains the same but its location changes in the stress space. Reference is made to *mixed hardening* when the size of the yield surface changes upon the development of plastic strains and translates in the stress space.

When plastic deformation makes the yield surface expanding in size, the material is said to have a *hardening behaviour*, which makes it more difficult to yield. In contrast, when plastic deformation makes the yield surface contracting in size, the material is said to have a *softening behaviour*, which makes it easier to yield. Hardening (and softening) can be linear or nonlinear.

The dependence of plastic deformation of hardening materials on the history of the stress state can be appreciated through Fig. 4.21 with reference to the idealised stress–strain relation characterising a material with a linear elastic behaviour and a nonlinear hardening behaviour. Points G and F are characterised by the same state of strain but different states of stress.

The internal variables that define the hardening are commonly assumed to be a function of plastic strains. In these situations, the material is characterised by a *strain hardening* behaviour and $\tilde{h} = \tilde{h}\left(\varepsilon_{ij}^{p}\right)$.

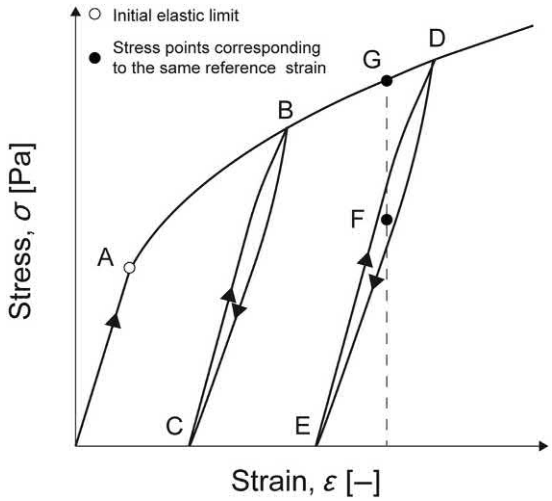

Figure 4.21 The importance of the stress history for hardening materials.

The stress conditions characterising the reversible and irreversible response of materials characterised by a thermoelastic (or elastic), plastic hardening behaviour are as follows

$$\text{Reversible behaviour} \qquad f\left(\sigma_{ij}, \tilde{h}_i\right) < 0 \ \text{ or } \ df \leq 0 \tag{4.94}$$

$$\text{Irreversible behaviour} \qquad f\left(\sigma_{ij}, \tilde{h}_i\right) = 0 \ \text{ and } \ df > 0 \tag{4.95}$$

To fully understand the previous equations, the loading–unloading conditions, or Karush–Kuhn–Trucker conditions (Karush, 1939; Kuhn and Tucker, 1951), must be considered:

$$\text{Unloading} \qquad f\left(\sigma_{ij}, \tilde{h}_i\right) = 0 \ \text{ and } \ df < 0 \tag{4.96}$$

$$\text{Neutral loading} \qquad f\left(\sigma_{ij}, \tilde{h}_i\right) = 0 \ \text{ and } \ df = 0 \tag{4.97}$$

$$\text{Loading} \qquad f\left(\sigma_{ij}, \tilde{h}_i\right) = 0 \ \text{ and } \ df > 0 \tag{4.98}$$

Eqs (4.96)–(4.98) represent criteria to model the mechanical behaviour of materials potentially characterised by hardening once the stress state is on the yield surface. Accordingly, the behaviour of these materials becomes irreversible (plastic deformations arise) only when the loading condition is satisfied (hardening occurs). Otherwise, for both unloading and neutral loading, the behaviour of these materials is reversible.

Eq. (4.96) represents the condition at which the material stress state moves towards the inside of the current yield surface. Eq. (4.97) corresponds to the condition in which the material stress state remains or travels on the current yield surface. Eq. (4.98) represents the condition in which the material condition has the tendency to go outside the yield surface, but because this phenomenon is not possible (i.e. stress states cannot lie outside the yield surface in the present framework) the current yield limit changes (i.e. it expands to a larger one for a hardening material while it contracts for a softening material).

According to Prager (1949), when loading of a material characterised by a plastic hardening behaviour happens, the material hardens while the stress state stays on a new expanded yield surface. This is the condition of consistency for hardening materials and indicates that loading from a plastic state leads to another plastic state. According to this condition, starting from a plastic sate with:

$$\text{Current yield surface} \qquad f\left(\sigma_{ij}, \tilde{h}_i\right) = 0 \ \text{ and } \ df\left(d\sigma_{ij}, d\tilde{h}_i\right) > 0 \tag{4.99}$$

the induced loading should result in a new plastic state where:

$$\text{New yield surface} \qquad f\left(\sigma_{ij} + d\sigma_{ij}, \tilde{h}_i + d\tilde{h}_i\right) = 0 \ \text{ and } \ df\left(d\sigma_{ij}, d\tilde{h}_i\right) = 0 \tag{4.100}$$

Therefore the condition of consistency for the yield function insensitive to temperature of a material characterised by hardening plasticity reads

$$df = \frac{\partial f}{\partial \sigma_{ij}} d\sigma_{ij} + \frac{\partial f}{\partial \tilde{h}_i} d\tilde{h}_i = 0 \tag{4.101}$$

For the case of a material characterised by a strain hardening behaviour, the hardening parameter may be the plastic strain. Accordingly, Eq. (4.101) can be written as

$$df = \frac{\partial f}{\partial \sigma_{ij}} d\sigma_{ij} + \frac{\partial f}{\partial \tilde{h}} \frac{\partial \tilde{h}}{\partial \varepsilon_{ij}^{p}} d\varepsilon_{ij}^{p} = 0 \tag{4.102}$$

The consistency equation is used to determine the plastic multiplier and the magnitude of plastic strains. This aspect is addressed later.

The stress conditions characterising the reversible and irreversible response of materials characterised by a thermoelastic, thermoplastic hardening behaviour are more complex. According to Prager (1949) and Prager (1958), the only admissible states of stress–temperature are those that lie inside or on the yield surface after the loading: if the material stress–temperature state is *inside* the elastic domain the response is purely elastic; if the material stress–temperature state is *on* the yield surface it is elastoplastic. Mathematically, the admissible states under nonisothermal conditions can be expressed as (Prager, 1958):

$$f = f\left(\sigma_{ij}, \tilde{h}_i, T\right) \leq 0 \tag{4.103}$$

Starting from an initial state (σ_{ij}, T) (for geomaterials, e.g. at a given void ratio) and considering changes in stress and temperature occurring at rates $d\sigma_{ij}$ and dT, the variation of f can be written as:

$$df = \frac{\partial f}{\partial \sigma_{ij}} d\sigma_{ij} + \frac{\partial f}{\partial \tilde{h}_i} d\tilde{h}_i + \frac{\partial f}{\partial T} dT \tag{4.104}$$

According to Hueckel and Borsetto (1990), the following situations are conceivable:

1. The initial state lies inside the yield surface ($f < 0$) and $d\sigma_{ij}$ and dT are such that the final state remains inside it (loading or unloading). In this case no plastic strain is produced. Mathematically (Di Donna, 2014): $d\tilde{h}_i = 0$ and df can be positive (loading), negative (unloading) or null (neutral loading).
2. The initial state lies on the yield surface ($f = 0$) and $d\sigma_{ij}$ and dT are such that the final state is inside it (unloading). In this case the plastic strain remains constant. Mathematically (Di Donna, 2014): $d\tilde{h}_i = 0$ and $df < 0$. Thus:

$$\frac{\partial f}{\partial \sigma_{ij}} d\sigma_{ij} + \frac{\partial f}{\partial T} dT < 0 \tag{4.105}$$

3. The initial state lies on the yield surface ($f = 0$) and $d\sigma_{ij}$ and dT are such that the final state remains on this setting. In this case, the condition of consistency for the yield function sensitive to temperature of a material characterised by hardening plasticity must stand true and reads:

$$df = \frac{\partial f}{\partial \sigma_{ij}} d\sigma_{ij} + \frac{\partial f}{\partial \tilde{h}_i} d\tilde{h}_i + \frac{\partial f}{\partial T} dT = 0 \tag{4.106}$$

In this latter situation, two possible phenomena can occur (Di Donna, 2014):

a. No plastic strain is produced ($d\tilde{h}_i = 0$) and the increment of stress is balanced by the increment of temperature (neutral loading):

$$\frac{\partial f}{\partial \sigma_{ij}} d\sigma_{ij} + \frac{\partial f}{\partial T} dT = 0 \tag{4.107}$$

b. Plastic strain is produced ($d\tilde{h}_i \neq 0$) (loading):

$$\frac{\partial f}{\partial \sigma_{ij}} d\sigma_{ij} + \frac{\partial f}{\partial T} dT > 0 \tag{4.108}$$

When $f = 0$, the continuity conditions postulated by Prager (1949) guarantee the possibility to have unloading (case 2), neutral loading (case 3.a) or loading (case 3.b) (Di Donna, 2014).

In the context of the modelling of hardening and softening of materials under non-isothermal conditions, it is noteworthy that soils exhibit a characteristic behaviour. Soils can exhibit strain hardening at constant temperature, that is the size of the elastic domain increases for increasing plastic strain. However, at constant void ratio, soils also show thermal softening for increasing temperature levels, that is the size of the elastic domain decreases with increasing temperature. In other words, the material undergoes plasticity earlier at higher temperatures. An in-depth analysis of this phenomenon has been presented, for example, by Hueckel and Baldi (1990).

4.10.6 Critical state plasticity

The concept of critical state plasticity is associated with the mechanical behaviour of materials for which a continuous distortion caused by shearing eventually leads to a well-defined state. The concept of critical state has been formulated independently by Roscoe et al. (1958) and Parry (1958), and it has found major applications in the analysis of geomaterials such as soils based on the works of Roscoe et al. (1958), Parry (1958), Schofield and Wroth (1968) and Roscoe and Burland (1968), for example.

Under critical state conditions, the material flows as a *frictional fluid* (Schofield and Wroth, 1968), so that yielding occurs at constant volume and constant stresses. The critical state is defined by the following two equations (Schofield and Wroth, 1968)

$$q = M_c p \tag{4.109}$$

$$\Gamma = v_e + \tilde{\lambda} \ln p \tag{4.110}$$

where M_c, Γ and $\tilde{\lambda}$ represent material parameters, v_e is the specific volume of the material ($v_e = 1 + e$, with e being the void ratio of the material) and p is the *relevant mean stress* (in general, the mean effective stress). Eq. (4.109) and (4.110) identify the so-called critical state line (CSL) in different planes (cf. Fig. 4.22). The CSL represented in the $v_e - \ln p$ plane is parallel to another key setting for the mechanical analysis of geomaterials, i.e. the Normal Compression (or Consolidation) Line (cf. Fig. 4.23). The slope of both of these lines represents the compression index, $\tilde{\lambda}$. Unloading a material from a stress state lying on the NCL (normal compression line) involves a stress path along the so-called unloading reloading line (URL). The slope of the URL represents the swelling index, $\tilde{\kappa}$. The intersection between the NCL and URL coincides with the preconsolidation pressure. Variations in void ratio of the material that are associated with elastic and plastic strains can be determined through an analysis of the stress paths along the NCL and URL.

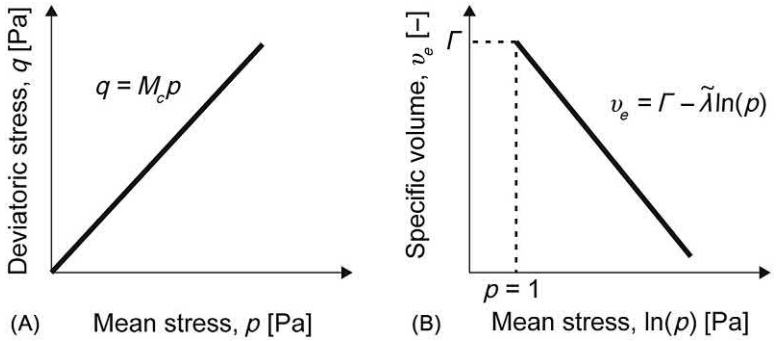

Figure 4.22 The concept of critical state: representation of the CLS in terms of (A) mean and deviatoric stress, and (B) mean stress and specific volume.

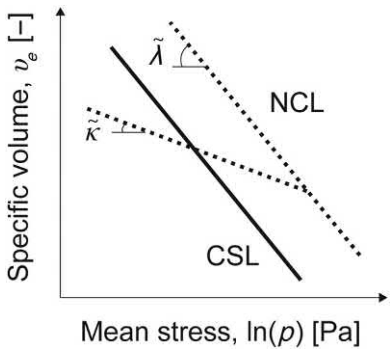

Figure 4.23 The critical state and normal compression lines.

The critical state concept is typically employed to address the mechanical behaviour of fine-grained soils (see, e.g. Roscoe and Burland, 1968), but it is also applicable to the analysis of coarse-grained soils (see, e.g. Atkinson and Bransby, 1978). Through the critical state theory, a unified characterisation of the mechanical behaviour of both fine- and coarse-grained soils can be achieved. In this context, the concept of *overconsolidation ratio* allows the former materials to be distinguished, for example in overconsolidated or normally consolidated, while the concept of *relative density* allows the latter materials to be denoted, for example as dense or loose.

The concept of critical state applied to the interpretation of the mechanical behaviour of geomaterials such as soils is represented in Fig. 4.24. When the material is sheared, after some progressive yielding states, it reaches a state in which shearing can continue without variation in volume. The corresponding void ratio to the achieved critical state is termed critical void ratio, e_c. At critical state, geomaterials exhibit lower

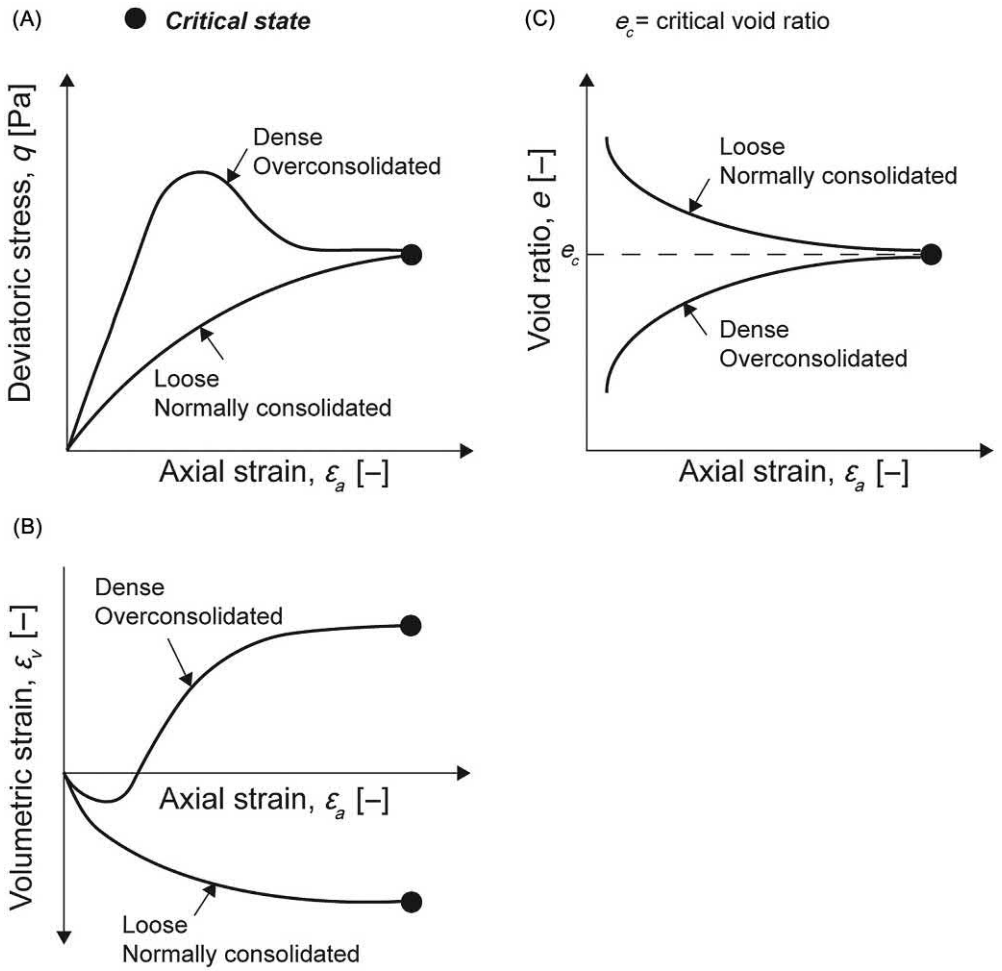

Figure 4.24 Representation of the achievement of the critical state with reference to the behaviour of soils: evolution of axial strain with (A) deviatoric stress, (B) volumetric strain and (C) void ratio.

shear strength compared to the maximum strength manifested under a dense or overconsolidated state. This aspect is shown in Fig. 4.25, considering values of cohesion and angle of shear strength in the Mohr plane, $\tau - \sigma_n$ (where τ is the shear stress and σ_n is the normal stress), for a dense or overconsolidated material, in correspondence of the maximum shear stress (at the peak) and at critical state (under constant volume conditions). In the former case, the values of the considered variables are typically termed peak cohesion, c, and peak angle of shear strength, φ. In the latter case, reference is made to cohesion and angle of shear strength under constant volume conditions, c_{cv} and φ_{cv}, respectively.

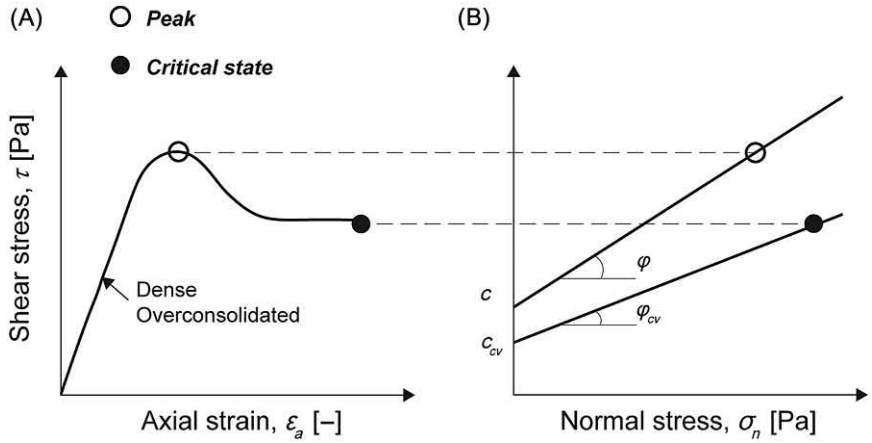

Figure 4.25 Shear resistance of materials at the peak or under constant volume conditions: representation in (A) the shear stress-axial strain plane and (B) the Mohr plane.

The first constitutive model that has been developed in the framework of the critical state theory is the Cam-Clay model. Two main versions of this model exist, differing from each other in their yield function equation and shape: the *Original Cam-Clay*, presented by Schofield and Wroth (1968), and the *Modified Cam-Clay*, presented by Roscoe and Burland (1968). The yield limit of the Modified Cam-Clay is elliptic while the Original Cam-Clay uses an almond shaped yield criterion. The modern thermoelastic, thermoplastic constitutive models for soils are often extensions of these two isothermal models (Di Donna, 2014). Hueckel and Borsetto (1990) have been the pioneers to introduce the shrinking of the elastic domain with increasing temperature at constant void ratio, developing the first thermoelastic, thermoplastic constitutive model for soils. Further developments have been proposed in other studies under continuous development (Modaressi and Laloui, 1997; Robinet et al., 1996; Cui et al., 2000; Graham et al., 2001; Abuel-Naga et al., 2007; Laloui and François, 2009). A state of the art on this topic has been provided, for example, by Hong et al. (2013).

4.10.7 Multisurface and bounding surface plasticity

The concepts of multisurface and bounding plasticity are aimed at capturing the mechanical behaviour of materials characterised by a smooth transition from a reversible to an irreversible behaviour, as well as subjected to reversal (i.e. cyclic) loadings. The mechanical behaviour of most materials showing the previous features can be difficult to capture with the modelling approaches described thus far. The concept of multisurface plasticity has been proposed for materials such as metals by Mrŏz (1967) and Iwan (1967), while the concept of bounding surface plasticity is due to Dafalias and Popov (1975) and Krieg (1975). However, both of the previous concepts have

found subsequent applications to the modelling of geomaterials. Early applications of the multisurface concept to geomaterials have been presented by Prévost (1977, 1978) and Mrŏz et al. (1978, 1979, 1981), for example. Early applications of the bounding surface concept to geomaterials have been proposed by Mrŏz et al. (1978, 1979), Dafalias and Herrmann (1982), Al-Tabbaa and Wood (1989), Whittle (1993) and Li and Meissner (2002), for example.

The theory of multisurface plasticity models the stress–strain relation of materials by various linear segments of constant tangential moduli. In the stress space, this concept is associated with various yield surfaces $f_1, f_2, f_3, \ldots, f_i$, with f_1 being the initial yield surface and $f_2, f_3, \ldots, f_i$ defining regions of constant plastic work hardening moduli (Yu, 2006). In this context, the yield surface moves (and may change in shape) upon loading.

The theory of bounding surface (or two surface) plasticity models the stress–strain behaviour of materials through two yield surfaces, that is an inner yield surface $f = 0$ and an outer yield surface $F = 0$. The theory bounding surface plasticity coincides with the multisurface theory proposed by Mrŏz (1967) with a continuum of intermediate loading surfaces where the distribution of these surfaces is analytically described a priori Krieg (1975). The location of the inner and outer surfaces completely describes the distribution of all intermediate surfaces so reference to them is not necessary (Yu, 2006).

Both of the previous theories can be extended to account for the influence of temperature on the irreversible behaviour of the material. Typically, these theories are coupled with those characterising hardening plasticity and critical state plasticity.

A constitutive model resorting to the theories of bounding and multi surface plasticity for geomaterials such as soils under nonisothermal conditions has been presented, for example, by Laloui and François (2009). The considered model, which is reported in Appendix C, has been based on successive developments presented by Laloui (1993), Modaressi and Laloui (1997) and Laloui and Cekerevac (2008). Models of this type may be employed in the analysis and design of energy geostructures to capture detailed aspects of the mechanical behaviour of geomaterials under nonisothermal conditions.

4.10.8 Thermoelastoplastic stress–strain relations

The increment of elastic strain at each point of a material characterised by a thermoelastic, plastic behaviour or by a thermoelastic, thermoplastic behaviour, can be written as (e.g. considering a single plastic mechanism)

$$d\varepsilon_{kl}^{e} = d\varepsilon_{kl} - d\varepsilon_{kl}^{p} = C_{klij} d\sigma'_{ij} - \beta_{kl} dT \tag{4.111}$$

The previous relations can be written as

$$d\sigma'_{ij} = D_{ijkl}\left(d\varepsilon_{kl} + \beta_{kl}dT - d\varepsilon^{p}_{kl}\right) \tag{4.112}$$

The increment of plastic deformation is given by the flow rule. Therefore Eq. (4.112) can be rewritten as

$$d\sigma'_{ij} = D_{ijkl}\left(d\varepsilon_{kl} + \beta_{kl}dT - d\lambda^{p}\frac{\partial g}{\partial \sigma_{kl}}\right) \tag{4.113}$$

Once an expression of the form introduced through Eq. (4.113) is established, the plastic multiplier must be defined. In this context, Eq. (4.113) must fulfil the uniqueness condition of the stress–strain solution formulated by Prager (1949). The value of the plastic multiplier can be computed by substituting Eq. (4.113) in either among the consistency Eqs (4.91), (4.101) and (4.106) written for a perfectly plastic material whose yield function is insensitive to temperature, for a hardening material whose yield function is insensitive to temperature, and for a hardening material whose yield function is sensitive to temperature, respectively. In this context, the vectorial notation instead of the tensorial one can be used for the strain and the stress tensors (Timoshenko and Goodier, 1951):

$$d\varepsilon_i = \begin{bmatrix} \varepsilon_x & \varepsilon_y & \varepsilon_z & \varepsilon_{xy} & \varepsilon_{xz} & \varepsilon_{yz} \end{bmatrix}^T \tag{4.114}$$

$$d\sigma_i = \begin{bmatrix} \sigma_x & \sigma_y & \sigma_z & \sigma_{xy} & \sigma_{xz} & \sigma_{yz} \end{bmatrix}^T \tag{4.115}$$

The consistency equation for a material characterised by a thermoelastic, perfectly plastic behaviour reads

$$\frac{\partial f}{\partial \sigma_i} D_{ij}\left(d\varepsilon_j + \beta_j dT - \lambda^{p}\frac{\partial g}{\partial \sigma_j}\right) = 0 \tag{4.116}$$

The consistency equation for a material characterised by a thermoelastic, plastic hardening behaviour reads

$$\frac{\partial f}{\partial \sigma_i} D_{ij}\left(d\varepsilon_j + \beta_j dT - \lambda^{p}\frac{\partial g}{\partial \sigma_j}\right) + \frac{\partial f}{\partial \tilde{h}_k}\frac{\partial \tilde{h}_k}{\partial \varepsilon^{p}_i}\lambda^{p}\frac{\partial g}{\partial \sigma_i} = 0 \tag{4.117}$$

The consistency equation for a material characterised by a thermoelastic, thermoplastic hardening behaviour reads

$$\frac{\partial f}{\partial \sigma_i} D_{\mathrm{ij}}\left(d\varepsilon_j + \beta_j dT - \lambda^{p}\frac{\partial g}{\partial \sigma_j}\right) + \frac{\partial f}{\partial T}dT + \frac{\partial f}{\partial \tilde{h}_k}\frac{\partial \tilde{h}_k}{\partial \varepsilon^{p}_i}\lambda^{p}\frac{\partial g}{\partial \sigma_i} = 0 \tag{4.118}$$

From Eq. (4.116), the plastic multiplier can be computed for a material characterised by a thermoelastic, perfectly plastic behaviour, and reads

$$d\lambda^p = \frac{\frac{\partial f}{\partial \sigma_i} D_{ij} \left(d\varepsilon_j + \beta_j dT \right)}{\frac{\partial f}{\partial \sigma_i} D_{ij} \frac{\partial g}{\partial \sigma_j}} \tag{4.119}$$

From Eq. (4.117), the plastic multiplier can be computed for a material characterised by a thermoelastic, plastic hardening behaviour, and reads

$$d\lambda^p = \frac{\frac{\partial f}{\partial \sigma_i} D_{ij} \left(d\varepsilon_j + \beta_j dT \right)}{\frac{\partial f}{\partial \sigma_i} D_{ij} \frac{\partial g}{\partial \sigma_j} - \frac{\partial f}{\partial \tilde{h}_k} \frac{\partial \tilde{h}_k}{\partial \varepsilon_i^p} \frac{\partial g}{\partial \sigma_i}} \tag{4.120}$$

From Eq. (4.118), the plastic multiplier can be computed for a material characterised by a thermoelastic, thermoplastic hardening behaviour, and reads

$$d\lambda^p = \frac{\frac{\partial f}{\partial \sigma_i} D_{ij} \left(d\varepsilon_j + \beta_j dT \right) + \frac{\partial f}{\partial T} dT}{\frac{\partial f}{\partial \sigma_i} D_{ij} \frac{\partial g}{\partial \sigma_j} - \frac{\partial f}{\partial \tilde{h}_k} \frac{\partial \tilde{h}_k}{\partial \varepsilon_i^p} \frac{\partial g}{\partial \sigma_i}} \tag{4.121}$$

Knowledge of the plastic multiplier(s) allows obtaining the complete stress−strain relation for the modelled material.

4.10.9 Three-dimensional thermoelastic, plastic or thermoelastic, thermoplastic modelling

The three-dimensional modelling of thermoelastic, plastic (or thermoelastic, thermoplastic) problems, assuming for simplicity the temperature distribution to be known, is more complex compared to the modelling of thermoelastic problems treated in Section 4.9.4. The reason for this is that additional functions and unknowns are associated with the mechanical behaviour of the modelled material(s).

Constitutive models accounting for the reversible and the irreversible behaviour of materials necessitate the definition of four key components: (1) the relations governing the reversible behaviour of the material (i.e. elastic deformation); (2) the criteria (yield functions) characterising the limit for which an irreversible behaviour may occur (i.e. plastic deformation); (3) the relations (plastic potential functions) characterising the irreversible behaviour of the material, including the definition of the mechanisms governing the development of plastic deformation and the direction of its evolution and potentially, (4) the expressions (hardening rules) describing the magnitude of plastic deformation. Aspects (1) and (2−4) characterise the elastic and plastic constitutive descriptions of the modelled material, respectively.

4.10.10 Constitutive modelling of materials involved with energy geostructures

In the context of the modelling of the mechanical behaviour of materials for the analysis and design of energy geostructures, the reinforced concrete that often characterises such structures can be described in most situations as linear thermoelastic. In contrast, the mechanical behaviour of the soil and rock surrounding energy geostructures is often described as either (1) thermoelastic, (2) thermoelastic, perfectly plastic, (3) thermoelastic, plastic with hardening or (4) thermoelastic, thermoplastic with hardening. Linear or nonlinear stress–strain relations are employed for the previous purpose, and the choice of accounting for plasticity depends on factors such as the stress state and the stress history characterising the modelled materials.

References

Abuel-Naga, H., Bergado, D.T., Bouazza, A., Ramana, G., 2007. Volume change behaviour of saturated clays under drained heating conditions: experimental and constitutive modelling. Can. Geotech. J. 44, 942–956.

Al-Tabbaa, A., Wood, D.M., 1989. An experimentally based "bubble" model for clay. In: Third International Conference on Numerical Models in Geomechanics, pp. 91–99.

Atkinson, J.H., Bransby, P., 1978. The Mechanics of Soils. McGraw-Hill.

Boley, B.A., Weiner, J.H., 1997. Theory of Thermal Stresses. Dover Publications, Mineola, NY.

Bourne-Webb, P., Bodas Freitas, T., Freitas Assunção, R., 2016a. Soil–pile thermal interactions in energy foundations. Geotechnique 66 (2), 167–171.

Bourne-Webb, P., Burlon, S., Javed, S., Kürten, S., Loveridge, F., 2016b. Analysis and design methods for energy geostructures. Renew. Sust. Energ. Rev. 65, 402–419.

Carpinteri, A., 1995. Scienza delle costruzioni 1. Pitagora Editrice Bologna, Bologna.

Cauchy, A.-L., 1823. Résumé des leçons données à l'école royale polytechnique sur le calcul infinitésimal. Imprimerie Royale.

Coulomb, C., 1773. Essai sur une application des règles de maximis et minimis à quelques problèmes de statique, relatifs à l'architecture. De l'Imprimerie Royale, Paris.

Cui, Y.J., Sultan, N., Delage, P., 2000. A thermomechanical model for saturated clays. Can. Geotech. J. 37 (3), 607–620.

Dafalias, Y., Herrmann, L., 1982. Bounding surface formulation of soil plasticity. In: Zienkiewicz, G.P.O. (Ed.), Soil Mechanics: Transient and Cyclic Loads. John Wiley & Sons.

Dafalias, Y., Popov, E., 1975. A model of nonlinearly hardening materials for complex loadingEin Modell für Werkstoffe mit nichtlinearer Verfestigung unter zusammengesetzter Belastung. Acta Mech. 21 (3), 173–192.

Davis, R.O., Selvadurai, A.P., 1996. Elasticity and Geomechanics. Cambridge University Press.

Di Donna, A., 2014. Thermo-mechanical aspects of energy piles. Laboratory of Soil Mechanics. Swiss Federal Institute of Technology in Lausanne (EPFL), Lausanne.

Drucker, D.C., Prager, W., 1952. Soil mechanics and plastic analysis for limit design. Q. Appl. Math. 10 (2), 157–165.

Drucker, D.C., Gibson, R.E., Henkel, D.J., 1957. Soil mechanics and work-hardening theories of plasticity, Trans., 122. *ASCE*, pp. 338–346.

Duhamel, J.M.C., 1835. Les phénomènes thermo-mécaniques. J. de l'école Polytech. Second Memoire 15, 1–57.

Einstein, A., 1916. Die grundlage der allgemeinen relativitätstheorie. Ann. Phys. 354 (7), 769–822.

Farouki, O.T., 1981. Thermal properties of soils. Cold Regions Sci. Technol. 5 (1), 67–75.

Graham, J., Tanaka, N., Crilly, T., Alfaro, M., 2001. Modified Cam-Clay modelling of temperature effects in clays. Can. Geotech. J. 38 (3), 608–621.
Hoek, E., Brown, E.T., 1980. Underground Excavations in Rock. CRC Press.
Hong, P.Y., Pereira, J.M., Tang, A.M., Cui, Y.J., 2013. On some advanced thermo-mechanical models for saturated clays. Int. J. Numer. Anal. Methods Geomech. 37 (17), 2952–2971.
Hooke, R., 1678. De Potentia Restitutiva. Printed for J. Martyn, London.
Hueckel, T., Baldi, G., 1990. Thermoplasticity of saturated clays—experimental constitutive study. J. Geotech. Eng. ASCE 116 (12), 1778–1796.
Hueckel, T., Borsetto, M., 1990. Thermoplasticity of saturated soils and shales—constitutive-equations. J. Geotech. Eng. ASCE 116 (12), 1765–1777.
Huotari, T., Kukkonen, I., 2004. Thermal expansion properties of rocks: literature survey and estimation of thermal expansion coefficient for Olkiluoto mica gneiss. Posiva Oy, Olkiluoto, Working Report 4, p. 62.
Iwan, W.D., 1967. On a class of models for the yielding behavior of continuous and composite systems. J. Appl. Mech. 34 (3), 612–617.
Jaeger, J.C., Cook, N.G., Zimmerman, R., 2009. Fundamentals of Rock Mechanics. John Wiley & Sons.
Karush, W., 1939. Minima of Functions of Several Variables With Inequalities as Side Constraints (M.Sc. dissertation), Department of Mathematics, University of Chicago.
Koiter, W.T., 1953. Stress–strain relations, uniqueness and variational theorems for elastic–plastic materials with a singular yield surface. Q. Appl. Math. 11 (3), 350–354.
Krieg, R., 1975. A practical two surface plasticity theory. J. Appl. Mech. 42 (3), 641–646.
Kuhn, H., Tucker, A., 1951. Nonlinear programming. In: Neyman, J. (Ed.), Second Berkeley Symposium on Mathematical Statistics and Probability. University of California Press, Berkeley, CA.
Lade, P.V., Duncan, J.M., 1975. Elastoplastic stress–strain theory for cohesionless soil. J. Geotech. Geoenviron. Eng. 101, 1037.
Laloui, L., 1993. Modélisation du comportement thermo-hydro-mécanique des milieux poreux anélastique (Ph.D. thesis), Ecole Centrale de Paris.
Laloui, L., Cekerevac, C., 2008. Non-isothermal plasticity model for cyclic behaviour of soils. Int. J. Numer. Anal. Methods Geomech. 32 (5), 437–460.
Laloui, L., François, B., 2009. ACMEG-T: soil thermoplasticity model. J. Eng. Mech. 135 (9), 932–944.
Laloui, L., Moreni, M., Vulliet, L., 2003. Comportement d'un pieu bi-fonction, fondation et échangeur de chaleur. Can. Geotech. J. 40 (2), 388–402.
Lamé, G., Clapeyron, B., 1831. Mémoire sur l'équilibre intérieur des corps solides homogènes. Journal für die reine und angewandte Mathematik 7, 145–169.
Lancellotta, R., 2008. Geotechnical Engineering. CRC Press.
Lévy, M., 1870. Mémoire sur les équations générales des mouvements intérieurs des corps solides ductiles au delà des limites où l'élasticité pourrait les ramener à leur premier état. Comptes Rendus Acad. Sci. 70, 1323–1325.
Li, T., Meissner, H., 2002. Two-surface plasticity model for cyclic undrained behavior of clays. J. Geotech. Geoenviron. Eng. 128 (7), 613–626.
Matsuoka, H., 1982. A new failure criterion for soils in three dimensional stresses. In: IUTAM Conference on Deformation and Failure of Granular Materials, Delft, The Netherlands, 1982, pp. 253–263.
Matsuoka, H., Nakai, T., 1974, Stress-deformation and strength characteristics of soil under three different principal stresses. In: Proceedings of the Japan Society of Civil Engineers, vol. 1974. Japan Society of Civil Engineers, pp. 59–70.
McKinstry, H.A., 1965. Thermal expansion of clay minerals. Am. Mineral. 50 (1–2), 212–222.
Melan, E., 1938. Zur plastizität des räumlichen kontinuums. Ing. Arch. 9 (2), 116–126.
Modaressi, H., Laloui, L., 1997. A thermo-viscoplastic constitutive model for clays. Int. J. Numer. Anal. Methods Geomech. 21 (5), 313–335.
Mrőz, Z., 1967. On the description of anisotropic workhardening. J. Mech. Phys. Solids 15 (3), 163–175.
Mrőz, Z., Norris, V., Zienkiewicz, O., 1978. An anisotropic hardening model for soils and its application to cyclic loading. Int. J. Numer. Anal. Methods Geomech. 2 (3), 203–221.

Mrŏz, Z., Norris, V., Zienkiewicz, O., 1979. Application of an anisotropic hardening model in the analysis of elasto-plastic deformation of soils. Geotechnique 29 (1), 1–34.
Mrŏz, Z., Norris, V., Zienkiewicz, O., 1981. An anisotropic, critical state model for soils subject to cyclic loading. Geotechnique 31 (4), 451–469.
Navier, C., 1821. Sur les ois des mouvement des fluides, en ayant regard à l'adhesion des molecules. Ann. Chim. Paris 19, 244–260.
Parry, R., 1958. Correspondence on "On yielding of soils". Geotechnique 8, 183–186.
Prager, W., 1949. Recent developments in the mathematical theory of plasticity. J. Appl. Phys. 20 (3).
Prager, W., 1958. Non-isothermal plastic deformation. Koninkl. Nederl. Akad. van Wetenschappen 61 (3), 176–182.
Prévost, J.H., 1977. Mathematical modelling of monotonic and cyclic undrained clay behaviour. Int. J. Numer. Anal. Methods Geomech. 1 (2), 195–216.
Prévost, J.H., 1978. Plasticity theory for soil stress-strain behavior. J. Eng. Mech. Div. 104 (5), 1177–1194.
Rankine, W.J.M., 1857. On the stability of loose earth. Philos. Trans. R. Soc. Lond. 147, 9–27.
Robertson, E.C., 1988. Thermal properties of rocks. Report 2331–1258.
Robinet, J.C., Rahbaoui, A., Plas, F., Lebon, P., 1996. A constitutive thermomechanical model for saturated clays. Eng. Geol. 41, 145–169.
Roscoe, K., Burland, J., 1968. On the generalized stress–strain behaviour of wet clay. Eng. Plasticity 535–609.
Roscoe, K.H., Schofield, A., Wroth, C., 1958. On the yielding of soils. Geotechnique 8 (1), 22–53.
Rotta Loria, A.F., 2019. Performance-based design of energy pile foundations. DFI J. 12 (2), 94–107.
Rotta Loria, A.F., Laloui, L., 2017. Thermally induced group effects among energy piles. Geotechnique 67 (5), 374–393.
Rotta Loria, A.F., Laloui, L., 2018. Group action effects caused by various operating energy piles. Geotechnique 68 (9), 834–841.
Saint Venant, B., 1870. Memoire sur l'etablissement des equations differentielles des mouvements interieurs operes dans les corps ductiles au dela des limites ou le elasticite pourtrait les ramener a leur premier etat. Comptes Rendus Acad. Sci. Paris 70, 473–480.
Schofield, A.N., Wroth, C.P., 1968. Critical State Soil Mechanics. McGraw-Hill.
Timoshenko, S., 1953. History of Strength of Materials: With a Brief Account of the History of Theory of Elasticity and Theory of Structures. Courier Corporation.
Timoshenko, S., Goodier, J.N., 1951. Theory of Elasticity. McGraw-Hill.
Timoshenko, S., Goodier, J., 1970. Theory of Elasticity. McGraw-Hill, New York.
Tresca, H., 1864. Sur l'ecoulement des corps solides soumis à de fortes pressions. Comptes-Rendus Acad. Sci. 59, 754–758.
von Mises, R., 1928. Mechanik der plastischen Formänderung von Kristallen. Z. Angew. Math. Mech. 8 (3), 161–185.
Whittle, A., 1993. Evaluation of a constitutive model for overconsolidated clays. Geotechnique 43 (2), 289–313.
Wood, D.M., 1990. Soil Behaviour and Critical State Soil Mechanics. Cambridge University Press.
Yu, H.-S., 2006. Plasticity and Geotechnics. Springer, Berlin.
Zienkiewicz, O.C., Taylor, R.L., 2005. The Finite Element Method for Solid and Structural Mechanics. Butterworth-Heinemann.

Questions and problems

Statements

a. Which is the fundamental kinematic variable that characterises most problems involved in mechanics?

b. Write the infinitesimal strain tensor. Define the relationship between the infinitesimal shear strain and the engineering shear strain.

c. Consider a square body subjected to a uniform temperature change in a two-dimensional rectangular Cartesian coordinate system (x, y). Write the normal strains in terms of displacement that are generated by the application of the temperature variation to the material.

d. Which are the two fundamental terms governing the thermally induced strain of materials subjected to thermal loads?

e. The unit measure of the linear thermal expansion coefficient is:

- **i.** °C
- **ii.** m/°C
- **iii.** °C/m
- **iv.** 1/°C

f. Write the infinitesimal strain tensor for an element that is free to deform and solely subjected to a thermal load. Specify if the produced strain is deviatoric or spherical.

g. Which is the physical meaning of the compatibility equations?

h. Define the features of the stress tensor and write it in matrix form.

i. The linear mapping $t_i^n = \sigma_{ji} n_i$ specifies that when the components σ_{ij} acting on any three mutually perpendicular planes through a point O are known, the stress vector on any plane through O can be determined. Prove that this is the case with reference to the equilibrium of a small portion of a continuum material in the shape of a tetrahedron. This demonstration will constitute the so-called Cauchy's theorem.

j. Write in compact form the stress tensor in terms of its deviatoric and spherical components.

k. Which are the portions that constitute the total strain in a thermoelastic problem?

l. Which can be the origin of stress in a thermoelastic problem?

m. Consider a body subjected to a mechanical force field, A (e.g. directed downward along the positive z coordinate of a Cartesian system), and to a temperature variation, B. Assume that the mechanical force field induces a displacement, strain and stress field termed $u_{i,A}, \varepsilon_{ij,A}$ and $\sigma_{ij,A}$ respectively. Suppose that the temperature variation induces a displacement, strain and stress field termed $u_{i,B}, \varepsilon_{ij,B}$ and $\sigma_{ij,B}$ respectively. Which is the resulting displacement, strain and stress field governing the considered body? To which fundamental principle of mechanics must be addressed this fact?

n. Consider a body subjected to a given force field. Assume that at a certain time an equal but opposite force field is applied to the same body. Which is the resulting displacement, strain and stress state characterising the considered body?

o. Can a material free to deform due to the application of a temperature variation be subjected to stress?

p. Write the stress–strain relations for a thermoelastic material in compact and extended forms.

q. In a three-dimensional case, to which parameter is proportional the thermally induced stress? Justify this answer.

r. Calculate the magnitude of the thermally induced stress for a reinforced concrete cubic sample subjected to a temperature variation of $\Delta T = 10°\text{C}$, characterised by a bulk modulus of $K = 20$ GPa and a linear thermal expansion coefficient of $\alpha = 10\ \mu\varepsilon/°\text{C}$, which is completely restrained to deform. Repeat the calculation for a soil cubic sample characterised by a bulk modulus of $K = 30$ MPa.

s. The stress tensor at a point in a thermoelastic material reads

$$\sigma_{ij} = \begin{bmatrix} 10 & 0 & 0 \\ 0 & 5 & 0 \\ 0 & 0 & 2 \end{bmatrix} [\text{kPa}]$$

i. Find the principal stresses and the orientation of the principal planes.

ii. Find the three principal invariants.

t. The stress tensor at a point in a thermoelastic material reads

$$\sigma_{ij} = \begin{bmatrix} 1 & 1 & 0 \\ 1 & -1 & 0 \\ 0 & 0 & 1 \end{bmatrix} [\text{kPa}]$$

Consider the surface passing through this point whose normal vector is parallel to $[1, 2, 3]$.

i. Find the components of the stress vector that acts on this surface.

ii. Find the magnitudes of normal and shear stress that act on this surface.

iii. Find the principal stresses of the stress tensor on this surface.

u. Prove that the temperature distribution in a three-dimensional body is a linear function of the rectangular Cartesian coordinates. That is prove that if $T(x, y, z, t) = a(t) + b(t)x + c(t)y + d(t)z$ [°C], then all the stress components are identically zero throughout the body, provided that all external restraints, body forces and displacement discontinuities are absent. Under the same conditions, prove that the considered temperature distribution is the unique one for which all stress components are identically zero.

v. Consider a three-dimensional body subjected to a uniform temperature variation $\Delta T(t)$ [°C], while zero displacements are maintained at all point of the bounding surface.
  i. Write the solution of the corresponding thermoelastic problem in terms of displacements u, v, w [m], stresses σ_{ij} [Pa] and strains ε_{ij} [−], in extended form.
  ii. Write the surface stress components, $\overline{X}, \overline{Y}, \overline{Z}$ [Pa] that are needed to maintain the considered state of stress.

w. Calculate the deformation of a steel bar characterised by a linear thermal expansion coefficient of $\alpha = 12\ \mu\varepsilon/^{\circ}\text{C}$ and subjected to a temperature variation of $\Delta T = 20^{\circ}\text{C}$ assuming that free deformation is ensured and referring to one-dimensional conditions. Assuming that the bar is 20 m in length, calculate the associated thermally induced displacement. Which would be the magnitude of this displacement in a completely restrained case?

x. Calculate the stress that is generated in a completely restrained steel bar characterised by a linear thermal expansion coefficient of $\alpha = 12\ \mu\varepsilon/^{\circ}\text{C}$ and Young's modulus of $E = 210$ GPa, subjected to a temperature variation of $\Delta T = 20^{\circ}\text{C}$. Refer to one-dimensional conditions.

y. How is the degree of freedom, *DOF*, of an energy pile mathematically defined? Specify the meaning of the terms involved in its definition.

z. Which is the magnitude of the displacement of a bar subjected to a temperature variation in a completely restrained case?

aa. Define the property of plasticity.

bb. In reality, a plastic behaviour directly follows an elastic behaviour, that is the transition is abrupt:
  a. True
  b. False

cc. When plasticity is addressed in the context of nonisothermal conditions, two main approaches can be considered to model the behaviour of materials. Describe these approaches.

dd. Define the physical meaning of a yield criterion. Express it mathematically.

ee. Write the generalised formulation for a flow rule in situations in which the unit normal to the plastic potential approaches a finite number of linearly independent limiting values as the stress point approaches the singular point in question.

ff. Materials behaving according to the theory of hardening plasticity are characterised by a size, location or shape of the yield surface that may change under the development of plastic deformations:
  a. True
  b. False

gg. The yield function of hardening materials only depends the stress state:
  a. True
  b. False

hh. Write the general mathematical formulation of the yield function of materials characterised by hardening and an elastic limit that is considered to be sensitive to temperature variations.

ii. Write the condition of consistency for materials characterised by hardening and an elastic limit that is considered to be sensitive to temperature variations.

jj. Describe the concept of critical state.

kk. The critical state theory can be employed to describe the mechanical behaviour of both coarse- and fine-grained materials.

ll. Write the mathematical expressions of the CSL in relevant planes.

mm. Describe the main features of multisurface and bounding surface plasticity.

Solutions

a. The variable that characterises most problems involved in mechanics is the displacement vector.

b. The infinitesimal strain tensor is a symmetric tensor characterised by nine components that in three-dimensional rectangular Cartesian coordinates reads:

$$\varepsilon_{ij} = \begin{bmatrix} \varepsilon_{xx} & \varepsilon_{xy} & \varepsilon_{xz} \\ \varepsilon_{yx} & \varepsilon_{yy} & \varepsilon_{yz} \\ \varepsilon_{zx} & \varepsilon_{zy} & \varepsilon_{zz} \end{bmatrix}$$

where the diagonal components ε_{kk} [-] are called normal strains and represent stretching of an element and the off-diagonal components ε_{kl} [-] are called infinitesimal shear strains and measure angular distortion. The infinitesimal shear strains are one half of the engineering shear strains, $\varepsilon_{kl} = \frac{1}{2}\gamma_{kl}$.

c. The normal strains are the diagonal components ε_{kk} of the infinitesimal strain tensor. They represent the stretching of an element. In a two-dimensional rectangular Cartesian coordinate system (x,y), the normal strains read:

$$\varepsilon_{xx} = -\frac{\partial u}{\partial x}$$

$$\varepsilon_{yy} = -\frac{\partial v}{\partial y}$$

where u and v [m] are the horizontal and vertical displacements, respectively.

d. The thermally induced strain of materials subjected to thermal loads is governed by the material linear thermal expansion coefficient α $[\mu\varepsilon/^{\circ}\mathrm{C}]$ and the applied temperature variation ΔT [°C].

e. The unit measure of the linear thermal expansion coefficient is:

i. °C

ii. m/°C

iii. °C/m

iv. 1/°C

f. For an infinitesimal element that is free to deform and solely subjected to a thermal load, the induced strain is spherical (volumetric) and can be expressed in tensor form as

$$\varepsilon_{ij} = \varepsilon_{ij,f}^{th} = \begin{bmatrix} -\alpha\Delta T & 0 & 0 \\ 0 & -\alpha\Delta T & 0 \\ 0 & 0 & -\alpha\Delta T \end{bmatrix}$$

where α $[\mu\varepsilon/^{\circ}\mathrm{C}]$ is the material linear thermal expansion coefficient and ΔT [°C] is the applied temperature variation.

g. The compatibility equations imply that the deformation of a continuum material occurs without creating any gaps or overlaps.

h. The stress tensor describes the stress state of any infinitesimal three-dimensional element of a considered material subjected to loading. It is a symmetric tensor characterised by nine stress components that in rectangular Cartesian coordinates reads:

$$\sigma_{ij} = \begin{bmatrix} \sigma_{xx} & \sigma_{xy} & \sigma_{xz} \\ \sigma_{yx} & \sigma_{yy} & \sigma_{yz} \\ \sigma_{zx} & \sigma_{zy} & \sigma_{zz} \end{bmatrix} = \begin{bmatrix} \sigma_x & \tau_{xy} & \tau_{xz} \\ \tau_{yx} & \sigma_y & \tau_{yz} \\ \tau_{zx} & \tau_{zy} & \sigma_z \end{bmatrix}$$

The diagonal components σ_{kk} [Pa] of the stress tensor expressed in relation act normal to the coordinate planes and are called normal stresses. The off-diagonal components σ_{kl} [Pa] act tangential to the coordinate planes and are called shear stresses.

The stress tensor is symmetric and this property can be proven considering the principle of balance of angular momentum. As a result, the complementary components of the shear stress are equal:

$$\sigma_{xy} = \sigma_{yx}$$

$$\sigma_{yz} = \sigma_{zy}$$

$$\sigma_{zx} = \sigma_{xz}$$

i. **To prove this statement, the equilibrium of a small portion of a continuum body in the shape of a tetrahedron, such as that reported in the following figure, is considered. If n_i is the unit outward vector normal to the surface ABC (whose components n_x, n_y, n_z are its direction cosines with respect to the coordinate axes), the components t_x^n, t_y^n, t_z^n acting on this surface can be obtained by considering the tetrahedron equilibrium.**

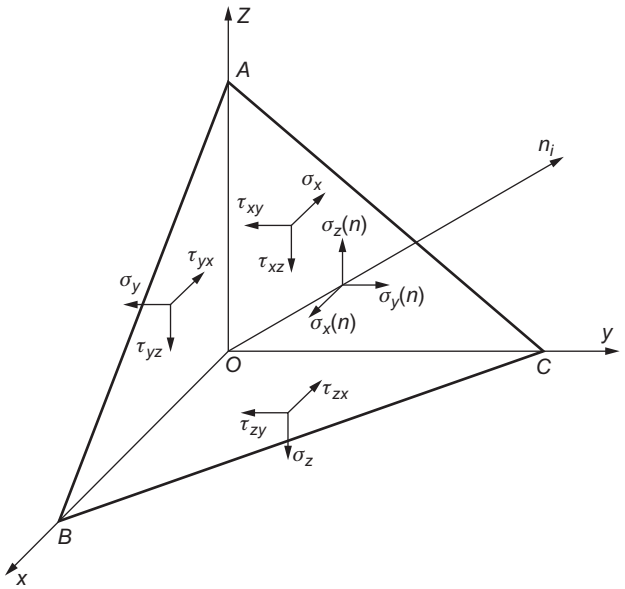

The force equilibrium in the x direction reads $\bar{t}_x^n \cdot (area\ ABC) = \overline{\sigma}_x \cdot (area\ AOC) + \overline{\tau}_{yx} \cdot (area\ AOB) + \overline{\tau}_{zx} \cdot (area\ BOC) - \rho b_x\ dV$ and similar equations are written in the y and z directions. In the previous equation, the vector b [N/kg] represents the body force per unit mass, ρ [kg/m^3] is the density, V [m^3] is the volume and the stresses are the average stresses acting on the faces of the tetrahedron. The volume of the tetrahedron can be expressed in the form $dV = 1/3(h \cdot dS)$, if dS [m^2] is the area of the surface ABC and h [m] is its distance from the point O.

If the limit for $h \to 0$ is considered, the term corresponding to body force vanishes and the average stresses reduce to the value reached at the point O. This value is expressed by the following limit

$$\lim_{dA \to 0} \left(\frac{d\mathfrak{I}}{dA} \right) = t_i$$

where the vector $d\mathfrak{I}$ applied at the point O is the reduction of the actions on the small element of surface dA, oriented by the unit outward normal vector n_i. The vector t_i is called traction or stress vector.

Therefore since:

$$n_x = \frac{area\ AOC}{area\ ABC}$$

$$n_y = \frac{area\ AOB}{area\ ABC}$$

$$n_z = \frac{area\ BOC}{area\ ABC}$$

the equilibrium equations can be written in the following matrix form:

$$\begin{Bmatrix} \bar{t}_x^n \\ \bar{t}_y^n \\ \bar{t}_z^n \end{Bmatrix} = \begin{bmatrix} \sigma_x & \tau_{xy} & \tau_{xz} \\ \tau_{yx} & \sigma_y & \tau_{yz} \\ \tau_{zx} & \tau_{zy} & \sigma_z \end{bmatrix} \begin{Bmatrix} n_x \\ n_y \\ n_z \end{Bmatrix}$$

and in tensor notation

$$\bar{t}_i^n = \sigma_{ij} n_j$$

j. The stress tensor in terms of its deviatoric and spherical components reads:

$$\sigma_{ij} = p\delta_{ij} + s_{ij}$$

where σ_{ij} [Pa] is the total stress tensor, p is the mean stress, δ_{ij} [-] is the Kronecker delta and s_{ij} [Pa] is the deviatoric stress tensor.
In matrix form, the stress tensor reads:

$$\begin{bmatrix} \sigma_{xx} & \sigma_{xy} & \sigma_{xz} \\ \sigma_{yx} & \sigma_{yy} & \sigma_{yz} \\ \sigma_{zx} & \sigma_{zy} & \sigma_{zz} \end{bmatrix} = \begin{bmatrix} p & 0 & 0 \\ 0 & p & 0 \\ 0 & 0 & p \end{bmatrix} + \begin{bmatrix} s_{xx} & \sigma_{xy} & \sigma_{xz} \\ \sigma_{yx} & s_{yy} & \sigma_{yz} \\ \sigma_{zx} & \sigma_{zy} & s_{zz} \end{bmatrix}$$

where σ_{kk} [Pa] are the normal stresses, σ_{kl} [Pa] are the shear stresses and s_{kk} [Pa] are the deviatoric stresses.

k. The first contribution comprises the strains induced by the application of a force (or displacement) field that is required to maintain the continuity of the material by means of the generalised Hooke's law. The second contribution comprises the strains induced by the application of a temperature change to the material that are required as well to maintain the continuity of the material.

l. Stresses arise in a material because of the application of temperature variations as a result of the presence of a restraint (i.e. development of the thermally induced strain prevented), of a nonuniform temperature distribution (i.e. differential thermal deformation) or of a combination of these causes.

m. Considering the elastic superposition principle, the combined effect of several loads acting simultaneously is equal to the algebraic sum of the effect of each load acting individually that can be computed separately. For the considered body subjected to the fields A and B:

$$u_{i,AB} = u_{i,A} + u_{i,B}$$

$$\varepsilon_{ij,AB} = \varepsilon_{ij,A} + \varepsilon_{ij,B}$$

$$\sigma_{ij,AB} = \sigma_{ij,A} + \sigma_{ij,B}$$

n. Assuming a reversible material response upon loading and unloading, the action of an equal but opposite force field than an initially applied field cancels the overall effect of these fields.

o. A material free to deform can be subjected to stress due to the application of a nonuniform temperature distribution causing differential thermal deformation.

p. In the thermoelasticity framework, the total strain at each point of a material subjected to a mechanical load and to a thermal load can be mathematically expressed in compact form as:

$$\varepsilon_{ij} = C_{ijkl}\sigma_{kl} - \beta_{kl}(T - T_0)$$

where σ_{kl} [Pa] is the stress tensor, C_{ijkl} [1/Pa] is the elastic compliance matrix, β_{kl} [1/°C] is the linear thermal expansion coefficient vector and

$(T - T_0)$ [°C] is the applied temperature variation. In matrix form, the above reads:

$$\begin{bmatrix} \varepsilon_{xx} \\ \varepsilon_{yy} \\ \varepsilon_{zz} \\ \varepsilon_{xy} \\ \varepsilon_{yz} \\ \varepsilon_{zx} \end{bmatrix} = \begin{bmatrix} 1/E & -\upsilon/E & -\upsilon/E & 0 & 0 & 0 \\ -\upsilon/E & 1/E & -\upsilon/E & 0 & 0 & 0 \\ -\upsilon/E & -\upsilon/E & 1/E & 0 & 0 & 0 \\ 0 & 0 & 0 & 1/(2G) & 0 & 0 \\ 0 & 0 & 0 & 0 & 1/(2G) & 0 \\ 0 & 0 & 0 & 0 & 0 & 1/(2G) \end{bmatrix} \begin{bmatrix} \sigma_{xx} \\ \sigma_{yy} \\ \sigma_{zz} \\ \sigma_{xy} \\ \sigma_{yz} \\ \sigma_{zx} \end{bmatrix} - \begin{bmatrix} \alpha \\ \alpha \\ \alpha \\ 0 \\ 0 \\ 0 \end{bmatrix} (T - T_0)$$

where for the considered material E [Pa] is the Young's modulus, υ [−] is the Poisson's ratio and G [Pa] is the shear modulus. In extended form, the above reads:

$$\varepsilon_{xx} = \frac{1}{E}\left[\sigma_{xx} - \upsilon\left(\sigma_{yy} + \sigma_{zz}\right)\right] - \alpha(T - T_0)$$

$$\varepsilon_{yy} = \frac{1}{E}\left[\sigma_{yy} - \upsilon(\sigma_{zz} + \sigma_{xx})\right] - \alpha(T - T_0)$$

$$\varepsilon_{zz} = \frac{1}{E}\left[\sigma_{zz} - \upsilon\left(\sigma_{xx} + \sigma_{yy}\right)\right] - \alpha(T - T_0)$$

$$\varepsilon_{xy} = \frac{1}{2G}\sigma_{xy}$$

$$\varepsilon_{yz} = \frac{1}{2G}\sigma_{yz}$$

$$\varepsilon_{zx} = \frac{1}{2G}\sigma_{zx}$$

q. If the stress tensor is expressed in terms of the strain tensor, it results

$$\sigma_{ij} = D_{ijkl}[\varepsilon_{kl} + \beta_{kl}(T - T_0)]$$

Thus the thermally induced stress is proportional to the elastic stiffness tensor of the material D_{ijkl}.

r. **For the cubic concrete sample**:

The thermally induced volumetric stress is proportional to the volumetric thermal strain:

$$\sigma^{th} = 3K\varepsilon^{th}$$

As the sample is fully restrained, the prevented strain is equal to the volumetric thermal strain $\varepsilon^{th} = \alpha\Delta T$.

Thus: $\sigma^{th} = 3\ K\alpha\Delta T = 3{\cdot}20{\cdot}10{\cdot}10^{-6}{\cdot}10 = 6$ **MPa**

For the cubic soil sample:

The same calculation is performed with a 30 MPa bulk modulus and an equal coefficient of thermal expansion.

Thus: $\sigma^{th} = 9$ **kPa**

s. **i. The principal stresses are the normal stresses acting on the principal planes, along which zero shear stresses are observed. For a stress tensor in the form of a diagonal matrix, the principal stresses are thus the diagonal components** σ_{kk} **of the tensor, that is**:

$\sigma_1 = 10$ kPa acting on the *yz* plane

$\sigma_2 = 5$ kPa acting on the *xz* plane

$\sigma_3 = 2$ kPa acting on the *xz* plane

ii. The three stress invariants are defined as

$$\begin{cases} I_1 = \mathrm{tr}(\sigma_{ij}) = \sigma_{ii} = \sigma_{xx} + \sigma_{yy} + \sigma_{zz} \\ I_2 = \frac{1}{2}\left(\sigma_{ii}\sigma_{jj} - \sigma_{ij}\sigma_{ij}\right) = \sigma_{xx}\sigma_{yy} + \sigma_{yy}\sigma_{zz} + \sigma_{zz}\sigma_{xx} - \sigma_{xy}^2 - \sigma_{yz}^2 - \sigma_{zx}^2 \\ I_3 = \det\sigma_{ij} = \sigma_{xx}\sigma_{yy}\sigma_{zz} + 2\sigma_{xy}\sigma_{yz}\sigma_{zx} - \sigma_{xx}\sigma_{yz}^2 - \sigma_{yy}\sigma_{zx}^2 - \sigma_{zz}\sigma_{xy}^2 \end{cases}$$

with

$$\sigma_{ij} = \begin{bmatrix} \sigma_{xx} & \sigma_{xy} & \sigma_{xz} \\ \sigma_{yx} & \sigma_{yy} & \sigma_{yz} \\ \sigma_{zx} & \sigma_{zy} & \sigma_{zz} \end{bmatrix} = \begin{bmatrix} 10 & 0 & 0 \\ 0 & 5 & 0 \\ 0 & 0 & 2 \end{bmatrix}$$

Thus

$$\begin{cases} I_1 = 10 + 5 + 2 = 17 \\ I_2 = 10{\cdot}5 + 5{\cdot}2 + 2{\cdot}10 = 80 \\ I_3 = 10{\cdot}5{\cdot}2 = 100 \end{cases}$$

The characteristic polynomial is defined as follows:

$$\lambda_*^3 - I_1\lambda_*^2 + I_2\lambda_* - I_3 = 0$$

The solution of the above equation is found for three real eigenvalues $\lambda_{*1}=\sigma_1$, $\lambda_{*2}=\sigma_2$ and $\lambda_{*3}=\sigma_3$.
That is:

$$\lambda_{*1}^3 - I_1\lambda_{*1}^2 + I_2\lambda_{*1} - I_3 = 10^3 - 17\cdot 10^2 + 80\cdot 10 - 100 = 0$$

$$\lambda_{*2}^3 - I_1\lambda_{*2}^2 + I_2\lambda_{*2} - I_3 = 5^3 - 17\cdot 5^2 + 80\cdot 5 - 100 = 0$$

$$\lambda_{*3}^3 - I_1\lambda_{*3}^2 + I_2\lambda_{*3} - I_3 = 2^3 - 17\cdot 2^2 + 80\cdot 2 - 100 = 0$$

t. i. According to Cauchy's stress theorem, the component of the stress vector that acts on this surface are:

$$t_i^n = \begin{bmatrix} 1 & 2 & 3 \end{bmatrix} \cdot \begin{bmatrix} 1 & 1 & 0 \\ 1 & -1 & 0 \\ 0 & 0 & 1 \end{bmatrix} = \begin{bmatrix} 3 & -1 & 3 \end{bmatrix}$$

ii. The magnitudes of the normal stresses are the diagonal components σ_{kk} of the stress tensor that is

$$\sigma_{11} = 1 \text{ kPa}$$

$$\sigma_{22} = -2 \text{ kPa}$$

$$\sigma_{33} = 1 \text{ kPa}$$

The magnitudes of the shear stresses are the off-diagonal components σ_{kl} of the stress tensor that is

$$\sigma_{12} = 1 \text{ kPa}$$

$$\sigma_{21} = 1 \text{ kPa}$$

$$\sigma_{13} = \sigma_{23} = \sigma_{31} = \sigma_{32} = 0 \text{ kPa}$$

iii. The principal stresses and the principal directions can be written as the eigenvalues and the eigenvectors of the stress tensor. By diagonalising the stress tensor in:

$$\sigma_{ij} = \begin{bmatrix} \sqrt{2} & 0 & 0 \\ 0 & 1 & 0 \\ 0 & 0 & -\sqrt{2} \end{bmatrix} [\text{kPa}]$$

The principal stresses are thus:

$$\sigma_1 = \sqrt{2}\ \text{kPa}$$

$$\sigma_2 = 1\ \text{kPa}$$

$$\sigma_3 = -\sqrt{2}\ \text{kPa}$$

u. If the compatibility equations are expressed in terms of stress components, in absence of external restraints, body forces and displacement discontinuities, it results

$$(1+\nu)\nabla^2\sigma_{xx} + \alpha E\left(\frac{1+\nu}{1-\nu}\nabla^2 T + \frac{\partial^2 T}{\partial x^2}\right) = 0$$

$$(1+\nu)\nabla^2\sigma_{yy} + \alpha E\left(\frac{1+\nu}{1-\nu}\nabla^2 T + \frac{\partial^2 T}{\partial y^2}\right) = 0$$

$$(1+\nu)\nabla^2\sigma_{zz} + \alpha E\left(\frac{1+\nu}{1-\nu}\nabla^2 T + \frac{\partial^2 T}{\partial z^2}\right) = 0$$

$$(1+\nu)\nabla^2\sigma_{xz} + \alpha E\frac{\partial^2 T}{\partial x \partial z} = 0$$

$$(1+\nu)\nabla^2\sigma_{yx} + \alpha E\frac{\partial^2 T}{\partial x \partial y} = 0$$

$$(1+\nu)\nabla^2\sigma_{yz} + \alpha E\frac{\partial^2 T}{\partial y \partial z} = 0$$

where ν [−] is the Poisson's ratio, α [με/°C] is the linear thermal expansion coefficient, E [Pa] is the Young's modulus, T [°C] is the temperature, x,y and z [m] are the Cartesian coordinates, σ_{kk} [Pa] are the normal stresses and σ_{kl} [Pa] are the shear stresses. For the considered temperature distribution $T(x,y,z,t) = a(t) + b(t)x + c(t)y + d(t)z$, all equations are homogeneous. Therefore the solution is

$$\sigma_{xx} = \sigma_{yy} = \sigma_{zz} = \sigma_{xy} = \sigma_{yz} = \sigma_{zx} = 0$$

If the solution of the previous problem is assumed to apply, the substitution in the compatibility equations then shows that the temperature distribution must satisfy the relations:

$$\frac{\partial^2 T}{\partial x^2} = \frac{\partial^2 T}{\partial y^2} = \frac{\partial^2 T}{\partial z^2} = \frac{\partial^2 T}{\partial x \partial y} = \frac{\partial^2 T}{\partial y \partial z} = \frac{\partial^2 T}{\partial z \partial x} = 0$$

and the temperature distribution must then be linear.

v. i. The solution of the thermoelastic problem is:

$$u = v = w = 0$$

$$\varepsilon_{xx} = \varepsilon_{yy} = \varepsilon_{zz} = \varepsilon_{xy} = \varepsilon_{yz} = \varepsilon_{zx} = \sigma_{xy} = \sigma_{yz} = \sigma_{zx} = 0$$

$$\sigma_{xx} = \sigma_{yy} = \sigma_{zz} = -3K\alpha\Delta T = -\frac{E\alpha}{1-2\upsilon}\Delta T$$

where x,y and z are the Cartesian coordinates, u,v and w [m] are the displacements in the associated directions, ε_{kk} [−] are the normal strains, ε_{kl} [−] are the shear strains, σ_{kk} [Pa] are the normal stresses, σ_{kl} [Pa] are the shear stresses, K [Pa] is the bulk modulus, α [με/°C] is the linear thermal expansion coefficient, T [°C] is the temperature, E [Pa] is the Young's modulus and ν [−] is the Poisson's ratio.

ii. The surface stress components $\overline{X}$,$\overline{Y}$ and $\overline{Z}$ that are needed to maintain the considered state of stress are:

$$\frac{\overline{X}}{n_x} = \frac{\overline{Y}}{n_y} = \frac{\overline{Z}}{n_z} = -\frac{E\alpha}{1-2\upsilon}\Delta T$$

where n_x, n_y and n_z are the coordinate vectors in the directions x, y and z.

w. The thermally induced deformation is the following:

$$\varepsilon^{th} = -\alpha \Delta T = 12 \cdot 20 = -240\ \mu\varepsilon$$

The thermally induced displacement for a bar characterised by a length $L = 20$ m would be:

$$\Delta L = -\varepsilon^{th} L = 240 \cdot 20 = 4.8\ \text{mm}$$

In a completely restrained case, this displacement would be equal to zero.

x. $\sigma_b^{th} = E\varepsilon_b^{th} = E\alpha\Delta T = 50.4$ **MPa**

y. The degree of freedom of an energy pile is defined as

$$DOF = \frac{\varepsilon_o^{th}}{\varepsilon_f^{th}}$$

where ε_o^{th} is the observed strain and ε_f^{th} is the strain under free expansion conditions.

z. The displacement of a bar subjected to a temperature variation in a completely restrained case is equal to zero.

aa. The property of plasticity, which involves irreversibility, is common to many materials whose deformation is caused by loads that exceed a certain limit.

bb. In reality, a plastic behaviour directly follows an elastic behaviour, that is the transition is abrupt:

a. True

b. False

cc. When plasticity is addressed in the context of nonisothermal conditions, two main approaches can be considered to model the behaviour of materials. The first approach resorts to the theory of thermoelasticity to account for the influence of temperature variations on the reversible mechanical behaviour of the material, and to the theory of isothermal plasticity to model the irreversible mechanical behaviour of the material. The second approach resorts to the theory of thermoelasticity to model the influence of temperature variations on the reversible mechanical behaviour of the material and to the theory of thermoplasticity to model the irreversible mechanical behaviour of the material while considering a dependence of the yield limit on temperature. In the former framework, the modelled material (or general system) is characterised by a thermoelastic, plastic behaviour. In the latter framework, the

modelled material (or general system) is characterised by a thermo-elastic, thermoplastic behaviour.

dd. The yield criterion defines all of the possible stress states that are associated with a reversible mechanical behaviour of the material as well as those that are associated with an irreversible mechanical behaviour of the material (depending on the loading situation). The limit of the elastic domain characterising the mechanical behaviour of a material can be expressed mathematically through the following general yield surface (or yield function)

$$f = 0$$

ee. If the unit normal to the plastic potential approaches a finite number of linearly independent limiting values as the stress point approaches the singular point in question, the following generalised flow rule can be considered:

$$d\varepsilon_{ij}^{p} = \sum_{k=1}^{N} d\lambda_{k}^{p} \frac{\partial g_{k}}{\partial \sigma_{ij}}$$

ff. Materials behaving according to the theory of hardening plasticity are characterised by a size, location or shape of the yield surface that may change under the development of plastic deformations:

a. True

b. False

gg. The yield function of hardening materials only depends the stress state:

a. True

b. False

hh. Materials characterised by hardening and an elastic limit that is considered to be sensitive to temperature are characterised by the following yield function:

$$f = f\left(\sigma_{ij}, \tilde{h}_{i}, T\right) = 0$$

ii. The condition of consistency for materials characterised by hardening and an elastic limit that is considered to be sensitive to temperature reads:

$$df = \frac{\partial f}{\partial \sigma_{ij}} d\sigma_{ij} + \frac{\partial f}{\partial \tilde{h}_{i}} d\tilde{h}_{i} + \frac{\partial f}{\partial T} dT = 0$$

jj. The concept of critical state plasticity is associated with the mechanical behaviour of materials for which a continuous distortion caused by shearing eventually leads to a well-defined critical state. Under critical state conditions, the material flows as a frictional fluid, so that yielding occurs at constant volume and constant stresses.

kk. The critical state theory can be employed to describe the mechanical behaviour of both coarse- and fine-grained materials.

a. True

b. False

ll. The critical state line (CSL) can be identified in the relevant planes $q - p$ and $v_e - \ln p$ as

$$q = M_c p$$

$$\Gamma = v_e + \tilde{\lambda} \ln p$$

mm. The concepts of multisurface and bounding plasticity are aimed at capturing with accuracy the mechanical behaviour of materials characterised by a smooth transition from a reversible to an irreversible behaviour, as well as subjected to reversal (i.e. cyclic) loadings.

PART C

Observations

CHAPTER 5

Thermohydromechanical behaviour of soils and soil–structure interfaces

5.1 Introduction

The ground represents the medium through which loads arising from energy geostructures are to be equilibrated by means of a transfer through the interfaces with such structures (i.e. soil–structure interfaces). Because of the multifunctional role of energy geostructures, thermal and mechanical loads are applied to soils and soil–structure interfaces. In this context, the multiphysical nature of the applied loads, together with the couplings that govern the behaviour of materials, makes the thermohydromechanical behaviour of soils and soil–structure interfaces paramount for the analysis and design of energy geostructures. Not only does this behaviour influence the deformation and capacity of energy geostructures depending on the material properties, but it also characterises the heat that can be exchanged via such structures. Understanding the behaviour of soils and soil–structure interfaces is thus critical to address the analysis and design of energy geostructures.

This chapter focuses on the experimental analysis of the thermohydromechanical behaviour of soils and soil–structure interfaces based on the results of laboratory tests. The behaviour of soils and soil–structure interfaces is expanded with a focus on their deformation and strength under nonisothermal conditions, and the influence of aspects that govern such behaviour are highlighted.

To address the aforementioned aspects, *idealisations and assumptions* are presented first: in this context, the objective is to propose a summary of the conceptual descriptions and hypotheses that are employed for describing the behaviour of soils and soil–structure interfaces under nonisothermal conditions. Second, the *characterisation of soils* is treated: the objective of this part is to summarise concepts for the characterisation of the behaviour of fine- and coarse-grained soils. Third, the *deformation and strength of soils under nonisothermal conditions* is discussed: in this context, the purpose is to address the influence of thermal and mechanical loads on the response of the considered materials. Next, the *thermally induced effects on soil parameters* are treated: in this framework, the purpose is to discuss the influence of thermal loads on parameters that describe the thermohydromechanical behaviour of soils. Afterward, the *characterisation of soil–structure interfaces* is discussed: the purpose of this part is to expand on features of interfaces with soils that can be employed to describe the related response to loading.

Analysis and Design of Energy Geostructures
DOI: https://doi.org/10.1016/B978-0-12-816223-1.00005-9

Then, the *strength of soil–concrete interfaces under nonisothermal conditions* is considered: in this context, the purpose is to comment on the response of interfaces between fine- and coarse-grained soils and concrete to thermal and mechanical loads. Finally, *questions and problems* are proposed: the purpose of this part is to fix and test the understanding of the subjects covered in this chapter by addressing a number of exercises.

5.2 Idealisations and assumptions

A key aspect related to the development of laboratory tests on core samples of soil, similar to other materials, is the representativeness of the obtained results with respect to the heterogeneities that characterise the tested material and the problem itself across scales. Based on the considerations proposed in Part B of this book, the concept of Representative Elementary Volume (REV) is employed in the following. The REV concept allows describing the behaviour of heterogeneous materials such as soils, rocks and concrete as if they were homogeneous, with the possibility to account for heterogeneities at greater scales than the scale characterising the REV.

In this context, the addressed materials are assumed multiphase systems characterised by one solid phase and one fluid phase. The previous assumption involves neglecting materials under partially saturated conditions [the thermohydromechanical behaviour of soils under partially saturated conditions has been investigated, for example by Bolzon and Schrefler (2005), François and Laloui (2008) and Gens (2010)] and accounting for soils that are either dry or fully saturated with water. When soils fully saturated with water are investigated, drained conditions are assumed upon thermal loading. These conditions are the result of testing procedures that do not cause excess pore water pressures upon thermal loading, despite the water present in the pores of soil matrices having a thermal expansion coefficient that is approximately 10 times greater than that of the solid particles and involving interactions with the solid phase. The considered conditions are representative of most energy geostructure applications because of the sufficiently slow rates of thermal loads applied to such structures that ensure drainage of the water embedded in the soil pores and negligible pore water pressure build-ups (Rotta Loria and Laloui, 2017).

Yet while the deformation and strength of soils and soil–structure interfaces under nonisothermal conditions is commented hereafter for temperature levels between 2°C and 90°C, temperature values between 2°C and 45°C should be considered representative for energy geostructure applications (Rotta Loria, 2019). In other words, results referring to temperature variations higher than 45°C are not representative of current energy geostructure applications, but they provide additional information on the subject matter treated herein.

The sign convention considered in the following coincides with that employed thus far. That is, contractive strains, downward displacements, compressive stresses and increases in angles in the anticlockwise direction are considered to be positive.

5.3 Characterisation of soils

5.3.1 Mineralogy and textural organisation of soils

Mineralogy is a primary attribute of soils because it influences the size, shape and properties of their solid particles. These properties, together with those of the pore fluid, characterise the overall behaviour of soils by means of interactions between the phases that constitute the material (e.g. solid and fluid). In this context, soil minerals can be classified in *clay* and *nonclay minerals*. An example of a soil structure composed by clay minerals is reported in Fig. 5.1.

Clay minerals belong to the family of phyllosilicates and are mostly characterised by a small platy shape, but may also be characterised by a needle or a tubular shape. These minerals are made of two structural units: the silicon tetrahedron, producing a silica sheet $(Si_4O_{10})^{4-}$ by the sharing of three of the four oxygen ions in each tetrahedron, and the aluminium or magnesium octahedron, forming an octahedral sheet by the sharing of oxygen or hydroxyls (Mitchell and Soga, 2005). The sharing of the aforementioned ions is achieved via strong bonds of primary valence type. Weaker Van der Waals bonds hold together the structural units in various ways depending on the type of clay, forming clay minerals (or lamellae), such as kaolinite, illite and smectite. Clay particles (or stacks) are formed by various lamellae. Clay aggregates are

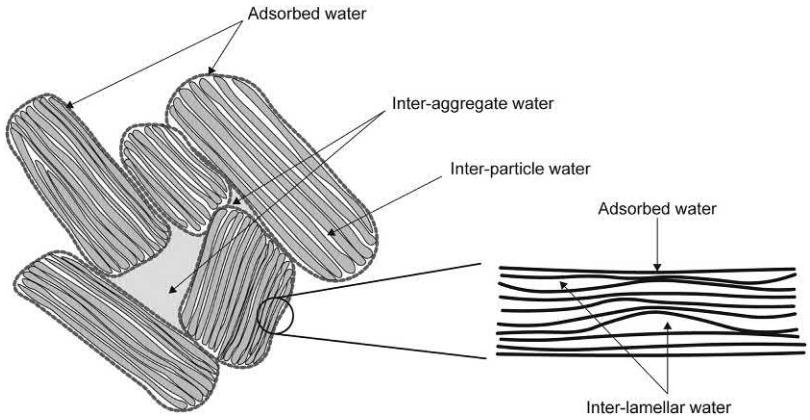

Figure 5.1 Schematic of the two main types of water in saturated soils: (i) free water, mainly in the interaggregate space and (ii) adsorbed water located in the interparticle and interlamellar spaces. *Redrawn after Cekerevac, C., 2003. Thermal effects on the mechanical behaviour of saturated clays: an experimental and numerical study. EPFL Lausanne.*

formed by various particles. Three classes of pore space can thus be determined by the textural organisation of clays: (1) an interlamellar space, with average size of 1.5−2.5 nm; (2) an interparticle porosity among connected clay clusters, with an average size of 20−150 nm; and (3) an interaggregate space between aggregates, defining a pore size of 1.5−16 μm (Touret et al., 1990; Robinet et al., 1996). The structure of clay minerals results in a residual negative charge on the surface of the particle that is balanced by the adsorption of cations from solution (Mitchell and Soga, 2005), resulting in so-called *adsorbed water*. The mechanical characteristics of adsorbed water are quite similar to those of the solid particles. For the previous reason, absorbed water is often considered a part of the solid particles (Hueckel, 2002). Cations in excess of those needed to neutralise the negative charge of the particle and the associated anions are present as salt precipitate, or in water solution when water is present (Di Donna and Laloui, 2013). The adsorbed cations try to diffuse away but are tightly held to the surface. The charged surface and the relative distributed charge in the adjacent phase are termed diffuse double layer (Chapman, 1913). Only at a given distance from the clay particles can water be considered free to move and is thus often termed *free water*. The water located in the interlamellar and interparticle space is typically absorbed, while that located in the interaggregate space is free (cf. Fig. 5.1). The amount of free and adsorbed water depends on the distribution and size of the pores and the chemical properties of the water.

Nonclay minerals are primarily characterised by a bulky shape. Quartz is probably the most abundant nonclay mineral occurring in soils, while feldspar and mica occur in smaller percentages (Mitchell and Soga, 2005). In many cases, nonclay minerals are relatively inert.

Based on the above, interactions between clay minerals are in most cases predominantly chemical in nature. In contrast, interactions between nonclay minerals are predominantly physical in nature. Because of the intrinsically different features of clay and nonclay minerals, the behaviour of soils is markedly influenced by the clay mineral fraction. The widely established soil classification depending on the size of the particles constituting the solid matrix of such materials allows the distinguishing of gravels, sands, silts and clays (ASTM D2487, 2017). The gravel, sand and most of the silt fraction of soils are composed of nonclay minerals. The clay fraction of soils is composed of clay minerals. Therefore in coarse-grained soils (i.e. sands and gravels), interactions between particles are predominantly physical in nature and self-weight forces are dominant; in contrast, in fine-grained soils (i.e. clays and silts), interactions between particles are predominantly chemical in nature and surface forces increasingly govern interactions with regards to self-weight forces for a decreasing particle size (Laloui, 1993; Mitchell and Soga, 2005). In general, for a given soil mineral and electrolyte, the magnitude of surface forces is proportional to

the surface area of the solid particles, while the magnitude of body forces is proportional to the volume of the solid particles. As particle size decreases, surface forces diminish with the square of the particle diameter, whereas volume forces diminish with the cube of the particle diameter.

Chemical interactions between particles inherently involve a higher sensitivity of the material to temperature compared to a material whose interactions between particles are predominantly physical. The previous fact implies a higher sensitivity to temperature of fine-grained soils compared to coarse-grained soils.

5.3.2 Effective stress

Different descriptions and interpretations of the mechanics of soils can be performed by means of the relevant stress to which deformations are associated. In principle, it is very unlikely that a stress expression is applicable to the full range of porous materials (Skempton, 1960, 1961; De Boer and Ehlers, 1990). The reason for this is that the adequate combination of total stresses, pore pressures and other interaction forces depends on the constitutive features and the internal structure of the material, losing in this way its desired universality (Gens et al., 2004). In practice, the effective stress expression proposed by Terzaghi (1943) may be considered valid for most energy geostructure applications. The effective stress represents the relevant stress that governs the macroscopic behaviour of porous materials, based on the principle that the external stress applied on a saturated porous medium with a fluid (e.g. water) is supported by the combination of the pore fluid pressure and the effective stress, that is

$$\sigma'_{ij} = \sigma_{ij} - p_w \delta_{ij} \tag{5.1}$$

where σ_{ij} the total stress tensor, p_w is the pore (water) pressure and δ_{ij} the Kroenecker's delta (equal to 1 if $i = j$ and to 0 otherwise). Provided that the assumptions governing the formulation of Eq. (5.1) hold, the deformation of porous materials is caused by a change in the effective stress.

The effective stress initially defined by Terzaghi (1936) may also be defined as the vector sum of all the interparticle forces in a given direction divided by the total area being considered (Mitchell and Soga, 2005). Based on the previous definition, a dependence of the effective stress on the physicochemical interactions between particles can be remarked. These interactions vary with the application of mechanical and thermal loads to soil structures.

5.3.3 Preconsolidation stress

The preconsolidation stress (or pressure) is the maximum vertical stress that a soil has ever supported and is a key parameter to characterise the mechanical behaviour of soils. Soils retain a memory of the maximum stress that they have supported

(Di Donna and Laloui, 2013). When soils are subjected to a stress that is lower than the preconsolidation stress, they are characterised by a small and reversible deformation. In contrast, when soils are subjected to a stress that becomes the preconsolidation stress, they are characterised by a significant and partially irreversible deformation. The preconsolidation stress corresponds to the maximum experienced density or the lowest void ratio (Di Donna and Laloui, 2013). It also represents the limit between a reversible and a partly irreversible mechanical behaviour of soils.

5.3.4 Overconsolidation ratio

The overconsolidation ratio (OCR) allows characterising the stress history of soils. This parameter can be computed from the preconsolidation stress, σ'_p, and the overburden vertical effective stress for a given soil, σ'_z, as

$$OCR = \frac{\sigma'_p}{\sigma'_z} \tag{5.2}$$

In principle, values of $OCR < 1$ are associated with a underconsolidated state for the soil. A value of $OCR = 1$ is associated with a normally consolidated (NC) state for the soil. Values of $OCR > 1$ are associated with an overconsolidated (OC) state for the soil.

In practice, soils are considered NC if the OCR is within the range of $1-2$, that is if the current stress state is close to the maximum that the soil has ever supported, while they are considered OC if the OCR is greater than 2, that is if the current stress state is lower than the maximum that the soil has ever supported.

Underconsolidation can result from processes including, for example deposition at a faster rate than consolidation, rapid drop in the groundwater table, insufficient time since the placement of a fill or other loading for consolidation to be completed, and disturbance that causes a material structure breakdown and decrease in effective stress (Mitchell and Soga, 2005). Normal consolidation can result from significant loading processes leading to effective stress equilibrium with the overburden effective stress. Overconsolidation can result from unloading phenomena caused, for example by the movement of the groundwater table, mechanical unloading, ageing, desiccation or physicochemical interactions (Lancellotta, 1995).

5.3.5 Relative density

The relative density can be considered as a proxy to characterise the stress history of coarse-grained soils. The considered parameter crucially characterises the mechanical behaviour of coarse-grained materials together with the effective stress state. It is a

measure of the current void ratio, e, in relation to the maximum void ratio, e_{max}, and minimum void ratio, e_{min}, and can be determined as

$$D_R = \frac{e_{max} - e}{e_{max} - e_{min}} \times 100\% \tag{5.3}$$

Values of $D_R = 0\%–20\%$ are associated with very loose coarse-grained soils. Values of $D_R = 20\%–40\%$ are associated with loose coarse-grained soils. Values of $D_R = 40\%–60\%$ are associated with medium-loose coarse-grained soils. Values of $D_R = 60\%–80\%$ are associated with dense coarse-grained soils. Values of $D_R = 80\%–100\%$ are associated with very dense coarse-grained soils.

5.4 Deformation of soils under nonisothermal conditions

5.4.1 Influence of mechanical and thermal loads on soil deformation

While mechanical loads can cause both volumetric and deviatoric deformations, thermal loads only induce volumetric deformations. Compressive mechanical loads cause contractive strains. Tensile mechanical loads cause expansive strains. Heating thermal loads induce an expansion of all of the soil constituents (i.e. solid grains and water in fully saturated conditions) according to their thermal expansion coefficient and the applied temperature variation. Cooling thermal loads induce a contraction of all of the soil constituents. Nevertheless, heating thermal loads can cause both expansive and contractive strains of soil matrices.

5.4.2 Volumetric behaviour of fine-grained soils caused by one thermal cycle

Experimental results about the volumetric behaviour of fine-grained soils subjected to one thermal cycle have been presented, for example by Campanella and Mitchell (1968), Plum and Esrig (1969), Demars and Charles (1982) and Baldi et al. (1988). Complementary results have been proposed by Towhata et al. (1993), Burghignoli et al. (2000), Sultan et al. (2002), Cekerevac and Laloui (2004), Romero et al. (2005) and Abuel-Naga et al. (2007). According to the previous results, heating fine-grained soils in *drained conditions* can produce a contractive or an expansive volume variation of such materials, while cooling produces a contractive volume variation. Experimental evidence supporting the previous considerations is reported in Fig. 5.2 with reference to the results of Baldi et al. (1988), Hueckel and Baldi (1990) and Abuel-Naga et al. (2007). Results are depicted in terms of the relationship between thermally induced volumetric strain, ε_v, and applied

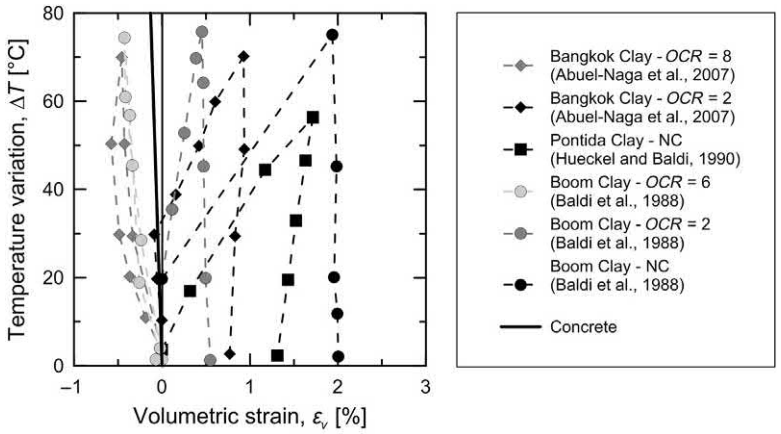

Figure 5.2 Volumetric behaviour of fine-grained soils subjected to temperature variations. *Redrawn after Di Donna, A., Laloui, L., 2013. Soil response under thermomechanical conditions imposed by energy geostructures. In: Laloui, L., Di Donna, A. (Eds.), Energy Geostructures: Innovation in Underground Engineering. Wiley, pp. 3–21.*

temperature variation, ΔT. The theoretical relationship between ε_v and ΔT for concrete is plotted for reference.

Under NC conditions, fine-grained soils contract when heated and a significant part of this deformation is not recovered upon cooling (Di Donna and Laloui, 2013). According to currently available experimental evidence, thermally induced volumetric strains of up to 6% can characterise NC soils upon heating (e.g. for temperature variations of up to $\Delta T = 80°C$). Such an irreversible mechanical behaviour is unusual for any material and is associated with a thermal contraction of the soil matrix (also termed thermal collapse).

Under highly OC conditions, fine-grained soils expand when heated and this deformation is entirely recovered upon cooling (Di Donna and Laloui, 2013). Thermally induced volumetric strains of up to -0.5% can characterise OC soils upon heating (e.g. for temperature variations of up to $\Delta T = 80°C$). Such a reversible mechanical behaviour is typical for most materials, such as metals and concrete.

Between the two aforementioned cases there is an intermediate one associated with slightly OC conditions (Di Donna and Laloui, 2013). Under slightly OC conditions, fine-grained soils show an initial expansion and subsequent contraction when heated, followed by a tendency towards contraction upon cooling. This mechanical behaviour represents a transition between the behaviour of soils under NC and OC conditions.

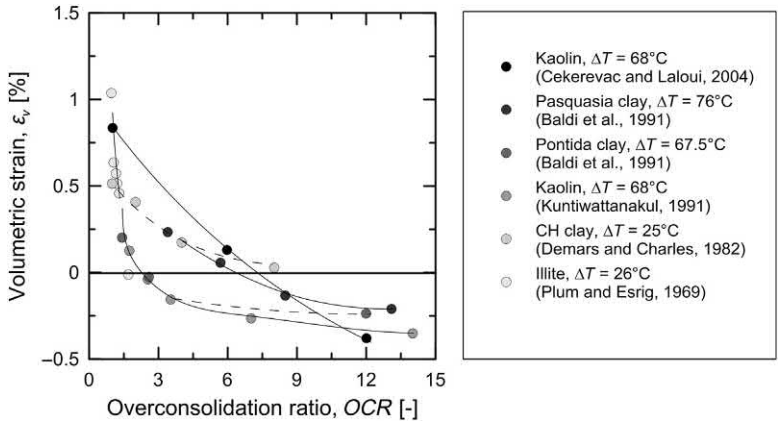

Figure 5.3 Influence of the overconsolidation ratio on the thermally induced volumetric strain of fine-grained soils. *Modified after Cekerevac, C., Laloui, L., 2004. Experimental study of thermal effects on the mechanical behaviour of a clay. Int. J. Numer. Anal. Methods Geomech. 28 (3), 209–228.*

The traditional approach employed for describing from a phenomenological perspective the volumetric behaviour of fine-grained soils subjected to temperature variations is in terms of the stress history, which can be assessed in terms of the *OCR*. This approach is illustrated in Fig. 5.3, in which the influence of the *OCR*, on the thermally induced volumetric strain, ε_v, of different soils tested by Plum and Esrig (1969), Demars and Charles (1982), Kuntiwattanakul (1991), Baldi et al. (1991) and Cekerevac and Laloui (2004) is shown. The thermal contraction of slightly OC to NC soils upon heating increases for a decrease in *OCR*, while the thermal expansion of OC soils upon heating increases for an increase in *OCR* (Cekerevac and Laloui, 2004).

A further interpretation of the volumetric behaviour of fine-grained soils resorting to the stress history can be carried out with reference to the relationship between the 'apparent' preconsolidation stress and the temperature. The word 'apparent' is used to remark that the mechanical load that is actually applied to the material does not change, so that the maximum load historically applied is always the same (Di Donna and Laloui, 2013). Extensive experimental evidence shows that the apparent preconsolidation pressure decreases *at constant void ratio* with increasing temperature (see, e.g. Eriksson, 1989; Tidfors and Sällfors, 1989; Boudali et al., 1994; Moritz, 1995; Laloui and Cekerevac, 2003). According to Boudali et al. (1994), this phenomenon is independent of viscous effects. Results that corroborate the variation of apparent preconsolidation pressure with temperature are summarised in Fig. 5.4, drawing from the investigations of Eriksson (1989), Tidfors and Sällfors (1989), Boudali et al. (1994) and Moritz (1995). Various analytical expressions have been formulated to capture the previous evidence (see, e.g. Hueckel and Baldi, 1990; Boudali et al., 1994; Moritz, 1995;

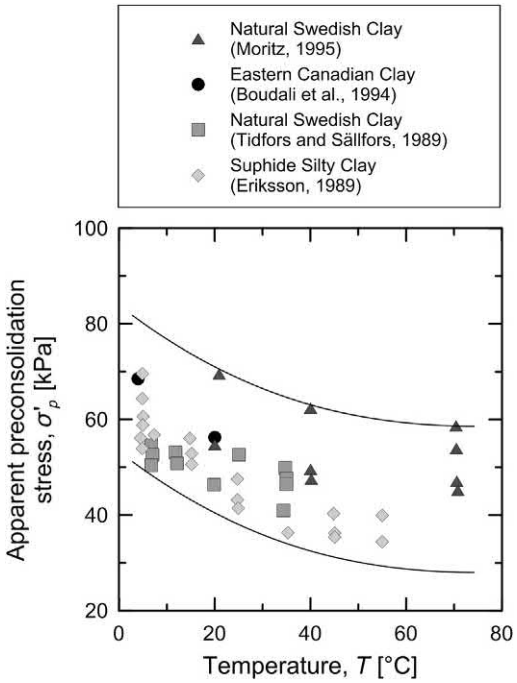

Figure 5.4 Effect of temperature on the apparent preconsolidation stress. *Redrawn after Laloui, L., Cekerevac, C., 2003. Thermoplasticity of clays: an isotropic yield mechanism. Comput. Geotech. 30 (8), 649–660.*

Cui et al., 2000; Laloui and Cekerevac, 2003). In general, these formulations link the isotropic preconsolidation pressure, p'_c, that is the maximum mean effective stress that the soil has ever supported, and the temperature, T (cf. Fig. 5.5).

Soils under NC conditions are characterised by a stress–temperature state that lies on the yield surface (state A in Fig. 5.5). In other words, the current mechanical pressure, p'_A, applied to the material at a temperature T_0 coincides with the preconsolidation pressure, p'_c. Because of the considered stress–temperature state, drained heating up to a temperature $T_1 > T_0$ from the initial state under a constant mean effective stress induces thermoplastic strain (i.e. path A–A'). Upon thermal unloading under a constant mean effective stress, the material becomes OC and strains are only partly recovered. For this reason, heating fine-grained soils under NC conditions leads to a so-called thermally induced overconsolidation (Di Donna and Laloui, 2013). Because heating under NC conditions causes plasticity and induces an increase in the elastic domain (i.e. path A–A' in Fig. 5.5), strain hardening is produced. Strain hardening can also be caused by isothermal mechanical loading (i.e. path A–A'' in Fig. 5.5). This phenomenon is the inverse of the thermal softening that involves the shrinkage of the elastic domain with an increase in temperature. Based on the previous

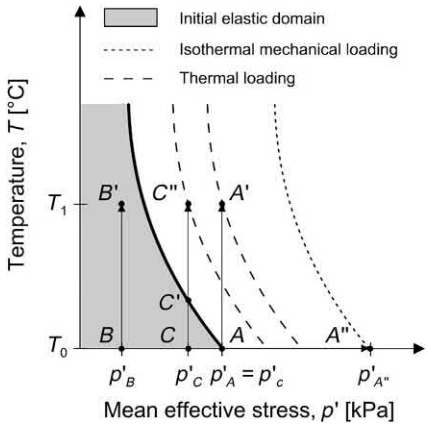

Figure 5.5 Temperature-stress paths in the mean effective stress–temperature plane. *Redrawn after Di Donna, A., Laloui, L., 2015. Response of soil subjected to thermal cyclic loading: experimental and constitutive study. Eng. Geol. 190 (1), 65–76.*

considerations, the volumetric behaviour of fine-grained soils under NC conditions upon a heating–cooling cycle is partly irreversible, that is thermoelastic, thermoplastic.

Soils under highly OC conditions are characterised by a stress–temperature state that lies within the yield surface (state B in Fig. 5.5). In other words, the current mechanical pressure, p'_B, applied to the material at a temperature T_0 is lower than the preconsolidation pressure, p'_c. Because of the considered stress–temperature state, drained heating up to a temperature $T_1 > T_0$ from the initial state under a constant mean effective stress induces thermoelastic strain (i.e. path $B–B'$). The reason for this phenomenon is because the stress–temperature state remains within the yield surface. Upon thermal unloading under a constant mean effective stress, the material still remains OC. Based on the previous considerations, the volumetric behaviour of fine-grained soils under highly OC conditions upon a heating–cooling cycle is reversible, that is thermoelastic.

Soils under slightly OC conditions are characterised by a stress–temperature state that lies within the yield surface (state C in Fig. 5.5). In other words, the current mechanical pressure, p'_C, applied to the material at a temperature T_0 is lower than the preconsolidation pressure, p'_c. Because of the considered stress–temperature state, drained heating from the initial state under a constant mean effective stress induces initial thermoelastic strain (i.e. path $C–C'$) and subsequent thermoplastic strain when loading from a stress–temperature state lying on the yield surface occurs (i.e. path $C'–C''$). Based on the previous considerations, the volumetric behaviour of fine-grained soils under slightly OC conditions upon a heating–cooling cycle can be reversible or partly irreversible.

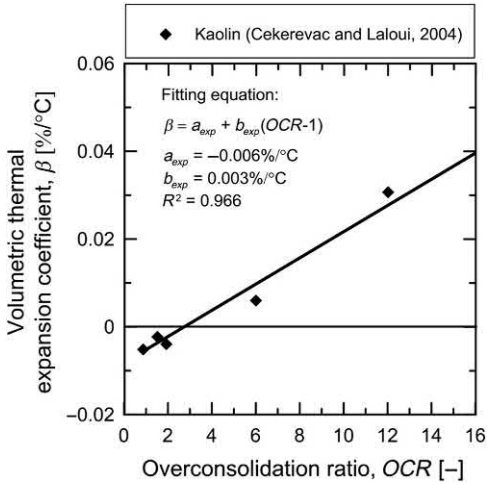

Figure 5.6 Relationship between the thermal expansion coefficient and overconsolidation ratio for the kaolin tested by Cekerevac and Laloui (2004). *Redrawn after Liu, H., Xiao, Y., McCartney, J.S., Liu, H., 2018. Influence of temperature on the volume change behavior of saturated sand. Geotechn. Test. J. 41 (4), 747–758.*

According to Liu et al. (2018), a linear increase of the volumetric thermal expansion coefficient of fine-grained soils, β, may be considered with the *OCR*. For the clay tested by Cekerevac and Laloui (2004), that is kaolin, the following relationship between β and *OCR* is found (Liu et al., 2018)

$$\beta = a_{exp} + b_{exp}(OCR - 1) \tag{5.4}$$

where a_{exp} and b_{exp} are material constants whose value is reported in Fig. 5.6.

An alternative approach to describe the volumetric behaviour of fine-grained soils subjected to temperature variations is in terms of the loading sequence. Details about the considered framework have been presented by Coccia and McCartney (2016a,b). In summary, thermally accelerated creep may provide closer thermal volume change predictions than thermal softening.

5.4.3 Volumetric behaviour of fine-grained soils for multiple thermal cycles

Experimental results on volumetric behaviour of fine-grained soils subjected to multiple thermal cycles have been presented, for example by Campanella and Mitchell (1968), Fleureau (1979), Hueckel et al. (1998), Vega and McCartney (2014) and Di Donna and Laloui (2015). These results show that the first heating–cooling cycle under drained conditions induces most of the irreversible volume change and the related hardening in NC materials. Subsequent thermal cycles of the *same magnitude*

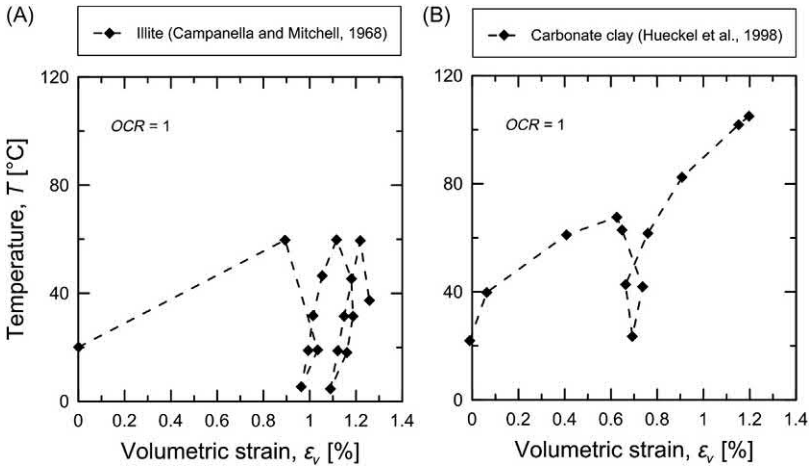

Figure 5.7 Thermal cyclic effects on normally consolidated (A) illite and (B) carbonate clay. *Redrawn after Campanella, R.G., Mitchell, J.K., 1968. Influence of temperature variations on soil behavior. J. Soil Mech. Found. Div. 94 (SM3), 709–734 and Hueckel, T., Pellegrini, R., Del Olmo, C., 1998. A constitutive study of thermoelasto-plasticity of deep carbonatic clays. Int. J. Numer. Anal. Methods Geomech. 22 (7), 549–574.*

and range produce small increments of irreversible deformation that decrease cycle after cycle. This phenomenon reveals an accommodation phenomenon and a soil behaviour that becomes progressively insensitive to temperature variations (Campanella and Mitchell, 1968). Experimental evidence in support of the previous considerations is presented in Fig. 5.7 with reference to the results of Campanella and Mitchell (1968) and Hueckel et al. (1998) (the latter highlight the influence of different magnitudes of heating thermal loads on the material response). Results are depicted in terms of the relationship between thermally induced volumetric strain, ε_v, and applied temperature variation, ΔT.

Complementary data corroborating the previous considerations are presented in Fig. 5.8 with reference to the study of Di Donna and Laloui (2015). Soils under OC conditions show a reversible deformation which corresponds to the thermoelastic expansion (and contraction) of the solid skeleton. Soils under NC conditions show a partly irreversible deformation upon the first heating–cooling cycle. Irreversible deformation is accumulated in all cases during the first heating–cooling cycle and then stabilises showing a thermoelastic behaviour (cf. Fig. 5.9). This phenomenon is called *plastic accommodation* (Di Donna and Laloui, 2015). The slope of the (unloading) curve associated with a thermoelastic behaviour of the material can be linked to the thermal expansion coefficient of the solid skeleton.

When cyclic thermal loading of NC soils occurs, the configuration of the solid particles becomes increasingly stable at each cycle (depending on the amount of

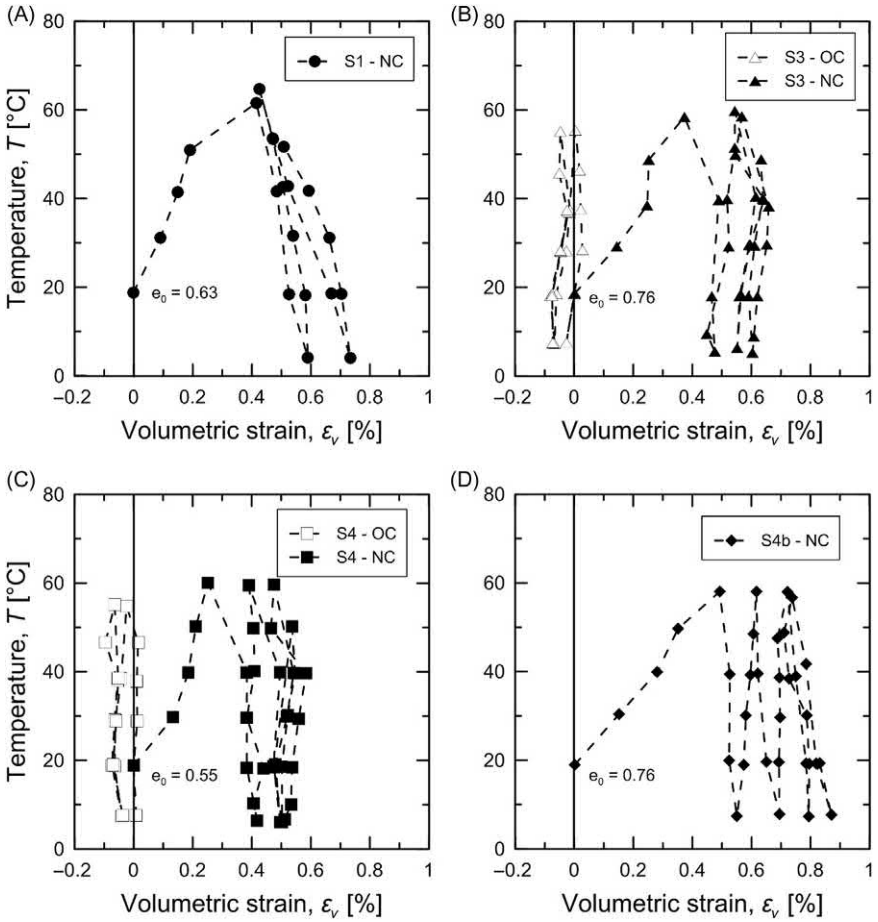

Figure 5.8 Volumetric behaviour of fine-grained soils subjected to thermal cycles. *Redrawn after Di Donna, A., Laloui, L., 2015. Response of soil subjected to thermal cyclic loading: experimental and constitutive study. Eng. Geol. 190 (1), 65–76.*

accumulated plastic deformation) and the available space for inducing additional collapse reduces, so that accommodation takes place. The thermal cycles result in a transition from a NC to an OC condition. The oedometric curve expressing a relationship between the void ratio, e, and the vertical effective stress, σ'_z, reported in Fig. 5.10 with reference to the results of Di Donna and Laloui (2015) highlights the aforementioned phenomenon. The material was first consolidated to 125 kPa (from point 1 to point 2 in Fig. 5.10), then subjected to four thermal cycles (from point 2 to point 3) and finally loaded up to 2000 kPa (from point 3 to point 5 in Fig. 5.10, with an unloading phase). During the final mechanical loading phase after thermal cyclic loading, the material shows a first phase of reversible behaviour (from point 3

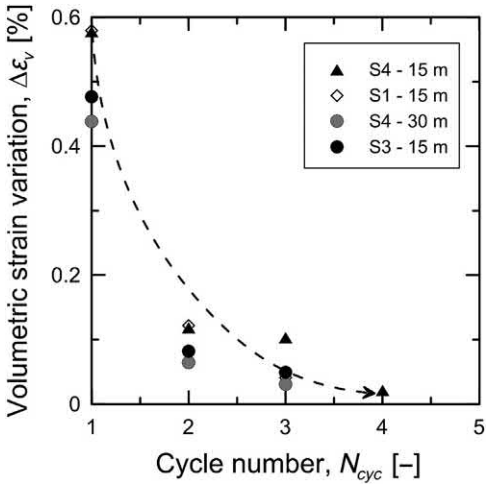

Figure 5.9 Accumulation of thermoplastic deformation at 20°C after each thermal cycle. *Redrawn after Di Donna, A., Laloui, L., 2015. Response of soil subjected to thermal cyclic loading: experimental and constitutive study. Eng. Geol. 190 (1), 65–76.*

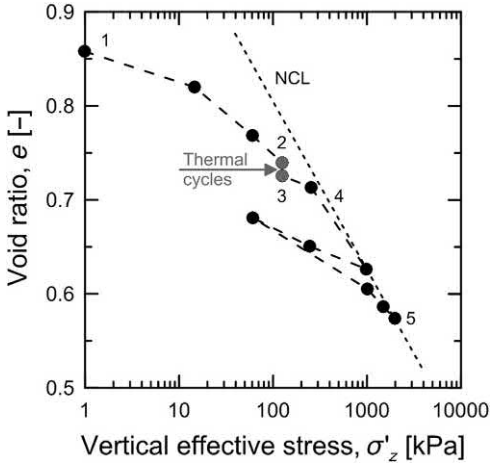

Figure 5.10 Effect of thermal cycles on the oedometric curve of a fine-grained soil. *Redrawn after Di Donna, A., Laloui, L., 2015. Response of soil subjected to thermal cyclic loading: experimental and constitutive study. Eng. Geol. 190 (1), 65–76.*

to point 4 in Fig. 5.10) and then undergoes plasticity again, joining the normal compression line (NCL). This behaviour results from the thermally induced overconsolidation caused by the heating of fine-grained soils under NC conditions, which requires (at the same temperature) a higher stress state to undergo plasticity (again) after thermal cycling.

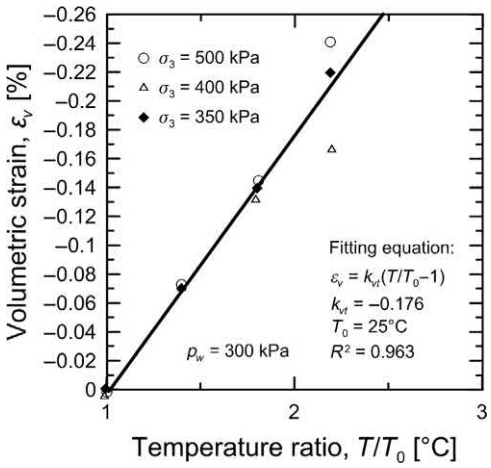

Figure 5.11 Relationship between the temperature ratio and volumetric strain for the Fujian sand tested by Liu et al. (2018). *Redrawn after Liu, H., Xiao, Y., McCartney, J.S., Liu, H., 2018. Influence of temperature on the volume change behavior of saturated sand. Geotechn. Test. J. 41 (4), 747–758.*

5.4.4 Volumetric behaviour of coarse-grained soils caused by one thermal cycle

Experimental results about the volumetric behaviour of coarse-grained soils subjected to one thermal cycle have been presented, for example by Demars and Charles (1982), Kosar (1983) and Agar et al. (1986, 1987). Complementary results have been proposed by Ng et al. (2016), Liu et al. (2018) and Sittidumrong et al. (2019).

Based on the previous results, it is widely considered that heating coarse-grained soils in *drained conditions* produces an expansive volume variation of such materials, while cooling produces a contractive volume variation. Experimental evidence supporting the previous considerations (for the influence of heating) is reported in Fig. 5.11 with reference to the results of Liu et al. (2018). Results are depicted in terms of the relationship between thermally induced volumetric strain, ε_v, and temperature ratio, T/T_0.

Nevertheless, available experimental evidence supports that heating coarse-grained soils in *drained conditions* can also produce a contractive volume variation of such materials. Based on the arguments of Ng et al. (2017) and considering the corroborating analyses presented by Chen et al. (2009), the reliability of the experimental results presented by Kosar (1983) and Agar et al. (1986) may be affected by boundary effects, despite the calibration of the apparatuses made. Such boundary effects have been controlled and eliminated in the experiments of Ng et al. (2016). In this context, heating coarse-grained soils in *drained conditions* can produce a contractive or an expansive volume variation of such materials. Experimental evidence supporting the previous considerations is reported in Fig. 5.12 with reference to the results of Ng et al. (2016).

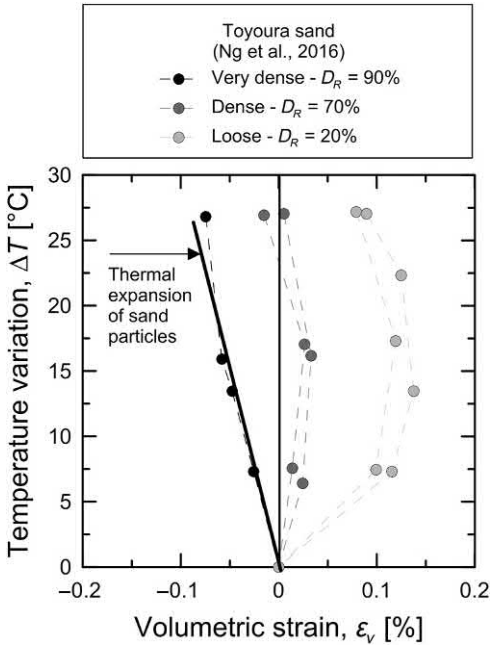

Figure 5.12 Volumetric behaviour of coarse-grained soils subjected to temperature variations. *Redrawn after Ng, C.W.W., Wang, S.H., Zhou, C., 2016. Volume change behaviour of saturated sand under thermal cycles. Géotech. Lett. 6 (2), 124–131.*

Results are depicted in terms of the relationship between thermally induced volumetric strain, ε_v, and applied temperature variation, ΔT. The volumetric strain purely due to the thermal expansion of the particles characterising the tested coarse-grained soil, that is Toyoura sand, is also plotted for reference [calculated by Ng et al. (2016) with reference to the work of Agar (1984)]. The considered values of relative density refer to the condition prior to thermal loading (not to the initial conditions).

Very dense coarse-grained soils expand when heated. The amount of thermal expansion is almost the same as that of the individual soil particles (Ng et al., 2016). Thermally induced volumetric strains of up to -0.1% (for temperature variations of up to approximately $\Delta T = 30°C$) can be observed.

In contrast, dense to loose coarse-grained soils show an initial contraction and a subsequent expansion when heated. Thermally induced volumetric strains ranging from 0.05% to 0.15% can characterise dense to loose coarse-grained soils upon heating (for temperature variations of $\Delta T = 12°C$, e.g. from a temperature $T = 23°C–35°C$). A further heating of these materials leads to thermally induced volumetric strains of up to -0.05% (for temperature variations of $\Delta T = 15°C$, from a temperature $T = 35°C–50°C$). For the same temperature variation, the observed thermal collapse of dense to loose coarse-grained soils is approximately ten times smaller than that

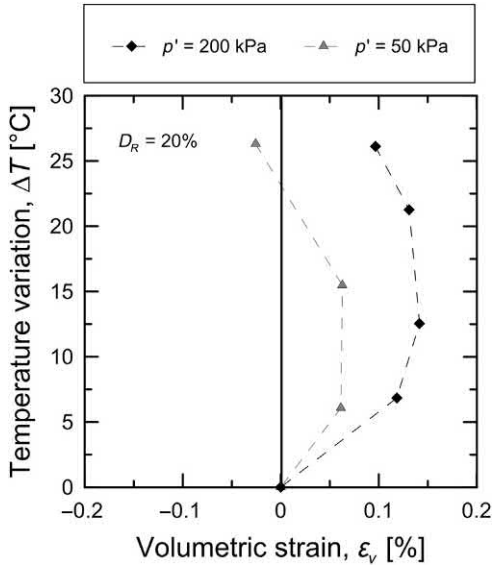

Figure 5.13 Volumetric response of coarse-grained soils subjected to temperature variations at different mean effective stresses. *Redrawn after Ng, C.W.W., Wang, S.H., Zhou, C., 2016. Volume change behaviour of saturated sand under thermal cycles. Géotech. Lett. 6 (2), 124–131.*

characterising NC fine-grained soils (Ng et al., 2016). Yet, the discussed behaviour of dense to loose coarse-grained soils is the inverse compared that characterising slightly OC fine-grained soils, which show an initial expansion and a subsequent contraction upon heating.

The significance of the thermal collapse of coarse-grained soils appears to depend on the stress state, which can be quantified in terms of the mean effective stress, p'. Experimental evidence supporting the previous consideration is reported in Fig. 5.13 with reference to the results of Ng et al. (2016). Results are depicted in terms of the relationship between thermally induced volumetric strain, ε_v, and applied temperature variation, ΔT. The relative density of the tested materials prior to heating is of $D_R = 20\%$. For the same relative density prior to heating, the thermal contraction increases with the mean effective stress. In the considered example, thermally induced volumetric contractions of 0.15% and 0.07% are observed at a mean effective stress of 200 and 50 kPa, respectively.

According to Ng et al. (2016), the observed volumetric behaviour of coarse-grained soils under thermal loads cannot be explained by most thermomechanical constitutive models (see, e.g. Hueckel and Borsetto, 1990; Cui et al., 2000; Laloui and François, 2009; Zhou and Ng, 2015). These models typically assume the stress history only to characterise the nonisothermal volumetric soil behaviour and describe contractive and

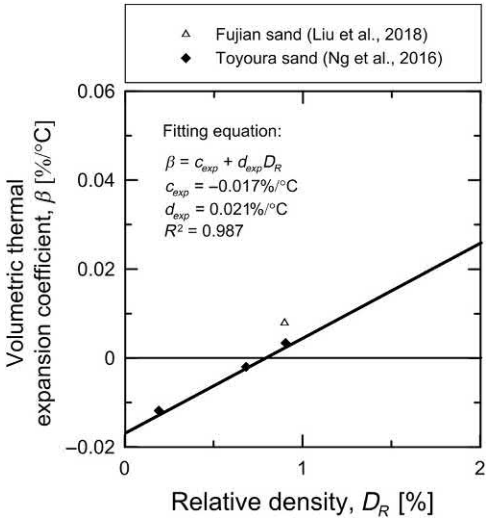

Figure 5.14 Relationship between the thermal expansion coefficient and relative density for the Toyoura and Fujian sands tested by Ng et al. (2016) and Liu et al. (2018), respectively. *Redrawn after Liu, H., Xiao, Y., McCartney, J.S., Liu, H., 2018. Influence of temperature on the volume change behavior of saturated sand. Geotechn. Test. J. 41 (4), 747–758.*

expansive responses under NC (loose) and highly overconsolidated (very dense) conditions, respectively, while an expansive and contractive response under slightly OC (dense and medium-loose) conditions. An attempt to model the volumetric behaviour of sands under nonisothermal conditions has been made by Zhou et al. (2017).

According to Liu et al. (2018), a linear increase of the volumetric thermal expansion coefficient of coarse-grained soils, β, may be considered with the D_R. For the sands tested by Ng et al. (2016) and Liu et al. (2018), that is Toyoura and Fujian sand, respectively, the following relationship between β and D_R is found (Liu et al., 2018)

$$\beta = c_{exp} + d_{exp}D_R \tag{5.5}$$

where c_{exp} and d_{exp} are material constants whose value is reported in Fig. 5.14. With an increase in the relative density of the sand, the volumetric thermal expansion coefficient of the material increases and involves from a contractive to an expansive behaviour (Liu et al., 2018).

5.4.5 Volumetric behaviour of coarse-grained soils for multiple thermal cycles

Experimental results on volumetric behaviour of coarse-grained soils subjected to multiple thermal cycles have been presented, for example by Chen et al. (2006) and

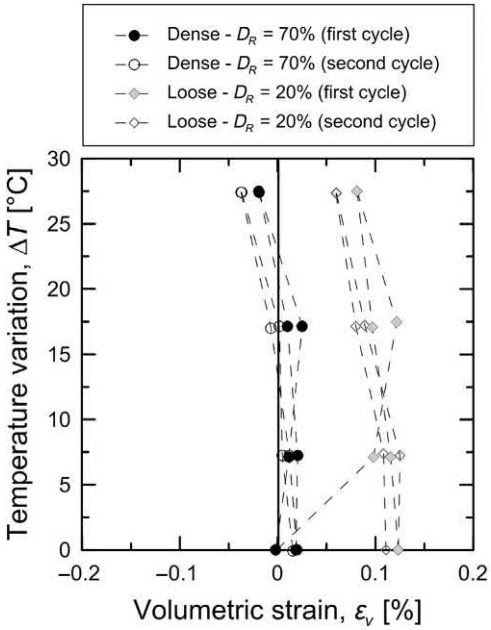

Figure 5.15 Volumetric behaviour of coarse-grained soils subjected to thermal cycles. *Redrawn after Ng, C.W.W., Wang, S.H., Zhou, C., 2016. Volume change behaviour of saturated sand under thermal cycles. Géotech. Lett. 6 (2), 124–131.*

Ng et al. (2016). These results show that the application of cyclic thermal loads under drained conditions to coarse-grained soils involves, after a first heating–cooling cycle (in which a contraction of the soil matrix during heating may be observed), an expansive volume variation of such materials upon heating and a contractive volume variation upon cooling. Experimental results that corroborate the previous considerations are shown in Fig. 5.15 with reference to the data of Ng et al. (2016). The observed cyclic effects are due to the irreversible contraction induced by the first cycle of heating and cooling. Soil response becomes stiffer during the second thermal cycle.

5.4.6 Micromechanics of the volumetric behaviour of soils under nonisothermal conditions

The effect of temperature on the volumetric behaviour of soils at the macroscale is a combination of microscale processes that govern the interactions between the soil phases. Predominantly chemical (besides physical) interactions between soil phases govern the volumetric behaviour of fine-grained soils under nonisothermal conditions. In contrast, predominantly physical interactions between soil phases govern the

volumetric behaviour of coarse-grained soils under nonisothermal conditions. Despite the inherently different nature of the processes that govern the behaviour of soils depending on their mineralogy, the following common underlying aspects can be highlighted for both fine- and coarse-grained soils.

If the soil particles were fixed, the thermal expansion of each soil constituent would produce a global dilation of the solid skeleton, with an associated increase in the pore size and the interparticle distance (François, 2008). However, soil particles are not fixed. Therefore, particle rearrangement can occur with an increase in temperature and is associated with the phenomenon of thermal collapse. In particular, while the volumetric behaviour of NC soils appears to be driven by particle rearrangement (whose effect is predominant with respect to the thermoelastic expansion of the soil particles), the behaviour of OC soils appears to be dominated by the thermoelastic expansion of the soil particles (with a minimum influence of particle rearrangement) (Di Donna and Laloui, 2013). In this context, the thermoplastic deformation of soils upon heating is associated with an unstable configuration of the solid particles, while the thermoelastic deformation of soils is associated with a particularly stable configuration of the particles. The presence of unstable voids is considered to facilitate the occurrence of thermal collapse in coarse-grained soils (Sitharam, 2003). In any case, the significance of the thermal collapse phenomenon appears to depend on the magnitude of the pores size (i.e. void ratio) prior to heating, because greater pores represent a higher potential for collapse (Di Donna and Laloui, 2015). Further considerations specifically apply to fine- and coarse-grained soils.

In fine-grained soils, the magnitude of the thermal collapse phenomenon appears to be proportional to the plasticity index, I_p, that is an indicator of the significance of chemical interactions in fine-grained soils (Demars and Charles, 1982; Abuel-Naga et al., 2006; Di Donna and Laloui, 2015). Data available in the literature on this aspect are collected in Fig. 5.16 and Table 5.1. Despite the scatter between the data, which prevents from an unequivocal relation between the plasticity index and the volumetric strain of the soil per unit temperature change, a more significant volumetric deformation per unit temperature change characterises soils with a higher plasticity index, I_p. In other words, the intensity of the irreversible part of deformation appears to be independent of the stress state in the NC range for fine-grained soils, but dependent on soil type and plasticity (Plum and Esrig, 1969).

Other phenomena contributing to the thermal collapse phenomenon in fine-grained soils appear to be (1) the degradation of the adsorbed water layer with an increase in temperature that tends to form larger voids (Fleureau, 1979; Pusch, 1986), (2) the modification of the contact forces network due to the differences between the rigidities and the thermal expansion of the different minerals involved (Kingery et al., 1976) and (3) and the changes in the equilibrium between the Van der Waals

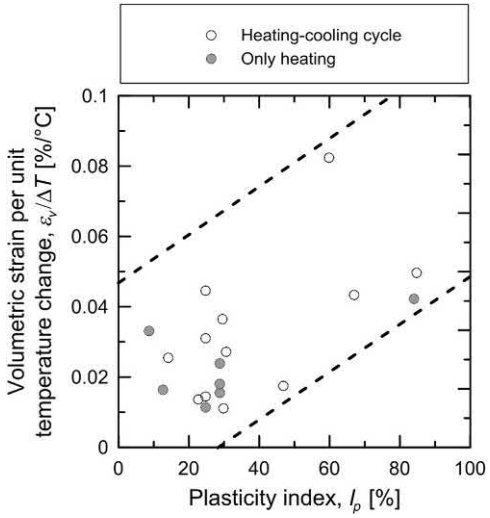

Figure 5.16 Relation between the plasticity index and the thermal collapse observed per unit temperature change.

attractive forces and the electrostatic repulsive forces (Laloui, 2001). All of these phenomena are associated with a decrease in the shearing strength of inter-particle contacts (governed by physicochemical interactions). This decrease in interparticle strength leads to an increase in the probability of particle slippage. The maximum probability of particle slippage occurs when the mobilised force producing such slippage is highest (i.e. under NC conditions). Under NC conditions, heating produces a partial collapse of the soil structure and a decrease in void ratio until a sufficient number of additional particle contacts are formed to allow the soil carrying stress at the higher temperature (Campanella and Mitchell, 1968). The reason why the thermal collapse is not observed in highly OC conditions is related to the stable soil structure and lower mobilised force. Such a reversible mechanical behaviour is typical for most materials and leaves valid the micromechanical processes associated with the thermoplasticity of NC soils observed upon heating.

5.4.7 Considerations for analysis and design of energy geostructures

Based on the results considered thus far, the temperature sensitivity of the volumetric behaviour of fine-grained soils may generally be considered more significant than coarse-grained soils. This sensitivity may preferably be considered in the analysis and design of energy geostructures. Nevertheless, the use of simplified analysis approaches (e.g. analytical models) may justify to neglect the temperature sensitivity of the volumetric behaviour of soils in situations wherein these materials have a thermal

Table 5.1 Thermal collapse (volumetric contraction) of different clayey soils induced by a temperature change at constant mean effective stress under normally consolidated conditions.

Authors	Clay type	T_0 [°C]	T_1 [°C]	ΔT [°C]	Thermal Cycle	I_p [%]	ε_v [%]	ε_v/°C [%/°C]
Demars and Charles (1982)	Atlantic Marine clay	25	50	25	Yes	25	1.24	0.049
	Atlantic Marine clay	25	50	25	Yes	84.7	1.08	0.043
	Atlantic Marine clay	25	50	25	Yes	66.9	0.68	0.027
	Atlantic Marine clay	25	50	25	Yes	30.8	0.64	0.025
Paaswell (1967)	Penn soil	30	60	30	No	8.9	1	0.033
Campanella and Mitchell (1968)	Remoulded illite	5	60	55	Yes	47	0.95	0.017
Plum and Esrig (1969)	Illite	24	50	26	No	84	1.1	0.042
Hueckel and Baldi (1990)	Boom clay Pontida clay	22	80	58	Yes	25	1.8	0.031
Towhata et al. (1993)	MC clay	20	90	70	No	25	1.66	0.023
	MC clay	20	90	70	No	29	1.08	0.015
	MC clay	20	90	70	No	29	1.26	0.018
Del Olmo et al. (1996)	Spanish clay	20	100	80	Yes	23	1.08	0.013
Robinet et al. (1997)	Parisian Basin clay	20	80	60	Yes	30	0.69	0.011
Burghignoli et al. (2000)	Todi clay	22	48	26	Yes	14.4	0.95	0.036
Sultan et al. (2002)	Boom clay	22	100	78	Yes	30	3.5	0.044
Laloui and Cekerevac (2003)	Kaolin clay	20	95	75	No	23	0.85	0.011
Abuel-Naga et al. (2007)	Bangkok clay	22	90	68	Yes	60	5.6	0.082

Correlation with the plasticity index of the soil. Thermal cycle: Yes: heating–cooling cycle; No: only heating.
Source: Data from François, B., 2008. Thermoplasticity of Fine Grained Soils At Various Saturation States: Application to Nuclear Waste Disposal (Ph.D. thesis), Swiss Federal Institute of Technology (EPFL), Lausanne, Switzerland

expansion coefficient that is lower than or equal to that of the embedded geostructures. Such a sensitivity should be considered when soils characterised by a greater thermal expansion coefficient than the one characterising geostructures may be encountered and in any case when dealing with fine-grained soils under NC conditions or particularly sensitive to time-dependent effects such as creep. According to

Bourne-Webb et al. (2016), the behaviour of NC fine-grained soils upon heating involves an action on the deformation of energy geostructures that is similar to the one applied by ground movements such as downdrag or negative skin friction and should be considered in analysis and design. Time-dependent effects such as creep may be accelerated by temperature increases (Leroueil and Soares Marques, 1996; Mitchell and Soga, 2005; Laloui et al., 2008) and result in additional long-term settlement. Limiting the settlement of energy geostructures under the influence of mechanical loads may limit time-dependent effects potentially accelerated by temperature.

5.5 Strength of soils under nonisothermal conditions

5.5.1 Yield surface at different temperatures

Along with the decrease of the preconsolidation pressure of fine-grained soils at constant void ratio with increasing temperature, a global shrinkage of the yield surface can be observed. Experimental results that corroborate the previous consideration have been reported, for example by Cekerevac and Laloui (2004) and are shown in Fig. 5.17. The yield surface is represented in two-dimensional space relating the mean effective stress, p', with the deviatoric stress, q. Both stresses are normalised by a scaling factor that represents the equivalent pressure on the NCL at the specific volume for which yielding is observed, p'_e.

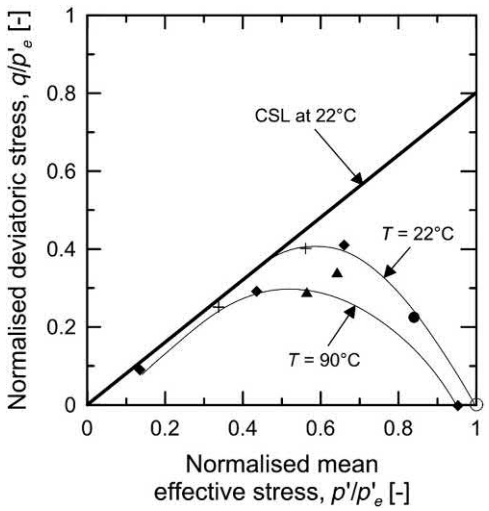

Figure 5.17 Normalised yield surfaces for kaolin at different temperatures. *Redrawn after Cekerevac, C., Laloui, L., 2004. Experimental study of thermal effects on the mechanical behaviour of a clay. Int. J. Numer. Anal. Methods Geomech. 28 (3), 209–228.*

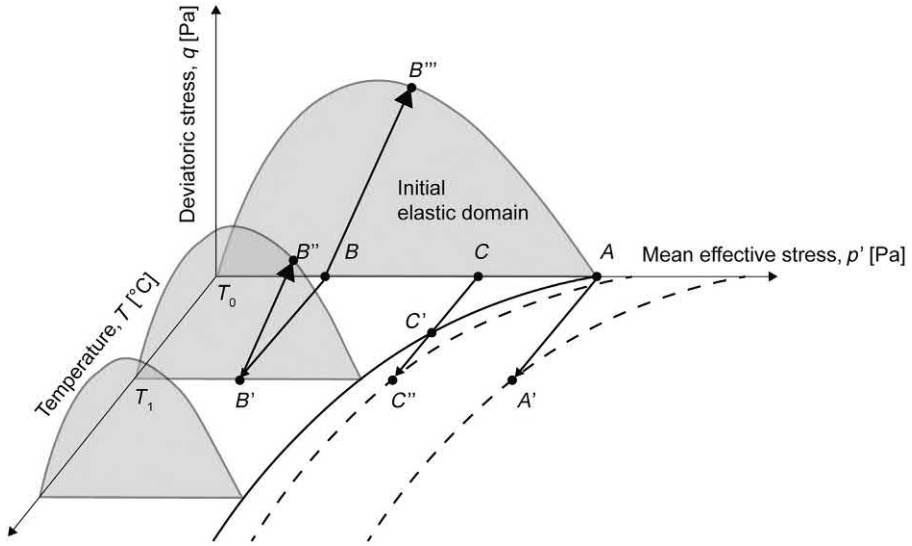

Figure 5.18 Thermal-stress paths in the mean effective stress–deviatoric stress–temperature space. *Redrawn after Di Donna, A., Laloui, L., 2013. Soil response under thermomechanical conditions imposed by energy geostructures. In: Laloui, L., Di Donna, A. (Eds.), Energy Geostructures: Innovation in Underground Engineering. Wiley, pp. 3–21.*

Based on the considered results, shrinkage of the yield limit with an increase in temperature is observed. This shrinkage is not homothetic, depends on the stress history and is associated with thermal softening. The influence of thermal softening on the variation of the yield surface of soils can be appreciated in the three-dimensional described by coordinate axes p', q and T. An example of this representation is proposed in Fig. 5.18 with reference to the yield surface described by the Advanced Constitutive Model for Environmental Geomechanics-Temperature effects, that is ACMEG-T (cf. Appendix C).

5.5.2 Shear strength

The assessment of the shear strength of fine-grained soils under nonisothermal conditions necessitates the consideration of the initial and current temperature level as well as the general loading conditions. Generalisations about the influence of temperature of the shear strength of soils lack of any significance without the previous information. The following aspects are worth noting with reference to the possible influence of temperature on the shear strength of fine-grained soils.

The main consequence of thermal softening under deviatoric stress states is that if an OC material (with a certain void ratio) is sheared at a high temperature (stress path

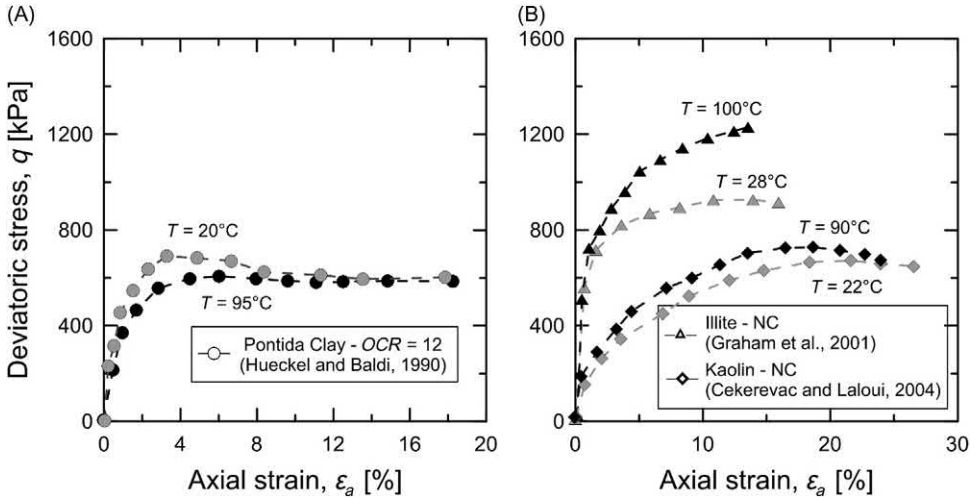

Figure 5.19 Shear strength at different constant temperatures of (A) overconsolidated and (B) normally consolidated fine-grained soils. *Data from Hueckel, T., Baldi, G., 1990. Thermoplasticity of saturated clays—experimental constitutive study. J. Geotech. Eng. 116 (12), 1778–1796, Graham, J., Tanaka, N., Crilly, T., Alfaro, M., 2001. Modified Cam-Clay modelling of temperature effects in clays. Can. Geotech. J 38 (3), 608–621. and Cekerevac, C., Laloui, L., 2004. Experimental study of thermal effects on the mechanical behaviour of a clay. Int. J. Numer. Anal. Methods Geomech. 28 (3), 209–228.*

$B'-B''$ in Fig. 5.18), it reaches the yield limit at a lower deviatoric stress with respect to shearing at the initial temperature (stress path $B-B'''$ in Fig. 5.18). In other words, the material undergoes plasticity earlier than in the isothermal case (Di Donna and Laloui, 2013). Conversely, in the case of a NC or slightly OC material, heating results in a combination of thermal softening and strain hardening, which compensate each other. An analysis of this phenomenon has been reported by Hueckel and Baldi (1990). Fig. 5.19 illustrates some experimental results reported by Hueckel and Baldi (1990), Graham et al. (2001) and Cekerevac and Laloui (2004) that corroborate the previous considerations. Additional results have been reported, for example by Kuntiwattanakul et al. (1995), Abuel-Naga et al. (2006) and Hueckel et al. (1998).

The initial *OCR* has also an effect on the shear strength of the material at ambient temperature after the application of one or more thermal cycles (Di Donna and Laloui, 2013). If the material is initially under OC conditions, a heating–cooling cycle (stress path $B-B'-B$ in Fig. 5.18) does not produce any plastic deformation (so that the dimension of the elastic domain remains the same after the entire cycle) and the response under shearing is not affected because no permanent change is induced on the void ratio. Conversely, if an initially NC or a slightly OC material is subjected to a heating–cooling cycle (stress path $A-A'-A$ or $C-C'-C''-C'-C$ in Fig. 5.18, respectively), strain hardening occurs as plastic deformation is produced. The material

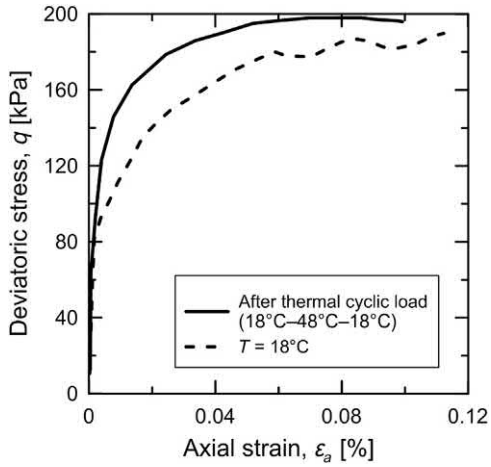

Figure 5.20 Effect of thermal cycles on the undrained shear strength of a normally consolidated Tody clay. *Redrawn after Burghignoli, A., Desideri, A., Miliziano, S., 2000. A laboratory study on the thermomechanical behaviour of clayey soils. Can. Geotech. J. 37 (4), 764–780.*

ends up being OC (at an ambient temperature T_0) because of the thermally induced overconsolidation and is characterised by an increase in shear strength. Experimental results that corroborate the previous phenomenon have been provided by Burghignoli et al. (2000) and are reported in Fig. 5.20. If a sample under initial NC conditions is heated and cooled under drained conditions, and then sheared, its undrained shear strength is higher than that of an equivalent sample tested at constant ambient temperature.

5.5.3 Flow rule

Upon distortional yielding, the flow rule defines the ratio between volumetric plastic strain increment $d\varepsilon_v^p$ and deviatoric plastic strain increment $d\varepsilon_q^p$. The associated flow rule postulates that, irrespective of the stress increment vector, on the yield limit the corresponding plastic strain increment vector should be normal to the yield limit (Schofield and Wroth, 1968). This normality assumption is essential to the validity of the limit (or bound) theorems, which provide the framework for many plastic mechanism analyses. Yet, it is often incorporated in critical state models (Schofield and Wroth, 1968). An analysis of the yield limit and plastic strain increment can be examined together by aligning $d\varepsilon_v^p$ with p' and $d\varepsilon_q^p$ with q. If normality is observed, then the yield surface also becomes the plastic potential surface (Roscoe and Burland, 1968). Most soils do not appear to obey to an associated flow rule (Wong and Mitchell, 1975).

Considerations about the flow rule of fine-grained soils and the potential influence of temperature on the deviation of the plastic strain increment vectors with respect to the normal to the yield limit have been reported, for example by Cekerevac and

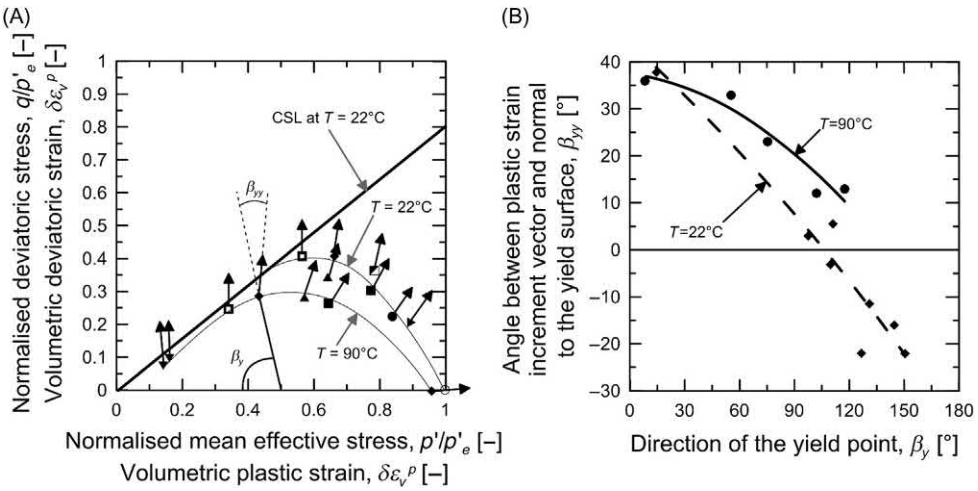

Figure 5.21 Effect of temperature on the flow rule of kaolin: (A) normalised yield surface and plastic strain increment vectors, (B) deviation of the plastic strain increment vector from normal to the yield envelope. *Redrawn after Cekerevac, C., Laloui, L., 2004. Experimental study of thermal effects on the mechanical behaviour of a clay. Int. J. Numer. Anal. Methods Geomech. 28 (3), 209–228.*

Laloui (2004). Supporting data for kaolin are reported in Fig. 5.21. From Fig. 5.21A it can be highlighted that the associated flow rule is not satisfied for the considered material. From Fig. 5.21B it can be highlighted that for highly OC materials the deviation of the plastic strain increment vectors is not affected by temperature, while as the *OCR* decreases the directions of plastic strain obtained at 90°C are quite different from those observed at 22°C. Therefore, temperature may have an effect on the flow rule. Despite the previous results, the effect of temperature on the flow rule is typically neglected in soil constitutive models.

5.6 Thermally induced effects on soil parameters

5.6.1 General

From a practical perspective, temperature variations associated with the geothermal operation of energy geostructures do not have a significant effect on the properties of most soils (Loveridge et al., 2017). Despite the previous consideration, a variation of some material properties is observed and may be included in constitutive models for developing advanced analyses of soil behaviour.

5.6.2 Temperature effect on compressibility parameters

Despite the effect of temperature on the preconsolidation pressure, it is generally recognised that, once that the yield surface is reached, the compressibility of the

material for subsequent mechanical loading is independent of temperature (Di Donna and Laloui, 2013). Key compressibility parameters are the compression index, C_c, the recompression index, C_r, and the swelling index, C_s. These parameters can be determined from the relationship between the mean effective stress (in logarithmic scale) and the void ratio. The slope of the NCL coincides with the value of C_c. By considering that this line is parallel to the critical state line (CSL), considerations about the critical state can also be performed through the value of C_c.

The slope of the compression line seems to be essentially independent of temperature (Finn, 1951; Campanella and Mitchell, 1968; Despax, 1976; Graham et al., 2001; Laloui and Cekerevac, 2003). Only a few contradictory experimental results show nonparallel consolidation curves at different temperatures (Plum and Esrig, 1969; Sultan et al., 2002). Similarly, the recompression index, C_r, and the swelling index, C_s, appear to be insensitive to temperature variations (Di Donna and Laloui, 2013). Experimental results supporting the previous considerations are reported in Fig. 5.22 with reference to the data presented by Di Donna and Laloui (2015) and Cekerevac and Laloui (2004). Further data highlighting the insensitivity to temperature of the compression, recompression and swelling indexes are reported in Table 5.2 drawing from the study of Di Donna and Laloui (2015).

From the values of C_s and C_c it is possible to compute the plastic rigidity index β_p and the bulk modulus K_{ref} at a reference mean effective stress p'_{ref}. According to the results reported by Di Donna and Laloui (2015), the plastic rigidity index of fine-

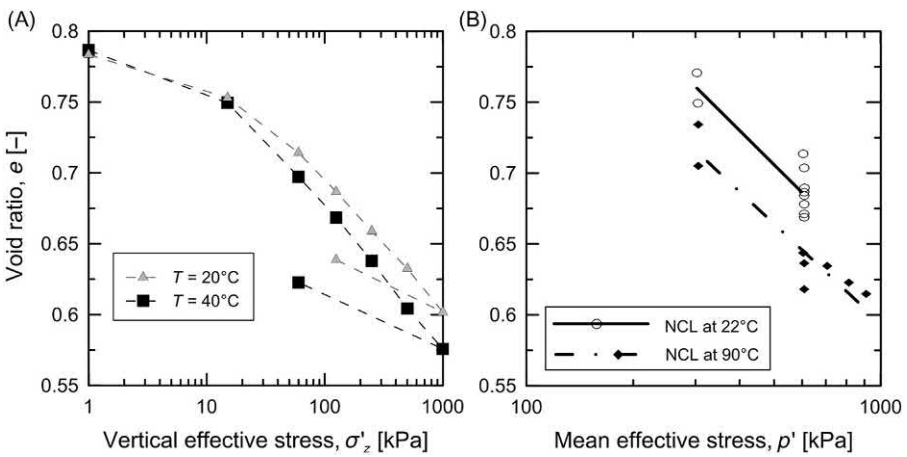

Figure 5.22 Effect of temperature on the compressibility parameters of fine-grained soils. *Data from Di Donna, A., Laloui, L., 2015. Response of soil subjected to thermal cyclic loading: experimental and constitutive study. Eng. Geol. 190 (1), 65–76 and Cekerevac, C., Laloui, L., 2004. Experimental study of thermal effects on the mechanical behaviour of a clay. Int. J. Numer. Anal. Methods Geomech. 28 (3), 209–228.*

Table 5.2 Compressibility parameters of fine-grained soils at different temperatures.

	T [°C]	C_r [–]	C_c [–]	C_s [–]
Sample S3	20	0.01	0.04	0.02
	40	0.01	0.05	0.02
	60	0.01	0.04	0.01
Sample S4	20	0.01	0.04	0.01
	40	0.01	0.04	0.02
	60	0.01	0.05	0.02

Source: Data from Di Donna, A., Laloui, L., 2015. Response of soil subjected to thermal cyclic loading: experimental and constitutive study. Eng. Geol. 190 (1), 65–76.

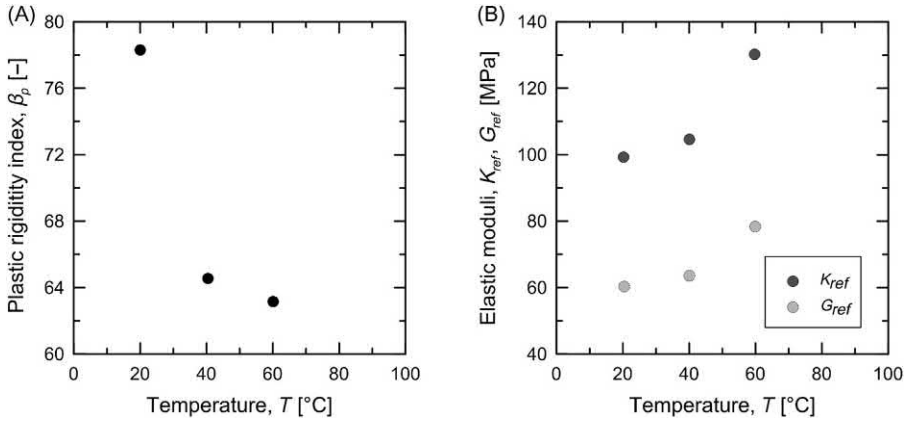

Figure 5.23 Effect of temperature on (A) the plastic rigidity index and (B) the elastic moduli of fine-grained soils. *Redrawn after Di Donna, A., Laloui, L., 2015. Response of soil subjected to thermal cyclic loading: experimental and constitutive study. Eng. Geol. 190 (1), 65–76.*

grained soils slightly decreases with temperature, while the bulk modulus slightly increases with temperature. Supporting data are presented in Fig. 5.23. The shear modulus at the reference mean effective stress is plotted for completeness (a Poisson's ratio of $\upsilon = 0.25$ is assumed for its calculation). While considering the variation of the plastic rigidity index and bulk modulus of the soil with temperature in analyses of energy geostructures may improve the accuracy of the obtained results, neglecting the considered variation is considered acceptable for practical design purposes.

Along with the previous results, the soil Young's modulus, E, appears to be insensitive to temperature for coarse-grained soils (Recordon, 1993; Saix et al., 2000), while characterised by potential variations for fine-grained soils. A slight increase of the Young's modulus with temperature is often considered for fine-grained soils under NC conditions due to the influence of the thermal collapse (Di Donna and Laloui, 2015).

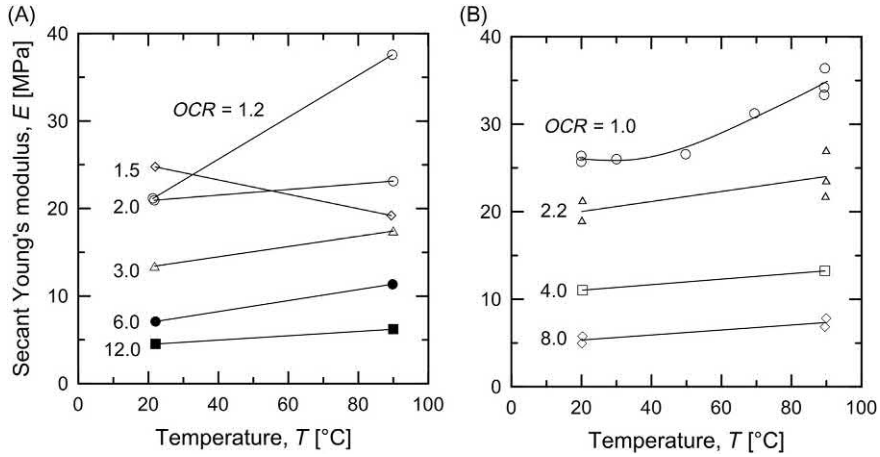

Figure 5.24 Effect of temperature on the secant elastic modulus of (A) kaolin (calculated at 0.5% strain) and (B) MC clay (calculated at 0.1% strain). The values of overconsolidation ratio are calculated at ambient temperature. *Redrawn after Cekerevac, C., Laloui, L., 2004. Experimental study of thermal effects on the mechanical behaviour of a clay. Int. J. Numer. Anal. Methods Geomech. 28 (3), 209–228 and Kuntiwattanakul, P., Towhata, I., Ohishi, K., Seko, I., 1995. Temperature effects on undrained shear characteristics of clay. Soils Found. 35 (1), 147–162.*

Nevertheless, a slight increase, decrease or actual insensitivity of the Young's modulus to temperature for various consolidation states can be observed (Highter, 1969; Murayama, 1969; Leroueil and Soares Marques, 1996; Burghignoli et al., 2000; Cekerevac and Laloui, 2004; Abuel-Naga et al., 2006; Fang and Daniels, 2006). Experimental data highlighting a variation of Young's modulus with temperature are reported in Fig. 5.24 with reference to the results of Cekerevac and Laloui (2004) and Kuntiwattanakul et al. (1995). Further data that show an undefined variation of the oedometric modulus, E_{oed}, which can be related to the soil Young's modulus, are reported in Fig. 5.25 with reference to the results of Di Donna and Laloui (2015). While considering the potential variation of the soil Young's modulus with temperature in analyses of energy geostructures may improve the accuracy of the obtained results, neglecting the considered aspect is considered acceptable for practical design purposes. In other words, unless particularly sensitive soils are encountered, considering a constant value of Young's modulus with temperature appears to be appropriate.

5.6.3 Temperature effect on angle of shear strength under constant volume conditions

A substantial amount of experimental data have been presented to characterise the influence of temperature on the angle of shear strength under constant volume

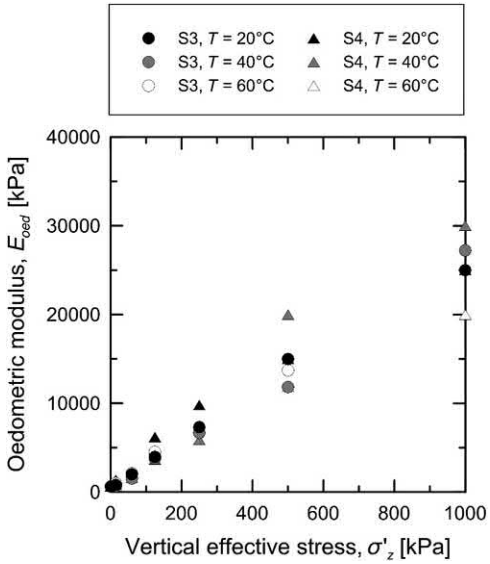

Figure 5.25 Effect of temperature on the oedometric modulus of fine-grained soils. *Redrawn after Di Donna, A., Laloui, L., 2015. Response of soil subjected to thermal cyclic loading: experimental and constitutive study. Eng. Geol. 190 (1), 65–76.*

conditions for both coarse- and fine-grained soils (Hueckel and Baldi, 1990; Hueckel and Pellegrini, 1992; Burghignoli et al., 2000; Graham et al., 2001; Cekerevac and Laloui, 2004; Robinet et al., 1997; Ghahremannejad, 2003; Yavari et al., 2016; Murphy and McCartney, 2014). Based on the previous results, an actual variation of the angle of shear strength under constant volume conditions with temperature can be observed in some cases. Experimental investigations have shown a slight dependency of the angle of shear strength for kaolin (Cekerevac and Laloui, 2004) and natural Boom clay (Hueckel and Pellegrini, 1989), whereas an insensitivity of the considered parameter for Illite (Graham et al., 2001) and smectite clay (Burghignoli et al., 2000; Hueckel and Baldi, 1990). However, potential variations of the angle of shear strength under constant volume conditions with temperature typically appear to be small and negligible from a practical perspective. The previous consideration agrees with the conclusions of Yavari et al. (2016). Supporting experimental evidence is reported in Fig. 5.26. Additional considerations can be found in Hueckel et al. (2009) and Hueckel et al. (2011). Based on the previous arguments, the angle of shear strength of soils can be considered independent of temperature. This fact is particularly relevant for the estimation of the capacity of energy geostructures, whose governing mathematical formulations depend in most cases on this parameter.

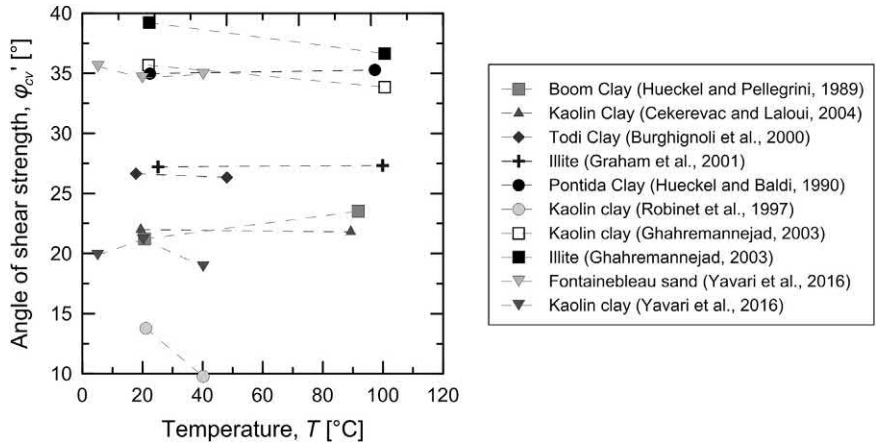

Figure 5.26 Influence of temperature on the angle of shear strength under constant volume conditions. *Redrawn after Yavari, N., Tang, A.M., Pereira, J.-M., Hassen, G., 2016. Effect of temperature on the shear strength of soils and the soil–structure interface. Can. Geotech. J. 53 (999), 1–9.*

5.6.4 Temperature effect on critical state line

Studies on the sensitivity to temperature of the slope of the CSL have been presented for example by Hueckel et al. (2009, 2011). Accordingly, the apparent preconsolidation pressure is not the only yield locus characteristic that may evolve with temperature. The slope of the CLS, similar to the angle of shear strength of soils, may exhibit a slight dependence on temperature. According to Hueckel et al. (2009), this temperature dependence is most likely material specific. The considered result has been verified, for example by Cekerevac and Laloui (2004) considering the results of shear tests on soil samples tested at temperatures of 22°C and 90°C. Fig. 5.27 presents the considered results in the semi-logarithmic plane of void ratio—mean effective stress. The slope of the CSL obtained at temperatures of 22°C and 90°C, which are expressed in terms of the compression index read $C_c = 0.181$ (at 22°C, based on 11 tests) and $C_c = 0.185$ (at 90°C, based on seven tests). Despite the actual differences between the results, a negligible influence of temperature on the slope of the CLS can be considered due to the significance involved. Fig. 5.28 presents additional results that corroborate the previous consideration in the $p' - q$ plane, with reference to the critical state parameter, M_c. The insensitivity of the CLS to temperature agrees with the corresponding insensitivity of the angle of shear strength under constant volume conditions observed in this case.

5.6.5 Temperature effect on consolidation parameters

The primary consolidation coefficient, c_v, is typically found to increase with temperature due to the reduction of water viscosity (Towhata et al., 1993; Delage et al., 2000;

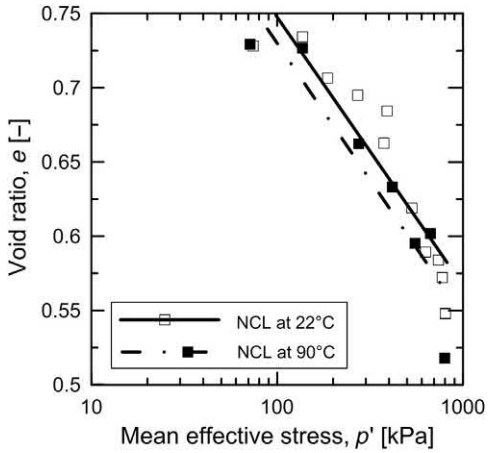

Figure 5.27 Influence of temperature on the critical state line of kaolin in the volumetric plane. *Redrawn after Cekerevac, C., Laloui, L., 2004. Experimental study of thermal effects on the mechanical behaviour of a clay. Int. J. Numer. Anal. Methods Geomech. 28 (3), 209–228.*

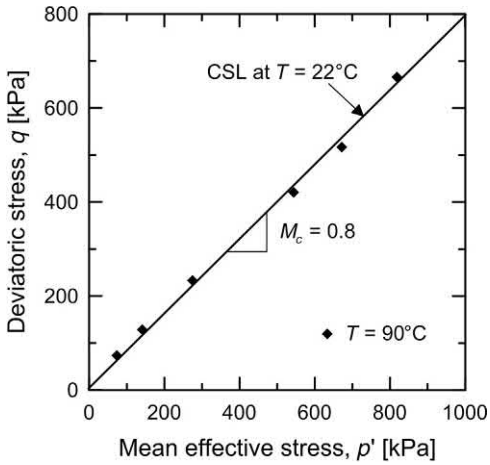

Figure 5.28 Critical state line for kaolin clay in the deviatoric plane at different temperatures. *Redrawn after Cekerevac, C., Laloui, L., 2004. Experimental study of thermal effects on the mechanical behaviour of a clay. Int. J. Numer. Anal. Methods Geomech. 28 (3), 209–228.*

Di Donna and Laloui, 2015). This result indicates a faster consolidation at higher temperature (Di Donna and Laloui, 2015). Data supporting the sensitivity of the primary consolidation coefficient to temperature are reported in Fig. 5.29 with reference to the results of Di Donna and Laloui (2015).

Based on the knowledge of the primary consolidation coefficient and the oedometric modulus, the hydraulic conductivity, k, can be calculated. Similar to the primary

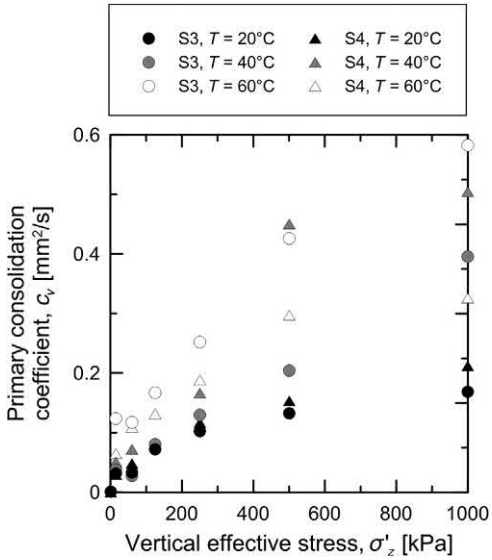

Figure 5.29 Effect of temperature on the primary consolidation coefficient of fine-grained soils. *Redrawn after Di Donna, A., Laloui, L., 2015. Response of soil subjected to thermal cyclic loading: experimental and constitutive study. Eng. Geol. 190 (1), 65–76.*

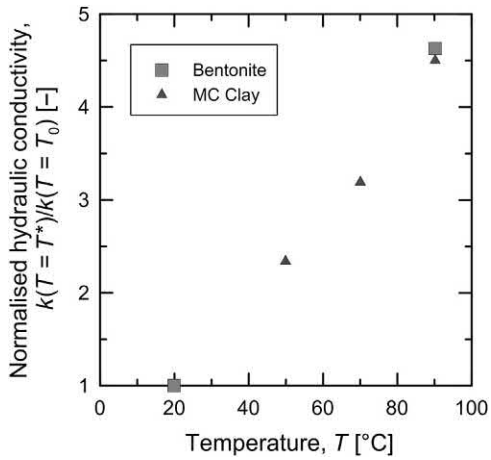

Figure 5.30 Influence of temperature on the hydraulic conductivity of fine-grained soils. *Data from Towhata, I., Kuntiwattanaul, P., Seko, I., Ohishi, K., 1993. Volume change of clays induced by heating as observed in consolidation tests. Soil Found. 33 (4), 170–183.*

consolidation coefficient, the hydraulic conductivity of soils increases with temperature, mainly as a consequence of the reduced viscosity of the heated water (Towhata et al., 1993; Burghignoli et al., 2000; Delage et al., 2000; Di Donna and Laloui, 2015). Fig. 5.30 illustrates the evolution of hydraulic conductivity with temperature, $k(T = T^*)$,

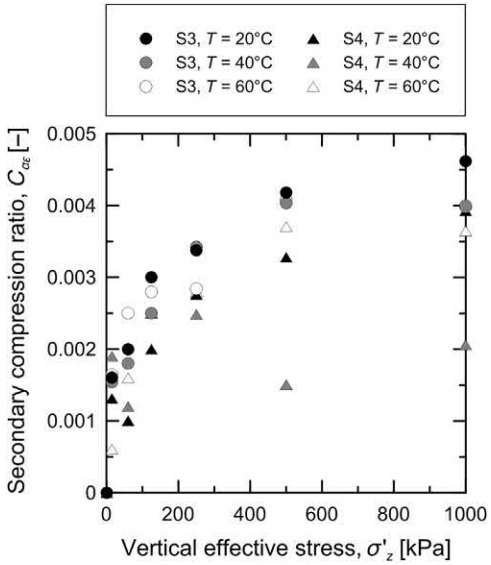

Figure 5.31 Effect of temperature on the secondary compression index of fine-grained soils. *Data from Di Donna, A., Laloui, L., 2015. Response of soil subjected to thermal cyclic loading: experimental and constitutive study. Eng. Geol. 190 (1), 65–76.*

normalised with respect to the value of the considered parameter measured at 20°C, $k(T = T_0)$, for two clays tested by Towhata et al. (1993). As the hydraulic conductivity governs the primary consolidation, the drainage conditions and the significance of potential groundwater flow, its variation with temperature may be considered in the analysis and design of energy geostructures.

Concerning the secondary compression index, C_α (alternatively defined as the secondary compression ratio, $C_{\alpha\varepsilon}$), experimental data support an increase of this parameter with temperature (Mitchell and Campanella, 1963; Meschyan and Galstyan, 1972; Eriksson, 1989), while others support an insensitivity with temperature (through the consideration of the coefficient $C_A = C_\alpha / C_c$) (Laloui et al., 2008; Marques et al., 2004; Boudali et al., 1994; Towhata et al., 1993). Further results that corroborate the last observation, which may be accounted for the analysis of energy geostructures, are reported in Fig. 5.31 with reference to the work of Di Donna and Laloui (2015).

5.7 Characterisation of soil–structure interfaces

5.7.1 General

Soil–structure interfaces represent a critical setting for the transfer of loads from structural elements to the ground. Soil–structure interfaces are typically defined as the thin

zone of soil between structures and surrounding ground masses. The thickness of these settings depends on soil and structure properties, but it is generally considered to vary from 5 to 10 times the average particle diameter (Boulon and Foray, 1986; Uesugi et al., 1988). In the context of energy geostructures, a characterisation of soil–structure interfaces is key for addressing phenomena such as mass transfer, heat transfer and deformation that may result from the influence of loads arising from the geostructure. In the following, the considered characterisation is investigated with a focus on the influence on the deformation of energy geostructures.

The exploitation of geothermal energy through energy geostructures involves the transfer of seasonally and daily cyclic thermal loads in addition to approximately constant mechanical loads to the ground, which result in a mobilisation of the shear strength of interfaces. The two following aspects of this problem can be distinguished (Di Donna et al., 2015):

1. Cyclic expansion and contraction of the geostructure during heating and cooling and the resulting mechanically cyclic mobilisation of the interface shear strength.
2. The direct effect of temperature on the soil at the interface and the resulting response of the soil–structure interface at different temperatures.

The mechanical mobilisation of the interface shear strength [i.e. aspect (1)] has been extensively addressed in the framework of offshore foundations with respect to the influence of the cyclic mechanical loads that are typically applied to such structures as a result of wind and wave actions (De Jong et al., 2003, 2006; Mortara et al., 2007). The influence of the mechanical solicitation of interfaces caused by mechanical loads is considered comparable to the one caused by thermal loads in the framework of energy geostructures. The direct effect of temperature on the soil at the interface (i.e. aspect 2) has been investigated in the framework of energy geostructures (Xiao et al., 2014; Di Donna et al., 2015; Yavari et al., 2016; Yazdani et al., 2019).

5.7.2 Structure roughness

The structure roughness is commonly identified through the normalised roughness, R_n, and is defined as follows (Uesugi and Kishida, 1986):

$$R_n = \frac{R_{max}}{D_{50}} \tag{5.6}$$

where R_{max} is the maximum vertical distance between the highest and lowest peaks of the structure asperities over a fixed length and D_{50} is the soil mean grain size (cf. Fig. 5.32).

Depending on the interface materials and conditions, it is possible to identify a critical value of roughness, R_{cr}, such that if $R_n < R_{cr}$ the interface is considered smooth,

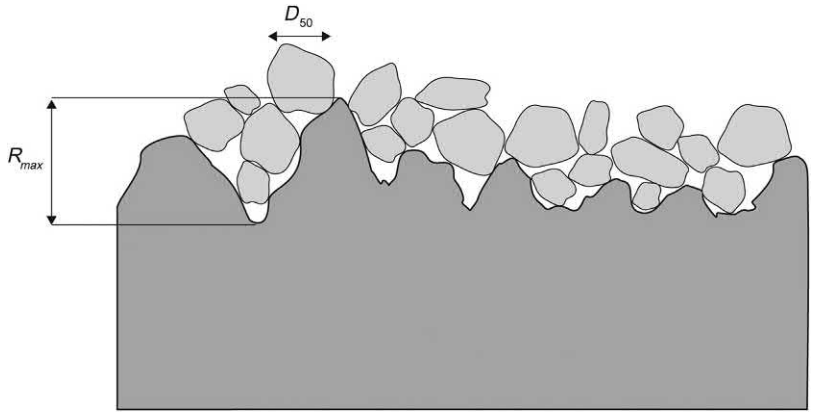

Figure 5.32 Representation of the soil–structure interface roughness.

and if $R_n > R_{cr}$ the interface is considered rough. In the first case, after an initial reversible range, the behaviour is generally perfectly plastic. As the roughness of the interface increases, after an initial reversible range, the behaviour become closer to that of the soil and can be analysed in the framework of the critical state plasticity (Schofield and Wroth, 1968). This fact has been proven to be valid for both sand– and clay–structure interfaces (Littleton, 1976; Tsubakihara et al., 1993; Yamamoto et al., 2003; Shakir and Zhu, 2009).

The shear strength of soil–structure interfaces is lower than the corresponding soil–soil strength or at most equal to it: the lowest value of shear strength is found in the case of smooth interfaces while the highest value is found in the case of rough interfaces (Littleton, 1976; Tsubakihara et al., 1993; Yamamoto et al., 2003; Shakir and Zhu, 2009). An example of this evidence for dry dense sand–aluminium interfaces tested under isothermal conditions by Porcino et al. (2003) is presented in Fig. 5.33 in terms of the relationships between shear stress, τ, horizontal displacement, δ_h, and normal displacement, δ_n. The interface shear resistance increases with the interface roughness and is always lower than the corresponding soil–soil strength (cf. Fig. 5.33A). The volumetric deformation of the interface is also lower with regards to the soil–soil one and the observed dilatant behaviour in this case is less and less evident with the reduction of the surface roughness (cf. Fig. 5.33B).

The lower shear strength of soil–structure interfaces compared to that of the same soils and the influence of the structure roughness on this discrepancy can also be highlighted in terms of the relationship between soil–structure interface angle of shear strength under constant volume conditions, δ_{cv}, and soil angle of shear strength under constant volume conditions, φ'_{cv}. An example of results for interfaces with sand and clay are reported in Fig. 5.34 with reference to the investigations of Potyondy (1961), Brumund and Leonards (1973), Littleton (1976), Tsubakihara et al. (1993),

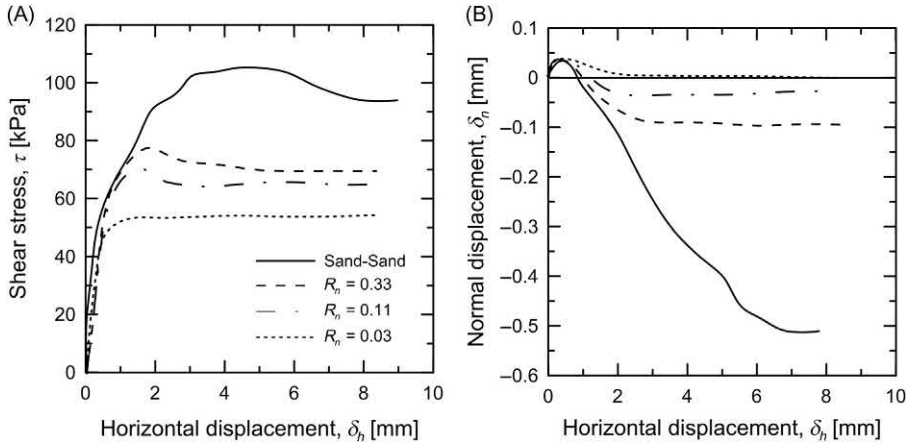

Figure 5.33 Effect of interface roughness on sand–aluminium interfaces: (A) deviatoric and (B) volumetric behaviour. *Redrawn after Porcino, D., Fioravante, V., Ghionna, V.N., Pedroni, S., 2003. Interface behavior of sands from constant normal stiffness direct shear tests. ASTM Geotech. Test. J. 26 (3), 289–301.*

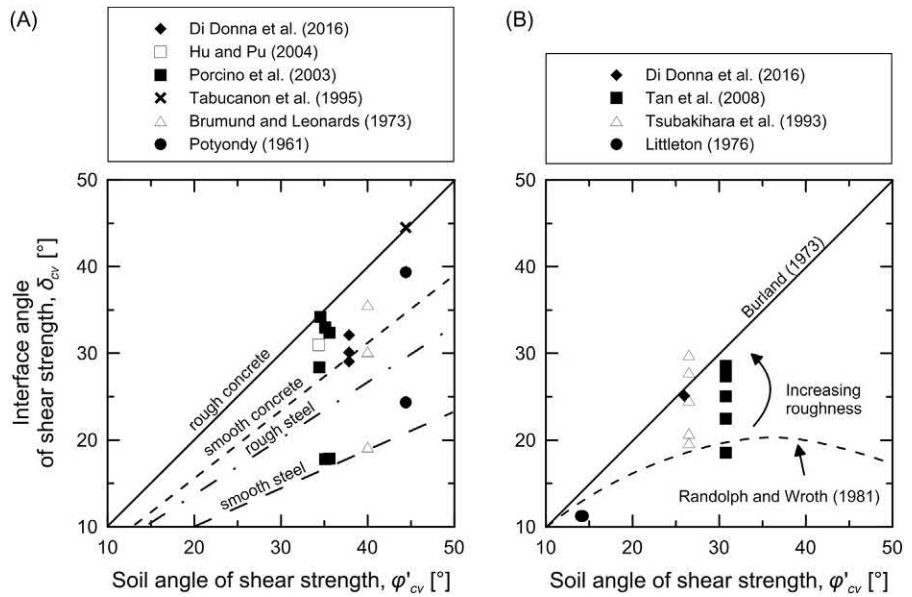

Figure 5.34 Relationship between (A) sand and sand–structure interface and (B) clay and clay–structure interface angles of shear strength under constant volume conditions. *Redrawn after Di Donna, A., Ferrari, A., Laloui, L., 2015. Experimental investigations of the soil–concrete interface: physical mechanisms, cyclic mobilisation and behaviour at different temperatures. Can. Geotech. J. 53 (4), 659–672.*

Tabucanon et al. (1995), Porcino et al. (2003), Hu and Pu (2004), Tan et al. (2008) and Di Donna et al. (2015). The higher the interface roughness, the higher the interface angle of shear strength and the closer this angle to the one of the soil. These data agree with the relationships proposed by Kulhawy et al. (1983) for interfaces with sands, as well as with those proposed by Burland (1973) and Randolph and Wroth (1981) for interfaces with clay.

Besides the structure roughness, the main factors that affect the behaviour of soil–structure interfaces are (1) the normal stress acting on the structure, (2) the soil density, (3) particle angularity and (4) the soil grain size distribution (Uesugi and Kishida, 1986).

5.7.3 Normal stress and soil density

Similar to soils, when interfaces are subjected to a greater effective normal stress, σ'_n, they have greater interface shear strengths, τ. Soil density influences behaviour of the interface because it is responsible, together with the stress state, for the dilative–contractive behaviour of the soil.

Dense soil–structure interfaces show dilatancy while loose soil–structure interfaces show a contractive behaviour (Fioravante et al., 1999). The behaviour of structural interfaces with clay is generally contractive, but might be dilative if the soil is subjected to highly OC conditions (Shakir and Zhu, 2009). These aspects are particularly important for the understanding of the response of interface of geostructures because the volumetric behaviour of the soil at the interface cannot freely develop as it is partially prevented by the presence of the surrounding ground (Di Donna et al., 2015).

5.7.4 Constant normal stiffness conditions

The far-field ground acts as a spring at soil–structure interface and reacts to the dilative–contractive behaviour of the interface according to Hooke's law. Such conditions are known as *constant normal stiffness* (CNS) conditions, in which the stiffness is equal to the stiffness of the equivalent far-field soil spring (Lehane et al., 1993). The considered conditions differ from the so-called *constant normal load* (CNL) conditions, wherein the stress (not the stiffness) remains constant upon loading and unloading.

Under CNS conditions, the normal effective stress applied to the interface varies as (Ooi and Carter, 1987; Tabucanon et al., 1995; Porcino et al., 2003; Mortara et al., 2007)

$$\sigma'_n = \sigma'_{n0} + \Delta\sigma'_n = \sigma'_{n0} - K_{int}\Delta\delta_n \tag{5.7}$$

where σ'_{n0} and $\Delta\sigma'_n$ are the initial and increment of the normal effective stress, respectively; K_{int} is the far-field normal stiffness; and $\Delta\delta_n$ is the variation of displacement

Table 5.3 Values of normal stiffness K_{int} for different soils.

Reference	Soil	Shear modulus, G_0 [MPa]	Stiffness, K_{int} [kPa/mm]			
			Radius, R [m]			
			0.5	0.8	1	1.2
Lo Presti (1989)	Cemented sand	300	1200	750	600	500
Ghionna et al. (1983)	Lightly cemented sand	280	1120	700	560	467
Ghionna et al. (1983)	Sand–gravel	125	500	313	250	208
Lo Presti (1989)	Gravel	100	400	250	200	167
Lo Presti (1989)	Fine-grained soil	50	200	125	100	83

Source: Data from Di Donna, A., 2014. Thermomechanical aspects of energy piles. In: Laboratory of Soil Mechanics. Swiss Federal Institute of Technology in Lausanne (EPFL), Lausanne.

normal to the interface. Using the cylindrical cavity expansion theory, the value of K can be deduced from the equilibrium equation, as suggested by (Wernick, 1978)

$$K_{int} = 2\frac{G_0}{R} \tag{5.8}$$

where G_0 is the shear modulus of the soil at small strains and R is the radius of the cavity (e.g. a pile). Theoretically, the value of K_{int} can vary from 0 (CNL) to infinite ('constant normal height', CNH). Reasonable values of K_{int} range between 100 and 1200 kPa/mm, being lower for clays, and are reported in Table 5.3 (Di Donna, 2014).

Fig. 5.35 compares the stress paths in the Mohr plane of dense sand–concrete and loose sand–concrete interfaces subjected to monotonic mechanical loading under isothermal CNS and CNL conditions by Fioravante et al. (1999). The interface angle of shear strength is identified by δ. In the case of dense soil (cf. Fig. 5.35A), the interface initially contracts and then dilates, so that in CNS conditions the normal effective stress decreases at the beginning and increases later, providing at the end a higher shear strength with respect the one observed under CNL conditions. In the case of loose sand (cf. Fig. 5.35B), the effect is almost negligible in terms of shear strength as the volumetric deformation is limited. However, in CNS conditions, the normal load decreases slightly due to the slight observed contraction. While the shear strength of a specific material under CNS conditions depends on the related volumetric behaviour, the interface angle of shear strength is unique for a given soil–structure interface (Di Donna et al., 2015).

Further results allowing to expand on the role of CNS and CNL conditions on the response of soil–structure interfaces are reported in Fig. 5.36 with reference to the results presented by Di Donna et al. (2015) for sand–concrete interfaces subjected to

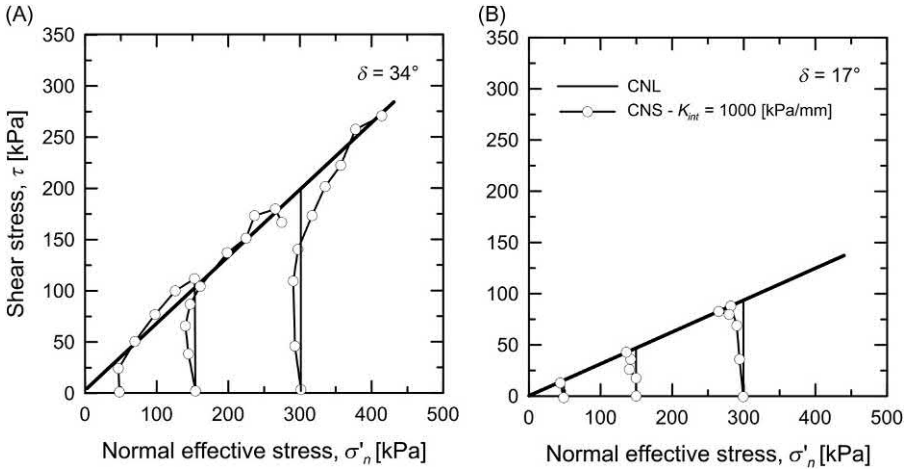

Figure 5.35 Stress paths for concrete interfaces with (A) dense and (B) loose sand under constant normal stiffness and constant normal load conditions. *Redrawn after Fioravante, V., Ghionna, V.N., Pedroni, S., Porcino, D., 1999. A constant normal stiffness direct shear box for soil-solid interface tests. Riv. Ital. Geotec. 33 (3), 7–22.*

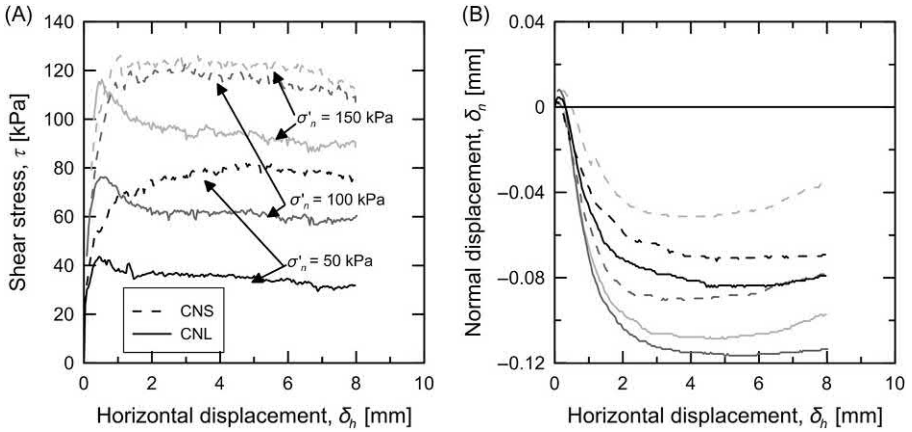

Figure 5.36 Sand–concrete interface (medium roughness) under constant normal load and constant normal stiffness conditions: (A) deviatoric and (B) volumetric behaviour. *Redrawn after Di Donna, A., Ferrari, A., Laloui, L., 2015. Experimental investigations of the soil–concrete interface: physical mechanisms, cyclic mobilisation and behaviour at different temperatures. Can. Geotech. J. 53 (4), 659–672.*

monotonic loading under isothermal conditions. A comparison of the results obtained from three tests under CNL conditions and three under CNS conditions is presented in terms of deviatoric and volumetric behaviour. Under CNL conditions, after the first compression phase, the interface shows a dilatant response. Hence, when the same tests

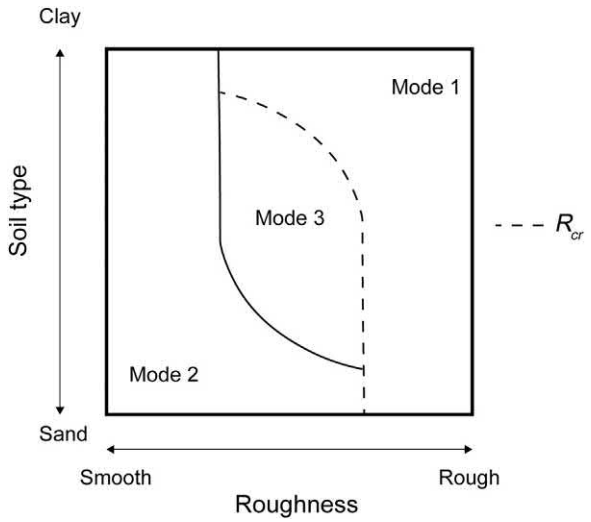

Figure 5.37 Modes of soil–structure interface failure. *Redrawn after Tsubakihara, Y., Kishida, H., Nishiyama, T., 1993. Friction between cohesive soils and steel. Soils Found. 33 (2), 145–156.*

are performed under CNS conditions, the volumetric dilation of the interface induces an increase in the normal effective stress and an increase in the available shear strength (cf. Fig. 5.36A). Simultaneously, the normal stiffness acts as a partial restraint for the free dilation of the interface and the samples tested under CNS conditions consistently dilate less than the corresponding samples under CNL conditions (cf. Fig. 5.36B).

5.7.5 Shearing and sliding of soil–structure interfaces

Different deformation mechanisms occur at soil–structure interfaces: shearing of the soil and sliding between the soil particles and the interface (involving a relative displacement between the two materials). Depending on the structure roughness, the two previous mechanisms can contribute in different ways to the formation of three failure modes of soil–structure interfaces (cf. Fig. 5.37): in mode 1, that is when the interface surface is rough, shear failure occurs in the soil; in mode 2, that is when the interface surface is smooth, full sliding occurs at the interface; in mode 3, shear failure and sliding displacement occur simultaneously.

Results corroborating the previous failure modes have been presented, for example by Uesugi et al. (1988), Tsubakihara et al. (1993) and De Jong et al. (2003). In the case of smooth interfaces, during the first phase of shearing a reorientation of the soil particles takes place so that they tend to turn parallel to the interface. In this phase, the sliding displacement is small and the soil shearing governs the interface deformation. Then, after a transitional phase and when all the particles are oriented parallel to the interface, sliding occurs with limited soil deformation (constant volume conditions).

In the case of rough interfaces, the sliding component is almost null as shearing occurs inside the soil (Shakir and Zhu, 2009).

In the development of the shearing and sliding mechanisms of soil–structure interfaces, a major influence is also played by the nature (e.g. monotonic or cyclic) of the loading. The magnitude of shearing inside the soil increases with the amplitude of cyclic loading but decreases with continuing cycles. The percentage of sliding (or slippage) between the soil and structural material increases with the number of loading cycles.

The volumetric behaviour of soil–structure interfaces changes at each cycle due to the continuous rearrangement of grains (Di Donna et al., 2015). A global contraction cycle after cycle and the reduction in the normal effective stress are typically observed and are responsible for cyclic degradation. The cyclic degradation phenomenon is particularly critical in coarse-grained soils. According to Mortara et al. (2007), the cyclic degradation is not recovered in the postcyclic phase when dealing with soils adjacent to smooth concrete, while it is partially recovered in the case of rough concrete. Yet, cyclic degradation increases with increasing normalised roughness, while postcyclic degradation decreases.

Irrespective of the nature of the loading, the constant volume envelope of soil–structure interfaces is unique. An example of this evidence is proposed in Fig. 5.38 with reference to the data presented by Di Donna et al. (2015).

5.8 Strength of soil–structure interfaces under nonisothermal conditions

5.8.1 Strength of sand–concrete interfaces

The strength of structural interfaces with coarse-grained soils under nonisothermal conditions is characterised by insensitivity to temperature variations. This evidence is related to the limited sensitivity of coarse-grained soils to temperature variations, both in terms of volumetric and deviatoric behaviour.

The typical response to monotonic shearing under CNL conditions of a sand–concrete interface at 60°C (first heated at the desired temperature and then sheared) and at the ambient temperature of 20°C is presented in Fig. 5.39 with reference to the result of Di Donna et al. (2015). No thermally induced effect characterises the deviatoric behaviour of the considered interface because the curves at 20°C and 60°C are comparable (cf. Fig. 5.39A). The same conclusion can be drawn for the volumetric behaviour of the interface (only the results under 100 and 150 kPa are available) (cf. Fig. 5.39B). Similar comments can be established considering the response of the considered interface subjected to cyclic shearing at different temperatures

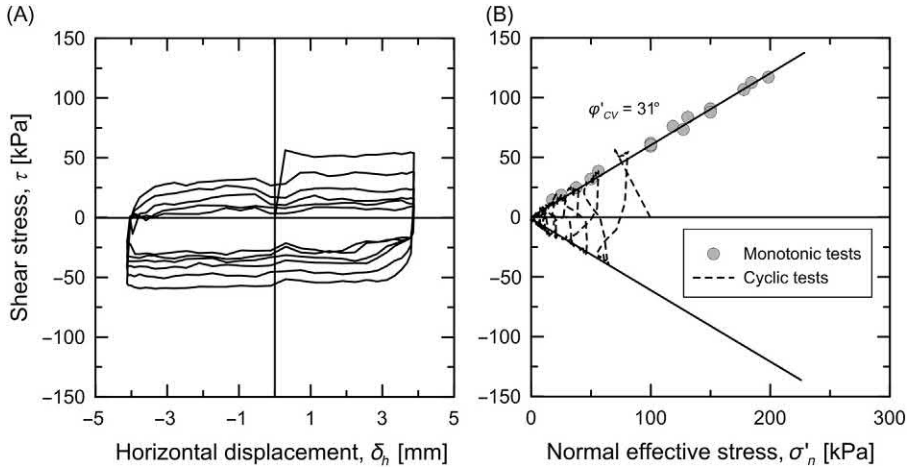

Figure 5.38 Sand–concrete interface (medium roughness) response subjected to cyclic and monotonic shearing under constant normal stiffness conditions: (A) shear stress–horizontal displacement plane; (B) Mohr plane. *Redrawn after Di Donna, A., Ferrari, A., Laloui, L., 2015. Experimental investigations of the soil–concrete interface: physical mechanisms, cyclic mobilisation and behaviour at different temperatures. Can. Geotech. J. 53 (4), 659–672.*

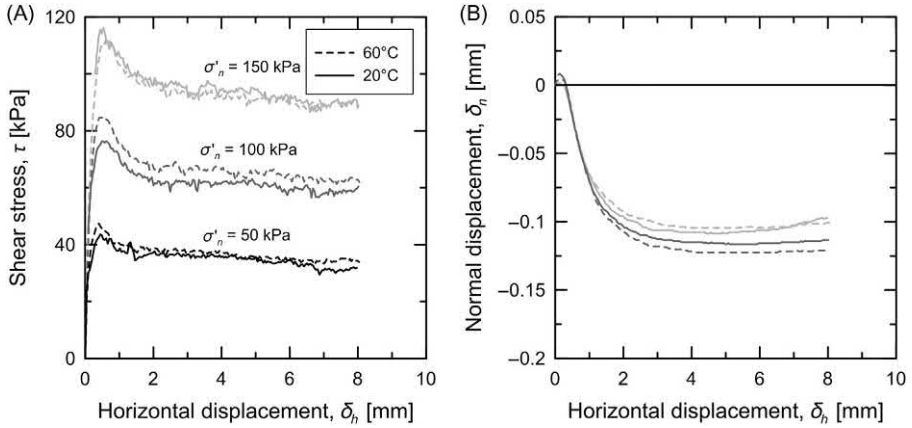

Figure 5.39 Sand–concrete interface (medium roughness) response subjected to monotonic shearing at 20°C and 60°C under constant normal load conditions: (A) shear stress–horizontal displacement plane; (B) Mohr plane. *Redrawn after Di Donna, A., Ferrari, A., Laloui, L., 2015. Experimental investigations of the soil–concrete interface: physical mechanisms, cyclic mobilisation and behaviour at different temperatures. Can. Geotech. J. 53 (4), 659–672.*

(cf. Fig. 5.40). No thermally induced effect is present because the failure envelopes at 20°C and 60°C coincide.

The results of various tests involving both cyclic and monotonic shearing of interfaces between concrete of varying roughness and dry sand at 20°C and 60°C under

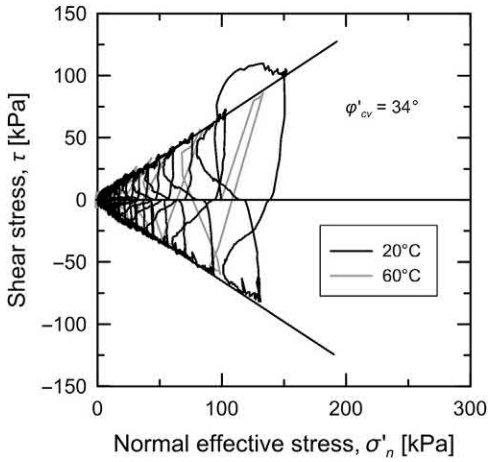

Figure 5.40 Sand–concrete interface (high roughness) response subjected to cyclic shearing at 20°C and 60°C under constant normal load conditions. *Redrawn after Di Donna, A., Ferrari, A., Laloui, L., 2015. Experimental investigations of the soil–concrete interface: physical mechanisms, cyclic mobilisation and behaviour at different temperatures. Can. Geotech. J. 53 (4), 659–672.*

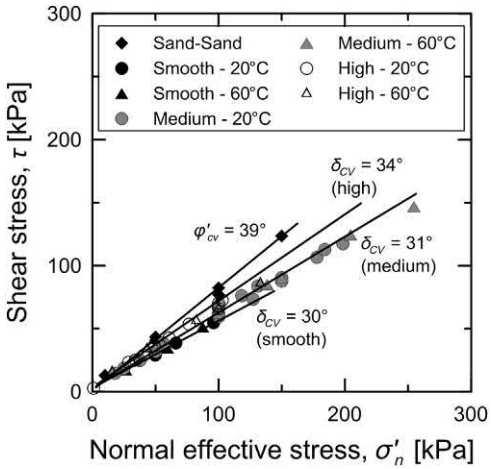

Figure 5.41 Dry sand–concrete interface responses at different temperatures under constant normal load and constant normal stiffness conditions. *Redrawn after Di Donna, A., Ferrari, A., Laloui, L., 2015. Experimental investigations of the soil–concrete interface: physical mechanisms, cyclic mobilisation and behaviour at different temperatures. Can. Geotech. J. 53 (4), 659–672.*

CNS and CNL conditions are summarised in Fig. 5.41 with reference to the results of Di Donna et al. (2015). A comparison with the response of the sand is made in the same plane. For each roughness, the interface angle of shear strength is independent of temperature, it increases with increasing roughness, and it is always lower than the corresponding soil one.

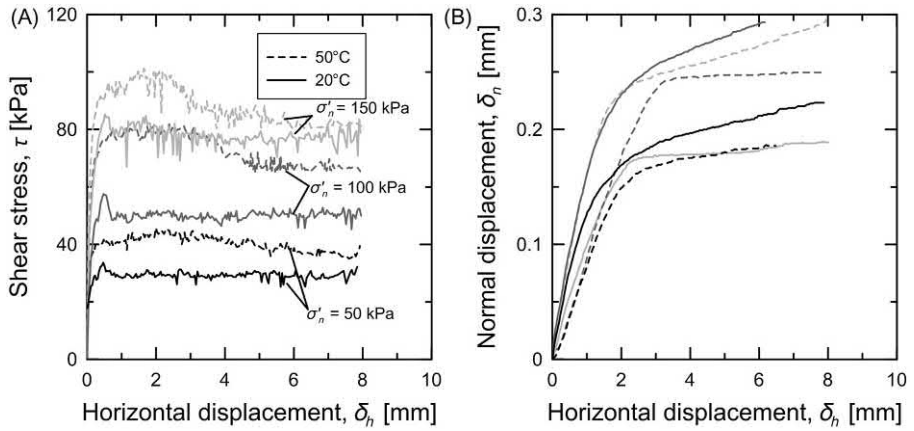

Figure 5.42 Constant normal load sand–concrete interface tests (rough) response subjected to monotonic shearing at 20°C and 50°C under constant normal load conditions: (A) shear stress–horizontal displacement plane; (B) Mohr plane. *redrawn after Di Donna, A., Ferrari, A., Laloui, L., 2015. Experimental investigations of the soil–concrete interface: physical mechanisms, cyclic mobilisation and behaviour at different temperatures. Can. Geotech. J. 53 (4), 659–672.*

5.8.2 Strength of clay–concrete interfaces

The strength of structural interfaces with fine-grained soils under nonisothermal conditions exhibits a slight sensitivity to temperature variations. This evidence is related to the more pronounced sensitivity of fine-grained soils to temperature variations compared to coarse-grained soils, both in terms of volumetric and deviatoric behaviour.

The typical response to monotonic shearing under CNL conditions of a clay–concrete interface at 50°C (initially under NC conditions, heated at the desired temperature and then sheared) and at the ambient temperature of 20°C is presented in Fig. 5.42 with reference to the result of Di Donna et al. (2015). The results at high temperature show an increase in the interface shear strength and a reduction in the contraction during shearing with respect to the response at ambient temperature. This response is attributed to the effect of the thermal collapse produced during the heating phase prior to the shearing phase. The considered phenomenon indicates that a higher force is necessary to shear a previously heated interface (as the material has a higher preconsolidation stress) compared to an interface at constant temperature. Yet, this phenomenon results in a peak strength (at small displacements) that is not present at ambient temperature, while generally in a greater shear strength at constant volume conditions (large displacements).

The increase of strength with increasing temperature for interfaces with fine-grained soils initially under NC conditions, then heated and eventually sheared can be

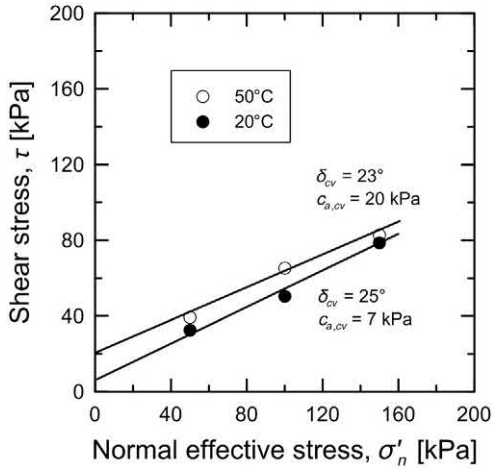

Figure 5.43 Clay–concrete interface (rough) failure envelope at 20°C and 50°C. *Redrawn after Di Donna, A., Ferrari, A., Laloui, L., 2015. Experimental investigations of the soil–concrete interface: physical mechanisms, cyclic mobilisation and behaviour at different temperatures. Can. Geotech. J. 53 (4), 659–672.*

appreciated in Fig. 5.43. The interface angle of shear strength reduces slightly at high temperature but the most significant thermal effect is found to be an increase of the adhesion (under constant volume conditions), $c_{a,cv}$, between the two tested materials. This is related to the thermal collapse of the clay, which results in an increase of the contact surface between the two materials. The same effect is shown for both high and medium rough interfaces, the second one having lower adhesion at both ambient and high temperatures because of the smaller asperities. The observed behaviour is different from the one known for clay itself (whose strength under constant volume conditions is recognised to be insensitive to temperature variations), as it is representative of the clay–concrete interface. The observed adhesion of the clay to the concrete increases from approximately 7 kPa at 20°C to approximately 20 kPa at 50°C, while the interface angle of shear strength decreases from 25 to 23 degrees for the same temperature difference.

Complementary data that support the previous considerations are reported in Fig. 5.44 with reference to data presented by Di Donna et al. (2015) for clay–concrete interfaces subjected to cyclic shearing under CNS conditions at the temperature levels of 20°C and 50°C. The lower normal stiffness value (200 kPa/mm) is responsible for the limited cyclic interface degradation that is likely to be encountered with geostructures installed in clays with respect to sands. While qualitatively similar observation to those highlighted for sand–concrete interfaces tested under CNS can be made, a higher number of cycles is required to degrade the strength of

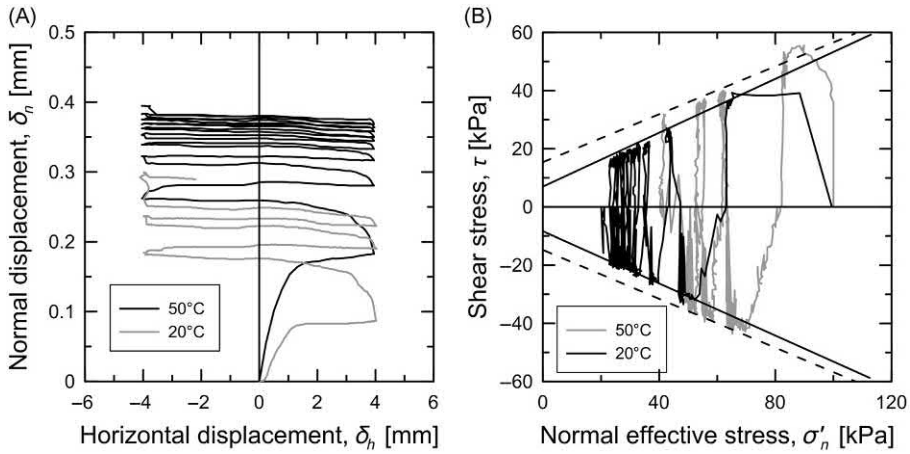

Figure 5.44 Clay–concrete interface (medium roughness) response subjected to cyclic shearing at 20°C and 50°C under constant normal stiffness conditions. (A) volumetric behaviour and (B) failure envelope. *Redrawn after Di Donna, A., Ferrari, A., Laloui, L., 2015. Experimental investigations of the soil–concrete interface: physical mechanisms, cyclic mobilisation and behaviour at different temperatures. Can. Geotech. J. 53 (4), 659–672.*

the clay–concrete interface. As for the monotonic clay–concrete interface tests with rough concrete, it appears that the higher the temperature, the lower the volume contraction during shearing cycles and thus the slower the cyclic degradation. Yet, the interface angle of shear strength reduces slightly at higher temperature but the adhesion between the two materials increases. The adhesion at 50°C (12 kPa) is three times higher than the one at 20°C (4 kPa), even if in this case it is lower with respect to the rough concrete case. This evidence confirms that it comes from the contact area between the soil and the concrete asperities, which is lower in the case of smoother surface.

5.9 Thermally induced effects on soil–concrete interface properties

Based on current experimental evidence (Xiao et al., 2014; Di Donna et al., 2015; Yavari et al., 2016; Yazdani et al., 2019), the behaviour of interfaces with coarse-grained soils does not appear to be affected by temperature variations, while that of interfaces with fine-grained soils shows a variation of strength with temperature. In particular, an increase in the strength with temperature is observed for concrete interfaces with fine-grained soils initially under NC conditions, then heated and eventually sheared (monotonically or cyclically). Based on the previous result, the direct effect of temperature on the soil–structure interface is absent in the case of concrete interfaces

with sand while globally appears to be on the safety side for interfaces with clay because it increases the interface strength (Di Donna et al., 2015).

When calculating the capacity of geostructures in terms of effective stress, the angle of shear strength of the interface is included while the adhesion is neglected. Therefore, a decrease of the strength of interfaces with fine-grained soils for an increase in temperature would arise from capacity formulations due to the decrease in the angle of shear strength of such interfaces. However, the actual increase in the shear strength of the considered interfaces with temperature by means of the contribution of the adhesion supports the use of a constant value of interface angle of shear strength (e.g. determined at ambient temperature) in capacity formulations.

A cyclic mechanical degradation of the interface shear stress induced by the thermoelastic expansion and contraction of the structural material at the interface with the soil may be observed. This effect is similar to the cyclic degradation phenomenon caused by cyclic mechanical loads applied to interfaces with conventional structures. It is typically more pronounced for coarse-grained soils compared to fine-grained soils because of the more significant volumetric cyclic contraction of the interface in the former case compared to the latter. In the case of interfaces with initially NC fine-grained soils, the cyclic volumetric contraction is even reduced by the increase in temperature, as the soil first undergoes a thermal collapse thus reducing the soil potential of collapse during shearing (Di Donna et al., 2015). Cyclic degradation effects may be considered in the analysis and design of energy geostructures. These effects are assumed to play a central role in the characterisation of the deformation of energy geostructures, especially for situations in which significant mechanical loads are applied. The reason for this is that, together with subsequently applied cyclic thermal loads, significant mechanical loads (even if approximately constant over time) may involve noteworthy degradation effects. When cyclic effects are considered limited in magnitude or absent, they can be omitted in the analysis and design of energy geostructures.

References

Abuel-Naga, H.M., Bergado, D.T., Ramana, G.V., Grino, L., Rujivipat, P., Thet, Y., 2006. Experimental evaluation of engineering behavior of soft Bangkok clay under elevated temperature. J. Geotech. Geoenviron. Eng. 132 (7), 902–910.

Abuel-Naga, H.M., Bergado, D.T., Lim, B.F., 2007. Effect of temperature on shear strength and yielding behavior of soft Bangkok clay. Soils Found. 47 (3), 423–436.

Agar, J.G., 1984. Geotechnical Behaviour of Oil Sands at Elevated Temperatures and Pressures. (Ph.D. thesis), Univerity of Alberta, Edmonton, AB.

Agar, J.G., Morgenstern, N.R., Scott, J.D., 1986. Thermal expansion and pore pressure generation in oil sands. Can. Geotech. J. 23 (3), 327–333.

Agar, J.G., Morgenstern, N.R., Scott, J.D., 1987. Shear strength and stress–strain behaviour of Athabasca oil sand at elevated temperatures and pressures. Can. Geotech. J. 24 (1), 1–10.

ASTM D2487, 2017. Standard Practice for Classification of Soils for Engineering Purposes (Unified Soil Classification System). ASTM international.
Baldi, G., Hueckel, T., Pellegrini, R., 1988. Thermal volume changes of the mineral–water system in low-porosity clay soils. Can. Geotech. J. 25 (4), 807–825.
Baldi, G., Hueckel, T., Peano, A. & Pellegrini, R. (1991) Developments in modelling of thermohydro-geomechanical behaviour of Boom clay and clay-based buffer materials (vol 2). Commission of the European Communities.
Bolzon, G., Schrefler, B.A., 2005. Thermal effects in partially saturated soils: a constitutive model. Int. J. Numer. Anal. Methods Geomech. 29 (9), 861–877.
Boudali, M., Leroueil, S., Srinivasa Murthy, B.R., 1994. Viscous behaviour of natural clays In: Proceedings of the 13th International Conference on Soil Mechanics and Foundation Engineering, vol. 1, New Delhi, India, pp. 411–416.
Boulon, M., Foray, P., 1986. Physical and numerical simulation of lateral shaft friction along offshore piles in sand. In: Proceedings of the 3rd International Conference on Numerical methods in Offshore Piling, Nantes, France, pp. 127–147.
Bourne-Webb, P., Burlon, S., Javed, S., Kürten, S., Loveridge, F., 2016. Analysis and design methods for energy geostructures. Renew. Sustain. Energy Rev. 65, 402–419.
Brumund, W., Leonards, G., 1973. Experimental study of static and dynamic friction between sand and typical constuction materials. J. Test. Eval. 1 (2), 162–165.
Burghignoli, A., Desideri, A., Miliziano, S., 2000. A laboratory study on the thermomechanical behaviour of clayey soils. Can. Geotech. J. 37 (4), 764–780.
Burland, J.B., 1973. Shaft friction of piles in clay - a simple fundamental approach. Ground Eng. 6 (3), 30–42.
Campanella, R.G., Mitchell, J.K., 1968. Influence of temperature variations on soil behavior. J. Soil Mech. Found. Div. 94 (SM3), 709–734.
Cekerevac, C., 2003. Thermal Effects on the Mechanical Behaviour of Saturated Clays: An Experimental and Numerical Study. EPFL Lausanne.
Cekerevac, C., Laloui, L., 2004. Experimental study of thermal effects on the mechanical behaviour of a clay. Int. J. Numer. Anal. Methods Geomech. 28 (3), 209–228.
Chapman, D.L., 1913. LI. A contribution to the theory of electrocapillarity. Philos. Mag. Ser. 6 25 (148), 475–481.
Chen, K., Cole, J., Conger, C., Draskovic, J., Lohr, M., Klein, K., et al., 2006. Granular materials: packing grains by thermal cycling. Nature 442 (7100), 257.
Chen, K., Harris, A., Draskovic, J., Schiffer, P., 2009. Granular fragility under thermal cycles. Granul. Matter 11, 237–242.
Coccia, C.J.R., McCartney, J.S., 2016a. Thermal volume change of poorly draining soils I: critical assessment of volume change mechanisms. Comput. Geotech. 80, 26–40.
Coccia, C.J.R., McCartney, J.S., 2016b. Thermal volume change of poorly draining soils II: model development and experimental validation. Comput. Geotech. 80, 16–25.
Cui, Y.J., Sultan, N., Delage, P., 2000. A thermomechanical model for saturated clays. Can. Geotech. J. 37 (3), 607–620.
De Boer, R., Ehlers, W., 1990. The development of the concept of effective stresses. Acta Mech. 83 (1–2), 77–92.
De Jong, J.T., Randolph, M., White, D.J., 2003. Interface load transfer degradation during cyclic loading: a microscale investigation. Soil Found. 43 (4), 81–93.
De Jong, J.T., White, D.J., Randolph, M., 2006. Microscale observation and modelling of soil–structure interface behaviour using particle image velocimetry. Soil Found. 46 (1), 15–28.
Delage, P., Sultan, N., Cui, Y.J., 2000. In the thermal consolidation of Boom clay. Can. Geotech. J. 37, 343–354.
Del Olmo, C., Fioravante, V., Gera, F., Hueckel, T., Mayor, J.C., Pellegrini, R., 1996. Thermomechanical properties of deep argillaceous formations. Eng. Geol. 41 (1-4), 87–102.
Demars, K.R., Charles, R.D., 1982. Soil volume changes induced by temperature cycling. Can. Geotech. J. 19 (2), 188–194.

Despax, D., 1976. Influence de la température sur les propriétés mécaniques des argiles saturées (Ph.D. Thesis), Ecole Centrale Paris, Paris, France.
Di Donna, A., 2014. Thermomechanical aspects of energy piles. Laboratory of Soil Mechanics. Swiss Federal Institute of Technology in Lausanne (EPFL), Lausanne, Switzerland.
Di Donna, A., Laloui, L., 2013. Soil response under thermomechanical conditions imposed by energy geostructures. In: Laloui, L., Di Donna, A. (Eds.), Energy Geostructures: Innovation in Underground Engineering. Wiley, pp. 3–21.
Di Donna, A., Laloui, L., 2015. Response of soil subjected to thermal cyclic loading: experimental and constitutive study. Eng. Geol. 190 (1), 65–76.
Di Donna, A., Ferrari, A., Laloui, L., 2015. Experimental investigations of the soil–concrete interface: physical mechanisms, cyclic mobilisation and behaviour at different temperatures. Can. Geotech. J. 53 (4), 659–672.
Eriksson, L.G., 1989. Temperature effects on consolidation properties of sulphide clays. In: Proceedings of 12th International Conference on Soil Mechanics and Foundation Engineering, vol. 3, pp. 2087–2090.
Fang, H.-Y., Daniels, J.L., 2006. Introductory Geotechnical Engineering: An Environmental Perspective. CRC Press.
Finn, F.N., 1951. The effects of temperature on the consolidation characteristics of remoulded clay. Report 126.
Fioravante, V., Ghionna, V.N., Pedroni, S., Porcino, D., 1999. A constant normal stiffness direct shear box for soil–solid interface tests. Riv. Ital. Geotec. 33 (3), 7–22.
Fleureau, J.-M., 1979. Influence d'un champ thermique ou électrique sur les phénomènes d'interaction solide–liquide dans les milieux poreux (Ph.D. Thesis). École Centrale Paris, Paris, France.
François, B., 2008. Thermoplasticity of Fine Grained Soils at Various Saturation States: Application to Nuclear Waste Disposal (Ph.D. Thesis), Swiss federal Institute of Technology (EPFL), Lausanne, Switzerland.
François, B., Laloui, L., 2008. ACMEG-TS: a constitutive model for unsaturated soils under non-isothermal conditions. Int. J. Numer. Anal. Methods Geomech. 32 (16), 1955–1988.
Gens, A., 2010. Soil–environment interactions in geotechnical engineering. Geotechnique 60 (1), 3.
Gens, A., Jardine, R., Hight, D., Coop, M., 2004. Developments in understanding soil behaviour. In: Advances in Geotechnical Engineering: The Skempton Conference. Thomas Telford, p. 103.
Ghahremannejad, B., 2003. Thermomechanical Behaviour of Two Reconstituted Clays (Ph.D. thesis), University of Sidney, Australia, p. 225.
Ghionna, V.N., Jamiolkowski, M., Lacasse, S., Ladd, C.C., Lancellotta, R. & Lunne, T. (1983) Evaluation of self-boring pressumeter. In: Proceedings of International Symposium on Soils and Rock Investigations by In-Situ Testing.
Graham, J., Tanaka, N., Crilly, T., Alfaro, M., 2001. Modified Cam-Clay modelling of temperature effects in clays. Can. Geotech. J. 38 (3), 608–621.
Highter, W.H., 1969. Temperature Effects on the Compaction and Strength Behavior of Clay. Report.
Hu, L., Pu, J., 2004. Testing and modeling of soil–structure interface. J. Geotech. Geoenviron. Eng. 130 (8), 851–860.
Hueckel, T., 2002. Reactive plasticity for clays during dehydration and rehydration. Part 1: concepts and options. Int. J. Plasticity 18, 281–312.
Hueckel, T., Baldi, G., 1990. Thermoplasticity of saturated clays—experimental constitutive study. J. Geotech. Eng. 116 (12), 1778–1796.
Hueckel, T., Borsetto, M., 1990. Thermoplasticity of saturated soils and shales: constitutive equations. J. Geotech. Eng. 116 (12), 1765–1777.
Hueckel, T., Pellegrini, R., 1989. Modelling of thermal failure of saturated clays. In: Pietruszczak, S. and Pande, G.N. (Eds.), Proceedings of International Symposium on Numerical Models in Geomechanics—NUMOG, pp. 81–90.
Hueckel, T., Pellegrini, R., 1992. Effective stress and water pressure in saturated clays during heating–cooling cycles. Can. Geotech. J. 29 (6), 1095–1102.

Hueckel, T., Pellegrini, R., Del Olmo, C., 1998. A constitutive study of thermoelasto-plasticity of deep carbonatic clays. Int. J. Numer. Anal. Methods Geomech. 22 (7), 549–574.
Hueckel, T., François, B., Laloui, L., 2009. Explaining thermal failure in saturated clays. Geotechnique 59 (3), 197–212.
Hueckel, T., François, B., Laloui, L., 2011. Temperature-dependent internal friction of clay in a cylindrical heat source problem. Geotechnique 61, 831–844.
Kingery, W.D., Bowen, H.K., Uhlmann, D.R., 1976. Introduction to Ceramics, 2nd Edition Wiley, New York.
Kosar, K.M., 1983. The Effect of Heated Foundations on Oil Sand (M. Sc. Thesis), Department of Civil Engineering, University of Alberta, Canada.
Kulhawy, F.H., O'Rourke, T., Stewart, J.P., Beech, J., 1983. Transmission Line Structure Foundations for Uplift-Compression Loading, Load Test Summaries: Appendix to EPRI Final Report EL-2870. Electric Power Research Institute.
Kuntiwattanakul, P., 1991. Effects of High Temperature on Mechanical Behavior of Clays (Ph.D. thesis), University of Tokyo, Tokyo, Japan.
Kuntiwattanakul, P., Towhata, I., Ohishi, K., Seko, I., 1995. Temperature effects on undrained shear characteristics of clay. Soils Found. 35 (1), 147–162.
Laloui, L., 1993. Modélisation du comportement thermohydromécanique des milieux poreux anélastique (Ph.D. thesis), Ecole Centrale de Paris.
Laloui, L., 2001. Thermomechanical behaviour of soils. Environmental Geomechanics. EPFL Press, Lausanne, pp. 809–843.
Laloui, L., Cekerevac, C., 2003. Thermoplasticity of clays: an isotropic yield mechanism. Comput. Geotech. 30 (8), 649–660.
Laloui, L., François, B., 2009. ACMEG-T: soil thermoplasticity model. J. Eng. Mech. 135 (9), 932–944.
Laloui, L., Leroueil, S., Chalindar, S., 2008. Modelling the combined effect of strain rate and temperature on one-dimensional compression of soils. Can. Geotech. J. 45 (12), 1765–1777.
Lancellotta, R., 1995. Geotechnical Engineering. Balkema, Rotterdam.
Lehane, B., Jardine, R., Bond, A.J., Frank, R., 1993. Mechanisms of shaft friction in sand from instrumented pile tests. J. Geotech. Eng. 119 (1), 19–35.
Leroueil, S., Soares Marques, M.E., 1996. Importance of strain rate and temperature effects in geotechnical engineering. Measuring and Modeling Time Dependent Soil Behavior. ASCE, pp. 1–60.
Littleton, I., 1976. An experimental study of the adhesion between clay and steel. J. Terramech. 13 (3), 141–152.
Liu, H., Xiao, Y., McCartney, J.S., Liu, H., 2018. Influence of temperature on the volume change behavior of saturated sand. Geotech. Test. J. 41 (4), 747–758.
Lo Presti, D.C.F., 1989. Proprietà dinamiche dei terreni. In: Proceedings of XIV Conferenza di Geotecnica di Torino.
Loveridge, F., Low, J., Powrie, W., 2017. Site investigation for energy geostructures. Quarterly Journal of Engineering Geology and Hydrogeology 50, 158–168.
Marques, M.E.S., Leroueil, S., Almeida, M.D.S., 2004. Viscous behaviour of St-Roch-de-l'Achigan clay, Quebec. Can. Geotech. J. 41 (1), 25–38.
Meschyan, S.R., Galstyan, R.R., 1972. Investigation of compressional creep of clay soil with consideration of temperature effects. Fundam. Mekhanika Grutov 4, 6–8.
Mitchell, J.K., Soga, K., 2005. Fundamentals of Soil Behavior. Wiley, New York.
Mitchell, J.K., Campanella, R.G., 1963. Creep studies on saturated clays. Proceedings of Laboratory Shear Testing of Soils. Institute of Transportation and Traffic Engineering, University of California.
Moritz, L., 1995. Geotechnical Properties of Clay at Elevated Temperatures. Swedish Geotechnical Institute Linköping, Sweden.
Mortara, G., Mangiola, A., Ghionna, V.N., 2007. Cyclic shear stress degradation and post-cyclic behaviour from sand–steel interface direct shear tests. Can. Geotech. J. 44 (7), 739–752.
Murayama, S., 1969. Effect of Temperature on Elasticity of Clays. HRB Special Report No. 103.
Murphy, K.D., McCartney, J.S., 2014. Thermal borehole shear device. Geotech. Test. J. 36 (3), 2014009.

Ng, C.W.W., Wang, S.H., Zhou, C., 2016. Volume change behaviour of saturated sand under thermal cycles. Géotech. Lett. 6 (2), 124–131.
Ng, C.W.W., Mu, Q., Zhou, C., 2017. Effects of boundary conditions on cyclic thermal strains of clay and sand. Géotech. Lett. 7 (1), 73–78.
Ooi, L.H., Carter, J.P., 1987. A constant normal stiffness direct shear device for static and cyclic loading. Geotech. Test. J. 10 (1), 3–12.
Paaswell, R.E., 1967. Temperature effects on clay soil consolidation. J. Soil Mech. Found. Div. 93 (SM3), 9–22.
Plum, R.L., Esrig, M.I., 1969. Some Temperature Effects on Soil Compressibility and Pore Water Pressure. Effect of Temperature and Heat on Engineering Behaviour of Soils. HRB, Special Report No. 103, pp. 231–242.
Porcino, D., Fioravante, V., Ghionna, V.N., Pedroni, S., 2003. Interface behavior of sands from constant normal stiffness direct shear tests. ASTM Geotech. Test. J. 26 (3), 289–301.
Potyondy, J.G., 1961. Skin friction between various soils and construction materials. Geotechnique 11 (4), 339–353.
Pusch, R., 1986. Permanent Crystal Lattice Contraction, a Primary Mechanism in Thermally Induced Alteration of Na Bentonite. In: MRS Online Proceedings Library, vol. 84.
Randolph, M.F., Wroth, C., 1981. Application of the failure state in undrained simple shear to the shaft capacity of driven piles. Geotechnique 31 (1), 143–157.
Recordon, E., 1993. Déformabilité des sols non saturés à diverses températures. Rev.Fr. Géotech. 65, 37–56.
Robinet, J.-C., Rahbaoui, A., Plas, F., Lebon, P., 1996. A constitutive thermomechanical model for saturated clays. Eng. Geol. 41, 145–169.
Robinet, J., Pasquiou, A., Jullien, A., Belanteur, N., Plas, F., 1997. Expériences de laboratoire sur le comportement thermohydromécanique de matériaux argileux remaniés gonflants et non gonflants. Rev. Fr. Géotech. 81, 53–80.
Romero, E., Villar, M., Lloret, A., 2005. Thermohydromechanical behaviour of two heavily overconsolidated clays. Eng. Geol. 81 (3), 255–268.
Roscoe, K.H., Burland, J.B., 1968. On the generalised stress–strain behaviour of 'wet' clay. In: Heyman, J., Leckie, F.A. (Eds.), Engineering Plasticity. Cambridge University Press, Cambridge, pp. 535–609.
Rotta Loria, A.F., 2019. Performance-based design of energy pile foundations. DFI J. 12 (2), 94–107.
Rotta Loria, A.F., Laloui, L., 2017. Thermally induced group effects among energy piles. Geotechnique 67 (5), 374–393.
Saix, C., Devillers, P., El Youssoufi, M., 2000. Eléments de couplage thermomécanique dans la consolidation de sols non saturés. Can. Geotech. J. 37 (2), 308–317.
Schofield, A., Wroth, P., 1968. Critical State Soil Mechanics. McGraw-Hill, London.
Shakir, R., Zhu, J., 2009. Behavior of compacted clay–concrete interface. Front. Archit. Civ. Eng. China 3 (1), 85–92.
Sitharam, T.G., 2003. Discrete element modelling of cyclic behaviour of granular materials. Geotech. Geol. Eng. 21 (4), 297–329.
Sittidumrong, J., Jotisankasa, A., Chantawarangul, K., 2019. Effect of thermal cycles on volumetric behaviour of Bangkok sand. Geomech. Energy Environ. 100127. https://doi.org/10.1016/j.gete.2019.100127.
Skempton, A., 1960. Significance of Terzaghi's concept of effective stress. From Theory to Practice in Soil Mechanics. Wiley.
Skempton, A., 1961. Effective stress in soils, concrete and rocks. In: Proceedings of Conference on Pore Pressure and Suction in Soils, London, pp. 4–16.
Sultan, N., Delage, P., Cui, Y., 2002. Temperature effects on the volume change behaviour of Boom clay. Eng. Geol. 64 (2–3), 135–145.
Tabucanon, J.T., Airey, D.W., Poulos, H.G., 1995. Pile skin friction in sands from constant normal stiffness tests. Geotech. Test. J. 18 (3), 350–364.
Tan, W., Lee, C., Sivadass, T., 2008. Behaviour of clay–steel interfaces. In: Proceedings of the International Conference on Construction and Building Technology, ICCBT, pp. 11–20.

Terzaghi, K., 1936. The shearing resistance of saturated soils and the angle between the planes of shear. In: First International Conference on Soil Mechanics,vol. 1, pp. 54–59.
Terzaghi, K., 1943. Theoretical Soil Mechanics. John Wiley & Sons, New York.
Tidfors, M., Sällfors, G., 1989. Temperature effect on preconsolidation pressure. Geotech. Test. J. 12 (1), 93–97.
Touret, O., Pons, C.H., Tessier, D., Tardy, Y., 1990. Etude de la repartition de l'eau dans des argiles saturees Mg^{2+} aux fortes teneurs en eau. Clay Miner. 25, 217–233.
Towhata, I., Kuntiwattanaul, P., Seko, I., Ohishi, K., 1993. Volume change of clays induced by heating as observed in consolidation tests. Soil Found. 33 (4), 170–183.
Tsubakihara, Y., Kishida, H., Nishiyama, T., 1993. Friction between cohesive soils and steel. Soils Found. 33 (2), 145–156.
Uesugi, M., Kishida, H., 1986. Frictional resistance at yield between dry sand mild steel. Soil Found. 26 (4), 139–149.
Uesugi, M., Kishida, H., Tsubakihara, Y., 1988. Behavior of sand particles in sand-steel friction. Soils Found. 28 (1), 107–118.
Vega, A., McCartney, J.S., 2014. Cyclic heating effects on thermal volume change of silt. Environ. Geotech. 2 (5), 257–268.
Wernick, E., 1978. Skin friction of cylindrical anchors in noncohesive soils. In: Symposium on Soil Reinforcing and Stabilising Techniques, pp. 201–219.
Wong, P.K.K., Mitchell, J.K., 1975. Yielding and plastic flow of sensitive cemented clay. Géotechnique 25, 763–782.
Xiao, S., Suleiman, M.T., McCartney, J.S., 2014. Shear behavior of silty soil and soil–structure interface under temperature effects. Geo-Congress 2014—Geo-Characterization and Modeling for Sustainability. ASCE, pp. 4105–4114.
Yamamoto, H., Morichi, K., Matsuoka, H., Tanaka, Y., Sun, D.A., 2003. Frictional behaviour between clay and steel by direct shear type apparatus. Deformation Characteristics of Geomaterials/ Comportement Des Sols Et Des Roches Tendres. Taylor & Francis.
Yavari, N., Tang, A.M., Pereira, J.-M., Hassen, G., 2016. Effect of temperature on the shear strength of soils and the soil–structure interface. Can. Geotech. J. 53 (999), 1–9.
Yazdani, S., Helwany, S., Olgun, G., 2019. Influence of temperature on soil–pile interface shear strength. Geomech. Energy Environ. 18, 69–78.
Zhou, C., Ng, C., 2015. A thermomechanical model for saturated soil at small and large strains. Can. Geotech. J. 52 (8), 1101–1110.
Zhou, C., Ng, C.W.W., Wang, S., 2017. Modelling volume changes of sand under thermal loads: a preliminary attempt. Géotech. Lett. 7 (1), 68–72.

Questions and problems

Statements

a. Gravity forces dominate interactions between phases in fine-grained soils:
  i. True
  ii. False

b. Coarse-grained soils are generally more sensitive to temperature variations than fine-grained soils:
  i. True
  ii. False

c. Define the *OCR*. State for which values of this parameter soils can typically be considered normally consolidated (NC) or overconsolidated (OC).

d. Describe the essential features of the behaviour of fine-grained soils to one heating–cooling cycle depending on the consolidation state.

e. The apparent preconsolidation pressure decreases at constant void ratio with increasing temperature:
  i. True
  ii. False

f. Fine-grained soils under NC conditions expand upon heating:
  i. True
  ii. False

g. Describe the phenomenon of plastic accommodation.

h. Describe the relationship between plasticity index and thermally induced volumetric strains of fine-grained soils.

i. Coarse-grained materials can be characterised by the thermal collapse phenomenon:
  i. True
  ii. False

j. The yield surface of fine-grained soils shrinks at constant void ratio with increasing temperature:
  i. True
  ii. False

k. The shrinkage of the yield surface with increasing temperature that is observed for fine-grained soils is not homothetic, depends on the stress history and is associated with thermal softening:
  i. True
  ii. False

l. Compressibility parameters can be considered insensitive to temperature variations:
  i. True
  ii. False

m. Employing a constant value of Young's modulus with temperature in the analysis and design of energy geostructures can be considered appropriate:
  i. True
  ii. False

n. The angle of shear strength of soils under constant volume conditions markedly varies with temperature:
  i. True
  ii. False

o. The slope of the critical state line depends on temperature:
  i. True
  ii. False

p. The primary consolidation coefficient markedly varies with temperature:
  i. True
  ii. False

q. Define the structure roughness and specify how this parameter can be used to characterise interfaces as smooth or rough.

r. Smooth interfaces show a higher shear resistance compared to rough interfaces:
  i. True
  ii. False

s. Smooth interfaces with a soil show a higher shear resistance compared to that of the soil:
  i. True
  ii. False

t. Define the main parameters that influence the mechanical response of soil–structure interfaces.

u. Define constant normal stiffness and constant normal load conditions. Which conditions is representative of the state of restraint characterising interfaces between geostructures and the surrounding ground?

v. Describe the three failure modes that can characterise soil–structure interfaces.

w. The shear strength of interfaces between concrete and coarse-grained soils is highly influenced by temperature variations:
  i. True
  ii. False

x. The shear strength of interfaces between concrete and fine-grained soils varies with temperature:
  i. True
  ii. False

y. The cyclic mechanical degradation of the interface shear stress induced by the thermoelastic expansion and contraction of the structural material at the interface with the soil should be considered in the analysis and design of energy geostructures, in all cases and irrespective of the magnitude of the applied loads:
  i. True
  ii. False

Solutions

a. Gravity forces dominate interactions between phases in fine-grained soils:
  i. True
  ii. False

b. Coarse-grained soils are generally more sensitive to temperature variations than fine-grained soils:
  i. True
  ii. False

c. The overconsolidation ratio, OCR [−], is defined as the ratio between the preconsolidation stress, $\sigma_p^{'}$ [Pa], and the overburden vertical effective stress, $\sigma_z^{'}$ [Pa]. soils are considered NC if the $1 \leq OCR \leq 2$, while they are considered OC if $OCR > 2$.

d. Under NC conditions, fine-grained soils contract when heated and a significant part of this deformation is not recovered upon cooling. Under highly OC conditions, fine-grained soils expand when heated and this deformation is entirely recovered upon cooling. Under slightly OC conditions, fine-grained soils show an initial expansion and subsequent contraction when heated, followed by a tendency towards contraction upon cooling.

e. The apparent preconsolidation pressure decreases at constant void ratio with increasing temperature:
  i. True
  ii. False

f. Fine-grained soils under NC conditions expand upon heating:
  i. True
  ii. False

g. The phenomenon of plastic accommodation involves a decrease of plastic volumetric strain over subsequent heating−cooling cycles applied to NC soils.

h. The contractive thermally induced volumetric strains that characterise fine-grained soils under NC conditions increase with the plasticity index of the soil.

i. Coarse-grained materials can be characterised by the thermal collapse phenomenon:
   i. True
   ii. False

j. The yield surface of fine-grained soils shrinks at constant void ratio with increasing temperature:
   i. True
   ii. False

k. The shrinkage of the yield surface with increasing temperature that is observed for fine-grained soils is not homothetic, depends on the stress history and is associated with thermal softening:
   i. True
   ii. False

l. Compressibility parameters can be considered insensitive to temperature variations:
   i. True
   ii. False

m. Employing a constant value of Young's modulus with temperature in the analysis and design of energy geostructures can be considered appropriate:
   i. True
   ii. False

n. The angle of shear strength of soils under constant volume conditions markedly varies with temperature:
   i. True
   ii. False

o. The slope of the critical state line depends on temperature:
   i. True
   ii. False

p. The primary consolidation coefficient markedly varies with temperature:
   i. True
   ii. False

q. The structure roughness is commonly identified through the normalised roughness, R_n [−], which is defined as the ratio between the maximum

vertical distance between the highest and lowest peaks of the structure asperities over a fixed length, R_{max} [m], the soil mean grain size, D_{50} [m]. Depending on the interface materials and conditions, it is possible to identify a critical value of roughness, R_{cr} [−], such that if $R_n < R_{cr}$ the interface is considered smooth, and if $R_n > R_{cr}$ the interface is considered rough.

r. Smooth interfaces show a higher shear resistance compared to rough interfaces:
   i. True
   ii. False

s. Smooth interfaces with a soil show a higher shear resistance compared to that of the soil:
   i. True
   ii. False

t. The main factors that affect the behaviour of soil−structure interfaces are (i) the structure roughness, (ii) the normal stress acting on the structure, (iii) the soil density, (iv) particle angularity and (v) the soil grain size distribution.

u. Under constant normal load conditions, the normal effective stress applied to the interface remains constant upon loading, so that $\sigma'_n = \text{const}$. Under constant normal stiffness conditions, the normal effective stress applied to the interface varies with loading as $\sigma'_n = \sigma'_{n0} + \Delta\sigma'_n = \sigma'_{n0} - K_{int}\Delta\delta_n$, where σ'_{n0} and $\Delta\sigma'_n$ are the initial and increment of the normal effective stress [Pa], respectively; K_{int} is the far-field normal stiffness [Pa/m]; and $\Delta\delta_n$ is the variation of displacement normal to the interface [m]. Constant normal stiffness conditions are representative of the state of restraint characterising interfaces between geostructures and the surrounding ground.

v. Depending on the structure roughness, three failure modes can characterise soil−structure interfaces: mode 1 characterises rough interface surfaces and involves shear failure in the soil; mode 2 characterises smooth interfaces surfaces and involves full sliding at the interface; mode 3 involves shear failure and sliding displacement occurring simultaneously.

w. The shear strength of interfaces between concrete and coarse-grained soils is highly influenced by temperature variations:
   i. True
   ii. False

x. The shear strength of interfaces between concrete and fine-grained soils varies with temperature:
   i. True
   ii. False

y. The cyclic mechanical degradation of the interface shear stress induced by the thermoelastic expansion and contraction of the structural material at the interface with the soil should be considered in the analysis and design of energy geostructures, in all cases and irrespective of the magnitude of the applied loads:
   i. True
   ii. False

CHAPTER 6

Thermomechanical behaviour of single energy piles

6.1 Introduction

Energy pile foundations, similar to conventional pile foundations, consist of two components: a group of piles and a pile cap (the latter being intended as the general structural element connecting the piles to the superstructure). Addressing the response of the piles in a group is crucial for a comprehensive understanding of the behaviour of any pile foundation. At the same time, in many practical cases, considering the piles as single isolated elements represents the starting point of any analysis and design. This approach is considered hereafter for energy piles subjected to the mechanical *and* thermal loads associated with their structural support and geothermal heat exchanger roles.

The application of mechanical and thermal loads to energy piles introduces novel aspects in the mechanical response of such foundations compared to that characterising conventional piles typically subjected to only mechanical loads because of their sole structural support role. The reason for this is because, as a consequence of the coupling between the heat transfer and the deformation of materials previously treated in Part B of this book, thermal loads induce thermal expansions and contractions of both the piles and the surrounding soil as well as modifications of the stress state. Understanding the influence of thermal loads, applied alone or in conjunction with mechanical loads, is key to address the thermomechanical behaviour of energy piles.

To investigate the response of single energy piles to mechanical and thermal loads, various approaches can be employed. Full-scale in situ tests, model-scale laboratory tests and centrifuge tests are example of experimental approaches. In general, more remarkable financial expenditures are required to run full-scale in situ tests compared to model-scale laboratory tests and centrifuge tests. Despite this limitation, the capability of full-scale in situ tests to provide data unaffected by scale effects that can potentially characterise the results of model-scale laboratory tests and centrifuge tests can make such an approach preferable for analysis and design purposes.

This chapter presents an analysis of the response of single energy piles subjected to mechanical and thermal loads based on the results of full-scale in situ tests. A focus is devoted to energy piles subjected to mechanical and heating thermal loads, although the influence of cooling thermal loads can be inferred from the results presented.

Analysis and Design of Energy Geostructures
DOI: https://doi.org/10.1016/B978-0-12-816223-1.00006-0

To address the aforementioned aspects, *idealisations and assumptions* are presented first: in this context, the objective is to propose a summary of the assumptions made to interpret the response of energy piles subjected to mechanical and thermal loads. Second, the *classification of single energy piles* is treated: the objective of this part is to summarise a characterisation of the types of single energy piles. Third, the *temperature variations* in energy piles are discussed: in this context the purpose is to expand on the thermal field characterising energy piles. Next, the *thermally induced vertical and radial strains* characterising energy piles are treated: in this framework the purpose is to discuss the influence of thermal loads on the deformation of energy piles. Afterward, the *thermally and mechanically induced variations in vertical displacement, shear stress and vertical stress* characterising energy piles are discussed: the purpose of this part is to expand on the variation of the considered variables along energy piles and to highlight crucial differences between the influence of thermal loads compared to mechanical loads. Then, the *variations in degree of freedom* are considered: in this context the purpose is to comment on the response of energy piles depending on the restraint provided by the ground and the superstructure characterising such foundations. Finally, *questions and problems* are proposed: the purpose of this part is to fix and test the understanding of the subjects covered in this chapter by addressing a number of exercises.

6.2 Idealisations and assumptions

As previously highlighted in Part B of this book, the materials constituting energy geostructures, soils and rocks are nonhomogeneous. However, in many cases, an effective analysis approach can resort to the continuum medium idealisation while considering the materials isotropic and homogeneous. This approach is again considered for the forthcoming interpretation of the thermomechanical behaviour of energy piles (cf. Fig. 6.1A).

While in practice piles are not often exactly characterised by a cylindrical shape and the surrounding soil layers are not fully horizontal, assuming the considered conditions markedly simplifies the analysis of pile response. Accordingly, these hypotheses are accounted for the following developments (cf. Fig. 6.1B).

Thermal and mechanical loads involve nonuniform variations of the temperature, stress, strain and displacement fields within (and around) energy piles (Abdelaziz and Ozudogru, 2016; Caulk et al., 2016; Rotta Loria and Laloui, 2017). Despite a fine analysis of the response of energy piles would require consideration of the actual nonuniform nature of the considered fields, in the following it is assumed that the reported variations in temperature, stress, strain and displacement are uniform and representative of the energy pile response (cf. Fig. 6.1C). The validity of this hypothesis increases at successive stages of the geothermal operation of energy piles and for more uniform pipe configurations within the cross-section of energy piles.

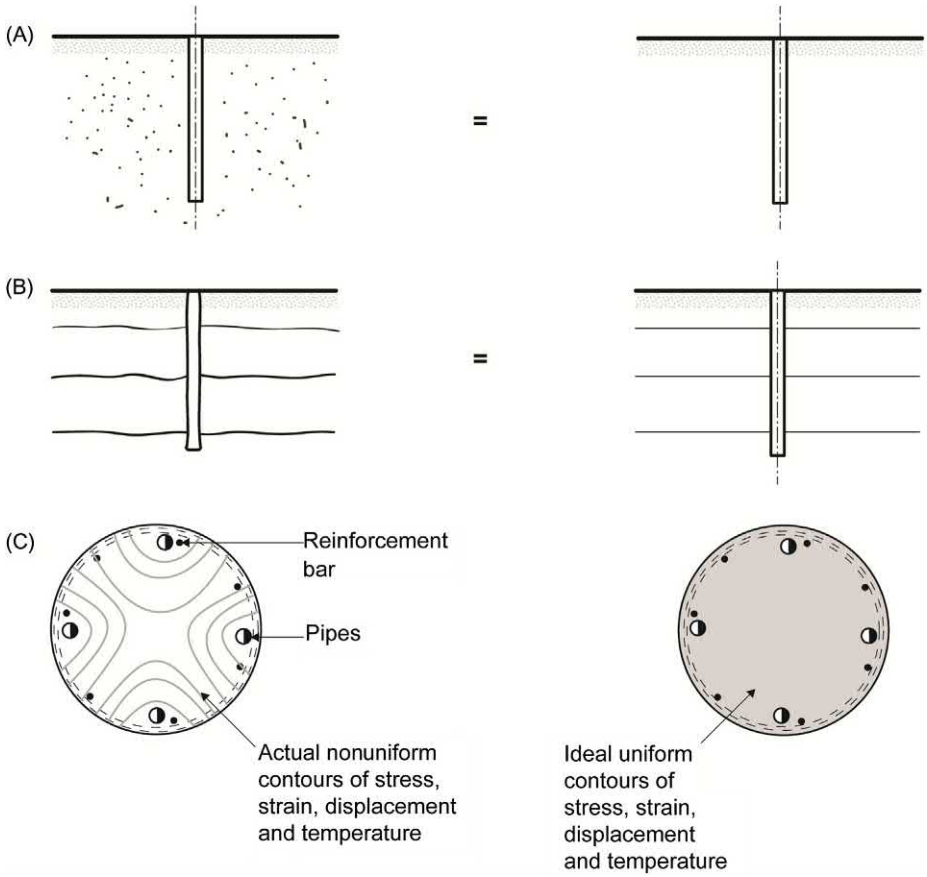

Figure 6.1 (A) Modelling approach of nonhomogeneous soil deposits; (B) modelling approach of nonhorizontal soil layers; and (C) idealisation of stress, strain, displacement and temperature fields within energy piles.

The sign convention considered in the following coincides with that employed thus far. That is contractive strains, downward displacements, compressive stresses and increases in angles in the anticlockwise direction are considered to be positive.

6.3 Classification of single energy piles

Energy piles can be classified in different types according to various criteria. These criteria can be considered to coincide with those available for conventional piles [see, e.g. Tomlinson and Woodward (1993) and Fleming et al. (2008)].

A widely used classification criterion refers to the pile installation technique because this aspect has the greatest influence on the response of such foundations to

loading (De Beer, 1988). Various pile installation techniques do exist and increasing combinations of such techniques are observed in practice. So-called *displacement piles* and *nondisplacement piles* can be broadly distinguished according to a classification criterion based on the pile installation technique. Displacement piles are installed by driving them into the ground and include, without being limited to, so-called driven piles. During installation, a marked disturbance of the ground is generated because of the penetration of the piles and noteworthy ground displacements in the radial direction are observed (Lancellotta, 1995). To highlight this phenomenon the term 'displacement' is employed to characterise such foundations. Nondisplacement piles are installed by excavating the ground for a successive filling with (reinforced) concrete and include, without being limited to, so-called bored piles. During installation the boring process causes lateral stresses in the ground to decrease with only a partial recovery upon concreting and limited ground displacements are observed (Lancellotta, 1995). To highlight this phenomenon the term 'nondisplacement' is employed to characterise such foundations.

Another classification criterion refers to the pile bearing behaviour. Piles subjected to loads that primarily influence the longitudinal (e.g. axial) pile response are characterised by the generation of shear stresses along the shaft and normal stresses at the toe ensuring equilibrium. These stresses contribute with those mobilised by the cap in the overall equilibrium of the foundation. So-called predominantly *end-bearing piles* and *friction* (or *floating*) *piles* can be broadly distinguished according to a classification criterion based on the pile bearing behaviour and associated contributions of load-carrying capacity provided by the shaft and the toe. Piles that penetrate a relatively soft layer of soil to found on a firmer stratum are generally referred to as end-bearing piles because the normal stresses mobilised at the pile toe (i.e. by the end-bearing) represent the higher contribution to the pile load-carrying capacity. Piles that do not found on a particularly firm stratum are generally referred to as floating piles because they derive most of their capacity from the shear stresses mobilised at the shaft. In fine-grained (e.g. cohesive) soil, the shaft capacity of both displacement and nondisplacement piles is generally paramount. In coarse-grained (e.g. noncohesive) soil, the overall pile capacity is more evenly divided between shaft and base.

6.4 Temperature variations

Notable temperature variations can develop in energy piles as a consequence of their geothermal operation. For given boundary conditions, the rate of these temperature variations depends on the thermal power applied to the energy piles as well as on the thermohydraulic properties of both the pile and the surrounding ground. For given applied thermal power and thermal conductivity of the grouting material characterising energy piles, lower values of thermal conductivity of the ground and groundwater

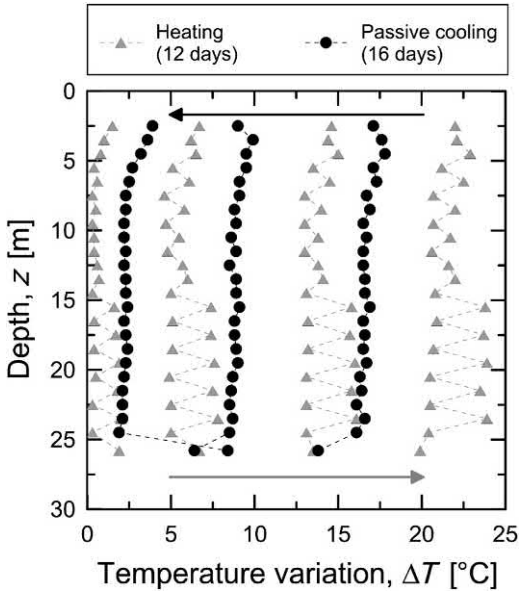

Figure 6.2 Temperature variations along an energy pile throughout a heating–passive cooling cycle. *Redrawn after Laloui, L., Moreni, M., Vulliet, L., 2003a. Comportement d'un pieu bi-fonction, fondation et échangeur de chaleur. Can. Geotech. J. 40 (2), 388–402.*

flow velocity result in greater temperature variations in energy piles. Variations of the boundary conditions at the surface can markedly influence the temperature field characterising energy piles (Bidarmaghz et al., 2016), especially when the piles are characterised by a limited length.

Maximum average temperature variations of $\overline{\Delta T} = 30°C$ and minimum average temperature variations of $\overline{\Delta T} = -15°C$ can be expected along energy piles for typical operating conditions. An example of the temperature variations along the depth z of a single energy pile free to move vertically at its head is shown in Fig. 6.2 with reference to the results presented by Laloui et al. (2003a). In the considered case study, the heating of the energy pile for a time of $t = 12$ days resulted in an average temperature variation along its length of $\overline{\Delta T} = 22°C$.

6.5 Thermally induced vertical strain variations

Thermal loads applied to energy piles generate expansive pile strains upon heating and contractive pile strains upon cooling. These strains are usually not uniform with depth. Their evolution depends on the end-restraint provided by the presence of the ground and the superstructure. The stiffer the ground surrounding energy piles, the lower the

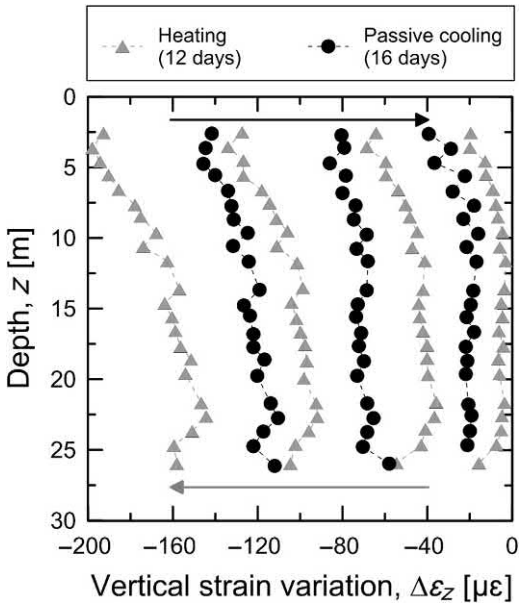

Figure 6.3 Vertical strain variations along an energy pile throughout a heating–passive cooling cycle. *Redrawn after Laloui, L., Moreni, M., Vulliet, L., 2003a. Comportement d'un pieu bi-fonction, fondation et échangeur de chaleur. Can. Geotech. J. 40 (2), 388–402.*

observed thermally induced strains. The same applies for the structural element potentially present at the head of energy piles.

Typical values of average expansive vertical strain variations caused by the temperature variations between $\overline{\Delta T} = 15°C$ and $30°C$ of approximately $\overline{\Delta\varepsilon_z} = -100$ to $-250\ \mu\varepsilon$ can be observed in energy piles. The opposite holds for cooling thermal loads applied to energy piles [see, e.g. Bourne-Webb et al. (2009)]. An example of thermally induced strains along a single energy pile free to move vertically at its head is shown in Fig. 6.3 with reference to the results presented by Laloui et al. (2003a). In the considered case study, an average temperature variation along the energy pile of $\overline{\Delta T} = 22°C$ resulted in average expansive vertical strains of $\overline{\Delta\varepsilon_z} = -180\ \mu\varepsilon$.

When energy piles are (at least theoretically) free to move vertically at their head, the thermally induced vertical strain variations approach those under free expansion conditions towards the pile head (Bourne-Webb et al., 2009; Mimouni and Laloui, 2013). An example of this phenomenon is shown in Fig. 6.4, which shows a comparison between the observed thermally induced vertical strain variation and the strain associated with free thermal expansion conditions along the energy pile tested by Laloui et al. (2003a). These findings are based on the linear thermal expansion coefficient of the pile, α_{EP}, and the average temperature variation applied along the pile length, $\overline{\Delta T}$ (i.e. $\overline{\Delta\varepsilon_f^{th}} = -\alpha_{EP}\overline{\Delta T}$).

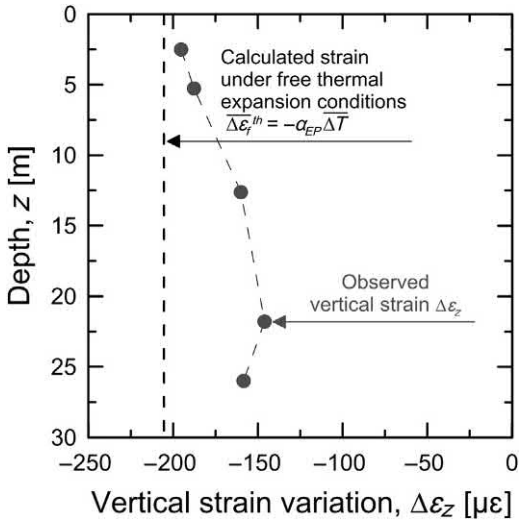

Figure 6.4 Comparison between the thermally induced vertical strain measured in a single energy pile free to move vertically at its head and the corresponding vertical strain under free expansion conditions. *Redrawn after Laloui, L., Moreni, M., Vulliet, L., 2003a. Comportement d'un pieu bi-fonction, fondation et échangeur de chaleur. Can. Geotech. J. 40 (2), 388–402.*

Observed thermally induced vertical strains in energy piles caused by heating thermal loads are often associated with a reversible, that is thermoelastic, character. This evidence was noted, for example, by Laloui et al. (2003a) and is reported in Fig. 6.5 considering the evolution of vertical strain variation at selected depths along a single energy pile free to move vertically at its head for different temperature variations applied to the pile.

6.6 Thermally induced radial strain variations

Radial strains develop in energy piles because of the applied thermal loads along with the thermally induced vertical strains. For the same temperature variation applied to energy piles, comparable vertical and radial strains caused by the temperature variations can be observed. However, due to the different dimensions characterising the length and the diameter of energy piles, the vertical and horizontal pile displacements associated with the considered strains are markedly different, the former being much more significant than the latter.

Observed thermally induced radial strain variations in energy piles can be associated with a reversible behaviour (Mimouni and Laloui, 2015; Rotta Loria and Laloui, 2017). In other words, lateral contact is maintained between the energy pile and the ground after a thermal cycle. Fig. 6.6 shows the evolution of radial strains for an

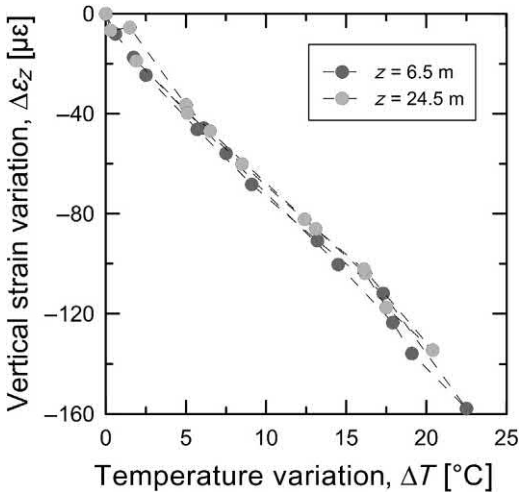

Figure 6.5 Evolution of thermally induced strains in an energy pile upon a heating−passive cooling cycle at depths of $z = 6.5$ m ($z/L = 0.25$) and $z = 24.5$ m ($z/L = 0.95$). *Redrawn after Laloui, L., Moreni, M., Vulliet, L., 2003a. Comportement d'un pieu bi-fonction, fondation et échangeur de chaleur. Can. Geotech. J. 40 (2), 388−402.*

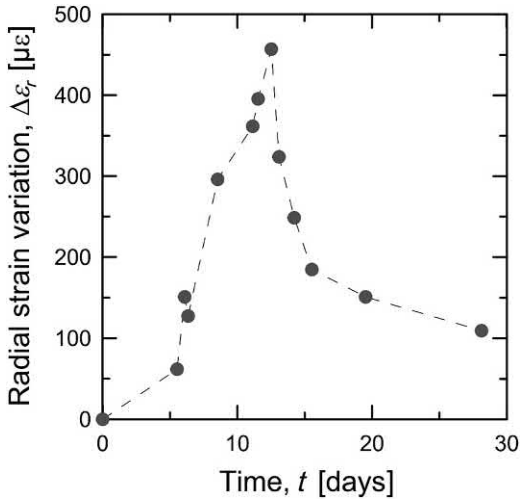

Figure 6.6 Evolution of thermally induced radial strain in an energy pile throughout a heating−passive cooling cycle. *Redrawn after Laloui, L., Nuth, M., Vulliet, L., 2006 Experimental and numerical investigations of the behaviour of a heat exchanger pile. Int. J. Numer. Anal. Methods Geomech. 30 (8), 763−781.*

energy pile free to move vertically at its head with reference to the results presented by Laloui et al. (2006). In this example, the strains do not completely recover at the end of the heating−passive cooling cycle because the initial and final temperature values characterising the energy pile are different.

6.7 Thermally and mechanically induced vertical displacement variations

The application of thermal loads along energy piles involves at best a linear distribution of the vertical displacement with depth and at worst a notably nonlinear distribution of the vertical displacement (becoming more pronounced with increasing pile compressibility and slenderness) (Rotta Loria et al., 2018). This consideration is applicable to the analysis of both rigid and deformable piles whether they have a predominantly floating or end-bearing character. In general, heating thermal loads cause energy pile head heaves while cooling thermal loads cause energy pile head settlements. The reason for this is due to the fact that thermal loads applied to energy piles generally involve two pile portions that displace in opposite directions from the so-called null point of the vertical displacement (located at a depth, $z_{NP,w}$) (Laloui et al., 2003a). The location of the null point depends on the end-restraint conditions (Mimouni and Laloui, 2014; Rotta Loria et al., 2015; Sutman et al., 2018). For an infinitely rigid base, the null point is located at the toe of energy piles. For an infinitely rigid slab, the null point is located at the pile head. In practice the null point is located somewhere along the length of the energy pile and always closer to the region of the system characterised by the higher restraint.

An example of the head heave of an energy pile free to move vertically at its head under the application of a heating–passive cooling cycle is shown in Fig. 6.7 with reference to the results presented by Laloui et al. (2003a). An average temperature variation along an energy pile free to move vertically at its head of $\overline{\Delta T} = 22°C$ can cause a vertical head displacement of approximately $w_h = -4$ mm. Higher head displacements can be expected for energy piles resting on stiff soil strata compared to energy piles floating in soft ground (the significant value of head displacement discussed with reference to the considered case is to be associated with the former situations). This phenomenon can be associated with the lower location of the null point in the former case compared to the latter for the same applied temperature variation. Higher energy pile displacements can be expected for longer piles. The reason for this is because, although the thermally induced deformation is independent of the pile length, the thermally induced displacement of energy piles is proportional to their length.

In contrast to the previous behaviour, the application of mechanical loads at the head of energy piles involves an approximately constant distribution of the vertical displacement with depth as well as a comparable distribution of shear stress (Rotta Loria et al., 2018). This consideration is particularly applicable to the analysis of rigid piles with a predominantly frictional character but is also acceptable for most piles. Compressive mechanical loads applied at the head of piles involve energy pile head settlements, while tensile mechanical loads involve energy pile head heaves. In particular, unless dealing with the phenomenon of negative skin friction, the action of

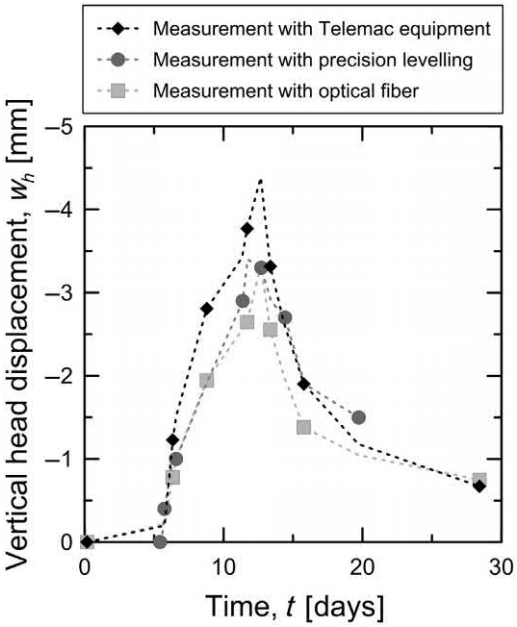

Figure 6.7 Evolution of thermally induced vertical head displacement in an energy pile free to move vertically at its head throughout a heating–passive cooling cycle. *Redrawn after Laloui, L., Moreni, M., Vulliet, L., 2003a. Comportement d'un pieu bi-fonction, fondation et échangeur de chaleur. Can. Geotech. J. 40 (2), 388–402.*

mechanical loads is associated with energy pile displacements in a unique direction (e.g. downward for compressive loads applied at the pile head).

Based on the previous considerations, the combined influence of mechanical and cooling thermal loads applied to energy piles involves an increase of their head settlement (with respect to the case of downward mechanical loading only). In contrast, the combined influence of mechanical and heating thermal loads applied to energy piles causes a decrease of their head settlement (with respect to the case of downward mechanical loading only) that can even result in an overall heave of such foundations. This latter phenomenon is associated with the opposite influence of downward mechanical loads and heating thermal loads on the behaviour of the pile head. It may be observed for piles subjected to limited mechanical loads and significant heating thermal loads. The commented influence of mechanical and heating thermal loads holds unless energy piles subjected to heating thermal loads in normally consolidated soils are considered. In these latter conditions the thermal collapse of the soil would result in a head settlement of the energy pile instead of a head heave, despite the pile expanding under the influence of the heating thermal load.

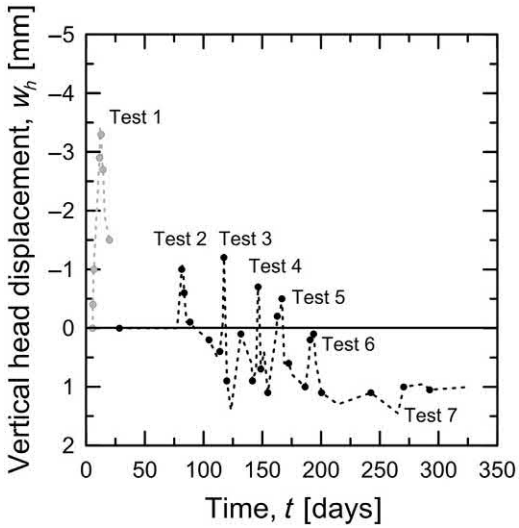

Figure 6.8 Vertical head displacement history caused by a thermal load (Test 1) and combined mechanical and thermal loads (Tests 2–7) in an energy pile. *Redrawn after Laloui, L., Moreni, M., Vulliet, L., 2003a. Comportement d'un pieu bi-fonction, fondation et échangeur de chaleur. Can. Geotech. J. 40 (2), 388–402.*

Fig. 6.8 shows a comparison between the vertical head displacement of the previously considered energy pile free to move vertically at its head and subjected to thermal loading only (labelled Test 1 in the plot), and the vertical head displacement of the same pile restrained at its head by a slab and subjected to both thermal loading and increasing mechanical loading (labelled Tests 2–7 in the plot). In the considered case study, thermal loading consisted of heating–passive cooling cycles applied to the energy pile of up to $\overline{\Delta T} = 22°C$, whereas mechanical loading involved increasing mechanical forces imposed at the head of the energy pile, following the construction of the storeys of a building supported by the tested foundation. The maximum mechanical load applied to the pile head was of $P = 1300$ kN. The thermally induced vertical head displacements of energy piles under free head conditions are higher than those actually observed under the influence of a head restraint. However, the influence of heating–passive cooling cycles can result in comparable and even greater head displacements than those caused by mechanical loads (Laloui et al., 2003a).

Fig. 6.9 summarises experimental measures of thermally induced vertical head displacements caused by thermal loads applied to full-scale energy piles, alone or in conjunction with mechanical loads. Data obtained by Laloui et al. (2003a), Murphy et al. (2015), Wang et al. (2014) and Akrouch et al. (2014) are presented. The upper and lower bounding interpolation lines refer to the results of Laloui et al. (2003a) and Wang et al. (2014), respectively. Thermally induced vertical head displacements from

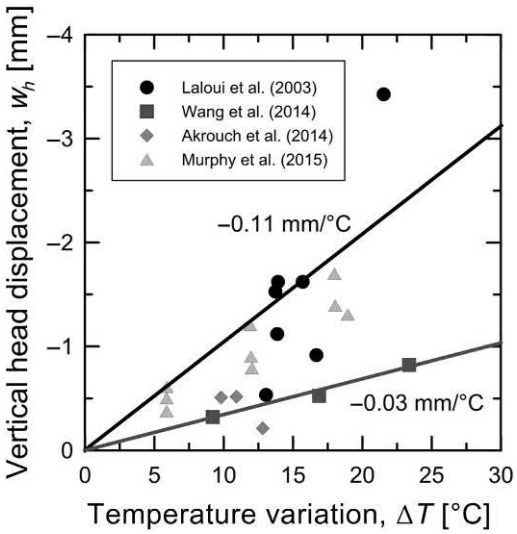

Figure 6.9 Summary of thermally induced vertical head displacements of full-scale energy piles. *Revised after Di Donna, A., Marco, B., Tony, A., 2017. Energy geostructures: analysis from research and systems installed around the world. In: Proceedings of 42nd DFI Conference.*

approximately -0.03 to -0.11 mm/°C can characterise energy piles subjected to heating thermal loads under different restraint conditions.

Complementary information on the vertical displacement variations caused by thermal or mechanical loads within energy piles is reported, for example: (1) through full-scale in situ tests by Bourne-Webb et al. (2009), McCartney and Murphy (2012, 2017), Murphy and McCartney (2015), Sutman et al. (2015), You et al. (2016), Sutman et al. (2017), Luo et al. (2017), Chen et al. (2017) and Allani et al. (2017); (2) through model-scale laboratory tests by Kalantidou et al. (2012), Yavari et al. (2014, 2016), Kramer and Basu (2014), Marto et al. (2015), Nguyen et al. (2017) and Liu et al. (2018); and (3) through centrifuge tests by Stewart and McCartney (2014), Ng et al. (2014, 2015, 2016) and Goode and McCartney (2015).

6.8 Thermally and mechanically induced shear stress variations

Following the thermally induced deformation of energy piles, shear stresses are mobilised in opposite directions at the pile shaft to ensure equilibrium with the surrounding soil from the so-called null point of the shear stress (generally located at a different depth, $z_{NP,\tau}$, than that of the null point of the vertical displacement) (Rotta Loria et al., 2018). The magnitude of the mobilised shear stresses depends on the restraint conditions.

An example of the thermally induced mobilised shear stress along an energy pile free to move vertically at its head and subjected to a heating thermal load is shown in

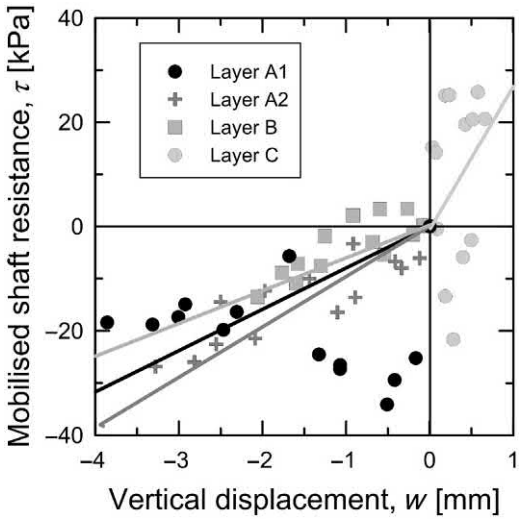

Figure 6.10 Mobilised shaft resistance by a heating thermal load along an energy pile free to move vertically at its head. *Redrawn after Laloui, L., Moreni, M., Vulliet, L., 2003a. Comportement d'un pieu bi-fonction, fondation et échangeur de chaleur. Can. Geotech. J. 40 (2), 388–402.*

Fig. 6.10 with reference to the results presented by Laloui et al. (2003a). Different magnitudes of shear stresses can be highlighted depending on the restraint provided by the soil layers surrounding the energy piles. Negative shear stresses develop because of the applied heating thermal load above the null point (in correspondence with the shallower portion of the energy pile adjacent to layers A1, A2 and B). Positive shear stresses develop because of the applied heating thermal load below the null point (in correspondence with the deeper portion of the energy pile adjacent to layer C). The opposite occurs because of cooling thermal loads applied to energy piles [see, e.g. Bourne-Webb et al. (2009)].

Positive shear stresses develop along energy piles subjected to compressive mechanical loads applied at their head to ensure equilibrium. An example of the magnitude of mobilised shaft resistance by the application of a mechanical load to an energy pile restrained at its head by a slab is shown in Fig. 6.11 with reference to the results presented by Laloui et al. (2003a). Different values of shaft resistance are mobilised along energy piles according to the increase in mean effective stress with depth and the properties of the soil surrounding the piles.

The direction of the mobilised shear stresses caused by compressive mechanical loads applied to energy piles is the same compared to that caused by cooling thermal loads above the null point of the shear stress, while it is opposite for heating thermal loads. The opposite is true for the portion of energy piles located below the null point. An example of this phenomenon is shown in Fig. 6.12 considering the

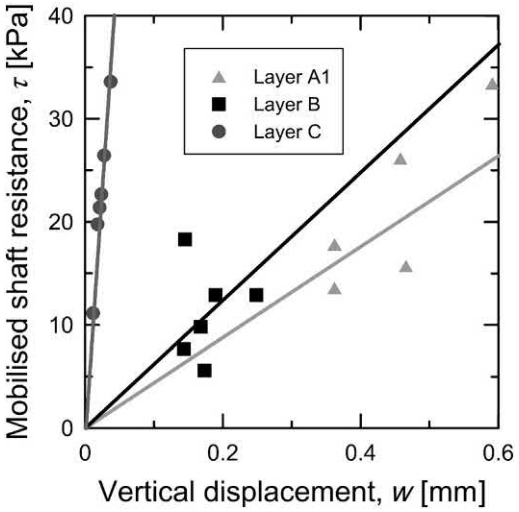

Figure 6.11 Relationship between the mobilised shaft resistance and the vertical displacement along an energy pile restrained at its head under the influence of a mechanical load. *Redrawn after Laloui, L., Moreni, M., Vulliet, L., 2003a. Comportement d'un pieu bi-fonction, fondation et échangeur de chaleur. Can. Geotech. J. 40 (2), 388−402.*

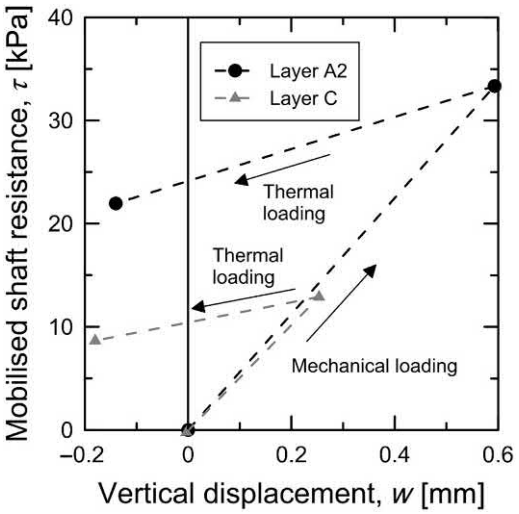

Figure 6.12 Mobilised shaft resistance and vertical displacement due to mechanical and heating thermal loading of an energy pile restrained at its head, above the null points of the vertical displacement and shear stress. *Redrawn after Laloui, L., Moreni, M., Vulliet, L., 2003a. Comportement d'un pieu bi-fonction, fondation et échangeur de chaleur. Can. Geotech. J. 40 (2), 388−402.*

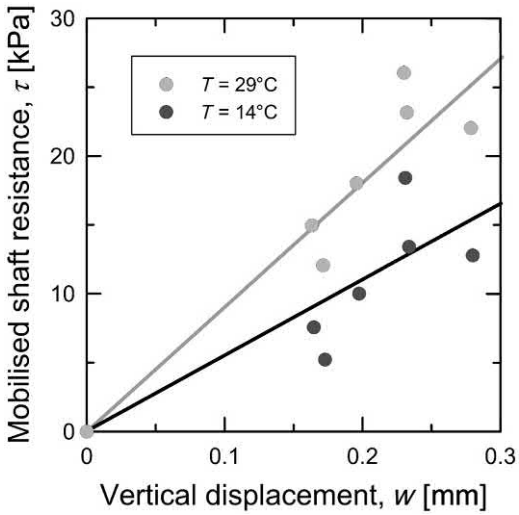

Figure 6.13 Mobilised shaft resistance and vertical displacement caused by different temperature variations in energy piles. *Redrawn after Laloui, L., Vulliet, L., Cekerevac, C., Moreni, M., 2003b. Heat exchanger pile: in-situ testing and constitutive modeling. In: Proceedings of an International Conference on Geo-Environment.*

combined effect of a mechanical load and a heating thermal load applied to an energy pile restrained at its head by a slab in terms of mobilised shaft resistance and vertical displacement with reference to the results presented by Laloui et al. (2003a).

More pronounced temperature variations applied to energy piles cause more significant mobilisations of shaft resistance. An example of this phenomenon is shown in Fig. 6.13 with reference to the results presented by Laloui et al. (2003b). At the same time, for a comparable temperature variation, lower shaft resistance is mobilised along energy piles under free and restrained head conditions. An example of this phenomenon can be observed by comparing the response of an energy pile free to move vertically at its head summarised in Fig. 6.10 with the response of the same energy pile restrained at its head under the action of comparable temperature variations that is presented in Fig. 6.14 with reference to the results presented by Laloui et al. (2003a).

Fig. 6.15 summarises experimental measures of thermally induced shaft resistance variations caused by thermal loads in full-scale energy piles, applied alone or in conjunction with mechanical loads. Data obtained by Laloui et al. (2003a), Bourne-Webb et al. (2009) and Murphy et al. (2015) are presented. The upper and lower bounding interpolation lines presented for temperature variations associated with positive shaft resistance variations refer to the results of Bourne-Webb et al. (2009) (measured at depths of $z =$ 1−17 and 17−30 m). The upper and lower bounding interpolation lines presented for temperature variations associated with negative shaft resistance variations refer to the results of Murphy et al. (2015) and Bourne-Webb et al. (2009)

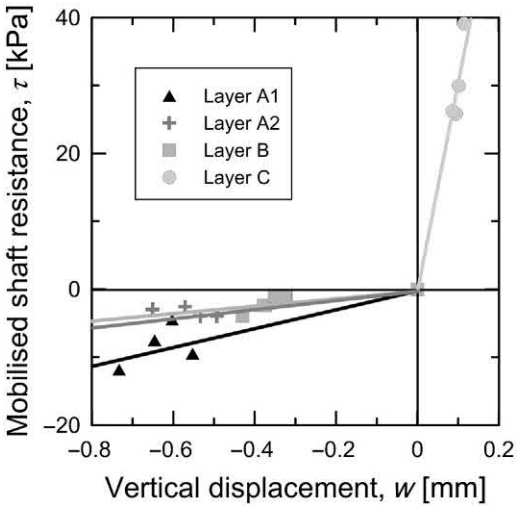

Figure 6.14 Mobilised shaft resistance by a heating thermal load along an energy pile restrained at its head. *Redrawn after Laloui, L., Moreni, M., Vulliet, L., 2003a. Comportement d'un pieu bi-fonction, fondation et échangeur de chaleur. Can. Geotech. J. 40 (2), 388−402.*

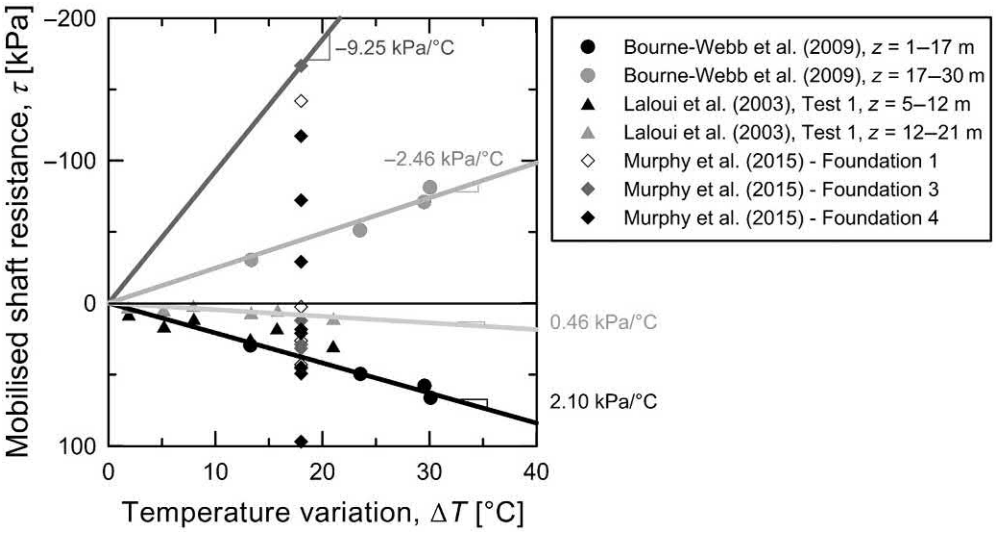

Figure 6.15 Summary of thermally induced shaft resistance variations in full-scale energy piles. *Extended after Amatya, B.L., Soga, K., Bourne-Webb, P.J., Amis, T., Laloui, L., 2012. Thermo-mechanical behaviour of energy piles. Geotechnique 62 (6), 503−519.*

(measured at a depth of $z = 17-30$ m), respectively. Positive shaft resistance variations from approximately 0.5 to 2 kPa/°C can characterise energy piles. Negative shaft resistance variations from approximately −2.5 to −9 kPa/°C can characterise energy piles.

Complementary information on the shear stress variations caused by thermal or mechanical loads along energy piles is reported, for example: (1) through full-scale in situ tests by McCartney and Murphy (2012, 2017), Murphy and McCartney (2015), Wang et al. (2014), Akrouch et al. (2014), Sutman et al. (2015, 2017), You et al. (2016), Chen et al. (2017) and Allani et al. (2017); (2) through model-scale laboratory tests by Yavari et al. (2014, 2016) and Kramer and Basu (2014); and (3) through centrifuge tests by Stewart and McCartney (2014), Ng et al. (2014) and Goode and McCartney (2015).

6.9 Thermally and mechanically induced vertical stress variations

Thermally induced stresses develop in energy piles because a proportion of the strain induced by the applied thermal loads is generally prevented by (1) the friction with the surrounding ground, (2) the presence of the superstructure at the pile head and (3) the end-bearing at the pile toe. Thermally induced compressive stresses comparable to those induced by the applied superstructure mechanical loads can be observed. As a result, the total vertical stress variations caused by combined mechanical and heating thermal loads can double that caused by only mechanical loads.

The influence of thermal loads with respect to mechanical loads can be appreciated in Fig. 6.16 for an energy pile restrained at its head by a slab that is subjected to a mechanical load $P =$ 1300 kN and a heating thermal load resulting in an average temperature variation along the pile of $\overline{\Delta T} =$ 13.4°C with reference to the results presented by Laloui et al. (2003a). The vertical stress variations are calculated based on the experimentally observed vertical strain variations using a one-dimensional scheme, that is $\Delta\sigma_z = \Delta\sigma_o^{th} = E_{EP}\Delta\varepsilon_b^{th} = E_{EP}\left(\Delta\varepsilon_o^{th} - \Delta\varepsilon_f^{th}\right) = E_{EP}(\Delta\varepsilon_z + \alpha_{EP}\Delta T)$ (where $\Delta\sigma_o^{th}$ is the thermally induced vertical stress, E_{EP} is the Young's modulus of the pile, $\Delta\varepsilon_b^{th}$ is the blocked thermally induced strain and $\Delta\varepsilon_o^{th}$ is the observed thermally induced strain). The profile of the thermally induced portion of vertical stress is determined as the difference between the total vertical stress variation measured along the energy pile and the variation caused by only the mechanical load applied at the pile head. In the considered case study, an increase in temperature of 1°C leads to an approximate increase in vertical stress of approximately 165 kPa (i.e. 100 kN/°C).

The vertical stress variation caused by mechanical loads generally decreases with depth. The vertical stress variation caused by thermal loads is often relatively uniform. The opposite can be expected for cooling thermal loads applied to energy piles, with the potential that the reduction of compressive stress caused by the cooling unloads and even causes tensile stresses in energy piles (especially for piles subjected to low magnitude of compressive loads at their head and significant cooling).

Fig. 6.17 proposes a summary of experimental measures of thermally induced vertical stresses caused by heating and cooling thermal loads in full-scale energy piles,

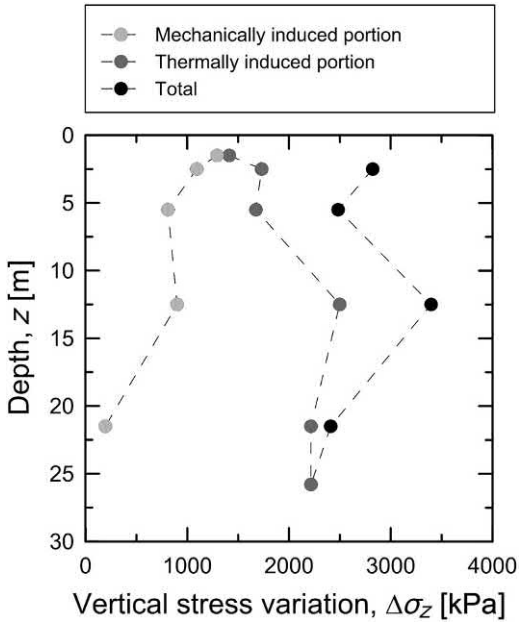

Figure 6.16 Vertical stress variations caused by a mechanical load and a heating thermal load applied to an energy pile restrained at its head. *Redrawn after Laloui, L., Moreni, M., Vulliet, L., 2003a. Comportement d'un pieu bi-fonction, fondation et échangeur de chaleur. Can. Geotech. J. 40 (2), 388–402.*

applied alone or in conjunction with mechanical loads. Data obtained by Laloui et al. (2003a), Bourne-Webb et al. (2009), McCartney and Murphy (2012), Murphy et al. (2015), Akrouch et al. (2014), Sutman et al. (2015) and You et al. (2016) are presented. The upper and lower bounding interpolation lines presented for temperature variations associated with heating thermal loads refer to the results of Laloui et al. (2003a) (measured at the toe of an energy pile) and Bourne-Webb et al. (2009) (measured at a depth of $z = 12$ m), respectively. The upper and lower bounding interpolation lines presented for temperature variations associated with cooling thermal loads refer to the results of Bourne-Webb et al. (2009) (measured at depths of $z = 6$ and 15 m, respectively). Heating thermal loads applied to energy piles can cause from approximately 40 to 360 kPa/°C of increase in compressive stress. Cooling thermal loads applied to energy piles can cause from approximately −15 to −180 kPa/°C of decrease in compressive stress.

The discussed influence of thermal loads on the thermally induced vertical stress variations in energy piles holds for all usual situations where the thermal expansion coefficient of the soil is (significantly) lower than or (at least theoretically) equal to that of the piles (Rotta Loria and Laloui, 2016, 2017). That is compressive stress is caused

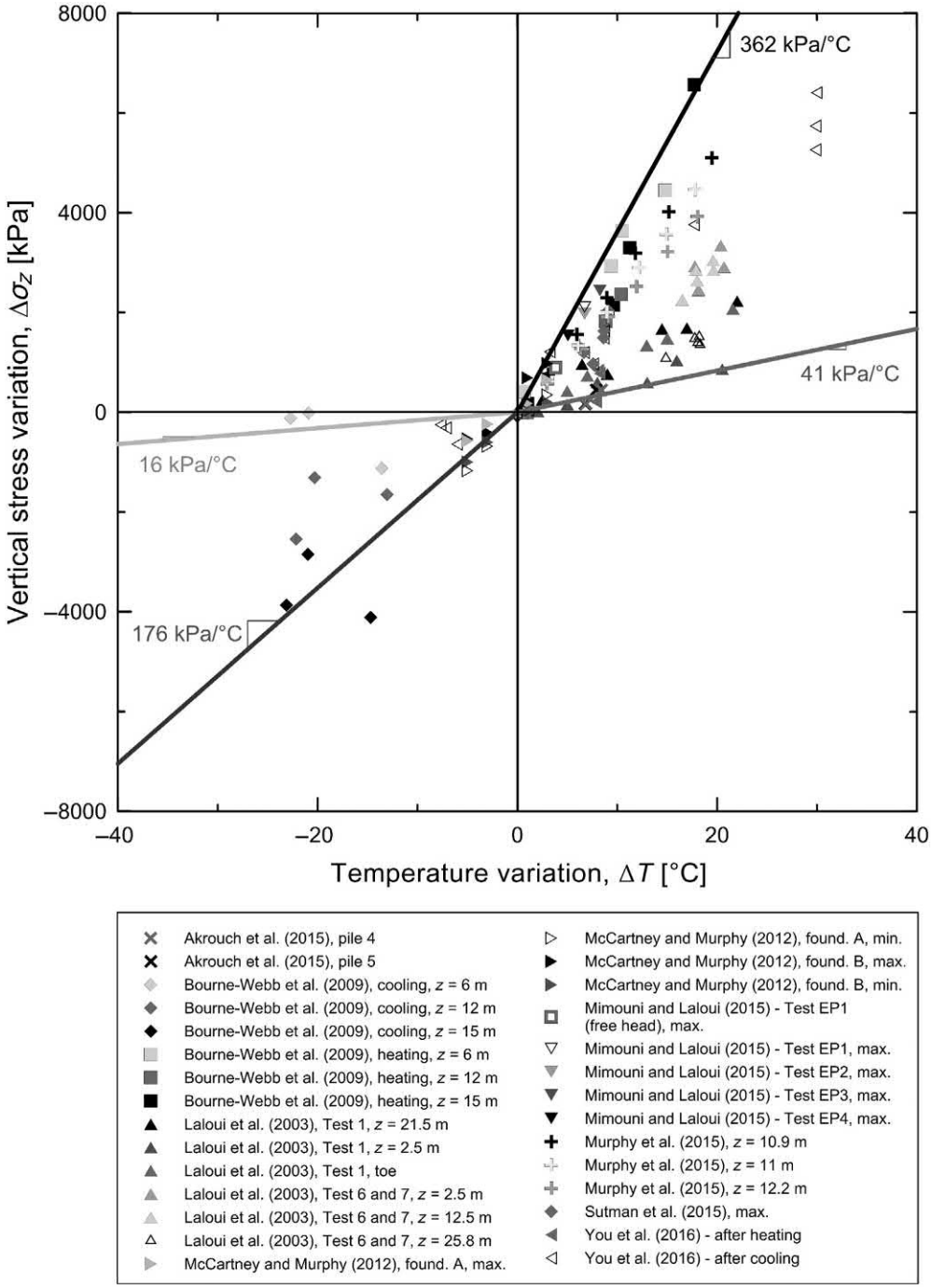

Figure 6.17 Summary of thermally induced stress variations in full-scale energy piles. *Extended after Amatya, B.L., Soga, K., Bourne-Webb, P.J., Amis, T., Laloui, L., 2012. Thermo-mechanical behaviour of energy piles. Geotechnique 62 (6), 503−519.*

by energy pile heating and tensile stress is caused by energy pile cooling (actually coinciding with a reduction of compressive stress). Only in situations where the thermal expansion coefficient of the soil is higher than that of the piles and successive stages of geothermal operations are considered can a different response be observed (Bourne-Webb et al., 2016; Rotta Loria and Laloui, 2017, 2018a). In these situations, thermally induced stress variations opposite to those that may be expected based on the type of applied thermal load can develop in piles surrounded by soil deposits in overconsolidated conditions (Rotta Loria and Laloui, 2018a). The reason for this is because the thermally induced soil deformation governs the deformation of the piles and can involve greater average thermally induced vertical strains than those associated with free expansion conditions by referring to the temperature variation applied to the piles and their linear thermal expansion coefficient. That is tensile stress is caused by energy pile heating and compressive stress is caused by energy pile cooling.

Complementary information on the vertical stress variations caused by thermal or mechanical loads within energy piles is reported, for example: (1) through full-scale in situ tests by Mimouni and Laloui (2015), Murphy and McCartney (2015, 2017), Wang et al. (2014), Sutman et al. (2017), Luo et al. (2017), Chen et al. (2017) and Allani et al. (2017); (2) through model-scale laboratory tests by Yavari et al. (2014), Kramer and Basu (2014), Marto et al. (2015), Nguyen et al. (2017) and Liu et al. (2018); and (3) through centrifuge tests by Stewart and McCartney (2014), Goode and McCartney (2015) and Ng et al. (2015).

6.10 Degree of freedom variations

The end-restraint conditions characterising energy piles crucially affect their response through the interplay between observed (and blocked) thermally induced strain and stress (Mimouni and Laloui, 2014; Sutman et al., 2018). The higher the restraint provided by the ground and the superstructure, the higher the blocked thermally induced strain, the lower the observed thermally induced strain and the greater the observed thermally induced stress along energy piles (Bourne-Webb et al., 2011; Rotta Loria and Laloui, 2018b). In this context, the degree of freedom can effectively characterise the degree of restraint of energy piles (Laloui et al., 2003a). For example a degree of freedom of $DOF = 0.5$ implies that 50% of the thermally induced strain that may be associated with a given temperature variation is blocked and results in an observed thermally induced stress.

An example of the evolution of degree of freedom along an energy pile is shown in Fig. 6.18 with reference to the results presented by Laloui et al. (2003a). With respect to a condition in which an energy pile is free to move vertically at its head (as in Test 1), the successive construction of building storeys causes a progressive decrease of the degree of freedom of the energy pile (as through Tests 2−7). The reason for

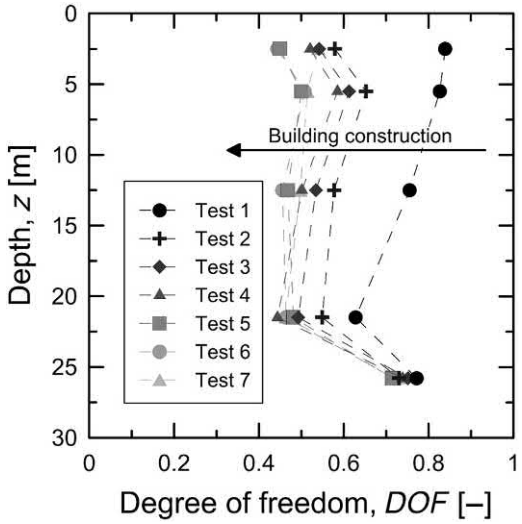

Figure 6.18 Variation of the degree of freedom along the depth of an energy pile for evolving restraint conditions associated with the construction of a building. *Redrawn after Laloui, L., Moreni, M., Vulliet, L., 2003a. Comportement d'un pieu bi-fonction, fondation et échangeur de chaleur. Can. Geotech. J. 40 (2), 388–402.*

this phenomenon can be attributed to the overall progressive increase of the stiffness characterising the pile–soil–superstructure system. The stiffness at the head of energy piles varies locally depending on their position within the foundation. This fact indicates that comparable energy piles subjected to the same thermal load in a given soil deposit but in different locations of a foundation are characterised by different degrees of freedom.

In all usual situations where the thermal expansion coefficient of the soil is (significantly) lower than or (at least theoretically) equal to that of the piles, it results in $0 \leq DOF \leq 1$. However, because of the previously mentioned role of the thermally induced soil deformation in the rare cases in which the thermal expansion coefficient of the soil is higher than that of the piles, it can result at successive stages of geothermal operation that $DOF > 1$.

References

Abdelaziz, S., Ozudogru, T.Y., 2016. Non-uniform thermal strains and stresses in energy piles. Environ. Geotech. 3 (4), 237–252.

Akrouch, G.A., Sánchez, M., Briaud, J.-L., 2014. Thermo-mechanical behavior of energy piles in high plasticity clays. Acta Geotech. 9 (3), 399–412.

Allani, M., Van Lysebetten, G., Huybrechts, N., 2017. Experimental and numerical study of the thermo-mechanical behaviour of energy piles for Belgian practice, Advances in Laboratory Testing and Modelling of Soils and Shales, vol. 1. Springer, pp. 405–412.

Amatya, B.L., Soga, K., Bourne-Webb, P.J., Amis, T., Laloui, L., 2012. Thermo-mechanical behaviour of energy piles. Geotechnique 62 (6), 503–519.
Bidarmaghz, A., Narsilio, G.A., Johnston, I.W., Colls, S., 2016. The importance of surface air temperature fluctuations on long-term performance of vertical ground heat exchangers. Geomech. Energy Environ. 6, 35–44.
Bourne-Webb, P.J., Amatya, B.L., Soga, K., Amis, T., Davidson, C., Payne, P., 2009. Energy pile test at Lambeth College, London: geotechnical and thermodynamic aspects of pile response to heat cycles. Geotechnique 59 (3), 237–248.
Bourne-Webb, P.J., Amatya, B., Soga, K., 2011. A framework for understanding energy pile behaviour. Proc. ICE Geotech. Eng. 166 (2), 170–177.
Bourne-Webb, P., Bodas Freitas, T., Freitas Assunção, R., 2016. Soil–pile thermal interactions in energy foundations. Geotechnique 66 (2), 167–171.
Caulk, R., Ghazanfari, E., McCartney, J.S., 2016. Parameterization of a calibrated geothermal energy pile model. Geomech. Energy Environ. 5, 1–15.
Chen, Y., Xu, J., Li, H., Chen, L., Ng, C.W., Liu, H., 2017. Performance of a prestressed concrete pipe energy pile during heating and cooling. J. Perform. Constr. Facil. 31 (3), 06017001.
De Beer, E., 1988. Different behavior of bored and driven piles. In: Impe, Van (Ed.), Deep Foundations on Bored and Auger Piles. Balkema, *Rotterdam*, pp. 47–82.
Di Donna, A., Barla, M., Amis, T., 2017. Energy geostructures: analysis from research and systems installed around the world. In: Proceedings of 42nd DFI Conference.
Fleming, K., Weltman, A., Randolph, M., Elson, K., 2008. Piling Engineering. CRC Press.
Goode III, J., McCartney, J.S., 2015. Centrifuge modeling of boundary restraint effects in energy foundations. J. Geotech. Geoenviron. Eng. 141 (8), 04015034.
Kalantidou, A., Tang, A.M., Pereira, J., Hassen, G., 2012. Preliminary study on the mechanical behaviour of heat exchanger pile in physical model. Geotechnique 62 (11), 1047–1051.
Kramer, C.A., Basu, P., 2014. Performance of a model geothermal pile in sand. In: Laloui, L., Di Donna, A. (Eds.), Proceedings of 8th International Conference on Physical Modelling in Geotechnics. CRC Press/Balkema, pp. 771–777.
Laloui, L., Moreni, M., Vulliet, L., 2003a. Comportement d'un pieu bi-fonction, fondation et échangeur de chaleur. Can. Geotech. J. 40 (2), 388–402.
Laloui, L., Vulliet, L., Cekerevac, C., Moreni, M., 2003b. Heat exchanger pile: in-situ testing and constitutive modelling. In: Proceedings of an International Conference on Geo-Environment.
Laloui, L., Nuth, M., Vulliet, L., 2006. Experimental and numerical investigations of the behaviour of a heat exchanger pile. Int. J. Numer. Anal. Methods Geomech. 30 (8), 763–781.
Lancellotta, R., 1995. Geotechnical Engineering. Balkema, Rotterdam.
Liu, H.-L., Wang, C.-L., Kong, G.-Q., Bouazza, A., 2018. Ultimate bearing capacity of energy piles in dry and saturated sand. Acta Geotech. 1–11.
Luo, J., Zhao, H., Gui, S., Xiang, W., Rohn, J., 2017. Study of thermal migration and induced mechanical effects in double U-tube energy piles. Comput. Geotech. 91, 1–11.
Marto, A., Amaludin, A., Hatta Bin Satar, M., 2015. Experiments on shallow geothermal energy model piles embedded in soft soil. Electron. J. Geotech. Eng. 20, 12687–12698.
McCartney, J.S., Murphy, K.D., 2012. Strain distributions in full-scale energy foundations. DFI J. 6 (2), 26–38.
McCartney, J.S., Murphy, K.D., 2017. Investigation of potential dragdown/uplift effects on energy piles. Geomech. Energy Environ. 10, 21–28.
Mimouni, T., Laloui, L., 2013. Full-scale in situ testing of energy piles. In: Laloui, L., Di Donna, A. (Eds.), Energy Geostructures: Innovation in Underground Engineering. Wiley-ISTE, pp. 23–43.
Mimouni, T., Laloui, L., 2014. Towards a secure basis for the design of geothermal piles. Acta Geotech. 9 (3), 355–366.
Mimouni, T., Laloui, L., 2015. Behaviour of a group of energy piles. Can. Geotech. J. 52 (12), 1913–1929.
Murphy, K., McCartney, J.S., 2015. Seasonal response of energy foundations during building operation. Geotech. Geol. Eng. 33 (2), 343–356.

Murphy, K.D., McCartney, J.S., Henry, K.S., 2015. Evaluation of thermo-mechanical and thermal behavior of full-scale energy foundations. Acta Geotech. 10 (2), 1–17.
Ng, C.W.W., Shi, C., Gunawan, A., Laloui, L., 2014. Centrifuge modelling of energy piles subjected to heating and cooling cycles in clay. Géotech. Lett. 4 (October–December), 310–316.
Ng, C.W.W., Shi, C., Gunawan, A., Laloui, L., Liu, H.L., 2015. Centrifuge modelling of heating effects on energy pile performance in saturated sand. Can. Geotech. J. 52 (8), 1045–1057.
Ng, C.W.W., Gunawan, A., Shi, C., Ma, Q., Liu, H., 2016. Centrifuge modelling of displacement and replacement energy piles constructed in saturated sand: a comparative study. Géotech. Lett. 6 (1), 34–38.
Nguyen, V.T., Tang, A.M., Pereira, J.-M., 2017. Long-term thermo-mechanical behavior of energy pile in dry sand. Acta Geotech. 12 (4), 729–737.
Rotta Loria, A.F., Laloui, L., 2016. The interaction factor method for energy pile groups. Comput. Geotech. 80, 121–137.
Rotta Loria, A.F., Laloui, L., 2017. Thermally induced group effects among energy piles. Geotechnique 67 (5), 374–393.
Rotta Loria, A.F., Laloui, L., 2018a. Group action effects caused by various operating energy piles. Geotechnique 68 (9), 834–841.
Rotta Loria, A.F., Laloui, L., 2018b. Thermo-mechanical schemes for energy piles. In: Proceedings of International Symposium on Energy Geotechnics, SEG 2018, pp. 218–225.
Rotta Loria, A.F., Gunawan, A., Shi, C., Laloui, L., Ng, C.W., 2015. Numerical modelling of energy piles in saturated sand subjected to thermo-mechanical loads. Geomech. Energy Environ. 1 (1), 1–15.
Rotta Loria, A.F., Vadrot, A., Laloui, L., 2018. Analysis of the vertical displacement of energy pile groups. Geomech. Energy Environ. 16, 1–14. Available from: https://doi.org/10.1016/j.gete.2018.04.001.
Stewart, M.A., McCartney, J.S., 2014. Centrifuge modeling of soil–structure interaction in energy foundations. J. Geotech. Geoenviron. Eng. 140 (4), 04013044.
Sutman, M., Olgun, C., Brettmann, T., 2015. Full-scale field testing of energy piles, Proceedings of IFCEE 2015, vol. 1. ASCE, pp. 1638–1647.
Sutman, M., Olgun, G., Laloui, L., Brettmann, T., 2017. Effect of end-restraint conditions on energy pile behavior. In: Geotechnical Frontiers 2017, pp. 165–174.
Sutman, M., Brettmann, T., Olgun, C.G., 2018. Full-scale in-situ tests on energy piles: head and base-restraining effects on the structural behaviour of three energy piles. Geomech. Energy Environ. 18, 56–68.
Tomlinson, M., Woodward, J., 1993. Pile design and Construction Practice. CRC Press.
Wang, B., Bouazza, A., Singh, R.M., Haberfield, C., Barry-Macaulay, D., Baycan, S., 2014. Posttemperature effects on shaft capacity of a full-scale geothermal energy pile. J. Geotech. Geoenviron. Eng. 141 (4), 04014125.
Yavari, N., Tang, A.M., Pereira, J.-M., Hassen, G., 2014. Experimental study on the mechanical behaviour of a heat exchanger pile using physical modelling. Acta Geotech. 9 (3), 385–398.
Yavari, N., Tang, A.M., Pereira, J.-M., Hassen, G., 2016. Mechanical behaviour of a small-scale energy pile in saturated clay. Geotechnique 66 (11), 878–887.
You, S., Cheng, X., Guo, H., Yao, Z., 2016. Experimental study on structural response of CFG energy piles. Appl. Therm. Eng. 96 (1), 640–651.

Questions and problems

Statements

a. Which is the most widely used criterion to classify piles?
b. What are the two basic methods that can be used to install piles?
c. What is the difference between displacement and nondisplacement piles? Is there any relation with floating and end-bearing piles?
d. Describe the difference between end-bearing and floating piles.
e. What is the order of magnitude of typical average temperature variations applied to energy piles, $\Delta\overline{T}$? What are the resulting temperature levels in such foundations for pile heating and pile cooling, if an average initial temperature with depth of $\overline{T}_0 = 15°C$ is considered?
f. Which is the typical magnitude of average vertical strain variations, $\Delta\overline{\varepsilon}_z$, caused by thermal loads applied along energy piles?
g. The blocked portion of thermally induced strains in energy piles results in:
  i. Thermally induced displacements
  ii. Thermally induced stresses
  iii. None of the above
h. Are the displacements associated with vertical strains of energy piles generally greater or smaller than those associated with radial strains? Justify your answer mathematically.
i. Describe the displacement evolution with depth caused by thermal loads and mechanical loads in energy piles.
j. What is the null point of the vertical displacement of an energy pile?
k. Discuss the effect of the restraint conditions on the position of the null point of the vertical displacement along energy piles.
l. The vertical displacement of an energy pile free to move vertically at its head, compared to that of the same pile restrained at its head will always be:
  i. Lower
  ii. Higher
  iii. Equal
m. Are the null points of the vertical displacement and shear stress generally coincident?
n. What are the typical orders of magnitude of mobilised shear stress developed along energy piles per unit temperature change?
o. Discuss the effect of the restraint conditions on the development of the thermally induced strain and stress in energy piles.
p. What are the typical orders of magnitude of vertical stress developed along energy piles per unit temperature change?

q. Discuss the physical meaning of the degree of freedom with respect to the influence that different values of this parameter have from a stress development perspective in energy piles.

Solutions

a. The most widely used criterion to classify piles refers to the pile installation technique, which has the greatest influence on the response of such foundations to loading. Even if various pile installation techniques do exist in practice, all of them can be classified either as so-called *displacement piles* or *nondisplacement piles*. This pile classification holds both for energy piles and conventional piles.

b. Pile boring and driving.

c. Displacement piles are installed by driving them into the ground. Because of the pile penetration into the ground, marked disturbance of the ground is generated and noteworthy ground displacement in the radial direction are observed. Nondisplacement piles are installed by excavating first the ground for a successive filling of (reinforced) concrete. During installation, the boring process causes lateral stresses in the ground to decrease with only a partial recovery upon concreting and limited displacements are observed. There is no particular relation between displacement and nondisplacement piles and end-bearing and friction piles.

d. End-bearing piles involve a predominant contribution to the pile load-carrying capacity provided by the normal stresses mobilised at the pile toe (by the end-bearing). Floating piles involve a predominant contribution to the pile load-carrying capacity provided by the shear stresses mobilised at the shaft.

e. For typical operating conditions, minimum and maximum average temperature variations are of approximately $\Delta T = -15^{\circ}\mathrm{C}$ and $\Delta T = +30^{\circ}\mathrm{C}$, respectively. Thus, for an initial average temperature with depth of $T_0 = 15^{\circ}\mathrm{C}$, temperature levels in energy piles can reach $T = 0^{\circ}\mathrm{C}$ and $T = 45^{\circ}\mathrm{C}$.

f. The magnitude of average vertical strain variations is almost the same weather heating thermal loads or cooling thermal loads are applied to energy piles. For temperature variations between $\Delta T = 15^{\circ}\mathrm{C}$ and $30^{\circ}\mathrm{C}$, average thermal induces vertical strain often vary from -100 to $-250\ \mu\varepsilon$.

g. The blocked portion of thermally induced strains in energy piles results in:

- i. Thermally induced displacements
- **ii. Thermally induced stresses**
- iii. None of the above

h. **In one-dimensional conditions, normal strains ε [−] are defined as**:

$$\varepsilon = -\frac{\Delta x}{x}$$

where Δx [m] is the displacement variation and x [m] is the reference length considered for the strain. For vertical strain, one can write:

$$\varepsilon_z = -\frac{\Delta L}{L}$$

where L [m] is the pile length. For radial strain, one can write:

$$\varepsilon_r = -\frac{\Delta D}{D}$$

where D [m] is the pile diameter. For the same temperature variation applied to energy piles, comparable vertical and radial strains caused by temperature variations can be observed, such that $\varepsilon_z = \varepsilon_r$. However, thermally induced vertical displacements are more significant than thermally induced radial displacements since $L \gg D$.

i. **The application of thermal loads to energy piles involves at best a linear distribution of the vertical displacement with depth, with zero displacement at the so-called null point, and at worst a notably nonlinear distribution of the vertical displacement. If the null point is not located at one of the pile extremities (i.e. the head or the toe), two pile portions displace vertically in opposite directions around the null point**.

   On the contrary, the application of mechanical loads at the head of energy piles involves an approximately constant distribution of the vertical displacement with depth. Compressive loads applied at the pile head involve pile settlements with depth. Tensile mechanical loads applied at the pile head involve pile heaves.

j. **The null point of the vertical displacement is the setting of an energy pile characterised by zero thermally induced displacement, referring to one-dimensional conditions. The null point divides the energy pile in two portions that displace in opposite directions when subjected to thermal load. The location of the null point depends on the end-restraint conditions of the energy pile**.

k. **The null point is always located closer to the region of the pile characterised by the higher restraint. This restraint is directly related to the stiffness of the system. For an infinity rigid base, the null point would be**

located at the toe of the energy pile. For an infinite rigid slab, the null point would be located at the pile head.

l. The vertical displacement of an energy pile free to move vertically at its head, compared to that of the same pile restrained at its head will always be:
  i. Lower
  ii. Higher
  iii. Equal

m. No, the null points of the vertical displacement and shear stress are generally not located at the same depth.

n. Shear stress applied from the soil at the shaft of the energy pile may vary in different magnitudes depending of the sign of shear stress. Positive shear stress may vary from approximately 0.5 to 2 kPa/°C. Negative shear stress may vary from approximately −2.5 to −9 kPa/°C.

o. The end-restraint conditions characterising energy piles crucially affect their response in terms of thermally induced strains and stresses. For increasing restraint provided by the superstructure or the soil, the observed thermal induces strain of energy piles decreases. Therefore the thermal blocked strain increases, leading to an increase in thermal induced stress. The opposite occurs for decreasing restraints characterising energy piles.

p. Thermally induced vertical stresses show different orders of magnitude depending on whether heating thermal loads or cooling thermal loads are applied to energy piles. For heating thermal loads, an increase in compression from approximately 40 to 360 kPa/°C may be observed. For cooling thermal loads, a decrease in compression from approximately −15 to −180 kPa/°C may be observed.

q. The degree of freedom can be expressed as

$$DOF = \frac{\varepsilon_o^{th}}{\varepsilon_f^{th}}[-]$$

where ε_o^{th} [−] is the observed thermally induced strain and ε_f^{th} [−] is the thermally induced strain associated with free thermal expansion conditions. In most practical cases a portion of the strain is blocked ε_b^{th}, with:

$$\varepsilon_f^{th} = \varepsilon_o^{th} - \varepsilon_b^{th}$$

Therefore thermally induced stresses characterise energy piles according to the following

$$\sigma_o^{th} = E_{EP}\varepsilon_b^{th} = E_{EP}\left(\varepsilon_o^{th} - \varepsilon_f^{th}\right) = E_{EP}\left(\varepsilon_o^{th} + \alpha_{EP}\Delta T\right) = E_{EP}\alpha_{EP}\Delta T(1 - DOF)\ \text{[Pa]}$$

where E_{EP} [Pa] is the Young's modulus of the pile material, α_{EP} [1/°C] is the linear thermal expansion coefficient of the pile material and ΔT [°C] is the applied temperature variation.

For an increasing restraint provided to energy piles, *DOF* tends to 0 and increasing thermally induced stresses are observed in the pile. For a decreasing restraint provided to energy piles, *DOF* tends to 1 and decreasing thermally induced stresses are observed in the pile.

CHAPTER 7

Thermomechanical behaviour of energy pile groups

7.1 Introduction

Energy pile foundations can involve *mixed groups* of conventional and energy piles, or *uniform groups* of energy piles for the purpose of a partial or entire geothermal heat operation of such elements, respectively. In either case, energy pile foundations do not consist of a single energy pile but of a group of energy piles that function as structural supports and geothermal heat exchangers.

Pile groups can be divided into two classes: widely and closely spaced. In widely spaced pile groups, the piles are located far enough from each other that their individual responses can be considered independent. In closely spaced pile groups, the piles are close enough to each other that their individual responses are influenced by the presence of and loadings on the neighbouring piles. Therefore while in widely spaced pile groups the individual pile responses can be associated with the response of a single isolated pile, the individual pile responses in closely spaced pile groups differ from that of an isolated pile.

The influences between the individual pile responses of any energy pile foundation represent interactions (thermal and mechanical) between the piles, the connecting structural element and the surrounding soil. These interactions characterise the deformation and flows (e.g. of thermal energy and mass) governing the considered geostructures and manifest through so-called *group effects*. Understanding the significance and influence of group effects and interactions among energy piles is crucial to comprehensively address the thermohydromechanical behaviour of such foundations.

This chapter presents an analysis of the response of energy pile groups subjected to mechanical and thermal loads based on the results of full-scale in situ tests. A focus is devoted to energy pile groups subjected to heating thermal loads, although the influence of cooling thermal loads can be inferred from the results presented.

To address the aforementioned aspects, *idealisations and assumptions* are presented first: in this context, the objective is to propose a summary of the assumptions made to interpret the response of energy piles subjected to mechanical and thermal loads. Second, the *classification of energy pile foundations* is treated: the objective of this part is to summarise a characterisation of the types of energy pile foundations. Third, the *temperature variations* in energy pile groups are discussed: in this context, the purpose is to

Analysis and Design of Energy Geostructures
DOI: https://doi.org/10.1016/B978-0-12-816223-1.00007-2

expand on the thermal field characterising the energy piles and the surrounding soil. Later, the *pore water pressure variations* characterising energy pile groups are considered: the aim of this section is to highlight the influence of thermal loads on the variation of the pore water pressure in the soil deposits surrounding energy piles. Next, the *thermally induced vertical strain and stress variations* characterising energy pile groups are treated: in this framework, the purpose is to discuss the influence of thermal loads on the deformation of energy piles. Afterward, the *effect of number of loaded energy piles on the vertical strain and stress variations* are considered: in this context, the purpose is to comment on the response of energy piles depending on the number of foundations subjected to thermal or mechanical loading. Then, the *key aspects governing the behaviour of energy pile foundations* are discussed: the purpose of this part is to expand on the design variables and parameters that play the major role in the variation of energy pile group response subjected to mechanical and thermal loads. Finally, *questions and problems* are proposed: the purpose of this part is to fix and test the understanding of the subjects covered in this chapter by addressing a number of exercises.

7.2 Idealisations and assumptions

The idealisation and assumptions made in this chapter coincide with those presented in Chapter 6, Thermomechanical behaviour of single energy piles. The quoted considerations find due justification in the referenced chapter and are only summarised for completeness in the following.

A continuum medium idealisation of the materials constituting energy pile foundations is employed while considering the materials isotropic and homogeneous. The piles are assumed to be characterised by a cylindrical shape. Layered (i.e. nonuniform) soil deposits are considered to be composed of fully horizontal layers. Uniform variations of the temperature, stress, strain and displacement fields within (and around) energy piles are considered. Contractive strains, downward displacements, compressive stresses and increases in angles in the anticlockwise direction are considered to be positive.

7.3 Classification of energy pile foundations

The rationale of pile foundations in the support of structures can be (1) to provide sufficient bearing capacity to a superstructure by transferring a load to a relatively deep and competent ground, (2) to reduce the deformation of a superstructure to an acceptable level, or (3) both of the previous purposes. In this regard, only the piles, only the cap or both the piles and the cap can be considered to address the requirements of structural support and deformation control. Based on the employed design

approach, two classes of both conventional and energy pile foundations can be distinguished: *pile groups* and *piled raft foundations*.

Pile groups are foundation systems whereby the purpose of load-carrying capacity or deformation control is assigned to the piles only. In this situation, while a cap such as a shallow foundation or a slab connected to the piles may be effectively present, no account of its role in the response of the foundation to loading is made in design. Piled raft foundations are systems whereby the purpose of load-carrying capacity or deformation control is assigned to one or both of these elements. In this situation, due account of the respective role of the pile cap and the piles in the response of the foundation to loading is made in design.

For example pile groups may be designed in such a way the number of piles entirely fulfils the required load-carrying capacity for a structure without accounting for the contribution of any shallow foundation connected to the piles. In contrast, piled raft foundations may be designed in such a way some proportion [typically 20%–40% (Randolph and Clancy, 1993)] of the total applied load is transferred directly from a slab to the ground while the remaining proportion is transferred through the piles. These foundations may also be designed considering that some proportion of the deformation of a slab is limited by the use of piles. At the extreme, shallow foundations supporting a required loading alone may be equipped with a limited number of piles working as deformation controllers. In conventional pile applications, reference is made in this latter context to the use of piles as 'settlement reducers', typically with reference to differential settlements (Burland et al., 1977). While a number of case studies in which conventional piles working as settlement reducers are available [see, e.g. Burland (1995)], to date no similar examples characterise energy piles.

7.4 Temperature variations

Notable temperature variations can develop in energy piles as a consequence of their geothermal operation (Laloui et al., 2003; Bourne-Webb et al., 2009; McCartney and Murphy, 2012). Because heat flows within media over time, comparable temperature variations can also affect other piles and the ground located in the surroundings of energy piles functioning as geothermal heat exchangers (Rotta Loria and Laloui, 2017, 2018). Based on the coupling between heat transfer, mass transfer and deformation, the considered temperature variations involve thermal and thermally induced mechanical interactions. The thermal interactions affect the thermohydraulic behaviour of energy piles operating as geothermal heat exchangers. The thermally induced mechanical interactions affect the thermomechanical behaviour of all types of piles, irrespective of whether they function or not as geothermal heat exchangers.

An example of the temperature variations along a group of piles retrained at their head by a slab, in which only one energy pile functions as a geothermal heat

exchanger, is shown in Fig. 7.1 with reference to the results presented by Rotta Loria and Laloui (2017). In plan view, the considered piles form a triangle within a 4.21 m^2 in which the central pile, EP1, is located 2.98 m from the others, EP2, 3 and 4. All the piles are located in the corner of a pile foundation comprising both energy and conventional piles [see, for further details Mimouni and Laloui (2015) and Rotta Loria and Laloui (2017)]. The energy piles are 28 m long and 0.9 m in diameter. In the considered case study, the heating of the central energy pile EP1 in a group for a time of $t = 2$, 8, 35 and 156 days resulted in average temperature variations of $\overline{\Delta T} = 5°C$, 10°C, 15°C and 20°C, respectively, along its portion in which the pipes were not

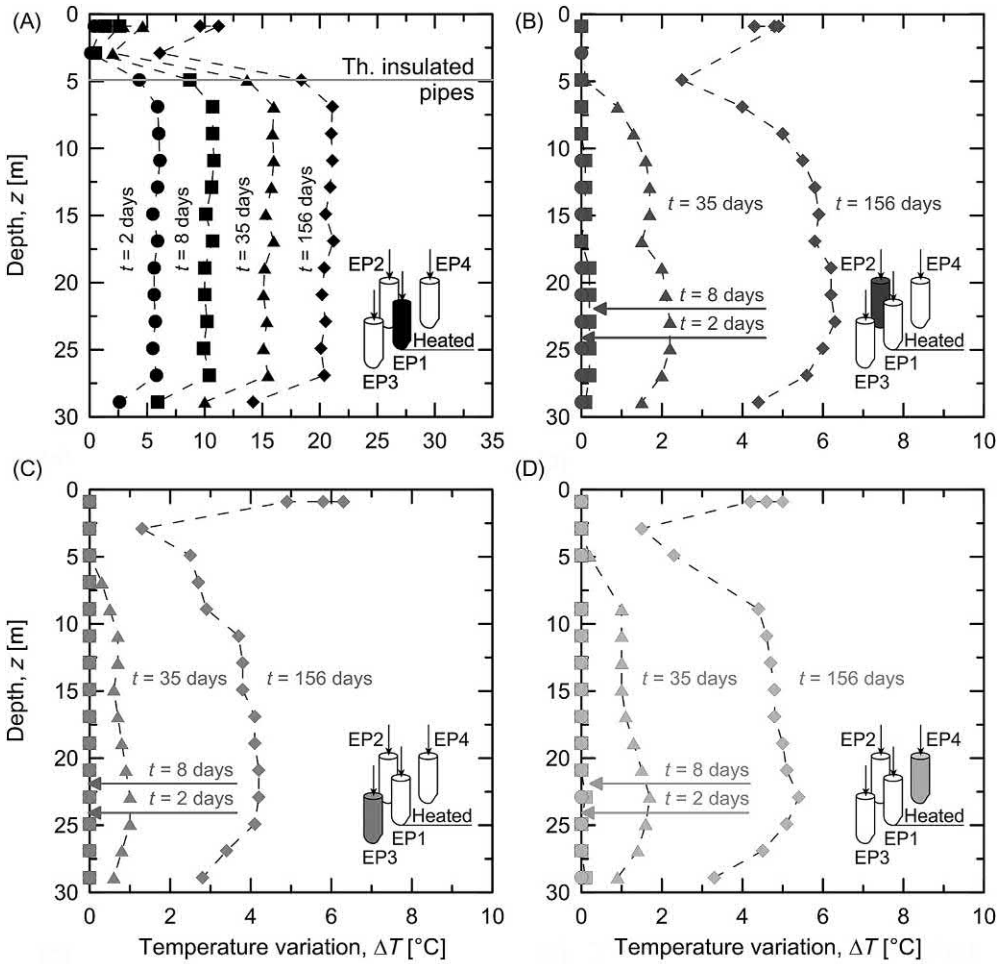

Figure 7.1 Temperature variations observed along a group of piles in which only one energy pile functions as a geothermal heat exchanger over time. *Modified after Rotta Loria, A.F., Laloui, L., 2017. Thermally induced group effects among energy piles. Geotechnique 67 (5), 374–393.*

thermally insulated (cf. Fig. 7.1A). After $t = 2$ and 8 days (i.e. during the early stages of the heating phase of the energy pile EP1), the corresponding portions of the piles EP2, 3 and 4 nonoperating as geothermal heat exchangers were characterised by no variations in temperature. However, temperature changes were observed over time because heat diffused through the soil from the central energy pile and indirectly heated them. After $t = 35$ and 156 days (i.e. during the successive stages of the heating phase of the energy pile EP1), heat diffusion resulted in average temperature variations of $\overline{\Delta T} = 1.6°C$, 0.7°C and 1.1°C and $\overline{\Delta T} = 5.3°C$, 3.6°C and 4.5°C along the piles EP2, 3 and 4, respectively. In addition to the observed temperature variations with time that corresponded to the portion of the energy pile EP1 in which the pipes were not thermally insulated, temperature variations also occurred in the shallowest 4 m of the piles EP2, 3 and 4 even though the pipes of the energy pile EP1 were thermally insulated at these depths. This phenomenon was attributed to the impact of the heat exchange operation of the energy pile EP1 on the thermal field characterising the shallower portion of the foundation. Variations in temperature approximately at the surface of the foundation (i.e. as a depth of $z = 0.9$ m) were also observed and were not characterised by the same magnitude within any reference pile. This phenomenon remarked a combined effect played by the variation of the surface thermal conditions and the inhomogeneity of the temperature field within the cross-section of the piles. Additional measurements of temperature variations in a group of energy piles are reported, for example by Mimouni and Laloui (2015).

An example of the temperature variations characterising the soil within a group piles in which only one energy pile functions as a geothermal heat exchanger is shown in Fig. 7.2 with reference to the results presented by Rotta Loria and Laloui (2017). In the considered case study, the heating of the energy pile EP1 had a notable impact on the temperature field of the surrounding soil. After $t = 156$ days, the soil profile at a radial distance of 1 m from the axis of the energy pile EP1 (i.e. P + T1) was subjected to an average temperature variation of $\overline{\Delta T} = 12°C$ (cf. Fig. 7.2A). At the same time, a lower average temperature variation of $\overline{\Delta T} = 5°C$ was observed along the profile at a radial distance of 2.2 m (i.e. P + T2; cf. Fig. 7.2B). The temperature variations observed at selected points along the lengths of the considered soil profiles with time followed the trend of the thermal loading path characterising the energy pile EP1 (cf. Fig. 7.2C). Inhomogeneity of the sandy-gravelly moraine was suggested by the different variations in temperature that were observed at the top and bottom of this layer (trends for points at $z = 9$ m and $z = 16.3$ m in P + T1; cf. Fig. 7.2C). A residual temperature variation was observed along the length of the soil profiles P + T1 and P + T2. This phenomenon reflected the impact of the residual temperature variation that characterised the heat carrier fluid circulating inside the pipes of the energy pile EP1 with reference to the initial condition on the thermal field of the foundation. These temperature variations caused in zones of the pile group residual strain and stress variations.

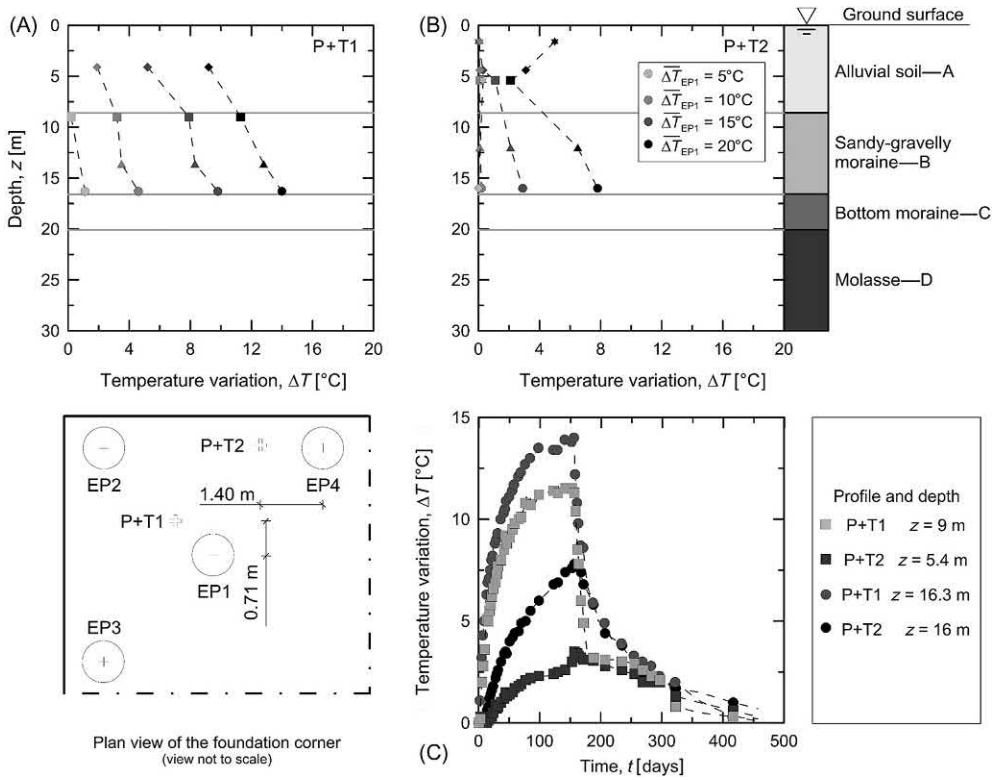

Figure 7.2 Temperature variations along soil profiles located within a group of piles in which only one energy pile functions as a geothermal heat exchanger over time. *Modified after Rotta Loria, A. F., Laloui, L., 2017. Thermally induced group effects among energy piles. Geotechnique 67 (5), 374–393.*

7.5 Pore water pressure variations

The variation of the temperature field in geomaterials, coupled with the variation of the displacement field of the material points and the influence of temperature on the properties of the material constituents (e.g. solid particles and water in a fully saturated case), causes changes in the hydraulic field. When the thermal expansion rate of the water filling the pores of geomaterials is too fast with respect to that of the solid particles pore water pressures can arise. This phenomenon is associated with the thermohydromechanical coupling that governs the behaviour of materials. Because the strength of materials is strictly related to the insurgence of pore water pressure variations [concept of effective stress (Terzaghi, 1923)], it is essential to understand the potential presence and influence of such pressures. The considered aspect governs the thermohydromechanical behaviour of energy piles and other energy geostructures.

An example of the pore water pressure variations characterising the soil within a group piles in which only one energy pile functions as a geothermal heat exchanger is shown in Figs 7.3–7.4, with reference to the results presented by Rotta Loria and Laloui (2017). The figures show the maximum pore water pressures that were observed throughout the considered test along two soil profiles (i.e. P + T1 and P + T2) and the trends of pore water pressure variations at selected points along the same soil profiles, respectively. In the considered case study, a negligible variation of the hydraulic field in the soil caused by the applied thermal load

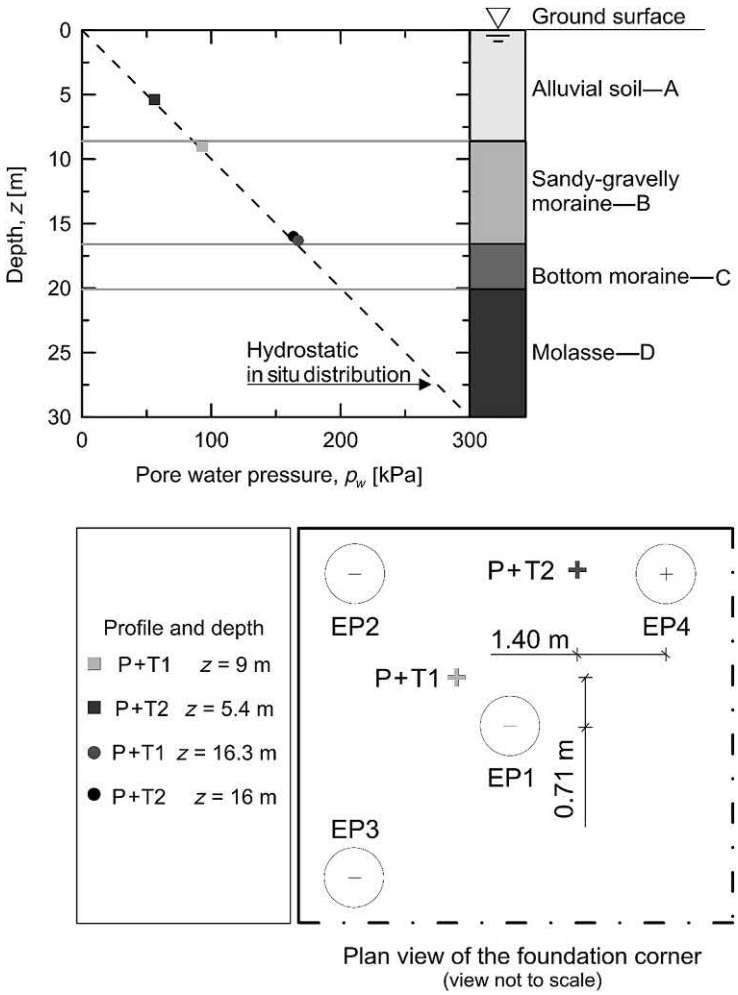

Figure 7.3 Maximum pore water pressure variations along soil profiles located within a group of piles in which only one energy pile functions as a geothermal heat exchanger. *Modified after Rotta Loria, A.F., Laloui, L., 2017. Thermally induced group effects among energy piles. Geotechnique 67 (5), 374–393.*

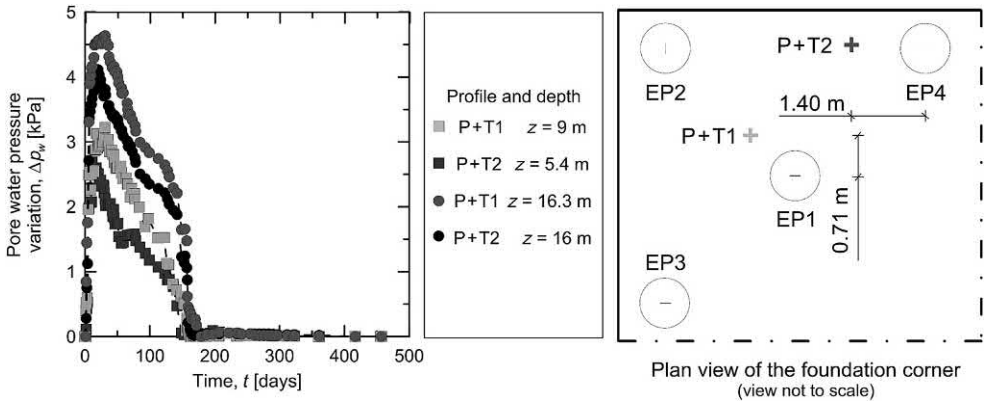

Figure 7.4 Maximum pore water pressure variations at selected settings along soil profiles located within a group of piles in which only one energy pile functions as a geothermal heat exchanger over time. *Modified after Rotta Loria, A.F., Laloui, L., 2017. Thermally induced group effects among energy piles. Geotechnique 67 (5), 374–393.*

to the foundation was observed. This result was in agreement with the experimental results presented by Mimouni and Laloui (2015). In the context of the numerical investigations carried out by Di Donna et al. (2016), it was observed that only when dealing with geomaterials characterised by remarkably low intrinsic permeability and coefficient of compressibility (e.g. values of intrinsic permeability lower than 1×10^{-17} m^2 and coefficient of compressibility of the solid particles forming the skeleton lower than 2.5×10^{-10} 1/Pa) do thermal loads cause significant pore water pressure variations. This results is in agreement with the investigations of Fuentes et al. (2016), in which reference values of intrinsic permeability lower than 1×10^{-17} m^2 and coefficient of compressibility of the solid particles forming the skeleton lower than 0.5×10^{-10} 1/Pa were shown to be associated with pore water pressures of comparable magnitude to the mobilisations of shaft friction along energy piles. Although in some practical cases characterised by the previous features pore water pressures caused by thermal loads may arise, the typical magnitude and rate of temperature variations characterising energy piles such as other energy geostructures can be considered in most situations to involve drained conditions. In other words, pore water pressures dissipate in most practical cases while thermal loads are applied to the ground surrounding energy geostructures.

7.6 Thermally induced vertical strain variations

Along with the influence of thermal loads applied to energy piles that generate expansive pile strains upon heating and contractive pile strains upon cooling, two phenomena occur in the surroundings (Rotta Loria and Laloui, 2016b):

1. Assuming the displacements of a considered system to be compatible, the thermally induced deformation of energy piles causes a variation of the displacement field and thus a disturbance of the mechanical response of neighbouring bodies. This phenomenon represents one effect of thermally induced mechanical interactions caused by thermal loads applied to piles and has a comparable influence to the mechanical interactions caused by mechanical loads applied such foundations.
2. Irrespective of the compatibility of the displacement field in a considered system, the temperature variations caused by the applied thermal loads to energy piles involve a thermally induced deformation and thus a disturbance of the mechanical response of neighbouring bodies. This phenomenon represents one additional effect caused by thermally induced mechanical interactions and can profoundly characterise the response of energy pile foundations depending on the significance of the thermal expansion potential of the soil with respect to that of the piles.

An example of the influence of thermal loads on the vertical strain variations within a group piles restrained at their head by a slab, in which only one energy pile functions as a geothermal heat exchanger, is shown in Fig. 7.5 with reference to the results presented by Rotta Loria and Laloui (2017). In the considered case study, the heating due to the geothermal operation of the energy pile EP1 resulted in an expansion of the pile portion in which the pipes were not thermally insulated and a contraction of the thermally insulated pile portion because of the entrapment with the slab (cf. Fig. 7.5A). The contraction of the shallower portion of the energy pile EP1 would not have occurred if the pipes were not thermally insulated in that region and the thermal field was more uniform along the pile length. Maximum expansive vertical strains of $\Delta\varepsilon_z = -22$, -56, -109 and $-167\,\mu\varepsilon$ were recorded along the uninsulated portion of the energy pile EP1 when it was subjected to temperature variations of $\overline{\Delta T} = 5°C$, 10°C, 15°C and 20°C, respectively (i.e. after $t = 2$, 8, 35 and 156 days, respectively). Maximum contractive vertical strains variations of $\Delta\varepsilon_z = 31$, 56, 68 and $79\,\mu\varepsilon$ were recorded along the insulated portion at the same reference times. Marked expansive vertical strains were observed with time in the bottom portion of this pile.

The heating of the energy pile EP1 also induced an expansion of the surrounding piles EP2, 3 and 4 nonoperating as geothermal heat exchangers (cf. Fig. 7.5B–D). After $t = 2$ and 8 days (i.e. during the early stages of the heating phase of the energy pile EP1), the expansions of the piles EP2, 3 and 4 were caused by (1) the expansion of the energy pile EP1 as a result of its direct heating and (2) the associated upward deformation of the slab. This deformation was thus purely mechanical (as described above, the temperature variations were zero or very small along the piles EP2, 3 and 4 at early stages of the geothermal operation of the energy pile EP1). The evolution of deformation along the piles (decreasing from top to bottom) indicates that the deformation was comparable to that caused by an upward force applied at their heads. After $t = 35$ and 156 days (i.e. during the successive stages of the heating phase of the energy

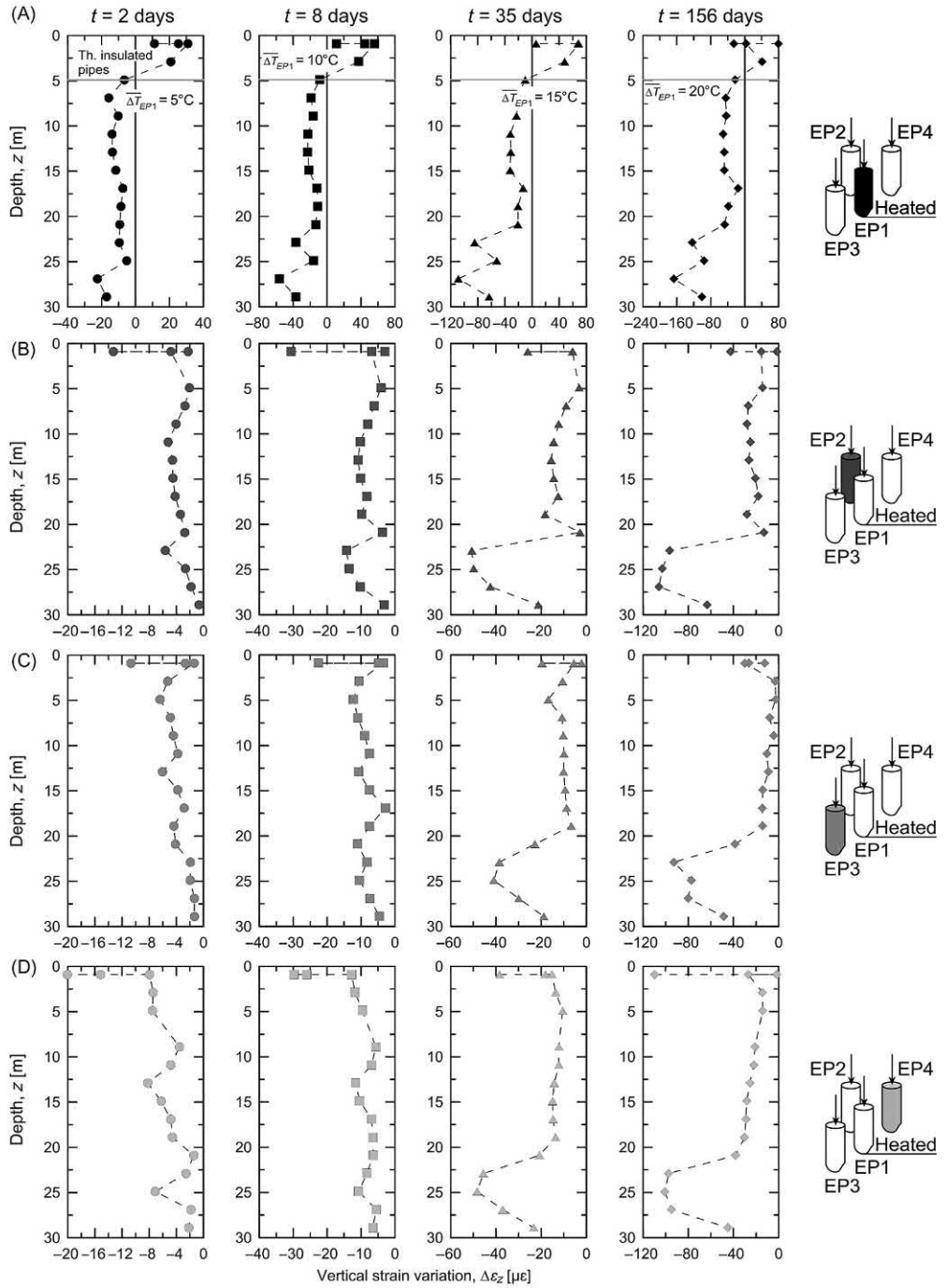

Figure 7.5 Variations in vertical strain observed along a pile group composed by (A) an energy pile operating as a geothermal heat exchanger (EP1) and (B−D) three nonoperating piles (EP2, 3 and 4), after $t = 2$, 8, 35 and 156 days. *Modified after Rotta Loria, A.F., Laloui, L., 2017. Thermally induced group effects among energy piles. Geotechnique 67 (5), 374−393.*

pile EP1), the expansions of piles EP2, 3 and 4 were caused by (1) the expansion of the energy pile EP1 as a result of its direct heating, (2) the associated upward deformation of the slab, (3) the expansions of these elements as a result of their indirect heating and (4) the expansion of the soil as a result of its heating. In contrast to the deformation of the piles EP2, 3 and 4 during the early stages of the geothermal operation of the energy pile EP1, this deformation was thus characterised by both mechanical and thermal contributions.

Marked expansions of up to $\Delta\varepsilon_z = -106\ \mu\varepsilon$ were observed after $t = 35$ and 156 days in the lower portions of piles EP2, 3 and 4. These expansions were significantly greater than those that developed in the top portions of these elements (i.e. between $\Delta\varepsilon_z = -10$ and $-30\ \mu\varepsilon$). They were also greater than the strain under free thermal expansion conditions, $\Delta\varepsilon_f^{th}$ (cf. Fig. 7.6 for the pile EP2 after $t = 156$ days, in which α_{EP} is the linear thermal expansion coefficient of the pile). The marked expansive vertical strains that were observed in the bottom portions of all of the piles during the successive stages of the heating phase of the energy pile EP1 occurred because as heat diffused through the system, the mechanical response of the foundation was governed by the thermally induced deformation of the bottom soil layer of molasse. These strain variations were caused not only by the interplay between the thermally induced deformations (direct and indirect) of the piles and the slab but also and primarily by the thermally induced deformation of the soil mass surrounding the piles. The key factor for this phenomenon was the greater value of the thermal expansion coefficient of the

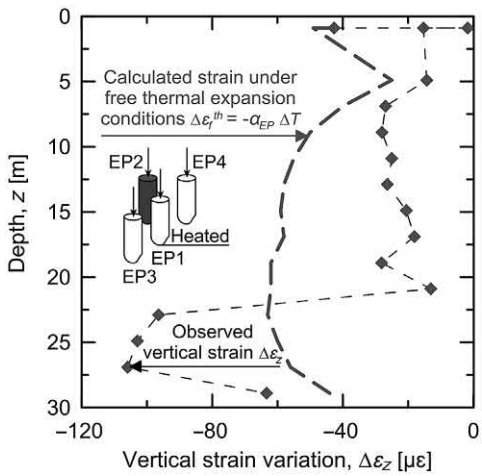

Figure 7.6 Comparison between the variation in vertical strain in a pile nonoperating as a geothermal heat exchanger after $t = 156$ days of geothermal operation of a neighbouring energy pile and the variation in vertical strain associated with free thermal expansion conditions. *Modified after Rotta Loria, A.F., Laloui, L., 2017. Thermally induced group effects among energy piles. Geotechnique 67 (5), 374–393.*

soil layer of molasse than that of the piles. Heating the very stiff molasse layer over time caused a marked expansion of this layer. This field was superimposed on the expansion field of the bottom portions of the piles. Remarkably high expansive vertical strains therefore developed in these settings. Relevant materials properties reported by Rotta Loria and Laloui (2017, 2018) for this site are summarised in Table 7.1 for reference.

7.7 Thermally induced stress variations

The insurgence of thermally induced strains in the surroundings of energy piles operating as geothermal heat exchangers is typically associated with stress variations because of the interplay between strain and stress. The considered thermally induced stress variations can profoundly vary depending on the significance of the thermal expansion potential of the soil relative to that of the piles.

An example of the influence of thermal loads on the vertical stress variations within a group piles restrained at their head by a slab, in which only one energy pile functions as a geothermal heat exchanger, is shown in Fig. 7.7 with reference to the results presented by Rotta Loria and Laloui (2017). The vertical stress variations are calculated based on the experimentally observed vertical strain variations using a one-dimensional

Table 7.1 Material properties of the energy pile foundation tested by Rotta Loria and Laloui (2017, 2018).

Material	Young's modulus, E [MPa]	Poisson's ratio, ν [–]	Volumetric heat capacity, ρc_p [kJ/(m^3 °C)]	Thermal conductivity, λ [W/(m °C)]	Linear thermal expansion coefficient, α [1/°C]
Soil layer A—alluvial soil	190	0.22	2612	1.40	3.3×10^{-6}
Soil layer B—sandy-gravelly moraine	84	0.4	3047	2.60	3.3×10^{-6}
Soil layer C—bottom moraine	90	0.4	2963	2.60	3.3×10^{-6}
Soil layer D—molasse (i.e. sandstone)	3000	0.3	2219	3.50	2.3×10^{-5}
Piles	28,000	0.25	2050	1.47	1×10^{-5}
Slab	35,000	0.25	2050	1.47	1×10^{-5}
Pipes	–	–	–	0.42	–

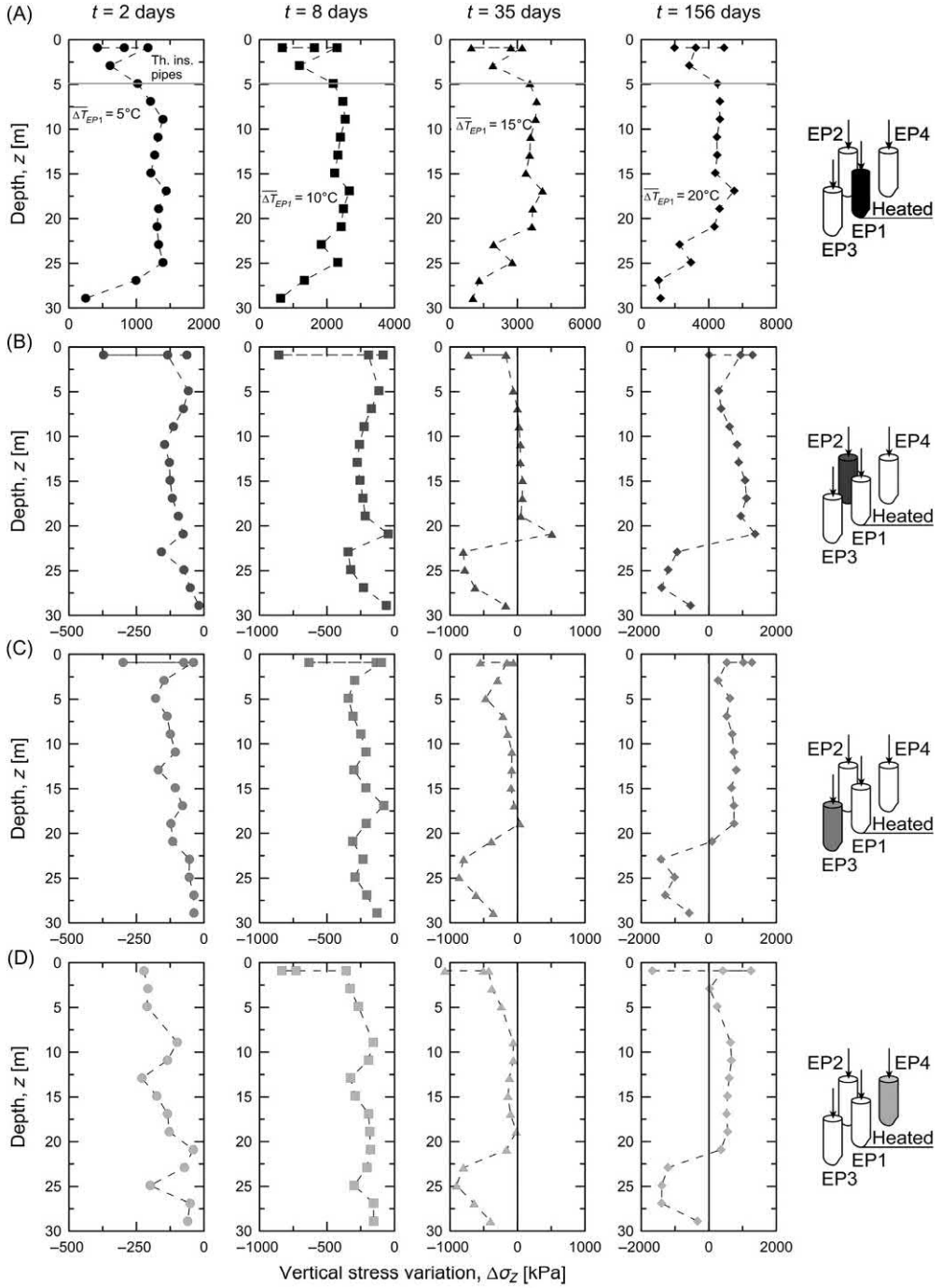

Figure 7.7 Comparison between the experimental and numerical vertical stress variations observed along (A) the operating energy pile EP1 and (B−D) the nonoperating energy piles EP2, 3 and 4, after $t = 2$, 8, 35 and 156 days of testing. *Modified after Rotta Loria, A.F., Laloui, L., 2017. Thermally induced group effects among energy piles. Geotechnique 67 (5), 374−393.*

scheme, i.e. $\Delta\sigma_z = \Delta\sigma_o^{th} = E_{EP}\Delta\varepsilon_b^{th} = E_{EP}\left(\Delta\varepsilon_o^{th} - \Delta\varepsilon_f^{th}\right) = E_{EP}(\Delta\varepsilon_z + \alpha_{EP}\Delta T)$ (where $\Delta\sigma_o^{th}$ is the thermally induced vertical stress, E_{EP} is the Young's modulus of the pile, $\Delta\varepsilon_b^{th}$ is the blocked thermally induced strain and $\Delta\varepsilon_o^{th}$ is the observed thermally induced strain). In the considered case study, the heating that was associated with the geothermal operation of the energy pile EP1 resulted in an increasing compressive vertical stress along its length (cf. Fig. 7.7A). The maximum compressive vertical stress variation of $\Delta\sigma_z = 5500$ kPa was observed after $t = 156$ days of geothermal operation. This phenomenon occurred because the expansive strain potential that is associated with the temperature variation in the pile was restrained by the presence of the soil and slab and caused an increase of the compressive stress in this element. The order of magnitude of the observed vertical stress variation was comparable to other experimental data from the literature (e.g. Murphy et al., 2015) that involved significant energy exploitations through the use of energy piles. Lower compressive vertical stress variations were observed in the bottom portion of the energy pile.

The heating of the energy pile EP1 also induced vertical stress variations in the surrounding piles EP2, 3 and 4 nonoperating as geothermal heat exchangers (cf. Fig. 7.7B–D). After $t = 2$ and 8 days (i.e. during the early stages of the heating phase of energy pile EP1), the piles EP2, 3 and 4 were subjected to tensile stress variations (actual reductions in compressive stress) of up to the maximum negative value of approximately $\Delta\sigma_z = -250$ kPa at their heads. Decreases in the tensile stress variations from the top to the bottom of these elements were observed during this stage of the test. These vertical stress variations were associated with the corresponding deformation field that was described previously. After $t = 35$ and 156 days (i.e. during the successive stages of the heating phase of energy pile EP1), maximum compressive vertical stress variations of up to $\Delta\sigma_z = 1370$ kPa and tensile vertical stress variations of up to $\Delta\sigma_z = -1419$ kPa were measured in the piles EP2, 3 and 4. The previously observed tensile vertical stress variations along the lengths of these elements decreased to compressive values in their top portions but increased towards higher tensile values in their bottom portions.

The effect of the more pronounced thermally induced deformation of the soil layer of molasse than the deformation in the bottom portions of the piles was again evident during the successive stages of the heating phase of energy pile EP1. The deformation of this layer pulled both the energy pile EP1 and the piles EP2, 3 and 4, and caused the reductions of the compressive thermally induced stress fields that were measured along the bottom portions of all of the piles. Because the energy pile EP1 was directly heated and the compressive thermally induced stress variation in this element was more pronounced than the tensile stress variation that was exerted by the molasse, a compressive stress field governed this foundation. Because the piles EP2, 3 and 4 were indirectly heated and the compressive thermally induced stress variations in these elements were smaller than the tensile stress variations that were exerted by the molasse,

a tensile stress field governed the bottom portions of these foundations. Together with the aforementioned phenomena, the presence of the slab played a crucial role in the variation of the stress fields in all the piles. The reason is because the deformation of the slab, which was caused by the thermally induced deformation of the energy pile EP1 and the soil, resulted in an imposed deformation on the piles EP2, 3 and 4 that caused stress variations in these elements. This phenomenon occurred as a consequence of (1) the continuity and compatibility of the displacements characterising the piles, the soil and the slab, and (2) the role of the slab as a constant stiffness boundary condition for the pile–soil system (which differently to a constant load boundary condition involves a load variation – and thus a stress variation – for a displacement variation in deformation-related problems). The bending rigidity per unit area of the slab is $D_b = \left(E_{slab}t_{slab}^3\right)/[12\left(1-\nu_{slab}^2\right)B_{slab}L_{slab}] = 10,080\ \mathrm{kN/m}$ where E_{slab} and ν_{slab} are the Young's modulus and Poisson's ratio of the slab, respectively, and B_{slab}, L_{slab} and t_{slab} are the breadth, length and thickness of the slab, respectively.

7.8 Effect of number of loaded energy piles on the vertical strain variations

When the number of energy piles subjected to thermal loading as a consequence of their geothermal operation increases in a closely spaced pile group, greater thermally induced vertical strains develop in the piles. The presence of thermally induced group effects governs the higher development of vertical strain for energy piles subjected to thermal loading in a group compared to single energy piles subjected to the same average load in an isolated case. In a similar way, when the number of piles subjected to the mechanical loading as a consequence of their structural support operation increases in a closely spaced pile group, greater mechanically induced vertical strain variations develop in the piles. The presence of mechanically induced group effects governs the higher development of vertical strain for energy piles subjected to mechanical loading in a group compared to single energy piles subjected to the same average load in an isolated case.

This feature of group effects has been widely studied in the framework of conventional pile groups subjected to only mechanical loads by means of full-scale in situ tests and is reported, for example by Berezantsev (1961) and O'Neill et al. (1981). In a similar way, it has also been studied in the framework of energy pile groups subjected to thermal and mechanical loads by means of full-scale in situ tests and is reported, for example by Rotta Loria and Laloui (2018). Because a greater vertical strain arises for the same average load applied to energy piles due to group effects, deformation analyses of single energy piles are not exhaustive and cannot represent the actual behaviour for energy piles operating in a group. Therefore these analyses are potentially

misleading in design. As a result, no energy pile analysis or design can be considered complete without accounting for the group effects.

An example of the effect of increasing number of energy piles subjected to the same average thermal load in a group on the thermally induced vertical strain variation along such foundations is shown in Fig. 7.8 with reference to the results presented by Rotta Loria and Laloui (2018). The variations in vertical strain along the length of an energy pile (EP1) when this pile was the only in the group operating as a geothermal heat exchanger (i.e. Test 20EP1) and along (on average) the lengths of four energy piles (EP1, 2, 3 and 4) when all of them operated as geothermal heat exchangers in the same group (i.e. Test 20EPall) are considered. The strain variations, $\Delta\varepsilon_z$, correspond to the average temperature variations along the uninsulated portion of the energy pile EP1 of $\overline{\Delta T}_{EP1} = 5°C$, 10°C, 15°C and 20°C (Fig. 7.8A–D, respectively)

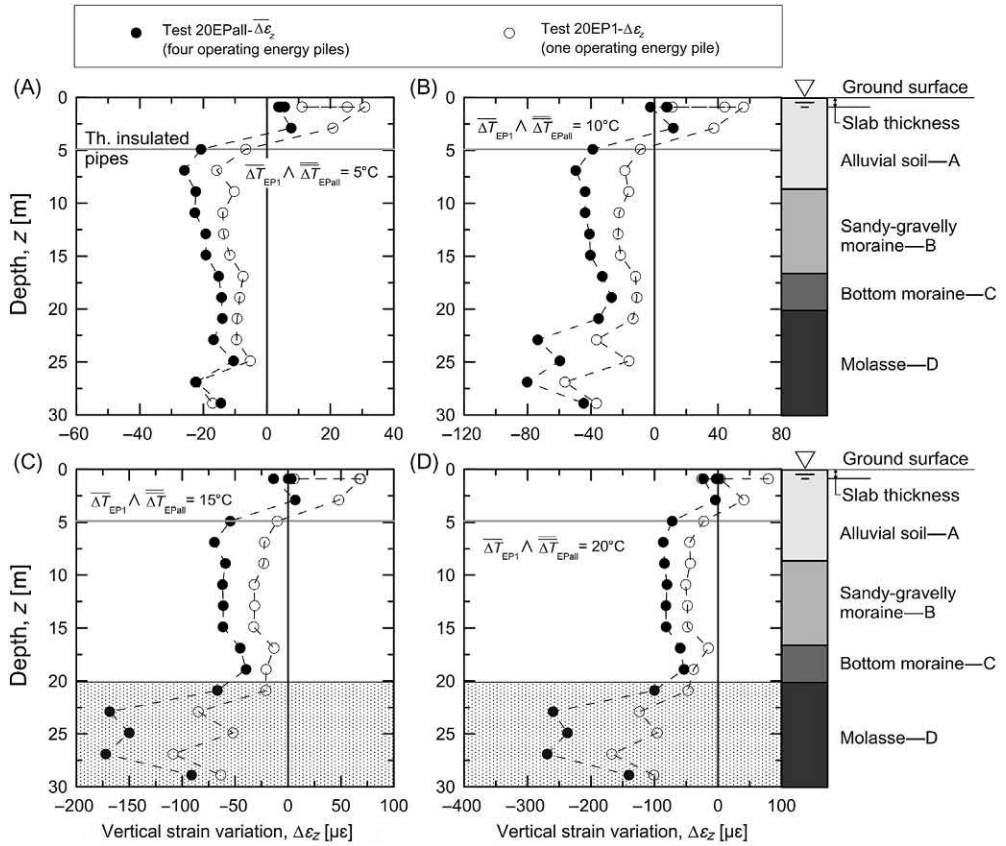

Figure 7.8 Effect of number of energy piles operating as geothermal heat exchangers on the thermally induced vertical strain variation in a group for average temperature variations along the piles of $\Delta T = 5°C$, 10°C, 15°C and 20°C. *Modified after Rotta Loria, A.F., Laloui, L., 2018. Group action effects caused by various operating energy piles. Geotechnique 68 (9), 834–841.*

after $t = 2$, 8, 35 and 156 days of its geothermal operation, respectively. The strain variations, $\overline{\Delta\varepsilon_z}$, correspond to the mean value of the average temperature variations along the uninsulated portions of the energy piles EP1, 2, 3 and 4 of $\overline{\overline{\Delta T}}_{EPall} = 5°C$, 10°C, 15°C and 20°C (Fig. 7.8A–D, respectively) after $t = 2$, 9, 28 and 60 days of their geothermal operation, respectively. When the number of operating energy piles in the group increased, the thermally induced vertical strain variation increased with depth for the same average temperature variation applied to the piles because of group effects. In the operation of multiple energy piles, this average temperature was achieved at a faster rate because of thermal interactions between the energy piles at successive stages of the geothermal operation.

Along with the aforementioned phenomena, the role of the thermally induced soil deformation on the overall response of energy pile groups becomes more pronounced with the increase in the number of energy piles operating as geothermal heat exchangers. The reason for this is that, for the same magnitude of applied thermal load and the same reference time, an increasing number of operating energy piles involves a more marked soil volume affected by a temperature variation. The larger this soil volume, the greater the variation of the mechanical response of the piles in the group irrespective of the thermal expansion coefficients of the materials involved.

An example of this phenomenon is shown in Fig. 7.9, which shows a comparison between the variation in average vertical strain along the previous four energy piles operating as geothermal heat exchangers after $t = 60$ days and the variations in vertical strain associated with free thermal expansion conditions considering the thermal expansion coefficients of the piles and the surrounding soil (Rotta Loria and Laloui, 2018). In the considered case study, similar to the phenomenon characterising piles nonoperating as geothermal heat exchangers in the case of a unique energy pile serving the considered purpose in a group, greater thermally induced vertical strain than may be associated with free expansion conditions were observed for the group of four energy piles operating as heat exchangers. These findings were based on the linear thermal expansion coefficient of the piles, α_{EP} and the applied temperature variation, ΔT (i.e. $\Delta\varepsilon_f^{th} = -\alpha_{EP}\Delta T$). This phenomenon is attributed to the impact of the thermally induced soil deformation on that of the energy piles due to the greater thermal expansion coefficient of the former relative to the latter. Furthermore, based on the results presented, this phenomenon can characterise both *nonoperating* and *operating* energy piles.

7.9 Effect of number of loaded energy piles on the vertical stress variations

When the number of energy piles subjected to thermal loading increases in a closely spaced pile group, lower thermally induced vertical stresses develop in the piles.

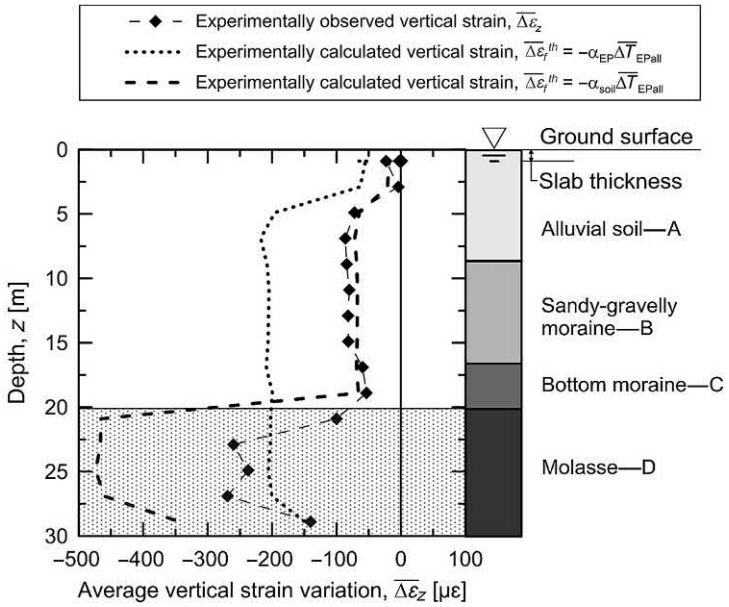

Figure 7.9 Comparison between the variation in average vertical strain in four energy piles operating as geothermal heat exchangers after $t = 60$ days and the variations in vertical strain associated with free thermal expansion conditions referring to the linear thermal expansion coefficient of the piles and that of the soil. *Modified after Rotta Loria, A.F., Laloui, L., 2018. Group action effects caused by various operating energy piles. Geotechnique 68 (9), 834–841.*

This phenomenon occurs due to the interplay between thermally induced blocked deformation and thermally induced observed stress and is detailed in the following.

An example of the effect of increasing number of energy piles subjected to the same average thermal load in a group on the thermally induced vertical stress variation along such foundations is shown in Fig. 7.10 with reference to the results presented by Rotta Loria and Laloui (2018). The variations in vertical stress along the length of an energy pile (EP1) when this pile was the only in the group operating as a geothermal heat exchanger (i.e. Test 20EP1) and along (on average) the lengths of four energy piles (EP1, 2, 3 and 4) when all of them operated as geothermal heat exchangers in the same group (i.e. Test 20EPall) are considered. The stress variations, $\Delta\sigma_z$, correspond to the average temperature variations along the uninsulated portion of the energy pile EP1 of $\overline{\Delta T}_{EP1} = 5°C$, 10°C, 15°C and 20°C (panels (a), (b), (c) and (d), respectively) after $t = 2$, 8, 35 and 156 days of its geothermal operation, respectively. The stress variations, $\overline{\Delta\sigma_z}$, correspond to the mean value of the average temperature variations along the uninsulated portions of the energy piles EP1, 2, 3 and 4 of $\overline{\overline{\Delta T}}_{EPall} = 5°C$, 10°C, 15°C and 20°C (Fig. 7.10A–D, respectively) after $t = 2$, 9, 28 and 60 days of their geothermal operation, respectively. The same time intervals

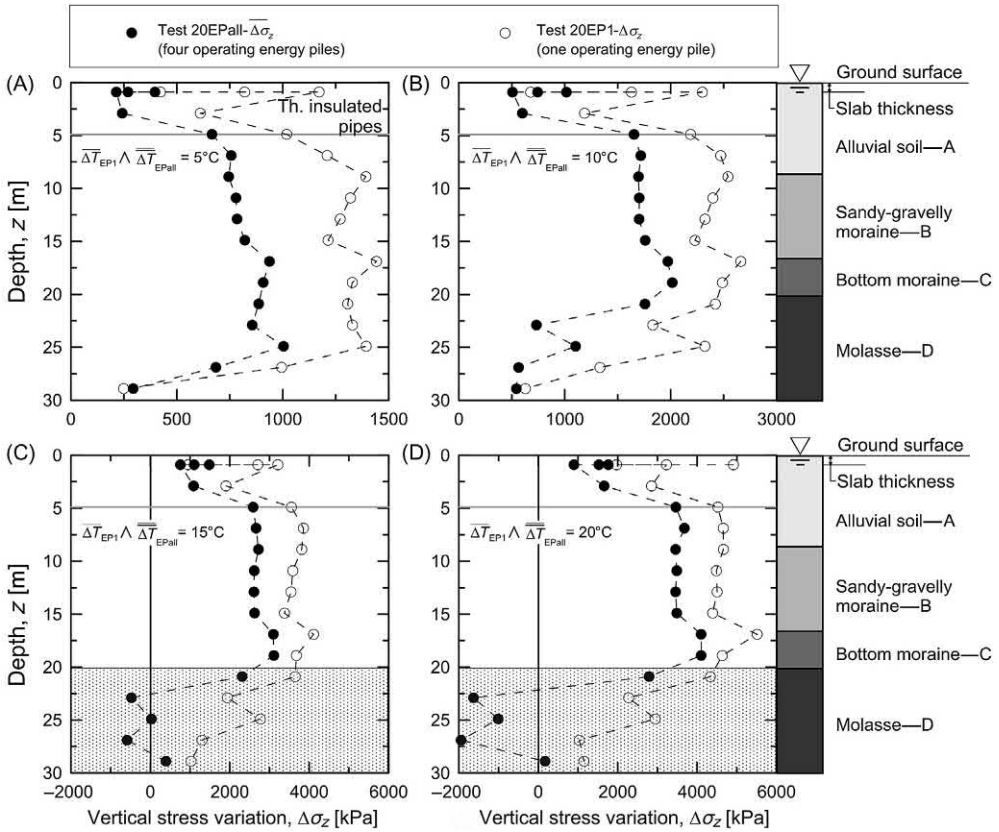

Figure 7.10 Effect of number of energy piles operating as geothermal heat exchangers on the thermally induced vertical stress variation in a group for average temperature variations along the piles of $\Delta T = 5°C$, 10°C, 15°C and 20°C. *Modified after Rotta Loria, A.F., Laloui, L., 2018. Group action effects caused by various operating energy piles. Geotechnique 68 (9), 834–841.*

accounted for thus far are considered. When the number of operating energy piles in the group was increased, the thermally induced vertical stress variation decreased with depth for the same temperature variation applied to the piles.

A notable phenomenon occurred at successive stages of the geothermal operation of the energy pile(s) in the considered tests (cf. Fig. 7.10C and D). In the test in which only one energy pile operated as a geothermal heat exchanger in a group (i.e. Test 20EP1), the presence of a soil layer with a greater linear thermal expansion coefficient than the piles (e.g. the molasse layer) resulted in a less pronounced increase in the vertical stress in the energy pile as the temperature increased in successive stages of geothermal operation. This phenomenon was caused by the thermally induced expansion of the soil, which resulted in a pulling action of the piles that reduced their vertical stress. Because only one operating energy pile was present in the considered test, the

variations in vertical stress remained compressive at successive stages of the geothermal operation, consistent with the soil layer characterised by a greater thermal expansion coefficient. That is the compressive stress variation induced in the energy pile by its restrained expansion was more pronounced than the tensile stress variation exerted by the surrounding soil layer (expanding more than the piles) under the applied heating thermal load. However, in the test in which four energy piles operated as geothermal heat exchangers (i.e. Test 20EPall), the more significant and widespread temperature variation experienced by the soil caused tensile stresses in the parts of the piles located in the soil layer with a thermal expansion coefficient greater than that of the piles. That is the compressive stress variation induced in the energy piles by their restrained expansion was less pronounced than the tensile stress variation exerted by the surrounding soil layer under the heating load. Therefore tensile stress can arise in energy piles when they are heated. This phenomenon experimentally confirms the evidence presented by Bourne-Webb et al. (2016). More generally, for more prolonged operation of various energy piles, when the soil has a greater thermal expansion coefficient than the pile, stress variations that are the opposite of the variations expected based on the type of applied thermal load (i.e. heating or cooling load) can develop in the piles. This phenomenon can be mathematically expressed as follows.

When the soil–pile thermal expansion coefficient ratio $X = \alpha_{soil}/\alpha_{EP} > 1$, in successive stages of geothermal operations, unlike in the usual framework

$$\varepsilon_o^{th} > \varepsilon_f^{th} = -\alpha_{EP}\Delta T \tag{7.1}$$

The reason for this response is that the thermally induced deformation of the energy pile is governed by the soil deformation. Therefore for energy piles subjected to heating thermal loads, the thermally induced stress can be negative (i.e. tensile stress):

$$\sigma_o^{th} = E_{EP}\varepsilon_b^{th} = E_{EP}\left(\varepsilon_o^{th} - \varepsilon_f^{th}\right) = E_{EP}(\varepsilon_o^{th} + \alpha_{EP}\Delta T) < 0 \tag{7.2}$$

The opposite is true for cooling thermal loads applied to energy piles.

Because during the more prolonged operation of various energy piles stress variations opposite those that may be expected based on the type of applied thermal load can develop in energy piles where the soil has a thermal expansion coefficient higher than that of the piles, attention must be paid to the geotechnical characterisation of sites. The use of unsuitable values of thermal expansion coefficients to characterise the energy piles and surrounding soil may generate results with marked pitfalls.

In addition to the previous considerations, the following summarising comments can be reported. Group effects and interactions imply increased deformation of the piles. That is when the same average temperature variation is applied to the energy piles, the proportion of the observed thermally induced vertical strain, ε_o^{th}, increases

with the number of thermally loaded piles. Consequently, under the same temperature variation, lower magnitudes of thermally induced blocked strain, $\varepsilon_b^{th} = \varepsilon_o^{th} - \varepsilon_f^{th}$, and observed vertical stress, $\sigma_o^{th} = E_{EP}\varepsilon_b^{th}$ develop in various operating energy piles than in a single operating energy pile. This phenomenon becomes more pronounced as the number of energy piles operating as geothermal heat exchangers increases. An example of this phenomenon is shown in Fig. 7.11 with reference to the average values of thermally induced strains and stress developed per unit temperature change along the length of the energy pile(s) operating as geothermal heat exchanger(s) observed in the tests reported by Rotta Loria and Laloui (2017, 2018). Under the same temperature variation, the proportion of the observed thermally induced vertical strain increases with the number of thermally loaded piles while the proportion of thermally induced stress decreases. Because the thermally induced vertical stress decreases under the same average temperature variation along the piles as the number of operating energy piles increases, analyses of a single energy pile are not exhaustive and cannot represent the actual behaviour for energy piles operating in a group. However, these analyses are considered useful in the preliminary design stages. Provided that similar head restraint conditions are accounted for a given energy pile in a soil deposit, considering the vertical stress of an isolated energy pile will always be conservative with regards to the thermally induced vertical stress of operating energy piles in a group.

7.10 Key aspects governing the behaviour of energy pile foundations

The results that were described in the previous sections highlight that the behaviour of groups of closely spaced piles that operate partially or entirely as geothermal heat

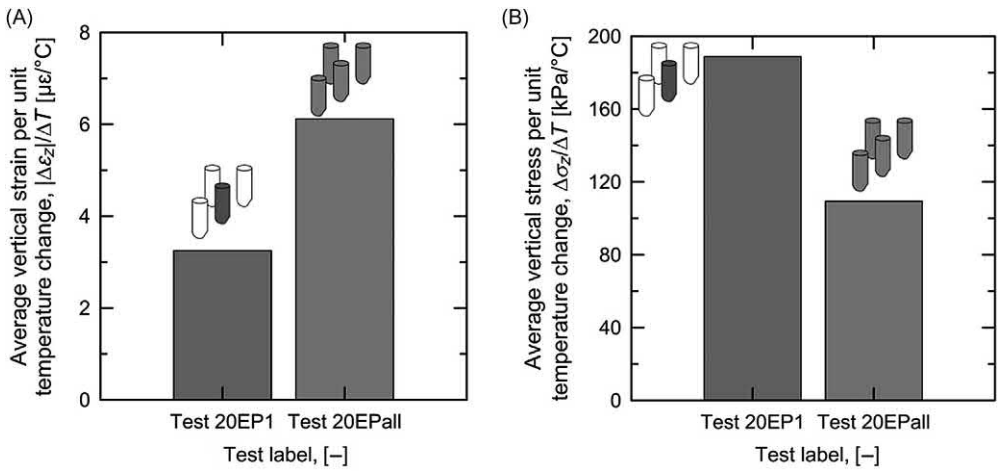

Figure 7.11 Impact of the number of operating energy piles on the group vertical strain and stress variations (Rotta Loria, 2019).

exchangers over time-scales that are typical of practical applications is characterised by significant *group effects*. These group effects can be caused by both the mechanical and thermal loads applied to the energy piles, that is they are mechanically and thermally induced. Mechanically induced group effects are evidenced through mechanical interactions among the piles, the soil and the slab. Thermally induced group effects are evidenced through thermal and thermally induced mechanical interactions between the piles, the soil and the slab.

Thermal interactions appear during successive stages of geothermal operations. For the same geometrical features of the pile group (e.g. the length of the piles and the centre-to-centre spacing between the piles) and a given thermal load applied to the operating energy piles, the magnitude and development of these interactions are governed by (1) the energy design solutions characterising the operating energy piles (e.g. the pipe configuration, the mass flow rate of the fluid circulating in the pipes and the fluid mixture composition), and (2) the thermal and hydraulic properties of the foundation.

Thermally induced mechanical interactions are always present throughout geothermal operations, similar to the mechanical interactions caused by mechanical loads. For the same geometrical features of the pile group (e.g. the length of the piles and the centre-to-centre spacing between the piles) and a given thermal load applied to the operating energy piles, the magnitude and development of these interactions are governed by (1) the relative amount of thermally induced deformation of soil to pile per unit temperature variation, (2) the relative stiffness of slab to soil and (3) the relative stiffness of pile to soil. Aspects (2) and (3) also characterise the mechanical interactions caused by mechanical loads. These characteristics of energy pile groups can be classified through three dimensionless ratios, that is (Rotta Loria and Laloui, 2017):

- *The soil–pile thermal expansion coefficient ratio*

$$X = \frac{\alpha_{soil}}{\alpha_{EP}} \tag{7.3}$$

  where α_{soil} is the linear thermal expansion coefficient of the soil. The soil–pile thermal expansion coefficient ratio allows envisaging the roles of the thermally induced deformations of the soil and the piles in the deformation of the energy pile group at *successive stages* of geothermal operations. Values of $X > 1$ correspond to a deformation of the energy pile group governed by the thermally induced deformation of the soil surrounding the piles, whereas values of $X \leq 1$ to a deformation of the energy pile group governed by the thermally induced deformation of the piles. Practical ranges of X are between 0.1 and 4. According to the findings provided by Bourne-Webb et al. (2016) for single isolated energy piles, the spatial extent of the field that involves temperature variations in the soil around the energy piles governs the effect of X on the thermally induced deformation of the energy pile group. The greater the volume of soil subjected to a temperature

variation is, the more pronounced the relative deformation between the energy piles and the soil is.

- The *slab–soil stiffness ratio*

$$K_{ss} = \frac{4E_{slab}B_{slab}t_{slab}^3(1-\nu_{soil}^2)}{3\pi E_{soil}L_{slab}^4(1-\nu_{slab}^2)} \tag{7.4}$$

where E_{soil} and ν_{soil} are the Young's modulus and the Poisson's ratio of the soil, respectively. The definition of this ratio is based on the work of Brown (1975) for the analysis of strip footings. It was formulated and exploited by Clancy and Randolph (1996) for the analysis of slabs connecting conventional piles and is extended herein to the analysis of slabs connecting energy piles. The slab–soil stiffness ratio allows estimating the impact of the presence of the slab on the load and displacement redistributions in the energy pile group. Values of $K_{ss} \approx 0.001$ correspond to a flexible slab whereas values of $K_{ss} \approx 0.1$ correspond to an almost rigid slab (Brown, 1975). Practical ranges of K_{ss} are between 0.001 and 10 (Clancy and Randolph, 1996).

- The *pile–soil stiffness ratio*

$$\Lambda = \frac{E_{EP}}{G_{soil}} \tag{7.5}$$

where G_{soil} is the shear modulus of the soil. The definition of this ratio is based on the work of Randolph and Wroth (1978) for the analysis of conventional piles subjected to solely mechanical loads and is extended herein to the analysis of energy pile groups subjected to both mechanical and thermal loads. It considers the shear modulus of the soil (which is preferred to the Young's modulus) because in pile-related problems the soil deforms primarily in shear and because the shear modulus is usually assumed to be unaffected by whether the loading is drained or undrained. The pile–soil stiffness ratio characterises the load-displacement relationship between each of the single piles in the group and the surrounding soil. Values of $\Lambda \approx 10$ correspond to a compressible pile whereas values of $\Lambda \approx 10{,}000$ to an almost rigid pile (Poulos and Davis, 1980). Practical ranges of Λ are between 100 and 10,000 (Randolph and Clancy, 1993).

Significant attention must be paid to the thermally (and mechanically) induced mechanical interactions because they are important in the analysis and design (i.e. geotechnical and structural) of energy pile groups.

Thermally induced mechanical interactions can also be classified depending on two criteria, that is (1) the time of heat exchange characterising the energy foundation (Rotta Loria and Laloui, 2016a) and (2) the objects of interaction (Rotta Loria and Laloui, 2018). The former classification includes the latter. Both classifications may be applied to

characterise thermal interactions with similar arguments. The latter classification may also be applied to characterise mechanical interactions caused by mechanical loads.

The classification of thermally induced mechanical interactions based on time includes two types of interactions (Rotta Loria and Laloui, 2016a):

1. *First-kind interactions*: this type of interactions develops during early stages of geothermal operations of energy piles and is primarily caused by the direct heating and associated thermally induced deformation of the operating energy piles.
2. *Second-kind interactions*: this type of interactions develops during successive stages of geothermal operations of energy piles and is caused by (1) the direct heating and related thermally induced deformation of the operating energy piles and (2) the indirect heating and related thermally induced deformation of the soil surrounding the operating energy piles as well as of the nonoperating energy piles. The magnitude and development of these interactions are governed by the interplay between the thermally induced responses of the operating and nonoperating energy piles and soil to temperature variations. The presence of the slab represents a key contribution for the development of all of the aforementioned interactions.

The classification of interactions based on the objects of interaction includes three types of interactions (Rotta Loria and Laloui, 2018):

1. *Pile–soil–pile interaction*: This type of interaction is governed by the relative influence between the deformation of the (i.e. operating) energy piles and the surrounding soil. This influence is primarily characterised by the deformation of the energy piles under the applied temperature variations during early stages of geothermal operations. However, it can be more strongly characterised by the deformation of the soil at successive stages of geothermal operations, especially where the thermal expansion coefficient of the soil may exceed that of the energy piles.
2. *Pile–slab–pile interaction*: This type of interaction is governed by the relative influence between the deformation of the energy piles and the connecting slab. This influence increases as the slab stiffness increases. Moreover, this interaction is less affected by the relative thermal expansion potential of the piles and the slab than the interaction between the piles and the soil. Indeed, in practice, the concrete mix design used for the piles and the slab will be generally the same, and as a result, (at least theoretically) these members will have the same thermal expansion coefficient.
3. *Slab–soil interaction*: This type of interaction is governed by the relative influence between the deformation of the slab and the soil. Similar to the pile–slab–pile interaction, the slab–soil interaction predominantly depends on the relative stiffness of the bodies in contact rather than on their relative thermal expansion coefficients. In practice, although different thermal expansion coefficients may characterise the soil and the slab connecting the energy piles, the shallower depths where the slab is located will not be significantly affected by the geothermal

operation of the piles due to the typical thermal insulation of the pipes. Nothing more unusual than the surface conditions may be expected to affect the interplay between the deformation of the slab and the underlying shallow soil. This phenomenon minimally contributes to the overall deformation of the system because, as in most applications, thermal insulation may be assumed between the slab floor and the upper environment. In any case, the influence of surface conditions may be considered negligible when compared to the effect of the geothermal operation of the energy piles on the deformation of the slab and soil.

References

Berezantsev, K., 1961. Load bearing capacity and deformation of piled foundations. In: Proceedings of 5th International Conference on Soil Mechanics and Foundation Engineering, vol. 1, p. 11.

Bourne-Webb, P.J., Amatya, B.L., Soga, K., Amis, T., Davidson, C., Payne, P., 2009. Energy pile test at Lambeth College, London: geotechnical and thermodynamic aspects of pile response to heat cycles. Geotechnique 59 (3), 237–248.

Bourne-Webb, P., Bodas Freitas, T., Freitas Assunção, R., 2016. Soil–pile thermal interactions in energy foundations. Geotechnique 66 (2), 167–171.

Brown, P., 1975. Strip footing with concentrated loads on deep elastic foundations. Geotech. Eng 6 (1), 1–13.

Burland, J., 1995. Piles as settlement reducers. In: Proceedings of 19th National Italian Geotechnical Conference, pp. 21–34.

Burland, J.B., Broms, B.B., de Mello, V.F., 1977. Behaviour of foundations and structures. In: 9th International Conference on Soil Mechanics and Foundation Engineering., vol. 2, Tokyo.

Clancy, P., Randolph, M., 1996. Simple design tools for piled raft foundations. Geotechnique 46 (2), 313–328.

Di Donna, A., Rotta Loria, A.F., Laloui, L., 2016. Numerical study on the response of a group of energy piles under different combinations of thermo-mechanical loads. Comput. Geotech. 72 (1), 126–142.

Fuentes, R., Pinyol, N., Alonso, E., 2016. Effect of temperature induced excess porewater pressures on the shaft bearing capacity of geothermal piles. Geomech. Energy Environ. 8, 30–37.

Laloui, L., Moreni, M., Vulliet, L., 2003. Comportement d'un pieu bi-fonction, fondation et échangeur de chaleur. Can. Geotech. J. 40 (2), 388–402.

McCartney, J.S., Murphy, K.D., 2012. Strain distributions in full-scale energy foundations. DFI J. 6 (2), 26–38.

Mimouni, T., Laloui, L., 2015. Behaviour of a group of energy piles. Can. Geotech. J. 52 (12), 1913–1929.

Murphy, K.D., McCartney, J.S., Henry, K.S., 2015. Evaluation of thermo-mechanical and thermal behavior of full-scale energy foundations. Acta Geotech. 10 (2), 1–17.

O'Neill, M.W., Hawkins, R.A., Mahar, L.J., 1981. Field study of pile group action. Final Report, p. 195.

Poulos, H.G., Davis, E.H., 1980. Pile Foundation Analysis and Design. Wiley, New York.

Randolph, M., Clancy, P., 1993. Efficient design of piled rafts. In: Impe, V. (Ed.), Deep Foundations on Bored and Auger Piles. Balkema, Rotterdam, pp. 119–130.

Randolph, M.F., Wroth, C.P., 1978. Analysis of deformation of vertically loaded piles. J. Geotech. Eng. Div. 104 (12), 1465–1488.

Rotta Loria, A.F., 2019. Performance-based design of energy pile foundations. DFI J. 12 (2), 94–107.

Rotta Loria, A.F., Laloui, L., 2016a. Analysis of thermally induced mechanical interactions in energy pile groups, Proceedings of First International Conference on Energy Geotechnics, ICEGT 2016, vol. 1. CRC Press, pp. 171–178.

Rotta Loria, A.F., Laloui, L., 2016b. The interaction factor method for energy pile groups. Comput. Geotech. 80, 121–137.
Rotta Loria, A.F., Laloui, L., 2017. Thermally induced group effects among energy piles. Geotechnique 67 (5), 374–393.
Rotta Loria, A.F., Laloui, L., 2018. Group action effects caused by various operating energy piles. Geotechnique 68 (9), 834–841.
Terzaghi, K., 1923. Die Berechnung des Durchlassigkeitszifferdes Tones aus dem Verlauf der hydrodynamischen Spannungserscheinungen. In: Wissen, S.A. (ed.), Wien MAth-naturw KI. Abt IIa, vol. 132, pp. 125–138.

Questions and problems

Statements

a. What are the two structural elements that constitute pile foundations?
b. What is the rationale of constructing pile foundations?
c. What is the difference between a mixed or uniform group of energy piles?
d. What is the difference between pile groups and piled raft foundations from a design perspective?
e. When designing pile groups:
  i. Due account is made of the contribution provided by the cap in the capacity and deformation control of the foundation
  ii. The contributions of capacity and deformation control provided by the cap are neglected
  iii. Only the contribution of capacity provided by the cap is considered
f. What is the responsible phenomenon for thermal interactions in energy pile groups?
g. What are the threshold values of intrinsic permeability and coefficient of compressibility of the solid particles forming the skeleton characterising geomaterials that allow distinguishing situations in which significant thermally induced pore water pressures are to be expected or not?
h. Are thermally induced pore water pressures a concern for the thermohydromechanical behaviour of energy pile foundations in most cases?
i. What are the physical phenomena that govern the development of the two types of mechanical interactions that can arise in energy pile foundations because of the applied thermal loads? Are both of these phenomena dependent on the compatibility of the displacement field?
j. Are heating thermal loads always associated with compressive stress variations in energy piles?
k. In which conditions heating thermal loads may be associated with tensile stress variations? Provide a mathematical explanation for this phenomenon.
l. The presence of group effects and mechanical interactions among piles, under the same average thermal load, involves:
  i. Lower thermally induced strains developed in a pile group compared to a situation involving an isolated pile representative of those of the group
  ii. Higher thermally induced strains developed in a pile group compared to a situation involving an isolated pile representative of those of the group
  iii. None of the above

m. The mechanical interactions caused by mechanical loads applied to energy piles cause a greater group deformation compared to the deformation of an isolated energy pile under the same average load:
  i. True
  ii. False

n. In the context of group effects and mechanical interactions among piles, the influence of thermal and mechanical loads is
  i. Different
  ii. Comparable
  iii. None of the above

o. When the number of energy piles operating as geothermal heat exchangers in a group increases:
  i. Greater thermally induced vertical strains develop in the piles under the same average temperature variation along the piles
  ii. Lower thermally induced vertical strains develop in the piles under the same average temperature variation along the piles
  iii. None of the above

p. When the number of energy piles operating as geothermal heat exchangers in a group increases:
  i. Greater thermally induced vertical stresses develop in the piles under the same average temperature variation along the piles
  ii. Lower thermally induced vertical stresses develop in the piles under the same average temperature variation along the piles
  iii. None of the above

q. Does an analysis of an energy pile that is considered to be in a single and isolated case provide a conservative estimate of its displacement? Why?

r. Thermal interactions are always present in closely spaced energy pile groups:
  i. True
  ii. False

s. Mechanical interactions caused by thermal and mechanical loads arise as soon as these loads are applied to closely spaced pile groups:
  i. True
  ii. False

t. Define mathematically the soil–pile thermal expansion coefficient ratio and specify why it is a key parameter in the characterisation of energy pile foundations.

u. Define mathematically the pile–soil stiffness ratio and specify why it is a key parameter in the characterisation of energy pile foundations. Provide values of this parameters associated with compressible or rigid piles

v. Define the three types of mechanical interactions characterising energy pile foundations based on the objects of interactions.

Solutions

a. **Pile foundations consist of two elements: a group of pile and a pile cap (the latter being intended as the general structural element connecting the piles to the superstructure).**
b. **The rationale of pile foundations in the support of structures can be (1) to provide sufficient capacity by transferring a load to a relatively deep competent ground, (2) to reduce the deformation to an acceptable level, (3) both of the previous purposes.**
c. **Mixed group of energy piles include both energy piles and conventional piles. Uniform group of energy piles include only energy piles.**
d. **Pile groups are foundation systems whereby the purpose of load-carrying capacity or deformation control is assigned to the piles only. Piles raft foundations are systems whereby the purpose of the load-carrying capacity or deformation control is assigned to one or both of these elements.**
e. **When designing pile groups**:
   i. Due account is made of the contribution provided by the cap in the capacity and deformation control of the foundation
   ii. **The contributions of capacity and deformation control provided by the cap are neglected**
   iii. Only the contribution of capacity provided by the cap is considered
f. **Thermal interactions in energy piles groups are caused by heat flow in the surrounding media as a consequence of the geothermal operations of the energy piles**.
g. **Significant thermally induced pore water pressures are to be expected for value of intrinsic permeability lower than 1×10^{-17} m^2 and coefficient of compressibility lower than 2.5×10^{-10} or 0.5×10^{-10} Pa^{-1}.**
h. **No, thermally induced pore water pressures do not represent a concern for the thermohydromechanical behaviour of energy pile foundations in most cases. Typical magnitudes and rates of temperature variations characterising energy piles such as other energy geostructures can be considered in most situations to involve drained conditions. Therefore pore pressures dissipate while thermal loads are applied to the ground surrounding energy geostructures**.
i. **The first phenomenon responsible for mechanical interactions caused by thermal loads is the thermally induced deformation of the energy piles, which causes a variation of the displacement field and thus a disturbance of the mechanical response of neighbouring bodies. This phenomenon depends on the compatibility of the displacement field of the pile–soil system**.

The second phenomenon responsible for mechanical interactions caused by thermal loads is the thermally induced deformation of the bodies located in the vicinity of the energy piles, which is associated with a disturbance of their mechanical response. This phenomenon does not depend on the compatibility of the displacement field of the pile–soil system.

j. No, heating thermal loads are not always associated with compressive stress variations in energy piles. Thermally induced stress variations can profoundly vary depending on the significance of the thermal expansion of the soil relative to that of the piles in case.

k. The vertical stress variation due to thermal loads using a one-dimensional scheme can be expressed as:

$$\Delta\sigma_z = E_{EP}\left(\Delta\varepsilon_o^{th} - \Delta\varepsilon_f^{th}\right)$$

where $\Delta\sigma_z$ [Pa] is the vertical stress variation positive in compression, E_{EP} [Pa] is the Young's modulus of the pile material, $\Delta\varepsilon_o^{th}$ [−] is the observed thermally induced strain and $\Delta\varepsilon_f^{th}$ [−] is the thermally induced strain under free thermal expansion conditions. $\Delta\sigma_z$ becomes negative when $\left(\Delta\varepsilon_o^{th} - \Delta\varepsilon_f^{th}\right)$ is negative, meaning that the observed thermally induced strain is greater than the thermally induced strain under free thermal expansion conditions. In the case of heating thermal loads application, tensile stress variations can occur when the thermally induced deformation of the soil is more pronounced than that of energy piles. In this case, the soil pulls the piles and exerts a tensile stress variation that reduces the compressive stress variation in the piles caused by their thermal expansion due to heating, even leading to a tensile stress variation in the piles.

l. The presence of group effects and mechanical interactions among piles, under the same average thermal load, involves:

- i. Lower thermally induced strains developed in a pile group compared to a situation involving an isolated pile representative of those of the group
- **ii. Higher thermally induced strains developed in a pile group compared to a situation involving an isolated pile representative of those of the group**
- iii. None of the above

m. The mechanical interactions caused by mechanical loads applied to energy piles cause a greater group deformation compared to

the deformation of an isolated energy pile under the same average load:

i. **True**
ii. False

n. **In the context of group effects and mechanical interactions among piles, the influence of thermal and mechanical loads is**:

i. Different
ii. **Comparable**
iii. None of the above

o. **When the number of energy piles operating as geothermal heat exchangers in a group increases**:

i. **Greater thermally induced vertical strains develop in the piles under the same average temperature variation along the piles**
ii. Lower thermally induced vertical strains develop in the piles under the same average temperature variation along the piles
iii. None of the above

p. **When the number of energy piles operating as geothermal heat exchangers in a group increases**:

i. Greater thermally induced vertical stresses develop in the piles under the same average temperature variation along the piles
ii. **Lower thermally induced vertical stresses develop in the piles under the same average temperature variation along the piles**
iii. None of the above

q. **No, it does not. The reason is because such an analysis neglects group effects, thus providing a lower estimate of the pile displacement**.

r. **Thermal interactions are always present in closely spaced energy pile groups**:

i. True
ii. **False**

s. **Mechanical interactions caused by thermal and mechanical loads arise as soon as these loads are applied to closely spaced pile groups**:

i. **True**
ii. False

t. **The soil–pile thermal expansion coefficient ratio is defined mathematically as**:

$$X = \frac{\alpha_{soil}}{\alpha_{EP}}$$

where α_{soil} [1/°C] and α_{EP} [1/°C] are the linear thermal expansion coefficients of the soil and the pile materials, respectively. The soil–pile

thermal expansion coefficient ratio is a key parameter in the characterisation of energy pile foundations because it provides information on the body (e.g. the pile or the soil) governing the thermally induced deformation of such geostructures at successive stage of the geothermal operation of energy piles.

u. **The pile−soil stiffness ratio is defined mathematically as**:

$$\Lambda = \frac{E_{EP}}{G_{soil}}$$

where E_{EP} [Pa] is the young's modulus of the energy pile and G_{soil} [Pa] is the shear modulus of the soil. The pile−soil stiffness ratio characterises the load-displacement relationship between any energy pile in a group and the surrounding soil. Values of $\Lambda \approx 10$ correspond to a compressible pile whereas values of $\Lambda \approx 10000$ correspond to an almost rigid pile.

v. **The mechanical interactions characterising energy pile foundations can be classified in the three following categories based on the objects of interactions**:
   i. **Pile−soil−pile interaction: this type of interaction is governed by the relative influence between the deformation of the (i.e. operating) energy piles and the surrounding soil.**
   ii. **Pile−slab−pile interaction: this type of interaction is governed by the relative influence between the deformation of the energy piles and the connecting slab.**
   iii. **Slab−soil interaction: this type of interaction is governed by the relative influence between the deformation of the slab and the soil**.

PART D

Analysis

CHAPTER 8

Analytical modelling of steady heat and mass transfers

8.1 Introduction

The heat and mass transfer phenomena associated with the operation of energy geostructures certainly do depend on time, that is they are time-dependent. The temperature changes applied to energy geostructures continuously vary together with the thermal loading and boundary conditions. Heating and cooling loads of superstructures typically vary depending on the changes in weather and occupation from an hourly to an annual basis. Boundary conditions such as the temperature in the shallowest portion of the ground vary depending on the weather conditions over the day as well as throughout the day–night and seasonal cycles.

However, there are some reference time (and space) scales that allow considering the heat and mass transfer phenomena as time-independent. These timescales are generally associated with so-called *steady* conditions and involve a time independence of the heat and mass transfer phenomena allowing for a relatively straightforward analysis of the problems involved. For example in the context of the analysis of the heat transfer characterising a body surrounded by a larger domain, under steady conditions (1) the capacity effect of the body becomes negligible, (2) the heat transfer phenomenon becomes a purely resistance process and (3) two distinct subprocesses can be considered to characterise the heat transfer. The first subprocess concerns the heat transfer occurring *within* the body and may be modelled via a time-independent approach. The second subprocess potentially refers to the heat transfer occurring in the domain *around* the body and may be modelled through a time-dependent approach. The considered body may typically be a pipe, a geothermal heat exchanger or a relevant zone of the ground surrounding the heat exchanger.

This chapter presents analytical approaches to characterise the time-independent heat and mass transfer phenomena governing energy geostructures under steady conditions. The analysis of these phenomena is treated for pipes, energy geostructures and the surrounding ground in an attempt to comprehensively characterise the operation of the investigated technology.

To address the aforementioned aspects, *idealisations and assumptions* are presented first: in this context, the objective is to propose a summary of assumptions that allow for expedient yet rigorous analyses of energy geostructures and other geothermal heat

Analysis and Design of Energy Geostructures
DOI: https://doi.org/10.1016/B978-0-12-816223-1.00008-4

exchangers. Second, an analysis of the *heat and mass transfers in pipes* is proposed: the objective of this part is to determine relevant temperature changes, the flow rate and the convection heat transfer coefficient for heat carrier fluids circulating in pipes, such parameters representing the basis to characterise the heat transfer within energy geostructures. Third, the *concept of thermal resistance* is defined by referring to bodies with no internal heat energy generation and with known temperature distribution: in this framework the purpose is to remark how thermal resistance describes heat transfer in the same way electrical resistance does for electric current flow. Next, the concept of thermal resistance is used for the time-independent analysis of the *heat transfer within energy piles and other circular heat exchangers*, as well as *within energy walls and other plane heat exchangers*: in this context the purpose is to show how plain and stratified cylindrical and planar geometries can be used to analyse problems involving energy geostructures of varying complexity, and to illustrate the case of internal heat generation for cylindrical and planar geometries. Afterward, approaches to estimate the *heat transfer and storage capacities of energy piles* are presented: the goal of this section is to highlight the importance of the heat transfer capacity for analyses devoted to assessing the heat extraction potential of cylindrical heat exchangers such as energy piles, while investigations into heat storage capacity aimed to assess the injection potential of such elements. Then, a digression on the *required thermally active dimension of energy geostructures* and the *effectiveness-NTU analysis method for energy geostructures* is proposed, with the goal of summarising the impact of various design solutions on the thermohydraulic behaviour of energy geostructures. Finally, *questions and problems* are proposed: the purpose of this part is to fix and test the understanding of the subjects covered in this chapter by addressing a number of exercises.

8.2 Idealisations and assumptions

In the analysis of the heat transfer, considering reference times, t^*, allows critical considerations to be made. For time intervals $t \leq t^*$, the heat transfer within a considered body cannot be associated with steady conditions and requires a time-dependent modelling approach to be described. In contrast, for time intervals $t > t^*$, the heat transfer within a considered body can be associated with steady conditions and may be meaningfully described through a time-independent modelling approach. In general, for $t > t^*$, *steady-flux conditions (not steady-state conditions)* can be considered to characterise the heat transfer. Steady-flux conditions are situations in which the variation of the potential variable governing a given phenomenon (e.g. temperature for heat transfer) is a result of quantities that evolve with time but are characterised by a constant difference over time. Steady-state conditions are situations in which the variation of the relevant potential variable is a result of quantities that are constant with time.

In the analysis of the heat transfer characterising geothermal heat exchangers such as energy geostructures *three reference times* are often of interest. The magnitude of the considered reference times can be estimated by working with the energy conservation equation and typically depends on a relevant characteristic length of the body and the associated problem under consideration (Eskilson, 1987; Claesson and Eskilson, 1988; Hellström, 1991). The first reference time is the so-called residence time of the fluid circulating in the pipes of energy geostructures and is proportional to the ratio between the heat exchanger depth and the velocity of the fluid circulating in the pipes, that is $t_p \propto L/v_f$ (Hellström, 1991). The second reference time is the characteristic time of the geothermal heat exchanger and for cylindrical bodies such as energy piles is proportional to the ratio between the pile radius and the thermal diffusivity of the grouting material characterising the heat exchanger, that is $t_{ghe} \propto R^2/\alpha_{d,ghe}$ (Eskilson, 1987; Claesson and Eskilson, 1988; Hellström, 1991; Li and Lai, 2015). The third reference time is proportional to the ratio between the radius of a zone of the ground around a given geothermal heat exchanger influenced by heat exchange and the thermal diffusivity of the ground, that is $t_g \propto r_{soil}^2/\alpha_{d,soil}$ (Li et al., 2014). As a consequence of these reference times, *four characteristic periods* can be considered to describe the heat transfer governing energy geostructures. Periods of time $t \leq t_p$ involve short timescales ranging from tens to a few hundreds of seconds and are needed to achieve a steady thermal regime in the pipes of geothermal heat exchangers. These periods are usually negligible from the perspective of the characterisation of the global heat transfer occurring in geothermal heat exchangers but are relevant for the processes occurring in the pipes. Periods of time $t_p < t \leq t_{ghe}$ involve short-to-medium timescales ranging from hours to days and govern the dynamic thermal response of the geothermal heat exchanger. These periods characterise the dynamic optimum control and operation of ground source heat pump and underground thermal energy storage systems. Periods of time $t_{ghe} < t \leq t_g$ characterise the relatively long timescales governing the operative thermal behaviour of the geothermal heat exchangers that are driven by the thermophysical properties of the surrounding ground. Periods of time $t > t_g$ characterise the heat transfer involved with the thermal influence of various potential geothermal heat exchangers. Together with the previous periods (i.e. $t > t_{ghe}$), these time intervals determine the overall feasibility of a system from the standpoint of the life cycle.

Unless otherwise specified, in the following developments devoted to characterising the heat (and mass) transfer in the pipes, the energy geostructures and the surrounding ground, reference is made to timescales $t > t^*$ of $t > t_p$, $t > t_{ghe}$ and $t > t_g$, respectively. Accordingly, the heat transfer occurring within the considered bodies can be considered to occur in steady conditions that can be meaningfully described through a time-independent approach (cf. Fig. 8.1A).

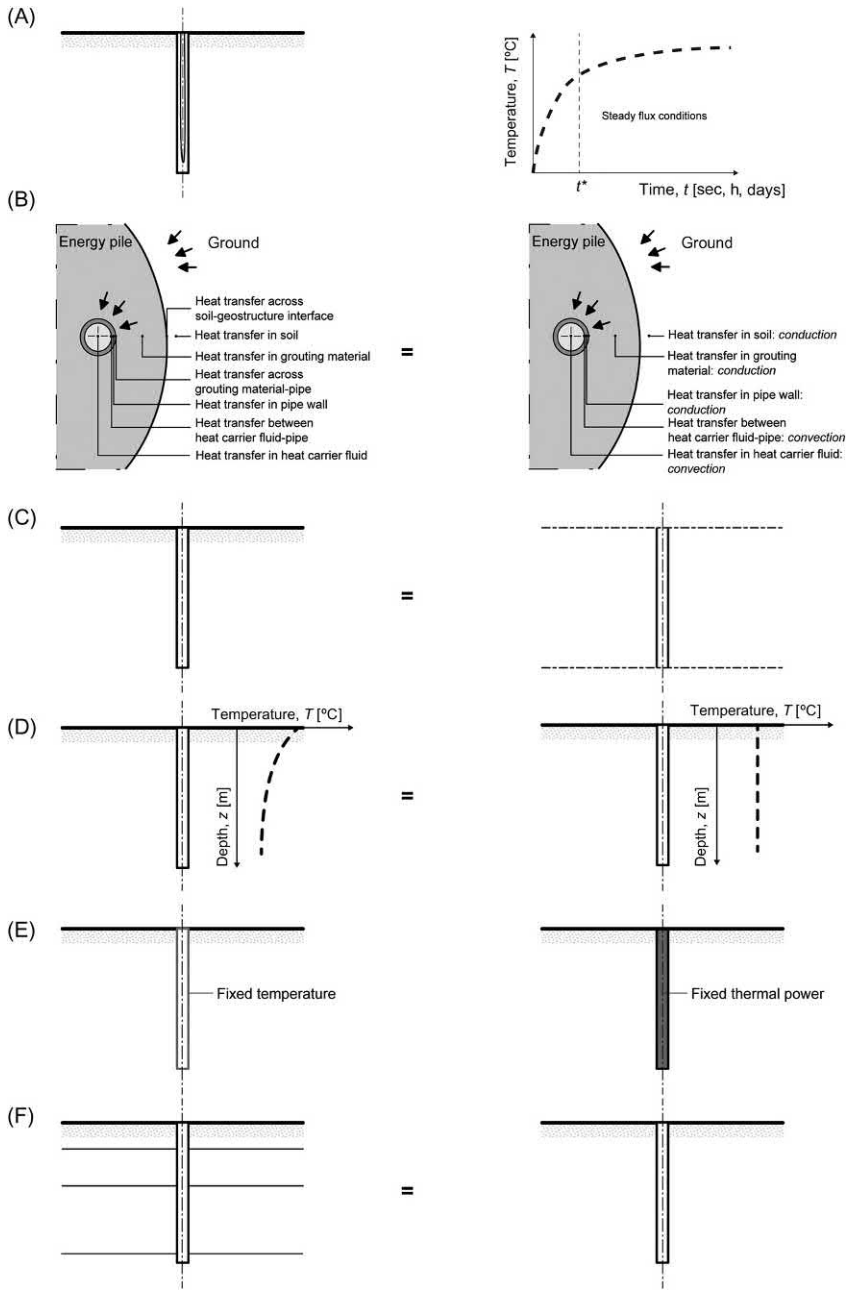

Figure 8.1 (A) Reference time for energy geostructures and physical meaning; (B) heat transfer phenomena accounted for the mathematical modelling of energy geostructures; (C) idealisation of an energy pile as an infinite heat exchanger; (D) idealisation of temperature distribution in the ground; (E) usually employed boundary conditions; (F) modelling of stratified and nonhomogeneous soil deposits.

In the following time-independent analytical modelling of the heat and mass transfers characterising geothermal heat exchangers such as energy geostructures, convection heat and mass transfers are considered to fully characterise the flow of the heat carrier fluid circulating in the pipes. Conduction represents the unique heat transfer mode occurring between the pipe wall and the grouting material of the heat exchanger, within the grouting material of this element, and in the ground around this body (cf. Fig. 8.1B). Convection may be considered by characterising the heat transfer between geothermal heat exchangers embedded in soil deposits with significant groundwater flow or constructed adjacent to a built environment presenting noteworthy airflows.

The ground and the energy geostructures are generally assumed to be infinite in extent (cf. Fig. 8.1C). A semiinfinite dimension of the problem may be considered to account for the influence of the surface conditions.

A uniform initial temperature is assumed to coincide with the undisturbed ground temperature (cf. Fig. 8.1D). Nonuniform temperature fields may also be considered with relatively low efforts once the temperature distribution would be known.

The thermal boundary conditions involve either a fixed constant flux or a fixed constant temperature (cf. Fig. 8.1E). The constant flux boundary condition is generally more convenient to develop thermal considerations, while the constant temperature condition is generally more convenient to develop mechanical considerations. The above particularly applies to situations where the discussed boundary conditions are imposed on the edge of the energy geostructures.

The materials are treated as isotropic and homogeneous media (cf. Fig. 8.1F). A unique equivalent thermal conductivity, λ_{eq}, is considered for layered soils. Despite this approximation, several numerical studies confirm that the considered assumption is appropriate for predicting the overall temperature response through analytical or semi-analytical formulations (Claesson and Eskilson, 1988; Eskilson, 1987; Lee, 2011). The equivalent thermal conductivity is a key parameter used in practical ground source heat pump system design (Ashrae, 2007) and there are several theoretical expressions for λ_{eq} (Bear, 1972). For a horizontally layered ground, the equivalent thermal conductivity can be calculated as

$$\lambda_{eq} = \frac{1}{\sum_{i=1}^{N} l_i} \sum_{i=1}^{N} \lambda_i l_i \tag{8.1}$$

where λ_i and l_i are the thermal conductivity and thickness of the ground layer, i, respectively, and N is the total number of ground layers. For a vertically layered ground, the equivalent thermal conductivity can be calculated as

$$\frac{1}{\lambda_{eq}} = \frac{1}{\sum_{i=1}^{N} l_i} \sum_{i=1}^{N} \frac{l_i}{\lambda_i} \tag{8.2}$$

8.3 Heat and mass transfers in pipes

8.3.1 Thermal and hydrodynamic entrance and fully developed regions in pipes

The heat and mass transfers involved with the flow of a heat carrier fluid in circular pipes is essentially influenced, for constant and uniform inflow velocity and temperature fields of the fluid over time, by (1) the flow regime of the fluid, that is *laminar* or *turbulent flow*, (2) the region in which the flow is considered, that is the *entrance region* or the *fully developed region* and (3) the boundary conditions considered for the temperature field across the boundary between the pipe and the surrounding concrete or soil, that is *constant temperature* or *constant heat flux boundary condition*. The need for considering the flow region makes the hydrodynamic problem of internal flow different compared to external flow, which is completely described based on the knowledge of the flow behaviour (Bergman et al., 2011).

The relevant heat transfer mode for heat carrier fluids circulating in the pipes of energy geostructures is *forced convection*. The reason for this is that a pump will always be present to make the fluid contained in the pipes of the system circulate.

Crucial characteristics of the heat and mass transfers in pipes can be analysed with reference to a circular pipe of internal radius r_p where laminar flow of a heat carrier fluid occurs. This heat carrier fluid is assumed to enter the tube at uniform velocity $v_{x,0}$ and uniform temperature field T_0 lower than the surface temperature of the pipes T_s (cf. Fig. 8.2).

Concerning the heat transfer problem, when the fluid makes contact with the surface of the pipe, convection heat transfer occurs and the *thermal boundary layer* develops with increasing distance x. Typically, the thermal boundary layer merges along the axis of the tube at a distance $x_{fd,th}$, called *thermal entry length*. From the entrance of the tube to the limit of $x_{fd,th}$, the region of the tube is the *entrance region* and the temperature field changes with the distance x. After the limit $x_{fd,th}$, the region of the tube is the *thermally fully developed region* and the relative shape of the temperature field no longer changes with the distance x for the same surface condition. The shape of the temperature profile in the fully developed region profoundly changes, however, depending on the surface condition (cf. Fig. 8.2A) (Bergman et al., 2011).

Concerning the mass transfer problem, when the fluid makes contact with the surface of the pipe, viscous effects come into play and the *velocity boundary layer* develops with increasing distance x. Typically, the velocity boundary layer merges along the

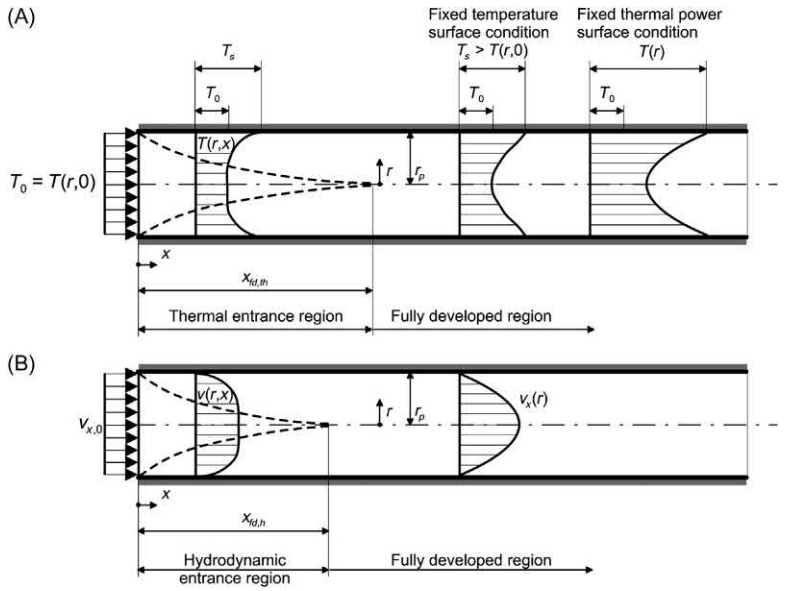

Figure 8.2 Peculiar regions characterising (A) heat and (B) mass transfer in circular pipes.

axis of the tube at a distance $x_{fd,h}$, called *hydrodynamic entry length*. From the entrance of the tube to the limit of $x_{fd,h}$, the region of the tube is the entrance region and the flow velocity changes with the distance x. After the limit $x_{fd,h}$, the region of the tube is the *hydrodynamically fully developed region*, viscous effects extend over the entire cross-section of the tube and the flow velocity no longer changes with the distance x. The velocity profile in the fully developed region is parabolic for laminar flow (cf. Fig. 8.2B), whereas it is flattened for turbulent flow due to turbulent mixing in the radial direction (Bergman et al., 2011).

The extent of the entrance regions depends on whether the flow regime is laminar or turbulent. This fact can be appreciated by referring to the Reynolds number for flow in a circular tube, which is defined as

$$Re_d \equiv \frac{\rho_f \overline{v}_x d_p}{\mu_f} = \frac{\overline{v}_x d_p}{\eta_f} \tag{8.3}$$

where ρ_f is the density of the heat carrier fluid, $\overline{v}_x$ is the fluid mean velocity along the longitudinal direction x, d_p is the inner diameter of the pipe and μ_f and η_f are the dynamic and kinematic viscosity of the fluid, respectively, with $\eta_f = \mu_f/\rho_f$. Fig. 8.3 presents the relationship between η_f and T for a typical heat carrier fluid.

Below the critical Reynolds number $Re_{d,c} = 2300$ laminar flow conditions occur. Above $Re_{d,c} \approx 10{,}000$ fully turbulent conditions exist. Between these values transient

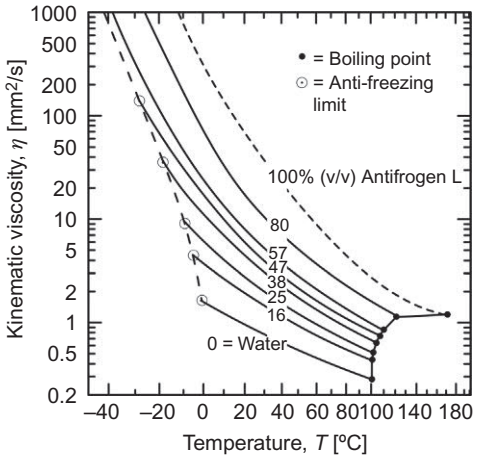

Figure 8.3 Kinematic viscosity of different mixtures of water with antifreeze liquid. *Redrawn after Brandl, H., 2006. Energy foundations and other thermo-active ground structures. Geotechnique 56 (2), 81–122.*

conditions occur. The transition to turbulence is likely to begin in the developing boundary layer of the entrance region (Bergman et al., 2011). Turbulence increases the diffusive transfer of energy, impulse and mass, such an effect increasing with flow velocity (Brandl, 2006).

In laminar flow, the streamlines of fluid movement are smooth, largely linear and highly ordered. Mass transfer is characterised by flow paths with different velocities $\overline{v}_x$ and interface friction τ, which is proportional to the velocity gradient $d\overline{v}_x/dx$ perpendicular to the flow direction. The coefficient of proportionality is the dynamic viscosity, μ_f, which decreases for an increase in temperature. Newton's friction law can be applied in this context and reads

$$\tau = \mu_f \frac{d\overline{v}_x}{dx} \tag{8.4}$$

In turbulent flow, the streamlines of turbulent flow are chaotic and the velocity is subjected to significant fluctuations. Mass transfer is characterised by a laminar zone close to the pipe surface where the local flow velocity is finally zero, while so-called 'turbulence balls' continuously enter and leave the laminar zone. In this context, Eq. (8.4) is only valid along the pipe surface, that is not within the core of the flux, and the shear stress τ_s along the surface is

$$\tau_s = f_M \frac{v_{x'}}{t_l} = \frac{f_M}{8} \rho_f v_{x,c}^2 \tag{8.5}$$

where f_M is the Moody (or Darcy) friction factor characterising the pressure drop within the pipe, v_x' is the velocity along the laminar edge zone, t_l is the thickness of the laminar zone and $v_{x,c}$ is the fluid velocity in the core. This thickness increases for higher concentrations of glycol mixed with water and hence reduces the turbulent zone.

For laminar flow, the thermal entry length may be obtained from an expression of the form (Kays et al., 2012)

$$\left(\frac{x_{fd,th}}{d_p}\right)_{lam} \approx 0.05 Re_d Pr \tag{8.6}$$

where Pr is the Prandtl number, which is a material parameter defined as

$$Pr = \frac{\eta_f}{\alpha_{d,f}} = \frac{\eta_f \rho_f c_{p,f}}{\lambda_f} \tag{8.7}$$

where $\alpha_{d,f}$, $c_{p,f}$ and λ_f are the thermal diffusivity, specific heat and thermal conductivity of the fluid, respectively. The Prandtl number is a measure of the relative importance of viscous diffusion to thermal diffusion.

For turbulent flow, the thermal entry length is approximately independent of the Prandlt number (Bergman et al., 2011) and the value

$$\left(\frac{x_{fd,th}}{d_p}\right)_{turb} \geq 10 \tag{8.8}$$

may be considered.

For laminar flow, the hydrodynamic entry length may be obtained from an expression of the form (Langhaar, 2016)

$$\left(\frac{x_{fd,h}}{d_p}\right)_{lam} \approx 0.05 Re_d \tag{8.9}$$

For turbulent flow, the hydrodynamic entry length is approximately independent of the Reynolds number (Bergman et al., 2011) and may be considered to occur for (Kays et al., 2012)

$$10 \leq \left(\frac{x_{fd,h}}{d_p}\right)_{turb} \leq 60 \tag{8.10}$$

From the above it is evident that if $Pr > 1$ the hydrodynamic boundary layer develops more rapidly than the thermal boundary layer, that is $x_{fd,h} < x_{fd,th}$. The opposite is true for $Pr < 1$.

For water and most other heat carrier fluids circulating in energy geostructures, the Prandtl number is greater than one at the relevant temperatures for the considered applications. Hence the thermal entry length for laminar flow is typically longer than the hydrodynamic entry length.

In energy geostructure applications, the establishment of the fully developed region in which heat transfer is stable typically dominates (Brandl, 2006). The reason for this is that turbulent flow conditions are generally preferred and in these conditions the entrance zone is typically up to 2 m (Loveridge, 2012). This length is markedly lower compared to that characterising laminar conditions, where distances of the entrance region of up to 30−50 m can be expected (Loveridge, 2012).

8.3.2 Mean fluid velocity and temperature

In internal flow problems, the velocity and temperature profiles of the fluid vary over the cross-section and there is no well-defined free stream. Therefore it is necessary to work with a mean velocity, $\overline{v}_x$, and with a mean fluid temperature, $\overline{T}_f$ (also termed core or bulk temperature).

The mean fluid velocity and temperature are essential variables to characterise the mass and heat transfer phenomena occurring in problems involved with internal flow. The mean fluid velocity can be used, for example to determine the flow regime and the mass flow rate. The mean temperature can be used (through the knowledge of the convection heat transfer coefficient and the use of Newton's law of cooling), for example to determine the heat transfer rate through a given convection surface.

The mean fluid velocity and temperature are defined as follows:

- *Mean fluid velocity*: This parameter is defined such that, when multiplied by the fluid density ρ_f and the cross-sectional area of the tube, A_p, it provides the rate of mass flow through the tube, $\dot{m}$ (Bergman et al., 2011), that is the flow of a mass m through a surface per unit time t:

$$\overline{v}_x = \frac{\dot{m}}{\rho_f A_p} \tag{8.11}$$

  Based on the above, the mass flow rate $\dot{m}$ can also be expressed in terms of the volumetric flow rate $\dot{V}$ as

$$\dot{m} = \rho_f \overline{v}_x A_p = \rho_f \dot{V} \tag{8.12}$$

  For laminar flow, the mean velocity is $\overline{v}_x = 0.5 v_{max,x}$ while for turbulent flow $\overline{v}_x = (0.80; 0.85) v_{max,x}$ (Brandl, 2006). From Eqs (8.3) and (8.11) it follows that, for flow in a circular tube of cross-sectional area $A_p = \pi d_p^2/4$, the Reynolds number reduces to

$$Re_d = \frac{4\dot{m}}{\pi d_p \mu_f} \tag{8.13}$$

For steady, incompressible flow in a tube of uniform cross-sectional area, $\dot{m}$ and $\overline{v}_x$ are constants independent of x. Furthermore, because the mass flow rate can be expressed as the integral of the mass flux, $\rho_f v_x$, it follows that for incompressible flow in a circular tube the mean velocity can be calculated at any location x from knowledge of the velocity profile $v_x(r)$ at that location (Bergman et al., 2011)

$$\overline{v}_x = \frac{\dot{m}}{\rho_f A_p} = \frac{\int_{A_p} \rho_f v_x dA_p}{\rho_f A_p} = \frac{2}{r_p^2}\int_0^{r_p} v_x(r,x) r dr \tag{8.14}$$

- *Mean fluid temperature*: This parameter can be defined starting from an alternative equation to Newton's law of cooling, which expresses the heat transferred by convection as

$$\dot{Q} = \dot{m} c_{p,f} \Delta T = \dot{m} c_{p,f} (T_{out} - T_{in}) \tag{8.15}$$

where T_{out} and T_{in} are the outlet and inlet fluid temperature, respectively. Eq. (8.15) can be determined from thermodynamics considerations (e.g. energy conservation), for steady flow in an open system with reference to a uniform temperature field across the inlet and outlet cross-sectional areas of the system [see for the full development, e.g. Bergman et al. (2011)]. The right-hand side of Eq. (8.15) represents the net rate of outflow enthalpy (i.e. thermal energy plus flow work) for an ideal gas or of thermal energy for an incompressible liquid.

Since the hypothesis of a uniform temperature is not true for convection heat transfer, the mean temperature has to be defined in a way such that the term $\dot{m} c_{p,f} \overline{T}_f$ is equal to the rate of thermal energy (or enthalpy) advection integrated over the cross-section. From this consideration and the use of Eq. (8.14) it follows that, for flow in a circular tube with constant ρ_f and $c_{p,f}$, the mean temperature reads (Bergman et al., 2011)

$$\overline{T}_f = \frac{2}{\overline{v}_x r_p^2}\int_0^{r_p} v_x(r,x) T r \; dr \tag{8.16}$$

By multiplying $\overline{T}_f$ by $\rho_f c_{p,f}$, the rate at which thermal energy (or enthalpy) is transferred by convection with the fluid through its movement in the tube is found.

In the analysis of internal flows, the mean temperature plays a comparable role to that of T_∞ expressed in the generalised formulation of Newton's law of cooling, which in this case can be rewritten as

$$\dot{q}_s = h_c \left(T_s - \overline{T}_f\right) \tag{8.17}$$

where $\dot{q}_s$ is the heat flux at the pipe surface, h_c is the local convection heat transfer coefficient and T_s is the temperature of the surface of the pipe. In this case, however $\overline{T}_f$ is not constant in the flow direction as T_∞, but varies along the flow direction, increasing with x if the heat transfer is from the surface to the fluid, that is for $T_s > \overline{T}_f$, while decreasing with x if the heat transfer is from the fluid to the surface, that is for $T_s < \overline{T}_f$. In other words, $d\overline{T}_f/dx$ is never zero when heat transfer occurs (Bergman et al., 2011).

8.3.3 Velocity, pressure gradient, friction factor and temperature in the fully developed region

In the fully developed region of a pipe where laminar flow occurs, both the radial velocity component, v_r, and the gradient of the axial velocity component, $\partial v_x/\partial x$, are everywhere zero. Hence, the axial velocity component, v_x, dependes only on r, that is $v_x(x, r) = v_x(r)$. The radial dependence of the axial velocity can be obtained by solving the appropriate form of the momentum equation along the x direction [see for the full development Bergman et al. (2011)]. As a result, it can be found that the velocity profile of an incompressible fluid with constant properties in the fully developed region under laminar flow conditions is characterised by a parabolic profile (cf. Fig. 8.4)

$$v_x(r) = -\frac{1}{4\mu_f}\left(\frac{dp_f}{dx}\right) r_p^2 \left[1 - \left(\frac{r}{r_p}\right)^2\right] \tag{8.18}$$

where p_f is the pressure of the fluid.

The parabolic profile of the fluid velocity is a function of the Prandtl number. For $Pr \to 0$, the velocity profile along x is equivalent to the profile of a piston flow. For $Pr \to \infty$, the velocity profile corresponds to the Hagen–Poiseuille flow (cf. Fig. 8.4). Common heat carrier fluids for energy geostructures exhibit values of the Prandtl number approximately of $Pr = 7$ for clean water close to the freezing point and $Pr = 70$ for a viscous fluids such as water–glycol mixtures (Brandl, 2006).

Substituting Eq. (8.18) in Eq. (8.14), the mean velocity reads

$$\overline{v}_x = -\frac{r_p^2}{8\mu_f}\frac{dp_f}{dx} \tag{8.19}$$

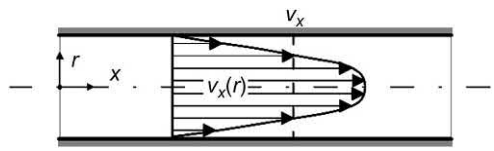

Figure 8.4 Velocity profile of a fluid circulating in laminar flow in a circular pipe.

Substituting Eq. (8.19) in Eq. (8.18) the velocity profile reads

$$\frac{v_x(r)}{\overline{v}_x} = 2\left[1 - \left(\frac{r}{r_p}\right)^2\right] \tag{8.20}$$

Since $\overline{v}_x$ can be computed from knowledge of the mass flow rate, Eq. (8.19) can be used to determine the pressure gradient needed to sustain an internal flow. Interest lies in determining this gradient to understand the pump power requirements (Bergman et al., 2011).

The pressure gradient can be determined through the Moody friction factor, which in its general expression reads

$$f_M \equiv -\frac{2(dp_f/dx)d_p}{\rho_f \overline{v}_x^2} \tag{8.21}$$

For fully developed laminar flow, the friction factor can be rewritten as

$$f_M = \frac{64}{Re_d} \tag{8.22}$$

For fully developed turbulent flow, the formulation of the friction factor is more complex and relies on experimental results, for example, given by Colebrook (Munson et al., 1990; Fox et al., 1985), and can be rewritten as

$$\frac{1}{\sqrt{f_M}} = -2\log\left[\frac{s_R}{3.7d_p} + \frac{2.51}{Re_d\sqrt{f_M}}\right] \tag{8.23}$$

where s_R is the pipe absolute surface roughness, that is the measure of the average height of the internal pipe roughness, which is often normalised by the pipe diameter d_p to obtain the relative surface roughness. Eqs (8.22) and (8.23) are usually depicted in the Moody diagram (cf. Fig. 8.5).

In contrast to the features of the velocity profile in the fully developed region of a pipe that involve that the radial velocity component, v_r, and the gradient of the axial velocity component, $\partial v_x/\partial x$, are everywhere zero, if there is heat transfer the terms $d\overline{T}_f/dx$ and $\partial T/\partial x$ must always be different from zero at any radial distance. For this reason, it is more challenging to find a formulation of the temperature such that $\partial T^*/\partial x = 0$ while $T(r)$ continuously changes with x. However, this temperature does exist for a fluid flowing in a tube with either a prescribed surface heat flux or a uniform surface temperature and is of the form $T^* = (T_s - T)/(T_s - \overline{T}_f)$ (Kays et al., 2012). Working with this temperature allows several considerations of practical interest to be drawn [see, e.g. Bergman et al. (2011)], such that (1) in the thermally fully developed region of a fluid with constant properties the local convection coefficient is

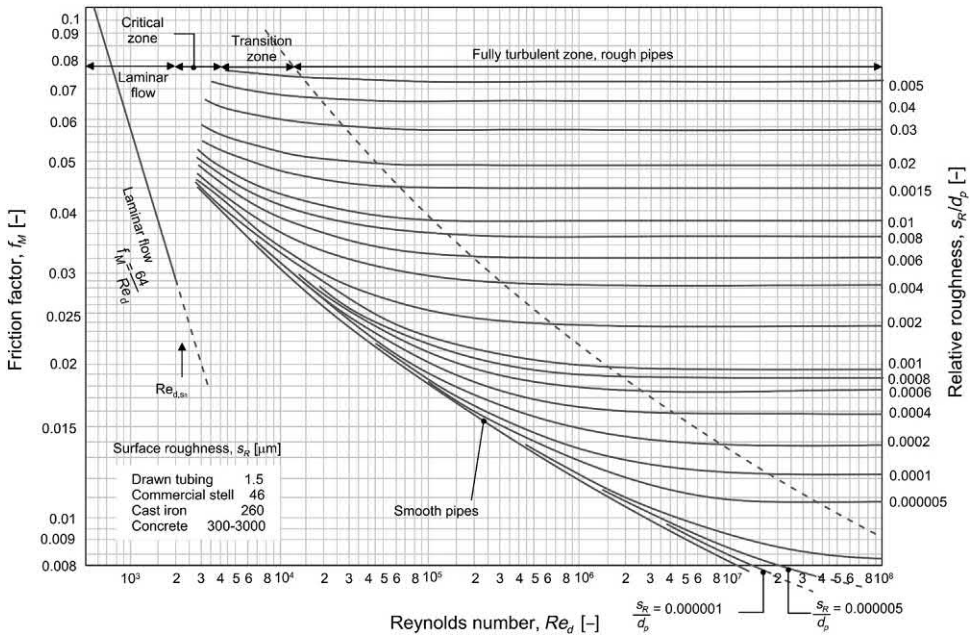

Figure 8.5 The Moody diagram [redrawn after Bergman et al. (2011)]. On the right of the fully dashed line, the flow is in fully turbulent conditions and the behaviour of the fluid is independent of its viscosity, that is f_M only depends on s_R/d_p and for this reason the curves are parallel to each other.

a constant independent of x, (2) in the case of uniform surface heat flux the axial temperature gradient is independent of the radial location and (3) in the case of constant surface temperature the axial temperature gradient depends on the radial location.

In any piping system, head losses are to be expected because of the chosen pipe diameter and flow velocity. These head losses govern the required pumping power. The Darcy–Weisbach equation can be employed to estimate the considered head losses as

$$h_L = f_M \frac{L_p}{d_p} \frac{\overline{v}_x^2}{2g} \tag{8.24}$$

where L_p is the pipe length. In terms of pressure drop, the Darcy–Weisbach equation reads

$$\frac{\Delta p_f}{L_p} = \frac{f_M}{d_p} \frac{\rho_f \overline{v}_x^2}{2} \tag{8.25}$$

To the previous losses must be added the local losses, which are independent of the pipe diameter and are associated with the local disruption of the flow caused by

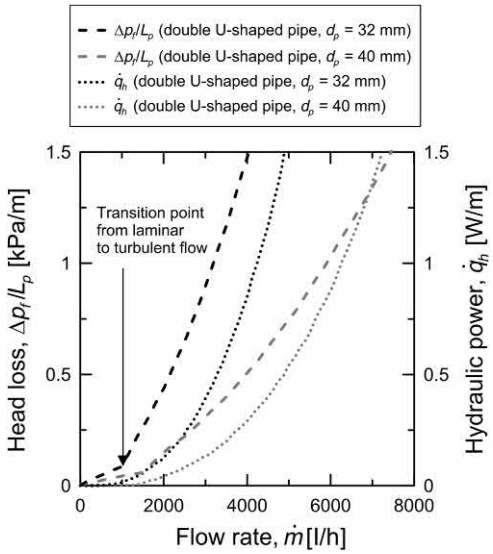

Figure 8.6 Relationship between head losses and hydraulic power with fluid flow rate. *Redrawn after SIA-384/6, 2010. Sondes géothermiques. The Swiss Society of Engineers and Architects, Zurich, Switzerland.*

the pipe bending, but also by fittings, valves and additional plumbing components. The considered head losses can be estimated as

$$h_L = K_L \frac{\overline{v}_x^2}{2g} \tag{8.26}$$

where K_L is a coefficient of local losses associated with the considered disturbing component. Note that the smaller the diameter, the smaller the bending radius of the pipe (usually around ten times the pipe diameter) and thus the higher installed pipe length (and bending), all of this resulting in higher losses. Typical head loss tables or charts are provided in the pipes' technical information. An example of these charts is reported in Fig. 8.6 with reference to the chart proposed by the SIA-384/6 (2010) for geothermal boreholes equipped with double U-shapes pipes, whereby a relationship for the head loss $\Delta p_f/L_p$ and hydraulic power $\dot{q}_h$ is established with the flow rate $\dot{m}$.

8.3.4 The energy balance and the mean temperature in pipes

The energy balance for the pipe allows determining the variation of $\overline{T}_f(x)$ with the pipe length and how the total convection heat transfer $\dot{Q}_{conv}$ is related to the difference in temperatures at the inlet and outlet. This energy balance is proposed hereafter for an incompressible liquid flowing in a tube at constant flow rate $\dot{m}$ with negligible viscous dissipation and negligible net heat transfer by conduction in the axial direction.

The considered assumptions yield to the treatment of a simplified steady-flow case in a tube of finite length that can be mathematically expressed as

$$\dot{Q}_{conv} = \dot{m} c_{p,f} \left(\overline{T}_{out} - \overline{T}_{in} \right) \tag{8.27}$$

where $\overline{T}_{out}$ and $\overline{T}_{in}$ are the mean outflow and inflow fluid temperatures, respectively. Eq. (8.27) is a general expression that applies irrespectively of the nature of the surface of the tube or the flow conditions in the tube.

Working with Eq. (8.15) with reference to a control volume of the tube and recalling that the mean temperature is defined such that its product with the flow rate and specific heat of the fluid represents the rate of thermal energy transferred by convection, integrated over the pipe cross-section, it can be proven that (Bergman et al., 2011)

$$\frac{d\overline{T}}{dx} = \frac{\dot{q}_s P_p}{\dot{m} c_{p,f}} = \frac{P_p}{\dot{m} c_{p,f}} h_c \left(T_s - \overline{T}_f \right) \tag{8.28}$$

where P_p is the surface perimeter of the tube. Eq. (8.28) allows determining the axial variation of the mean temperature $\overline{T}_f$. Where $T_s > \overline{T}_f$, heat is transferred to the fluid and $\overline{T}_f$ increases with x. The opposite is true for $T_s < \overline{T}_f$.

The solution of Eq. (8.28) depends on the surface thermal boundary condition. For a constant temperature boundary condition, it can be proven that (Bergman et al., 2011)

$$\overline{T}_f(x) = T_s - \left(T_s - \overline{T}_{in} \right) \exp\left(- \frac{P_p x}{\dot{m} c_{p,f}} \overline{h}_c \right) \tag{8.29}$$

where $\overline{h}_c$ is the average value of h_c from the tube inlet to x. Eq. (8.29) implies that the term $T_s - \overline{T}_f$ decays exponentially along the tube axis, while T_s is constant (cf. Fig. 8.7A). The heat transfer rate by convection reads in this case

$$\dot{Q}_{conv} = \overline{U} A_p \Delta T_{lm} = \overline{U} A_p \frac{(\Delta T_{out} - \Delta T_{in})}{\ln\left(\Delta T_{out} / \Delta T_{in} \right)} \tag{8.30}$$

where $\overline{U}$ is the average overall heat transfer coefficient, while the ratio comprising the temperature differences and expressing ΔT_{lm} is the so-called log mean temperature difference, that is an appropriate average of the temperature difference over the pipe length, L_p.

For a constant heat flux boundary condition, it can be proven that (Bergman et al., 2011)

$$\overline{T}_f(x) = \overline{T}_{in} + \frac{\dot{q}_s P_p x}{\dot{m} c_{p,f}} \tag{8.31}$$

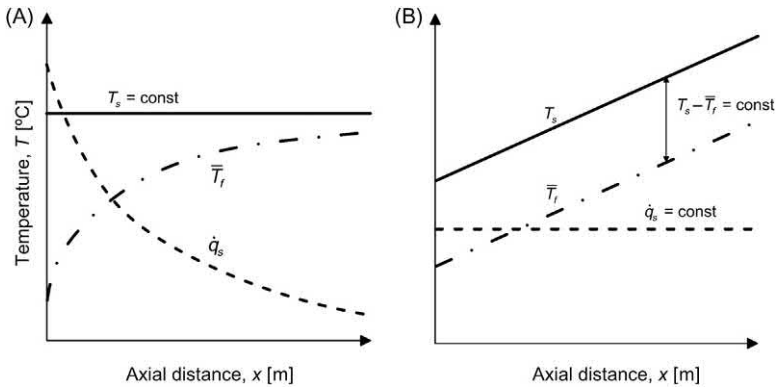

Figure 8.7 Axial temperature variations for heat transfer in a pipe characterised by two different boundary conditions in the fully developed region: (A) fixed constant surface temperature and (B) fixed constant surface heat flux.

Eq. (8.31) implies that the term $T_s - \overline{T}_f$ is constant along the tube axis while the $\dot{q}_s$ is also constant (cf. Fig. 8.7B). The heat transfer rate by convection reads in this case

$$\dot{Q}_{conv} = \dot{q}_s A_p = \dot{q}_s P_p L_p = \dot{q}_s \pi d_p L_p \tag{8.32}$$

The common hypothesis that is made when analysing the heat and mass transfer problem of the heat carrier fluid circulating in the pipes of energy geostructures is that the surface walls of the absorber pipes are characterised by a constant heat flux boundary condition. In this condition, the mean temperature is equal to the arithmetic mean between the mean inflow and outflow temperatures of the fluid, that is $\overline{T}_f = (\overline{T}_{in} + \overline{T}_{out})/2$. However, in reality the constant temperature boundary condition may be more appropriate for the considered problem (Brandl, 2006).

8.3.5 Relevant coefficients for the heat and mass transfer analysis in pipes

To use many of the foregoing results, the convection heat transfer coefficient must be known. Knowledge of this coefficient, through Newton's law of cooling, allows characterising the convection heat transfer characterising a convection surface (e.g. a pipe wall) via the determination of the temperature difference between the mean fluid temperature and the temperature of the wall.

The convection heat transfer coefficient h_c depends on the pipe diameter d_p, the pipe length L_p, the flow velocity $\overline{v}_{f,i}$, the fluid dynamic viscosity μ_f, the fluid density ρ_f and the fluid specific heat $c_{p,f}$ or thermal conductivity λ_f, respectively (Brandl, 2006). The convection heat transfer coefficient is typically larger for turbulent flow compared to laminar flow, such a phenomenon justifying the general preference of

turbulent conditions to laminar conditions for the associated enhancement of the heat transfer. Although turbulent flow in the pipes of energy geostructures is often recommended, in the case of long heat extraction (or storage), the critical point may not the heat transfer but the quantity of thermal energy economically extracted from or stored in the ground (Brandl, 2006). In these conditions, high-performance pumps would be required to create turbulent conditions, thus reducing the seasonal performance factor of the overall geothermal system and making the establishment of turbulent conditions unfavourable.

The convection heat transfer coefficient h_c is strictly related to the Nusselt number Nu_d. For laminar flow, h_c can be determined theoretically via Nu_d. For turbulent flow, h_c is defined experimentally via Nu_d. The Nusselt number expresses the ratio of convective to conductive heat transfer across (normal to) a boundary that undergoes the influence of the flow of a fluid. For a circular tube of diameter d_p, it is defined as

$$Nu_d = \frac{h_c d_p}{\lambda_f} \tag{8.33}$$

The Nusselt number Nu_d is a valuable parameter to describe the heat transfer intensity from the absorber fluid to a particular section of the absorber pipe, the heat transfer between the pipe wall and the heat carrier fluid increasing with Nu_d (Brandl, 2006). However, this number does not describe the overall heat extraction (or storage) of the entire absorber system, which depends on the time period for the absorber fluid to circulate within the heat exchanger.

Relevant formulations of the Nusselt number are determined in the following for an incompressible fluid with constant properties flowing in laminar conditions in a circular tube. The case of turbulent conditions is considered thereafter.

Considering the simplified steady flow Eq. (8.15) with reference to an annular element of tube in which the effects of net axial conduction are neglected and no convection through the radial control surfaces is considered because the radial velocity is zero in the fully developed region, a balance between axial convection and radial conduction is obtained (Bergman et al., 2011). This balance coincides with the following form of the Fourier heat conduction equation

$$\rho_f c_{p,f} v_x(r) \frac{\partial T}{\partial x} = \lambda_f \frac{1}{r} \frac{\partial}{\partial r} \left(r \frac{\partial T}{\partial r} \right) \tag{8.34}$$

For a constant surface temperature T_s along the entire pipe length and a mean fluid temperature $\overline{T}_f$

$$\frac{\partial T}{\partial x} = \frac{T_s - T}{T_s - \overline{T}_f} \frac{d\overline{T}_f}{dx} \tag{8.35}$$

the heat transfer problem can be described according to Eq. (8.34) as

$$\rho_f c_{p,f} v_x(r)\left(\frac{T_s - T}{T_s - \overline{T}_f}\frac{d\overline{T}_f}{dx}\right) = \lambda_f \frac{1}{r}\frac{\partial}{\partial r}\left(r\frac{\partial T}{\partial r}\right) \tag{8.36}$$

whose iterative solution leads to the temperature profile $T(r, x)$. The Nusselt number can then be shown to read (Kays et al., 2012)

$$Nu_d = 3.66 \tag{8.37}$$

If instead of having a constant surface temperature at the pipe surface there is a constant heat flux density $\dot{q}_s = h_c(T_s - \overline{T}_f)$, the convection heat transfer coefficient h_c is constant

$$h_c = \frac{\dot{q}_s}{T_s - \overline{T}_f} = \frac{\lambda_f}{r_p}\left[\frac{\partial}{\partial(z/r_p)}\left(\frac{T_s - T}{T_s - \overline{T}_f}\right)\right]_s \tag{8.38}$$

and the temperature difference $T_s - \overline{T}_f$ is also constant, leading to

$$\frac{\partial T}{\partial x} = \frac{dT_s}{dx} = \frac{d\overline{T}_f}{dx} \tag{8.39}$$

Accordingly, the heat transfer problem can be described according to Eq. (8.34) as

$$\rho_f c_{p,f} v_x(r)\frac{d\overline{T}_f}{dx} = \lambda_f \frac{1}{r}\frac{\partial}{\partial r}\left(r\frac{\partial T}{\partial r}\right) \tag{8.40}$$

From knowledge of the temperature profile $T(r, x)$ that can be defined by integrating Eq. (8.40), the mean temperature $\overline{T}_f(x)$ can be defined. Hence, combining the expression for $\overline{T}_f(x) - T_s(x)$ with Newton's law of cooling, the Nusselt number can be then be shown to read (Bergman et al., 2011)

$$Nu_d = 4.36 \tag{8.41}$$

Eqs (8.37) and (8.41) show that the Nusselt number in circular tubes characterised by laminar flow in the fully developed region is a constant independent of the Reynolds and Prandtl numbers as well as axial location. Fluid flow in laminar conditions depends on how long the fluid is embedded in the absorber pipes as well as on the density, thermal conductivity and specific heat of the absorber fluid. The former aspect is typically related to (1) the pump performance, (2) the pump efficiency and (3) the pipe length. The latter aspects are related to (1) the fluid composition and (2) the temperature. With regards to energy geostructure applications, it is typically observed that heat transfer between absorber pipe wall and fluid increases with (1)

decreasing operating temperature, (2) decreasing concentration of the water–glycol mixture, (3) decreasing pipe length, (4) increasing pipe diameter, (5) increasing pump performance and flow velocity and (6) increasing temperature of the pipe wall (Brandl, 2006). Laminar conditions usually characterise almost all pipes characterised by a small diameter and in such cases the Nusselt number can hardly increase by increasing the pump performance. Turbulent conditions can be achieved rapidly in pipes of large diameter by increasing the pump performance. Therefore installing pumps with higher capacity is of no use when employing small diameter pipes (Brandl, 2006).

For turbulent flow, similar to laminar flow, the Nusselt number is still a constant with the axial location in the pipe as far as the flow is considered in the fully developed region, but it depends on the Reynolds and Prandtl numbers. In this context, the Prandtl's basic equation establishing the relationship between heat transfer and flow resistance may be used for estimating the Nusselt number with reference to fully thermal and hydrodynamically developed conditions as

$$Nu_d = Re_d Pr \frac{f_M}{8} \frac{1}{1 + (Pr - 1)\left(v_x^{'}/v_{x,c}\right)} \tag{8.42}$$

for which the velocity ratio $v_x^{'}/v_{x,c}$ may be substituted by $12.7\sqrt{f_M/8}$.

One alternative formulation is that proposed by Dittus and Boelter for turbulent flow in circular tubes (Bejan and Kraus, 2003)

$$Nu_d = 0.0023 Re_d^{4/5} Pr^{c_{DB}} \tag{8.43}$$

where $c_{DB} = 0.4$ when the fluid is heated and $c_{DB} = 0.3$ when the fluid is cooled, such a formulation being valid for Prandtl and Reynolds numbers approximately in the ranges $0.7 \leq Pr \leq 120$ and $2500 \leq Re_d \leq 124,000$, respectively.

Another approach, often preferred to the Dittus and Boelter Eq. (8.43) because it is more accurate for applications relevant to energy geostructures, also referring to turbulent flow in a smooth circular tube, may consist of considering the Gnielinski equation (Gnielinski, 1976)

$$Nu_d = \frac{\left(f_M/8\right)(Re_d - 1000)Pr}{1 + 12.7\sqrt{(f_M/8)}\left(\sqrt{Pr^2} - 1\right)} \tag{8.44}$$

which is typically valid for Prandtl and Reynolds numbers approximately in the ranges $0.5 \leq Pr \leq 2000$ and $3000 \leq Re_d \leq 50,000$, respectively, and may be applied with reference to $\overline{T}_f$.

One alternative expression of the Gnielinski Eq. (8.44) that also considers the length of the pipe system reads (Brandl, 2006)

$$Nu_d = \frac{(f_M/8)(Re_d - 1000)Pr}{1 + 12.7\sqrt{(f_M/8)}\left(\sqrt{Pr^2} - 1\right)} f_{L_p} \tag{8.45}$$

with

$$f_{L_p} = 1 + \sqrt{\left(\frac{d_p}{L_p}\right)^2} \tag{8.46}$$

and is valid for $0.5 < Pr < 10^4$, $2300 < Re_d < 10^6$ and $0 < d_p/L_p < 1$.

One alternative formulation of the Gnielinski Eq. (8.44) may also consider the factor f_D, instead of f_M, proposed by Haaland (1983)

$$f_D = \left[-1.8\log\left(\frac{6.9}{Re_d}\right)\right]^{-1} \tag{8.47}$$

Fig. 8.8 considers laminar and turbulent flow conditions depending on the dimensionless Reynolds, Nusselt and Prandtl numbers according to Brandl (2006). When determining these parameters, a possible temperature dependence of the material properties has to be taken into account, whereby in practice only the dynamic viscosity is influenced by temperature changes in a relevant way. Thus the Nusselt number becomes (Kays et al., 2012)

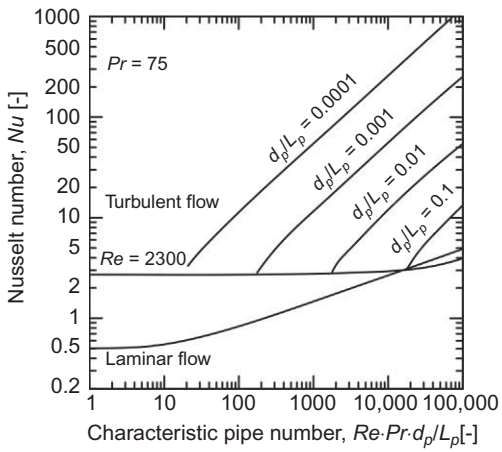

Figure 8.8 Heat transfer from surface of absorber pipe wall to heat carrier fluid for different conditions. *Redrawn after Brandl, H., 2006. Energy foundations and other thermo-active ground structures. Geotechnique 56 (2), 81–122.*

$$Nu_{d,T} = Nu_d \left(\frac{\overline{\mu}_f}{\mu_s} \right)^{0.14} \tag{8.48}$$

where $\overline{\mu}_f$ is the fluid dynamic viscosity at the mean temperature $\overline{T}_f$ and μ_s is the dynamic viscosity at the surface temperature of T_s.

The above relations are approximately valid for both of the surface boundary conditions of constant surface temperature and constant surface heat flux (Bergman et al., 2011). When dealing with turbulent flow conditions in rough tubes, some changes have however to be applied to the above equations. In these conditions, the convection heat transfer coefficient increases with wall surface roughness and may be approximately determined according to the Gnielinski Eq. (8.44) with friction factors obtained from the Moody diagram. This approach is however approximate because the increase in f_M with surface roughness is larger than that of h_c, so that when f_M is approximately four times larger than the corresponding value for smooth surface, h_c no longer changes with an additional increase in f_M (Bergles and Webb, 1970). Accurate alternative procedures to consider the effect of surface roughness on the Nusselt number are proposed by Kakaç et al. (1987).

8.4 Thermal resistance concept for time-independent solutions

The consideration of the Fourier heat conduction equation, together with the use of appropriate boundary conditions, allows determining the temperature distribution within (and around) any considered medium. Hence, by using the fundamental expressions describing conduction, convection or radiation heat transfer, that is Fourier's law, Newton's law of cooling or the linearised Stefan–Boltzmann's law, the temperature distribution may be used for calculating the heat transfer rate by conduction, convection or radiation, respectively, within the considered media. Any of the aforementioned expressions may in particular be written as

$$\dot{Q} = \dot{q}_i A = \frac{\Delta T}{R_{ghe}} \tag{8.49}$$

where $\dot{q}_i$ is the heat flux density exchanged by the considered mode of heat transfer, A is the area normal to the direction of the heat transfer, ΔT is a relevant temperature difference and R_{ghe} the so-called time-independent *thermal resistance* of the geothermal heat exchanger.

The thermal resistance has great utility in solving complex heat transfer problems (Bergman et al., 2011). It takes different forms for different modes of heat transfer and usually includes the influences of the geometry of the heat exchanger

(Bourne-Webb et al., 2016). If steady-state heat transfer is considered to occur, the thermal resistance is a constant equal to the temperature difference between, for example the absorber pipes and the energy geostructure edge. In other words, the thermal resistance expresses the temperature difference that is generated as a consequence of the heat extraction (or injection) of an energy geostructure between the temperature of the heat carrier fluid and the temperature of the surrounding ground irrespective of whether the geological conditions are favourable or not (SIA-D0190, 2005).

The thermal resistance is usually defined through the following three approaches:

1. *One-dimensional modelling approaches*: for the particular case of one-dimensional heat transfer with no internal energy generation and media with constant properties, an analogy exists between the heat diffusion and the electrical charge. Just as an electrical resistance is associated with the transfer of electricity, a thermal resistance may be associated with the conduction of heat (Bergman et al., 2011). In this context, complex geometries can be reduced to a one-dimensional geometry for which the solution of the temperature distribution, and thus the thermal resistance, may be estimated through relevant heat transfer laws. For example simplification of complex geometries may involve considering energy piles as cylinders of infinite length or energy walls or slabs as prisms with plane surfaces infinite in extent. Other problems, which do not involve the modelling of the energy geostructures but of the pipes installed within them, may include reducing any number of pipes to a unique pipe of equivalent diameter through the so-called equivalent pipe approach [see, e.g. Bauer et al. (2011) and Yang et al. (2010)].
2. *Two-dimensional modelling approaches*: for the case of two-dimensional heat transfer, the heat transfer problem is solved through the so-called multipole method [see, e.g. Bennet et al. (1987)].
3. *Quasi three-dimensional modelling approaches*: with reference to a three-dimensional problem for which negligible vertical effects and uniform temperature can be considered, the heat transfer problem is solved by taking into account the thermal interaction between the pipes and the fluid temperature profile with depth [see, e.g. Lamarche et al. (2010)].

The definition of the thermal resistance may also be categorised depending on the nature of the considered modelling approach, that is empirical or theoretical. Empirical approaches are based on empirical constants that may be determined by fitting (experimental or computational) data to the model for a particular geometry. They are widely used because of their simplicity, but provide little insight into the underlying heat transfer problem, differently to theoretical models.

8.5 Heat transfer within energy piles and other circular heat exchangers

8.5.1 General

To characterise the heat transfer of long, slender, circular heat exchangers such as energy piles and vertical boreholes, the thermal power can be conveniently expressed per metre length of the thermally active portion of the element, L [not of the actual length of the pipes embedded into it (Grassi et al., 2015)]. In such situations Eq. (8.49) takes the form

$$\frac{\dot{Q}}{L} = \dot{q}_l = \frac{\Delta T}{R'_{ghe}} \tag{8.50}$$

Heat transfer within heat exchangers such as energy piles, for a given geometry of the pile and stratigraphy of the surrounding ground, depends on (1) the configuration of pipes, (2) the number of pipes, (3) the flow rate (and related regime) of the fluid circulating in the pipes, (4) the thermal properties of the grouting material and (5) the thermal properties of the ground. To describe this phenomenon via analytical or semi-analytical solutions, *three processes* and *two modes of heat transfer* are generally considered (Li and Lai, 2015): (1) *convection* heat transfer between the circulating heat carrier fluid and the inner surface of the pipes; (2) *conduction* heat transfer through the wall of the pipes; and (3) *conduction* heat transfer through the grouting material of the geothermal heat exchanger (cf. Fig. 8.9). Under steady-flux conditions, that is for periods of time t that exceed values from $t_{ghe} = 2.5R^2/\alpha_{d,ghe}$ (Hellström, 1991) to $t_{ghe} = 5R^2/\alpha_{d,ghe}$ (Li and Lai, 2015), *two types of thermal resistances*, that is a thermal resistance associated with convection, R'_{conv}, and a thermal resistance associated with conduction, R'_{cond}, can be formulated and assumed to be connected in series to describe the *three aforementioned processes*. These thermal resistances yield to the time-independent effective thermal resistance of the geothermal heat exchanger as

$$R'_{ghe} = R'_{conv,p} + R'_{cond,p} + R'_{cond,c} \tag{8.51}$$

where $R'_{conv,p}$, $R'_{cond,p}$ and $R'_{cond,c}$ are the effective thermal resistances that account for the aforementioned phenomena (1), (2) and (3), respectively, with $R'_{conv,p} + R'_{cond,p} = R'_p$ the thermal resistance of the pipe and $R'_{cond,c} = R'_c$ the thermal resistance of the grouting material (e.g. concrete).

In general, the lower the effective thermal resistance of the geothermal heat exchanger is, the greater the quality of the heat exchanger from an energy point of view will be. According to Loveridge and Powrie (2014), the resistance of energy piles is less in cases where there are more pipes installed with less concrete cover. Larger

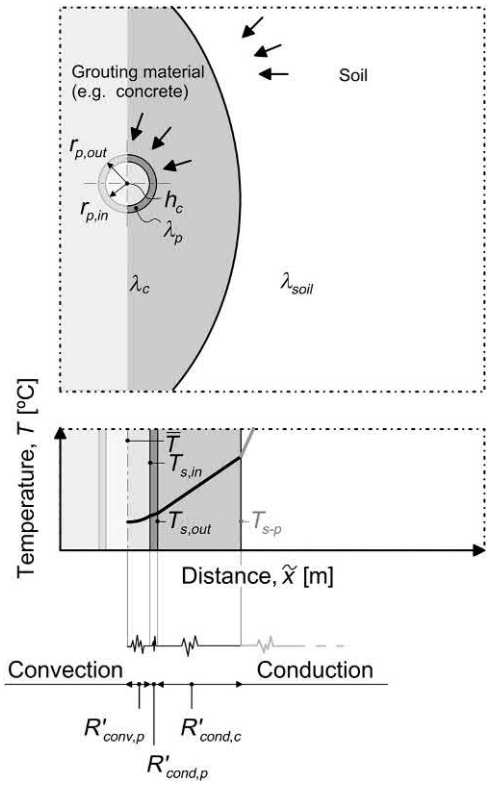

Figure 8.9 The thermal resistance concept applied to energy piles.

energy piles tend to have a larger thermal resistance unless they have a large number of pipes installed. Where the concrete cover is particularly large, the number and arrangement of pipes has less influence on the resistance.

With respect to the magnitude of R'_{ghe}, R'_p usually accounts for 35% whereas $R'_{cond,c}$ accounts for 65%. Because $R'_{conv,p}$ often constitutes 2%−3% of the effective thermal resistance (Li and Lai, 2013), $R'_{cond,p}$ may be inferred to account for 32%−33%. Typical values of R'_{ghe} calculated for energy piles through numerical analyses are reported in Fig. 8.10. Measured values of thermal resistance of energy piles are reported in Table 8.1. Improvements of the effective thermal resistance generally address $R'_{cond,c}$, by lowering it through, for example an increase of the thermal conductivity of the grouting material or increasing the shape factor. A summary on this topic is proposed by Faizal et al. (2016).

In the following, a one-dimensional modelling approach is presented to define the convective thermal resistance R'_{conv} and the conductive thermal resistance R'_{cond}. Knowledge of these thermal resistances allows defining all of the terms $R'_{conv,p}$,

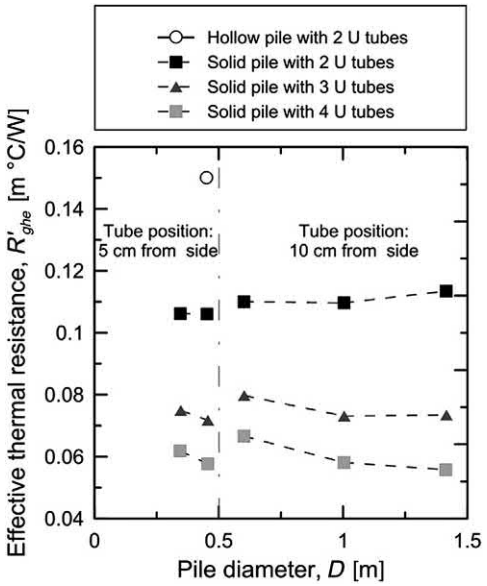

Figure 8.10 Typical simulated values of effective thermal resistance of energy piles. *Redrawn after SIA-D0190, 2005. Utilisation de la Chaleur du Sol par des Ouvrages de Fondation et de Soutènement en Béton. Guide pour la Conception, la Realisation et la Maintenance. The Swiss Society of Engineers and Architects, Zurich, Switzerland.*

Table 8.1 Typical measured values of effective thermal resistance of energy piles.

Pile diameter, D [m]	Pile type	Pipe arrangement	Total thermal resistance, R'_{ghe} [m °C/W]	Source
0.3	Continuous flight auger	Single U-tube	0.22	Wood et al. (2010)
0.6	Cast *in situ*	Single U-tube	0.25	Gao et al. (2008)
		Double U-tube in series	0.15–0.2	
		Triple U-tube in series	0.125–0.15	
0.27	Square driven	Single U-tube	0.17	Lennon et al. (2008)
0.244	Drive steel tube	Single U-tube	0.11	

Source: Data from Loveridge, F., 2012. The Thermal Performance of Foundation Piles Used as Heat Exchangers in Ground Energy Systems (Ph.D. thesis), University of Southampton.

$R'_{cond,p}$ and $R'_{cond,c}$. Two-dimensional or quasi three-dimensional analytical or empirical approaches are afterward presented because of one main shortcoming related to the one-dimensional analysis approach that will be expanded hereafter in some cases.

8.5.2 One-dimensional solutions for heat transfer without internal energy generation

The fundamental problem that allows determining via a one-dimensional modelling approach the thermal resistances R'_{conv} and R'_{cond} is represented by an *infinite hollow cylinder* of constant properties (e.g. thermal conductivity λ), whose inner and outer surfaces are exposed to fluids at different temperatures, without internal heat generation (cf. Fig. 8.11). For this problem, it can be shown that the general Fourier heat conduction equation reduces to

$$\frac{1}{r}\lambda\frac{d}{dr}\left(r\frac{dT}{dr}\right)=0 \tag{8.52}$$

The temperature distribution may be obtained integrating twice Eq. (8.52) and imposing appropriate boundary conditions. For a fixed temperature boundary condition, that is $T(r=r_{in})=T_{s,in}$ and $T(r=r_{out})=T_{s,out}$, where r_{in} and r_{out} are the distances from the origin axis of the internal and outer radii of the hollow cylinder, $T(r=r_{in})$ and $T(r=r_{out})$ are the corresponding temperatures, and $T_{s,in}$ and $T_{s,out}$ are the temperatures of the fluid adjoining the inner and outer surfaces of the cylinder, respectively, this temperature distribution reads

$$T(r)=\frac{T_{s,in}-T_{s,out}}{\ln\left(r_{in}/r_{out}\right)}\ln\left(\frac{r}{r_{out}}\right)+T_{s,out} \tag{8.53}$$

Because the temperature distribution is known, the thermal resistance characteristic of the convective heat transfer problem occurring in the inner cavity of the cylinder and the conductive problem occurring in the wall of the cylinder can be determined with reference to Eq. (8.50), and to Newton's law of cooling and Fourier's law, respectively. In this case, Newton's law of cooling reads

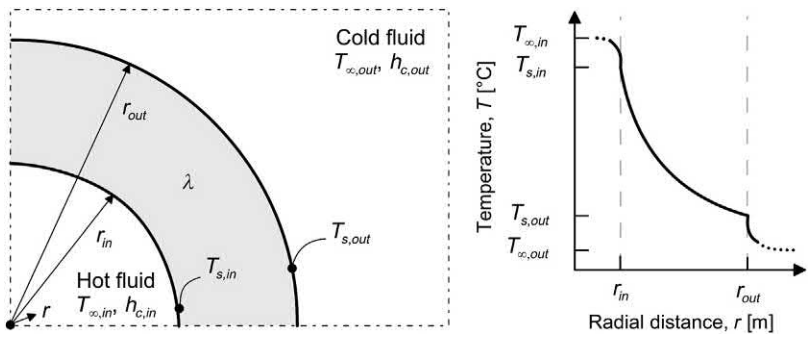

Figure 8.11 Idealisation of hollow pipe with convective surface conditions and related temperature distribution.

$$\dot{q}_l = \frac{\dot{Q}}{L} = \frac{h_c A(T_s - T_\infty)}{L} = 2\pi r_{in} h_c (T_{s,in} - T_\infty) \tag{8.54}$$

while Fourier's law reads

$$\dot{q}_l = \frac{\dot{Q}}{L} = \frac{-\lambda A(dT/dr)}{L} = \frac{2\pi\lambda\left(T_{s,in} - T_{s,out}\right)}{\ln\left(r_{out}/r_{in}\right)} \tag{8.55}$$

It is worth noting that Fourier's law dictates that the heat transfer rate (not the heat flux $\dot{Q}/A$) is a constant in the radial direction because $\lambda r dT/dr$ in Eq. (8.52) is independent of r.

Based on the above, the convective thermal resistance of the hollow cylinder, R'_{conv}, can be found by substituting Eq. (8.54) in Eq. (8.50) with the appropriate formulation of temperature obtained through Eq. (8.53) as

$$R'_{conv} = \frac{\Delta T}{\dot{q}_l} = \frac{T_s - T_\infty}{\dot{q}_l} = \frac{1}{h_c A/L} = \frac{1}{2\pi r_{in} h_c} \tag{8.56}$$

In a similar way, the conductive thermal resistance of the hollow cylinder, R'_{cond}, can be found by substituting Eq. (8.55) in Eq. (8.50) with the appropriate formulation of temperature obtained through Eq. (8.53) as

$$R'_{cond} = \frac{\Delta T}{\dot{q}_l} = \frac{T_{s,in} - T_{s,out}}{\dot{q}_l} = \frac{\ln\left(r_{out}/r_{in}\right)}{2\pi\lambda} \tag{8.57}$$

In the context of the analysis of energy piles or other circular heat exchangers, the aforementioned hollow cylinder may typically be considered to be representative of pipes characterised by internal and outer radii $r_{p,in}$ and $r_{p,out}$, respectively, and a thermal conductivity λ_p. Accordingly, the convective thermal resistance of the pipe reads

$$R'_{conv,p} = \frac{1}{2\pi r_{p,in} h_c} \tag{8.58}$$

while the conductive thermal resistance of the pipe reads

$$R'_{cond,p} = \frac{\ln\left(r_{p,out}/r_{p,in}\right)}{2\pi\lambda_p} \tag{8.59}$$

For an energy pile whose cross-section is characterised by n_p pipes in parallel, the thermal resistance associated with convection in the pipes may be expressed as (Loveridge and Powrie, 2014)

$$R'_{conv,p} = \frac{1}{2\pi r_{p,in} h_c n_p} \tag{8.60}$$

while the thermal resistance associated with conduction through the walls of the pipes may be expressed as (Loveridge and Powrie, 2014)

$$R'_{cond,p} = \frac{\ln\left(r_{p,out}/r_{p,in}\right)}{2\pi\lambda_p n_p} \tag{8.61}$$

Referring to the heat exchange problem characterising a hollow cylinder also allows the estimation of the conductive thermal resistance of the grout $R'_{cond,c}$ to be carried out. In this case, a similar method to that considered for determining $R'_{cond,c}$ can be used, with the main difference that in this case the object of study is a hollow energy pile or vertical borehole (not the pipes embedded within it) characterised by inner and outer radii R_{eff} and R, respectively, and by a thermal conductivity of the grout λ_c. The inner radius of the heat exchanger can be defined as (Shonder and Beck, 2000)

$$R_{eff} = r_{p,out}\sqrt{n_p} \tag{8.62}$$

Assuming a uniform temperature distribution at the outer boundary of the heat exchanger (which may vary with time and depth), the conductive thermal resistance of the grout can then be defined as

$$R'_{cond,c} = \frac{\ln\left(R/R_{eff}\right)}{2\pi\lambda_c} \tag{8.63}$$

8.5.3 Two- and three-dimensional solutions for heat transfer

While the assumption of a temperature distribution around the hollow cylinder may be considered to be accurate for the one-dimensional modelling of the conductive thermal resistance of pipes, $R'_{cond,p}$, this is often not the case for the modelling referring to the conductive thermal resistance of the grout, $R'_{cond,c}$. The reason for this is because in contrast to the uniform temperature field that characterises pipes, the circumferential temperature characterising the cross-section of larger heat exchangers such as piles and vertical boreholes can vary significantly. This phenomenon particularly characterises energy piles with heat exchange pipes located close to the edge of the pile and relatively widely spaced (Loveridge and Powrie, 2014). Furthermore, the one-dimensional solution for R'_{cond} takes no account for the features of the pipe layout, e.g. the offset from the edge of the pile of the pipes and their distance from each other (Loveridge and Powrie, 2014). As a result, unless the pipes may be located in an impractical and inefficient configuration in contact with each other, Eq. (8.63) will lead to an

overestimate of the conductive the thermal resistance of the grout (Sharqawy et al., 2009). To overcome the limitations associated with a one-dimensional modelling approach for the evaluation of $R'_{cond,c}$, two- and three-dimensional modelling approaches may be considered for heat exchangers such as energy piles and vertical boreholes.

An empirical, two-dimensional expression for R'_c is proposed by Loveridge and Powrie (2014) for energy piles characterised by various pipe configurations based on results of finite element analyses and reads

$$R'_{cond,c} = \frac{1}{\lambda_c S_c} \tag{8.64}$$

where S_c is a shape factor that can be determined as

$$S_c = \frac{A_L}{B_L \ln\left(r_{p,out}/R\right) + C_L \ln\left(r_{p,out}/c_c\right) + \left(r_{p,out}/R\right)^{D_L} + \left(r_{p,out}/c_c\right)^{E_L} + F_L} \tag{8.65}$$

where A_L, B_L, C_L, D_L, E_L and F_L are constants whose values depend on the number of pipes and the conductivity ratio between the grouting material and the surrounding ground (cf. Table 8.2), and c_c is the grout cover.

Table 8.2 Constants describing the empirical model proposed by Loveridge and Powrie (2014).

	2 pipes			**4 pipes**		
	$\lambda_c = \lambda_{soil}$	$\lambda_c = 2\lambda_{soil}$	$2\lambda_c = \lambda_{soil}$	$\lambda_c = \lambda_{soil}$	$\lambda_c = 2\lambda_{soil}$	$2\lambda_c = \lambda_{soil}$
A_L	4.919	4.34	4.853	3.33	3.284	3.369
B_L	0.3549	0.317	0.345	0.1073	0.1051	0.1091
C_L	− 0.07127	− 0.001228	− 0.1676	− 0.07727	− 0.05823	− 0.09659
D_L	− 11.41	− 10.18	− 16.76	− 10.9	− 11.98	− 11.79
E_L	− 2.88	− 2.953	− 3.611	− 2.9	− 2.782	− 3.032
F_L	0.06819	− 0.002101	0.1938	0.1278	0.1027	0.1535
	6 pipes			**8 pipes**		
	$\lambda_c = \lambda_{soil}$	$\lambda_c = 2\lambda_{soil}$	$2\lambda_c = \lambda_{soil}$	$\lambda_c = \lambda_{soil}$	$\lambda_c = 2\lambda_{soil}$	$2\lambda_c = \lambda_{soil}$
A_L	3.171	3.162	3.18	3.203	3.201	3.208
B_L	0.08526	0.08669	0.08386	0.0609	0.06157	0.05989
C_L	− 0.07458	− 0.06736	− 0.08085	− 0.06795	− 0.06399	− 0.06839
D_L	− 1.28	− 1.256	− 1.304	− 1.391	− 1.378	− 1.394
E_L	− 2.743	− 2.686	− 2.791	− 2.503	− 2.466	− 2.499
F_L	0.05347	0.03534	0.06954	0.07836	0.06846	0.08188

Table 8.3 Remund (1999) model parameters.

Coefficient value, [-]	Pipes located centrally in the ground heat exchanger and touching each other	Intermediately located and equally spaced pipes in the ground heat exchanger	Pipes touching the edge of the ground heat exchanger located along its diameter
β_0	20.10	17.44	21.91
β_1	− 0.9447	− 0.6052	− 0.3796

The expression proposed by Loveridge and Powrie (2014) is an advanced formulation tailored for energy piles of the original empirical expression proposed by Remund (1999) for boreholes equipped with one pair of pipes. In this latter formulation, the shape factor S_c reads

$$S_c = \beta_0 \left(\frac{R}{r_{p,out}} \right)^{\beta_1} \tag{8.66}$$

where β_0 and β_1 are empirical constants that attempt to capture the effects of pipe separation and placement within the ground heat exchanger (cf. Table 8.3). The rationale of the modification of the expression proposed by Remund (1999) is that it can be difficult to know accurately the positions of the installed pipes and it is also not applicable to most energy piles characterised by more than one pair of pipes (Loveridge and Powrie, 2014).

Other theoretical and empirical models, which were originally proposed for borehole heat exchangers, are available in the literature and may be considered with some degree of accuracy for the analysis of energy piles. Theoretical models based on a two-dimensional modelling approach assume that each pipe in the geothermal heat exchanger is a line source or a multipole, that is a numerical derivative of a line source. By using Duhamel's theorem and the associated superposition principle [see for further details Carslaw and Jaeger (1959)], these models allow to calculate the heat flux related to each pipe and hence the value of thermal resistance. The problem is in this case two-dimensional because the temperature of the heat carrier fluid circulating in the pipes varies with the heat exchanger depth, as a consequence of the fact that (1) heat capacity effects are not taken into account, (2) heat conduction in the axial direction is considered to be negligible, (3) uniform edge temperature of the geothermal heat exchanger is considered and (4) both the heat exchanger and soil properties are considered to be homogeneous with temperature and with independent thermophysical properties (Conti et al., 2016). In principle, two-dimensional models are advantageous compared to one-dimensional models because they allow considering the actual position of and thermal interaction between the pipes in the geothermal heat exchanger. In practice, a single average value of temperature is considered in most cases along the

cross-section of the heat exchanger with depth [see, e.g. Hellström (1991), Diao et al. (2004) and Lamarche et al. (2010)], so neither the thermal interference among the pipes nor the temperature profile of the heat carrier fluid with depth are accounted for. Theoretical models based on a three-dimensional modelling approach do account for an axial variation of the heat carrier fluid temperature with depth, being thus more advanced than models that rely on a two-dimensional approach. Table 8.4 summarises a number of expressions for estimating the effective thermal resistance, R'_{ghe}, of vertical geothermal boreholes that may also be used with some accuracy for energy piles.

8.5.4 One-dimensional solutions for heat transfer with internal energy generation

Heat generation may be considered to occur in cylindrical bodies. These bodies may be modelled as a long solid cylinder in which there is a uniform heat energy generation per unit volume, $\dot{q}_v$, and for which the external surfaces are maintained at T_s (cf. Fig. 8.12). To maintain the surface temperature at a fixed value equal to T_s in steady conditions, the rate at which heat is generated within the cylinder must equal the rate at which heat is convected from the surface of the cylinder to the surrounding (e.g. constituted by a moving fluid). For this problem, it can be shown that the Fourier heat conduction equation reads

$$\frac{1}{r}\frac{d}{dr}\left(r\frac{dT}{dr}\right)+\frac{\dot{q}_v}{\lambda}=0 \tag{8.67}$$

The temperature distribution may be obtained by twice integrating Eq. (8.52) and imposing appropriate boundary conditions. For the following boundary conditions, $(dT/dr)_{r=0}=0$ and $T(r_{in})=T_s$, the former of which is defined by exploiting the symmetry of the system and the fact that along the symmetry axis the temperature gradient must be zero, this temperature distribution reads

$$T(r)=\frac{\dot{q}_v r_{in}^2}{4\lambda}\left(1-\frac{r^2}{r_{in}^2}\right)+T_s \tag{8.68}$$

Being the temperature distribution known, the heat rate at any radius in the cylinder may be evaluated using Fourier's law. To relate the surface temperature, T_s, with that of the cold fluid, T_∞, an overall energy balance may be used to yield

$$T_s=\frac{\dot{q}_v r_{in}}{2h_c}+T_\infty \tag{8.69}$$

It is worth noting that where heat generation is present, the heat transfer rate is not a constant, independent of the spatial coordinate (Bergman et al., 2011).

Table 8.4 Models of effective thermal resistance of energy piles and other circular heat exchangers.

	Expressions for R'_{ghe}	Comments
Empirical models	$\frac{1}{\beta_0 \lambda_c \left(R/r_{p,out}\right)^{\beta_1}}$	This expression uses the shape-factor in heat conduction. The empirical coefficients β_0 and β_1 are obtained by fitting experimental data (Paul, 1996).
	$\frac{1}{2\pi\lambda_c} \ln \frac{R}{\sqrt{n_p} r_{p,out}}$	This expression is derived from the equivalent-diameter assumption (Shonder and Beck, 2000).
	$\frac{1}{2\pi\lambda_c} \ln\left(\frac{R}{R'_p} \sqrt{\frac{R}{x_c}}\right)$	This expression is for ground heat exchangers with a single U-shaped pipe. It is also derived from the equivalent-diameter assumption (Gu and O'Neal, 1998).
Two-dimensional models	$\frac{1}{4\pi\lambda_c} \left\{ \ln\left[\left(\frac{R^2}{2x_c r_{p,out}}\right) \left(\frac{R^4}{R^4 - x_c^4}\right)^{\lambda_n} \right] - \xi \right\} + \frac{R'_p}{2}$	The influence of λ_{soil} is represented by the dimensionless ratio λ_n. $\xi = 0$ for configurations employing a single U-shaped pipe. Otherwise, it can be calculated through the multiple method as (Hellström, 1991) $\xi = \frac{\left[\frac{r_{p,out}}{2x_c}\left(1 - \frac{4\lambda_n x_c^4}{R^4 - x_c^4}\right)\right]^2}{\frac{1 + 2\pi\lambda R'_p}{1 - 2\pi\lambda R'_p} + \frac{r_{p,out}^2}{4x_c^2}\left[1 + \frac{16\lambda_n x_c^4 R^4}{(R^4 - x_c^4)^2}\right]'}$ where x_c is half of the shank spacing between two U-legs.
Quasi-three-dimensional models	$\frac{1}{8\pi\lambda_c} \left[\ln\left(\frac{R}{r_{p,out}}\right) + 2\ln\left(\frac{R}{\sqrt{2}x_c}\right) + \ln\left(\frac{R}{2x_c}\right) - \lambda_n \ln\left(\frac{R^8 - x_c^8}{R^8}\right) \right] + \frac{R'_p}{4}$	T_{out} is obtained by solving energy equations for up- and down-flow channels (Zeng et al., 2003).
	$\frac{L}{\rho_f c_{p,f} \dot{V}} \left(\frac{T_{in} - T}{T_{in} - T_{out}} - \frac{1}{2}\right)$	
	$\frac{L}{\dot{m} c_{p,f} \ln(1/1 - \epsilon_{ghe_{3D}})}$	$\epsilon_{ghe_{3D}}$ is the three-dimensional effectiveness, which varies for depending on the pipe configuration (Conti et al., 2016).

Source: Data from Li, M., Lai, A.C., 2013. Thermodynamic optimization of ground heat exchangers with single U-tube by entropy generation minimization method. Energy Convers. Manag. 65, 133–139 and Conti, P., Testi, D., Grassi, W., 2016. Revised heat transfer modeling of double-U vertical ground-coupled heat exchangers. Appl. Therm. Eng. 106, 1257–1267.

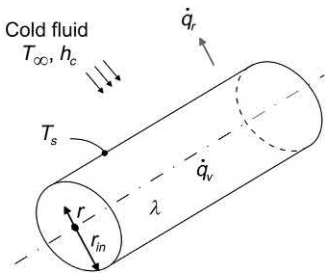

Figure 8.12 Conduction in a solid cylinder with uniform heat generation. *Redrawn after Bergman, T., Incropera, F., Lavine, A., DeWitt, D., 2011. Fundamentals of Heat and Mass Transfer. Wiley, Hoboken, NJ.*

Therefore it would be incorrect to use the thermal resistance concept and the related heat rate equation developed previously.

8.6 Heat transfer in energy walls and other plane heat exchangers

8.6.1 General

To characterise the heat transfer of plane heat exchangers such as energy walls and energy slabs, the thermal resistance R''_{ghe} may be preferably expressed as a function of the thermally active heat exchange surface of these elements. In such situations Eq. (8.49) takes the form

$$\frac{\dot{Q}}{A} = \dot{q}_i = \frac{\Delta T}{R''_{ghe}} \tag{8.70}$$

Heat transfer in plane geothermal heat exchangers such as energy walls may be considered to be dependent, similar to energy piles, on (1) the configuration of pipes, (2) the number of pipes, (3) the flow rate (and related regime) of the fluid circulating in the pipes, (4) the thermal properties of the grouting material and (5) the thermal properties of the ground. In addition to these aspects, (6) the flow rate (and related regime) of the fluid circulating in a potential cavity constituting the underground built environment adjacent to the geostructure may crucially characterise the heat transfer problem governing such heat exchangers. Thermal resistances accounting for convection R''_{conv} and conduction R''_{cond} may be defined in this case through a one-dimensional modelling approach to develop similar considerations to those proposed for cylindrical geometries. Their determination is presented hereafter.

8.6.2 One-dimensional solutions for heat transfer without internal energy generation

The fundamental problem that allows determining via a one-dimensional modelling approach the thermal resistances R''_{conv} and R''_{cond} is represented by an *infinite plane wall*

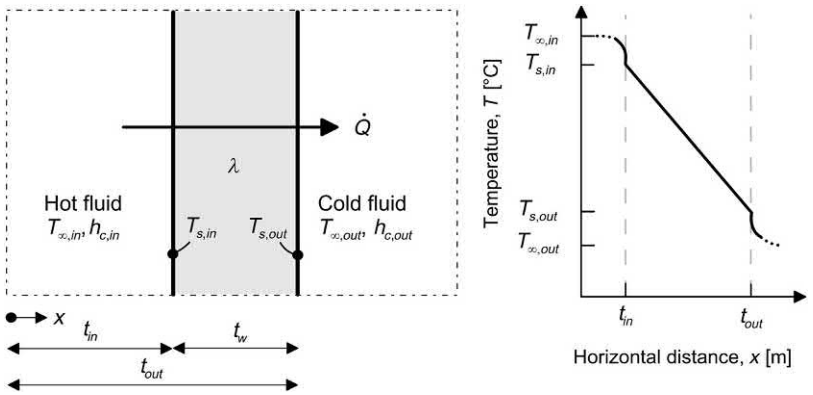

Figure 8.13 Idealisation of plane wall with convective surface conditions and related temperature distribution.

of constant properties (e.g. thermal conductivity λ), whose inner and outer surfaces are exposed to fluids at different temperatures, without internal heat generation (cf. Fig. 8.13). For this problem, it can be shown that the Fourier heat conduction equation reduces to

$$\lambda \frac{d}{dx}\left(\frac{dT}{dx}\right) = 0 \tag{8.71}$$

The temperature distribution may be obtained integrating twice Eq. (8.52) and imposing appropriate boundary conditions. For a fixed temperature boundary condition, that is $T(x = t_{in}) = T_{s,in}$ and $T(x = t_{out}) = T_{s,out}$, where t_{in} and t_{out} are the distances from the origin axis of the internal and outer surface of the plane wall of thickness $t_{out} - t_{in} = t_w$, $T(x = t_{in})$ and $T(x = t_{out})$ are the corresponding temperatures, and $T_{s,in}$ and $T_{s,out}$ are the temperatures of the fluid adjoining the inner and outer surfaces of the wall, respectively, this temperature distribution reads

$$T(x) = (T_{s,out} - T_{s,in})\frac{x}{t_w} + T_{s,in} \tag{8.72}$$

Eq. (8.72) shows how for one-dimensional steady conduction in a plane wall with no internal heat generation and constant thermal conductivity, the temperature varies linearly with the distance x (not logarithmically as in the case of the cylinder problem).

Because the temperature distribution is known, the thermal resistance characteristic of the convective heat transfer problem occurring in the cavity adjacent to the wall and the conductive problem occurring in the wall can be determined with reference to Eq. (8.70), and to Newton's law of cooling and Fourier's law, respectively. In this case, Newton's law of cooling reads

$$\dot{q}_x = \frac{\dot{Q}}{A} = \frac{h_c A(T_s - T_\infty)}{A} = h_c(T_{s,in} - T_\infty) \tag{8.73}$$

while Fourier's law reads

$$\dot{q}_x = \frac{\dot{Q}}{A} = \frac{-\lambda A(dT/dx)}{A} = \frac{\lambda\left(T_{s,in} - T_{s,out}\right)}{t_w} \tag{8.74}$$

It is worth noting that Fourier's law dictates that the heat transfer rate *and* the heat flux $\dot{Q}/A$ are constants independent of x.

Based on the above, the convective thermal resistance of the plane wall, R''_{conv}, can be found by substituting Eq. (8.73) in Eq. (8.70) with the appropriate formulation of temperature obtained through Eq. (8.72) as

$$R''_{conv} = \frac{\Delta T}{\dot{q}_x} = \frac{T_s - T_\infty}{\dot{q}_x} = \frac{1}{h_c} \tag{8.75}$$

In a similar way, the conductive thermal resistance of the plane wall, R''_{cond}, can be found by substituting Eq. (8.74) in Eq. (8.70) with the appropriate formulation of temperature obtained through Eq. (8.72) as

$$R''_{cond} = \frac{\Delta T}{\dot{q}_x} = \frac{T_{s,in} - T_{s,out}}{\dot{q}_x} = \frac{t_w}{\lambda} \tag{8.76}$$

8.6.3 Solutions for heat transfer with internal energy generation

Heat generation may be considered to occur in plane solid bodies such as energy walls, energy slabs and other heat exchangers. The plane wall geometry may in particular become useful to describe the heat transfer problem governing plane bodies in which there is a uniform heat energy generation per unit volume, $\dot{q}_v$, and for which the external surfaces are maintained at $T_{s,in}$ and $T_{s,out}$, with $T_{s,in} \neq T_{s,out}$ (cf. Fig. 8.14). For this problem, it can be shown that the Fourier heat conduction equation reads

$$\frac{d^2T}{dx^2} + \frac{\dot{q}_v}{\lambda} = 0 \tag{8.77}$$

The temperature distribution may be obtained by twice integrating Eq. (8.52) and imposing appropriate boundary conditions. For the following boundary conditions, $T\left(x = -t_{w,r}\right) = T_{s,in}$ and $T\left(x = t_{w,r}\right) = T_{s,out}$, where $t_{w,r}$ is half of the plane wall thickness t_w, this temperature distribution reads

$$T(x) = \frac{\dot{q}_v t_{w,r}^2}{2\lambda}\left(1 - \frac{x^2}{t_{w,r}^2}\right) + \frac{T_{s,out} - T_{s,in}}{2}\frac{x}{t_{w,r}} + \frac{T_{s,in} + T_{s,out}}{2} \tag{8.78}$$

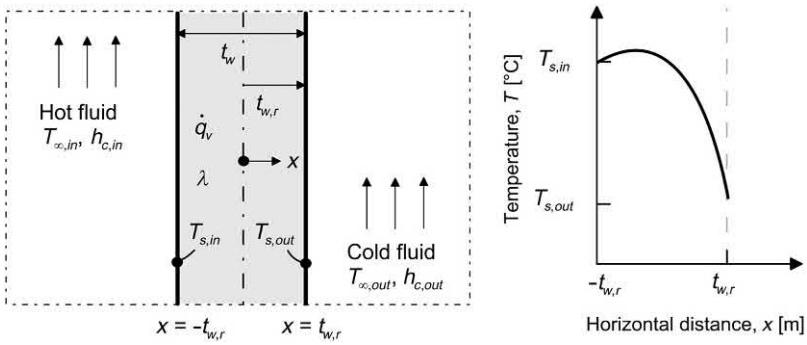

Figure 8.14 Conduction in a plane wall with uniform heat generation and asymmetrical boundary condition.

Being the temperature distribution known, the heat flux at any distance in the plane wall may be evaluated using Fourier's law. It is worth noting that when internal heat generation characterises a plane wall, the heat flux is no longer independent of the distance x.

When dealing with a plane wall whose surface temperatures $T_{s,in}$ and $T_{s,out}$ are $T_{s,in} = T_{s,out} = T_s$ (cf. Fig. 8.15A), Eq. (8.78) simplifies because the temperature distribution is then symmetrical with respect to the centre plane. Hence

$$T(x) = \frac{\dot{q}_v t_{w,r}^2}{2\lambda}\left(1 - \frac{x^2}{t_{w,r}^2}\right) + T_s \tag{8.79}$$

At the plane of symmetry the temperature gradient is equal to zero, $(dT/dx)_{x=0} = 0$. Therefore there is no heat transfer across this plane, which effectively means that the plane is characterised by an adiabatic surface (cf. Fig. 8.15B). Eq. (8.78) is thus valid also for plane walls that are perfectly insulated on one side (e.g. $x = 0$) and maintained at a fixed constant temperature T_s on the other side ($x = t_{w,r}$). However, to use the considered expression there is the need to know the magnitude of T_s, which in most cases is unknown in spite of the knowledge of T_∞. This temperature can however be related through an overall energy balance to the plane wall and yield the resulting formulation

$$T_s = \frac{\dot{q}_v t_{w,r}}{h_c} + T_\infty \tag{8.80}$$

As for the case of the cylinder with internal energy generation, it is worth noting that where heat generation is present in plane walls, the heat transfer rate is not a constant, independent of the spatial coordinate (Bergman et al., 2011). Therefore it would be incorrect to use the thermal resistance concept and the related heat rate equation developed previously.

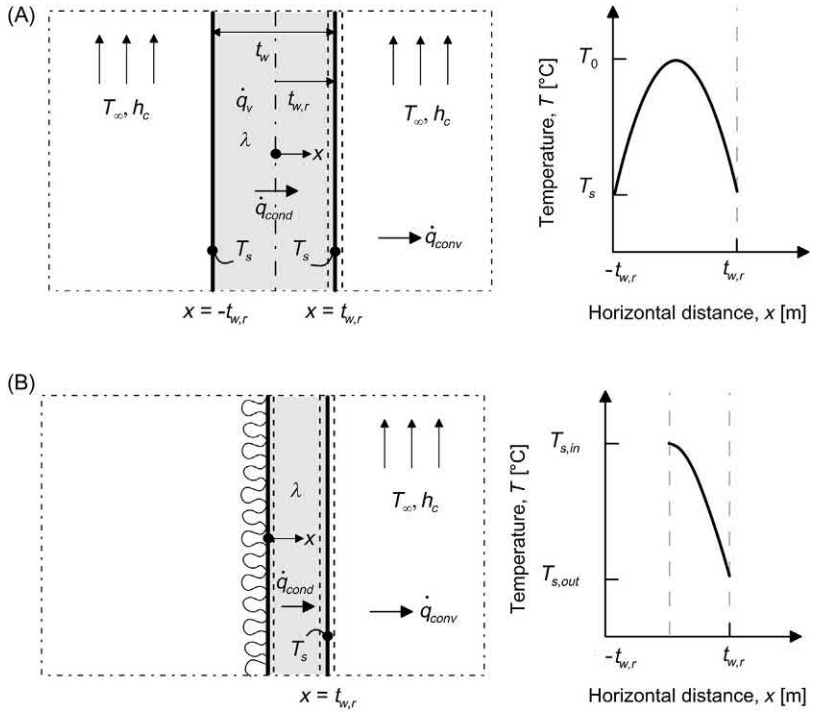

Figure 8.15 Conduction in a plane wall with uniform heat generation and (A) symmetrical boundary condition and (B) adiabatic surface at mid plane.

8.7 Heat transfer analysis through equivalent composite thermal circuits

8.7.1 Application of thermal circuits to basic cylindrical and plane problems

Thermal resistances can efficiently be associated with the transfer of heat and represented in circuits similarly to electrical resistances. Circuit representations provide a useful tool for both conceptualising and quantifying heat transfer problems (Bergman et al., 2011). Fig. 8.16 shows an example of thermal circuits for the previously considered problems of the infinite cylinder and plane wall.

For the cylinder, since $\dot{Q}$ is constant throughout the network, it follows that

$$\dot{q}_l = \frac{\dot{Q}}{L} = \frac{T_{\infty,in} - T_{s,in}}{1/(2\pi r_{in} h_{c,in})} = \frac{T_{s,in} - T_{s,out}}{(\ln(r_{out}/r_{in}))/2\pi\lambda} = \frac{T_{s,out} - T_{\infty,out}}{1/(2\pi r_{out} h_{c,out})} \tag{8.81}$$

The thermal power per unit length may also be expressed in terms of the overall temperature difference, $T_{\infty,in} - T_{\infty,out}$, and the total thermal resistance, R'_{tot}, as

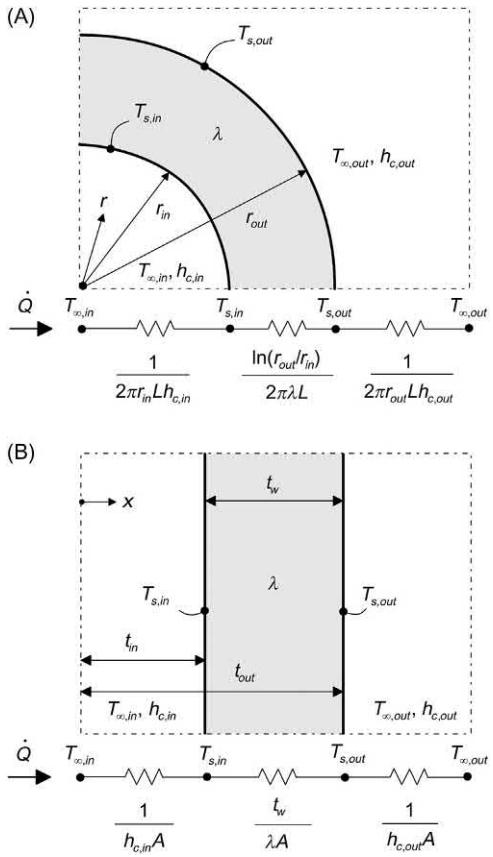

Figure 8.16 Equivalent thermal circuits for (A) a hollow cylinder and (B) a plane wall.

$$\dot{q}_l = \frac{\dot{Q}}{L} = \frac{T_{\infty,in} - T_{\infty,out}}{R'_{tot}} \tag{8.82}$$

where, considering the analysed thermal circuit in series,

$$R'_{tot} = \frac{1}{2\pi r_{in} h_{c,in}} + \frac{\ln\left(r_{out}/r_{in}\right)}{2\pi\lambda} + \frac{1}{2\pi r_{out} h_{c,out}} \tag{8.83}$$

For the wall, since $\dot{Q}$ is constant throughout the network, it follows that

$$\dot{q}_i = \frac{\dot{Q}}{A} = \frac{T_{\infty,in} - T_{s,in}}{1/h_{c,in}} = \frac{T_{s,in} - T_{s,out}}{t_w/\lambda} = \frac{T_{s,out} - T_{\infty,out}}{1/h_{c,out}} \tag{8.84}$$

The thermal power per unit surface may also be expressed in terms of the overall temperature difference, $T_{\infty,in} - T_{\infty,out}$, and the total thermal resistance, R''_{tot}, as

$$\dot{q}_i = \frac{\dot{Q}}{A} = \frac{T_{\infty,in} - T_{\infty,out}}{R''_{tot}} \tag{8.85}$$

where, considering the analysed thermal circuit in series,

$$R''_{tot} = \frac{1}{h_{c,in}} + \frac{t_w}{\lambda} + \frac{1}{h_{c,out}} \tag{8.86}$$

8.7.2 Radiation thermal resistance

In a similar way as performed for the case of convection, a thermal resistance for radiation may be defined according to the linearised form of the Stefan–Boltzmann's equation. For the cylinder the thermal resistance for radiation reads

$$R'_{rad} = \frac{1}{2\pi r_{in} h_r} \tag{8.87}$$

while for the plane wall it reads

$$R''_{rad} = \frac{1}{h_r} \tag{8.88}$$

Surface radiation and convection resistance act in parallel, and if $T_\infty = T_{sur}$, they may be combined to obtain a single effective surface resistance (Bergman et al., 2011).

8.7.3 Application of thermal circuits to complex cylindrical and plane problems

Equivalent thermal circuits may be used to model more complex bodies that may be approximated as composite cylinders and composite walls. These systems may be modelled through any combination of resistances connected in series or in parallel due to the presence of layers of different materials. Fig. 8.17 shows an example of composite thermal circuits (in series) for the previously considered problems of the infinite cylinder and plane wall.

For the cylinder the thermal power per unit length may be expressed as

$$\begin{aligned}\dot{q}_l &= \frac{\dot{Q}}{L} = \frac{T_{\infty,in} - T_{\infty,out}}{\sum R'_i} \\ &= \frac{T_{\infty,in} - T_{\infty,out}}{(1/(2\pi r_{in} h_{c,in})) + ((\ln(r_1/r_{in}))/2\pi\lambda_1) + ((\ln(r_2/r_1))/2\pi\lambda_2) + ((\ln(r_{out}/r_2))/2\pi\lambda_3) \\ &\quad + (1/(2\pi r_{out} h_{c,out}))}\end{aligned} \tag{8.89}$$

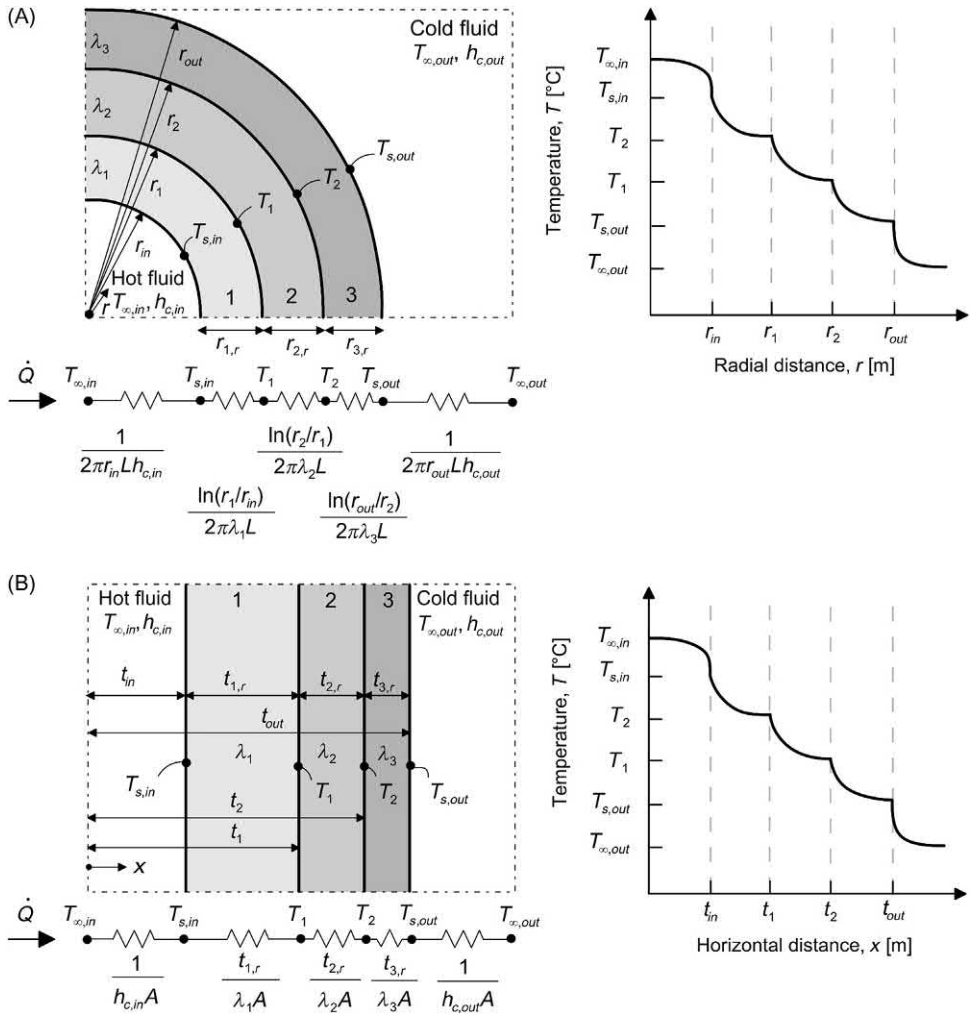

Figure 8.17 Equivalent thermal circuits for (A) a composite hollow cylinder and (B) a composite plane wall.

where $T_{\infty,in} - T_{\infty,out}$ is the overall temperature difference, R'_i are the ith thermal resistances of the circuit, and $r_{1,r} = r_1 - r_{in}$, $r_{2,r} = r_2 - r_1$ and $r_{3,r} = r_{out} - r_2$ and λ_1, λ_2 and λ_3 are the thicknesses and thermal conductivities of layers 1, 2 and 3, respectively.

For the wall the thermal power per unit surface may be expressed as

$$\dot{q}_i = \frac{\dot{Q}}{A} = \frac{T_{\infty,in} - T_{\infty,out}}{\sum R''_i} = \frac{T_{\infty,in} - T_{\infty,out}}{(1/h_{c,in}) + (t_{1,r}/\lambda_1) + (t_{2,r}/\lambda_2) + (t_{3,r}/\lambda_3) + (1/(h_{c,out}))} \tag{8.90}$$

where R''_i are the ith thermal resistances of the circuit and $t_{1,r} = t_1 - t_{in}$, $t_{2,r} = t_2 - t_1$ and $t_{3,r} = t_{out} - t$ are the thicknesses of layers 1, 2 and 3, respectively.

With composite systems, it is often useful to work with an overall heat transfer coefficient, U, through the following expression (similar to Newton's law of cooling)

$$\dot{Q} = UA\Delta T \tag{8.91}$$

where ΔT is the overall temperature difference.

From Eq. (8.91) the heat transfer capacity is derived as

$$UA = \frac{\dot{Q}}{\Delta T} = \frac{1}{R_{tot}} \tag{8.92}$$

In general, it can also be written that

$$R_{tot} = \sum R_i = \frac{\Delta T}{\dot{Q}} = \frac{1}{UA} \tag{8.93}$$

8.8 Heat transfer and storage capacities of energy piles

Until now, attention has been devoted to the time-independent analysis of heat (and mass) transfer phenomena that occur *within* geothermal heat exchangers. A number of considerations can also be carried out through a time-independent analysis approach with reference to the phenomena that occur *around* geothermal heat exchangers under steady conditions. In the following, two applications of this modelling approach are presented with reference to energy piles.

8.8.1 Heat transfer capacity of energy piles

The heat transfer capacity, UA, is a key parameter for the thermal characterisation of energy piles because it represents the thermal power that can be transferred from or into the ground under steady-flux conditions for a temperature variation of 1°C between the mean temperature of the heat carrier fluid circulating in the energy piles, $\overline{T}_f$, and the mean temperature of the soil in the zone affected by the heat exchange, $\overline{T}_{soil}$, that is

$$\dot{Q} = UA\left(\overline{T}_f - \overline{T}_{soil}\right) \tag{8.94}$$

For a group of n_{EP} energy piles of active length L at a given spacing s, the heat transfer capacity can be estimated for the case of steady-flux state and pure conduction in the ground as

$$UA = \frac{n_{EP} L}{R'_{ghe} + R'_{soil}} \tag{8.95}$$

where R'_{ghe} and R'_{soil} are the energy piles and the ground thermal resistances, respectively. The time after which Eq. (8.95) may be applied can be estimated as (Hellström, 1991)

$$t_g = 0.065 \frac{A_{th,soil}}{\alpha_{d,soil}} \tag{8.96}$$

where $A_{th,soil}$ is the plan area of ground for one energy pile in the group interested by the heat exchange (for a square group of energy piles located at s from each other, $A_{th,soil} = s^2$) and $\alpha_{d,soil}$ is the ground thermal diffusivity (cf. Fig. 8.18). For typical values of ground thermal diffusivity and pile spacing (e.g. $\alpha_{d,soil} = 8 \times 10^{-7}$ m^2/s and $s = 4$ m), t_g is approximately equal to 15 days (Pahud, 2002).

According to previous developments, the ground thermal resistance can be determined by considering the region influenced by the heat transfer as a thermally homogeneous ring around an energy pile as (SIA-D0190, 2005)

$$R'_{soil} = \frac{\ln\left(r_{soil}/R\right)}{2\pi\lambda_{soil}} \tag{8.97}$$

where λ_{soil} is the ground thermal conductivity and r_{soil} is the radius of the ground volume associated with one energy pile (for energy piles characterised by a spacing s, $r_{soil} = s/\sqrt{\pi}$, cf. Fig. 8.18). A more accurate formulation of ground thermal resistance than the one expressed in Eq. (8.97) is that provided by Hellström (1991)

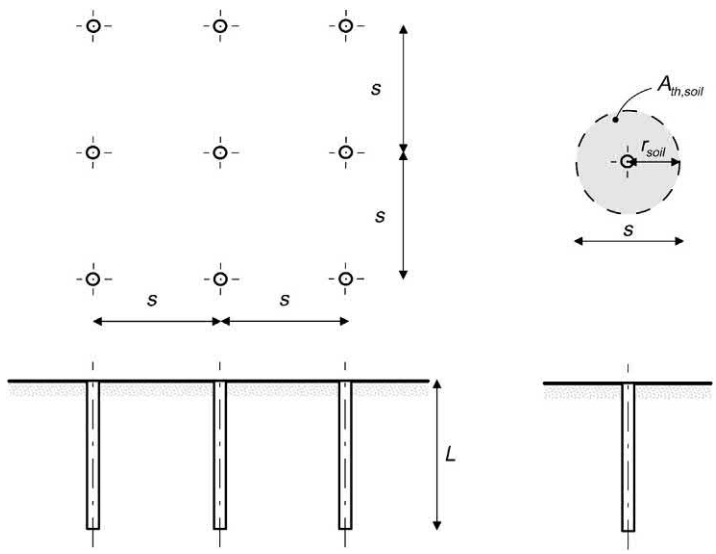

Figure 8.18 Plan area influenced by heat exchange for one energy pile in a group.

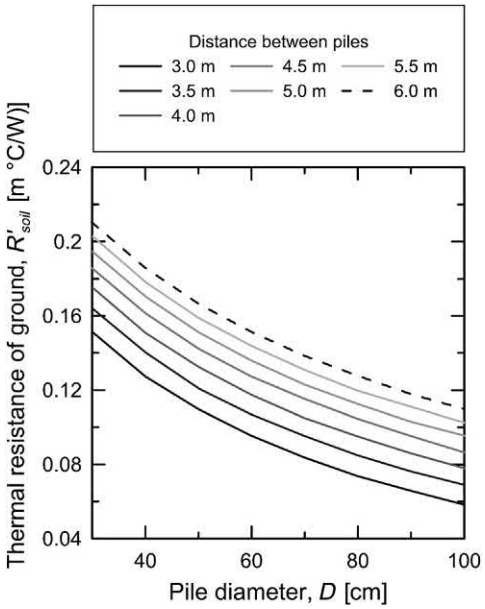

Figure 8.19 Typical simulated values of thermal resistance of ground. *Redrawn after SIA-D0190, 2005. Utilisation de la Chaleur du Sol par des Ouvrages de Fondation et de Soutènement en Béton. Guide pour la Conception, la Realisation et la Maintenance. The Swiss Society of Engineers and Architects, Zurich, Switzerland.*

$$R'_{soil} = \frac{1}{2\pi\lambda_{soil}} \left\{ \left[\frac{{r_{soil}}^2}{{r_{soil}}^2 - R^2} \right]^2 \ln\left(\frac{r_{soil}}{R}\right) - \frac{3}{4} - \frac{R^2}{2({r_{soil}}^2 - R^2)} \right\} \tag{8.98}$$

Fig. 8.19 shows typical values of ground thermal resistance calculated through Eq. (8.98) for different pile diameters and spacing (Pahud, 2002). The considered values refer to a thermal conductivity of the soil of $\lambda_{soil} = 1.8$ W/(m °C), but may be corrected for other values of λ_{soil} according to Eq. (8.98).

8.8.2 Heat storage capacity of energy piles

The specific heat storage capacity C_{sp} of a group of piles is defined as the heat Q that can be extracted for a reduction of the mean ground temperature of 1°C as

$$Q = C_{sp}\Delta\overline{T}_{soil} = C_{sp}\left(T_{soil,0} - \overline{T}_{soil}\right) \tag{8.99}$$

where $\Delta\overline{T}_{soil}$ is the mean ground temperature variation caused by the heat exchange operation of the energy piles. The specific heat storage capacity depends on the volumetric heat capacity and the volume of ground involved in the heat exchange as

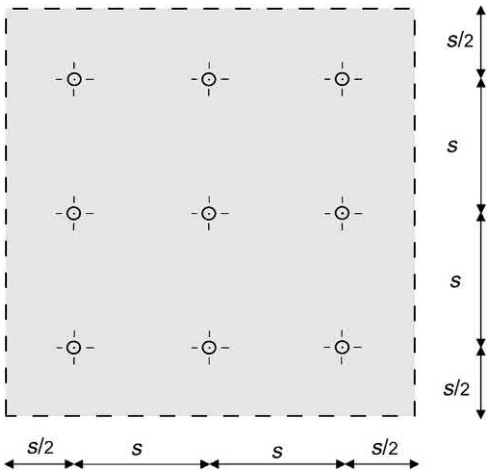

Figure 8.20 Schematic of the plan area influenced by heat exchange in an energy pile group.

$$C_{sp} = \rho_{soil} c_{p,soil} L A_{inf} \tag{8.100}$$

where ρ_{soil} and $c_{p,soil}$ are the bulk density and specific heat of the ground, respectively, and A_{inf} is the plan area of the involved ground volume. The area A_{inf} may be estimated as the plan area of ground embedded in the simplest polygon that includes the group of energy piles, augmented from the perimeter of the group of $s/2$ (cf. Fig. 8.20).

8.9 Required thermally active dimension of energy geostructures

The use of energy geostructures characterised by a predominant slender or stubby geometry, or by a vertical or horizontal geometry is generally a function of (1) structural and geotechnical considerations related to the significance of the superstructure (or general environment) to be supported, (2) architectural needs and (3) land availability. Once the type of energy geostructure is chosen, the estimation of the thermally active dimension of the energy geostructure that exchanges heat with the ground becomes an essential step in analysis and design. In the context of vertical ground heat exchangers such as energy piles, this parameter allows defining the total length and number of energy piles to be installed. In the context of energy walls or tunnels, this parameter allows defining the total thermally active surface of energy walls to be installed.

In early stages of the analysis and design of energy geostructures, rule of thumb values of the thermal power that can be extracted from or injected in the ground were proposed, among others, by Brandl (2006) and are as follows:

- Energy piles with diameter $D = 0.3-0.5$ m: 40−60 W/m (of thermally active run);
- Energy piles with diameter $D \geq 0.6$ m: 35 W/m^2 (of earth-contact area);
- Diaphragm walls, pile walls (fully embedding the soil): 30 W/m^2 (of earth-contact area);
- Base slabs: 10−30 W/m^2 (of earth-contact area).

As specified by Bourne-Webb (2013), the aforementioned values may not be conservative in some situations and may be excessively so in others. The reason for this is that, according to Narsilio et al. (2014), there are a number of factors which can have a significant influence on the thermohydraulic behaviour of energy geostructures, including (1) the geology, (2) the geomaterial thermal properties, (3) the location where the energy geostructure has to be constructed, (4) its elevation, (5) the configuration of the pipes, (6) the location and orientation of the pipes (e.g. on ground-side or air-side for energy walls and tunnels, although the former solution is more common for practical reasons related to the maintenance of the geostructure), (7) the energy geostructure size, (8) the backfill/grout thermal properties, (9) the pipe sizes and spacing, (10) the evolution over time of the geothermal operation (e.g. continuous or intermittent, the latter leading to much higher performances), and most importantly, (11) the balance and relative magnitude between the heating and cooling thermal loads exchanged with the ground.

At successive stages of the analysis and design, because of the aforementioned uncertainties, more sophisticated methods are preferable to assess the thermohydraulic behaviour of energy geostructures than the previous rule of thumb values and numerical methods are a powerful means to address this problem. Methods of pipe design may be found in manuals such as IGSHPA (2000) and CGC (2010).

In the following, the relatively simple method proposed by IGSHPA (2000) to estimate the total length of vertical ground heat exchangers such as energy piles is presented. The considered method refers to a geothermal system operating for the heating of the superstructure and composed of energy piles equipped with single U-shaped pipes and estimates the total required thermally active length of vertical energy piles as (IGSHPA, 2000):

$$L_{tot} = \frac{Q_h\left((COP-1)/COP\right)\left(R'_{ghe} + R'_{soil}F_h\right)}{T_{soil} - \left((T_{in,min} + T_{out,min})/2\right)} \tag{8.101}$$

where Q_h is the design ground source heat pump system heating capacity, COP is the design value of coeffient of performance of the heat pump, F_h is the the run fraction of the GSHP during the design heating month (i.e. the proportion of the time the pump has to run to provide the required heat), T_{soil} is the steady-state ground temperature adjacent to the energy pile, and $T_{in,min}$ and $T_{out,min}$ are the inlet and outlet minimum design temperatures of the fluid circulating in the pipes of the energy pile.

While the design parameters Q_h, COP, $T_{in,min}$ and $T_{out,min}$ are generally known, F_h can be estimated based on the use of the superstructure, the remaining parameters being analytically defined as proposed previously.

8.10 The effectiveness-NTU analysis method for energy geostructures

An analysis of the thermohydraulic behaviour of geothermal heat exchanger such as energy geostructures must be able to predict the thermal power extracted or injected from or in the heat exchanger, $\dot{Q}$, as well as the return temperature of the fluid circulating in the pipes, T_{out}, for heat pump dimensioning and operation considerations. In particular, the evolutions of these parameters with time and operative parameters such as T_{in} and $\dot{m}$ are relevant.

When steady conditions are attained, the enthalpy drop of the fluid from the inlet to the outlet section of the pipes corresponds to the thermal power exchanged at the outer surface of the energy geostructure (i.e. the surface in contact with the ground) (Batini et al., 2015). Under such conditions, the heat capacity effects are negligible and the energy geostructure can be considered to behave as a typical heat exchanger characterised by an equivalent thermal resistance between the pipes and the ground. The classical effectiveness–number of transfer units ($\epsilon_{ghe} - NTU$) method for heat exchangers (Bergman et al., 2011) can be used in such situations to evaluate the heat transfer occurring in energy geostructures and to compare the thermal behaviour of these heat exchangers for different pipe configurations installed.

When considering the $\epsilon_{ghe} - NTU$ method to energy piles, for example, the following equations apply (Conti et al., 2016)

$$\dot{Q} = \dot{q}_l L = \dot{m} c_{p,f} \left(\overline{T}_{in} - \overline{T}_{out}\right) = UA\left(\overline{T_f - T_{s-p}}\right) = UA\left(\overline{T}_f - \overline{T}_{s-p}\right) \tag{8.102}$$

$$\dot{q}_l = \frac{\left(\overline{T}_f - \overline{T}_{s-p}\right)}{L} \tag{8.103}$$

$$UA = \frac{L}{R'_{ghe}} \tag{8.104}$$

where $\overline{T}_{s-p}$ is the average temperature at the surface of the soil–pile interface. The convenient formulation of the arithmetic mean temperature $\overline{T}_f$ can be used in the analysis through Eq. (8.102), because of the small deviation among $\overline{T}_{in}$ and $\overline{T}_{out}$.

Under a uniform surface temperature of the soil–pile interface, $\overline{T}_{s-p} = T_{s-p}$, the heat exchanger effectiveness, ϵ_{ghe}, which represents the ratio between the actual heat transfer rate and the maximum possible heat transfer rate of the heat exchanger, can be defined as (Bergman et al., 2011)

$$\epsilon_{ghe} = \frac{\overline{T}_{out} - \overline{T}_{in}}{T_{s-p} - \overline{T}_{in}} \tag{8.105}$$

with

$$\epsilon_{ghe} = f(NTU) = f\left(\frac{1}{\dot{m}c_{p,f}}\frac{L}{R'_{ghe}}\right) \tag{8.106}$$

There is one main advantage associated with the use of the effectiveness−NTU method for the analysis of energy geostructures: the thermal power at the surface of the geostructure can always be considered to be coherent with the temperature variation of the fluid, $\overline{T}_{in} - \overline{T}_{out}$. The reason for this is that the outlet fluid temperature is imposed to be always greater or lower than the temperature at the soil−pile interface depending on the heat flux direction for the cooling or heating mode of the energy geostructure, respectively. This fact allows the avoidance of inconsistent analysis results that may arise as a consequence of the use of the mean temperature in terms of local direction of heat transfer (e.g. $\overline{T}_{out} < \overline{T}_{s-p}$ when $\overline{T}_f > \overline{T}_{s-p}$ and $\dot{Q} > 0$) because of the small temperature drop between the fluid and the ground (Conti et al., 2016). The $\epsilon_{ghe} - NTU$ method is a powerful tool for performing sensitivity analyses on the impact of different design solutions on the thermohydraulic behaviour of energy geostructures.

References

Ashrae, A.H., 2007. HVAC Applications. Inch-Pound Edition.

Batini, N., Rotta Loria, A.F., Conti, P., Testi, D., Grassi, W., Laloui, L., 2015. Energy and geotechnical behaviour of energy piles for different design solutions. Appl. Therm. Eng. 86 (1), 199−213.

Bauer, D., Heidemann, W., Diersch, H.J.G., 2011. Transient 3D analysis of borehole heat exchanger modeling. Geothermics 40 (4), 250−260.

Bear, J., 1972. Dynamics of Fluids in Porous Media. American Elsevericer Pubishing Company Inc, New York.

Bejan, A., Kraus, A.D., 2003. Heat Transfer Handbook. John Wiley & Sons.

Bennet, J., Claesson, J., Hellstrom, G., 1987. Multipole Method to Compute the Conductive Heat Flows To and Between Pipes in a Composite Cylinder, p. 84 (Master thesis). Department of Building Technology and Mathematical Physics, University of Lund, Lund, Sweden.

Bergles, A., Webb, R.L., 1970. Augmentation of Convective Heat and Mass Transfer. American Society of Mechanical Engineers.

Bergman, T., Incropera, F., Lavine, A., DeWitt, D., 2011. Fundamentals of Heat and Mass Transfer. Wiley, Hoboken, NJ.

Bourne-Webb, P.J., 2013. Observed response of energy geostructures. In: Laloui, L., Di Donna, A. (Eds.), Energy Geostructures. Wiley, pp. 45−77.

Bourne-Webb, P., Burlon, S., Javed, S., Kürten, S., Loveridge, F., 2016. Analysis and design methods for energy geostructures. Renew. Sustain. Energy Rev. 65, 402−419.

Brandl, H., 2006. Energy foundations and other thermo-active ground structures. Geotechnique 56 (2), 81−122.

Carslaw, H., Jaeger, J., 1959. Conduction of Heat in Solids. Oxford University Press, Oxford.
CGC, 2010. Design and Installation of Residential Ground Source Heat Pump Systems. CGC.
Claesson, J., Eskilson, P., 1988. Conductive heat extraction to a deep borehole: Thermal analyses and dimensioning rules. Energy 13 (6), 509–527.
Conti, P., Testi, D., Grassi, W., 2016. Revised heat transfer modeling of double-U vertical ground-coupled heat exchangers. Appl. Therm. Eng. 106, 1257–1267.
Diao, N., Zeng, H., Fang, Z., 2004. Improvement in modeling of heat transfer in vertical ground heat exchangers. HVAC&R Res. 10 (4), 459–470.
Eskilson, P., 1987. Thermal Analysis of Heat Extraction Boreholes (Ph.D. thesis). Department of Mathematical Physics, University of Lund, Lund, Sweden.
Faizal, M., Bouazza, A., Singh, R.M., 2016. Heat transfer enhancement of geothermal energy piles. Renew. Sustain. Energy Rev. 57, 16–33.
Fox, R.W., McDonald, A.T., Pritchard, P.J., 1985. Introduction to Fluid Mechanics. John Wiley & Sons, New York.
Gao, J., Zhang, X., Liu, J., Li, K., Yang, J., 2008. Numerical and experimental assessment of thermal performance of vertical energy piles: an application. Appl. Energy 85 (10), 901–910.
Gnielinski, V., 1976. New equations for heat and mass transfer in turbulent pipe and channel flow. Int. Chem. Eng. 16 (1), 359–368.
Grassi, W., Conti, P., Schito, E., Testi, D., 2015. On sustainable and efficient design of ground-source heat pump systems, Journal of Physics: Conference Series, vol. 655. IOP Publishing, p. 012003.
Gu, Y., O'Neal, D.L., 1998. Development of an equivalent diameter expression for vertical U-tubes used in ground-coupled heat pumps. ASHRAE Trans. 104, 347.
Haaland, S., 1983. Simple and explicit formulas for the friction factor in turbulent flow. J. Fluids Eng. Trans. ASME 103 (1), 89–90.
Hellström, G., 1991. Ground Heat Storage: Thermal Analyses of Duct Storage Systems. Theory (Ph.D. thesis). Department of Mathematical Physics, University of Lund, Lund.
IGSHPA, 2000. Grouting for Vertical Geothermal Heat Pump Heat Pump Systems, Engineering Design and Field Procedures Manual. Hoklaoma State University, Stillwater, OK.
Kakaç, S., Shah, R.K., Aung, W., 1987. Handbook of Single-Phase Convective Heat Transfer. Wiley, New York, et al.
Kays, W.M., Crawford, M.E., Weigand, B., 2012. Convective Heat and Mass Transfer. Tata McGraw-Hill Education.
Lamarche, L., Kajl, S., Beauchamp, B., 2010. A review of methods to evaluate borehole thermal resistances in geothermal heat-pump systems. Geothermics 39 (2), 187–200.
Langhaar, H.L., 2016. Energy Methods in Applied Mechanics. Courier Dover Publications.
Lee, C.K., 2011. Effects of multiple ground layers on thermal response test analysis and ground-source heat pump simulation. Appl. Energy 88 (12), 4405–4410.
Lennon, D., Watt, E., Suckling, T., 2008. Energy piles in Scotland. In: Fifth International Symposium on Deep Foundations on Bored and Auger Piles, pp. 349–355.
Li, M., Lai, A.C., 2013. Thermodynamic optimization of ground heat exchangers with single U-tube by entropy generation minimization method. Energy Convers. Manag. 65, 133–139.
Li, M., Lai, A.C., 2015. Review of analytical models for heat transfer by vertical ground heat exchangers (GHEs): a perspective of time and space scales. Appl. Energy 151, 178–191.
Li, M., Li, P., Chan, V., Lai, A.C., 2014. Full-scale temperature response function (G-function) for heat transfer by borehole ground heat exchangers (GHEs) from sub-hour to decades. Appl. Energy 136, 197–205.
Loveridge, F., 2012. The Thermal Performance of Foundation Piles Used as Heat Exchangers in Ground Energy Systems (Ph.D. thesis). University of Southampton.
Loveridge, F., Powrie, W., 2014. 2D thermal resistance of pile heat exchangers. Geothermics 50, 122–135.
Munson, B.R., Young, D.F., Okiishi, T.H., 1990. Fundamentals of fluid mechanics, 3. Wiley, New York (4).

Narsilio, G.A., Bidarmaghz, A., Colls, S., 2014. Geothermal energy: introducing an emerging technology. In: Proceedings of International Conference on Advances in Civil Engineering for Sustainable Development, pp. 141–154.

Pahud, D. 2002. Geothermal Energy and Heat Storage. SUPSI – DCT – LEEE Laboratorio di Energia, Ecologia ed Economia, p. 133.

Paul, N.D., 1996. The effect of grout thermal conductivity on vertical geothermal heat exchanger design and performance (Ph.D. thesis). Mechanical Engineering Department, South Dakota State University.

Remund, C.P., 1999. Borehole thermal resistance: laboratory and field studies. ASHRAE Trans. 105, 439.

Sharqawy, M.H., Mokheimer, E.M., Badr, H.M., 2009. Effective pipe-to-borehole thermal resistance for vertical ground heat exchangers. Geothermics 38 (2), 271–277.

Shonder, J.A., Beck, J.V., 2000. Field test of a new method for determining soil formation thermal conductivity and borehole resistance. ASHRAE Trans. 106, 843–850.

SIA-384/6, 2010. Sondes géothermiques. The Swiss Society of Engineers and Architects, Zurich, Switzerland.

SIA-D0190, 2005. Utilisation de la Chaleur du Sol par des Ouvrages de Fondation et de Soutènement en Béton. Guide pour la Conception, la Realisation et la Maintenance. The Swiss Society of Engineers and Architects, Zurich, Switzerland.

Wood, C., Liu, H., Riffat, S., 2010. Comparison of a modelled and field tested piled ground heat exchanger system for a residential building and the simulated effect of assisted ground heat recharge. Int. J. Low-Carbon Technol. 5 (3), 137–143.

Yang, H., Cui, P., Fang, Z., 2010. Vertical-borehole ground-coupled heat pumps: a review of models and systems. Appl. Energy 87 (1), 16–27.

Zeng, H., Diao, N., Fang, Z., 2003. Heat transfer analysis of boreholes in vertical ground heat exchangers. Int. J. Heat Mass Transf. 46 (23), 4467–4481.

Questions and problems

Statements

a. Under steady conditions, the heat transfer occurring *within* energy geostructures can be modelled with:
  i. A time-dependent approach
  ii. A time-independent approach
  iii. None of the above

b. The concept of thermal resistance can be used:
  i. To characterise heat transfer as a purely resistance process
  ii. To characterise electrical current flow as a purely resistance process
  iii. To characterise groundwater flow as a purely resistance process

c. Within the entrance regions describing heat and mass transfers in pipes:
  i. The temperature and velocity profiles do not change with the axial distance
  ii. The temperature and velocity profiles are constant
  iii. The temperature and velocity profiles change with the axial distance

d. Laminar flow typically occurs in cylindrical pipes for:
  i. Values of Reynolds number greater than 10,000
  ii. Values of Reynolds number approximately greater than 2300
  iii. Values of Reynolds number approximately lower than 2300
  iv. None of the above

e. A useful parameter to define the convection heat transfer coefficient is:
  i. The Reynolds number
  ii. The Nusselt number
  iii. The Prandtl number
  iv. None of the above

f. The convection heat transfer coefficient is useful to determine:
  i. The conduction thermal resistance of heat exchangers
  ii. The radiation thermal resistance of heat exchangers
  iii. The convection thermal resistance of heat exchangers

g. The time-independent thermal resistance of ground heat exchangers typically includes
  i. Two convective thermal resistances and one conductive thermal resistance
  ii. Two conductive thermal resistances
  iii. One conductive thermal resistance
  iv. Two conductive thermal resistances and one convective thermal resistance

h. The unit measure of the thermal resistance per metre length of heat exchanger is
  i. W/m
  ii. W/(m °C)

iii. °C/m
iv. m
v. m °C/W

i. What are the conditions that allow treating heat transfer as a time-independent process?
j. Explain the difference between steady-state and steady-flux conditions.
k. Discuss about the key features of the thermal and hydrodynamic entrance regions in pipes.
l. Is the friction factor for fully developed flow always affected by the wall roughness?
m. Define Prandtl number.
n. Define Nusselt number.
o. Consider fully developed conditions in a circular pipe with constant surface temperature $T_s < T_m$. Determine whether a small or large diameter pipe is more effective in minimising heat loss from the flowing fluid characterised by a mass flow rate of $\dot{m}$.
p. Hot air flows with a mass flow rate of $\dot{m} = 0.1$ kg/s through an uninsulated pipe of diameter $d_p = 0.2$ m. The hot air enters at $T_{in} = 50°C$ and cools at $T_{out} = 4°C$ after a distance of $L_p = 5$ m. The convection heat transfer coefficient between the pipe outer surface and the ambient air at $T_\infty = 10°C$ is known to be $h_{c,out} = 6$ W/(m^2 °C). Calculate the heat loss $\dot{Q}$ [W] from the pipe over the length and determine the heat flux $\dot{q}_s$ [W/m^2] and the pipe surface temperature T_s [°C] at $x = L^*$.
q. Consider water around ambient temperature entering in a circular pipe characterised by a diameter of $d_p = 50$ mm and a length of $L_p = 10$ m with a velocity of $v_x = 2$ m/s. Find the internal convection heat transfer coefficient h_c [W/(m^2°C)].
r. What is the difference between the temperature distribution in plane energy walls and energy piles?
s. A one-dimensional plane energy wall characterised by a thickness of $2t_w = 0.50$ m and an area of $A = 10$ m^2 experiences a uniform thermal energy generation of $\dot{q}_v = 100$ W/m^3 and is convectively cooled at $x = \pm 0.25$ m by an ambient fluid characterised by a far field temperature of $T_\infty = 28°C$. If the steady-state temperature distribution within the wall is:

$$T(x) = a\left(t_w{}^2 - x^2\right) + b$$

where $a = 100°C/m^2$ and $b = 30°C$, find the thermal conductivity of the wall λ [W/(m °C)] and the value of the convection heat transfer coefficient h_c [W/(m^2 °C)].
t. A system for heating water from an inlet temperature of $\overline{T}_{f,in} = 10°C$ to an outlet temperature of $\overline{T}_{f,out} = 50°C$ involves passing the water through a

thick-walled pipe having inner and outer diameters of $d_{p,in} = 20$ and $d_{p,out} = 40$ mm, respectively. The outer surface of the pipe is well insulated, and a heat source within the wall provides a uniform volumetric heat generation rate of $\dot{q}_v = 10^6$ W/m^3. For a mass flow rate of $\dot{m} = 0.2$ kg/s, how long must be the pipe to achieve the desired outlet temperature? If the inner surface temperature of the pipe is $T_s = 60°C$ at the outlet, what is the local convection heat transfer coefficient at the outlet $h_{c,out}$ [W/(m^2°C)]? Assume that the specific heat of water reads $c_p = 4200$ J/(kg °C).

u. Water flowing at $\dot{m} = 1$ kg/s through a 20-mm-diameter pipe is to be heated from $\overline{T}_{in} = 3°C$ to $\overline{T}_{out} = 10°C$ by maintaining the pipe surface temperature at $T_s = 15°C$. What is the required pipe length L_p [m] for these conditions? Assume an internal convection heat transfer coefficient equal to $\overline{h_c} = 5000$ W/(m^2 °C) and a specific heat of water of $c_p = 4186$ J/(kg °C).

v. A plane energy wall of thermal conductivity $\lambda = 2$ W/(m °C) and thickness $t_w = 0.5$ m is characterised by no internal heat generation and experiences one-dimensional conduction under steady-state conditions with reference to the configuration depicted in the following figure.

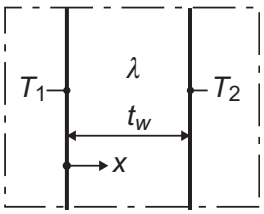

Determine the unknown quantity for each of the following cases, together with the heat flux $\dot{q}_x$ [W/m^2]. Specify the direction of the heat flux based on the relevant sign.

Case	T_1 [°C]	T_2 [°C]	dT/dx [°C/m]
1	30	20	
2	10	20	
3	20		2
4		10	−2
5		15	1

w. A plane energy wall 50 cm thick has a thermal conductivity $\lambda = 1.5$ W/(m °C). Steady-state conditions characterise the inner and outer surfaces of the wall following the temperatures of $T_1 = 15°C$ and $T_2 = 20°C$, respectively. Determine the heat flux $\dot{q}_x$ [W/m^2] and the temperature gradient dT/dx [°C/m] for the temperature distribution with the coordinate systems shown in the following figure.

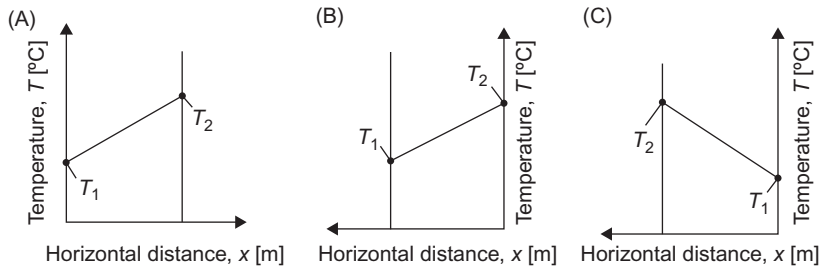

x. The thermal conductivity of a thermal insulator sheet is of $\lambda = 0.2$ W/(m °C). The measured temperature difference across a 10-mm-thick sheet of the material is $T_1 - T_2 = 0.5$°C. Answer the following questions:

i. What is the heat flux $\dot{q}_x$ [W/m^2] through a 2 m × 1 m insulation sheet?

ii. What is the rate of heat transfer $\dot{Q}_x$ [W] through the insulation sheet?

y. An uninsulated pipe passes at the ground surface where the air temperature is $T_\infty = 20$°C. The outside radius of the pipe is $r_{p,out} = 25$ mm and its surface temperature and emissivity are of $T_s = 40$°C and $\epsilon = 0.8$, respectively. What are the heat flux density emission, $\dot{q}_{rad,e}$, and radiation, $\dot{q}_{rad,a}$ [W/m^2]? If the coefficient associated with free convection heat transfer from the surface to the air is $h_c = 10$ W/(m^2 °C), what is the rate of heat loss from the surface per unit length of pipe, $\dot{q}_l$ [W/m]? Assume steady-state conditions and that radiation exchange between the pipe and the exterior occurs in a much large environment. The Stefan–Boltzmann constant is $\sigma_{SB} = 5.67 \times 10^{-8}$ W/(m^2 K^4) and the surface emissivity and absorptivity are the same.

z. The temperature distribution across a 0.3 m-thick energy wall at a certain instant of time is:

$$T(x) = a + bx + cx^2$$

where T [°C] is the temperature, x [m] is the horizontal distance, $a = 20$°C, $b = -20$°C/m and $c = 3$°C/m^2. The wall has a thermal conductivity of 2 W/(m °C). For this problem:

- On a unit surface area basis, determine the rate of heat transfer inside and outside of the wall, $\dot{q}_{x,in}$ and $\dot{q}_{x,out}$ [W/m^2], respectively.
- If the cold surface is exposed to a fluid at $T_f = 10$°C, what is the convection coefficient h_c [W/(m^2 °C)]?

aa. The following steady-state linear temperature distribution within a composite wall composed of two materials A and B occurs in a given problem. No internal generation occurs, and the conduction is monodimensional. For each of the following cases, which material has the higher thermal conductivity?

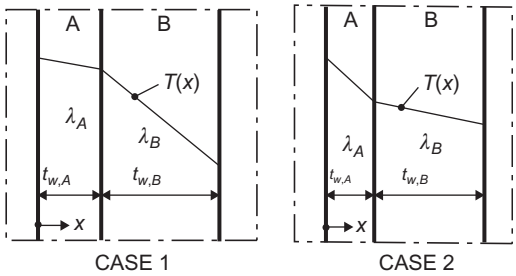

bb. A pipe containing a hot heat carrier fluid has a temperature T_1 at an outside radius $r_{p,1}$. A thick insulation layer, applied to reduce the heat loss, has an outer radius $r_{p,2}$ and is characterised by a temperature T_2. Sketch the temperature distribution in the insulation material for one-dimensional, steady-state heat transfer with constant properties.

cc. A plane energy wall is a composite of two materials A and B. Material A is characterised by a uniform heat generation of $\dot{q}_{v,A} = 30$ W/m^3, a thermal conductivity of $\lambda_A = 0.5$ W/(m °C) and a thickness of $t_{w,A} = 60$ cm. Material B has no heat generation, with $\lambda_B = 1.5$ W/(m °C) and $t_{w,B} = 20$ cm. The inner surface of material A is well insulated, while the outer surface of material B is cooled by an airstream with an undisturbed temperature of $T_\infty = 20$°C and a convection heat transfer coefficient of $h_c = 10$ W/(m^2 °C). For this problem:

- Sketch the temperature distribution that exists in the composite under steady-state conditions.
- Determine the temperature T_{in} [°C] of the insulated surface and the temperature T_{out} [°C] of the cooled surface.

dd. A plane concrete slab has thickness t_{slab} [m] and thermal conductivity λ_{slab} [W/(m °C)]. Above the slab, ambient air flows at a temperature T_∞ [°C] with a convection heat transfer coefficient h_c [W/(m^2 °C)]. Below the slab, a soil layer with thermal conductivity of the solid particles λ_s [W/(m °C)], with pores fully filled with a fluid of thermal conductivity λ_f [W/(m °C)] according to a porosity n [−], is present. During winter, at a depth t_{tot} [m] in the soil, there is a temperature $T_{soil} > T_\infty$ [°C]. For this problem, which is illustrated in the following figure:

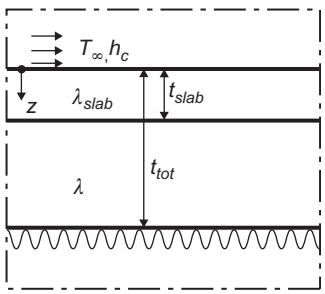

- Sketch the temperature distribution that exists under steady-state conditions, considering the thermal contact resistance between slab and soil.
- Determine the temperatures $T_{slab,1}$ and $T_{slab,2}$ [°C] of the two surfaces of the slabs (neglect thermal contact resistance).

ee. A thin-walled pipe of radius $r_{p,in}$ [m], carrying a low-temperature refrigerant, is at a temperature T_i [°C] that is less than that of the ambient air around the pipe at T_∞ [°C]. Which is the optimum thickness $t_{w,opt}$ [m] associated with the addition of insulation to the pipe?

The thermal conductivity of the insulation is λ [W/(m °C)] and the outer surface convection coefficient is h_c [W/(m^2 °C)].

Assume:

1. Steady-state conditions.
2. One-dimensional radial conduction
3. Negligible pipe wall thermal resistance.
4. Constant properties.
5. Outer surface adiabatic.

ff. A long pipe, insulated at the outer radius $r_{p,out}$ [m] and cooled at the inner radius $r_{p,in}$ [m], experiences uniform volumetric heat generation $\dot{q}_v$ [W/m^3] within the solid. For this problem:

- Obtain the general formulation of the temperature distribution within the pipe, $T(r)$ [°C].
- A limit would be placed on the maximum allowable temperature at the insulated surface ($r = r_{p,out}$) in a real application. Considering this limit as T_{out} [°C], identify appropriate boundary conditions that may be used to determine the arbitrary constants appearing in the general formulation. Determine these constants and the corresponding form of the temperature distribution.
- Calculate the heat removal rate per unit length of pipe $\dot{q}_l$ [W/m].
- If the coolant is available at a temperature T_∞ [°C], obtain the formulation of the expression for the convection coefficient h_c [W/(m^2°C)] that would have to be maintained at the inner surface in order to allow the conditions at prescribed values of T_{out} and $\dot{q}_l$.

Assume:

1. Steady-state conditions.
2. One-dimensional radial conduction.
3. Constant properties.

4. Uniform volumetric heat generation.
5. Outer surface adiabatic.

gg. A composite energy wall, such as the one reproduced in the following figure, consists of three materials, two of which are of known thermal conductivity $\lambda_A = 2$ W/(m °C) and $\lambda_C = 0.5$ W/(m °C), and known thickness $t_{w,A} = 0.30$ m and $t_{w,C} = 0.15$ m. The third material B, which is sandwiched between materials A and C, is of known thickness, $t_{w,B} = 0.15$ m, but unknown thermal conductivity λ_B [W/(m °C)].

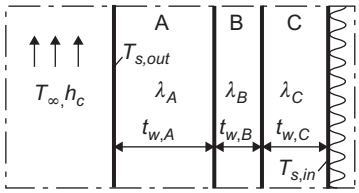

For this problem:

- Under steady-state operating conditions in winter, measurements reveal an outer surface temperature of $T_{s,out} = 5$°C, an inner surface temperature of $T_{s,in} = 20$°C, and a heat pump air temperature of $T_\infty = 23$°C. The inside convection coefficient is known to be of $h_c = 1$ W/(m^2 °C). What is the value of λ_B?
- Imagine that materials A, B and C are three different materials that characterise the wall of an underground car parking, with the temperature $T_{s,out}$ almost constant during the year. Find a relationship among the physical quantities that gives the temperature of the air T_∞ coming from a heat pump, knowing all the other parameters shown in the picture.

hh. Explain the differences between R_{ghe}, R'_{ghe} and R''_{ghe}. What are the units of these quantities?

ii. Describe heat transfer capacity and heat storage capacity of energy piles.

jj. An energy pile of 60 cm in diameter has a thermal resistance of $R'_{ghe} = 0.06$ (m °C)/W. The pile is included in a square group in which the piles are characterised by a centre-to-centre spacing of $s = 6$ m. The soil surrounding the piles has a thermal conductivity of $\lambda_{soil} = 1.8$ W/(m °C). Which is the thermal power per unit length $\dot{q}_l$ [W/m] that can be extracted with a difference of temperature between the fluid and the soil of $\Delta T = \overline{T} - \overline{T}_{soil} = 5$°C? Refer to the following figure for the calculations.

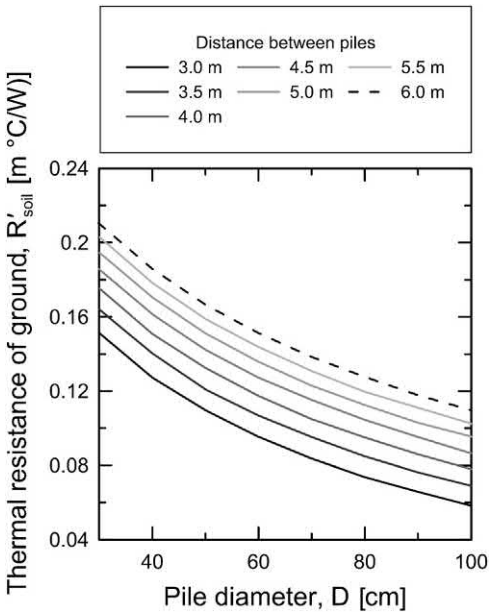

kk. The thermal power per unit of length that can be extracted from an energy pile with a difference of temperature between the fluid and the soil of $\Delta T = \overline{T} - \overline{T}_{soil} = 6°C$ reads $\dot{q}_l = 30$ W/m. The thermal resistance of the energy pile is $R'_{ghe} = 0.08$ (m °C)/W. The pile is included in a square group in which the foundations are characterised by a centre-to-centre spacing of $s = 3.5$ m. The soil surrounding the piles has a thermal conductivity of $\lambda_{soil} = 1.8$ W/(m °C). Which is the diameter of the energy pile, D [m]? Refer to the previous figure for the calculations.

ll. Calculate the specific heat storage capacity C_{sp} [J/°C] of a square group of nine energy piles characterised by a spacing of $s = 5$ m. The length of the piles is $L = 20$ m, the soil bulk density is $\rho_{soil} = 2500$ kg/m^3 and the soil specific heat is $c_{p,soil} = 800$ J/(kg °C).

mm. In steady-state conditions, an energy geostructure supplies a house requiring heat for $\dot{Q}_h = 10$ kW. The manufacturer's data sheets of a selected heat pump indicate that the Coefficient of Performance reads $COP = 4$ as well as that water enters in the pump at the minimum design temperature $\overline{T}_{in,min} = 8°C$ and leaves at $\overline{T}_{out,min} = 4°C$. The piping of the geostructure has a total length of $L_{p,tot} = 200$ m and the average ground temperature around the geostructure is of $\overline{T}_{soil} = 16°C$. Calculate the thermal resistance of the geothermal heat exchanger R'_{ghe} [(m °C)/W], considering a thermal resistance of the soil of $R'_{soil} = 0.5$ (m °C)/W and a run fraction of the pump of $F_h = 0.5$.

nn. In steady-state conditions, an energy geostructure supplies a building that requires heat for $\dot{Q}_h = 15$ kW. The manufacturer's data sheet of the selected heat pump indicates that the Coefficient of Performance reads $COP = 4$ as well as that water enters in the pump at the minimum design temperature $\overline{T}_{in,min} = 7°C$ and leaves at $\overline{T}_{out,min} = 3°C$. The average ground temperature around the geostructure is $\overline{T}_{soil} = 17°C$ and the time-independent thermal resistance of the geothermal heat exchanger has been evaluated as $R'_{ghe} = 0.1$ (m °C)/W, while the thermal resistance of soil has been evaluated as $R'_{soil} = 0.6$ (m °C)/W with a pump run factor equal to $F_h = 0.5$. Calculate the required piping length.

oo. Calculate the heat exchange effectiveness of an energy pile where water enters at a temperature equal to $\overline{T}_{in} = 10°C$ and leaves at a temperature equal to $\overline{T}_{out} = 14°C$. Consider a uniform temperature of the soil–pile interface equal to $T_{s-p} = 15°C$. Steady-state conditions are attained.

pp. In steady-state conditions, an energy geostructure operates with a heat exchange effectiveness equal to $\epsilon_{ghe} = 0.6$ [–]. Knowing that water enters at $\overline{T}_{in} = 18°C$ and leaves at $\overline{T}_{out} = 15°C$, calculate the temperature of the soil–pile interface.

Solutions

a. Under steady conditions, the heat transfer occurring *within* energy geostructures can be modelled with:
- **i.** A time-dependent approach
- **ii.** **A time-independent approach**
- **iii.** None of the above

b. The concept of thermal resistance can be used:
- **i.** **To characterise heat transfer as a purely resistance process**
- **ii.** To characterise electrical current flow as a purely resistance process
- **iii.** To characterise groundwater flow as a purely resistance process

c. Within the entrance regions describing heat and mass transfers in pipes:
- **i.** The temperature and velocity profiles do not change with the axial distance
- **ii.** The temperature and velocity profiles are constant
- **iii.** **The temperature and velocity profiles change with the axial distance**

d. Laminar flow typically occurs in cylindrical pipes for:
- **i.** Values of Reynolds number greater than 10,000
- **ii.** Values of Reynolds number approximately greater than 2300
- **iii.** **Values of Reynolds number approximately lower than 2300**
- **iv.** None of the above

e. A useful parameter to define the convection heat transfer coefficient is:

i. The Reynolds number
ii. **The Nusselt number**
iii. The Prandtl number
iv. None of the above

f. The convection heat transfer coefficient is useful to determine:
i. The conduction thermal resistance of heat exchangers
ii. The radiation thermal resistance of heat exchangers
iii. **The convection thermal resistance of heat exchangers**

g. The time-independent thermal resistance of ground heat exchangers typically includes
i. Two convective thermal resistances and one conductive thermal resistance
ii. Two conductive thermal resistances
iii. One conductive thermal resistance
iv. **Two conductive thermal resistances and one convective thermal resistance**

h. The unit measure of the thermal resistance per metre length of heat exchanger is
i. W/m
ii. W/(m °C)
iii. °C/m
iv. m
v. **m °C/W**

i. Some reference time (and space) scales allow considering the heat transfer as a time-independent process. These timescales are generally associated with so-called steady conditions and involve a time independence of the heat transfer process. The reason for this is because the temperature field at each given point of a system is either constant with time or characterised by a constant rate of change.

j. Steady-flux conditions are situations in which the relevant temperature is a result of quantities that evolve with time but are characterised by a constant difference over time. Steady-flux conditions differ from steady-state conditions in that in the latter the temperatures that yield to the relevant temperature change are constant with time.

k. When a fluid makes contact with the surface of a pipe at a different temperature, convection heat transfer occurs and the thermal boundary layer develops with increasing distance x. Typically, the thermal boundary layer merges along the axis of the pipe at a distance $x_{fd,th}$, called thermal entry length. From the entrance of the pipe to the limit of $x_{fd,th}$, the

region of the pipe is the entrance region and the temperature field changes with the distance x. After the limit $x_{fd,h}$, the region of the pipe is the thermally fully developed region and the relative shape of the temperature field no longer changes with the distance x for the same surface condition.

When a fluid makes contact with the surface of a pipe, viscous effects come into play and the velocity boundary layer develops with increasing distance x. Typically, the velocity boundary layer merges along the axis of the pipe at a distance $x_{fd,h}$, called hydrodynamic entry length. From the entrance of the pipe to the limit of $x_{fd,h}$, the region of the pipe is the entrance region and the flow velocity changes with the distance x. After the limit $x_{fd,h}$, the region of the pipe is the hydrodynamic fully developed region, viscous effects extend over the entire cross-section of the pipe and the flow velocity no longer changes with the distance x.

l. **For fully developed laminar flow, the friction factor reads $f_M = 64/Re_d$. Therefore under these conditions, the friction factor is not affected by the wall roughness. For fully developed turbulent flow, the analysis is more complicated and there is the need to rely on experimental results. In addition to depending on the Reynolds number, the friction factor is a function of the surface condition and increases with surface roughness.**

m. **The Prandtl number is defined as the ratio of the kinematic viscosity, also referred to as the momentum diffusivity η [m^2/s] to the thermal diffusivity α_d [m^2/s]. It is therefore a fluid property. The Prandtl number provides a measure of the relative effectiveness of momentum and energy transport by diffusion in the velocity and thermal boundary layers, respectively.**

$$Pr = \frac{\eta}{\alpha_d}\ [-]$$

n. **In the heat transfer at a boundary (surface) within a fluid, the Nusselt number Nu_x is the ratio of convective to conductive heat transfer across (normal to) the boundary. In this context, convection includes both advection and diffusion.**

$$Nu_x = \frac{h_{c,x}x}{\lambda}\ [-]$$

where $h_{c,x}$ [W/(m^2 °C)] is the convection heat transfer coefficient, x [m] is the characteristic length of the problem and λ [W/(m °C)] is the thermal conductivity of the medium.

o. The heat loss is directly proportional to the surface of the pipe. Therefore in these conditions, a small diameter pipe is more effective to minimising heat loss.

p. The specific heat of air between 40 and 50°C is $c_p = 1006$ kJ/(kg°C), the thermal conductivity is $\lambda = 0.0275$ W/(m °C), the dynamic viscosity is $\mu = 1.96 \times 10^{-5}$ Ns/m^2 and the Prandtl number is $Pr = 0.704$. The heat loss from the pipe over the length is $\dot{Q} = \dot{m} c_p (T_{in} - T_{out}) = 0.1 \cdot 1006 \cdot (50 - 40) = 1009$ W.

An expression for the heat flux at $x = L^*$ can be inferred from the following resistance network

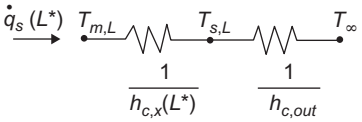

where $h_{c,x}(L^*)$ is the inside convection heat transfer coefficient at $x = L^*$. Hence, the heat loss reads

$$\dot{q}_s(L^*) = \frac{T_{m,L} - T_\infty}{\frac{1}{h_{c,x}(L^*)} + \frac{1}{h_{c,out}}}$$

where $T_{m,L}$ [°C] is the bulk temperature of air at $x = L^*$.

The inside convection heat transfer coefficient can be obtained from knowledge of the Reynolds number, which reads

$$Re_d = \frac{4\dot{m}}{\pi d_p \mu} = \frac{4 \cdot 0.1}{\pi \cdot 0.2 \cdot 1.96 \cdot 10^{-5}} = 32{,}480$$

Hence, the flow is turbulent. Moreover, with

$$\frac{L^*}{d_p} = \frac{5}{0.2} = 25$$

it is reasonable to assume fully developed conditions at $x = L^*$. The Nusselt number can be evaluated as

$$Nu_d = \frac{h_{c,x}(L^*) d_p}{\lambda} = 0.023 Re_d^{\frac{4}{5}} Pr^{0.3} = 0.023 \cdot 32480^{\frac{4}{5}} \cdot 0.704^{0.3} = 84.2$$

Therefore

$$h_{c,x}(L^*) = Nu_d \frac{\lambda}{d_p} = 84.2 \cdot \frac{0.0275}{0.2} = 11.58 \ \ \mathrm{W/(m^2{}^\circ C)}.$$

Additionally

$$\dot{q}_s(L^*) = \frac{40 - 10}{\frac{1}{12} + \frac{1}{6}} = 120 \ \mathrm{W/m^2}.$$

Referring to the resistance network associated with this problem, it also follows that

$$\dot{q}_s(L^*) = \frac{T_{m,L} - T_{s,L}}{\frac{1}{h_{c,x}(L^*)} + \frac{1}{h_{c,0}}}$$

Therefore the pipe surface temperature at $x = L^*$ reads

$$T_{s,L} = T_{m,L} - \frac{\dot{q}_s(L^*)}{h_{c,x}(L^*)} = 40 - \frac{120}{11.58} = 29.64^\circ C.$$

q. Considering an average water temperature of 20°C, for which the density, the specific heat, the kinematic viscosity and the thermal conductivity read respectively $\rho = 1000\ \mathrm{kg/m^3}$, $c_p = 4187\ \mathrm{J/(kg\ ^\circ C)}$, $\eta = 5 \cdot 10^{-6}\ \mathrm{m^2/s}$, $\lambda = 0.6\ \mathrm{W/(m\ ^\circ C)}$, the Reynolds number can be calculated to understand the type of flow within the pipe as

$$Re_d = \frac{v_x d_p}{\eta} = \frac{2 \cdot 0.05}{5 \cdot 10^{-6}} = 20{,}000$$

As $Re_d > 10{,}000$, turbulent flow occurs and the Dittus-Boelter relationship can be used to find the Nusselt number as

$$Nu = 0.023 Re_d^{0.8} Pr^{0.4} \ [-]$$

where Pr [−] is the Prandtl number which can be calculated as

$$Pr = \frac{\eta_x \rho c_p}{\lambda} = \frac{5 \cdot 10^{-6} \cdot 1000 \cdot 4187}{0.6} = 34.9$$

Therefore the Nusselt number reads

$$Nu = 0.023 Re_d^{0.8} Pr^{0.4} = 0.023 \cdot 20000^{0.8} \cdot 34.9^{0.4} = 18.42$$

From the Nusselt number, the internal convection heat transfer coefficient can be calculated as

$$h_c = \frac{\lambda}{d_p} Nu = \frac{0.6}{0.05} \cdot 18.42 = 221.04 \ \mathrm{W/(m^2{}^\circ C)}$$

r. For a plane energy wall, the energy conservation equation in steady-state conditions and with no internal heat generation reads

$$\frac{d^2T}{dx^2} = 0$$

For a cylindrical energy pile, the energy conservation equation in steady-state conditions and with no internal heat generation reads

$$\frac{1}{r}\frac{d}{dr}\left(r\frac{dT}{dr}\right) = 0$$

Hence, the temperature distribution in plane energy walls is linear while in energy piles is logarithmic.

s. At $x = 0$, the temperature is $T(x=0) = a\left(t_w{}^2 - x^2\right) + b = 100 \cdot 0.25^2 + 30 = 36.25^\circ C$.

At $x = \pm t_w$, the temperature is $T(x = \pm t_w) = a\left(t_w{}^2 - x^2\right) + b = 100 \cdot \left(0.25^2 - 0.25^2\right) + 30 = 30^\circ C$.

In the control volume of dimensions $2t_w A = 0.50 \ \mathrm{m} \cdot 10 \ \mathrm{m}^2$, the thermal energy generation leads to a thermal power of $\dot{Q} = \dot{q_v} 2t_w A = 100 \cdot 0.5 \cdot 10 = 500 \ \mathrm{W}$. According to the energy balance through the wall, the thermal power internally generated in the control volume is equal to the thermal power by conduction and to the thermal power by convection:

$$\dot{Q} = \dot{Q}_{cond} = \dot{Q}_{conv}$$

where

$$\dot{Q}_{cond} = \frac{\lambda(T_{x=0} - T_{x=t_w})}{t_w} A$$

and

$$\dot{Q}_{conv} = h_c A(T_{x=t_w} - T_\infty)$$

The energy balance leads to

$$\dot{Q}_{cond} = \dot{Q}_{conv} = 500 \ \mathrm{W}.$$

Based on the above, the thermal conductivity of the wall can be calculated as

$$\lambda = \dot{Q}_{cond}\frac{t_w}{A(T_{x=0} - T_{x=t_w})} = 500\cdot\frac{0.25}{10\cdot(36.25-30)} = 2\ \mathrm{W/(m^{\circ}C)}$$

and the convection heat transfer coefficient can be calculated as

$$h_c = \frac{\dot{Q}_{conv}}{A(T_{x=t_w} - T_{\infty})} = \frac{500}{10\cdot(30-28)} = 25\ \mathrm{W/(m^{2\circ}C)}.$$

t. Since the outer surface of the pipe is adiabatic, the rate at which energy is generated within the pipe wall must equal the rate at which it is convected to the water: $\dot{E}_g = \dot{q}_{conv} = \dot{Q}\frac{\pi}{4}\left(d_{p,out}^2 - d_{p,in}^2\right)L_p$, which is equal to $\dot{m}c_p(\overline{T}_{f,out} - \overline{T}_{f,in})$ for the conservation of energy, where $\dot{Q}$ [W] is the rate of heat transfer and L_p [m] is the total length of pipe.

It follows that

$$L_p = \frac{4\dot{m}c_p}{\pi\left(d_{p,out}^2 - d_{p,in}^2\right)\dot{q}_v}\left(\overline{T}_{f,out} - \overline{T}_{f,in}\right) = \frac{4\cdot 0.1\cdot 4200}{\pi\left(0.04^2 - 0.02^2\right)10^6}(50-10) = 35.67\ \mathrm{m}.$$

Assuming that uniform heat generation in the wall provides a constant surface heat flux, it is found

$$\dot{q}_s = \frac{\dot{E}_g}{\pi d_{p,in}L_p} = \frac{\dot{q}_v}{4}\frac{d_{p,out}^2 - d_{p,in}^2}{d_{p,in}} = \frac{10^6}{4}\cdot\frac{\left(0.04^2 - 0.02^2\right)}{0.02} = 1.5\cdot 10^4\ \mathrm{W/m^2}.$$

Therefore the local convection heat transfer coefficient reads

$$h_{c,out} = \frac{\dot{q}_s}{T_{s,out} - \overline{T}_{f,out}} = \frac{1.5\cdot 10^4}{(60-50)} = 1500\ \mathrm{W/\left(m^{2\circ}C\right)}.$$

u. The energy balance leads to

$$\dot{m}c_p(\overline{T}_{out} - \overline{T}_{in}) = \overline{h_c}S\Delta T_{LM} = \overline{h_c}\pi d_p L_p \Delta T_{LM}\ [\mathrm{W}]$$

where $S = \pi d_p L_p$ [$\mathrm{m^2}$] is the surface of the pipe with a diameter d_p [m] and ΔT_{LM} [°C] is the logarithmic mean temperature.

It results that

$$\Delta T_{LM} = \frac{\left(T_s - \overline{T}_{in}\right) - \left(T_s - \overline{T}_{out}\right)}{\ln\left(\frac{T_s - \overline{T}_{in}}{T_s - \overline{T}_{out}}\right)} = \frac{(15-3)-(15-10)}{\ln\left(\frac{15-3}{15-10}\right)} = 8^{\circ}\text{C}.$$

Therefore the required pipe length is

$$L_p = \frac{\dot{m} c_p (\overline{T}_{out} - \overline{T}_{in})}{\overline{h}_c \pi d_p \Delta T_{LM}} = \frac{1 \cdot 4186 \cdot 7}{5000 \cdot \pi \cdot 0.02 \cdot 8} = 11.66 \text{ m}.$$

v. In the considered case, Fourier's law can be written as $\dot{q}_x = -\lambda \frac{dT}{dx}$ to determine the heat flux. In the following, a positive heat flux occurs towards the positive x-axis direction whereas a negative flux occurs towards the negative x-axis direction.

Case	T_1 [°C]	T_2 [°C]	dT/dx [°C/m]	$\dot{q}_x$ [W/m^2]
1	30	20	−20	40
2	10	20	20	−40
3	20	19	−2	4
4	9	10	2	−4
5	15.5	15	−1	2

w.

a. The temperature gradient is $\frac{dT}{dx} = \frac{20-15}{0.5} = 10\ ^{\circ}\text{C/m}$. The related heat flux is $\dot{q}_x = -\lambda \frac{dT}{dx} = -15\ \text{W/m}^2$.
b. The temperature gradient is $\frac{dT}{dx} = \frac{15-20}{0.5} = -10\ ^{\circ}\text{C/m}$. The related heat flux is $\dot{q}_x = -\lambda \frac{dT}{dx} = 15\ \text{W/m}^2$.
c. The temperature gradient is $\frac{dT}{dx} = \frac{20-15}{0.5} = 10\ ^{\circ}\text{C/m}$. The related heat flux is $\dot{q}_x = -\lambda \frac{dT}{dx} = -15\ \text{W/m}^2$.

The positive sign indicates that the heat flux goes in the positive x-axis direction whereas the negative sign indicates that the heat flux goes in the negative x-axis direction.

x. In this case, Fourier's law allows determining the heat flux as $\dot{q}_x = -\lambda \frac{dT}{dx} = -0.2 \frac{-0.5}{0.01} = 10\ \text{W/m}^2$. The rate of heat transfer through the area of $A = 2\ \text{m} \cdot 1\ \text{m} = 2\ \text{m}^2$ the insulation sheet is $\dot{Q}_x = \dot{q}_x A = 10 \cdot 2 = 20\ \text{W}$.
y. The heat flux density emission can be evaluated as

$$\dot{q}_{rad,e} = \epsilon \sigma_{SB} T_s^4 = 0.8 \cdot \left(5.67 \cdot 10^{-8}\right)(40+273)^4 = 435\ \text{W/m}^2.$$

The heat flux density by radiation is

$$\dot{q}_{rad,a} = \epsilon \sigma_{SB} T_s^4 = 0.8 \cdot \left(5.67 \cdot 10^{-8}\right)(20+273)^4 = 418\ \text{W/m}^2.$$

The rate of heat loss from the surface per unit pipe length L_p [m] can be evaluated as

$$\dot{q}_l = \frac{\dot{Q}_{conv} + \dot{Q}_{rad}}{L_p} \left[\mathrm{W/m}\right]$$

where $\dot{Q}_{conv}$ [W] is the convective rate of heat transfer, that reads

$$\dot{Q}_{conv} = h_c 2\pi r_{p,out} L_p (T_s - T_\infty) \,[\mathrm{W}]$$

and $\dot{Q}_{rad}$ [W] is the radiative rate of heat transfer, that reads

$$\dot{Q}_{rad} = \epsilon 2\pi r_{p,out} L_p \sigma_{SB} \left(T_s^4 - T_\infty^4\right) \,[\mathrm{W}].$$

Hence

$$\begin{aligned}\dot{q}_l &= \frac{\dot{Q}_{conv} + \dot{Q}_{rad}}{L_p} = h_c 2\pi r_{p,out}(T_s - T_\infty) + \epsilon 2\pi r_{p,out}\sigma_{SB}\left(T_s^4 - T_\infty^4\right) \\ &= 10 \cdot 2\pi \cdot 0.025 \cdot (40 - 20) + 0.8 \cdot 2\pi \cdot 0.025 \cdot 5.67 \cdot 10^{-8} \\ &\quad \cdot \left[(40+273)^4 - (20+273)^4\right] = 47 \ \mathrm{W/m}.\end{aligned}$$

z. The rate of heat transfer entering and leaving the wall on a unit surface area basis can be obtained by using the given temperature distribution.

$$\dot{q}_{x,in} = -\lambda \frac{\partial T}{\partial x}\Big|_{x=0} = -\lambda (b + 2cx)_{x=0} = 20 \cdot 2 = 40 \ \mathrm{W/m}.$$

$$\dot{q}_{x,out} = -\lambda \frac{\partial T}{\partial x}\Big|_{x=L} = -\lambda (b + 2cx)_{x=L} = -2 \cdot (-20 + 2 \cdot 3 \cdot 0.3) = 36.4 \ \mathrm{W/m}.$$

The temperatures of the surfaces are

$$T(x = 0) = 20^\circ \mathrm{C}$$

and

$$T(x = L) = 14.27^\circ \mathrm{C}.$$

The energy balance through the cold surface leads to

$$\dot{q}_{x,out} = \dot{q}_{x,conv} = h_c (T_{x=L} - T_f) \,[\mathrm{W/m^2}].$$

Hence, the convection heat transfer coefficient reads

$$h_c = \frac{\dot{q}_{x,conv}}{T_{x=L} - T_f} = \frac{36.4}{14.27 - 10} = 8.52 \ \mathrm{W/(m^2{}^\circ C)}.$$

aa. For case 1, since the temperature gradient is higher through material B, material A has a higher thermal conductivity than material B. For case 2, since the temperature gradient is higher through material A, material B has a higher thermal conductivity than material A.

bb.

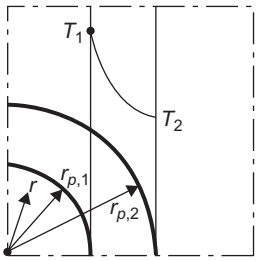

cc.

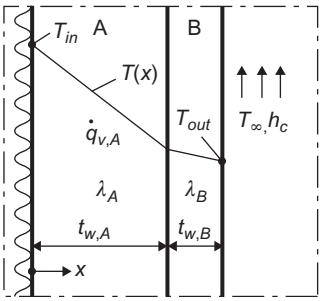

The energy balance leads to

$$t_{w,A}\dot{q}_{v,A} = \dot{q}_{x,cond,A} = \dot{q}_{x,cond,B} = \dot{q}_{x,conv} \ [\mathrm{W/m^2}]$$

where $\dot{q}_{x,cond,A}$ and $\dot{q}_{x,cond,B}$ are the conductive heat flux through material A and B, respectively, and $\dot{q}_{x,conv}$ is the convective heat flux between material B and air. Because the heat flux by convection reads

$$\dot{q}_{x,conv} = h_c(T_{out} - T_\infty)$$

the temperature of the cooled surface can be determined as

$$T_{out} = \frac{t_{w,A}\dot{q}_{v,A}}{h_c} + T_\infty = \frac{0.6 \cdot 30}{10} + 20 = 21.8^\circ \mathrm{C}.$$

The temperature of the insulated surface can be calculated as:

$$T_{in} = t_{w,A}\dot{q}_{v,A}R''_{tot} + T_{out} \ [^\circ \mathrm{C}]$$

where $R''_{tot} = \frac{t_{w,A}}{\lambda_A} + \frac{t_{w,B}}{\lambda_B}$ $[(\mathrm{m^2}\,^\circ \mathrm{C})/\mathrm{W}]$ is the total thermal resistance between the inner and the outer surfaces of materials A and B, respectively. Hence:

$$T_{in} = t_{w,A}\dot{q}_{v,A}R''_{tot} + T_{out} = 0.6 \cdot 30 \cdot \left(\frac{0.6}{0.5} + \frac{0.2}{1.5}\right) + 21.8 = 45.8^{\circ}\text{C}.$$

dd.

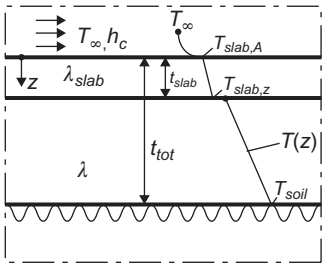

Once the temperature difference $(T_{soil} - T_\infty)$ [°C] is known, the heat flux can be calculated as

$$\dot{q}_z = \frac{T_{soil} - T_\infty}{R''_{tot}} \ [\text{W/m}^2]$$

where R''_{tot} [(m² °C)/W] is the total thermal resistance between the soil at a depth t_{tot} and the air. Neglecting the contact resistance, R''_{tot} can be calculated as

$$R''_{tot} = R''_{soil} + R''_{slab} + R''_{conv} \ [(\text{m}^2{}^{\circ}\text{C})/\text{W}]$$

where R''_{soil} is the equivalent conductive thermal resistance of soil considering its porosity, R''_{slab} is the conductive thermal resistance of the slab and R''_{conv} is the convective thermal resistance between the slab and air.

The equivalent conductive thermal resistance of soil can be calculated as

$$R''_{soil} = \frac{t_{tot} - t_{slab}}{\lambda}$$

where λ [W/(m °C)] is the thermal conductivity of the soil that can be calculated as

$$\lambda = \lambda_s(1 - n) + \lambda_f n \ [\text{W}/(\text{m}^{\circ}\text{C})].$$

The conductive thermal resistance of the slab can be determined as

$$R''_{slab} = \frac{t_{slab}}{\lambda_{slab}}$$

The convective thermal resistance between the slab and air can be calculated as

$$R''_{conv} = \frac{1}{h_c}$$

Once $\dot{q}_z$ is known, the temperature of the two surfaces of the slab can be calculated as

$$T_{slab,2} = T_{soil} - \dot{q}_z R_{eq,soil} \ [^\circ\mathrm{C}]$$

and

$$T_{slab,1} = T_{slab,2} - \dot{q}_z R_{slab} \ [^\circ\mathrm{C}].$$

ee. The total thermal resistance between the refrigerant and the air is composed by conduction and convection resistances. Its expression per unit length reads

$$R'_{tot} = \frac{\ln\left(\frac{r}{r_{p,in}}\right)}{2\pi\lambda} + \frac{1}{2\pi r h_c} \ [(\mathrm{m}^\circ\mathrm{C})/\mathrm{W}]$$

where r [m] is radial coordinate of the pipe.

The thermal power per unit length reads

$$\dot{q}_l = \frac{T_\infty - T_i}{R'_{tot}} \ [\mathrm{W/m}].$$

To optimise the insulation thickness, it is necessary to obtain the value of r which minimises $\dot{q}_l$ or maximises R'_{tot}. This value can be obtained from the requirement that

$$\frac{dR'_{tot}}{dr} = 0$$

That is

$$\frac{1}{2\pi\lambda r} - \frac{1}{2\pi r^2 h_c} = 0$$

The previous equation leads to

$$r = \frac{\lambda}{h_c}$$

To understand if this result maximises or minimises the total resistance, the second derivative has to be evaluated:

$$\frac{d^2R'_{tot}}{dr^2} = \frac{1}{2\pi\lambda r^2} - \frac{1}{\pi r^3 h_c}$$

At $r = \frac{\lambda}{h_c}$:

$$\frac{d^2R'_{tot}}{dr^2} = \frac{1}{\pi\left(\frac{\lambda}{h_c}\right)^2}\left(\frac{1}{\lambda} - \frac{1}{2\lambda}\right) = \frac{1}{\frac{2\pi\lambda^3}{h_c^2}} > 0$$

The result is always positive. This means that $r = \frac{\lambda}{h_c}$ **is the insulation radius that minimises the total thermal resistance and leads to state that an optimum insulation thickness does not exist. It is more correct to define a critical insulation radius which maximises heat transfer: above this value the heat transfer decreases with increasing the insulation radius, below this value the heat transfer increases with increasing the insulation radius. The considered critical radius reads**

$$r_{cr} = \frac{\lambda}{h_c}\ [\mathrm{m}].$$

ff. To determine the temperature distribution $T(r)$ **within the pipe it is necessary to consider the Fourier heat conduction equation for this case, which reads**

$$\frac{1}{r}\frac{d}{dr}\left(r\frac{dT}{dr}\right) + \frac{\dot{q}_v}{\lambda} = 0$$

where r **[m] is radial coordinate of the system and** λ **[W/(m °C)] is**

Separating the variables and assuming uniform volumetric heat generation, this expression may be integrated to obtain

$$r\frac{dT}{dr} = -\frac{\dot{q}_v}{2\lambda}r^2 + C_1$$

where C_1 **is the constant of first integration**.

Repeating the procedure, the general formulation of the temperature distribution within the pipe can be found as

$$T(r) = -\frac{\dot{q}_v}{4\lambda}r^2 + C_1 \ln r + C_2$$

where C_2 is the constant of second integration.

Two boundary conditions are necessary to evaluate the constant C_1 and C_2. Applying the prescribed temperature limit

$$T\left(r_{p,out}\right) = T_{out}$$

and applying the adiabatic condition at the outer surface

$$\frac{dT}{dr}\Big|_{r_{p,2}} = 0$$

the temperature at the outer radius reads

$$T_{out} = -\frac{\dot{q}_v}{4\lambda} r_{p,out}^2 + C_1 \ln r_{p,out} + C_2.$$

Similarly

$$0 = -\frac{\dot{q}_v}{2\lambda} r_{p,out}^2 + C_1.$$

Hence

$$C_1 = \frac{\dot{q}_v}{2\lambda} r_{p,out}^2$$

and

$$C_2 = T_{out} + \frac{\dot{q}_v}{4\lambda} r_{p,out}^2 - \frac{\dot{q}_v}{2\lambda} r_{p,out}^2 \ln r_{p,out}.$$

Substituting the values of C_1 and C_2 in the temperature distribution, it follows that

$$T(r) = T_{out} + \frac{\dot{q}_v}{4\lambda}\left(r_{p,out}^2 - r^2\right) - \frac{\dot{q}_v}{2\lambda} r_{p,out}^2 \ln \frac{r_{p,out}}{r}$$

The heat removal rate can be calculated by obtaining the conduction rate at $r_{p,in}$ or evaluating the total heat generation rate for the pipe. The Fourier's law for this case states

$$\dot{q}_l = -\lambda 2\pi r \frac{dT}{dr}$$

Substituting in the previous equation and evaluating the results at $r_{p,in}$

$$\dot{q}_l\left(r_{p,in}\right) = -\lambda 2\pi r_{p,in}\left(-\frac{\dot{q}_v}{2\lambda} r_{p,in} - \frac{\dot{q}_v}{2\lambda}\frac{r_{p,out}^2}{r_{p,in}}\right) = -\pi \dot{q}_v (r_{p,out}^2 - r_{p,in}^2)$$

To obtain an expression for the convection heat transfer coefficient at radius $r_{p,in}$, the energy conservation has to be applied to the inner surface. It follows that

$$\dot{q}_{l,cond} = \dot{q}_{l,conv}$$

or

$$\dot{q}_v \pi \left(r_{p,out}^2 - r_{p,in}^2 \right) = h_c 2\pi r_{p,in} (T_{in} - T_\infty).$$

Hence

$$h_c = \frac{\dot{q}_v \left(r_{p,out}^2 - r_{p,in}^2 \right)}{2 r_{p,in} (T_{in} - T_\infty)}$$

where T_{in} can be obtained by evaluating the temperature $T(r)$ at $r = r_{p,in}$.

gg. Applying the energy conservation equation, it follows that the conductive heat flux within the wall is equal to the convective heat flux between the fluid and the wall. It follows that

$$\dot{q}_{x,cond} = \dot{q}_{x,conv} = h_c \left(T_\infty - T_{s,in} \right) = 10 \cdot (23 - 20) = 30 \ \mathrm{W/m^2}.$$

The conductive heat flux between the composite wall is

$$\dot{q}_{x,cond} = \frac{T_{s,in} - T_{s,out}}{R''_{tot}}$$

where R''_{tot} [$(\mathrm{m^2\,^\circ C})/\mathrm{W}$] is the total thermal resistance equal to

$$R''_{tot} = \frac{t_{w,A}}{\lambda_A} + \frac{t_{w,B}}{\lambda_B} + \frac{t_{w,C}}{\lambda_C}.$$

Hence

$$30 = \frac{T_{s,in} - T_{s,out}}{\frac{t_{w,A}}{\lambda_A} + \frac{t_{w,B}}{\lambda_B} + \frac{t_{w,C}}{\lambda_C}} = \frac{20 - 5}{\frac{0.3}{2} + \frac{0.15}{\lambda_B} + \frac{0.15}{0.5}}$$

It follows that

$$\lambda_B = 3 \ \mathrm{W/(m^\circ C)}.$$

With the same energy balance, it is possible to express the value of the temperature T_∞ related to the other parameters shown:

$$h_c\left(T_\infty - T_{s,in}\right) = \frac{T_{s,in} - T_{s,out}}{\frac{t_{w,A}}{\lambda_A} + \frac{t_{w,B}}{\lambda_B} + \frac{t_{w,C}}{\lambda_C}}$$

Hence

$$T_\infty = \frac{T_{s,in} - T_{s,out}}{h_c\left(\frac{t_{w,A}}{\lambda_A} + \frac{t_{w,B}}{\lambda_B} + \frac{t_{w,C}}{\lambda_C}\right)} + T_{s,in}\ [^\circ\mathrm{C}].$$

hh. R_{ghe} **[°C/W] is the so-called time-independent thermal resistance of the geothermal heat exchanger.** R'_{ghe} **[(m °C)/W] is the time-independent thermal resistance of the geothermal heat exchanger expressed as a function of the thermally active length of this body.** R''_{ghe} **[(m² °C)/W] is the time-independent thermal resistance of the geothermal heat exchanger expressed as a function of the thermally active heat exchange surface of this body.**

ii. The heat transfer capacity represents the thermal power that can be transferred from (or in) the ground under steady-flux conditions for a temperature change of 1°C between the mean temperature of the heat carrier fluid circulating in the energy piles and the mean temperature of the soil in the zone affected by the heat exchange.

The specific heat storage capacity of a group of piles is defined as the heat that can be extracted for a reduction of the mean soil temperature of 1°C.

jj. The equivalent thermal resistance of soil for this case can be obtained from the graph and is of $R'_{soil} = 0.16$ **(m °C)/W. The thermal power per unit length** $\dot{q}_l$ **that can be extracted with a difference of temperature between the fluid and the soil equal to 5°C can be calculated as**

$$\frac{\dot{Q}}{L} = \dot{q}_l = \frac{\overline{T} - \overline{T}_{soil}}{R'_{ghe} + R'_{soil}} = \frac{5}{0.06 + 0.16} = 22.72\ \mathrm{W/m}$$

where $\dot{Q}$ **[W] is the rate of heat transfer and** L **[m] is the total length of the geostructure.**

kk. From the equation

$$\dot{q}_l = \frac{\overline{T} - \overline{T}_{soil}}{R'_{ghe} + R'_{soil}}\ [\mathrm{W}]$$

The equivalent thermal resistance of soil can be calculated as

$$R'_{soil} = \frac{\overline{T} - \overline{T}_{soil}}{\dot{q}_l} - R'_{ghe} = \frac{6}{30} - 0.08 = 0.12\ \frac{\mathrm{m^\circ C}}{\mathrm{W}}$$

From the previous graph, it can be obtained that the pile diameter related to such a resistance is $D = 50$ cm.

ll. The specific heat storage capacity depends on the volumetric thermal capacity and the volume of soil involved in the heat exchange as

$$C_{sp} = \rho_{soil} c_{p,soil} L A_{inf}$$

where A_{inf} [m^2] is the plan area of the involved soil volume. The area A_{inf} may be estimated as the plan area of soil embedded in the simplest polygon that includes the group of energy piles, augmented from the perimeter of the group of $s/2$. For this specific case, this approach yields to a specific heat storage capacity of

$$C_{sp} = \rho_{soil} c_{p,soil} L A_{inf} = 2500 \cdot 800 \cdot 20 \cdot 225 = 9 \cdot 10^9 \text{ J}/^\circ\text{C}.$$

mm. The relationship between the total length of the piping and the heating capacity is

$$L_{p,tot} = \frac{\dot{Q}_h \left(\frac{COP-1}{COP}\right) \left(R'_{ghe} + R'_{soil} F_h\right)}{\overline{T}_{soil} - \frac{\overline{T}_{in,min} + \overline{T}_{out,min}}{2}} \text{ [m]}.$$

Based on the above, the thermal resistance of the heat exchanger can be calculated as

$$R'_{ghe} = \frac{L_{tot} \left(\overline{T}_{soil} - \frac{\overline{T}_{in,min} + \overline{T}_{out,min}}{2}\right)}{\dot{Q}_h \left(\frac{COP-1}{COP}\right)} - R'_{soil} F_h = \frac{200 \cdot \left(16 - \frac{8+4}{2}\right)}{10{,}000 \left(\frac{3-1}{3}\right)} - 0.5 \cdot 0.5 = 0.05 \text{ (m}^\circ\text{C)/W}.$$

nn. The relationship between the total length of the piping and the heating capacity is

$$L_{tot} = \frac{\dot{Q}_h \left(\frac{COP-1}{COP}\right) \left(R'_{ghe} + R'_{soil} F_h\right)}{\overline{T}_{soil} - \frac{\overline{T}_{in,min} + \overline{T}_{out,min}}{2}} \text{ [m]}$$

Hence, the required piping length is

$$L_{tot} = \frac{15{,}000 \cdot \left(\frac{4-1}{4}\right)(0.1 + 0.6 \cdot 0.5)}{17 - \frac{7+3}{2}} = 375 \text{ m}.$$

oo. Under steady-state conditions and uniform surface temperature of the soil–pile interface, $\overline{T}_{s-p} = T_{s-p}$, the heat exchanger effectiveness can be evaluated as

$$\epsilon_{ghe} = \frac{\overline{T}_{out} - \overline{T}_{in}}{\overline{T}_{s-p} - \overline{T}_{in}} = \frac{14 - 10}{15 - 10} = 0.8$$

pp. Under steady-state conditions and uniform surface temperature of the soil−pile interface, $\overline{T}_{s-p} = T_{s-p}$, the heat exchanger effectiveness can be evaluated as

$$\epsilon_{ghe} = \frac{\overline{T}_{out} - \overline{T}_{in}}{\overline{T}_{s-p} - \overline{T}_{in}}[-]$$

Hence the temperature of the soil−pile interface can be calculated as

$$\overline{T}_{s-p} = \frac{\overline{T}_{out} - \overline{T}_{in}}{\epsilon_{ghe}} + \overline{T}_{in} = \frac{14 - 10}{0.6} + 18 = 13^{\circ}\text{C}.$$

CHAPTER 9

Analytical modelling of transient heat transfer

9.1 Introduction

The continuously varying energy requirements of built environments, together with the weather conditions, can cause different magnitudes and frequencies of temperature changes in the subsurface. These temperature changes vary over time and can be classified in two types: (1) high-frequency temperature changes occurring within hours to days (i.e. for relatively short-to-medium timescales) of small magnitudes (from 5°C to 10°C) and (2) low-frequency temperature changes occurring throughout seasons and years (i.e. for relatively long timescales) of remarkable magnitudes (from 10°C to 30°C).

Based on the previous evidence, the heat transfer phenomena occurring in the subsurface and characterising energy geostructures also vary with time, that is they are time-dependent. The time-dependence of *unsteady* or *transient* heat transfer typically is the result of a variation in the boundary conditions in a system and lasts until a steady-state temperature distribution is reached. Understanding and modelling time-dependent heat transfer phenomena is crucial to characterise the transient thermohydraulic behaviour of energy geostructures as well as to comprehensively understand the functioning of both Ground Source Heat Pump Systems and Underground Thermal Energy Storage Systems. In fact, both high- and low-frequency temperature changes have a direct impact on the response of heat pumps and thus significantly influence the overall system behaviour. Although a time-independent modelling of the heat transfer phenomena involved with energy geostructures can provide important insights for analysis and design purposes, time-dependent investigations must thus be carried out for a sound characterisation of the thermohydraulic behaviour of energy geostructures and the associated energy systems. The rationale of the time-dependent modelling of heat transfer phenomena is to address the temperature distribution in bodies during a transient process as well as the heat transfer between such bodies and their surroundings. Typical problems of interest can involve the determination of the temperature variation with time or the analysis of the temperature variation with both location and time. In the context of energy geostructure applications, the latter problem is often of primary interest and analytical models can be employed for such purpose.

Analysis and Design of Energy Geostructures
DOI: https://doi.org/10.1016/B978-0-12-816223-1.00009-6

This chapter presents analytical approaches to characterise the time-dependent heat transfer phenomena governing energy geostructures under transient conditions. The analysis of these phenomena focuses on the influence of low-frequency temperature changes characterising energy geostructures over relatively long timescales, but the influence of high-frequency temperature changes associated with small-to-medium timescales is also treated in an attempt to comprehensively characterise the operation of the investigated technology.

To address the aforementioned aspects, *idealisations and assumptions* are presented first: in this context, the objective is to propose a summary of assumptions that allow for expedient yet rigorous analyses of energy geostructures and other geothermal heat exchangers. Second, the *analysis approaches* are proposed: the objective of this part is to present two effective approaches allowing for the time-dependent modelling of heat transfer problems to be carried out. Next, the *Duhamel's theorem* is presented: in this context, the purpose is to expand on the superposition principle and the ways superposition can be considered over time and in space to address complex problems. Next, the *concept of thermal resistance* for the time-dependent analysis of heat transfer is expanded: in this framework, the purpose is to complement previously addressed knowledge about the concept of thermal resistance for a comprehensive time-dependent modelling of the heat transfer. Afterward, analytical solutions for the time-dependent analysis of the *heat transfer around energy piles and other circular heat exchangers*, as well as *around energy walls and other plane heat exchangers* are considered: in this context, the purpose is to show analytical solutions that can effectively capture the heat transfer characterising relatively simple geometries representative of geothermal heat exchangers such as energy geostructures. Then, the analysis of *heat transfer at short-to-medium timescales* is presented: the goal of this section is to highlight analytical solutions that can address the response of geothermal heat exchangers subjected to high-frequency temperature fluctuations at the timescales addressed. Finally, *questions and problems* are proposed: the purpose of this part is to fix and test the understanding of the subjects covered in this chapter by addressing a number of exercises.

9.2 Idealisations and assumptions

In the following time-dependent modelling of the heat transfer characterising geothermal heat exchanger such as energy geostructures, the same idealisation and assumptions presented in Chapter 8, Analytical modelling of steady heat and mass transfers, are accounted for unless otherwise specified. The quoted considerations find due justification in the referenced chapter and are only summarised for completeness in the following prior to the detailed description and justification of additional hypotheses.

The ground is considered to be infinite or semiinfinite in extent. A uniform initial temperature is assumed in any modelled domain. Constant flux or constant

Figure 9.1 Modelling strategy to account for groundwater flow.

temperature boundary conditions are considered. The materials are assumed to be isotropic, homogeneous and characterised by effective properties. When considered in the investigations, convection is the unique heat transfer mode occurring in the pipes of the geothermal heat exchangers, while conduction entirely characterises heat transfer across the pipes and within the grouting material of the geothermal heat exchangers. Solutions including the effect of convection at fluid-solid interfaces are considered for bodies that may be assumed adjacent to built environments filled with a fluid (i.e. air). Conduction is generally considered to characterise heat transfer in the ground around the geothermal heat exchangers.

When the effect of groundwater flow is considered in the analysis of heat transfer around geothermal heat exchangers, a homogeneous groundwater flow with parallel streamlines to the surface is assumed (cf. Fig. 9.1). This approach is common to the analytical solutions available to date for the analysis of this phenomenon (i.e. Dupuit seepage theory).

Other (coupled) phenomena, such as heat and moisture transfers (Luikov, 1975), may occur in applications of geothermal heat exchangers such as energy geostructures. However, no solutions currently exist to account for these problems (Li and Lai, 2015). Despite this limitation, as far as potential variations in the thermal properties of the materials are considered due to moisture migration, the contribution of moisture transfer to the global heat transfer phenomenon can be considered negligible for practical considerations.

9.3 Analysis approaches

9.3.1 General

Two analytical approaches can be typically used to model time-dependent heat transfer phenomena. A first approach, termed the *lumped capacitance method*, resorts to the solution of an energy balance and allows modelling time-dependent heat transfer problems for bodies characterised by a spatially uniform temperature within them during the transient process (i.e. temperature gradients within the body are negligible). This approach can be used to determine the variation of temperature with time. A second

approach resorts to the solution of the Fourier heat conduction equation and allows modelling time-dependent heat transfer problems for bodies in which the temperature is not spatially uniform within them during the transient process (i.e. temperature gradients within the body cannot be neglected) and heat transfer is typically one-dimensional. This approach can be used to determine the variation of temperature with both space and time.

Both of the aforementioned approaches can address key aspects of the time-dependent modelling of heat transfer and are covered in the following. However, while the lumped capacitance method is summarised hereafter with the main purpose of presenting useful parameters for the time-dependent analysis of heat transfer, a focus is devoted to the analytical solutions of the Fourier heat conduction equation due to their capability of accounting for the temperature gradients within and around bodies that are of particular interest in the context of energy geostructures.

9.3.2 The lumped capacitance method

The lumped capacitance method can effectively address the temperature variation with time of bodies experiencing a sudden change in thermal environment when the temperature distribution within them is spatially uniform. This situation may be considered to characterise a body at a uniform initial temperature T_0 that is immersed in a larger domain at a temperature, for example $T_\infty < T_0$, for which heat transfer occurs from a time $t \geq 0$ until a thermal steady-state is reached ($T_\infty = T_0$). In this context, for example, when a solid is immersed in a fluid at a different temperature, or when a fluid is suddenly put in contact with a solid, heat transfer takes place due to convection at the solid-fluid interface.

The absence of a temperature gradient in the body implies an infinite thermal conductivity of this medium based on Fourier's law and makes Fourier heat conduction equation useless for characterising this time-dependent problem because such an equation governs the distribution of temperature in space. Based on these considerations, the transient temperature response must be tackled through the formulation of an overall energy balance for the entire body, which relates the rate of heat loss (or heat gain) to the rate of change of the internal energy. Mathematically, the energy balance for the considered problem can be expressed as

$$-h_c A_{si}(T - T_\infty) = \rho V c_p \frac{dT}{dt} \tag{9.1}$$

where h_c is the convection heat transfer coefficient, A_{si} is the surface of the body immersed in the fluid at uniform constant temperature T_∞, ρ and c_p are the density and specific heat of the body, V is the volume of the body and T is the temperature. By introducing the relevant temperature changes

$$\tilde{\tilde{\theta}} = T - T_\infty \tag{9.2}$$

and

$$\tilde{\tilde{\theta}}_i = T_0 - T_\infty \tag{9.3}$$

and by working with Eq. (9.1), the time required for the body to reach some temperature T can be determined as (Bergman et al., 2011)

$$\frac{\rho V c_p}{h_c A_{si}} \ln \frac{\tilde{\tilde{\theta}}_i}{\tilde{\tilde{\theta}}} = t \tag{9.4}$$

Equivalently, the temperature reached by the body at some time t can be determined as (Bergman et al., 2011)

$$\frac{\tilde{\tilde{\theta}}}{\tilde{\tilde{\theta}}_i} = \frac{T - T_\infty}{T_0 - T_\infty} = \exp\left(- \frac{h_c A_{si}}{\rho V c_p} t \right) \tag{9.5}$$

In Eq. (9.4), the factor

$$\frac{\rho V c_p}{h_c A_{si}} = \frac{R''_{conv} C_t}{A_{si}} = \tau_t \tag{9.6}$$

represents the *thermal time constant* for the considered body, where R''_{conv} and C_t are the resistance to convection heat transfer and the lumped thermal capacitance of the solid, respectively. The considered thermal time constant can be useful to analyse the exponential decay expressed in Eq. (9.5) of the temperature difference between the body and the fluid to zero as t approaches infinity (cf. Fig. 9.2).

In the context of the present analysis, the infinite value of thermal conductivity for the body is clearly unrealistic. However, from a physical perspective, this condition can be associated with a thermal resistance to conduction within the body that is much smaller than the thermal resistance to heat transfer between the body and its surroundings (Bergman et al., 2011). Verifying the occurrence of a thermal resistance to conduction in a body that is much less than the resistance to convection across the fluid boundary layer is essential for the lumped capacitance method to be meaningfully applied. The parameter that must be used to verify this condition is the *Biot number*, which is a dimensionless parameter that can be determined through an energy balance for all bodies as

$$Bi = \frac{h_c L_c}{\lambda} \tag{9.7}$$

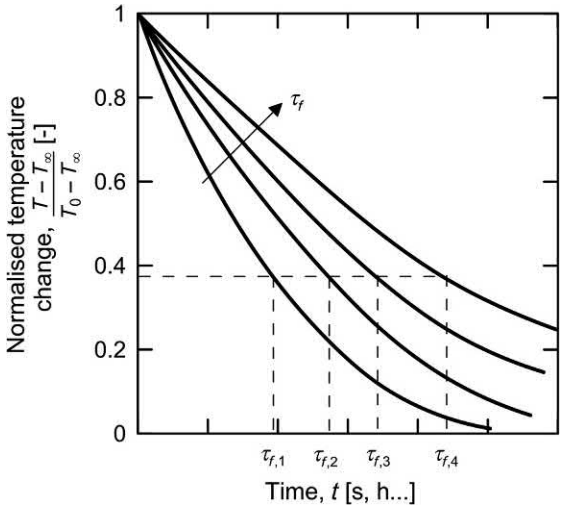

Figure 9.2 Transient temperature response of lumped capacitance bodies for different thermal time constants. *Modified after Bergman, T., Incropera, F., Lavine, A., DeWitt, D., 2011. Fundamentals of Heat and Mass Transfer. Wiley, Hoboken, NJ.*

where L_c is the characteristic length of the considered body and λ is the thermal conductivity of the body. Theoretically, L_c is defined as the ratio of the body volume to surface area $L_c \equiv V/A_{si}$, but is often conservatively considered as the length scale corresponding to the maximum spatial temperature difference. As a consequence of this latter approach: for a wall of thickness t_w, L_c is equal to half thickness $t_w/2$; for a long cylinder or a sphere or radius R, L_c is equal to R.

For the lumped capacitance method to be applied with a small error, it must be verified that $Bi \ll 1$ and in particular $Bi < 0.1$ (Bergman et al., 2011). Under these conditions, the assumption of a uniform temperature distribution within a considered body is reasonable, that is $T(x,t) \approx T(t)$. When the previous condition is not verified, the temperature distribution within a body cannot be considered uniform, that is $T = T(x,t)$. An example of this concept is shown in Fig. 9.3 for a plane wall initially at a uniform temperature T_0 that experiences convection cooling when it is immersed in a fluid of temperature $T_\infty < T_0$.

Based on the definition of the Biot number and considering $L_c \equiv V/A_{si}$, the exponent of Eq. (9.5) can be expressed as

$$\frac{h_c A_{si}}{\rho V c_p} t = Bi \cdot Fo \tag{9.8}$$

where

$$Fo \equiv \frac{\alpha_d t}{L_c^2} \tag{9.9}$$

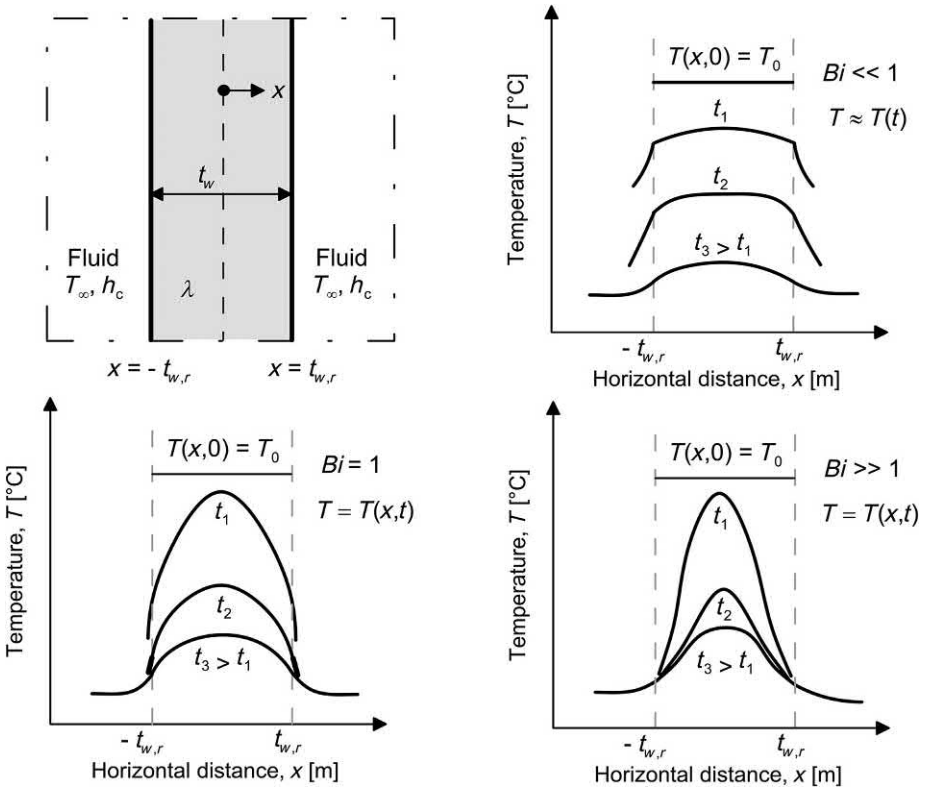

Figure 9.3 Thermal response of a plane wall depending on the value of Biot number. *Modified after Bergman, T., Incropera, F., Lavine, A., DeWitt, D., 2011. Fundamentals of Heat and Mass Transfer. Wiley, Hoboken, NJ.*

with *Fo* being the *Fourier number* and α_d the thermal diffusivity. The Fourier number is a dimensionless time providing key information together with the Biot number about transient conduction problems (e.g. the validity of analytical solutions).

Substituting Eq. (9.8) in Eq. (9.5) it results

$$\frac{\tilde{\tilde{\theta}}}{\tilde{\tilde{\theta}}_i} = \frac{T - T_\infty}{T_0 - T_\infty} = \exp(-Bi \cdot Fo) \tag{9.10}$$

9.3.3 Solution of the Fourier heat conduction equation

The solution of the Fourier heat conduction equation can address the temperature variation with both time and spatial coordinates when the temperature distribution within bodies cannot be considered spatially uniform (i.e. when the Biot number is not small and temperature gradients are not negligible). Different approaches can be

employed to solve the Fourier heat conduction equation. These approaches include, for example dimension reduction, reduction by similarity, separation of variables, Green's function integrals and Laplace's transforms (see, e.g. Carslaw and Jaeger, 1959; Schneider, 1955; Kakac and Yener, 2008; Poulikakos, 1994).

In the time-dependent modelling of heat transfer, the temperature evolution depends on the relevant spatial coordinates, the time, the material as well as geometrical properties characterising any considered problem. For the plane wall depicted in Fig. 9.3, it results

$$T = T(x, T, T_0, T_\infty, t_w, \lambda, \alpha_d, h_c) \tag{9.11}$$

where x is the relevant spatial coordinate. The rationale of Eq. (9.11) can be highlighted by solving the Fourier heat conduction equation, for example by dimension reduction (heat transfer depends only on one dimensional coordinate and hence the Fourier heat conduction equation can be simplified). By assuming no internal energy generation and a constant thermal conductivity, Fourier heat conduction equation reads in this case

$$\frac{\partial^2 T}{\partial x^2} = \frac{1}{\alpha_d}\frac{\partial T}{\partial t} \tag{9.12}$$

To solve Eq. (9.12) and obtain the temperature distribution $T(x, t)$, one initial condition and two boundary conditions are needed. A typical initial condition prescribing a uniform initial temperature at the time $t = 0$ reads

$$T(x, 0) = T_0 \tag{9.13}$$

For the considered problem, a first boundary condition can be set to express the symmetry of the system along the midplane of the wall as

$$\frac{\partial T}{\partial x}|_{x=0} = 0 \tag{9.14}$$

A second boundary condition can also be set to characterise the convection condition for time $t > 0$ as

$$-\lambda \frac{\partial T}{\partial x}|_{x=t_{w,r}} = h_c\left[T\left(t_{w,r}, t\right) - T_\infty\right] \tag{9.15}$$

To broadly characterise time-dependent heat transfer problems, reference is often made to suitable groups of variables and dimensionless solutions. For example by expressing the following dimensionless parameters

$$\tilde{\theta}^* \equiv \frac{\tilde{\tilde{\theta}}}{\tilde{\tilde{\theta}}_i} = \frac{T - T_\infty}{T_0 - T_\infty} \tag{9.16}$$

$$\tilde{x}^* \equiv \frac{x}{t_w} \tag{9.17}$$

$$\tilde{t}^* \equiv \frac{\alpha_d t}{t_w^2} \equiv Fo \tag{9.18}$$

The functional dependence expressed in Eq. (9.11) can be formulated as

$$\tilde{\theta}^* \equiv f(\tilde{x}^*, Bi, Fo) \tag{9.19}$$

In other words, for a prescribed geometry, the transient temperature distribution is a universal function of $\tilde{x}^*$, Bi and Fo. That is the dimensionless solution (9.19) has a prescribed form that does not depend on any particular value of T, T_0, T_∞, t_w, λ, α_d or h_c (Bergman et al., 2011).

9.4 Thermal resistance concept for time-dependent solutions

In the time-independent modelling of heat transfer, an analogy between heat and electrical current flows has been made through the concept of time-independent thermal resistance. This concept has been shown to be particularly effective in modelling heat transfer problems characterised by (at least) one body surrounded by a larger domain, considering reference times t^*. In this context, solutions to time-independent heat transfer problems within (at least) one body surrounded by a larger domain have been presented for $t > t^*$, with the rationale that steady conditions can be assumed to occur within the former while unsteady conditions characterise the latter.

In the treatment of the time-dependent modelling of heat transfer, the concept of thermal resistance can still be used, but must be expressed through a time-dependent formulation to account for the transient phenomena occurring in the larger domain surrounding the previously considered single or multiple bodies for $t > t^*$ (typically, the ground surrounding the geothermal heat exchanger(s)). The considered thermal resistance is often referred to as the *total thermal resistance*, $R_T(t)$, and is decomposed into a time-independent part and a time-dependent part as

$$R_T(t) = R_{ghe} + G_f(x_i, t) \tag{9.20}$$

where R_{ghe} is the time-independent part of the total thermal resistance, typically coinciding with the thermal resistance of the geothermal heat exchanger, and $G_f(x_i, t)$ is the time-dependent part of the total thermal resistance, often called *G-function* (with x_i the coordinates of a considered point and t the time). The approach of expressing the total thermal resistance as in Eq. (9.20) draws from the work of Li and Lai (2015). In

fact, although G-functions have originally been expressed in dimensionless forms (Ingersoll et al., 1954; Claesson and Eskilson, 1988; Eskilson, 1987), in this context they have the same unit measure of a thermal resistance and express the temperature response in the ground due to a unit-step change in heat transfer rate $\dot{Q}$ (Li and Lai, 2015).

The previous concept of total thermal resistance that simplifies the global heat transfer characterising geothermal heat exchangers in a time-independent and time-dependent processes within and around these bodies, respectively, should be considered for $t > t_{ghe}$, that is for the relatively long timescales that govern the optimum control and operation of Ground Source Heat Pump and Underground Thermal Energy Storage Systems, and are associated with daily (or monthly) energy load profiles. In general, the previous concept of total thermal resistance should not be applied for $t_p < t \leq t_{ghe}$, that is for relatively short-to-medium timescales that govern the overall feasibility of Ground Source Heat Pump and Underground Thermal Energy Storage Systems for the standpoint of the life cycle, and are associated with hourly energy load profiles. The reason for this is that, for time intervals $t_p < t \leq t_{ghe}$ and the high-frequency temperature changes characterising heat transfer, the hypotheses made to obtain the analytical solutions of the G-function and the assumptions made to obtain the time-independent portion of the thermal resistance (i.e. referring to steady conditions within the geothermal heat exchanger) make this approach inappropriate in contrast to time periods $t > t_{ghe}$ at which the low-frequency temperature changes govern heat transfer.

Based on the previous considerations, when dealing with the time-dependent modelling of heat transfer in the context of the analysis and design of geothermal heat exchangers such as energy geostructures (e.g. for $t > t_{ghe}$), two aspects typically need to be addressed (Li and Lai, 2015): (a) what the heat transfer rate of the geothermal heat exchanger as a function of time is, given a particular temperature difference between the circulating fluid and the ground, and (b) what the temperature difference as a function of time is, given a required heat exchange rate. These two aspects can be mathematically expressed as

$$\dot{Q} = \dot{q}_i A = \frac{\overline{T}_f(t) - T_0}{R_T(t)} = \frac{\Delta T}{R_T(t)} \tag{9.21}$$

where $\dot{q}_i$ is the heat flux density, A is the area normal to the direction of heat transfer, $\overline{T}_f(t)$ is the average temperature of the heat carrier fluid circulating in the pipes of the geothermal heat exchanger and T_0 is the initial ground temperature. Based on Eq. (9.20), Eq. (9.21) can be rewritten as

$$\Delta T = \dot{Q}\left[R_{ghe} + G_f(x_i, t)\right] \tag{9.22}$$

When problem (a) is considered, the term $\overline{T}_f(t) - T_0$ is known and R_{ghe} and $G_f(x_i, t)$ need to be determined to estimate $\dot{Q}$. When problem (b) is considered, the term $\dot{Q}$ is known and R_{ghe} and $G_f(x_i, t)$ need to be determined for estimating the average temperature of the heat carrier fluid, $\overline{T}_f(t)$. Once $\overline{T}_f(t)$ is known, the inlet temperature of the fluid, $\overline{T}_{in}(t)$, and the outlet temperature of the fluid, $\overline{T}_{out}(t)$, can be calculated. In many cases, it is assumed that $\overline{T}_f(t) = \left[\overline{T}_{in}(t) + \overline{T}_{out}(t)\right]/2$ (ASHRAE, 2011). Therefore the inlet and outlet fluid temperatures can be computed as (Li and Lai, 2015)

$$\begin{cases} \overline{T}_{in}(t) = \overline{T}_f(t) + \dfrac{\dot{Q}}{2\rho_f c_{p,f} \dot{V}} \\ \overline{T}_{out}(t) = \overline{T}_f(t) - \dfrac{\dot{Q}}{2\rho_f c_{p,f} \dot{V}} \end{cases} \tag{9.23}$$

where ρ_f and $c_{p,f}$ are the density and specific heat of the heat carrier fluid circulating in the pipes, respectively, and $\dot{V}$ is the volumetric flow rate. Eq. (9.23) can be equivalently expressed as

$$\dot{Q} = \rho_f c_{p,f} \dot{V} \left(\overline{T}_{in}(t) - \overline{T}_{out}(t)\right) \tag{9.24}$$

The inlet and outlet temperature of the heat carrier fluid circulating in the pipes of geothermal heat exchangers, together with the flow rate, typically represent the parameters that drive the operation of the related energy systems (Spitler and Bernier, 2016). In most cases, inlet temperature and flow rate represent boundary conditions for geothermal heat exchanger models. However, according to Spitler and Bernier (2016), the design of energy systems usually resorts to loads in the form of imposed heat transfer rates or energy consumptions to the geothermal heat exchangers of the heat pumps.

9.5 Duhamel's theorem

Applied thermal loads are never constant with time in energy systems (Bourne-Webb et al., 2016) (cf. Fig. 9.4). The reason for this is that the response of energy systems is designed to vary over time according to the change in boundary conditions. Despite this fact, in most cases and especially when employing analytical solutions, constant loads or some form of load aggregation are employed over time (Claesson and Javed, 2012). In addition to the previous considerations, the temperature distribution that characterises the geothermal heat exchangers and the surrounding ground is generally different compared to the distribution associated with single isolated geothermal heat exchangers. The reason for this is because geothermal heat exchangers often interact

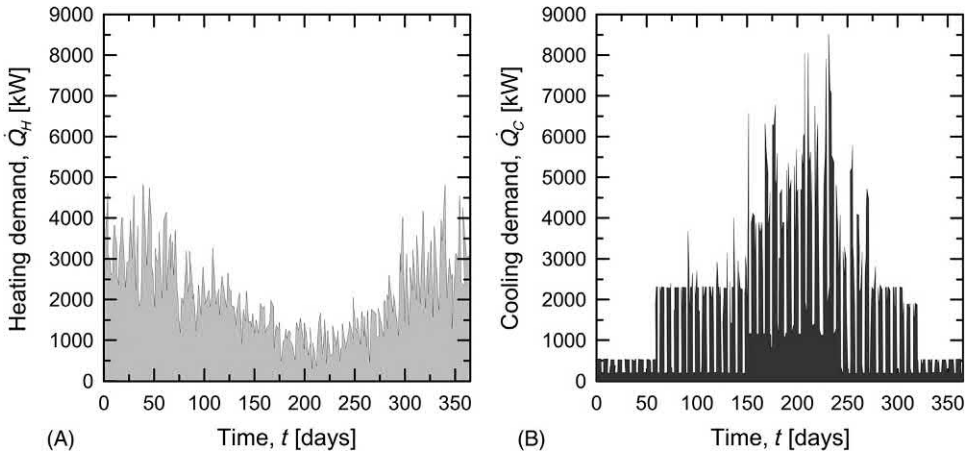

Figure 9.4 (A) Heating and (B) cooling energy demand in a general building.

with other sources located in the surroundings (e.g. other heat exchangers) that modify the temperature profile caused by the operation of a geothermal heat exchanger in an isolated case. Despite this fact, in most cases and especially when employing analytical solutions, the response of isolated geothermal heat exchangers represents the starting point of the investigations.

The rationale for developing analyses referring to constant loads over time or to isolated subjects is due to the existence of the superposition principle. Duhamel's theorem is typically employed to express this (temporal) principle with respect to the evolution of a relevant variable over time (Carslaw and Jaeger, 1959; Ozisik, 1993). Based on the superposition principle, analyses of the response of any system subjected to a complex total load profile evolving with time can be tackled by considering the superposition of the responses of the same system to an appropriate number of constant unit-step loads that decompose the total load profile over time (cf. Fig. 9.5). Similarly, analyses of the response of a system composed of different representative and distinct sources interacting in space can be tackled by considering the superposition of the responses of the individual sources under a given representative load (cf. Fig. 9.6). In other words, the superposition principle can be applied both *temporally* and *spatially*.

The superposition principle applied to the analysis of heat transfer problems relies on the linear nature of the Fourier heat conduction equation and the boundary conditions (Claesson and Dunand, 1983). This principle can also be applied in other contexts, such as in the mechanical analysis of bodies subjected to loading through similar considerations about the governing master equation and associated boundary conditions. When boundary conditions involving nonlinearity in the solution are considered, the superposition principle can only be applied approximately. In the analysis of heat transfer, boundary conditions that involve nonlinearity of the solution are those

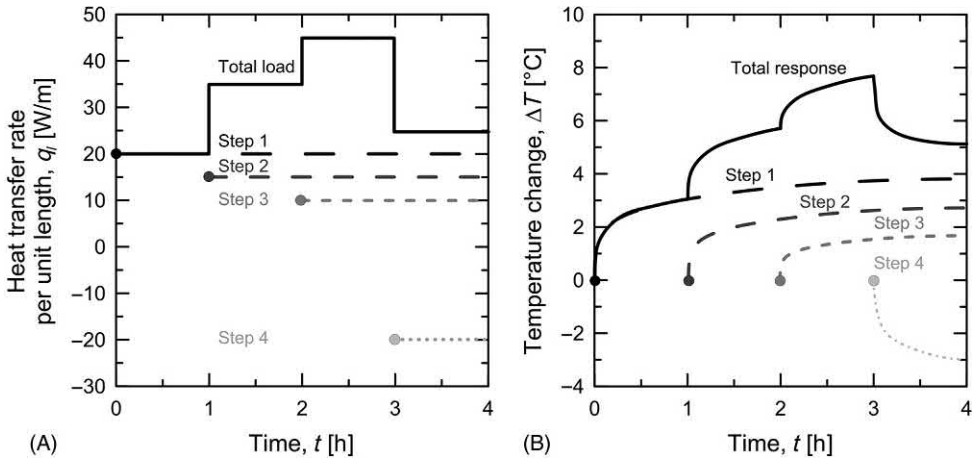

Figure 9.5 Example of (A) total hourly load represented through the superposition of constant step functions and (B) corresponding temperature responses of a borehole heat exchanger. *Redrawn after Spitler, J., Bernier, M., 2016. Vertical borehole ground heat exchanger design methods. In: Advances in Ground-Source Heat Pump Systems. Elsevier, pp. 29–61.*

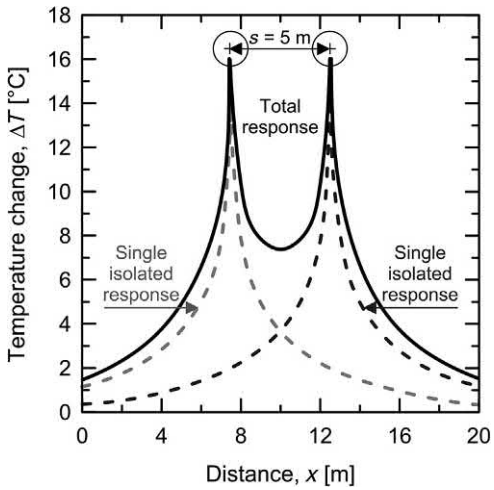

Figure 9.6 Example of total thermal response of two borehole heat exchangers located at a centre-to-centre spacing of $s = 5$ m given by the spatial superposition of the single isolated responses. *Redrawn after Spitler, J., Bernier, M., 2016. Vertical borehole ground heat exchanger design methods. In: Advances in Ground-Source Heat Pump Systems. Elsevier, pp. 29–61.*

associated with, for example, radiation heat transfer at the surface, time-dependent heat transfer coefficients for the surface, and time-dependent convection and groundwater flows.

According to Duhamel's theorem, problems of time-dependent loads can easily be tackled by using the problem solution for a unit-step load (Li and Lai, 2015)

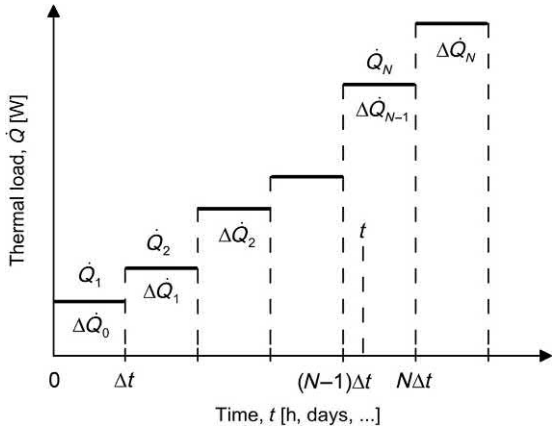

Figure 9.7 Concept of step-unit load varying over time. *Modified after Li, M., Li, P., Chan, V., Lai, A. C., 2014. Full-scale temperature response function (G-function) for heat transfer by borehole ground heat exchangers (GHEs) from sub-hour to decades. Appl. Energy 136, 197–205.*

$$T_1(x_i, t) = T_0 + \int_0^t \dot{Q} \frac{\partial G_f(x_i, t - x_t)}{\partial t} dx_t \tag{9.25}$$

where x_t is an integral variable with the dimension of a time. The function G_f is the response function for unit-step change in the thermal load of the geothermal heat exchanger.

Because the heating and cooling loads applied to geothermal heat exchangers are commonly available as stepwise constant values (on an hourly, daily, weekly or monthly base), Eq. (9.25) is often expressed as (Ozisik, 1993)

$$T_1(x_i, t) = T_0 + \sum_{j=0}^{N-1} \Delta\dot{Q}_j G_f(x_i, t - j\Delta t) \tag{9.26}$$

where $\Delta\dot{Q}_j$ is the stepwise change in $\dot{Q}$ at the beginning of the jth time interval (cf. Fig. 9.7).

According to Li and Lai (2015), Eqs (9.25) and (9.26) imply that the response function of any time-dependent load $\dot{Q}$ is readily determined once the G-function, that is temperature response to the unit-step load, is available.

9.6 Heat transfer around energy piles and other circular heat exchangers

9.6.1 General

To characterise the heat transfer of long, slender, circular heat exchangers such as energy piles and vertical boreholes, Eqs (9.21) and (9.22) are usually expressed as a

function of the thermal power per metre length of the thermally active portion of the element $\dot{q}_l$ as

$$\dot{q}_l = \frac{\overline{T}_f(t) - T_0}{R'_T(t)} = \frac{\Delta T}{R'_T(t)} \tag{9.27}$$

and

$$\Delta T = \dot{q}_l \left[R'_{ghe} + G'_f(x_i, t) \right] = \dot{q}_l R'_T(t) \tag{9.28}$$

where $R'_T(t)$ is the total thermal resistance of the slender heat exchanger while R'_{ghe} and $G'_f(x_i, t)$ are the time-independent and time-dependent portions of the thermal resistance, respectively. Eqs (9.27) and (9.28) are the typical expressions used in the thermohydraulic analysis of geothermal heat exchangers for addressing the previously considered problems (a) and (b) highlighted by Li and Lai (2015) (cf. Section 9.4).

In the following several analytical models allowing to define G-functions are presented to address the time-dependent heat transfer around bodies (i.e. for the relatively long timescales associated with $t > t_{ghe}$ and low-frequency temperature fluctuations). The geometries that are typically employed in these models to investigate the thermal response of long, slender, circular heat exchangers are cylinders or lines that are often considered to be infinite in extent. A number of mathematical developments allow referring also to geometries more adherent to reality, such as finite cylinders and lines. In all cases, the considered models have been proven to capture essential aspects of the time-dependent heat transfer.

9.6.2 Infinite cylindrical surface source model

The infinite cylindrical surface source model finds its roots in the work of Ingersoll et al. (1954). The model provides a solution for the radial heat transfer from a hollow cylinder surrounded by an infinite medium in which heat transfer occurs via conduction (cf. Fig. 9.8).

The cylinder, which can represent the outer boundary of the geothermal heat exchanger, is assumed to have a constant heat flux (or temperature) around its outer surface. The model is expressed mathematically as

$$\begin{cases} \dfrac{\partial^2 T}{\partial r^2} + \dfrac{1}{r}\dfrac{\partial T}{\partial r} = \dfrac{1}{\alpha_{d,soil}}\dfrac{\partial T}{\partial t} \\ r = R \quad -2\pi R \lambda_{soil} \dfrac{\partial T}{\partial r} = \dot{q}_l \\ r \to \infty \quad T = T_0 \\ t = 0 \quad T = T_0 \end{cases} \tag{9.29}$$

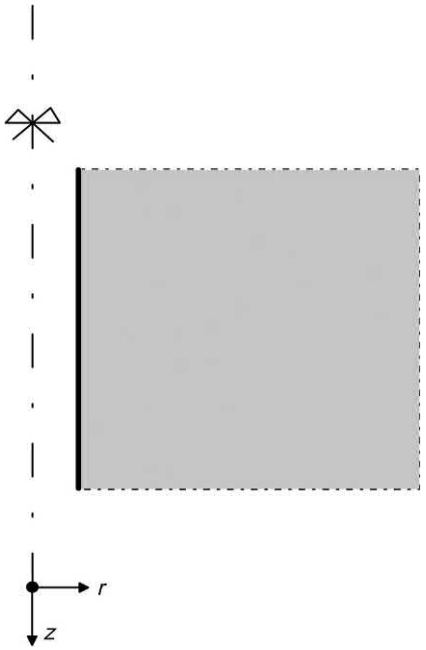

Figure 9.8 Schematic of the infinite cylindrical surface source model.

where r is the radial distance from the axis of the cylinder, $\alpha_{d,soil}$ is the thermal diffusivity of the ground and λ_{soil} is the thermal conductivity of the ground. The solution of this problem can be found by simplifying the Fourier heat conduction equation through the Laplace transformation method and reads (Carslaw and Jaeger, 1959)

$$T(t,R) = T_0 + \dot{q}_l G_f'(t,R) = \\ T_0 + \dot{q}_l \frac{1}{\pi^2 R \lambda_{soil}} \int_0^\infty \left(e^{-\alpha_{d,soil} u^2 t} - 1\right) \frac{J_{B,0}(uR)Y_{B,1}(uR) - Y_{B,0}(uR)J_{B,1}(uR)}{u^2\left[J_{B,1}^2(uR) + Y_{B,1}^2(uR)\right]} du \tag{9.30}$$

where $J_{B,0}$ and $J_{B,1}$, and $Y_{B,0}$ and $Y_{B,1}$ are Bessel functions of the first and second kind of first and second order. For large values of $\alpha_{d,soil}t/R^2 = Fo$, the solution of the G-function can be written as

$$G_f'(r,t) = \frac{1}{4\pi\lambda_{soil}}\left[\ln\frac{4\alpha_{d,soil}t}{r^2} - \gamma_E + \frac{r^2}{2\alpha_{d,soil}t}\left(\ln\frac{4\alpha_{d,soil}t}{r^2} - \gamma_E + 1\right)\right] \tag{9.31}$$

where $\gamma_E = 0.5772$ is the Euler's constant.

The infinite cylindrical surface model can be employed to simulate long vertical geothermal heat exchangers such as energy piles and energy wells, and also the lower part of piles or energy diaphragm walls embedded on either side (Brandl, 2006).

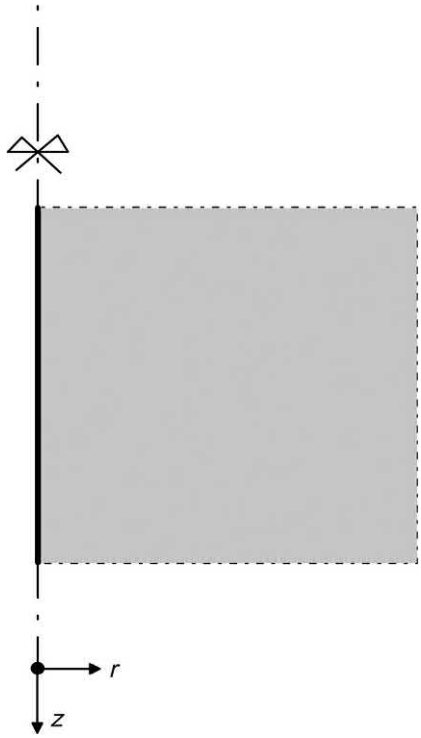

Figure 9.9 Schematic of the infinite line source model.

9.6.3 Infinite line source model

The infinite line source model also finds its roots in the work of Ingersoll et al. (1954) and is based on the work of Kelvin (1882) successively expanded by Whitehead (1927). The model provides a solution for the radial heat transfer from a line (e.g. a cylinder of vanishingly small radius) characterised by a constant heat flux towards (or from) an infinite medium in which heat transfer occurs via conduction (cf. Fig. 9.9).

The model is given mathematically by

$$\begin{cases} \dfrac{\partial^2 T}{\partial r^2} + \dfrac{1}{r}\dfrac{\partial T}{\partial r} = \dfrac{1}{\alpha_{d,soil}}\dfrac{\partial T}{\partial t} \\ r \to 0 \quad -2\pi\lambda_{soil} \lim\limits_{r\to 0} r\dfrac{\partial T}{\partial r} = \dot{q}_l \\ r \to \infty \quad T = T_0 \\ t = 0 \quad T = T_0 \end{cases} \tag{9.32}$$

The solution of this problem is (Carslaw and Jaeger, 1959; Ingersoll et al., 1954)

$$T(t,R) = T_0 + \dot{q}_l G_f'(t,R) = T_0 + \dot{q}_l \frac{1}{4\pi\lambda_{soil}} \int_{R^2/(4\alpha_{d,soil}t)}^{\infty} \frac{e^{-u}}{u}\, du = T_0 + \dot{q} \frac{1}{4\pi\lambda_{soil}} E_1\left(\frac{R^2}{4\alpha_{d,soil}t}\right) \tag{9.33}$$

where E_1 is the exponential integral. For large values of $\alpha_{d,soil}t/R^2$, the solution of the exponential integral can be approximated as (Carslaw and Jaeger, 1959)

$$G_f'(t,R) = \frac{1}{4\pi\lambda_{soil}} E_1\left(\frac{R^2}{4\alpha_{d,soil}t}\right) = \frac{1}{4\pi\lambda_{soil}} \left(\ln\frac{4\alpha_{d,soil}t}{R^2} - \gamma_E\right) \tag{9.34}$$

with a maximum error of 2% for $t > 5t_{ghe} \sim 5R^2/\alpha_{d,ghe}$ (Hellström, 1991), where $\alpha_{d,ghe}$ is the thermal diffusivity of the geothermal heat exchanger.

Similar to the infinite cylindrical surface model, the infinite line source model can be employed to simulate long vertical geothermal heat exchangers such as energy piles. However, the infinite line source model is worse applicable to analyses addressing short-to-medium timescales compared to the infinite cylindrical surface model, because of the line source assumption (Li and Lai, 2015). The relative error between these two models is less than about 10% when $t \approx 5t_{ghe}$ (Hellström, 1991) and 2% when $t \approx 20t_{ghe}$ (Ingersoll et al., 1954). However, the more complex formulation of the infinite cylindrical surface source model than the infinite line source model makes the former tool less advantageous than the latter at the considered timescales. In general, both the infinite cylindrical surface and line source models are poorly applicable in analyses addressing long timescales because they neglect the finite extent of the problem characterising heat transfer. This aspect involves edge effects under these timescales caused by the actual presence of the ground surface and the limited length of the geothermal heat exchangers due to their bluffness.

9.6.4 Finite line source model

For geothermal heat exchangers such as energy piles, edge effects become relevant approximately after one year of geothermal operation and continue to be important throughout the life of the system (Li and Lai, 2015). While the influence of the ground surface cannot be addressed by the infinite cylindrical surface source model and the infinite line source model, it can be treated analytically through the method of images and Kelvin's theory of heat sources (Eckert and Drake Jr., 1987). Considering the ground as a reflecting plane, a constant temperature (or an adiabatic boundary condition) can be assumed at the ground surface and the finite line source model can capture this edge effect (Zeng et al., 2002; Lamarche and Beauchamp, 2007a) (cf. Fig. 9.10).

According to Li and Lai (2015), the finite line source model requires a double integral to obtain the integral average temperature of the geothermal heat exchanger wall, which leads to a marked increase in computational cost. However, Lamarche and

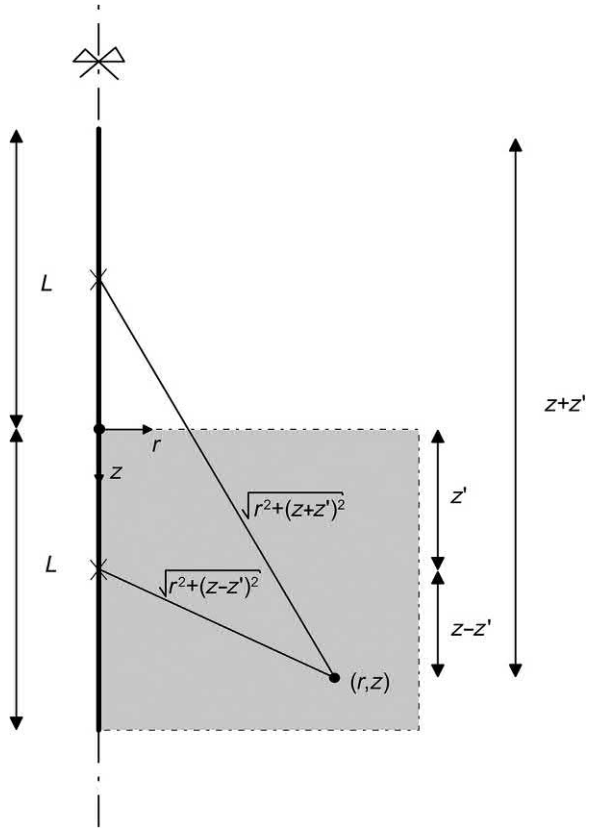

Figure 9.10 Schematic of the finite line source model.

Beauchamp (2007a) and Claesson and Javed (2012) have reformulated the finite line source model to avoid this need. The formulation of the G-function derived from the finite line source model reads

$$G_f'(t,R,z) = \frac{1}{4\pi\lambda_{soil}} \int_0^L \left[\frac{\operatorname{erfc}\left(\sqrt{R^2+(z-z')^2}/2\sqrt{\alpha_{d,soil}t} \right)}{\sqrt{R^2+(z-z')^2}} - \frac{\operatorname{erfc}\left(\sqrt{R^2+(z+z')^2}/2\sqrt{\alpha_{d,soil}t} \right)}{\sqrt{R^2+(z+z')^2}} \right] dz' \tag{9.35}$$

where z' is a characteristic coordinate and erfc is the complementary Gaussian error function of the error function erf, which is defined as follows and needs to be solved numerically

$$\mathrm{erfc}(\xi) = 1 - \mathrm{erf}(\xi) = 1 - \frac{2}{\sqrt{\pi}} \int_0^{\xi} e^{-\varpi^2} d\varpi = \frac{2}{\sqrt{\pi}} \int_{\xi}^{\infty} e^{-\varpi^2} d\varpi \tag{9.36}$$

where ξ is the integration limit and ϖ the integration variable.

9.6.5 Infinite moving line source model

Groundwater flow can involve significant heat convection, which plays a noteworthy role for the thermohydraulic behaviour of geothermal heat exchangers (Pavlov and Olesen, 2012). A conservative design of an application involving heat extraction only may assume no benefit from groundwater flow (Kavanaugh and Rafferty, 1997), although the resulting solution may not eventually be cost effective. An estimate of the influence of groundwater flow on heat transfer may be desirable, especially for situations in which heat injection in the ground is foreseen because thermal dispersion induced by groundwater flow may occur (Erol et al., 2015; Molina-Giraldo et al., 2011a; Bear, 2013).

In general, groundwater flow can be vertical, horizontal or both, and is complex to be modelled. Currently available analytical models assume a homogeneous groundwater flow parallel to the surface (Li and Lai, 2015). Most analytical models address the coupled convection heat and mass transfer problem via the moving heat source method. This method was first proposed by Ingersoll et al. (1954) and was further explored or extended by Diao et al. (2004), Sutton et al. (2002), Molina-Giraldo et al. (2011a,b), Chiasson and O'Connell (2011) and Tye-Gingras and Gosselin (2014). The rationale of the moving heat source method lies in the formal mathematical equivalence through which heat and mass transfers can be modelled. According to the arguments of Li et al. (2016) and Carslaw and Jaeger (1959), moving heat source problems can be analysed either as problems in which heat sources move through a fixed medium or as problems in which a uniformly moving medium flows through fixed heat sources. As a consequence of this approach, the energy conservation equation accounting for conduction and convection but neglecting any heat source can be effectively solved through a change of variables.

The model presented by Diao et al. (2004) is based on the previous considerations and is associated with a G-function that reads

$$G_f'(t, R) = \frac{1}{4\pi\lambda_{soil}} \exp\left(\frac{U_r x}{2\alpha_{d,soil}}\right) \int_0^{R^2/4\alpha_{d,soil}t} \frac{1}{\eta_*} \exp\left(-\frac{1}{\eta_*} - \frac{U_r^2 R^2 \eta_*}{16\alpha_{d,soil}^2}\right) d\eta_* \tag{9.37}$$

where $U_r = v_x \rho_w c_{p,w} / \rho_{soil} c_{p,soil}$ is the normalised velocity of the moving medium parallel to the horizontal axis x (with v_x the horizontal velocity, $\rho_w c_{p,w}$ the volumetric heat

capacity of the water flowing in the ground, and $\rho_{soil}c_{p,soil}$ the volumetric heat capacity of the ground) and $\eta_* = 4\alpha_{d,soil}(t - t')/R^2$ is an integration variable.

When limited magnitudes of groundwater flow would occur in a given deposit, purely conductive analytical solutions may approximately be employed to address time-dependent heat transfer instead of the previous solutions. In this context, a higher value of effective thermal conductivity of the ground may be employed to include the effect of groundwater flow on the enhanced heat transfer (Lazzari et al., 2010; Piller and Scorpo, 2013). According to Bourne-Webb et al. (2016), however, this approach can represent a significant oversimplification because the reference timescales for conduction and convection heat transfer are markedly different.

9.6.6 Other analytical models

In addition to the previous models, other analytical solutions do exist for addressing a variety of problems involving long, slender, circular geothermal heat exchangers. Those include, but are not limited to, the following:

- The operation of vertical geothermal heat exchangers characterised by peculiar pipe configurations: in this context, Man et al. (2010) developed the infinite solid cylindrical surface source model for energy piles embedded in a homogeneous medium to simplify a spiral pipe configuration as a cylindrical surface. An extension of this model to a finite cylinder embedded in a homogeneous medium was also presented by Man et al. (2010), while the presence of a nonhomogeneous medium was addressed by Li and Lai (2012a). Cui et al. (2011) and Zhang et al. (2012) developed the ring-coil heat source model for energy piles equipped with spiral coils. All of the aforementioned 'solid' models represent an evolution of the classical line and cylinder models because they account for the heat capacity effect given by the geothermal heat exchanger and may also be applied for addressing time-dependent heat transfer at short-to-medium timescales. However, they all assume homogeneous properties for a unique material characterising the ground and the geothermal heat exchanger and neglect the actual number and position of the pipes. Therefore these models do not allow for an accurate description of the thermal field evolution as the quoted timescales and they do not explicitly relate the heat delivered/removed by the generation surface/lines to the temperature of the heat carrier fluid. Li and Lai (2012b) proposed the continuous line source in composite media solution that can account for the actual pipes number, configuration and position, as well as for different ground thermophysical properties, being particularly suitable to address heat transfer at short-to-medium timescales. Based on this solution, Li et al. (2014) developed timescale models that can be employed to calculate the so-called multistage model for a full-scale temperature response function, that is a G-function that is valid from short-to-medium timescales up to long

timescales. Zhang et al. (2016) further extended the work of Li et al. (2014). Hu et al. (2014) proposed a simplified cylindrical model for energy piles equipped with multi-U pipes.

- The modelling of other long, circular heat exchangers such as energy tunnels: in this context, Zhang et al. (2013) proposed an analytical solution for the analysis of heat transfer around an energy tunnel lining.
- The analysis of special conditions involving a phase change of the materials involved due to ground freezing: in this context, when dealing with conventional geothermal heat exchanger applications involving water-to-air configurations, it may be suggested to use so-called extended-range heat pumps ASHRAE (2011), that is machines specifically designed to operate when the heat carrier fluid entering the pump has a temperature of −4°C in the heating mode and 38°C in the cooling mode (Li and Lai, 2015). Temperatures lower than 0°C may induce ground freezing as soon as the capacity effect of geothermal heat exchangers would involve the achievement of the considered temperatures in the ground. According to Ingersoll et al. (1954), ground freezing involves less relevant effects compared to those induced by moisture transfer from an energy perspective and for this reason may be foreseen or allowed in conventional geothermal heat exchanger applications. The model proposed by Ingersoll et al. (1954) may be employed to capture the considered heat transfer problem. When dealing with energy geostructure applications, ground freezing involves detrimental effects from a geotechnical perspective and for this reason should be avoided. To this aim, the temperature of the heat carrier fluid circulating in the pipes should not be less than 0°C (SIA-D0190, 2005; VDI 4640, 2009) or 2°C (Phillips et al., 2010).

9.6.7 Other analysis approaches

A number of additional approaches are available to model the time-dependent heat transfer associated with geothermal heat exchangers. These approaches have originally been formulated for borehole heat exchangers but may be applied with some approximations to the analysis of energy piles. Among the available approaches, Bourne-Webb et al. (2016) report the ASHRAE handbook method, which is based on the work of Kavanaugh and Rafferty (1997), the superposition borehole model (Eskilson, 1987) and the duct ground heat storage model (Hellström, 1989).

The ASHRAE Handbook method employs a set of equations derived from the cylindrical surface source model for calculating the size of the geothermal application. This method is found to perform less satisfactorily than other methods (Fossa and Rolando, 2015; Bourne-Webb et al., 2016).

The superposition borehole model is based on the finite line source model and employs nondimensional thermal response solutions to a unit-step load (i.e. the classical nondimensional G-functions, which are determined in this context in a numerically exact way) for the analysis and design borehole heat exchangers. It usually represents the most common approach for the sizing and understanding of geothermal applications involving boreholes (Bourne-Webb et al., 2016), although it may be applied for time greater than 200 hours (Yavuzturk, 1999).

The duct ground heat storage model is an analysis approach for regular configurations of vertical borehole heat exchanger that allows even markedly large problems to be considered effectively. The model is usually employed through numerical codes, such as TRNSYS (Klein et al., 2011) and PILESIM2 (Pahud, 2007).

9.7 Heat transfer around energy walls and other plane heat exchangers

9.7.1 General

To characterise the heat transfer of plane heat exchangers such as energy walls and slabs, Eqs (9.21) and (9.22) are usually expressed as a function of the thermal power per square metre of the thermally active portion of the element $\dot{q}_i$ as

$$\dot{q}_i = \frac{\overline{T}_f(t) - T_0}{R''_T(t)} = \frac{\Delta T}{R''_T(t)} \tag{9.38}$$

and

$$\Delta T = \dot{q}_i \left[R''_{ghe} + G''_f(x_i, t) \right] = \dot{q}_i R''_T(t) \tag{9.39}$$

where $R''_T(t)$ is the total thermal resistance of the plane heat exchanger while R''_{ghe} and $G''_f(x_i, t)$ are the time-independent and time-dependent portions of the thermal resistance, respectively.

In the following some analytical models allowing to define G-functions are presented to address the time-dependent heat transfer around bodies. The geometry that is employed in these models to investigate the thermal response of long, plane heat exchangers is the semiinfinite medium. This assumption, that is a medium extending to infinity in all but one direction and thus characterised by a unique identifiable surface, is often associated to a sudden change of conditions at its surface. This sudden change of conditions can be due to the application of a constant heat flux at the surface, a constant temperature or a convection boundary condition, but also because of a periodic temperature or heat flux boundary condition applied over time. For small values of the Fourier number [i.e. $Fo = \alpha_d t / L^2 \leq 0.2$ (Bergman et al., 2011)], the

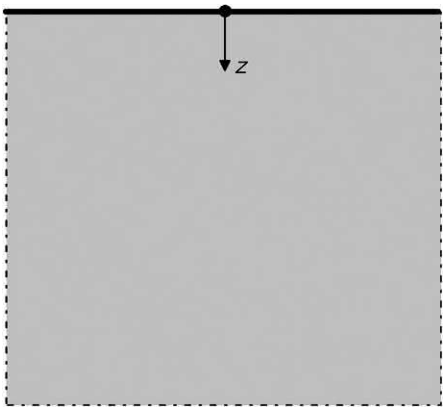

Figure 9.11 Schematic of the semiinfinite medium source model.

time-dependent heat transfer in geometries including thick slabs characterised by a finite dimension or the ground surface, for example, can be modelled effectively.

9.7.2 Semiinfinite medium source model

The semiinfinite medium source model represents a classical heat transfer problem (cf. Fig. 9.11) (Ozisik, 1993; Carslaw and Jaeger, 1959). The considered problem can be solved for a number of boundary conditions at the surface, which include the sudden application of a constant heat flux at the surface $\dot{q}_z = \dot{q}_s$, a constant temperature $T = T_s$, or a convection condition $-\lambda_{soil}\left(\partial T/\partial z\right)|_{z=0} = h_c[T_\infty - T(0,t)]$. The solutions to these problems are given mathematically as follows.

For the constant heat flux condition, the temperature evolution in the semiinfinite medium reads

$$T(t,z) = T_0 + \dot{q}_s\left[\frac{2}{\lambda_{soil}}\sqrt{\frac{\alpha_{d,soil}t}{\pi}}\exp\left(-\frac{z^2}{4\alpha_{d,soil}t}\right) - \frac{z}{\lambda_{soil}}\operatorname{erfc}\left(\frac{z}{2\sqrt{\alpha_{d,soil}t}}\right)\right] \tag{9.40}$$

from which the following G-function can be obtained

$$G_f(x_i,t) = \left[\frac{2}{\lambda_{soil}}\sqrt{\frac{\alpha_{d,soil}t}{\pi}}\exp\left(-\frac{z^2}{4\alpha_{d,soil}t}\right) - \frac{z}{\lambda_{soil}}\operatorname{erfc}\left(\frac{z}{2\sqrt{\alpha_{d,soil}t}}\right)\right] \tag{9.41}$$

For the constant temperature condition, the temperature evolution in the semiinfinite medium reads

$$T(t,z) = T_0 + (T_s - T_0)\operatorname{erfc}\left(\frac{z}{2\sqrt{\alpha_{d,soil}t}}\right) \tag{9.42}$$

with

$$\dot{q}_s(t) = \frac{\lambda_{soil}(T_s - T_0)}{\sqrt{\pi \alpha_{d,soil} t}} \tag{9.43}$$

For the convection condition, the temperature evolution in the semiinfinite medium reads

$$\begin{aligned} T(t,z) = T_0 + (T_s - T_0)\mathrm{erfc}\left(\frac{z}{2\sqrt{\alpha_{d,soil}t}}\right) \\ - \left[\exp\left(\frac{h_c z}{\lambda_{soil}} + \frac{h_c^2 \alpha_{d,soil} t}{\lambda_{soil}^2}\right)\right]\left[\mathrm{erfc}\left(\frac{z}{2\sqrt{\alpha_{d,soil}t}} + \frac{h_c\sqrt{\alpha_{d,soil}t}}{\lambda_{soil}}\right)\right] \end{aligned} \tag{9.44}$$

When dealing with the time-dependent modelling of heat transfer in a semiinfinite medium, interest may lie in understanding the zone within the medium that is significantly influenced by a temperature change over time. This analysis is usually performed with reference to the *thermal penetration depth*, which can be defined through Eq. (9.42) and with reference to a depth z at which $(T_0 - T_s) = 0.90$ as $\delta_p = 2.3\sqrt{\alpha_{d,soil}t}$ (Bergman et al., 2011). Based on the definition of thermal penetration depth, considerations about the validity of the semiinfinite medium assumption for describing actual problems of finite dimensions can be done. For example according to Bergman et al. (2011), to apply the semiinfinite approximation to a plane wall of thickness t_w it must be verified that $\delta_p < t_w/2$. Substituting $\delta_p = t_w/2$ in the expression of the thermal penetration depth suggests that the semiinfinite approximation is valid for $Fo \leq 0.2$.

9.7.3 Periodic source model for a semiinfinite medium

In addition to the previous solutions including constant boundary conditions for the time-dependent heat transfer in the semiinfinite medium, additional solutions addressing more complex conditions at the surface do exist. These solutions typically refer to a periodic temperature or heat flux condition at the surface (cf. Fig. 9.12). In the context of the analysis of geothermal heat exchangers such as energy geostructures, they may be useful to address problems including, for example temperature variations caused by fluctuations in the environmental conditions at the ground surface as well as at the surface of an energy wall or an energy tunnel in an underground built environment. Both daily and seasonal temperature changes occur in practice in those situations and after a sufficient time can be associated with a quasi-steady-state in which the ground surface exchanges heat with the air that is characterised by a temperature fluctuating about a periodically time-invariant mean value (cf. Fig. 9.13). According to Bergman et al. (2011), in the semiinfinite medium the temperature fluctuations have a time lag relative to the surface temperature and their amplitude decays exponentially from the surface because of the thermal inertia of the semiinfinite medium.

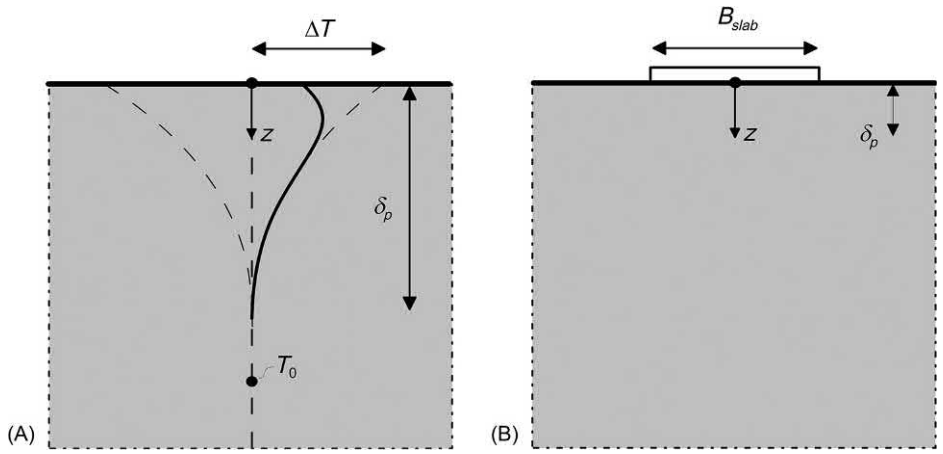

Figure 9.12 Schematic of the semiinfinite medium source model including periodic conditions at the surface for (A) the temperature and (B) the heat flux.

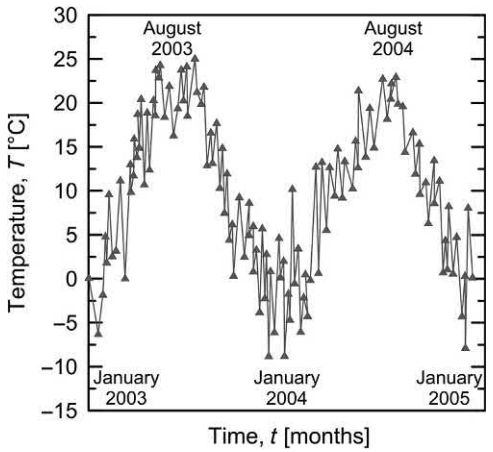

Figure 9.13 Example of outside air temperature in Vienna. *Redrawn after Brandl, H., 2006. Energy foundations and other thermo-active ground structures. Geotechnique 56 (2), 81–122.*

The periodic fluctuation of the surface temperature may be modelled through the function

$$T(0,t) = T_0 + \Delta T \sin \omega t \tag{9.45}$$

where ΔT is the temperature amplitude of the considered function over the average (initial) temperature T_0 and ω is the angular frequency. A solution of the Fourier heat conduction equation for expression (9.45) can be found through the approach of reduction by similarity. Assuming a quasi-steady-state to occur, this formulation reads (Bergman et al., 2011)

$$T(t,z) = T_0 + \Delta T \exp\left(-z\sqrt{\frac{\omega}{2\alpha_{d,soil}}}\right)\sin\left[\omega t - z\sqrt{\frac{\omega}{2\alpha_{d,soil}}}\right] \tag{9.46}$$

where z is the depth of the semiinfinite medium and $\sqrt{\omega/2\alpha_{d,soil}} = \sqrt{\pi/(\alpha_{d,soil}\overline{T}_P)}$ is the damping depth (with $\overline{T}_P$ the period duration of the temperature oscillation). Associated with this temperature distribution is a thermal penetration depth of $\delta_p = 4\sqrt{\alpha_{d,soil}/\omega}$ (Bergman et al., 2011). The heat flux associated with the considered temperature distribution can be calculated according to Fourier's law as

$$\dot{q}_s(t) = \lambda_{soil}\Delta T\sqrt{\frac{\omega}{\alpha_{d,soil}}}\sin\left(\omega t + \frac{\pi}{4}\right) \tag{9.47}$$

Based on Eq. (9.47), it can be noted that the heat flux is also a periodic function, which is characterised by an average value over time equal to zero.

The periodic fluctuation of surface temperature may also be modelled through the function

$$T(0,t) = T_0 + \Delta T\overline{\eta}_B\cos[\omega(t-\overline{\epsilon})] \tag{9.48}$$

where

$$\overline{\eta}_B = \frac{1}{\sqrt{1+2k_B+2k_B^2}} \tag{9.49}$$

$$\overline{\epsilon} = \arctan\frac{k_B}{1+k_B} \tag{9.50}$$

$$k_B = \frac{\lambda_{soil}}{h_c}\sqrt{\frac{\pi}{\alpha_{d,soil}\overline{T}_P}} \tag{9.51}$$

A solution of the Fourier heat conduction equation for expression (9.48) can be found through the approach of reduction by similarity. Assuming a quasi-steady-state to occur, this formulation reads (Brandl, 2006)

$$T(t,z) = T_0 + \Delta T\overline{\eta}_B\exp\left(-z\sqrt{\frac{\omega}{2\alpha_{d,soil}}}\right)\cos\left[\omega(t-\overline{\epsilon}) - z\sqrt{\frac{\omega}{2\alpha_{d,soil}}}\right] \tag{9.52}$$

As highlighted by Brandl (2006), the amplitude of the surface temperature decreases by a factor $\eta_B < 1$ in relation to the air temperature and undergoes a time lag of $\overline{\epsilon}$. Comparing the response of the semiinfinite medium to yearly and daily periods yields the following ratio

$$\frac{\overline{P}_{yearly}}{\overline{P}_{daily}} = \sqrt{365} = 19.1 \tag{9.53}$$

which reveals that a yearly temperature wave penetrates approximately 19 times deeper in the semiinfinite medium (e.g. the ground) than the daily wave.

In addition to the previous solutions, a periodic heat flux applied at the surface may also be considered. One possible function for this heat flux, applied below a strip placed upon the semiinfinite medium, reads

$$\dot{q}_s(0,t) = \Delta\dot{q}_s + \Delta\dot{q}_s \sin\omega t \tag{9.54}$$

The relationship between the amplitude of the applied sinusoidal temperature change and the amplitude of the temperature response can be approximated as (Cahill, 1990)

$$\Delta T \approx \frac{\Delta\dot{q}_s}{L_{slab}\pi\lambda_{soil}}\left[-\frac{1}{2}\ln\left(\frac{\omega}{2}\right) - \ln\left(\frac{B_{slab}}{4\alpha_{d,soil}}\right) + C_1\right] = \frac{\Delta\dot{q}_s}{L_{slab}\pi\lambda_{soil}}\left[-\frac{1}{2}\ln\left(\frac{\omega}{2}\right) + C_2\right] \tag{9.55}$$

where L_{slab} and B_{slab} are the width and breadth of the strip present at the surface, respectively, (with $L_{slab} \gg B_{slab}$) and C_1 and C_2 are two integration constants. Associated with this temperature distribution is a thermal penetration depth of $\delta_p = \sqrt{\alpha_{d,soil}/\omega}$ (Bergman et al., 2011).

9.8 Heat transfer at short-to-medium timescales

As previously highlighted, in most cases Eq. (9.20) is employed to address the time-dependent analysis of geothermal heat exchangers for $t > t^*$ by considering that $t^* \propto t_{ghe}$. This approach allows simplifying the heat transfer phenomenon in a time-independent portion, occurring within the geothermal heat exchanger and addressed through the time-independent thermal resistance, and a time-dependent portion, occurring around the geothermal heat exchanger and addressed through the G-function.

Based on the previous considerations, no matter which formulations for time-independent portion of thermal resistance R_{ghe} and for the G-function are used, the approach of employing the total thermal resistance to express an associated temperature change as in Eq. (9.22) is unsuitable when a rapidly varying heat flux is to be addressed. The reason for this is that, under the considered short-to-medium timescales, steady conditions do not characterise the heat transfer within the geothermal heat exchanger and the heat capacity of the grouting materials of the considered bodies plays a crucial role in conjunction with the pipe layout.

The more common analytical approach to tackle the modelling of heat transfer at short-to-medium timescales is to consider an equivalent diameter for the pipes located in the heat exchanger that simplifies the actual geometry involved as an equivalent

hollow cylinder (Lamarche and Beauchamp, 2007b; Young, 2004). Details of this approach are summarised by Li and Lai (2015), among others.

To overcome the limitation that the actual response of heat exchangers characterised by more complex pipe layouts than a U-shaped type cannot be captured through the previous approach, Li and Lai (2012b) proposed the continuous line source in composite media solution that is capable of addressing the considered challenge. The continuous line source in composite media solution consists of an infinite line heat source placed in a two-dimensional infinite plane domain made of two purely-conductive materials: the first one extends from $r = 0$ to $r = R$ and the second one extends from $r = R$ to infinite. A heat source is located at $r = r'$ and $\phi = \phi'$. The mathematical formulation of the problem reads

$$\begin{cases} r < R & \dfrac{\partial T_{ghe}}{\partial t} - \alpha_{d,ghe}\nabla^2 T_{ghe} = 0 \\ r \geq R & \dfrac{\partial T_{soil}}{\partial t} - \alpha_{d,soil}\nabla^2 T_{soil} = 0 \\ \begin{cases} T_{soil} = T_{ghe} \\ -\lambda_{soil}\nabla T_{soil} = -\lambda_{ghe}\nabla T_{ghe} \end{cases} & r = R \\ t = 0 & T = T_0 \\ r \to \infty & T_{soil} = T_0 \\ -\lambda_{ghe}(2\pi r)\frac{\partial T}{\partial r}\Big|_{r\to r'} = \dot{q}_l \end{cases} \tag{9.56}$$

where T_{soil} and T_{ghe} are the temperature of the ground and geothermal heat exchanger, respectively, and λ_{ghe} is the thermal conductivity of the geothermal heat exchanger. According to Li and Lai (2012b), the solution of the previous problem (expressed in terms of dimensionless temperatures $\Theta = (T - T_0)\lambda_{ghe}/\dot{q}_l$) reads

$$\Theta_{ghe}\left(Fo, \tilde{R}^*, \phi\right) = \frac{1}{2\pi}\sum_{n=-\infty}^{+\infty} \cos n(\phi - \phi') \int_0^{+\infty} \left[1 + -\exp\left(-\nu^2 Fo\right)\right] \frac{J_{B,n}\left(\nu\tilde{R}^*\right) J_{B,n}\left(\nu\tilde{\tilde{R}}^*\right)\left(\varphi_n g_n - \psi_n f_n\right)}{\nu\left(\varphi_n^2 + \psi_n^2\right)} d\nu \tag{9.57}$$

$$\Theta_{soil}\left(Fo, \tilde{R}^*, \phi\right) = -\frac{1}{\pi^2}\sum_{n=-\infty}^{+\infty} \cos n\left(\phi - \phi'\right) \int_0^{+\infty} \left[1 + -\exp\left(-\nu^2 Fo\right)\right] \frac{J_{B,n}\left(\nu\tilde{\tilde{R}}^*\right)\left[\psi_n J_{B,n}\left(A_d\nu\tilde{R}^*\right) - \varphi_n Y_{B,n}\left(A_d\nu\tilde{R}^*\right)\right]}{\nu^2\left(\varphi_n^2 + \psi_n^2\right)} d\nu \tag{9.58}$$

with

$$Fo = \frac{\alpha_{d,ghe} t}{R^2} \tag{9.59}$$

$$\tilde{R}^* = \frac{r}{R} \tag{9.60}$$

$$\tilde{\tilde{R}}^* = \frac{r'}{R} \tag{9.61}$$

$$\mathrm{A}_d = \sqrt{\frac{\alpha_{d,ghe}}{\alpha_{d,soil}}} \tag{9.62}$$

$$\Lambda_l = \frac{\lambda_{soil}}{\lambda_{ghe}} \tag{9.63}$$

$$\begin{aligned}
\varphi_n(\nu) &= A_d \Lambda_l J_n(\nu) \frac{dJ_{B,n}}{d\beta^*}(A_d\nu) - \frac{dJ_{B,n}}{d\beta^*}(\nu) J_{B,n}(A_d\nu) \\
\psi_n(\nu) &= A_d \Lambda_l J_{B,n}(\nu) \frac{dY_{B,n}}{d\beta^*}(A_d\nu) - \frac{dJ_{B,n}}{d\beta^*}(\nu) Y_{B,n}(A_d\nu) \\
f_n(\nu) &= A_d \Lambda_l Y_{B,n}(\nu) \frac{dJ_{B,n}}{d\beta^*}(A_d\nu) - \frac{dY_{B,n}}{d\beta^*}(\nu) J_{B,n}(A_d\nu) \\
g_n(\nu) &= A_d \Lambda_l Y_{B,n}(\nu) \frac{dY_{B,n}}{d\beta^*}(A_d\nu) - \frac{dY_{B,n}}{d\beta^*}(\nu) Y_{B,n}(A_d\nu)
\end{aligned} \tag{9.64}$$

where $J_{B,n}$ and $Y_{B,n}$ are the Bessel functions of the first and second kind of order n, respectively.

References

ASHRAE, 2011. ASHRAE Handbook: HVAC Applications. ASHRAE, Atlanta.
Bear, J., 2013. Dynamics of Fluids in Porous Media. Courier Corporation, North Chelmsford.
Bergman, T., Incropera, F., Lavine, A., DeWitt, D., 2011. Fundamentals of Heat and Mass Transfer. Wiley, Hoboken, NJ.
Bourne-Webb, P., Burlon, S., Javed, S., Kürten, S., Loveridge, F., 2016. Analysis and design methods for energy geostructures. Renew. Sustain. Energy Rev. 65, 402–419.
Brandl, H., 2006. Energy foundations and other thermo-active ground structures. Geotechnique 56 (2), 81–122.
Cahill, D.G., 1990. Thermal conductivity measurement from 30 to 750 K: the 3ω method. Rev. Sci. Instrum. 61 (2), 802–808.
Carslaw, H., Jaeger, J., 1959. Conduction of Heat in Solids. Oxford University Press, Oxford.

Chiasson, A., O'Connell, A., 2011. New analytical solution for sizing vertical borehole ground heat exchangers in environments with significant groundwater flow: Parameter estimation from thermal response test data. HVAC&R Res. 17 (6), 1000–1011.
Claesson, J., Dunand, A., 1983. Heat Extraction from Ground by Horizontal Pipes—A Mathematical Analysis. Swedish Council for Building Research, Stokholm.
Claesson, J., Eskilson, P., 1988. Conductive heat extraction to a deep borehole: thermal analyses and dimensioning rules. Energy 13 (6), 509–527.
Claesson, J., Javed, S., 2012. A load-aggregation method to calculate extraction temperatures of borehole heat exchangers. ASHRAE Trans. 118 (1), 530–539.
Cui, P., Li, X., Man, Y., Fang, Z., 2011. Heat transfer analysis of pile geothermal heat exchangers with spiral coils. Appl. Energy 88 (11), 4113–4119.
Diao, N., Li, Q., Fang, Z., 2004. Heat transfer in ground heat exchangers with groundwater advection. Int. J. Therm. Sci. 43 (12), 1203–1211.
Eckert, E.R.G., Drake Jr., R.M., 1987. Analysis of Heat and Mass Transfer. McGraw-Hill, New York.
Erol, S., Hashemi, M.A., François, B., 2015. Analytical solution of discontinuous heat extraction for sustainability and recovery aspects of borehole heat exchangers. Int. J. Therm. Sci. 88, 47–58.
Eskilson, P., 1987. Thermal Analysis of Heat Extraction Boreholes (Ph.D. thesis). Lund University, Sweden
Fossa, M., Rolando, D., 2015. Improving the Ashrae method for vertical geothermal borefield design. Energy Build. 93, 315–323.
Hellström, G., 1989. Duct Ground Heat Storage Model, Manual for Computer Code. Department of Mathematical Physics, University of Lund, Sweden.
Hellström, G., 1991. Ground Heat Storage: Thermal Analyses of Duct Storage Systems. Lund University, Lund.
Hu, P., Zha, J., Lei, F., Zhu, N., Wu, T., 2014. A composite cylindrical model and its application in analysis of thermal response and performance for energy pile. Energy Build. 84, 324–332.
Ingersoll, L.R., Zabel, O.J., Ingersoll, A.C., 1954. Heat Conduction with Engineering, Geological, and Other Applications. Mc-Graw Hill, New York.
Kakac, S., Yener, Y., 2008. Heat Conduction. CRC Press.
Kavanaugh, S.P., Rafferty, K., 1997. Ground-Source Heat Pumps: Design of Geothermal Systems for Commercial and Institutional Buildings. American Society of Heating, Refrigerating and Air-Conditioning Engineers.
Kelvin, T.W., 1882. Mathematical and Physical Papers. Cambridge University Press, London.
Klein, A., Beckman, A., Mitchell, W., Duffie, A., Duffie, N., Freeman, T., 2011. TRNSYS 17—A Transient System Simulation Program. Solar Energy Laboratory, University of Wisconsin, Madison.
Lamarche, L., Beauchamp, B., 2007a. A new contribution to the finite line-source model for geothermal boreholes. Energy Build. 39 (2), 188–198.
Lamarche, L., Beauchamp, B., 2007b. New solutions for the short-time analysis of geothermal vertical boreholes. Int. J. Heat Mass Transf. 50 (7), 1408–1419.
Lazzari, S., Priarone, A., Zanchini, E., 2010. Long-term performance of BHE (borehole heat exchanger) fields with negligible groundwater movement. Energy 35 (12), 4966–4974.
Li, M., Lai, A.C., 2012a. Heat-source solutions to heat conduction in anisotropic media with application to pile and borehole ground heat exchangers. Appl. Energy 96, 451–458.
Li, M., Lai, A.C., 2012b. New temperature response functions (G functions) for pile and borehole ground heat exchangers based on composite-medium line-source theory. Energy 38 (1), 255–263.
Li, M., Lai, A.C., 2015. Review of analytical models for heat transfer by vertical ground heat exchangers (GHEs): a perspective of time and space scales. Appl. Energy 151, 178–191.
Li, M., Li, P., Chan, V., Lai, A.C., 2014. Full-scale temperature response function (G-function) for heat transfer by borehole ground heat exchangers (GHEs) from sub-hour to decades. Appl. Energy 136, 197–205.
Li, M., Zhu, K., Fang, Z., 2016. Analytical methods for thermal analysis of vertical ground heat exchangers. Advances in Ground-Source Heat Pump Systems. Elsevier, pp. 157–183.

Luikov, A.V., 1975. Systems of differential equations of heat and mass transfer in capillary-porous bodies (review). Int. J. Heat Mass Transf. 18 (1), 1–14.
Man, Y., Yang, H., Diao, N., Liu, J., Fang, Z., 2010. A new model and analytical solutions for borehole and pile ground heat exchangers. Int. J. Heat Mass Transf. 53 (13), 2593–2601.
Molina-Giraldo, N., Bayer, P., Blum, P., 2011a. Evaluating the influence of thermal dispersion on temperature plumes from geothermal systems using analytical solutions. Int. J. Therm. Sci. 50 (7), 1223–1231.
Molina-Giraldo, N., Blum, P., Zhu, K., Bayer, P., Fang, Z., 2011b. A moving finite line source model to simulate borehole heat exchangers with groundwater advection. Int. J. Therm. Sci. 50 (12), 2506–2513.
Ozisik, M.N., 1993. Heat Conduction. John Wiley & Sons.
Pahud, D., 2007. PILESIM2: Simulation Tool for Heating/Cooling Systems with Energy Piles or Multiple Borehole Heat Exchangers. Project Report.
Pavlov, G.K., Olesen, B.W., 2012. Thermal energy storage—a review of concepts and systems for heating and cooling applications in buildings: Part 1—seasonal storage in the ground. HVAC&R Res. 18 (3), 515–538.
Phillips, A., Raynor, D., Pantelidou, H., Gornali, D., Nicholson, D., 2010. Efficient Design of Piled Foundations for Low-Rise Housing—Design Guide. NHBC Foundation.
Piller, M., Scorpo, A.L., 2013. Numerical investigation of forced convection from vertical boreholes. Geothermics 45, 41–56.
Poulikakos, D., 1994. Conduction Heat Transfer. Prentice Hall.
Schneider, P.J., 1955. Conduction Heat Transfer. Addison-Wesley Pub. Co.
SIA-D0190, 2005. Utilisation de la Chaleur du Sol par des Ouvrages de Fondation et de Soutènement en Béton. Guide pour la Conception, la Realisation et la Maintenance. The Swiss Society of Engineers and Architects, Zurich.
Spitler, J., Bernier, M., 2016. Vertical borehole ground heat exchanger design methods. Advances in Ground-Source Heat Pump Systems. Elsevier, pp. 29–61.
Sutton, M.G., Couvillion, R.J., Nutter, D.W., Davis, R.K., 2002. An algorithm for approximating the performance of vertical bore heat exchangers installed in a stratified geological regime. ASHRAE Trans. 108 (2), 177–184.
Tye-Gingras, M., Gosselin, L., 2014. Generic ground response functions for ground exchangers in the presence of groundwater flow. Renew. Energy 72, 354–366.
VDI 4640, 2009. Thermal use of the underground. Ground Source Heat Pump Systems. Association of German Engineers, Dusseldorf.
Whitehead, S., 1927. Determining temperature distribution: a contribution to the evaluation of the flow of heat in isotropic media. Electrician 19 (August), 225–226.
Yavuzturk, C., 1999. Modeling of Vertical Ground Loop Heat Exchangers for Ground Source Heat Pump Systems. Oklahoma State University, USA.
Young, T.R., 2004. Development, Verification, and Design Analysis of the Borehole Fluid Thermal Mass Model for Approximating Short Term Borehole Thermal. Oklahoma State University.
Zeng, H., Diao, N., Fang, Z., 2002. A finite line-source model for boreholes in geothermal heat exchangers. Heat Transf. Asian Res. 31 (7), 558–567.
Zhang, W., Yang, H., Lu, L., Fang, Z., 2012. Investigation on heat transfer around buried coils of pile foundation heat exchangers for ground-coupled heat pump applications. Int. J. Heat Mass Transf. 55 (21–22), 6023–6031.
Zhang, G., Xia, C., Sun, M., Zou, Y., Xiao, S., 2013. A new model and analytical solution for the heat conduction of tunnel lining ground heat exchangers. Cold Reg. Sci. Technol. 88, 59–66.
Zhang, L., Zhang, Q., Huang, G., 2016. A transient quasi-3D entire time scale line source model for the fluid and ground temperature prediction of vertical ground heat exchangers (GHEs). Appl. Energy 170, 65–75.

Questions and problems

Statements

a. How does transient heat transfer differ from steady-state heat transfer?

b. Which are the main analytical approaches typically used in the time-dependent modelling of heat transfer problems?

c. Under what conditions may the lumped capacitance method be used to predict the transient response of a solid to a change in its thermal environment?

d. The lumped capacitance method implies the presence of

1. Infinite heat transfer coefficient between solid and fluid

2. Infinite thermal conductivity of the solid

3. Infinite conductive thermal resistance of the solid

4. Infinite convective thermal resistance of the solid

e. Write and discuss the energy balance deriving from the lumped capacitance method assumptions.

f. How is the thermal time constant defined? How it can be used?

g. Sketch the influence of the thermal time constant on the normalised temperature change of the body.

h. What is the physical interpretation of the Biot number?

i. Sketch the temperature distribution within the plane wall shown in the following figure, which is initially at a uniform temperature T_0 and subsequently experiences convection cooling when it is immersed in a fluid of temperature $T_\infty < T_0$ at different temperature, for the following Biot numbers:

1. $Bi \ll 1$

2. $Bi = 1$

3. $Bi \gg 1$

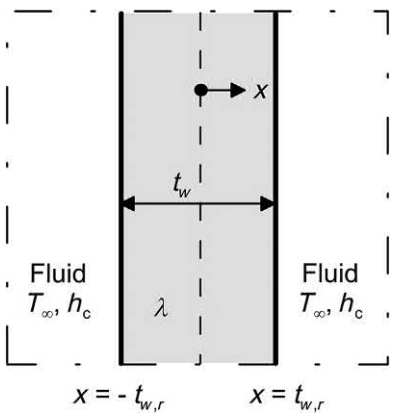

j. The thermal diffusivity α_d [m^2/s] is the controlling transport property for transient

conduction. Using the following values of thermal conductivity λ [W/(m °C)], density ρ [kg/m^3] and specific heat c_p [J/(kg °C)] at ambient temperature, calculate α_d for the following materials. Is concrete material A or material B?

1. Material A: $\lambda_A = 240$ W/(m °C), $\rho_A = 2700$ kg/m^3, $c_{p_A} = 900$ J/(kg °C);
2. Material B: $\lambda_B = 1.6$ W/(m °C), $\rho_B = 1800$ kg/m^3, $c_{p_B} = 750$ J/(kg °C).

k. What is the physical interpretation of the Fourier number?

l. Write the Fourier heat conduction equation for a one-dimensional heat transfer problem assuming no internal energy generation and constant material properties.

m. Explain the concept of thermal resistance in the treatment of the time-dependent modelling of heat transfer.

n. Which are the two aspects that typically need to be addressed when dealing with the time-dependent modelling of heat transfer in the context of the analysis and design of geothermal heat exchangers such as energy geostructures?

1. The heat transfer rate of the geothermal heat exchanger as a function of time and the temperature difference at the steady-state.
2. The heat transfer rate of the geothermal heat exchanger as a function of time and the temperature difference as a function of time.
3. The heat transfer rate of the geothermal heat exchanger at the steady-state and the temperature difference as a function of time.
4. The heat transfer rate of the geothermal heat exchanger at the steady-state and the temperature difference at the steady-state.

o. How can the heat transfer rate of a geothermal heat exchanger as a function of time and the temperature difference as a function of time be mathematically related?

p. How can energy systems with significantly time-changing applied thermal loads be analytically studied?

q. According to Duhamel's theorem, how can problems of time-dependent loads be treated?

r. Sketch an example of total thermal response of two borehole heat exchangers located at a centre-to-centre spacing of $s = 5$ m given by the spatial superposition of the single isolated responses.

s. The infinite cylindrical surface source model provides a solution for:

1. The axial heat transfer from a solid cylinder surrounded by an infinite medium in which heat transfer occurs via radiation.
2. The radial heat transfer from a hollow cylinder surrounded by an infinite medium in which heat transfer occurs via radiation and convection.
3. The axial and circumferential heat transfer from a hollow cylinder surrounded by an infinite medium in which heat transfer occurs via conduction.
4. The radial heat transfer from a hollow cylinder surrounded by an infinite medium in which heat transfer occurs via conduction.

t. Provide the mathematical formulation of the infinite cylindrical surface source model of a geothermal heat exchanger with a constant heat flux around its surface at $r = R$ equal to $\dot{q}_l$, initially at a temperature $T = T_0$.

u. The infinite line source model provides a solution for
   1. The radial heat transfer from a line characterised by a constant heat flux towards (or from) an infinite medium in which heat transfer occurs via conduction.
   2. The radial heat transfer from a cylinder characterised by a constant heat flux towards (or from) an infinite medium in which heat transfer occurs via convection and radiation.
   3. The axial and circumferential heat transfer from a line characterised by a constant heat flux towards (or from) an infinite medium in which heat transfer occurs via conduction.
   4. The radial heat transfer from a line characterised by a constant heat flux towards (or from) an infinite medium in which heat transfer occurs via convection and radiation.

v. Provide the mathematical formulation of the infinite line source model of heat transfer from a line characterised by a constant heat flux equal to $\dot{q}$ towards (or from) an infinite medium in which heat transfer occurs via conduction initially at a temperature $T = T_0$.

w. For geothermal heat exchangers such as energy piles, edge effects become relevant approximately after one year of geothermal operation and continue to be important throughout the life of the system. In these problems, the finite line source model can capture the influence of the ground surface:
   1. Considering the ground as a heat source/sink, applying a fixed conductive heat flux on the surface.
   2. Considering the ground as a reflecting plane with a constant temperature (or an adiabatic) boundary condition applied at the ground surface.
   3. Applying a convective heat flux at the ground surface.
   4. Applying a radiative heat flux at the ground surface.

x. A pipe within an energy geostructure has a wall thickness of $t_p = 3$ mm. In order to avoid seasonal temperature changes, it is good practice to insulate the pipe on the outside in the first metres of depth. With the initiation of flow, hot water is pumped through the pipe, creating a convective condition corresponding to $h_c = 500$ W/(m^2 °C) at the inner surface of the pipe. Calculate the Biot and Fourier numbers after 8 minutes from the initiation of flow. The properties of the pipe are: thermal conductivity $\lambda = 0.5$ W/(m °C), density $\rho = 550$ kg/m^3, specific heat $c_p = 2250$ J/(kg °C), thermal diffusivity $\alpha_d = 4 \times 10^{-7}$ m^2/s.

y. A pipe within an energy geostructure has a wall thickness of $t_p = 2$ mm. In order to avoid seasonal temperature changes, it is good practice to insulate the pipe on the outside in the first metres of depth. With the initiation of flow, hot water is pumped through the pipe, creating a convective condition corresponding to $h_c = 250$ W/(m^2 °C) at the inner surface of the pipe and the Biot and Fourier numbers after 1 minute from the initiation of flow are $Bi = 1.25$ and $Fo = 4.5$, respectively. Knowing that the density of the pipe material is $\rho = 600$ kg/m^3, find the specific heat of the pipe material, c_p [J/(kg °C)].

z. What is the main implication in considering the first term approximation of the infinite series solution of transient conduction equation for plane walls?

aa. How can the periodic temperature or heat flux changes occurring in boundary conditions of time-dependent heat transfer problems be taken into account?

bb. A The temperature distribution across a 1 m-thick energy wall at a certain instant of time is:

$$T(x) = a + bx + cx^2$$

where T is in degrees Celsius and x is in metres, while $a = 30$°C, $b = -10$°C/m and $c = -5$°C/m^2. A uniform heat generation of $\dot{q}_v = 30$ W/m^3 is present. The wall of area is of $A = 10$ m^2 and the properties of the wall are as follows: bulk density $\rho = 2400$ kg/m^3, thermal conductivity $\lambda = 2$ W/(m °C) and specific heat $c_p = 880$ J/(kg °C).

1. Determine the rate of heat transfer entering the wall $\dot{Q}_{in}$ ($x = 0$ m) [W] and leaving the wall $\dot{Q}_{out}$ ($x = L = 1$ m) [W].
2. Determine the rate of change of energy storage in the wall $\dot{Q}_{st}$ [W].
3. Determine the rate of temperature change ΔT [°C] at $x = 0$, 0.25 and 0.5 m.

cc. As a first approximation, uniform internal heat generation at $\dot{q}_v = 25$ W/m^3 is occurring in an energy pile characterised by a diameter of $D = 1$ m and a length of $L = 30$ m. Under steady-state conditions, the temperature distribution is of the form:

$$T(r) = a + br^2$$

where T is in degrees Celsius and r is in metres, while $a = 30$°C and $b = -2$°C/m^2. The pile concrete properties are as follows: thermal conductivity $\lambda = 2$ W/(m °C), bulk density $\rho = 2400$ kg/m^3 and specific heat $c_p = 850$ J/(kg °C).

1. What is the rate of heat transfer of the pile at $r = 0$ m (the pile axis) and at $r = 0.5$ m (the pile shaft) per unit length $\dot{q}_l$ [W/m]?
2. Determine the rate of change of energy storage in the pile $\dot{Q}_{st}$ [W].
3. If the power level is suddenly increased to $\dot{q}_v = 50$ W/m^3, what is the initial time rate of temperature change $\partial T/\partial t$ [°C/s] at $r = 0$ m and at $r = 0.5$ m? Consider mono-dimensional heat transfer.

Solutions

a. Transient problems typically arise when the boundary conditions of a system are changed. For example, if the surface temperature of a system is altered, the temperature at each point in the system will also to change. The changes will continue to take place until a steady-state temperature distribution is reached.

b. Two analytical approaches can be typically used to model time-dependent heat transfer phenomena. A first approach, termed the lumped capacitance method, resorts to the solution of an energy balance and allows modelling time-dependent heat transfer problems for bodies characterised by a spatially uniform temperature within them during the transient process (i.e. temperature gradients within the body are negligible). This approach can be used to determine the variation of temperature with time. A second approach resorts to the solution of the Fourier heat conduction equation and allows modelling time-dependent heat transfer problems for bodies in which the temperature is not spatially uniform within them during the transient process (i.e. temperature gradients within the body cannot be neglected) and heat transfer is typically one-dimensional. This approach can be used to determine the variation of temperature with both space and time.

c. In the lumped capacitance method, the assumption is that the temperature of the solid is spatially uniform at any instant during the transient process. This assumption implies that temperature gradients within the solid are negligible.

d. The lumped capacitance method implies the presence of:

1. Infinite heat transfer coefficient between solid and fluid
2. **Infinite thermal conductivity of the solid**
3. Infinite conductive thermal resistance of the solid
4. Infinite convective thermal resistance of the solid

e. The absence of a temperature gradient in the body implies an infinite thermal conductivity of this medium based on Fourier's law and makes Fourier heat conduction equation useless for characterising this time-dependent problem because such an equation governs the distribution of temperature in space. Based on these considerations, the transient temperature response must be tackled through the formulation of an overall energy balance for the entire body, which relates the rate of heat loss (or heat gain) to the rate of change of the internal energy. Mathematically, the energy balance for the considered problem can be expressed as

$$-h_c A_s (T - T_\infty) = \rho V c_p \frac{dT}{dt}$$

where h_c [W/(m^2 °C)] is the convection coefficient, A_s [m^2] is the surface of the body immersed in the fluid at uniform temperature T_∞ [°C], ρ [kg/m^3] and c_p [J/(kg °C)] are the density and the specific heat of the body, respectively, V [m^3] is the volume of the body, T [°C] is the temperature and t [s] is the time.

f. The thermal time constant is defined as

$$\tau_t = \frac{R''_{conv} C_t}{A_s} \text{ [s]}$$

where R''_{conv} [(m^2 °C)/W] and C_t [J/°C] are the resistance to convection heat transfer and the lumped thermal capacitance of the solid, respectively, and A_{si} [m^2] is the surface of the body exchanging the heat. The considered thermal time constant can be useful to analyse the exponential decay of the temperature difference between the body and the fluid to zero as the time approaches infinity.

g. The influence of the thermal time constant on the normalised temperature change of the body can be represented as proposed in the following figure.

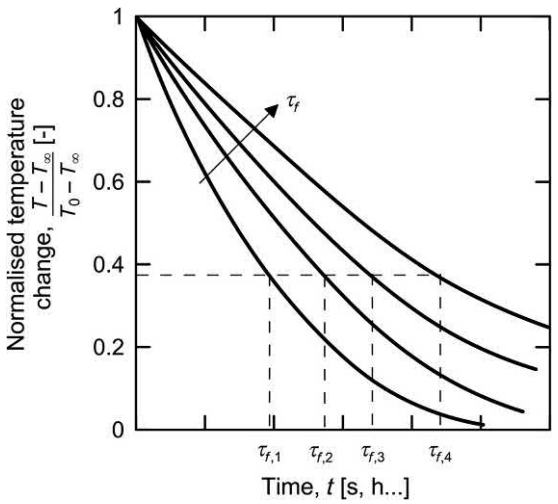

h. The Biot number is a dimensionless parameter that can be determined through an energy balance for all bodies as

$$Bi = \frac{h_c L_c}{\lambda} \text{ [-]}$$

where h_c [W/(m^2 °C)] is the convective heat transfer coefficient between the body and the fluid, L_c [m] is the characteristic length of the considered body and λ [W/(m °C)] is the thermal conductivity of the body. The Biot number provides a measure of the temperature drop in the solid relative to the temperature difference between the solid's surface and the fluid and it is also evident that it may be interpreted as a ratio of thermal resistances. In particular, if $Bi \ll 1$, the resistance to conduction within the solid is much less than the resistance to convection across the fluid boundary layer. Hence, the assumption of a uniform temperature distribution within the solid is reasonable if the Biot number is small, while when $Bi \gg 1$, the temperature difference across the solid is much larger than that between the surface and the fluid.

i. **The temperature distribution within the plane wall for the different cases is shown in the following.**

   1. **For $Bi \ll 1$, the temperature distribution is:**

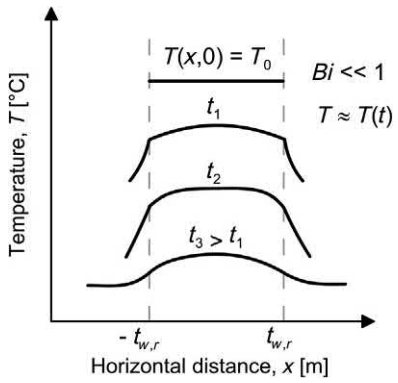

   2. **For $Bi = 1$, the temperature distribution is:**

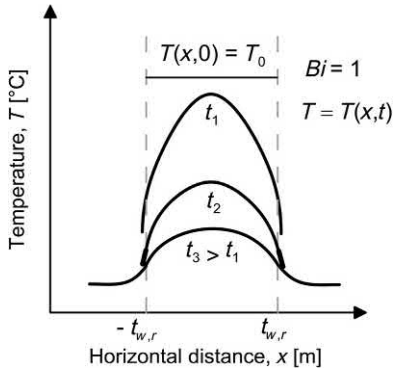

3. **For $Bi \gg 1$, the temperature distribution is**:

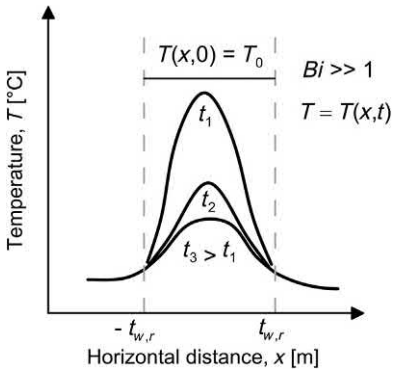

j. **The thermal diffusivity is defined as**

$$\alpha_d = \frac{\lambda}{\rho c_p} \left[\mathrm{m}^2/\mathrm{s}\right]$$

For material A, the thermal diffusivity reads

$$\alpha_{d_A} = \frac{\lambda_A}{\rho_A c_{pA}} = \frac{240}{2700 \cdot 900} = 9.88 \times 10^{-6}\,\mathrm{m}^2/\mathrm{s}$$

For material B, the thermal diffusivity reads

$$\alpha_{d_B} = \frac{\lambda_B}{\rho_B c_{pB}} = \frac{1.6}{1800 \cdot 750} = 1.18 \times 10^{-6}\,\mathrm{m}^2/\mathrm{s}.$$

Material B is likely to be concrete, whereas material A is likely to be aluminium.

k. **The Fourier number is a dimensionless time providing key information together with the Biot number in characterising transient conduction problems (e.g. the validity of analytical solutions) defined as**

$$Fo \equiv \frac{\alpha_d t}{L_c^2} \left[-\right]$$

where α_d [m^2/s] is the thermal diffusivity of the body, t [s] is time and L_c [m] is the characteristic length of the considered body.

l. **By assuming no internal energy generation and a constant thermal conductivity, Fourier heat conduction equation reads in this case**

$$\frac{\partial^2 T}{\partial x^2} = \frac{1}{\alpha_d}\frac{\partial T}{\partial t}$$

where T [°C] is the temperature of the body, x [m] is the coordinate of the direction along which the heat transfer occurs, α_d [m^2/s] is the thermal diffusivity of the body and t [s] is the time.

m. The thermal resistance in the treatment of the time-dependent modelling of heat transfer takes into account the transient phenomena occurring in a larger domain surrounding a single body or multiple bodies for $t > t^*$ (typically, the ground surrounding the geothermal heat exchanger (s)). The considered thermal resistance is often referred to as the total thermal resistance, $R_T(t)$, and is decomposed into a time-independent part and a time-dependent part as

$$R_T(t) = R_{ghe} + G_f(x_i, t)\ [^\circ\mathrm{C/W}]$$

where R_{ghe} [°C/W] is the time-independent part of the total thermal resistance, typically coinciding with the thermal resistance of the geothermal heat exchanger, and $G_f(x_i,t)$ [°C/W] is the time-dependent part of the total thermal resistance, often called G-function (with x_i [m] the coordinates of a considered point and t [s] the time).

n. Which are the two aspects that typically need to be addressed when dealing with the time-dependent modelling of heat transfer in the context of the analysis and design of geothermal heat exchangers such as energy geostructures?

1. The heat transfer rate of the geothermal heat exchanger as a function of time and the temperature difference at the steady-state.
2. **The heat transfer rate of the geothermal heat exchanger as a function of time and the temperature difference as a function of time**.
3. The heat transfer rate of the geothermal heat exchanger at the steady-state and the temperature difference as a function of time.
4. The heat transfer rate of the geothermal heat exchanger at the steady-state and the temperature difference at the steady-state.

o. The heat transfer rate of the geothermal heat exchanger as a function of time and the temperature difference as a function of time can be mathematically related as

$$\dot{Q} = \dot{q}_i A = \frac{\overline{T}_f(t) - T_0}{R_T(t)} = \frac{\Delta T}{R_T(t)}\ [\mathrm{W}]$$

where $\dot{q}_i$ [W/m^2] is the heat flux density, A [m^2] is the area normal to the direction of heat transfer, $\overline{T}_f(t)$ [°C] is the average temperature of

the heat carrier fluid circulating in the pipes of the geothermal heat exchanger, T_0 [°C] is the initial ground temperature and $R_T(t)$ [°C/W] is the total thermal resistance.

p. Analyses of the response of any system subjected to a complex total load profile evolving with time can be tackled by considering the superposition of the responses of the same system to an appropriate number of constant unit-step loads that decompose the total load profile over time. Similarly, analyses of the response of a system composed of different representative and distinct sources interacting in space can be tackled by considering the superposition of the responses of the individual sources under a given representative load. In other words, the superposition principle can be applied both temporally and spatially.

q. According to Duhamel's theorem, problems of time-dependent loads can easily be tackled by using the problem solution for a unit-step load

$$T_1(x_i, t) = T_0 + \int_0^t \dot{Q} \frac{\partial G_f(x_i, t - x_t)}{\partial t} dx_t \text{ [°C]}$$

where T_1 [°C] is the temperature function, x_i [m] is the spatial coordinate, t [s] is time, T_0 [°C] is the initial temperature, $\dot{Q}$ [W] is the thermal load, the function G_f is the response function for unit-step change in the thermal load of the geothermal heat exchanger and x_t is an integral variable with the dimension of a time. Because the heating and cooling loads applied to geothermal heat exchangers are commonly available as stepwise constant values (on an hourly, daily, weekly or monthly base), the previous equation is often expressed as

$$T_1(x_i, t) = T_0 + \sum_{j=0}^{N-1} \Delta \dot{Q}_j G_f(x_i, t - j\Delta T) \text{ [°C]}$$

where N [−] is the number of intervals and $\Delta \dot{Q}_j$ [W] is a stepwise change in $\dot{Q}$ at the beginning of the jth time interval.

r. An example of total thermal response of two borehole heat exchangers located at a centre-to-centre spacing of $s = 5$ m given by the spatial superposition of the single isolated responses is proposed in the following figure.

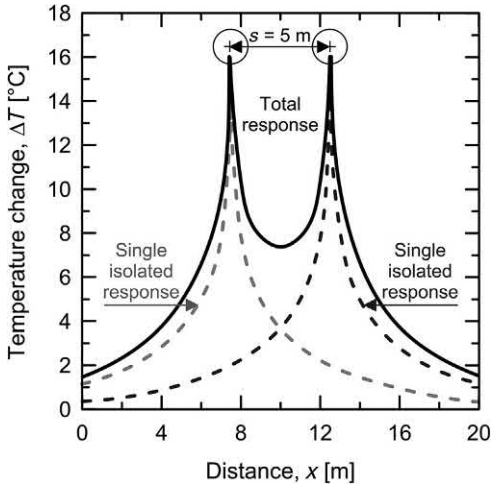

s. The infinite cylindrical surface source model provides a solution for:

1. The axial heat transfer from a solid cylinder surrounded by an infinite medium in which heat transfer occurs via radiation.
2. The radial heat transfer from a hollow cylinder surrounded by an infinite medium in which heat transfer occurs via radiation and convection.
3. The axial and circumferential heat transfer from a hollow cylinder surrounded by an infinite medium in which heat transfer occurs via conduction.
4. **The radial heat transfer from a hollow cylinder surrounded by an infinite medium in which heat transfer occurs via conduction**.

t. The model is expressed mathematically as

$$\begin{cases} \dfrac{\partial^2 T}{\partial r^2} + \dfrac{1}{r}\dfrac{\partial T}{\partial r} = \dfrac{1}{\alpha_d}\dfrac{\partial T}{\partial t} \\ r = R \; -2\pi R\lambda \dfrac{\partial T}{\partial t} = \dot{q}_l \\ r \to \infty \quad T = T_0 \\ t = 0 \quad T = T_0 \end{cases}$$

where r [m] is the radial distance from the axis of the cylinder, T [°C] is the temperature of the body, α_d [m^2/s] is the thermal diffusivity, R [m] is the radius of the cylindrical surface, λ [W/(m °C)] is the thermal conductivity, $\dot{q}_l$ [W/m] is the heat flux per unit length, T_0 [°C] is the initial temperature and t [s] is the time.

u. The infinite line source model provides a solution for
   1. **The radial heat transfer from a line characterised by a constant heat flux towards (or from) an infinite medium in which heat transfer occurs via conduction**.
   2. The radial heat transfer from a cylinder characterised by a constant heat flux towards (or from) an infinite medium in which heat transfer occurs via convection and radiation.
   3. The axial and circumferential heat transfer from a line characterised by a constant heat flux towards (or from) an infinite medium in which heat transfer occurs via conduction.
   4. The radial heat transfer from a line characterised by a constant heat flux towards (or from) an infinite medium in which heat transfer occurs via convection and radiation.

v. The model is expressed mathematically as

$$\begin{cases} \dfrac{\partial^2 T}{\partial r^2} + \dfrac{1}{r}\dfrac{\partial T}{\partial r} = \dfrac{1}{\alpha_d}\dfrac{\partial T}{\partial t} \\ r \to \infty \quad -2\pi\lambda\dfrac{\partial T}{\partial t} = \dot{q} \\ r \to \infty \quad T = T_0 \\ t = 0 \quad T = T_0 \end{cases}$$

where r [m] is the radial distance from the axis of the cylinder, T [°C] is the temperature of the body, α_d [m^2/s] is the thermal diffusivity, λ [W/(m °C)] is the thermal conductivity, $\dot{q}$ [W/m^2] is the heat flux, T_0 [°C] is the initial temperature and t [s] is the time.

w. For geothermal heat exchangers such as energy piles, edge effects become relevant approximately after one year of geothermal operation and continue to be important throughout the life of the system. In these problems, the finite line source model can capture the influence of the ground surface
   1. Considering the ground as a heat source/sink, applying a fixed conductive heat flux on the surface.
   2. **Considering the ground as a reflecting plane with a constant temperature (or an adiabatic) boundary condition applied at the ground surface.**
   3. Applying a convective heat flux at the ground.
   4. Applying a radiative heat flux at the ground.

x. **After $t = 8$ min from the initiation of flow, the Biot and Fourier numbers are**:

$$Bi = \frac{h_c t_p}{\lambda} = \frac{500 \cdot 0.003}{0.5} = 3\ [-]$$

$$Fo = \frac{\alpha_d t}{t_p^2} = \frac{4 \times 10^{-7} \cdot 8 \cdot 60}{0.003^2} = 21.3\ [-]$$

y. **From the Biot number definition, it is possible to find the value of the thermal conductivity, λ [W/(m °C)]**:

$$Bi = \frac{h_c t_p}{\lambda}$$

Hence

$$\lambda = \frac{h_c t_p}{Bi} = \frac{250 \cdot 0.002}{1.25} = 0.4\ \mathrm{W/(m^{\circ}C)}$$

From the Fourier number definition, it is possible to find the value of the thermal diffusivity, α_d [m^2/s]:

$$Fo = \frac{\alpha_d t}{t_p^2}$$

Hence

$$\alpha_d = \frac{Fo \cdot t_p^2}{t} = \frac{4.5 \cdot 0.002^2}{60} = 3 \times 10^{-7}\ \mathrm{m^2/s}.$$

From the thermal diffusivity definition, it is possible to find the desired value of the specific heat:

$$\alpha_d = \frac{\lambda}{\rho c_p}$$

That is

$$c_p = \frac{\lambda}{\rho \alpha_d} = \frac{0.4}{600 \cdot 3 \times 10^{-7}} = 2222\ \mathrm{J/(kg^{\circ}C)}$$

z. **The main implication of the first term approximation is that the time dependence of the temperature at any location within the wall is the same as that of the midplane temperature**.

aa. In addition to the solutions including constant boundary conditions for the time-dependent heat transfer in the semiinfinite medium, additional solutions addressing more complex conditions at the surface do exist. These solutions typically refer to a periodic temperature or heat flux condition at the surface. In the context of the analysis of geothermal heat exchangers such as energy geostructures, they may be useful to address problems including, for example temperature variations caused by fluctuations in the environmental conditions at the ground surface as well as at the surface of an energy wall or an energy tunnel in an underground built environment. Both daily and seasonal temperature changes occur in practice in those situations and after a sufficient time can be associated with a quasi-steady-state in which the ground surface exchanges heat with the air that is characterised by a temperature fluctuating about a periodically time-invariant mean value. In the semiinfinite medium the temperature fluctuations have a time lag relative to the surface temperature and their amplitude decays exponentially from the surface because of the thermal inertia of the semiinfinite medium. The periodic fluctuation of the surface temperature may be modelled through the function

$$T(0,t) = T_0 + \Delta T \sin(\omega t)$$

where ΔT [°C] is the temperature amplitude of the considered function over the average (initial) temperature T_0 [°C] and ω [rad/s] is the angular frequency.

bb. It is possible to obtain the required quantities according the following steps.

1. **The rate of heat transfer entering and leaving the wall can be obtained by using the given temperature distribution.**

$$\dot{Q}_{in} = -\lambda A \frac{\partial T}{\partial x}\Big|_{x=0} = -\lambda A (b + 2cx)_{x=0} = -b\lambda A = 200\,\mathrm{W}$$

$$\dot{Q}_{out} = -\lambda A \frac{\partial T}{\partial x}\Big|_{x=L} = -\lambda A (b + 2cx)_{x=L} = -\lambda A (b + 2cL) = 400\,\mathrm{W}$$

2. **The rate of change of energy storage in the wall can be calculated by applying an overall energy balance to the wall.**

$$\dot{Q}_{st} = \dot{Q}_{in} - \dot{Q}_{out} + AL\dot{q}_v = 200 - 400 + 10 \cdot 1 \cdot 30 = 100\,\mathrm{W}$$

3. **The rate of temperature change at a certain point can be evaluated by using the heat equation for a monodimensional heat transfer in a plane wall**:

$$\frac{\partial T}{\partial t} = \frac{\lambda}{\rho c_p}\frac{\partial^2 T}{\partial x^2} + \frac{\dot{q}_v}{\rho c_p}$$

It follows that

$$\frac{\partial^2 T}{\partial x^2} = \frac{\partial}{\partial x}\left(\frac{\partial T}{\partial x}\right) = \frac{\partial}{\partial x}(b + 2cx) = 2c = 2\cdot(-5) = -10^{\circ}\mathrm{C/m^2}$$

Note that this derivative is independent of position in the medium. Hence

$$\frac{\partial T}{\partial t} = \frac{2}{2400\cdot 880}\cdot(-10) + \frac{30}{2400\cdot 880} = -1.04\cdot 10^{-5} + 1.42\cdot 10^{-5} = 3.8\cdot 10^{-6^{\circ}}\mathrm{C/s}.$$

cc. **It is possible to obtain the required quantities according the following steps**.

1. **The rate of heat transfer at the pile axis reads**

$$\dot{Q}_{r=0} = -\lambda A\frac{\partial T}{\partial r}\Big|_{r=0} = -\lambda A_l(2br) = -2\cdot\pi\cdot 1\cdot 30(0) = 0\,\mathrm{W}$$

were A_l [m^2] is the pile shaft surface. The rate of heat transfer at the pile shaft reads

$$\dot{Q}_{r=0.5} = -\lambda A\frac{\partial T}{\partial r}\Big|_{r=0.5} = -\lambda A_l(2br) = -2\cdot\pi\cdot 1\cdot 30(2\cdot -2\cdot 0.5) = 377\,\mathrm{W}$$

The rate of heat transfer at the pile shaft per unit length reads

$$\dot{q}_{l\,r=0.5} = \frac{\dot{Q}_{r=0.5}}{L} = \frac{377}{30} = 12.6\,\mathrm{W/m}.$$

2. **The rate of change of energy storage in the wall can be calculated by applying an overall energy balance to the pile**.

$$\dot{Q}_{st} = \dot{Q}_{in} - \dot{Q}_{r=0.5} + A_b L\dot{q}_v = 0 - 377 + \pi\cdot 0.5^2\cdot 30\cdot 25 = 212\,\mathrm{W}$$

were A_b [m^2] is the pile base surface.

3. **The rate of temperature change at a certain point can be evaluated by using the heat equation for a mono-dimensional heat transfer in cylindrical coordinates**:

$$\frac{\partial T}{\partial t} = \frac{\lambda}{\rho c_p}\frac{\partial^2 T}{\partial r^2} + \frac{\dot{q}_v}{\rho c_p}$$

It follows that

$$\frac{\partial^2 T}{\partial r^2} = \frac{\partial}{\partial r}\left(\frac{\partial T}{\partial r}\right) = \frac{\partial}{\partial r}(2br) = 2b = 2\cdot(-2) = -4^{\circ}\mathrm{C/m^2}.$$

Note that this derivative is independent of position in the medium. Hence

$$\frac{\partial T}{\partial t} = \frac{2}{2400\cdot 850}\cdot(-4) + \frac{50}{2400\cdot 850} = -3.92\cdot 10^{-6} + 2.45\cdot 10^{-5} = 2.06\cdot 10^{-5\,\circ}\mathrm{C/s}.$$

CHAPTER 10

Analytical modelling of capacity and deformation of single energy piles

10.1 Introduction

Estimating the response of single energy piles subjected to the mechanical and thermal loads associated with their structural support and heat exchanger operation represents the starting point for any comprehensive analysis of energy pile foundations. In this context, two key aspects must be addressed for any characteristic pile constituting energy pile foundations: the pile *capacity* and the pile *deformation*. Addressing the capacity of energy piles involves determining the maximum load that is likely to be associated with an inadmissible state in the soil (or in the pile) and may cause the collapse or failure of the structure or its components. Addressing the deformation of energy piles involves assessing the maximum load that is likely to be associated with an inadmissible state in the soil (or in the pile) and may cause the loss of functionality, appearance and durability of the structure or its components. The referenced 'maximum load' for the previous considerations may in principle consist of a unique load, but in the majority of cases it consists of a combination of loads.

While the capacity of piles markedly depends on their method of installation, the deformation of such foundations is crucially characterised by the adopted construction details. However, both of these aspects are a function of the properties of any considered site. In this context, understanding and being capable of describing the load-transfer relationship between the pile and the surrounding ground is essential to address the thermomechanical behaviour of such foundations. Experimental evidence obtained from full-scale field tests can yield the most realistic information on the load-transfer relationship of energy piles. Particularly rigorous theoretical analysis approaches such as the finite element method are accessible to tackle this problem as well. However, analytical approaches can in many cases represent an effective solution to address the load-transfer relationship of energy piles, with the advantage of being expediently applicable in sensitivity analyses for even large pile foundations, potentially via relatively simple computer software.

This chapter focuses on analytical and semianalytical approaches to characterise the capacity and the deformation of single energy piles subjected to mechanical and thermal loads. Attention is given to the influence of axial (e.g. vertical and compressive) mechanical loads as well as to both heating and cooling thermal loads.

Analysis and Design of Energy Geostructures
DOI: https://doi.org/10.1016/B978-0-12-816223-1.00010-2

The analysis of the influence lateral loads can be considered separately and is not treated in the following.

To address the aforementioned aspects, *idealisations and assumptions* are presented first: in this context the objective is to propose a summary of the assumptions made to model the response of energy piles subjected to mechanical and thermal loads. Second, the *generalised axial capacity formulation* for energy piles is treated: the objective of this part is to define mathematical expressions that can be employed to investigate the failure of such foundations. Third, the *capacity in coarse-grained soil, fine-grained soil and rock* is analysed: in this context the purpose is to expand on approaches for estimating the capacity of energy piles in many of the situations that are likely to be encountered in practice. Next, the *generalised axial deformation formulation* characterising energy piles is treated: in this framework the purpose is to define mathematical expressions governing the deformation of such foundations. Afterward, *thermomechanical schemes* for energy piles are described: the purpose of this part is to expand on theoretical diagrams describing the influence of axial mechanical loads and thermal loads on the response of energy piles. Then, *displacement charts* are presented: in this context the aim is to provide charts summarising the vertical head displacement of single energy piles caused by mechanical and thermal loads in various situations. Later, the *load-transfer analysis approach* is discussed: the objective of this part is to provide the essentials of a powerful method for the analysis of the failure and deformation of energy piles. In addition to this, a discussion about the *modelled and observed response* of energy piles is proposed: in this framework, the aim is to expand on the capabilities of the foregoing theoretical approaches in modelling the actual response of energy piles. Finally, *questions and problems* are proposed: the purpose of this part is to fix and test the understanding of the subjects covered in this chapter by addressing a number of exercises.

10.2 Idealisations and assumptions

Most of the idealisation and assumptions made in this chapter coincide with those presented in Chapter 7, Thermomechanical behaviour of energy pile groups. The quoted considerations find due justification in the referenced chapter and are only summarised for completeness in the following, prior to a detailed description and justification of additional hypotheses.

A continuum medium idealisation of the materials constituting energy pile foundations is employed while considering the materials to be isotropic and homogeneous. The piles are assumed to be characterised by a cylindrical shape. Layered (i.e. nonuniform) soil deposits are considered to be composed of fully horizontal layers. Uniform variations of the temperature, stress, strain and displacement fields within energy piles are assumed.

The ground is considered to be insensitive to temperature variations, that is an *infinite heat reservoir* that remains at a fixed constant temperature (cf. Fig. 10.1A). Although approximate, this approach has been proven to be effective (Rotta Loria and Laloui, 2016; Rotta Loria and Laloui, 2017a) because (1) it develops solutions that are independent of the actual heat exchange occurring in the ground surrounding energy piles and (2) it takes advantage of the negligible role of the thermally induced soil deformation on the pile response characterising all usual situations where the thermal expansion coefficient of the soil is (significantly) lower than or (at least theoretically) equal to that of the piles (Rotta Loria and Laloui, 2017b; Rotta Loria and Laloui, 2016). Mechanical loads applied to energy piles are modelled via a prescribed force to their head, P. Thermal loads applied along energy piles are modelled via prescribed temperature variations, $\Delta T = T - T_0$, where T is an actual temperature value and T_0 is the initial uniform temperature of the pile

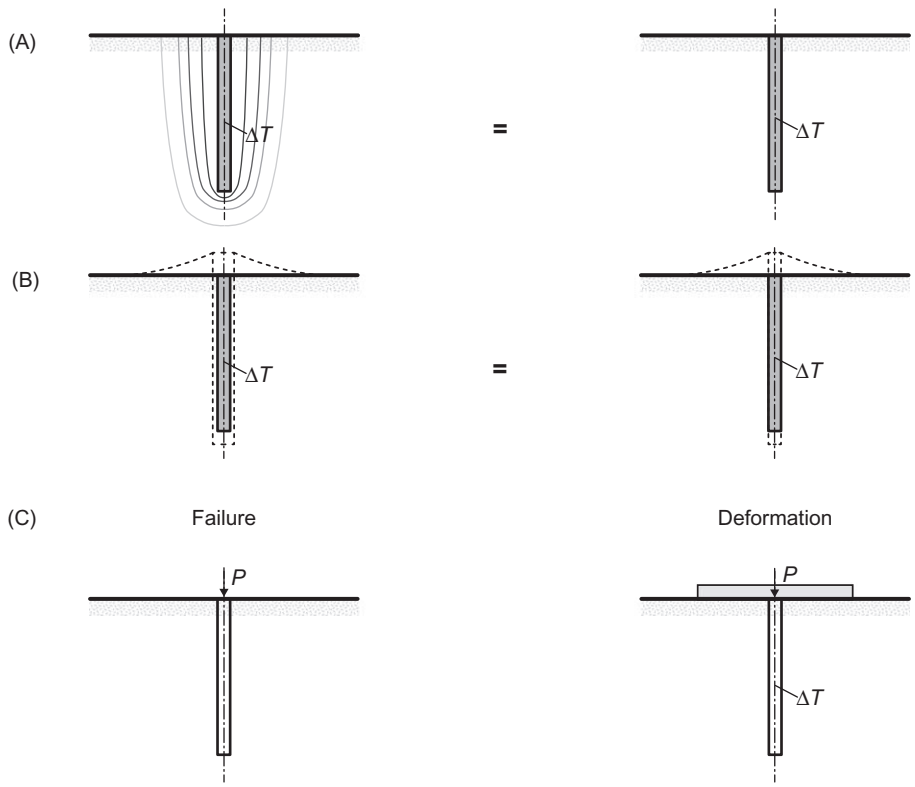

Figure 10.1 (A) Modelling approach to account for the effects of thermal loads; (B) modelling approach to describe the deformation of energy piles subjected to thermal loads; and (C) relevant loads and conditions considered for the analysis of the failure and deformation of single energy piles.

and surrounding ground. The temperature variation applied to the energy piles is assumed to be (1) instantaneously and uniformly imposed along the piles and (2) constant with time. The pipes inside the energy piles are not modelled. This choice involves considering the temperature field in these domains as that of the heat carrier fluid circulating inside the pipes in the reality.

Energy piles are modelled employing a one-dimensional scheme unless otherwise specified. Accordingly, the radial pile displacements are neglected (cf. Fig. 10.1B). This choice appears to be justified based on the small values of radial displacements characterising energy piles (Laloui et al., 2003; Olgun et al., 2014) and the consequent limited impact of these displacements on the axial response of such foundations. The material properties of the pile are constant with depth and do not change with temperature. The soil and soil–pile interaction properties (deformation and shearing resistance properties) also do not change with temperature. Variations of the soil deformation properties (e.g., Eslami et al., 2017) and the soil shear strength properties (e.g., Cekerevac and Laloui, 2004) with temperature variations have been observed in some cases. However, while it may be worth accounting for the former phenomenon particularly for energy piles embedded in fine-grained soil rather than in coarse-grained soil and may increase the accuracy of the analyses, considering the latter phenomenon is considered negligible from a practical perspective. In general the weight of the pile is considered when addressing the axial load capacity of the piles, whereas it is neglected when addressing the axial deformation of such foundations. The constitutive models that characterise the interaction of the pile with the surroundings are known and are considered to be unaffected by any potential temperature effects. Although these effects were clearly remarked for single energy piles in some situations (McCartney and Rosenberg, 2011; Wang et al., 2011; Ng et al., 2015) they were small and/or negligible in others (Regueiro et al., 2012; Goode et al., 2014; Kramer and Basu, 2014). Considering these effects may increase the accuracy of the analyses where the behaviour of the soil surrounding the piles may be sensitive to temperature effects.

The analysis of the capacity of energy piles is associated with the combination and the effects of only mechanical loads, whereas that of the deformation of such foundations is associated with the combination and the influence of both mechanical and thermal loads (cf. Fig. 10.1C). This hypothesis is supported by the consideration that thermal loads are unlikely to involve the failure of energy piles but only to characterise the deformation of such foundations (Rotta Loria et al., 2019a). Yet, while no account of the pile cap is made when addressing the capacity of energy piles, the contribution of this structural element is considered when addressing the deformation of such foundations unless otherwise specified. This assumption neglects the actual presence of the cap in the former case as often occurs in practice to perform simpler and safer analyses

than otherwise. Due account of the cap is made in the latter case because this structural element predominantly characterises the deformation of energy piles via the provided head restraint.

Contractive strains, downward displacements, compressive stresses and increases in angles in the anticlockwise direction are considered to be positive.

10.3 Generalised axial capacity formulation

The net axial load capacity of a single pile, Q_u, is generally accepted to be equal to the sum of the shaft capacity, Q_s, and the base capacity, Q_b, less than the weight of the pile, W:

$$Q_u = Q_s + Q_b - W \tag{10.1}$$

In Eq. (10.1) the shaft and base capacity contributions are computed independently from each other, thus neglecting the different displacement values for which they may be effectively mobilised in practice. While this assumption simplifies the analysis, it is worth noting that the shaft capacity of piles is mobilised for much smaller pile displacements than the base capacity. The shaft capacity may be fully mobilised for pile displacements typically of the order of 0.5%–2% of the pile diameter (i.e. displacements usually in the range of 5–15 mm) whereas the base capacity may require displacements as large as 5%–10% of the pile (base) diameter (even larger for low-displacement piles in coarse-grained soil) to be fully mobilised (Fleming et al., 2008). In practice the axial capacity of piles is considered to be achieved for either the load for which a further increase in settlement does not induce an increase in load or for the load causing a settlement of 10% of the pile base diameter.

Following the approach of Poulos and Davis (1980), the shaft capacity can be estimated by integrating the pile–soil interface shear strength along the external surface of the pile shaft and the base capacity can be evaluated from bearing capacity theory. This approach yields to the generalised expression for the pile capacity, which can be written as

$$Q_u = q_s A_s + q_b A_b - W = \left(\bar{\tau}_a + \overline{\sigma}_z \overline{K} \tan\delta\right) A_s + \left(cN_c s_c d_c + \sigma_{zb} N_q s_q d_q + \frac{1}{2}\gamma D N_\gamma s_\gamma d_\gamma\right) A_b - W \tag{10.2}$$

where q_s is the average shear strength down the pile shaft; $A_s = 2\pi RL$ is the area of the pile shaft (with R and L being the pile radius and length, respectively); q_b is the base resistance; $A_b = \pi R^2$ is the cross-sectional area of the pile base; $\bar{\tau}_a$ is the average pile–soil interface adhesion; $\overline{\sigma}_z$ is some average vertical stress; $\overline{K}$ is some average

Table 10.1 Values and expressions for the term $cN_cs_cd_c$.

Term $cN_cs_cd_c$				
Author	**Cohesion, c [Pa]**	**Bearing capacity factor, N_c [−]**	**Shape factor, s_c [−]**	**Depth factor, d_c [−]**
Terzaghi (1943)	Actual value	$(N_q - 1)\cot\varphi$	1.3	-
Meyerhof (1963)	Actual value	Same as suggested by Terzaghi (1943)	$1 + 0.2K_p$ where $K_p = \tan^2\left(45 + \frac{\varphi}{2}\right)$ is the passive coefficient of earth pressure	$1 + 0.2\sqrt{K_p}\left(\frac{L}{D}\right)$
Hansen (1970)	Actual value	Same as suggested by Terzaghi (1943)	Drained conditions: $1 + \frac{N_q}{N_c}$ Undrained conditions ($\varphi = 0$ degree): 0.2	Drained conditions: $1 + 0.4k_H$ Undrained conditions ($\varphi = 0$ degree): $0.4k_H$ with $k_H = \tan^{-1}\left(\frac{L}{D}\right)$ and k_H in radians
Vesic (1975, 1977)	Actual value	Same as suggested by Terzaghi (1943)	$1 + \frac{N_q}{N_c}$	Same as suggested by Hansen (1970)

coefficient of lateral pressure; δ is some angle of pile−soil interface shear strength; c is the soil cohesion; σ_{zb} is some vertical stress at the level of the pile base; γ is some unit weight of the soil; D is the pile diameter; N_c, N_q and N_γ are bearing capacity factors; s_c, s_q and s_γ are shape factors; and d_c, d_q and d_γ are depth factors.

If the capacity for a sudden loading scenario is to be computed, $\bar{\tau}_a$, δ, c and γ should be values appropriate to undrained conditions, and $\overline{\sigma}_z$ and σ_{zb} should be *total* vertical stresses. If the capacity for a slow loading scenario is to be computed, the material parameters should be values appropriate for drained conditions and $\overline{\sigma}'_z$ and σ'_{zb} should be *effective* vertical stresses. Bearing in mind these considerations, Tables 10.1−10.3 summarise expressions of the terms involved in the generalised formulation of the base resistance q_b in Eq. (10.2) referring to four classical capacity formulations (Terzaghi, 1943; Meyerhof, 1963; Hansen, 1970; Vesic, 1975, 1977). Note that, under the assumption of undrained conditions, the formulation for the base resistance provided by Hansen (1970) reads $q_b = (2 + \pi)c_u(1 + s_c + d_c) + \sigma_{zb}$ (where c_u is the undrained soil cohesion at the level of the pile base) instead of the formulation proposed in Eq. (10.2).

Table 10.2 Values and expressions for the term $\sigma_{zb}N_qs_qd_q$.

Term $\sigma_{zb}N_qs_qd_q$				
Author	**Vertical stress, σ_{zb} [Pa]**	**Bearing capacity factor, N_q [–]**	**Shape factor, s_q [–]**	**Depth factor, d_q [–]**
Terzaghi (1943)	Actual value	$N_q = \frac{a_T^2}{a_T \cos^2\left(45+\frac{\varphi}{2}\right)}$ with $a_T = e^{\left(0.75\pi-\frac{\varphi}{2}\right)\tan\varphi}$	–	–
Meyerhof (1963)	Actual value	$K_p e^{\pi\tan\varphi}$	Drained conditions: $1+0.1K_p$ Undrained conditions ($\varphi = 0$ degree): 1	Drained conditions: $1+0.1\sqrt{K_p}\left(\frac{L}{D}\right)$ Undrained conditions ($\varphi = 0$ degree): 1
Hansen (1970)	Actual value	Same as suggested by Meyerhof (1963)	$1+\sin\varphi$	$1+2\tan\varphi(1-\sin\varphi)^2 k_H$
Vesic (1975, 1977)	Actual value	Same as suggested by Meyerhof (1963)	Same as suggested by Hansen (1970)	Same as suggested by Hansen (1970)

Table 10.3 Values and expressions for the term $\frac{1}{2}\gamma DN_\gamma s_\gamma d_\gamma$.

Term $\frac{1}{2}\gamma DN_\gamma s_\gamma d_\gamma$					
Author	**Unit weight, γ [N/m^3]**	**Pile diameter, D [m]**	**Bearing capacity factor, N_γ [–]**	**Shape factor, s_γ [–]**	**Depth factor, d_γ [–]**
Terzaghi (1943)	Actual value	Actual value	$\frac{\tan\varphi}{2}\left(\frac{K_{p\gamma}}{\cos^2\varphi}-1\right)$ (see Table 10.4 for the values of $K_{p\gamma}$)	0.6	-
Meyerhof (1963)	Actual value	Actual value	$(N_q-1)\tan(1.4\varphi)$	Drained conditions: $1+0.1K_p$ Undrained conditions ($\varphi = 0$ degree): 1	Drained conditions: $1+0.1\sqrt{K_p}\left(\frac{L}{D}\right)$ Undrained conditions ($\varphi = 0$ degree): 1
Hansen (1970)	Actual value	Actual value	$1.5\left(N_q-1\right)\tan\varphi$	0.6	1
Vesic (1975, 1977)	Actual value	Actual value	$2\left(N_q+1\right)\tan\varphi$	Same as suggested by Hansen (1970)	Same as suggested by Hansen (1970)

Table 10.4 Values of the term $K_{p\gamma}$.

Angle of shear strength, φ [degree]	Bearing capacity factor, N_c [−]	Bearing capacity factor, N_q [−]	Bearing capacity factor, N_γ [−]	Pressure coefficient, $K_{p\gamma}$ [−]
0	5.7[a]	1.0	0.0	10.8
5	7.3	1.6	0.5	12.2
10	9.6	2.7	1.2	14.7
15	12.9	4.4	2.5	18.6
20	17.7	7.4	5.0	25.0
25	25.1	12.7	9.7	35.0
30	37.2	22.5	19.7	52.0
34	52.6	36.5	36.0	–
35	57.8	41.4	42.4	82.0
40	95.7	81.3	100.4	141.0
45	172.3	173.3	297.5	298.0
48	258.3	287.9	780.1	–
50	347.5	415.1	1153.2	800.0

[a] $N_c = 1.5\pi + 1$ according to Terzaghi (1943).

10.4 Capacity in coarse-grained soil

10.4.1 General

For piles in coarse-grained soil, drained conditions may be assumed upon loading so that an effective stress analysis can be considered. Assuming in Eq. (10.2) that the cohesive components are equal to zero, neglecting the term $\frac{1}{2}\gamma' D N_\gamma s_\gamma d_\gamma$ because it is small in relation to the term involving N_q and considering by means of a conservative approach both s_q and $d_q = 1$ (when these terms appear in the employed base capacity formulation), the pile capacity formulation becomes

$$Q_u = q_s A_s + q_b A_b - W = \overline{\sigma'}_z \overline{K} \tan\delta' A_s + \sigma'_{zb} N_q A_b - W \tag{10.3}$$

10.4.2 Displacement piles

The shaft resistance is often expressed in the form $\overline{\sigma'}_z \overline{K} \tan\delta' = \overline{\sigma'}_z \beta^f$. Accordingly, the considered approach to estimate the shaft resistance of piles is termed the 'Beta Method' (Burland, 1973). The coefficient $\beta^f = \overline{K} \tan\delta'$ must be defined considering its two components $\overline{K}$ and $\tan\delta'$, and is analysed in detail by Randolph et al. (1994).

The coefficient $\overline{K}$ relates the normal stress acting on the pile–soil interface after pile installation, $\overline{\sigma'}_n$, to the in situ vertical effective stress, $\overline{\sigma'}_z$, and is the crucial governing factor of the shaft resistance of displacement piles in coarse-grained soils. For a chosen pile installation method, $\overline{K}$ depends on the in situ coefficient of earth pressure at rest, K_0, and the stress variation produced by the installation (related to the initial

soil density) (Fleming et al., 2008; Lancellotta, 1995). The values of $\overline{K}$ can vary from values equal to the coefficient of passive earth pressure, K_p, near the ground surface, to values equal to the coefficient of the earth pressure at rest, K_0, near the pile toe.

The quoted values of $\overline{K}$ compensate the increase in vertical effective stress with depth, thus leading to an asymptotic trend of the shaft resistance with depth. This characteristic is in accordance with the phenomenon of shaft resistance limitation or even degradation that is observed, for example with increasing depths in highly permeable soils (Vesic, 1969, 1977; Lehane et al., 1993).

An example of the phenomenon of shaft resistance limitation observed experimentally by Vesic (1967) along a pile is reported in Fig. 10.2. An example of the phenomenon of shaft resistance degradation observed experimentally by Lehane et al. (1993) in three instrument clusters at different distances r from the toe of a 6 m long and 0.1 m diameter pile as it is jacked into the ground is reported in Fig. 10.3. The evolution of the cone resistance, q_c, factored down by 100, is plotted for reference.

Typical values of $\overline{K}$ for driven cast in situ piles are 1 if wet concrete is placed, while they are up to 1.2 if dry concrete is rammed into the pile shaft (Fleming et al., 2008). Alternative approaches to quantify $\overline{K}$ have been proposed by Kulhawy et al. (1983), Kraft (1990), Randolph et al. (1994), Jardine and Chow (1996) and

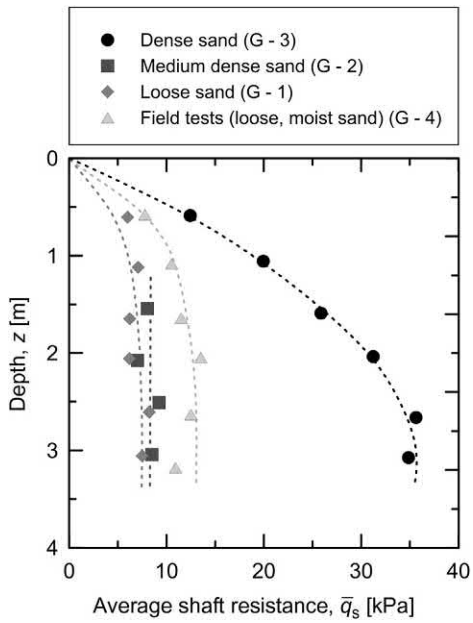

Figure 10.2 Asymptotic evolution of shaft resistance with increasing depth for piles in coarse-grained soil. *Redrawn after Vesic, A.S., 1967. A Study of the Bearing Capacity of Deep Foundations. Georgia Institute of Technology, Atlanta, GA.*

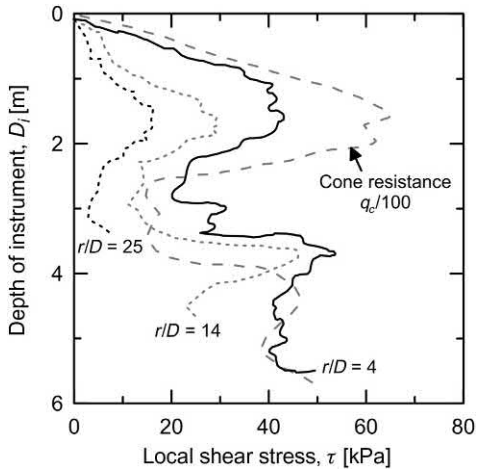

Figure 10.3 Phenomenon of shaft resistance degradation with increasing depth for a pile in coarse-grained soil. *Redrawn after Lehane, B., Jardine, R., Bond, A.J., Frank, R., 1993. Mechanisms of shaft friction in sand from instrumented pile tests. J. Geotech. Eng. 119 (1), 19–35. and Fleming, K., Weltman, A., Randolph, M., Elson, K., 2008. Piling Engineering. CRC Press.*

Fleming et al. (2008). Considering $\overline{K} = K_0$ may be typically appropriate according to Kulhawy et al. (1983).

The pile–soil interface angle of shear strength, δ', is usually assumed to be equal to the angle of shear strength under constant volume conditions of the soil, φ'_{cv}, in the absence of interface shear tests results, although the former is generally found to be a little lower than the latter (Randolph et al., 1994). The approach of considering $\delta' = \varphi'_{cv}$ may be justified on the basis that no dilation is to be expected between the soil and the pile shaft at failure (Fleming et al., 2008).

One alternative approach to estimate the pile–soil interface angle of shear strength resorts to the definition of the angle of shear strength of the soil. For silica sands and calcareous sands, Kraft (1990) proposes $\delta' = 0.7\varphi'$ and $\delta' = 0.6\varphi'$, respectively. Although the values δ' resulting from this approach are not necessarily consistent with laboratory data (Randolph et al., 1994), they have been successfully applied in predicting the axial capacity of piles in sand (Rotta Loria et al., 2014). When the dilatancy angle of the soil ψ is available, the stress–dilatancy relationship $\varphi' = \varphi'_{cv} + 0.8\psi$ for plane shear of Rowe (1962) may also be employed to estimate the soil angle of shear strength under constant volume conditions, φ'_{cv}.

Kulhawy et al. (1983) propose ratios between δ' and the soil angle of shear strength φ' to be used in design for different soil–structure interfaces (cf. Table 10.5). Kishida and Uesugi (1987) relate the pile–soil interface angle of shear strength with the soil angle of shear strength through a normalised roughness coefficient. Jardine et al. (1993) provide further information on this topic. For typical pile–soil interface

Table 10.5 Values of normalised angle of shear strength for interfaces between different materials.

Interface material	Normalised angle of shear strength, δ'/φ' [−]
Sand−concrete (rough)	1.0
Sand−concrete (smooth)	0.8−1.0
Sand−steel (corrugated)	0.7−0.9
Sand−steel (smooth)	0.5−0.9
Sand−timber	0.8−0.9

Source: Data from Kulhawy, F.H., O'Rourke, T., Stewart, J.P., Beech, J., 1983. Transmission Line Structure Foundations for Uplift-compression Loading, Load Test Summaries: Appendix to EPRI Final Report EL-2870. Electric Power Research Institute.

roughness, the pile−soil interface angle of shear strength is 0.75−1 times that of the soil (Fleming et al., 2008).

Simplified approaches linking the shaft resistance of driven piles directly to the cone resistance, q_c, are also available in addition to the previous theoretical approaches. Expressions of this type have been proposed by De Beer (1985, see Lancellotta, 1995) and Lehane et al. (2005) based on the tradition of using empirical relations resorting to in situ tests to design piles (Van Impe, 1991).

The base resistance is a function of the vertical effective stress at the level of the pile toe and the bearing capacity factor, whose determination depends on the considered collapse mechanism occurring at the pile toe. The factor N_q has been proven to depend on the soil characteristics and on the relative depth of the pile toe (Lancellotta, 1995), both aspects having an impact on controlling factors such as the shear strength of the soil and the rigidity index of the material, G_{soil}/p' (where G_{soil} is the shear modulus of the soil and p' is the mean effective stress) (Randolph et al., 1994), as well as on the in situ stresses (Houlsby and Hitchman, 1988). A dramatic variation of the factor N_q is observed depending on the reference collapse mechanisms among the four proposed, for example by (1) Caquot (1934), Buisman (1935) and Terzaghi (1943), (2) Meyerhof (1951, 1953), (3) Berezantsev (1961) and (4) Skempton et al. (1953) and Vesic (1975, 1977), through which this factor is calculated. According to Fleming et al. (2008), the relationship between the bearing capacity factor N_q and the soil angle of shear strength derived by Berezantsev (1961) is the most used for the design of circular deep foundations such as energy piles (cf. Fig. 10.4). The previous relationship can be considered in the approach discussed by Kulhawy (1984) and Randolph et al. (1994) to define through the following iterative procedure the appropriate value of N_q, starting from given values of the soil angle of shear strength at constant volume, φ'_{cv}, relative density, D_R, and vertical effective stress, σ'_z:

1. Chose a first trial value of the bearing capacity factor N_q;
2. Determine the value of the mean effective stress p' as follows:

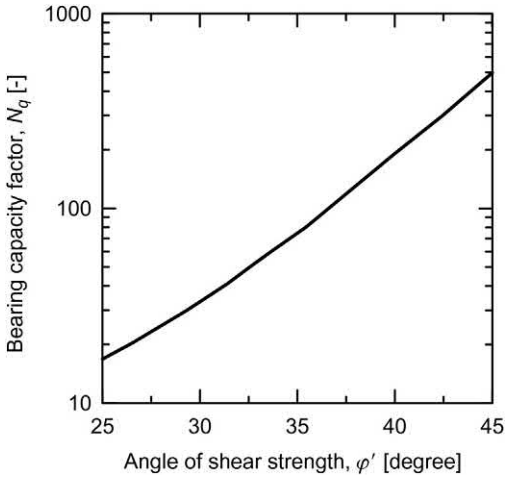

Figure 10.4 Variation of the bearing capacity factor N_q with the soil angle of shear strength φ'. *Redrawn after Berezantsev, K., 1961. Load bearing capacity and deformation of piled foundations. In: Proceedings of 5th International Conference on Soil Mechanics and Foundation Engineering, vol. 1, p. 11.*

$$p' = \sqrt{N_q \sigma'_{zb}} \tag{10.4}$$

3. With this value of p', determine the relative dilatancy index I_R according to Bolton (1986, 1987):

$$\begin{aligned} I_R &= D_R \left[5.4 - \ln\left(\frac{p'}{p_a}\right) \right] - 1 \quad \text{for } p' > 150 \text{ kN/m}^2 \\ I_R &= 5D_R - 1 \qquad\qquad\qquad\quad \text{for } p' \leq 150 \text{ kN/m}^2 \end{aligned} \tag{10.5}$$

4. Compute the angle of shear strength, φ', according to Bolton (1986):

$$\varphi' = \varphi'_{cv} + 3I_R \tag{10.6}$$

5. By entering the computed value of φ' into Fig. 10.4, evaluate the corresponding value of N_q.

6. Iterate until the trial value of the factor N_q obtained in step 5 is equal to the value considered in step 1.

The previous approach can consider the gradually decreasing gradient of pile base resistance with depth often observed in practice (e.g. in a uniform sand deposit), which is in contrast to the linearly increasing resistance that would arise from the simple consideration of the product $\sigma'_{zb}N_q$. Therefore no limiting value of base resistance should be stipulated (Randolph et al., 1994).

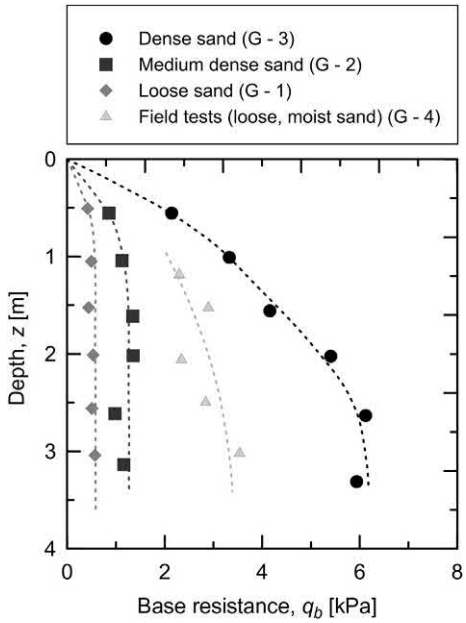

Figure 10.5 Phenomenon of decreasing gradient of base resistance with increasing depth for piles in coarse-grained soil. *Redrawn after Vesic, A.S., 1967. A Study of the Bearing Capacity of Deep Foundations. Georgia Institute of Technology, Atlanta, GA.*

An example of the decreasing gradient characterising the base resistance of piles observed by Vesic (1967) is reported in Fig. 10.5. Further charts proposed by Fleming et al. (2008) that corroborate the considered phenomenon by expressing the relationship between the base resistance q_b and the bearing capacity factor N_q for different values of the soil angle of shear strength under constant volume conditions φ'_{cv} and relative density D_R are presented in Fig. 10.6.

Another analytical approach to estimate the base resistance of piles is provided, for example by Hansen (1970) (cf. Tables 10.1, 10.2 and 10.3). According to Bowles (1988), the approach proposed by Hansen (1970) provides a particularly suitable estimate of the base resistance.

Additional theoretical approaches available to determine the base resistance are proposed, for example by Janbu (1976), Lang and Huder (1978), Coyle and Castello (1981), Tomlinson and Woodward (1993), Jardine and Chow (1996), Randolph (2003) and Powrie (2013).

Alternative empirical approaches to estimate the base resistance are also available and resort to penetration test results because of the similarities between the cone employed in such tests and the axially loaded pile. Adjustments to the cone resistance must be made due to scale effects and the limited displacements appropriate for pile

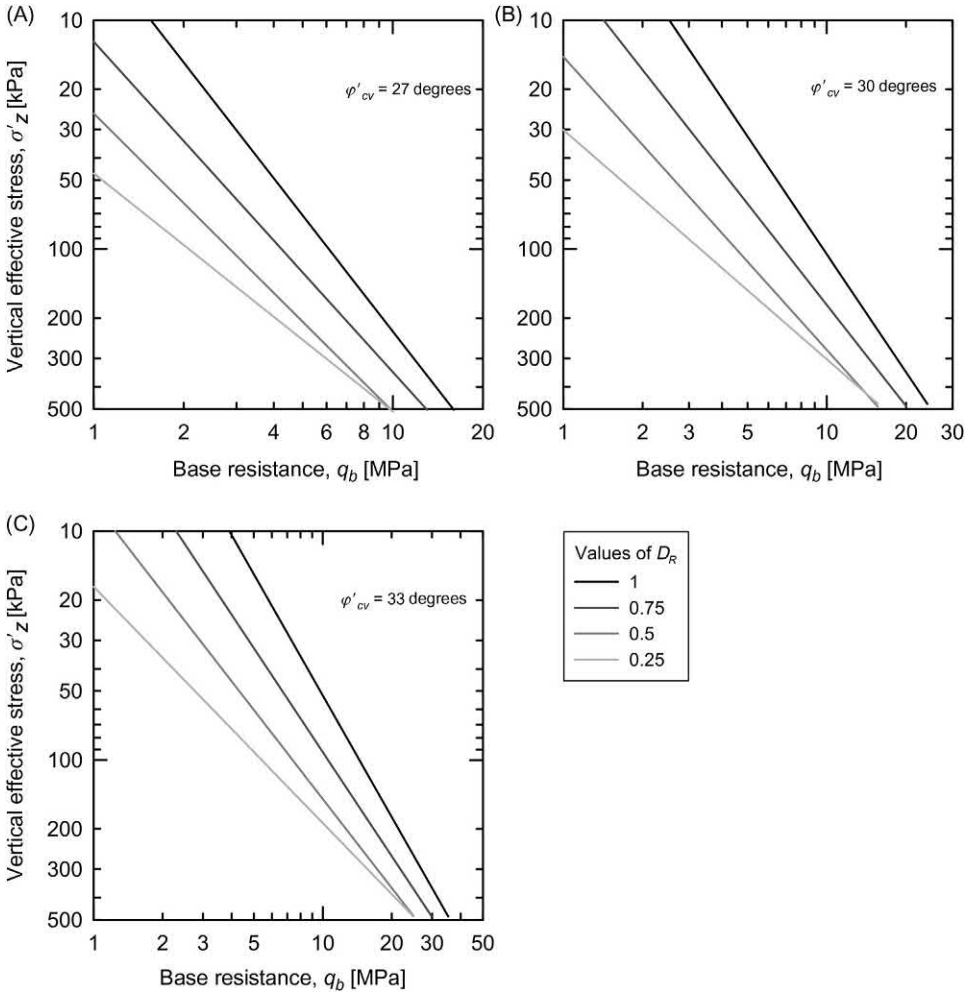

Figure 10.6 Relationship between the base resistance q_b and the bearing capacity factor N_q for different values of the soil angle of shear strength under constant volume conditions φ'_{cv} and the soil relative density D_R. *Redrawn after Fleming, K., Weltman, A., Randolph, M., Elson, K., 2008. Piling Engineering. CRC Press.*

design. Examples of empirical approaches linking the base resistance of the pile q_b to the cone resistance q_c are those proposed by Nordlund (1963), Meyerhof (1976) (although this approach considers no correction of q_c) and Fleming and Thorburn (1984). Typical ratios of q_b/q_c for (e.g. closed-ended) driven piles range from 0.2 (Jardine and Chow, 1996) to 0.5 (Kraft, 1990; De Nicola and Randolph, 1997) or 0.6 (Lehane et al., 2005). An example of the minimum values of normalised base resistance q_b/q_c for piles driven in coarse-grained soil of varying relative density D_R

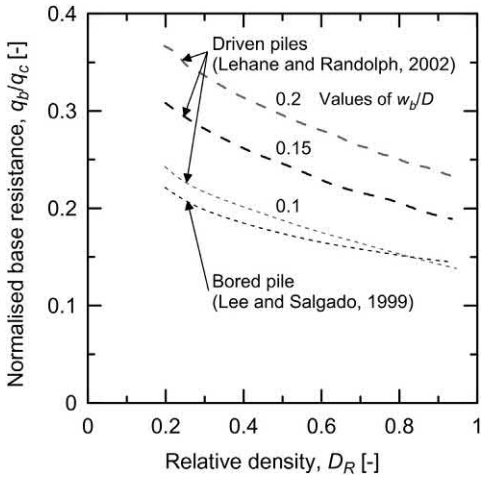

Figure 10.7 Normalised end-bearing pressures for driven open-ended piles and bored piles embedded in coarse-grained soils of varying relative density. *Redrawn after Fleming, K., Weltman, A., Randolph, M., Elson, K., 2008. Piling Engineering. CRC Press.*

proposed by Lehane and Randolph (2002) and enriched with the data for bored piles presented by Lee and Salgado (1999) and Fleming et al. (2008) are presented in Fig. 10.7. The curves refer to values of the vertical displacement of the pile base, w_b, normalised by the pile diameter, D.

10.4.3 Nondisplacement piles

The shaft resistance of nondisplacement piles is generally lower compared to that of displacement piles because during excavation lateral stresses in the ground are reduced and the initial in situ conditions are only partly restored upon concreting. The magnitude of the lateral pressure, which governs the shaft resistance, depends significantly on the excavation method and on the characteristics of the concrete (Lancellotta, 1995).

Based on investigations performed by Bernal and Reese (1983), Reese and O'Neill (1989) proposed an empirical formula for β^f (with the limiting value of $\overline{\sigma'}_z\beta^f \leq 200$ kPa). However, the use of a single lumped parameter β^f may be inaccurate.

A suitable approach to estimate the shaft resistance of nondisplacement piles is to consider the typical values of $\overline{K}$ for conventional bored piles of 0.7, while for continuous-flight auger piles the values are 0.9 in sands and gravels, and from 0.5 to 0.6 in silts and silty sands (Fleming et al., 2008). These values are in accordance with the recommendations of Kulhawy et al. (1983), who proposed $\overline{K} = 0.7K_0$.

The arguments summarised above for displacement piles about the choice of the pile–soil interface angle of shear strength are also valid for nondisplacement piles.

To account for potential loosening of the soil during the installation process, values of δ' between φ' and φ'_{cv} may be considered.

Particularly for relatively short piles, the shaft resistance of bored piles may be less than half the resistance of driven piles of the same nominal size, once excess pore pressures generated during installation have dissipated (Fleming et al., 2008). Moreover, because swelling processes and stress relief associated with ground excavation occur when dealing with nondisplacement piles, the displacements required to attain the failure state are much higher than those usually found for displacement piles (Lancellotta, 1995).

Meyerhof (1976) and Vesic (1977), referring to data presented by De Beer (1988), Reese and O'Neill (1988) and Hirayama (1990), stated that if the base resistance is considered to be mobilised for the conventional relative displacement of 10% of the pile base diameter, then the base resistance of bored piles is of the order of one half to one third that of driven piles. That is the displacements required to fully mobilise the base resistance of bored piles are much higher compared to those of driven piles and generally incompatible with structural integrity. Approaches to limit loads that are associated to specific displacements are available to tackle this issue (Van Impe, 1991; De Beer, 1988; Reese and O'Neill, 1988; Jamiolkowski and Lancellotta, 1988) and need to be considered to avoid serviceability problems. An example of the empirical approach proposed by Jamiolkowski and Lancellotta (1988) on the basis of 15 load tests is presented in Fig. 10.8 by linking the critical pressure $q_{0.05}$ to a relative

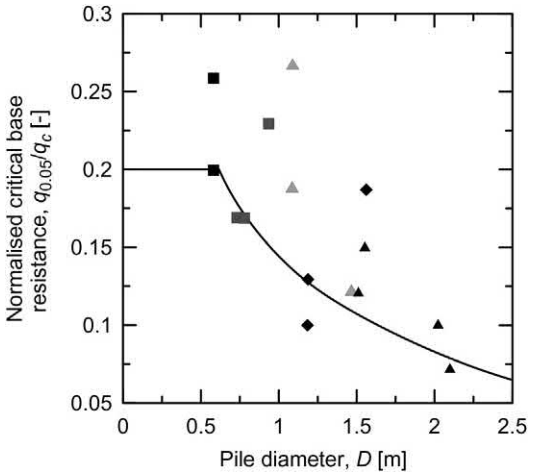

Figure 10.8 End-bearing load of bored piles characterised by different diameters. *Redrawn after Jamiolkowski, M., Lancellotta, R., 1988. Relevance of in-situ test results for evaluation of allowable base resistance of bored piles in sands. In: Proceedings of 1st International Geotechnical Seminar on Deep Foundations on Bored and Auger Piles, pp. 107–120.*

settlement of 5%. Typical empirical ratios of q_b/q_c for bored piles range from 0.15 to 0.22 (Lee and Salgado, 1999).

10.5 Capacity in fine-grained soil

10.5.1 General

For piles in fine-grained soil, undrained conditions may be assumed upon loading so that a total stress analysis has been historically considered. Assuming in Eq. (10.2) that the pile–soil interface angle of shear strength δ and the factor N_γ (considering the undrained angle of shear strength of the soil to be zero) are equal to zero, and the shape factors s_c, d_c, s_q and d_q are equal to one by means of a conservative approach (when these terms appear in the employed base capacity formulation) as well as the factor N_q, the pile capacity formulation becomes

$$Q_u = q_s A_s + q_b A_b - W = \bar{\tau}_a A_s + (c_u N_c + \sigma_{zb}) A_b - W \tag{10.7}$$

where N_c is the bearing capacity factor proposed by Skempton (1951) for a circular area (cf. Fig. 10.9), which may be taken to be equal to 9 for depths relevant for piles (Lancellotta, 1995). Interpolation may be considered from values of 6–9 with the increasing penetration depth of the pile up to values of three pile diameters (Fleming et al., 2008).

The pile–soil interface adhesion, $\bar{\tau}_a$, varies considerably with many factors including (1) pile type, (2) soil type and (3) method of installation (Poulos and Davis, 1980). Many attempts have been made to correlate this parameter with the undrained soil cohesion in the form $\bar{\tau}_a = \alpha^f c_u$, such as those by Meyerhof and Murdock (1953), Golder and Leonard (1954), Golder (1957), Tomlinson (1957, 1971), Peck (1958), Skempton (1959), Mohan and Chandra (1961), Woodward and Boitano (1961), Coyle and Reese (1966), Vesic (1967), Morgan and Poulos (1968), McClelland et al. (1969, 1972, 1974). Accordingly, the considered approach to estimate the shaft resistance of piles is often referred to as the 'Alpha method' (Tomlinson, 1971). Typical relationships between the adhesion factor $\alpha^f = \bar{\tau}_a/c_u$ and c_u summarised by McClelland (1974) for displacement piles in fine-grained soil are presented in Fig. 10.10. The value of α^f deduced from pile load tests reduces from unity or more for piles in clay of low strength, down to 0.5 or less for clay of strength greater than about 100 kPa (Fleming et al., 2008). Further insights about the values of the adhesion factor are provided for displacement piles in Table 10.6 and Fig. 10.11, based on the results presented by Tomlinson (1971) and elaborated by Poulos and Davis (1980). Values of the adhesion factor are provided for nondisplacement piles in Table 10.7, based on the results of Golder and Leonard (1954), Golder (1957), Tomlinson (1957) and Mohan and Chandra (1961).

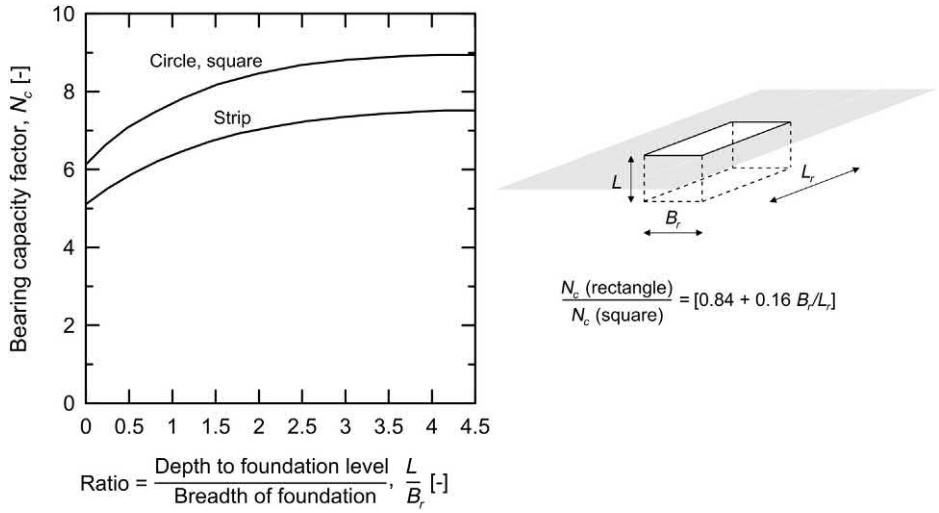

Figure 10.9 Values of bearing capacity factor N_c for foundations in fine-grained soils. Note that for the case of a circle or a square, $B_r = L_r$. *Redrawn after Skempton, A., 1951. The bearing capacity of clays. In: Proceedings of Building Research Congress, vol. 1, pp. 180–189.*

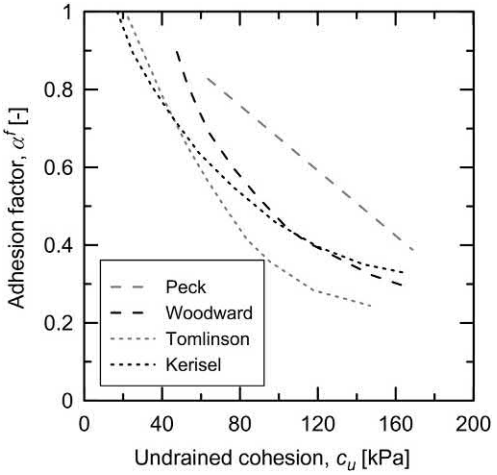

Figure 10.10 Relationship between adhesion factor and undrained soil cohesion for displacement piles embedded in fine-grained soils. *Redrawn after McClelland, B., 1974. Design of deep penetration piles for ocean structures. J. Geotech. Eng. Div. 100 (GT7), 705–747.*

In all cases, a significant variation of the adhesion factor can be noted, such an aspect being a cause for concern for design purposes (Fleming et al., 2008). In an attempt to overcome this limitation, other approaches addressing the definition of the adhesion factor by considering the full stress history of the soil in the vicinity of piles have been proposed with reference to the strength ratio c_u/σ'_z. These other approaches

Table 10.6 Values of adhesion factors for displacement piles in stiff fine-grained soil.

Case	Soil conditions	Penetration depth, z/D [–]	Adhesion factor, α^f [–]
I	Sands or sandy soils overlying stiff cohesive soil	<20	1.25
		>20	Cf. Fig. 10.11A
II	Soft clays or silts overlying stiff cohesive soils	<20	0.40
		>20	0.70
III	Stiff cohesive soils without overlying strata	<20	0.4
		>20	Cf. Fig. 10.11B

Source: Modified after Poulos, H.G., Davis, E.H., 1980. Pile Foundation Analysis and Design. Wiley, New York., data from Tomlinson, M., 1971. Some effects of pile driving on skin friction. In: Behaviour of Piles. Thomas Telford Publishing, pp. 107–114.

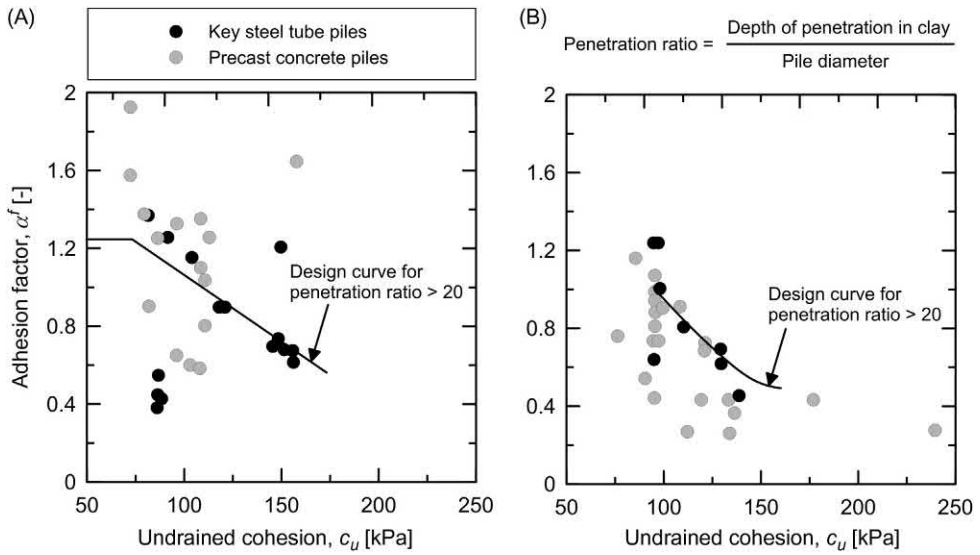

Figure 10.11 Adhesion factors for (A) sands and gravels overlying stiff to very stiff cohesive soils and (B) stiff to very stiff clays without overlying soil strata. *Redrawn after Tomlinson, M., 1971. Some effects of pile driving on skin friction. In: Behaviour of Piles. Thomas Telford Publishing, pp. 107–114.*

are considered, for example by Randolph and Wroth (1981), Olson and Dennis (1982), Stas and Kulhawy (1984), Semple and Rigden (1984), Randolph and Murphy (1985), Kulhawy and Jackson (1989), Sladen (1992), API (1993), Coduto (1994), Kolk and der Velde (1996) and Cherubini and Yves (1998). For example the expressions proposed by the American Petroleum Institute read (API, 1993)

$$\alpha^f = \frac{0.5}{\left(\frac{c_u}{\overline{\sigma'_z}}\right)^{0.5}} \quad \text{for} \quad c_u/\overline{\sigma'_z} \leq 1.0 \tag{10.8}$$

Table 10.7 Values of adhesion factors for nondisplacement piles in clay.

Soil type	Definition of adhesion factor	Adhesion factor, α^f [−]	Reference
London clay	$\bar{\tau}_a/c_u$	0.25−0.70 (average of 0.45)	Golder and Leonard (1954), Tomlinson (1957) and Mohan and Chandra (1961)
Sensitive clay	$\bar{\tau}_a/c_r$, with c_r being the remoulded soil strength	1	Golder (1957)
Highly expansive clay	$\bar{\tau}_a/c_u$	0.5	Mohan and Chandra (1961)

Source: Modified after Poulos, H.G., Davis, E.H., 1980. Pile Foundation Analysis and Design. Wiley, New York.

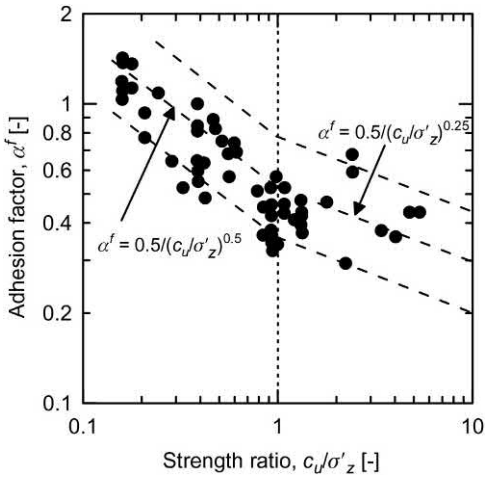

Figure 10.12 Variation of adhesion factor with the strength ratio. *Redrawn after Fleming, K., Weltman, A., Randolph, M., Elson, K., 2008. Piling Engineering. CRC Press.*

$$\alpha^f = \frac{0.5}{\left(\frac{c_u}{\overline{\sigma'_z}}\right)^{0.25}} \quad \text{for} \quad c_u/\overline{\sigma'_z} > 1.0 \tag{10.9}$$

An application of these formulations is proposed in Fig. 10.12 with reference to data summarised by Fleming et al. (2008) for displacement piles.

A somewhat different approach to estimate the shaft resistance for piles in fine-grained soils has been proposed by Vijayvergiya and Focht (1972). In this approach,

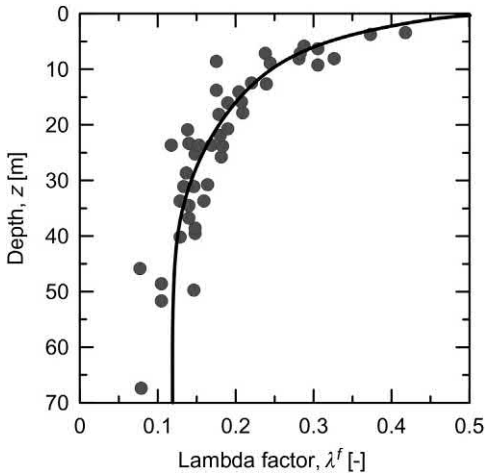

Figure 10.13 Variation of the factor λ^f with increasing pile penetration depth. *Redrawn after Vijayvergiya, V., Focht, J., 1972. A new way to predict the capacity of piles in clay. In: Fourth Annual Offshore Technology Conference, Houston, vol. 2, pp. 865–874.*

which is often referred to as the 'Lambda Method', the shaft resistance of piles is determined as

$$q_s = \lambda^f(\overline{\sigma}_z + 2c_u) \tag{10.10}$$

where λ^f is a factor that depends on the length of the pile and applies over its total embedment length. Values of λ^f can be determined by referring to Fig. 10.13, with reference to the data summarised by Vijayvergiya and Focht (1972) for full-scale piles in overconsolidated fine-grained soils. The reduction in λ^f is linked to the pile installation process, which involves longer pile portions passing at shallow depths when driven into the soil compared to deeper depths and causes a higher reduction of shaft resistance in the former regions compared to the latter (Kraft et al., 1981). The factor λ^f includes both the effects of α^f and β^f (Bowles, 1988). For piles characterised by a length $L \leq 15$ m, it is preferable to use $0.2 \leq \lambda^f \leq 0.4$ to avoid an overprediction of the shaft resistance (Kraft et al., 1981). The maximum value of $\lambda^f = 0.4$ should be considered (Bowles, 1988). Despite all of the previous considerations, the unique value of λ^f over the pile length appears to be a marked limitation of the Lambda Method (Bowles, 1988).

Empirical approaches are also available to estimate the capacity of both displacement and nondisplacement piles in fine-grained soil. These approaches are discussed by Fleming et al. (2008) but they are not covered here.

A final alternative approach to estimate the capacity of piles in fine-grained soil assumes drained conditions upon loading so that an effective stress approach is

considered. This approach was originally proposed by Vesic (1967) and Chandler (1968), and further expanded by Burland (1973) based on the argument that although high excess pore water pressures are developed upon pile construction they are dissipated when the pile is loaded. The reason for this is because failure occurs in the very thin region of soil adjacent to or in the vicinity of the pile where drained conditions are prevalent. This approach has the great advantage of considering the whole actual stress history of the pile from its installation to its operation and is nowadays considered more appropriate than the previous approaches. Assuming in Eq. (10.2) the cohesive component is equal to zero (which especially at the pile–soil interface can be considered to be destroyed by remoulding during pile installation), neglecting the term $\frac{1}{2}\gamma' D N_\gamma s_\gamma d_\gamma$ because it is small in relation to the term involving N_q and considering both s_q and $d_q = 1$ by means of a conservative approach (when these terms appear in the employed base capacity formulation), the same expression as that summarised for piles in coarse-grained soils in Eq. (10.3) is obtained. As a result, the formulation of pile capacity is purely frictional. Nowadays, according to the arguments of Fleming et al. (2008), no pile design should be considered complete without an assessment of the effective stress state in the soil around displacement and nondisplacement piles. Based on this consideration, attention is given in the following to the determination of the parameters included in this last considered capacity formulation.

10.5.2 Displacement piles

Original approaches to estimate the coefficient $\overline{K}$ used in Eq. (10.3) were proposed by Burland (1973), Parry and Swain (1977) and Flaate and Selnes (1977). For piles in soft normally consolidated or slightly overconsolidated clay, the values of $\overline{K}$ may range between the lower bound $K_0 = 1 - \sin\varphi'$ (see Jaky, 1944) or the value $K_0 = (1 - \sin^2\varphi')/(1 + \sin^2\varphi')$. For piles in overconsolidated clay, the value of $\overline{K}$ may be considered as $K_0 = (1 - \sin\varphi')\sqrt{OCR}$, where OCR is the overconsolidation ratio of the soil (see Schmidt, 1966). In all of the above relationships, the soil angle of shear strength under constant volume conditions φ'_{cv} may be considered for the terms including both φ' and δ' (especially for piles longer than 30–40 m (Lancellotta, 1995)). If the soil angle of shear strength φ' would be available it may be considered that $\varphi'_{cv} = \arctan\left((\sin\varphi'\cos\varphi')/(1 + \sin^2\varphi')\right)$ (Randolph and Wroth, 1981). In the absence of contrary data, $\overline{\sigma'}_z$ and σ'_{zb} may be calculated according to the in situ vertical effective stress and the values of the factor N_q may be taken as equal to those for coarse-grained soil (Poulos and Davis, 1980). Examples of the trends of average shaft resistance along displacement piles in soft and stiff clays reported by Burland (1973), including data from Tomlinson (1957), Eide et al. (1961) and Hutchinson and Jensen (1968), and considering the factor β^f to be calculated according to the previous considerations, are shown in Fig. 10.14A and B, respectively.

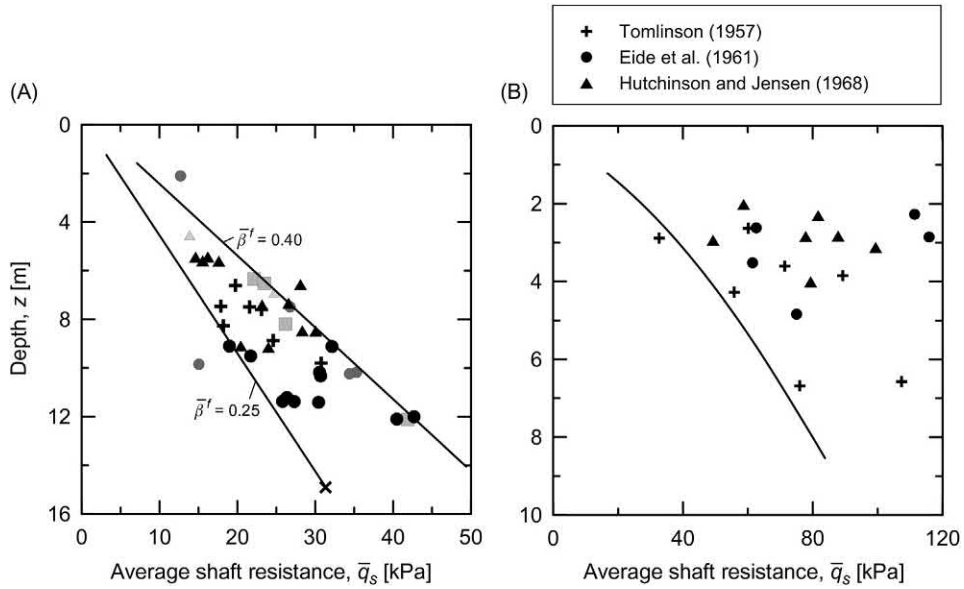

Figure 10.14 Average shaft resistance along displacement piles in (A) soft and (B) stiff clays. *Redrawn after Burland, J.B., 1973. Shaft friction of piles in clay—a simple fundamental approach. Ground Eng. 6 (3), 30–42.*

Although the above approaches may be valid to estimate the shaft resistance of piles in fine-grained soil in terms of effective stress, Fleming et al. (2008) argument that none of them takes due account of the stress variations that occur during and after pile installation. This phenomenon results in changes of the parameter $\overline{K}$ during installation and loading following the evolution of the pore water pressure (Fleming et al., 2008), and has been analysed in detail by Jardine and Chow (1996), Chow (1997) and Randolph (2003) through the development of more advanced approaches.

10.5.3 Nondisplacement piles

The estimation of the shaft capacity of nondisplacement piles in fine-grained soil through the effective stress approach is generally more straightforward than that for displacement piles.

The shaft resistance of nondisplacement piles in fine-grained soils may be accurately estimated assuming $\overline{K} = K_0$ because little variations of the soil stress state around the pile occur due to pile construction if concrete is promptly poured. In heavily overconsolidated clay some allowance for stress relaxation should be made reducing the value of $\overline{K}$ by 20% or the mean stress between the in situ horizontal stress and that due to the concrete poured into the pile shaft may be taken replacing $\overline{K}$ by $(1+K_0)/2$ (Fleming et al., 2008).

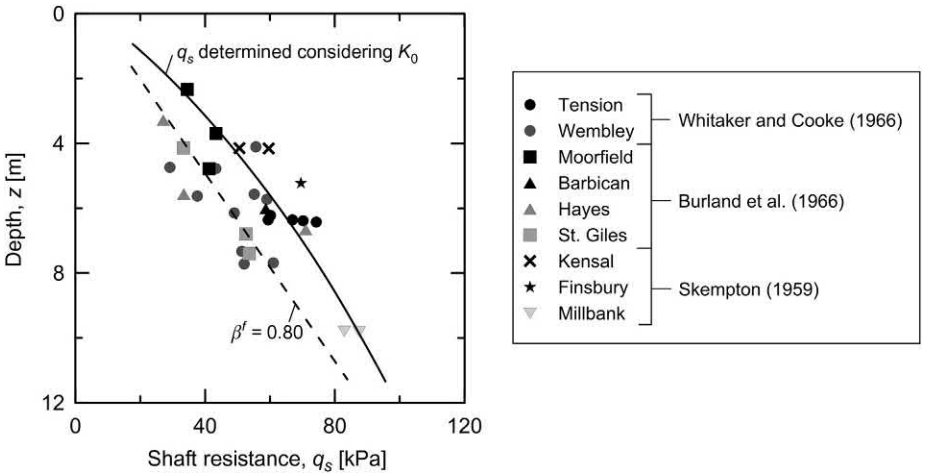

Figure 10.15 Shaft resistance of nondisplacement piles in stiff clays. *Redrawn after Burland, J.B., 1973. Shaft friction of piles in clay—a simple fundamental approach. Ground Eng. 6 (3), 30–42.*

The soil angle of shear strength under constant volume conditions φ'_{cv} may be considered for the terms including both φ' and δ' according to Burland and Twine (1988) for piles in overconsolidated clay. The previous approach may be unsuitable for very rough nondisplacement piles whereby failure may occur in the soil and not at the pile–soil interface. The parameters $\overline{\sigma'}_z$, σ'_{zb} and N_q may be determined as above.

An example of the trend of the average shaft resistance along nondisplacement piles in stiff clays reported by Burland (1973), including data from Whitaker and Cooke (1966), Burland et al. (1966) and Skempton (1959), and considering the factor β^f to be calculated according to the previous considerations, are shown in Fig. 10.15. As can be noted, determining the shaft resistance via the coefficient $\overline{K} = K_0$ yields an upper bound of the observed data, such an aspect corroborating the suggestions of Fleming et al. (2008) to consider $\overline{K} = (1+K_0)/2$.

10.6 Capacity in rock

10.6.1 General

Piles constructed in rock are generally characterised by a capacity contribution provided by the base that is significantly higher than the contribution provided by the shaft. This statement appears to be valid irrespective of whether piles founded on rock and socketed in soil or piles embedded in a rock mass are considered. In the former case, the intrinsically different properties characterising soil and rock yield to a higher base capacity than the shaft capacity. In the latter case, the disturbance of the rock surrounding the shaft is likely to involve a much lower shaft capacity

than the base capacity for the same material surrounding the pile. Although considerable shear transfer can characterise shallower soil layers embedding piles in rock (Fleming et al., 2008), the shaft capacity is thus often neglected in design in spite of the base capacity. Because of the significant stiffness and strength of rocks, the maximum load applicable to piles founded on these materials may not be associated with the capacity provided by the rock. In contrast, the maximum applicable load should be determined with reference to the stresses developed in the pile. Neglecting this aspect may involve the failure of the pile material before that of the ground.

When piles are embedded in soil, the approaches described in the previous sections to estimate the shaft capacity can be employed. Different approaches must be considered when piles are embedded in rock or they simply rest on this material. In general, both the shaft and base capacity piles in rock are customarily considered as proportional to the unconfined compressive strength of the rock, *UCS* (Horvath et al., 1980; Williams and Pells, 1981; Rowe and Armitage, 1987; Zhang and Einstein, 1998).

10.6.2 Shaft capacity

According to Fleming et al. (2008), shear forces are developed at the interface between piles and rocks depending on (1) the frictional characteristics of the rock, (2) the degree of roughness of the socket and (3) the strength properties of the host rock. Most approaches indicate that the shaft resistance is proportional to the square root of the rock unconfined compressive strength (Kulhawy and Phoon, 1993; Randolph and Wroth, 1981; Fleming et al., 2008). At the same time, a remarkable discontinuity in the transition zone between hard soils and soft rocks is highlighted by Fleming et al. (2008) and can be noted in Fig. 10.16. The plotted lines follow the following expressions

$$q_s = p_a \psi \left(\frac{c_u}{p_a} \right)^{0.5} \quad \text{for hard soils} \tag{10.11}$$

$$q_s = p_a \psi \left(\frac{UCS}{p_a} \right)^{0.5} \quad \text{for rocks} \tag{10.12}$$

where p_a is the atmospheric pressure, $\psi = 0.5$ for the fine-grained soil data and $\psi = 2$ for the main soft rock data.

According to Poulos and Davis (1980) and Fleming et al. (2008), failure of reinforced concrete piles embedded in nonfractured rock may occur at shaft resistance levels of the order of 5% to 20% of the compressive strength of concrete. Values of adhesion for piles embedded in fractured rock at failure are likely to range between 75 and 150 kPa (Poulos and Davis, 1980).

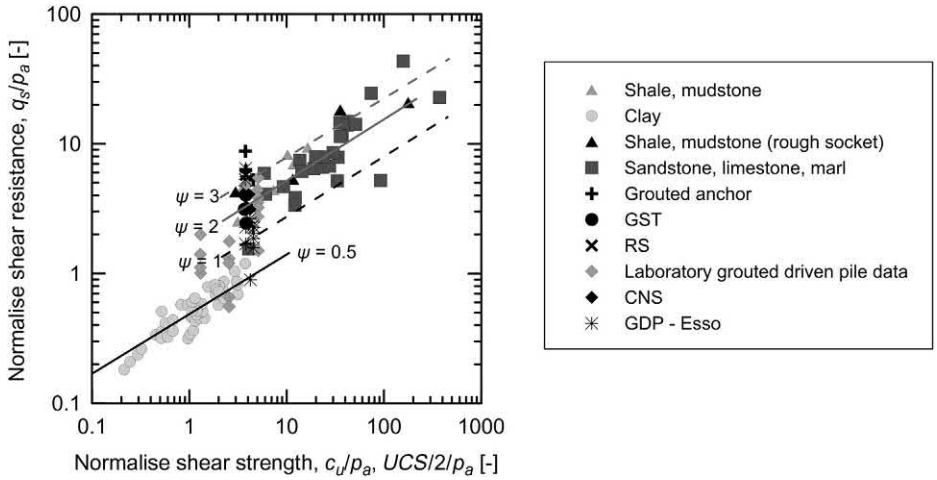

Figure 10.16 Relationship between normalised shaft resistance and shear strength of piles in hard soils and rocks. *Redrawn after Fleming, K., Weltman, A., Randolph, M., Elson, K., 2008. Piling Engineering. CRC Press.*

10.6.3 Base capacity

According to Zhang and Einstein (1998), the base resistance of piles resting on rock (e.g. associated with a normalised displacement of 10% of the pile diameter) is proportional to the square root of the rock unconfined compressive strength as

$$q_b \approx 15\left(\frac{UCS}{p_a}\right)^{0.5} \tag{10.13}$$

Besides the previous formulation that may be employed to limit the end-bearing pressures for piles resting on rock, other formulations do exist and are discussed by Poulos and Davis (1980) and Fleming et al. (2008). However, the usual consideration of pile capacity associated with a normalised displacement of 10% of the pile diameter suggests using the approach proposed by Zhang and Einstein (1998) that has also been verified through model tests and experimental tests by Randolph et al. (1998). Fig. 10.17 shows the application of the considered formulation with reference to the results reported by Randolph et al. (1998).

10.7 Generalised axial deformation formulation

The general equation that governs the axial deformation of energy piles, neglecting the contribution of the pile weight W, reads

$$P + \frac{\pi D^2}{4} K_h w_h + Q_{s,mob} + Q_{b,mob} = 0 \tag{10.14}$$

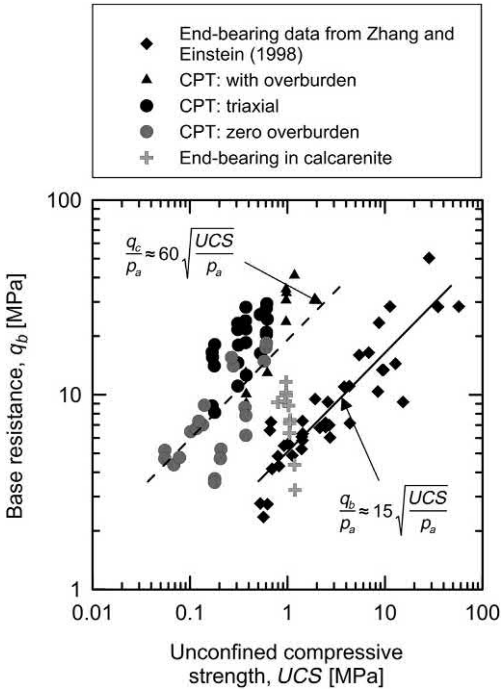

Figure 10.17 Relationship between base resistance and unconfined compressive strength of hard soils and rocks. *Redrawn after Fleming, K., Weltman, A., Randolph, M., Elson, K., 2008. Piling Engineering. CRC Press.*

where P is the applied mechanical load, K_h is the head stiffness of the structural element connected to the pile head, w_h is the pile head vertical displacement, $Q_{s,mob}$ is the mobilised portion of the pile shaft capacity Q_s and $Q_{b,mob}$ is the mobilised portion of pile base capacity Q_b (cf. Fig. 10.18). The term $Q_{s,mob}$ is associated with the mobilised shaft resistance τ along the external surface of the pile shaft A_s, and the term $Q_{b,mob}$ is proportional to a relevant vertical stress σ_{zb} mobilised at the level of the pile base characterised by a cross-sectional area A_b.

To distinguish the different mechanical response of energy piles subjected to mechanical and thermal loads, $Q_{s,mob}$ and $Q_{b,mob}$ can be written in terms of a mechanical and a thermal contribution as (Mimouni and Laloui, 2014)

$$Q_{s,mob} = Q^{m}_{s,mob} + Q^{th}_{s,mob} \tag{10.15}$$

and

$$Q_{b,mob} = Q^{m}_{b,mob} + Q^{th}_{b,mob} \tag{10.16}$$

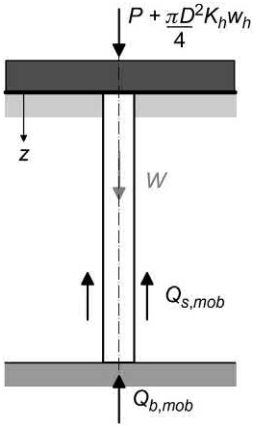

Figure 10.18 Axial equilibrium of a pile.

The reason for this is that, in contrast to the influence of conventionally applied mechanical loads that cause a pile displacement in a unique direction (e.g. downward), thermal loads applied to energy piles generally involve two pile portions that displace in opposite directions (e.g. upward and downward) from the so-called null point of the vertical displacement (located at a depth, $z_{NP,w}$) (Laloui et al., 2003). Accordingly, shear stress is mobilised in opposite directions at the pile shaft to ensure equilibrium with the surrounding soil from the so-called null point of the shear stress [generally located at a different depth, $z_{NP,\tau}$, than that of the null point of the vertical displacement (Rotta Loria et al., 2018)]. Based on the above, $Q^{th}_{s,mob}$ can also be written in terms of two contributions as (Mimouni and Laloui, 2014)

$$Q^{th}_{s,mob} = Q_{s,mob,up} + Q_{s,mob,down} \tag{10.17}$$

where, for cylindrical energy piles,

$$Q_{s,mob,up} = \pi D \int_0^{z_{NP,\tau}} \tau dz \tag{10.18}$$

and

$$Q_{s,mob,down} = \pi D \int_{z_{NP,\tau}}^{L} \tau dz \tag{10.19}$$

The presence of the null points of the vertical displacement and shear stress in energy piles subjected to thermal loads involves a key difference for modelling the response of such foundations compared to conventional piles subjected to only mechanical loads. Closed form analytical expressions are available to describe the axial

response of piles subjected to mechanical loads (Randolph and Wroth, 1978; Cooke, 1974; Frank, 1975). The reason for this is that the deformation caused by mechanical loads can be associated with a plane state of strain and described via relatively simple mathematical developments. However, as plane strain conditions cannot be associated with the influence of thermal loads because of the presence of the null point (Rotta Loria et al., 2018), iterative solutions are employed to solve the vertical equilibrium equation of energy piles subjected to the latter considered loads. The foregoing considerations suggest that semianalytical methods or numerical approaches are needed to address the mechanical response of energy piles under the action of thermal loads, applied alone or in conjunction with mechanical loads.

10.8 Thermomechanical schemes

10.8.1 General

When no semianalytical or numerical tools may be available to address the response of energy piles to thermal loads, applied alone or in conjunction with mechanical loads, schemes addressing the influence of the considered loads become powerful tools to characterise the response of such foundations. Original thermomechanical schemes have been proposed by Bourne-Webb et al. (2009, 2011) with reference to results of full-scale in situ tests of single energy piles and may be considered for the previous purpose. However, schemes based on theoretical principles may more closely reflect the predictions made for the analysis and design of energy piles. Thermomechanical schemes based on elastic theory have been proposed by Rotta Loria and Laloui (2018b) and are presented in the following. In these schemes, the energy piles are considered to follow a linear thermoelastic behaviour, whereas the surrounding soil is considered to follow a linear elastic behaviour (i.e. the soil is considered as an infinite heat reservoir that remains at a constant fixed temperature).

As the proposed schemes are based on (thermo-)elasticity theory:

- They are representative of the response of single energy piles at any stage of their geothermal operation when the soil−pile thermal expansion coefficient ratio reads $X = \alpha_{soil}/\alpha_{EP} \leq 1$ (where α_{soil} and α_{EP} are the linear thermal expansion coefficients of the soil and pile, respectively), while only at early stages of geothermal operations when $X > 1$. The reason for this is because considering the soil to be isothermal inherently implies that the thermally induced deformation of this medium is negligible. The previous condition always holds when the thermal expansion of the soil is lower than or equal to that of the pile, that is for $X \leq 1$, whereas it holds when the thermal expansion coefficient of the soil is greater than that of the pile, that is for $X > 1$, only at early stages of geothermal operations at which the influence of soil deformation on that of the pile is limited (Bourne-Webb et al., 2016; Rotta Loria and Laloui, 2017b, 2018a).

- They describe nonlinear variations of the thermally induced vertical stress (and strain), whereas linear variations of the thermally induced shear stress (and displacement), as predicted by continuum mechanics theory. This feature is in contrast with the schemes presented by Bourne-Webb et al. (2009, 2011) that consider linear variations of the thermally induced vertical stress (and strain), whereas constant stepwise variations of the thermally induced shear stress. Nonlinearity actually characterises all of the considered fields and increases for increasing nonuniformity and decreasing relative stiffness between the energy pile and the soil.
- They describe linearly greater variations of the stress, strain and displacement along energy piles without any movement of the null points for greater magnitudes of applied loads. This feature vanishes as soon as the hypothesis of a linear (thermo-) elastic behaviour of the pile–soil system no longer applies (Rotta Loria et al., 2015).
- They involve symmetrical variations of stress, strain and displacement along energy piles subjected to the same magnitude of temperature variation associated with heating and cooling thermal loads. This feature vanishes as soon as the (thermo-) elastic hypothesis no longer applies (Rotta Loria and Laloui, 2016, 2017a).

In the following, thermomechanical schemes representative of energy piles (1) with no base and head restraints, (2) with base *or* head restraints and (3) with base *and* head restraints are presented. The analysed situations may be assumed to characterise energy piles (1) free at their head and embedded in soft soil, (2) free at their head and bearing on stiff soil *or* restrained at their head and embedded in soft soil and (3) restrained at their head *and* bearing on stiff soil, respectively.

10.8.2 Energy piles with no base and head restraints

The mechanical response of an energy pile with no base and head restraints to an axial mechanical load, a heating or cooling thermal load, and a mechanical and thermal load is depicted in Fig. 10.19. For the case of vertical mechanical loading only (cf. Fig. 10.19A), Eq. (10.14) can be written as

$$P + Q_{s,mob}^{m} = 0 \tag{10.20}$$

The application of an axial mechanical load to the pile head causes an approximately linearly decreasing distribution of compressive vertical stress σ_z along the pile and uniform and approximately constant distributions of positive shear stress τ at the pile–soil interface and downward pile displacement w with depth z. The higher the pile stiffness, the more uniform and linear the distribution of σ_z with z, and the more uniform and constant the distributions of τ and w with z. Soil layering causes a less uniform distribution of all the considered variables. Stronger mechanical loads cause linearly greater stress and displacement variations.

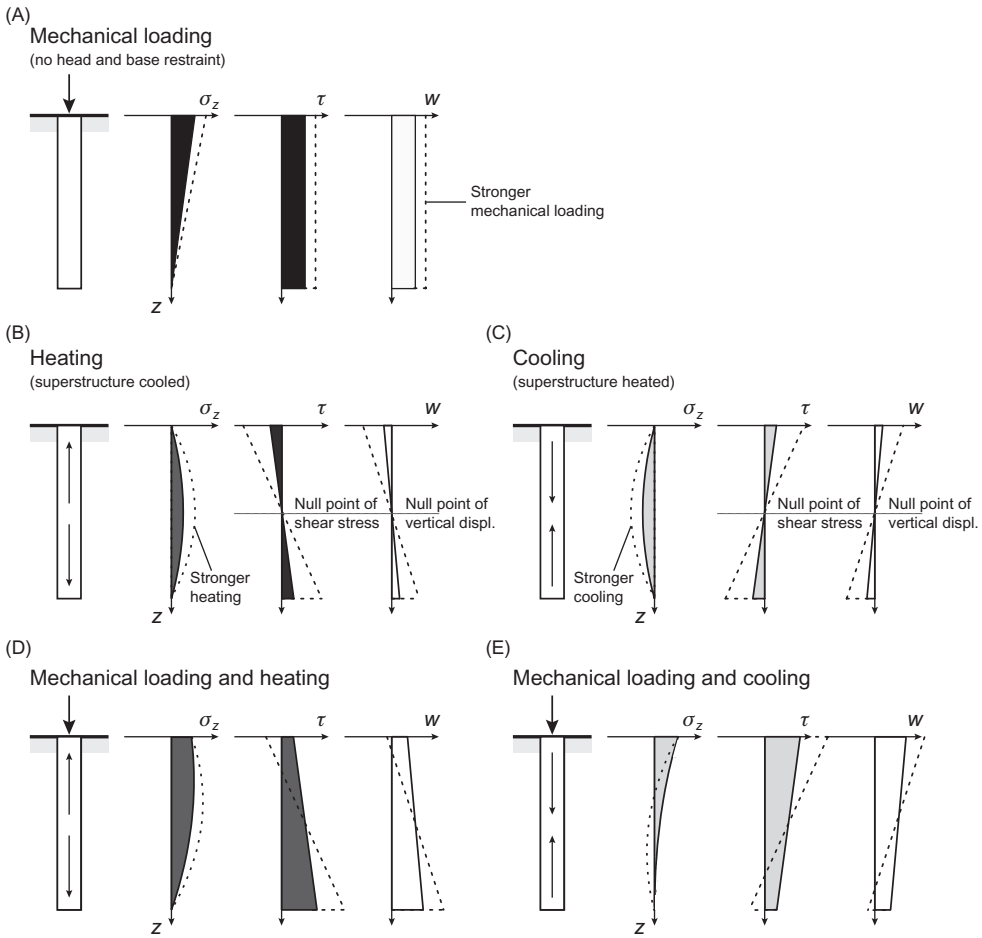

Figure 10.19 Thermomechanical schemes for energy piles characterised by no base and head restraints (Rotta Loria and Laloui, 2018b).

For the case of thermal loading only (cf. Fig. 10.19B and C), Eq. (10.14) can be rewritten as

$$Q_{s,mob}^{th} = Q_{s,mob,up} + Q_{s,mob,down} = 0 \tag{10.21}$$

The application of a heating or cooling thermal load to the pile causes a nonlinear distribution of σ_z with z (symmetrical for heating and cooling), which is characterised by a maximum that coincides with the mid-length of the energy pile, where the null points of the vertical displacement and shear stress are also located. The application of a heating thermal load mobilises negative shear stress and causes heave for the energy pile portion above the null points, while it mobilises positive shear stress and causes

settlement for the pile portion below the null points. The shear stress and vertical displacement caused by a heating thermal load develop in the opposite direction compared to those caused by a mechanical load above the null points, whereas these develop in the same direction below the null points. The opposite is true for a cooling thermal load. Shear stress and vertical displacement evolve approximately linearly with depth. The higher the pile stiffness, the more uniform the evolution of σ_z with z, and the lower the variation of σ_z for the same applied thermal load. Similarly, the higher the pile stiffness, the more uniform the evolutions of τ and w but the higher their variation. Stronger thermal loads cause linearly greater stress and displacement variations.

For the case of mechanical and thermal loading (cf. Fig. 10.19D and E), Eq. (10.14) can be rewritten as

$$P + Q_{s,mob} = P + Q^{m}_{s,mob} + Q^{th}_{s,mob} = 0 \tag{10.22}$$

The distributions of vertical stress and shear stress with depth as well as of vertical displacement can be obtained via superposition of the previous ones. Tensile stress along the energy piles can arise for low magnitudes of applied mechanical loads and significant cooling.

10.8.3 Energy piles with base or head restraints

The mechanical response of an energy pile with base or head restraints to an axial mechanical load, a heating thermal load, and a mechanical and heating thermal load is depicted in Fig. 10.20. For the case of vertical mechanical loading only (cf. Fig. 10.20A and B), Eq. (10.14) can be rewritten as

$$P + Q^{m}_{s,mob} + Q^{m}_{b,mob} = 0 \tag{10.23}$$

where only the base restraint is present, whereas

$$P + \pi \frac{D^2}{4} K_h w^{m}_{h} + Q^{m}_{s,mob} = 0 \tag{10.24}$$

where only the head restraint is present (with w^{m}_{h} the pile vertical head displacement caused by the mechanical load).

When a base restraint is present, a greater average vertical stress σ_z (with a value corresponding to P at the pile head) and lower shear stress τ and vertical displacement w develop along the pile compared to the case of no base and head restraints. This phenomenon arises because of the contribution provided by the base capacity to the vertical pile equilibrium. In these schemes, the base capacity mobilises at the same time as the shaft capacity for any magnitude of applied load, even though this is not necessarily the case in reality.

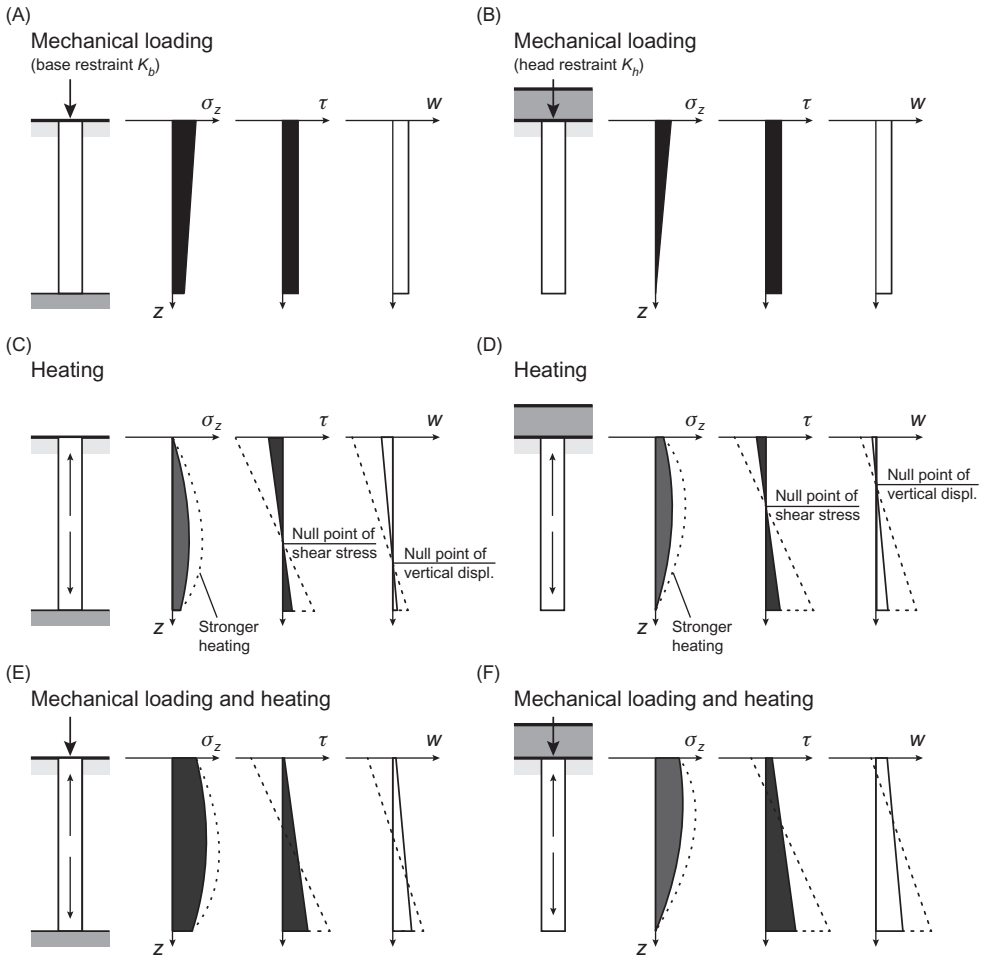

Figure 10.20 Thermomechanical schemes for energy piles characterised by base or head restraints (Rotta Loria and Laloui, 2018b).

When a head restraint is present, a smaller average vertical stress σ_z (with a corresponding value lower than that of P at the pile head) and lower shear stress and vertical displacement variations develop along the pile compared to the case of no base and head restraints. This phenomenon arises because the head restraint reduces the effect of the downward mechanical load. This effect vanishes when the interplay between the mechanical load and the head restraint is not considered because the latter term is neglected. The consequence of such an approach is a pile response to mechanical loading equal to that of the case of no base and head restraints.

For the case of heating thermal loading only (cf. Fig. 10.20C and D), Eq. (10.14) can be rewritten as

$$Q_{s,mob}^{th} + Q_{b,mob}^{th} = 0 \tag{10.25}$$

where only the base restraint is present, whereas

$$\pi \frac{D^2}{4} K_h w_h^{th} + Q_{s,mob}^{th} = 0 \tag{10.26}$$

where only the head restraint is present (with w_h^{th} the pile vertical head displacement caused by the thermal load).

Different from the situation where no base or head restraints are present, when either a base or head restraint is present, vertical stress σ_z is generated at the restrained pile end by the applied thermal load. The vertical stress distribution is greater than that in the case with no base and head restraints, in accordance with the discussed effect of the higher restraint of the system. The null points of the vertical displacement and shear stress do not coincide but are shifted towards the region of the system characterised by the higher restraint. Lower vertical displacement develops towards the region of the system characterised by higher restraint, while higher displacement develops towards the region characterised by lower restraint compared to the case where the null points are located at the mid-length of the pile. A cooling thermal load yields a symmetrical response of the energy pile. In reality, the reduction of the compressive stress experienced at the pile toe for the case where a base restraint is present can attain at most the sum of any vertical mechanical load applied to the pile and its weight. This phenomenon occurs because soils generally cannot withstand tensile stress.

For the case of mechanical and heating thermal loading (cf. Fig. 10.20E and F), Eq. (10.14) can be rewritten as

$$P + Q_{s,mob} + Q_{b,mob} = 0 \tag{10.27}$$

where the base restraint is present, whereas

$$P + \pi \frac{D^2}{4} K_h w_h^{m+th} + Q_{s,mob} = 0 \tag{10.28}$$

where the head restraint is present (with w_h^{m+th} the pile vertical head displacement caused by the mechanical and thermal loads).

The distributions of vertical stress and shear stress with depth as well as of vertical displacement can be obtained via superposition of the previous ones.

10.8.4 Energy piles with base and head restraints

The mechanical response of an energy pile with base and head restraints to an axial mechanical load, a heating thermal load, and a mechanical and heating thermal load is

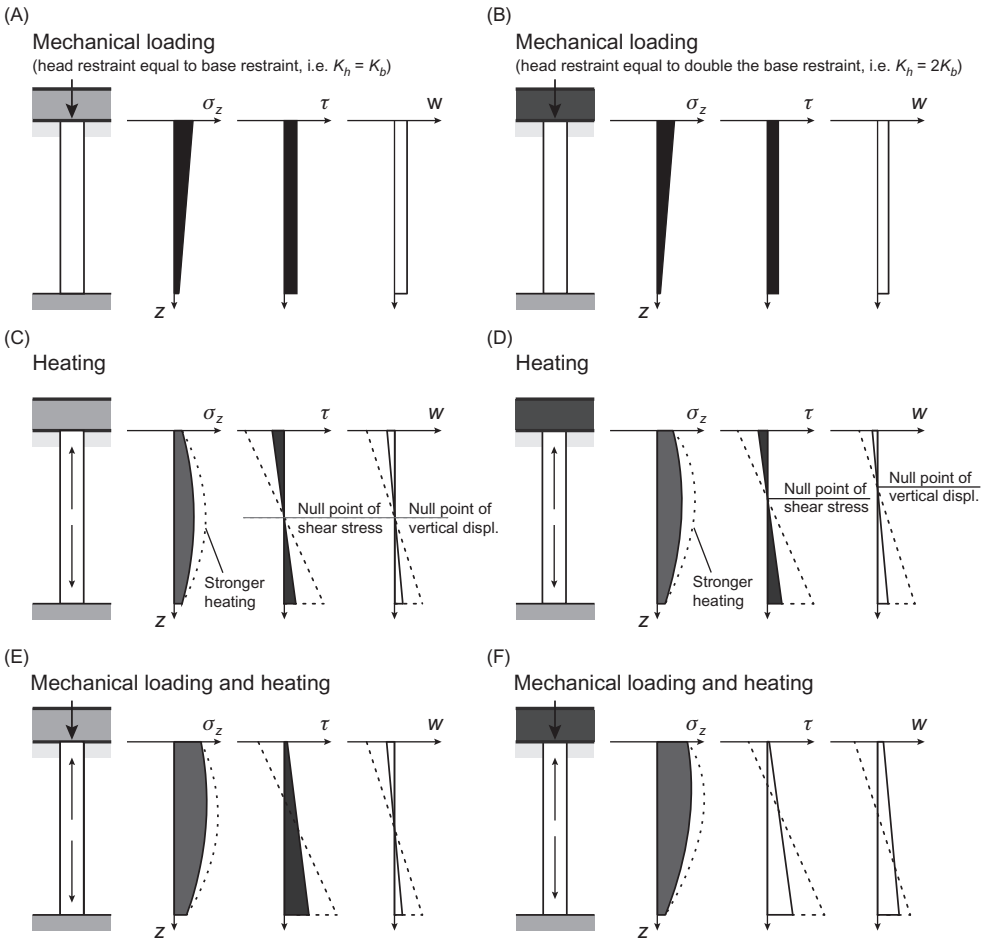

Figure 10.21 Thermomechanical schemes for energy piles characterised by base and head restraints (Rotta Loria and Laloui, 2018b).

depicted in Fig. 10.21. Two different cases involving a base restraint equal to the head restraint and a base restraint equal to one half of the head restraint are considered. For the case of vertical mechanical loading only (cf. Fig. 10.21A and B), Eq. (10.14) can be rewritten as

$$P + \pi \frac{D^2}{4} K_h w_h^m + Q_{s,mob}^m + Q_{b,mob}^m = 0 \tag{10.29}$$

In the proposed schemes, the effect of the presence of the slab on the influence of the mechanical load on the pile response is considered. Hence, lower developments of vertical stress and shear stress as well as of vertical displacement are observed for a

higher head restraint, compared to the case of a base restraint only. This behaviour may be expected in reality. However, many analyses and designs usually do not account for the interplay between the action of the mechanical load and the head restraint, neglecting the latter term.

For the case of heating thermal loading only (cf. Fig. 10.21C and D), Eq. (10.14) can be rewritten as

$$\pi \frac{D^2}{4} K_h w_h^{th} + Q_{s,mob}^{th} + Q_{b,mob}^{th} = 0 \tag{10.30}$$

The vertical stress σ_z caused by the thermal load is characterised by a symmetrical distribution with depth z when the base and head restraints are of the same magnitude, whereas by an asymmetrical distribution when different magnitudes characterise the end-restraints. Higher stress develops towards the region of the system characterised by higher restraint. The higher the restraint provided by the end conditions, the higher the vertical stress and the lower the mobilised shear stress and vertical displacement.

For the case of mechanical and heating thermal loading (cf. Fig. 10.21E and F), Eq. (10.14) governs the system, the response of which can be obtained via superposition of the analysed situations.

10.9 Displacement charts

10.9.1 General

Another useful tool for characterising the response of single energy piles subjected to mechanical and thermal loads, with a focus on the axial deformation of such foundations, is represented by charts. A comprehensive number of charts based on the integral equation method or the boundary element method have been proposed to predict the load distribution and the settlement of piles subjected to only mechanical loads by Poulos and Davis (1968), Poulos and Mattes (1969), Butterfield and Banerjee (1971) and Banerjee and Davies (1978). Additional charts based on the load-transfer method and the finite element method have been proposed to describe the load distribution, the settlement or the heave of piles subjected to thermal loads by Burlon et al. (2013), Mimouni and Laloui (2014), Chen and McCartney (2016), Rotta Loria and Laloui (2016, 2017a) and Rammal et al. (2018).

Simplified yet effective charts have been often based on linear elastic theory. The reason for this is because the load-settlement behaviour of piles is essentially linear to a load well beyond half of the failure load (Poulos and Davis, 1980), and the results of the considered theory may thus be representative for deformation-related

considerations. However, it must be borne in mind that soil deformation can often be nonlinear and may involve reversible (i.e. elastic) or irreversible (i.e. plastic) stress–strain behaviour (Rotta Loria et al., 2017).

As a consequence of the nonlinear character of soil deformation, different deformation modulus values can be associated with the varying shear strain levels that characterise the soil surrounding piles (e.g. as a result of loading or construction effects). The soil region adjacent to or in the vicinity of the shaft of single piles subjected to mechanical loads undergoes high shear strains in the order of 0.005%–0.015% (Randolph, 1994). These strain levels are associated with lower soil modulus values and generally correspond to reversible or irreversible soil behaviour that remains localised close to the pile (Caputo and Viggiani, 1984; Jardine et al., 1986; Chow, 1986a). The bulk of the soil between piles experiences low shear strains that may be orders of magnitude smaller than those near the piles and typically less than approximately 0.001% (Randolph, 1994). These strain levels are associated with higher soil modulus values and generally correspond to a soil behaviour that may be considered to be reversible, as are the interactions between the piles (Caputo and Viggiani, 1984; Chow, 1986a).

Based on the aforementioned considerations, soil modulus values that are associated with high strain levels can be used to characterise the vertical displacement behaviour of the single piles composing any group. On the other hand, soil modulus values that are associated with low strain levels can be used to estimate the interaction between the piles. The previous approach can make analyses based on linear elastic theory capable of addressing the nonlinear stress–strain response of the soil, once the absence of failure or relative slip between pile and soil have been verified. The usefulness of this approach, however, rests on the degree of accuracy with which values of soil modulus may be chosen (Fleming et al., 2008). The correlations proposed for fine-grained soils by Weltman and Healy (1978), Jardine et al. (1986), Kagawa (1992) and Viggiani (2001), and for coarse-grained soils by Carriglio et al. (1990), Baldi et al. (1989), Robertson (1991), Wroth (1979) and Randolph (1981), for example can be used for choosing appropriate values of soil deformation modulus.

Besides the previous considerations, the vertical deformation of single energy piles caused by a given magnitude and combination of mechanical and thermal loads depends on (1) the pile and soil stiffness, (2) the pile geometry, (3) the features of the end-restraints, (4) the thermal expansion potential of pile and soil, (5) the time characterising the geothermal operation of the energy pile and (6) the rate of loading. Assuming drained conditions to be preserved upon loading involves that in most practical cases aspects (1)–(5) govern the response of single energy piles.

In the following, charts summarising the vertical head displacement of piles per unit mechanical load or temperature change applied to such foundations are presented

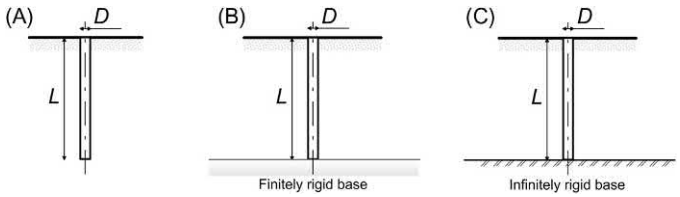

Figure 10.22 The modelled problems: energy pile (A) embedded in a uniform half space, (B) embedded in a shallower uniform soil layer and resting on a finitely rigid uniform soil layer and (C) embedded in a shallower uniform soil layer and resting on an infinitely rigid uniform soil layer.

for varying slenderness ratios, L/D, and pile–soil stiffness ratios, $\Lambda = E_{EP}/G_{soil}$ (where E_{EP} is the pile Young's modulus and G_{soil} is the soil shear modulus). Predominantly floating piles embedded in a uniform soil mass as well as predominantly end-bearing piles embedded in a uniform soil layer and resting on an either finitely or infinitely rigid soil stratum are considered (cf. Fig. 10.22).

The charts draw from the results of axisymmetric thermomechanical finite element analyses performed by Rotta Loria and Laloui (2016, 2017a). These analyses consider linear thermoelastic pile behaviour and linear elastic soil behaviour (the soil is an infinite heat reservoir whose response is independent of the time characterising the geothermal operation of the energy pile). They do not account for the influence of the pile weight, whereas they do account for radial deformations of the piles depending on the value of soil Poisson's ratio, ν_{soil}. In all cases, the piles are assumed free to move at their head (i.e. infinitely flexible slab), with the advantage of conservatively analysing the vertical (e.g. head) displacement of piles according to the widely used assumption of a negligible contribution of the uppermost slabs or other shallow foundations in the deformation of piles, at least for preliminary analyses and designs (Poulos and Davis, 1980; Bowles, 1988; Fleming et al., 2008).

The elastic assumption characterising the following charts involves that the reported displacement variations caused by a unit compressive mechanical load or by a unit temperature change associated with a heating thermal load are the same in absolute value than those caused by a unit tensile mechanical load or by a unit temperature change associated with a cooling thermal load, respectively (Rotta Loria and Laloui, 2016, 2017a). The consideration of uniform soil layers also involves that the following charts may be rigorously applied only for piles embedded in soil deposits characterised by similar properties. However, according to Poulos and Davis (1980), the following charts may also be approximately employed for piles in layered (i.e. nonuniform) soil deposits where the variation of the deformation moduli between successive layers is not large, with reference to an average soil deformation modulus that can be estimated as follows

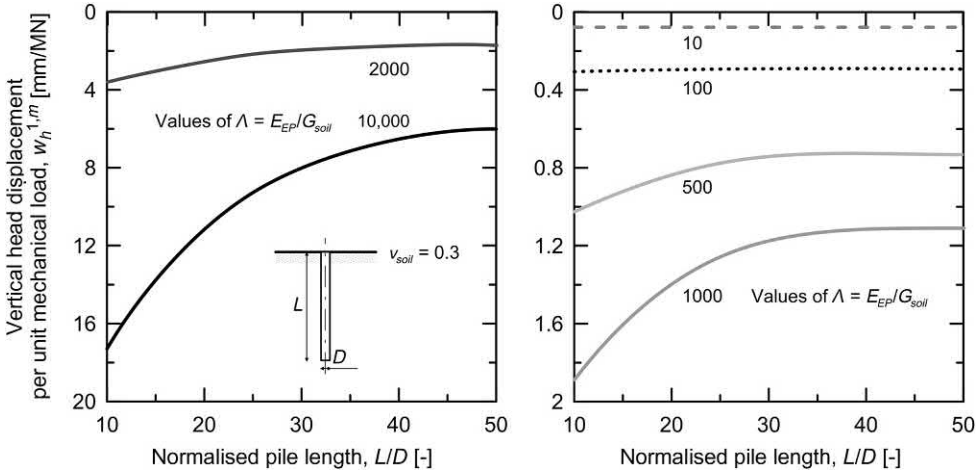

Figure 10.23 Vertical head displacement per unit mechanical load for different L/D—predominantly floating energy pile embedded in uniform mass.

$$\overline{G}_{soil} = \frac{1}{\sum_{k=1}^{N} l_k} \sum_{k=1}^{N} G_{soil,k} l_k \tag{10.31}$$

where l_k is the height of layer k composing a layered soil deposit of total number of layers N and $G_{soil,k}$ is the shear modulus of the layer k.

10.9.2 Charts for mechanical loads

The vertical head displacement $w_h^{1,m}$ per unit mechanical load $P = 1$ MN of a predominantly floating energy pile characterised by varying slenderness ratios L/D is presented in Fig. 10.23 for the case of a uniform soil deposit of varying pile–soil stiffness ratios $\Lambda = E_{EP}/G_{soil}$. Reference is made to a Poisson's ratio of the soil of $\nu_{soil} = 0.3$. For the same Λ, decreasing values of $w_h^{1,m}$ are observed for increasing normalised pile lengths (i.e. slenderness ratios L/D). The significance of this pile head settlement decrease with increasing pile length becomes less pronounced for a decrease in the pile–soil stiffness ratio. For the same L/D, the values of $w_h^{1,m}$ decrease with Λ. Complementary charts for piles subjected to mechanical loads in a uniform soil deposit are reported by Poulos and Davis (1980).

The vertical head displacement $w_h^{1,m}$ per unit mechanical load $P = 1$ MN of a predominantly end-bearing energy pile characterised by varying slenderness ratios L/D is presented from Figs 10.24–10.28 for the case of a soil deposit composed of a shallower uniform soil layer embedding the pile of varying pile–soil stiffness ratio $\Lambda = E_{EP}/G_{soil,s}$ (where $G_{soil,s}$ is the shear modulus of the soil socketing the pile shaft) and a deeper soil stratum. Increasing stiffness with respect of the soil layer surrounding

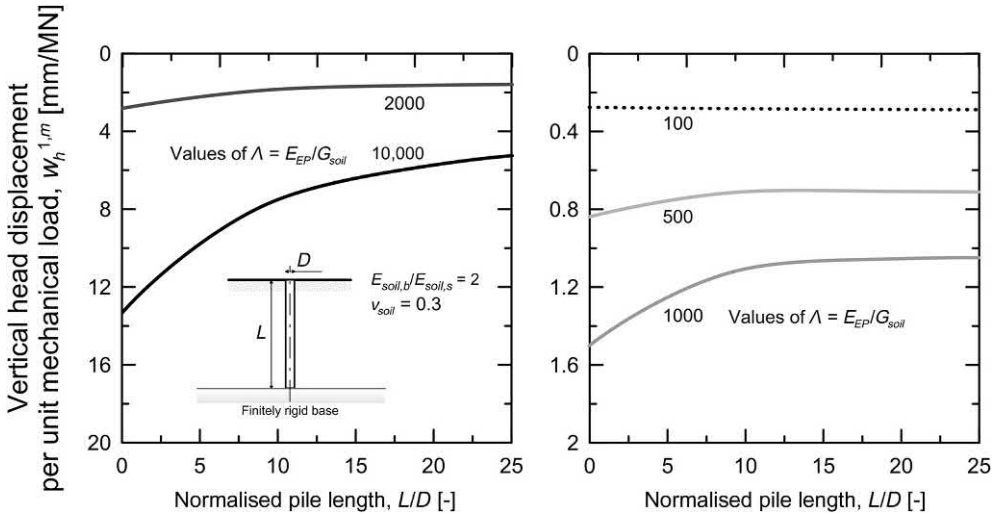

Figure 10.24 Vertical head displacement per unit mechanical load for different L/D—predominantly end-bearing pile resting on finitely rigid soil strata ($E_{soil,b}/E_{soil,s} = 2$).

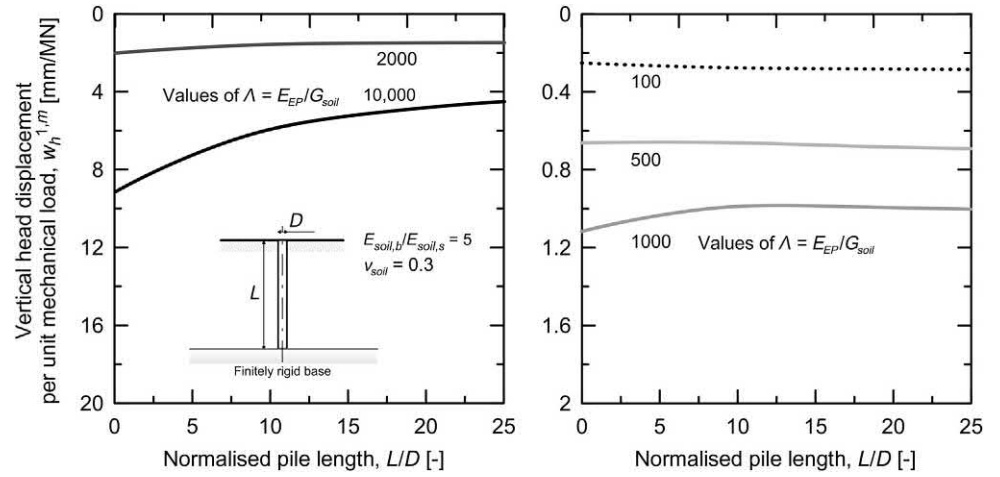

Figure 10.25 Vertical head displacement per unit mechanical load for different L/D—predominantly end-bearing pile resting on finitely rigid soil strata ($E_{soil,b}/E_{soil,s} = 5$).

the pile shaft are considered for the bearing stratum. This feature is characterised by the base-to-shaft soil Young's modulus ratio $E_{soil,b}/E_{soil,s}$. For values of $E_{soil,b}/E_{soil,s}$ greater than 1000 the effect of the rigidity of the bearing soil layer involves a pile response comparable to that for the case of an infinitely rigid base. Lower values of Λ are associated with lower head settlements for piles characterised by the same L/D. However, while decreasing values of $w_h^{1,m}$ are observed for an increase in L/D with

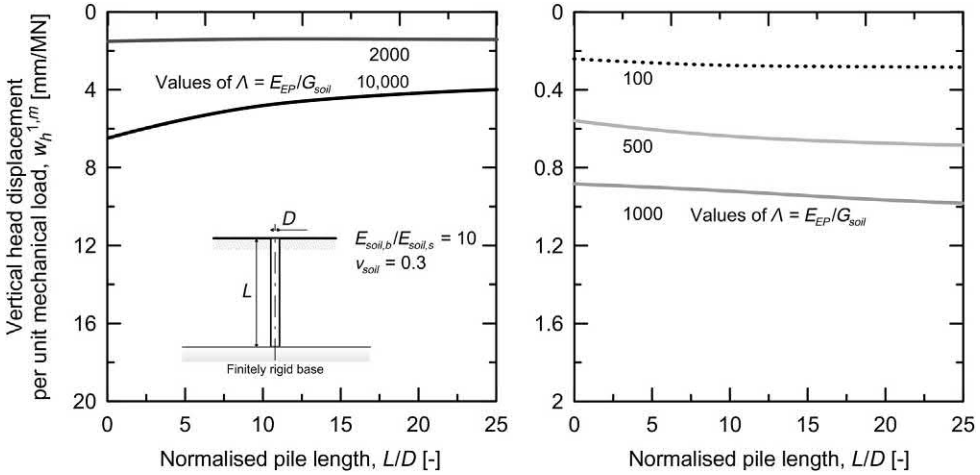

Figure 10.26 Vertical head displacement per unit mechanical load for different L/D—predominantly end-bearing pile resting on finitely rigid soil strata ($E_{soil,b}/E_{soil,s} = 10$).

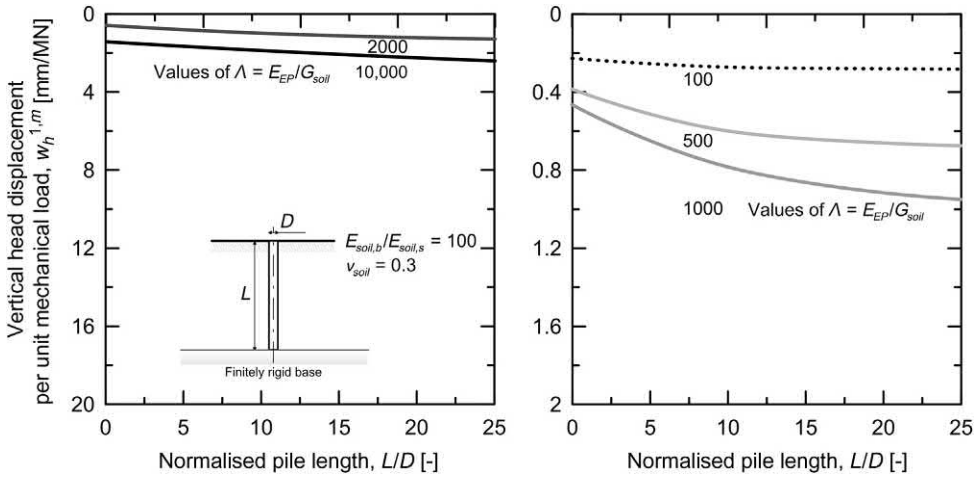

Figure 10.27 Vertical head displacement per unit mechanical load for different L/D—predominantly end-bearing pile resting on finitely rigid soil strata ($E_{soil,b}/E_{soil,s} = 100$).

reference to the more significant values of Λ and the smaller values of $E_{soil,b}/E_{soil,s}$, the opposite occurs for a further decrease of Λ and an increase of $E_{soil,b}/E_{soil,s}$. That is pile head settlement values increase with the increase of L/D for a given value of Λ. This phenomenon can be attributed to the influence of the stiffness of the base layer on the relative pile to soil deformation. Complementary charts for piles subjected to mechanical loads in a nonuniform soil deposit are reported by Poulos and Davis (1980).

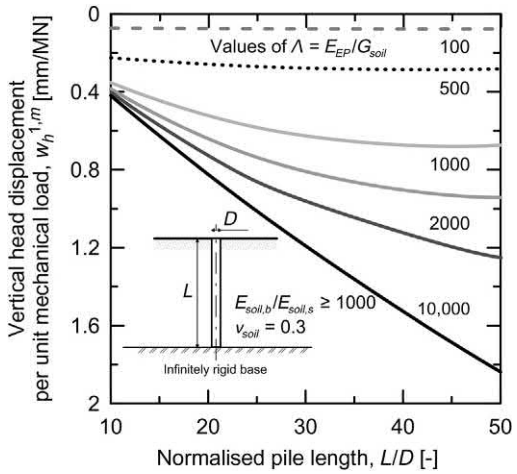

Figure 10.28 Vertical head displacement per unit mechanical for different L/D—predominantly end-bearing pile resting on soil strata that can be considered to be infinitely rigid ($E_{soil,b}/E_{soil,s} \geq 1000$).

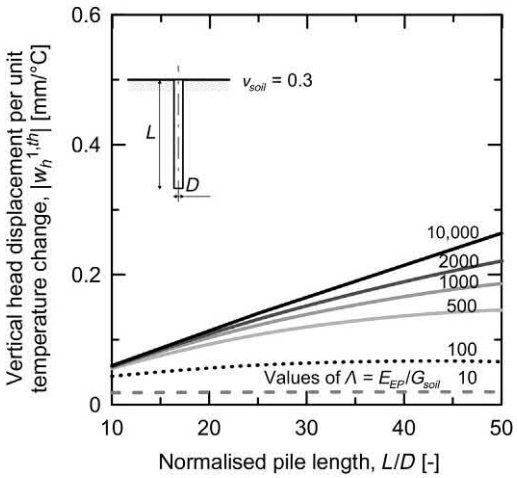

Figure 10.29 Vertical head displacement per unit temperature change for different L/D—predominantly floating energy pile embedded in uniform mass. *Modified after Rotta Loria, A. F., Laloui, L., 2016. The interaction factor method for energy pile groups. Comput. Geotech. 80, 121–137.*

10.9.3 Charts for thermal loads

Absolute values of the vertical head displacement $w_h^{1,th}$ per unit temperature change $\Delta T = 1°C$ of a predominantly floating energy pile characterised by varying slenderness ratios L/D is presented in Fig. 10.29 for the case of a uniform soil deposit of varying pile–soil stiffness ratios $\Lambda = E_{EP}/G_{soil}$. Reference is made to a Poisson's ratio of the

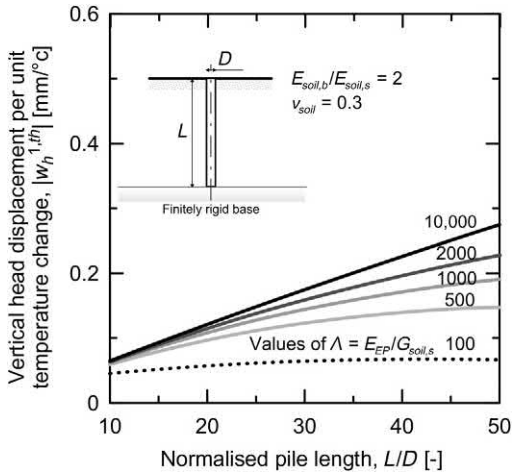

Figure 10.30 Vertical head displacement per unit temperature change for different L/D—predominantly end-bearing pile resting on finitely rigid soil strata ($E_{soil,b}/E_{soil,s} = 2$). *Modified after Rotta Loria, A.F., Laloui, L., 2017a. Displacement interaction among energy piles bearing on stiff soil strata. Comput. Geotech. 90, 144–154.*

soil of $\nu_{soil} = 0.3$. For the same Λ, increasing values of $w_h^{1,th}$ are observed for increasing L/D. This phenomenon indicates an opposite influence of the pile slenderness ratio on the vertical head displacement of piles subjected to thermal loads compared to mechanical loads. The significance of the considered pile head settlement increases with increasing pile length becomes less pronounced for a decrease in the pile–soil stiffness ratio. For the same L/D, the values of $w_h^{1,th}$ decrease with Λ. This phenomenon is caused by the increasing restraint provided by the soil surrounding the pile on the observed thermally induced pile deformation for decreasing values of Λ.

Similar evolutions of vertical head displacement per unit temperature change are observed for a predominantly end-bearing energy pile embedded in a soil deposit composed of a shallower uniform soil layer of varying $\Lambda = E_{EP}/G_{soil,s}$ and a deeper soil stratum of increasing $E_{soil,b}/E_{soil,s}$, as shown from Figs 10.30–10.34. For values of $E_{soil,b}/E_{soil,s}$ greater than 1000 the effect of the rigidity of the bearing soil layer involves a pile response comparable to that for the case of an infinitely rigid base. The vertical head displacement increases with the presence and increasing stiffness of a bearing soil stratum until the limiting case of a pile resting on an infinitely rigid layer is considered.

10.10 Load-transfer analysis approach

10.10.1 Background

The load-transfer method is an analysis approach originally proposed by Coyle and Reese (1966) to describe the load-displacement behaviour of conventional piles subjected to only mechanical loads. In recent years, this approach has been extended to

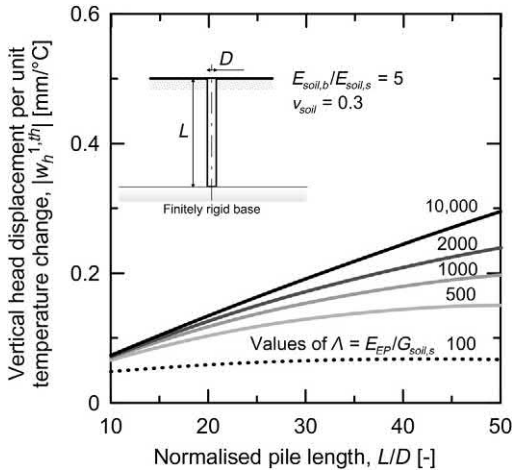

Figure 10.31 Vertical head displacement per unit temperature change for different L/D—predominantly end-bearing pile resting on finitely rigid soil strata ($E_{soil,b}/E_{soil,s} = 5$). *Modified after Rotta Loria, A.F., Laloui, L., 2017a. Displacement interaction among energy piles bearing on stiff soil strata. Comput. Geotech. 90, 144–154.*

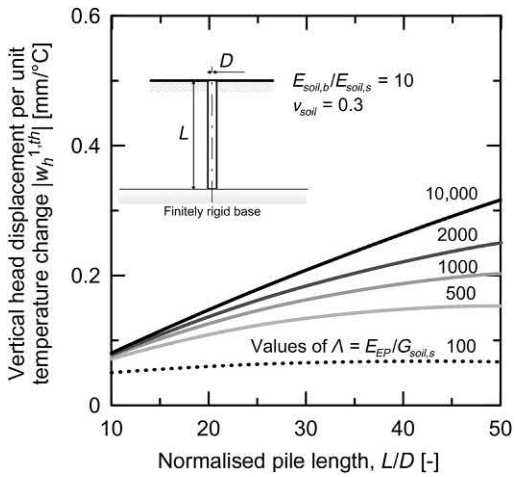

Figure 10.32 Vertical head displacement per unit temperature change for different L/D—predominantly end-bearing pile resting on finitely rigid soil strata ($E_{soil,b}/E_{soil,s} = 10$). *Modified after Rotta Loria, A.F., Laloui, L., 2017a. Displacement interaction among energy piles bearing on stiff soil strata. Comput. Geotech. 90, 144–154.*

describe the response of energy piles subjected to both mechanical and thermal loads by Knellwolf et al. (2011), Pasten and Santamarina (2014), Suryatriyastuti et al. (2014) and Chen and McCartney (2016) and Sutman et al. (2018). This method can solve the axial pile equilibrium equation and thus provides more comprehensive information

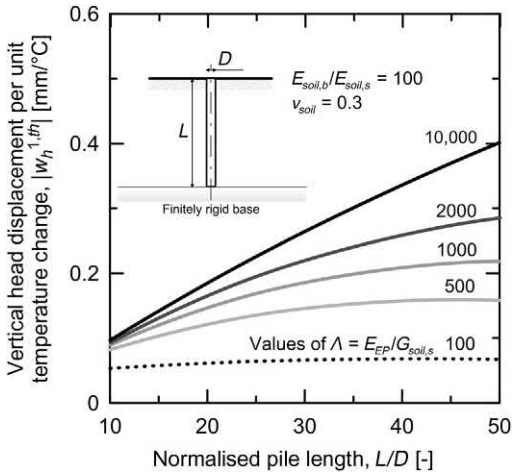

Figure 10.33 Vertical head displacement per unit temperature change for different L/D—predominantly end-bearing pile resting on finitely rigid soil strata ($E_{soil,b}/E_{soil,s} = 100$). *Modified after Rotta Loria, A.F., Laloui, L., 2017a. Displacement interaction among energy piles bearing on stiff soil strata. Comput. Geotech. 90, 144–154.*

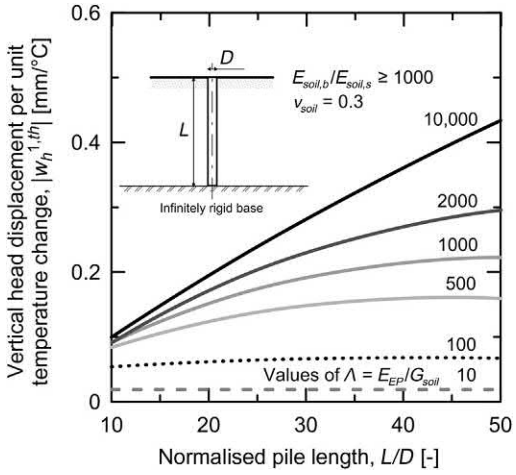

Figure 10.34 Vertical head displacement per unit temperature change for different L/D—predominantly end-bearing pile resting on soil strata that can be considered to be infinitely rigid ($E_{soil,b}/E_{soil,s} \geq 1000$). *Modified after Rotta Loria, A.F., Laloui, L., 2017a. Displacement interaction among energy piles bearing on stiff soil strata. Comput. Geotech. 90, 144–154.*

to account for the influence of both mechanical and thermal loads on the response of single energy piles than the previous approaches resorting to schemes or charts.

The load-transfer analysis approach relies on modelling single piles as being composed of several rigid elements that are linked with unconnected springs (i.e. springs

whose response does not depend on the response of the others along the pile) and interact with the surroundings through additional springs. Each of these springs is characterised by a constitutive law that determines the behaviour of the springs upon loading (or unloading) as well as the consequent response of the various pile elements. In the context of load-transfer analyses, the considered constitutive law is typically termed *load-transfer function* or *load-displacement relationship*. The discretisation of the pile in a number of elements allows considering various soil layers with distinct properties and the variation of the soil properties with depth. This fact makes the load-transfer method effective to model the response of piles in many practical situations.

Besides the previous capabilities and advantages, however, according to Poulos and Davis (1980) the load-transfer analysis approach should be considered as a fundamentally inferior method to numerical approaches such as the finite element method. Corroborating statements are as follows:

1. In using the load-transfer relationships, similar to the theory of subgrade reaction (Winkler, 1867), it is inherently assumed that the movement of the pile at any element is related only to the stress developed at that element and is independent of the stress occurring elsewhere along the pile. No proper account is thus taken of the continuity within the pile and the soil mass, and the previous approach to model pile behaviour may be defined as a 'layer model' (Chow, 1986b; Rotta Loria et al., 2018).
2. The underlying assumption about the discontinuity of the soil characterising the load-transfer method yields to a number of differences compared to other 'continuous' approaches that do account for the influence of a pile element on the other, such as the equations of Mindlin (1936). Therefore the load-transfer method may be applied with judgement to the analysis of the load-displacement response of piles.
3. To obtain load-transfer relationships, data obtained from field tests on full-scale instrumented piles or laboratory tests on model-scale piles are needed. To carry out the considered tests, considerably more instrumentation is required on a pile compared than in a more usual pile test. Yet, extrapolation of data from one site to another may not be entirely adequate. Therefore load-transfer analyses may be characterised by drawbacks in situations where piles are embedded in soil deposits for which detailed information is unavailable.

Various load-transfer functions can be employed to characterise the response of piles to loading. Examples of these functions have been proposed by Seed and Chan (1966), Coyle and Reese (1966), Coyle and Sulaiman (1967), Reese et al. (1969), Randolph and Wroth (1978), Frank and Zhao (1982), Armaleh and Desai (1987) and Frank et al. (1991) for piles embedded in both fine- and coarse-grained soil.

According to Poulos and Davis (1980), a number of load-transfer relationships may be required to describe the load-transfer along the whole pile length. In this context, the following aspects should be considered to characterise the axial pile response (Randolph, 2003): the axial capacity of piles markedly depends on (1) the effective

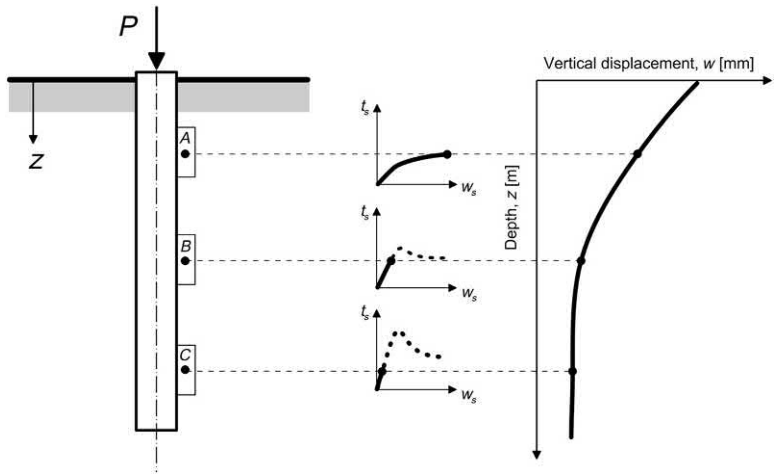

Figure 10.35 Load-transfer functions along a pile. *Modified after Randolph, M.F., 2003. Science and empiricism in pile foundation design. Geotechnique 53 (10), 847–875.*

stress level and (2) the fabric conditions at the pile–soil interface for any given pile installation technique; in contrast, the axial deformation of piles depends on (1) the soil conditions and (2) the soil properties slightly farther from the pile–soil interface. Typical features of load-transfer functions describing the interaction between a displacement pile and the adjacent soil are reported in Fig. 10.35.

10.10.2 Load-displacement relationships

In the following, a focus is given to the load-transfer relationships and a number of mathematical expressions that have been implemented at the Swiss Federal Institute of Technology in Lausanne in a computer software called Thermo-Pile (https://lms.epfl.ch/thermopile), which allows the analysis of the axial response of energy piles subjected to mechanical and thermal loads to be carried out via the load-transfer method (Knellwolf et al., 2011). In the considered load-transfer analysis approach, single energy piles are modelled as being composed of several rigid elements that are connected by springs. Each of the elements constituting the pile is characterised at its side by an interaction with the soil that follows a load-transfer function expressing a relationship between the soil shear strength and the pile shaft displacement, $t_s - w_s$. The element at the toe of the pile is characterised at its base by an interaction with the soil that follows another load-transfer function expressing a relationship between the normal stress developed at the pile toe and the pile toe displacement, $t_b - w_b$. The element at the head of the pile is characterised at its top by an interaction with the general structural element connected to the pile that follows a load-transfer function expressing a relationship between the normal stress developed in the structural element and the pile head displacement, $t_h - w_h$.

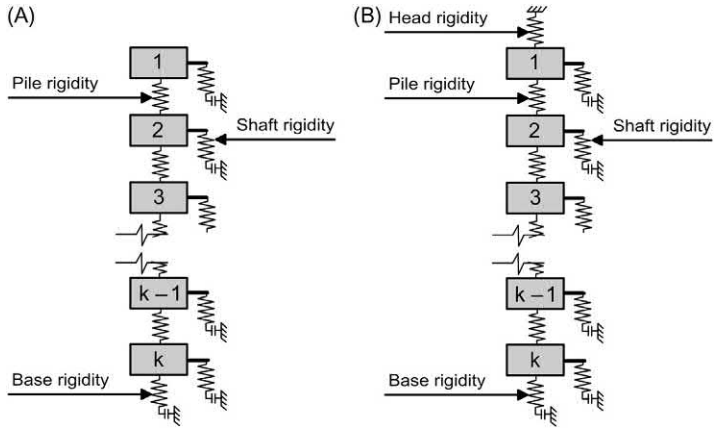

Figure 10.36 Schematic of a single pile employed in (A) the original load-transfer method proposed by Coyle and Reese (1966) and (B) the extended load-transfer method proposed by Knellwolf et al. (2011).

In the original load-transfer method proposed by Coyle and Reese (1966) for piles subjected to mechanical loads, only springs on the side of the pile elements and on the base of the pile element at the level of the toe were considered (cf. Fig. 10.36A). The inclusion of these aspects has been proposed by Knellwolf et al. (2011) to account for the noteworthy influence of the head restraint in the axial deformation of piles subjected to thermal loads (cf. Fig. 10.36B). It is only considered upon thermal loading according to the hypotheses described thus far.

The pile response obeys a linear thermoelastic behaviour, whereas the pile cap follows a linear elastic behaviour. The soil obeys trilinear elastoplastic behaviour according to the load-displacement relationships depicted in Fig. 10.37A and B for the shaft and base of the energy pile, respectively. The schematics of those relationships have been extended to energy piles by Knellwolf et al. (2011) based on those presented by Frank and Zhao (1982) for single conventional piles. The shape of these functions is characterised by (1) a first loading/unloading linear branch that describes the elastic response of the shaft/base of the energy pile, (2) a next loading linear branch that refers to the inelastic response of the shaft/base of the energy pile, (3) an unloading linear branch that describes the elastic response of the shaft/base when unloading occurs from a stress state along the inelastic branch and (4) a final *plateau* that can be associated with the perfectly plastic response of the shaft/base of the energy pile when the shaft/base resistance value is attained.

In the original formulations of Frank and Zhao (1982), in contrast with those extended by Knellwolf et al. (2011), no unloading branch was foreseen for both the shaft and base load-transfer functions and the load-transfer function referring to the elements of the pile shaft was defined only with reference to compressive stresses and

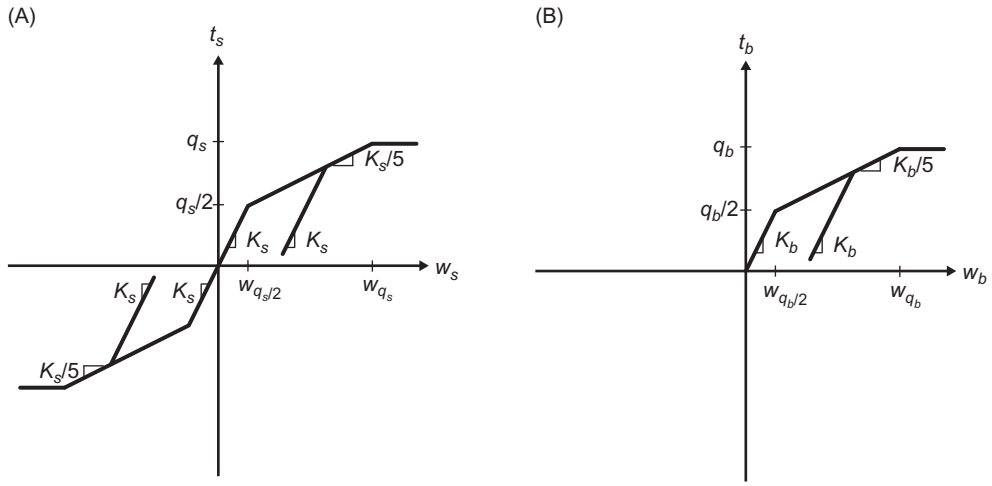

Figure 10.37 Load-displacement relationships for the (A) shaft and (B) base of energy piles. *Redrawn after Knellwolf, C., Peron, H., Laloui, L., 2011. Geotechnical analysis of heat exchanger piles. J. Geotech. Geoenviron. Eng. 137 (10), 890–902.*

settlements (i.e. this function was not symmetrical like the one depicted in Fig. 10.37A by including the possible presence of tensile stresses and heaves). The considered modifications have been proposed to include the unloading effect of cooling thermal loads applied to energy piles with respect to the loading effect caused by mechanical loads or heating thermal loads.

The first linear parts of the shaft and the base load-displacement functions cover shaft and base displacements of $w_{q_s/2}$ and $w_{q_b/2}$ until shaft and base resistances of $q_s/2$ and $q_b/2$ are mobilised, respectively. According to Frank and Zhao (1982), these values of shaft and base resistances are half of the shaft and base resistances of q_s and q_b of the energy pile, respectively. The slopes K_s and K_b of the loading/unloading elastic branches of the load-displacement functions represent the stiffness of the shaft and base springs that govern the elastic pile–soil interaction, respectively. The considered parameters can be defined according to Frank et al. (1991) as

$$K_s = 0.8\frac{E_M}{D} \qquad K_b = 4.8\frac{E_M}{D} \qquad \text{for coarse–grained soils} \tag{10.32}$$

$$K_s = 2\frac{E_M}{D} \qquad K_b = 11\frac{E_M}{D} \qquad \text{for fine–grained soils} \tag{10.33}$$

Table 10.8 Values of the rheological coefficient α_r.

	Value of rheological coefficient, α_r [−]				
Soil consolidation state/density state	Peat	Clay	Silt	Sand	Sand and gravel
Overconsolidated/dense	−	1	2/3	1/2	1/3
Normally consolidated/loose	1	2/3	1/2	1/3	1/4
Weathered or altered	−	1/2	1/2	1/3	1/4

Source: Data from Menard, L., 1975. Interpretation and application of pressuremeter test results. Sols Soils No. 26-1975.

where E_M is the Menard pressuremeter modulus. The Menard pressuremeter modulus can be related to the Young's modulus of the soil according to different methods available in the literature (Clarke, 1994; Frank, 2009). According to Amar et al. (1991) and Amar and Jézéquel (1998), one typical relationship links the Menard pressuremeter modulus, E_M, and the elastic modulus in plane strain conditions, E_{oed} (associable to the conditions of the cavity characterising the pressuremeter test), through a rheological coefficient, α_r, presented by Menard (1975), and reads

$$E_M = \alpha_r E_{oed} \tag{10.34}$$

with

$$E_{oed} = \frac{E_{soil}(1-\nu_{soil})}{(1+\nu_{soil})(1-2\nu_{soil})} \tag{10.35}$$

Typical values of the rheological coefficient α_r are reported in Table 10.8.

The loading inelastic branches of the shaft and base load-displacement functions cover shaft and base displacements greater than $w_{q_s/2}$ and $w_{q_b/2}$ until the shaft and base resistances of q_s and q_b are mobilised, respectively. According to Frank and Zhao (1982), the slopes of the inelastic branches related to the shaft and base are equal to $K_s/5$ and $K_b/5$, respectively.

The shaft and base resistances q_s and q_b, respectively, may be determined considering (1) the type of soil surrounding the piles and (2) the method (and order) of installing the piles. Approaches to account for these aspects are proposed earlier in this chapter.

The stiffness of the pile can be determined as $K_{EP} = E_{EP}/h_k$, where h_k is the height of the element k characterising the pile. The stiffness characterising the pile−structure interaction can finally be determined with reference to a rigid rectangular plate resting vertically loaded on a semiinfinite isotropic elastic half space as (Gorbunov-Posadov and Serebrjanyi, 1961)

$$K_h = \frac{E_{soil}\sqrt{B_{slab}L_{slab}}}{(1-\nu_{soil}{}^2)\rho_0} \tag{10.36}$$

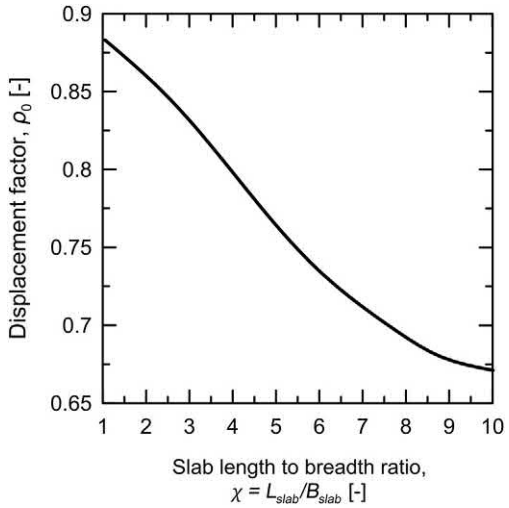

Figure 10.38 Relationship between length to breadth ratio and displacement factor of an infinitely rigid plate resting on a semiinfinite elastic half space. *Redrawn after Gorbunov-Posadov, M.I., Serebrjanyi, R.V., 1961. Design of structures on elastic foundation. In: 5th International Conference on Soil Mechanics and Foundation Engineering, vol. 1, pp. 643–648.*

where B_{slab} and L_{slab} are the dimensions of the slab or general structural element connected at the pile head and ρ_0 is a displacement factor that can be evaluated as a function of the length to breadth ratio of the considered element $\chi = L_{slab}/B_{slab}$ (cf. Fig. 10.38). The load-displacement function for the element of the pile head reads in particular $t_h = K_h w_h$.

When layered (i.e. nonuniform) soil deposits are encountered and the variation of the deformation moduli between successive layers is not large, Eq. (10.36) may be approximately applied by considering average values of the Young's modulus and Poisson's ratio characterising the soil deposit determined as follows

$$\overline{E}_{soil} = \frac{1}{\sum_{k=1}^{N} l_k} \sum_{k=1}^{N} E_{soil,k} l_k \tag{10.37}$$

$$\overline{\nu}_{soil} = \frac{1}{\sum_{k=1}^{N} l_k} \sum_{k=1}^{N} \nu_{soil,k} l_k \tag{10.38}$$

where $E_{soil,k}$ and $\nu_{soil,k}$ are the Young's modulus and Poisson's ratio of the soil layer k. According to Poulos and Davis (1980), variations of ν_{soil} along piles may be ignored because the displacement of such foundations is slightly dependent on the Poisson's ratio of the soil.

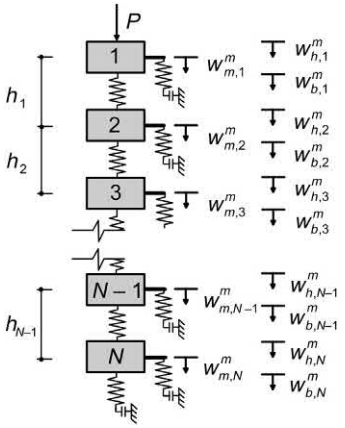

Figure 10.39 Discretisation of a pile subjected to mechanical loading in a number of elements according to the load-transfer method. *Modified after Knellwolf, C., Peron, H., Laloui, L., 2011. Geotechnical analysis of heat exchanger piles. J. Geotech. Geoenviron. Eng. 137 (10), 890–902.*

The previous Eqs (10.37) and (10.38) may also be applied when dealing with piles embedded in layered soil deposits of comparable deformation properties and resting on a very stiff bearing layer by ignoring the properties of the base stratum.

10.10.3 Solution for mechanical loading only

To characterise the axial response of an energy pile to mechanical loading, the following iterative procedure can be employed (Coyle and Reese, 1966):

1. The pile is divided in a number of elements $k = 1, 2, \ldots, N$ (actually consisting of segments as reference is made to one-dimensional conditions) characterised by a height h_k, a cross-sectional area A_{EP} and a diameter D (cf. Fig. 10.39). Under the influence of a mechanical load, a value of axial displacement is assumed to characterise the toe, $w^m_{b,k}$, the middle, $w^m_{m,k}$, and the head, $w^m_{h,k}$, of each element. Associated with those displacements are values of axial force $N^m_{b,k}$, $N^m_{m,k}$ and $N^m_{h,k}$ for the base, middle and head of each element, respectively.
2. A small axial displacement for the base of element N of the pile toe, $w^m_{b,N}$, is assumed. According to Poulos and Davis (1980), this displacement may be taken equal to zero, but this approach is generally not employed because unless piles are resting on rock they are characterised by some movement at the toe.
3. The mobilised portion of base capacity by the previous displacement, $N^m_{b,N}$, is calculated. This may be done considering the pile toe as a rigid circular area in a semiinfinite isotropic elastic half space and employing the solution of Boussinesq (1878)

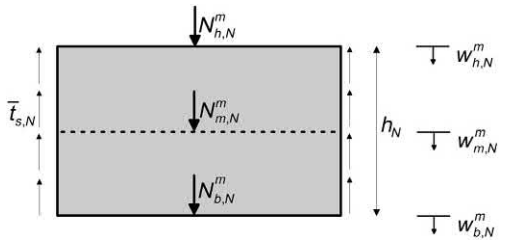

Figure 10.40 Schematic of the bottom element of a pile. *Redrawn after Knellwolf, C., Peron, H., Laloui, L., 2011. Geotechnical analysis of heat exchanger piles. J. Geotech. Geoenviron. Eng. 137 (10), 890–902.*

$$N^m_{b,N} = \frac{2DE_{soil}w^m_{b,N}}{1-\nu^2_{soil}} \tag{10.39}$$

4. An axial displacement $w^m_{m,N}$ for the middle of the bottom element N, which is associated with an axial force $N^m_{m,N}$, is assumed (cf. Fig. 10.40). When considering this step for the first time, it is typically assumed that $w^m_{m,N} = w^m_{b,N}$. With reference to the considered element, $N^m_{b,N}$ and $N^m_{h,N}$ are the axial forces acting at the base and head of the element, respectively. The corresponding axial displacements are $w^m_{b,N}$ and $w^m_{h,N}$, respectively.
5. Referring to the relevant load-displacement relationship, the average shear stress $\bar{t}_{s,N}(w^m_{m,N})$ mobilised by the soil for the estimated axial displacement at the middle of the element is determined.
6. Referring to the value of $\bar{t}_{s,N}$ and assuming a constant shear stress along the considered element, the axial force at the head of the bottom element can be calculated as

$$N^m_{h,N} = N^m_{b,N} + \bar{t}_{s,N}(w^m_{m,N})h_N\pi D \tag{10.40}$$

7. Assuming a linear variation of axial load along the element, the axial force $N^m_{m,N}$ at the middle reads

$$N^m_{m,N} = \frac{\left(N^m_{b,N} + N^m_{h,N}\right)}{2} = N^m_{b,N} + \bar{t}_{s,N}(w^m_{m,N})\frac{h_N\pi D}{2} \tag{10.41}$$

Therefore application of Hooke's law yields a relative displacement, Δw^m_N, from the bottom to the middle of the element N that reads

$$\Delta w^m_N = \frac{N^m_{b,N} + N^m_{m,N}}{2}\frac{1}{A_{EP}E_{EP}}\frac{h_N}{2} = \left[N^m_{b,N} + \bar{t}_{s,N}\left(w^m_{m,N}\right)\frac{h_N\pi D}{4}\right]\frac{1}{A_{EP}E_{EP}}\frac{h_N}{2} \tag{10.42}$$

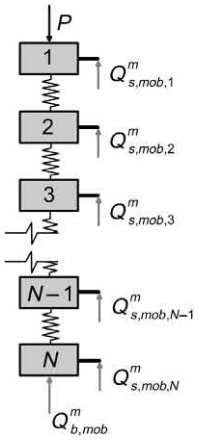

Figure 10.41 Vertical equilibrium of external forces along a discretised pile subjected to mechanical loading. *Modified after Knellwolf, C., Peron, H., Laloui, L., 2011. Geotechnical analysis of heat exchanger piles. J. Geotech. Geoenviron. Eng. 137 (10), 890–902.*

8. From the above, a new axial displacement can be determined for the middle of the element as

$$w^m_{m,N}{}' = w^m_{b,N} + \Delta w^m_N \tag{10.43}$$

9. The axial displacement $w^m_{m,N}{}'$ determined in step 8 is compared with $w^m_{m,N}$ determined in step 4. If the difference between the considered displacements is greater than a prescribed value, steps 2–8 are repeated iteratively until a reliable value of $w^m_{m,N}{}'$ is obtained.

10. When convergence is achieved, the next element up k is considered and so on, until the axial force of the element at the pile head, $N^m_{h,1}$, is equal to the applied load, P, following Eq. (10.23) (cf. Fig. 10.41):

$$P + Q^m_{s,mob} + Q^m_{b,mob} = 0 \tag{10.44}$$

where

$$Q^m_{s,mob} = \sum_{k=1}^{N} Q^m_{s,k} \tag{10.45}$$

In the particular case in which an axial load is equal to the axial capacity of the pile, Eq. (10.44) coincides with Eq. (10.1).

10.10.4 Solution for thermal loading only

To characterise the axial response of an energy pile to thermal loading, a different iterative procedure than the one previously described for the case of mechanical loading

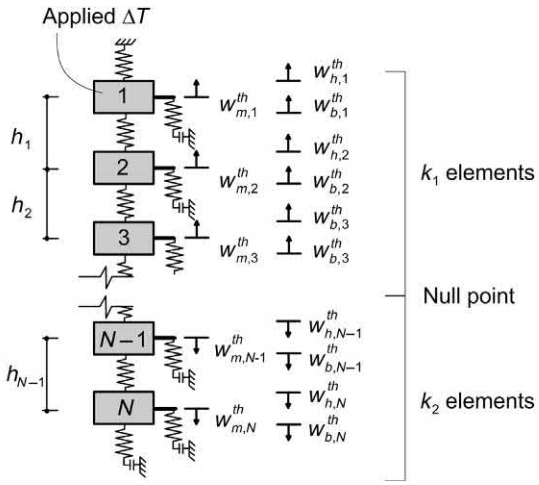

Figure 10.42 Discretisation of a pile subjected to thermal loading in a number of elements according to the load-transfer method. *Modified after Knellwolf, C., Peron, H., Laloui, L., 2011. Geotechnical analysis of heat exchanger piles. J. Geotech. Geoenviron. Eng. 137 (10), 890–902.*

only is employed. The iterative character of this procedure aims to determine a position for the null point of the shear stress along the energy pile that satisfies the vertical pile equilibrium within a specified tolerance. In this context, it is worth noting that the assumed discontinuity of the soil involves that the null points of the shear stress and axial displacement coincide. Therefore reference is simply made to a single null point in the following, but it must be borne in mind that this result is a simple outcome of a particular modelling approach that simplifies reality.

The features of the considered procedure are as follows:

1. The pile is divided in a number of elements $k = 1, 2, \ldots, N$ characterised by a height h_k, a cross-sectional area A_{EP} and a diameter D (cf. Fig. 10.42).
2. A value of thermally induced observed deformation, ε_o^{th}, is chosen. When considering this step for the first time, it is typically assumed that the observed deformation develops under free thermal expansion conditions, that is $\varepsilon_o^{th} = \varepsilon_f^{th} = -\alpha_{EP}\Delta T$ (Knellwolf et al., 2011). The assumed value of thermally induced observed deformation results in a displacement variation for each element that reads

$$\Delta w_k^{th} = h_k \alpha_{EP} \Delta T \tag{10.46}$$

3. A location z_{NP} of the null point of the axial displacement is chosen. The behaviour of the pile can be analysed by separately investigating the parts of the pile below and above the null point. Each of these parts is characterised by a number k_1 of elements above the null point and a number k_2 of elements below the null point (cf. Fig. 10.42).

4. Considering that there is no axial displacement in correspondence with the null point (i.e. $w^{th} = 0$ at $z = z_{NP}$), a distribution of axial displacement along the energy pile is calculated. Assuming the pile subjected to a heating thermal load, a settlement of all the elements below the null point can be expected. The axial displacement at the head, middle and base of the element $(k_1 + 1)$ downward to element N can be calculated as (Chen and McCartney, 2016)

$$w_{h,k}^{th} = \begin{cases} 0 & \text{for } k = k_1 + 1 \\ w_{b,k-1}^{th} & \text{for } k \text{ located at } z \neq z_{NP} \end{cases} \tag{10.47}$$

$$w_{m,k}^{th} = w_{h,k}^{th} + \frac{\Delta w_k^{th}}{2} \tag{10.48}$$

$$w_{b,k}^{th} = w_{h,k}^{th} + \Delta w_k^{th} \tag{10.49}$$

5. By using the load-transfer relationships, the mobilised forces at the base, middle and head of each element of the pile from element N to element $(k_1 + 1)$ can be determined as

$$N_{b,k}^{th} = \begin{cases} \bar{t}_{b,k}\left(w_{b,k}^{th}\right)\pi D h_k & \text{for } k = N \\ N_{h,k+1}^{th} & \text{for } k \neq N \end{cases} \tag{10.50}$$

$$N_{m,k}^{th} = N_{b,k}^{th} + \bar{t}_{s,k}\left(w_{m,k}^{th}\right)\pi D \frac{h_k}{2} \tag{10.51}$$

$$N_{h,k}^{th} = 2N_{m,k}^{th} - N_{b,k}^{th} = N_{b,k}^{th} + \bar{t}_{s,k}\left(w_{m,k}^{th}\right)\pi D h_k \tag{10.52}$$

and the thermally induced axial stress at the middle of each element can be calculated as follows

$$\sigma_{b,k}^{th} = \frac{N_{h,k}^{th} + N_{b,k}^{th}}{2}\frac{1}{A_{EP}} \tag{10.53}$$

6. A new value (i.e. lower) of the actual axial displacement of each segment, which is lower than the initial guess Δw_k^{th}, can now be determined as

$$\Delta w_k^{th\prime} = \Delta w_k^{th} - \frac{\sigma_{b,k}^{th} h_k}{E_{EP}} = h_k\left(\alpha_{EP}\Delta T - \frac{\sigma_{b,k}^{th}}{E_{EP}}\right) \tag{10.54}$$

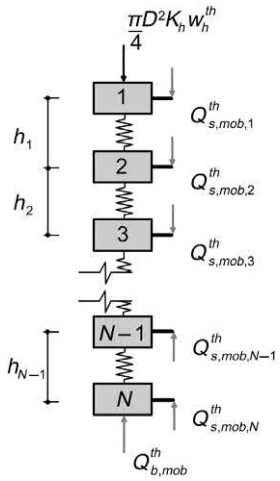

Figure 10.43 Vertical equilibrium of external forces along a discretised pile subjected to thermal loading. *Modified after Knellwolf, C., Peron, H., Laloui, L., 2011. Geotechnical analysis of heat exchanger piles. J. Geotech. Geoenviron. Eng. 137 (10), 890–902.*

7. Steps 4 and 5 must be repeated with reference to the updated value of axial displacement determined via Eq. (10.54) until a prescribed tolerance is achieved. The same procedure should be applied for the elements above the null point considering the appropriate terms.
8. When convergence is achieved for the portion(s) below and/or above the null point of the energy pile and a resulting axial displacement distribution is obtained, axial equilibrium must be verified via the following equation (which represents a discretised version of Eq. (10.30)) for the pile subjected to thermal loading:

$$\frac{\pi D^2}{4} K_h w_h^{th} + \sum_{k=1}^{k_1} Q_{s,mob,k}^{th} + \sum_{k=k_1+1}^{N} Q_{s,mob,k}^{th} + Q_{b,mob}^{th} = 0 \qquad (10.55)$$

9. If equilibrium is reached, the estimated position of the null point can be considered representative for the modelled problem. Otherwise, a new location of the null point must be assumed and the aforementioned procedure should be repeated until Eq. (10.55) is satisfied (cf. Fig. 10.43).

10.10.5 Solution for mechanical and thermal loading

In this case, the solution of the problem resorts to a preliminary characterisation of the energy pile response under mechanical loading only. The results of the considered analysis are assumed as initial conditions for the analysis addressing the influence of thermal loads. The procedure previously described for thermal loading is

Table 10.9 Summary of the modelled full-scale in situ tests by Rotta Loria et al. (2019b).

Reference	Pile type	Soil	Head restraint	Loading
Briaud et al. (1989)	Conventional pile	Medium-dense sand	Free	Mechanical
O'Neill et al. (1981)	Conventional pile	Overconsolidated clay	Free	Mechanical
Mandolini and Viggiani (1992)	Conventional pile	Slightly overconsolidated clay	Free	Mechanical
Mimouni and Laloui (2015)	Energy pile	Overconsolidated clay and dense sand resting on rock	Free	Thermal
Rotta Loria and Laloui (2017b)	Energy pile	Overconsolidated clay and dense sand resting on rock	Restrained	Mechanical and thermal

then applied to solve the considered problem involving a pile subjected to mechanical and thermal loading.

10.11 Modelled and observed response

10.11.1 General

This section expands on the capabilities of the load-transfer method in predicting the response of piles subjected to mechanical and thermal loads. To this aim, the observed behaviour through full-scale in situ tests of conventional piles subjected to mechanical loads as well as of energy piles subjected to mechanical and/or thermal loads is compared with predictions made with the load-transfer method.

The following predictions are reported by Rotta Loria et al. (2019b). Table 10.9 summarises essential features of the considered full-scale in situ tests of single piles.

Additional prediction examples via the load-transfer method of the response of energy piles tested in situ and in the centrifuge under the action of mechanical and thermal loads have been reported by Knellwolf et al. (2011) and Chen and McCartney (2016), respectively.

10.11.2 Tests by Briaud et al. (1989)

Briaud et al. (1989) reported the results of full-scale in situ tests performed on six conventional piles subjected to vertical mechanical loading, including one experiment on a single reference pile. The piles were driven in a clean medium-dense sand deposit and consisted of closed-end tubular steel pipes of an external diameter of $D = 273$ mm, a wall thickness of $t_w = 9.27$ mm, and an embedded length of

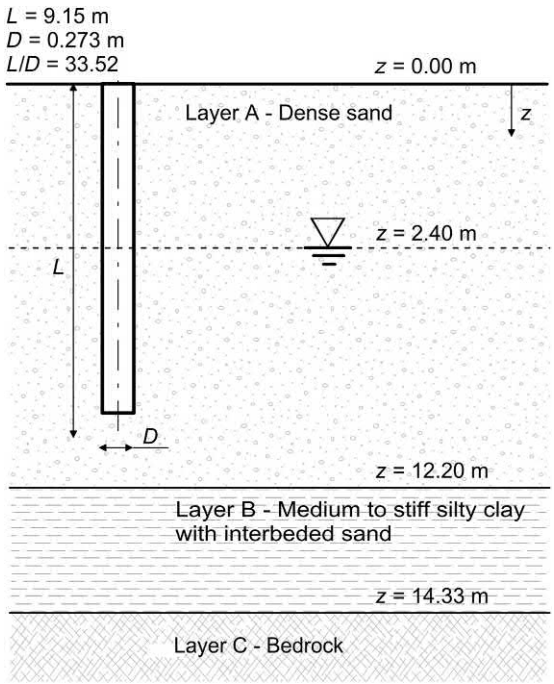

Figure 10.44 Features of the test site described by Briaud et al. (1989). *Modified after Rotta Loria, A.F., Català Oltra, J.V., Laloui, L., 2019b. Equivalent pier analysis of full-scale pile groups subjected to mechanical and thermal loads. (Under review).*

$L = 9.15$ m (cf. Fig. 10.44). Without accounting for a 1.37 m-thick shallow layer made of sandy gravel that was removed prior to testing the piles, the clean sand deposit reached a depth of $z = 12.20$ m from surface. Below the sand layer, a medium-stiff to stiff silty clay with interbedded sand layer was found until reaching the bedrock at a depth of $z = 14.33$ m. The groundwater table was found at a depth of $z = 2.40$ m.

Relevant parameters were extracted from the work of Briaud et al. (1989), Castelli and Maugeri (2002) and Castelli and Motta (2003) and are reported in Tables 10.10 and 10.11. Values written in regular font were found in the referenced publications, those written in italic were assumed and those written in bold resulted from calculations based on the parameters presented.

The Young's modulus of the modelled pile was calculated with reference to an equivalent homogeneous circular cross-section characterised by a pile diameter of $D = 273$ mm based on the actual value of axial pile stiffness. This value was determined for the hollow pile referring to its actual steel area as well as to a Young's modulus of the steel assumed to be equal to 210 GPa. The soil deposit was considered to be dry and fully saturated with water above and below the groundwater table level of

Table 10.10 Soil properties considered for modelling the single pile test of Briaud et al. (1989).

Reference depth, z [m]	Variable	Value
[0; 2.40]	Dry unit weight, γ_d [kN/m^3]	15.7
[2.40; 9.15)	Saturated unit weight, γ_{sat} [kN/m^3]	19.3
[0; 9.15)	Angle of shear strength under constant volume conditions, φ'_{cv} [degree]	35.4
	Young's modulus, E_{soil} [MPa]	63
	Poisson's ratio, ν_{soil} [−]	*0.35*
	Menard pressuremeter modulus, E_M [MPa]	**50.6**
	Slope of the pile shaft load-transfer elastic branch, K_s [kPa/m]	**148,148**
	Slope of the pile base load-transfer elastic branch, K_b [kPa/m]	**888,889**

Source: Modified after Rotta Loria, A.F., Català Oltra, J.V., Laloui, L., 2019b. Equivalent pier analysis of full-scale pile groups subjected to mechanical and thermal loads. (Under review).

Table 10.11 Pile properties considered for modelling the single pile test of Briaud et al. (1989).

Variable	Value
Young's modulus, E_{EP} [GPa]	**27.6**
Shaft capacity, Q_s [kN]	**130.9**
Base capacity, Q_b [kN]	**282.7**
Total pile axial capacity, Q_u [kN]	**413.6**

Source: Modified after Rotta Loria, A.F., Català Oltra, J.V., Laloui, L., 2019b. Equivalent pier analysis of full-scale pile groups subjected to mechanical and thermal loads. (Under review).

$z = 2.40$ m, respectively. The Menard pressuremeter modulus E_M was calculated via the expression proposed by Amar et al. (1991) based on the Young's modulus and Poisson's ratio of the soil and considering a rheological coefficient $\alpha_r = 1/3$ according to Menard (1975). The slopes K_s and K_b of the elastic branches of the load-displacement functions proposed by Knellwolf et al. (2011) were determined according to the formulations of Frank et al. (1991) for coarse-grained soils. The shaft capacity was determined considering $\delta' = \varphi'_{cv}$ as well as $\overline{K} = K_0$ following the approach proposed by Kulhawy et al. (1983) for displacement piles, whereby $K_0 = 1 - \sin\varphi'_{cv}$. The base capacity was calculated considering the approach proposed by Hansen (1970) assuming $s_q = 1$ but considering the contribution of d_q, and resorting to the soil angle of shear strength φ'_{cv}.

Fig. 10.45 shows the measured and computed load-settlement curves for the head of the single reference pile. Both the applied mechanical load and the resulting vertical displacement are normalised values. The applied mechanical load is normalised with respect to the pile axial capacity, which is estimated to be $Q_{u,exp} = 414$ kN with

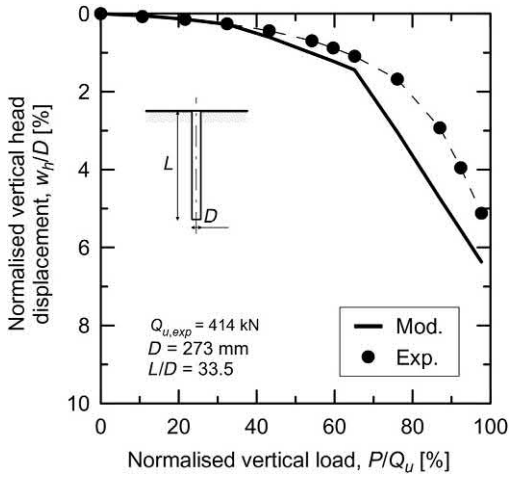

Figure 10.45 Experimental and modelled pile head load-settlement curves with reference to the single pile test of Briaud et al. (1989). *Modified after Rotta Loria, A.F., Català Oltra, J.V., Laloui, L., 2019b. Equivalent pier analysis of full-scale pile groups subjected to mechanical and thermal loads. (Under review).*

reference to the experimental data reported by Briaud et al. (1989). The vertical head displacement of the pile is normalised by its diameter D.

The prediction results are closely comparable to the experimental data. The two typical branches characterising pile load-settlement curves can be remarked with reference to the considered data. A first approximately linear branch associated with a reversible response of the soil surrounding the pile is observed for head settlements of up to $w_h = 1 - 2\%D$. A second nonlinear branch associated with an irreversible response of the soil surrounding the pile is subsequently observed.

Fig. 10.46 shows the measured and computed evolutions of the vertical load with depth for the single reference pile. Both the applied mechanical load and the depth are normalised values. The applied mechanical load is normalised with respect to the experimentally determined pile axial capacity of $Q_{u,exp} = 414$ kN. The depth is normalised by the pile length L.

The prediction results match the experimental measurements, with a closer adherence between the data for mechanical loads of up to $P = 0.5Q_{u,exp}$ than for higher values of applied loads. This result also characterises the load-settlement curve of the tested pile and is attributed to a more realistic description of the stress redistribution along the pile for relatively low magnitudes of loading compared to higher magnitudes of loading at which a yielding occurs in the soil. The typical evolution characterising the vertical load distribution of piles subjected to vertical mechanical loads can be remarked with reference to the considered data, whereby a more pronounced

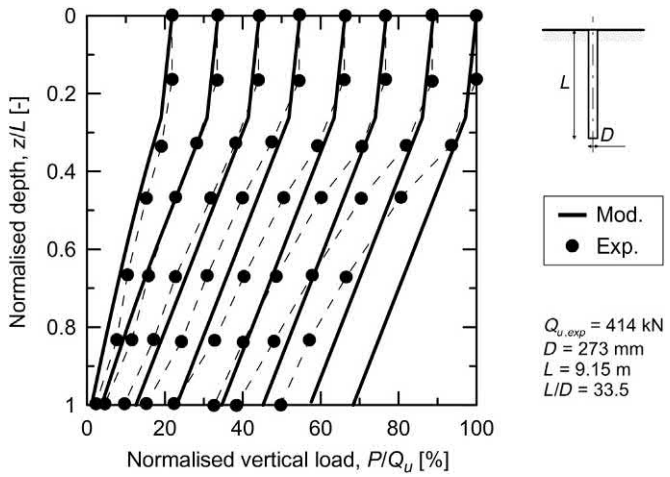

Figure 10.46 Experimental and modelled evolutions of the normalised vertical load along the normalised pile depth referring to the single pile test of Briaud et al. (1989). *Modified after Rotta Loria, A.F., Català Oltra, J.V., Laloui, L., 2019b. Equivalent pier analysis of full-scale pile groups subjected to mechanical and thermal loads. (Under review).*

contribution of the base capacity is mobilised along with that of the shaft capacity for higher values of applied mechanical load at the pile head.

10.11.3 Tests by O'Neill et al. (1981)

O'Neill et al. (1981) reported the results of full-scale in situ tests performed on eleven conventional piles subjected to vertical mechanical loading, including two experiments on two single reference piles. The piles were driven in an overconsolidated clayey soil deposit and consisted of closed-end tubular steel pipes of an external diameter of $D = 273$ mm, a wall thickness of $t_w = 9.27$ mm, and an embedded length of $L = 13.11$ m (cf. Fig. 10.47). The soil profile approximately consisted of two layers. The first layer was composed by stiff overconsolidated clay and reached a depth of $z = 14.11$ m. Below this layer, a second layer a very stiff sandy clay and silts was found. The groundwater table was found at a depth of $z = 2.135$ m.

Relevant parameters were extracted from the work of O'Neill et al. (1981) and are reported in Tables 10.12 and 10.13. Values written in regular font were found in the referenced publication, those written in italic were assumed and those written in bold resulted from calculations based on the parameters presented.

The Young's modulus of the modelled pile was calculated with reference to an equivalent homogeneous circular cross-section characterised by a pile diameter of $D = 273$ mm based on the actual value of axial pile stiffness. This value was determined for the hollow pile referring to its actual steel area as well as to a Young's modulus of the steel assumed to be equal to 210 GPa. The soil deposit was considered to

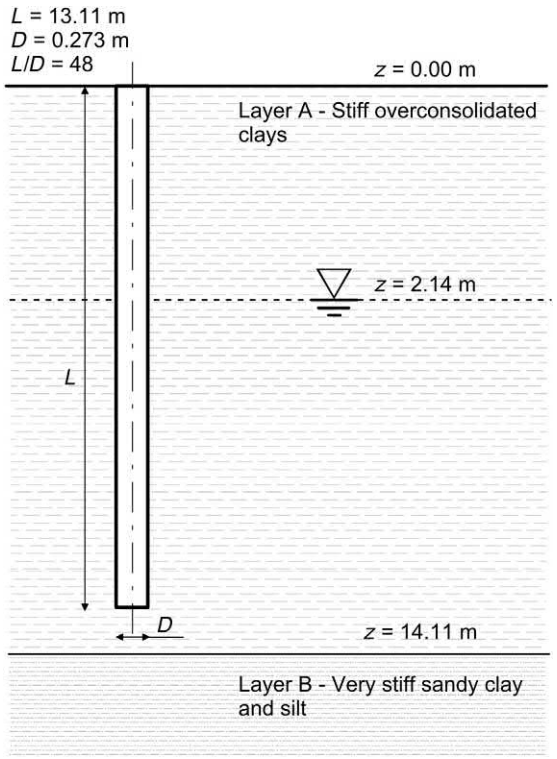

Figure 10.47 Features of the test site described by O'Neill et al. (1981). *Modified after Rotta Loria, A.F., Català Oltra, J.V., Laloui, L., 2019b. Equivalent pier analysis of full-scale pile groups subjected to mechanical and thermal loads. (Under review).*

be dry and fully saturated with water above and below the groundwater table level of $z = 2.135$ m, respectively. For each of these layers, a constant value of Young's modulus of the soil was determined as the average of the approximately linearly increasing values of Young's modulus measured with depth by O'Neill et al. (1981). The Menard pressuremeter modulus E_M was calculated via the expression proposed by Amar et al. (1991) based on the Young's modulus and Poisson's ratio of the soil and considering a rheological coefficient $\alpha_r = 1$ according to Menard (1975). The slopes K_s and K_b of the elastic branches of the load-displacement functions proposed by Knellwolf et al. (2011) were determined according to the formulations of Frank et al. (1991) for fine-grained soils. The values of angle of shear strength under constant volume conditions, overconsolidation ratio and relevant unit weight of the dry and saturated parts of the clay layer surrounding the pile were determined as average values of the experimental data reported by O'Neill et al. (1981). The shaft capacity was determined considering $\delta' = \varphi'_{cv}$ as well as $\overline{K} = K_0$ following the approach proposed by Kulhawy et al. (1983) for displacement piles, whereby $K_0 = (1 - \sin\varphi'_{cv})\sqrt{OCR}$

Table 10.12 Soil properties considered for modelling the single pile tests of O'Neill et al. (1981).

Reference depth, z [m]	Variable	Value
[0; 2.14]	Dry unit weight, γ_d [kN/m^3]	**17.4**
	Angle of shear strength under constant volume conditions, φ'_{cv} [degree]	**17**
	Young's modulus, E_{soil} [MPa]	**49.0**
	Poisson's ratio, ν_{soil} [−]	*0.45*
	Menard pressuremeter modulus, E_M [MPa]	**185.9**
	Slope of the pile shaft load-transfer elastic branch, K_s [kPa/m]	**1,361,627**
	Overconsolidation ratio, OCR [−]	**7.2**
[2.14; 13.10)	Saturated unit weight, γ_{sat} [kN/m^3]	**20.9**
	Angle of shear strength under constant volume conditions, φ'_{cv} [degree]	**19.9**
	Young's modulus, E_{soil} [MPa]	**49.0**
	Poisson's ratio, ν_{soil} [−]	*0.45*
	Menard pressuremeter modulus, E_M [MPa]	**185.9**
	Slope of the pile shaft load-transfer elastic branch, K_s [kPa/m]	**1,361,627**
	Slope of the pile base load-transfer elastic branch, K_b [kPa/m]	**7,488,948**
	Overconsolidation ratio, OCR [−]	**4.5**

Source: Modified after Rotta Loria, A.F., Català Oltra, J.V., Laloui, L., 2019b. Equivalent pier analysis of full-scale pile groups subjected to mechanical and thermal loads. (Under review).

Table 10.13 Pile properties considered for modelling the single pile tests of O'Neill et al. (1981).

Variable	Value
Young's modulus, E_{EP} [GPa]	**27.6**
Shaft capacity, Q_s [kN]	**505.6**
Base capacity, Q_b [kN]	**80.6**
Total pile axial capacity, Q_u [kN]	**586.2**

Source: Modified after Rotta Loria, A.F., Català Oltra, J.V., Laloui, L., 2019b. Equivalent pier analysis of full-scale pile groups subjected to mechanical and thermal loads. (Under review).

according to Schmidt (1966). The base capacity was calculated considering the approach proposed by Hansen (1970) assuming $s_q = 1$ but considering the contribution of d_q, and resorting to the soil angle of shear strength φ'_{cv}.

Fig. 10.48 shows the measured and computed load-settlement curves for the head of the single reference piles. The experimental data represent an average of the load-settlement curves characterising the two tests on the single reference piles. Both the applied mechanical load and the resulting vertical displacement are normalised values. The applied mechanical load is normalised with respect to the pile axial capacity, which is

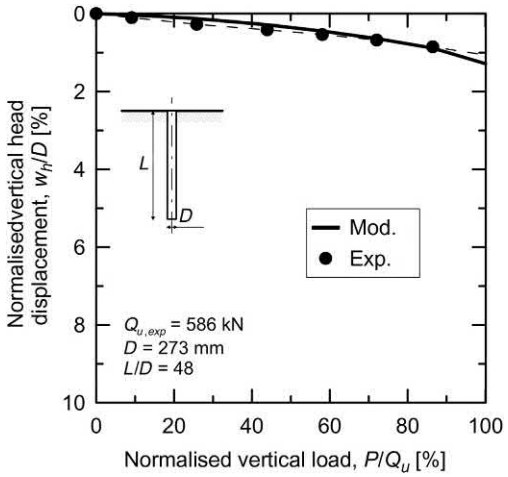

Figure 10.48 Experimental and modelled pile head load-settlement curves referring to the single pile tests of O'Neill et al. (1981). *Modified after Rotta Loria, A.F., Català Oltra, J.V., Laloui, L., 2019b. Equivalent pier analysis of full-scale pile groups subjected to mechanical and thermal loads. (Under review).*

estimated to be $Q_{u,exp} = 586$ kN referring to the experimental data reported by O'Neill et al. (1981). The vertical head displacement of the pile is normalised by its diameter D.

The prediction results are closely comparable to the experimental data. Different from the previously considered experimental results of Briaud et al. (1989), the load-settlement curve follows a linear evolution for increasing loading. This aspect highlights the remarkable load capacity provided by soil surrounding the pile shaft, which together with its stiffness involves relatively reversible pile behaviour upon loading.

Fig. 10.49 shows the measured and computed evolutions of the vertical load with depth for the single reference pile. Both the applied mechanical load and the depth are normalised values. The applied mechanical load is normalised with respect to the experimentally determined pile axial capacity of $Q_{u,exp} = 586$ kN. The depth is normalised by the pile length L.

The prediction results match the experimental measurements, with a closer adherence between the data for greater values of applied mechanical load. A lower contribution of the shaft capacity is mobilised according to the modelling results compared to the experimental data for the lower value of applied mechanical load to the pile head.

10.11.4 Tests by Mandolini and Viggiani (1992)

Mandolini and Viggiani (1992) reported the results of full-scale in situ tests performed on a series of micropiles supporting bridge piers subjected to vertical mechanical loading, including one experiment on a single reference pile. The piles were driven in a normally to slightly overconsolidated silty clay soil deposit and consisted of closed-end

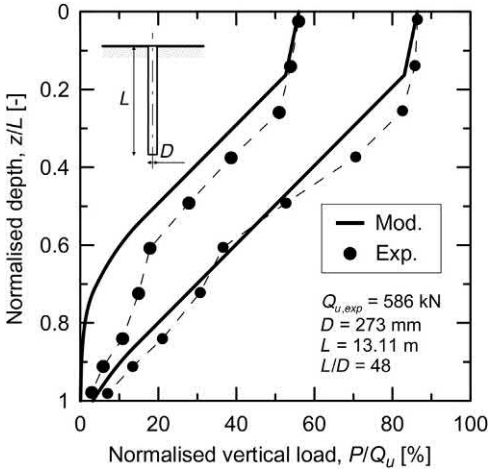

Figure 10.49 Experimental and modelled evolutions of the normalised vertical load along the normalised pile depth referring to the single pile tests of O'Neill et al. (1981). *Modified after Rotta Loria, A.F., Català Oltra, J.V., Laloui, L., 2019b. Equivalent pier analysis of full-scale pile groups subjected to mechanical and thermal loads. (Under review).*

tubular steel pipes filled with concrete of an external diameter of $D = 385$ mm and an embedded length from $L = 40-50$ m (cf. Fig. 10.50). A geotechnical characterisation of the site was performed and is reported by Mandolini and Viggiani (1992). The soil profile was particularly uniform along the piles. The groundwater table was found to be approximately at the surface of the deposit.

Relevant parameters were extracted from the work of Mandolini and Viggiani (1992) and are reported in Tables 10.14 and 10.15. Values written in regular font were found in the referenced publication, those written in italic were assumed and those written in bold resulted from calculations based on the parameters presented.

The pile length was assumed to be of $L = 45$ m. The soil deposit was considered to be fully saturated with water. A constant value of Menard pressuremeter modulus E_M with depth was determined as the average of the values of oedometric modulus measured in the soil with depth by Mandolini and Viggiani (1992). This parameter was calculated via the expression proposed by Amar et al. (1991) considering a rheological coefficient $\alpha_r = 2/3$ according to Menard (1975). The slopes K_s and K_b of the elastic branches of the load-displacement functions proposed by Knellwolf et al. (2011) were determined according to the formulations of Frank et al. (1991) for fine-grained soils. The saturated unit weight of the soil was determined as the average of the experimental data reported by Mandolini and Viggiani (1992) with depth. The shaft capacity was determined considering $\delta' = \varphi'_{cv}$ as well as $\overline{K} = K_0$ following the approach proposed by Kulhawy et al. (1983) for displacement piles, whereby $K_0 = (1 - \sin\varphi'_{cv})\sqrt{OCR}$ according to Schmidt (1966). The base capacity

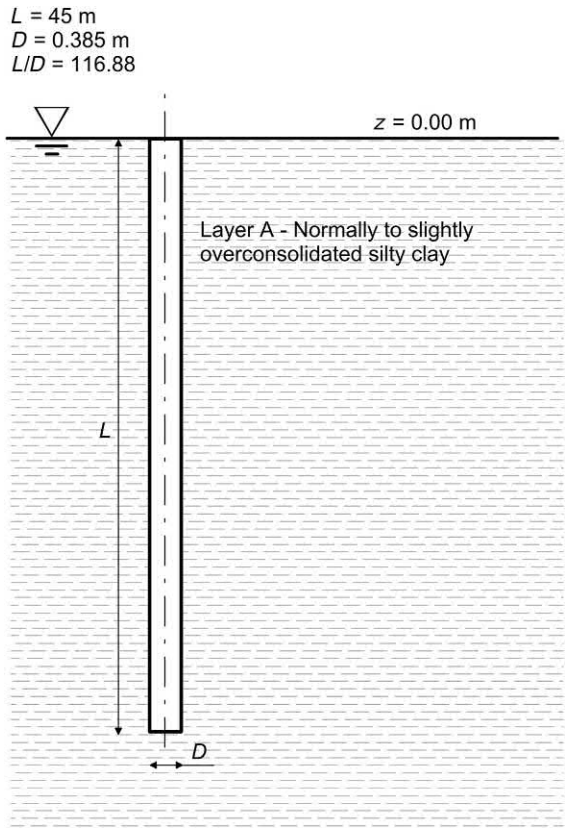

Figure 10.50 Features of the test site described by Mandolini and Viggiani (1992). *Modified after Rotta Loria, A.F., Català Oltra, J.V., Laloui, L., 2019b. Equivalent pier analysis of full-scale pile groups subjected to mechanical and thermal loads. (Under review).*

Table 10.14 Soil properties considered for modelling the single pile test of Mandolini and Viggiani (1992).

Reference depth, *z* [m]	Variable	Value
[0; 45)	Saturated unit weight, γ_{sat} [kN/m^3]	**17.8**
	Angle of shear strength under constant volume conditions, φ'_{cv} [degree]	35
	Menard pressuremeter modulus, E_M [MPa]	**47.3**
	Slope of the pile shaft load-transfer elastic branch, K_s [kPa/m]	**24,567**
	Slope of the pile base load-transfer elastic branch, K_b [kPa/m]	**135,119**
	Overconsolidation ratio, *OCR* [−]	*2*

Source: Modified after Rotta Loria, A.F., Català Oltra, J.V., Laloui, L., 2019b. Equivalent pier analysis of full-scale pile groups subjected to mechanical and thermal loads. (Under review).

Table 10.15 Pile properties considered for modelling the single pile test of Mandolini and Viggiani (1992).

Variable	Value
Young's modulus, E_{EP} [GPa]	30
Shaft capacity, Q_s [kN]	**2611**
Base capacity, Q_b [kN]	**1892**
Total pile axial capacity, Q_u [kN]	**4503**

Source: Modified after Rotta Loria, A.F., Català Oltra, J.V., Laloui, L., 2019b. Equivalent pier analysis of full-scale pile groups subjected to mechanical and thermal loads. (Under review).

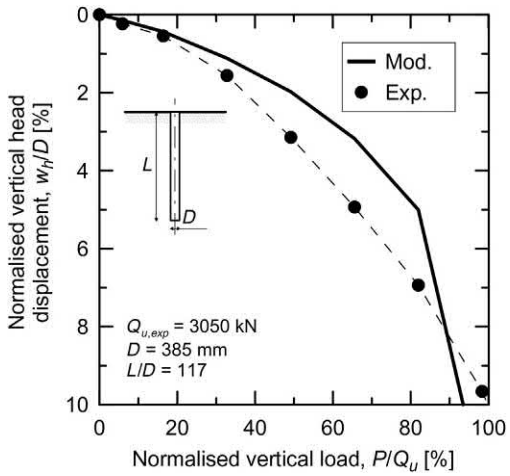

Figure 10.51 Experimental and modelled pile head load-settlement curves referring to the single pile test of Mandolini and Viggiani (1992). *Modified after Rotta Loria, A.F., Català Oltra, J.V., Laloui, L., 2019b. Equivalent pier analysis of full-scale pile groups subjected to mechanical and thermal loads. (Under review).*

was calculated considering the approach proposed by Hansen (1970) assuming $s_q = 1$ but considering the contribution of d_q, and resorting to the soil angle of shear strength φ'_{cv}.

Fig. 10.51 shows the measured and computed load-settlement curves for the head of the single reference pile. Both the applied mechanical load and the resulting vertical displacement are normalised values. The applied mechanical load is normalised with respect to the pile axial capacity, which is estimated to be $Q_{u,exp} = 3050$ kN referring to the experimental data reported by Mandolini and Viggiani (1992). The vertical head displacement of the pile is normalised by its diameter D.

The prediction results capture the overall evolution of the experimental data. A different transition from the linear to the nonlinear branches of the load-settlement curves can be highlighted. Despite this limitation, a very similar value of the load that

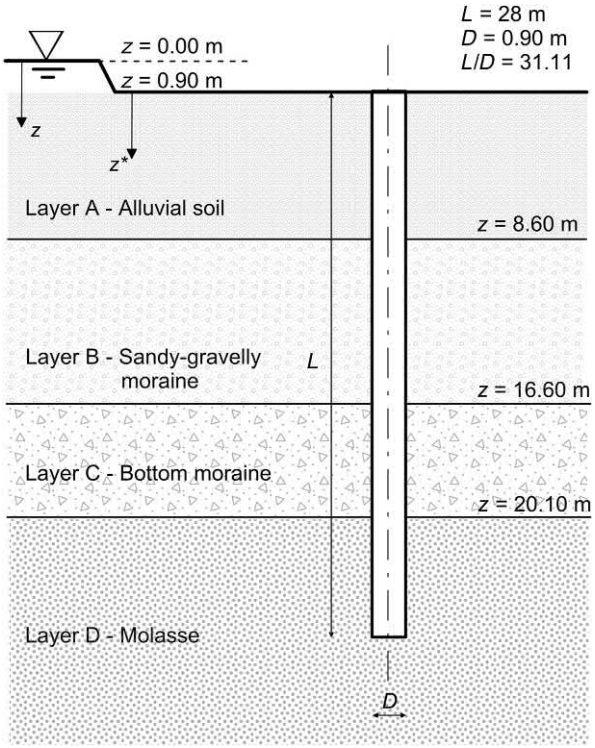

Figure 10.52 Features of the test site described by Mimouni and Laloui (2015). *Modified after Rotta Loria, A.F., Català Oltra, J.V., Laloui, L., 2019b. Equivalent pier analysis of full-scale pile groups subjected to mechanical and thermal loads. (Under review).*

may be associated with the failure of the pile because associated with a vertical had displacement of $w_h = 10\%D$ can be remarked.

10.11.5 Tests by Mimouni and Laloui (2015)

Mimouni and Laloui (2015) reported the results of full-scale in situ tests performed on four energy piles subjected to thermal loading, applied alone or in conjunction with vertical mechanical loading, including one experiment on one energy pile free to move vertically at its head and subjected to thermal loading only. This thermal loading resulted in an average temperature variation of $\Delta T = 3.4°C$ along the pile portion in which the pipes were not thermally insulated (i.e. below 4 m from the pile head). The piles were bored in a stratified overconsolidated soil deposit and consisted of reinforced concrete piles of a diameter of $D = 900$ mm and a length of $L = 28$ m (cf. Fig. 10.52). The soil deposit consisted of a shallow alluvial soil layer from the surface (coinciding with the level of the successively built 0.9-m thick slab) to a depth of $z = 8.6$ m. Below the alluvial soil layer, a sandy-gravelly moraine layer was found to reach a depth

of $z = 16.6$ m. A layer of bottom moraine was present below the sandy-gravelly moraine layer, down to a depth of $z = 20.1$ m. A molasse layer was found at greater depths below the bottom moraine. The groundwater table was located at the surface.

Relevant parameters were extracted from the investigations of Di Donna et al. (2016) and Rotta Loria and Laloui (2017b) and are reported in Tables 10.16 and 10.17. Values written in regular font were found in the referenced publications, those written in italic were assumed and those written in bold resulted from calculations based on the parameters presented.

The soil deposit was considered to be fully saturated with water. A constant value of Menard pressuremeter modulus E_M was considered for each soil layer according to the constant values of Young's modulus reported by Di Donna et al. (2016) and Rotta Loria and Laloui (2017b). This parameter was calculated via the expression proposed by Amar et al. (1991) considering a value of $\alpha_r = 2/3$ for the alluvial soil layer, whereas a value of $\alpha_r = 1$ for the sandy-gravelly moraine and the bottom moraine layers according to Menard (1975). The slopes K_s and K_b of the elastic branches of the load-displacement functions proposed by Knellwolf et al. (2011) were determined according to the formulations of Frank et al. (1991) for fine-grained soils when referring to the alluvial soil layer, while for coarse-grained soils when referring to the sandy-gravelly moraine and bottom moraine layers. The slope K_b of the elastic branches characterising the load-displacement function of the molasse layer was considered to range between the two limiting values proposed by Knellwolf et al. (2011) for a molasse deposit encountered in a site located 200 m far from the one under investigation. This approach was employed because no information on this material parameter was available for the present site and because the value of this parameter calculated referring to the Young's modulus value reported by Di Donna et al. (2016) and Rotta Loria and Laloui (2017b) via the approach proposed by Amar et al. (1991) was considered unreliable. This approach also resulted in two different predictions of the pile under investigation. In these analyses, a different value of the parameter K_s was associated to each value of K_b. Each of these values was determined through the formulation proposed by Frank et al. (1991) for the shaft of piles in fine-grained soils with reference to the pile diameter D and a value of E_M calculated from the formulation proposed by Frank et al. (1991) for the base of piles in fine-grained soils via the assumed value of K_b. The shaft capacity was determined considering δ' and φ'_{cv}, where entering in the formulations as well as $\overline{K} = 0.7K_0$ following the approach proposed by Kulhawy et al. (1983) for nondisplacement piles, whereby $K_0 = (1 - \sin\varphi'_{cv})\sqrt{OCR}$ according to Schmidt (1966). The base capacity was calculated considering the approach proposed by Zhang and Einstein (1998). The temperature variation measured by Mimouni and Laloui (2015) at the end of the heating phase of the energy pile was applied along the entire pile length due to the incapability of the considered load-transfer method in imposing temperature variations on bounded pile portions.

Table 10.16 Soil properties considered for modelling the single energy pile test of Mimouni and Laloui (2015).

Reference depth, z [m]	Variable	Value
[0; 3.1]	Saturated unit weight, γ_{sat} [kN/m^3]	15.6
	Angle of shear strength under constant volume conditions, φ'_{cv} [degree]	24
	Pile–soil interface angle of shear strength, δ' [degree]	19.1
	Menard pressuremeter modulus, E_M [MPa]	**144.6**
	Slope of the pile shaft load-transfer elastic branch, K_s [kPa/m]	**321,364**
	Overconsolidation ratio, OCR [−]	4
[3.1; 8.6]	Saturated unit weight, γ_{sat} [kN/m^3]	15.6
	Angle of shear strength under constant volume conditions, φ'_{cv} [degree]	21
	Pile–soil interface angle of shear strength, δ' [degree]	18.5
	Menard pressuremeter modulus, E_M [MPa]	**144.6**
	Slope of the pile shaft load-transfer elastic branch, K_s [kPa/m]	**321,364**
	Overconsolidation ratio, OCR [−]	4
[8.6; 16.6]	Saturated unit weight, γ_{sat} [kN/m^3]	11.1
	Angle of shear strength under constant volume conditions, φ'_{cv} [degree]	17
	Pile–soil interface angle of shear strength, δ' [degree]	16.1
	Menard pressuremeter modulus, E_M [MPa]	**60**
	Slope of the pile shaft load-transfer elastic branch, K_s [kPa/m]	**53,333**
	Overconsolidation ratio, OCR [−]	4
[16.6; 20.1]	Saturated unit weight, γ_{sat} [kN/m^3]	11.9
	Angle of shear strength under constant volume conditions, φ'_{cv} [degree]	21
	Pile–soil interface angle of shear strength, δ' [degree]	18.9
	Menard pressuremeter modulus, E_M [MPa]	**64.3**
	Slope of the pile shaft load-transfer elastic branch, K_s [kPa/m]	**57,143**
	Overconsolidation ratio, OCR [−]	4
[20.1; 28.9)	Saturated unit weight, γ_{sat} [kN/m^3]	10.3
	Angle of shear strength under constant volume conditions, φ'_{cv} [degree]	29
	Pile–soil interface angle of shear strength, δ' [degree]	24.5
	Menard pressuremeter modulus, E_M [MPa]	**109.3; 54.6**
	Slope of the pile shaft load-transfer elastic branch, K_s [kPa/m]	**242,800; 121,400**
	Slope of the pile base load-transfer elastic branch, K_b [kPa/m]	*1,335,400; 667,700*
	Overconsolidation ratio, OCR [−]	4

Source: Modified after Rotta Loria, A.F., Català Oltra, J.V., Laloui, L., 2019b. Equivalent pier analysis of full-scale pile groups subjected to mechanical and thermal loads. (Under review).

Table 10.17 Pile properties considered for modelling the single pile test of Mimouni and Laloui (2015).

Variable	Value
Young's modulus, E_{EP} [GPa]	28
Shaft capacity, Q_s [kN]	**2288**
Base capacity, Q_b [kN]	**10,074**
Total pile axial capacity, Q_u [kN]	**12,362**

Source: Modified after Rotta Loria, A.F., Català Oltra, J.V., Laloui, L., 2019b. Equivalent pier analysis of full-scale pile groups subjected to mechanical and thermal loads. (Under review).

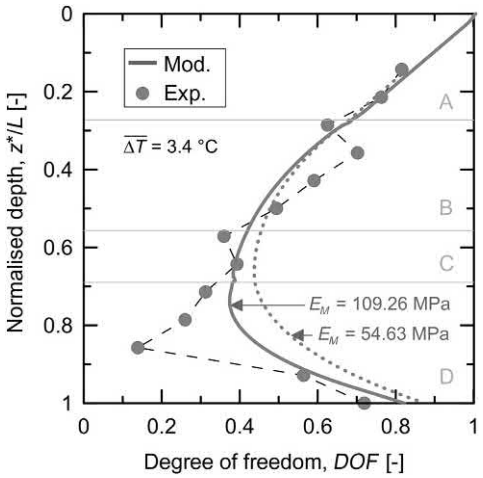

Figure 10.53 Experimental and modelled evolutions of the degree of freedom along the single energy pile tested by Mimouni and Laloui (2015). *Modified after Rotta Loria, A.F., Català Oltra, J.V., Laloui, L., 2019b. Equivalent pier analysis of full-scale pile groups subjected to mechanical and thermal loads. (Under review).*

Fig. 10.53 shows the measured and computed evolutions of the degree of freedom along the single energy pile, $DOF = \varepsilon_o^{th}/\varepsilon_f^{th}$, where ε_o^{th} and ε_f^{th} are the observed thermally induced strain and the strain under free thermal expansion conditions calculated according to a one-dimensional scheme. The relative depth z^* is normalised by the pile length L.

Close agreement between the experimental data and the results of the predictions is observed. The prediction results meaningfully tend to a value of degree of freedom $DOF = 1$ at the pile head, thus reflecting the free character of this setting because of the absence of restraint provided by any structural element connected at the pile head throughout the considered test. The DOF decreases with depth and increases again towards the pile toe. The greater differences between the experimental and predictions results can be highlighted in the molasse layer, although both simulations can be

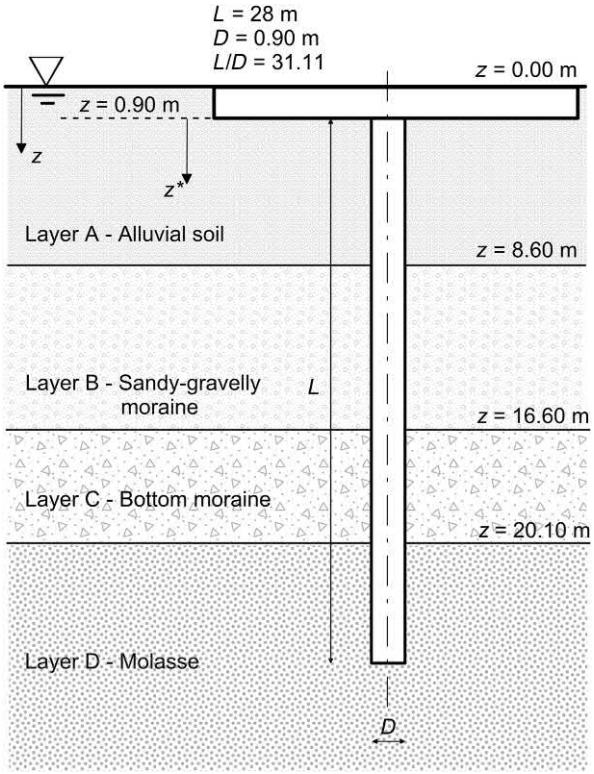

Figure 10.54 Features of the test site described by Rotta Loria and Laloui. *Modified after Rotta Loria, A.F., Català Oltra, J.V., Laloui, L., 2019b. Equivalent pier analysis of full-scale pile groups subjected to mechanical and thermal loads. (Under review).*

considered to capture the overall evolution of the pile degree of freedom with depth. The use of different values of E_M reasonably involves a noteworthy difference between the predictions results in molasse layer, with a decreasing influence on the variation of the *DOF* along the shallower soil layers.

10.11.6 Tests by Rotta Loria and Laloui (2017b)

Rotta Loria and Laloui (2017b) reported the results of a full-scale in situ test performed on the same facility tested by Mimouni and Laloui (2015), with the main difference that thermal loading was applied for typical time-scales of practical geothermal operations to an energy pile restrained at its head by the presence of a slab (cf. Fig. 10.54). The thermal loading applied to the energy pile over time resulted in an average temperature variation of $\overline{\Delta T} = 5°C$, 10°C, 15°C and 20°C along its portion in which the pipes were not thermally insulated (i.e. below 4 m from the pile head).

Relevant parameters are the same as those previously reported in Tables 10.16 and 10.17 for the test of Mimouni and Laloui (2015). The same modelling considerations previously made were employed for the present analyses, with the two main following differences. (1) A head restraint was accounted for taking into consideration the presence and influence of the slab on the energy pile response. A value of the head stiffness of $K_{slab} = 2744.4$ MN/m was estimated according to the expression provided by Gorbunov-Posadov and Serebrjanyi (1961), with reference to average values of the

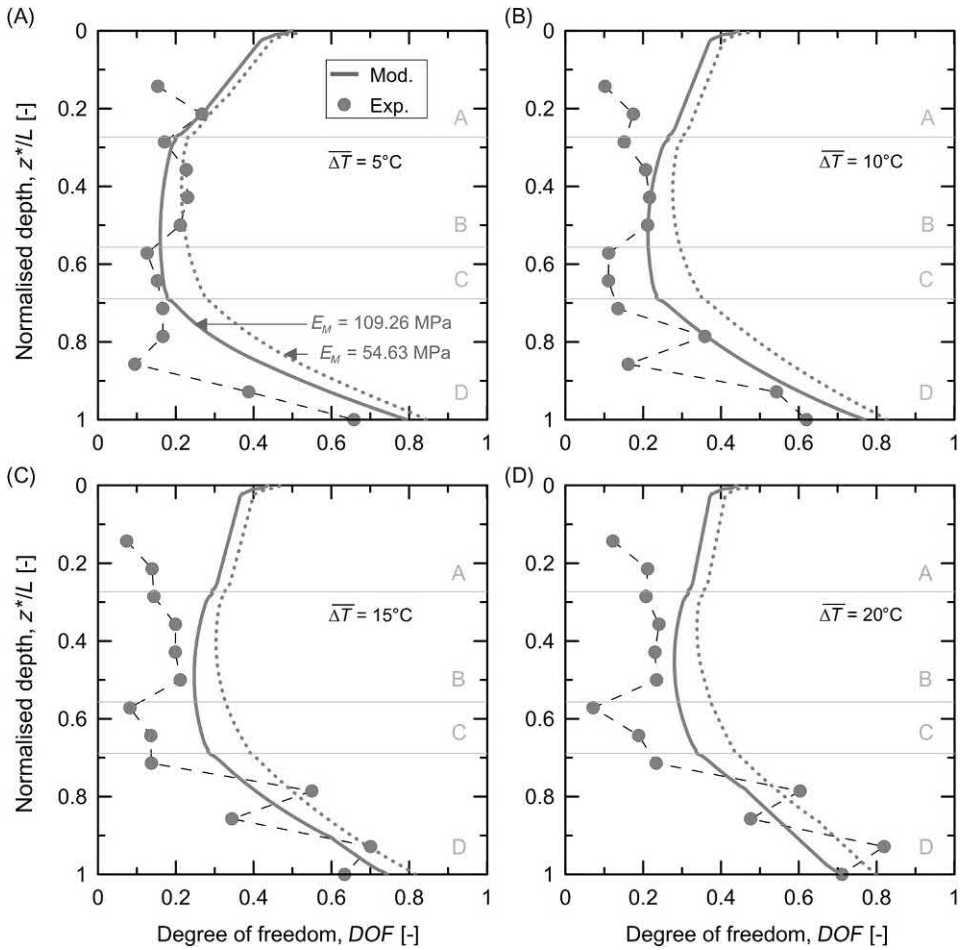

Figure 10.55 Experimental and modelled evolutions of the degree of freedom along the single energy pile tested by Rotta Loria and Laloui (2017b). Panels (A), (B), (C) and (D) refer to average temperature variations along the uninsulated portion of the energy pile of $\overline{\Delta T} = 5°C$, 10°C, 15°C and 20°C. *Modified after Rotta Loria, A.F., Català Oltra, J.V., Laloui, L., 2019b. Equivalent pier analysis of full-scale pile groups subjected to mechanical and thermal loads. (Under review).*

Young's modulus and the Poisson's ratio of the soil as well as to the slab dimensions of $L_{slab} = 26$ m and $B_{slab} = 10$ m. In the estimation of the average Young's modulus and Poisson's ratio of the soil no account was made of the properties of the molasse layer. The previous value of head stiffness resulted in a head restraint of $K_h = 4313.9$ MPa/m applied to the head of the modelled pile. (2) According to the hypothesis of an infinitely rigid plate representing the slab, a vertical mechanical load calculated as the average of the mechanical loads applied to the piles in the foundation of $P = 495$ kN was considered.

Fig. 10.55 shows the measured and computed evolutions of the degree of freedom, $DOF = \varepsilon_o^{th}/\varepsilon_f^{th}$, along the normalised along depth, z^*/L, of the single energy pile. The results of two different sets of simulations associated with different values of the Menard pressuremeter modulus for the molasse layer are reported.

The predictions capture the overall evolution of the experimental data. An increasing difference between the experimental and modelling results in correspondence with the shallower portion of the energy pile is observed for successive stages of its geothermal operation, that is when temperature variations of $\overline{\Delta T} = 15°C$ and $20°C$ are considered. This difference is attributed to the incapability of the present load-transfer analysis approach in capturing the effects (e.g. stress redistribution) associated with the more pronounced thermally induced deformation of the soil (the molasse layer) than the deformation of the pile that was observed by Rotta Loria and Laloui (2017b) at the considered stages of the experimental test. Values of $DOF \neq 1$ are meaningfully observed at the pile head because of the presence of the head restraint.

References

Amar, S., Jézéquel, J.-F., 1998. Propriétés mécaniques des sols déterminées en place. Tech. Ing. Constr. 1 (C220), C220. 1-C220. 24.

Amar, S., Clarke, B., Gambin, M., Orr, T., 1991. The application of pressuremeter test results to foundation design in Europe, Part 1: predrilled pressuremeters-self-boring pressuremeters. In: European Soil Mechanics and Foundation Engineering, European Regional Technical Committee(4).

API, 1993. Recommended Practice for Planning, Designing and Constructing Fixed Offshore Platforms. API, Dallas, TX.

Armaleh, S., Desai, C., 1987. Load-deformation response of axially loaded piles. J. Geotech. Geoenviron. Eng. 113 (12), 1483–1500.

Baldi, G., Bellotti, R., Ghionna, V., Jamiolkowski, M., Lo Presti, D., 1989. Modulus of sands from CPTs and DMTs. In: Proceedings of 12th ICSMFE, vol. 1, pp. 165–170.

Banerjee, P., Davies, T., 1978. The behaviour of axially and laterally loaded single piles embedded in nonhomogeneous soils. Geotechnique 28 (3), 309–326.

Berezantsev, K., 1961. Load bearing capacity and deformation of piled foundations. In: Proceedings of 5th International Conference on Soil Mechanics and Foundation Engineering, vol. 1, p. 11.

Bernal, J.B., Reese, L.C., 1983. Study of the Lateral Pressure of Fresh Concrete as Related to the Design of Drilled Shafts. Research Report 308–1F. The Center for Transportation Research, The University of Texas at Austin, Austin, TX.

Bolton, M., 1986. The strength and dilatancy of sands. Geotechnique 36 (1), 65–78.

Bolton, M., 1987. Discussion on the strength and dilatancy of sands. Geotechnique 37 (2), 219–226.
Bourne-Webb, P.J., Amatya, B.L., Soga, K., Amis, T., Davidson, C., Payne, P., 2009. Energy pile test at Lambeth College, London: geotechnical and thermodynamic aspects of pile response to heat cycles. Geotechnique 59 (3), 237–248.
Bourne-Webb, P.J., Amatya, B., Soga, K., 2011. A framework for understanding energy pile behaviour. Proc. ICE Geotech. Eng. 166 (2), 170–177.
Bourne-Webb, P., Bodas Freitas, T., Freitas Assunção, R., 2016. Soil–pile thermal interactions in energy foundations. Geotechnique 66 (2), 167–171.
Boussinesq, J., 1878. Équilibre d'élasticité d'un sol isotrope sans pesanteur, supportant différents poids. C. R. Acad. Sci. 86 (86), 1260–1263.
Bowles, J.E., 1988. Foundation Analysis and Design. McGraw-Hill, Singapore.
Briaud, J., Tucker, L. & Ng, E., 1989. Axially loaded 5 pile group and single pile in sand. In: Proceedings of, 12th International Conference on Soil Mechanics and Foundation Engineering, vol. 2, Balkema, Rotterdam, pp. 1121–1124.
Buisman, A., 1935. De weerstand van paalpunten in zand. De Ingenieur 50 (Bt. 25–28), 31–35.
Burland, J.B., 1973. Shaft friction of piles in clay—a simple fundamental approach. Ground Eng. 6 (3), 30–42.
Burland, J., Twine, D., 1988. The shaft friction of bored piles in terms of effective strength. In: Proceedings of 1st International Conference on Deep Foundations, Bored and Augered Piles, pp. 411–420.
Burland, J.B., Butler, F.G., Dunican, P., 1966. The behaviour and design of large diameter bored piles in stiff clay. Symposium on Large Bored Piles. Thomas Telford Publishing, London, pp. 51–71.
Burlon, S., Habert, J., Szymkievicz, F., Suryatriyastuti, M., Mroueh, H., 2013. Towards a design approach of bearing capacity of thermo-active piles. In: European Geothermal Congress, pp. 1–6.
Butterfield, R., Banerjee, P., 1971. The elastic analysis of compressible piles and pile groups. Geotechnique 21 (1), 43–60.
Caputo, V., Viggiani, C., 1984. Pile foundation analysis: a simple approach to nonlinearity effects. Riv. Ital. Geotec. 18 (2), 32–51.
Caquot, A.I., 1934. Équilibre des massifs à frottement interne: stabilité des terres, pulvérulentes ou cohérentes. Gauthier-Villars.
Carriglio, F., Ghionna, V., Jamiolkowski, M., Lancellotta, R., 1990. Stiffness and penetration resistance of sands versus state parameter. J. Geotech. Eng. 116 (6), 1015–1020.
Castelli, F., Maugeri, M., 2002. Simplified nonlinear analysis for settlement prediction of pile groups. J. Geotech. Geoenviron. Eng. 128 (1), 76–84.
Castelli, F., Motta, E., 2003. Settlement prevision of piles under vertical load. Proc. Inst. Civ. Eng. Geotech. Eng. 156 (4), 183–191.
Cekerevac, C., Laloui, L., 2004. Experimental study of thermal effects on the mechanical behaviour of a clay. Int. J. Numer. Anal. Methods Geomech. 28 (3), 209–228.
Chandler, R.J., 1968. The shaft friction of piles in cohesive soils in terms of effective stress. Civ. Eng. Public Works Rev. 63, 48–51.
Chen, D., McCartney, J.S., 2016. Parameters for load transfer analysis of energy piles in uniform nonplastic soils. Int. J. Geomech. 17 (7), 04016159.
Cherubini, C., Yves, R., 1998. A few comments on pile design: discussion/reply. Can. Geotech. J. 35 (5), 905.
Chow, F., 1997. Investigations into the Behaviour of Displacement Piles for Offshore Structures (Ph.D. thesis). University of London Imperial College, London.
Chow, Y., 1986a. Analysis of vertically loaded pile groups. Int. J. Numer. Anal. Methods Geomech. 10 (1), 59–72.
Chow, Y., 1986b. Discrete element analysis of settlement of pile groups. Comput. Struct. 24 (1), 157–166.
Clarke, B.G., 1994. Pressuremeters in Geotechnical Design. CRC Press.
Coduto, D., 1994. Foundation Design: Principles and Practices. Prentice-Hall Inc., Englewood Clifs, NJ.
Cooke, R., 1974. Settlement of friction pile foundations. In: Proceedings of Conference on Tall Buildings, pp. 7–19.

Coyle, H.M., Castello, R.R., 1981. New design correlations for piles in sand. J. Geotech. Geoenviron. Eng. 107 (GT7), 965–986 **(ASCE 16379)**.
Coyle, H.M., Reese, L.C., 1966. Load transfer for axially loaded piles in clay. J. Soil Mech. Found. Div. 92, 1–26 **(SM2, Proc Paper 4702)**.
Coyle, H.M., Sulaiman, I.H., 1967. Skin friction for steel piles in sand. J. Soil Mech. Found. Div 92, **(SM5, Proc Paper 490)**.
De Beer, E., 1988. Different behavior of bored and driven piles. In: Van Impe, W. (Ed.), Deep Foundations on Bored and Auger Piles. Balkema, Rotterdam, pp. 47–82.
De Nicola, A., Randolph, M., 1997. The plugging behaviour of driven and jacked piles in sand. Geotechnique 47 (4), 841–856.
Di Donna, A., Rotta Loria, A.F., Laloui, L., 2016. Numerical study on the response of a group of energy piles under different combinations of thermo-mechanical loads. Comput. Geotech. 72 (1), 126–142.
Eide, O., Hutchinson, J., Landva, A., 1961. Short and long-term test loading of a friction pile in clay. In: 5th International Conference on Soil Mechanics and Foundation Engineering, vol. 2, Paris, France, pp. 45–53.
Eslami, H., Rosin-Paumier, S., Abdallah, A., Masrouri, F., 2017. Pressuremeter test parameters of a compacted illitic soil under thermal cycling. Acta Geotech. 1–14.
Flaate, K., Selnes, P., 1977. Side friction of piles in clay. In: Proceedings of the 9th International Conference on Soil Mechanics and Foundation Engineering, Tokyo, pp. 517–522.
Fleming, W., Thorburn, S., 1984. Recent piling advances. Piling and Ground Treatment. Thomas Telford Publishing, pp. 1–16.
Fleming, K., Weltman, A., Randolph, M., Elson, K., 2008. Piling Engineering. CRC Press.
Frank, R., 1975. Etude théorique du comportement des pieux sous charge verticale: Introduction de la dilatance (Ph.D. thesis). Laboratoires des Ponts et Chaussées, p. 243.
Frank, R., 2009. Design of foundations in France with the use of Menard pressuremeter tests (MPM). Soil Mech. Found. Eng. 46 (6), 219–231.
Frank, R., Zhao, S., 1982. Estimation par les paramètres pressiométriques de l'enfoncement sous charge axiale de pieux forés dans des sols fins. Bull. Liaison Labo. P. et Ch. 119, 17–24.
Frank, R., Kalteziotis, N., Bustamante, M., Christoulas, S., Zervogiannis, H., 1991. Evaluation of performance of two piles using pressuremeter method. J. Geotech. Eng. 117 (5), 695–713.
Golder, H., 1957. A note on piles in sensitive clays. Geotechnique 7 (4), 192–195.
Golder, H., Leonard, M., 1954. Some tests on bored piles in London Clay. Geotechnique 4 (1), 32–41.
Goode III, J., Zhang, M., McCartney, J.S., 2014. Centrifuge modeling of energy foundations in sand. Proceedings of 8th International Conference on Physical Modelling in Geotechnics (ICPMG2014). Taylor and Francis, London, pp. 729–736.
Gorbunov-Posadov, M.I., Serebrjanyi, R.V., 1961. Design of structures on elastic foundation. In: 5th International Conference on Soil Mechanics and Foundation Engineering, vol. 1, pp. 643–648.
Hansen, J.B., 1970. A revised and extended formula for bearing capacity. Danish Geotech. Inst. Bull. 28, 5–11.
Hirayama, H., 1990. Load-settlement analysis for bored piles using hyperbolic transfer functions. Soils Found. 30 (1), 55–64.
Horvath, R., Kenney, T., Trow, W., 1980. Results of tests to determine shaft resistance of rock-socketed drilled piers. In: International Conference on Structural Foundations on Rock, vol. 1, Sydney, Australia.
Houlsby, G., Hitchman, R., 1988. Calibration chamber tests of a cone penetrometer in sand. Geotechnique 38 (1), 39–44.
Hutchinson, J.N., Jensen, E., 1968. Loading tests on piles driven into estuarine clays at Port Kharramashahr, Iran, and observations of the effect of bitumen coatings on shaft bearing capacity. Nor. Geotech. Inst. Publ. 78, 1–12.
Jaky, J., 1944. The coefficient of earth pressure at rest. J. Soc. Hung. Archit. Eng. 78 (22), 355–358.
Jamiolkowski, M., Lancellotta, R., 1988. Relevance of in-situ test results for evaluation of allowable base resistance of bored piles in sands. In: Proceedings of 1st International Geotechnical Seminar on Deep Foundations on Bored and Auger Piles, pp. 107–120.

Janbu, N., 1976. Static bearing capacity of friction piles. In: Sechste Europaeische Konferenz Fuer Bodenmechanik Und Grundbau, vol. 1.
Jardine, R., Chow, F., 1996. New Design Methods for Offshore Piles. Marine Technology Directorate, London.
Jardine, R., Fourie, A., Potts, D., Burland, J., 1986. Studies of the influence of non-linear stress-strain characteristics in soil–structure interaction. Geotechnique 36 (3), 377–396.
Jardine, R., Lehane, B., Everton, S., 1993. Friction coefficients for piles in sands and silts. Offshore Site Investigation and Foundation Behaviour. Springer, pp. 661–677.
Kagawa, T., 1992. Moduli and damping factors of soft marine clays. J. Geotech. Eng. 118 (9), 1360–1375.
Kishida, H., Uesugi, M., 1987. Tests of the interface between sand and steel in the simple shear apparatus. Geotechnique 37 (1), 45–52.
Knellwolf, C., Peron, H., Laloui, L., 2011. Geotechnical analysis of heat exchanger piles. J. Geotech. Geoenviron. Eng. 137 (10), 890–902.
Kolk, H., der Velde, E., 1996. A reliable method to determine friction capacity of piles driven into clays. In: Proceedings of Offshore Technology Conference, Houston.
Kraft, L., 1990. Computing axial pile capacity in sands for offshore conditions. Mar. Geotechnol. 9 (1), 61–92.
Kraft, L., Focht, J., Amerasinghe, S., 1981. Friction capacity of piles driven into clay. J. Geotech. Geoenviron. Eng. 107, 1521–1541 (ASCE 16663 Proceeding).
Kramer, C.A., Basu, P., 2014. Performance of a model geothermal pile in sand. Proceedings of 8th International Conference on Physical Modelling in Geotechnics. Balkema/CRC Press, pp. 771–777.
Kulhawy, F.H., 1984. Limiting tip and side resistance: fact or fallacy? Analysis and Design of Pile Foundations. ASCE, pp. 80–98.
Kulhawy, F.H., Jackson, C.S., 1989. Some observations on undrained side resistance of drilled shafts. Foundation Engineering: Current Principles and Practices. ASCE, pp. 1011–1025.
Kulhawy, F.H., Phoon, K.-K., 1993. Drilled shaft side resistance in clay soil to rock. Design and Performance of Deep Foundations: Piles and Piers in Soil and Soft Rock. ASCE, pp. 172–183.
Kulhawy, F.H., O'Rourke, T., Stewart, J.P., Beech, J., 1983. Transmission Line Structure Foundations for Uplift-Compression Loading, Load Test Summaries: Appendix to EPRI Final Report EL-2870. Electric Power Research Institute.
Laloui, L., Moreni, M., Vulliet, L., 2003. Comportement d'un pieu bi-fonction, fondation et échangeur de chaleur. Can. Geotech. J. 40 (2), 388–402.
Lancellotta, R., 1995. Geotechnical Engineering. Balkema, Rotterdam.
Lang, H.J., Huder, J., 1978. Bodenmechanik und Grundbau: Das Verhalten von Böden und die wichtigsten grundbaulichen Konzepte. Springer, Berlin.
Lee, J., Salgado, R., 1999. Determination of pile base resistance in sands. J. Geotech. Geoenviron. Eng. 125 (8), 673–683.
Lehane, B., Randolph, M.F., 2002. Evaluation of a minimum base resistance for driven pipe piles in siliceous sand. J. Geotech. Geoenviron. Eng. 128 (3), 198–205.
Lehane, B., Jardine, R., Bond, A.J., Frank, R., 1993. Mechanisms of shaft friction in sand from instrumented pile tests. J. Geotech. Eng. 119 (1), 19–35.
Lehane, B.M., Schneider, J.A., Xu, X., 2005. A Review of Design Methods for Offshore Driven Piles in Siliceous Sand. The University of Western Australia.
Mandolini, A., Viggiani, C. (Eds.), 1992. Terreni ed opere di fondazione di un viadotto sul fiume Garigliano. Riv. Ital. Geotec. 26 (2), 95–113.
McCartney, J.S., Rosenberg, J.E., 2011. Impact of heat exchange on side shear in thermo-active foundations. Proceedings of Geo-Frontiers: Advances in Geotechnical Engineering. ASCE, pp. 488–498.
McClelland, B., 1972. Design and performance of deep foundations. In: Proceedings of Special Conference on Performance of Earth and Earth-Supported Structures, vol. 2, p. 111.
McClelland, B., 1974. Design of deep penetration piles for ocean structures. J. Geotech. Eng. Div. 100 (GT7), 705–747.

McClelland, B., Focht, J.A., Emrich, W.J., 1969. Problems in design and installation of offshore piles. J. Soil Mech. Found. Eng. Div. 95 (SM6).
Menard, L. (1975) Interpretation and application of pressuremeter test results. Sols Soils No. 26-1975.
Meyerhof, G., 1951. The ultimate bearing capacity of foudations. Geotechnique 2 (4), 301–332.
Meyerhof, G., 1953. Some recent foundation research and its application to design. Struct. Eng. 31 (6), 151–167.
Meyerhof, G.G., 1963. Some recent research on the bearing capacity of foundations. Can. Geotech. J. 1 (1), 16–26.
Meyerhof, G., 1976. Bearing capacity and settlement of pile foundations. J. Geotech. Eng. Div. GT3 (1), 197–228.
Meyerhof, G., Murdock, L., 1953. An investigation of the bearing capacity of some bored and driven piles in London Clay. Geotechnique 3 (7), 267–282.
Mimouni, T., Laloui, L., 2014. Towards a secure basis for the design of geothermal piles. Acta Geotech. 9 (3), 355–366.
Mimouni, T., Laloui, L., 2015. Behaviour of a group of energy piles. Can. Geotech. J. 52 (12), 1913–1929.
Mindlin, R.D., 1936. Force at a point in the interior of a semi-infinite solid. J. Appl. Phys. 7 (5), 195–202.
Mohan, D., Chandra, S., 1961. Frictional resistance of bored piles in expansive clays. Geotechnique 11 (4), 294–301.
Morgan, J., Poulos, H., 1968. Settlement and stability of deep foundations. In: Lee, I.K. (Ed.), Proceedings of Soil Mechanics—Selected Topics. Butterworths, pp. 528–609.
Ng, C.W.W., Shi, C., Gunawan, A., Laloui, L., Liu, H.L., 2015. Centrifuge modelling of heating effects on energy pile performance in saturated sand. Can. Geotech. J. 52 (8), 1045–1057.
Nordlund, R., 1963. Bearing capacity of piles in cohesionless soils. J. Soil Mech. Found. Div. 89 (3), 1–36.
Olgun, C.G., Ozudogru, T.Y., Arson, C., 2014. Thermo-mechanical radial expansion of heat exchanger piles and possible effects on contact pressures at pile–soil interface. Géotech. Lett. 4 (July–September), 170–178.
Olson, R.E., Dennis, N.D., 1982. Review and Compilation of Pile Test Results: Axial Pile Capacity. Geotechnical Engineering Center, Department of Civil Engineering, University of Texas, Dallas, TX.
O'Neill, M.W., Hawkins, R.A., Mahar, L.J., 1981. Field Study of Pile Group Action. Final Report No. FHWA/RD-81/001, p. 195.
Parry, R., Swain, C., 1977. Effective stress methods of calculating skin friction on driven piles in soft clay. Ground Eng. 10 (3), 24–26 **(Analytic)**.
Pasten, C., Santamarina, J.C., 2014. Thermally induced long-term displacement of thermoactive piles. J. Geotech. Geoenviron. Eng. 140 (5), 06014003.
Peck, R., 1958. A Study of the Comparative Behaviour of Friction Piles. Highway Research Board, Special Report No. 36.
Poulos, H.G., Davis, E.H., 1968. The settlement behaviour of single axially loaded incompressible piles and piers. Geotechnique 18 (3), 351–371.
Poulos, H.G., Davis, E.H., 1980. Pile Foundation Analysis and Design. Wiley, New York.
Poulos, H.G., Mattes, N.S., 1969. The behaviour of axially loaded end-bearing piles. Geotechnique 19 (2), 285–300.
Powrie, W., 2013. Soil Mechanics: Concepts and Applications. CRC Press.
Rammal, D., Mroueh, H., Burlon, S., 2018. Impact of thermal solicitations on the design of energy piles. Renew. Sustain. Energy Rev. 92, 111–120.
Randolph, M.F., 1981. Piles subjected to torsion. J. Soil Mech. Found. Div. 107 (8), 1095–1111.
Randolph, M., 1994. Design methods for pile groups and piled rafts. In: Proceedings of XIII ICSMFE, pp. 61–82.
Randolph, M.F., 2003. Science and empiricism in pile foundation design. Geotechnique 53 (10), 847–875.

Randolph, M.F., Murphy, B., 1985. Shaft capacity of driven piles in clay. In: Proceedings of 7th Offshore Technology Conference, Houston.
Randolph, M.F., Wroth, C.P., 1978. Analysis of deformation of vertically loaded piles. J. Geotech. Eng. Div. 104 (12), 1465–1488.
Randolph, M.F., Wroth, C., 1981. Application of the failure state in undrained simple shear to the shaft capacity of driven piles. Geotechnique 31 (1), 143–157.
Randolph, M., Dolwin, R., Beck, R., 1994. Design of driven piles in sand. Geotechnique 44 (3), 427–448.
Randolph, M.F., Joer, H.A., Airey, D.W., 1998. Foundation design in cemented sands. In: Proceedings of 2nd International Seminar on Hard Soils, vol. 3.
Reese, L.C., O'Neill, M.W., 1988. Drilled Shafts: Construction Procedures and Design Methods. Prepared for US Department of Transportation, Federal Highway Administration, Office of Implementation.
Reese, L., O'Neill, M., 1989. New design method for drilled shafts from common soil and rock tests. Foundation Engineering: Current Principles and Practices. ASCE, pp. 1026–1039.
Reese, L., Hudson, W., Vijayvergiya, V., 1969. An investigation of the interaction between bored piles and soil. In: 7th International Conference on Soil Mechanics and Foundation Engineering, vol. 2.
Regueiro, R.A., Wang, W., Stewart, M.A., McCartney, J.S., 2012. Coupled thermo-poro-mechanical finite element analysis of an energy foundation centrifuge experiment in saturated silt. Proceedings of GeoCongress. ASCE, pp. 4406–4415.
Robertson, P., 1991. Estimation of foundation settlements in sand from CPT. Geotechnical Engineering Congress—1991. ASCE, pp. 764–775.
Rotta Loria, A.F., Laloui, L., 2016. The interaction factor method for energy pile groups. Comput. Geotech. 80, 121–137.
Rotta Loria, A.F., Laloui, L., 2017a. Displacement interaction among energy piles bearing on stiff soil strata. Comput. Geotech. 90, 144–154.
Rotta Loria, A.F., Laloui, L., 2017b. Thermally induced group effects among energy piles. Géotechnique 67 (5), 374–393.
Rotta Loria, A.F., Laloui, L., 2018a. Group action effects caused by various operating energy piles. Geotechnique 68 (9), 834–841.
Rotta Loria, A.F., Laloui, L., 2018b. Thermo-mechanical schemes for energy piles. In: Proceedings of International Symposyum on Energy Geotechnics, SEG 2018, pp. 218–225.
Rotta Loria, A.F., Orellana, F., Minardi, A., Furbringer, J.-M., Laloui, L., 2014. Predicting the axial capacity of piles in sand. Comput. Geotech. 69 (1), 485–495.
Rotta Loria, A.F., Gunawan, A., Shi, C., Laloui, L., Ng, C.W., 2015. Numerical modelling of energy piles in saturated sand subjected to thermo-mechanical loads. Geomech. Energy Environ. 1 (1), 1–15.
Rotta Loria, A.F., Vadrot, A., Laloui, L., 2017. Effect of non-linear soil deformation on the interaction among energy piles. Comput. Geotech. 86, 9–20.
Rotta Loria, A.F., Vadrot, A., Laloui, L., 2018. Analysis of the vertical displacement of energy pile groups. Geomech. Energy Environ. 16, 1–14.
Rotta Loria, A.F., Bocco, M., Garbellini, C., Muttoni, A., Laloui, L., 2019a. The role of thermal loads in the performance-based design of energy piles. Geomech. Energy Environ. doi.10.1016/j.gete.2019.100153.
Rotta Loria, A.F., Català Oltra, J.V., Laloui, L., 2019b. Equivalent pier analysis of full-scale pile groups subjected to mechanical and thermal loads. (Under review).
Rowe, P.W., 1962. The stress-dilatancy relation for static equilibrium of an assembly of particles in contact. Report 1364-5021, pp. 500–527.
Rowe, R., Armitage, H., 1987. A design method for drilled piers in soft rock. Can. Geotech. J. 24 (1), 126–142.
Schmidt, B., 1966. Earth pressures at rest related to stress history. Can. Geotech. J. 3 (4), 239–242.
Seed, H.B., Chan, C.K., 1966. Clay strength under earthquake loading conditions. J. Soil Mech. Found. 92 (6), 105–134.

Semple, R.M., Rigden, W.J., 1984. Shaft capacity of driven pipe piles in clay. Analysis and Design of Pile Foundations. ASCE, pp. 59–79.
Skempton, A., 1951. The bearing capacity of clays. In: Proceedings of Building Research Congress, vol. 1, pp. 180–189.
Skempton, A.W., 1959. Cast in-situ bored piles in London clay. Geotechnique 9 (4), 153–173.
Skempton, A., Yassin, A., Gibson, R., 1953. Theorie de la force portante des pieux. Annales de l'Institut Technique du Batiment et des Travaux Publics vol. 6, 285–290.
Sladen, J., 1992. The adhesion factor: applications and limitations. Can. Geotech. J. 29 (2), 322–326.
Stas, C.V., Kulhawy, F.H., 1984. Critical Evaluation of Design Methods for Foundations Under Axial Uplift and Compression Loading. Electric Power Research Institute.
Suryatriyastuti, M., Mroueh, H., Burlon, S., 2014. A load transfer approach for studying the cyclic behavior of thermo-active piles. Comput. Geotech. 55 (1), 378–391.
Sutman, M., Olgun, C.G., Laloui, L., 2018. Cyclic load–transfer approach for the analysis of energy piles. J. Geotech. Geoenviron. 145 (1), 04018101.
Terzaghi, K., 1943. Theoretical Soil Mechanics. John Wiley & Sons, New York.
Tomlinson, M., 1957. The adhesion of piles driven in clay soils. In: Proceedings of the 4th International Conference on Soil Mechanics and Foundation Engineering, vol. 2, pp. 66–71.
Tomlinson, M., 1971. Some effects of pile driving on skin friction. Behaviour of Piles. Thomas Telford Publishing, pp. 107–114.
Tomlinson, M., Woodward, J., 1993. Pile Design and Construction Practice. CRC Press.
Van Impe, W., 1991. Deformation of deep foundations. General Report. In: Proceedings of the 13th ISSMFE Conference.
Vesic, A.S., 1967. A Study of the Bearing Capacity of Deep Foundations. Georgia Institute of Technology, Atlanta, GA.
Vesić, A., 1969. Experiments with instrumented pile groups in sand. Performance of Deep Foundations. ASTM International.
Vesic, A.S., 1975. Bearing capacity of shallow foundations. Foundation Engineering Handbook. Van Nostrand Reinhold Company, New York, pp. 121–147.
Vesic, A.S., 1977. Design of Pile Foundations. NCHRP Synthesis of Highway Practice Issue No. 42. Transportation Research Board.
Viggiani, C., 2001. Analysis and design of piled foundations. Riv. Ital. Geotec. 35 (1), 47–75.
Vijayvergiya, V., Focht, J., 1972. A new way to predict the capacity of piles in clay. In: Fourth Annual Offshore Technology Conference, vol. 2, Houston, pp. 865–874.
Wang, B., Bouazza, A., Haberfield, C., 2011. Preliminary observations from laboratory scale model geothermal pile subjected to thermal-mechanical loading. Proceedings of Geo-Frontiers 2011: Advances in Geotechnical Engineering. ASCE, pp. 430–439.
Weltman, A., Healy, P., 1978. Piling in Boulder Clay and other Glacial Tills. Report G5 Monograph.
Whitaker, T., Cooke, R.W., 1966. An investigation of the shaft and base resistance of large bored piles in London clay. Symposium on Large Bored Piles. Thomas Teldford Publishing, London, pp. 7–49.
Williams, A., Pells, P., 1981. Side resistance rock sockets in sandstone, mudstone, and shale. Can. Geotech. J. 18 (4), 502–513.
Winkler, E., 1867. Die Lehre von der Elasticitaet und Festigkeit: mit besonderer Rücksicht auf ihre Anwendung in der Technik für polytechnische Schulen, Bauakademien, Ingenieue, Maschinenbauer, Architecten, etc. Dominicus.
Woodward, R., Boitano, J., 1961. Pile loading tests in stiff clays. In: 5th International Conference of Soil Mechanics and Foundation Engineering, vol. 2.
Wroth, C., 1979. Correlations of some engineering properties of soils. In: Proceedings of the Second International Conference on the Behaviour of Off-Shore Structures, held at Imperial College, London, England.
Zhang, L., Einstein, H.H., 1998. End bearing capacity of drilled shafts in rock. J. Geotech. Geoenviron. Eng. 124 (7), 574–584.

Questions and problems

Statements

a. Express mathematically the equation that governs the axial load capacity of piles and define all of the involved terms

b. The shaft and base capacities of piles are characterised by the fact that:
- **i.** They are mobilised at the same time
- **ii.** The shaft capacity is mobilised after the base capacity
- **iii.** The shaft capacity is mobilised before the base capacity

c. Briefly provide a description of the 'Alpha, Beta and Lambda Methods' for calculating the shaft resistance of piles.

d. Explain why it can be considered meaningful to consider the pile–soil interface angle of shear strength to be equal to the soil angle under constant volume conditions when calculating the shaft capacity of piles.

e. Are there any relationships that link the angle of shear strength of soils to their angle of shear strength under constant volume conditions via the contribution of dilatancy? Express mathematically possible formulations if available.

f. The shaft capacity of displacement piles can generally be calculated according to the same considerations for nondisplacement piles:
- **i.** True
- **ii.** False

g. Explain why it is preferable to employ an effective stress approach to calculate the axial load capacity of piles compared to a total stress approach.

h. Consider the geotechnical model characterised by the material properties reported in the following figure. Assume that the applied mechanical load to the pile head is known. Evaluate the minimum length of the displacement pile to carry the applied load referring to an analysis in terms of total stresses and an analysis in terms of effective stresses. For the former analysis, estimate the shaft capacity by using the approach proposed by the American Petroleum Institute read (API, 1993) for determining the empirical parameter $\overline{\alpha^f}$ and calculate the base capacity according to the approach proposed by Terzaghi (1943). For the latter analysis, estimate the base capacity by applying the approach proposed by Hansen (1970). Use appropriate values of angle of shear strength. Compare the obtained results.

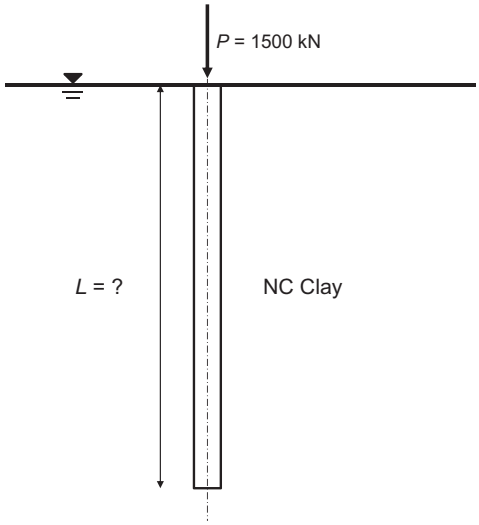

i. With reference to the geotechnical model reported in the following figure, evaluate the load applicable to the considered nondisplacement pile founded on rock. To evaluate the shaft capacity, use appropriate values of the coefficient $\overline{K}$ according to Kulhawy et al. (1983) and of the angle of shear strength. To estimate the base capacity, use the formulation proposed by Zhang and Einstein (1998). Think about and specify which contributions are relevant for the bearing capacity of the considered pile. Which is the minimum concrete class that should be used for the pile? Justify your choice.

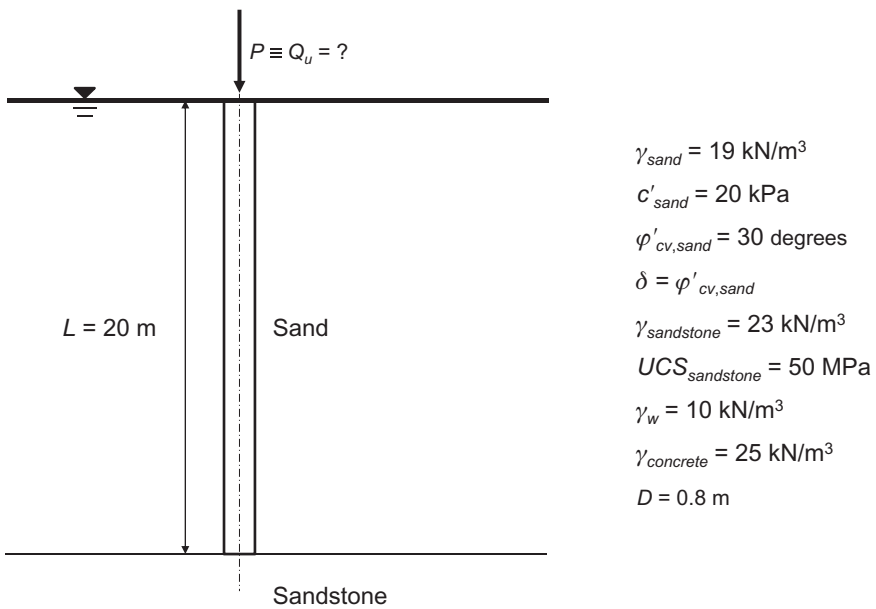

j. With reference to the geotechnical model reported in the following figure, evaluate the load capacity of the pile, considered as both displacement (e.g. driven) and nondisplacement (e.g. bored). To evaluate the shaft capacity, use appropriate values of the coefficient $\overline{K}$ according to Kulhawy et al. (1983) and of the angle of shear strength. To evaluate the base capacity, use the approaches proposed by (1) Berezantsev (1961) (considering the iterative approach proposed by Kulhawy (1984) and Fleming et al. (2008) for the bearing capacity factor estimation), (2) Hansen (1970) and (3) Janbu (1976). Compare the total bearing capacity obtained with the different analysis approaches.

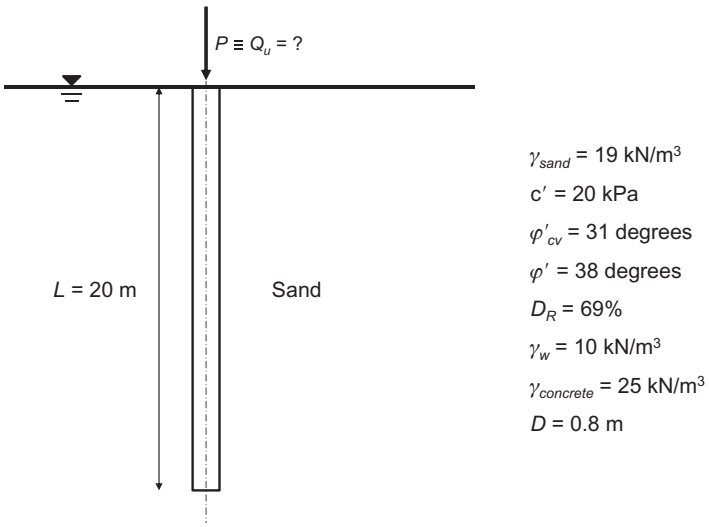

k. Consider the geotechnical model reported in the following figure. Evaluate the load capacity of the pile through an analysis in terms of total stresses and an analysis in terms of effective stresses. For the total stress analysis, estimate the shaft capacity by using the approach proposed by the American Petroleum Institute read (API, 1993) for determining the empirical parameter $\overline{\alpha^f}$ and calculate the base capacity according to the approach proposed by Terzaghi (1943). For the effective stress analysis, estimate the base capacity by applying the approach proposed by Hansen (1970). Use appropriate values of angle of shear strength. Compare the obtained results.

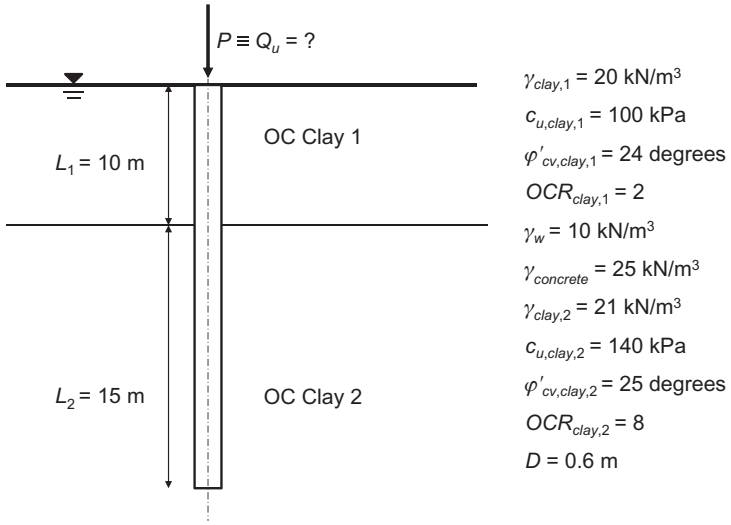

l. Consider the geotechnical model reported in the following figure. Evaluate the load capacity of the pile through an effective stress analysis. For the evaluation of the shaft capacity, consider the pile as a displacement pile (e.g. driven). For the evaluation of the base capacity, use the formulation proposed by Hansen (1970). Use appropriate values of angle of shear strength.

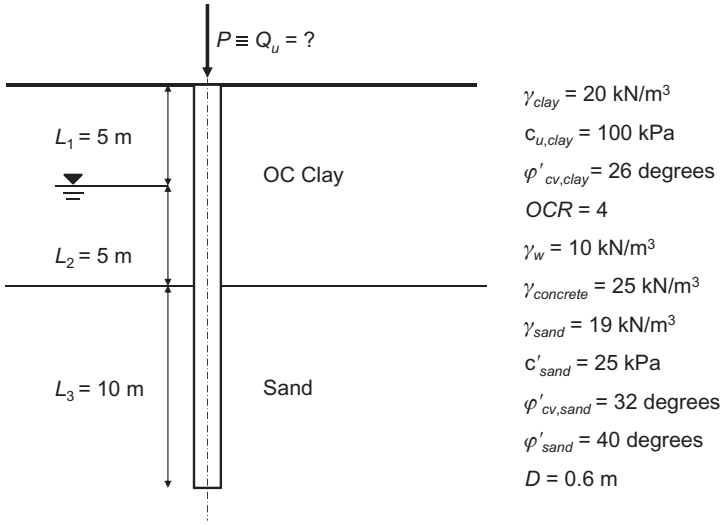

m. Express mathematically the equation that governs the axial deformation of energy piles and define all of the involved terms

n. The presence of the null point in energy piles subjected to thermal loads involves that:
  i. Energy pile equilibrium cannot be solved via closed form solutions
  ii. Energy pile equilibrium can be solved via closed form solutions
  iii. None of the above

o. The discussed thermomechanical schemes for energy piles are developed under the fundamental hypothesis of:
  i. (Thermo-)elastic conditions
  ii. (Thermo-)plastic conditions
  iii. Anisotropic conditions
  iv. None of the above

p. With reference to a thermoelastic framework, sketch the vertical stress and vertical displacement variations caused by the application of a mechanical load at the head of an energy pile that is characterised by no head and base restraints (i.e. fully floating pile). Consider compressive stresses and downward displacements to be positive.

q. With reference to a thermoelastic framework, sketch the vertical stress and vertical displacement variations caused by the application of a positive temperature variation (heating thermal load) along an energy pile that is characterised by no head and base restraints (i.e. fully floating pile). Consider compressive stresses and downward displacements to be positive.

r. With reference to a thermoelastic framework, sketch the vertical stress and vertical displacement variations caused by the application of a positive temperature variation (heating thermal load) along an energy pile that is characterised by no head restraint but by a strong base restraint (i.e. end-bearing pile). Consider compressive stresses and downward displacements to be positive.

s. To which stress and material parameters there is the need to refer when estimating analytically the bearing capacity of energy piles through short-term and long-term analyses?

t. Describe the essential features of the load-transfer method for energy piles.

u. Sketch the trilinear load-transfer curve *referring to energy piles* that has been proposed by Knellwolf et al. (2011), based on the work of Frank and Zhao (1982), to describe the interaction between the pile shaft and the surrounding soil. Consider positive shear stresses developed with positive displacement values, i.e. settlements.

v. Describe the physical meaning behind each of the three branches of the trilinear load-transfer curve referring to energy piles that has been proposed by Knellwolf et al. (2011), based on the work of Frank and Zhao (1982), and describes the interaction between the pile shaft and the surrounding soil.

w. The load-transfer approach allows considering
- **i.** Pile radial strains
- **ii.** Different soil layers
- **iii.** None of the above

x. Consider an energy pile of 20 m in length and 0.8 m in diameter that is a part of the square group of energy piles reported in the following figure. Assume that the energy pile is socketed in a saturated sand deposit and that a 12×12 m rigid slab (resting on the ground) made of reinforced concrete connects all the energy piles. The sand and the pile proprieties are reported in the following two tables, respectively.

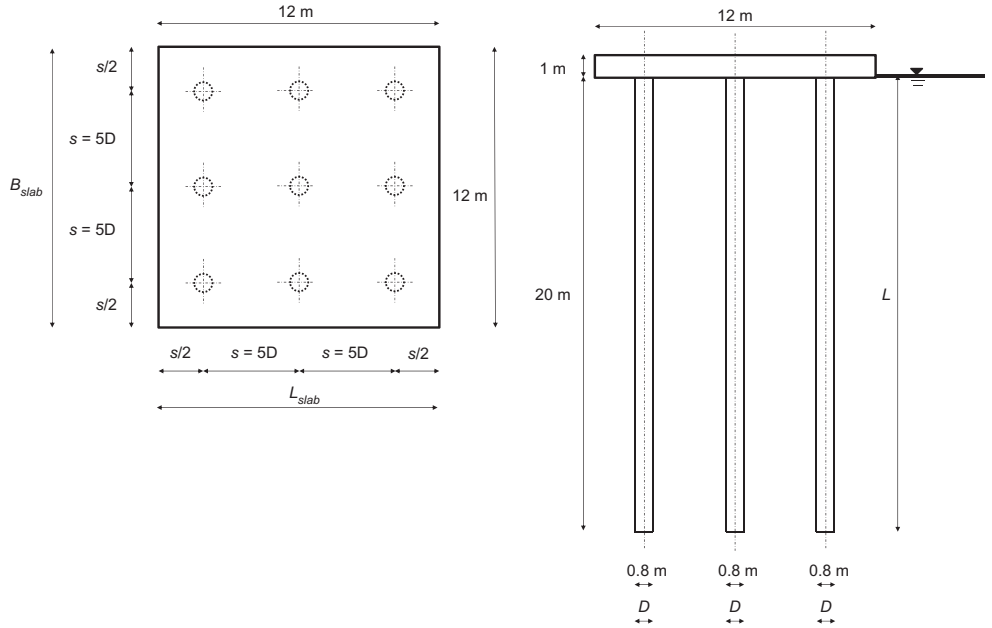

	γ_{soil}	c'	φ'_{cv}	φ'	E_{soil}	ν_{soil}	α_r
	[kN/m^3]	[kPa]	[degree]	[degree]	[MPa]	[–]	[–]
Sand	19	20	31	38	78	0.3	0.33

	$\gamma_{concrete}$	E_{EP}	ν_{EP}	α_{EP}
	[kN/m^3]	[MPa]	[–]	[με/°C]
Pile	25	30,000	0.25	10

Evaluate the bearing capacity of the energy pile (1) assuming it as a nondisplacement pile, (2) by using an analysis in terms of effective stresses and (3) considering the Hansen's method (Hansen, 1970) for the evaluation of the base contribution of capacity.

By using the software Thermo-Pile (Knellwolf et al., 2011) and referring to the relations proposed by Frank et al. (1991) for piles in coarse-grained soils, evaluate the vertical stresses and displacements developed in the considered energy pile, assumed to be a single isolated element, in five different cases:

- CASE 1: pile free at the head subjected to a vertical load of $P = 500$ kN and to a temperature variation of $\Delta T = 0°C$.
- CASE 2: pile free at the head subjected to a vertical load of $P = 0$ kN and to a temperature variation of $\Delta T = 10°C$.
- CASE (1 + 2): pile assumed to be characterised by the effects induced by the loads considered in CASE 1 and CASE 2 through an elastic superposition principle.
- CASE 3: pile free at the head subjected to a vertical load of $P = 500$ kN and to a temperature variation of $\Delta T = 10°C$.
- CASE 4: pile restrained at the head by the presence of the slab and subjected to a vertical load of $P = 500$ kN and to a temperature variation of $\Delta T = 10°C$. Assume that the slab stiffness can be estimated through the following equation, with reference to a rigid rectangular plate resting vertically loaded on an isotropic elastic half space (Gorbunov-Posadov and Serebrjanyi, 1961):

$$K_h = \frac{E_{soil}\sqrt{B_{slab}L_{slab}}}{(1 - \nu_{soil}{}^2)\rho_0}$$

where E_{soil} is the Young's modulus of the soil, B_{slab} and L_{slab} are the dimensions of the slab, ν_{soil} is the Poisson's ratio of the soil, and ρ_0 is a displacement coefficient. Consider that the displacement coefficient can be evaluated as a function of the ratio $\chi = L_{slab}/B_{slab}$.

For each case, plot the evolutions along the length of the energy pile (discretised in 200 elements in Thermo-Pile) of the vertical stress, shear stress and vertical displacement induced by the applied mechanical and/or thermal loads. Compare and discuss the differences between the obtained results through a short resume for each case, with a particular focus on the reason why CASE (1 + 2) and CASE 3 differ. Compare as well in each case the obtained results with the thermomechanical schemes discussed during the course. To which extent are these charts representative of the actual behaviour of energy piles?

Solutions

a. The general equation that governs the axial load capacity of piles is:

$$Q_u = Q_s + Q_b - W$$

where Q_s [N] is the shaft capacity, Q_b [N] is the base capacity and W [N] is the weight of the pile.

b. The shaft and base capacities of piles are characterised by the fact that:

i. They are mobilised at the same time

ii. The shaft capacity is mobilised after the base capacity

iii. The shaft capacity is mobilised before the base capacity

c. The 'Alpha method', mainly used for fine-grained soils, aims to determine the shaft resistance of piles through a relationship between the pile–soil interface adhesion $\bar{c}_a$ [Pa] and the undrained shear strength of the surrounding soil c_u [Pa] described by the adhesion factor $\alpha^f = \bar{c}_a / c_u$ [–].

The 'Beta method', used for both fine- and coarse-grained soils, aims to determine the shaft resistance of piles through a drained approach in the form $\overline{\sigma'}_z \beta^f$, where $\overline{\sigma'}_z$ [Pa] is the in situ effective vertical stress and $\beta^f = \overline{K} \tan\delta'$, with $\overline{K}$ [–] that relates the normal stress acting on the pile–soil interface after pile installation and δ' [degree] the pile–soil interface angle of shear strength.

The 'Lambda method' aims to determine the shaft resistance of piles through the expression $\lambda^f(\overline{\sigma}_z + 2c_u)$, where λ^f is a factor that depends on the length of the pile, applies over its total embedment length and includes both the effects of α^f and β^f, and $\overline{\sigma}_z$ [Pa] is the in situ total vertical stress.

d. The pile–soil interface angle of shear strength, δ', may be assumed to be equal to the angle of shear strength under constant volume conditions of the soil, φ'_{cv}, because no dilation is to be expected between the soil and the pile shaft at failure.

e. The angle of shear strength of soil may be linked to its angle of shear strength under constant volume conditions via the contribution of dilatancy through the following expression:

$$\varphi' = \varphi'_{cv} + 0.8\psi$$

where φ' [degree] is the soil angle of shear strength, φ'_{cv} [degree] is the soil angle of shear strength under constant volume conditions and ψ [degree] is the soil dilatancy angle.

f. **The shaft capacity of displacement piles can generally be calculated according to the same considerations for nondisplacement piles:**
   i. True
   ii. **False**

g. **An effective stress approach is preferable compared to a total stress approach to estimate the axial load capacity of piles because the former can account for the history characterising the soil surrounding the pile while the latter cannot.**

h. *Total stress analysis*

To evaluate the length of the pile there is the need to impose the condition for vertical pile equilibrium:

$$Q_u = Q_s + Q_b - W$$

In this case, the applied load $P = Q_u$ is of 1500 kN. The shaft capacity, Q_s, the base capacity, Q_b, and the weight, W, of the pile are all functions of its length, L, which is unknown. Therefore to solve the problem, the equilibrium equation of the pile must be written in parametric form as a function of the pile length and to be solved for the given input data.

Based on the available data and the use of the relevant formulation for $\overline{\alpha^f}$, the shaft capacity can be calculated according to the approach proposed by the American Petroleum Institute (API, 1993):

$$Q_s = q_s A_s = \overline{\alpha^f} c_u A_s = \frac{0.5}{\left(\frac{c_u}{\overline{\sigma'_z}}\right)^{0.5}} c_u \pi D L = \frac{0.5}{\left(\frac{50}{(19-10)\cdot\frac{L}{2}}\right)^{0.5}} \cdot 50 \cdot \pi \cdot 0.5L = \frac{39.3}{\left(\frac{11.1}{L}\right)^{0.5}} L$$

The base capacity, assuming a shape factor for the term N_c of $s_c = 1$ and considering that for $\varphi = 0$ (with reference to undrained conditions) the factor $N_q = 1$ and the factor $N_\gamma = 0$, can be estimated following the approach proposed by Terzaghi (1943) as:

$$Q_b = q_b A_b = (c_u N_c + \sigma_{zb}) A_b = \left(c_u N_c + \gamma_{clay} L\right) \pi \left(\frac{D}{2}\right)^2$$
$$= (50 \cdot 9 + 19 \cdot L) \pi \left(\frac{0.5}{2}\right)^2 = 88.36 + 3.73L$$

The weight of the pile reads:

$$W = \gamma_{concrete} \pi \left(\frac{D}{2}\right)^2 L = 25\pi \left(\frac{0.5}{2}\right)^2 L = 4.91L$$

By substituting the aforementioned formulations in the equation of vertical pile equilibrium, an equation for the unknown L is obtained:

$$P \equiv Q_u = Q_s(L) + Q_b(L) - W(L)$$

$$1500 = \frac{39.3}{\left(\frac{11.1}{L}\right)^{0.5}} L + 88.36 + 3.73L - 4.91L$$

$$\frac{39.3}{\left(\frac{11.1}{L}\right)^{0.5}} L + 88.36 + 3.73L - 4.91L - 1500 = 0$$

By solving the aforementioned equation, a pile length of $L = 24.7$ m is obtained.

Effective stress analysis

Based on the available data, the shaft capacity can be calculated with reference to a value of $\overline{K}$ for a displacement pile estimated according to Kulhawy et al. (1983) as follows:

$$Q_s = q_s A_s = \overline{K}\overline{\sigma'_z}\tan\delta' A_s = \left(1 - \sin\varphi'_{cv}\right)\overline{\sigma'_z}\tan\varphi'_{cv} A_s$$
$$= (1 - \sin 28)9\frac{L}{2}\tan 28 \cdot \pi 0.5L = 1.99L^2$$

The base capacity, assuming the terms involving N_c and N_γ to be negligible with respect to that involving N_q, can be estimated following the approach proposed by Hansen (1970) as:

$$Q_b = q_b A_b = \sigma'_{zb} N_q d_q A_b = \sigma'_{zb} K_p e^{\pi \tan\varphi'_{cv}} d_q \pi \left(\frac{D}{2}\right)^2$$

$$= \sigma'_{zb}\frac{1 + \sin\varphi'_{cv}}{1 - \sin\varphi'_{cv}} e^{\pi\tan\varphi'_{cv}} \left(1 + 2\tan\varphi'_{cv}\left(1 - \sin\varphi'_{cv}\right)^2 k_H\right)\pi\left(\frac{D}{2}\right)^2$$

$$= \sigma'_{zb}\frac{1 + \sin\varphi'_{cv}}{1 - \sin\varphi'_{cv}} e^{\pi\tan\varphi'_{cv}} \left(1 + 2\tan\varphi'_{cv}\left(1 - \sin\varphi'_{cv}\right)^2 \tan^{-1}\left(\frac{L}{D}\right)\right)\pi\left(\frac{D}{2}\right)^2$$

$$= (19 - 10)L\frac{1 + \sin 28}{1 - \sin 28} e^{\pi\tan 28}\left(1 + 2\tan 28(1 - \sin 28)^2 \tan^{-1}\left(\frac{L}{0.5}\right)\right)\pi\left(\frac{0.5}{2}\right)^2$$

$$= 9L \cdot 14.72 \cdot \left(1 + 0.3 \cdot \tan^{-1}\left(\frac{L}{0.5}\right)\right) \cdot \pi 0.0625$$

$$= 26.01L\left(1 + 0.3 \cdot \tan^{-1}\left(\frac{L}{0.5}\right)\right)$$

By substituting the aforementioned formulations in the equation of vertical pile equilibrium, an equation for the unknown L is obtained:

$$P \equiv Q_u = Q_s(L) + Q_b(L) - W(L)$$

$$1500 = 1.99L^2 + 26.01L\left(1 + 0.3\tan^{-1}\left(\frac{L}{0.5}\right)\right) - 4.91L$$

$$1.99L^2 + 26.01L\left(1 + 0.3\tan^{-1}\left(\frac{L}{0.5}\right)\right) - 4.91L - 1500 = 0$$

By solving the aforementioned equation, a pile length of $L = 20.4$ m is obtained.

Comments:

The total stress analysis yields to a length of the pile approximately 4 m longer than that determined through the effective stress analysis. It is possible to conclude that the total analysis is more restrictive than the effective stress analysis.

i. When dealing with piles founded on rock, an approach that can be considered is to assume that only the base capacity contributes to the total pile capacity, so that:

$$Q_u \cong Q_b$$

The above approach performs a conservative analysis and is often employed for its expediency because the magnitudes of the shaft capacity and weight of the pile are low compared to the base capacity. A proof of this aspect is proposed in the following.

Based on the available data, the base capacity can be estimated through the approach proposed by Zhang and Einstein (1998) as:

$$Q_b = q_b A_b = 15 p_a \sqrt{\frac{UCS_{sandstone}}{p_a}} A_b = 15 \cdot 101 \cdot \sqrt{\frac{50000}{101}} \cdot \pi \cdot 0.4^2$$
$$= 33708 \cdot \pi \cdot 0.4^2 = 16944 \text{ kN}$$

It is worth noting that the maximum pressure applicable is smaller than the *UCS* of the sandstone. However, due to its high value, it must be compared also with the *UCS* of the concrete. In this case, to avoid failure of the concrete, at least a concrete class of C32/40 must be used.

The shaft capacity can be calculated with reference to a value of $\overline{K}$ for a nondisplacement pile estimated according to Kulhawy et al. (1983) as follows:

$$Q_s = q_s A_s = \overline{K}\overline{\sigma'_z}\tan\delta' A_s = 0.7\left(1-\sin\varphi'_{cv,sand}\right)\gamma'_{sand}\frac{L}{2}\tan\delta'\pi DL$$

$$= 0.7\cdot(1-\sin 30)\cdot 9\cdot 10\cdot\tan 30\cdot\pi\cdot 0.8\cdot 20 = 18.2\cdot\pi\cdot 0.8\cdot 20 = 914\ \text{kN}$$

It is approximately the 5% of the base capacity. The weight of the pile reads:

$$W = \gamma_{concrete}\pi\left(\frac{D}{2}\right)^2 L = 25\pi\left(\frac{0.8}{2}\right)^2 20 = 251\ \text{kN}$$

It is approximately 1.5% of the base capacity. Based on the above, the load capacity of the pile is approximately equal to:

$$Q_u \cong Q_b = 16{,}944\ \text{kN}$$

j. The shaft capacity of the pile must be determined considering if the pile is displacement or nondisplacement. The following equation can be generally used:

$$Q_s = q_s A_s = \overline{K}\overline{\sigma'_z}\tan\delta' A_s$$

For a displacement pile, the coefficient $\overline{K}$ can be taken according to Kulhawy et al. (1983) as:

$$\overline{K} = K_0 = 1-\sin\varphi'_{cv} = 1-\sin 31 = 0.48$$

while the pile–soil interface angle of shear strength, δ', can be considered according to Kraft (1990) as $\delta' = 0.7\varphi'$ so that:

$$\tan\delta' = \tan(0.7\varphi') = 0.50$$

Therefore the shaft capacity reads:

$$Q_s = q_s A_s = \overline{K}\overline{\sigma'_z}\tan\delta' A_s = 0.48\cdot(19-10)\cdot\frac{20}{2}\cdot 0.50\cdot\pi\cdot 0.8\cdot 20 = 1086\ \text{kN}$$

For a nondisplacement pile, the coefficient $\overline{K}$ can be taken according to Kulhawy et al. (1983) as:

$$\overline{K} = 0.7K_0 = 0.7(1 - \sin\varphi'_{cv}) = 0.7(1 - \sin 31) = 0.34$$

while the pile–soil interface angle of shear strength, δ', can be considered to be $\delta' = \varphi'_{cv}$ so that:

$$\tan\delta' = \tan\varphi'_{cv} = 0.6$$

Therefore the shaft capacity reads:

$$Q_s = q_s A_s = \overline{K}\overline{\sigma'_z}\tan\delta' A_s = 0.34 \cdot (19 - 10) \cdot \frac{20}{2} \cdot 0.6 \cdot \pi \cdot 0.8 \cdot 20 = 923 \text{ kN}$$

Evaluating the base capacity with three different methods allows appreciating how the base capacity can vary in practical analyses and drawing some comments on the impact of the hypotheses made on the design.

Berezantsev's Method

The base capacity, neglecting the terms involving the bearing capacity factors N_c and N_γ, can be evaluated according to this method as:

$$Q_b = q_b A_b = \sigma'_{zb} N_q A_b = \gamma'_{sand} L N_q \pi \left(\frac{D}{2}\right)^2$$

While σ'_{zb} and A_b can be straightforwardly determined, an iterative procedure is needed to determine the factor N_q. The first trial value of $N_q^{(1)} = 50$ is chosen. The value of the mean effective stress p' is evaluated as:

$$p' = \sqrt{N_q \sigma'_{zb}} = \sqrt{50 \cdot (19 - 10) \cdot 20} = 94.87 \text{ kPa}$$

With this value of p', the I_R index is evaluated as Bolton (1986; 1987):

$$I_R = 5D_R - 1 = 5 \cdot 0.69 - 1 = 2.45$$

The peak angle of shear strength, φ', is then computed as Bolton (1986):

$$\varphi' = \varphi'_{cv} + 3I_R = 31 + 3 \cdot 2.45 = 38.35 \text{ degrees}$$

By entering in the following figure with the computed value of φ', it is possible to evaluate the corresponding value of N_q, which is equal to 139. This value is different from the trial value so it is necessary to iterate till when the trial value will be equal to the computed value.

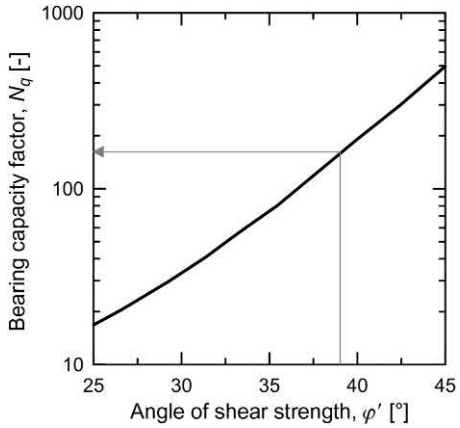

The second trial value $N_q^{(2)} = 139$ is chosen. It follows that:

$$p' = \sqrt{N_q \sigma'_{zb}} = \sqrt{139 \cdot (19 - 10) \cdot 20} = 158.20 \text{ kPa}$$

$$I_R = D_R \left[5.4 - \ln\left(\frac{p'}{p_a}\right) \right] - 1 = 0.69 \cdot \left[5.4 - \ln\left(\frac{158}{101}\right) \right] - 1 = 2.42$$

$$\varphi' = \varphi'_{cv} + 3I_R = 31 + 3 \cdot 2.42 = 38.25 \text{ degrees}$$

$$N_q = 136$$

The third trial value $N_q^{(3)} = 136$ is chosen. It follows that:

$$p' = \sqrt{N_q \sigma'_{zb}} = \sqrt{136 \cdot (19 - 10) \cdot 20} = 156.65 \text{ kPa}$$

$$I_R = D_R \left[5.4 - \ln\left(\frac{p'}{p_a}\right) \right] - 1 = 0.69 \cdot \left[5.4 - \ln\left(\frac{156.65}{101}\right) \right] - 1 = 2.42$$

$$\varphi' = \varphi'_{cv} + 3I_R = 31 + 3 \cdot 2.42 = 38.27 \text{ degrees}$$

$$N_q = 137$$

The fourth trial value $N_q^{(4)} = 137$ is chosen. It follows that:

$$p' = \sqrt{N_q \sigma'_{zb}} = \sqrt{137 \cdot (19 - 10) \cdot 20} = 156.96 \text{ kPa}$$

$$I_R = D_R \left[5.4 - \ln\left(\frac{p'}{p_a}\right) \right] - 1 = 0.69 \cdot \left[5.4 - \ln\left(\frac{156.96}{101}\right) \right] - 1 = 2.42$$

$$\varphi' = \varphi'_{cv} + 3I_R = 31 + 3 \cdot 2.42 = 38.27 \text{ degrees}$$

$$N_q = 137$$

So the base capacity is equal to:

$$Q_b = q_b A_b = N_q \sigma'_{zb} A_b = 137 \cdot 180 \cdot \pi \cdot \left(\frac{0.8}{2}\right)^2 = 12395 \text{ kN}$$

Hansen's method

The base capacity, neglecting the terms involving the bearing capacity factors N_c and N_γ and assuming a shape factor $s_q = 1$, can be evaluated according to this method as:

$$Q_b = q_b A_b = \sigma'_{zb} N_q d_q A_b = \gamma'_{sand} L K_p e^{\pi \tan\varphi'_{cv}} \left(1 + 2\tan\varphi'_{cv} \left(1 - \sin\varphi'_{cv}\right)^2 k_H\right) \pi \left(\frac{D}{2}\right)^2$$
$$= \gamma'_{sand} L \frac{\left(1 + \sin\varphi'_{cv}\right)}{\left(1 - \sin\varphi'_{cv}\right)} e^{\pi \tan\varphi'_{cv}} \left(1 + 2\tan\varphi'_{cv} \left(1 - \sin\varphi'_{cv}\right)^2 k_H\right) \pi \left(\frac{D}{2}\right)^2$$

Based on the available data:

$$K_p = \frac{\left(1 + \sin\varphi'_{cv}\right)}{\left(1 - \sin\varphi'_{cv}\right)} = \frac{(1 + \sin 31)}{(1 - \sin 31)} = 3.12$$

$$N_q = K_p e^{\pi \tan\varphi'_{cv}} = 3.12 \cdot e^{\pi \cdot \tan 31} = 20.6$$

$$k_H = \tan^{-1}\left(\frac{L}{D}\right) = 1.53$$

$$d_q = 1 + 2\tan\varphi'_{cv} \left(1 - \sin\varphi'_{cv}\right)^2 k_H = 1 + 2 \cdot \tan 31 \cdot (1 - \sin 31)^2 \cdot 1.53 = 1.43$$

Therefore the base capacity is:

$$Q_b = q_b A_b = \sigma'_{zb} N_q d_q A_b = 180 \cdot 20.6 \cdot 1.43 \cdot \pi \cdot \left(\frac{0.8}{2}\right)^2 = 2670 \text{ kN}$$

Janbu's method

In this case, the value of base resistance needed to estimate the base capacity of the pile has the same formulation of the method proposed by Hansen (1970), except for the coefficient N_q that can be calculated as:

$$N_q = \left(\tan\varphi'_{cv} + \sqrt{1+\tan^2\varphi'_{cv}}\right)^2 \exp\left(2\psi_J \tan\varphi'_{cv}\right)$$

Based on the available data, this involves:

$$N_q = \left(\tan 31 + \sqrt{1+\tan^2 31}\right)^2 \cdot \exp(2 \cdot \text{rad}(75) \cdot \tan 31) = 15.1$$

Therefore neglecting again the terms involving the bearing capacity factors N_c and N_γ and assuming a shape factor $s_q = 1$, the base capacity is equal to:

$$Q_b = q_b A_b = \sigma'_{zb} N_q d_q A_b = 180 \cdot 15.1 \cdot 1.43 \cdot \pi \cdot \left(\frac{0.8}{2}\right)^2 = 1954 \text{ kN}$$

Considering that the weight of the pile can be determined as:

$$W = \gamma_{concrete} \pi \left(\frac{D}{2}\right)^2 L = 25 \cdot \pi \cdot \left(\frac{0.8}{2}\right)^2 \cdot 20 = 251 \text{ kN}$$

The load capacity can finally be determined for the various cases considered as:

$$Q_u = Q_s + Q_b - W$$

Pile type	Displacement			
Method used to estimate Q_b	Shaft capacity, Q_s	Base capacity, Q_b	Weight, W	Load capacity, Q_u
[–]	[kN]	[kN]	[kN]	[kN]
Berezantsev	1086	12,395	251	13,230
Hansen	1086	2670	251	3505
Janbu	1086	1954	251	2789

Pile type	Nondisplacement			
Method used to estimate Q_b	Shaft capacity, Q_s	Base capacity, Q_b	Weight, W	Load capacity, Q_u
[–]	[kN]	[kN]	[kN]	[kN]
Berezantsev	923	12,395	251	13,067
Hansen	923	2670	251	3342
Janbu	923	1954	251	2626

Comments:

It is worth considering the impact of the chosen angle of shear strength for the base capacity estimation on the resulting magnitude. Although the iterative procedure proposed by Kulhawy (1984) and Fleming et al. (2008), which is based on the formula proposed by Berezantsev (1961) to estimate the base capacity, is considered optimal to evaluate the base capacity, it results in a marked overestimation of this contribution compared to the estimations provided by Hansen's and Janbu's methods. The reason for this is that, while in the former approach a peak angle of shear strength is considered to estimate the base capacity, in the latter approaches an angle of shear strength at constant volume conditions is employed according to the arguments proposed by Powrie (2013). Attention has to be paid to this aspect as it involves a marked variation of the bearing capacity estimation for any considered pile.

k. *Total stress analysis*

Based on the available data and using the relevant formulation for $\overline{\alpha_s}$ proposed by the American Petroleum Institute (API, 1993), the shaft capacity reads

$$\begin{aligned} Q_s &= q_s A_s = \overline{\alpha^f}\, c_u A_s = \overline{\alpha^{f,1}} c_{u,1} A_{s,1} + \overline{\alpha^{f,2}} c_{u,2} A_{s,2} \\ &= \frac{0.5}{\left(\frac{c_{u,1}}{\sigma'_{z,1}}\right)^{0.25}} c_{u,1} \pi D L_1 + \frac{0.5}{\left(\frac{c_{u,2}}{\sigma'_{z,2}}\right)^{0.5}} c_{u,2} \pi D L_2 \\ &= \frac{0.5}{\left(\frac{100}{50}\right)^{0.25}} \cdot 100 \cdot \pi \cdot 0.6 \cdot 10 + \frac{0.5}{\left(\frac{140}{182.5}\right)^{0.5}} \cdot 140 \cdot \pi \cdot 0.6 \cdot 15 \\ &= 0.42 \cdot 100 \cdot \pi \cdot 0.6 \cdot 10 + 0.57 \cdot 140 \cdot \pi \cdot 0.6 \cdot 15 = 3052 \text{ kN} \end{aligned}$$

The base capacity, assuming a shape factor for the term N_c of $s_c = 1$ and considering that for $\varphi = 0$ (with reference to undrained conditions)

the factor $N_q = 1$ and the factor $N_\gamma = 0$, can be estimated following the approach proposed by Terzaghi (1943) as:

$$Q_b = (c_u N_c + \sigma_{zb}) A_b = \left(c_{u,2} N_c + \sigma_{zb}\right) \pi \left(\frac{D}{2}\right)^2$$
$$= [140 \cdot 9 + (10 \cdot 20 + 21 \cdot 15)] \pi \left(\frac{0.6}{2}\right)^2 = 502 \text{ kN}$$

The weight of the pile reads:

$$W = \gamma_{concrete} \pi \left(\frac{D}{2}\right)^2 L = 25\pi \left(\frac{0.6}{2}\right)^2 25 = 177 \text{ kN}$$

Therefore the load capacity of the pile can be evaluated as

$$Q_u = Q_s + Q_b - W = 3052 + 502 - 177 = 3377 \text{ kN}$$

Effective stress analysis

The shaft capacity reads:

$$Q_s = q_s A_s = \overline{K} \overline{\sigma'_z} \tan\delta' A_s$$

For a displacement pile, according to Flaate and Selnes (1977) and Kulhawy et al. (1983), the coefficient $\overline{K}$ can be taken as:

$$\overline{K} = K_0(NC) OCR^{0.5} = \left(1 - \sin\varphi'_{cv}\right) OCR^{0.5}$$

Therefore based on the available data,

$$\overline{K_1} = K_0(NC) OCR^{0.5} = \left(1 - \sin\varphi'_{cv,1}\right) OCR^{0.5} = (1 - \sin 24) \cdot 2^{0.5} = 0.84$$

$$\overline{K_2} = K_0(NC) OCR^{0.5} = \left(1 - \sin\varphi'_{cv,1}\right) OCR^{0.5} = (1 - \sin 25) \cdot 8^{0.5} = 1.63$$

The pile–soil interface angle of shear strength, δ', can be taken as equal to φ'_{cv}:

$$\tan\delta'_1 = \tan\left(\varphi'_{cv,1}\right) = \tan(24) = 0.45$$

$$\tan\delta'_2 = \tan\left(\varphi'_{cv,2}\right) = \tan(25) = 0.47$$

Therefore the shaft capacity reads:

$$Q_s = q_s A_s = \overline{K}\overline{\sigma'_z}\tan\delta' A_s = \overline{K_1}\overline{\sigma'_{z,1}}\tan\delta' A_{s,1} + \overline{K_2}\overline{\sigma'_{z,2}}\tan\delta' A_{s,2}$$
$$= 0.84 \cdot 50 \cdot 0.45 \cdot \pi \cdot 0.6 \cdot 10 + 1.63 \cdot 182.5 \cdot 0.47 \cdot 0.6 \cdot \pi \cdot 15 = 348 + 3869 = 4301 \text{ kN}$$

The base capacity, neglecting the terms involving the bearing capacity factors N_c and N_γ and assuming a shape factor $s_q = 1$, can be evaluated according to the method proposed by Hansen (1970) as:

$$Q_b = q_b A_b = \sigma'_{zb} N_q d_q A_b$$
$$= \gamma'_{sand} L K_p e^{\pi \tan\varphi'_{cv}} \left(1 + 2\tan\varphi'_{cv}\left(1 - \sin\varphi'_{cv}\right)^2 k_H\right) \pi \left(\frac{D}{2}\right)^2$$
$$= \gamma'_{sand} L \frac{\left(1 + \sin\varphi'_{cv}\right)}{\left(1 - \sin\varphi'_{cv}\right)} e^{\pi \tan\varphi'_{cv}} \left(1 + 2\tan\varphi'_{cv}\left(1 - \sin\varphi'_{cv}\right)^2 k_H\right) \pi \left(\frac{D}{2}\right)^2$$

Based on the available data:

$$K_p = \frac{\left(1 + \sin\varphi'_{cv,2}\right)}{\left(1 - \sin\varphi'_{cv,2}\right)} = \frac{(1 + \sin 25)}{(1 - \sin 25)} = 2.46$$

$$N_q = K_p e^{\pi \tan\varphi'_{cv,2}} = 2.46 e^{\pi \tan 25} = 10.66$$

$$k_H = \tan^{-1}\left(\frac{L}{D}\right) = \tan^{-1}\left(\frac{25}{0.6}\right) = 1.55$$

$$d_q = 1 + 2\tan\varphi'_{cv,2}\left(1 - \sin\varphi'_{cv,2}\right)^2 k_H = 1 + 2\tan 25 \cdot (1 - \sin 25)^2 \cdot 1.55 = 1.48$$

Therefore the base capacity can be estimated to be:

$$Q_b = q_b A_b = \sigma'_{zb} N_q d_q A_b = 265 \cdot 10.66 \cdot 1.48 \cdot \pi \cdot \left(\frac{0.6}{2}\right)^2 = 1182 \text{ kN}$$

The weight of the pile can be evaluated as:

$$W = \gamma_{concrete}\pi\left(\frac{D}{2}\right)^2 L = 25\pi\left(\frac{0.6}{2}\right)^2 25 = 177 \text{ kN}$$

Therefore the load capacity of the pile can be evaluated as:

$$Q_u = Q_s + Q_b - W = 4301 + 1182 - 177 = 5306 \text{ kN}$$

l. The shaft capacity can be estimated as:

$$Q_s = q_s A_s = \overline{K}\overline{\sigma'_z}\tan\delta' A_s$$

For a displacement pile, according to Flaate and Selnes (1977) and Kulhawy et al. (1983), the coefficient $\overline{K}$ can be taken equal to:

$$\overline{K_{clay}} = K_0(NC)OCR^{0.5} = \left(1 - \sin\varphi'_{cv,clay}\right)OCR^{0.5} = (1 - \sin 26)\cdot 4^{0.5} = 1.12$$

$$\overline{K_{sand}} = K_0 = \left(1 - \sin\varphi'_{cv}\right) = (1 - \sin 32) = 0.47$$

The pile–soil interface angle of shear strength, δ', can be taken as equal to $\delta' = 0.7\varphi'$ for the sand according to Kraft (1990) and equal to $\delta' = \varphi'_{cv}$ for the clay, so that:

$$\tan\delta'_{sand} = \tan\left(0.7\varphi'_{sand}\right) = \tan(0.7\cdot 40) = 0.53$$

$$\tan\delta'_{clay} = \tan\left(\varphi'_{cv,clay}\right) = \tan(26) = 0.49$$

The profiles of σ'_z and $\overline{K}\sigma'_z$ are reported in the following figure. Based on the above,

$$\begin{aligned} Q_s &= q_s A_s = \overline{K}\overline{\sigma'_z}\tan\delta' A_s \\ &= \overline{K}\overline{\sigma'_{z(0\div 5m)}}\tan\delta' A_{s(0\div 5m)} + \overline{K}\overline{\sigma'_{z(5\div 10m)}}\tan\delta' A_{s(5\div 10m)} \\ &\quad + \overline{K}\overline{\sigma'_{z(10\div 20m)}}\tan\delta' A_{s(10\div 20m)} \\ &= 56\cdot 0.49\cdot\pi\cdot 0.6\cdot 5 + 140\cdot 0.49\cdot\pi\cdot 0.6\cdot 5 + 91.7\cdot 0.53\cdot\pi\cdot 0.6\cdot 10 \\ &= 259 + 647 + 916 = 1822 \text{ kN} \end{aligned}$$

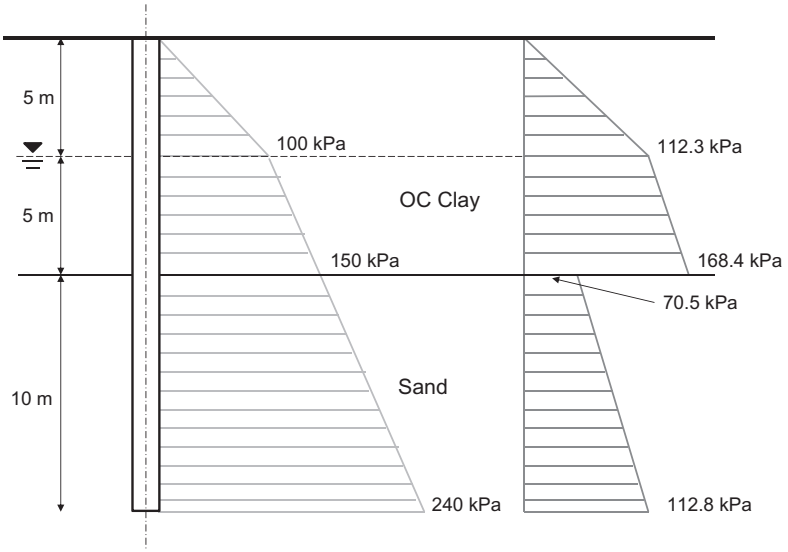

The base capacity, neglecting the terms involving the bearing capacity factors N_c and N_γ and assuming a shape factor $s_q = 1$, can be evaluated according to the method proposed by Hansen (1970) as:

$$Q_b = q_b A_b = \sigma'_{zb} N_q d_q A_b = \gamma'_{sand} L K_p e^{\pi \tan\varphi'_{cv}} \left(1 + 2\tan\varphi'_{cv}\left(1-\sin\varphi'_{cv}\right)^2 k_H\right)\pi\left(\frac{D}{2}\right)^2$$

$$= \gamma'_{sand} L \frac{\left(1+\sin\varphi'_{cv}\right)}{\left(1-\sin\varphi'_{cv}\right)} e^{\pi \tan\varphi'_{cv}} \left(1 + 2\tan\varphi'_{cv}\left(1-\sin\varphi'_{cv}\right)^2 k_H\right)\pi\left(\frac{D}{2}\right)^2$$

Based on the available data:

$$K_p = \frac{\left(1+\sin\varphi'_{cv,sand}\right)}{\left(1-\sin\varphi'_{cv,sand}\right)} = \frac{(1+\sin 32)}{(1-\sin 32)} = 3.25$$

$$N_q = K_p e^{\pi \tan\varphi'_{cv,sand}} = 3.25 \cdot e^{\pi \tan 32} = 23.18$$

$$k_H = \tan^{-1}\left(\frac{L}{D}\right) = 1.54$$

$$d_q = 1 + 2\tan\varphi'_{cv,sand}\left(1-\sin\varphi'_{cv,sand}\right)^2 k_H = 1 + 2\tan 32(1-\sin 32)^2 \cdot 1.54 = 1.43$$

Therefore the base capacity reads:

$$Q_b = q_b A_b = \sigma'_{zb} N_q d_q A_b = 240 \cdot 23.18 \cdot 1.43 \pi \left(\frac{0.6}{2}\right)^2 = 2249 \text{ kN}$$

The weight of the pile can be estimated as:

$$W = \gamma_{concrete} \pi \left(\frac{D}{2}\right)^2 L = 25 \pi \left(\frac{0.6}{2}\right)^2 \cdot 20 = 141 \text{ kN}$$

The load capacity of the pile can finally be evaluated as:

$$Q_u = Q_s + Q_b - W = 1822 + 2249 - 141 = 3930 \text{ kN}$$

m. The general equation that governs the axial deformation of energy piles is:

$$P + \frac{\pi D^2}{4} K_h w_h + W + Q_{s,mob} + Q_{b,mob} = 0$$

where P [N] is the applied mechanical load, D [m] is the pile diameter, K_h [Pa/m] is the head stiffness of the structural element connected to the pile head, w_h [m] is the pile vertical head displacement, W [N] is the pile weight, $Q_{s,mob}$ [N] is the mobilised portion of the pile shaft capacity Q_s and $Q_{b,mob}$ [N] is the mobilised portion of the pile base capacity Q_b.

n. The presence of the null point in energy piles subjected to thermal loads involves that:

i. Energy pile equilibrium cannot be solved via closed form solutions

ii. Energy pile equilibrium can be solved via closed form solutions

iii. None of the above

o. The discussed thermomechanical schemes for energy piles are developed under the fundamental hypothesis of:

i. (Thermo-)elastic conditions

ii. (Thermo-)plastic conditions

iii. Anisotropic conditions

iv. None of the above

p.

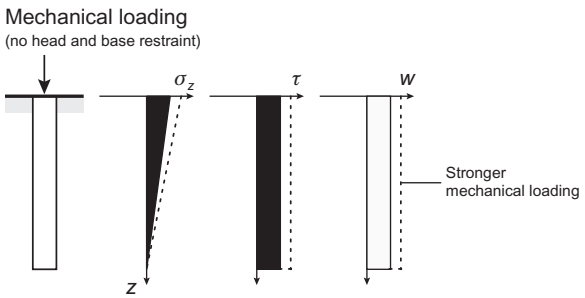

q.

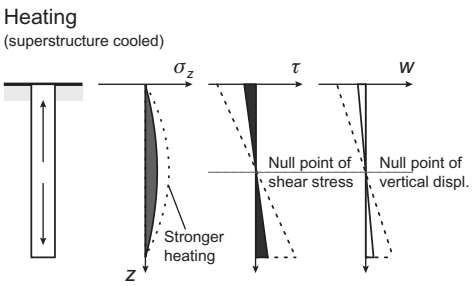

r.

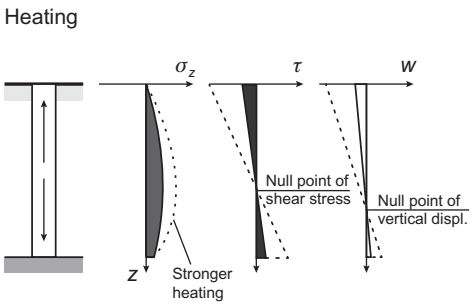

s. Total stress analysis: undrained material parameters.
Effective stress analysis: drained material parameters.

t. Discretisation of the pile in a number of segments/elements to consider soil layers of different properties;
Soil and pile properties remain constant with temperature but can be imposed to vary with depth;
Soil and soil–pile interaction properties do not change with temperature;
The relationships between the shaft friction–shaft displacement, head stress–head displacement and base stress–base displacement are assumed to be known through load-transfer curves;
Pile radial strains are neglected.

u. The trilinear load-transfer curve *referring to energy piles* that has been proposed by Knellwolf et al. (2011), based on the work of Frank and Zhao (1982), to describe the interaction between the pile shaft and the surrounding soil is as follows

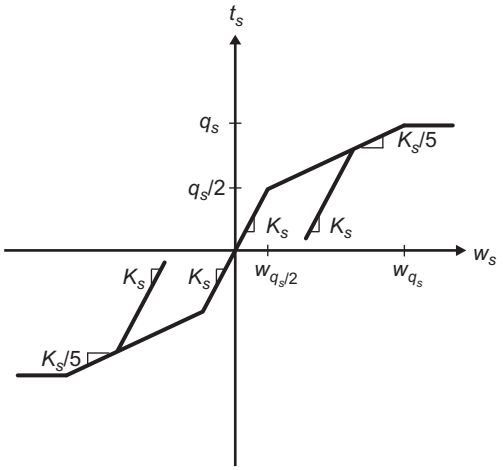

v. **First branch: linear elastic part characterising a reversible behaviour; Second branch: linear plastic part characterising a partly reversible behaviour; Third branch (plateau): perfectly plastic part characterising an irreversible behaviour where displacement increases under constant load.**

w. **The load-transfer approach allows considering**
   i. Pile radial strains
   ii. **Different soil layers**
   iii. None of the above

x. **For a nondisplacement pile, the coefficient $\overline{K}$ can be taken according to Kulhawy et al. (1983) as:**

$$\overline{K} = 0.7K_0 = 0.7(1 - \sin\varphi'_{cv}) = 0.7(1 - \sin 31) = 0.34$$

while the pile–soil interface angle of shear strength, δ', can be considered to be $\delta' = \varphi'_{cv}$ so that:

$$\tan\delta' = \tan\varphi'_{cv} = 0.6$$

Therefore the shaft capacity reads:

$$Q_s = q_s A_s = \overline{K}\overline{\sigma'_z}\tan\delta' A_s = 0.34(19 - 10)\frac{20}{2}0.6\pi \cdot 0.8 \cdot 20 = 923 \text{ kN}$$

The base capacity, neglecting the terms involving the bearing capacity factors N_c and N_γ and assuming a shape factor $s_q = 1$, can be evaluated according to the method proposed by Hansen (1970) as:

$$\begin{aligned} Q_b &= q_b A_b = \sigma'_{zb} N_q d_q A_b \\ &= \gamma'_{sand} L K_p e^{\pi \tan\varphi'_{cv}} \left(1 + 2\tan\varphi'_{cv}\left(1-\sin\varphi'_{cv}\right)^2 k_H\right)\pi\left(\frac{D}{2}\right)^2 \\ &= \gamma'_{sand} L \frac{\left(1+\sin\varphi'_{cv}\right)}{\left(1-\sin\varphi'_{cv}\right)} e^{\pi \tan\varphi'_{cv}} \left(1 + 2\tan\varphi'_{cv}\left(1-\sin\varphi'_{cv}\right)^2 k_H\right)\pi\left(\frac{D}{2}\right)^2 \end{aligned}$$

Based on the available data:

$$K_p = \frac{\left(1+\sin\varphi'_{cv}\right)}{\left(1-\sin\varphi'_{cv}\right)} = \frac{(1+\sin 31)}{(1-\sin 31)} = 3.12$$

$$N_q = K_p e^{\pi \tan\varphi'_{cv}} = 3.12 e^{\pi \tan 31} = 20.6$$

$$k_H = \tan^{-1}\left(\frac{L}{D}\right) = 1.53$$

$$d_q = 1 + 2\tan\varphi'_{cv}\left(1-\sin\varphi'_{cv}\right)^2 k_H = 1 + 2\tan 31(1-\sin 31)^2 \cdot 1.53 = 1.43$$

Therefore the base capacity is:

$$Q_b = q_b A_b = \sigma'_{zb} N_q d_q A_b = 180 \cdot 20.6 \cdot 1.43 \cdot \pi \cdot \left(\frac{0.8}{2}\right)^2 = 2665 \text{ kN}$$

For the analyses to be run with the software Thermo-Pile, a number of parameters must be determined. These are the Menard pressuremeter modulus, E_M, and the stiffness of the slab, K_h.

The Menard pressuremeter modulus of the sand that can be estimated as follows:

$$E_M = E_{oed} \alpha_r$$

where E_{oed} is the oedometric modulus.

The oedometric modulus can be calculated as:

$$E_{oed} = \frac{E_{soil}(1 - \nu_{soil})}{(1 + \nu_{soil})(1 - 2\nu_{soil})} = \frac{78{,}000 \cdot (1 - 0.3)}{(1 + 0.3) \cdot (1 - 2 \cdot 0.3)} = 105{,}000 \text{ kPa}$$

Therefore the Menard pressuremeter modulus reads:

$$E_M = E_{oed}\alpha_r = 10{,}5000 \cdot 0.33 = 34{,}650 \text{ kPa}$$

To evaluate the slab stiffness, the following equation can be used:

$$K_h = \frac{E_s\sqrt{B_{slab}L_{slab}}}{(1 - \nu_{soil}^2)\rho_0} = \frac{78{,}000 \cdot \sqrt{12 \cdot 12}}{\left(1 - 0.3^2\right) \cdot 0.88} = 1{,}168{,}831 \text{ kN/m}$$

Hence, the stiffness of the slab per unit cross-sectional area of energy pile is:

$$K_h^* = \frac{K_h}{A_{EP}} = \frac{1{,}168{,}831}{0.503} = 2{,}323{,}720 \text{ kPa/m}$$

The results obtained with the Thermo-Pile software are reported below.

CASE 1

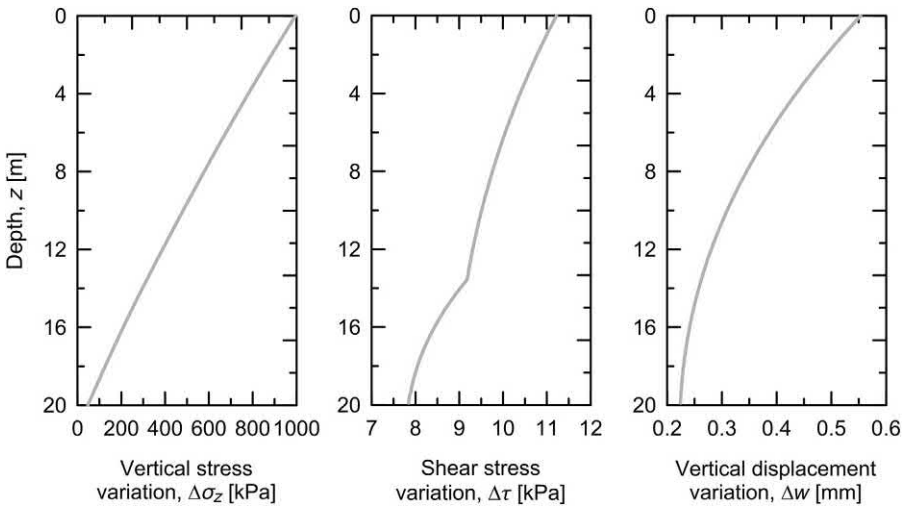

CASE 2

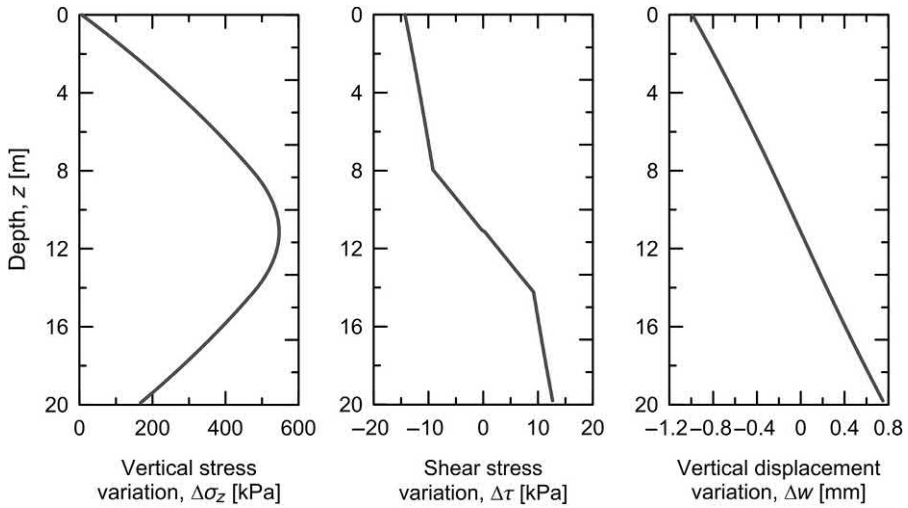

CASE 1 + 2

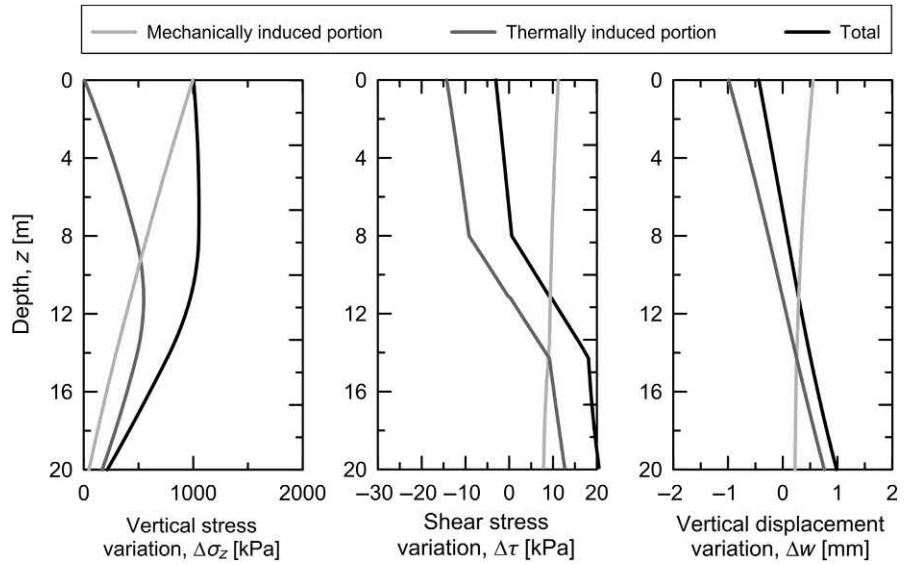

CASE 3

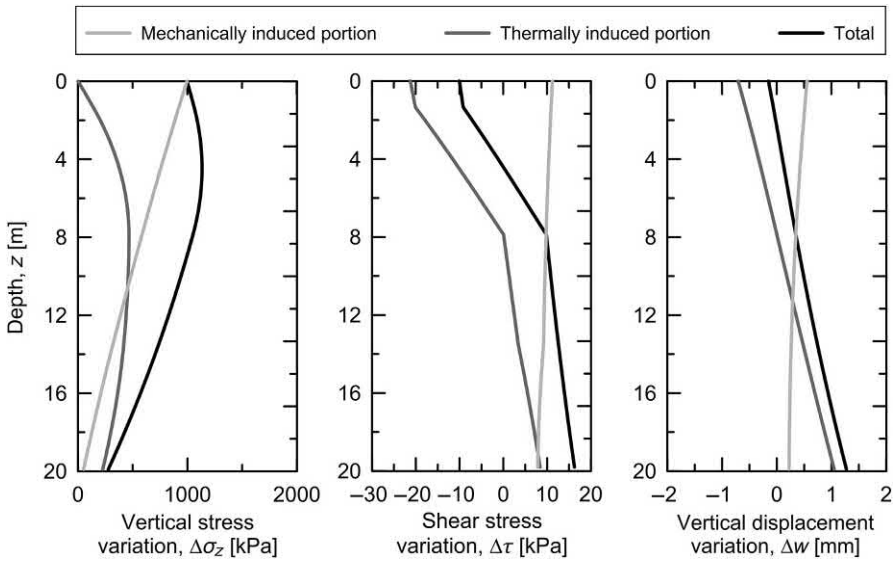
Mechanically induced portion
Thermally induced portion
Total
Depth, z [m]
0
4
8
12
16
20
0
1000
2000
Vertical stress variation, Δσz [kPa]
−30 −20 −10 0 10 20
Shear stress variation, Δτ [kPa]
−2 −1 0 1 2
Vertical displacement variation, Δw [mm]

CASE 4

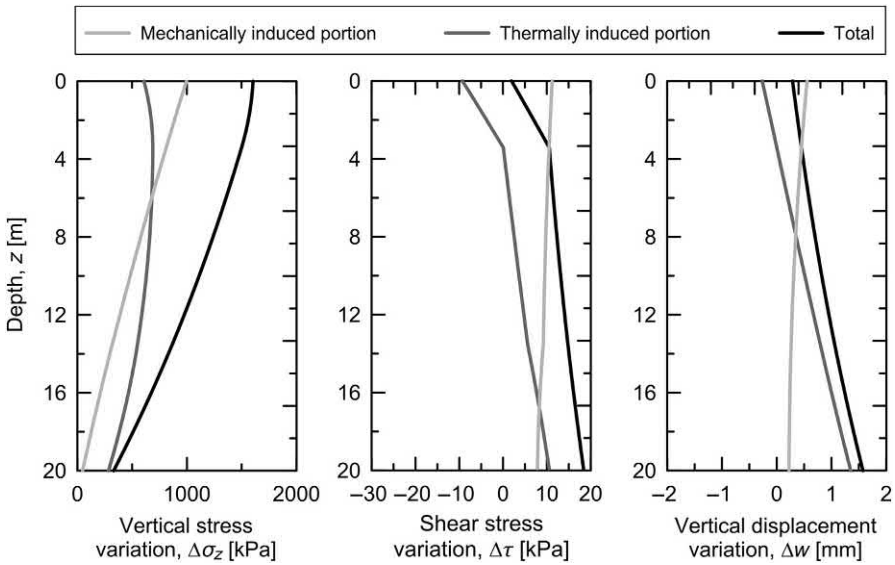
Mechanically induced portion
Thermally induced portion
Total
Depth, z [m]
0
4
8
12
16
20
0
1000
2000
Vertical stress variation, Δσz [kPa]
−30 −20 −10 0 10 20
Shear stress variation, Δτ [kPa]
−2 −1 0 1 2
Vertical displacement variation, Δw [mm]

CHAPTER 11

Analytical modelling of capacity and deformation of energy pile groups

11.1 Introduction

Estimating the response of energy pile groups subjected to the mechanical and thermal loads associated with their structural support and heat exchanger operation represents a crucial complementary point to the characterisation of the single pile responses for any comprehensive analysis of energy pile foundations. Two key aspects must be addressed for energy pile groups: the group *capacity* and the group *deformation*. Addressing the capacity of energy pile groups involves investigating the potential failure of the individual piles composing the group and that of the pile group as a block. Addressing the deformation of pile groups involves considering the vertical displacement – differential and average – of the piles in the group and the load redistribution among the piles in the group.

The rationale for distinguishing the analysis of the capacity and deformation of energy pile groups from that characterising single energy piles is related to the presence and influence of group effects. Considering these phenomena may be omitted when dealing with widely spaced energy pile groups. However, these phenomena and the related analysis should be considered for closely spaced energy pile groups because of the different response to loading that characterise the piles in the group with reference to the same piles in a single isolated case. No analysis and design of closely spaced energy piles can be considered complete without addressing the behaviour of piles as both isolated elements and in a group. In this context, understanding and being capable to describe the potential interactions characterising energy pile groups is essential to address the thermomechanical behaviour of such foundations.

This chapter focuses on analytical and semianalytical approaches to characterise the capacity and the deformation of energy pile groups subjected to mechanical and thermal loads. Attention is given to the influence of axial (e.g. vertical and compressive) mechanical loads as well as to both heating and cooling thermal loads. The analysis of the influence of lateral loads can be considered separately and is not treated in the following.

To address the aforementioned aspects, *idealisations and assumptions* are presented first: in this context, the objective is to propose a summary of the assumptions made to model the response of energy piles subjected to mechanical and thermal loads.

Analysis and Design of Energy Geostructures
DOI: https://doi.org/10.1016/B978-0-12-816223-1.00011-4

Second, the *generalised axial capacity formulation* for energy pile groups is treated: the objective of this part is to define mathematical expression that can be employed to investigate the failure of such foundations. Third, the *capacity in coarse-grained soil* and *fine-grained soil* is analysed: in this context, the purpose is to expand on approaches for estimating the capacity of energy pile groups in many of the situations that are likely to be encountered in practice. Next, the *generalised axial deformation formulation* characterising energy pile groups is treated: in this framework, the purpose is to comment on the mathematical formulation expressing the vertical equilibrium of energy piles in a group and to present a summary of the approaches that can address the axial deformation of such foundations. Afterwards, the *interaction factor method based on charts and analytical models* is described: the purpose of this part is to expand on a simplified yet effective analysis approach addressing the deformation of energy pile groups subjected to axial mechanical loads and thermal loads, based on the analysis of a single energy pile. Then, the *equivalent pier method* is presented: in this context, the aim is to present a second method addressing both the axial failure and deformation of energy pile groups, based on the analysis of a single solid element representative of the group. Later, a *comparison with rigorous solutions* is discussed for a number of predictions obtained with the discussed analysis approaches: the objective of this part is to expand on the capabilities of the considered theoretical methods in modelling the response of energy pile groups to loading. In addition to this, a discussion about the *modelled and observed response* of energy piles is proposed: in this framework, the aim is to expand on the capabilities of the foregoing theoretical approaches in modelling the actual response of energy pile groups. Finally, *questions and problems* are proposed: the purpose of this part is to fix and test the understanding of the subjects covered in this chapter by addressing a number of exercises.

11.2 Idealisations and assumptions

Most of the idealisation and assumptions made in this chapter coincide with those presented in Chapter 7, Thermomechanical behaviour of energy pile groups, and Chapter 10, Analytical modelling of capacity and deformation of single energy piles. The quoted considerations find due justification in the referenced chapters and are only summarised for completeness in the following prior to a detailed description and justification of one additional hypothesis.

A continuum medium idealisation of the materials constituting energy pile foundations is employed while considering the materials isotropic and homogeneous. The piles are characterised by a cylindrical shape. Layered (i.e. nonuniform) soil deposits are considered to be composed of fully horizontal layers. Uniform variations of the temperature, stress, strain and displacement fields within energy piles are assumed. Mechanical loads applied to energy piles are modelled via a prescribed force to their

head, P. Thermal loads applied along energy piles are modelled via prescribed temperature variations, $\Delta T = T - T_0$, where T is an actual temperature value and T_0 is the initial uniform temperature of the pile and surrounding ground. These temperature variations are assumed to be (1) instantaneously and uniformly imposed along the piles and (2) constant with time. The pipes inside the energy piles are not modelled. The material properties of the pile are constant with depth and do not change with temperature. The soil and soil–pile interaction properties (deformation and shearing resistance properties) do not change with temperature as well. The constitutive models that characterise the interaction of the pile with the surroundings are known and are considered to be unaffected by any potential temperature effects. The analysis of the capacity of energy piles is associated with the combination and the effects of only mechanical loads, whereas that of the deformation of such foundations is associated with the combination and the influence of both mechanical and thermal loads. Unless otherwise specified, the following assumptions are also assumed to be valid. The ground is considered to be insensitive to temperature variations, that is an *infinite heat reservoir* that remains at a fixed constant temperature. Energy piles are modelled employing a one-dimensional scheme and the radial pile displacements are neglected. The weight of the pile is neglected. No account of the pile cap is made unless otherwise specified, that is reference is made to energy piles that are (1) free to move vertically at their heads (i.e. no head restraint) and (2) characterised by an infinitely flexible slab.

As an additional hypothesis, the energy piles composing the modelled groups are assumed to be characterised by the same geometry (cf. Fig. 11.1). Although energy piles of different dimensions may characterise practical applications, this assumption can representatively describe the behaviour energy pile groups as long as appropriate average dimensions of the piles are employed.

Contractive strains, downward displacements, compressive stresses and increases in angles in the anticlockwise direction are considered to be positive.

11.3 Generalised axial capacity formulation

Piles will always be applied in groups. For centre-to-centre spacing between the piles approximately greater than or equal to $s = 8D$ (e.g. widely spaced piles), where D is

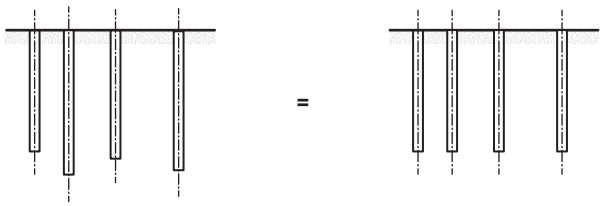

Figure 11.1 Modelling approach considered for energy piles in a group.

the pile diameter, disturbance between the piles as a consequence of construction effects is unlikely to occur and the capacity of the individual piles in the group may be assumed to coincide with that of the same piles in an isolated case. In those situations, the piles may fail as single isolated foundations. For centre-to-centre spacing lower than $s = 8D$ (e.g. closely spaced piles), disturbance between the piles as a consequence of construction effects is likely to occur and the capacity of the individual piles in the group may differ from that of the same piles in an isolated case. In those situations, block failure may occur especially when a slab would be in contact with the ground. Block failure would almost certainly occur if inappropriate design may have been considered for spacing lower than $s = 3D$.

Historically, an analysis approach relying on the concept of 'group efficiency' has been considered to estimate the capacity of pile groups, based on a comparison of the capacity of the individual piles in a group with that of the surrounding block – given by the sum of the individual pile capacities (see Poulos and Davis, 1980). Nowadays, this approach appears to be inappropriate (Fleming et al., 2008). Two failure modes of pile groups caused by that of the individual piles and by the group as block should be appraised independently, and the block capacity of a group should not be confused with the sum of the individual pile capacities by the use of an efficiency factor (Fleming et al., 2008). The concept of efficiency of pile groups is more appropriate to characterise the stiffness of such foundations.

In general, the block capacity of a pile group may be estimated as

$$Q_{u,b} = q_{s,g} A_{g,s} + q_{b,g} A_g - W_g \tag{11.1}$$

where $q_{s,g}$ is the shaft resistance for block failure of the pile group, $A_{g,s}$ is the area of the block shaft, $q_{b,g}$ is the base resistance for block failure of the pile group, A_g is the plan area of the block and W_g is the weight of the pile group. The area A_g may be considered as the plan area of soil and piles delimited by the simplest polygon that better reproduces the shape of the group.

According to Fleming et al. (2008), the settlement needed to mobilise the base capacity of the block is usually very large (e.g. 5%–10% of the width of the group). Block failure is also more likely to occur for groups composed by a large number of long slender piles at a particular spacing than for groups consisting of a few short stubby piles at the same spacing because it is governed by relevant proportions of block shaft resistance compared to block base resistance. Following the same arguments, group failure is less likely for piles in sand (where $q_{b,g}/q_{s,g}$ usually varies from 50 to 200) than for piles in clay (where $q_{b,g}/q_{s,g}$ usually varies from 10 to 20) (Fleming et al., 2008). Individual pile failure may be analysed through proper considerations.

The formulae and approaches presented below to tackle the capacity of pile groups are relevant for analysis and design purposes. However, verifications of deformation

rather than capacity requirements often dominate the design of both pile groups in coarse- and fine-grained soil.

11.4 Capacity in coarse-grained soil

Calculation of the block capacity of a pile group in coarse-grained soil follows a similar procedure to that described for single piles, except that failure is now likely to occur in the soil (not at the pile–soil interface) and the self-weight of this material may be significant. Accordingly, an effective stress approach is considered and involves calculating the block capacity as

$$Q_{u,b} = q_{s,g}A_{g,s} + q_{b,g}A_g - W_g = \overline{\sigma'}_z K_0 \tan\varphi' A_{g,s} + (\sigma'_{zb}N_q + \frac{1}{2}\gamma' L_g N_\gamma)A_g - W_g \quad (11.2)$$

where $\overline{\sigma'}_z$ is an average value of the effective vertical stress with depth, K_0 is the coefficient of earth pressure at rest, φ' is the soil angle of shear strength, σ'_{zb} is the vertical effective stress at the level of the pile base, γ' is the buoyant unit weight, L_g is the width of the pile group in plan view (considered approximately square) and N_q and N_γ are bearing capacity factors.

The individual capacity of displacement piles characterising most closely spaced pile groups in coarse-grained soil is generally greater than the capacity that may be defined with reference to a single isolated case. This phenomenon occurs because of the densification process induced by pile installation. In contrast, the individual capacity of nondisplacement piles in most groups in coarse-grained soil is often found to be lower than the capacity estimated with reference to a single isolated case. While capacities of displacement pile groups of up to 1.5–2 times those obtained by the sum of the individual pile capacities have been observed, nondisplacement pile group capacities reduced to two third of the sum have been remarked (Lo, 1967; Vesić, 1969).

As a general approximation, the capacity of pile groups in coarse-grained soil may generally be assumed to be equal to the sum of the individual pile capacities, except where a slab in contact with the ground is present. In this latter case, the group capacity is likely to be closer to that of the block estimated through Eq. (11.2), which is generally well in excess of the sum of the individual pile capacities.

11.5 Capacity in fine-grained soil

Calculation of the block capacity of a pile group in fine-grained soil follows a similar procedure to that described for single piles, except that failure is now likely to occur around the periphery of the block. Accordingly, a total stress approach may be considered and involves calculating the block capacity as

$$Q_{u,b} = q_{s,g}A_{g,s} + q_{b,g}A_g - W_g = \bar{\tau}_a A_{g,s} + (c_u N_c + \sigma_{zb})A_g - W_g \tag{11.3}$$

where $\bar{\tau}_a$ is the pile–soil interface adhesion, c_u is the undrained soil cohesion, N_c is the bearing capacity factor proposed by Skempton (1951) for a rectangular area (cf. Fig. 13.9) and σ_{zb} is the total vertical stress at the level of the toe of the piles in the group.

In addition to the previous total stress analysis approach, an effective stress approach may also be considered for calculating the block capacity of pile groups in fine-grained soil. This choice represents a matter of discussions among designers.

Concerns about the occurrence of individual pile capacities in fine-grained soil lower than those associated with the same piles in a single isolated case have been remarked (Meyerhof, 1976; Lancellotta, 1995). However, experimental results (O'Neill et al., 1981) have shown that the group capacity in fine-grained soil rarely falls below that calculated from the sum of the individual pile capacities and in the cases in which this may occur the reduction may not be significant.

Based on the previous considerations, similar to pile groups in coarse-grained soil, the capacity of pile groups in fine-grained soil may be assumed to be equal to the sum of the individual pile capacities, except where a slab in contact with the ground is present.

11.6 Generalised axial deformation formulation

To address the axial deformation of energy pile groups, various analytical or semianalytical methods are available. The majority of these methods have been originally presented for the analysis of conventional pile groups subjected to only mechanical loads. However, some of these methods have been modified and extended for the analysis of energy pile groups subjected to thermal loads, applied alone or in conjunction with mechanical loads.

The methods addressing the axial deformation of pile groups include:

1. The interaction factor method, applied to the analysis of both conventional piles (e.g. Poulos, 1968; O'Neill et al., 1977; Randolph and Wroth, 1979b; Chow, 1986; Mylonakis and Gazetas, 1998) and energy piles (Rotta Loria and Laloui, 2016, 2017; Rotta Loria et al., 2017). In this method, the concept of interaction factor and the principle of superposition are employed.
2. The equivalent pier method, applied to the analysis of both conventional piles (e.g. Poulos and Davis, 1980; Butterfield and Douglas, 1981; Poulos, 1993; Randolph, 1994) and energy piles (Rotta Loria and Laloui, 2017b). In this method, the pile groups are modelled as an equivalent pier constituted by the piles and the soil between them.

3. The equivalent raft method, applied to the analysis of only conventional piles (e.g. Van Impe, 1991; Poulos, 1993; Tomlinson and Boorman, 2001). In this method, the pile groups are represented by an equivalent raft acting at some depth along the piles.
4. The settlement ratio method, applied to the analysis of only conventional piles (e.g. Skempton, 1953; Meyerhof, 1959; Vesić, 1969; Poulos, 1989; Kaniraj, 1993; McCabe and Lehane, 2006). In this method, the settlement of a single pile at the average load level is multiplied by a group settlement ratio reflecting the effects of the interactions in the pile group.
5. The modified load–transfer method, applied to the analysis of both conventional piles (e.g. Randolph and Clancy, 1993; Randolph, 1994; Lee and Xiao, 2001) and energy piles (Ravera et al., 2019). In this method, the load–settlement curves of single piles are modified to account for the influence of group effects.

Especially at early stages of the analysis and design of pile foundations, the previous methods can well replace more rigorous, although often time-consuming, numerical methods. These latter methods include, for example the finite element and difference methods [to date applied to the analysis of both conventional piles (e.g. Butterfield and Banerjee, 1971; Ottaviani, 1975; Banerjee and Davies, 1978; Pressley and Poulos, 1986) and energy piles (e.g. Jeong et al., 2014; Salciarini et al., 2015; Di Donna et al., 2016; Suryatriyastuti et al., 2016; Saggu and Chakraborty, 2016)] and the boundary element method [to date only applied to the analysis of conventional piles (e.g. Poulos, 1994)].

Poulos (1989) has compared various among the previous methods in the context of the analysis of conventional pile groups, concluding that most of them are capable of providing comparable results despite differences in the fundamental basis of the analysis approach. According to Poulos et al. (2002), the reason for this is that the key to successful analyses of the deformation of pile groups lies in the selection of appropriate pile–soil parameters and the reliable quantification of the relationship between the deformation of a single pile and a pile group, but not in the method of analysis used.

Table 11.1 reports parameters of particular interest for the analysis of the deformation of energy pile groups. Table 11.2 lists groups of dimensionless parameters that are useful for the same purpose, their typical ranges of variation and the values that are used in many instances in this chapter to expand on the features of the considered analysis approaches.

In the following, the features of the interaction factor method and the equivalent pier method are proposed, with the main advantage that the considered approaches can be potentially applied together in the analysis and design of very large pile groups, irrespective of whether the piles are subjected to mechanical loads, applied alone or in conjunction with thermal loads.

Table 11.1 Parameters of interest for the analysis of energy pile groups (Rotta Loria and Laloui, 2016).

Pile	Notation	Soil	Notation
Length	L	Depth of layer	h
Diameter	D	Shear modulus	G_{soil}[a]
Spacing	s	Poisson's ratio	ν_{soil}[a]
Young's modulus	E_{EP}	Linear thermal expansion coefficient	α_{soil}[a]
Linear thermal expansion coefficient	α_{EP}		

[a]When labelled with the subscript s or b, the soil parameters refer to the soil portion located in correspondence of the shaft or base of energy piles.

Table 11.2 Dimensionless groups of parameters of interest for energy pile groups, typical values and values used hereafter in a number of examples (Rotta Loria and Laloui, 2016).

Dimensionless group	Notation	Practical rage	Considered values
Normalised pile spacing	s/D	3–10	1.05, 1.25, 1.5, 2, 2.5, 3, 5, 10, 20
Normalised breadth	D/s	0.33–0.1	0.95, 0.8, 0.67, 0.5, 0.4, 0.33, 0.2, 0.1, 0.05
Pile slenderness ratio	L/D	10–50	10, 25, 50
Pile–soil stiffness ratio (piles surrounded by uniform soil deposit or resting on infinitely rigid base)	$\Lambda = E_{EP}/G_{soil}$	100–10,000	10, 100, 500, 1000, 2000, 10,000
Pile–soil stiffness ratio (piles resting on finitely rigid base)	$\Lambda = E_{EP}/G_{soil,s}$	100–10,000	100, 500, 1000, 2000
Poisson's ratio of soil	ν_{soil}	0.1–0.5	0.1, 0.15, 0.2, 0.3, 0.4, 0.5
Soil–pile thermal expansion coefficient ratio	$X = \alpha_{soil}/\alpha_{EP}$	0.25–4	0, 0.5, 1, 2
Depth of soil layer	h_l/L	–	1, 1.05, 1.1, 1.25, 2.5, $\rightarrow \infty$
Base-to-shaft soil Young's modulus ratio	$E_{soil,b}/E_{soil,s}$	1–10,000	1, 2, 5, 10, 100, 1000, 10,000

11.7 Interaction factor method based on charts

11.7.1 Background

The interaction factor method is an analysis approach originally proposed by Poulos (1968) for conventional piles subjected to mechanical loads that has been extended to energy piles subjected to thermal loads by Rotta Loria and Laloui (2016).

The considered method assumes that the vertical displacement of any pile group, for example under serviceability conditions, may be estimated through *elastic theory* and the *superposition principle* by knowing (1) the vertical displacement of a single pile under unit load, (2) the displacement interaction relationship – quantified by an interaction factor – among two characteristic piles of the group considered in an isolated pair and (3) the loads applied to the piles. The expediency and capability of this method have played a major role for its diffusion.

Originally, charts for floating and end-bearing conventional piles subjected to mechanical loads have been proposed via the boundary element method by Poulos (1968) and Poulos and Mattes (1974), respectively, to serve the interaction factor method. In recent years, charts have been proposed via the finite element method for floating and end-bearing energy piles subjected to thermal loads by Rotta Loria and Laloui (2016, 2017a), respectively.

In the following, the interaction factor concept and the resulting method are described, and charts for the analysis of the displacement interaction between two identical piles under a broad range of design conditions are presented. Although Rotta Loria and Laloui (2016, 2017a) proposed charts addressing the influence of only thermal loads based on the results of thermomechanical finite element analyses, additional charts addressing the influence of mechanical loads have been derived and are presented here to treat the interaction factor method in a unified framework. Further original charts and tables are presented by Poulos and Davis (1980) and may be considered with the procedure proposed hereafter for an approximate analysis of problems not treated in the following. According to Poulos (1977), although it is not possible to present theoretical solutions that cover all possible cases, those presented in the following are considered to be sufficient to enable an approximation of the vertical displacement of energy pile groups to be made for most cases likely to be encountered in practice.

11.7.2 Hypotheses and considerations

In addition to the hypotheses and considerations presented in Section 11.2, those described hereafter apply to the following developments. Both predominantly floating and end-bearing energy piles subjected to a mechanical load and a temperature variation are treated. The soil is assumed to be a semiinfinite, isotropic and homogeneous mass where predominantly floating energy piles are considered. The soil is a semiinfinite mass characterised by an isotropic and homogeneous layer surrounding the shaft of the energy piles and an isotropic homogeneous layer located below the toe of the energy piles where predominantly end-bearing energy piles are considered.

The thermomechanical finite element analyses run to obtain the following charts consider linear thermoelastic pile behaviour and linear elastic soil behaviour (i.e. the

soil is an infinite heat reservoir that remains at a fixed constant temperature). These analyses do account for radial deformations of the piles depending on the value of soil Poisson's ratio, ν_{soil}.

No slip or yielding occurs between each of the energy piles and the adjacent soil (perfect contact between the pile and soil is assumed), and thus, reference is made to loading situations in which reversible conditions prevail. Although not valid in situations where mechanical and thermal loads of significant magnitudes are applied to energy piles (especially if predominantly floating) (Rotta Loria et al., 2015), these conditions have been demonstrated to characterise normal working situations based on the results of full-scale experimental tests (Wang et al., 2014; Murphy et al., 2015; Mimouni and Laloui, 2015; Rotta Loria and Laloui, 2017c, 2018) and numerical analyses (Di Donna et al., 2016).

The elastic assumption involves the reported displacement variations caused by a unit compressive mechanical load or by a unit temperature change associated with a heating thermal load being the same in absolute value as those caused by a unit tensile mechanical load or by a unit temperature change associated with a cooling thermal load, respectively (Rotta Loria and Laloui, 2016, 2017a). The elastic assumption also involves the principle of superposition allowing the addressing of mechanical and thermal loads via *separate analyses* addressing the respective influences of the considered loads.

11.7.3 The interaction factor concept

The simplest system representing an energy pile group can be considered as consisting of two energy piles in a deep soil deposit. The energy piles may be predominantly floating and embedded in a uniform soil layer. They may also be predominantly end-bearing, surrounded by a shallow uniform soil layer and rest on a deep uniform soil stratum.

The application of mechanical loads P to the head of energy piles induces a movement of the pile (and surroundings) in the same direction of the applied load along the entire pile length. The application of temperature variations ΔT along energy piles involves one portion of the pile that moves upwards while the other portion that moves downwards around the so-called null point of the vertical displacement (Laloui et al., 2003). As a consequence of the application of either of the aforementioned loads, the displacement field generated in energy piles is transmitted in the adjacent soil. Interaction of the displacement fields generated by the deformation of the energy piles thus occurs.

Assuming that the resulting deformation field of a group of two energy piles subjected to loading can be representatively decomposed through the superposition principle, two individual systems can be considered to describe the analysed problem. When the piles are equally loaded, these systems are symmetrical. Fig. 11.2 provides

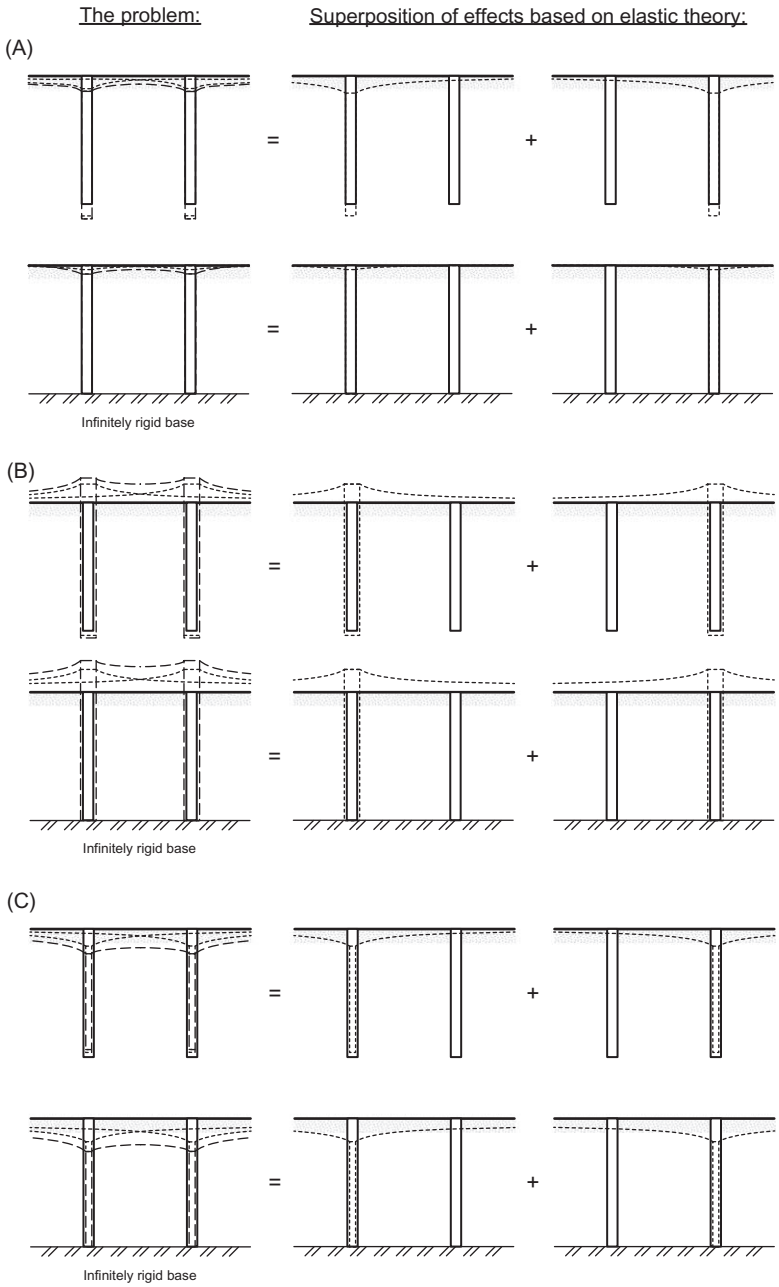

Figure 11.2 The interaction factor modelling approach employed for energy piles subjected to (A) compressive mechanical loading, (B) heating thermal loading and (C) cooling thermal loading.

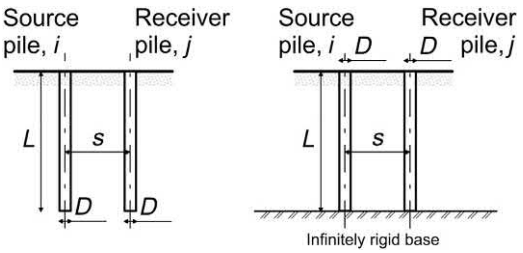

Figure 11.3 The elementary unit.

an example of this decomposition for situations in which a compressive mechanical load, a positive temperature variation or a negative temperature variation are applied to a pair of predominantly floating and end-bearing energy piles.

In the analysis of the previous problem, each of the individual systems can be considered to represent an *elementary unit* (cf. Fig. 11.3) involving a source pile i subjected to loading (e.g. represented by a mechanical load applied at the pile head P or by a temperature variation ΔT applied along the pile) and a receiver pile j located at a certain spacing s in a soil layer. The interaction factor method addresses the displacement analysis of general pile groups by considering the displacement response of a pair of piles with reference to the response of a source pile in an isolated case. The piles in the pair include a loaded 'source' pile and a 'receiver' neighbouring pile in the previous elementary unit. The source pile in the isolated case is considered to be subjected to the same loading of the source pile in the pair and to be embedded in a soil deposit characterised by the same material properties as those for the piles in the pair.

The essence of the displacement interaction between a source pile and a neighbouring receiver pile is shown in Fig. 11.4, with reference to the influence of a mechanical load (e.g. $P = 1\,\text{MN}$) and a temperature variation (e.g. $\Delta T = 10^{\circ}\text{C}$), respectively. The figures present the evolution of the normalised vertical displacement caused by mechanical loading, w_h^m, and thermal loading, w_h^{th}, at the head of a pair of piles in an elementary unit with a normalised centre-to-centre distance between the piles as well as at level of the ground surface for a single isolated pile with a normalised horizontal distance. The displacement of predominantly floating energy piles in a deep, uniform and compressible soil layer is considered with reference to that of geometrically identical predominantly end-bearing energy piles in a deep soil deposit consisting of a (shallower) uniform and compressible soil layer and a (deeper) uniform and infinitely rigid soil stratum. The stiffness of the soil layer characterising the case of the predominantly floating energy pile(s) is considered to be the same as that of the soil layer surrounding the shaft of the predominantly end-bearing energy pile(s). In Fig. 11.4A and B, the vertical displacement is normalised with respect to the pile diameter, D. In Fig. 11.4C and D, the vertical displacement is normalised with respect

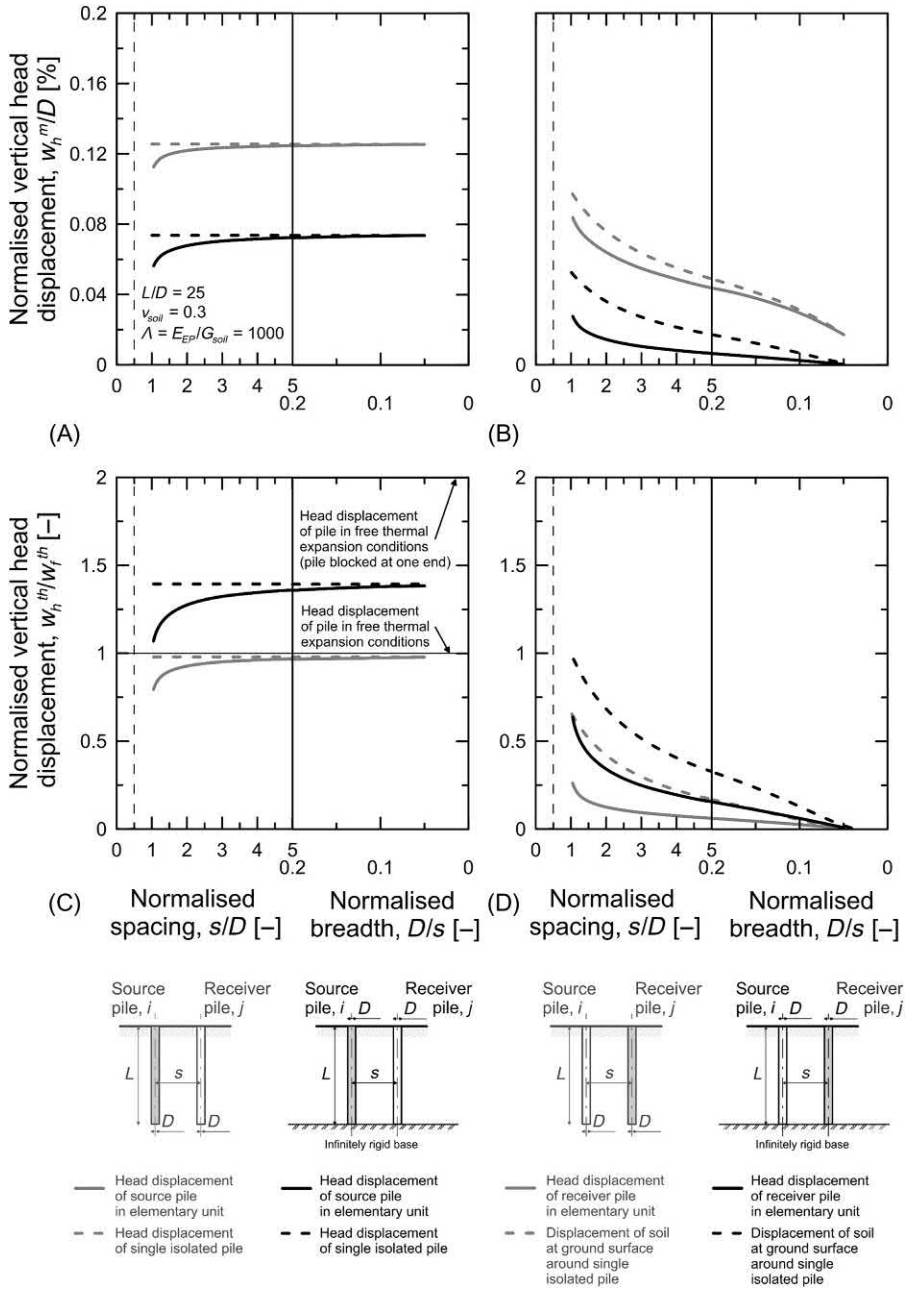

Figure 11.4 Vertical head displacement characterising a source and receiver pile in the elementary units, as well as corresponding single isolated piles subjected to the same load applied to the source piles. Panels (A and B) refer to mechanical loading. Panels (C and D) refer to thermal loading. *Modified after Rotta Loria, A.F., Laloui, L., 2016. The interaction factor method for energy pile groups. Comput. Geotech. 80, 121–137.*

to the head displacement of the single pile under free thermal expansion conditions, $w_f^{th} = -\alpha_{EP}\Delta TL/2$. Energy piles characterised by a slenderness ratio of $L/D = 25$ and pile–soil stiffness ratio of $\Lambda = E_{EP}/G_{soil} = 1000$, and embedded in a soil of Poisson's ratio $\nu_{soil} = 0.3$ are considered.

The application of the mechanical load and the thermal load to the source pile induces a mechanically and thermally induced deformation of this element, respectively, which involves a modification of the displacement field along its length. This displacement is lower for smaller centre-to-centre distances to the receiver pile, whereas this displacement increases and tends to the displacement of a single isolated pile subjected to the same temperature variation for centre-to-centre distances that approach infinity (cf. Fig. 11.4A and C). This result is caused by the effect of the stiffness of the receiver pile on the deformation of the source pile. For both mechanical and thermal loading, the effect of the stiffness of the receiver pile on the deformation of the source pile is less pronounced for predominantly floating piles surrounded by a uniform soil deposit compared to predominantly end-bearing piles resting on an infinitely rigid soil stratum.

The pile vertical head displacement is higher for predominantly floating piles surrounded by uniform soil deposits compared to that for predominantly end-bearing piles resting on infinitely rigid soil strata subjected to the same mechanical load. In contrast, the pile vertical head displacement is lower for predominantly floating piles surrounded by uniform soil deposits compared to that for predominantly end-bearing piles resting on infinitely rigid soil strata subjected to the same temperature variation. Considering the influence of mechanical loading, this phenomenon occurs because of the damping effect provided by the bottom soil layer characterising predominantly end-bearing energy piles on the related vertical deformation, which is less noteworthy for predominantly floating energy piles. Considering the influence of thermal loading, this phenomenon occurs because of the partial and complete upward pile deformation under the application of the temperature variation characterising predominantly floating and end-bearing energy piles, respectively, as a consequence of the different null point position (above the pile toe in the former and at the toe in the latter).

The deformation of the source pile is transmitted to the surrounding soil and influences the displacement field of the receiver pile (cf. Fig. 11.4B and D). This displacement is equal to that of the source pile for zero spacing between the two, whereas this displacement decreases and tends to zero for centre-to-centre distances that approach infinity. Yet, this displacement is always smaller than the displacement characterising the soil at the ground surface around a single isolated pile subjected to the same loading applied to the source pile in the elementary unit. This result is caused by the higher stiffness of the receiver pile compared to the stiffness of the soil. The impact of the difference in stiffness between the receiver pile and the soil on the displacement of the

receiver pile becomes more pronounced with increasing pile spacing for predominantly end-bearing piles resting on infinitely rigid soil strata compared to predominantly floating piles surrounded by uniform soil deposits. The previous phenomenon occurs irrespective of whether the influence of mechanical or thermal loading is considered.

The displacement interaction between piles implies that, when subjected to loading in a group, they present greater displacements compared to the case in which they are isolated and characterised by the same loading. The additional displacement of a pile due to the loading of an adjacent pile can be expressed in terms of an interaction factor Ω, where (Poulos, 1968; Rotta Loria and Laloui, 2016)

$$\Omega = \frac{\text{additional displacement due to adjacent pile}}{\text{displacement of single isolated pile}} = \frac{w_j}{w_i} \tag{11.4}$$

In defining the interaction factor, w_j is the vertical head displacement of a receiver pile in a pair, whereas w_i is the vertical head displacement of a single isolated pile subjected to the same load applied to the source pile in the elementary unit. This definition of the interaction factor relates the effect of loading a source pile on a receiver pile in a pair with the response of the source pile in an isolated case.

11.7.4 Peculiarities of the displacement interaction caused by mechanical and thermal loads

Fig. 11.5 presents the typical evolution of the interaction factor referring to the head of two predominantly floating piles located at a normalised centre-to-centre distance between each other in the case of mechanical and thermal loading. The interaction decreases with increasing centre-to-centre distance between the piles. Mechanical loading causes a more pronounced displacement interaction between the piles compared to thermal loading. The schematic proposed in Fig. 11.5 meaningfully refers to a vertical head displacement of the source pile in an isolated case, w_i, that is greater than the vertical head displacement of the same pile subjected to the same loading in a pair, w_i^*, and is employed with the vertical head displacement of the receiver pile in a pair, w_j, to calculate the interaction factor.

Figs 11.6 and 11.7 present the typical evolution of the interaction factors caused by mechanical loading, Ω^m, and thermal loading, Ω^{th}, between the piles in the elementary units previously considered with a normalised centre-to-centre distance. For energy piles subjected to mechanical loading, the interaction factor for predominantly end-bearing piles resting on infinitely rigid soil strata is lower than that for predominantly floating piles embedded in uniform soil deposits (cf. Fig. 11.6). In contrast, for energy piles subjected to thermal loading, the interaction factor for

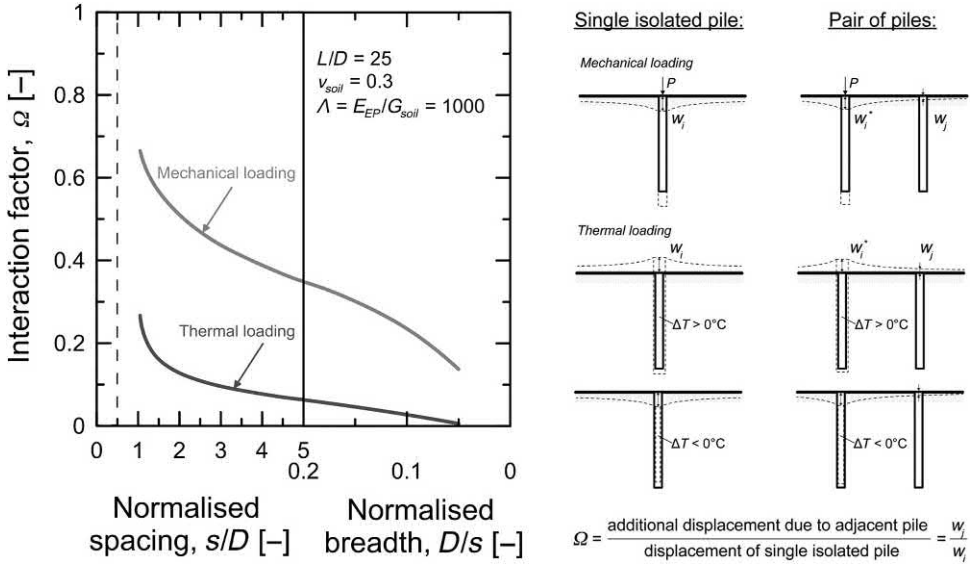

Figure 11.5 Displacement interaction between two predominantly floating piles in a deep soil layer. *Modified after Rotta Loria, A.F., Laloui, L., 2016. The interaction factor method for energy pile groups. Comput. Geotech. 80, 121−137.*

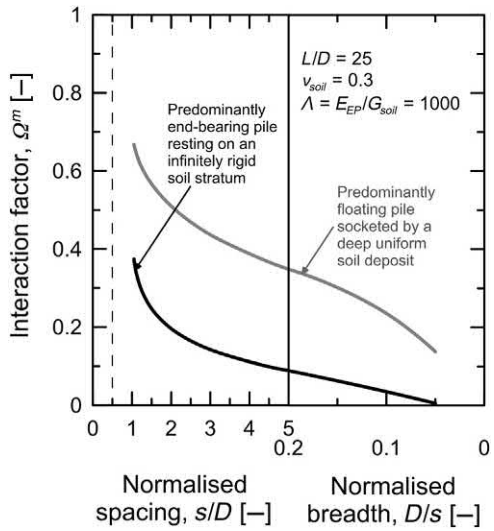

Figure 11.6 Interaction factor for predominantly floating and end-bearing energy piles resting on infinitely rigid soil strata and socketed in uniform soil deposits, respectively, under the application of a mechanical load.

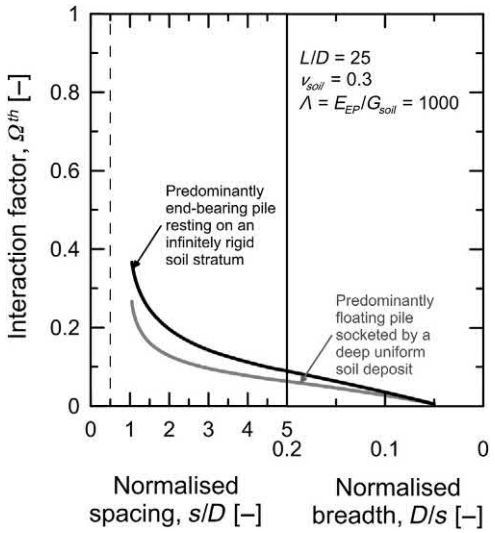

Figure 11.7 Interaction factor for predominantly floating and end-bearing energy piles resting on infinitely rigid soil strata and socketed in uniform soil deposits, respectively, under the application of a thermal load. *Modified after Rotta Loria, A.F., Laloui, L., 2016. The interaction factor method for energy pile groups. Comput. Geotech. 80, 121–137.*

predominantly end-bearing energy piles resting on infinitely rigid soil strata is greater than that for predominantly floating energy piles embedded in uniform soil deposits (cf. Fig. 11.7). These phenomena are generally observed for any pile spacing and pile slenderness ratio.

The above indicates that, irrespective of whether the influence of mechanical or thermal loads is considered, the interaction factor for energy piles resting on finitely rigid soil strata generally lies between the interaction factor for energy piles resting on infinitely rigid soil strata and the interaction factor for energy piles surrounded by deep uniform soil deposits. Attention has thus to be paid in the geotechnical characterisation of sites to the presence and rigidity of bearing soil strata because these characteristics have a marked effect on the vertical displacement of pile groups subjected to mechanical and thermal loads (Poulos and Mattes, 1974; Rotta Loria and Laloui, 2017a). The group effects among piles may be poorly estimated if reference may be made to predominantly floating rather than end-bearing pile groups.

Drawing from the investigations of Poulos and Mattes (1974), the corrected interaction factor for energy piles resting on finitely rigid soil strata may be expressed as (Rotta Loria and Laloui, 2017a)

$$\Omega(\text{corrected}) = \Omega(\text{floating}) + F_b(\Omega(\text{end}-\text{bearing}) - \Omega(\text{floating})) \tag{11.5}$$

where Ω(floating) is the interaction factor for predominantly floating energy piles, F_b is a correction factor indicating the effect of the bearing stratum and Ω(end−bearing) is the interaction factor for predominantly end-bearing energy piles resting on infinitely rigid soil strata.

The term F_b is a function of (1) the base-to-shaft soil Young's modulus ratio, $E_{soil,b}/E_{soil,s}$, (2) the pile slenderness ratio, L/D, (3) the normalised pile spacing, s/D and (4) the ratio of base-to-shaft soil Poisson's ratio, $\nu_{soil,b}/\nu_{soil,s}$. The characteristics governing the variation of F_b are aspects (1) and (2). Aspect (3) causes a notable variation of F_b for the impractical centre-to-centre distances between energy piles of approximately $s \leq 3D$, whereas a negligible variation of F_b for the most practical distances of $s > 3D$ and certainly of $s \geq 5D$. Aspect (4) has a negligible influence on the variation of F_b. Based on the above, aspects (1) and (2) are considered herein whereas aspect (4) is neglected. Aspect (3) is accounted for by referring to the commonly utilised centre-to-centre distance between energy piles of $s = 5D$.

The limiting values for F_b are $F_b = 0$ for predominantly floating piles socketed in a deep uniform soil deposit, that is $E_{soil,b}/E_{soil,s} = 1$, and $F_b = 1$ for predominantly end-bearing energy piles resting on an infinitely rigid soil stratum, that is $E_{soil,b}/E_{soil,s} = \infty$.

11.7.5 Basic analysis procedure

The analysis procedure characterising the interaction factor method based on charts consists of three key steps (cf. Fig. 11.8):

1. The analysis of a single isolated pile subjected to a mechanical load or a temperature variation to define the unitary pile vertical head displacements $w_h^{1,m}$ and $w_h^{1,th}$ caused by these actions, respectively. This analysis can be carried out by referring to the charts presented in Chapter 10, Analytical modelling of capacity and

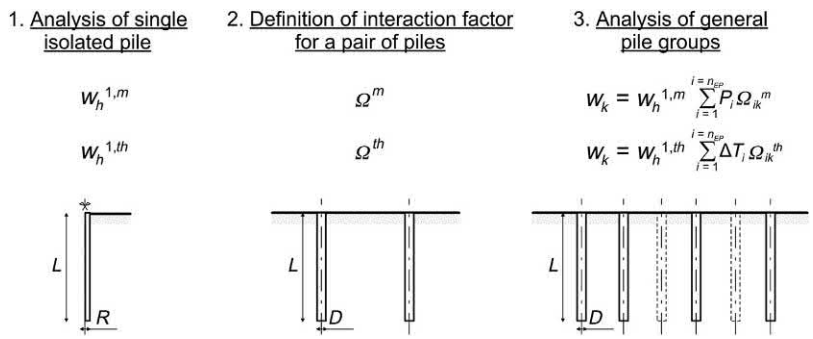

Figure 11.8 Key steps for the application of the interaction factor method based on charts. *Modified after Rotta Loria, A.F., Laloui, L., 2016. The interaction factor method for energy pile groups. Comput. Geotech. 80, 121−137.*

deformation of single energy piles, in which values of $w_h^{1,m}$ and $w_h^{1,th}$ for various design situations are depicted. Otherwise, it may be performed with any numerical method available for such purpose.

2. The definition of Ω for a pair of two piles at any given centre-to-centre distance. This step can be accomplished by referring to the charts reported in the following.
3. The analytical analysis of the displacement behaviour of the pile group, which is suggested to be applied for $s/D \geq 5$ (Rotta Loria and Laloui, 2016). This analysis allows determining the vertical head displacement w_k of any pile, k, composing a general pile group with a total number of piles, n_{EP}, in which some or all of the piles may be subjected to mechanical and/or thermal loading, supposing the superposition principle to be valid. In the case of piles subjected to mechanical loads, the interaction factor analysis of pile groups can be performed as (Poulos, 1968)

$$w_k = w_h^{1,m} \sum_{i=1}^{i=n_{EP}} P_i \Omega_{ik}^m \tag{11.6}$$

where P_i is the applied mechanical load to the head of pile i and Ω_{ik}^m is the interaction factor referring to the head of two piles subjected to mechanical loading in a pair corresponding to the centre-to-centre distance between pile i and pile k. In the case of piles subjected to thermal loads, this analysis can be performed as (Rotta Loria and Laloui, 2016)

$$w_k = w_h^{1,th} \sum_{i=1}^{i=n_{EP}} \Delta T_i \Omega_{ik}^{th} \tag{11.7}$$

where ΔT_i is the applied temperature variation to pile k and Ω_{ik}^{th} is the interaction factor referring to the head of two piles subjected to thermal loading in a pair corresponding to the centre-to-centre distance between pile i and pile k.

The proposed approach for the displacement analysis of energy pile groups is indeed a simplified method because it involves approximations to obtain an answer even for the idealised situation (Poulos, 1968; Rotta Loria and Laloui, 2016). Some inaccuracy may result from the approximations made in the formulation of the proposed method. According to Poulos (1968), these approximations appear however to be justified because their consideration would result in an increase in complexity of the solution not commensurate with any increase in accuracy that might be obtained. The proposed approach thus represents a simplified yet effective method for the displacement analysis of energy pile groups.

A notable feature of the proposed method is that it allows performing the displacement analysis of general energy pile groups also in situations in which some of the piles may be subjected to significant mechanical loads or temperature variations

that may induce nonlinear phenomena (e.g. plastic strains) in the narrow region of soil adjacent to or in the vicinity of such elements, that is the pile–soil interface (Rotta Loria and Laloui, 2016). The reason is because displacement interactions among piles are essentially elastic (Chow, 1986). Reference to situations in which the soil surrounding the piles may be approximated to behave according to an elastic-perfectly plastic constitutive law allows considering that only the elastic component of strain is transmitted from source piles (e.g. subjected to significant loads) to receiver piles (e.g. potentially subjected to less pronounced loads). Yet, in situations in which the soil region adjacent to receiver piles is in a (perfectly) plastic state no deformation is transmitted from source piles to receiver piles. The reason for these phenomena is that when the shear strength of the pile–soil interface is fully mobilised, full slippage between the soil and the pile can be considered to occur due to the formation of a displacement discontinuity at the pile–soil interface. Based on the previous considerations, the displacement resulting from an elastic component of strain (potentially associated to a plastic state at the pile–soil interface) of a source pile is transmitted in the surrounding bulk of the soil. In contrast, the displacement induced by an elastic component of strain of a source pile is no more transmitted to a receiver pile if its interface is in a plastic state. The elastic character of displacement interactions indicates that a nonlinear response of piles subjected to significant loads can be copresent to a linear response of piles subjected to less remarkable loads in the same group (Caputo and Viggiani, 1984). In these situations, the estimation of the displacement of the piles in the group may be performed by calculating through a suitable analysis the displacement of these elements with reference to a single isolated case and by applying the interaction factors only up to the limit corresponding to the elastic component of this displacement as well as only to the piles whose interface is not in a plastic state.

11.7.6 Charts for mechanical loads

The evolution of the interaction factor for varying design features characterising a group of two energy piles subjected to mechanical loading, including the pile spacing, the pile slenderness ratio, the pile–soil stiffness ratio, the depth of a finite layer and the base-to-shaft soil Young's modulus ratio, is presented in the following. The following solutions are valid for both compressive and tensile mechanical loads applied to the energy piles.

11.7.6.1 Effect of pile spacing, pile slenderness ratio and pile–soil stiffness ratio – piles embedded in uniform soil mass

Figs 11.9–11.11 present the evolution of the interaction factor for a group of two predominantly floating energy piles embedded in a uniform mass as a function of the normalised centre-to-centre distance between the piles for various slenderness ratios

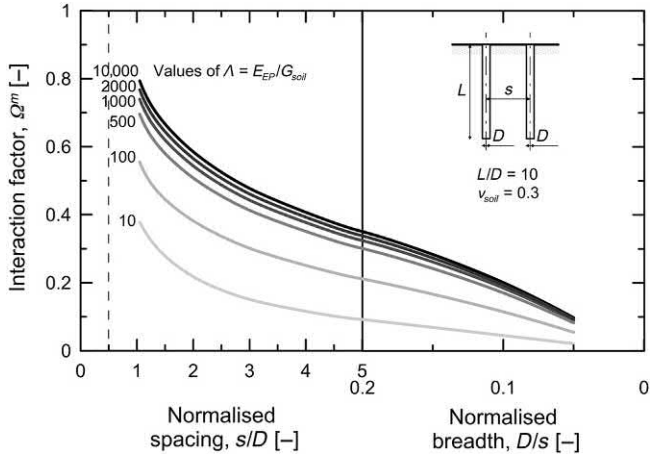

Figure 11.9 Interaction factors for predominantly floating energy piles of $L/D = 10$ subjected to mechanical loading.

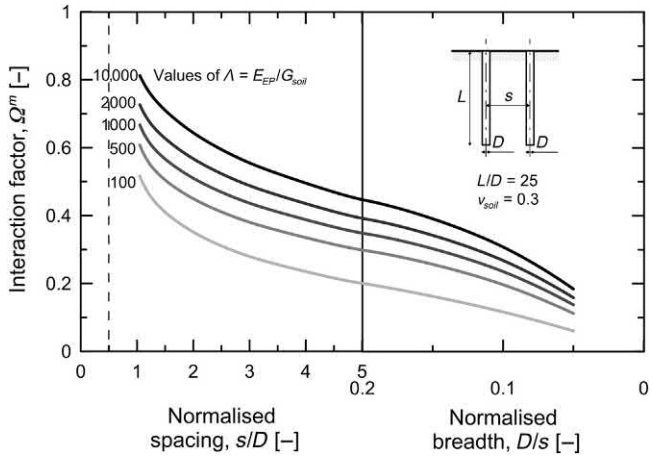

Figure 11.10 Interaction factors for predominantly floating energy piles of $L/D = 25$ subjected to mechanical loading.

L/D and pile–soil stiffness ratios $\Lambda = E_{EP}/G_{soil}$. The decreasing interaction with increasing centre-to-centre distance is shown according to the aforementioned comments. According to Poulos (1968), the interaction increases as L/D and Λ increase, that is as the piles become slender or stiffer.

11.7.6.2 Effect of pile spacing, pile slenderness ratio and pile–soil stiffness ratio – piles resting on infinitely rigid soil strata

Figs 11.12–11.14 present the evolution of the interaction factor for a group of two predominantly end-bearing energy piles resting on infinitely rigid soil strata as a function of

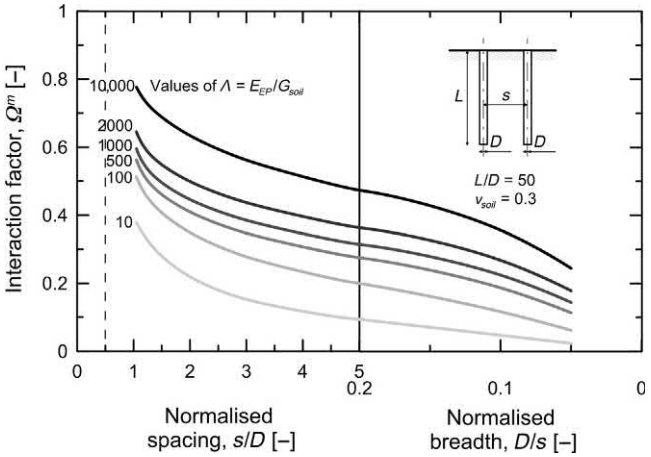

Figure 11.11 Interaction factors for predominantly floating energy piles of $L/D = 50$ subjected to mechanical loading.

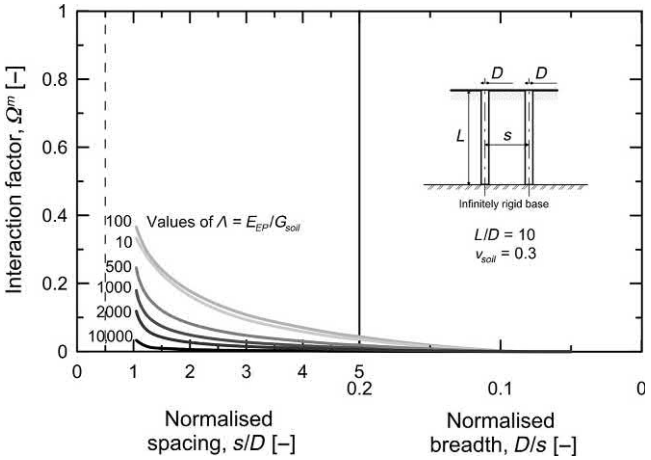

Figure 11.12 Interaction factors for predominantly end-bearing energy piles of $L/D = 10$ subjected to mechanical loading.

the normalised centre-to-centre distance between the piles for various slenderness ratios L/D and pile–soil stiffness ratios $\Lambda = E_{EP}/G_{soil}$. The interaction decreases with increasing centre-to-centre distance. According to Poulos and Mattes (1974), the interaction increases as L/D increases and Λ decreases, that is as the piles become slender or less stiff. The latter result indicates an opposite role of the stiffness compared to that found by Poulos (1968) for predominantly floating piles subjected to mechanical loads, that is increasing interaction as Λ increases and thus as the piles become stiffer.

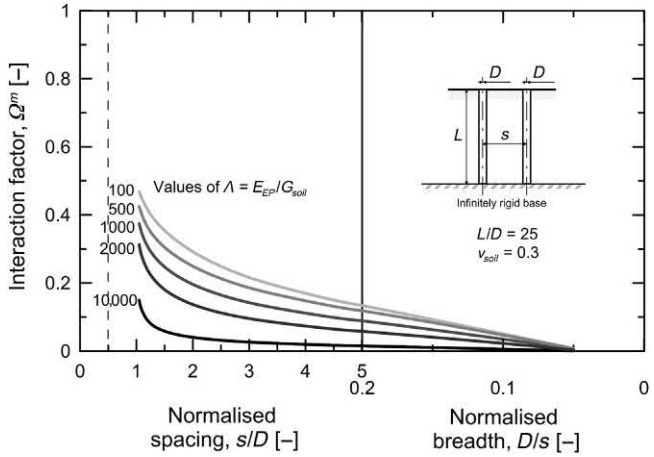

Figure 11.13 Interaction factors for predominantly end-bearing energy piles of $L/D = 25$ subjected to mechanical loading.

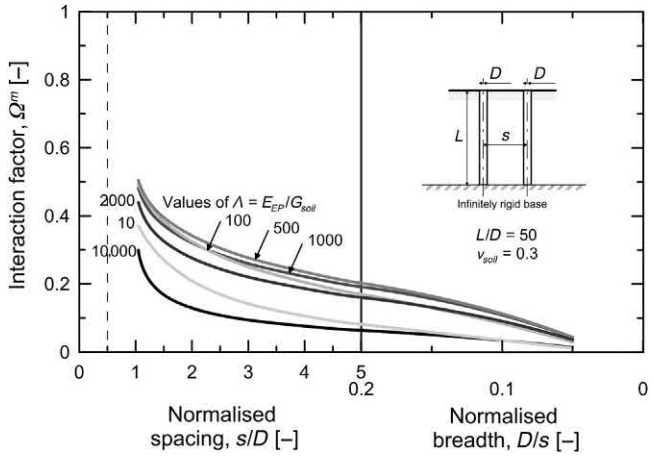

Figure 11.14 Interaction factors for predominantly end-bearing energy piles of $L/D = 50$ subjected to mechanical loading.

11.7.6.3 Effect of pile slenderness ratio, pile–soil stiffness ratio and base-to-shaft modulus ratio – piles resting on finitely rigid soil strata

Figs 11.15 and 11.16 present the evolution of the correction factor for a group of two predominantly end-bearing energy piles resting on finitely rigid soil strata as a function of the base-to-shaft soil Young's modulus ratio $E_{soil,b}/E_{soil,s}$ for various slenderness ratios L/D and pile–soil stiffness ratios $\Lambda = E_{EP}/G_{soil,s}$. According to Poulos and Mattes (1974), the correction factor F_b generally increases with decreasing Λ and increasing $E_{soil,b}/E_{soil,s}$. The larger the value of L/D or the smaller the value of Λ, the

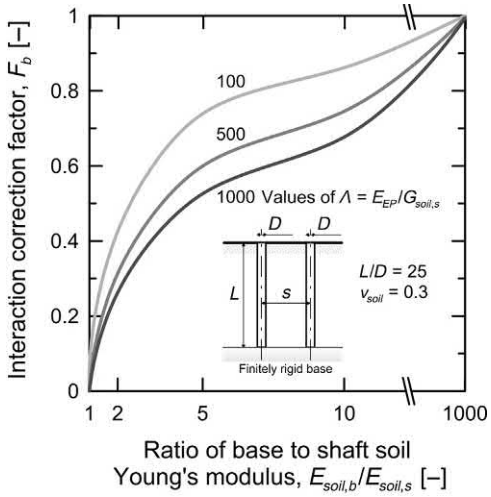

Figure 11.15 Correction factor F_b to account for the effect of a finitely rigid bearing stratum for $L/D = 25$ for energy piles subjected to mechanical loading.

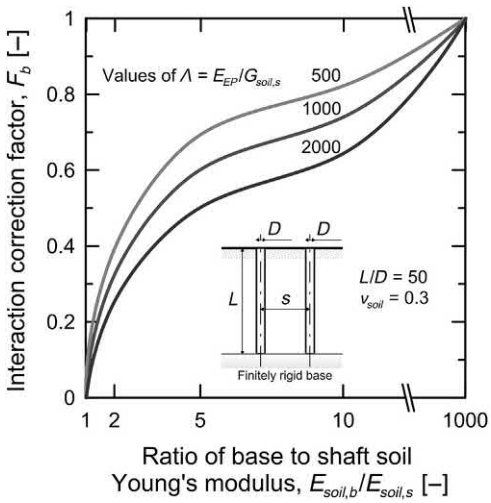

Figure 11.16 Correction factor F_b to account for the effect of a finitely rigid bearing stratum for $L/D = 50$ for energy piles subjected to mechanical loading.

smaller the value of $E_{soil,b}/E_{soil,s}$ for which F_b tends to 1, that is the corrected interaction factor tends to the interaction factor for predominantly end-bearing energy piles resting on infinitely rigid soil strata. Although the values of F_b shown are exact only for a normalised pile spacing of $s/D = 5$, they apply to other centre-to-centre distances between the piles sufficiently accurately for practical purposes. Note that for values of $E_{soil,b}/E_{soil,s}$ greater than 1000 the value of F_b remains approximately unchanged, that

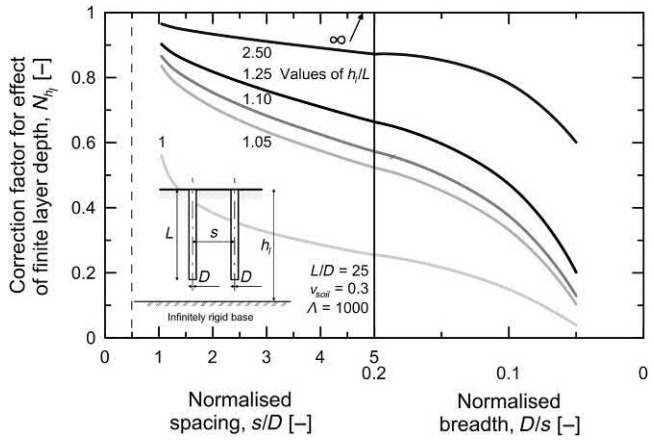

Figure 11.17 Correction factor N_{h_l} for effect of finite layer depth for energy piles subjected to mechanical loading.

is the effect of the rigidity of the bearing soil layer involves a pile response comparable to that for the case of an infinitely rigid base.

11.7.6.4 Effect of finite layer depth

Fig. 11.17 presents the effect of the finite layer depth h_l, where a correction factor N_{h_l} is plotted for $L/D = 25$ and $\Lambda = 1000$. The interaction factor for any value of h_l/L is given by

$$\Omega = N_{h_l}\Omega_{h_l/L\to\infty} \tag{11.8}$$

where $\Omega_{h_l/L\to\infty}$ is the interaction factor for the deep soil layer ($h_l/L\to\infty$). According to Poulos (1968), the interaction increases as the value of h_l/L increases. This effect becomes more notable as L/D increases and Λ decreases. Although presented for specific values of L/D and Λ, the values of the factor N_{h_l} presented in Fig. 11.17 can be approximately applied for other values of L/D and Λ.

A possible application of Eq. (11.8) is as follows: for $s/D = 1$ and a value of $h_l/L = 1$, that is representing the theoretical situation of energy piles resting on an infinitely rigid soil stratum, N_{h_l} can be estimated to read 0.58 from Fig. 11.17; the interaction factor for a pair of predominantly floating energy piles referring to the same values of s/D and Λ reads 0.68 from Fig. 11.11; consideration of Eq. (11.8) with reference to the previous values yield to an interaction factor of $\Omega = N_{h_l}\Omega_{h_l/L\to\infty} = 0.58\cdot 0.68 = 0.39$ for a pile resting on an infinitely rigid soil stratum that can be appreciated from Fig. 11.13 referring to the relevant values of s/D and Λ.

11.7.7 Charts for thermal loads

The evolution of the interaction factor for varying design features characterising a group of two energy piles subjected to thermal loading, including the pile spacing, the pile slenderness ratio, the pile–soil stiffness ratio, the Poisson's ratio of the soil, the depth of a finite layer, nonuniform soil moduli, the soil–pile thermal expansion coefficient ratio and the base-to-shaft soil Young's modulus ratio, is presented in the following. The following solutions are valid for both positive and negative temperature variations applied to the energy piles.

11.7.7.1 Effect of pile spacing, pile slenderness ratio and pile–soil stiffness ratio – piles embedded in uniform soil mass

Figs 11.18–11.20 present the evolution of the interaction factor for a group of two predominantly floating energy piles embedded in a uniform mass as a function of the normalised centre-to-centre distance between the piles for various slenderness ratios L/D and pile–soil stiffness ratios $\Lambda = E_{EP}/G_{soil}$. The decreasing interaction with increasing centre-to-centre distance is shown according to the aforementioned comments. The interaction increases as L/D increases and Λ decreases, that is as the piles become slender or less stiff. The latter result indicates an opposite role of the stiffness compared to that found by Poulos (1968) for piles subjected to mechanical loads, that is increasing interaction as Λ increases and thus as the piles become stiffer.

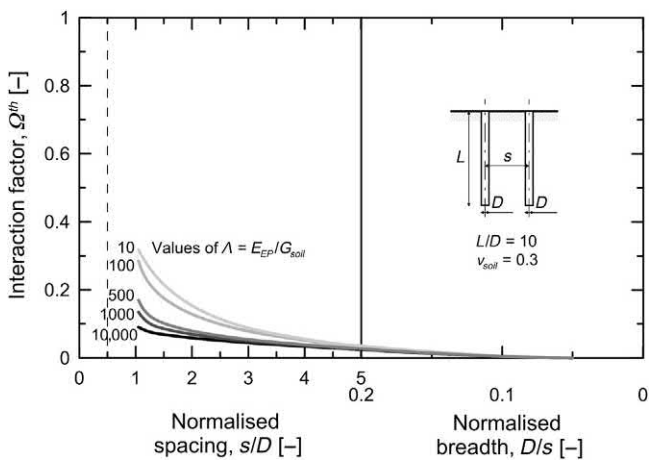

Figure 11.18 Interaction factors for predominantly floating energy piles of $L/D = 10$ subjected to thermal loading. *Modified after Rotta Loria, A.F., Laloui, L., 2016. The interaction factor method for energy pile groups. Comput. Geotech. 80, 121–137.*

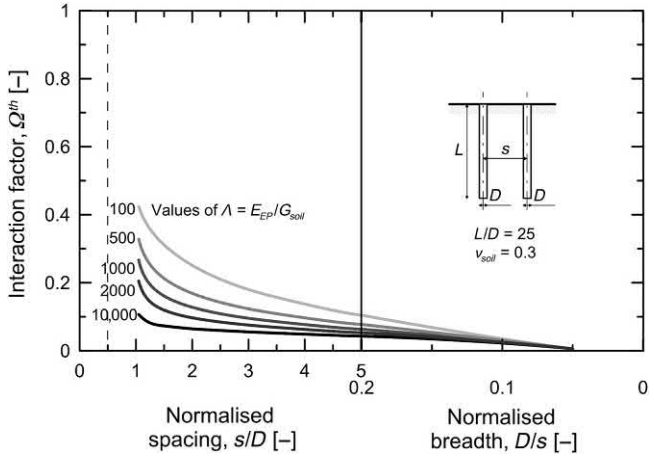

Figure 11.19 Interaction factors for predominantly floating energy piles of $L/D = 25$ subjected to thermal loading. *Modified after Rotta Loria, A.F., Laloui, L., 2016. The interaction factor method for energy pile groups. Comput. Geotech. 80, 121–137.*

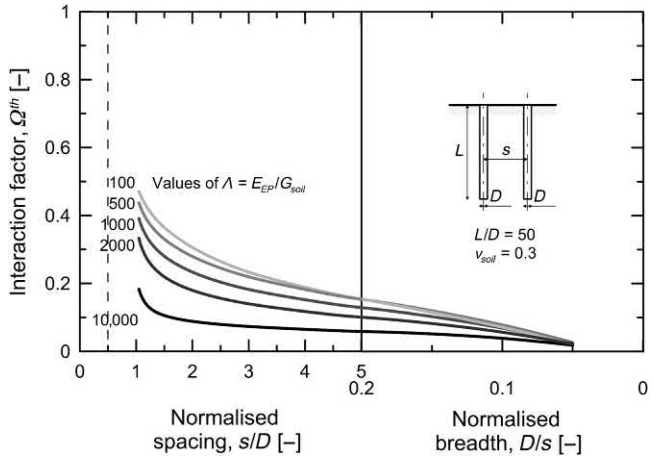

Figure 11.20 Interaction factors for predominantly floating energy piles of $L/D = 50$ subjected to thermal loading. *Modified after Rotta Loria, A.F., Laloui, L., 2016. The interaction factor method for energy pile groups. Comput. Geotech. 80, 121–137.*

11.7.7.2 Effect of pile spacing, pile slenderness ratio and pile–soil stiffness ratio – piles resting on infinitely rigid soil strata

Figs 11.21–11.23 present the evolution of the interaction factor for a group of two predominantly end-bearing energy piles resting on infinitely rigid soil strata as a function of the normalised centre-to-centre distance between the piles for various slenderness ratios L/D and pile–soil stiffness ratios $\Lambda = E_{EP}/G_{soil}$. The interaction decreases with increasing centre-to-centre distance. The interaction increases as L/D increases

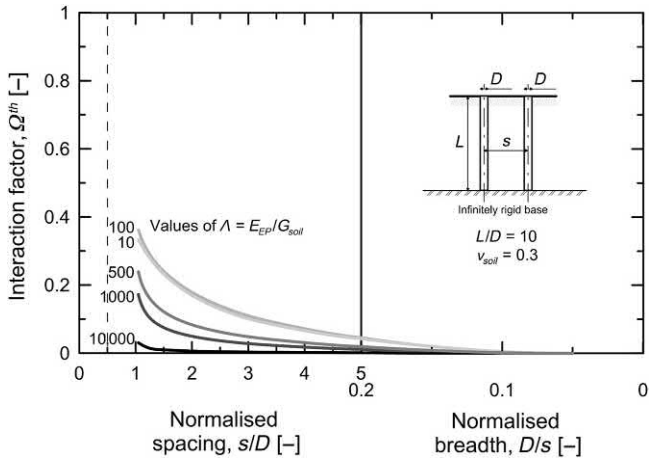

Figure 11.21 Interaction factors for predominantly end-bearing energy piles of $L/D = 10$ subjected to thermal loading. *Modified after Rotta Loria, A.F., Laloui, L., 2017a. Displacement interaction among energy piles bearing on stiff soil strata. Comput. Geotech. 90, 144–154.*

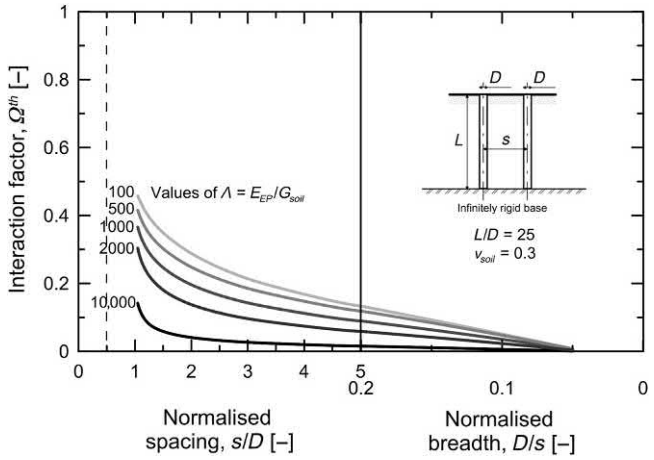

Figure 11.22 Interaction factors for predominantly end-bearing energy piles of $L/D = 25$ subjected to thermal loading. *Modified after Rotta Loria, A.F., Laloui, L., 2017a. Displacement interaction among energy piles bearing on stiff soil strata. Comput. Geotech. 90, 144–154.*

and Λ decreases, that is as the piles become slender or less stiff. The latter result indicates (1) the same role of the stiffness compared to that found for predominantly floating energy piles subjected to thermal loads; (2) the same role of the stiffness compared to that found by Poulos and Mattes (1974) for predominantly end-bearing conventional piles subjected to mechanical loads and (3) the opposite role of the stiffness compared to that found by Poulos (1968) for predominantly floating conventional

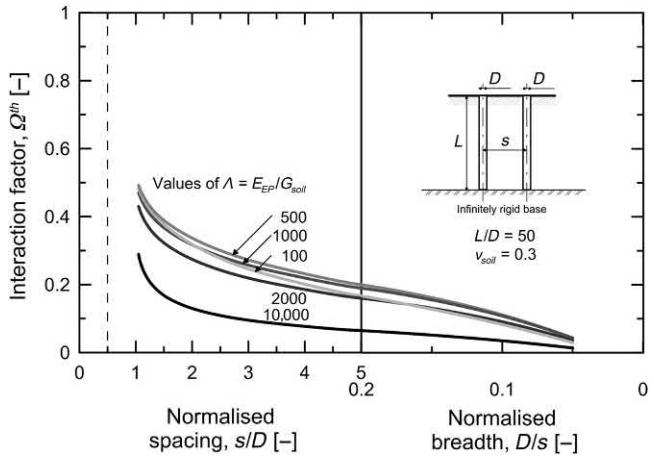

Figure 11.23 Interaction factors for predominantly end-bearing energy piles of $L/D = 50$ subjected to thermal loading. *Modified after Rotta Loria, A.F., Laloui, L., 2017a. Displacement interaction among energy piles bearing on stiff soil strata. Comput. Geotech. 90, 144–154.*

piles subjected to mechanical loads, that is increasing interaction as Λ increases and thus as the piles become stiffer.

11.7.7.3 Effect of pile slenderness ratio, pile–soil stiffness ratio and base-to-shaft modulus ratio – piles resting on finitely rigid soil strata

Figs 11.24 and 11.25 present the evolution of the correction factor for a group of two predominantly end-bearing energy piles resting on finitely rigid soil strata as a function of the base-to-shaft soil Young's modulus ratio $E_{soil,b}/E_{soil,s}$ for various slenderness ratios L/D and pile–soil stiffness ratios $\Lambda = E_{EP}/G_{soil,s}$. The correction factor generally increases with increasing Λ and $E_{soil,b}/E_{soil,s}$. This result indicates the opposite role of Λ compared to that found by Poulos and Mattes (1974) for predominantly end-bearing piles subjected to mechanical loads, that is increasing F_b as Λ decreases and thus as the piles become less stiff. The smaller the value of L/D or the greater the value of Λ, the smaller the value of $E_{soil,b}/E_{soil,s}$ for which F_b tends to 1, that is the corrected interaction factor tends to the interaction factor for predominantly end-bearing energy piles resting on infinitely rigid soil strata. Although the values of F_b shown are exact only for a normalised pile spacing of $s/D = 5$, they apply to other centre-to-centre distances between the piles sufficiently accurately for practical purposes. Note that for values of $E_{soil,b}/E_{soil,s}$ greater than 1000 the value of F_b remains approximately unchanged, that is the effect of the rigidity of the bearing soil layer involves a pile response comparable to that for the case of an infinitely rigid base.

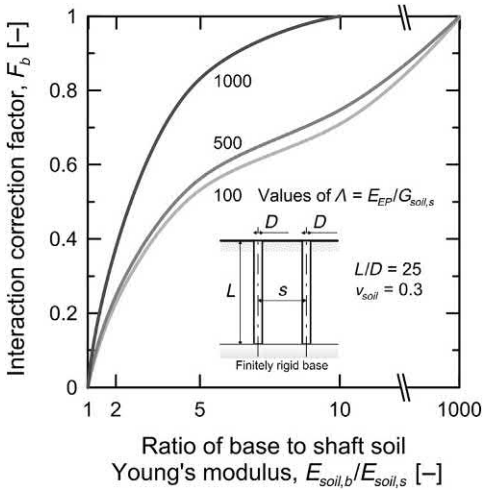

Figure 11.24 Correction factor F_b to account for the effect of a finitely rigid bearing stratum for $L/D = 25$ for energy piles subjected to thermal loading. *Modified after Rotta Loria, A.F., Laloui, L., 2017a. Displacement interaction among energy piles bearing on stiff soil strata. Comput. Geotech. 90, 144–154.*

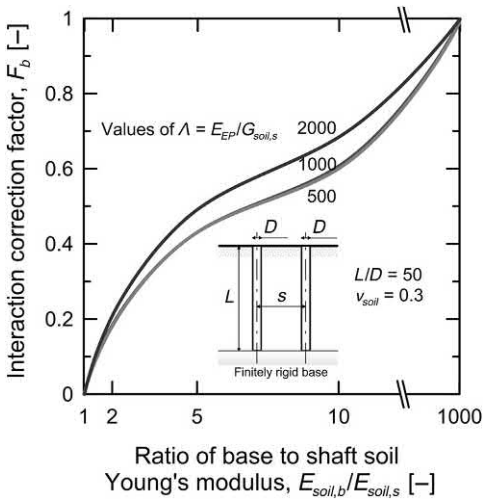

Figure 11.25 Correction factor F_b to account for the effect of a finitely rigid bearing stratum for $L/D = 50$ for energy piles subjected to thermal loading. *Modified after Rotta Loria, A.F., Laloui, L., 2017a. Displacement interaction among energy piles bearing on stiff soil strata. Comput. Geotech. 90, 144–154.*

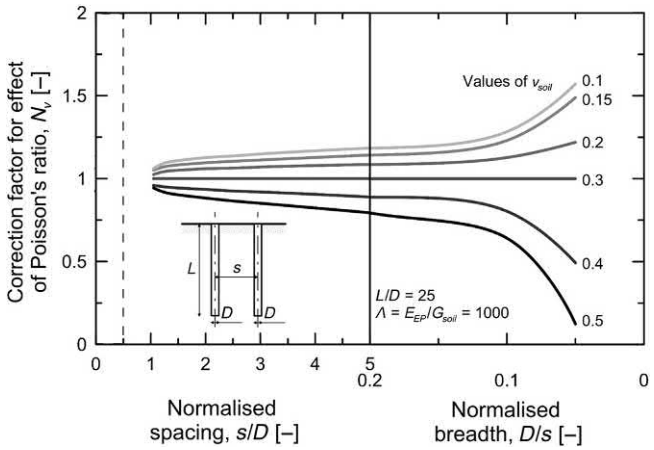

Figure 11.26 Correction factor N_ν for effect of Poisson's ratio of soil for energy piles subjected to thermal or mechanical loading (Rotta Loria and Laloui, 2016).

11.7.7.4 Effect of Poisson's ratio of soil

Fig. 11.26 presents the effect of the Poisson's ratio of the soil ν_{soil}, where a correction factor N_ν is plotted for $L/D = 25$ and $\Lambda = 1000$. The interaction factor for any value of ν_{soil} is given by

$$\Omega = N_\nu \Omega_{\nu_{soil}=0.3} \tag{11.9}$$

where $\Omega_{\nu_{soil}=0.3}$ is the interaction factor for $\nu_{soil} = 0.3$. The interaction increases as the value of ν_{soil} decreases. This effect becomes more notable as the centre-to-centre distance between the piles increases. Although the considered chart has been obtained for piles subjected to thermal loading can be employed approximately in the analysis of piles subjected to mechanical loading.

11.7.7.5 Effect of finite layer depth

Fig. 11.27 presents the effect of the finite layer depth h_l in terms of a correction factor N_{h_l} referring to $L/D = 25$ and $\Lambda = 1000$ that allows calculating the interaction factor for any value of h_l/L according to Eq. (11.8). The interaction increases as the value of h_l/L decreases. This effect becomes more notable as L/D increases and Λ decreases. Although presented for specific values of L/D and Λ, the values of the factor N_{h_l} presented in Fig. 11.27 can be approximately applied for other values of L/D and Λ. The results demonstrate an opposite role of the depth of the soil layer compared to that found by Poulos (1968) for conventional piles subjected to mechanical loads, that is decreasing interaction as h_l/L decreases.

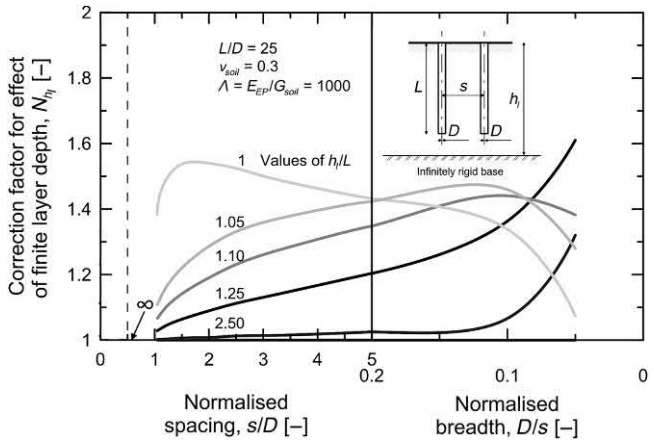

Figure 11.27 Correction factor N_{h_l} for effect of finite layer depth for energy piles subjected to thermal loading (Rotta Loria and Laloui, 2016).

11.7.7.6 Effect of nonuniform soil modulus

The solutions presented above for the interaction factor all assume a uniform soil modulus along the pile shaft. In some cases, a closer approximation to reality is to consider the soil modulus as increasing linearly with depth (Gibson's soil) (Poulos, 1968).

Fig. 11.28 shows the effect of a nonuniform soil modulus along the pile shaft on the interaction factor. A comparison between the interaction factor evolutions with normalised centre-to-centre distance between the piles for a constant and a linearly increasing soil modulus with depth (the latter being equal, on average, to the constant distribution along the pile length) is presented. The variation of the soil modulus with depth is as follows

$$E_{soil}(z) = 0.5E_{soil} + \frac{z}{L}E_{soil} \tag{11.10}$$

where z is the depth of the soil deposit. The value of Ω^{th} for the piles in the nonhomogeneous soil is up to 2% smaller than for the homogeneous soil at any considered centre-to-centre distance. Thus, the use of interaction factors for the case of piles in a homogeneous soil gives conservative estimates of the interaction for cases in which the modulus increases with depth. The effect of nonuniform soil moduli on the displacement interaction between piles subjected to thermal loads is less marked compared to that characterising piles subjected to mechanical loads, for which the difference with the uniform case ranges from 20% to 25% (Poulos and Davis, 1980).

11.7.7.7 Effect of soil–pile thermal expansion coefficient ratio

The solutions presented above for the interaction factor all assume an isothermal soil (infinite heat reservoir) that is characterised by an elastic behaviour. The effect of the

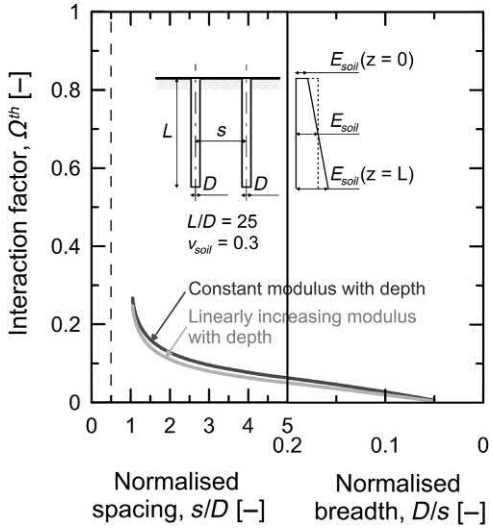

Figure 11.28 Effect of nonuniform soil modulus on interaction factor for energy piles subjected to thermal loading. *Modified after Rotta Loria, A.F., Laloui, L., 2016. The interaction factor method for energy pile groups. Comput. Geotech. 80, 121–137.*

ratio between the linear thermal expansion coefficient of soil and that of the pile $X = \alpha_{soil}/\alpha_{EP}$ on the interaction factor is investigated herein. The solutions have been obtained through time-dependent finite element analyses referring to a heating time of the source pile of $t = 6$ months. In these analyses, the thermal expansion coefficient of the receiver pile is set to zero to highlight only the effect of thermally induced volumetric variations in the soil on the interaction previously defined with reference to the elastic soil.

Fig. 11.29 presents the effect of the soil–pile thermal expansion coefficient ratio on the interaction factor. The interaction increases with increasing thermal expansion coefficient of the soil. Values of $X = 0.5$ and 1 have a similar impact on the interaction factor compared to $\nu_{soil} = 0.15$, that is they induce a relative average increase of 12% compared to the increase of 15% from the reference value of Ω^{th}. Values of the thermal expansion coefficient of soil greater than that of the pile (e.g. $X = \alpha_{soil}/\alpha_{EP} = 2$) have a considerably stronger effect on the interaction, that is up to an average increase of 200% compared to the reference value of Ω^{th}. The time (and thus the spatial extent) of heat diffusion in the soil crucially characterises the effect of the soil–pile thermal expansion coefficient ratio on the interaction because it involves varying amounts of mobilised thermal expansion coefficient of soil.

11.7.8 Modified analysis procedure

The previously proposed interaction factor analysis procedure considers the soil to be characterised by an *elastic* behaviour. This involves assuming the soil to be an infinite

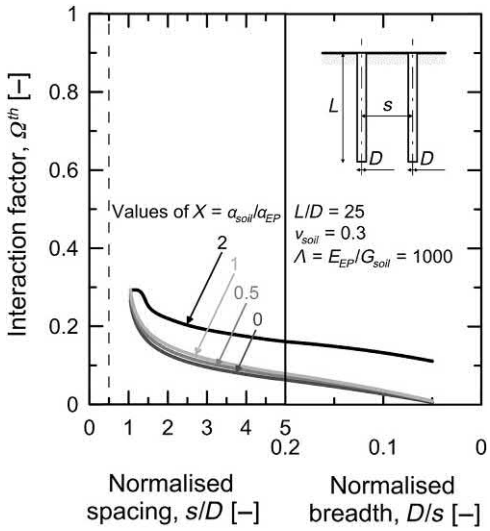

Figure 11.29 Effect of soil thermal expansion coefficient on interaction factor. *Modified after Rotta Loria, A.F., Laloui, L., 2016. The interaction factor method for energy pile groups. Comput. Geotech. 80, 121–137.*

heat reservoir that remains at a constant fixed temperature. Hence, no influence caused by any temperature sensitivity of the soil or thermal interaction between the source pile and the receiver pile is considered. Although approximate, this approach has been proven to be valuable (Rotta Loria and Laloui, 2016, 2017a) because (1) it develops solutions of the interaction factor that are independent of the actual heat exchange occurring in the energy pile group and (2) it takes advantage of the negligible role of the thermally induced soil deformation on the interaction between piles characterising all usual situations where the thermal expansion coefficient of the soil is lower than or equal to that of the piles (Rotta Loria and Laloui, 2016, 2017c).

Only in situations where the thermal expansion coefficient of the soil is higher than that of the piles does the thermally induced soil deformation have a marked effect on the pile interaction, especially at successive stages of geothermal operations of the piles (Rotta Loria and Laloui, 2017c). In these situations, a simplified yet valuable approach for capturing the group displacement via charts has been proven to result from interaction factors still referring to pile pairs in isothermal soil (Rotta Loria and Laloui, 2016, 2017a).

The modified interaction factor analysis procedure for the analysis of energy pile groups in which the thermal expansion coefficient of the soil is in excess to that of the piles relies on the steps detailed in Section 11.7.5 with a revision of step 1. In this context, the consideration of a unitary displacement obtained through a numerical analysis in which the soil, as the energy pile, is characterised by a *thermoelastic* behaviour

(in contrast to the idealisation of the pile group when applying the interaction factor concept), makes the interaction factor method suitable to describe the displacement response of energy pile groups also in situations in which the soil thermal expansion coefficient is higher than that of the piles. This capability is associated with the higher vertical displacement value resulting from the analysis of the single isolated pile that better approaches reality through application of interaction factors still referring to pile pairs in isothermal soil.

11.8 Interaction factor method based on analytical models

11.8.1 Background

The original interaction factor method proposed by Poulos (1968) for conventional piles subjected to only mechanical loads as well as by Rotta Loria and Laloui (2016) for energy piles subjected to thermal loads resorts to charts. However, as an alternative to charts, analytical models have been later proposed in both cases, the rationale being that analytical models can estimate the interaction factor in a broader range of conditions and perform more comprehensively and flexibly than the charts in the analysis of pile groups.

To address the vertical displacement of floating and end-bearing conventional piles subjected to mechanical loads, early analytical models have been proposed by Randolph and Wroth (1979a,b), respectively. An alternative formulation of these models by Chow (1986) and an improvement related to the definition of the interaction factor by Mylonakis and Gazetas (1998) have been later presented. Modifications and more advanced formulations of the original approaches have also been proposed by Lee (1993), Costanzo and Lancellotta (1998), Lee and Xiao (2001), Wong and Poulos (2005), Zhang et al. (2010), Wang et al. (2012, 2016) and Sheil et al. (2018). To address the vertical displacement of floating and end-bearing energy piles subjected to thermal loads, Rotta Loria et al. (2018) unified, modified and extended the analytical models that have been developed by Randolph and Wroth (1979b), Chow (1986) and Mylonakis and Gazetas (1998).

In the following, the features of a *layer model* and a *continuous model* presented by Rotta Loria et al. (2018) are summarised to address through the interaction factor method the displacement analysis of general configurations of energy pile groups subjected to mechanical and thermal loads, based on the analysis of a single isolated pile.

11.8.2 Hypotheses and considerations

In principle, a complete description of the interaction between a source pile and a receiver pile in the pair addressed by the interaction factor method would require three-dimensional (3D) time-dependent numerical analyses because of its 3D and

time-dependent character. For example the vertical displacement field is generally not homogeneous in the 3D space because of the stiffness and presence of the piles. Bending moments occur in the piles. The heat exchange involves temperature variations with time that cause thermally induced deformations of the soil and potentially of the receiver pile.

In practice, an approximate yet realistic analytical description of the considered problem can be performed analytically based on the analysis of a single *isolated* pile subjected to the same load of the source pile in the pair based on a number of simplifying hypotheses and considerations presented below (Rotta Loria et al., 2018). These hypotheses and considerations complement those presented in Section 11.2.

The displacement field characterising the loaded source pile in the pair is assumed to be equal to that in the single isolated case. This assumption disregards the effect of the stiffness of the receiver pile on the deformation of the source pile, which appears to be justified in view of the impractical spacing between the piles for which this effect is observed and is significant (e.g. for $s/D \leq 3$ considering Fig. 11.4).

The displacement field characterising the receiver pile in the pair is considered to be lower than that of the soil around the source pile in an isolated case. This assumption accounts for the greater stiffness of piles than that of the surrounding soil.

The displacement field in the soil around a single isolated pile is assumed to be homogeneous, whereas that around a pair of piles is considered to be nonhomogeneous. As will be shown through the results presented in the following, this approach captures the actual deformation behaviour of the source and receiver piles in a pair with accuracy.

The displacement field within the piles is assumed to be homogeneous. This hypothesis is justified in view of the notable stiffness that usually characterises energy piles compared to that of the soil.

The effect of bending moments on the displacement field of the piles and the soil is neglected. This consideration is justified in view of the small impact of bending moments on the vertical displacement of the piles in the considered problem.

11.8.3 Basic analysis procedure

The analysis procedure characterising the interaction factor method based on analytical models consists of five key steps (cf. Fig. 11.30):

1. The analysis of a single isolated source pile subjected to mechanical or thermal loading to define the vertical displacement, $w_i(z)$, and the shear stress, $\tau_i(z)$, along the pile shaft (z is the vertical coordinate). This analysis may preferably resort to the finite element method. In principle, load-transfer analyses may also be employed for the same purpose. In practice, because of some different underlying hypotheses, the load-transfer method appears less suitable than the finite element method in serving interaction factor analyses.

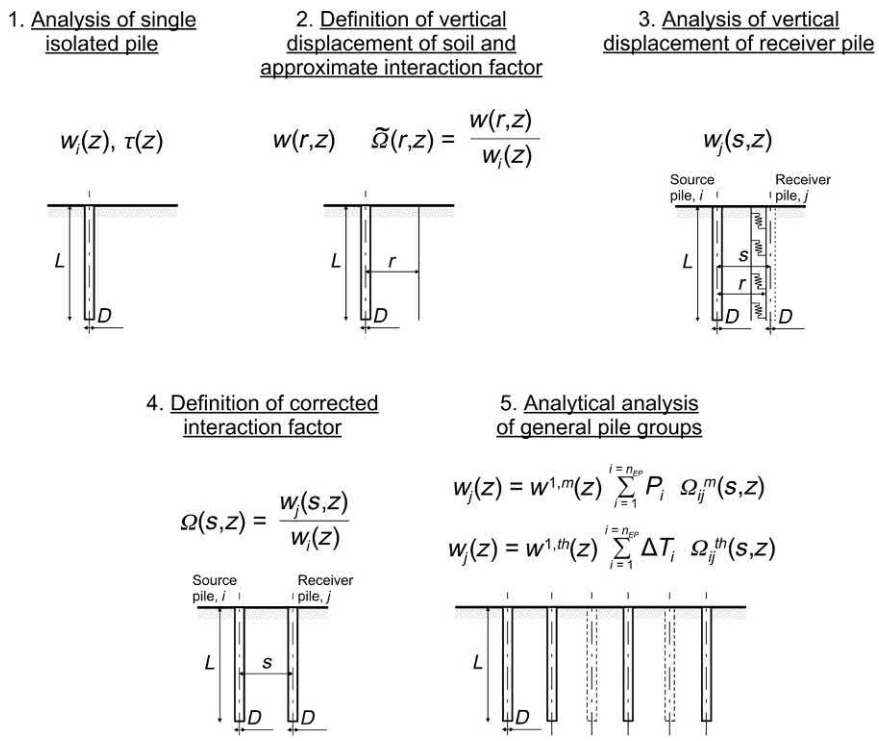

Figure 11.30 Key steps for the application of the interaction factor method based on analytical models. *Modified after Rotta Loria, A.F., Vadrot, A., Laloui, L., 2018. Analysis of the vertical displacement of energy pile groups. Geomech. Energy Environ. 16, 1–14.*

2. The determination of the vertical displacement field of the soil, $w(r, z)$, at any given radial distance, r, from the axis of the previously analysed single isolated pile subjected to loading, and along the vertical coordinate, z. This step can be performed using the analytical models presented hereafter and determines the approximate pile–soil interaction factor as

$$\tilde{\Omega}(r, z) = \frac{w(r, z)}{w_i(z)} \tag{11.11}$$

3. The analysis of the vertical displacement, $w_j(s, z)$, of a receiver pile located at a spacing $s = r + R$ (where $R = 0.5D$ is the pile radius) from the source pile that was previously considered to be isolated. This step can also be performed with the models presented in the following.

4. The determination of the corrected pile–soil–pile interaction factor as (Randolph and Wroth, 1979b; Mylonakis and Gazetas, 1998; Rotta Loria and Laloui, 2016)

$$\Omega(s, z) = \frac{w_j(s, z)}{w_i(z)} \tag{11.12}$$

5. The analysis of the vertical displacement $w_j(z)$ of any pile, j, composing a general group with a total number of piles, n_{EP}, in which some or all of the piles may be subjected to loading through the interaction factor method.

   In the case of piles subjected to mechanical loads, this analysis can be performed as (Poulos, 1968)

$$w_j(z) = w_h^{1,m}(z) \sum_{i=1}^{i=n_{EP}} P_i \Omega_{ij}^m(s,z) \tag{11.13}$$

   where $w_h^{1,m}(z)$ is the vertical displacement along the length of a single isolated pile per unit mechanical load, P_i is the applied mechanical load to the head of pile i and Ω_{ij}^m is the interaction factor for two piles subjected to mechanical loading in a pair corresponding to the centre-to-centre distance between pile i and pile j.

   In the case of piles subjected to thermal loads, this analysis can be performed as (Rotta Loria et al., 2018)

$$w_j(z) = w_h^{1,th}(z) \sum_{i=1}^{i=n_{EP}} \Delta T_i \Omega_{ij}^{th}(s,z) \tag{11.14}$$

   where $w_h^{1,th}(z)$ is the vertical displacement along the length of a single isolated pile per unit temperature variation, ΔT_i is the applied temperature variation to pile i and Ω_{ij}^{th} is the interaction factor for two piles subjected to thermal loading in a pair corresponding to the centre-to-centre distance between pile i and pile j.

In the context of the interaction factor method resorting to charts, it has been remarked the need of a modified procedure for the analysis of energy pile groups in situations where the thermal expansion coefficient of the soil is in excess to that of the piles (Rotta Loria and Laloui, 2016, 2017a). The quoted approach is not needed for capturing the group displacement via the analytical models (Rotta Loria et al., 2018). The reason for this is because these models give the lower and upper boundaries of the displacement that may be expected for energy pile groups embedded in soils characterised by all of thermal expansion coefficient values likely to be found in practice.

Throughout the following development of the models that constitute the core of steps 2 and 3, $w_i(z)$ and $\tau_i(z)$ are assumed to be known.

11.8.4 Layer model

11.8.4.1 Soil vertical displacement and approximate pile–soil interaction factor

The considered model assumes that the soil around the shaft of piles subjected to loads that induce vertical deformation may be idealised as consisting of any number of concentric cylindrical elements, with shear stresses distributed on the surface of each element (cf. Fig. 11.31A). For vertical equilibrium, the magnitude of the shear stress on

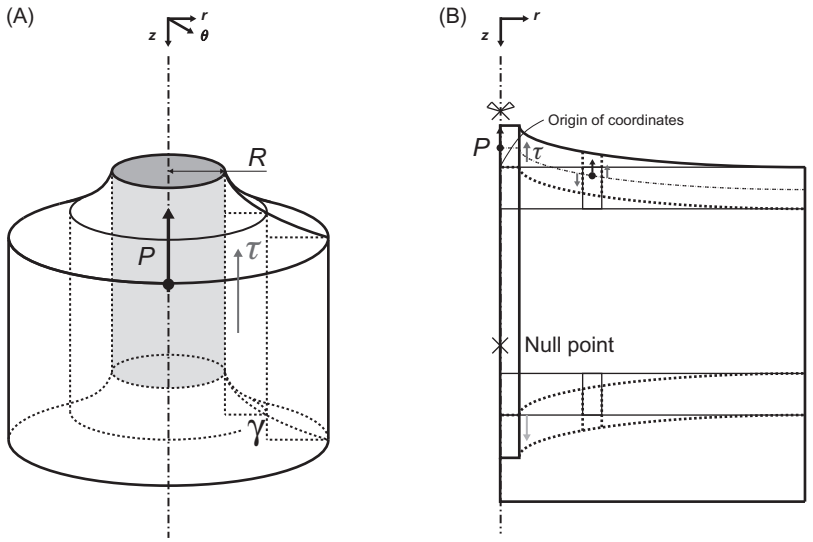

Figure 11.31 The layer model concept for an energy pile subjected to a heating thermal load: (A) the mode of deformation of a layer of cylindrical elements characterising any pile–soil system and (B) the effect of this mode of deformation (Rotta Loria et al., 2018).

each cylindrical element must decrease inversely with the vertical surface area of the element (Cooke et al., 1981).

According to the previous considerations, a simplification of the equilibrium equation along z written for an element with regards to a cylindrical coordinate system (r, θ, z) yields the general solution for the vertical displacement of the soil. When the effects of volume forces due to body loads are neglected, the solution for the vertical displacement of the soil reads (Randolph and Wroth, 1978)

$$w(r,z) = w_i(z) - \frac{\tau_i(z)R}{G_{soil}} \ln\left(\frac{r}{R}\right) \tag{11.15}$$

Eq. (11.15) highlights that the layer model *does not* consider the effects of the shear stress acting on any element of a source pile on all of the elements of the surrounding soil in a 'continuous' way (cf. Fig. 11.31A). This is the rationale for defining the present model as 'layer' model.

The general solution for $w(r,z)$ expressed in Eq. (11.15) can be normalised with respect to $w_i(z)$ to give the approximate pile–soil interaction factor as

$$\tilde{\Omega}(r,z) = 1 - \frac{\tau_i(z)R}{w_i(z)G_{soil}} \ln\left(\frac{r}{R}\right) \tag{11.16}$$

The parameter $\tilde{\Omega}(r,z)$ expresses the effect of loading a single isolated source pile on the surrounding soil in terms of a displacement variation.

Randolph and Wroth (1978) determined the displacement of the pile at its shaft, w_i, by introducing a 'magical radius', r_m, at which the shear stresses (and thus the vertical displacements) in the soil become vanishingly small. Randolph and Wroth (1979b) also obtained a general expression for the vertical displacement of the soil expressed in Eq. (11.15) that is independent of w_i and heavily dependent on r_m. In the framework of conventional piles subjected to mechanical loads, the magical distance r_m has been found (Randolph and Wroth, 1978) to be (1) almost constant with depth as a consequence of the plane state of strain characterising the piles and (2) greater than the length of the pile, that is $r_m = 2.5L(1 - \nu_{soil})$ for predominantly friction piles. In the framework of energy piles subjected to thermal loads, this magical distance has been found (Rotta Loria et al., 2018) to be (1) not constant with depth because of the absence of the plane state of strain characterising the piles and (2) generally smaller than the length of the pile, for example $r_m = 0.5L(1 - \nu_{soil})$ at the ends of predominantly floating piles. Based on these considerations, the application of relationships such as those proposed by Randolph and Wroth (1978, 1979b) for describing piles subjected to mechanical loads appears to be unsuitable for describing piles subjected to thermal loads. The above relationships would be valid only for certain regions of piles subjected to thermal loads because of the variable character of r_m with depth.

The dependence on the depth of the layer model expressed in Eq. (11.15), together with the assumption of no interaction between the elements and associated layers in the surrounding soil, make this model easily applicable to analysing the vertical displacement of stratified (nonuniform) soil deposits.

11.8.4.2 Receiver pile vertical displacement and corrected pile–soil–pile interaction factor

The presence of a receiver pile usually decreases the displacement of the soil (Mylonakis and Gazetas, 1998). This effect becomes larger with increasing relative stiffness of the receiver pile compared to that of the soil.

To account in a simple yet realistic way for the interplay between a receiver pile and the soil, the receiver pile is modelled as a beam supported with springs of a given stiffness characteristic of the surrounding soil medium, K_s. A possible formulation for K_s reads (Mylonakis, 2001)

$$K_s \approx \frac{1.3G_{soil}}{\pi D}\left(\frac{E_{EP}}{E_{soil}}\right)^{-\frac{1}{40}}\left(1 + 7\left(\frac{L}{D}\right)^{-0.6}\right) \tag{11.17}$$

Considering the vertical equilibrium of an element of a receiver pile whose axis is located at a spacing s from that of a corresponding element of the thermally loaded source pile gives the following simplified equation (cf. Fig. 11.32)

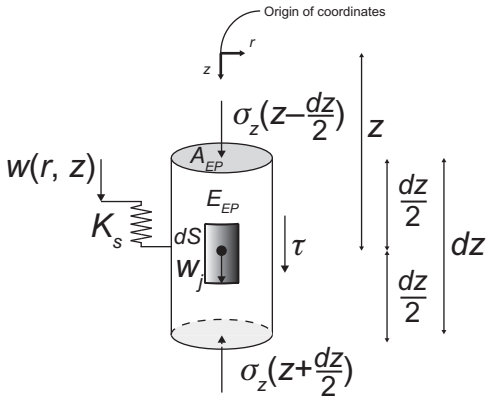

Figure 11.32 Vertical equilibrium of an element of a receiver pile (Rotta Loria et al., 2018).

$$\frac{d\sigma_z}{dz}A_{EP}dz - \pi DK_s\left(w(r,z) - w_j(s,z)\right)dz = 0 \tag{11.18}$$

where σ_z is the vertical stress acting on an element of a receiver pile and A_{EP} is the cross-sectional surface of the considered element. Using the constitutive equations, Eq. (11.18) can be rewritten in the form of the second-order differential equation governing the equilibrium of *each element* of the receiver pile (Mylonakis and Gazetas, 1998)

$$\frac{\partial^2 w_j}{\partial z^2} - \lambda_{lt}^2\left(w(r,z) - w_j(s,z)\right) = 0 \tag{11.19}$$

where λ_{lt} is a load-transfer coefficient given by

$$\lambda_{lt} = \sqrt{\frac{\pi DK_s}{A_{EP}E_{EP}}} \tag{11.20}$$

Eq. (11.19) needs two boundary conditions to be solved. The first boundary condition is chosen with reference to the state of restraint that characterises the head of the receiver pile. Based on the consideration that because the pile is free to displace vertically at its head no vertical stress will be present in this setting. This condition can be mathematically expressed through the constitutive equations as (Mylonakis and Gazetas, 1998)

$$\left.\frac{\partial w_j}{\partial z}\right|_{z=0} = 0 \tag{11.21}$$

The second boundary condition needs to be preferably chosen by considering whether the source pile is subjected to mechanical or thermal loading. The application

of this boundary condition must also refer to the shear stress induced by either mechanical or thermal loading separately. In the case of mechanical loading, the second boundary condition is chosen with reference to the base of the receiver pile. Because the pile base acts as a rigid punch on the lower layer of soil (Randolph and Wroth, 1979b), there is a specific relation between the point load applied at the pile base, $P_b = A_{EP}\sigma_z(z = L)$ (where $\sigma_z(z = L)$ is the normal stress acting on A_{EP} at the pile base) and the displacement of the rigid circular disc, $w_j(z = L)$ (Timoshenko and Goodier, 1970) (cf. Fig. 11.33). This relation can be mathematically expressed through the constitutive equations (Mylonakis and Gazetas, 1998) to become the second boundary condition for the case of mechanical loading as

$$E_{EP}A_{EP}\frac{\partial w_j}{\partial z}\bigg|_{z=L} + K_b w_j(z = L) = 0 \tag{11.22}$$

where (Boussinesq, 1878)

$$K_b = \frac{2DG_{soil}}{1 - \nu_{soil}} \tag{11.23}$$

In the case of thermal loading, the second boundary condition is chosen with reference to the so-called null point of the shear stress of the receiver pile (Rotta Loria et al., 2018). As the layer model does not account for interaction between the

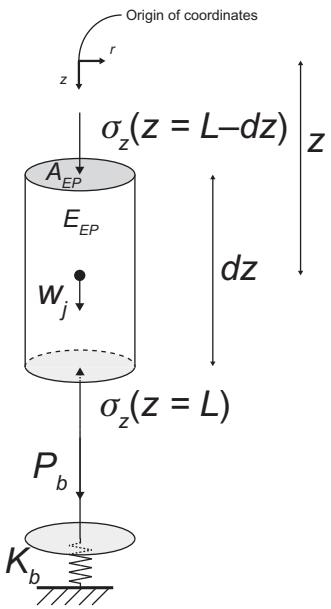

Figure 11.33 Vertical equilibrium of a base element of a receiver pile (Rotta Loria et al., 2017).

different layers of elements, in correspondence with this setting the displacement of the receiver pile is the same as that of the soil (i.e. $w(r,z) - w_j(s,z) = 0$). This phenomenon arises because, for compatibility, upward, downward and zero vertical displacements will be caused if and only if upward, downward and zero shear stresses are applied *at the corresponding element* in the *adjacent soil*. This location can be determined from the analysis of a single isolated pile according to Eq. (11.15). The discussed boundary condition can be mathematically expressed as

$$w_j(s, z = z|_{w=0}) = w(r, z = z|_{w=0}) = 0 \tag{11.24}$$

Eq. (11.19), together with the boundary conditions expressed in Eqs (11.21) and (11.24), can calculate the values of $w_j(s,z)$. These values finally determine the values of the corrected pile–soil–pile interaction factor, $\Omega(s,z)$.

11.8.5 Continuous model

11.8.5.1 Soil vertical displacement and approximate pile–soil interaction factor

The considered model assumes that the continuous distribution of the shear stresses at the pile shaft can be approximated as a distribution of point loads acting at the centre of the elements composing these piles as if they were linear entities generated by nodes (cf. Fig. 11.34A). At some distance, the effects of such stresses and point loads are indistinguishable (Chow, 1986).

The assumption highlighted above involves the equations of Mindlin (1936) for a vertical point load acting in a semiinfinite, homogeneous and isotropic elastic half-space being exploited to determine through the superposition principle the vertical displacement caused by a distribution of point loads acting on a single isolated (mechanically and/or thermally loaded) source pile at any location in the surrounding soil. The vertical displacement of the soil can be defined as (Mindlin, 1936)

$$w(r,z) = \sum_{l=1}^{m} w_{kl} = \sum_{l=1}^{m} \frac{P_l}{16\pi G_{soil}(1-\nu_{soil})} \left(\frac{3-4\nu_{soil}}{R_1} + \frac{8(1-\nu_{soil})^2 - (3-4\nu_{soil})}{R_2} + \frac{(z_l - z_k)^2}{R_1^3} + \frac{(3-4\nu_{soil})(z_l+z_k)^2 - 2z_l z_k}{R_2^3} + \frac{6z_l z_k (z_l+z_k)^2}{R_2^5} \right) \tag{11.25}$$

where w_{kl} is the vertical displacement of any soil node, k, caused by a point load, $P_l = 2\pi R L_{seg} \tau_l$, applied to the node, l, of a source pile (for which L_{seg} is the length of the element and τ_l is the shear stress acting along it); m are the elements of the source pile from which the effects of the point loads are calculated; $R_1 = \sqrt{r_k^2 + (z_k - z_l)^2}$ (for which r_k is the horizontal distance between node l at which the load is applied

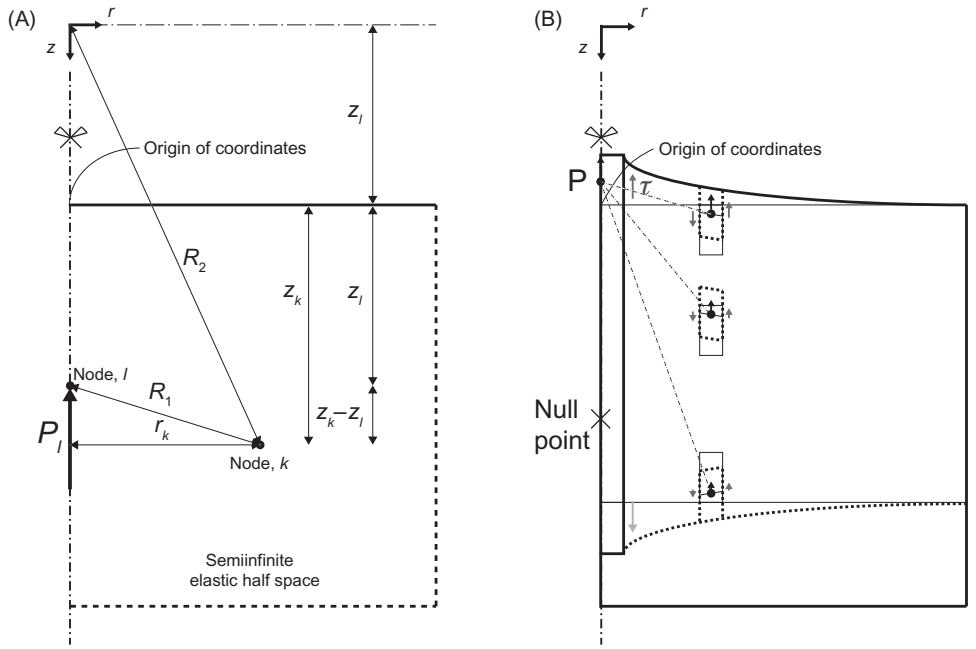

Figure 11.34 The continuous model concept for an energy pile subjected to a heating thermal load: (A) the reference situation for Mindlin's problem (Mindlin, 1936) and (B) the transposition of this problem to that of a single isolated pile subjected to thermal loading (Rotta Loria et al., 2018).

and node k at which the influence is considered, z_k is the depth of node k, and z_l is the depth of node l); and $R_2 = \sqrt{r_k^2 + (z_k + z_l)^2}$.

The equations of Mindlin (1936) indicate that the present continuous model allows the vertical displacement of stratified (nonhomogeneous) soil deposits to be estimated only approximately. However, an effective and accurate procedure has been shown in this context to consider a mean value of the shear modulus of the soil layer where the displacement is calculated at any soil node, k, and the shear modulus of the soil layer where the point load is applied at any pile node, l (Poulos and Davis, 1980).

Eq. (11.25) highlights that the continuous model considers the effects of the shear stress acting on any element of a source pile on all of the elements of the surrounding soil in a 'continuous' way, regardless of the layer (cf. Fig. 11.34B). This is the rationale for defining the present model as 'continuous' model.

The general solution for the vertical displacement of the soil expressed in Eq. (11.25) can be normalised with respect to the vertical displacement at the pile shaft to give the approximate pile–soil interaction factor, as suggested by Eq. (11.11).

11.8.5.2 Receiver pile vertical displacement and corrected pile–soil–pile interaction factor

In order to solve Eq. (11.19) for energy piles subjected to mechanical loads the same boundary conditions expressed in Eqs (11.21) and (11.22) can be employed. In contrast, while the first boundary condition expressed in Eq. (11.21) may also be used for energy piles subjected to thermal loads, a different second boundary condition must be employed with the continuous model to properly address the hypotheses and considerations characterising the continuous model. The reason for this is related to the incapability of Eq. (11.22) of explicitly considering the presence of the null point. This fact has been verified to lead to an overestimate of the vertical displacement of receiver piles when source piles in a pair are subjected to thermal loads (Rotta Loria et al., 2017). Therefore Eq. (11.22) is considered unsuitable to model piles subjected to thermal loads but only piles subjected to mechanical loads.

Unlike the layer model, the continuous model accounts for interaction between the different layers of elements. According to this hypothesis and to continuum mechanics theory, it may be considered that the location where zero thermally induced shear stress occurs does not coincide with the location where zero thermally induced vertical displacement occurs. Knowledge of the location where the vertical displacement of the soil is $w(r,z) = w_j(s,z) \neq 0$ is thus of interest to define the second boundary condition. To overcome the issue that the specific value of $w(r,z) \neq 0$ and the associated location where $\tau(r,z) = 0$ is not known a priori, the equations of Mindlin (1936) can be exploited to determine through the superposition principle the shear stress caused by a distribution of point loads acting on a single isolated source pile at any location in the surrounding soil. This approach, which accounts for the continuous character of the present model, approximately allows for the direct determination of the location in the soil where $\tau(r,z) = 0$ and thus where $w(r,z) = w_j(s,z) \neq 0$ from the analysis of a single isolated pile (Rotta Loria et al., 2018). The shear stress in the soil can be defined as (Mindlin, 1936)

$$\tau(r,z) = \sum_{l=1}^{m} \tau_{kl} = \sum_{l=1}^{m} \frac{P_l r_k}{8\pi(1-\nu_{soil})} \left(-\frac{1-2\nu_{soil}}{R_1^3} + \frac{1-2\nu_{soil}}{R_2^3} - \frac{3(z_k - z_l)^2}{R_1^5} - \frac{3(3-4\nu_{soil})z_k(z_k+z_l) - 3z_l(3z_k+z_l)}{R_2^5} - \frac{30 z_k z_l (z_k+z_l)^2}{R_2^7} \right) \tag{11.26}$$

where τ_{kl} is the shear stress acting on any soil node, k, caused by a point load, P_l, applied to the node, l, of a source pile. The second discussed boundary condition for energy piles subjected to thermal loads can thus be mathematically expressed as

$$w_j(s, z = z|_{\tau=0}) = w(r, z = z|_{\tau=0}) \tag{11.27}$$

Eq. (11.19), together with Eqs (11.21) and (11.27), can calculate the values of $w_j(s, z)$. As before, these values can determine the values of $\Omega(s, z)$.

11.8.6 Effect of nonlinear soil deformation on energy pile interaction

With the increasing understanding of the response of both conventional piles subjected to mechanical loads and energy piles subjected to thermal and mechanical loads, a number of experimental (Caputo and Viggiani, 1984) and theoretical (O'Neill et al., 1981; Chow, 1986; Jardine et al., 1986; Poulos, 1988, 2006; Randolph, 1994; Mandolini and Viggiani, 1997; Leung et al., 2010; Rotta Loria et al., 2017) investigations based on interaction factor analyses have been performed to address the effect of nonlinear soil deformation on the vertical displacement of and interaction between such foundations. Soil deformation can often be nonlinear and may involve reversible (i.e. elastic) or irreversible (i.e. plastic) stress–strain behaviour. As a consequence of this nonlinearity, different deformation modulus values can be associated with the varying shear strain levels that characterise the soil surrounding piles (e.g. as a result of loading or construction effects). Consideration of these deformation modulus values has been proven to be essential to analyse and design pile groups (O'Neill et al., 1981; Poulos, 1988; Randolph, 1994).

The aforementioned considerations justify a specific approach for the interaction factor analysis of pile groups (O'Neill et al., 1981; Jardine et al., 1986; Poulos, 1988; Randolph, 1994; Mandolini and Viggiani, 1997). Soil modulus values that are associated with high strain levels can be used to characterise the vertical displacement behaviour of the single piles composing any group. On the other hand, soil modulus values that are associated with low strain levels can be used to estimate the interaction between the piles. With this approach, interaction factor analyses based on appropriate soil modulus values can capture the vertical displacement of conventional pile groups subjected to mechanical loads almost irrespective of the mathematical formulation employed for describing soil behaviour and the related pile response (Mandolini and Viggiani, 1997; Leung et al., 2010).

The above is justified by the close adherence to reality of results of interaction factor analyses of conventional pile groups that exploit either different (Poulos, 1988, 2006) or varying (Chow, 1986; Randolph, 1994; Leung et al., 2010; Zhang et al., 2010; Wang et al., 2012) soil modulus values, and linear elastic (Poulos, 1988, 2006), nonlinear elastic (Randolph, 1994; Leung et al., 2010) or nonlinear elastoplastic (Chow, 1986; Zhang et al., 2010; Wang et al., 2012) stress–strain relationships. It is also justified by interaction factor analysis of energy pile groups that exploit different soil modulus values and a linear elastic stress–strain relationship (Rotta Loria et al., 2017).

11.8.7 Modified analysis procedure

The previously proposed interaction factor analysis procedures based on charts or analytical models (cf. Sections 11.7.5 and 11.8.3) ignore nonlinear soil deformation. This is caused by the fact that the considered procedures account for a unique soil modulus value to characterise both the single pile response and the interactions among the piles. To address this challenge, a modified and extended procedure proposed by Rotta Loria et al. (2017) of that presented by Poulos (1988) is described to model the response of energy pile groups subjected to mechanical and thermal loads in nonlinearly deforming soils.

The use of linear elastic theory, constant material properties and linear mathematical formulations are the fundamental assumptions underlying the procedure presented here to describe nonlinear soil deformation and the related vertical displacement of piles and interaction between them. Although this procedure is approximate in principle, it has in practice been capable of accurately and expediently reproducing the vertical displacement of pile groups.

Currently, both $w_i(z)$ (step 1 of the analysis approach presented in Section 11.8.3) and $w_j(s,z)$ (steps 2 and 3) are computed using the same value of soil Young's modulus adjacent to the pile, that is the 'near-pile' soil modulus E_{soil}. The resulting interaction factor analysis does not account for nonlinear soil deformation.

In the modified interaction factor analysis procedure, the vertical displacement of the single isolated source pile, $w_i(z)$, is calculated (step 1) using the near-pile soil modulus, E_{soil}, whereas the vertical displacement of the receiver pile in the pair, $w_j(s,z)$, is calculated (steps 2 and 3) using an average soil modulus, $\overline{E}_{soil}$, which accounts for the smaller strain levels between the piles. The resulting modified interaction factor analysis accounts for nonlinear soil deformation.

The average soil modulus is given by the following expressions (cf. Fig. 11.35)

$$\begin{aligned} \overline{E}_{soil}(s) &= E_{soil}\left(1+\frac{(\mu_E-1)(s-D)}{2s_t}\right) \quad \text{for } s<s_t+D \qquad \text{(a)} \\ \overline{E}_{soil}(s) &= E_{soil}\left(\mu_E+\frac{(1-\mu_E)s_t}{2(s-D)}\right) \quad \text{for } s\geq s_t+D \qquad \text{(b)} \end{aligned} \tag{11.28}$$

where $\mu_E = E_{soil,m}/E_{soil}$ (for which $E_{soil,m}$ is the soil 'mass' modulus between the piles) is likely to lie within the range of 3 and 10 and s_t is a transition distance likely to be between $3D$ and $6D$ (Poulos, 1988).

The described distribution of soil modulus to determine $\overline{E}_{soil}$ for calculating $w_j(s,z)$ is indeed simplified for a number of reasons (Rotta Loria et al., 2017). In principle, experimental evidence may be of help for formulating a procedure more adherent to reality. In practice, the success of theoretical investigations proposed by Poulos (1988)

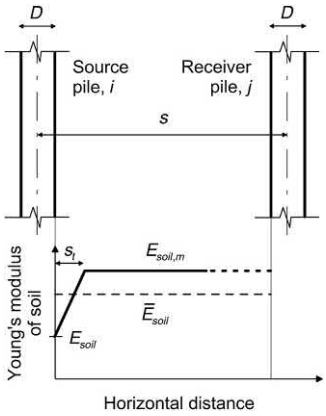

Figure 11.35 Assumed distribution of soil modulus between two piles. E_{soil} = near−pile soil modulus (characteristic of high strain levels); $E_{soil,m} = \mu_E E_{soil}$ (with $\mu_E \geq 1$) = soil mass modulus (characteristic of low strain levels); $\bar{E}_{soil}$ = average soil modulus for computing interactions; s_t = transition distance (Rotta Loria et al., 2017).

and Rotta Loria et al. (2017) corroborate the use of the considered approach despite the lack of the previous evidence.

Although the foregoing modified analysis procedure includes the previous simplifications, such an approach does approximately account for nonlinear soil deformation (through a linear elastic behaviour of the soil surrounding the piles) depending on the geometrical configuration of the piles in any group, in addition to the material properties characterising the group. An example of this capability is proposed in Fig. 11.36, which presents the values of the normalised average soil Young's modulus corresponding to the centre-to-centre spacing between different pairs of piles that are used in the modified interaction factor analysis approach to define the interaction factor and the vertical displacement for different numbers and locations of piles subjected to loading. The average Young's modulus of soil is normalised by the near-pile Young's modulus. Although for any given distance between two piles a constant soil mass modulus value is used, the normalised average soil Young's modulus varies nonlinearly for different pile spacing according to Eq. (11.28).

11.9 Equivalent pier method

11.9.1 Background

The *equivalent pier method* represents another approach to address the displacement response of pile groups by considering the response to loading of a solid block composed of piles and the soil contained between them. The roots of the equivalent pier method, similar to the interaction factor method, date back to studies originally

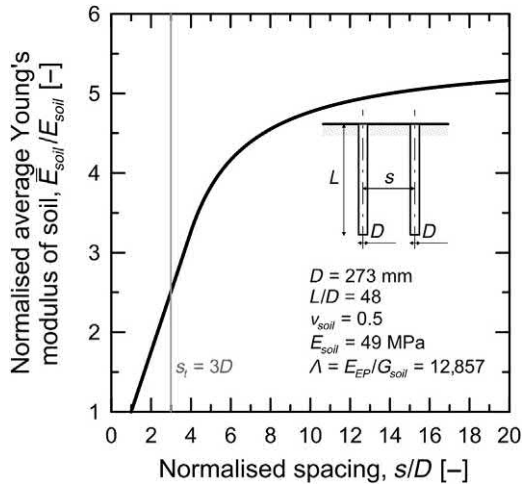

Figure 11.36 Values of the normalised average soil Young's modulus corresponding to the centre-to-centre spacing between different pairs of piles that are used in the modified interaction factor analysis approach (Rotta Loria et al., 2017).

developed for conventional pile groups subjected to mechanical loads that highlighted the effectiveness and suitability of replacing any pile group by a single equivalent pier that displaces an equal amount (Poulos, 1968; Poulos and Davis, 1980; Butterfield and Douglas, 1981). This method has also been modified and extended to energy pile groups subjected to thermal loads (Rotta Loria and Laloui, 2017b).

Two types of approximations have generally been considered for the equivalent pier approach: (1) a single pier of the same circumscribed plan area as the group with an equivalent length (Poulos, 1968) and (2) a single equivalent pier of the same length as the piles with an equivalent diameter (Poulos, 1993). The equivalent pier method is useful for a number of purposes, including the estimation of (1) the average vertical displacement of any relatively small pile group and (2) the average and differential vertical displacement of any large foundation comprising a number of pile groups with the aid of other methods (e.g. the interaction factor method) to consider intergroup interaction.

The equivalent pier method has been applied to the analysis of conventional pile groups in various forms, including early formulations based on an elastic description of the pier–soil interaction that were applied through the boundary element method (Poulos and Davis, 1980; Poulos, 1993) and successive formulations based on an elastoplastic description of the pier–soil interaction that were applied through the load-transfer method (Randolph and Clancy, 1993; Randolph, 1994; Clancy and Randolph, 1996; Horikoshi and Randolph, 1998; Castelli and Maugeri, 2002; Castelli and Motta, 2003; McCabe and Lehane, 2006; Sheil and McCabe, 2014). Based on the

previous developments, the equivalent pier method has been modified and extended to the analysis of energy pile groups based on the load-transfer method (Rotta Loria and Laloui, 2017b). In the following, this latter formulation of the equivalent pier method for estimating the average vertical displacement of energy pile groups subjected to mechanical and thermal loads is presented.

11.9.2 Hypotheses and considerations

In addition to the hypotheses and considerations presented in Section 11.2, those described hereafter apply to the following developments. Although reference is made to energy piles and equivalent piers that are (1) free to move vertically at their heads (i.e. no head restraint) and (2) characterised by an infinitely flexible slab, considering the presence of a slab connecting the energy piles and characterising the equivalent piers may indeed be feasible. In those cases, an effective approach may consist in assuming the slab as infinitely rigid and calculate an associated value of stiffness for the head restraint. Poulos and Davis (1980) remark, however, that the average vertical displacement of a pile group characterised by an infinitely flexible slab is approximately equal to that of the same group with an infinitely rigid slab.

The energy piles are approximated as solid cylindrical prisms and form a regular geometry in plan view (e.g. square groups of energy piles). The equivalent piers are also considered to be solid cylindrical prisms.

The materials constituting the energy piles and the equivalent piers follow a linear thermoelastic behaviour. The soil follows an elastoplastic behaviour and is thus generally considered as an infinite (isothermal) heat reservoir. The impact of the temperature variations observed in reality in the soil on the response of the pile group is implicitly considered in the analyses only in situations where the thermal expansion coefficient of the soil is in excess to that of the piles. In these situations, the dominant mode of heat transfer is assumed to be conduction. Moisture migration is negligible. The impact of ground water advection is considered to be negligible. Thermal contact resistance between the energy piles and the soil is discounted. The variation of the thermal field at the ground surface as a consequence of a potential variation in the environmental conditions is assumed to be negligible. The temperature at the far fields from the pile group, that is the (bottom) horizontal and vertical boundaries that may be considered to characterise the deep soil domain surrounding the piles, is assumed to remain constant with time and equal to $T_\infty = T_0$. The horizontal (top) boundary described by the soil surface is treated as adiabatic.

The energy piles are considered to be embedded in a deep soil layer at the same initial temperature T_0 and are subjected to a temperature variation, $\Delta T = T - T_0$. This temperature variation is assumed to be equal for all the piles. The same temperature variation is assumed to be applied to the equivalent piers.

The load–displacement behaviour of the equivalent piers is modelled using the one-dimensional load-transfer method proposed by Coyle and Reese (1966). The load–displacement relationship characterising the equivalent piers relies on a modification to account for group effects of the relationships proposed by Knellwolf et al. (2011) and by Frank and Zhao (1982). This modified load-transfer relationship has been implemented in the Thermo-Pile software developed at the Swiss Federal Institute of Technology in Lausanne (https://lms.epfl.ch/thermopile).

11.9.3 Analysis procedure

The analysis procedure characterising the equivalent pier method consists of three key steps (cf. Fig. 11.37):

1. The analysis of the features of a single pile as well as of the soil embedding the piles composing the group, that is pile geometry, capacity and deformation properties as well as soil deformation properties. This analysis can be carried out referring to the theory presented in Chapter 10, Analytical modelling of capacity and deformation of single energy piles.
2. The definition of the characteristics of the pier, that is pier geometry, capacity and deformation properties. This step can be accomplished by referring to the theoretical developments proposed in the following.
3. The analysis of the average displacement of the pile group, $\overline{w}$, which is suggested to be applied for $s/D < 5$ (Rotta Loria and Laloui, 2017b).

11.9.4 Geometry of the equivalent pier

The key concept of the equivalent pier approach is that any regular pile group can be modelled as a single equivalent pier by considering the soil region in which the piles are embedded as a homogenised continuum (cf. Fig. 11.38). Such an equivalent pier is

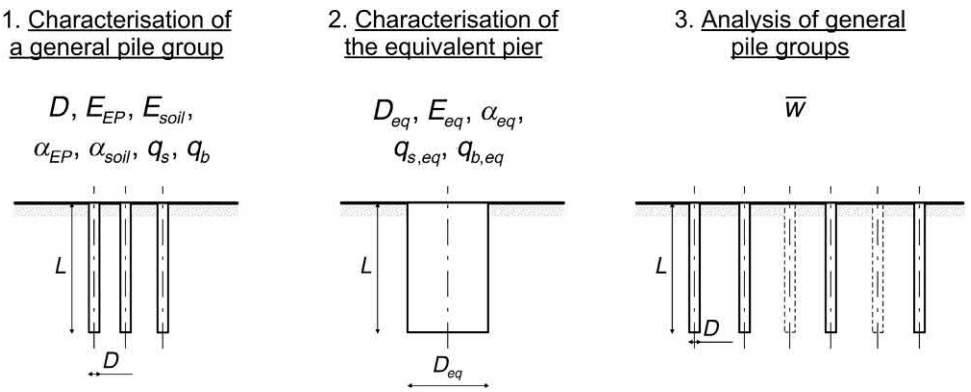

Figure 11.37 Key steps for the application of the equivalent pier method.

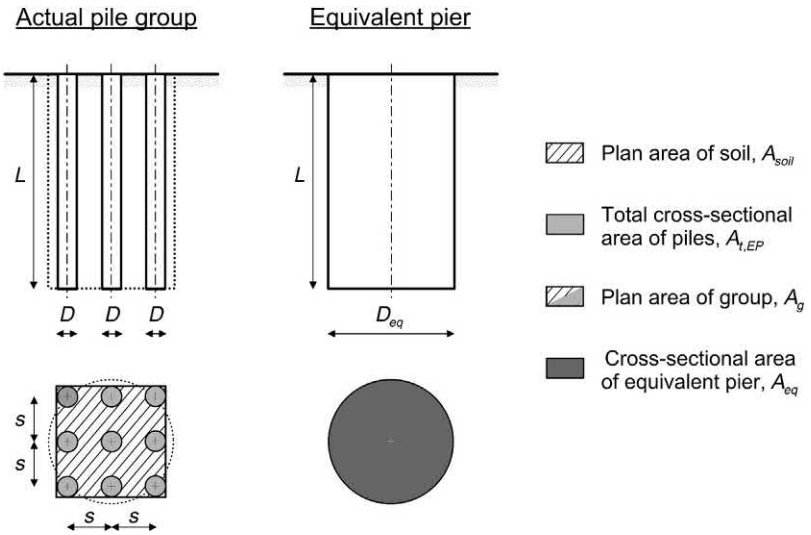

Figure 11.38 Schematic for the calculation of the dimensions of the equivalent pier (Rotta Loria and Laloui, 2017b).

characterised by a length coincident with the average length of the piles and by an equivalent diameter that can be calculated as (Poulos, 1993)

$$\begin{aligned} D_{eq} &\approx 1.27\sqrt{A_g} && \text{for predominantly floating piles} && \text{(a)} \\ D_{eq} &= \frac{2}{\sqrt{\pi}}\sqrt{A_g} \approx 1.13\sqrt{A_g} && \text{for predominantly end-bearing piles} && \text{(b)} \end{aligned} \tag{11.29}$$

For any general configuration of piles, A_g can be determined as

$$A_g = A_{t,EP} + A_{soil} \tag{11.30}$$

where $A_{t,EP}$ is the total cross-sectional area of the piles composing the group ($A_{t,EP} = n_{EP}A_{EP}$) and A_{soil} is the plan area of soil surrounding the piles delimited by the simplest polygon that better reproduces the shape of the pile group. For a square geometry of piles, A_g can be calculated as

$$A_g = \left[\left(\sqrt{n_{EP}} - 1\right)s + D\right]^2 \tag{11.31}$$

Considering an equivalent pier of the same (average) length of the piles in the group and of an equivalent diameter appears to be preferable to considering an equivalent pier of the same circumscribed plan area as the group and an equivalent length. Reference to the same length of the piles allows considering the properties (e.g. thermal and mechanical) of the soil layers that may surround the pile group and govern its deformation and capacity.

Based on the considered approach, any pile group with a total cross-sectional area of piles

$$A_{t,EP} = \pi \frac{D^2}{4} n_{EP} \tag{11.32}$$

is replaced by a single equivalent pier of cross-sectional area

$$A_{eq} = \pi \frac{{D_{eq}}^2}{4} \tag{11.33}$$

The shape of the pile group can be categorised by the 'aspect ratio', which can be determined for a square geometry of piles in plan view as (Randolph and Clancy, 1993)

$$AR = \sqrt{\frac{n_{EP} s}{L}} \tag{11.34}$$

where L is the (average) length of the piles. The equivalent pier approach has been proven to provide a representative description of the behaviour (e.g. deformation and capacity) of conventional pile groups subjected to mechanical loads for values of AR smaller than 4 and certainly less than 2 (Randolph, 1994). This approach has also been suggested to provide sufficiently accurate results for practical purposes (characterised by a 20% variation with those obtained with more rigorous approaches) for pile groups with a centre-to-centre pile spacing of up to five diameters (Poulos et al., 2002). The reason for this is that for larger aspect ratios ($AR > 3 \div 4$) and wider pile spacing ($s > 5D$), the pile group resembles a 'shallow' foundation more than a 'deep' foundation, so the hypothesis of a block behaviour of the group is no longer valid. Analyses performed over a broad range of design conditions suggest that the considerations summarised above for conventional pile groups subjected to axial mechanical loads are also valid for energy pile groups subjected to thermal loads (Rotta Loria and Laloui, 2017b).

11.9.5 Homogenised material properties of the equivalent pier

The equivalent pier can be characterised by an equivalent Young's modulus effectively homogenising that of the piles and of the soil embedded between them that can be calculated as the weighted average of the Young's modulus of these bodies as (Poulos, 1993)

$$E_{eq} = \frac{A_{t,EP} E_{EP} + A_{soil} E_{soil}}{A_{t,EP} + A_{soil}} = E_{EP} \frac{A_{t,EP}}{A_g} + E_{soil} \left(1 - \frac{A_{t,EP}}{A_g}\right) \tag{11.35}$$

This definition of the equivalent pier modulus accounts for the effect that the excess stiffness of the piles compared to that of the soil has on the deformability

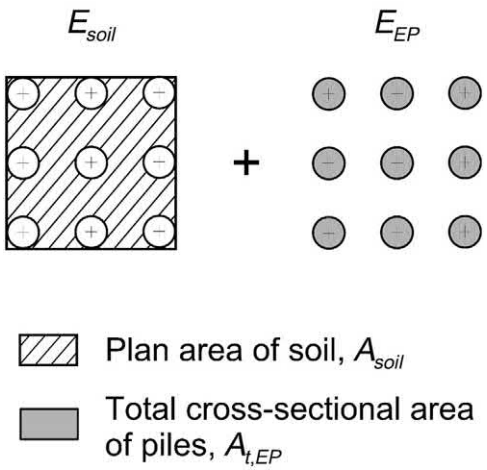

Figure 11.39 Schematic for the calculation of the Young's modulus of the equivalent pier (Rotta Loria and Laloui, 2017b).

problem by considering superposition of the representative areas involved (cf. Fig. 11.39).

The equivalent pier can then be characterised by an equivalent linear thermal expansion coefficient that can be calculated as (Rotta Loria and Laloui, 2017b)

$$\begin{aligned} &\alpha_{eq} = \alpha_{EP} && \text{for } X = \alpha_{soil}/\alpha_{EP} \leq 1 && \text{(a)} \\ &\alpha_{eq} = \frac{A_{EP}\alpha_{EP} + A_{exc}\alpha_{soil}\Upsilon}{A_{EP} + A_{exc}} = \alpha_{EP}\frac{A_{EP} + A_{exc}X\Upsilon}{A_{EP} + A_{exc}} && \text{for } X = \alpha_{soil}/\alpha_{EP} > 1 && \text{(b)} \end{aligned} \tag{11.36}$$

where Υ is a coefficient that relates the average temperature variation in the soil to that in the energy piles within the plan area A_{exc} in which the thermal strain potential of the soil is in excess compared to the thermal strain potential of the energy piles (cf. Fig. 11.40).

Formulation (a) of Eq. (11.36) expresses that when $X = \alpha_{soil}/\alpha_{EP} \leq 1$, the deformation of the energy pile group may be interpreted and described by considering only the thermal expansion coefficient of the piles and the related thermally induced deformation because it governs that of the group. Formulation (b) of Eq. (11.36) highlights that when $X = \alpha_{soil}/\alpha_{EP} > 1$, the deformation of the energy pile group may be interpreted and described by considering also the thermal expansion coefficient of the soil surrounding the piles and the related thermally induced deformation because it profoundly characterises that of the group. In particular, the definition of formulation (b) of Eq. (11.36) is based on a similar concept to that characterising Eq. (11.35). Formulation (b) of Eq. (11.36) accounts for the impact of a linear thermal expansion

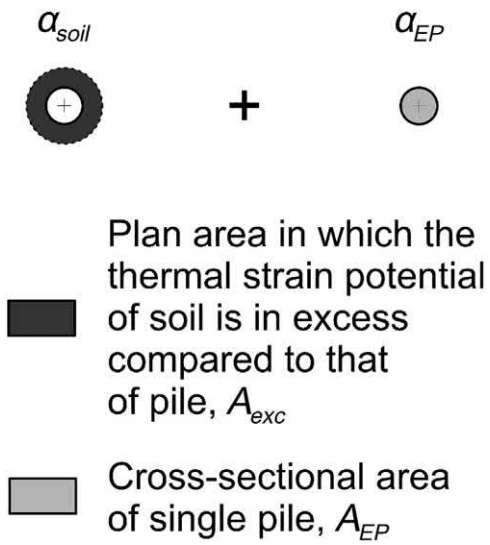

Figure 11.40 Schematic for the calculation of the linear thermal expansion coefficient of the equivalent pier (Rotta Loria and Laloui, 2017b).

coefficient of the soil in excess compared to that of the piles on the deformability problem by considering superposition of the representative areas involved.

The fundamental assumption that allows obtaining the formulation of the equivalent linear thermal expansion coefficient expressed in formulation (b) of Eq. (11.36) is that thermal interactions between the energy piles in any considered group are negligible. This choice may represent an approximation of the real temperature field around the energy piles for long-term durations of applied thermal loads and may rarely characterise reality. However, this choice is valuable because it involves determining the temperature field around the energy piles as if they were isolated heat sources, with a consequent effective determination of the parameters Υ and A_{exc}.

The rationale behind the definition of Υ and A_{exc} is as follows (Rotta Loria and Laloui, 2017b). In situations characterised by $X = \alpha_{soil}/\alpha_{EP} > 1$, interest lies in determining the extent of the plan area of soil A_{exc} in which the thermal strain potential of this body is in excess compared to the thermal strain potential of the energy piles. There is a radial distance, R_{exc}, in the soil for which this condition is satisfied and coincides with a temperature variation, ΔT_{soil}, that can be expressed with reference to free thermal expansion conditions as

$$\left|\varepsilon^{th}_{f,soil}\right| > \left|\varepsilon^{th}_{f,EP}\right| \rightarrow |-\alpha_{soil}\Delta T_{soil}| > |-\alpha_{EP}\Delta T_{EP}| \rightarrow |\Delta T_{soil}| > \frac{\alpha_{EP}}{\alpha_{soil}}|\Delta T_{EP}| \longrightarrow \Delta T_{soil} = \frac{\Delta T_{EP}}{X}$$

where $\varepsilon_{f,soil}^{th}$ and $\varepsilon_{f,EP}^{th}$ are the thermal strains of the soil and the energy piles under free thermal expansion conditions and ΔT_{EP} is the temperature variation applied to the energy piles. In normalised form, this temperature variation is

$$\frac{\Delta T_{soil}}{\Delta T_{EP}} = \frac{1}{X} \tag{11.37}$$

Knowledge of the evolution in space and with time of the temperature field around a single isolated energy pile enables R_{exc} to be determined with reference to the normalised temperature variation expressed in Eq. (11.37). The availability of R_{exc} allows calculating the plan area of interest as

$$A_{exc} = \pi \frac{D_{exc}^2 - D^2}{4} \tag{11.38}$$

where $D_{exc} = 2R_{exc}$.

The hypothesis of no thermal interactions allows the temperature field around a single isolated energy pile to be expediently assessed through a number of analytical and semianalytical solutions. In the following, the energy piles are considered to be a single isolated infinite heat source with a spherical gap subjected to a constant temperature variation according to the conditions described in Section 11.9.2. Consideration of the heat source as a continuous infinite spherical body eliminates the need for the two boundary conditions related to the top and bottom boundaries of the soil domain described in Section 11.9.2. The evolution of the temperature field for radial distances, r, greater than the energy pile radius, R, with time, t, can consequently be determined semianalytically as

$$T(r,t) = T_\infty + (T_R - T_\infty)\frac{R}{r} erfc\left(\frac{r-R}{\sqrt{4t\alpha_d}}\right) \tag{11.39}$$

where T_R is the temperature at the energy pile radius (constant and uniform in the pile domain), *erfc* is the complementary Gaussian error function and $\alpha_d = \lambda/(\rho c_p)$ is the soil thermal diffusivity (where λ is the thermal conductivity, ρ is the bulk density and c_p is the specific heat). The parameter α_d may be calculated as an average value from the thermal diffusivity of different soil layers surrounding the pile length. This fact makes the present equivalent pier approach capable of approximately considering the thermal (and mechanical) behaviour of energy pile groups in layered soils.

The plan area of soil A_{exc} is characterised by an average temperature variation, $\overline{\Delta T}_{soil}$, that can be determined analytically based on the results of Eq. (11.39). This average temperature variation in the soil is related to the temperature variation in the energy piles through the factor

$$\Upsilon = \frac{\overline{\Delta T}_{soil}}{\Delta T_{EP}} \text{with} \frac{1}{X} < \Upsilon \leq 1 \tag{11.40}$$

Neglecting the thermal interactions among the energy piles involves disregarding the effect of the spacing among and position of the energy piles on the definition of A_{exc} and Υ. A dependence of the thermal expansion coefficient of the equivalent pier on these features may be present in reality.

11.9.6 Load–displacement description of the equivalent pier

An advantageous feature of the equivalent pier method is that the analysis of the displacement behaviour of the equivalent pier under loading can be based on solutions or methods proposed for the analysis of single isolated piles. However, these solutions must be modified for considering the group effects caused by the displacement interactions among the piles on the load–displacement response of the pile group. Such group effects involve a more pronounced average group displacement and thus a greater displacement of the equivalent pier.

To characterise the load–displacement relationship of the equivalent pier, reference is made in the following to a characteristic energy pile in the group that is subjected to the displacement interactions highlighted above. This characteristic energy pile should be considered to be representative of the displacement behaviour of most of the piles in the group.

The load-transfer method considered for analysing the load–displacement behaviour of the equivalent pier relies on modelling this body as being composed of several rigid elements that are connected by springs representing the elastic pier stiffness (Coyle and Reese, 1966). Each of these rigid elements is characterised at its side (i.e. a proportion of the shaft) by an elastoplastic interaction with the soil. The element at the toe of the pier is characterised at its base by an elastoplastic interaction with the soil. The element at the head of the pier is characterised at its top by a spring representing the elastic pier–structure interaction.

The elastoplastic load–displacement relationships characterised by the features depicted in Fig. 11.41A and B are considered to govern the shaft and base resistance mobilisation for shaft and base displacement of the equivalent pier, respectively. The schematics of those relationships have been extended to energy pile groups from those that were proposed by Knellwolf et al. (2011) (cf. Fig. 11.41C and D) for single isolated energy piles based on the ones presented by Frank and Zhao (1982) for single isolated conventional piles. The shape of these functions is characterised by (1) a first loading/unloading linear branch that describes the elastic response of the shaft/base of the equivalent pier/energy pile, (2) a next loading linear branch that refers to the inelastic response of the shaft/base of the equivalent pier/energy pile, (3) an unloading linear branch that describes the elastic response of the shaft/base when unloading

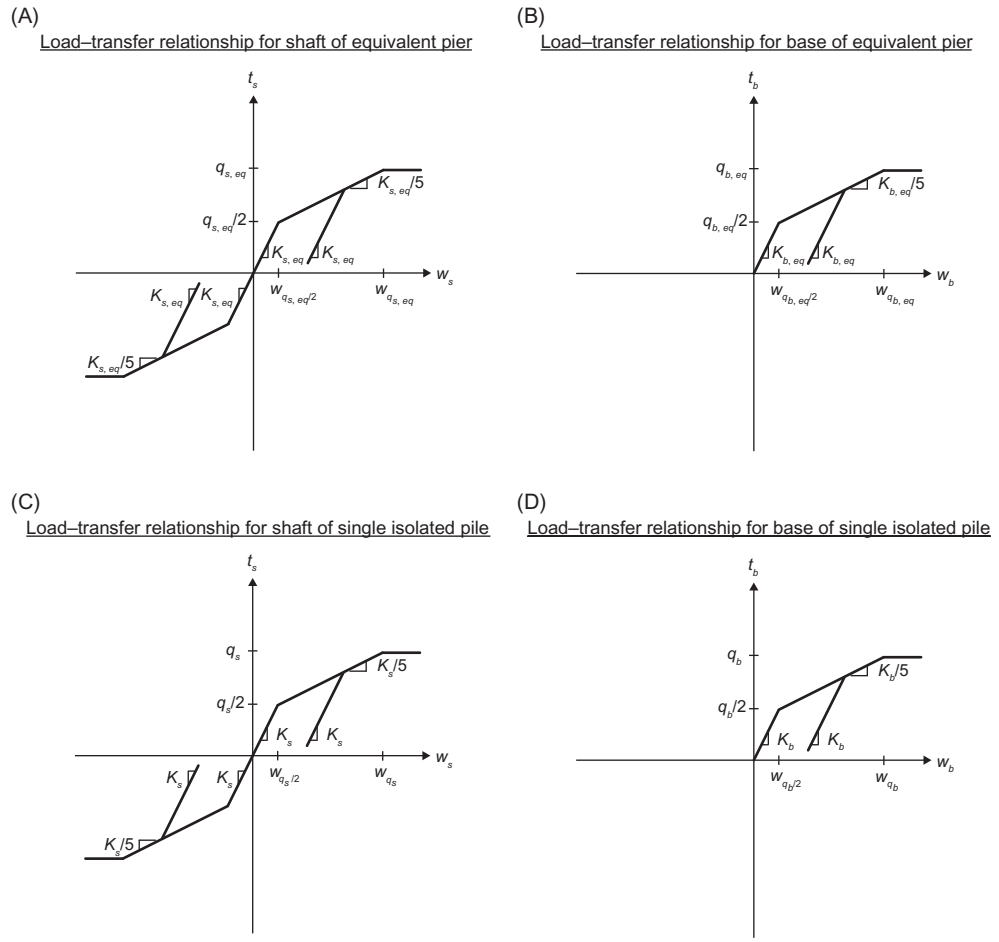

Figure 11.41 Load–displacement relationships for the shaft and base of equivalent piers (A and B) and single isolated energy piles (C and D) (Rotta Loria and Laloui, 2017b).

occurs from a stress state along the inelastic branch and (4) a final *plateau* that can be associated with the perfectly plastic response of the shaft/base of the equivalent pier/energy pile when the ultimate shaft/base resistance value is attained.

The first linear parts of the shaft and the base load–displacement (or load-transfer) functions of the equivalent pier cover shaft and base displacements of $w_{q_{s,eq}/2}$ and $w_{q_{b,eq}/2}$ until shaft and base resistances of $q_{s,eq}/2$ and $q_{b,eq}/2$ are mobilised, respectively. These values of shaft and base resistances are half of the ultimate shaft and base resistances of $q_{s,eq}$ and $q_{b,eq}$ of the equivalent pier, respectively. The same condition was considered by Frank and Zhao (1982) for single isolated piles, with reference to shaft and base displacements of $w_{q_s/2}$ and $w_{q_b/2}$, intermediate shaft and base resistances of $q_s/2$ and $q_b/2$,

and ultimate shaft and base resistances of q_s and q_b, respectively. The slopes $K_{s,eq}$ and $K_{b,eq}$ of the loading/unloading elastic branches of the load–displacement functions of the equivalent pier represent the stiffness of the shaft and base springs that govern the elastic pier–soil interaction, respectively. The same physical meaning was considered by Frank and Zhao (1982) for single isolated piles, with reference to the shaft and base stiffness K_s and K_b, respectively. The slopes of the loading/unloading elastic branches of the shaft and base load–displacement functions of the equivalent pier are determined based on an extrapolation from the definitions presented by Frank et al. (1991) for single isolated piles and a correction through a novel parameter to account for group effects as (Rotta Loria and Laloui, 2017b)

$$\begin{aligned} K_{s,eq} &= 0.8\frac{E_M}{D}\zeta \quad \text{(a)} \\ K_{b,eq} &= 4.8\frac{E_M}{D}\zeta \quad \text{(b)} \end{aligned} \qquad \text{for coarse–grained soils} \qquad (11.41)$$

$$\begin{aligned} K_{s,eq} &= 2\frac{E_M}{D}\zeta \quad \text{(a)} \\ K_{b,eq} &= 11\frac{E_M}{D}\zeta \quad \text{(b)} \end{aligned} \qquad \text{for fine–grained soils} \qquad (11.42)$$

where E_M is the Menard pressuremeter modulus and ζ is a stiffness reduction factor.

The stiffness reduction factor, ζ, represents the key parameter to account for the group effects caused by the displacement interactions among energy piles on the displacement response of the equivalent pier with reference to the behaviour of the characteristic energy pile. The definition of this parameter is based on a statement proposed by Randolph and Clancy (1993) for which the interaction between the piles in any group can be broadly quantified through the ratio between the length of the piles and their centre-to-centre spacing, that is L/s. It thus appears rational to define a reduction factor for the stiffness of a single characteristic energy pile in any considered pile group that accounts for the interaction effects on the increase in displacement as (Rotta Loria and Laloui, 2017b)

$$\zeta = \frac{s}{L} \qquad (11.43)$$

The factor ζ varies between 0.04 and 0.5 in the practical pile applications for which the use of the equivalent pier method is suggested. It physically represents a softening of the shaft and base load-transfer curves of single isolated piles for characterising those of the equivalent pier and addresses the difference in the displacement

behaviour between single isolated energy piles and groups of energy piles under the same conditions. When this stiffness reduction factor attains the theoretical upper value of $\zeta = 1$, Eqs (11.41) and (11.42) become the original relations proposed by Frank et al. (1991) for describing K_s and K_b.

The loading inelastic branches of the shaft and base load–displacement functions of the equivalent pier cover shaft and base displacements greater than $w_{q_{s,eq}/2}$ and $w_{q_{b,eq}/2}$ until the ultimate shaft and base resistances of $q_{s,eq}$ and $q_{b,eq}$ are mobilised, respectively. The slopes of the inelastic branches of the equivalent pier related to the shaft and base are equal to $K_{s,eq}/5$ and $K_{b,eq}/5$, respectively. The same condition was considered by Frank and Zhao (1982) for single isolated piles with reference to $K_s/5$ and $K_b/5$.

The ultimate shaft and base resistances of the equivalent pier $q_{s,eq}$ and $q_{b,eq}$, respectively, may be determined considering (1) the type of soil surrounding the piles, (2) the method and order of installing the piles and (3) the shaft and base resistances of the single piles composing the group q_s and q_b, respectively.

11.10 Comparison with rigorous solutions

11.10.1 Application of the interaction factor method based on charts

11.10.1.1 General

Solutions for the displacement behaviour of general energy pile groups obtained through the application of the interaction factor method based on charts are presented in the following. In some instances, a comparison with the results of 3D thermomechanical finite element analyses is made. The analysis is based on results presented by Rotta Loria and Laloui (2016).

Reference is made to situations in which all the piles are subjected to the same temperature variation of $\Delta T = 10°C$ and are free of any head restraint. Attention is devoted to square groups of 4, 9, 16 and 25 energy piles, which are referred to in the following as 2×2, 3×3, 4×4 and 5×5 pile groups, respectively.

The analyses consider energy piles embedded in uniform soil deposits with the material properties reported in Table 11.3. Unless otherwise specified, the analyses resorting to the interaction factor method consider the piles to be embedded in elastic soil following the basic analysis procedure detailed in Section 11.7.5. In those situations, reference is made to a soil–pile thermal expansion coefficient ratio of $X = \alpha_{soil}/\alpha_{EP} = 0$. To model these problems, stationary 3D thermomechanical analyses are carried out. Situations in which the soil can be subjected to thermally induced volumetric variations according to $X = 0.5$, 1 and 2 are also modelled. To model these problems, the analyses resorting to the interaction factor method follow the modified analysis procedure detailed in Section 11.7.8, while time-dependent 3D thermomechanical analyses for a time of $t = 6$ months rigorously consider the problem wherein the soil can be subjected to thermally induced volumetric variations.

Table 11.3 Material properties used for the numerical analysis.

Reinforced concrete pile parameters	Value (thermoelastic description)	Soil parameters	Value (elastic description)	Value (thermoelastic description)
E_{EP}: [MPa]	30,000	G_{soil}: [MPa]	30[a]	
ν_{EP}: [−]	0.25	ν_{soil}: [−]	0.30[a]	
ρ_{EP}: [kg/m^3]	2450	ρ_{soil}: [kg/m^3]	1537	
α_{EP}: [1/°C]	1×10^{-5}	α_{soil}: [1/°C]	–	1×10^{-5}[a]
λ_{EP}: [W/(m °C)]	1.47	λ_{soil}: [W/(m °C)]	–	0.25
$c_{p,EP}$: [J/(kg °C)]	854	$c_{p,soil}$: [J/(kg °C)]	–	961

[a]Parameter varied throughout the simulations.
Source: Modified after Rotta Loria, A.F., Laloui, L., 2016. The interaction factor method for energy pile groups. Comput. Geotech. 80, 121−137.

11.10.1.2 Maximum average vertical head displacement

In analysing the displacement characterising energy pile groups, knowledge of a parameter defined as the displacement ratio D_r appears convenient. The definition of the displacement ratio has been extended for energy piles by Rotta Loria and Laloui (2016) from that of the settlement ratio R_s proposed by Poulos (1968) for conventional piles subjected to mechanical loads. The rationale of this extension is that, in the majority of practical cases, energy piles subjected to mechanical and thermal loads are characterised by both pile settlements and heaves while conventional piles subjected to only mechanical loads are characterised by settlements. The displacement ratio is defined as

$$D_r = \frac{\text{average displacement of group}}{\text{displacement of single pile subjected to same average load}} \tag{11.44}$$

Reference is made to the pile head vertical displacement. One way to determine the displacement ratio with reference to the displacement of a single isolated energy pile, w_i, subjected to a given load consist in determining analytically the increase in displacement of the group in which all the piles are subjected to the same load through superposition with the use of the interaction factor Ω. For example the displacement ratio for a group of 2, 3 and 4 piles can be determined as follows

$$D_r = \frac{w_i(1 + \Omega_{s/D})}{w_i} = 1 + \Omega_{s/D} \quad \text{for a } 2\text{−pile group}$$

$$D_r = \frac{w_i(1 + 2\Omega_{s/D})}{w_i} = 1 + 2\Omega_{s/D} \quad \text{for a } 3\text{−pile group}$$

$$D_r = \frac{w_i(1 + 2\Omega_{s/D} + \Omega_{s\sqrt{2}/D})}{w_i} = 1 + 2\Omega_{s/D} + \Omega_{s\sqrt{2}/D} \text{ for } a \text{ } 4-\text{pile group}$$

where $\Omega_{s/D}$ is the interaction factor between two piles at any normalised centre-to-centre distance and $\Omega_{s\sqrt{2}/D}$ is the interaction factor between two piles in the 4-pile group along the diagonal of the square, whose side has a normalised length of s/D.

Fig. 11.42 presents the evolution of the displacement ratio with the normalised centre-to-centre distance between energy piles subjected to thermal loading in groups of 3×3, 4×4 and 5×5 piles. Predominantly floating energy piles of slenderness ratio of $L/D = 25$ and pile–soil stiffness ratio of $\Lambda = E_{EP}/G_{soil} = 1000$ are considered. The displacement ratio increases with increasing number of piles in the group, with such a phenomenon becoming less pronounced for increased centre-to-centre distances between the piles in the group because of the weaker interactions. The displacement ratio for the same group of energy piles in a soil mass with a greater Poisson's ratio decreases because of the weaker interactions among the piles.

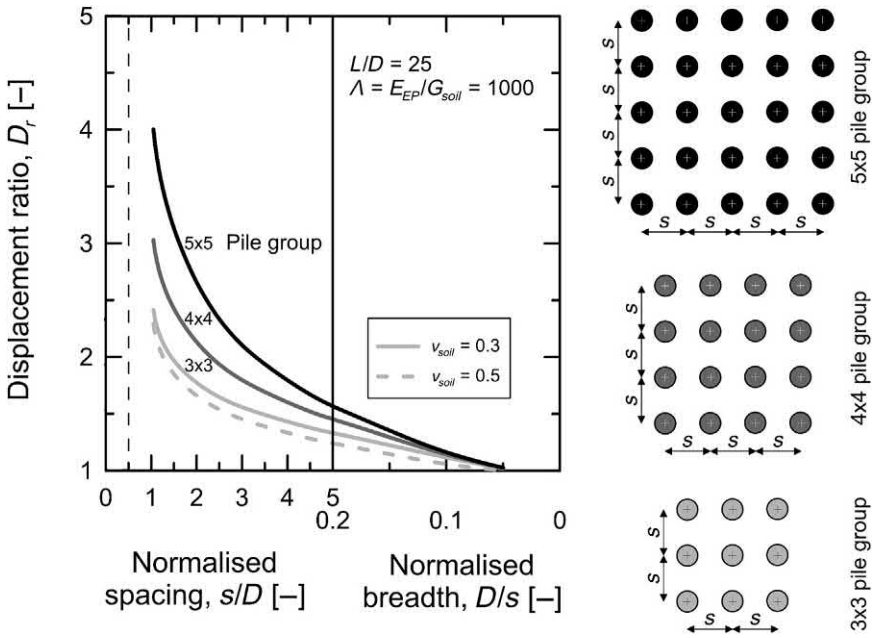

Figure 11.42 Effect of Poisson's ratio of soil on the displacement ratio (Rotta Loria and Laloui, 2016).

11.10.1.3 Maximum vertical head displacement

Fig. 11.43 presents the evolution of the normalised vertical head displacement for the centre, side and corner energy piles in a 3×3 group of piles with normalised centre-to-centre distance between the piles. Predominantly floating energy piles characterised by varying values of $L/D = 25$ and 50, and the pile–soil stiffness ratio of $\Lambda = 1000$, are investigated. For a general square group of energy piles in which all the piles are subjected to the same temperature variation, the maximum vertical head displacement occurs at the centre pile(s), whereas the minimum displacement occurs at the corner piles. The vertical head displacement of the side piles is intermediate. This result is also found in groups of conventional piles subjected to the same mechanical load because of the more pronounced interaction among the piles in the centre zone of the group. Such a result is a consequence of the greater number of surrounding piles (and stronger associated interaction) characterising a given pile in the centre zone of the group compared to an external pile. The vertical displacement of piles, whose arrangement in two corresponding groups is the same, increases with increasing slenderness ratio of the piles.

11.10.1.4 Maximum differential vertical head displacement

Fig. 11.44 shows the evolution of the maximum differential displacement normalised by the maximum displacement as a function of the normalised centre-to-centre distance between energy piles. Groups of 3×3, 4×4 and 5×5 predominantly floating energy piles of $L/D = 25$ and $\Lambda = 1000$ are considered. The normalised

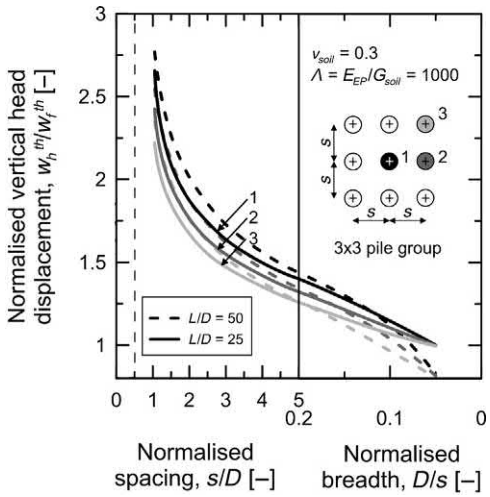

Figure 11.43 Effect of position on the vertical displacement of the piles. *Modified after Rotta Loria, A.F., Laloui, L., 2016. The interaction factor method for energy pile groups. Comput. Geotech. 80, 121–137.*

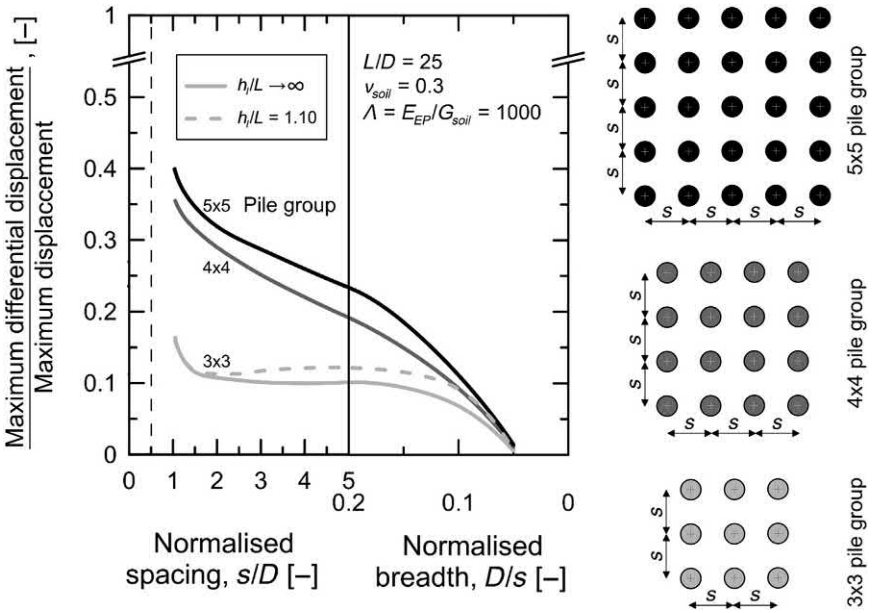

Figure 11.44 Effect of finite layer depth on the differential displacement of the piles (Rotta Loria and Laloui, 2016).

maximum differential displacement increases as the number of piles in the group increases, although increasingly less markedly for greater numbers of piles in the group. The normalised differential displacement increases with decreasing depth of a bearing layer.

11.10.1.5 Illustrative example

This section presents an introduction to the types of predictions possible through the application of the interaction factor method based on charts. The square group of four predominantly floating energy piles represented in Fig. 11.45 with the material properties specified in Table 11.3 is considered.

A comparison between the average vertical head displacement obtained through the interaction factor method and more rigorous 3D thermomechanical finite element analyses is made. Values of soil–pile thermal expansion coefficient ratios of $X = 0$, 0.5, 1 and 2 are considered through the modelling approaches highlighted in Section 11.10.1.

Following the basic analysis procedure described in Section 11.7.5, the average displacement of the pile group can be determined through the interaction factor method as follows:

1. An axisymmetric stationary finite element analysis of a single pile subjected to the considered temperature variation in an elastic soil gives

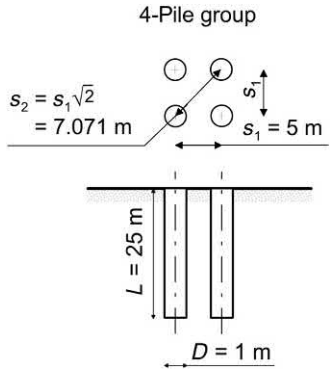

Figure 11.45 Configuration of the practical example (Rotta Loria and Laloui, 2016).

$w_h^{1,th} = -0.122\ \text{mm}/^{\circ}\text{C}$

that is a vertical head displacement of the energy pile of $w_i = -1.22$ mm.

2. The charts presented in this work enable the definition of the interaction factors for the two characteristic centre-to-centre distances between the piles

   $\Omega_{s_1} = 0.063$

   $\Omega_{s_2} = 0.045$

3. By applying the superposition principle, the average vertical head displacement of the group is determined analytically as

$$w_k = \overline{w}_h^{th} = w_h^{1,th} \sum_{i=1}^{i=n_{EP}} \Delta T_i \Omega_{ik} = w_i + 2\left(w_h^{1,th} \Delta T \Omega_{s_1}\right) + w_h^{1,th} \Delta T \Omega_{s_2} = -1.43\ \text{mm}$$

Table 11.4 presents a comparison between the average vertical head displacement of the group estimated through the interaction factor method and that determined through the more rigorous finite element method. The percentage error obtained when applying the proposed simplified method and the finite element approach is also presented. For the analysed pile group, the consideration of a displacement of unity, obtained through an axisymmetric finite element analysis in which the soil is characterised by an elastic behaviour, enables an estimate of the average vertical head displacement of the group that can be considered on the side of safety for most practical cases in which the soil thermal expansion coefficient is lower than or equal to that of the piles. This does not appear to be the case for soil–pile thermal expansion coefficient ratios of greater that unity. An approach that appears suitable for overcoming this issue relies in the modified analysis procedure described in Section 11.7.8. In such a case, the resulting analysis of the average vertical head displacement of the group that can be considered on the representative for most cases. This result is corroborated by the data proposed in the last column of Table 11.4.

Table 11.4 Comparison of predicted results for a 2 × 2 group of energy piles (Rotta Loria and Laloui, 2016).

	Reference prediction analysis	Interaction factor method – analytical (use of $w_{i,\alpha_{soil}/\alpha_{EP}=0}$)	Interaction factor method – analytical (use of $w_{i,\alpha_{soil}/\alpha_{EP}=2}$)
	Estimated average head displacement [mm]	**−1.43**	**−1.56**
Type of alternative analysis	**Calculated average head displacement [mm]**	**Prediction error[a] [%]**	**Prediction error[a] [%]**
3D FE – elastic isothermal soil – $\alpha_{soil}/\alpha_{EP} = 0$	− 1.37	4.38	12.29
3D FE – thermoelastic soil – $\alpha_{soil}/\alpha_{EP} = 0.5$	− 1.43	0.43	8.67
3D FE – thermoelastic soil – $\alpha_{soil}/\alpha_{EP} = 1$	− 1.48	− 3.51	5.05
3D FE – thermoelastic soil – $\alpha_{soil}/\alpha_{EP} = 2$	− 1.60	− 11.40	− 2.18

[a]Positive sign indicates a prediction on the side of safety.

11.10.1.6 Analysis of 2 × 2, 3 × 3, 4 × 4 and 5 × 5 square energy pile groups

Fig. 11.46 presents a comparison between the results obtained through the application of the basic and modified analysis procedures constituting the interaction factor method based on charts and more rigorous 3D thermomechanical finite element analyses devoted to investigating the displacement behaviour of square groups of energy piles. Groups of 4, 9, 16 and 25 predominantly floating energy piles characterised by a slenderness ratio of $L/D = 25$ with the material properties presented in Table 11.3 are considered to be embedded in soil deposits with different thermal expansion coefficients. The evolution of the normalised average vertical head displacement with practical values of the normalised centre-to-centre distance between the piles is presented.

The estimates of average vertical head displacement of the considered pile groups are always greater than the vertical head displacement characterising a single pile under free thermal expansion conditions. These estimates are also greater than the vertical head displacement characterising a single isolated pile subjected to the same temperature variation, such an effect becoming more pronounced for situations in which the soil–pile thermal expansion coefficient ratio exceeds unity.

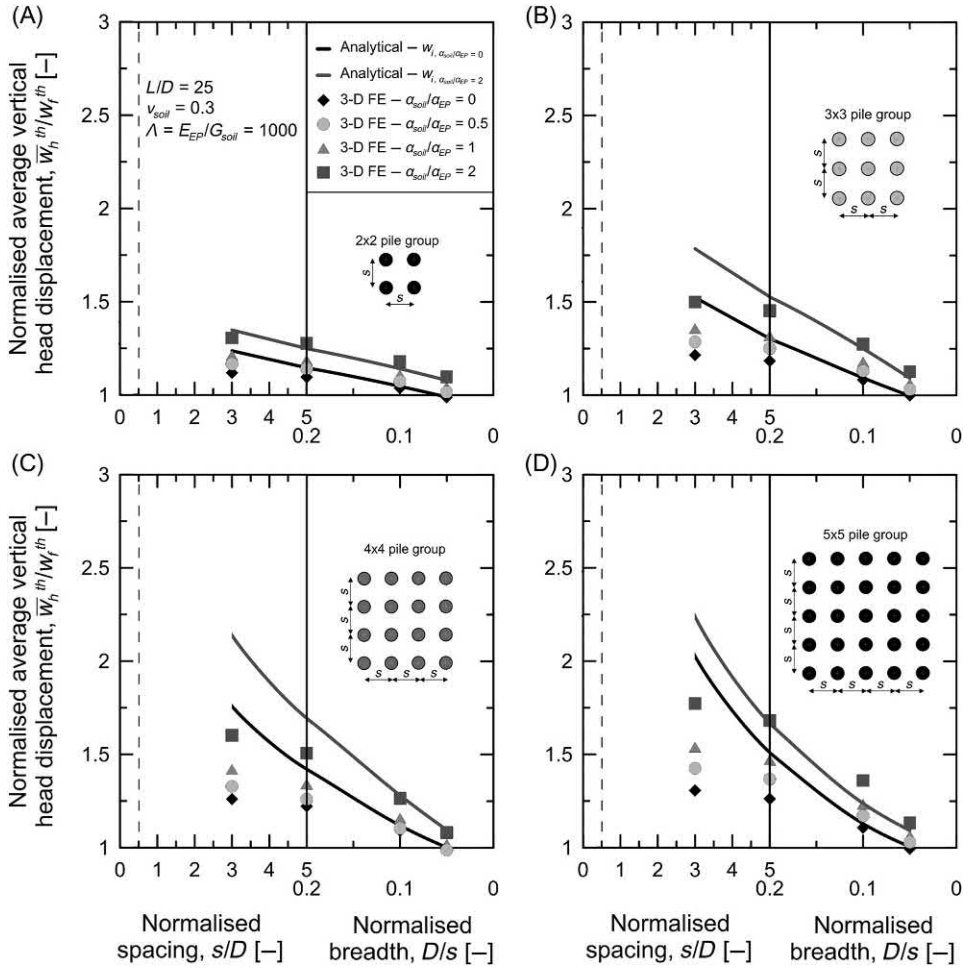

Figure 11.46 Comparison between the results obtained through the interaction factor method based on charts and those obtained through more rigorous 3D thermomechanical finite element analyses. *Modified after Rotta Loria, A.F., Laloui, L., 2016. The interaction factor method for energy pile groups. Comput. Geotech. 80, 121–137.*

Fig. 11.47 presents a further comparison between the results obtained by applying the basic and modified analysis procedures constituting the interaction factor method and more rigorous 3D thermomechanical finite element analyses devoted to investigating the displacement behaviour of square groups of energy piles. Groups of 9 predominantly end-bearing energy piles characterised by a centre-to-centre distance between the piles of $s/D = 6$ and the pile slenderness ratio of $L/D = 25$ are considered. The evolution of the normalised average vertical head displacement with the base-to-shaft soil Young's modulus ratio is presented for the different values of the pile–soil stiffness

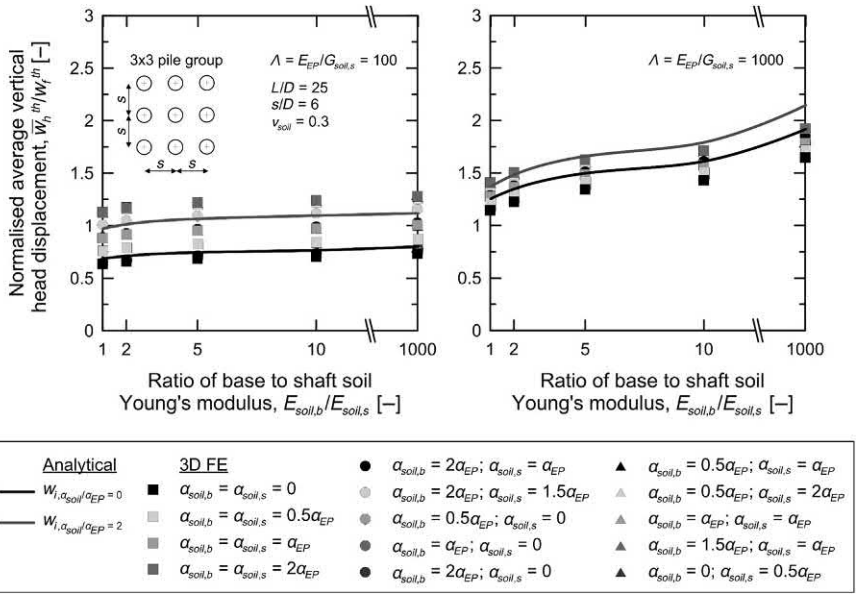

Figure 11.47 Comparison between the results obtained using the interaction factor method based on charts and those obtained using more rigorous 3D thermomechanical finite element analyses. *Modified after Rotta Loria, A.F., Laloui, L., 2017a. Displacement interaction among energy piles bearing on stiff soil strata. Comput. Geotech. 90, 144–154.*

ratio of $\Lambda = E_{EP}/G_{soil,s} = 100$ and 1000 and the soil–pile thermal expansion coefficient ratio X.

A greater increase of the average vertical head displacement of the group is observed for a greater pile–soil stiffness ratio and any given base-to-shaft modulus ratio. This evidence can be attributed to the increase of the thermally induced pile displacement with increasing pile–soil stiffness ratio, irrespective of the presence of interactions among the piles. The use of the two approaches referring to a unitary displacement of a single isolated energy pile in an elastic or thermoelastic soil mass for estimating the displacement behaviour of the group, is again considered to be validated based on the obtained results where $\alpha_{soil,b} \vee \alpha_{soil,s} > \alpha_{EP}$.

The impact of Λ and $E_{soil,b}/E_{soil,s}$ on the vertical displacement confirms that the interaction among pile groups subjected to thermal loads increases with decreasing pile–soil stiffness ratio as well as with the presence (and increasing rigidity) of a bearing soil stratum below the pile toe.

The impact of $\alpha_{soil,b}$ and $\alpha_{soil,s}$ on the vertical displacement confirms that the thermally induced deformation of energy pile groups is markedly characterised by that of the surrounding soil in situations where the linear thermal expansion coefficient of the soil is higher than that of the piles. Increasing values of average vertical head

displacement are generally observed for situations where $\alpha_{soil,b} \vee \alpha_{soil,s} > \alpha_{EP}$, the highest value of displacement characterising the situation where $\alpha_{soil,b} = \alpha_{soil,s} = 2\alpha_{EP}$. The considered situations markedly differ from usual situations where $\alpha_{soil,b} \wedge \alpha_{soil,s} \leq \alpha_{EP}$, for which the thermally induced deformation of energy pile groups predominantly depends on that of the energy piles rather than on the thermally induced deformation of the soil. The usual occurrence of situations where $\alpha_{soil,b} \wedge \alpha_{soil,s} \leq \alpha_{EP}$ and the associated negligible impact of the thermally induced soil deformation on the pile group deformation corroborate the formulation of interaction factors using an isothermal soil as reference. The impact of $\alpha_{soil,b}$ and $\alpha_{soil,s}$ on the variation of the average vertical head displacement decreases with increasing values of Λ.

11.10.2 Application of the interaction factor method based on analytical models

11.10.2.1 General

Solutions for the displacement behaviour of general energy pile groups obtained through the application of the interaction factor method based on analytical models are presented in the following. Results of axisymmetric and 3D thermomechanical finite element analyses are also proposed. The former simulations address the behaviour of single isolated source piles. They provide the evolutions of $w_i(z)$ and $\tau_i(z)$ that are needed in the application of the models and results for comparison. The latter simulations address the behaviour of energy pile groups and provide additional results for comparison. The analysis is based on results presented by Rotta Loria et al. (2018).

The analyses consider a temperature variation of $\Delta T = 10°C$ applied to energy piles free of any head restraint. In all cases except in Section 11.10.2.5, the finite element analyses are stationary and neglect – as the interaction factor analyses based on the layer and continuous models – the temperature sensitivity of the soil (i.e. they refer to soils characterised by a soil–pile thermal expansion coefficient ratio of $X = 0$). In Section 11.10.2.5, the 3D finite element analyses are time-dependent, consider the applied temperature variation to be constant for $t = 6$ months and account for the temperature sensitivity of the soil (i.e. they refer to soils characterised by soil–pile thermal expansion coefficient ratios of $X = 1$ and 2).

Unless stated otherwise, energy piles with a slenderness ratio of $L/D = 25$ are considered to be embedded in uniform soil characterised by $\Lambda = 1000$, based on the material properties specified in Table 11.3. Piles with $L/D = 50$ and nonuniform soil are also investigated.

11.10.2.2 Analysis of vertical displacement of a single isolated pile

Fig. 11.48 presents the evolution of the vertical displacement against the shear stress along the shaft of a single isolated energy pile subjected to thermal loading. The vertical displacement along the pile length, w, is normalised with respect to the absolute

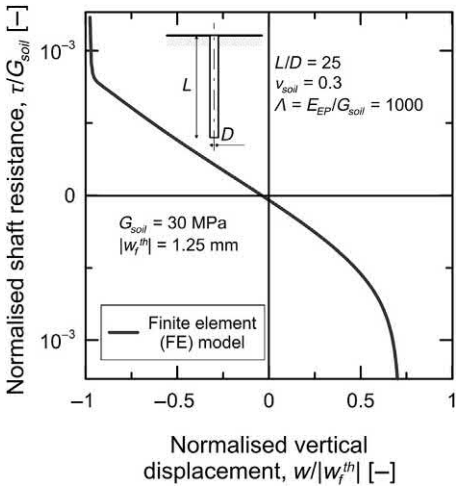

Figure 11.48 Vertical displacement–shear stress relationship estimated through an axisymmetric finite element analysis (Rotta Loria et al., 2018).

value of the head displacement of a single pile under free thermal expansion conditions, $|w_f^{th}| = |-\alpha_{EP}\Delta T\ L/2|$. The shear stress mobilised along the pile length, τ, is normalised by the soil shear modulus.

The typical nonlinear variation of the $\tau - w$ curve (especially at the pile ends), which is asymmetric with respect to the mid-length of the piles, is observed. The location of the null point of the shear stress differs from that of the vertical displacement, involving a $\tau - w$ relationship that does not cross the origin of the axes. This phenomenon is caused by the capability of the finite element analysis to capture the effects of the shear stress acting on any element of a source pile on all of the elements of the pile in a continuous way.

11.10.2.3 Analysis of corrected interaction factor

Fig. 11.49 presents a comparison between the evolutions obtained via the analytical models and thermomechanical finite element analyses of the corrected interaction factor with the normalised depth of two piles in a pair for normalised spacing of $s/D = 3$ and 5. In general, the evolution of the corrected pile–soil–pile interaction factor with depth is thoroughly captured by the analytical models. The evolution of the corrected interaction factor suggested by the layer model may be considered to be representative of the average displacement behaviour of a receiver pile.

Notable variations of the interaction factor at locations that are close to the null point of the vertical displacement can be observed. These variations are addressed to a movement of the null point with increasing horizontal distance from the axis of a thermally loaded source pile (Rotta Loria et al., 2018). They involve values of the

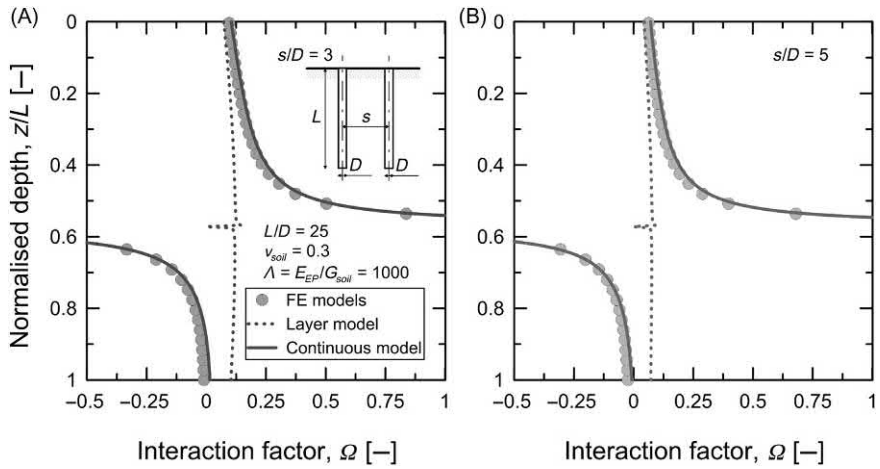

Figure 11.49 Evolution of the corrected interaction factor with the normalised depth for a normalised spacing of (A) $s/D = 3$ and (B) $s/D = 5$. *Modified after Rotta Loria, A.F., Vadrot, A., Laloui, L., 2018. Analysis of the vertical displacement of energy pile groups. Geomech. Energy Environ. 16, 1–14.*

interaction factor that may be lower than 0 and greater than 1 (these values have not been included in the present figures for clarity). This is a crucial difference compared to the values of the interaction factor that characterise conventional piles subjected to mechanical loads (Randolph and Wroth, 1979b; Poulos, 1968), that is varying between 0 and 1, and almost constant with depth because of the absence of the null point.

Positive values of the corrected interaction factor indicate a displacement of the receiver pile that is developed in the same direction as that characterising the source pile. Negative values of the corrected interaction factor indicate a displacement of the receiver pile that is developed in the opposite direction as that characterising the source pile.

11.10.2.4 Corrected interaction factor for a range of design situations

Figs 11.50 and 11.51 compare the evolution of the corrected interaction factor with the normalised horizontal distance for the head of pile pairs of $L/D = 25$ and 50. The piles are characterised by pile–soil stiffness ratios of $\Lambda = E_{EP}/G_{soil} = 100$, 1000 and 10,000.

The displacement interaction factor curves described by the analytical models accurately reproduce the curves obtained using more rigorous finite element analyses despite some differences. The layer model tends to underestimate the corrected pile–soil–pile interaction factor compared to the values estimated by the continuous model and the finite element analyses, especially for decreasing values of the pile–soil stiffness ratio. However, in reality, the nonlinear nature of soil deformation leads to

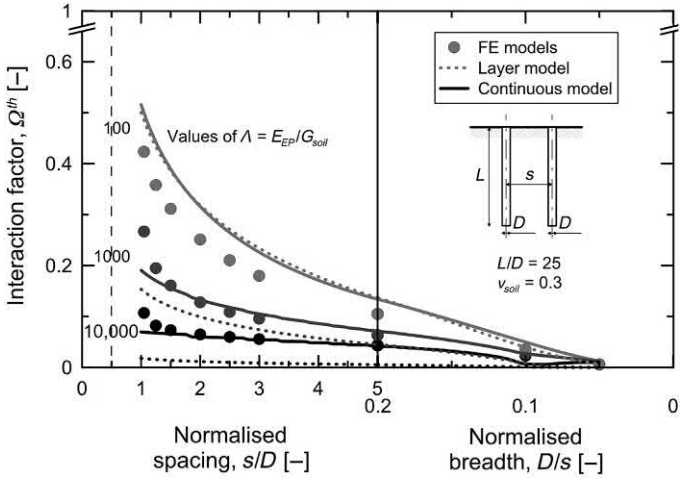

Figure 11.50 Corrected interaction factors referred to the pile head for $L/D = 25$ in various design conditions. *Modified after Rotta Loria, A.F., Vadrot, A., Laloui, L., 2018. Analysis of the vertical displacement of energy pile groups. Geomech. Energy Environ. 16, 1–14.*

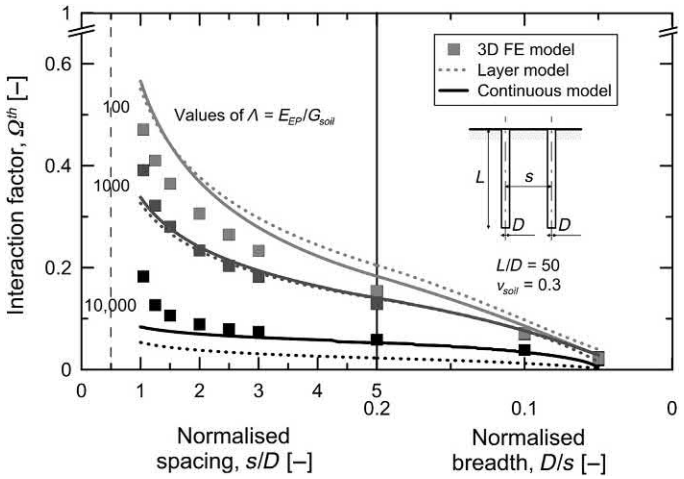

Figure 11.51 Corrected interaction factors referred to the pile head for $L/D = 50$ in various design conditions. *Modified after Rotta Loria, A.F., Vadrot, A., Laloui, L., 2018. Analysis of the vertical displacement of energy pile groups. Geomech. Energy Environ. 16, 1–14.*

less interaction than that predicted from a linear elastic analysis because the deformation is more confined to the immediate vicinity of the pile (Randolph and Wroth, 1979b; Poulos, 1988; Rotta Loria et al., 2017). Based on this consideration, the layer model may provide more realistic predictions of pile interaction than those given by the continuous model. Both models are still considered of paramount importance for a

comprehensive displacement analysis of piles because they provide lower and upper boundaries of the pile interaction that may be encountered in practice.

11.10.2.5 Analysis of 5 × 5 square energy pile groups

This section presents evidence for a validation of the interaction factor method based on the layer and continuous analytical models. Two different design situations for energy pile groups composed of 25 energy piles (5 × 5 group, cf. Fig. 11.52) are modelled: (1) predominantly floating energy piles embedded in uniform soil and (2) predominantly end-bearing energy piles embedded in nonuniform soil constituted by two layers. Piles with a typical slenderness ratio of $L/D = 25$ are analysed for values of normalised centre-to-centre spacing of $s/D = 3$, 5 and 10, and pile–soil stiffness ratios of $\Lambda = E_{EP}/G_{soil} = 1000$ and 10,000. The nonuniform soil is characterised by a deeper soil layer with the same material properties of the shallower layer, except for a double shear modulus. Soil deposits characterised by soil–pile thermal expansion coefficient ratios of $X = \alpha_{soil}/\alpha_{EP} = 0$, 1 and 2 are considered.

The average vertical head displacement of the modelled pile groups can be estimated according to the five steps that constitute the analysis approach based on the layer and continuous models presented in Section 11.8.3 as follows.

Step 1: The vertical displacement, $w_i(z)$, and the shear stress, $\tau_i(z)$, along the shaft of a single isolated pile are determined.

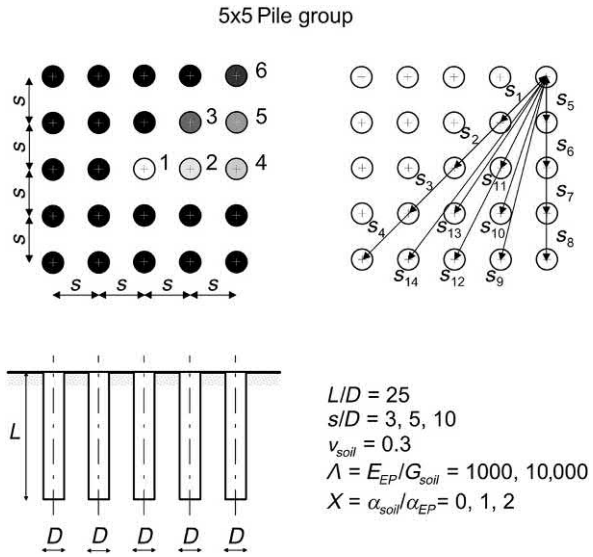

Figure 11.52 Configuration of the practical example.

Steps 2–4: The approximate pile–soil interaction factors, $\tilde{\Omega}^{th}(r,z)$, and corrected pile–soil–pile interaction factors, $\Omega^{th}(s,z)$, are calculated for the characteristic centre-to-centre distances that describe all of the singular pile pairs constituting the energy pile group. Because in this example the vertical displacements of interest are those of the pile heads, the relevant interaction factors are $\tilde{\Omega}^{th}(r=r_1,r_2,\ldots,r_{14},z=0)$ and $\Omega^{th}(s=s_1,s_2,\ldots,s_{14},z=0)$, where $s_1,s_2,\ldots,s_{14}$ are the fourteen characteristic centre-to-centre distances between the pile pairs that describe the considered energy pile group (cf. Fig. 11.52). For the design situation involving piles in nonuniform soil, the layer model directly accounts for the different properties of the soil layers with depth while the continuous model implicitly considers the different properties of the soil layers according to the procedure proposed by Poulos and Davis (1980) (cf. Section 11.8.5.1).

Step 5: The vertical head displacement of each of the characteristic energy piles of the groups is determined. In this example, six characteristic energy piles, 1, 2, …, 6 (cf. Fig. 11.52), describe the pile group. The associated vertical head displacements that need to be determined for calculating the average vertical head displacement of the group are $w_{h,1}^{th},w_{h,2}^{th},\ldots,w_{h,6}^{th}$ (i.e. $w_{h,1}^{th}(z=0)$, $w_{h,2}^{th}(z=0),\ldots,w_{h,6}^{th}(z=0)$). A calculation example of the vertical head displacement is given below for the centre pile 1 and the corner pile 6, considering in Eq. (11.14) $w_j(z)=w_j(z=0)=w_j$, $w_h^{1,th}(z)=w_h^{1,th}(z=0)=w_h^{1,th}$, $\Delta T_i=\Delta T$, $w_h^{1,th}\Delta T=w_i$, and $\Omega_{ij}^{th}(s,z)=\Omega^{th}(s=s_1,s_2,\ldots,s_{14},z=0)=\Omega_{s_1,s_2,\ldots,s_{14}}^{th}$.

$$w_{h,1}^{th}=w_i\left[1+4\Omega_{s_1}+4\Omega_{s_2}+4\Omega_{s_5}+4\Omega_{s_6}+8\Omega_{s_{11}}\right]$$

$$w_{h,6}^{th}=w_i\left[\begin{array}{c}1+\Omega_{s_1}+\Omega_{s_2}+\Omega_{s_3}+\Omega_{s_4}\\+2\Omega_{s_5}+2\Omega_{s_6}+2\Omega_{s_7}+2\Omega_{s_8}+2\Omega_{s_9}+2\Omega_{s_{10}}+2\Omega_{s_{11}}+2\Omega_{s_{12}}+2\Omega_{s_{13}}+2\Omega_{s_{14}}\end{array}\right]$$

Once the vertical head displacement of all of the characteristic energy piles is known, the average vertical head displacement of the group, which is below normalised by the head displacement of a single pile under free thermal expansion conditions, can be calculated as

$$\frac{\overline{w}_h^{th}}{D}=\frac{w_{h,1}^{th}+4w_{h,2}^{th}+4w_{h,3}^{th}+4w_{h,4}^{th}+8w_{h,5}^{th}+4w_{h,6}^{th}}{25D}$$

Fig. 11.53 compares absolute values of the normalised average vertical head displacement of the considered energy pile groups given by the analyses performed. In almost cases, the results of the layer and continuous model bound those of the 3D finite element analyses for any values of X. The above can be considered to be valid not only for varying pile–soil stiffness ratios, but also for different types of energy piles.

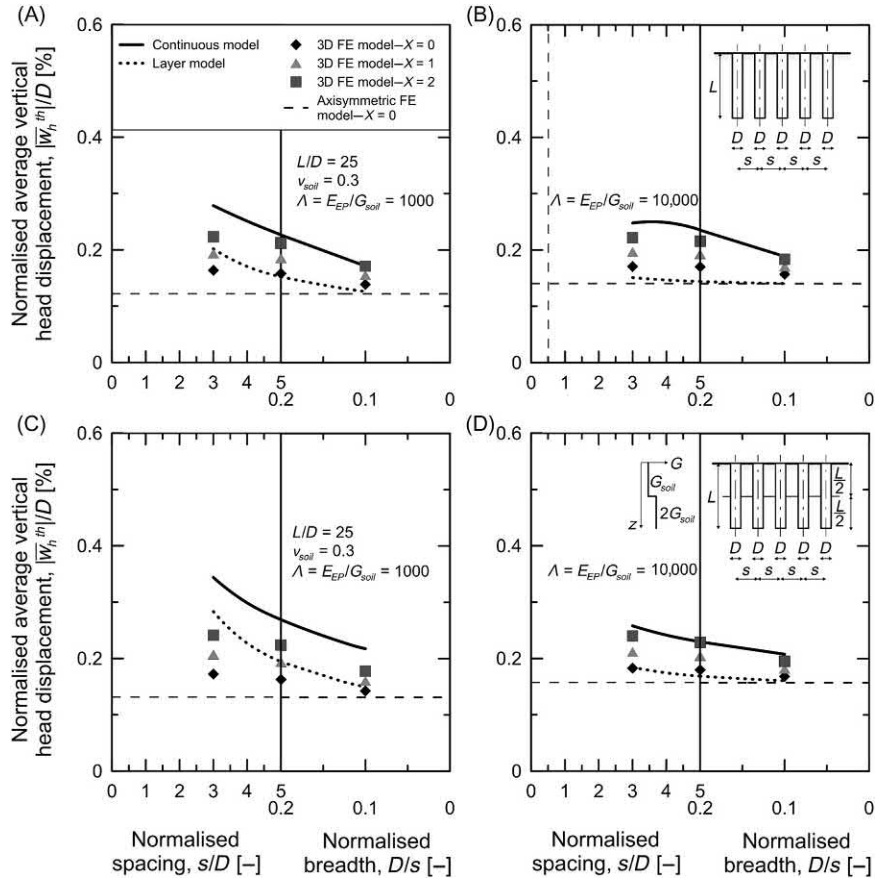

Figure 11.53 Analysis of 5×5 energy pile groups in various design conditions: (A and B) uniform soil mass and (C and D) nonuniform soil mass. *Modified after Rotta Loria, A.F., Vadrot, A., Laloui, L., 2018. Analysis of the vertical displacement of energy pile groups. Geomech. Energy Environ. 16, 1—14.*

The differences observed between the predictions of the analytical models and the finite element analyses result from the diverse capabilities of these models in capturing the displacement interaction among piles. Greater values of pile group displacements are observed for decreasing values of s/D, increasing values of Λ and X, and because of the presence of a bearing stratum. The higher values of group displacement observed for increasing values of Λ, in contrast to the lower displacement interaction among the piles for greater values of the considered parameter, is caused by the higher displacement of each of the piles in the group due to the lower restraint provided by the soil to the pile deformation.

11.10.3 Application of the equivalent pier method

11.10.3.1 General

Solutions for the displacement behaviour of general energy pile groups obtained through the application of the equivalent pier method are presented in the following. Results of analyses resorting to the interaction factor method based on charts and the 3D thermomechanical finite element simulations are also presented for comparison. The analysis is based on results presented by Rotta Loria and Laloui (2017b).

The analyses consider a temperature variation of $\Delta T = 10°C$ applied to energy piles free of any head restraint and embedded in uniform soil deposits with the material properties specified in Table 11.3. Predominantly floating energy piles with a slenderness ratio of $L/D = 25$ are considered to be embedded in uniform soil deposits characterised by values of $X = 0$, 0.5, 1 and 2. Complementary features of the modelled energy piles via the load-transfer approach to those reported in Table 11.3 are summarised in Table 11.5. The shaft and base resistances of the equivalent piers are calculated by distributing the total shaft and base capacities of each group (calculated as the shaft and base capacities of the single isolated energy piles multiplied by the number of piles in the group for hypothesis) on the shaft and base area of the equivalent piers, respectively. This implies that

$$q_{s,eq} = q_s \frac{D}{D_{eq}} n_{EP} \tag{11.45}$$

and

$$q_{b,eq} = q_b \frac{D^2}{D_{eq}^2} n_{EP} \tag{11.46}$$

The analyses resorting to the equivalent pier method consider the analysis procedure detailed in Section 11.9.5 and assume the soil to be insensitive to temperature variations (by considering $\alpha_{eq} = \alpha_{EP}$) wherein $X \leq 1$, whereas they implicitly account

Table 11.5 Complementary features of the modelled energy piles and soil via the load-transfer approach to those reported in Table 11.3.

Pile–soil interaction parameters	
K_s: [MPa/m]	28
K_b: [MPa/m]	168
Pile shaft and base resistances	
q_s: [kPa]	38
q_b: [kPa]	377

for the temperature sensitivity of the soil (by considering $\alpha_{eq} \neq \alpha_{EP}$) wherein $X > 1$. The analyses resorting to the interaction factor method based on charts and the 3D thermomechanical analyses consider or neglect the temperature sensitivity of the soil depending on whether $X = 0$ or $X = 0.5$, 1 and 2, respectively, according to the details reported in Section 11.10.1.1.

11.10.3.2 Analysis of 2 × 2, 3 × 3, 4 × 4 and 5 × 5 square energy pile groups

Fig. 11.54 presents a comparison between the results obtained through the application of the equivalent pier method as well as the results obtained using the interaction factor method and more rigorous 3D thermomechanical finite element analyses to investigate the displacement behaviour of square groups of 2 × 2, 3 × 3, 4 × 4 and 5 × 5 energy piles. The evolution of the normalised average vertical head displacement with

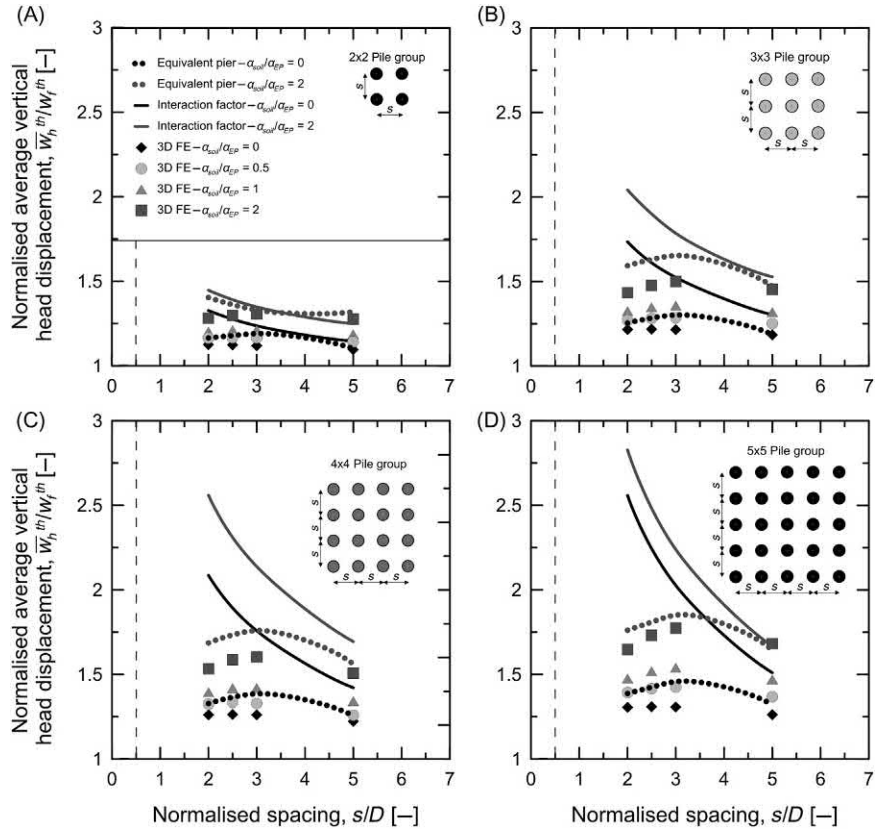

Figure 11.54 Comparison between the results obtained using the proposed equivalent pier method, the interaction factor method and 3D thermomechanical finite element analyses. *Modified after Rotta Loria, A.F., Laloui, L., 2017b. The equivalent pier method for energy pile groups. Geotechnique 67 (8), 691–702.*

close values of the normalised centre-to-centre distance between energy piles that may be encountered in practice is presented. The vertical displacement is normalised with respect to the head displacement of a single energy pile under free thermal expansion conditions, $w_f^{th} = -\alpha_{EP}\Delta T\ L/2$.

The use of the equivalent pier method through the approaches described in Section 11.9.5 captures the behaviour of energy pile groups. The estimates of the average vertical head displacement appear to be on the conservative side in most of the considered cases, if reference is made to the more rigorous finite element solutions.

11.11 Modelled and observed response

11.11.1 Analysis of single and groups of piles in nonlinearly deforming soil

11.11.1.1 General

This section expands on the capabilities of the modified analysis procedure constituting the interaction factor method, coupled with the use of the continuous model presented by Rotta Loria et al. (2018), in predicting the response of single and group of piles subjected to loading (e.g. mechanical), once the theory discussed in this chapter is employed with appropriate material parameters and engineering judgement. To this aim, the observed behaviour through full-scale in situ tests of conventional piles subjected to mechanical loads by O'Neill et al. (1981) is compared with predictions made with the considered analysis approach. The following predictions have been reported by Rotta Loria et al. (2017).

11.11.1.2 Tests by O'Neill et al. (1981)

O'Neill et al. (1981) reported the results of full-scale in situ tests performed on eleven conventional piles subjected to vertical mechanical loading, including three experiments on a 9-pile group, a 5-pile group and a 4-pile group and two experiments on distinct single reference piles. The piles were driven in an overconsolidated clayey soil deposit and consisted in closed-end tubular steel pipes of an external diameter of $D = 273$ mm, a wall thickness of $t_w = 9.27$ mm, and an embedded length of $L = 13.11$ m. Two reference piles were driven as isolated piles. Nine other piles were driven in a square 3×3 arrangement. The two reference piles were located at a spacing of $s = 10.4D$ from the centre of the pile group. The piles in the group were located at spacing of $s = 3D$ apart from each other. A rigid slab made of reinforced concrete connected the piles in the group without being in contact with the ground. The soil profile consisted of two layers. The first layer was composed by stiff overconsolidated clay and reached a depth of $z = 14.11$ m. Below this layer, a second layer a very stiff sandy clay and silts was found. The groundwater table was found at a depth of $z = 2.135$ m.

11.11.1.3 Analyses by Rotta Loria et al. (2017)

To serve the interaction factor analyses of the modelled tests on single and groups of piles, an axisymmetric finite element analysis was performed. This analysis simulates the response of the single piles tested by O'Neill et al. (1981) under mechanical loading. In the following developments: (1) the piles are assumed to be isotropic and homogeneous cylindrical solids that are considered to be representatively described by linear elastic behaviour; (2) the soil layer is assumed to be an isotropic and homogeneous mass that can be considered to be semiinfinite and representatively described by linear elastic behaviour; (3) the same loads that are applied to the piles in the single case are also considered to be applied uniformly to the piles in the groups; (4) no head restraint is considered at the head of any pile; and (5) the reference experimentally observed vertical mechanical load of $Q_{u,exp} = 586$ kN is considered as limiting value of the single pile capacity.

Table 11.6 reports the material parameters used in this study. Differently to the experimental observation, the piles are characterised by a uniform and homogeneous cross section made of steel, and the soil is characterised by constant values with depth of the near-pile modulus (steps 1–3 in the basic interaction factor analysis procedure and step 1 in the modified interaction factor approach) and average modulus (steps 2–3 in the modified interaction factor analysis procedure). A transition distance of $s_t = 3D$, as suggested by Poulos (1988), is considered in the modified interaction factor analysis approach.

11.11.1.4 Effect on nonlinear soil deformation on the response of mechanically loaded piles

Fig. 11.55A presents a comparison between the numerically modelled and experimentally observed head load–displacement curves for the single pile. The vertical head displacement of the pile is normalised by the pile diameter, D. The applied vertical load is normalised by the value of mechanical load corresponding to failure, $Q_{u,exp}$.

Table 11.6 Material parameters used to model the considered problem.

Soil parameters		Pile parameters	
Near-pile Young's modulus, E_{soil}: [MPa]	49	Young's modulus, E_{EP}: [MPa]	210,000
Mass Young's modulus, $E_{soil,m}$: [MPa]	272.6	Poisson's ratio, ν_{EP}: [−]	0.3
Poisson's ratio, ν_{soil}: [−]	0.5	Normalised transition distance, s_t/D: [−]	3

Source: Modified after Rotta Loria, A.F., Vadrot, A., Laloui, L., 2017. Effect of non-linear soil deformation on the interaction among energy piles. Comput. Geotech. 86, 9–20.

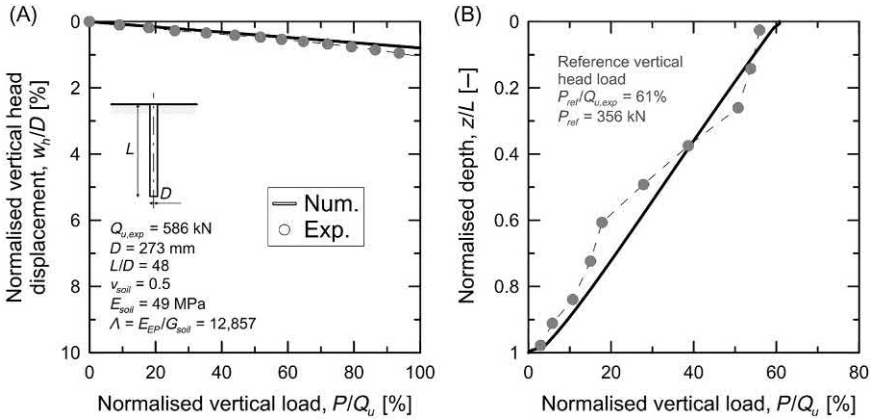

Figure 11.55 Comparison between the numerically modelled and experimentally observed (A) load–displacement curves for the single pile and (B) evolution of the normalised vertical load with the normalised depth in the pile. *Modified after Rotta Loria, A.F., Vadrot, A., Laloui, L., 2017. Effect of non-linear soil deformation on the interaction among energy piles. Comput. Geotech. 86, 9–20.*

The numerical results are in close agreement with the experimental observations, although the former fail in capturing the latter when plastic strains occur in the soil surrounding the pile. This result is in accordance with the linear elastic soil behaviour considered in the numerical analysis and the associated incapability of the analysis of capturing plastic strains.

Fig. 11.55B presents a comparison between the numerically modelled and experimentally observed evolution of the normalised vertical load in the pile with the normalised pile depth. The normalised reference mechanical load applied at the pile head of $P_{ref}/Q_{u,exp} = 61\%$ is considered. The numerical results are highly comparable to the experimental data.

Fig. 11.56 presents a comparison between the modelled and experimentally observed evolutions of the normalised vertical displacement with the normalised radial distance from the pile axis. Reference is made to a normalised depth of $z/L = 0.047$. The results of two different analyses are presented:

- An analysis that addresses linear soil deformation based on steps 1 and 2 of the basic interaction factor analysis procedure. In this analysis, the soil displacement, $w(r, z)$, is calculated analytically (step 2) based on the vertical displacement, $w_i(z)$, and shear stress, $\tau_i(z)$, distributions characterising the single isolated source pile using the same value of near-pile soil modulus, E_{soil}, that is used in the numerical analysis to define $w_i(z)$ and $\tau_i(z)$ (step 1).
- An analysis that addresses nonlinear soil deformation based on steps 1 and 2 of the modified interaction factor analysis procedure. In this analysis, the soil displacement, $w(r, z)$, is calculated analytically (step 2) based on the vertical

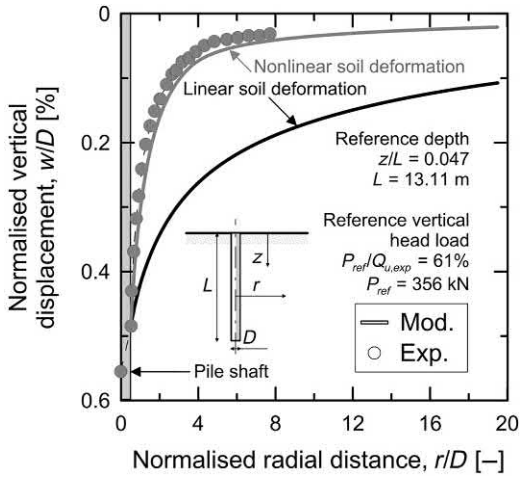

Figure 11.56 Comparison between the modelled and experimentally observed evolutions of the normalised vertical displacement with the normalised radial distance from the pile axis. *Modified after Rotta Loria, A.F., Vadrot, A., Laloui, L., 2017. Effect of non-linear soil deformation on the interaction among energy piles. Comput. Geotech. 86, 9–20.*

displacement, $w_i(z)$, and shear stress, $\tau_i(z)$, distributions characterising the single isolated source pile using a different value of soil modulus, $\overline{E}_{soil}$, compared to the near-pile soil modulus, E_{soil}, that is used in the numerical analysis to define $w_i(z)$ and $\tau_i(z)$ (step 1).

The close comparison between the modelling results addressing the nonlinear soil deformation and the experimental results proves the occurrence of the considered phenomenon. This phenomenon was originally remarked by O'Neill et al. (1981).

Fig. 11.57 presents a comparison between the modelled and experimentally observed evolutions of the normalised average vertical head displacement of the piles, $\overline{w}_h$, with the number of directly (mechanically) loaded piles, n_{LP}, for the reference pile tests, the 9-pile group test, the 5-pile subgroup test and the 4-pile subgroup test. The normalised reference mechanical load applied at the pile heads of $P_{ref}/Q_{u,exp} = 61\%$ is considered. The results of two different investigations addressing linear soil deformation based on the basic interaction factor analysis procedure and nonlinear soil deformation based on the modified interaction factor analysis procedure are presented. The results of the modified interaction factor analysis procedure considering nonlinear soil deformation are in close agreement with the experimental observations for the pile groups considered, differently from the results obtained through the basic interaction factor analysis procedure. This evidence underscores the tendency of the basic interaction factor analysis procedure to overestimate group effects and displacement interactions among the piles, and thus, the average vertical displacement of pile groups subjected to mechanical loads. This result also highlights the capability of the modified

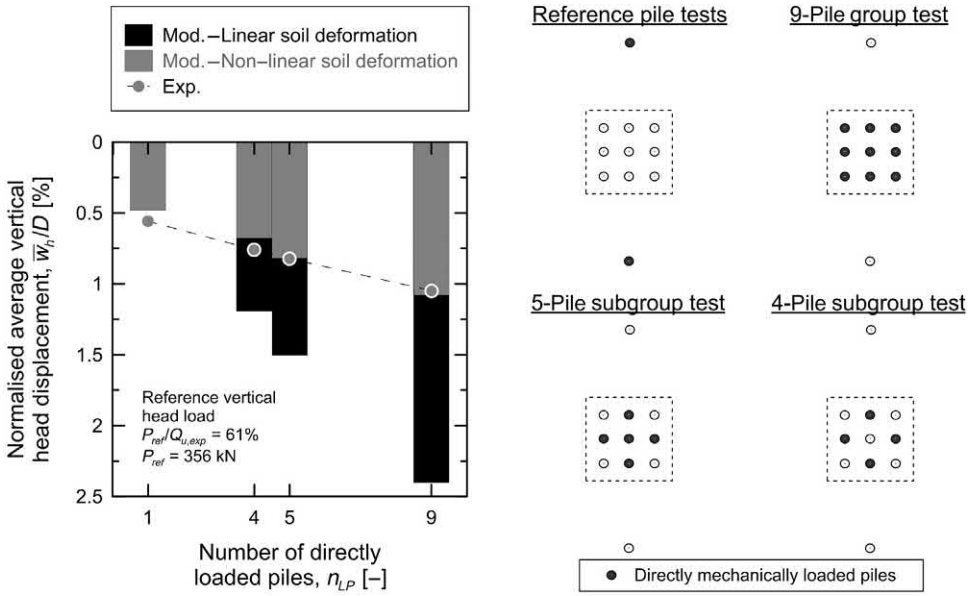

Figure 11.57 Comparison between the modelled and experimentally observed evolutions of the normalised average vertical head displacement of the piles with the number of directly mechanically loaded piles for the different pile tests considered. *Modified after Rotta Loria, A.F., Vadrot, A., Laloui, L., 2017. Effect of non-linear soil deformation on the interaction among energy piles. Comput. Geotech. 86, 9–20.*

interaction factor analysis procedure of capturing the vertical displacement of pile groups in nonlinearly deforming soils.

11.11.2 Analysis of pile groups subjected to mechanical and thermal loads

11.11.2.1 General

This section expands on the capabilities of the load-transfer method, coupled with the equivalent pier analysis approach, in predicting the response of pile groups subjected to mechanical and thermal loads, once the theory discussed in this chapter is employed with appropriate material parameters and engineering judgement. To this aim, the observed behaviour through full-scale in situ tests of conventional piles subjected to mechanical loads as well as of energy piles subjected to mechanical and/or thermal loads is compared with predictions made with the considered analysis approaches. The present pile group analyses are complementary to the single pile analyses discussed in Chapter 10, Analytical modelling of capacity and deformation of single energy piles.

The following predictions have been reported by Rotta Loria et al. (2019). Table 11.7 summarises essential features of the considered full-scale in situ tests of pile groups.

Table 11.7 Summary of the modelled full-scale in situ tests by Rotta Loria et al. (2019).

Reference	Pile group type	Soil	Head restraint	Loading
Briaud et al. (1989)	Conventional pile group	Medium-dense sand	Restrained	Mechanical
O'Neill et al. (1981)	Conventional pile group	Overconsolidated clay	Restrained	Mechanical
Mandolini and Viggiani (1992)	Conventional pile group	Slightly overconsolidated clay	Restrained	Mechanical
Rotta Loria and Laloui (2018)	Energy pile group	Overconsolidated clay and dense sand resting on rock	Restrained	Mechanical and thermal

11.11.2.2 Tests by Briaud et al. (1989)

Briaud et al. (1989) reported the results of full-scale in situ tests performed on six conventional piles subjected to vertical mechanical loading, including one experiment on a group of five piles. The piles were driven in a clean medium-dense sand deposit and consisted in closed-end tubular steel pipes of an external diameter of $D = 273$ mm, a wall thickness of $t_w = 9.27$ mm and an embedded length of $L = 9.15$ m. One reference pile was driven as isolated pile. Five other piles were driven in a square arrangement. The reference pile was located at a spacing of $s = 15.48D$ from the centre of the pile group. The outer piles in the group were located at spacing of $s = 4.24D$ apart from each other (cf. Fig. 11.58). A rigid slab made of reinforced concrete connected the piles in the group without being in contact with the ground. Without accounting for a 1.37-m-thick shallow layer made of sandy gravel that was removed prior to testing the piles, the clean sand deposit reached a depth of $z = 12.20$ m from surface. Below the sand layer, a medium-stiff to stiff silty clay with interbedded sand layer was found until reaching the bedrock at a depth of $z = 14.33$ m. The groundwater table was found at a depth of $z = 2.40$ m.

Relevant parameters were extracted from the work of Briaud et al. (1989), Castelli and Maugeri (2002) and Castelli and Motta (2003) and are reported in Tables 11.8 and 11.9. Values written in regular font were found in the referenced publications, those written in italic were assumed and those written in bold resulted from calculations based on the parameters presented. Complementary information of the material properties employed for modelling the single piles and the soil is summarised in Section 10.11.2.

The diameter of the equivalent pier was determined according to the expression proposed by Poulos (1993) for end-bearing piles. The slopes $K_{s,eq}$ and $K_{b,eq}$ of the elastic branches of the load–displacement functions proposed by Rotta Loria and

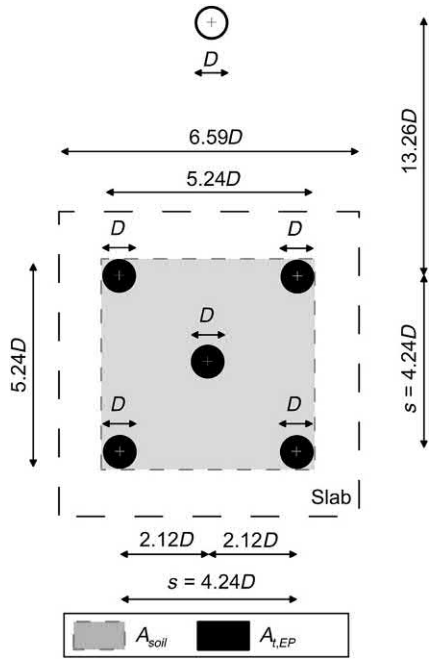

Figure 11.58 Features of the pile group described by Briaud et al. (1989). *Modified after Rotta Loria, A.F., Català Oltra, J.V., Laloui, L., 2019. Equivalent pier analysis of full-scale pile groups subjected to mechanical and thermal loads. (Under review).*

Table 11.8 Soil properties considered for modelling the pile group test of Briaud et al. (1989).

Reference depth, z [m]	Variable	Value
[0; 2.40]	Dry unit weight, γ_d [kN/m^3]	15.7
[2.40; 9.15)	Saturated unit weight, γ_{sat} [kN/m^3]	19.3
[0; 9.15)	Angle of shear strength under constant volume conditions, φ'_{cv} [degrees]	35.4
	Young's modulus, E_{soil} [MPa]	63
	Poisson's ratio, ν_{soil} [−]	*0.35*
	Menard pressuremeter modulus, E_M [MPa]	**50.6**
	Slope of the load-transfer elastic branch for the equivalent pier shaft, $K_{s,eq}$ [kPa/m]	**18,749**
	Slope of the load-transfer elastic branch for the equivalent pier base, $K_{b,eq}$ [kPa/m]	**112,495**

Source: Modified after Rotta Loria, A.F., Català Oltra, J.V., Laloui, L., 2019. Equivalent pier analysis of full-scale pile groups subjected to mechanical and thermal loads. (Under review).

Table 11.9 Equivalent pier properties considered for modelling the pile group test of Briaud et al. (1989).

Variable	Value
Equivalent Young's modulus, E_{eq} [GPa]	**4.0**
Equivalent shaft capacity, $Q_{s,eq}$ [kN]	**654.5**
Equivalent base capacity, $Q_{b,eq}$ [kN]	**1413.5**
Total pier axial capacity, $Q_{u,eq}$ [kN]	**2068**
Plan area of pile group, A_g [m^2]	**2.1**
Representative pile spacing, s [m]	**1.16**
Equivalent diameter, D_{eq} [m]	**1.6**

Source: Modified after Rotta Loria, A.F., Català Oltra, J.V., Laloui, L., 2019. Equivalent pier analysis of full-scale pile groups subjected to mechanical and thermal loads. (Under review).

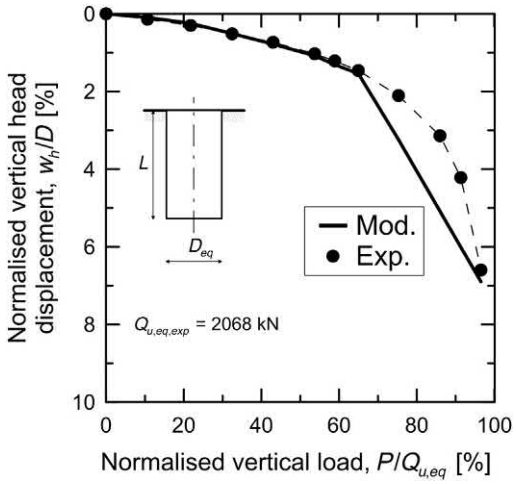

Figure 11.59 Experimental and modelled head load–settlement curves referring to the pile group test of Briaud et al. (1989). *Modified after Rotta Loria, A.F., Català Oltra, J.V., Laloui, L., 2019. Equivalent pier analysis of full-scale pile groups subjected to mechanical and thermal loads. (Under review).*

Laloui (2017b) were determined with reference to the spacing of $s = 4.24D$. The shaft and base capacities of the equivalent pier were determined by multiplying the shaft and base capacities of the single isolated piles multiplied by the number of piles in the group. This approach conservatively analyses the bearing capacity of driven pile groups in coarse-grained soil as remarked in this chapter. No contribution of the slab was accounted for modelling the response of the equivalent pier according to the freestanding character of the slab connecting the pile in the experimental test.

Fig. 11.59 shows the measured and computed load–settlement curves for the considered pile group. Both the applied mechanical load and the resulting vertical

displacement are normalised values. The applied mechanical load is normalised with respect to the axial capacity of the pile group, which is estimated to be $Q_{u,eq,exp} = 2068$ kN referring to the experimental data reported by Briaud et al. (1989). The vertical head displacement, which represents the average head displacement of the piles in the group for the measured values whereas the head displacement of the equivalent pier for the modelled values, is normalised by the pile diameter D.

The prediction results are closely comparable to the experimental data. The two typical branches characterising pile load–settlement curves can be remarked with reference to the considered data. The shape of the obtained load–settlement curve for the equivalent pier resembles that of the single pile tested by Briaud et al. (1989) except that similar values of displacement are mobilised under the influence of a much greater mechanical load.

11.11.2.3 Tests by O'Neill et al. (1981)

O'Neill et al. (1981) reported the results of full-scale in situ tests performed on eleven conventional piles subjected to vertical mechanical loading, including three experiments on a 9-pile group, a 5-pile group and a 4-pile group. The site is described in Section 11.11.1.2 and relevant features are summarised in Fig. 11.60.

Relevant parameters were extracted from the work of O'Neill et al. (1981) and are reported in Tables 11.10 and 11.11. Values written in regular font were found in the referenced publication, those written in italic were assumed and those written in bold resulted from calculations based on the parameters presented. Complementary information of the material properties employed for modelling the single piles and the soil is summarised in Section 10.11.3.

In each pile group test, the diameter of the equivalent pier was determined according to the expression proposed by Poulos (1993) for end-bearing piles. The slopes $K_{s,eq}$ and $K_{b,eq}$ of the elastic branches of the load–displacement functions proposed by Rotta Loria and Laloui (2017b) were determined with reference to the spacing of $s = 3D$, $s = 3\sqrt{2}D$ and $s = 3\sqrt{2}D$ for the 9-pile group, the 5-pile group and the 4-pile group test, respectively. The shaft and base capacities of the equivalent pier were determined by multiplying the shaft and base capacities of the single isolated piles multiplied by the number of piles in the group. This approach conservatively analyses the bearing capacity of driven pile groups in fine-grained soil as remarked in this chapter. No contribution of the slab was accounted for modelling the response of the equivalent pier according to the freestanding character of the slab connecting the pile in the experimental test. The equivalent Young's modulus was calculated considering an average value of soil Young's modulus with depth.

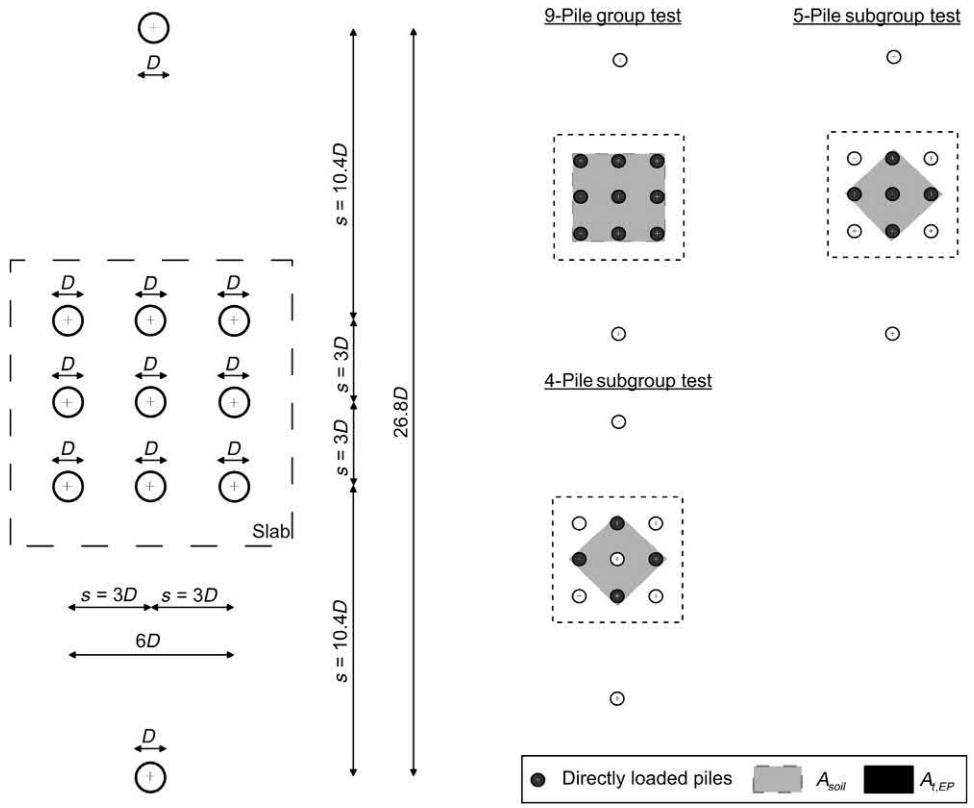

Figure 11.60 Features of the pile group and related pile group tests described by O'Neill et al. (1981). *Modified after Rotta Loria, A.F., Català Oltra, J.V., Laloui, L., 2019. Equivalent pier analysis of full-scale pile groups subjected to mechanical and thermal loads. (Under review).*

Fig. 11.61 shows the measured and computed load–settlement curves for the considered 9-, 5- and 4-pile groups. Both the applied mechanical load and the resulting vertical displacement are normalised values. The applied mechanical load is normalised with respect to the axial capacity of the pile group, which is estimated to be $Q_{u,eq,exp} = 5276$, 2931 and 2345 kN referring to the experimental data reported by O'Neill et al. (1981) in the 9-, 5- and 4-pile group test, respectively. The vertical head displacement, which represents the average head displacement of the piles in the groups for the measured values whereas the head displacement of the equivalent piers for the modelled values, is normalised by the pile diameter D.

The prediction results are closely comparable to the experimental data. Different from the previously considered experimental results of Briaud et al. (1989), the load–settlement curve follows a linear evolution for increasing loading. This aspect characterises both the single pile and pile group tests.

Table 11.10 Soil properties considered for modelling the pile group tests of O'Neill et al. (1981).

Reference depth, z [m]	Variable	Value
[0; 2.14]	Dry unit weight, γ_d [kN/m^3]	**17.4**
	Angle of shear strength under constant volume conditions, φ'_{cv} [degrees]	**17**
	Young's modulus, E_{soil} [MPa]	**49.0**
	Poisson's ratio, ν_{soil} [−]	*0.45*
	Menard pressuremeter modulus, E_M [MPa]	**185.9**
	Slope of the load-transfer elastic branch for the equivalent pier shaft, $K_{s,eq}$ [kPa/m] − 9-pile group test	**85,128**
	Slope of the load-transfer elastic branch for the equivalent pier shaft, $K_{s,eq}$ [kPa/m] − 5-pile group test	**120,364**
	Slope of the load-transfer elastic branch for the equivalent pier shaft, $K_{s,eq}$ [kPa/m] − 4-pile group test	**120,364**
	Overconsolidation ratio, OCR [−]	**7.2**
[2.14; 13.10)	Saturated unit weight, γ_{sat} [kN/m^3]	**20.9**
	Angle of shear strength under constant volume conditions, φ'_{cv} [degrees]	**19.8**
	Young's modulus, E_{soil} [MPa]	**49.0**
	Poisson's ratio, ν_{soil} [−]	*0.45*
	Menard pressuremeter modulus, E_M [MPa]	**185.9**
	Slope of the load-transfer elastic branch for the equivalent pier shaft, $K_{s,eq}$ [kPa/m] − 9-pile group test	**85,128**
	Slope of the load-transfer elastic branch for the equivalent pier shaft, $K_{s,eq}$ [kPa/m] − 5-pile group test	**120,364**
	Slope of the load-transfer elastic branch for the equivalent pier shaft, $K_{s,eq}$ [kPa/m] − 4-pile group test	**120,364**
	Slope of the load-transfer elastic branch for the equivalent pier base, $K_{b,eq}$ [kPa/m] − 9-pile group test	**468,202**
	Slope of the load-transfer elastic branch for the equivalent pier base, $K_{b,eq}$ [kPa/m] − 5-pile group test	**662,000**
	Slope of the load-transfer elastic branch for the equivalent pier base, $K_{b,eq}$ [kPa/m] − 4-pile group test	**662,000**
	Overconsolidation ratio, OCR [−]	**4.47**

Source: Modified after Rotta Loria, A.F., Català Oltra, J.V., Laloui, L., 2019. Equivalent pier analysis of full-scale pile groups subjected to mechanical and thermal loads. (Under review).

11.11.2.4 Tests by Mandolini and Viggiani (1992)

Mandolini and Viggiani (1992) reported the results of full-scale in situ tests performed on a series of micropiles supporting bridge piers subjected to vertical mechanical loading, including one experiment on a group of 20 piles. The piles were driven in a normally to slightly overconsolidated silty clay soil deposit and consisted in closed-end tubular steel pipes filled with concrete of an external diameter of $D = 385$ mm and an

Table 11.11 Equivalent pier properties considered for modelling the pile group tests of O'Neill et al. (1981).

Test	Variable	Value
9-Pile group test	Equivalent Young's modulus, E_{eq} [GPa]	**4.0**
	Equivalent shaft capacity, $Q_{s,eq}$ [kN]	**4550.4**
	Equivalent base capacity, $Q_{b,eq}$ [kN]	**725.4**
	Total pier axial capacity, $Q_{u,eq}$ [kN]	**5275.8**
	Plan area of pile group, A_g [m^2]	**3.7**
	Representative pile spacing, s [m]	**0.82**
	Equivalent diameter, D_{eq} [m]	**2.43**
5-Pile group test	Equivalent Young's modulus, E_{eq} [GPa]	**2.8**
	Equivalent shaft capacity, $Q_{s,eq}$ [kN]	**2528**
	Equivalent base capacity, $Q_{b,eq}$ [kN]	**403**
	Total pier axial capacity, $Q_{u,eq}$ [kN]	**2931**
	Plan area of pile group, A_g [m^2]	**2.8**
	Representative pile spacing, s [m]	**1.16**
	Equivalent diameter, D_{eq} [m]	**2.1**
4-Pile group test	Equivalent Young's modulus, E_{eq} [GPa]	**2.3**
	Equivalent shaft capacity, $Q_{s,eq}$ [kN]	**2022.4**
	Equivalent base capacity, $Q_{b,eq}$ [kN]	**322.4**
	Total pier axial capacity, $Q_{u,eq}$ [kN]	**2344.8**
	Plan area of pile group, A_g [m^2]	**2.9**
	Representative pile spacing, s [m]	**1.16**
	Equivalent diameter, D_{eq} [m]	**2.1**

Source: Modified after Rotta Loria, A.F., Català Oltra, J.V., Laloui, L., 2019. Equivalent pier analysis of full-scale pile groups subjected to mechanical and thermal loads. (Under review).

embedded length from $L = 40$ to 50 m (cf. Fig. 11.62). A rigid slab made of reinforced concrete connected the piles in the group without being in contact with the ground. A geotechnical characterisation of the site was performed and is reported by Mandolini and Viggiani (1992). The soil profile was particularly uniform along the piles. The groundwater table was found to be approximately at the surface of the deposit.

Relevant parameters were extracted from the work of Mandolini and Viggiani (1992) and are reported in Tables 11.12 and 11.13. Values written in regular font were found in the referenced publication, those written in italic were assumed and those written in bold resulted from calculations based on the parameters presented. Complementary information of the material properties employed for modelling the single piles and the soil is summarised in Section 10.11.4.

The pile length was assumed to be of $L = 45$ m. The diameter of the equivalent pier was determined according to the expression proposed by Poulos (1993) for end-bearing piles. The slopes $K_{s,eq}$ and $K_{b,eq}$ of the elastic branches of the

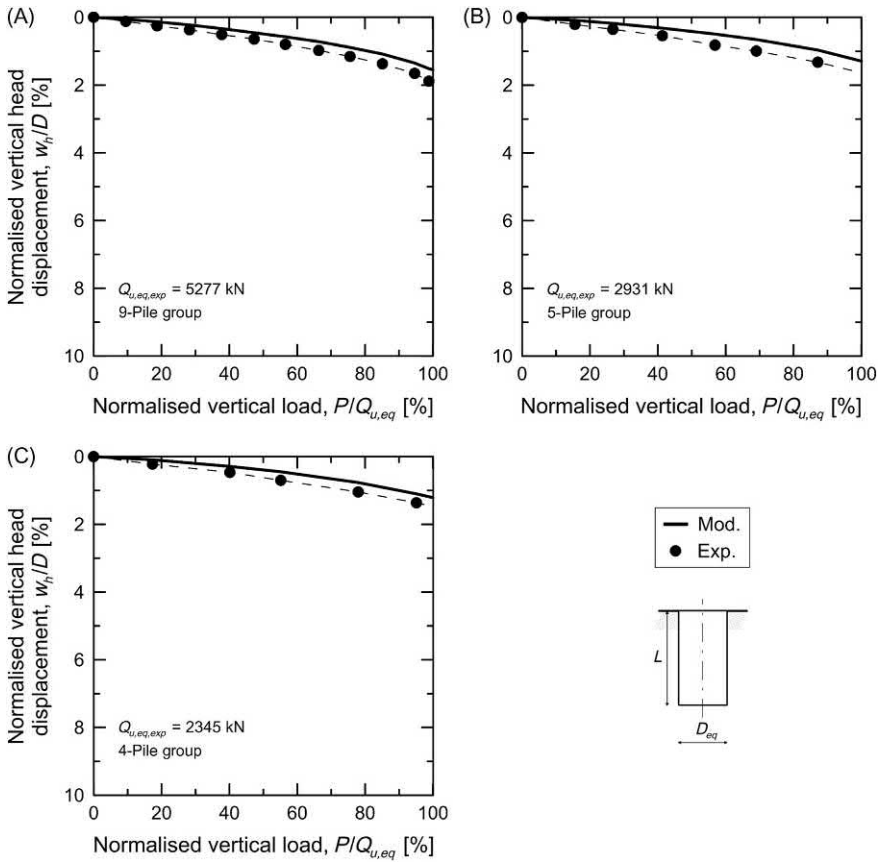

Figure 11.61 Experimental and modelled pile head load–settlement curves referring to the (A) 9-pile group test, (B) 5-pile group test and (C) 4-pile group test of O'Neill et al. (1981). *Modified after Rotta Loria, A.F., Català Oltra, J.V., Laloui, L., 2019. Equivalent pier analysis of full-scale pile groups subjected to mechanical and thermal loads. (Under review).*

load–displacement functions proposed by Rotta Loria and Laloui (2017b) were determined with reference to the spacing of $s = 5.71D$. The shaft and base capacities of the equivalent pier were determined by multiplying the shaft and base capacities of the single isolated piles multiplied by the number of piles in the group. This approach conservatively analyses the bearing capacity of driven pile groups in coarse-grained soil as remarked in this chapter. No contribution of the slab was accounted for modelling the response of the equivalent pier according to the freestanding character of the slab connecting the pile in the experimental test.

Fig. 11.63 shows one value of normalised vertical load against the corresponding head settlement for the pile group referring to the experimental and modelling results.

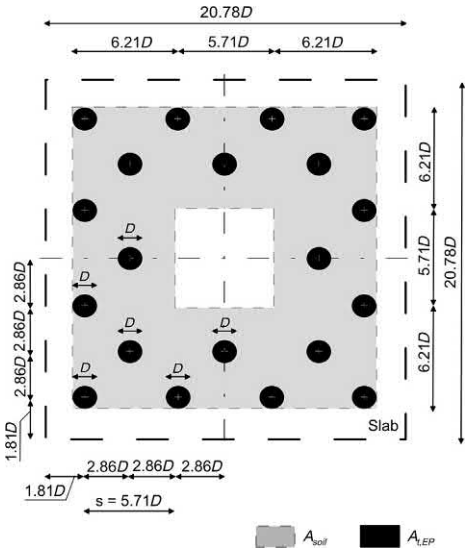

Figure 11.62 Features of the pile group described by Mandolini and Viggiani (1992). *Modified after Rotta Loria, A.F., Català Oltra, J.V., Laloui, L., 2019. Equivalent pier analysis of full-scale pile groups subjected to mechanical and thermal loads. (Under review).*

Table 11.12 Soil properties considered for modelling the pile group test of Mandolini and Viggiani (1992).

Reference depth, z [m]	Variable	Value
[0; 45)	Saturated unit weight, γ_{sat} [kN/m^3]	**17.8**
	Angle of shear strength under constant volume conditions, φ'_{cv} [degrees]	35
	Menard pressuremeter modulus, E_M [MPa]	**47.3**
	Slope of the load-transfer elastic branch for the equivalent pier shaft, $K_{s,eq}$ [kPa/m]	**1201**
	Slope of the pile base load-transfer elastic branch for the equivalent pier base, $K_{b,eq}$ [kPa/m]	**6606**
	Overconsolidation ratio, OCR [−]	*2*

Source: Modified after Rotta Loria, A.F., Català Oltra, J.V., Laloui, L., 2019. Equivalent pier analysis of full-scale pile groups subjected to mechanical and thermal loads. (Under review).

Both the applied mechanical load and the resulting vertical displacement are normalised values. The applied mechanical load is normalised with respect to the axial capacity of the pile group, which is estimated analytically to be $Q_{u,eq,mod} = 90,060$ kN. The vertical head displacement of the pile is normalised by its diameter D.

Table 11.13 Equivalent pier properties considered for modelling the pile group test of Mandolini and Viggiani (1992).

Variable	Value
Equivalent Young's modulus, E_{eq} [GPa]	**1.6**
Equivalent shaft capacity, Q_s [kN]	**52,220**
Equivalent base capacity, Q_b [kN]	**37,840**
Total pier axial capacity, Q_u [kN]	**90,060**
Plan area of pile group, A_g [m^2]	**43.9**
Representative pile spacing, s [m]	**2.20**
Equivalent diameter, D_{eq} [m]	**7.5**

Source: Modified after Rotta Loria, A.F., Català Oltra, J.V., Laloui, L., 2019. Equivalent pier analysis of full-scale pile groups subjected to mechanical and thermal loads. (Under review).

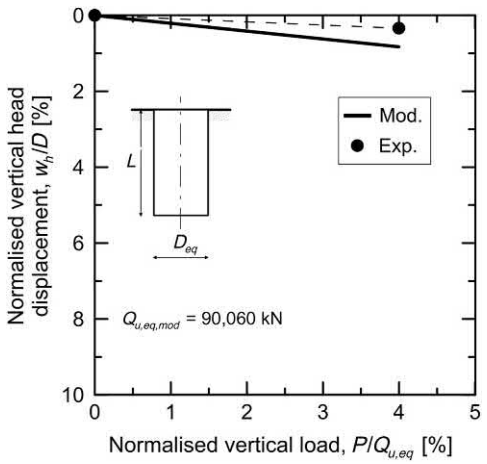

Figure 11.63 Experimental and modelled head load–settlement curves referring to the pile group test of Mandolini and Viggiani (1992). *Modified after Rotta Loria, A.F., Català Oltra, J.V., Laloui, L., 2019. Equivalent pier analysis of full-scale pile groups subjected to mechanical and thermal loads. (Under review).*

The prediction results predict a more remarkable head settlement of the pile group compared to the experimental results. Despite this shortcoming, the modelling results may be considered representative of the modelled problem to a given extent.

11.11.2.5 Tests by Rotta Loria and Laloui (2018)

Rotta Loria and Laloui (2018) reported the results of a full-scale in situ test performed on four energy piles subjected to thermal loading, applied in conjunction with vertical mechanical loading. The thermal loading applied to the energy piles over time resulted in an average temperature variation of $\overline{\overline{\Delta T}} = 5°C$, 10°C, 15°C and 20°C along their

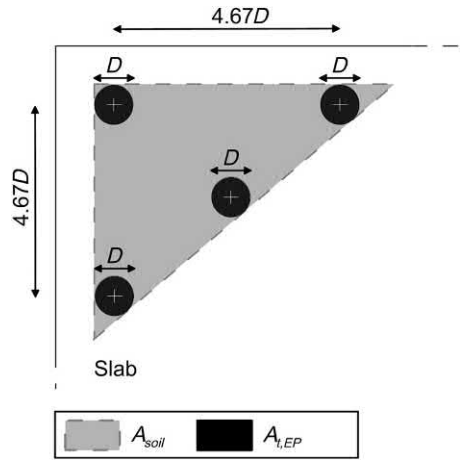

Figure 11.64 Features of the pile group described by Rotta Loria and Laloui (2018). *Modified after Rotta Loria, A.F., Català Oltra, J.V., Laloui, L., 2019. Equivalent pier analysis of full-scale pile groups subjected to mechanical and thermal loads. (Under review).*

portion in which the pipes were not thermally insulated (i.e. below 4 m from the pile heads). The piles were bored in a stratified overconsolidated soil deposit and consisted in reinforced concrete piles of a diameter of $D = 900$ mm and a length of $L = 28$ m. A 0.9-m-thick slab characterised by the dimensions of $L_{slab} = 2$ m and $B_{slab} = 10$ mm and made of reinforced concrete connected the four energy piles, which are a part of a larger pile group of other 16 conventional piles (cf. Fig. 11.64). A value of the head stiffness of $K_{slab} = 2744.4$ MN/m was estimated according to the expression provided by Gorbunov-Posadov and Serebrjanyi (1961). A value of mechanical load of $P = 495$ kN was assumed to be applied to each pile in the foundation. The soil deposit consisted of a shallow alluvial soil layer from the surface (coinciding with the level of the built 0.9-m-thick slab) to a depth of $z = 8.6$ m. Below the alluvial soil layer, a sandy-gravelly moraine layer was found to reach a depth of $z = 16.6$ m. A layer of bottom moraine was present below the sandy-gravelly moraine layer, down to a depth of $z = 20.1$ m. A molasse layer was found at greater depths below the bottom moraine. The groundwater table was located at the surface.

Relevant parameters were extracted from the investigations of Di Donna et al. (2016) and Rotta Loria and Laloui (2017c) and are reported in Tables 11.14 and 11.15. Values written in regular font were found in the referenced publications, those written in italic were assumed and those written in bold resulted from calculations based on the parameters presented. Complementary information of the material properties employed for modelling the single piles and the soil is summarised in Section 10.11.5.

Table 11.14 Soil properties considered for modelling the energy pile group test of Rotta Loria and Laloui (2018).

Reference depth, z [m]	Variable	Value
[0; 3.1]	Saturated unit weight, γ_{sat} [kN/m^3]	15.6
	Angle of shear strength under constant volume conditions, φ'_{cv} [degrees]	24
	Pile–soil interface angle of shear strength, δ' [degrees]	19.1
	Menard pressuremeter modulus, E_M [MPa]	**144.6**
	Slope of the load-transfer elastic branch for the equivalent pier shaft, $K_{s,eq}$ [kPa/m]	**48,319**
	Overconsolidation ratio, OCR [−]	4
[3.1; 8.6]	Saturated unit weight, γ_{sat} [kN/m^3]	15.6
	Angle of shear strength under constant volume conditions, φ'_{cv} [degrees]	21
	Pile–soil interface angle of shear strength, δ' [degrees]	18.5
	Menard pressuremeter modulus, E_M [MPa]	**144.6**
	Slope of the load-transfer elastic branch for the equivalent pier shaft, $K_{s,eq}$ [kPa/m]	**48,319**
	Overconsolidation ratio, OCR [−]	4
[8.6; 16.6]	Saturated unit weight, γ_{sat} [kN/m^3]	11.1
	Angle of shear strength under constant volume conditions, φ'_{cv} [degrees]	17
	Pile–soil interface angle of shear strength, δ' [degrees]	16.1
	Menard pressuremeter modulus, E_M [MPa]	**60**
	Slope of the load-transfer elastic branch for the equivalent pier shaft, $K_{s,eq}$ [kPa/m]	**8019**
	Overconsolidation ratio, OCR [−]	4
[16.6; 20.1]	Saturated unit weight, γ_{sat} [kN/m^3]	11.9
	Angle of shear strength under constant volume conditions, φ'_{cv} [degrees]	21
	Pile–soil interface angle of shear strength, δ' [degrees]	18.9
	Menard pressuremeter modulus, E_M [MPa]	**64.3**
	Slope of the load-transfer elastic branch for the equivalent pier shaft, $K_{s,eq}$ [kPa/m]	**8592**
	Overconsolidation ratio, OCR [−]	4
[20.1; 28.9)	Saturated unit weight, γ_{sat} [kN/m^3]	10.3
	Angle of shear strength under constant volume conditions, φ'_{cv} [degrees]	29
	Pile–soil interface angle of shear strength, δ' [degrees]	24.5
	Menard pressuremeter modulus, E_M [MPa]	**109.3; 54.6**
	Slope of the load-transfer elastic branch for the equivalent pier shaft, $K_{s,eq}$ [kPa/m]	**36,507; 18,253**
	Slope of the load-transfer elastic branch for the equivalent pier base, $K_{b,eq}$ [kPa/m]	**200,787; 100,393**
	Overconsolidation ratio, OCR [−]	4

Source: Modified after Rotta Loria, A.F., Català Oltra, J.V., Laloui, L., 2019. Equivalent pier analysis of full-scale pile groups subjected to mechanical and thermal loads. (Under review).

Table 11.15 Equivalent pier properties considered for modelling the energy pile group test of Rotta Loria and Laloui (2018).

Variable	Value
Equivalent Young's modulus, E_{eq} [GPa]	**5.4**
Equivalent shaft capacity, $Q_{s,eq}$ [kN]	**9152**
Equivalent base capacity, $Q_{b,eq}$ [kN]	**40,296**
Total pier axial capacity, $Q_{u,eq}$ [kN]	**49,448**
Plan area of pile group, A_g [m^2]	**15.6**
Representative pile spacing, s [m]	**4.21**
Equivalent diameter, D_{eq} [m]	**4.5**

Source: Modified after Rotta Loria, A.F., Català Oltra, J.V., Laloui, L., 2019. Equivalent pier analysis of full-scale pile groups subjected to mechanical and thermal loads. (Under review).

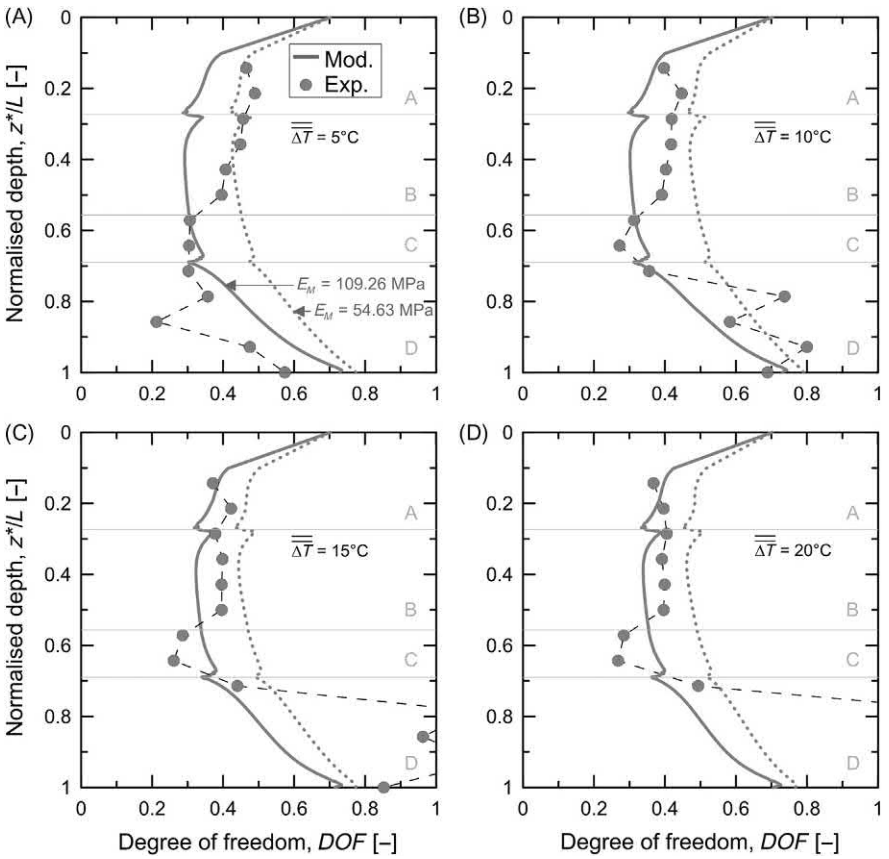

Figure 11.65 Experimental and modelled evolutions of the degree of freedom along the energy piles tested by Rotta Loria and Laloui (2018). Panels (A–D) refer to average temperature variations along the uninsulated portion of the energy piles of $\overline{\overline{\Delta T}} = 5°C$, 10°C, 15°C and 20°C. *Modified after Rotta Loria, A.F., Català Oltra, J.V., Laloui, L., 2019. Equivalent pier analysis of full-scale pile groups subjected to mechanical and thermal loads. (Under review).*

The diameter of the equivalent pier was determined according to the expression proposed by Poulos (1993) for end-bearing piles. The slopes $K_{s,eq}$ and $K_{b,eq}$ of the elastic branches of the load–displacement functions proposed by Rotta Loria and Laloui (2018) were determined with reference to the spacing of $s = 4.67D$. The shaft and base capacities of the equivalent pier were determined by multiplying the shaft and base capacities of the single isolated piles multiplied by the number of piles in the group. The previous value of head stiffness resulted in a head restraint of $K_h =$ 1078.5 MPa/m applied to the head of the equivalent pier. A value of mechanical load of $P = 1980$ kN was assumed to be applied to the equivalent pier based on the mechanical loads applied to the four energy piles represented by the pier. The equivalent Young's modulus was calculated considering an average value of soil Young's modulus with depth referring to all the soil layers except the bottom molasse layer.

Fig. 11.65 shows the measured and computed evolutions of the degree of freedom, $DOF = \varepsilon_o^{th}/\varepsilon_f^{th}$, along the normalised depth, z^*/L, of the equivalent pier, whereby z^* expresses the depth from the head of the piles and pier. The relative depth z^* is normalised by the pile length L. The results of two different sets of simulations associated with different values of the Menard pressuremeter modulus for the molasse layer are reported.

The predictions capture the overall evolution of the experimental data. An increasing difference between the experimental and modelling results in correspondence with the deeper portion of the energy piles is observed for successive stages of their geothermal operation, that is when temperature variations of $\overline{\overline{\Delta T}} = 15°C$ and 20°C are considered. This difference is attributed to the incapability of the present load-transfer analysis approach in capturing the effects (e.g. stress redistribution) associated with the more pronounced thermally induced deformation of the soil (the molasse layer) than the deformation of the piles that was observed by Rotta Loria and Laloui (2018) at the considered stages of the experimental test. Values of $DOF > 1$ are meaningfully observed in correspondence with the soil layer expanding more than the piles because of the greater thermally induced deformation of the piles compared to the one associated with free thermal expansion conditions by referring to the linear thermal expansion coefficient of the pile and the applied temperature variation to the pile. Values of $DOF \neq 1$ are meaningfully observed at the pile head because of the presence of the head restraint.

References

Banerjee, P., Davies, T., 1978. The behaviour of axially and laterally loaded single piles embedded in nonhomogeneous soils. Geotechnique 28 (3), 309–326.

Boussinesq, J., 1878. Équilibre d'élasticité d'un sol isotrope sans pesanteur, supportant différents poids. C. R. Acad. Sci. 86 (86), 1260–1263.

Briaud, J., Tucker, L., Ng, E., 1989. Axially loaded 5 pile group and single pile in sand, Proceedings of 12th International Conference on Soil Mechanics and Foundation Engineering, vol. 2. Balkema, Rotterdam, pp. 1121–1124.
Butterfield, R., Banerjee, P., 1971. The elastic analysis of compressible piles and pile groups. Geotechnique 21 (1), 43–60.
Butterfield, R., Douglas, R., 1981. Flexibility Coefficients for the Design of Piles and Pile Groups. Report 086017171X, p. 81.
Caputo, V., Viggiani, C., 1984. Pile foundation analysis: a simple approach to nonlinearity effects. Riv. Ital. Geotec. 18 (2), 32–51.
Castelli, F., Maugeri, M., 2002. Simplified nonlinear analysis for settlement prediction of pile groups. J. Geotech. Geoenviron. Eng. 128 (1), 76–84.
Castelli, F., Motta, E., 2003. Settlement prevision of piles under vertical load. Proc. Inst. Civ. Eng. Geotech. Eng. 156 (4), 183–191.
Chow, Y., 1986. Analysis of vertically loaded pile groups. Int. J. Numer. Anal. Methods Geomech. 10 (1), 59–72.
Clancy, P., Randolph, M., 1996. Simple design tools for piled raft foundations. Geotechnique 46 (2), 313–328.
Cooke, R., Sillett, D., Smith, D., Gooch, M., 1981. Some observations of the foundation loading and settlement of a multi-storey building on a piled raft foundation in London clay, ICE Proceedings, vol. 70. Thomas Telford, pp. 433–460.
Costanzo, D., Lancellotta, R., 1998. A note on pile interaction factors. Soils Found. 38 (4), 251–253.
Coyle, H.M., Reese, L.C., 1966. Load transfer for axially loaded piles in clay. J. Soil Mech. Found. Div. 92, 1–26.
Di Donna, A., Rotta Loria, A.F., Laloui, L., 2016. Numerical study on the response of a group of energy piles under different combinations of thermo-mechanical loads. Comput. Geotech. 72 (1), 126–142.
Fleming, K., Weltman, A., Randolph, M., Elson, K., 2008. Piling Engineering. CRC Press.
Frank, R., Zhao, S., 1982. Estimation par les paramètres pressiométriques de l'enfoncement sous charge axiale de pieux forés dans des sols fins. Bull. Liaison Labo. P. et Ch. 119, 17–24.
Frank, R., Kalteziotis, N., Bustamante, M., Christoulas, S., Zervogiannis, H., 1991. Evaluation of performance of two piles using pressuremeter method. J. Geotech. Eng. 117 (5), 695–713.
Gorbunov-Posadov, M.I., Serebrjanyi, R.V., 1961. Design of structures on elastic foundation. In: 5th International Conference on Soil Mechanics and Foundation Engineering, vol. 1, pp. 643–648.
Horikoshi, K., Randolph, M., 1998. A contribution to optimum design of piled rafts. Geotechnique 48 (3), 301–317.
Jardine, R., Fourie, A., Potts, D., Burland, J., 1986. Studies of the influence of non-linear stress-strain characteristics in soil-structure interaction. Geotechnique 36 (3), 377–396.
Jeong, S., Min, H., Lee, J.K., 2014. Thermally induced mechanical response of energy piles in axially loaded pile groups. Appl. Therm. Eng. 71 (1), 608–615.
Kaniraj, S.R., 1993. A semi-empirical equation for settlement ratio of pile foundations in sand. Soils Found. 33 (2), 82–90.
Knellwolf, C., Peron, H., Laloui, L., 2011. Geotechnical analysis of heat exchanger piles. J. Geotech. Geoenviron. Eng. 137 (10), 890–902.
Laloui, L., Moreni, M., Vulliet, L., 2003. Comportement d'un pieu bi-fonction, fondation et échangeur de chaleur. Can. Geotech. J. 40 (2), 388–402.
Lancellotta, R., 1995. Geotechnical Engineering. Balkema, Rotterdam.
Lee, C., 1993. Pile group settlement analysis by hybrid layer approach. J. Geotech. Eng. 119 (6), 984–997.
Lee, K., Xiao, Z., 2001. A simplified method for nonlinear analysis of single piles in multilayered soils. Can. Geotech. J. 38 (5), 1063–1080.
Leung, Y., Soga, K., Lehane, B., Klar, A., 2010. Role of linear elasticity in pile group analysis and load test interpretation. J. Geotech. Geoenviron. Eng. 136 (12), 1686–1694.
Lo, M.B., 1967. An experimental study of the load distribution in pile groups in sand by Y.O. Beredugo (vol. III, no. 3: 145–66). Can. Geotech. J. 4 (3), 353–356.

Mandolini, A., Viggiani, C., 1992. Terreni ed opere di fondazione di un viadotto sul fiume Garigliano. Riv. Ital. Geotec. 26 (2), 95–113.
Mandolini, A., Viggiani, C., 1997. Settlement of piled foundations. Geotechnique 47 (4), 791–816.
McCabe, B., Lehane, B., 2006. Behavior of axially loaded pile groups driven in clayey silt. J. Geotech. Geoenviron. Eng. 132 (3), 401–410.
Meyerhof, G., 1959. Compaction of sands and bearing capacity of piles. J. Soil Mech. Found. Div. 85 (6), 1–30.
Meyerhof, G., 1976. Bearing capacity and settlement of pile foundations. J. Geotech. Eng. Div. GT3 (1), 197–228.
Mimouni, T., Laloui, L., 2015. Behaviour of a group of energy piles. Can. Geotech. J. 52 (12), 1913–1929.
Mindlin, R.D., 1936. Force at a point in the interior of a semi-infinite solid. J. Appl. Phys. 7 (5), 195–202.
Murphy, K.D., McCartney, J.S., Henry, K.S., 2015. Evaluation of thermo-mechanical and thermal behavior of full-scale energy foundations. Acta Geotech. 10 (2), 1–17.
Mylonakis, G., 2001. Winkler modulus for axially loaded piles. Geotechnique 51 (5), 455–462.
Mylonakis, G., Gazetas, G., 1998. Settlement and additional internal forces of grouped piles in layered soil. Geotechnique 48 (1), 55–72.
O'Neill, M.W., Ghazzaly, O.I., Ha, H.B., 1977. Analysis of three-dimensional pile groups with nonlinear soil response and pile-soil-pile interaction. In: 9th Annual Offshore Technology Conference, Houston, TX, pp. 245–256.
O'Neill, M.W., Hawkins, R.A., Mahar, L.J., 1981. Field study of pile group action. Final Report, p. 195.
Ottaviani, M., 1975. Three-dimensional finite element analysis of vertically loaded pile groups. Geotechnique 25 (2), 159–174.
Poulos, H.G., 1968. Analysis of the settlement of pile groups. Geotechnique 18 (4), 449–471.
Poulos, H.G., 1977. Estimation of pile group settlements. Ground Eng. 10 (2), 40–50.
Poulos, H.G., 1988. Modified calculation of pile-group settlement interaction. J. Geotech. Eng. 114 (6), 697–706.
Poulos, H.G., 1989. Pile behaviour—theory and application. Geotechnique 39 (3), 365–415.
Poulos, H.G., 1993. Settlement prediction for bored pile groups. Proceedings of Deep Foundations on Bored and Auger Piles. Balkema, Rotterdam, pp. 103–117.
Poulos, H.G., 1994. An approximate numerical analysis of pile–raft interaction. Int. J. Numer. Anal. Methods Geomech. 18 (2), 73–92.
Poulos, H.G., 2006. Pile group settlement estimation: research to practice, GeoShanghai International Conference 2006, vol. 153. ASCE Geotechnical Special Publication, Shanghai, pp. 1–22.
Poulos, H.G., Davis, E.H., 1980. Pile Foundation Analysis and Design. Wiley, New York.
Poulos, H.G., Mattes, N.S., 1974. Settlement of pile groups bearing on stiffer strata. J. Geotech. Geoenviron. Eng. 100 (GT2), 185–190.
Poulos, H.G., Carter, J.P., Small, J.C., 2002. Foundations and retaining structures—research and practice, International Conference on Soil Mechanics and Geotechnical Engineering, vol. 4. Balkema, pp. 2527–2606.
Pressley, J.S., Poulos, H.G., 1986. Finite element analysis of mechanisms of pile group behaviour. Int. J. Numer. Anal. Methods Geomech. 10 (2), 213–221.
Randolph, M., 1994. Design methods for pile groups and piled rafts. In: Proceedings of XIII ICSMFE, pp. 61–82.
Randolph, M., Clancy, P., 1993. Efficient design of piled rafts. In: Van Impe, W. (Ed.), Deep Foundations on Bored and Auger Piles. Balkema, Rotterdam, pp. 119–130.
Randolph, M.F., Wroth, C.P., 1978. Analysis of deformation of vertically loaded piles. J. Geotech. Eng. Div. 104 (12), 1465–1488.
Randolph, M., Wroth, C., 1979a. A simple approach to pile design and the evaluation of pile tests. Behavior of Deep Foundations. ASTM International.
Randolph, M.F., Wroth, C., 1979b. An analysis of the vertical deformation of pile groups. Geotechnique 29 (4), 423–439.

Ravera, E., Sutman, M., Laloui, L., 2019. Load transfer method for energy piles in a group with pile-soil-slab-pile interaction. J. Geotech. Geoenviron. Eng. (Under review).
Rotta Loria, A.F., Laloui, L., 2016. The interaction factor method for energy pile groups. Comput. Geotech. 80, 121–137.
Rotta Loria, A.F., Laloui, L., 2017a. Displacement interaction among energy piles bearing on stiff soil strata. Comput. Geotech. 90, 144–154.
Rotta Loria, A.F., Laloui, L., 2017b. The equivalent pier method for energy pile groups. Geotechnique 67 (8), 691–702.
Rotta Loria, A.F., Laloui, L., 2017c. Thermally induced group effects among energy piles. Geotechnique 67 (5), 374–393.
Rotta Loria, A.F., Laloui, L., 2018. Group action effects caused by various operating energy piles. Geotechnique 68 (9), 834–841.
Rotta Loria, A.F., Gunawan, A., Shi, C., Laloui, L., Ng, C.W., 2015. Numerical modelling of energy piles in saturated sand subjected to thermo-mechanical loads. Geomech. Energy Environ. 1 (1), 1–15.
Rotta Loria, A.F., Vadrot, A., Laloui, L., 2017. Effect of non-linear soil deformation on the interaction among energy piles. Comput. Geotech. 86, 9–20.
Rotta Loria, A.F., Vadrot, A., Laloui, L., 2018. Analysis of the vertical displacement of energy pile groups. Geomech. Energy Environ. 16, 1–14.
Rotta Loria, A.F., Català Oltra, J.V. & Laloui, L., 2019. Equivalent pier analysis of full-scale pile groups subjected to mechanical and thermal loads. (Under review).
Saggu, R., Chakraborty, T., 2016. Thermomechanical response of geothermal energy pile groups in sand. Int. J. Geomech. 16 (4), 04015100.
Salciarini, D., Ronchi, F., Cattoni, E., Tamagnini, C., 2015. Thermomechanical effects induced by energy piles operation in a small piled raft. Int. J. Geomech. 15 (2), 04014042.
Sheil, B.B., McCabe, B.A., 2014. A finite element–based approach for predictions of rigid pile group stiffness efficiency in clays. Acta Geotech. 9 (3), 469–484.
Sheil, B.B., McCabe, B.A., Comodromos, E.M., Lehane, B.M., 2018. Pile groups under axial loading: an appraisal of simplified nonlinear prediction models. Geotechnique 1–51. Available from: https://doi.org/10.1680/jgeot.17.
Skempton, A., 1951. The bearing capacity of clays. In: Proceedings of Building Research Congress, vol. 1, pp. 180–189.
Skempton, A., 1953. Discussion: piles and pile foundations. In: 3rd International Conference for Soil Mechanics and Foundation Engineering, Zurich, Switzerland.
Suryatriyastuti, M., Burlon, S., Mroueh, H., 2016. On the understanding of cyclic interaction mechanisms in an energy pile group. Int. J. Numer. Anal. Methods Geomech. 40 (1), 3–24.
Timoshenko, S., Goodier, J., 1970. Theory of Elasticity. McGraw-Hill, New York.
Tomlinson, M.J., Boorman, R., 2001. Foundation Design and Construction. Pearson Education.
Van Impe, W., 1991. Deformation of deep foundations. General Report. In: Proceedings of the 13th ISSMFE Conference.
Vesić, A., 1969. Experiments with instrumented pile groups in sand. Performance of Deep Foundations. ASTM International.
Wang, Z., Xie, X., Wang, J., 2012. A new nonlinear method for vertical settlement prediction of a single pile and pile groups in layered soils. Comput. Geotech. 45, 118–126.
Wang, B., Bouazza, A., Singh, R.M., Haberfield, C., Barry-Macaulay, D., Baycan, S., 2014. Posttemperature effects on shaft capacity of a full-scale geothermal energy pile. J. Geotech. Geoenviron. Eng. 141 (4), 04014125.
Wang, A., Wang, W., Huang, M., Wu, J., 2016. Interaction factor for large pile groups. Géotech. Lett. 6 (1), 58–65.
Wong, S.C., Poulos, H.G., 2005. Approximate pile-to-pile interaction factors between two dissimilar piles. Comput. Geotech. 32 (8), 613–618.
Zhang, Q.-Q., Zhang, Z.-M., He, J.-Y., 2010. A simplified approach for settlement analysis of single pile and pile groups considering interaction between identical piles in multilayered soils. Comput. Geotech. 37 (7), 969–976.

Questions and problems

Statements

a. Which is the typical centre-to-centre spacing that distinguishes a closely spaced energy pile group from a widely spaced energy pile group, in terms of the pile diameter?

b. The concept of group efficiency is an appropriate method to estimate the axial capacity of pile groups:
- **i.** True
- **ii.** False

c. Does the consideration of an axial load capacity of pile groups that is equal to the sum of the individual load capacities of the single piles always represent a conservative analysis and design approach?

d. Briefly enumerate the five analytical or semianalytical analysis and design approaches that can be employed to address the axial deformation of pile groups.

e. Considering w_j the additional displacement due to the loading of an adjacent pile and w_i the displacement of a single pile, the interaction factor reads:
- **i.** w_j/w_i
- **ii.** w_i/w_j
- **iii.** $w_j/(n_{EP}w_i)$

f. The damping effect played by a receiver pile on the deformation of a source pile in a pair:
- **i.** Increases with the pile spacing
- **ii.** Decreases with the pile spacing
- **iii.** It is independent of the pile spacing

g. Write the formulation for the interaction factor between piles resting on finitely rigid soil strata.

h. Are both the interaction factors for predominantly end-bearing energy piles subjected to mechanical and thermal loads greater than those for predominantly floating energy piles? Justify your answer resorting to a description of the response of the considered piles to mechanical and thermal loads.

i. Can the superposition principle be employed to investigate the effects of the interactions caused by both mechanical and thermal loads among energy piles?

j. Express mathematically how the superposition principle can be employed in the interaction factor analysis procedure based on charts to determine the vertical head displacement w_k of any pile, k, composing a general pile group with a total number of piles, n_{EP}, in which some or all of the piles may be subjected to mechanical and/or thermal loading. Define all of the involved terms appearing in the formulations.

k. Can the considered interaction factor charts referring to a Poisson's ratio of the soil $\nu_{soil} = 0.3$ be employed to calculate the interaction factor for piles embedded in soil deposits with a different value of Poisson's ratio? If this result can be achieved, specify how.

l. The use of interaction factors for the case of piles in a homogeneous soil gives conservative estimates of the interaction for cases in which the soil deformation modulus increases with depth:
- **i.** True
- **ii.** False
- **iii.** It depends on whether the influence of mechanical or thermal loading is considered

m. The development of interaction factor charts referring to isothermal soil deposits may be considered:
- **i.** An effective approach to describe the interaction between piles in any type of soil deposit, provided that an appropriate unitary displacement of a single pile is considered in the analyses
- **ii.** An effective approach to describe the interaction between piles in any type of soil deposit, irrespective of the unitary displacement of a single pile that is considered in the analyses

n. Consider a group of two identical energy piles characterised by a slenderness ratio of $L/D = 25$ that are surrounded by an isotropic, homogeneous and deep thermoelastic soil mass. Assume that one pile in the group is subjected to a temperature variation. If the piles are characterised by a Young's modulus of $E_{EP} = 30$ GPa and the soil by a Young's modulus of $E_{soil} = 78$ MPa and a Poisson's ratio of $\nu_{soil} = 0.3$, which is the value of interaction factor between the two piles for a normalised spacing of $s/D = 3$? Consider the following interaction factor chart to answer to this question.

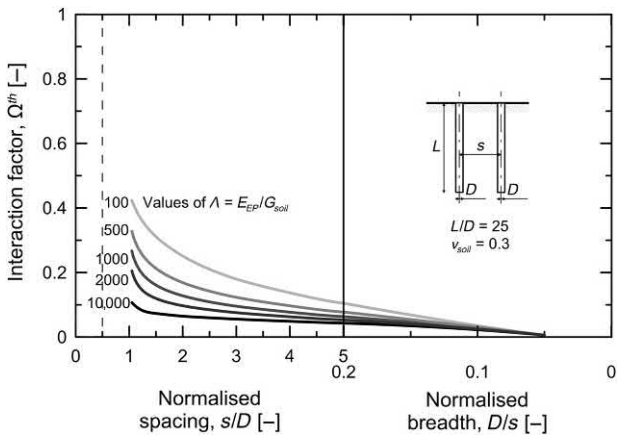

o. Consider a group of two identical energy piles that are surrounded by an isotropic, homogeneous and deep thermoelastic soil mass. Assume that both piles in the group are subjected to the same temperature variation. Write the expression for the vertical displacement of each pile of the group w_k by considering that the vertical displacement of the piles in the single isolated case subjected to the same temperature variation reads w_i and the interaction factor between the piles in the group is Ω.

p. Obtain the analytical expression constituting the layer model for the vertical displacement at any given distance in the soil from a loaded source pile starting from the indefinite equilibrium equations governing the response of bodies to loading, written for a pile element.

q. Can the same two boundary conditions needed to correct the interaction factor to account for the stiffness of the receiver pile on the definition of this parameter via analytical models be used for both mechanical and thermal loading? Explain why.

r. The evolution of the interaction factor associated with thermal loads can be considered approximately constant with depth, similar to the evolution of the interaction factor associated with mechanical loads:
- **i.** Yes, it can be considered constant with depth because the response of pile to thermal loads can be considered in a plane state of strain
- **ii.** No, it cannot be considered constant with depth because the response of pile to thermal loads can be considered in a plane state of strain

s. The interaction factor characterising piles subjected to thermal loads can be greater than 1:
- **i.** Yes, it can be greater than 1
- **ii.** No, it cannot be greater than 1

t. When using the layer and continuous model in interaction factor analyses of energy piles embedded in soil deposits whose thermal expansion coefficient is in excess than that of the piles, a unitary pile displacement resulting from an analysis that accounts for the temperature sensitivity of the soil is needed:
- **i.** Yes, because the layer and continuous models are incapable of accounting for this phenomenon
- **ii.** No, because the layer and continuous model already provide the lower and upper boundaries of pile interaction and resulting displacement that may be expected in reality irrespective of the soil−pile thermal expansion coefficient ratio

u. Soil modulus values that are associated with high strain levels can be used to characterise:
- **i.** The vertical displacement behaviour of the single piles composing any group
- **ii.** The interactions between the piles composing any group

iii. Both of the previous subjects

v. The equivalent pier method can be applied for aspect ratios of the group and for normalised spacing between the piles of
   i. $AR < 4$ and $s/D \leq 5$
   ii. $AR > 4$ and $s/D \leq 5$
   iii. $AR \leq 4$ and $s/D > 5$
   iv. $AR > 4$ and $s/D > 5$

w. Which is the basic concept behind the equivalent pier method?

x. For which design situations can the coupled use of the interaction factor and equivalent pier methods be particularly useful?

y. Consider the group of energy piles of 20 m in length and 0.8 m in diameter that is reported in the following figure and has already been analysed previously. Remember that the energy piles are socketed in a saturated sand deposit and that a 12×12 m^2 rigid slab (resting on the ground) made of reinforced concrete connects all the energy piles. The sand and the pile proprieties are reported in the two following tables, respectively. Assume that the behaviour of the considered energy pile group can be analysed with accuracy with the equivalent pier method, that is by modelling the pile group as a single equivalent pier.

For the considered pier, calculate the parameters needed for its geometrical and material description, that is the equivalent diameter, D_{eq}, the equivalent Young's modulus, E_{eq}, and the equivalent linear thermal expansion coefficient of the pier, α_{eq}. When calculating α_{eq}, assume that $X = \alpha_{soil}/\alpha_{EP} \leq 1$, where α_{soil} and α_{EP} are the linear thermal expansion coefficients of the soil and energy piles, respectively.

With reference to the bearing capacity of one of the energy piles in the group, determine the bearing capacity of the equivalent pier by distributing the total shaft and base capacities of the group (calculated as the shaft and base capacities of the single isolated energy piles multiplied by the number of piles in the group for hypothesis) on the shaft and base area of the equivalent pier, respectively. This implies that

$$q_{s,eq} = q_s \frac{D}{D_{eq}} n_{EP}$$

and

$$q_{b,eq} = q_b \frac{D^2}{D_{eq}^2} n_{EP}$$

To construct the load-transfer relationships for the shaft and base of the equivalent pier, consider that it can be reproduced by a revision of the relationships proposed by Frank et al. (1991) for piles in coarse-grained soils, that is

$$K_{s,eq} = 0.8\frac{E_M}{D}\zeta$$

$$K_{b,eq} = 4.8\frac{E_M}{D}\zeta$$

where

$$\zeta = \frac{s}{L}$$

for which s is the centre-to-centre spacing between the piles and L is the pile length.

By using the software Thermo-Pile (Knellwolf et al., 2011) evaluate the average vertical displacement of the equivalent pier with depth in five different cases:

- CASE 1: pier free at the head subjected to a vertical load of $P = 4500$ kN and to a temperature variation of $\Delta T = 0°C$.
- CASE 2: pier free at the head subjected to a vertical load of $P = 0$ kN and to a temperature variation of $\Delta T = 10°C$.
- CASE (1 + 2): pier assumed to be characterised by the effects induced by the loads considered in CASE 1 and CASE 2 through the elastic superposition principle.
- CASE 3: pier free at the head subjected to a vertical load of $P = 4500$ kN and to a temperature variation of $\Delta T = 10°C$.
- CASE 4: pier restrained at the head by the presence of the slab and subjected to a vertical load of $P = 4500$ kN and to a temperature variation of $\Delta T = 10°C$. Assume that the slab stiffness can be estimated through the following equation, with reference to a rigid rectangular plate resting vertically loaded on an isotropic elastic half-space (Gorbunov-Posadov and Serebrjanyi, 1961):

$$K_{slab} = \frac{E_{soil}\sqrt{B_{slab}L_{slab}}}{(1-\nu_{soil}{}^2)\rho_0}$$

where E_{soil} is the Young's modulus of the soil, B_{slab} and L_{slab} are the dimensions of the slab, ν_{soil} is the Poisson's ratio of the soil, and ρ_0 is a displacement coefficient. Consider that the displacement coefficient can be evaluated as a function of the ratio $\chi = L_{slab}/B_{slab}$.

For each case, compare the vertical displacement distributions of the equivalent pier (discretised in 200 elements in Thermo-Pile) with those characterising one of the piles of the group obtained through a previous analysis with reference to a single isolated situation. Comment on the impact of group effects on the vertical displacement distribution of an energy pile group compared to that of a single isolated energy pile under mechanical and/or thermal loads.

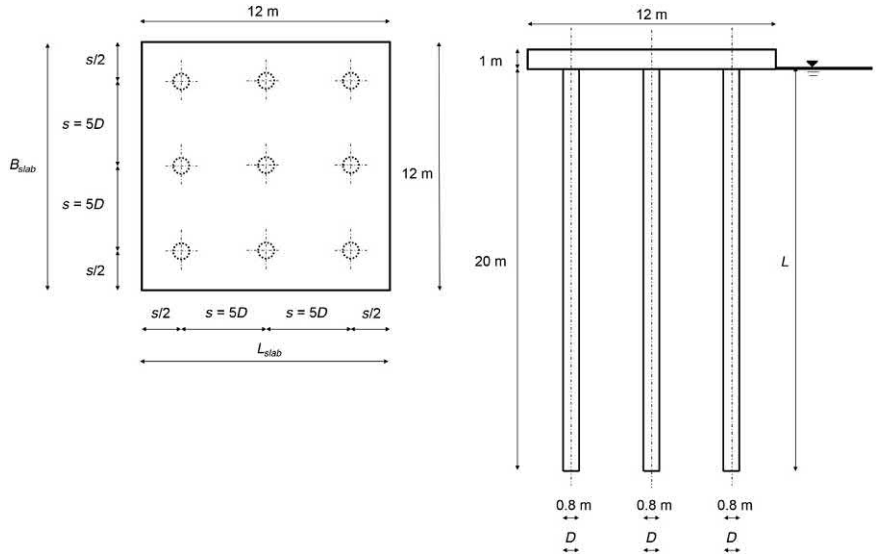

	γ_{soil}	c'	φ'_{cv}	φ'	E_{soil}	v_{soil}	α_r
	[kN/m^3]	[kPa]	[degrees]	[degrees]	[MPa]	[−]	[−]
Sand	19	20	31	38	78	0.3	0.33

	$\gamma_{concrete}$	E_{EP}	v_{EP}	α_{EP}
	[kN/m^3]	[MPa]	[−]	[με/°C]
Pile	25	30,000	0.25	10

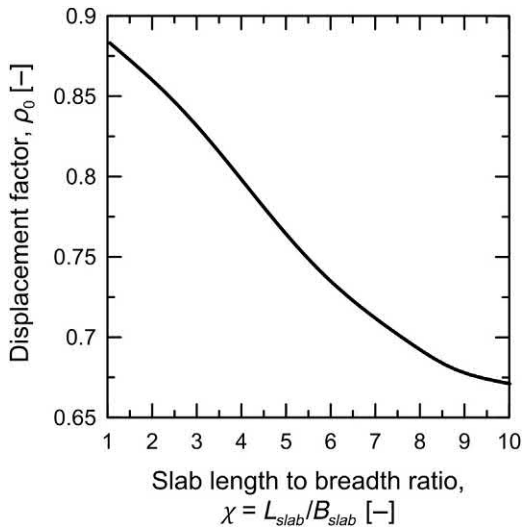

Solutions

a. The typical centre-to-centre spacing that distinguishes a closely spaced energy pile group from a widely spaced energy pile group, in terms of the pile diameter, reads $\frac{s}{D} = 8$

b. The concept of group efficiency is an appropriate method to estimate the axial capacity of pile groups:

i. True

ii. False

c. Considering the load capacity of pile groups as the sum of the individual load capacities of the single piles does not always represent a conservative analysis, although this assumption if often considered as an approximation of reality. For example in coarse-grained soil, the individual capacity of nondisplacement piles in a group is often found to be lower than the capacity estimated with reference to a single isolated case, involving an overestimation of the pile group capacity if calculated as the sum of the individual piles capacities.

d. The methods addressing the axial deformation of pile groups include:

i. The interaction factor method;

ii. The equivalent pier method;

iii. The equivalent raft method;

iv. The settlement ratio method;

v. The modified load−settlement method;

e. Considering w_j the additional displacement due to the loading of an adjacent pile and w_i the displacement of a single pile, the interaction factor reads:

i. $\boldsymbol{w_j/w_i}$

ii. w_i/w_j

iii. $w_j/(n_{EP}w_i)$

f. The damping effect played by a receiver pile on the deformation of a source pile in a pair:

i. Increases with the pile spacing

ii. Decreases with the pile spacing

iii. It is independent of the pile spacing

g. The corrected interaction factor for energy piles resting on finitely rigid soil strata may be expressed as

$$\boldsymbol{\Omega(\text{corrected}) = \Omega(\text{floating}) + F_b(\Omega(\text{end}-\text{bearing}) - \Omega(\text{floating}))}$$

where Ω(floating) is the interaction factor for predominantly floating energy piles, F_b is a correction factor indicating the effect of the bearing

stratum and Ω(end−bearing) is the interaction factor for predominantly end-bearing energy piles resting on infinitely rigid soil strata.

h. For energy piles subjected to mechanical loading, the interaction factor for predominantly end-bearing piles resting on infinitely rigid soil strata is lower than that for predominantly floating piles embedded in uniform soil deposits. In contrast, for energy piles subjected to thermal loading, the interaction factor for predominantly end-bearing energy piles resting on infinitely rigid soil strata is greater than that for predominantly floating energy piles embedded in uniform soil deposits. These phenomena are generally observed for any pile spacing and pile slenderness ratio.

i. Yes, the superposition principle can be employed to investigate the effects of the interactions caused by both mechanical and thermal loads among energy piles. The reason for this is that, although the response of energy piles to mechanical and thermal loads is different, as soon as the loading conditions are reversible the superposition principle can be applied to analyse the displacement field caused by any type of loading (e.g. mechanical or thermal).

j. In the case of piles subjected to mechanical loads, the superposition principle allows estimating the vertical head displacement w_k [m] of any pile in a group as

$$w_k = w_h^{1,m} \sum_{i=1}^{i=n_{EP}} P_i \Omega_{ik}^m$$

where $w_h^{1,m}$ [m] is the vertical head displacement of the source pile considered in a single isolated case and subjected to an applied mechanical load, P_i [N] is the applied mechanical load to the head of pile i and Ω_{ik}^m [−] is the interaction factor referring to the head of two piles subjected to mechanical loading in a pair corresponding to the centre-to-centre distance between pile i and pile k.

In the case of piles subjected to thermal loads, the superposition principle allows estimating the vertical head displacement w_k [m] of any pile in a group as

$$w_k = w_h^{1,th} \sum_{i=1}^{i=n_{EP}} \Delta T_i \Omega_{ik}^{th}$$

where $w_h^{1,th}$ [m] is the vertical head displacement of the source pile considered in a single isolated case and subjected to an applied temperature variation, ΔT_i [°C] is the applied temperature variation to pile k and Ω_{ik}^{th}

[−] is the interaction factor referring to the head of two piles subjected to thermal loading in a pair corresponding to the centre-to-centre distance between pile i and pile k.

k. Yes, the interaction factor charts referring to a Poisson's ratio of the soil $\nu_{soil} = 0.3$ can be employed to calculate the interaction factor for piles embedded in soil deposits with a different value of Poisson's ratio. This result can be achieved by employing the following expression:

$$\Omega = N_\nu \Omega_{\nu_{soil}=0.3}$$

where Ω [−] is the interaction for a general value of Poisson's ratio of the soil, N_ν [−] is a correction factor for the effect of the Poisson's ratio on the interaction among piles and $\Omega_{\nu_{soil}=0.3}$ [−] is the interaction factor for $\nu_{soil} = 0.3$.

l. The use of interaction factors for the case of piles in a homogeneous soil gives conservative estimates of the interaction for cases in which the soil deformation modulus increases with depth:

i. True

ii. False

iii. It depends on whether the influence of mechanical or thermal loading is considered

m. The development of interaction factor charts referring to isothermal soil deposits may be considered:

i. An effective approach to describe the interaction between piles in any type of soil deposit, provided that an appropriate unitary displacement of a single pile is considered in the analyses

ii. An effective approach to describe the interaction between piles in any type of soil deposit, irrespective of the unitary displacement of a single pile that is considered in the analyses

n. Based on the available parameters, $G_{soil} = 30$ MPa, so $\Lambda = 1000$ and $\Omega \approx 0.1$.

o. $w_k = w_i(1 + \Omega)$

p. The equilibrium equation along z written for an element with regards to a reference cylindrical coordinate system (r,θ, z) in which the effects of volume forces due to body loads are neglected, is

$$\frac{\partial \tau_{rz}}{\partial r} + \frac{\tau_{rz}}{r} + \frac{\partial \sigma_{zz}}{\partial z} = 0 \tag{1}$$

where $\tau_{rz} = \tau$ is the shear stress increment and $\sigma_{zz} = \sigma_z$ is the vertical stress increment. Eq. (1) inherently resorts to the assumption of an elastic

behaviour of the considered material, such that the effects due to body loads in the system are neglected and may be accounted for at any time due to the validity of the superposition principle. Neglecting these effects in the present application focuses on the only effects of mechanical and thermal loads.

The application of mechanical and thermal loads to energy piles indicates that $\partial\tau/\partial r \gg \partial\sigma/\partial z$. This phenomenon characterises regions of soil in the vicinity of the pile shaft. From this consideration, it follows that Eq. (1) may be approximated to become

$$\frac{\partial\tau}{\partial r} + \frac{\tau}{r} = 0 \tag{2}$$

Integration of Eq. (2), with reference to an element of the source pile, i, whose centre is located at a depth, z, from the surface yields the general solution for the shear stress in the soil as

$$\frac{\partial\tau}{\partial r} = -\frac{\tau}{r} \Rightarrow \frac{\partial\tau}{\tau} = -\frac{\partial r}{r} \Rightarrow \int_{\tau_i(z)}^{\tau} \frac{1}{\tau}\partial\tau = -\int_{R}^{r} \frac{1}{r}\partial r \Rightarrow [\ln(\tau)]_{\tau_i(z)}^{\tau} = -[\ln(r)]_{R}^{r}$$

$$\Rightarrow \ln\tau - \ln\tau_i(z) = -\ln(r) + \ln(R) \Rightarrow \ln\frac{\tau}{\tau_i(z)} = \ln\frac{R}{r} \Rightarrow \frac{\tau}{\tau_i(z)} = \frac{R}{r}$$

Finally

$$\tau(r,z) = \frac{\tau_i(z)R}{r} \tag{3}$$

The shear strain associated with the aforementioned shear stress can be computed according to the elastic theory as

$$\gamma = -\left(\frac{\partial w}{\partial r} + \frac{\partial u}{\partial z}\right) = \frac{\tau}{G_{soil}} \tag{4}$$

where u is the radial displacement and G_{soil} is the shear modulus of the soil. In the present problem, both u and w, respectively, depend only on r and z, and not on the angular coordinate, θ. This aspect arises because there is an invariance of the displacement field around the latter axis. Moreover, because no twist characterises the pile, there is no orthoradial component, v, in the displacement field.

The application of mechanical and thermal loads to energy piles indicates that $\partial w/\partial r \gg \partial u/\partial z$. This phenomenon characterises regions of soil in the

vicinity of the pile shaft. Together with the assumption of a negligible variation of $\partial\sigma/\partial z$, it physically represents a negligible interaction between different soil layers with depth. From the above consideration and the combination of Eqs (3) and (4), the first-order partial differential equation is found

$$\frac{\partial w}{\partial r} = -\frac{\tau_i(z)R}{rG_{soil}} \tag{5}$$

Integration of Eq. (5) yields the general solution for the vertical displacement of the soil as

$$\partial w = -\frac{\tau_i(z)R}{G_{soil}}\frac{1}{r}\partial r \Rightarrow \int_{w_i(z)}^{w(r,z)} \partial w = -\frac{\tau_i(z)R}{G_{soil}}\int_R^r \frac{1}{r}\partial r$$

$$\Rightarrow w(r,z) - w_i(z) = -\frac{\tau_i(z)R}{G_{soil}}(\ln r - \ln R) \Rightarrow w(r,z) - w_i(z) = -\frac{\tau_i(z)R}{G_{soil}}\ln\left(\frac{r}{R}\right)$$

Finally

$$w(r,z) = w_i(z) - \frac{\tau_i(z)R}{G_{soil}}\ln\left(\frac{r}{R}\right) \tag{6}$$

q. No, the two boundary conditions needed to correct the interaction factor to account for the stiffness of the receiver pile on the definition of this parameter via analytical models change for piles subjected to mechanical and thermal loading. This is due to the fact that, although the first boundary conditions referring to the pile head does not change, the second boundary condition does change. The first boundary condition is chosen with reference to the state of restraint that characterises the head of the receiver pile, irrespective of whether the pile is subjected to mechanical or thermal load. The second boundary condition needs to be preferably chosen by considering whether the source pile is subjected to mechanical or thermal loading. In the case of mechanical loading, the second boundary condition is chosen with reference to the base of the receiver pile. In the case of thermal loading, the second boundary condition is chosen with reference to the so-called null point of the shear stress of the receiver pile.

r. The evolution of the interaction factor associated with thermal loads can be considered approximately constant with depth, similarly to the evolution of the interaction factor associated with mechanical loads:

i. Yes, it can be considered constant with depth because the response of pile to thermal loads can be considered in a plane state of strain

ii. No, it cannot be considered constant with depth because the response of pile to thermal loads can be considered in a plane state of strain

s. The interaction factor characterising piles subjected to thermal loads can be greater than 1:

i. Yes, it can be greater than 1

ii. No, it cannot be greater than 1

t. When using the layer and continuous model in interaction factor analyses of energy piles embedded in soil deposits whose thermal expansion coefficient is in excess than that of the piles, a unitary pile displacement resulting from an analysis that accounts for the temperature sensitivity of the soil is needed:

i. Yes, because the layer and continuous models are incapable of accounting for this phenomenon

ii. No, because the layer and continuous model already provide the lower and upper boundaries of pile interaction and resulting displacement that may be expected in reality irrespective of the soil–pile thermal expansion coefficient ratio

u. Soil modulus values that are associated with high strain levels can be used to characterise:

i. The vertical displacement behaviour of the single piles composing any group

ii. The interactions between the piles composing any group

iii. Both of the previous subjects

v. The equivalent pier method can be applied for aspect ratios of the group and for normalised spacing between the piles of

i. $AR < 4$ and $s/D \leq 5$

ii. $AR > 4$ and $s/D \leq 5$

iii. $AR \leq 4$ and $s/D > 5$

iv. $AR > 4$ and $s/D > 5$

w. The basic concept behind the equivalent pier method is that the mechanical behaviour of any energy pile group can be reproduced with sufficient accuracy for practical purposes by modelling the group as a single equivalent pier whose material properties are a homogenisation of those characterising the actual pile group. This pier will also need to be characterised by a modified load-transfer relationship compared to that of a single isolated pile to account for group effects and interaction between piles.

x. The coupled use of the interaction factor and equivalent pier methods is particularly useful to analyse the displacement response of very large pile groups, by considering pile subgroups as equivalent piers and characterising the overall displacement response of the foundation through the interaction factor method.

y. The equivalent diameter of the pier, D_{eq}, for a group of end-bearing piles can be evaluated as

$$D_{eq} = \frac{2}{\sqrt{\pi}}\sqrt{A_g} = \frac{2}{\sqrt{\pi}}\sqrt{77.44} = 9.93 \text{ m}$$

where A_g is the plan area of the group and for a square group of energy piles is evaluated as

$$A_g = \left[\left(\sqrt{n_{EP}}-1\right)s+D\right]^2 = \left[\left(\sqrt{n_{EP}}-1\right)5D+D\right]^2 = \left[\left(\sqrt{9}-1\right)\cdot 5\cdot 0.8+0.8\right]^2 = 77.44 \text{ m}^2$$

The homogenised Young's modulus of the equivalent pier, E_{eq}, can be estimated as:

$$E_{eq} = \frac{A_{t,EP}E_{EP} + A_{soil}E_{soil}}{A_{t,EP}} = E_{EP}\frac{A_{t,EP}}{A_g} + E_{soil}\left(1 - \frac{A_{t,EP}}{A_g}\right)$$

$$= 30000\cdot\frac{4.52}{77.44} + 78\cdot\left(1 - \frac{4.52}{77.44}\right) = 1751.03 + 73.45 = 1824.48 \text{ MPa}$$

$$A_{t,EP} = \pi\frac{D^2}{4}n_{EP} = \pi\cdot\frac{0.8^2}{4}\cdot 9 = 4.52 \text{ m}^2$$

For the evaluation of the equivalent linear thermal expansion coefficient of the pier, α_{eq}, it is assumed that $X = \alpha_{soil}/\alpha_{EP} \leq 1$. Hence:

$$\alpha_{eq} = \alpha_{EP}$$

The shaft and base resistances of the group read

$$q_{s,eq} = q_s\frac{D}{D_{eq}}n_{EP} = 18.36\cdot\frac{0.8}{9.93}\cdot 9 = 13.31 \text{ kPa}$$

$$q_{b,eq} = q_b\frac{D^2}{D_{eq}^2}n_{EP} = 5302.44\cdot\frac{0.8^2}{9.93^2}\cdot 9 = 309.74 \text{ kPa}$$

The slopes of the load-transfer relationships that govern the interaction between the shaft and base of the group with the surrounding soil read

$$K_{s,eq} = 0.8\frac{E_M}{D}\zeta = 0.8\frac{E_M}{D}\frac{s}{L} = 0.8\frac{E_M}{D}\frac{5D}{L} = 0.8\cdot\frac{34650}{0.8}\cdot\frac{5\cdot 0.8}{20} = 6930\ \text{kPa}$$

$$K_{b,eq} = 4.8\frac{E_M}{D}\zeta = 4.8\frac{E_M}{D}\frac{s}{L} = 4.8\frac{E_M}{D}\frac{5D}{L} = 4.8\cdot\frac{34650}{0.8}\cdot\frac{5\cdot 0.8}{20} = 41{,}580\ \text{kPa}$$

To evaluate the slab stiffness, the following equation can be used:

$$K_{slab} = \frac{E_s\sqrt{B_{slab}L_{slab}}}{(1-\nu_{soil}{}^2)\rho_0} = \frac{78{,}000\cdot\sqrt{12\cdot 12}}{\left(1-0.3^2\right)\cdot 0.88} = 1{,}168{,}831\ \text{kN/m}$$

Hence, the stiffness of the slab per unit cross-sectional area of equivalent pier is

$$K^*_{slab} = \frac{K_{slab}}{A_{t,EP}} = \frac{1{,}168{,}831}{4.52} = 258{,}591\ \text{kPa/m}$$

The results obtained with the Thermo-Pile software are reported below.

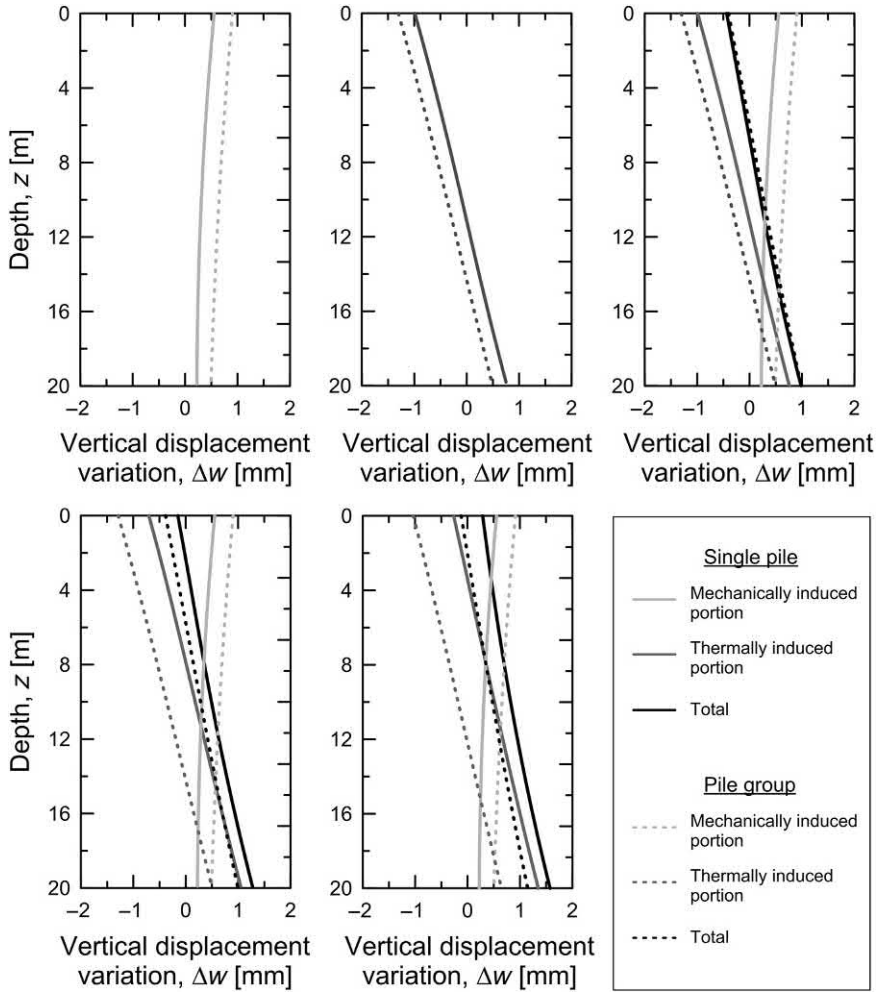
Depth, z [m]
0
4
8
12
16
20
−2
−1
0
1
2
Vertical displacement variation, Δw [mm]
Single pile
Mechanically induced portion
Thermally induced portion
Total
Pile group
Mechanically induced portion
Thermally induced portion
Total

CHAPTER 12

Numerical modelling of energy geostructures

12.1 Introduction

The analysis of the thermohydromechanical behaviour of energy geostructures requires the consideration of the relevant heat transfer, mass transfer and deformation phenomena that characterise the subsurface throughout the geothermal and structural support operation of such technologies. These phenomena take place within and around energy geostructures, and are associated with a different thermohydromechanical behaviour depending on the intrinsically different geometrical features, heat transfer potential and construction methods characterising such geostructures.

From the perspective of the geothermal heat exchanger role of energy geostructures, the following noteworthy aspects can be highlighted. The different geometrical features and related heat transfer potential involve energy piles representing an effective means for energy harvesting at the building scale, while energy tunnels and energy walls can be considered for energy harvesting from the building to the city scale (e.g. via district heating networks). Energy piles are in most applications completely bounded by an interface with a soil or rock deposit. In contrast, energy tunnels and energy walls are also characterised by an interface wherein airflows are encountered. The presence of an interface with air involves the possibility of harvesting aerothermal energy in addition to geothermal energy. This feature makes the energy exploitation achievable through energy tunnels and walls particularly flexible yet challenging, because different heat sources can be employed for the energy harvesting. Based on the previous aspects, the energy harvesting achievable via energy geostructures can involve (1) heat and mass transfer by convection in the built environment adjacent to the energy geostructure, (2) heat transfer dominated by conduction within the filling material of the geostructure and across the wall of the pipes, (3) heat and mass transfer dominated by convection within the pipes of the geostructure and (4) heat transfer dominated by conduction in the ground, unless a significant groundwater flow leads to convection dominated heat transfer. Phenomena (1)−(4) typically characterise energy geostructures such as energy tunnels and energy walls. Phenomena (2)−(4) usually characterise energy geostructures such as energy piles.

From the perspective of the structural support role of energy geostructures, the following aspects can be noted. The mechanics of energy geostructures such as energy

Analysis and Design of Energy Geostructures
DOI: https://doi.org/10.1016/B978-0-12-816223-1.00012-6

piles is typically characterised by a predominant axial character. In contrast, the mechanics of energy geostructures such as energy walls is characterised by a predominant flexural character. Strong perturbations of the stress and displacement fields can characterise the ground surrounding all types of energy geostructures because of the loadings associated with their construction or operation. These perturbations can cause reversible or irreversible deformations (e.g. in the ground surrounding energy geostructures). However, the relative significance of mechanical loads to thermal loads that is associated with the construction and operational phases of energy geostructures is much more pronounced for energy tunnels and walls compared to energy piles, for example.

Various critical aspects of the thermohydromechanical behaviour of energy geostructures can be effectively captured through analytical and semianalytical modelling approaches. However, with the progress of the analysis or design process, numerical modelling approaches become essential to obtain comprehensive information on the heat transfer, mass transfer and deformation phenomena that characterise the behaviour of energy geostructures.

This chapter focuses on the numerical modelling of the thermohydromechanical behaviour of energy geostructures for typical technical solutions and site conditions that can characterise such applications. The analysis resorts to the results of finite element and computational fluid dynamics simulations, and is devoted to expanding on the influence of factors that can significantly characterise the response of energy geostructures.

To this aim, *idealisations and assumptions* are presented first: in this context the objective is to propose a summary of the conceptual descriptions and hypotheses that can be employed for the numerical modelling of the heat transfer, mass transfer and deformation phenomena that occur within and around energy geostructures. Next, the *thermohydromechanical behaviour of energy piles, energy tunnels and energy walls* is addressed: the purpose of this part is to investigate the response of such geostructures for a variation in typical technical solutions and site conditions. Later, the *modelled and observed response* is commented: the objective of this part is to propose a summary of currently available numerical simulations of the observed behaviour of energy geostructures. Finally, *questions and problems* are proposed: the purpose of this part is to fix and test the understanding of the subjects covered in this chapter by addressing a number of exercises.

12.2 Idealisations and assumptions

The numerical modelling of the thermohydromechanical behaviour of energy geostructures typically differs depending on the following aspects: (1) the choice of the relevant modes of heat and mass transfers that are assumed to characterise energy

geostructures, and the model domains (or boundaries) wherein these phenomena are considered to occur; (2) the approach employed to account for the influence of the nonisothermal flow of the heat carrier fluid circulating in the pipes of energy geostructures; (3) the approach used to account for the influence of the nonisothermal airflow potentially present in built environments (e.g. located in the underground) adjacent to energy geostructures; (4) the selection of the constitutive model(s) used to address the behaviour of energy geostructures and (5) the extent of the coupling between the phenomena that are modelled in the analysis. Various mathematical formulations can be employed to address the previous aspects.

In the following, a specific thermohydromechanical formulation that may be considered for the analysis of heat transfer, mass transfer and deformation phenomena characterising energy geostructures is presented. This mathematical formulation is not common to all of the results presented in the following, but may be considered as a representative approach for simulating the behaviour of energy geostructures in many practical cases. Other mathematical formulations may be employed. Contractive strains, downward displacements, compressive stresses and increases in angles in the anticlockwise direction are considered to be positive.

The idealisation and assumptions governing the following mathematical formulation are as follows: (1) conduction heat transfer characterises the ground, the filling material of the energy geostructures and the pipe walls; convection heat and mass transfers characterise the heat carrier fluid circulating in the pipes as well as the air flowing in the built environment adjacent to relevant energy geostructures (e.g. energy tunnels and walls); (2) the nonisothermal fluid flow of the heat carrier fluid circulating in the pipes (modelled as lines) is explicitly considered in the analyses by solving the relevant governing equations along the pipes; (3) the nonisothermal airflow characterising underground built environments embedded by energy geostructures is implicitly considered in the analyses through appropriate boundary conditions; (4) the materials that constitute the energy geostructures and the surrounding ground are assumed to be isotropic, homogeneous and characterised by a linear thermoelastic behaviour; the displacements and deformations of these materials are described through a linear kinematic approach under quasistatic conditions (i.e. negligible inertial effects); the materials characterising the ground and the energy geostructures are characterised by pores that are fully filled with a fluid (e.g. water or air) and are assumed to have equivalent thermophysical properties that are given by the fluid and the solid phases; and (5) in this context, the master equations governing the heat transfer, mass transfer and deformation phenomena (continuity equation, momentum equation, energy conservation equation) are coupled numerically in a time-dependent framework.

The continuity and momentum equations allowing to model the flow of an incompressible fluid within the pipes read, respectively:

$$\nabla \cdot \left(A_p \rho_f \overline{v}_{f,i} \right) = 0 \tag{12.1}$$

and

$$\rho_f \left(\frac{\partial \overline{v}_{f,i}}{\partial t} \right) = -\nabla p_f - f_D \frac{\rho_f}{2 d_p} \left| \overline{v}_{f,i} \right| \overline{v}_{f,i} \tag{12.2}$$

where $\nabla\cdot$ represents the divergence operator, ∇ represents the gradient, $A_p = \pi r_{p,in}^2$ is the pipe cross-sectional area (defined by the internal pipe radius $r_{p,in} = 0.5 d_p$, where d_p is the hydraulic diameter of the pipe), ρ_f is the heat carrier fluid density, $\overline{v}_{f,i}$ is the average velocity vector of the fluid circulating in the pipes, t is the time, p_f is the heat carrier fluid pressure and f_D is the Darcy friction factor.

The energy conservation equation describing the convective−conductive heat transfer in the pipes for an incompressible fluid is evaluated over the lines representing the pipes (characterised by the curvilinear coordinate x_p). With this approach, a one-dimensional energy conservation equation for the circulating fluid is assumed and the influence of the actual pipe diameter is neglected in terms of heat transfer within the energy geostructure according to the following expression

$$\lambda_f \nabla^2 \overline{T}_f + f_D \frac{\rho_f}{2 d_p} \left| \overline{v}_{f,i} \right| \overline{v}_{f,i}^2 + \frac{\dot{q}_p}{A_p} = \rho_f c_{p,f} \frac{\partial \overline{T}_f}{\partial t} + \rho_f c_{p,f} \overline{v}_{f,i} \cdot \nabla \overline{T}_f \tag{12.3}$$

where λ_f, $c_{p,f}$ and $\overline{T}_f$ are the thermal conductivity, specific heat and mean temperature of the heat carrier fluid, respectively, and $\dot{q}_p$ represents the heat flux per unit length exchanged through the pipe wall given by

$$\dot{q}_p = U P_p \left(T_s - \overline{T}_f \right) \tag{12.4}$$

where U is an effective value of the pipe heat transfer coefficient, $P_p = 2\pi r_{p,in}$ is the wetted perimeter of the cross section and T_s is the temperature at the outer side of the pipe. The overall heat transfer coefficient, including the internal film resistance and the wall resistance, is evaluated as follows:

$$U = \frac{1}{\frac{1}{h_c} + \frac{r_{p,in}}{\lambda_p} \ln \left(\frac{r_{p,out}}{r_{p,in}} \right)} \tag{12.5}$$

where h_c is the convection heat transfer coefficient, λ_p is the thermal conductivity of the pipe and $r_{p,out}$ is the pipe outer radius. The convection heat transfer coefficient is evaluated through the Gnielinski formula (Gnielinski, 1976) for turbulent flow and the Colebrook equation (Fox et al., 1985; Munson et al., 1990).

The previous equations are solved for the pressure p_f, the velocity $\overline{v}_{f,i}$ and the temperature of the heat carrier fluid $\overline{T}_f$, and are coupled to the temperature field T obtained from the conductive energy conservation equation solved for the energy geostructure(s) and the surrounding ground.

The energy conservation equation allowing to model the purely conductive heat transfer within the energy geostructure(s) and the surrounding ground reads:

$$\lambda \nabla^2 T = \rho c_p \frac{\partial T}{\partial t} \tag{12.6}$$

where λ is the thermal conductivity of the material (determined via the porosity of the material, n, through the thermal conductivity of water λ_w or air λ_a and the thermal conductivity of the solid particles λ_s), ∇^2 represents the Laplacian operator, ρ is the density of the material (determined analogously through the density of water ρ_w or air ρ_a and the density of the solid particles ρ_s) and c_p is the specific heat of the material (determined analogously through the specific heat of water $c_{p,w}$ or air $c_{p,a}$ and the specific heat of the solid particles $c_{p,s}$).

The momentum conservation equation written in terms of a simplified indefinite equilibrium equation that neglects the influence of body forces reads

$$\nabla \cdot \sigma_{ij} = 0 \tag{12.7}$$

where σ_{ij} is the total stress tensor. The stress tensor can be expressed as

$$\sigma_{ij} = D_{ijkl}\left[\varepsilon_{kl} + \beta_{kl}(T - T_0)\right] \tag{12.8}$$

where D_{ijkl} is the elastic stiffness tensor, which contains the material parameters (i.e. Young's modulus, E, and Poisson's ratio, ν), ε_{kl} is the total strain tensor, β_{kl} is a vector that comprises the linear thermal expansion coefficient of the material, α, and $T - T_0 = \Delta T$ is the applied temperature variation.

Appropriate initial and boundary conditions are needed to solve the previous system of equations under time-dependent conditions. For the energy conservation equation, typical initial conditions involve a uniform temperature field in all the modelled domains, that is T_0. For the momentum conservation equation, zero initial perturbations in terms of displacement or stress are typically considered for the model domains. The influence of body forces (e.g. gravity) may be simulated.

Time-dependent evolutions of the inlet temperature, $\overline{T}_{in}$, and velocity, $\overline{v}_{in}$, of the heat carrier fluid circulating in the pipes are imposed as boundary conditions. Constant temperature, adiabatic, convection or radiation boundary conditions are applied on relevant boundaries. These conditions respectively read

$$T_\infty = T_0 \tag{12.9}$$

$$-n_i \cdot (-\lambda \nabla T) = 0 \tag{12.10}$$

$$\dot{q}_{conv} = h_c(T_\infty - T) \tag{12.11}$$

$$\dot{q}_{rad} = \epsilon \sigma_{SB}(T_\infty^4 - T^4) \tag{12.12}$$

where T_∞ is the temperature of the relevant far field boundary, n_i is the outward vector from the relevant boundary, ϵ is the surface emissivity and σ_{SB} is the Stefan–Boltzmann constant. Typically, T_∞ is considered to coincide with the air temperature T_a. In general: Eq. (12.9) is employed for boundaries that are considered to be at a given uniform initial temperature; Eq. (12.10) is employed to prescribe no heat flux across a boundary and involves considering an ideal thermal insulation on the selected boundary; Eq. (12.11) is employed to reproduce a nonisothermal flow occurring over a boundary without the need of explicitly modelling it through computational fluid dynamics tools; and Eq. (12.12) is employed to reproduce a radiation phenomenon over a boundary.

Restrictions are applied to both the vertical and horizontal displacements on the bases of the models (i.e. pinned boundary) and to the horizontal displacements on the sides (i.e. roller boundaries). The following equation is used for the previous purpose

$$u_i = \mathcal{F}_i(\mathcal{H}) \tag{12.13}$$

where u_i is the displacement vector, $\mathcal{F}_i$ is a vector containing prescribed displacement functions and $\mathcal{H}$ is each of the points of the bounding surface at which Eq. (12.13) needs to be satisfied.

Examples of the application of the previous initial and boundary conditions to numerical models of energy piles, energy tunnels and energy walls are reported in Fig. 12.1.

Some remarks are worth noting with respect to the previous mathematical expressions:

1. At least in principle, time-dependent numerical simulations allow modelling the response of energy systems for any timescale. In practice, many numerical simulations addressing the geothermal operation of energy geostructures (similar to other heat exchangers) employ simplified thermal loading paths until steady thermal conditions are reached. In other words, the geothermal operation of energy geostructures is not modelled for the actual duration that is likely to be expected in practice (e.g. several decades), but various 'short-term' simulations are run to address the response of the considered heat exchangers (Cousin et al., 2019). The rationale for this approach is that, according to the superposition principle

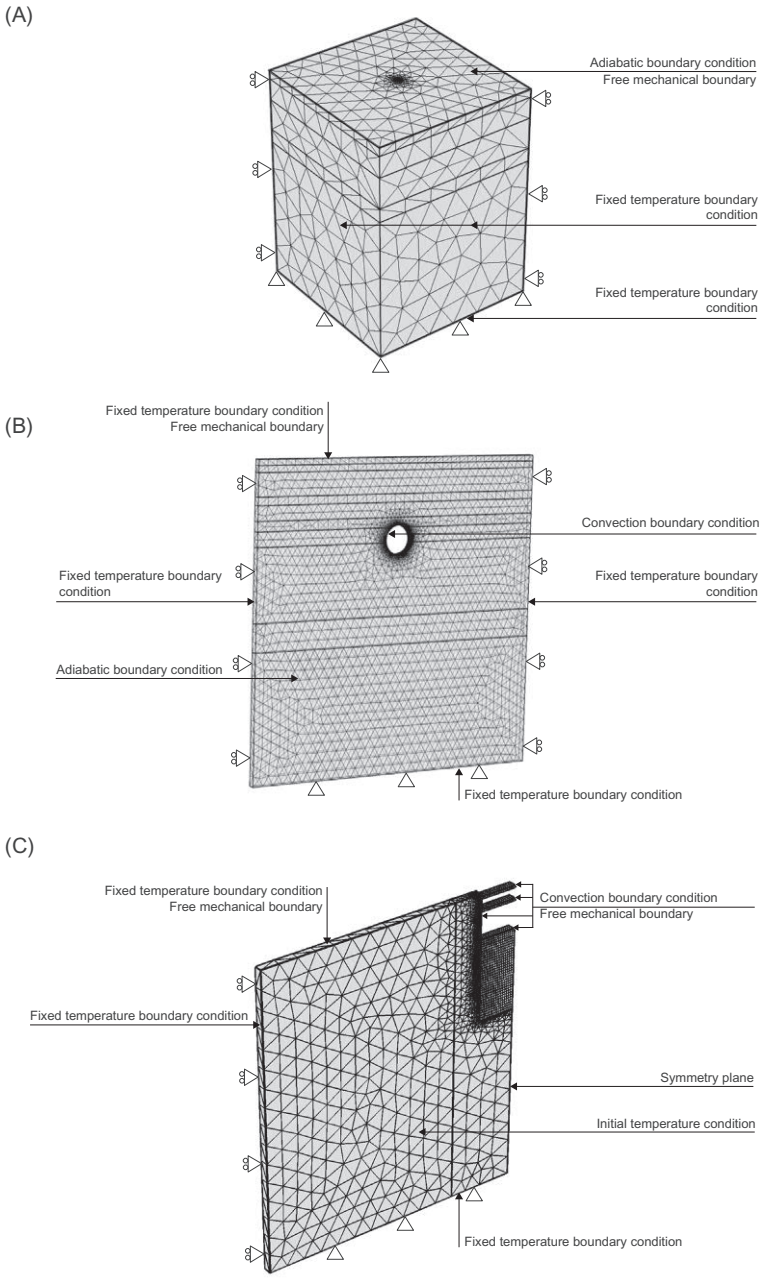

Figure 12.1 Examples of boundary and initial conditions employed to simulate aspects involved with the structural support and geothermal operation of (A) energy piles, (B) energy tunnels and (C) energy walls.

(cf. Chapter 9, Analytical modelling of transient heat transfer), the transient thermohydraulic behaviour of geothermal heat exchangers can be reproduced by the superposition of numerous steady responses.

2. The rationale for neglecting the influence of body forces when dealing with elastic problems is that their effect can be superimposed at any time based on the superposition principle (cf. Chapter 4, Deformation in the context of energy geostructures). Dealing with elastic problems also involves any load of the same magnitude but of opposite sign (e.g. a temperature variation of $\Delta T = 10°C$ or $-10°C$) inducing a symmetrical (equal in absolute value) mechanical response for the modelled system (Rotta Loria and Laloui, 2016).

12.3 Thermohydromechanical behaviour of energy piles

12.3.1 General

In the following, the response of energy piles is expanded for a variation in (1) the pipe configuration, (2) the pile slenderness ratio, (3) the heat carrier fluid flow rate, (4) the heat carrier fluid mixture composition, (5) the soil–pile thermal expansion coefficient ratio and (6) the loading magnitude and sequence.

12.3.2 Influence of the pipe configuration

The configuration of the pipes embedded within energy piles probably represents the technical solution that most influences the thermohydromechanical behaviour of such geothermal heat exchangers (Batini et al., 2015). Different pipe configurations involve a different length and number of pipes installed in energy piles, thus influencing the thermal resistance of such geothermal heat exchangers.

Installing a greater number of pipes in energy piles appears to be preferable for maximising the heat transfer (Loveridge and Powrie, 2014; Cecinato and Loveridge, 2015). Therefore a double U-pipe configuration (series connection) or a W-shaped pipe configuration should always be preferable to a single U-shaped pipe configuration (Gao et al., 2008a,b; Park et al., 2013; Gashti et al., 2014; Yoon et al., 2015; Bezyan et al., 2015; Batini et al., 2015; Zhao et al., 2016; Carotenuto et al., 2017). Compared to the previous pipe configurations, the spiral-shaped pipe configuration generally appears superior from the perspective of the energy harvesting (Man et al., 2010; Zarrella et al., 2013; Go et al., 2014; Yoon et al., 2015; Bezyan et al., 2015; Zhao et al., 2016, 2017; Park et al., 2016; Carotenuto et al., 2017). The reason for the previous result can be associated with the greater pipe length installed in energy piles for the same available volume. The benefits associated with the more significant heat transfer that can be achieved with a spiral-shaped pipe configuration may however be

hindered by the greater difficulties associated with its installation compared to a W-shaped pipe configuration, for example.

For any given pipe configuration, careful determination of the appropriate pipe embedment, spacing or pitch (for spiral pipes) should be foreseen because this aspect markedly influences the energy that can be harvested from the ground (Loveridge and Powrie, 2014; Cecinato and Loveridge, 2015; Bezyan et al., 2015; Park et al., 2016; Zhao et al., 2017). Inappropriate pipe embedment can yield to a higher thermal resistance, while unsuitable pipe spacing or pitches can involve thermal interactions between the pipes. Both of the previous results are associated with a negative effect on the energy yield. The installation depth associated with a thermally active surface of pipes should also be carefully determined based on the site and geostructure characteristics (Park et al., 2017). The ground surface boundary conditions can profoundly influence the thermohydromechanical behaviour of energy piles (Fadejev and Kurnitski, 2015; Bidarmaghz et al., 2016). The previous considerations are noteworthy for general geothermal heat exchangers.

In the following, the influence of the pipe configuration on the thermohydromechanical behaviour of energy piles is expanded with reference to the results of Batini et al. (2015). A single U-, a double U- and a W-shaped pipe configuration are considered.

Fig. 12.2 presents an example of the influence of the pipe configuration on the axial evolution of the temperature variation along energy piles over time. In the

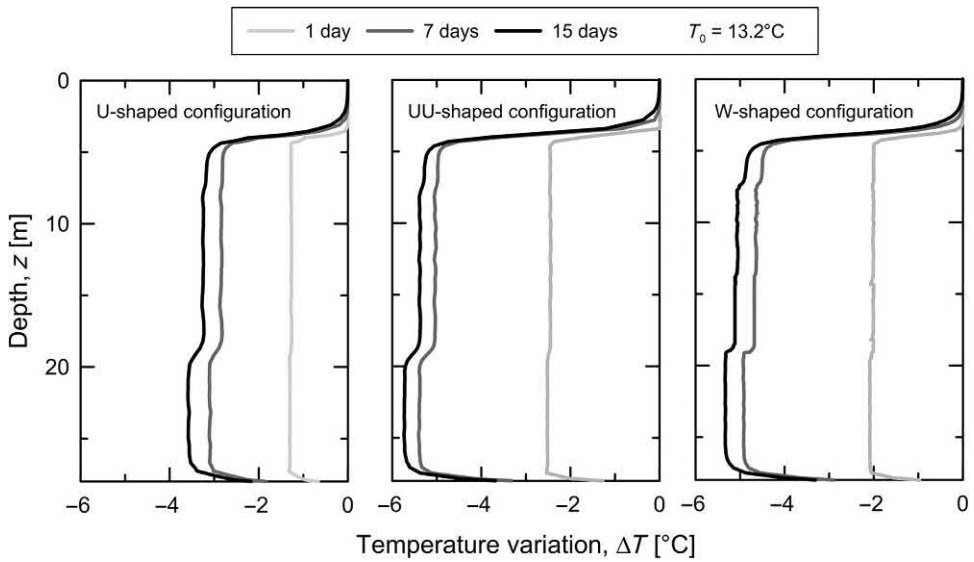

Figure 12.2 Axial temperature evolution along an energy pile equipped with a single U-, a double U- and a W-shaped pipe configuration. *Redrawn after Batini, N., Rotta Loria, A.F., Conti, P., Testi, D., Grassi, W., Laloui, L., 2015. Energy and geotechnical behaviour of energy piles for different design solutions. Appl. Therm. Eng. 86 (1), 199–213.*

considered case study, no remarkable temperature variations characterise the energy pile in correspondence to the region in which the pipes are thermally insulated (i.e. within the shallower 4 m). The heat carrier fluid circulating in the pipe(s) is characterised by a constant inflow velocity and temperature over time of $\overline{v}_{in} = 0.2$ m/s and $\overline{T}_{in} = 5°C$, respectively. These conditions cause temperature variations over time along the energy pile. However, the temperature distribution along the axis of the energy pile does not remarkably vary between $t = 7$ and 15 days, indicating that in the considered case study the thermal conditions inside the pile approach a steady scenario from the first week of operation onwards. Greater temperature variations are observed in correspondence with the soil layers characterised by a lower thermal conductivity. A lower heat transfer with the ground occurs in those settings and a more pronounced amount of heat remains within the energy pile. The highest temperature variation is reached with the double U-shaped pipe configuration because it involves the highest quantity of cold heat carrier fluid in the heat exchange process.

The evolution of axial stress induced by the previous temperature variations along the energy piles are shown in Fig. 12.3. Maximum axial stress values of $\Delta\sigma_z = -800$, -1400 and -1300 kPa are observed for the single U-, double U- and W-shaped pipe configurations, respectively. The greatest stress variations are associated with the highest temperature variations along the pile depending on the pipe configuration.

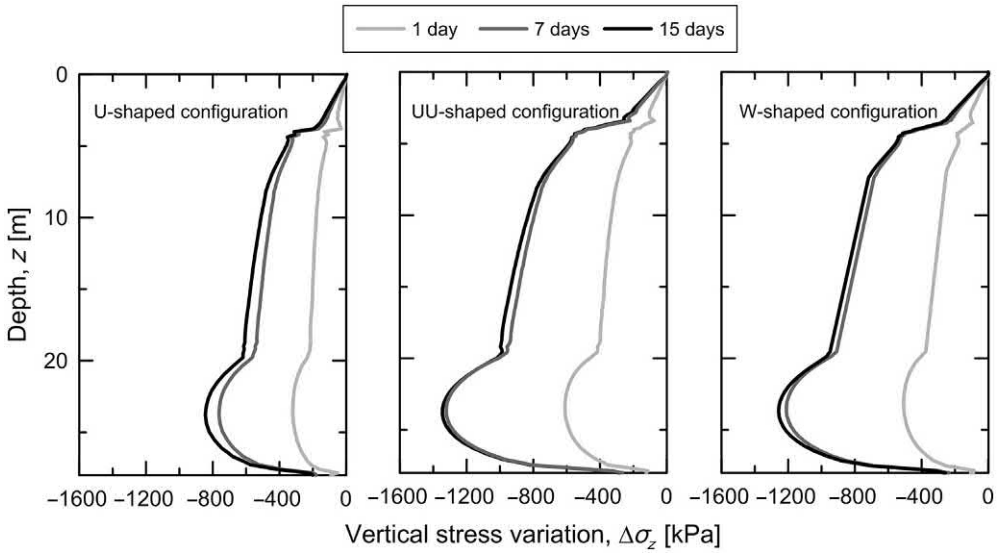

Figure 12.3 Axial stress evolution caused by temperature variations along an energy pile equipped with a single U-, a double U- and a W-shaped pipe configuration. *Redrawn after Batini, N., Rotta Loria, A.F., Conti, P., Testi, D., Grassi, W., Laloui, L., 2015. Energy and geotechnical behaviour of energy piles for different design solutions. Appl. Therm. Eng. 86 (1), 199–213.*

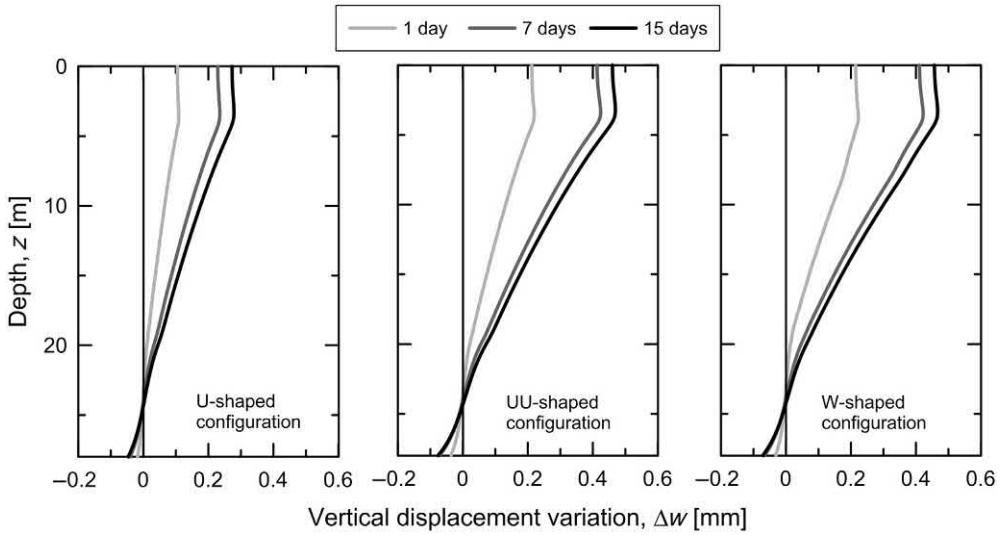

Figure 12.4 Axial displacement evolution caused by temperature variations along an energy pile equipped with a single U-, a double U- and a W-shaped pipe configuration. *Redrawn after Batini, N., Rotta Loria, A.F., Conti, P., Testi, D., Grassi, W., Laloui, L., 2015. Energy and geotechnical behaviour of energy piles for different design solutions. Appl. Therm. Eng. 86 (1), 199–213.*

The stress variation values are equal to zero at the pile head because of the absence of any restraint.

Fig. 12.4 shows the axial evolution of the vertical displacement associated with each of the previously considered pipe configurations. Consistent with the distributions of the temperature and stress, maximum pile head settlements of $\Delta w = 0.28$, 0.47 and 0.46 mm are observed for the single U-, double U- and W-shaped pipe configurations, respectively. The null point, which represents the setting where zero thermally induced displacement occurs within the energy pile (Laloui et al., 2003), is in all cases close to pile toe because of the significant restraint provided by the bottom soil layer.

Fig. 12.5 shows an example of the influence of the pipe configuration on the temperature evolution of the heat carrier fluid along the pipe(s) length, x_p. The heat carrier fluid temperature linearly increases along the flow direction according to its lower temperature level compared to that of the ground. The slight changes of the slope of the curves indicate that this increase is not uniform, as it can be expected in practice. The reason for this is because the progressive increase of the heat carrier fluid temperature along the pipe reduces the heat transfer potential with the ground, thus leading to smaller relative temperature variations. The outflow fluid temperature, $\overline{T}_{out}$, is higher for the single U-shaped pipe configuration with respect to the double U-shaped configuration. The previous phenomenon is attributed to a thermal interference that

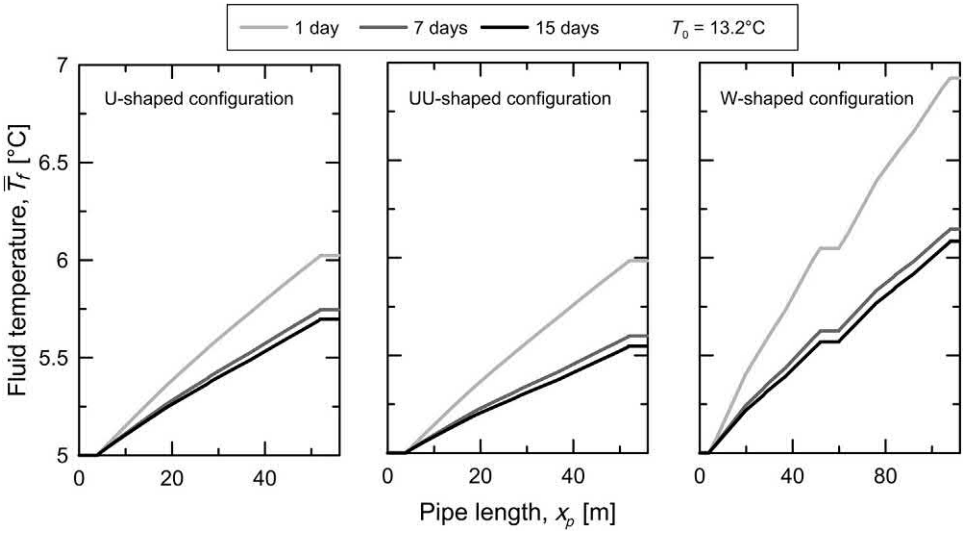

Figure 12.5 Temperature evolution of the heat carrier fluid along the pipe of an energy pile equipped with a single U-, a double U- and a W-shaped pipe configuration. *Redrawn after Batini, N., Rotta Loria, A.F., Conti, P., Testi, D., Grassi, W., Laloui, L., 2015. Energy and geotechnical behaviour of energy piles for different design solutions. Appl. Therm. Eng. 86 (1), 199–213.*

occurs between the pipes characterising the energy pile equipped with a double U-shaped pipe configuration. The highest temperature increase is obtained for the W-shaped pipe configuration.

An example of the influence of the pipe configuration on the trend of thermal power harvested from energy piles equipped with a single U-, a double U- and a W-shaped pipe configuration is shown in Fig. 12.6. Complementary data referring to a geothermal operation of $t = 15$ days are summarised in Table 12.1. A decrease of the thermal power per metre length of pile, $\dot{q}_l = \dot{Q}/L$, can be observed over time. Higher absolute values of thermal powers are obtained through the double U- and W-shaped pipe configurations, whereas a lower thermal power is associated with the single U-shaped pipe configuration. After $t = 15$ days, the energy pile equipped with the double U-shaped pipe configuration has a 57% higher heat transfer rate than that characterising the same pile equipped with a single U-shaped pipe configuration. However, the double U-shaped pipe configuration is only 3% more efficient than the W-shaped pipe configuration, being thus 54% more efficient than the same pile equipped with a single U-shaped pipe configuration. According to Batini et al. (2015), the W-shaped pipe configuration should be considered the best trade-off among the considered design solutions, owing to (1) a significantly higher energy extraction with respect to the single U-shaped pipe configuration, which justifies its higher installation cost, and (2) a negligibly lower energy extraction with respect to the double U-shaped pipe

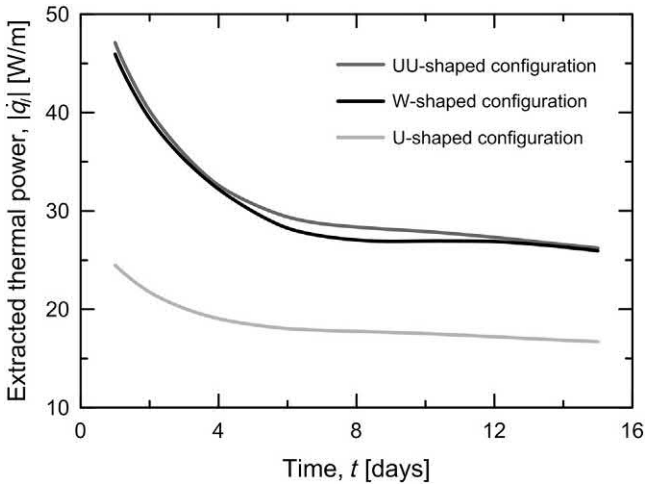

Figure 12.6 Trends of the thermal power extracted from the ground via an energy pile equipped with a single U-, a double U- and a W-shaped pipe configuration. *Redrawn after Batini, N., Rotta Loria, A.F., Conti, P., Testi, D., Grassi, W., Laloui, L., 2015. Energy and geotechnical behaviour of energy piles for different design solutions. Appl. Therm. Eng. 86 (1), 199–213.*

Table 12.1 Thermohydraulic data characterising an energy pile equipped with a single U-, a double U- and a W-shaped pipe configuration.

Pipe configuration	Outflow temperature, $\overline{T}_{out}$ [°C]	Temperature variation, $\overline{\Delta T}$ [°C]	Temperature at the pile–soil interface, $\overline{T}_{s-p}$ [°C]	Heat exchanger effectiveness, ϵ_{ghe} [–]	Volumetric flow rate, $\dot{V}$ [L/min]	Thermal power per unit length, $\lvert\dot{q}_l\rvert$ [W/m]
Single U-shaped	5.70	0.70	10.73	0.122	9.7	16.9
Double U-shaped	5.55	0.55	9.06	0.135	19.3	26.5
W-shaped	6.08	1.08	9.15	0.260	9.7	26.1

Source: Data from Batini, N., Rotta Loria, A.F., Conti, P., Testi, D., Grassi, W., Laloui, L., 2015. Energy and geotechnical behaviour of energy piles for different design solutions. Appl. Therm. Eng. 86 (1), 199–213.

configuration, operating via double of the volumetric flow rate, $\dot{V}$ (thus entailing a significantly lower pumping power). The reason for the similar thermal behaviour of the energy piles equipped with a double U-shaped and a W-shaped pipe configuration is associated with the low effectiveness of these relatively short heat exchangers, ϵ_{ghe}.

12.3.3 Influence of the pile slenderness ratio

The pile slenderness ratio can be varied through a modification of the pile diameter or length (Loveridge and Powrie, 2014; Cecinato and Loveridge, 2015; Batini et al., 2015;

Carotenuto et al., 2017). The increase of the slenderness ratio of energy piles results in an approximately linear increase of the exchanged heat, independent of the configuration of the pipes (Batini et al., 2015). This phenomenon influences the thermal power that can be exchanged per metre length of energy pile.

Fig. 12.7 shows the influence of the pile slenderness ratio on the axial evolution of temperature variation along energy piles characterised by different slenderness ratios L/D, where D is the pile diameter, with reference to the results of Batini et al. (2015). Energy piles characterised by slenderness ratios of $L/D = 10$, 20, 31 and 40 and equipped with a single U-, a double U- and a W-shaped pipe configuration are considered after a geothermal operation of $t = 15$ days. The depth from surface, z, is normalised by the energy pile length, L. Different temperature evolutions with depth are observed for the various slenderness ratios depending on the relative influence of the thermal properties of the various soil layers and the extent of the region in which the pipes are thermally insulated with respect to the total pile length. The highest temperature variations are obtained for the energy pile characterised by the double U-shaped pipe configuration. This phenomenon is attributed to the highest quantity of cold heat carrier fluid involved in the heat exchange process for the energy pile equipped with a double U-shaped pipe configuration compared to the single U- and W-shaped pipe configurations.

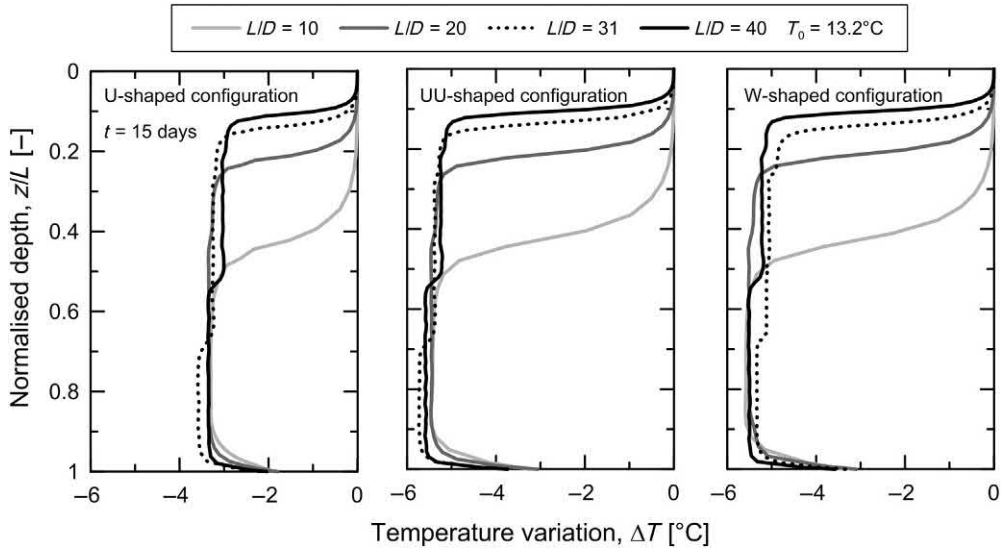

Figure 12.7 Axial temperature evolution along energy piles equipped with a single U-, a double U- and a W-shaped pipe configuration for different pile slenderness ratios. *Redrawn after Batini, N., Rotta Loria, A.F., Conti, P., Testi, D., Grassi, W., Laloui, L., 2015. Energy and geotechnical behaviour of energy piles for different design solutions. Appl. Therm. Eng. 86 (1), 199–213.*

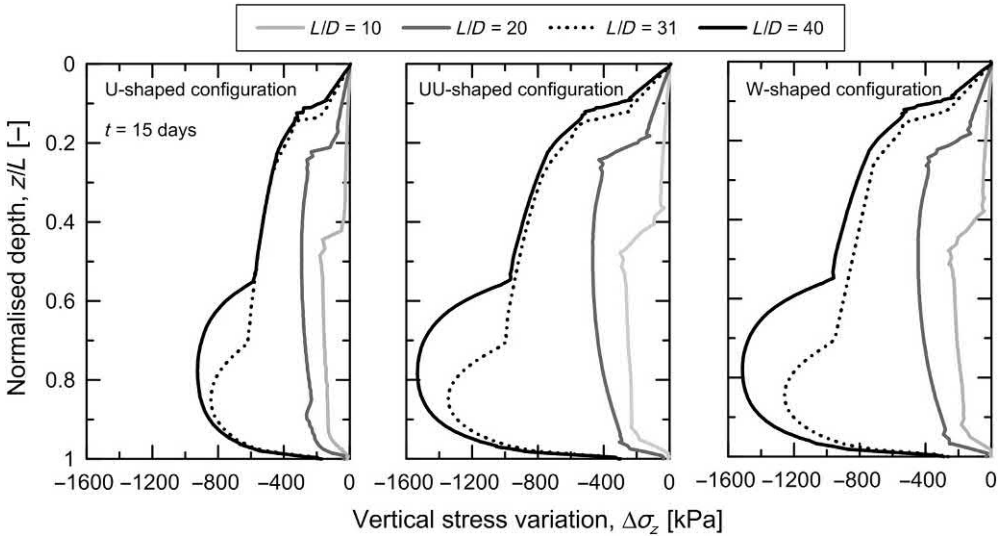

Figure 12.8 Axial stress evolution caused by temperature variations along energy piles equipped with a single U-, a double U- and a W-shaped pipe configuration for different pile slenderness ratios. *Redrawn after Batini, N., Rotta Loria, A.F., Conti, P., Testi, D., Grassi, W., Laloui, L., 2015. Energy and geotechnical behaviour of energy piles for different design solutions. Appl. Therm. Eng. 86 (1), 199–213.*

The evolution of axial stress induced by the previous temperature variations along the energy piles are shown in Fig. 12.8. Lower and more homogeneous distributions of thermally induced axial stress are observed for the lower slenderness ratios. This result is associated with (1) the different bearing behaviour that characterises the energy pile for the various slenderness ratios (i.e. predominantly frictional down to a depth corresponding to $L/D = 18$ and predominantly end-bearing beyond this depth) and (2) the impact of the thermal properties of the various soil layers on the heat exchange process and the related thermally induced stress.

Fig. 12.9 shows the axial evolution of the vertical displacement associated with each of the previously considered pile slenderness ratios. The null point location moves downwards for an increase in the slenderness ratio L/D because of the more pronounced influence of the base restraint. Upper bound values of axial head settlements caused by the imposed temperature variations of $\Delta w = 0.3$, 0.7 and 0.65 mm are observed for the slenderness ratio of $L/D = 36$ and a single U-, a double U- and a W-shaped pipe configuration, respectively. Lower bound values of $\Delta w = 0.27$, 0.47 and 0.47 mm are observed for the slenderness ratio of $L/D = 9$ and the same pipe configurations.

Fig. 12.10 shows an example of the influence of the pile slenderness ratio on the temperature evolution of the heat carrier fluid along the pipe(s) of energy piles

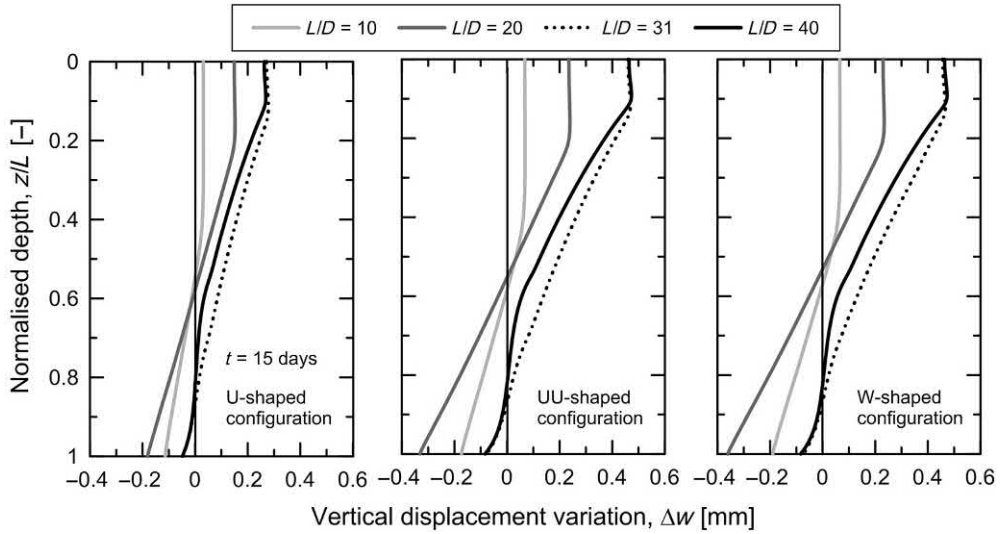

Figure 12.9 Axial displacement evolution caused by temperature variations along energy piles equipped with a single U-, a double U- and a W-shaped pipe configuration for different pile slenderness ratios. *Redrawn after Batini, N., Rotta Loria, A.F., Conti, P., Testi, D., Grassi, W., Laloui, L., 2015. Energy and geotechnical behaviour of energy piles for different design solutions. Appl. Therm. Eng. 86 (1), 199–213.*

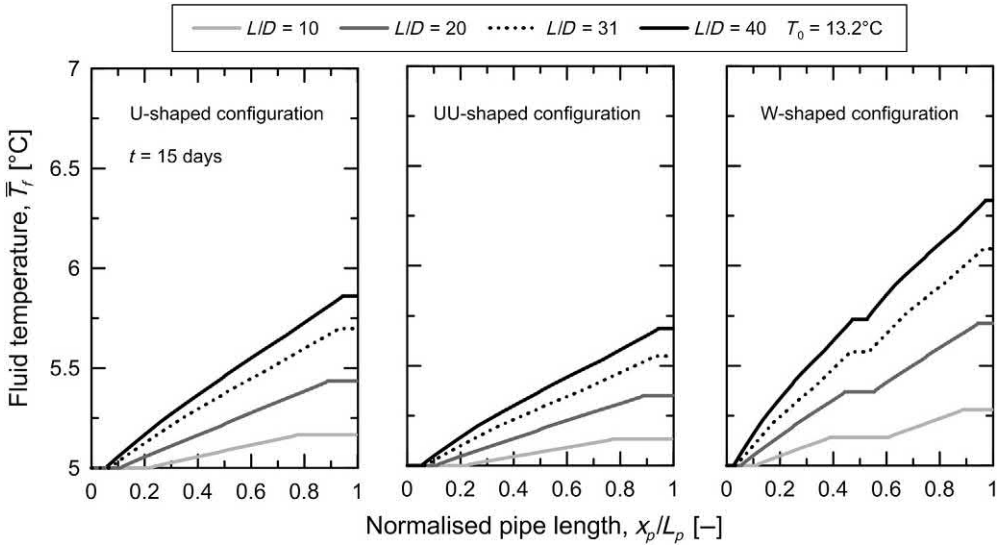

Figure 12.10 Temperature evolution of the heat carrier fluid along the pipe of energy piles equipped with a single U-, a double U- and a W-shaped pipe configuration for different pile slenderness ratios. *Redrawn after Batini, N., Rotta Loria, A.F., Conti, P., Testi, D., Grassi, W., Laloui, L., 2015. Energy and geotechnical behaviour of energy piles for different design solutions. Appl. Therm. Eng. 86 (1), 199–213.*

characterised by a single U-, a double U- and a W-shaped pipe configuration, after a geothermal operation of $t = 15$ days. The curvilinear coordinate describing the pipe axis, x_p, is normalised by the total pipe length, L_p. The temperature of the heat carrier fluid circulating in the pipes increases with the aspect ratio of the pile due to the increase in the heat transfer surface. This phenomenon is observed irrespective of the considered pipe configuration. Complementary data related to the same time interval analysed above are presented in Table 12.2. In the considered case study, the thermal power extracted from the ground via energy piles equipped with a double U-shaped pipe configuration is always larger than that associated (in order) with energy piles equipped with a W- and single U-shaped pipe configuration, irrespective of the pile slenderness ratio. Doubling the energy pile slenderness ratio from 10 to 20 involves an increase of the thermal power extraction between 152% and 170% depending on the configuration of the pipes. Doubling the energy pile slenderness ratio from 20 to 40 results in a lower relative increase between 87% and 100%, which can be attributed to the tendency of the heat exchanger to become saturated from a thermal perspective with the increase in the heat transfer surface.

Charts summarising the influence of the pipe configuration and the pile slenderness ratio are presented in Figs 12.11–12.14 with reference to the results of Achich (2018). Values of thermal power that can be harvested from energy piles of varying diameters when steady thermal conditions are achieved within such foundations are depicted for varying pipe configurations and values of effective thermal conductivity of the ground. Absolute values of thermal power extracted from the ground via energy piles characterised by a diameter ranging from $D = 0.5$ to 1.2 m and a length ranging from $L = 10$ to 50 m are comprised between approximately $|\dot{q}_l| = 30–70$ W/m.

Increasing the number of U-loops in energy piles does not necessarily lead to higher values of thermal power because of thermal interactions occurring between the pipes. For the various pile lengths, pile diameters and pipe configurations considered, a successive increase in the effective thermal conductivity of the ground of 0.5 W/(m °C) from a value of $\lambda_{soil} = 1.5$ W/(m °C) to a value of $\lambda_{soil} = 3.0$ W/(m °C) results in an average increase of thermal power harvested via the energy piles of 14.2% [for $\lambda_{soil} = 1.5–2.0$ W/(m °C)], 13.6% [for $\lambda_{soil} = 2.0–2.5$ W/(m °C)] and 9% [for $\lambda_{soil} = 2.5–3$ W/(m °C)]. In other words, doubling the effective thermal conductivity of the ground from $\lambda_{soil} = 1.5–3.0$ W/(m °C) can improve the thermal power harvested via energy piles of approximately 40%.

12.3.4 Influence of the heat carrier fluid flow rate

The flow rate of the heat carrier fluid circulating in the pipes can be varied through a modification of the inner pipe diameter, d_p, or the fluid velocity, $\overline{v}_{in}$. Increasing the flow rate of the heat carrier fluid circulating in the pipes yields to a more significant

Table 12.2 Thermohydraulic data characterising energy piles equipped with a single U-, a double U- and a W-shaped pipe configuration for different pile slenderness ratios.

Slenderness ratio, L/D [−]	Outflow temperature, $\overline{T}_{out}$ [°C]	Temperature variation, $\overline{\Delta T}$ [°C]	Temperature at the pile−soil interface, $\overline{T}_{s-p}$ [°C]	Heat exchanger effectiveness, ϵ_{ghe} [−]	Volumetric flow rate, $\dot{V}$ [L/min]	Thermal power per unit length, $\lvert\dot{q}_l\rvert$ [W/m]
Single U-shaped pipe						
10	5.17	0.17	10.85	0.028	9.7	12.5
20	5.44	0.44	10.71	0.077	9.7	16.5
31	5.70	0.70	10.73	0.122	9.7	16.9
40	5.86	0.86	10.65	0.152	9.7	16.1
Double U-shaped pipes						
10	5.14	0.14	9.20	0.032	19.3	20.3
20	5.35	0.35	9.05	0.086	19.3	26.3
31	5.55	0.55	9.06	0.135	19.3	26.5
40	5.69	0.69	8.80	0.182	19.3	25.9
W-shaped pipe						
10	5.28	0.28	9.02	0.070	9.7	21.0
20	5.71	0.71	8.94	0.180	9.7	26.6
31	6.08	1.08	9.15	0.260	9.7	26.1
40	6.33	1.33	8.82	0.347	9.7	24.9

Source: Data from Batini, N., Rotta Loria, A.F., Conti, P., Testi, D., Grassi, W., Laloui, L., 2015. Energy and geotechnical behaviour of energy piles for different design solutions. Appl. Therm. Eng. 86 (1), 199−213.

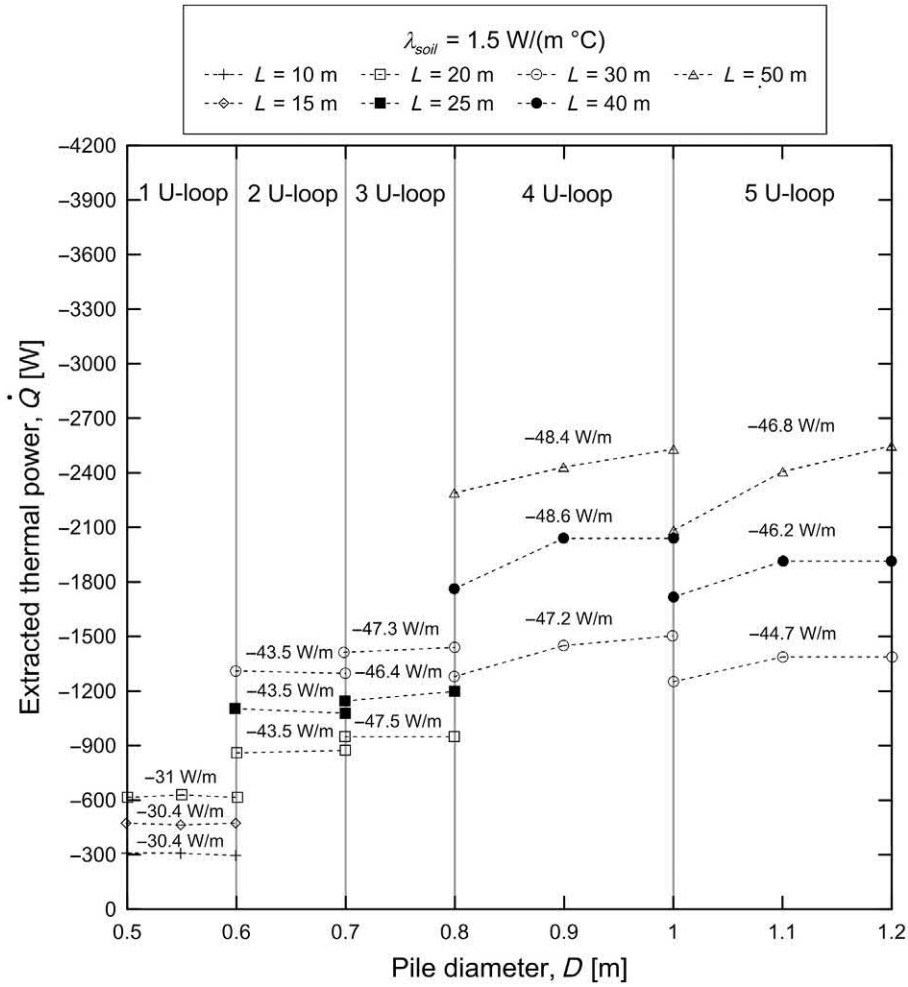

Figure 12.11 Thermal power extracted from energy piles of different diameter and length, which are equipped with varying pipe configurations, in a uniform soil deposit of $\lambda_{soil} = 1.5$ W/(m °C). *Redrawn after Achich, A., 2018. Numerical simulation of deck de-icing using energy pile systems (M.Sc. degree). Laboratory of Soil Mechanics, Swiss Federal Institute of Technology in Lausanne, Lausanne.*

amount of exchanged heat with the surrounding environment (Gao et al., 2008a; Loveridge and Powrie, 2014; Cecinato and Loveridge, 2015; Batini et al., 2015; Cui and Zhu, 2017; Carotenuto et al., 2017). Therefore the heat carrier fluid flow rate circulating in the pipes can have a remarkable influence on the thermohydraulic behaviour of energy piles. However, a flow rate increase does not necessarily have a positive influence of the efficiency of energy systems. Aspects related to the interplay between the electrical power required to run the heat pump for varying flow rates and the cost

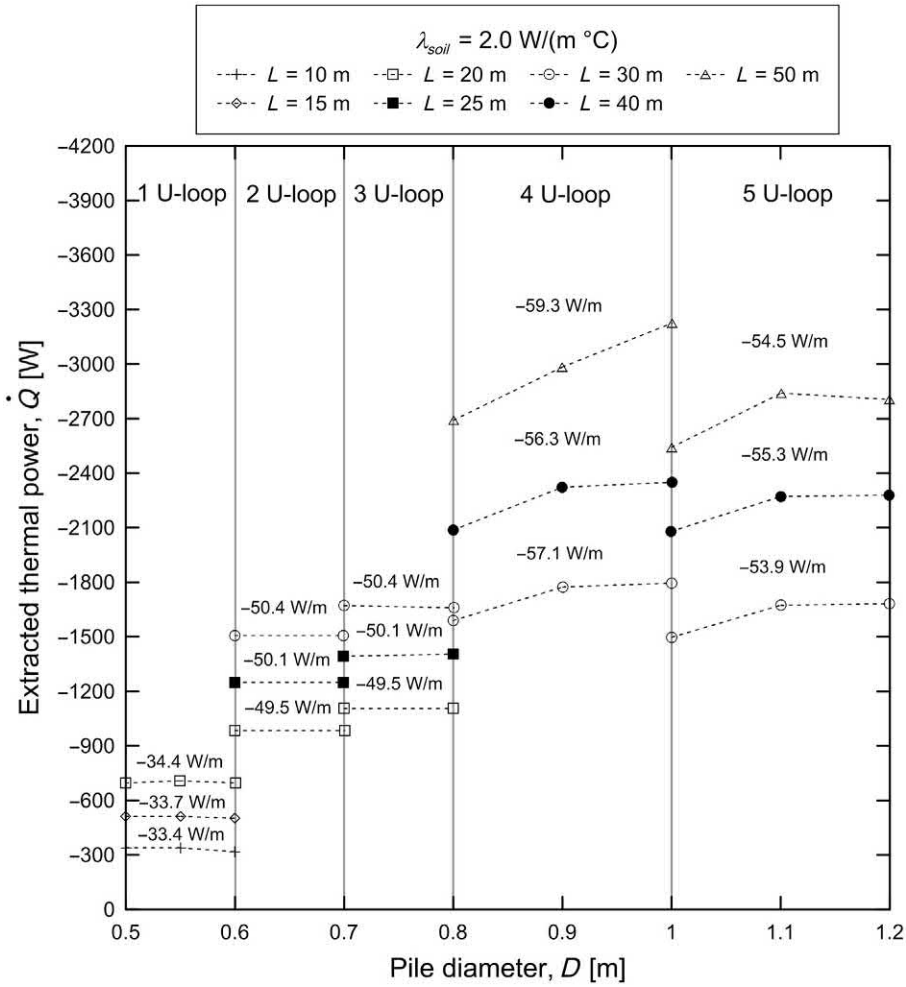

Figure 12.12 Thermal power extracted from energy piles of different diameter and length, which are equipped with varying pipe configurations, in a uniform soil deposit of $\lambda_{soil} = 2.0$ W/(m °C). *Redrawn after Achich, A., 2018. Numerical simulation of deck de-icing using energy pile systems (M.Sc. degree). Laboratory of Soil Mechanics, Swiss Federal Institute of Technology in Lausanne, Lausanne.*

of the considered solution should be considered to define the optimal flow rate. In contrast to the remarkable role played by a variation of the heat carrier fluid flow rate on the thermohydraulic behaviour of energy piles, the considered variable plays a negligible role on the mechanical behaviour of such geostructures (Batini et al., 2015).

In the following, the influence of the flow rate of the heat carrier fluid circulating in the pipes on the thermohydromechanical behaviour of energy piles is expanded with reference to the results of Batini et al. (2015). Flow rates of the heat carrier fluid circulating in the pipes associated with pipe diameters of $d_p = 25$, 32 and 40 mm

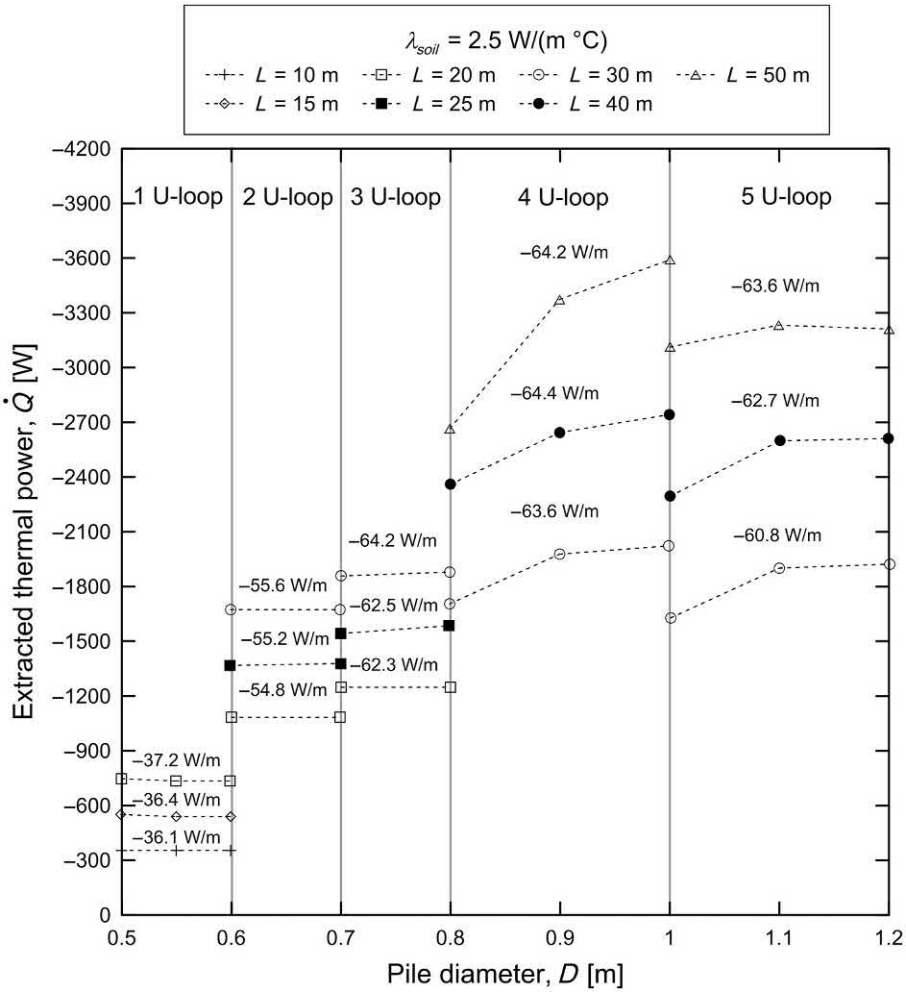

Figure 12.13 Thermal power extracted from energy piles of different diameter and length, which are equipped with varying pipe configurations, in a uniform soil deposit of $\lambda_{soil} = 2.5$ W/(m °C). *Redrawn after Achich, A., 2018. Numerical simulation of deck de-icing using energy pile systems (M.Sc. degree). Laboratory of Soil Mechanics, Swiss Federal Institute of Technology in Lausanne, Lausanne.*

(with a flow velocity of $\overline{v}_{in} = 0.2$ m/s) and flow velocities of $\overline{v}_{in} = 0.2$, 0.5 and 1 m/s (with a pipe diameter of $d_p = 32$ mm) are considered.

12.3.4.1 Pipe diameter variation

Fig. 12.15 shows the influence of a variation in the diameter of the pipes embedded in energy piles on the axial temperature evolution along such foundations for a single U-, a double U- and a W-shaped pipe configuration with varying pipe diameters of $d_p = 25$, 32 and 40 mm. A geothermal operation of $t = 15$ days is considered.

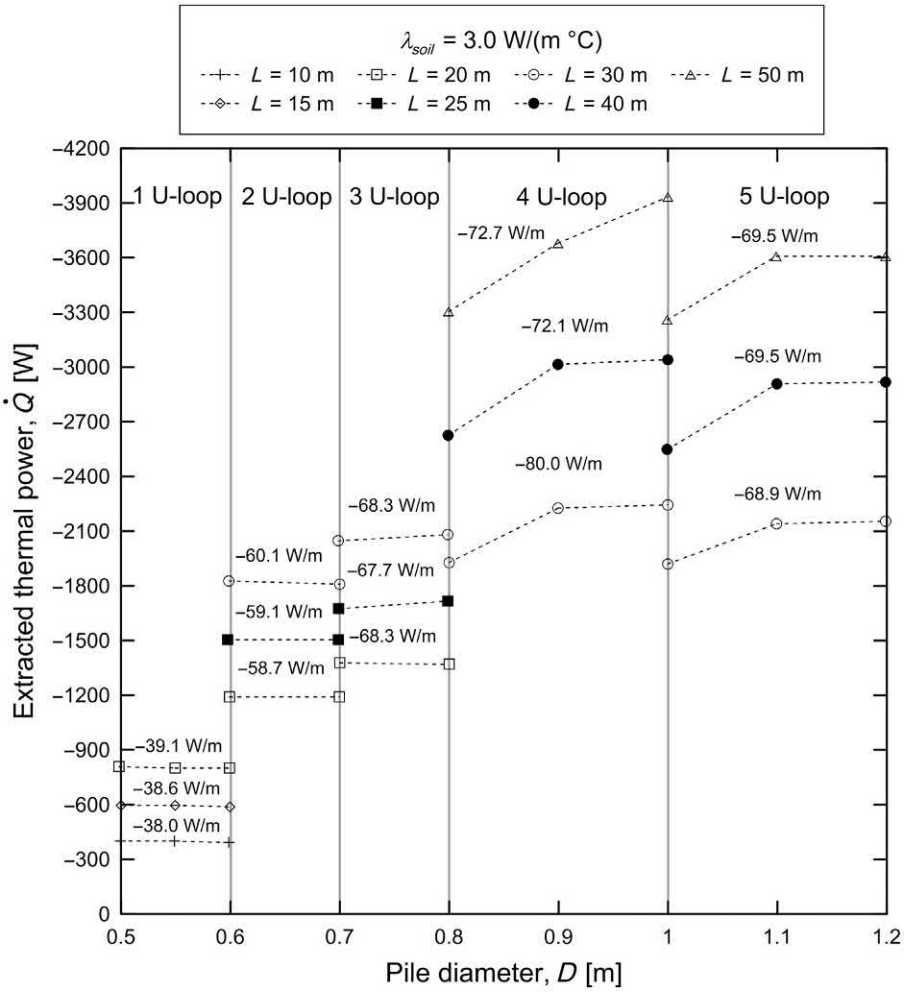

Figure 12.14 Thermal power extracted from energy piles of different diameter and length, which are equipped with varying pipe configurations, in a uniform soil deposit of $\lambda_{soil} = 3.0$ W/(m °C). *Redrawn after Achich, A., 2018. Numerical simulation of deck de-icing using energy pile systems (M.Sc. degree). Laboratory of Soil Mechanics, Swiss Federal Institute of Technology in Lausanne, Lausanne.*

An increase in the axial temperature variation along the energy pile is observed for an increase in the fluid flow rate associated with a variation of the pipe diameter. The most significant temperature variation (achieved with the largest pipe diameter) characterises the energy pile equipped with a W-shaped pipe configuration. The previous phenomenon is related to the higher heat transfer associated with the longer duration of the contact between the heat carrier fluid and the surroundings in the W-shaped pipe configuration.

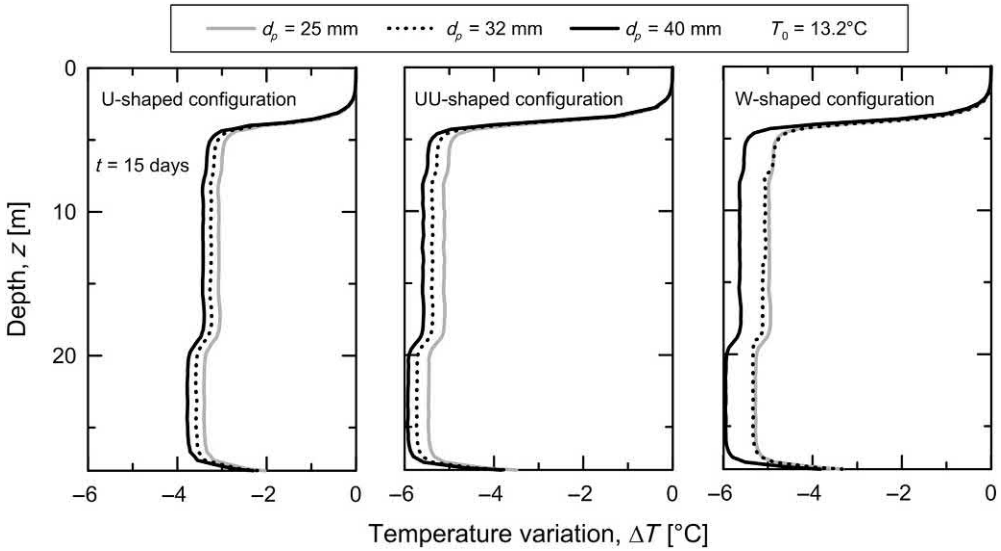

Figure 12.15 Axial temperature evolution along an energy pile equipped with a single U-, a double U- and a W-shaped pipe configuration for different pipe diameters. *Redrawn after Batini, N., Rotta Loria, A.F., Conti, P., Testi, D., Grassi, W., Laloui, L., 2015. Energy and geotechnical behaviour of energy piles for different design solutions. Appl. Therm. Eng. 86 (1), 199–213.*

Fig. 12.16 presents the influence of a variation in the diameter of the pipes embedded in energy piles on the evolution of the heat carrier fluid temperature along the pipe length as well as on the trend of thermal power associated with the geothermal operation of such foundations. Results refer to a geothermal operation of $t = 15$ days. Complementary data are summarised in Table 12.3. A lower variation of the outflow temperature of the heat carrier fluid is observed when the diameter of the pipe is reduced. This phenomenon is attributed to the lower heat transfer that is associated with less pronounced flow rates. The trends of thermal power extracted from the ground show that up to 10% of the heat transfer rate can be gained when the diameter of the pipes is increased from 25 to 40 mm.

12.3.4.2 Flow velocity variation

Fig. 12.17 presents the influence of a variation in the velocity of the heat carrier fluid circulating in the pipes embedded in energy piles on the axial temperature evolution along such foundations for a single U-, a double U- and a W-shaped pipe configuration and a velocity of the heat carrier fluid of $\overline{v}_{in} = 0.2$, 0.5 and 1 m/s. A geothermal operation of $t = 15$ days is considered. An increase in the axial temperature variation along the energy pile is observed for an increase in the fluid flow rate associated with a variation of the flow velocity.

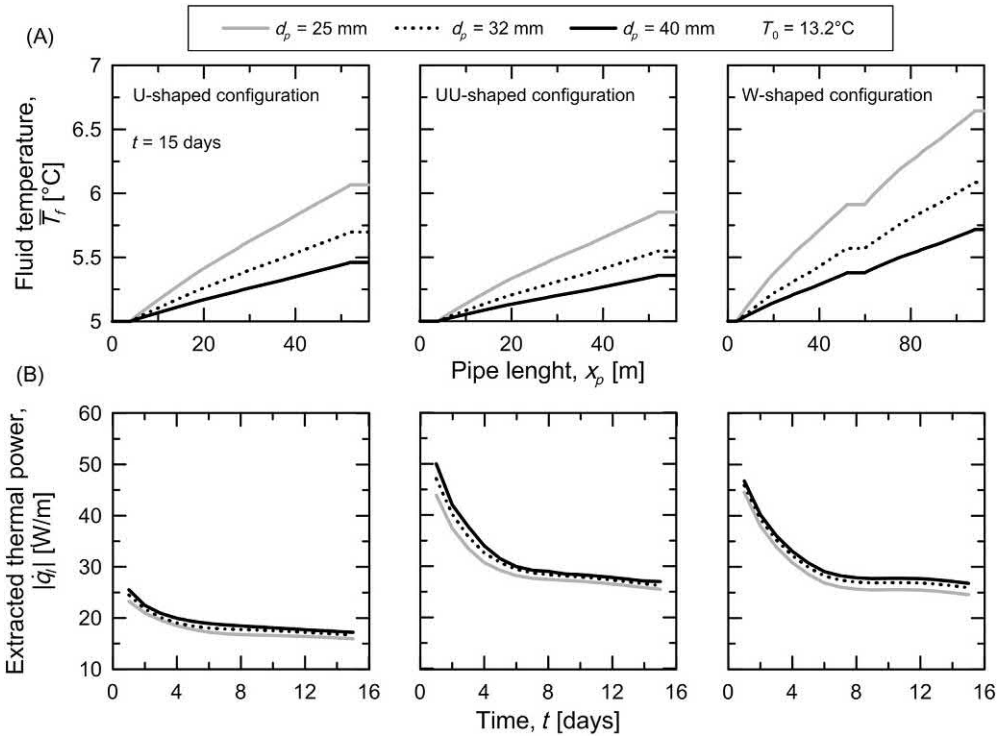

Figure 12.16 (A) Evolution of the heat carrier fluid temperature along the pipe and (B) trends of thermal power of an energy pile equipped with a single U-, a double U- and a W-shaped pipe configuration for different pipe diameters. *Redrawn after Batini, N., Rotta Loria, A.F., Conti, P., Testi, D., Grassi, W., Laloui, L., 2015. Energy and geotechnical behaviour of energy piles for different design solutions. Appl. Therm. Eng. 86 (1), 199–213.*

Fig. 12.18 shows the influence of a variation in the velocity of the heat carrier fluid on the evolution of its temperature along the pipe length as well as on the trend of thermal power associated with the geothermal operation of energy piles equipped with a single U-, a double U- and a W-shaped pipe configuration. A geothermal operation of $t = 15$ days is considered. Complementary data are summarised in Table 12.4. The trends of thermal power extracted from the ground show a sensible growth when the fluid velocity is increased, despite their typical decay with time. An increase in the heat carrier fluid velocity from 0.2 to 0.5 m/s induces an increase of approximately 7% in the heat transfer rate, while an increase from 0.2 to 1 m/s results in an increase of approximately 11%. These variations depend on the pipe configuration although the most relevant effects are observed for the W-shaped pipe configuration.

Table 12.3 Thermohydraulic data characterising an energy pile equipped with a single U-, a double U- and a W-shaped pipe configuration for different pipe diameters.

Pipe diameter, d_p [mm]	Outflow temperature, $\overline{T}_{out}$ [°C]	Temperature variation, $\overline{\Delta T}$ [°C]	Temperature at the pile−soil interface, $\overline{T}_{s-p}$ [°C]	Heat exchanger effectiveness, ϵ_{ghe} [−]	Volumetric flow rate, $\dot{V}$ [L/min]	Thermal power per unit length, $\lvert\dot{q}_l\rvert$ [W/m]
Single U-shaped pipe						
25	6.07	1.07	10.67	0.189	5.9	15.8
32	5.70	0.70	10.73	0.122	9.7	16.9
40	5.46	0.46	10.44	0.085	15.1	17.3
Double U-shaped pipes						
25	5.85	0.85	9.03	0.211	11.8	25.0
32	5.55	0.55	9.06	0.135	19.3	26.5
40	5.36	0.36	8.67	0.098	30.2	27.1
W-shaped pipe						
25	6.64	1.64	9.25	0.386	5.9	24.2
32	6.08	1.08	9.15	0.260	9.7	26.1
40	5.72	0.72	8.56	0.201	15.1	27.0

Source: Data from Batini, N., Rotta Loria, A.F., Conti, P., Testi, D., Grassi, W., Laloui, L., 2015. Energy and geotechnical behaviour of energy piles for different design solutions. Appl. Therm. Eng. 86 (1), 199−213.

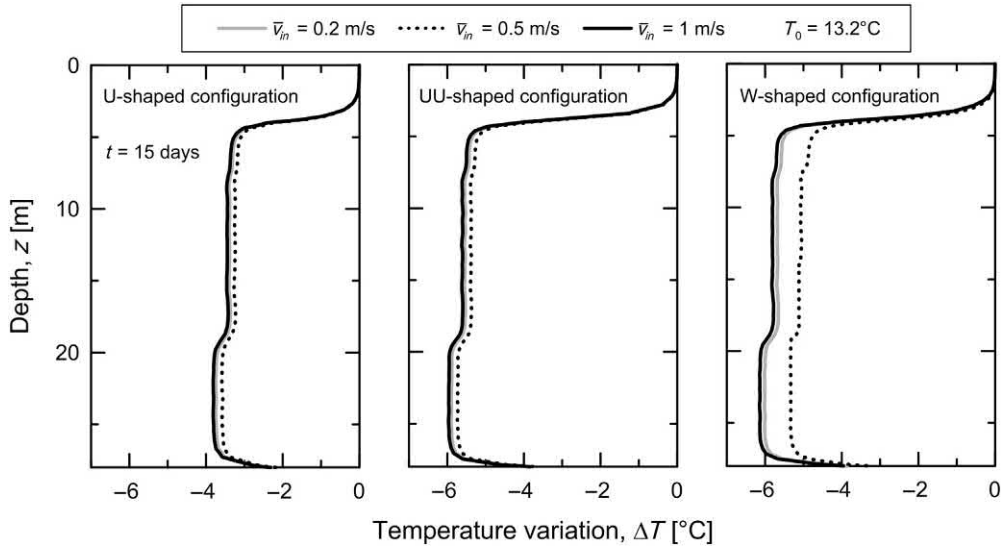

Figure 12.17 Axial temperature evolution along an energy pile equipped with a single U-, a double U- and a W-shaped pipe configuration for different pipe diameters. *Redrawn after Batini, N., Rotta Loria, A.F., Conti, P., Testi, D., Grassi, W., Laloui, L., 2015. Energy and geotechnical behaviour of energy piles for different design solutions. Appl. Therm. Eng. 86 (1), 199–213.*

12.3.5 Influence of the heat carrier fluid composition

Antifreeze chemicals are typically mixed with pure water to lower the freezing point of the heat carrier fluid circulating in the pipes, especially when dealing with working conditions characterised by low temperature regimes (Batini et al., 2015). The role of antifreeze chemicals mixed with water plays a nonnegligible role on the thermohydraulic behaviour of energy piles and other energy geostructures. However, the influence of the previous variable may be considered negligible for the mechanical behaviour of such geostructures.

In the following, the influence of the heat carrier fluid composition on the thermohydromechanical behaviour of energy piles is expanded with reference to the results of Batini et al. (2015). Heat carrier fluid compositions represented by pure water, MEG 25 and MEG 50 are considered.

Fig. 12.19 presents the influence of the heat carrier fluid composition on the axial temperature evolution along energy piles equipped with a single U-, a double U- and a W-shaped pipe configuration for a geothermal operation of $t = 15$ days. The evolution of the heat carrier fluid temperature along the pipes after $t = 15$ days and the trends of thermal power extracted through the same energy piles over time are reported in Fig. 12.20. Complementary data referring to a geothermal operation of $t = 15$ days are summarised in Table 12.5. The use of antifreeze does not appreciably

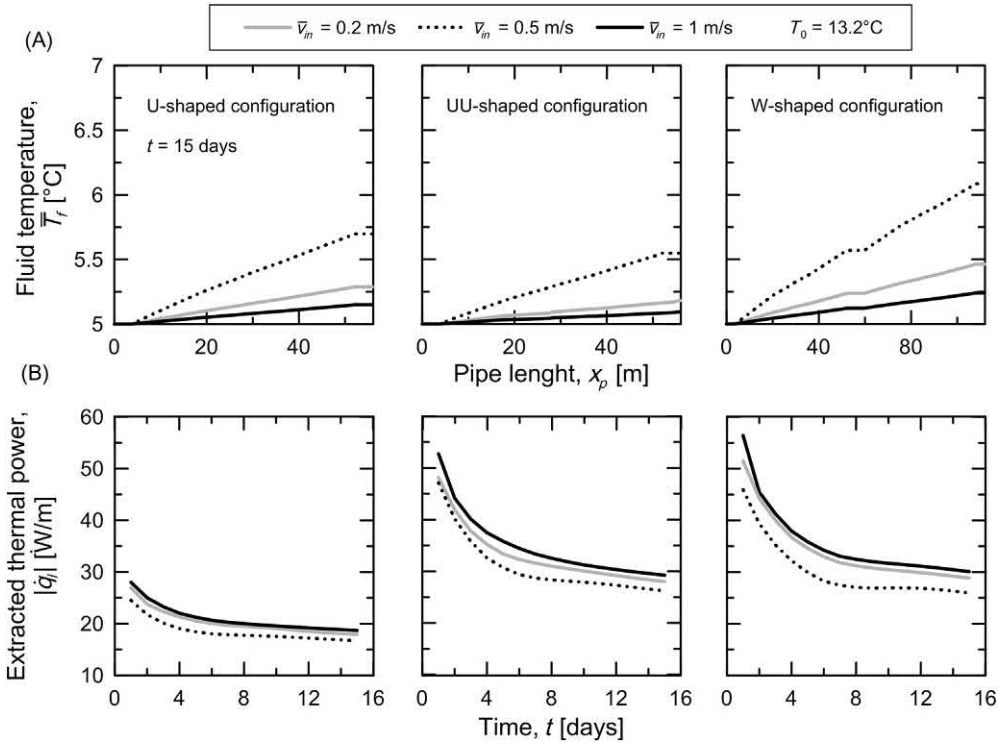

Figure 12.18 (A) Evolution of the heat carrier fluid temperature along the pipe and (B) trends of thermal power of an energy pile equipped with a single U-, a double U- and a W-shaped pipe configuration for different flow velocities. *Redrawn after Batini, N., Rotta Loria, A.F., Conti, P., Testi, D., Grassi, W., Laloui, L., 2015. Energy and geotechnical behaviour of energy piles for different design solutions. Appl. Therm. Eng. 86 (1), 199–213.*

affect the temperature of the heat carrier fluid circulating in the pipes. However, the variations (e.g. decrease) in the thermal power that can be harvested through energy piles can be significant for concentrations of antifreeze greater than 25%.

12.3.6 Influence of the soil–pile thermal expansion coefficient ratio

The relative significance of the thermal expansion of the ground to that of energy piles critically influences the thermomechanical behaviour of such geostructures (Bourne-Webb et al., 2016a; Rotta Loria and Laloui, 2017). The reason for this evidence is because the contribution of developed thermally induced deformation causes displacement, whereas the contribution of restrained deformation causes stress: both of these contributions depend on the restraint provided by the ground.

The relative significance of the thermal expansion of the ground to that of energy piles depends on (1) the thermal field characterising the energy pile(s) and (2) the relative thermal expansion coefficient of soil to pile. Aspect (1) indicates that the greater

Table 12.4 Thermohydraulic data characterising an energy pile equipped with a single U-, a double U- and a W-shaped pipe configuration for different flow velocities.

Inlet velocity, $\overline{v}_{in}$ [m/s]	Outflow temperature, $\overline{T}_{out}$ [°C]	Temperature variation, $\overline{\Delta T}$ [°C]	Temperature at the pile−soil interface, $\overline{T}_{s-p}$ [°C]	Heat exchanger effectiveness, ϵ_{ghe} [−]	Volumetric flow rate, $\dot{V}$ [L/min]	Thermal power per unit length, $\lvert\dot{q}_l\rvert$ [W/m]
Single U-shaped pipe						
0.2	5.70	0.70	10.73	0.122	9.7	16.9
0.5	5.29	0.29	10.47	0.052	24.1	17.2
1	5.15	0.15	10.41	0.028	48.3	18.1
Double U-shaped pipes						
0.2	5.55	0.55	9.06	0.135	19.3	26.5
0.5	5.23	0.23	8.71	0.061	48.3	27.4
1	5.12	0.12	8.67	0.033	96.5	29.0
W-shaped pipe						
0.2	6.08	1.08	9.15	0.260	9.7	26.1
0.5	5.46	0.46	8.51	0.132	24.1	27.9
1	5.24	0.24	8.38	0.071	48.3	29.0

Source: Data from Batini, N., Rotta Loria, A.F., Conti, P., Testi, D., Grassi, W., Laloui, L., 2015. Energy and geotechnical behaviour of energy piles for different design solutions. Appl. Therm. Eng. 86 (1), 199−213.

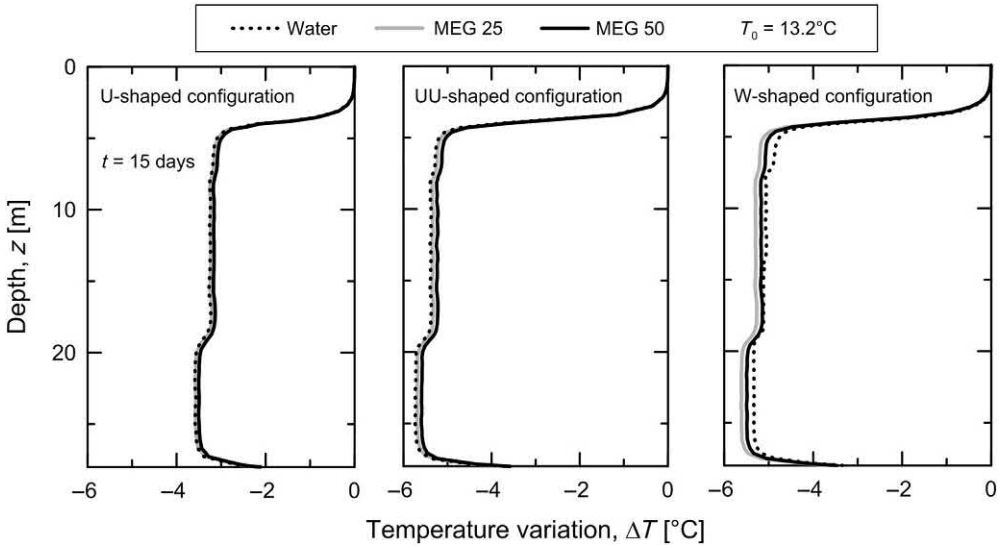

Figure 12.19 Axial temperature evolution along an energy pile equipped with a single U-, a double U- and a W-shaped pipe configuration for different heat carrier fluid compositions. *Redrawn after Batini, N., Rotta Loria, A.F., Conti, P., Testi, D., Grassi, W., Laloui, L., 2015. Energy and geotechnical behaviour of energy piles for different design solutions. Appl. Therm. Eng. 86 (1), 199–213.*

the volume of soil subjected to a temperature variation is, the more pronounced the impact of the deformation of the soil on that of the pile is. Aspect (2) can be assessed through the soil–pile thermal expansion coefficient ratio, that is the ratio between the linear thermal expansion coefficient of the soil and the linear thermal expansion coefficient of the pile, $X = \alpha_{soil}/\alpha_{EP}$, where α_{soil} and α_{EP} are the linear thermal expansion coefficients of the soil and energy piles, respectively. Considering these aspects in the analysis and design of energy piles is important because they profoundly characterise the deformation of such foundations (Rotta Loria and Laloui, 2017).

According to Bourne-Webb et al. (2016a), ignoring the thermally induced deformation of the ground or using inappropriate values of its thermal expansion coefficient can lead to incorrect predictions of the pile–soil interactions generated by thermal loading. In particular, employing unsuitable values of the thermal expansion coefficient can involve opposite predictions of thermally induced stresses along energy geostructures (Rotta Loria and Laloui, 2017, 2018). The adherence to reality of simulations inappropriately dealing with the relative deformation of the ground to that of energy piles becomes less accurate for higher values of X (Bourne-Webb et al., 2016a). Assuming that the ground is insensitive to temperature variations only provides conservative estimates of thermally induced stresses over a limited range of conditions and only for energy geostructures in overconsolidated ground (Bourne-Webb et al., 2016a).

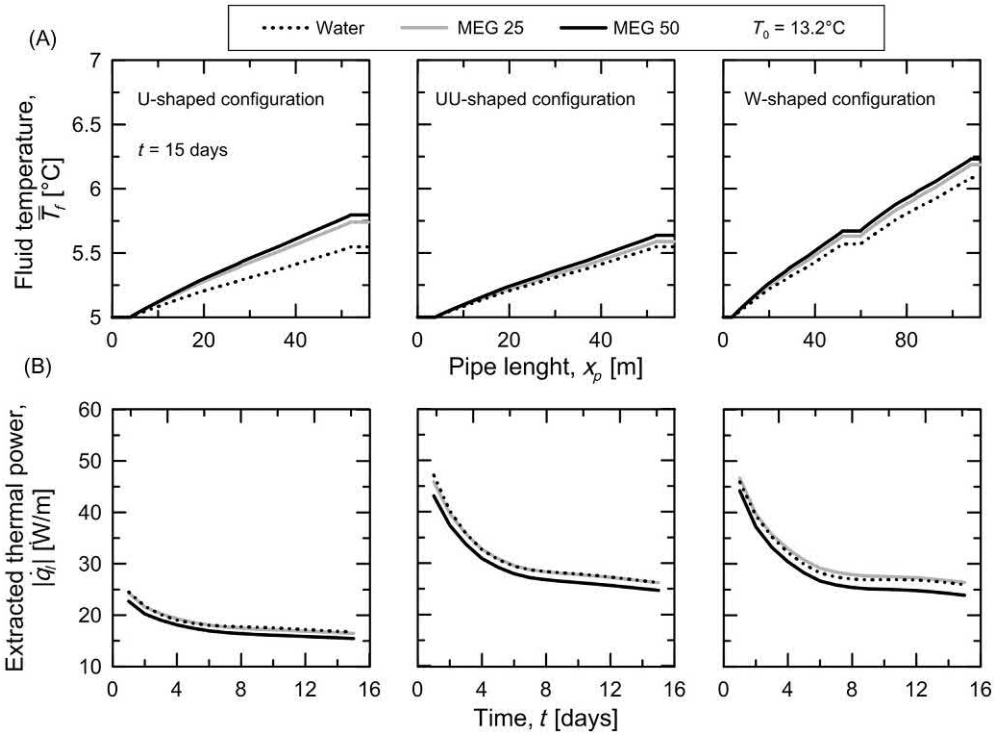

Figure 12.20 (A) Evolution of the heat carrier fluid temperature along the pipe and (B) trends of thermal power of an energy pile equipped with a single U-, a double U- and a W-shaped pipe configuration for different heat carrier fluid compositions. *Redrawn after Batini, N., Rotta Loria, A.F., Conti, P., Testi, D., Grassi, W., Laloui, L., 2015. Energy and geotechnical behaviour of energy piles for different design solutions. Appl. Therm. Eng. 86 (1), 199–213.*

In the following, the influence of the soil–pile thermal expansion coefficient ratio on the thermomechanical behaviour of energy piles is expanded with reference to the results of Rotta Loria and Laloui (2017). A full-scale group of energy piles in which only one energy pile operates as a geothermal heat exchanger is simulated considering the bottom soil layer with a value of $X < 1$ (prediction 1) or $X > 1$ (prediction 2). The shallower soil layers are characterised by values of $X < 1$.

Fig. 12.21 compares the variations in vertical strain determined through the predictions 1 and 2 along an operating energy pile (EP1) and a neighbouring nonoperating energy pile (EP2) for average temperature variations applied to the former pile of $\overline{\Delta T} = 5°C$, 10°C, 15°C and 20°C. At the early stages of the heating phase of energy pile EP1, a small difference between the variations in vertical strain determined through the numerical analyses characterises the energy piles. At these stages, a limited volume of soil is subjected to a temperature variation. Thus despite the

Table 12.5 Thermohydraulic data characterising an energy pile equipped with a single U-, a double U- and a W-shaped pipe configuration for different heat carrier fluid compositions.

Fluid composition	Outflow temperature, $\overline{T}_{out}$ [°C]	Temperature variation, $\overline{\Delta T}$ [°C]	Temperature at the pile−soil interface, $\overline{T}_{s-p}$ [°C]	Heat exchanger effectiveness, ϵ_{ghe} [−]	Volumetric flow rate, $\dot{V}$ [L/min]	Thermal power per unit length, $\lvert\dot{q}_l\rvert$ [W/m]
Single U-shaped pipe						
Pure water	5.70	0.70	10.73	0.122	9.7	16.9
MEG 25	5.74	0.74	10.59	0.132	10.1	18.6
MEG 50	5.80	0.80	10.65	0.141	10.5	20.9
Double U-shaped pipes						
Pure water	5.55	0.55	9.06	0.135	19.3	26.5
MEG 25	5.59	0.59	8.96	0.148	20.2	29.6
MEG 50	5.64	0.64	8.94	0.161	21.0	33.4
W-shaped pipe						
Pure water	6.08	1.08	9.15	0.260	9.7	26.1
MEG 25	6.19	1.19	8.83	0.310	10.1	29.9
MEG 50	6.23	1.23	8.94	0.312	10.5	32.3

Source: Data from Batini, N., Rotta Loria, A.F., Conti, P., Testi, D., Grassi, W., Laloui, L., 2015. Energy and geotechnical behaviour of energy piles for different design solutions. Appl. Therm. Eng. 86 (1), 199−213.

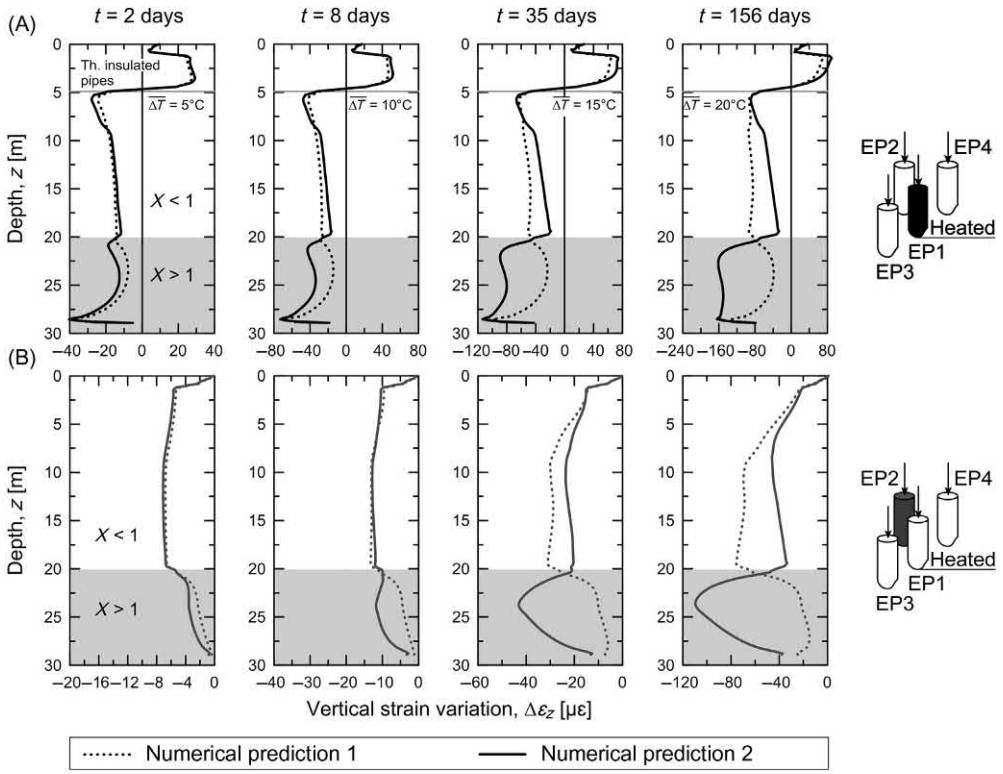

Figure 12.21 Evolution of the vertical strain along (A) an operating energy pile and (B) a nonoperating energy pile in a group for different values of soil–pile thermal expansion coefficient ratio. *Redrawn after Rotta Loria, A.F., Laloui, L., 2017. Thermally induced group effects among energy piles. Geotechnique 67 (5), 374–393.*

different values of thermal expansion coefficient used in the predictions, the thermally induced deformation of the soil is limited and involves a negligible influence on the deformation of both the operating and nonoperating energy piles. At the successive stages of the heating phase of energy pile EP1, an increasing difference between the variations in vertical strain estimated through the numerical analyses can be noted. In general, greater variations in vertical strain are observed in the layers characterised by the greater thermal expansion coefficients. Greater strain variations are determined in the shallower portions of the energy piles by prediction 1 compared to the smaller variations determined by prediction 2. Smaller strain variations are determined in the deeper portions of the energy piles by prediction 1 compared to the greater variations determined by the prediction 2. The reason for the observed difference between the predictions results is because, at the successive stages of the heating phase of energy pile EP1, a noteworthy volume of soil becomes subjected to a temperature variation

and the thermally induced deformation of soil consequently has a marked impact on the deformation of both the operating and nonoperating energy piles.

Based on the previous results, at the early stages of geothermal operations of energy piles, the deformation of such geostructures is governed by the thermally induced deformation of the piles, almost irrespectively of whether $X \leq 1$ or $X > 1$. In contrast, at the successive stages of geothermal operations of energy piles, values of $X \leq 1$ correspond to a deformation of such geostructures that is governed by the thermally induced deformation of the piles, while values of $X > 1$ correspond to a deformation that is governed by the thermally induced deformation of the soil surrounding the piles.

12.3.7 Influence of loading magnitude and sequence

The loading magnitude and sequence critically characterise the thermohydromechanical behaviour of energy piles. Higher magnitudes of loading (e.g. mechanical and thermal) cause more significant variations of variables such as temperature, stress and displacement in both the energy piles and surrounding ground, with an influence on both the mechanics and the energy yield of the considered geostructures. The loading sequence can also involve different responses of energy piles from the aforementioned perspectives. The previous considerations are valid for general energy geostructures. Attention is devoted in the following to the influence of the loading magnitude and sequence on the mechanics governing energy piles.

According to Randolph (2003), the response of individual piles in a group predominantly depends on the conditions and properties of the pile–soil interface, while the overall response of pile groups predominantly depends on the conditions and properties of the bulk of the soil contained between them. The previous considerations also apply to energy piles and must be accounted for the development of numerical analyses (Rotta Loria et al., 2017). One consequence associated with significant magnitudes of loads (e.g. mechanical and thermal) applied to energy piles is the potential development of plastic strains at the pile–soil interface.

When plastic phenomena develop in the ground, stress redistribution occurs for further loading. From one side, this phenomenon can cause a variation of the restraint conditions and yield to short-term implications for the response of the considered geostructures [e.g. variations of the null point position (Rotta Loria et al., 2015b; Di Donna and Laloui, 2014)]. From the other side, this phenomenon can cause cyclic effects related to the successive (e.g. daily and seasonal) thermal loading and unloading and yield to long-term implications for the response of the considered geostructures [e.g. progressive settlements (Suryatriyastuti et al., 2013; Olgun et al., 2014; Dupray et al., 2014; Saggu and Chakraborty, 2015a; Ozudogru et al., 2015; Salciarini et al., 2015, 2017; Suryatriyastuti et al., 2015; Ng et al., 2016; Vieira and Maranha, 2016; Adinolfi et al., 2018; Sutman et al., 2018; Akrouch et al., 2018)].

12.4 Thermohydromechanical behaviour of energy tunnels

12.4.1 General

In the following, the response of energy tunnels is expanded for a variation in (1) the tunnel shape, (2) the airflow regime within the tunnel, (3) the surface wall roughness, (4) the pipe configuration, (5) the pipe embedment, (6) the heat carrier fluid flow rate and (7) the groundwater flow significance.

12.4.2 Influence of tunnel shape

The shape of energy tunnels markedly influences their thermohydromechanical behaviour. From one side, the tunnel shape influences the development of the boundary layers within energy tunnels, thus characterising the related thermohydraulic behaviour. From the other side, the tunnel shape influences the static features of energy tunnels, thus characterising the related thermomechanical behaviour. Attention is devoted in the following to the influence of the shape of energy tunnels on the development of the thermal and velocity boundary layers within such environments. Information about the thermomechanical behaviour of energy tunnels characterised by different shapes by means of numerical simulation results has been presented by Mimouni et al. (2014), Nicholson et al. (2014) and Barla and Di Donna (2018).

In energy tunnels, convection heat transfer caused by an airflow at a different temperature compared to that of the inner surface of the structure wall(s) occurs. Under these conditions, the airflow in the underground environment represents a nonisothermal problem of internal flow (i.e. the flow presents temperature gradients and is completely bounded by a surface) characterised by the development of the thermal and velocity boundary layers (Peltier et al., 2019). The development of the boundary layers involves the establishment of two types of regions along the direction of the flow: the thermal and hydrodynamic entrance regions and the thermally and hydrodynamically fully developed regions (Bergman et al., 2011). The relative significance of the entrance and fully developed regions is associated with the so-called thermal entry length, $x_{fd,th}$, and hydrodynamic entry length, $x_{fd,h}$. The development of the thermal and velocity boundary layers as well as the significance of the entrance and fully developed regions crucially characterise the convection heat transfer in the context of nonisothermal problems of internal flow. The reason for this fact is that the convection heat transfer between a surface and a moving fluid is a function of the velocity of the moving fluid via the convection heat transfer coefficient, as well as of the difference between the surface temperature and the undisturbed temperature of the fluid (cf. Eq. 12.11). Therefore as the temperature and velocity fields of a moving fluid vary with the distance as a function of the development of the boundary layers, the variation of these variables can lead to marked changes in the convection heat transfer phenomenon.

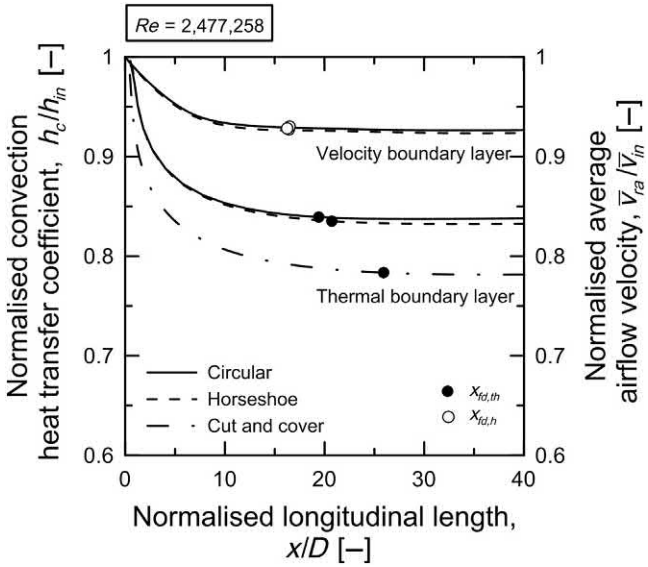

Figure 12.22 Development of the thermal and velocity boundary layers for different shapes of tunnel cross section. *Redrawn after Peltier, M., Rotta Loria, A.F., Lepage, L., Garin, E., Laloui, L., 2019. Numerical investigation of the convection heat transfer driven by airflows in underground tunnels. Appl. Therm. Eng. 159, 113844.*

Fig. 12.22 shows an example of the variations of the normalised convection heat transfer coefficient and flow velocity along the normalised longitudinal length of tunnels characterised by three equivalent cross sections with reference to the results of Peltier et al. (2019). Tunnels characterised by a circular, horseshoe and cut-and-cover cross section of the same equivalent hydraulic diameter are considered. An airflow parallel to the longitudinal length of the tunnel, x, with a constant uniform inlet temperature $\overline{T}_{in}$ and a constant uniform inlet velocity $\overline{v}_{in}$ is simulated. Reference is made to a Reynolds number of $Re = 2{,}477{,}258$ as well as to a smooth surface embedding the flow, that is $k_s = 0$ mm, where k_s is the wall surface roughness. The convection heat transfer coefficient h_c and the average airflow velocity $\overline{v}_{ra}$ are normalised by the convection heat transfer coefficient h_{in} and the airflow velocity $\overline{v}_{in}$ at the tunnel entrance, respectively.

For any considered shape of tunnel cross section, the thermal and hydrodynamic entry lengths differ from each other, with the former being greater than the latter. The obtained values for both the thermal and hydrodynamic entry lengths agree with the values commonly encountered for nonisothermal problems of internal flow involving pipes, that is $x_{fd,th}/D \geq 10$ and $10 \leq x_{fd,h}/D \leq 60$ (Bergman et al., 2011). Considering that the obtained entrance lengths are on average approximately equal to $20D$ and that the usual diameters characterising tunnels range between 5 and 20 m,

thermal entrance regions between 100 and 400 m can be expected in practice. The previous consideration indicates that significant portions of these environments may often be in a continuous entrance region. The considered aspect may be accounted for the energy exploitation targeted through energy tunnels.

The shape of the tunnel cross section markedly characterises the significance of the thermal entry length, while it involves a negligible variation of the hydrodynamic entry length in tunnels. In other words, the shape of the cross section of tunnels influences the development of the thermal boundary layer while it does not influence the development of the velocity boundary layer. Similar thermal entry lengths characterise tunnels with equivalent circular and horseshoe cross sections, whereas a different thermal entry length characterises tunnels with an equivalent cut-and-cover cross section (the thermal entry length is greater in the latter case compared to the former two cases). Undistinguishable hydrodynamic entry lengths characterise tunnels with equivalent circular, horseshoe and cut-and-cover cross sections. Based on the previous results, modelling tunnels characterised by an actual horseshoe cross section with an equivalent circular cross section can be a meaningful and representative approach, with the further advantage of considerably decreasing the computational time. In contrast, this approach should be avoided to model tunnels characterised by a cut-and-cover cross section as markedly different results can be obtained.

Greater variations of the convection heat transfer coefficient along the longitudinal length respectively characterise tunnels with equivalent circular, horseshoe and cut-and-cover cross sections. In any case, the variation of the convection heat transfer coefficient with the normalised longitudinal length involves different values of this parameter in the thermal entrance region and the thermally fully developed region. A more significant convection heat transfer coefficient is associated with the thermal entrance region compared to the thermally fully developed region of tunnels, that is $h_{c,ent} > h_{c,fd}$. At least in principle, the previous result involves a higher energy exploitation of the tunnel simply because of the considered location with respect to the development of the thermal and velocity boundary layers. Nevertheless, a slight difference between the *average* convection heat transfer coefficient characterising the thermal entrance region and the convection heat transfer coefficient associated with the thermally fully developed region can be highlighted. This phenomenon is evidenced in Fig. 12.23 with reference to the relationship between the average values of convection heat transfer coefficient with the longitudinal distance in the thermal entrance region, $\overline{h}_{c,ent}$, and the thermally fully developed region, $h_{c,fd}$, with the associated values of airflow velocity, $\overline{v}_{ra}$. Correlations previously identified in the literature between the convection heat transfer coefficient and the associated average value of airflow velocity are presented for reference (ASHRAE, 2007; EN ISO 6946, 2007; Palyvos, 2008; Lee et al., 2009). Even if markedly different values of h_c are reached locally in the thermal entrance region compared to the thermally fully developed region of tunnels, their

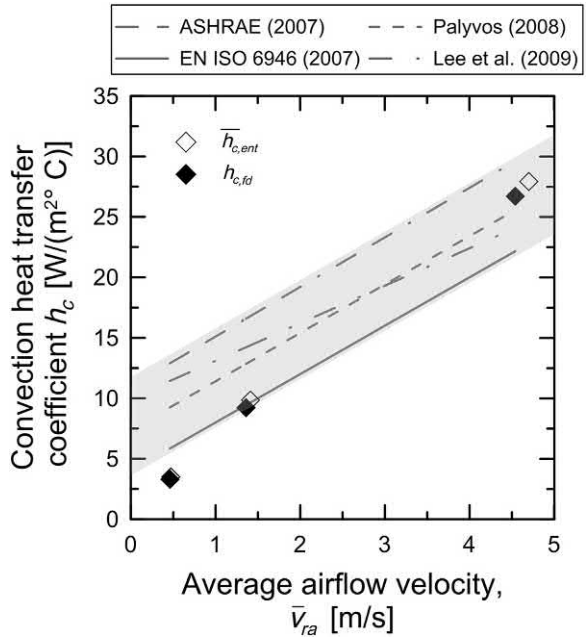

Figure 12.23 Correlations between convection heat transfer coefficient and airflow velocity for different regions of the flow in tunnels. *Redrawn after Peltier, M., Rotta Loria, A.F., Lepage, L., Garin, E., Laloui, L., 2019. Numerical investigation of the convection heat transfer driven by airflows in underground tunnels. Appl. Therm. Eng. 159, 113844.*

magnitude drops very quickly with the longitudinal distance to the value of the convection heat transfer coefficient in the thermally fully developed region. Therefore as long as no disturbances of the thermal and velocity boundary layers are encountered in practice, the *average* amount of energy that can be harvested through energy tunnels in correspondence with the entrance or fully developed regions may be considered unaffected by the development of the thermal and velocity boundary layers.

12.4.3 Influence of airflow regime within the tunnel

The airflow regime within energy tunnels strongly characterises their thermohydromechanical behaviour. Higher flow regimes are associated with a more substantial heat transfer via energy tunnels, which may represent a beneficial or unfavourable aspect for the energy harvesting and mechanical response characterising the tunnel. Higher heat transfers with the tunnel environment involve, for example, varying temperature and stress variations within the tunnel wall (Zhang et al., 2013; Nicholson et al., 2014; Bourne-Webb et al., 2016b; Barla et al., 2016; Bidarmaghz et al., 2017).

The airflow regime within energy tunnels does not necessarily influence the thermal and velocity boundary layers within such environments. The previous result

particularly applies once turbulent conditions are established (Bergman et al., 2011). As these conditions are likely to characterise most energy tunnels due to the typical airflow velocities of $\overline{v}_{ra} = 0.5-5$ m/s and tunnel diameters of $D = 5$ and 20 m (Peltier et al., 2019), this aspect may be considered in the thermohydraulic analysis of such geostructures.

Fig. 12.24 illustrates an example of the variations of the normalised convection heat transfer coefficient and flow velocity along the normalised longitudinal length of tunnels for varying Reynolds numbers with reference to the results of Peltier et al. (2019). Reynolds numbers of $Re = 247{,}753$, 743,528 and 2,477,258, which correspond to inlet velocities of $\overline{v}_{in} = 0.5$, 1.5 and 5 m/s, are considered. A tunnel characterised by a circular cross section and a smooth surface wall ($k_s = 0$ mm) is modelled. The Reynolds number does not significantly affect the thermal and hydrodynamic entry lengths in tunnels. This result is in accordance with the approximations available for turbulent flow characterising nonisothermal problems of internal flow involving pipes (Bergman et al., 2011). The Reynolds number markedly influences the variation of the normalised convection heat transfer coefficient with the normalised longitudinal length of tunnels, whereas it does not lead to noteworthy variations of the normalised flow velocity. Increasing the Reynolds number leads to higher values of the convection heat transfer coefficient h_c. This result confirms previous evidence available in the literature about the

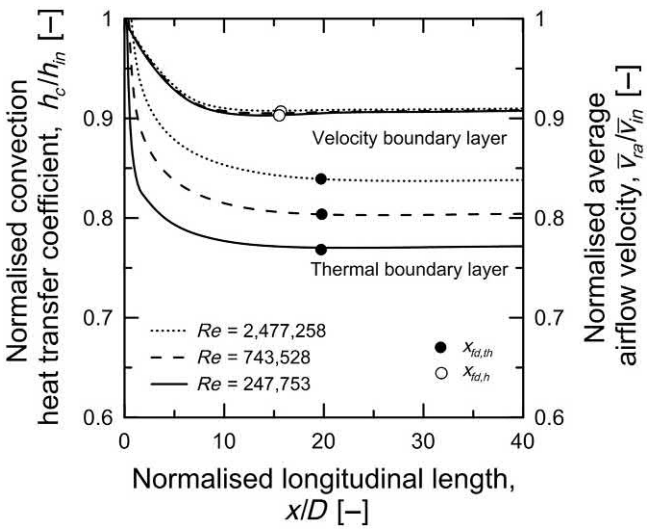

Figure 12.24 Development of the thermal and velocity boundary layers for different Reynolds numbers. *Redrawn after Peltier, M., Rotta Loria, A.F., Lepage, L., Garin, E., Laloui, L., 2019. Numerical investigation of the convection heat transfer driven by airflows in underground tunnels. Appl. Therm. Eng. 159, 113844.*

dependence of the convection heat transfer coefficient on the airflow velocity (Bourne-Webb et al., 2016b).

The influence of the significance of an airflow in the environment enclosed by energy tunnels on the related thermohydraulic behaviour is expanded in Fig. 12.25 with reference to a chart drawing from the study of Cousin et al. (2019). Absolute values of the thermal power that can be harvested from energy tunnels when steady thermal conditions are achieved within such geostructures is depicted for varying values of air temperature, airflow velocity and effective thermal conductivity of the ground. Values of thermal power comprised between approximately 15 and 50 W/m^2 can be associated with the same energy tunnel in different site conditions because of a variation of the considered variables. Further results on how the tunnel air temperature affects the thermal behaviour of energy tunnels have been presented, for example, by Ogunleye et al. (2020).

12.4.4 Influence of surface wall roughness

The surface roughness of the wall(s) characterising energy tunnels critically characterises their thermohydromechanical behaviour through a strong influence on the development of both the thermal and velocity boundary layers. Rough surfaces

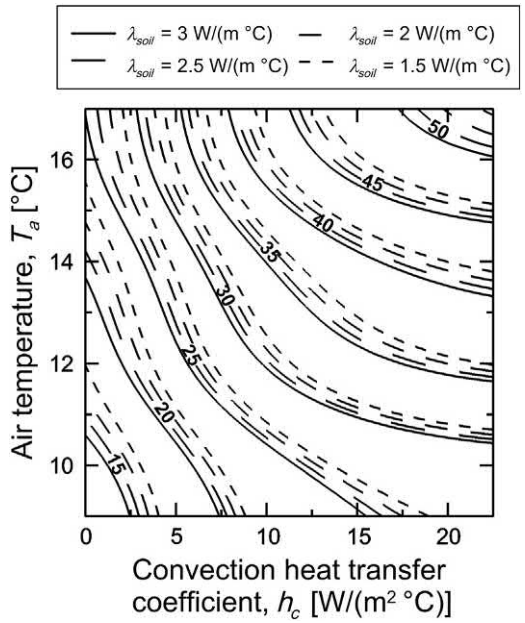

Figure 12.25 Thermal power per unit surface that can be extracted via energy tunnels for varying values of air temperature, convection heat transfer coefficient associated with an airflow and effective thermal conductivity of the ground.

typically cause a shortening of the entrance regions compared to smooth surface(s), but increasing wall roughness lead to higher values of the convection heat transfer coefficient (Peltier et al., 2019). This latter phenomenon can be considered to enhance the energy exploitation targeted through energy tunnels.

The influence of the surface wall roughness on the development of the boundary layers and the related convection heat transfer driven by airflows is presented in the following with reference to the results of Peltier et al. (2019). Values of surface wall roughness of $k_s = 0$, 3, 8 and 11 mm are modelled. The lowest and highest values of the surface roughness can be associated with a smooth or a shotcrete-like surface of the wall(s).

Fig. 12.26 shows the variations of the normalised convection heat transfer coefficient and flow velocity along the normalised longitudinal length of tunnels for different values of surface wall roughness. A tunnel characterised by a circular cross section and airflow with an associated Reynolds number of $Re = 2{,}477{,}258$ is considered. The roughness of the surface bounding the flow markedly characterises the thermal and hydrodynamic entry lengths in tunnels. A shortening of the thermal and hydrodynamic entry lengths is observed for an increase of the surface wall roughness. The previous result indicates that tunnels with rough walls are characterised by shorter thermal and hydrodynamic entrance regions compared to tunnels with smooth walls, and thus

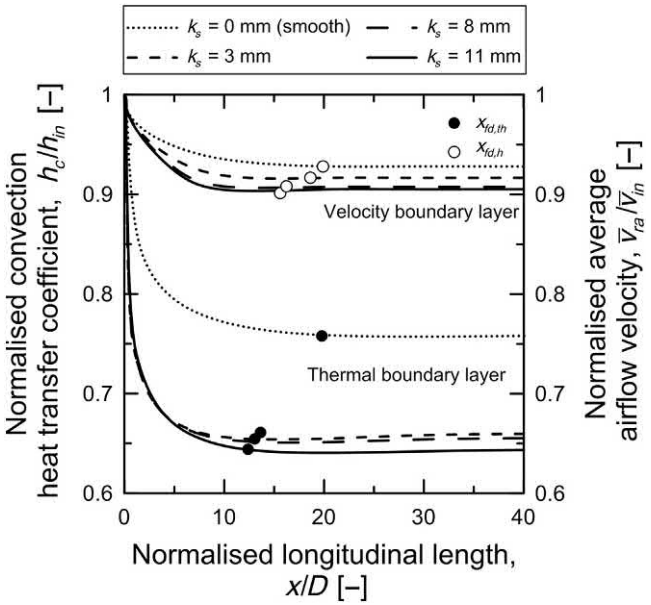

Figure 12.26 Development of the thermal and velocity boundary layers for different surface wall roughness. *Redrawn after Peltier, M., Rotta Loria, A.F., Lepage, L., Garin, E., Laloui, L., 2019. Numerical investigation of the convection heat transfer driven by airflows in underground tunnels. Appl. Therm. Eng. 159, 113844.*

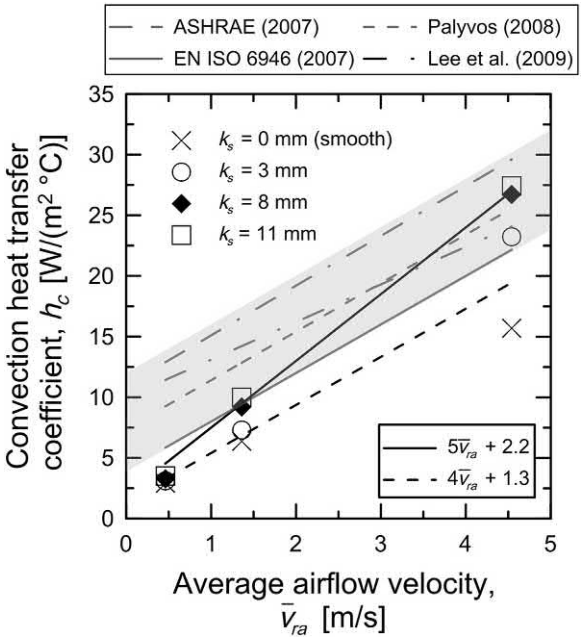

Figure 12.27 Correlations between convection heat transfer coefficient and airflow velocity for different surface roughness. *Redrawn after Peltier, M., Rotta Loria, A.F., Lepage, L., Garin, E., Laloui, L., 2019. Numerical investigation of the convection heat transfer driven by airflows in underground tunnels. Appl. Therm. Eng. 159, 113844.*

by longer fully developed regions where h_c is constant. The roughness of the surface(s) bounding the flow also characterises the variations of the normalised convection heat transfer coefficient and normalised airflow velocity with the normalised longitudinal length of tunnels. The influence of the surface wall roughness on the variation of the convection heat transfer coefficient is more pronounced compared to the influence represented by the flow velocity.

Fig. 12.27 presents the relationship between the convection heat transfer coefficient and the associated average value of airflow velocity measured in the thermally fully developed region of a tunnel characterised by a circular shape of the cross section for different values of surface wall roughness. Correlations previously identified in the literature are plotted for reference (ASHRAE, 2007; EN ISO 6946, 2007; Palyvos, 2008; Lee et al., 2009). For a given airflow velocity, a higher wall roughness leads to a higher magnitude of coefficient h_c. The reason for this phenomenon is attributed to the tendency of h_c to increase with the surface wall roughness, thus leading to an increase in the actual heat transfer rate occurring at the wall–air interface, irrespective of cooling or heating. The previous result agrees with evidence available in the literature highlighting that rough surfaces cause an increased transport of heat and mass (Bergman et al., 2011; Li et al., 2016).

12.4.5 Influence of pipe configuration

The pipe configuration represents a key technical solution for the optimisation of the thermohydromechanical behaviour of energy tunnels. Pipes can be installed perpendicular or parallel to the axis of energy tunnels (Barla and Di Donna, 2018; Cousin et al., 2019). A notable degree of freedom is associated with their installation when dealing with tunnels equipped with energy textiles over their surface (Lee et al., 2012). In contrast, noteworthy constraints arise when dealing with energy segmental linings, that is tunnels constructed by laying a permanent support made of prefabricated concrete segments that embed the pipes into them right after the 'tail' of the so-called full-face tunnel boring machines, while pursuing the excavation process. In fact, as far as minimum values of pipe spacing and bending radius are considered as a function of the pipe diameter, varying the layout or diameter of pipes installed in linings results in varying pipe configurations for the same surface of lining available. For example varying the pipe diameter involves changing the minimum pipe spacing and bending radius and thus the density of pipes per unit surface of tunnel lining (Cousin et al., 2019).

In the following, the influence of the pipe configuration on the thermohydraulic behaviour of energy tunnels is expanded with reference to the results of Cousin et al. (2019). Pipe configurations considering pipes located parallel to the tunnel axis and perpendicular to the tunnel axis, with diameters of 32 and 20 mm, are considered. Accordingly, four pipe configurations result from the previous pipe diameters and pipe layouts: (1.1) 32 mm diameter pipes installed parallel to the tunnel axis, (1.2) 20 mm diameter pipes installed parallel to the tunnel axis, (2.1) 32 mm diameter pipes installed perpendicular to the tunnel axis, (2.2) 20 mm diameter pipes installed perpendicular to the tunnel axis. A graphical representation of the previous pipe configurations is presented in Fig. 12.28. Energy tunnels in which the influence of airflow is considered through a constant value of convection heat transfer coefficient h_c are considered.

An example of the average extracted thermal power under steady conditions per unit surface of tunnel lining, $\dot{q}_i$, is reported in Fig. 12.29 for four pipe configurations

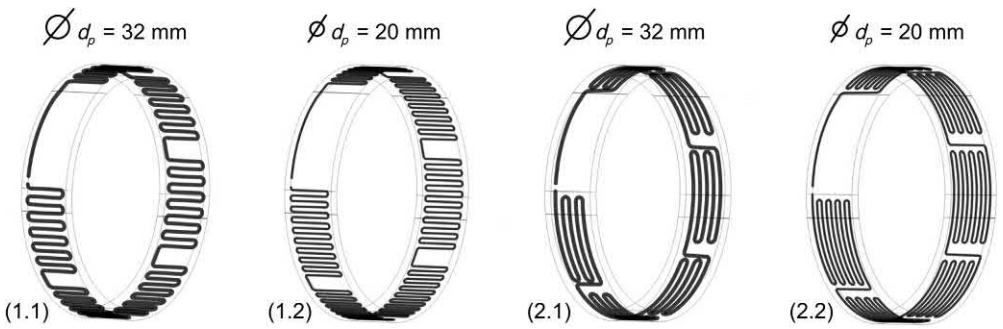

Figure 12.28 Example of the pipe density per unit surface of tunnel lining depending on the pipe configuration (Cousin et al., 2019).

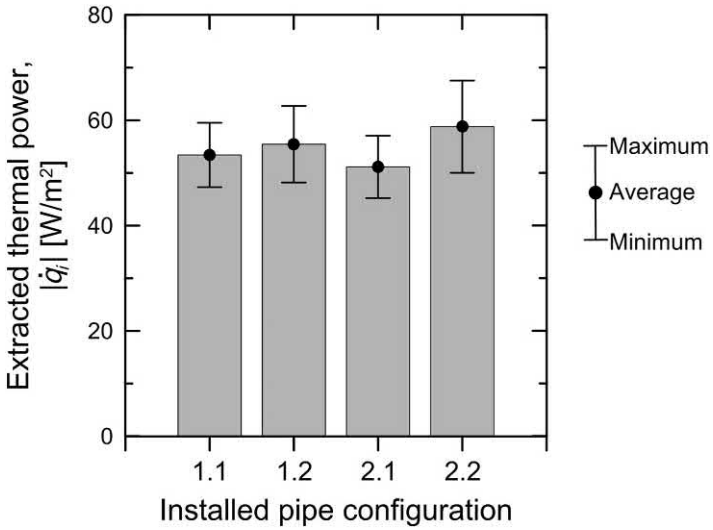

Figure 12.29 Average extracted thermal power for four different pipe configurations after 16 days of geothermal operation through an energy tunnel: (1.1) 32 mm diameter pipes installed parallel to the tunnel axis, (1.2) 20 mm diameter pipes installed parallel to the tunnel axis, (2.1) 32 mm diameter pipes installed perpendicular to the tunnel axis, (2.2) 20 mm diameter pipes installed perpendicular to the tunnel axis. *Modified after Cousin, B., Rotta Loria, A.F., Bourget, A., Rognon, F., Laloui, L., 2019. Energy performance and economic feasibility of energy segmental linings for subway tunnels. Tunn. Undergr. Space Technol. 91, 102997.*

involving layouts parallel and perpendicular to the tunnel axis and different pipe diameters, after a geothermal operation of $t = 16$ days. The variation of the considered variable depending on varying values of the Reynolds number and pipe embedment is proposed for reference. The configuration involving the smaller diameter pipes installed perpendicular to the tunnel axis yields to the greatest pipe length per segment and represents the optimal solution in terms of extracted thermal power per unit surface of tunnel lining. Numerical results corroborating the previous evidence are given in Table 12.6, along with the percentage increase of extracted thermal power calculated with respect to the minimum reference value corresponding to a pipe configuration involving 32 mm diameter pipes installed perpendicular to the tunnel axis (i.e. configuration 2.1). Installing larger diameter pipes leads to a higher yield of thermal power per metre of pipe, despite a smaller pipe length per ring being installed. However, the previous approach does not represent the optimal design solution from a strictly energy performance-related point of view.

12.4.6 Influence of pipe embedment

Reducing the pipe embedment facilitates the conduction heat transfer between the heat carrier fluid and the tunnel air, thus minimising the conduction heat transfer

Table 12.6 Influence of the pipe configuration on the extracted thermal power from a tunnel after 16 days. Configuration (1.1): 32 mm diameter pipes installed parallel to the tunnel axis; configuration (1.2): 20 mm diameter pipes installed parallel to the tunnel axis; configuration (2.1): 32 mm diameter pipes installed perpendicular to the tunnel axis; and configuration (2.2): 20 mm diameter pipes installed perpendicular to the tunnel axis.

Configuration	1.1	1.2	2.1	2.2
Average extracted thermal power per ring [W]	2920	3032	2796	3214
Extracted thermal power per unit of lining surface [W/m^2]	53	55	51	59
Configuration influence (w.r.t. min) [%]	+ 4.43	+ 8.44	−	+ 14.95
Extracted thermal power per metre length of pipe [W/m]	22	16	23	15

Source: Data from Cousin, B., Rotta Loria, A.F., Bourget, A., Rognon, F., Laloui, L., 2019. Energy performance and economic feasibility of energy segmental linings for subway tunnels. Tunn. Undergr. Space Technol. 91, 102997.

resistance of the lining (Cousin et al., 2019). This influence increases with a successive decrease of the pipe embedment and an increase of the Reynolds number, because the latter reduces the convection thermal resistance in the pipes.

In the following, the influence of the pipe embedment on the thermohydraulic behaviour of energy tunnels is expanded with reference to the results of Cousin et al. (2019). Values of pipe embedment from the tunnel intrados of $s_i/t_l = 0.5$, 0.625 and 0.75, where s_i is the distance from the tunnel intrados and t_l is the lining thickness, are considered. A graphical representation of the considered pipe embedment is provided in Fig. 12.30.

Fig. 12.31 presents an example of thermal power harvested per unit surface of tunnel lining, considering three different values of pipe embedment and three different flow rates. A tunnel lining characterised by a pipe configuration with 20 mm diameter pipes installed perpendicular to the tunnel axis after 16 days of geothermal operation is considered. Examples of percentages of harvested thermal power variation for a change in the pipe embedment are provided in Table 12.7 for varying values of Reynolds numbers. Decreasing the pipe embedment markedly improves the harvested thermal power.

12.4.7 Influence of heat carrier fluid flow rate

Increasing the Reynolds number enhances the convection heat transfer between the heat carrier fluid and the surrounding environment, thus minimising the convection heat transfer resistance in the pipes (Cousin et al., 2019). This influence increases with a decreasing pipe embedment, because reducing the spacing between the pipes and the tunnel intrados reduces the conduction thermal resistance of the geostructure.

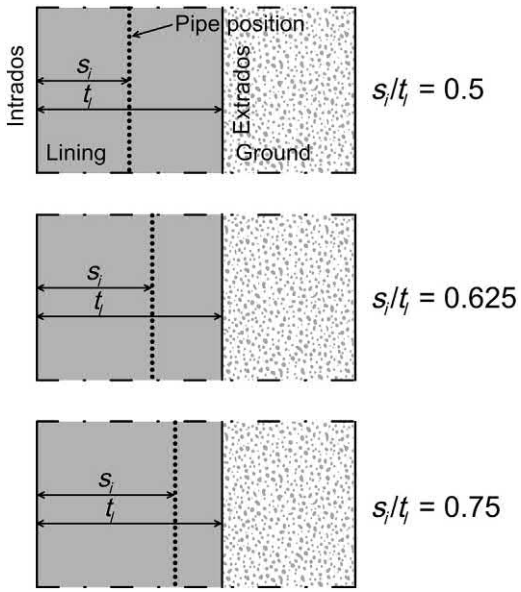

Figure 12.30 Examples of pipe embedment. The sketches represent portions of vertical cross sections of the lining that are perpendicular to the tunnel axis (Cousin et al., 2019).

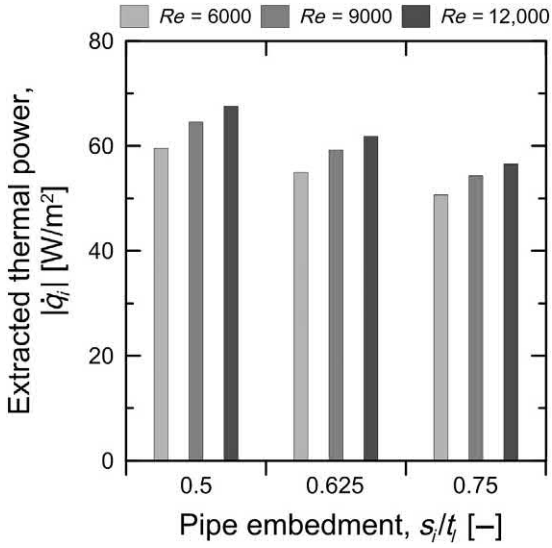

Figure 12.31 Extracted thermal power through an energy tunnel equipped with a pipe configuration involving 20 mm diameter pipes installed perpendicular to the tunnel axis, for three pipe embedment and three flow rates, after 16 days of geothermal operation. *Modified after Cousin, B., Rotta Loria, A.F., Bourget, A., Rognon, F., Laloui, L., 2019. Energy performance and economic feasibility of energy segmental linings for subway tunnels. Tunn. Undergr. Space Technol. 91, 102997.*

Table 12.7 Influence of the pipe embedment on the extracted thermal power through an energy tunnel equipped with a pipe configuration involving 20 mm diameter pipes installed perpendicular to the tunnel axis, for three Reynolds number, after 16 days of geothermal operation.

Reynolds number, *Re* [−]	Pipe embedment, s_i/t_l [−]	
	0.75 → 0.625	**0.75 → 0.5**
6000	+ 8.45%	+ 17.48%
9000	+ 9.04%	+ 18.85%
12,000	+ 9.30%	+ 19.46%

Source: Data from Cousin, B., Rotta Loria, A.F., Bourget, A., Rognon, F., Laloui, L., 2019. Energy performance and economic feasibility of energy segmental linings for subway tunnels. Tunn. Undergr. Space Technol. 91, 102997.

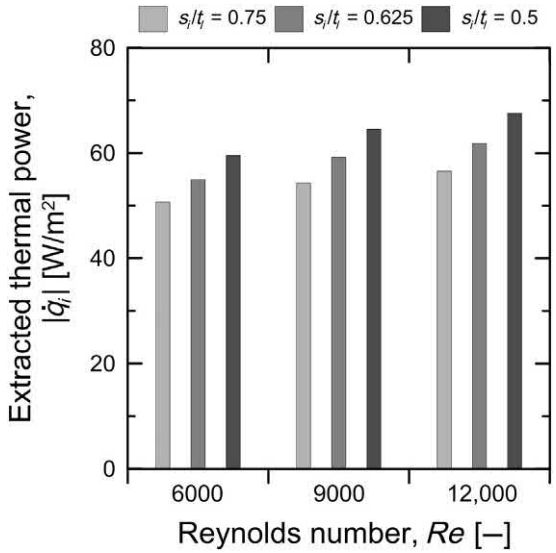

Figure 12.32 Extracted thermal power through an energy tunnel equipped with a pipe configuration involving 20 mm diameter pipes installed perpendicular to the tunnel axis, for three flow rates and three pipe embedment, after 16 days of geothermal operation. *Modified after Cousin, B., Rotta Loria, A.F., Bourget, A., Rognon, F., Laloui, L., 2019. Energy performance and economic feasibility of energy segmental linings for subway tunnels. Tunn. Undergr. Space Technol. 91, 102997.*

In the following, the influence of the heat carrier fluid flow rate circulating in the pipes on the thermohydraulic behaviour of energy tunnels is expanded with reference to the results of Cousin et al. (2019). Reynolds numbers of $Re = 6000$, 9000 and 12,000 are considered. Complementary numerical results about the influence of the flow rate on the effectiveness of the energy harvesting achievable via energy tunnels have been reported, for example, by Barla et al. (2016).

An example of the extracted thermal power per unit surface of tunnel lining, considering three different flow rates and three different pipe embedment, is presented in Fig. 12.32 for a pipe configuration with 20 mm diameter pipes installed perpendicular

Table 12.8 Influence of the Reynolds number on the extracted thermal power through an energy tunnel equipped with a pipe configuration involving 20 mm diameter pipes installed perpendicular to the tunnel axis, for three pipe embedment, after 16 days of geothermal operation.

Pipe embedment, s_i/t_l [−]	Reynolds number, *Re* [−]	
	6000 → 9000	6000 → 12,000
0.5	+ 8.43%	+ 13.46%
0.625	+ 7.76%	+ 12.46%
0.75	+ 7.18%	+ 11.59%

Source: Data from Cousin, B., Rotta Loria, A.F., Bourget, A., Rognon, F., Laloui, L., 2019. Energy performance and economic feasibility of energy segmental linings for subway tunnels. Tunn. Undergr. Space Technol. 91, 102997.

to the tunnel axis after 16 days of geothermal operation. The improvement of thermal power harvested from the tunnel that is achieved by increasing the fluid flow rate increases less markedly for a successive increase of the Reynolds number because it reduces the heat exchanger effectiveness. Examples of percentage of harvested thermal power variation with varying flow rates are provided in Table 12.8 for varying values of pipe embedment.

Based on the aforementioned results related to the influence of the pipe configuration, pipe embedment and heat carrier fluid flow rate, the following technical solutions appear to be particularly effective for achieving an effective geothermal exploitation via energy tunnels (Cousin et al., 2019): (1) densify the heat exchanger segment with smaller diameter pipes whenever possible; (2) apply a moderately turbulent flow rate to trade-off between high heat exchange and acceptable pumping power; (3) reduce the pipe embedment (when providing heat in the case of hot tunnels) and (4) equip several times shorter tunnel sections instead of a unique, long tunnel. An example of the influence of the considered technical solutions on the energy yield achievable through energy segmental lining is provided in Fig. 12.33 with reference to the results of Cousin et al. (2019). In the considered case studies, a 49% variation between the lowest and highest value of extracted thermal power can be observed.

12.4.8 Influence of groundwater flow

The presence of groundwater flow around energy tunnels can markedly characterise their thermohydromechanical behaviour. Similar to the influence of the airflow in the tunnel environment, more significant groundwater flows are associated with a more substantial heat transfer between energy tunnels and the surrounding ground (Di Donna and Barla, 2016; Bidarmaghz and Narsilio, 2018). Similar considerations are valid for other energy geostructures presenting an interface with air and another one with the ground such as energy walls and slabs.

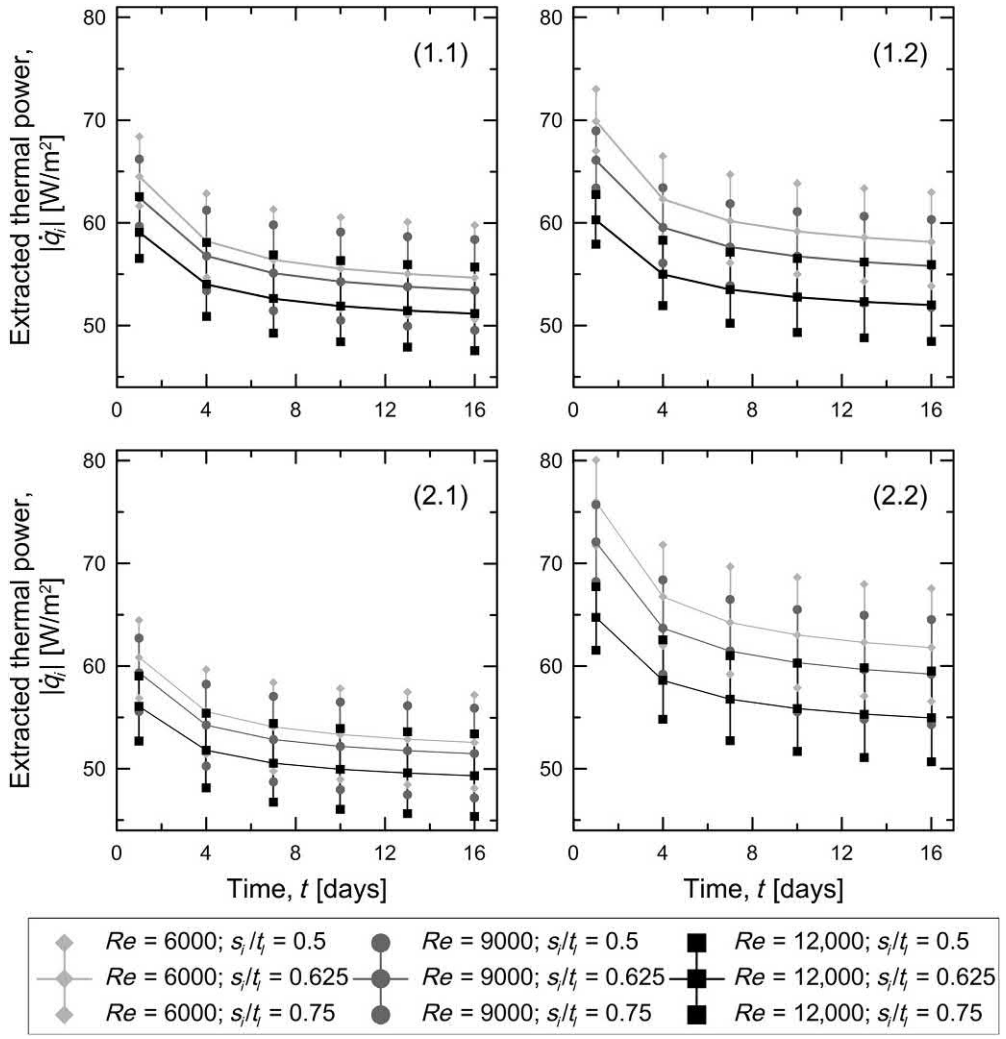

Figure 12.33 Extracted thermal power per unit of tunnel lining surface over 16 days for different pipe configurations, flow rates and pipe embedment. Configuration (1.1): 32 mm diameter pipes installed parallel to the tunnel axis; configuration (1.2): 20 mm diameter pipes installed parallel to the tunnel axis; configuration (2.1): 32 mm diameter pipes installed perpendicular to the tunnel axis and configuration (2.2): 20 mm diameter pipes installed perpendicular to the tunnel axis. *Modified after Cousin, B., Rotta Loria, A.F., Bourget, A., Rognon, F., Laloui, L., 2019. Energy performance and economic feasibility of energy segmental linings for subway tunnels. Tunn. Undergr. Space Technol. 91, 102997.*

In the absence of groundwater flow, the ground thermal conductivity plays a primary role in the energy yield that can be achieved via energy tunnels (e.g., under steady conditions). In these conditions, an increase in the effective thermal conductivity of the ground from $\lambda_{soil} = 0.9{-}3.9$ W/(m °C) for both summer and winter operation

modes can more than double the exchanged heat (Di Donna and Barla, 2016; Barla and Di Donna, 2018). The extent of the region in which the temperature field of the ground is significantly disturbed by the geothermal operation of energy tunnels is typically limited in the absence of groundwater flow (Cousin et al., 2019), while it can be remarkable in the presence of groundwater flow and achieve approximately 10 m (Barla et al., 2016; Bidarmaghz and Narsilio, 2018). Intermittent operations can help to restrain the region of the ground surrounding energy tunnels that is influenced by the heat exchange (Ogunleye et al., 2020).

In the presence of groundwater flow, the most influential factor on the overall heat transfer process governing the thermohydraulic behaviour of energy tunnels is the intensity of groundwater velocity rather than the value of effective thermal conductivity of the ground. In these conditions, an increase of Darcy's velocity from $\overline{v}_{rw} = 0$ to 2 m/day can involve an increase of the exchanged heat by a factor of three to eight times (Di Donna and Barla, 2016; Barla and Di Donna, 2018). Significant values of groundwater flow require the assessment of the risk of thermal pollution (Di Donna and Barla, 2016; Barla and Di Donna, 2018). The presence and significance of groundwater flow significantly influence the temperature distribution in the ground, the tunnel and the tunnel air (Bidarmaghz and Narsilio, 2018).

Charts summarising the influence of the presence and significance of groundwater flow on the thermohydraulic behaviour of energy tunnels is expanded in Fig. 12.34

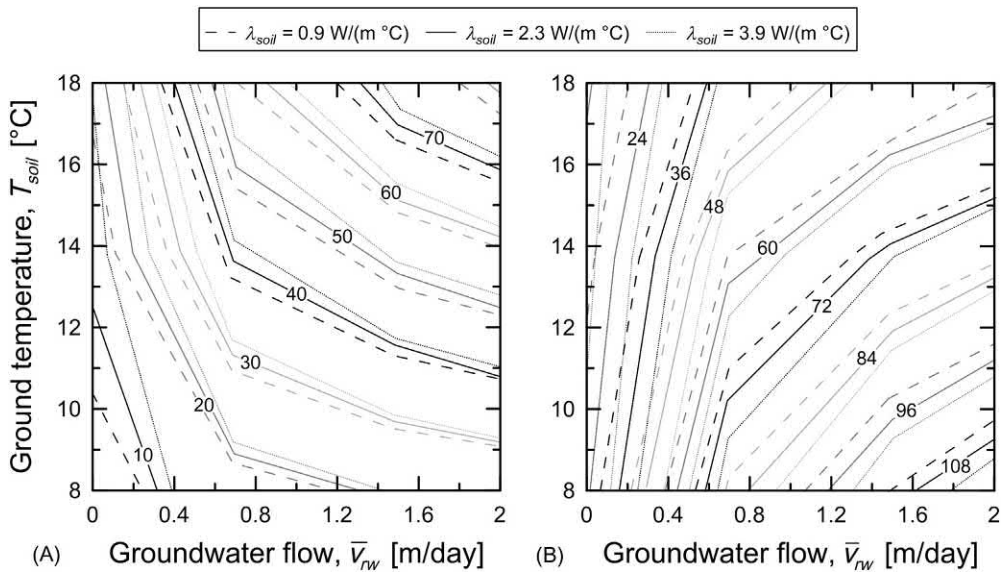

Figure 12.34 Thermal power (A) extracted and (B) injected via energy tunnels for varying values of ground temperature, groundwater flow velocity and effective thermal conductivity of the ground. *Redrawn after Di Donna, A., Barla, M., 2016. The role of ground conditions on energy tunnels' heat exchange. Environ. Geotech. 3 (4), 214–224.*

with reference to the results of Di Donna and Barla (2016). Absolute values of the thermal power that can be harvested from energy tunnels when steady thermal conditions are achieved within such geostructures are depicted for varying values of ground temperature, groundwater flow velocity and effective thermal conductivity of the ground. Thermal powers comprised between approximately 10 and 100 W/m^2 can be associated with the same energy tunnel in different site conditions because of a variation of the considered variables.

12.5 Thermohydromechanical behaviour of energy walls

12.5.1 General

In the following, the thermohydromechanical behaviour of energy walls is expanded for a variation in (1) the pipe configuration, (2) the surface wall thermal condition, (3) the soil–wall thermal conductivity ratio, (4) the soil–wall thermal expansion coefficient ratio and (5) the groundwater flow significance.

12.5.2 Influence of pipe configuration

The pipe configuration represents a key technical solution for the optimisation of the thermohydromechanical behaviour of energy walls, similar to other energy geostructures. In particular, the pipe configuration more pronouncedly affects the energy harvesting rather the mechanics of energy walls. This aspect may be considered to characterise other energy geostructures such as energy tunnels and slabs.

Energy walls offer broad choices for the pipe configuration (Sterpi et al., 2017). Various pipe layouts can be foreseen due to the more remarkable freedom related to the pipe installation compared to other energy geostructures such as energy piles. Pipes can be installed only towards the air or the ground side, or on both sides of energy walls (Bourne-Webb et al., 2016b). The pipe layout, rather than the pipe length, critically influences the thermohydraulic behaviour of energy walls (Sterpi et al., 2017).

The pipe configurations installed in energy walls characterise the temperature gradients within the wall panels and their consequent thermohydromechanical behaviour (Sterpi et al., 2017; Kürten et al., 2015; Bourne-Webb et al., 2016b; Di Donna et al., 2017). Temperature gradients in the energy wall plane develop in both the vertical and horizontal directions due to the nonnegligible distance that typically characterise the geostructure between the cool and warm portions of the heat exchangers (Coletto and Sterpi, 2016). The previous aspect involves that different vertical cross sections are subjected to thermal loads of different magnitude and their mutual interaction leads to three-dimensional effects for the thermomechanical response of energy walls. Based on the previous consideration, conventional

plane strain analyses of wall structures are considered inaccurate for energy walls (Sterpi et al., 2017).

In the following, the influence of the pipe location on the thermomechanical behaviour of energy walls is expanded with reference to the results of Bourne-Webb et al. (2016b). Pipe configurations involving pipes located on the air or ground side are considered.

An example of the relative effect caused by mechanical loads, thermal loads associated with the thermal equilibration of the underground environment after the geostructure construction and thermal loads associated with a geothermal operation is discussed in Fig. 12.35 in terms of the bending moment distribution along the energy wall. After the end construction, the next major alteration in the thermomechanical behaviour of the energy wall is caused by the thermal equilibration of the underground environment. Different pipe locations involve a limited influence on the thermomechanical behaviour of the energy wall compared to the influences played by the mechanical loads associated with the construction and the thermal loads occurring during the successive thermal equilibration of the underground environment. However, when considered in terms of variations from the previous

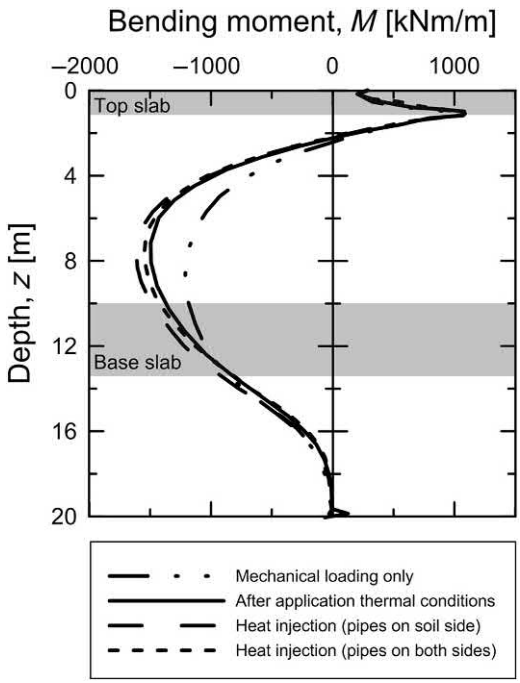

Figure 12.35 Bending moments in a tunnel energy wall from construction to operation. *Redrawn after Bourne-Webb, P., Freitas, T.B., da Costa Gonçalves, R., 2016b. Thermal and mechanical aspects of the response of embedded retaining walls used as shallow geothermal heat exchangers. Energy Build. 125, 130–141.*

state characterising the wall, different pipe locations do involve noteworthy different mechanical responses. According to Bourne-Webb et al. (2016b), other configurations and/or material properties characterising energy walls may be associated with different effects.

The commented behaviour of energy walls highlights the different structural function provided with respect to other energy geostructures such as energy piles. According to Sterpi et al. (2017), this structural function is governed by horizontal pressures that are contrasted by the wall flexural response and by the supporting action of possible anchors and struts. Variations of contact pressures caused by the influence of mechanical loads at the soil–structure interface are generally paramount, while those caused by the applications of thermal loads are likely to be limited in practice (Sterpi et al., 2017; Rui and Yin, 2017; Sailer et al., 2019). The possible detrimental action induced by cyclic thermal loads of this interface may be neglected due to the limited influence of the shear strength of this setting on the overall structural response of energy walls (Sterpi et al., 2017). The effects caused by the thermally induced deformation of anchors on the thermohydromechanical behaviour of tunnel energy walls are remarkable (Mimouni et al., 2014).

12.5.3 Influence of surface wall thermal condition

The surface wall thermal condition profoundly influences the thermohydromechanical behaviour of energy walls and other relevant energy geostructures. Strictly related to the presence and significance of airflow in the adjacent built environment, the surface wall thermal condition characterises the temperature field in the energy wall and the surrounding ground. This aspect, in turn, markedly influences the energy harvesting and the mechanics characterising the considered geostructures (Bourne-Webb et al., 2016b). The airflow condition particularly characterises the temperature difference between the underground built environment and the wall, such a feature playing a crucial role in the behaviour of energy walls (Di Donna et al., 2017; Rui and Yin, 2017).

In the following, the effect of the surface wall thermal conditions on the thermohydromechanical behaviour of energy walls is expanded with reference to the results of Bourne-Webb et al. (2016b). Surface wall thermal conditions involving a fixed constant temperature or a convection boundary condition characterised by increasing values of convection heat transfer coefficient of $h_c = 2.5$ and $25\ \mathrm{W/(m^2\,^\circ C)}$ are considered.

Fig. 12.36 presents an example of the influence of the surface wall thermal condition on the heat flow characterising the depth of energy walls towards the air and ground sides. When an airflow resulting in a convection heat transfer coefficient that tends to zero characterises the surface of energy walls and other relevant energy

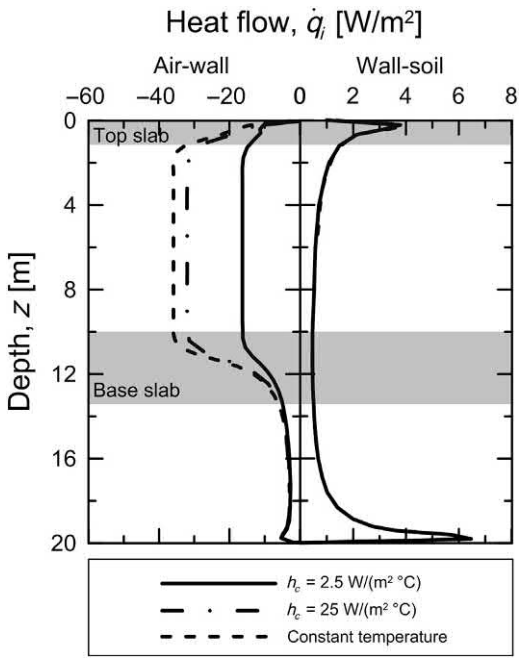

Figure 12.36 Effect of surface wall thermal condition on the lateral heat flow across energy walls. *Redrawn after Bourne-Webb, P., Freitas, T.B., da Costa Gonçalves, R., 2016b. Thermal and mechanical aspects of the response of embedded retaining walls used as shallow geothermal heat exchangers. Energy Build. 125, 130–141.*

geostructures, the highest interface temperatures and lowest temperature gradients are observed, and thus the lowest heat flow is established. When a constant temperature characterises the surface of energy walls and other relevant energy geostructures, the lowest interface temperatures and highest temperature gradients are observed, and thus the highest heat flow is established. According to Bourne-Webb et al. (2016b), the previous two cases act as bounds to the other cases considered. As the airflow velocity and related value of convection heat transfer coefficient increase, heat is more readily conducted across the wall interface and heat flow increases.

Fig. 12.37 presents an example of the influence of the surface wall thermal condition on the bending moment characterising the depth of energy walls. The surface wall thermal condition has a comparable effect to the location of the pipes in the variation of bending moment upon thermal equilibration of the underground environment. According to Bourne-Webb et al. (2016b), this effect may be considered negligible in absolute value compared to the bending moment variation that is caused by the occurrence of the thermal equilibration itself after the construction of the considered energy geostructures.

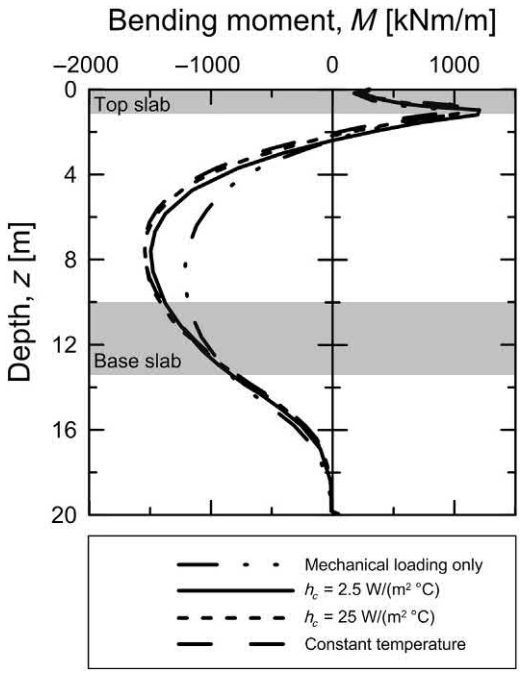

Figure 12.37 Effect of surface wall thermal condition on the bending moment distribution along energy walls. *Redrawn after Bourne-Webb, P., Freitas, T.B., da Costa Gonçalves, R., 2016b. Thermal and mechanical aspects of the response of embedded retaining walls used as shallow geothermal heat exchangers. Energy Build. 125, 130–141.*

12.5.4 Influence of soil–wall thermal conductivity ratio

The relative significance of the thermal conductivity of the ground to that of energy walls markedly influences the thermohydraulic behaviour of such geostructures (Bourne-Webb et al., 2016b). Different magnitudes of thermal conductivity of the ground and the geostructure characterise the significance of the heat that is exchanged via the energy wall: from one side, with the underground built environment and, from the other side, with the surrounding ground.

An example of the influence of the thermal conductivity of the ground and an energy wall on the exchanged heat with depth is presented in Fig. 12.38 with reference to the results of Bourne-Webb et al. (2016b). Situations in which the thermal conductivity of the material constituting energy walls is half, equal or double the thermal conductivity of the surrounding ground are considered. This yields soil–wall thermal conductivity ratios of $\lambda_{soil}/\lambda_{EW} = 2$, 1 and 0.5, where λ_{soil} and λ_{EW} are the thermal conductivity of the soil and energy wall, respectively. Different values of the thermal conductivity of the material constituting energy walls significantly influence

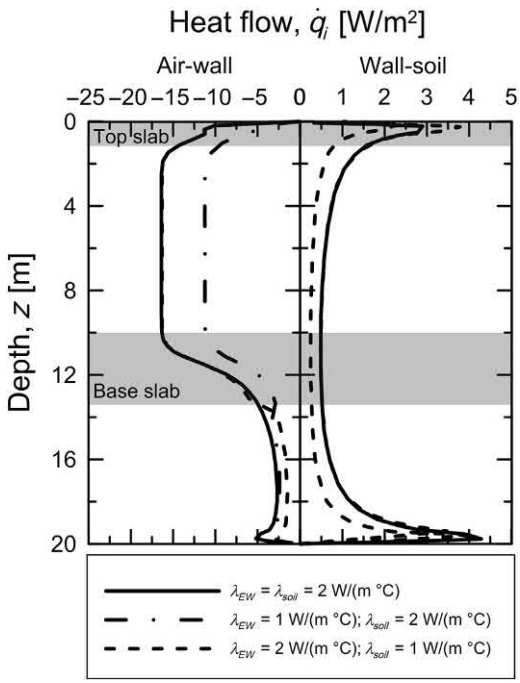

Figure 12.38 Effect of thermal conductivity ratio on the lateral heat flow across energy walls. *Redrawn after Bourne-Webb, P., Freitas, T.B., da Costa Gonçalves, R., 2016b. Thermal and mechanical aspects of the response of embedded retaining walls used as shallow geothermal heat exchangers. Energy Build. 125, 130–141.*

the heat flow across the wall interface with the underground built environment, while having almost no impact on heat flow across the wall interface with the soil. Different values of the thermal conductivity of the soil significantly influence the heat flow across the wall interface with medium, while having a limited impact on the heat flow across the wall interface with the underground built environment. According to Bourne-Webb et al. (2016b), the application of thermal gradients in the wall section is likely to lead to moisture movement and changes in the thermal conductivity over time. The influence of this time-dependent effect, similar to others highlighted by Sailer et al. (2019), may be considered in the analysis of energy walls and other relevant energy geostructures.

12.5.5 Influence of soil–wall thermal expansion coefficient ratio

The relative significance of the thermal expansion of the ground to that of energy walls critically influences the thermomechanical behaviour of such geostructures (Bourne-Webb et al., 2016b). Different values of soil–wall thermal expansion coefficient ratio, $X = \alpha_{soil}/\alpha_{EW}$, where α_{EW} is the linear thermal expansion coefficient of

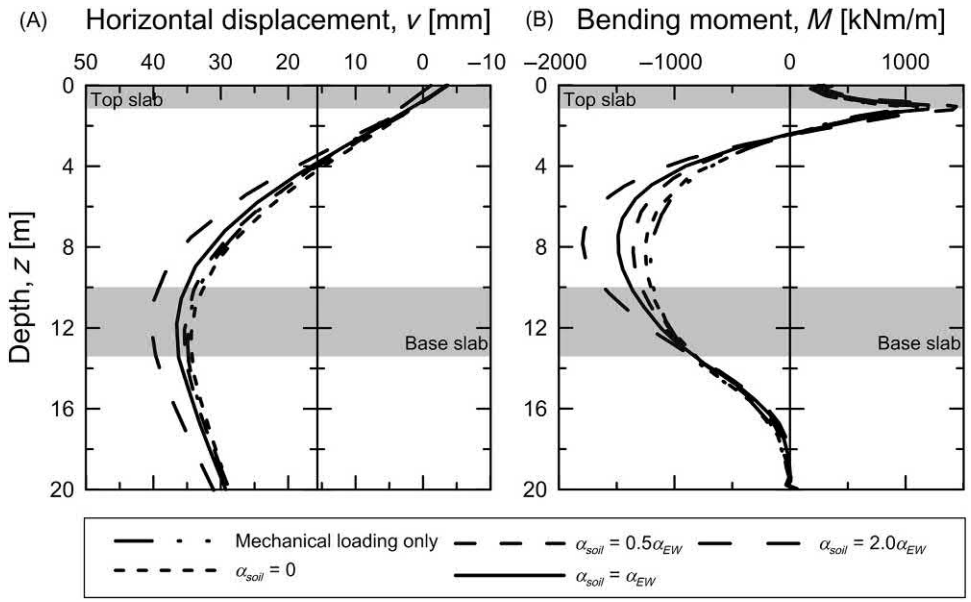

Figure 12.39 Effect of the thermal expansion coefficient ratio on the distributions of (A) horizontal displacement and (B) bending moment along energy tunnels. *Redrawn after Bourne-Webb, P., Freitas, T.B., da Costa Gonçalves, R., 2016b. Thermal and mechanical aspects of the response of embedded retaining walls used as shallow geothermal heat exchangers. Energy Build. 125, 130–141.*

the energy wall, can markedly affect the distributions of horizontal displacement and bending moment along such geostructures.

An example of the influence of the soil–wall thermal expansion coefficient ratio on the distributions of horizontal displacement and bending moment along energy walls is presented in Fig. 12.39 with reference to the results of Bourne-Webb et al. (2016b). Values of $X = \alpha_{soil}/\alpha_{EW} =$ 0, 0.5, 1 and 2 are considered. The overall effect of the imposed surface and tunnel conditions differs significantly depending on the thermal expansion coefficient of the soil. Compared to the situation in which $X = 1$, values of $X = 0$ and 2 involve values of the maximum bending moment of about 40% less or 90% larger, respectively, while values of the maximum displacements about 10% less and 40% larger, respectively.

12.5.6 Influence of groundwater flow

The presence of groundwater flow around energy tunnels can markedly characterise their thermohydromechanical behaviour. Similar to the influence of the airflow in the tunnel environment, more significant groundwater flows are associated with a more substantial heat transfer between energy tunnels and the surrounding ground (Piemontese et al., 2018; Zannin et al., 2018; Delerablée et al., 2018).

12.6 Modelled and observed response

Many different numerical approaches can be employed to simulate the thermohydro-mechanical behaviour of energy geostructures and the literature presents various comparisons between modelled and observed responses of energy geostructures. To date, the most significant proportion of experimental results obtained by means of full-scale field testing, centrifuge testing or laboratory testing is available for energy piles (see, e.g., Laloui et al., 2003; Bourne-Webb et al., 2009; Akrouch et al., 2014; Wang et al., 2014a; You et al., 2016; Sutman et al., 2018; Ng et al., 2014, 2015; Stewart and McCartney, 2012; Goode and McCartney, 2015; Kalantidou et al., 2012; Yavari et al., 2014, 2016; McCartney and Murphy, 2012; Murphy and McCartney, 2015; Mimouni and Laloui, 2015; Rotta Loria and Laloui, 2017, 2018; Nguyen et al., 2017). A markedly less developed amount of experimental results characterises other energy geostructures such as energy tunnels (Adam and Markiewicz, 2009; Buhmann et al., 2016; Barla et al., 2019) and energy walls (Xia et al., 2012; Sterpi et al., 2018a). Because of the previous evidence, the largest amount of numerical simulations currently available focuses on modelling aspects involved with the structural support and geothermal operation of energy piles rather than with other energy geostructures such as energy tunnels and energy walls.

The numerical simulation of the observed behaviour of energy piles has been addressed, for example, by Laloui et al. (2006), Wang et al. (2014b), Rotta Loria et al. (2015a,b), Saggu and Chakraborty (2015b), Di Donna et al. (2016) and Gawecka et al. (2016). The numerical simulation of the observed behaviour of energy walls has been addressed, for example, by Di Donna et al. (2017) and Sterpi et al. (2018b).

Due to the significant challenges and limited knowledge associated with energy tunnels and energy walls, the numerical analysis of the considered structures is expected to increase in the future.

References

Achich, A., 2018. Numerical simulation of deck de-icing using energy pile systems (M.Sc. degree). Laboratory of Soil Mechanics, Swiss Federal Institute of Technology in Lausanne, Lausanne.

Adam, D., Markiewicz, R., 2009. Energy from earth-coupled structures, foundations, tunnels and sewers. Geotechnique 59 (3), 229–236.

Adinolfi, M., Maiorano, R.M.S., Mauro, A., Massarotti, N., Aversa, S., 2018. On the influence of thermal cycles on the yearly performance of an energy pile. Geomech. Energy Environ. 16, 32–44.

Akrouch, G.A., Sánchez, M., Briaud, J.-L., 2014. Thermo-mechanical behavior of energy piles in high plasticity clays. Acta Geotech. 9 (3), 399–412.

Akrouch, G.A., Sánchez, M., Briaud, J.-L., 2018. Thermal performance and economic study of an energy piles system under cooling dominated conditions. Renew. energy. Avaliable from: https://doi.org/10.1016/j.renene.2018.11.101.

ASHRAE, A.H., 2007. HVAC applications. ASHRAE Handbook, Fundamentals, 2003.

Barla, M., Di Donna, A., 2018. Energy tunnels: concept and design aspects. Undergr. Space 3 (4), 268–276.

Barla, M., Di Donna, A., Perino, A., 2016. Application of energy tunnels to an urban environment. Geothermics 61, 104–113.
Barla, M., Di Donna, A., Insana, A., 2019. A novel real-scale experimental prototype of energy tunnel. Tunn. Undergr. Space Technol. 87, 1–14.
Batini, N., Rotta Loria, A.F., Conti, P., Testi, D., Grassi, W., Laloui, L., 2015. Energy and geotechnical behaviour of energy piles for different design solutions. Appl. Therm. Eng. 86 (1), 199–213.
Bergman, T., Incropera, F., Lavine, A., DeWitt, D., 2011. Fundamentals of Heat and Mass Transfer. Wiley, Hoboken, NJ.
Bezyan, B., Porkhial, S., Mehrizi, A.A., 2015. 3-D simulation of heat transfer rate in geothermal pile-foundation heat exchangers with spiral pipe configuration. Appl. Therm. Eng. 87, 655–668.
Bidarmaghz, A., Narsilio, G.A., 2018. Heat exchange mechanisms in energy tunnel systems. Geomech. Energy Environ. 16, 83–95.
Bidarmaghz, A., Narsilio, G.A., Johnston, I.W., Colls, S., 2016. The importance of surface air temperature fluctuations on long-term performance of vertical ground heat exchangers. Geomech. Energy Environ. 6, 35–44.
Bidarmaghz, A., Narsilio, G.A., Buhmann, P., Moormann, C., Westrich, B., 2017. Thermal interaction between tunnel ground heat exchangers and borehole heat exchangers. Geomech. Energy Environ. 10, 29–41.
Bourne-Webb, P.J., Amatya, B.L., Soga, K., Amis, T., Davidson, C., Payne, P., 2009. Energy pile test at Lambeth College, London: geotechnical and thermodynamic aspects of pile response to heat cycles. Geotechnique 59 (3), 237–248.
Bourne-Webb, P., Bodas Freitas, T., Freitas Assunção, R., 2016a. Soil–pile thermal interactions in energy foundations. Geotechnique 66 (2), 167–171.
Bourne-Webb, P., Freitas, T.B., da Costa Gonçalves, R., 2016b. Thermal and mechanical aspects of the response of embedded retaining walls used as shallow geothermal heat exchangers. Energy Build. 125, 130–141.
Buhmann, P., Moormann, C., Westrich, B., Pralle, N., Friedemann, W., 2016. Tunnel geothermics—a German experience with renewable energy concepts in tunnel projects. Geomech. Energy Environ. 8, 1–7.
Carotenuto, A., Marotta, P., Massarotti, N., Mauro, A., Normino, G., 2017. Energy piles for ground source heat pump applications: comparison of heat transfer performance for different design and operating parameters. Appl. Therm. Eng. 124, 1492–1504.
Cecinato, F., Loveridge, F.A., 2015. Influences on the thermal efficiency of energy piles. Energy 82, 1021–1033.
Coletto, A., Sterpi, D., 2016. Structural and geotechnical effects of thermal loads in energy walls. Procedia Eng. 158, 224–229.
Cousin, B., Rotta Loria, A.F., Bourget, A., Rognon, F., Laloui, L., 2019. Energy performance and economic feasibility of energy segmental linings for subway tunnels. Tunn. Undergr. Space Technol. 91, 102997.
Cui, Y., Zhu, J., 2017. 3D transient heat transfer numerical analysis of multiple energy piles. Energy Build. 134, 129–142.
Delerablée, Y., Rammal, D., Mroueh, H., Burlon, S., Habert, J., Froitier, C., 2018. Integration of thermoactive metro stations in a smart energy system: feedbacks from the Grand Paris Project. Infrastructures 3 (4), 56.
Di Donna, A., Barla, M., 2016. The role of ground conditions on energy tunnels' heat exchange. Environ. Geotech. 3 (4), 214–224.
Di Donna, A., Laloui, L., 2014. Numerical analysis of the geotechnical behaviour of energy piles. Int. J. Numer. Anal. Methods Geomech. 39 (8), 861–888.
Di Donna, A., Rotta Loria, A.F., Laloui, L., 2016. Numerical study on the response of a group of energy piles under different combinations of thermo-mechanical loads. Comput. Geotech. 72 (1), 126–142.
Di Donna, A., Cecinato, F., Loveridge, F., Barla, M., 2017. Energy performance of diaphragm walls used as heat exchangers. Proc. Inst. Civ. Eng. Geotech. Eng. 170 (3), 232–245.

Dupray, F., Li, C., Laloui, L., 2014. Heat-exchanger piles for the de-icing of bridges. Acta Geotech. 9 (3), 413–423.
EN ISO 6946, 2007. BS EN ISO 6946: 2007 Building Components and Building Elements—Thermal Resistance and Thermal Transmittance—Calculation Method. International Organization for Standardization, Geneva.
Fadejev, J., Kurnitski, J., 2015. Geothermal energy piles and boreholes design with heat pump in a whole building simulation software. Energy Build. 106, 23–34.
Fox, R.W., McDonald, A.T., Pritchard, P.J., 1985. Introduction to Fluid Mechanics. John Wiley & Sons, New York.
Gao, J., Zhang, X., Liu, J., Li, K., Yang, J., 2008a. Numerical and experimental assessment of thermal performance of vertical energy piles: an application. Appl. Energy 85 (10), 901–910.
Gao, J., Zhang, X., Liu, J., Li, K.S., Yang, J., 2008b. Thermal performance and ground temperature of vertical pile-foundation heat exchangers: a case study. Appl. Therm. Eng. 28 (17–18), 2295–2304.
Gashti, E.H.N., Malaska, M., Kujala, K., 2014. Evaluation of thermo-mechanical behaviour of composite energy piles during heating/cooling operations. Eng. Struct. 75 (1), 363–373.
Gawecka, K.A., Taborda, D.M., Potts, D.M., Cui, W., Zdravković, L., Haji Kasri, M.S., 2016. Numerical modelling of thermo-active piles in London Clay. Proc. Inst. Civ. Eng. Geotech. Eng. 170 (3), 201–2194.
Gnielinski, V., 1976. New equations for heat and mass transfer in turbulent pipe and channel flow. Int. Chem. Eng. 16 (1), 359–368.
Go, G.-H., Lee, S.-R., Yoon, S., Kang, H.-B., 2014. Design of spiral coil PHC energy pile considering effective borehole thermal resistance and groundwater advection effects. Appl. Energy 125, 165–178.
Goode III, J., McCartney, J.S., 2015. Centrifuge modeling of boundary restraint effects in energy foundations. J. Geotech. Geoenviron. Eng. 141 (8), 04015034.
Kalantidou, A., Tang, A.M., Pereira, J., Hassen, G., 2012. Preliminary study on the mechanical behaviour of heat exchanger pile in physical model. Geotechnique 62 (11), 1047–1051.
Kürten, S., Mottaghy, D., Ziegler, M., 2015. Design of plane energy geostructures based on laboratory tests and numerical modelling. Energy Build. 107, 434–444.
Laloui, L., Moreni, M., Vulliet, L., 2003. Comportement d'un pieu bi-fonction, fondation et échangeur de chaleur. Can. Geotech. J. 40 (2), 388–402.
Laloui, L., Nuth, M., Vulliet, L., 2006. Experimental and numerical investigations of the behaviour of a heat exchanger pile. Int. J. Numer. Anal. Methods Geomech. 30 (8), 763–781.
Lee, Y., Choi, M.-S., Yi, S.-T., Kim, J.-K., 2009. Experimental study on the convective heat transfer coefficient of early-age concrete. Cem. Concr. Compos. 31 (1), 60–71.
Lee, C., Park, S., Won, J., Jeoung, J., Sohn, B., Choi, H., 2012. Evaluation of thermal performance of energy textile installed in tunnel. Renew. Energy 42, 11–22.
Li, A., Yang, C., Ren, T., 2016. Modeling and parametric studies for convective heat transfer in large, long and rough circular cross-sectional underground tunnels. Energy Build. 127, 259–267.
Loveridge, F., Powrie, W., 2014. 2D thermal resistance of pile heat exchangers. Geothermics 50, 122–135.
Man, Y., Yang, H., Diao, N., Liu, J., Fang, Z., 2010. A new model and analytical solutions for borehole and pile ground heat exchangers. Int. J. Heat Mass Transf. 53 (13), 2593–2601.
McCartney, J.S., Murphy, K.D., 2012. Strain distributions in full-scale energy foundations. DFI J. 6 (2), 26–38.
Mimouni, T., Laloui, L., 2015. Behaviour of a group of energy piles. Can. Geotech. J. 52 (12), 1913–1929.
Mimouni, T., Dupray, F., Laloui, L., 2014. Estimating the geothermal potential of heat-exchanger anchors on a cut-and-cover tunnel. Geothermics 51, 380–387.
Munson, B.R., Young, D.F., Okiishi, T.H., 1990. Fundamentals of fluid mechanics. John Wiley & Sons, New York.
Murphy, K., McCartney, J.S., 2015. Seasonal response of energy foundations during building operation. Geotech. Geol. Eng. 33 (2), 343–356.
Ng, C.W.W., Shi, C., Gunawan, A., Laloui, L., 2014. Centrifuge modelling of energy piles subjected to heating and cooling cycles in clay. Géotech. Lett. 4 (October–December), 310–316.

Ng, C.W.W., Shi, C., Gunawan, A., Laloui, L., Liu, H.L., 2015. Centrifuge modelling of heating effects on energy pile performance in saturated sand. Can. Geotech. J. 52 (8), 1045–1057.
Ng, C.W.W., Ma, Q.J., Gunawan, A., 2016. Horizontal stress change of energy piles subjected to thermal cycles in sand. Comput. Geotech. 78, 54–61.
Nguyen, V.T., Tang, A.M., Pereira, J.-M., 2017. Long-term thermo-mechanical behavior of energy pile in dry sand. Acta Geotech. 12 (4), 729–737.
Nicholson, D.P., Chen, Q., de Silva, M., Winter, A., Winterling, R., 2014. The design of thermal tunnel energy segments for Crossrail, UK, Proceedings of the Institution of Civil Engineers-Engineering Sustainability, vol. 167. Thomas Telford Ltd, pp. 118–134.
Ogunleye, O., Singh, R.M., Cecinato, F., Choi, J.C., 2020. Effect of intermittent operation on the thermal efficiency of energy tunnels under varying tunnel air temperature. Renew. Energy 146, 2646–2658.
Olgun, C.G., Ozudogru, T.Y., Abdelaziz, S.L., Senol, A., 2014. Long-term performance of heat exchanger piles. Acta Geotech. 10 (5), 553–569. Available from: https://doi.org/10.1007/s11440-014-0334-z.
Ozudogru, T.Y., Ghasemi-Fare, O., Olgun, C.G., Basu, P., 2015. Numerical modeling of vertical geothermal heat exchangers using finite difference and finite element techniques. Geotech. Geol. Eng. 33 (2), 291–306.
Palyvos, J., 2008. A survey of wind convection coefficient correlations for building envelope energy systems' modeling. Appl. Therm. Eng. 28 (8), 801–808.
Park, H., Lee, S.-R., Yoon, S., Choi, J.-C., 2013. Evaluation of thermal response and performance of PHC energy pile: Field experiments and numerical simulation. Appl. Energy 103, 12–24.
Park, S., Lee, S., Lee, D., Lee, S.S., Choi, H., 2016. Influence of coil pitch on thermal performance of coil-type cast-in-place energy piles. Energy Build. 129, 344–356.
Park, S., Lee, D., Lee, S., Chauchois, A., Choi, H., 2017. Experimental and numerical analysis on thermal performance of large-diameter cast-in-place energy pile constructed in soft ground. Energy 118, 297–311.
Peltier, M., Rotta Loria, A.F., Lepage, L., Garin, E., Laloui, L., 2019. Numerical investigation of the convection heat transfer driven by airflows in underground tunnels. Appl. Therm. Eng. 159, 113844.
Piemontese, M., Barla, M., Di Donna, A., Loveridge, F., 2018. Preliminary assessment of energy walls efficiency under different underground scenarios. Extended abstract. In: Symposium on Energy Geotechnics, Lausanne, September 2018.
Randolph, M.F., 2003. Science and empiricism in pile foundation design. Geotechnique 53 (10), 847–875.
Rotta Loria, A.F., Laloui, L., 2016. The interaction factor method for energy pile groups. Comput. Geotech. 80, 121–137.
Rotta Loria, A.F., Laloui, L., 2017. Thermally induced group effects among energy piles. Geotechnique 67 (5), 374–393.
Rotta Loria, A.F., Laloui, L., 2018. Group action effects caused by various operating energy piles. Geotechnique 68 (9), 834–841.
Rotta Loria, A.F., Di Donna, A., Laloui, L., 2015a. Numerical study on the suitability of centrifuge testing the thermal-induced mechanical behavior of energy piles. J. Geotech. Geoenviron. Eng. 141 (10), 04015042.
Rotta Loria, A.F., Gunawan, A., Shi, C., Laloui, L., Ng, C.W., 2015b. Numerical modelling of energy piles in saturated sand subjected to thermo-mechanical loads. Geomech. Energy Environ. 1 (1), 1–15.
Rotta Loria, A.F., Vadrot, A., Laloui, L., 2017. Effect of non-linear soil deformation on the interaction among energy piles. Comput. Geotech. 86, 9–20.
Rui, Y., Yin, M., 2017. Thermo-hydro-mechanical coupling analysis of a thermo-active diaphragm wall. Can. Geotech. J. 55 (5), 720–735.
Saggu, R., Chakraborty, T., 2015a. Cyclic thermo-mechanical analysis of energy piles in sand. Geotech. Geol. Eng. 33 (1), 1–22.
Saggu, R., Chakraborty, T., 2015b. Thermal analysis of energy piles in sand. Geomech. Geoeng. 10 (1), 10–29.

Sailer, E., Taborda, D.M., Zdravković, L., Potts, D.M., 2019. Fundamentals of the coupled thermo-hydro-mechanical behaviour of thermo-active retaining walls. Comput. Geotech. 109, 189–203.
Salciarini, D., Ronchi, F., Cattoni, E., Tamagnini, C., 2015. Thermomechanical effects induced by energy piles operation in a small piled raft. Int. J. Geomech. 15 (2), 04014042.
Salciarini, D., Ronchi, F., Tamagnini, C., 2017. Thermo-hydro-mechanical response of a large piled raft equipped with energy piles: a parametric study. Acta Geotech. 12 (4), 703–728. Available from: https://doi.org/10.1007/s1144:1-26.
Sterpi, D., Coletto, A., Mauri, L., 2017. Investigation on the behaviour of a thermo-active diaphragm wall by thermo-mechanical analyses. Geomech. Energy Environ. 9, 1–20.
Sterpi, D., Angelotti, A., Habibzadeh-Bigdarvish, O., Jalili, D., 2018a. Assessment of thermal behaviour of thermo-active diaphragm walls based on monitoring data. J. Rock Mech. Geotech. Eng. 10 (6), 1145–1153.
Sterpi, D., Tomaselli, G., Angelotti, A., 2018b. Energy performance of ground heat exchangers embedded in diaphragm walls: field observations and optimization by numerical modelling. Renew. Energy .
Stewart, M.A., McCartney, J.S., 2012. Strain distributions in centrifuge model energy foundations. Proceedings of GeoCongress. ASCE, pp. 25–29.
Suryatriyastuti, M.E., Mroueh, H., Burlon, S., 2013. Numerical analysis of the bearing capacity of thermoactive piles under cyclic axial loading. In: Laloui, L., Di Donna, A. (Eds.), Energy Geostructures: Innovation in Underground Engineering. Wiley-ISTE, pp. 139–155.
Suryatriyastuti, M., Burlon, S., Mroueh, H., 2015. On the understanding of cyclic interaction mechanisms in an energy pile group. Int. J. Numer. Anal. Methods Geomech. Available from: https://doi.org/10.1002/nag.2382.
Sutman, M., Brettmann, T., Olgun, C.G., 2018. Full-scale in-situ tests on energy piles: head and base-restraining effects on the structural behaviour of three energy piles. Geomech. Energy Environ. 18, 56–68.
Vieira, A., Maranha, J.R., 2016. Thermoplastic analysis of a thermoactive pile in a normally consolidated clay. Int. J. Geomech. 17 (1), 04016030.
Wang, B., Bouazza, A., Singh, R.M., Haberfield, C., Barry-Macaulay, D., Baycan, S., 2014a. Posttemperature effects on shaft capacity of a full-scale geothermal energy pile. J. Geotech. Geoenviron. Eng. 141 (4), 04014125.
Wang, W., Regueiro, R., McCartney, J., 2014b. Coupled axisymmetric thermo-poro-mechanical finite element analysis of energy foundation centrifuge experiments in partially saturated silt. Geotech. Geol. Eng. 33 (2), 291–306.
Xia, C., Sun, M., Zhang, G., Xiao, S., Zou, Y., 2012. Experimental study on geothermal heat exchangers buried in diaphragm walls. Energy Build. 52, 50–55.
Yavari, N., Tang, A.M., Pereira, J.-M., Hassen, G., 2014. Experimental study on the mechanical behaviour of a heat exchanger pile using physical modelling. Acta Geotech. 9 (3), 385–398.
Yavari, N., Tang, A.M., Pereira, J.-M., Hassen, G., 2016. Mechanical behaviour of a small-scale energy pile in saturated clay. Geotechnique 66 (11), 878–887.
Yoon, S., Lee, S.-R., Xue, J., Zosseder, K., Go, G.-H., Park, H., 2015. Evaluation of the thermal efficiency and a cost analysis of different types of ground heat exchangers in energy piles. Energy Convers. Manage. 105, 393–402.
You, S., Cheng, X., Guo, H., Yao, Z., 2016. Experimental study on structural response of CFG energy piles. Appl. Therm. Eng. 96 (1), 640–651.
Zannin, J., Ferrari, A., Pousse, M., Laloui, L., 2018. A flowchart for early-stage thermal design of energy walls. In: International Symposium on Energy Geotechnics, SEG 2018, Lausanne, Switzerland.
Zannin, J., Ferrari, A., Pousse, M., Laloui, L., 2019. Optimization of the energy exploitation and design of the heat exchangers embedded in an energy wall. (Under review).
Zarrella, A., De Carli, M., Galgaro, A., 2013. Thermal performance of two types of energy foundation pile: helical pipe and triple U-tube. Appl. Therm. Eng. 61 (2), 301–310.
Zhang, G., Xia, C., Sun, M., Zou, Y., Xiao, S., 2013. A new model and analytical solution for the heat conduction of tunnel lining ground heat exchangers. Cold Reg. Sci. Technol. 88, 59–66.
Zhao, Q., Chen, B., Liu, F., 2016. Study on the thermal performance of several types of energy pile ground heat exchangers: U-shaped, W-shaped and spiral-shaped. Energy Build. 133, 335–344.
Zhao, Q., Liu, F., Liu, C., Tian, M., Chen, B., 2017. Influence of spiral pitch on the thermal behaviors of energy piles with spiral-tube heat exchanger. Appl. Therm. Eng. 125, 1280–1290.

Questions and problems

Statements

a. What are the typical technological solutions that can be varied in most energy geostructure applications?

b. The configuration of the pipes embedded within energy piles probably represents the technical solution that most influences the thermohydromechanical behaviour of such geothermal heat exchangers:
- **i.** True
- **ii.** False

c. From the perspective of the structural support role of energy geostructures, what predominant behaviour will characterise the mechanics of energy piles compared to energy walls?

d. Which aspects typically cause differences in the numerical modelling of the thermohydromechanical behaviour of energy geostructures?

e. In many instances, the numerical modelling of energy geostructures assumes that conduction heat transfer characterises the ground, the filling material of the energy geostructures and the pipe walls, while convection heat and mass transfers characterise the heat carrier fluid circulating in the pipes as well as the air flowing in the built environment adjacent to relevant energy geostructures (e.g. energy tunnels and walls):
- **i.** True
- **ii.** False

f. What initial and boundary conditions are typically considered to characterise thermomechanical problems under time-dependent conditions?

g. What is the rationale for employing simplified thermal loading paths until steady thermal conditions are reached, instead of modelling the actual duration of geothermal operations of energy geostructures that is likely to be expected in practice (e.g. several decades)?

h. When dealing with energy piles, increasing the number of U-loops necessarily leads to higher values of thermal power:
- **i.** True
- **ii.** False

i. The ground surface boundary conditions can profoundly influence the thermohydromechanical behaviour of energy piles:
- **i.** True
- **ii.** False

j. What cost-related aspect should be considered when trying to define the optimal flow rate of an energy geostructure?

k. The use of antifreeze chemicals mixed with water plays a nonnegligible role on the mechanical behaviour of energy geostructures.
  i. True
  ii. False

l. Explain in mathematical terms why the flow rate of the heat carrier fluid circulating in the pipes of energy geostructures can change both by a variation of the wetted pipe diameter, d_p, and by the fluid velocity, $\overline{v}_f$.

m. The shape of energy tunnels markedly influences their thermohydromechanical behaviour:
  i. True
  ii. False

n. In energy tunnel applications, what are the two regions established along the direction of the flow as a result of the development of the boundary layers?

o. Why does the development of the thermal and velocity boundary layers as well as the significance of the entrance and fully developed regions crucially characterise the convection heat transfer in the context of nonisothermal problems of internal flow?

p. The airflow regime within energy tunnels does not necessarily influence the thermal and velocity boundary layers within such environments:
  i. True
  ii. False

q. Rough surfaces typically cause a shortening of the entrance regions compared to smooth surfaces:
  i. True
  ii. False

r. What is the typical constraint related to the consideration of several pipe configurations when dealing with energy segmental linings?

s. The thermal power harvested from energy tunnels characterised by a given operation mode may be varied up to 50% by optimising the various design solutions:
  i. True
  ii. False

t. The presence of groundwater flow around energy tunnels can markedly characterise their thermohydromechanical behaviour:
  i. True
  ii. False

u. In the presence of groundwater flow, the most influential factor on the overall heat transfer process governing the thermohydraulic behaviour of energy tunnels is still the value of effective thermal conductivity of the ground rather than the intensity of groundwater velocity:
  i. True
  ii. False

v. Why may one consider that energy walls offer broader choices of pipe configurations compared to other energy geostructures applications?

w. The relative significance of the thermal conductivity of the ground to that of energy walls markedly influences the thermohydraulic behaviour of such geostructures:

i. True

ii. False

Solutions

a. The typical technological solutions that can be varied in different energy geostructure applications are:

i. Pipe configuration

ii. Pipes location

iii. Heat carrier fluid flow rate

iv. Heat carrier fluid composition

v. Thermal insulation length of pipes

vi. Available space for connecting lines

vii. Position of header block (distributor/collector)

viii. Position of heat pump machine(s) and technical service centre

ix. Features of heat pump machine(s)

x. Runout length of pipes.

b. The configuration of the pipes embedded within energy piles represents the technical solution that most influences the thermohydromechanical behaviour of such geothermal heat exchangers:

i. True

ii. False

c. The mechanics of energy geostructures such as energy piles is typically characterised by a predominant axial character. In contrast, the mechanics of energy geostructures such as energy walls is characterised by a predominant flexural character.

d. The numerical modelling of the thermohydromechanical behaviour of energy geostructures typically differs depending on the following aspects: (1) the choice of the relevant modes of heat and mass transfers that are assumed to characterise energy geostructures, and the model domains (or boundaries) wherein these phenomena are considered to occur; (2) the approach employed to account for the influence of the nonisothermal flow of the heat carrier fluid circulating in the pipes of energy geostructures; (3) the approach used to account for the influence of the nonisothermal airflow potentially present in built environments (e.g. located

in the underground) adjacent to energy geostructures; (4) the selection of the constitutive model(s) used to address the behaviour of energy geostructures; and (5) the extent of the coupling between the phenomena that are modelled in the analysis.

e. In many instances, the numerical modelling of energy geostructures assumes that conduction heat transfer characterises the ground, the filling material of the energy geostructures and the pipe walls, while convection heat and mass transfers characterise the heat carrier fluid circulating in the pipes as well as the air flowing in the built environment adjacent to relevant energy geostructures (e.g. energy tunnels and walls):
   i. True
   ii. False

f. For the energy conservation equation, typical initial conditions involve a uniform temperature field in all the modelled domains. For the momentum conservation equation, zero initial perturbations in terms of displacement or stress are considered for the model domains. Prescribed thermal and mechanical loads are typically applied as boundary conditions. Displacement boundary conditions are typically applied.

g. The rationale for employing simplified thermal loading paths until steady thermal conditions are reached, instead of modelling the actual duration that is likely to be expected in practice, is that according to the superposition principle the transient thermohydraulic behaviour of geothermal heat exchangers can be reproduced by the superposition of numerous steady responses.

h. When dealing with energy piles, increasing the number of U-loops necessarily leads to higher values of thermal power:
   i. True
   ii. False

i. The ground surface boundary conditions can profoundly influence the thermohydromechanical behaviour of energy piles:
   i. True
   ii. False

j. Aspects related to the interplay between the electrical power required to run the heat pump for varying flow rates and the cost of the considered solution should be considered to define the optimal flow rate.

k. The use of antifreeze chemicals mixed with water plays a nonnegligible role on the mechanical behaviour of energy geostructures:
   i. True
   ii. False

l. **The volumetric fluid flow rate can be generally expressed as**

$$\dot{V} = \overline{v}_f \cdot A = \overline{v}_f \frac{\pi d_p^2}{4} [\mathrm{m}^3/\mathrm{s}]$$

where $\overline{v}_f$ [m/s] is the flow velocity, A_p [m^2] is the cross-sectional area of the pipe and d_p [m] is the wetted pipe diameter. Based on the previous considerations, the flow rate of the heat carrier fluid circulating in the pipes of an energy geostructure can change both by a variation of the wetted pipe diameter, d_p, and by the fluid velocity, $\overline{v}_f$.

m. The shape of energy tunnels markedly influences their thermohydromechanical behaviour.
   i. **True**
   ii. False

n. **The two regions characterising nonisothermal flows such as those encountered in energy tunnels are the thermal and hydrodynamic entrance regions and the thermally and hydrodynamically fully developed regions**.

o. **The reason for this fact is that the convection heat transfer between a surface and a moving fluid is a function of the velocity of the moving fluid via the convection heat transfer coefficient, as well as of the difference between the surface temperature and the undisturbed temperature of the fluid. Therefore as the temperature and velocity fields of a moving fluid vary with the distance as a function of the development of the boundary layers, the variation of these variables can lead to marked changes in the convection heat transfer phenomenon**.

p. The airflow regime within energy tunnels does not necessarily influence the thermal and velocity boundary layers within such environments:
   i. **True**
   ii. False

q. Rough surfaces typically cause a shortening of the entrance regions compared to smooth surfaces:
   i. **True**
   ii. False

r. **As far as minimum values of pipe spacing and bending radius are considered as a function of the pipe diameters, varying the layout or diameter of pipes installed in linings results in varying pipe configurations for the same surface of lining available. For example varying the pipe diameter involves changing the minimum pipe spacing and bending radius and thus the density of pipes per unit surface of tunnel lining**.

s. The harvested thermal power from energy tunnels characterised by a given operation mode may be varied up to 50% by optimising the various design solutions:
   i. True
   ii. False

t. The presence of groundwater flow around energy tunnels can markedly characterise their thermohydromechanical behaviour:
   i. True
   ii. False

u. In the presence of groundwater flow, the most influential factor on the overall heat transfer process governing the thermohydraulic behaviour of energy tunnels is still the value of effective thermal conductivity of the ground rather than the intensity of groundwater velocity:
   i. True
   ii. False

v. Various pipe layouts can be foreseen due to the more remarkable freedom related to the pipe installation compared to other energy geostructures such as energy piles. Pipes can be installed only towards the air or the ground side, or on both sides of energy walls.

w. The relative significance of the thermal conductivity of the ground to that of energy walls markedly influences the thermohydraulic behaviour of such geostructures:
   i. True
   ii. False

PART E

Design

CHAPTER 13

Performance-based design in the context of energy geostructures

13.1 Introduction

Nowadays it is established that energy geostructures have major capabilities to provide energy supply and structural support to the built environment. To date, the energy requirements of various constructions have been met via energy geostructures and no examples showing the lack of structural support requirements have been documented. Based on the previous fact, the *performance* of energy geostructures, that is the feature to *verify* a given *requirement* while interacting with general perturbations, may be considered satisfactory.

However, the absence of applications of energy geostructures characterised by a lack of required performance (e.g. energy, geotechnical and structural) is often not representative of an adequate design. In contrast, the previous evidence is the consequence of a design created (at least theoretically) to overly conservatively tackle the challenging multiphysical phenomena associated with the structural support and geothermal operations of energy geostructures. Designs of structures aimed at achieving a trouble-free performance instead of an optimal performance have the marked limitation of being uneconomical. Only by understanding any problem in a theoretical and empirical sense and by developing analysis tools and design methodologies can adequate and economical designs can obtained.

So-called performance-based design approaches are key methodologies to achieve adequate and economical designs. The reason for this is that, compared to so-called prescriptive design approaches that resort to deterministic specifications and are consequently of limited applicability, performance-based design approaches resort to statistical concepts and provide verifications of broad applicability to ensure an optimal performance.

In the context of the design project of constructions, various norms rely on a performance-based design approach. For example a framework for the structural and geotechnical performance-based design of structures has been available for several decades in the European Union and is detailed in norms often called the Eurocodes. In relatively recent years, integrations to the previous normative framework have been proposed to address the optimal geotechnical and structural design of energy geostructures, based on three main reasons: (1) the different nature of thermal actions applied to energy geostructures compared to that of thermal actions typically applied to more

Analysis and Design of Energy Geostructures
DOI: https://doi.org/10.1016/B978-0-12-816223-1.00013-8

conventional structures and infrastructures; (2) the shortcomings described in prescriptive design guidelines about the influence of thermal actions, applied alone or in conjunction with mechanical loads, on the actual response of energy geostructures; and (3) the lack of appropriate performance-based design methodologies addressing the influence of thermal actions applied to energy geostructures.

This chapter presents the theoretical essentials constituting the performance-based design of general geostructures drawing from the Eurocodes framework, with a focus on novel aspects and practical approaches to address the geotechnical and structural performance-based design of energy geostructures. While not claiming to be comprehensive of all design situations that may characterise energy geostructures and to be valid for all normative contexts, this analysis is aimed at expanding on key aspects characterising the geotechnical and structural design of many energy geostructures.

To this aim, *holistic integrated design considerations* are proposed first: the objective of this part is to summarise essential features of the design project of constructions and to focus on key aspects characterising the design of energy geostructures. Second, the *available design recommendations* for energy geostructures are summarised: in this context the purpose is to expand on currently available guidelines for the design of the considered structures. Next, the *Eurocode Programme* is introduced: the purpose of this part is to expand on features of norms available in the European Union for the common performance-based design of structures. Then, the concepts of *limit states* and *design situations* as well as the *classification of actions* characterising general structures are presented: in this framework the aim is to propose essential features characterising the performance-based design of structures. Afterward, the *verification of requirements through a partial factor method*, the *performance-based design approach for energy geostructures* and the *combinations of actions at ultimate and serviceability limit states* are described: the aim of this part is to highlight typical steps constituting the performance-based design of structures as well as to propose an appropriate design approach for energy geostructures drawing from the Eurocodes. The *design data for some materials* are subsequently summarised: the purpose of this section is to report design data for concrete and reinforcing steel, based on the rationale that these materials characterise most energy geostructures. Later, the *design for ultimate and serviceability limit states* is discussed: the goal of this part is to present theoretical essentials and practical design approaches to tackle typical design problems in the framework of the Eurocodes. Finally, *questions and problems* are proposed: the purpose of this part is to fix and test the understanding of the subjects covered in this chapter by addressing a number of exercises.

13.2 Holistic integrated design considerations

The design project of buildings and infrastructures is certainly complex and a holistic integrated approach is required for achieving the features desired for any construction.

In the framework of the design project of constructions using energy geostructures, the complexity of such process may be considered to increase, requires consideration of many aspects that are provided by different contributors, and resorts to strongly multidisciplinary competences (cf. Fig. 13.1). The focus is given here to the features of the *design activities* characterising the *design project* of constructions, because such activities crucially contribute to the suitable operation of the built environment.

Aspects involved in the architectural, structural, geotechnical and energy design of constructions are reported in Tables 13.1, 13.2, 13.3 and 13.4, respectively, with a focus on applications using energy geostructures. The competences that are typically required to successfully carry out the considered designs include planning, analysis, construction and maintenance competences.

When considering the analysis and design of the energy geostructures, various challenges arise due to the multifunctional operation of such technology. From one side, the challenges characterising the analysis and design of energy geostructures are related to the thermohydraulic behaviour and the associated energy performance of such technology. From the other side, the challenges characterising the analysis and design of

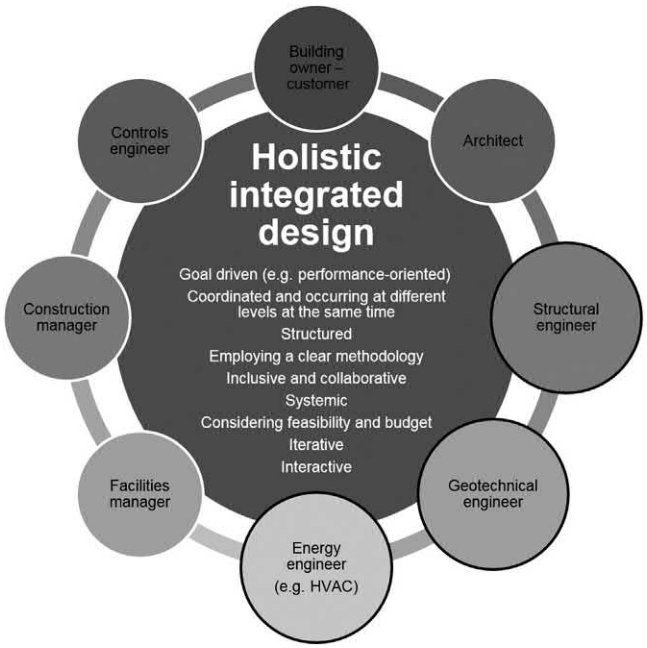

Figure 13.1 Essential features of the holistic, integrated design of constructions, with a focus on applications employing energy geostructures.

Table 13.1 Examples of aspects involved in the architectural design of constructions involving energy geostructures.

Architectural design

• **Establishes the architectural and distributive features of the construction, considering**:
  • The resources (e.g. economic and financial) available to the project
  • The location and interaction of the construction with the surrounding systems and environments (e.g. urban, ambient, etc.)
  • The requirements for occupants' use and/or accessibility
• **Defines the environmental systems and units characterising the construction**
• **Defines the classes of technological systems, the technological systems, the technological elements (e.g. for building envelope and interior environment, etc.), and the related features, considering**:
  • The resources (e.g. economic and financial) available to the project
  • The features of the environmental systems and units characterising the construction
  • The requirements for occupants use or accessibility (e.g. ambient temperature, relative humidity, etc.)
  • Other complementary requirements targeted by the construction design (e.g. associated with energy performance, environmental impact, etc.)
  • The capability of the technological solutions to be demounted, maintained, repaired, deconstructed and reconstructed
  • The life cycle of the technological solutions applied (with regards to the design working life of the structure)

Table 13.2 Examples of aspects involved in the structural design of constructions involving energy geostructures.

Structural design

• **Defines the features (e.g. dimensional and technological) of the superstructure system upon**
  • The choice of the type of superstructure systems based on
  • *The architectural and distributive features of the construction*
  • *The location, use and features of the construction from the perspective of the actions and effects of actions applied to the structure*
  • *The feasibility of the solution foreseen (e.g. economic, financial and technical)*
  • The establishment of a target structural performance of the superstructure system, based on the verification of the requirements and the consideration of
  • *The actions and effects of actions characteristics of the features, location and use of the construction*
  • *The actions and effects of actions potentially arising from the foundation*
• **Contributes with the geotechnical design to define the features (e.g. dimensional and technological) of the geostructure system upon**
  • The verification of the structural performance of the geostructure with reference to target requirements and based on the estimate of
  • *The actions arising from the superstructure that have to be carried by the geostructure*
  • *The actions characteristics of a specific use or location of the geostructure*
• **Ensures a target structural performance of the superstructure and geostructure systems to a certain probable extent in the design working life of the construction**

Table 13.3 Examples of aspects involved in the geotechnical design of constructions involving energy geostructures.

Geotechnical design

• **Defines the features (e.g. dimensional and technological) of the geostructure system upon**
  ◦ The choice of the type of geostructure systems based on
  ▪ *The architectural and distributive features of the construction*
  ▪ *The features of the superstructure system and the actions involved*
  ▪ *The geotechnical characterisation of the site*
  ▪ *The feasibility of the solution foreseen (e.g. economic, financial and technical)*
  ◦ The establishment of a target geotechnical performance of the geostructure system, based on the verification of the requirements and the consideration of
  ▪ *The actions and effects of actions arising from the superstructure system (e.g. thermal and mechanical actions)*
  ▪ *The actions and effects of actions potentially arising from the ground*
  ▪ *The mutual interaction with the solution foreseen by the energy design for the energy geostructure*
• **Ensures a target geotechnical performance of the geostructure system to a certain probable extent in the design working life of the construction**

Table 13.4 Examples of aspects involved in the energy design of constructions involving energy geostructures.

Energy design

• **Defines the features of the systems and plants (e.g. for the production of hot water, the allowance of conditioning, the distribution of electrical power, etc.) foreseen to satisfy the energy needs associated with the features and use of the construction, considering**
  ◦ The resources (e.g. economic and financial) available to the project
  ◦ The location and interaction of the construction with the surrounding environment
  ◦ The requirements for occupants use in terms of thermohygrometric comfort, indoor air quality, etc.
  ◦ The feasibility and sustainability of the solution
  ◦ Other complementary requirements targeted by the construction design (e.g. associated with energy performance, environmental impact, etc.)
• **Contributes with the geotechnical design to define the features (e.g. dimensional and technological) of the geostructure system**
• **Ensures a target energy performance of the construction to a certain probable extent in its design working life**

energy geostructures are related to the thermo-(hydro-)mechanical behaviour and the associated geotechnical and structural performance of such technology. Treating these challenges for any site and energy geostructure is essential for the successfulness of any application of this technology.

13.3 Available design recommendations

One documentation in Germany (VDI 4640, 2009), one guide in Switzerland (SIA-D0190, 2005), one standard in the United Kingdom (Ground Source Heat Pump Association, 2012) and one recommendation in France (CFMS-SYNTEC-SOFFONS-FNTP, 2017) offer guidance for the design of energy geostructures. However, while the German documentation (VDI 4640, 2009) only focuses on the energy design of energy geostructures, the Swiss (SIA-D0190, 2005), United Kingdom (Ground Source Heat Pump Association, 2012) and French (CFMS-SYNTEC-SOFFONS-FNTP, 2017) documents also treat the geotechnical and structural design of energy geostructures. The French recommendations (CFMS-SYNTEC-SOFFONS-FNTP, 2017) integrate and expand most of the knowledge included in the previous guidelines.

All of the previous contributions represent valuable references for practitioners because they have been proposed since early years of the research and development of energy geostructures. At the same time, these contributions currently suffer from drawbacks, especially considering the recommendations for the geotechnical and structural design of energy geostructures. The reasons for the previous statement are expanded in the following.

Both the Swiss code (SIA-D0190, 2005) and the United Kingdom standard (Ground Source Heat Pump Association, 2012) are mainly focused on the geotechnical and structural design of energy piles, providing little information about the design of other energy geostructures. In addition to suffering from the previous drawback, the recommendations included in these documents are applicable to only a limited number of design situations because they are characterised by prescriptive and not performance-based features, and neglect relevant aspects for the design (Rotta Loria et al., 2019). In most cases, the United Kingdom standard (Ground Source Heat Pump Association, 2012) also involves an excessive oversizing of the treated energy geostructures (i.e. energy piles). The reason for this result is associated with the worst-case scenario considerations suggested in the standard to verify energy geostructures (e.g. the thermally induced stresses and displacements characterising energy piles may be verified assuming the piles are completely restrained or free to deform, respectively, which are conditions hardly achievable in practice).

The French recommendations (CFMS-SYNTEC-SOFFONS-FNTP, 2017) may in principle be considered the best reference for the geotechnical and structural design of energy geostructures because they adopt a performance-based design approach, being based on the Eurocodes. However, they are considered to suffer from three main limitations (Rotta Loria et al., 2019). First, the recommendations do not include

a comprehensive methodological framework for the design process of energy geostructures (intended as a complex iterative process of design and verification phases) and focus on only the verification, not the design, of such geostructures. Second, the recommendations rely on the arguable proposition of establishing verifications addressing the failure and the deformation of energy geostructures by combining the results of specific analyses referring to the deformation of such structures. Third, the recommendations account for the influence of thermal loads in a way that may not be conservative in many design situations.

In addition to the previous recommendations, investigations focusing on the performance-based design of energy piles have been reported, for example by Xiao et al. (2016) and Jelušič and Žlender (2018). Along with the previous investigations, a methodology for the performance-based design of energy piles drawing from the Eurocodes has been presented by Rotta Loria et al. (2019).

The crucial difference characterising the methodology proposed by Rotta Loria et al. (2019) compared to all of the previous references is related to the way thermal loads are considered in the performance-based design. Because of the theoretical basis and effectiveness characterising the quoted methodology, the following developments are based on this approach and may be considered for the design of other energy geostructures than energy piles.

13.4 The Eurocode programme

In 1975 the Commission of the European Community initiated a programme devoted to create, promote and establish common technical rules for the design of buildings and civil engineering works in the various Member States, that is the Eurocode programme. Nowadays, the Eurocode programme consists of ten sets of European Norms, that is the Eurocodes, comprising a head key code, that is EN 1990, and nine other complementary codes, that is EN 1991 to EN 1999 (cf. Table 13.5).

EN 1990 covers the fundamentals of the *limit state design* of structures and is the head code established for all Eurocodes: (1) principles and requirements for the safety, serviceability and durability of structures and infrastructures, (2) application rules for the basis of the design and verification of these structures, (3) guidelines for related aspects of structural reliability (structural resistance and serviceability, durability, and quality control of structures), and (4) provisions applicable to EN 1991 to EN 1996. EN 1991 considers the actions on structures. EN 1992 to EN 1996 and EN 1999 deal with different material categories and construction types, and for this reason are often called 'material' Eurocodes. EN 1997 focuses on the geotechnical design of structures. EN 1998 expands on the design of structures against earthquakes. The previous characterisation of the Eurocodes is reported in a complementary form in Fig. 13.2.

Table 13.5 The Eurocodes.

European norm code	European norm title
EN 1991	Eurocode: Basis of Structural Design
EN 1991	Eurocode 1: Actions on Structures
EN 1992	Eurocode 2: Design of Concrete Structures
EN 1993	Eurocode 3: Design of Steel Structures
EN 1994	Eurocode 4: Design of Composite Steel and Concrete Structures
EN 1995	Eurocode 5: Design of Timber Structures
EN 1996	Eurocode 6: Design of Masonry Structures
EN 1997	Eurocode 7: Geotechnical Design
EN 1998	Eurocode 8: Design of Structures for Earthquake Resistance
EN 1999	Eurocode 9: Design of Aluminium Structures

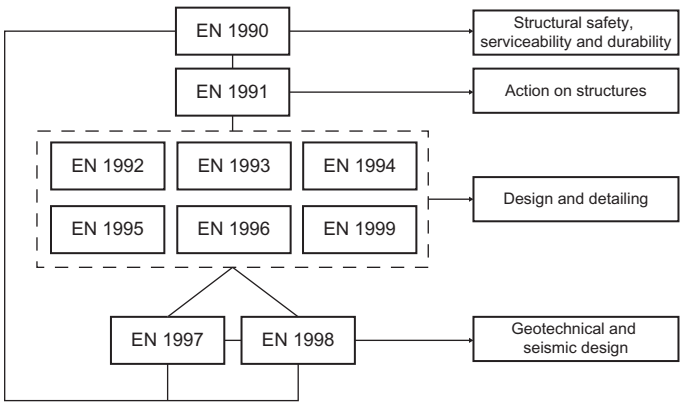

Figure 13.2 Characterisation of the Eurocode programme.

Eurocodes are implemented as National Standards under the responsibility of each National Standards Body. Once implemented, the full text of Eurocodes (annexes comprised) is to be considered without any alterations as published by the European Committee for Standardization. The European Commission recognises the responsibility of authorities in each European Union Member State to determine in a National Annex values of parameters, known as nationally determined parameters, which are to be used for the design of buildings and civil engineering works to be constructed in the country concerned. The National Annex cannot change or modify the content of Eurocodes in any way other than where it indicates that national choices may be made by means of nationally determined parameters. More detailed information of these aspects can be found in the guide to EN 1990 (2002) presented by Gulvanessian et al. (2002).

13.5 Limit states

In structural design, *limit states* are the states whose achievement involves the loss of functioning or required performance for which the structure is designed. According to the EN 1990 (2002), distinction shall be made between two groups of limit states:

i. *Ultimate limit states*: associated with the collapse or failure of the structure or components and thus involving the safety of people. They generally govern the strength of the structure or components. These states are often attained through the (1) loss of equilibrium of the structure or of one of its components (considered as rigid bodies); (2) failure by excessive deformation, transformation of the structure or any part of it into a mechanism, rupture, loss of stability of the structure or any part of it, including supports and foundations; and (3) failure caused by fatigue or other time-dependent effects.
ii. *Serviceability limit states*: associated with the loss of functionality of a structure with reference to the requirements of its normal use, comfort, appearance and durability, and thus not involving the safety of people. They generally govern the stiffness of the structure or components. These states may be reversible or irreversible and are often attained due to an excessive deformation of the structure involving fissures and incompatible displacements. Reversible serviceability limit states are states where no consequences of actions exceeding any specified serviceability requirement would remain when these actions may be removed. Irreversible serviceability limit states are states where some consequences of actions exceeding any specified serviceability requirement would remain when these actions may be removed.

The category of causes (1) refers to the 'EQU' (equilibrium) ultimate limit state, related to the loss of static equilibrium of the structure or any part of it considered as a rigid body. The category of causes (2) refers to the 'STR' (structural) ultimate limit state, related to internal failure or excessive deformation of the structure or structural members, and/or the 'GEO' (geotechnical) ultimate limit state, related to failure or excessive deformation of the ground. The category of causes (3) refers to the 'FAT' (fatigue) ultimate limit state, related to fatigue failure of the structure or structural members, and/or the 'UPL' (uplift) ultimate limit state, related to the loss of equilibrium of the structure or the ground due to uplift by water pressure, that is buoyancy, or other vertical actions, and the 'HYD' (hydraulic) ultimate limit state, related to hydraulic heave, internal erosion and piping in the ground caused by hydraulic gradients.

The relevant ultimate limit states for most energy geostructure applications may generally be considered to be the EQU, STR and GEO. All of the previous limit states characterise, for example energy wall applications, whereas only the latter two usually characterise, for example energy pile applications.

13.6 Design situations

Design situations are sets of physical conditions representing the real conditions occurring during a certain time interval for which the design demonstrates that relevant limit states are not exceeded. According to the EN 1990 (2002), distinction shall be made between four groups of design situations:

1. *Persistent design situations*: relevant for conditions of normal use, that is for periods of the same order as the design working life of the structure.
2. *Transient design situations*: relevant for temporary conditions applicable to the structure, that is for periods much shorter than the design working life of the structure, and characterised by a high probability of occurrence.
3. *Accidental design situations*: referred to exceptional conditions applicable to the structure or its exposure.
4. *Seismic design situations*: referred to exceptional conditions applicable when the structure may be subjected to the action of a seismic event.

Design situations shall be sufficiently severe and varied to encompass all conditions that can reasonably be foreseen to occur during the execution and use of the structure (EN 1990, 2002). The execution and the use of the structure are generally associated with its design working life. For example EN 1990 (2002) classifies four categories of design working life for structures, ranging from 10 to 100 years (these values are specified for each country in the National Annex). The design working life for building structures and other structures is generally of 50 years. Structural resistance and serviceability, durability and quality control (where applicable) should be ensured throughout the design working life of structures.

13.7 Classification of actions

Actions are sets of forces, imposed deformations or accelerations applied to the structure. According to the EN 1990 (2002), actions may be classified based on different criteria, including their variation in time, origin, spatial variation and nature.

The classification of actions based on time foresees (examples of these actions are summarised in Table 13.6)

1. *Permanent actions*: actions that are likely to act throughout a given reference period and for which the variation in magnitude with time is negligible, or for which the variation is always in the same direction (monotonic) until the actions attain a certain limit value.
2. *Variable actions*: actions whose variation in magnitude with time is neither negligible nor monotonic, which can have either a long or short duration with reference to the design working life.
3. *Accidental actions*: actions, usually of short duration but of significant magnitude, which are unlikely to occur (they have a very low probability of occurrence and are hardly predictable) on a given structure during the design working life.

Table 13.6 Examples of actions.

Permanent actions	Variable actions	Accidental actions
Self-weight of structures, fittings and fixed equipment	Imposed deformations caused, for example by temperature variations	Seismic actions
Prestressing forces	Imposed loads on building floors, beams and roofs	Explosions
Water and earth loads	Wind actions[b]	Impacts from vehicles
Actions caused by shrinkage or uneven settlements[a]	Snow loads[b]	

[a]May be considered to be permanent or variable actions.
[b]May be considered to be variable or accidental actions.

The classification of actions based on their origin foresees

1. *Direct actions*: loads applied to the structure.
2. *Indirect actions*: imposed deformations or accelerations.

The classification of actions based on their spatial variation foresees

1. *Fixed actions*: actions of a fixed distribution and position over the structure or structural members, such that the magnitude and direction of these actions are determined unambiguously for the whole structure or structural members if determined at one point of the structure or structural members;
2. *Free actions*: actions of various spatial distributions over the structure.

The classification of actions based on their nature foresees

1. *Static actions*: actions that do not cause significant acceleration of the structure or structural members.
2. *Dynamic actions*: actions that cause significant acceleration of the structure or structural members.

Thermal actions currently considered in the Eurocodes for structures such as buildings and bridges may be classified as *variable, indirect, free and static actions*. Thermal actions applied to energy geostructures may be considered in a similar way as *variable, indirect, free and static actions*.

Thermal actions are variable actions because related to the aleatory and varied nature of the conditions and factors that characterise the outer environment (e.g. for bridges), and/or the interaction between the outer environment and the inner environment (e.g. for buildings and energy geostructures). They are indirect actions because resulting from imposed loads that cause a temperature variation. They are free actions because characterised by an intrinsic variable distribution in space. They are static actions because not associated with accelerations.

Daily and seasonal variations in shade air temperature, solar radiation, and reradiation are typical examples of thermal actions for buildings and bridges (EN 1991, 2003). Temperature variations associated with the heating or cooling of superstructures are typical examples of thermal actions for energy geostructures.

The temperature variations applied to energy geostructures can be defined with reference to the heat inputs involved in the building energy design, the associated thermal powers for heating and cooling, the operation time and the thermal properties of the piles and ground. Because the temperature variations in energy geostructures are generally nonuniform within the structure, best practice methods for selecting the appropriate temperature variation should be considered in the design (Loveridge and Powrie, 2016; Abdelaziz and Ozudogru, 2016; Rammal et al., 2018).

13.8 Verification of requirements through a partial factor method

13.8.1 General

The actions and resistances governing the performance of structures, and the relation between them, are aleatory variables because they cannot be defined in a deterministic way. From one side, because of the intrinsic uncertainty in their value, time of application and variability throughout the lifetime of the structure (especially for imposed deformations such as those caused by thermal actions). From the other side, due to the intrinsic uncertainty on the measures performed for determining directly these quantities or the parameters needed to define these quantities.

The aleatory character of actions and resistances in the design of structures are tackled in norms referring to a limit state design approach such as the Eurocodes through a *semiprobabilistic safety framework* and an associated *partial factor design approach*. In this approach, different aspects of the performance of structures are attempted to be classified and analysed through diverse 'security levels' and associated design conditions. Yet, differently to conventional deterministic design approaches where the uncertainties are treated by applying a unique safety factor, in this approach the uncertainties of the variables are treated right at the sources by introducing partial safety factors.

The four key aspects to consider in the design of structures are the actions, the effects of actions, the material properties and the resulting resistances. These aspects are treated in the following.

13.8.2 Actions and effects of actions

According to the EN 1990 (2002), the design effects of actions, E_d, can be considered a function of the representative values of the actions, $F_{rep,i}$, and the material or product

properties, $X_{k,i}$, which are transformed in design values, $F_{d,i}$, $X_{d,i}$ or $R_{d,i}$, through the use partial safety factors γ_i (where i are the numbers of the specific variables considered), and the design values of the geometrical data of the structure, a_d. Partial factors may be applied either to the actions themselves or to their effects. This can be mathematically expressed as

$$E_d = E\left\{\gamma_{F,i}F_{rep,i}; \frac{X_{k,i}}{\gamma_{M,i}}; a_d\right\}, \text{with } i \geq 1 \tag{13.1}$$

or

$$E_d = \gamma_{E,i}E\left\{F_{rep,i}; \frac{X_{k,i}}{\gamma_{M,i}}; a_d\right\}, \text{with } i \geq 1 \tag{13.2}$$

The representative values of actions $F_{rep,i}$ may be characteristic values of actions $F_{k,i}$ or accompanying values of actions $\psi_i F_{k,i}$, where ψ_i are combination factors.

The *characteristic value* of an action is its main representative value and shall be specified as a mean value, as an upper or lower value, as a nominal value (which does not refer to a known statistical distribution), or in the project documentation. The characteristic values of the temperature variations associated with the geothermal operation of energy geostructures may be considered nominal values, ΔT_k (Rotta Loria et al., 2019). Characteristic values with an aleatory statistical distribution may be defined in such a way of having a prescribed or intended probability of being exceeded. In general, the fractile of 5% of an assumed statistical distribution is considered for such purpose (cf. Fig. 13.3).

The *accompanying value* of an action is usually considered for variable actions. This value accounts for the probability of a simultaneous occurrence of variable actions in

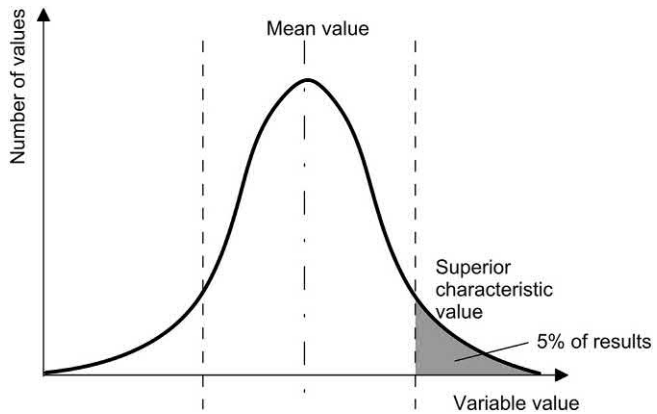

Figure 13.3 Approach defining the characteristic value of an action with an aleatory statistical distribution.

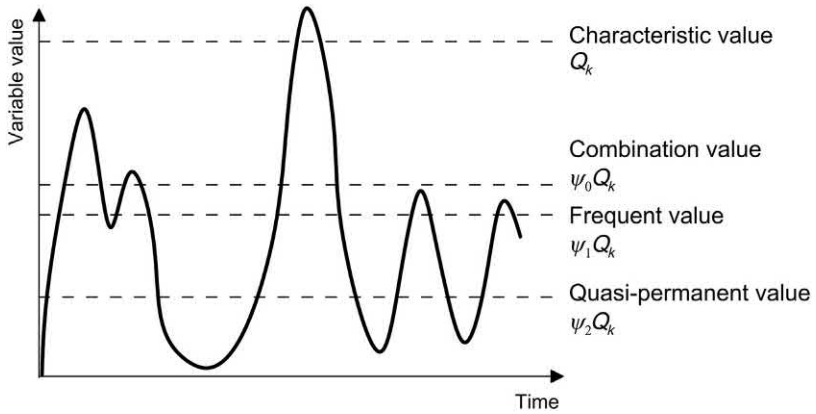

Figure 13.4 Approach defining the accompanying values of variable actions with an aleatory statistical distribution.

specific design situations referred to the design working life of the structure and is related to the intensity of the variable action within the reference period. According to the EN 1990 (2002), three accompanying values of variable actions can be distinguished (cf. Fig. 13.4):

i. The *combination value*, represented as a product $\psi_0 Q_k$, used for the verification of ultimate limit states (e.g. related to the normal use of the structure during construction or repair) and irreversible serviceability limit states (e.g. stress checks for reinforcement). It is defined to account for the low probability of a simultaneous occurrence of at least two variable actions that are characterised by close values to their characteristic values and may be chosen so that the probability that the effects caused by the combination will be exceeded is approximately the same as by the characteristic value of an individual action.

ii. The *frequent value*, represented by a product $\psi_1 Q_k$, used for the verification of ultimate limit states involving accidental actions (e.g. exceptional conditions involving fire, explosion impact, etc.) and for verifications of reversible serviceability limit states (e.g. crack width or decompression checks in prestressed concrete structures). It is defined with reference to a value of the variable action that may generally be exceeded within a short period of time compared to the reference period and the working life of the structure.

iii. The *quasipermanent value*, represented as a product $\psi_2 Q_k$, used for the verification of ultimate limit states involving accidental actions and for the verification of reversible serviceability limit states (e.g. crack width checks in reinforced concrete structures). It is defined with reference to a value of the variable action that can be exceeded for a large period of time compared to the reference period and the working life of the structure and is generally close the mean of the statistical

distribution (if available, otherwise it may be an averaged value over a reference period of time) of the action values.

The factors ψ_i lead to a determined part of the characteristic value of any variable action ($\psi_i \leq 1$, where $\psi_i = 1$ is for the case of a unique variable load) and together with the factors γ_i vary with each load. The factors γ_i, except for designs dealing with the equilibrium of structures and/or components, generally read $\gamma_i \geq 1$ depending on the limit state, the favourable or unfavourable impact of the action or action effect on the design effects of actions and the design approach.

13.8.3 Material properties and resulting resistances

According to the EN 1990 (2002), the representative values of material or product properties $X_{k,i}$ may be characteristic values with a prescribed or intended probability of being inferior, or nominal values. In general, the fractile of 5% of an assumed statistical distribution is considered for such purpose (cf. Fig. 13.5).

The characteristic values of geotechnical parameters shall be selected as a cautious estimate of the value affecting the occurrence of the limit state (EN 1997, 2004). The safety factors $\gamma_{F,i} = \gamma_{Sd}\gamma_{f,i}$ (as the factors $\gamma_{E,i}$) account for the possibility of unfavourable deviation of the action values from the representative values and inaccuracies in the analyses related to the modelling of the effects of actions or to the modelling of the actions themselves. The safety factors $\gamma_{M,i} = \gamma_{Rd}\gamma_{m,i}$ account for the uncertainty in the resistance model and geometric deviations if these are not modelled explicitly, and the possible unfavourable deviation of the material or product properties from the representative values.

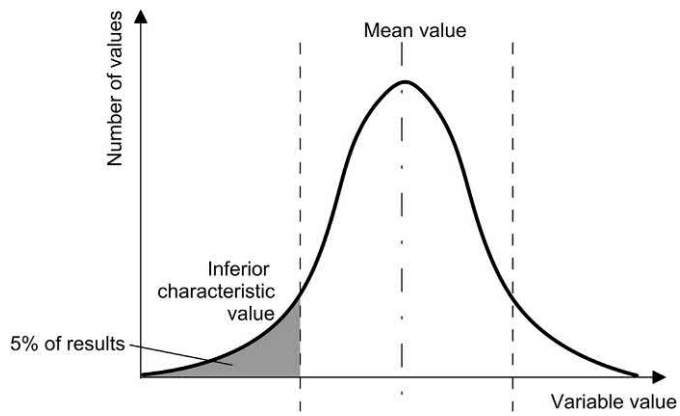

Figure 13.5 Approach defining the characteristic value of a material or product property with an aleatory statistical distribution.

The design values of the geometrical data of the structure may be nominal values, a_{nom}, or modified values where deviations in geometrical data may be significant, $a_{nom} \pm \Delta a$.

The dependence of the design effects of actions on the material or product properties is characteristic of geotechnical applications where the material or product properties of the ground may have an impact on the action exerted by this body on the structure (EN 1997, 2004). This dependence is generally not considered for the effects of actions applied to concrete structures (EN 1992, 2004).

In some design situations, the application of partial factors coming from or through the ground could lead to unreasonable or even impossible design values. In these situations, the partial factors may be applied directly to the effects of actions derived from representative values of the actions (EN 1997, 2004).

The design resistances, R_d, can be considered a function of the representative values of the actions, $F_{rep,i}$, and the material or product properties, $X_{k,i}$, or resistances, $R_{k,i}$, which are transformed in design values through the use of partial safety factors γ_i, and the design values of the geometrical data of the structure, a_d. Partial factors may be applied either to the material properties or to the resistances, or to both. This can be mathematically expressed as

$$R_d = R\left\{\gamma_{F,i}F_{rep,i}; \frac{X_{k,i}}{\gamma_{M,i}}; a_d\right\}, \text{with } i \geq 1 \tag{13.3}$$

or

$$R_d = R\frac{\left\{\gamma_{F,i}F_{rep,i}; X_{k,i}; a_d\right\}}{\gamma_{R,i}}, \text{with } i \geq 1 \tag{13.4}$$

or

$$R_d = R\frac{\left\{\gamma_{F,i}F_{rep,i}; \frac{X_{k,i}}{\gamma_{M,i}}; a_d\right\}}{\gamma_{R,i}}, \text{with } i \geq 1 \tag{13.5}$$

In cases where the design resistance may be obtained directly from the characteristic value of a material or product resistance, explicit determination of design values for individual basic variables may be avoided and the above would become

$$R_d = \frac{R_k}{\gamma_M} \tag{13.6}$$

The material or product properties, $X_{k,i}$, or resistances, $R_{k,i}$, may generally be considered to depend on multiplying partial safety factors η_i accounting for volume or scale effects, effects of moisture or temperature effects, or other effects that may affect the estimation of such properties and resistances (EN 1990, 2002). This dependence is

neglected in the prescriptions for geotechnical problems because the material or product properties or resistances are defined to be those relevant to the field situation and thus include the factors η_i in their definition.

The dependence of the design resistances on the design values of actions is characteristic of geotechnical applications where the design actions may affect the values of the geotechnical resistances (EN 1997, 2004). This dependence is generally not considered for the design resistances of concrete structures (EN 1992, 2004).

13.8.4 Verification

A design based on the partial factor method is considered to be sufficient if no limit state is exceeded in all relevant design situations when design values for actions or effects of actions and resistances are introduced into the analysis models (EN 1990, 2002). According to the EN 1997 (2004), it shall generally be verified that limit states EQU, STR, GEO, UPL and HYD are not exceeded. Meanwhile, as previously specified in Section 13.5, the relevant limit states for most energy geostructure applications may be considered the EQU, STR and GEO. In the EN 1997 (2004) it is specified that the limit state GEO is often critical to the sizing of structural elements involved in foundations or retaining structures and sometimes to the strength of structural elements. Based on the previous consideration, the verification of static equilibrium EQU is disregarded in the following and only the joint verification of resistance for structural and ground limit states in persistent and transient situations GEO and STR are considered.

The prescription (e.g. *inequality*) that shall be verified when considering a limit state of rupture or failure of a section, member, connection or medium, that is an ultimate limit state STR and/or GEO, is (EN 1990, 2002)

$$E_d \leq R_d \tag{13.7}$$

The prescription (e.g. *inequality*) that shall be verified when considering a limit state of loss of functionality of a section, member, connection or medium, that is a serviceability limit state, is (EN 1990, 2002)

$$E_d \leq C_d \tag{13.8}$$

where E_d and C_d are the design value of the effects of actions and the limiting design value for the serviceability criterion, respectively.

Values of the safety factors γ_i for serviceability limit states should normally be taken as $\gamma_i = 1$ (EN 1990, 2002). Characteristic values should be changed appropriately if variations of ground properties may occur during the life of the structure (EN 1997, 2004).

Bearing in mind the previous inequalities, the design for any limit state requires the definition of four aspects: (1) the appropriate loading and analysis methods to establish the design load effects; (2) the design material properties to be used in the verification; (3) the criteria establishing the limit of satisfactory performance; and (4) the suitable methods for the performance prediction.

13.9 Performance-based design approach for energy geostructures

The most appropriate and effective design approach for energy piles appears as follows (Rotta Loria et al., 2019): verify the performance of the energy geostructure against the action of only mechanical loads at ultimate limit states and verify the performance of the energy geostructure against the combined action of mechanical and thermal loads at serviceability limit states. The previous approach proposed by Rotta Loria et al. (2019) through theoretical considerations for energy piles may be employed to design other types of energy geostructures, such as energy walls, energy tunnels and energy slabs, provided that the sufficient ductility and rotation capacity of the elements are ensured. The reason for this is because, as far as a sufficient ductility capacity is ensured, imposed deformations, such as those caused by thermal actions, can be neglected at ultimate limit states because they are absorbed by the structure (Rotta Loria et al., 2019). The importance of a ductility-oriented design approach to deal with the influence of thermal actions applied to structures such as energy geostructures will represent a novelty of revised versions of the Eurocodes to be published in the foreseeable future.

From the foregoing developments, it is considered that thermal loads applied to energy geostructures involve effects that can be neglected in the performance-based design at ultimate limit states, both from a geotechnical and a structural perspective, and that can only be considered relevant at serviceability limit states.

13.10 Combination of actions at ultimate limit states

For each critical load case, the design values of the effects of actions shall be determined by combining the values of actions that are considered to occur simultaneously. According to the EN 1990 (2002), each combination of actions should include a leading variable action or an accidental action. Thermal actions applied to energy geostructures as a consequence of their geothermal operation may be neglected at ultimate limit states according to the design approach highlighted in Section 13.9.

In situations where there may be more than one variable action and it may be difficult to establish the leading variable action along with the accompanying variable actions, each of the variable actions shall in turn be considered as the leading action and the others as accompanying actions. In cases where the results of verifications may

be very sensitive to variations in magnitude of actions (e.g. permanent actions) the inferior and superior values of these actions (or the unfavourable and favourable parts of these actions) shall be considered as individual actions.

The general format of design effects of actions for persistent and transient design situations at ultimate limit states can be written according to the EN 1990 (2002) as

$$E_d = \gamma_{Sd} E\left\{\gamma_{g,j} G_{k,j}; \gamma_p P_c; \gamma_{q,1} Q_{k,1}; \gamma_{q,i} \psi_{0,i} Q_{k,i}\right\}, \text{ with } j \geq 1 \text{ and } i \geq 1 \tag{13.9}$$

where $\gamma_{g,j}$, γ_p, $\gamma_{q,1}$ and $\gamma_{q,i}$ are the partial factors for the permanent, precompression, leading variable and accompanying variable combination loads, $G_{k,j}$, P_c, $Q_{k,1}$ and $Q_{k,i}$, respectively. The above may also be expressed as

$$E_d = E\left\{\gamma_{G,j} G_{k,j}; \gamma_P P_c; \gamma_{Q,1} Q_{k,1}; \gamma_{Q,i} \psi_{0,i} Q_{k,i}\right\}, \text{with } j \geq 1 \text{ and } i \geq 1 \tag{13.10}$$

The *fundamental combination* of design effects of actions for persistent and transient design situations at ultimate limit states associated with expression (13.10) can be written as

$$\sum_{j \geq 1} \gamma_{G,j} G_{k,j} + \gamma_P P_c + \gamma_{Q,1} Q_{k,1} + \sum_{i \geq 1} \gamma_{Q,i} \psi_{0,i} Q_{k,i} \tag{13.11}$$

where the symbol '+' may be read as 'combined with' and the symbol '$\sum$' implies 'the combined effect of'. For situations involving geotechnical actions and the resistance of the ground in persistent and transient situations (STR and GEO limit states), the less of the two favourable expressions may be alternatively considered to expression (13.11)

$$\sum_{j \geq 1} \gamma_{G,j} G_{k,j} + \gamma_P P_c + \gamma_{Q,1} \psi_{0,1} Q_{k,1} + \sum_{i \geq 1} \gamma_{Q,i} \psi_{0,i} Q_{k,i} \tag{13.12}$$

$$\sum_{j \geq 1} \xi_j \gamma_{G,j} G_{k,j} + \gamma_P P_c + \gamma_{Q,1} Q_{k,1} + \sum_{i \geq 1} \gamma_{Q,i} \psi_{0,i} Q_{k,i} \tag{13.13}$$

where $\xi_j \leq 1$ are factors for unfavourable permanent actions. The magnitude of the design effect of actions resulting from the application of expression (13.11) will always be greater than that resulting from expressions (13.12) and (13.13) (Narayanan and Beeby, 2005). This is the reason why expression (13.11) is usually considered for the analysed design situations.

Table 13.7 presents values of the partial safety factors γ_G and γ_Q for permanent and variable actions applied to building structures at ultimate limit states, respectively, according to the EN 1990 (2002). Table 13.8 summarises values of partial factors ψ_0, ψ_1 and ψ_2 for variable actions according to the EN 1990 (2002), Rotta Loria et al.

Table 13.7 Partial factors γ_G and γ_Q for permanent and variable actions applied to building structures at ultimate limit states, respectively—persistent and transient design situations (EN 1990, 2002).

Action type	Effect of action for verification	Factor value in fundamental load combination
Permanent (stability check)	Unfavourable	1.10
	Favourable	0.90
Permanent (other checks)	Unfavourable	1.35
	Favourable	1.00
Variable	Unfavourable	1.50
Accidental	–	–

Table 13.8 Values of partial factors ψ_0, ψ_1 and ψ_2 for variable actions.

Variable action type	Subject of application	Factor ψ_0 value	Factor ψ_1 value	Factor ψ_2 value
Imposed loads[a]	Dwellings	0.7	0.5	0.3
	Offices	0.7	0.5	0.3
	Shopping and congregation areas	0.7	0.7	0.6
	Storage	1.0	0.9	0.8
	Parking	0.7	0.7	0.6
Wind loads[a]	–	0.5	0.2	0.0
Snow loads (for altitudes lower than or equal to 1000 m)[a]	–	0.7	0.2	0.0
Thermal loads	Buildings[a]	0.6[b]	0.5	0.0
	Bridges[a]	0.6[b]	0.6	0.5
	Energy geostructures[c]	0.6[d]	0.5	0.5

[a]Values reported by EN 1990 (2002).
[b]According to the EN 1990 (2002), the recommended value of ψ_0 may in most cases be reduced at 0 for ultimate limit states EQU, STR and GEO.
[c]Values reported by Rotta Loria et al. (2019) [values of $\psi_0 = 0.6$, $\psi_1 = 0.5$ and $\psi_2 = 0.2$ were proposed by Burlon et al. (2013) and are recommended by CFMS-SYNTEC-SOFFONS-FNTP (2017)].
[d]According to Rotta Loria et al. (2019), the recommended value of ψ_0 may be reduced at 0 for ultimate limit states EQU, STR and GEO considering the results proposed for axially loaded energy piles. Following the approach reported in the EN 1990 (2002), the recommended value of ψ_0 may be reduced at 0 for ultimate limit states EQU, STR and GEO referring to other energy geostructures.

(2019) and Burlon et al. (2013). Table 13.9 summarises examples of partial factors for load combination at ultimate limit states according to the EN 1990 (2002).

For STR and GEO limit states, inequality (13.7) should be verified, with reference to expression (13.11) [or expressions (13.12) and (13.13)], by using one of the following Design Approaches (the choice of the design approach is for national

Table 13.9 Partial factors γ_G, γ_Q and γ_P for the fundamental combination at ultimate limit states (EN 1990, 2002).

Load combination	Permanent load		Imposed load		Wind load[a]	Prestressing load
Expression (13.11) considered	Adverse effect	Beneficial effect	Adverse effect	Beneficial effect	–	–
Permanent + imposed load	1.35	1.00	1.50	0	–	1.0
Permanent + wind load	1.35	1.00	–	–	1.50	1.0
Permanent + imposed + wind load	1.35	1.00	1.50	0	0.9	1.0

[a]It is assumed that the wind load is not the leading action.

determination and should be stated in the National Annex; different design problems may be treated using different design approaches) – 'A' stands for actions of effects of actions and the use of the related partial factors for actions, γ_F, or effects of actions, γ_E, 'M' stands for material parameters and the use of the related partial factors for the strength (material) parameters, γ_M, and 'R' stands for resistances and the use of the related partial factors for the resistances, γ_R (EN 1997, 2004):

1. *Design Approach 1*

   It shall be verified that a limit state of rupture or excessive deformation will not occur with *either* of the following combinations of sets of partial factors.

   Except for the design of axially loaded piles and anchors:

   Combination 1: A1 ' + ' M1 ' + ' R1

   Partial factors are applied to actions alone and to ground strength parameters.

   Combination 2: A2 ' + ' M2 ' + ' R1

   Partial factors are applied to actions alone and to ground strength parameters.

   Specifically for the design of axially loaded piles and anchors:

   Combination 1: A1 ' + ' M1 ' + ' R1

   Partial factors are applied to actions alone and to ground strength parameters.

   Combination 2: A2 ' + ' (M1 or M2) ' + ' R4

   Partial factors are applied to actions, to ground resistances and sometimes to ground strength parameters.

   In practice, the use of Design Approach 1, Combination 1, is reported as DA1-C1, and the same approach may be used for other relevant acronyms.

2. *Design Approach 2*

   It shall be verified that a limit state of rupture or excessive deformation will not occur with the following combinations of sets of partial factors.

   Combination: A1 ' + ' M1 ' + ' R2

   Partial factors are applied to actions and resistances simultaneously.

3. *Design Approach 3*

It shall be verified that a limit state of rupture or excessive deformation will not occur with the following combinations of sets of partial factors.

Combination: (A1* or A2^{+}) ' + ' M2 ' + ' R3

Partial factors are applied to actions of action effects from the structure and to ground strength parameters (in case '*' the partial factors are applied to structural actions whereas in case '$^{+}$' to geotechnical actions).

Design Approach 1 is generally a 'material factoring approach' at load side and a 'resistance factoring approach' at resistance side (Bauduin, 2002). In principle, it requires design checks for two combinations of factors. In practice, in those cases where it is obvious that one of the two combinations governs the design, it is not necessary to carry out calculations for both sets. In Design Approach 1, Combination 1, $\gamma_F \neq 1$ and $\gamma_E = 1$ are generally applied in Eq. (13.1) and (13.2), respectively, together with $\gamma_M = \gamma_R = 1$ in Eq. (13.5) (EN 1990, 2002). In Design Approach 1, Combination 2, $\gamma_E = 1$ is always used with $\gamma_F \neq 1$ only for variable actions in Eq. (13.1) and (13.2), and (e.g. for piles and anchorages) $\gamma_M = 1$ and $\gamma_R > 1$ are used in Eq. (13.4) (EN 1990, 2002). In most cases, the sizing of foundation is governed by the sets of parameters associated with Combination 2 and the structural resistance is governed by the sets of parameters associated with Combination 1. For pile foundations, unlike all other geotechnical structures, Design Approach 1 is a partial resistance factor rather than a material factor approach (Bond et al., 2013). This is because, for combinations 1 and 2, the design resistance is obtained by applying partial resistance factors R1 or R4 (mostly $\gamma_R \geq 1$), respectively, to the characteristic base and shaft resistances, and applying partial material factors M1 ($\gamma_M = 1$). Material factors M2 involving $\gamma_M > 1$ are in fact only used to calculate unfavourable actions on piles owing, for example to negative skin friction.

Design Approach 2 is a 'load and resistance factoring approach' and is in several aspects close to a deterministic approach (Bauduin, 2002). In Design Approach 2, either $\gamma_E \neq 1$ and $\gamma_F = 1$ or $\gamma_E = 1$ and $\gamma_F \neq 1$ are used in Eq. (13.1) and (13.2), together with $\gamma_M = 1$ in Eq. (13.4) (EN 1990, 2002).

Design Approach 3 is a material factoring approach at both load and resistance sides. In Design Approach 3, either $\gamma_E \neq 1$ and $\gamma_F = 1$ or $\gamma_E = 1$ and $\gamma_F \neq 1$ are used in Eq. (13.1) and (13.2), and $\gamma_M > 1$ and $\gamma_R = 1$ are used in Eq. (13.3) (EN 1990, 2002). This approach may not be used to design piles from load tests or resistances calculated from profiles of test results as it provides no safety on resistance ($\gamma_R = 1$) (Bond et al., 2013).

13.11 Combination of actions at serviceability limit states

The combinations of actions to be considered in the relevant design situations should be appropriate for the serviceability requirements and performance criteria being verified. Thermal actions applied to energy geostructures as a consequence of their geothermal

operation should be considered in the combinations of actions at serviceability limit states (Rotta Loria et al., 2019). The characteristic temperature variations employed for the previous purpose should be considered as nominal values, ΔT_k (Rotta Loria et al., 2019).

According to the EN 1990 (2002), similar to the considerations governing the combination of actions at ultimate limit states, in situations where there may be more than one variable action and it may be difficult to establish the leading variable action along with the accompanying variable actions, each of the variable actions shall in turn be considered as the leading action and the others as accompanying actions. This approach should be considered when other variable actions may be applied in conjunction with thermal actions to energy geostructures, whereby different load combinations for different leading variable actions should be carried out.

The design effects of actions involving the characteristic combination can be written according to the EN 1990 (2002) as

$$E_d = E\left\{G_{k,j};P_c;Q_{k,1};\psi_{0,i}Q_{k,i}\right\},\ \text{with}\ j \geq 1\ \text{and}\ i \geq 1 \tag{13.14}$$

The *characteristic combination* associated with expression (13.14) is normally used to refer to irreversible limit states and can be expressed as

$$\sum_{j \geq 1} G_{k,j} + P_c + Q_{k,1} + \sum_{i \geq 1} \psi_{0,i} Q_{k,i} \tag{13.15}$$

The design effects of actions involving the frequent combination can be written according to the EN 1990 (2002) as

$$E_d = E\left\{G_{k,j};P_c;\psi_{1,1}Q_{k,1};\psi_{2,i}Q_{k,i}\right\},\ \text{with}\ j \geq 1\ \text{and}\ i \geq 1 \tag{13.16}$$

The *frequent combination* associated with expression (13.16) is normally used to refer to reversible limit states and can be expressed as

$$\sum_{j \geq 1} G_{k,j} + P_c + \psi_{1,1} Q_{k,1} + \sum_{i \geq 1} \psi_{2,i} Q_{k,i} \tag{13.17}$$

The design effects of actions involving the quasipermanent combination can be written according to the EN 1990 (2002) as

$$E_d = E\left\{G_{k,j};P_c;\psi_{2,i}Q_{k,i}\right\},\ \text{with}\ j \geq 1\ \text{and}\ i \geq 1 \tag{13.18}$$

The *quasipermanent combination* associated with expression (13.18) is normally used to refer to conditions involving long-term effects and the appearance of the structure, and can be expressed as

$$\sum_{j \geq 1} G_{k,j} + P_c + \sum_{i \geq 1} \psi_{2,i} Q_{k,i} \tag{13.19}$$

In the aforementioned load combinations, the value of the characteristic temperature variation ΔT_k, rather than the value of the effect of this temperature variation $Q_k(\Delta T_k)$, must be used (Rotta Loria et al., 2019). This approach is generally valid irrespective of whether analyses accounting for a reversible or potentially irreversible mechanical behaviour of the ground are performed, as a hypothesis of superposition between the actions and their effects, which characterises the former type of analyses but not the latter, is not made.

Based on the previous considerations, an example in which an energy geostructure is subjected to a permanent compressive mechanical load, G_k, and a variable compressive mechanical load, Q_k, in addition to a thermal load, ΔT_k (e.g. considered for the heating of the energy geostructure through a positive value ΔT_k^+, whereas for the cooling through a negative value, ΔT_k^-), is shown in the following. The aim of this example is to illustrate the combinations of actions that govern the design of energy geostructures in this case at serviceability limit states.

1. *Characteristic combination accounting for mechanical and thermal actions*

A key aspect of the characteristic combination of actions involving more than one variable load relies in identifying the dominant variable load. The dominant variable load will be considered in the combination of actions through the characteristic value of such load, whereas the other variable load(s) will be combined through the accompanying value of such load(s) via the factor ψ_0.

a. When interest lies in combining the effects of a heating thermal load and any number of compressive mechanical loads, it is not known a priori whether these effects make the thermal load the dominant variable load. For example the increase in compressive stress caused in the energy geostructure by the heating thermal load may or may not be greater compared to that caused by the compressive variable mechanical load(s). Thus different design combinations must be considered.

In this example, the discussed approach results in two load combinations. One combination assumes that the effects of the heating thermal load make it the dominant variable load with respect to the variable compressive mechanical load ($\Delta T_k^+ = Q_{k,1}$), that is

$$E_d = G_k + \Delta T_k^+ + \psi_0 Q_k \tag{13.20}$$

The other combination assumes that the effects of the heating thermal load do not make it the dominant variable load with respect to the variable compressive mechanical load ($Q_k = Q_{k,1}$), that is

$$E_d = G_k + Q_k + \psi_0 \Delta T_k^+ \tag{13.21}$$

b. When interest lies in combining the effects of a cooling thermal load and any number of compressive mechanical loads, it is known a priori that these effects

make the thermal load the dominant variable load. For example the decrease in compressive stress caused in the energy geostructure by the cooling thermal load is associated with an opposite effect compared to that caused by the compressive variable mechanical load(s). Thus a unique design combination must be considered.

In this example, the combination considers that the effects of the cooling thermal load make it the dominant variable load with respect to the variable compressive mechanical load ($\Delta T_k^- = Q_{k,1}$), that is

$$E_d = G_k + \Delta T_k^- + \psi_0 Q_k \tag{13.22}$$

2. *Frequent combination accounting for mechanical and thermal actions*

A key aspect of the frequent combination of actions involving more than one variable load relies in identifying the dominant variable load, similar to the characteristic combination of actions. However, different to the characteristic combination of actions, in the frequent combination the dominant variable load will be considered in the combination of actions through the accompanying value of such load via the factor ψ_1, whereas the other variable load(s) will be combined through the accompanying value of such load(s) via the factor ψ_2.

a. In this example, two load combinations are considered to account for the combined influence of Q_k and ΔT_k^+. One combination assumes that $\Delta T_k^+ = Q_{k,1}$, that is

$$E_d = G_k + \psi_1 \Delta T_k^+ + \psi_2 Q_k \tag{13.23}$$

The other combination assumes that $Q_k = Q_{k,1}$, that is

$$E_d = G_k + \psi_1 Q_k + \psi_2 \Delta T_k^+ \tag{13.24}$$

b. In this example, a unique load combination is considered to account for the combined influence of Q_k and ΔT_k^-. This combination considers that $\Delta T_k^- = Q_{k,1}$, that is

$$E_d = G_k + \psi_1 \Delta T_k^- + \psi_2 Q_k \tag{13.25}$$

3. *Quasipermanent combination accounting for mechanical and thermal actions*

A key aspect of the quasipermanent combination of actions is that any variable load is considered in the combination through the accompanying value of such load via the factor ψ_2. Thus no considerations about the dominance of a variable load must be made when more than one of these loads are applied to any structure. In contrast, only considerations related to the effects of the variable loads for the purpose of the verification are required.

a. In this example, only one load combination allows to account for the combined influence of Q_k and ΔT_k^+, that is

$$E_d = G_k + \psi_2 \Delta T_k^+ + \psi_2 Q_k \tag{13.26}$$

b. In a similar way, only one load combination also allows to account for the combined influence of Q_k and ΔT_k^-, that is

$$E_d = G_k + \psi_2 \Delta T_k^- + \psi_2 Q_k \tag{13.27}$$

13.12 Design data for some materials

13.12.1 General

In many instances, energy geostructures are made of reinforced concrete. Recalling fundamental design data for concrete and reinforcing steel that compose reinforced concrete structures appear thus of interest. A summary of the design data characterising concrete and reinforcing steel is proposed in the following with reference to the limit state design approach included in the Eurocodes.

Essential design data for concrete of strength up to 90 MPa as well as for steel ribbed bars, decoiled rods, welded fabrics and lattice girders are reported in EN 1992 (2004). Extensive theoretical treatment of the features of concrete and reinforcing steel as well as of the theory of reinforced concrete structures is proposed, for example by MacGregor et al. (1997), Jirásek and Bažant (2001), Nilson et al. (2004) and McCormac and Brown (2015).

13.12.2 Concrete

The typical idealised *stress–strain relationship for the analysis of concrete* is reported in Fig. 13.6. This relationship refers to short-term uniaxial loading and is valid for strain levels of the concrete ε_c reading $0 < |\varepsilon_c| < |\varepsilon_{cu1}|$, where ε_{cu1} is the nominal ultimate strain of the concrete. The mathematical expression associated with this relationship reads (EN 1992, 2004)

$$\frac{\sigma_c}{f_{cm}} = \frac{k_c \eta_\varepsilon - \eta_\varepsilon^2}{1 + (k_c - 2)\eta_\varepsilon} \tag{13.28}$$

where $\eta_\varepsilon = \varepsilon_c / \varepsilon_{c1}$, ε_{c1} is the strain of concrete at peak stress f_{cm} and $k_c = 1.1 E_{cm} |\varepsilon_{c1}| f_{cm}$, with $E_{cm} = 22\left(f_{cm}/10\right)^{0.3}$ (f_{cm} in MPa) and $f_{cm} = f_{ck} + 8$ MPa. In the previous relations, E_{cm} is the mean secant modulus of elasticity of concrete, f_{cm} is the mean value of cylinder concrete compressive strength and f_{ck} the characteristic compressive cylinder strength of concrete at 28 days.

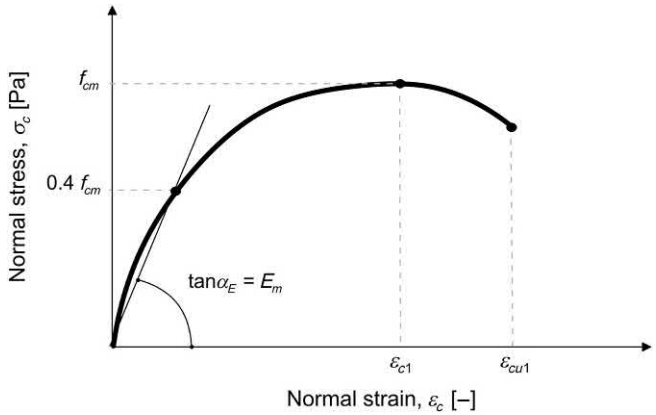

Figure 13.6 Stress–strain relationship for the analysis of concrete. *Redrawn after EN 1992, 2004. Design of Concrete Structures – Part 1-1: General Rules and Rules for Buildings. British Standards Institution, London, p. 225.*

The secant mean modulus of elasticity of concrete, E_{cm}, such as other deformation parameters that may be employed to characterise such material, critically depends on the composition of concrete and in particular on the modulus of elasticity of its aggregates. The characteristic compressive cylinder strength of concrete, f_{ck}, is generally employed to denote the concrete class. Compressive strength classes are denoted by the letter 'C' followed by two numbers that indicate the cylinder and cube characteristic strength (expressed in MPa), for example C30/37. The compressive cube strength is denoted as $f_{ck,cube}$. The characteristic compressive cylinder strength of concrete is typically defined with respect to the fractile of 5% characterising the statistical distribution of reference cylindrical concrete samples, being thus defined as the strength below which not more than 5% of all test results are likely to fall.

Relevant values of the material parameters characterising concrete are shown in Table 13.10. According to the EN 1992 (2004), the Poisson's ratio of concrete may normally be taken as equal to $\nu_c = 0.2$ for uncracked concrete and $\nu_c = 0$ for cracked concrete, whereas the linear thermal expansion coefficient of concrete may be considered of $\alpha_c = 10\,\mu\varepsilon/°C$ in the absence of more accurate information.

In addition to the idealised stress–strain relationship for the analysis of concrete, two different idealised *stress–strain relationships for the design of concrete* cross sections are available and may be used for such purpose: the parabola–rectangle relationship (cf. Fig. 13.7) and the bilinear relationship (cf. Fig. 13.8). In general, the parabola–rectangle idealisation is preferred over the bilinear relationship. For this reason, the features of the parabola–rectangle relationship are detailed hereafter.

Table 13.10 Strength and deformation characteristics for concrete.

Strength classes for concrete														
Characteristic compressive cylinder strength, f_{ck} [MPa]	12	16	20	25	30	35	40	45	50	55	60	70	80	90
Characteristic compressive cube strength, $f_{ck,cube}$ [MPa]	15	20	25	30	37	45	50	55	60	67	75	85	95	105
Characteristic (inferior) axial tensile strength, $f_{ctk,0.05}$ [MPa]	1.1	1.3	1.5	1.8	2.0	2.2	2.5	2.7	2.9	3.0	3.1	3.2	3.4	3.5
Mean secant modulus of elasticity, E_{cm} [GPa]	27	29	30	31	33	34	35	36	37	38	39	41	42	44
Compressive strain at the peak stress, ε_{c1} [‰]	1.8	1.9	2.0	2.1	2.2	2.25	2.3	2.4	2.45	2.5	2.6	2.7	2.8	2.8
Ultimate compressive strain, ε_{cu1} [‰]	3.5									3.2	3.0	2.8	2.8	2.8
Compressive strain at the peak stress, ε_{c2} [‰]	2.0									2.2	2.3	2.4	2.5	2.6
Ultimate compressive strain, ε_{cu2} [‰]	3.5									3.1	2.9	2.7	2.6	2.6
Compressive strain at the peak stress, ε_{c3} [‰]	1.75									1.8	1.9	2.0	2.2	2.3
Ultimate compressive strain, ε_{cu3} [‰]	3.5									3.1	2.9	2.7	2.6	2.6

Source: Modified after EN 1992, 2004. Design of Concrete Structures – Part 1-1: General Rules and Rules for Buildings. British Standards Institution, London, p. 225.

The mathematical formulation of the parabola–rectangle relationship reads (EN 1992, 2004)

$$\begin{gathered}\sigma_c = f_{cd}\left[1-\left(1-\frac{\varepsilon_c}{\varepsilon_{c2}}\right)^{n_{pr}}\right] \quad \text{for} \quad 0 \le |\varepsilon_c| < |\varepsilon_{c2}| \\ \sigma_c = f_{cd} \quad \text{for} \quad |\varepsilon_{c2}| \le |\varepsilon_c| \le |\varepsilon_{cu2}|\end{gathered} \tag{13.29}$$

where f_{cd} is the value of design compressive strength of concrete, n_{pr} is an exponent that depends on the concrete class, ε_{c2} is the strain at reaching the maximum strength and ε_{cu2} is the ultimate strain of concrete.

The value of design compressive strength of concrete is defined according to the EN 1992 (2004) as

$$f_{cd} = \alpha_{cc}\frac{f_{ck}}{\gamma_C} \tag{13.30}$$

where α_{cc} is a coefficient considering long-term effects on the compressive strength and unfavourable effects resulting from the way the load is applied [recommended

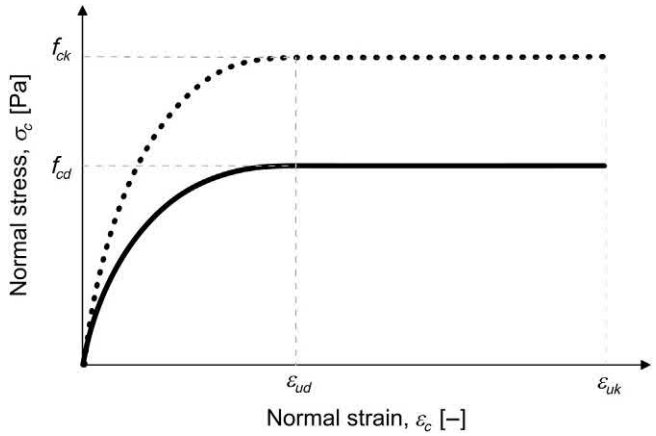

Figure 13.7 Stress–strain relationship for the design of concrete cross sections: parabola–rectangle model. *Redrawn after EN 1992, 2004. Design of Concrete Structures – Part 1-1: General Rules and Rules for Buildings. British Standards Institution, London, p. 225.*

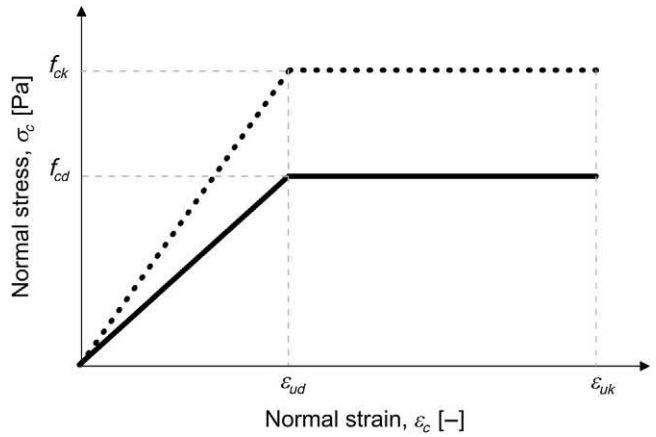

Figure 13.8 Stress–strain relationship for the design of concrete cross sections: bilinear model. *Redrawn after EN 1992, 2004. Design of Concrete Structures – Part 1-1: General Rules and Rules for Buildings. British Standards Institution, London, p. 225.*

value of 1.0 according to the EN 1992 (2004)] and γ_C is the partial factor for concrete. Values of γ_C are summarised in Table 13.11 according to the EN 1992 (2004). Following a similar approach, the value of design tensile strength of concrete is defined according to the EN 1992 (2004) as

$$f_{ctd} = \alpha_{ct} \frac{f_{ctk,0.05}}{\gamma_C} \tag{13.31}$$

Table 13.11 Value of the partial factor γ_C for concrete[a].

Design situations	Value of γ_C [−]
Persistent and transient	1.5
Accidental	1.2

[a]Note that the partial factor for concrete γ_C should be multiplied by a factor k_{cp} for calculation of design resistance of cast in place piles without permanent casing. The recommended value is $k_{cp} = 1.1$.
Source: Modified after EN 1992, 2004. Design of Concrete Structures – Part 1-1: General Rules and Rules for Buildings. British Standards Institution, London, p. 225.

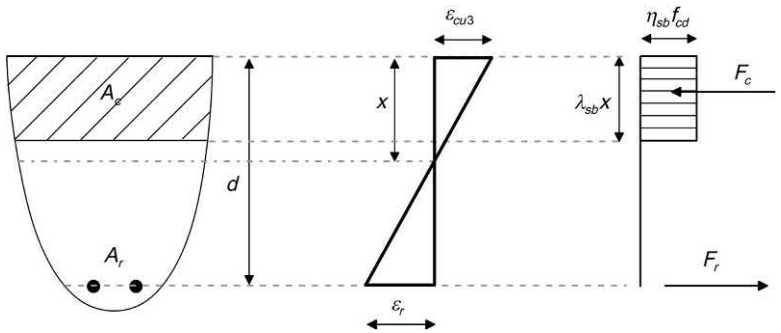

Figure 13.9 Stress–strain relationship for the design of concrete cross sections: bilinear model. *Redrawn after EN 1992, 2004. Design of Concrete Structures – Part 1-1: General Rules and Rules for Buildings. British Standards Institution, London, p. 225.*

where α_{ct} is a coefficient considering long-term effects on the tensile strength and unfavourable effects resulting from the way the load is applied [recommended value of 1.0 according to the EN 1992 (2004)].

In addition to the previous approaches for cross section design, a rectangular stress block relationship may also be employed. A schematic representation of this modelling approach is presented in Fig. 13.9 with reference to a reinforced concrete cross section characterised by a reinforcement sectional area A_r, a concrete sectional area A_c, a neutral axis depth x (i.e. the setting of a cross section along which there are no longitudinal stresses or strains, thus dividing the cross section in two portions in which all fibres are subjected to compression and tension), an effective depth of the cross section d, a normal strain level of the reinforcement ε_r and resulting forces given by the compressed concrete cross section and traction steel cross section of F_c and F_r, respectively. According to the EN 1992 (2004), the mathematical expression for the rectangular stress block approximation depends on two parameters, that is λ_{sb} and η_{sb}. These parameters are a function of the concrete strength. For the relevant characteristic compressive cylinder strength of concrete employed in energy geostructure applications of $f_{ck} \leq 50$ MPa, λ_{sb} and η_{sb} have constant values of 0.8 and 1.0, respectively (EN 1992,

2004). The factor λ_{sb} defines the effective height of the compression zone in a cross section. The factor η_{sb} defines the effective strength of the cross section.

Confinement of concrete results in a modification of the effective stress–strain relationship of such material. As highlighted in the EN 1992 (2004), higher strength and higher critical strains characterise confined concrete with respect to these same properties for (at least theoretically) the same concrete under unconfined conditions. Accounting for this phenomenon may be of particular interest for the design of energy piles due to the confinement provided by the soil surrounding such foundations. However, it is common practice to neglect this phenomenon following a conservative approach and refer to the basic stress–strain relationships described thus far.

13.12.3 Reinforcing steel

The typical idealised *stress–strain relationships for the analysis of reinforcing steel* are reported in Fig. 13.10. The (1) yield strength, (2) tensile strength and (3) ductility of steel are crucial properties for analysis and design purposes. The yield strength of steel, which can be determined as the characteristic yield load by the nominal cross section of the steel bar, is typically associated with the characteristic yield stress, f_{yk}. Different grades of reinforcing steel can be distinguished according to the value of f_{yk}. Another reference property for the yield strength of steel for products without a pronounced yield stress is the 0.2% proof-stress, $f_{0.2k}$. The tensile strength of steel, which can be determined as the characteristic maximum load in direct axial tension by the nominal cross section of the steel bar, is typically associated with the characteristic tensile strength f_{tk} (or f_t). The ductility of steel is inversely related to its yield stress and can be characterised by the characteristic strain at maximum load, ε_{uk}, and the ratio between the maximum and the yield strengths, $k_f = f_t/f_{yk}$. Ductility is an essential property if the full benefit of the plastic behaviour of structures wants to be obtained. The greater the ductility, the greater the elongation in axially loaded members, and the greater the rotation capacity in members subjected to flexure.

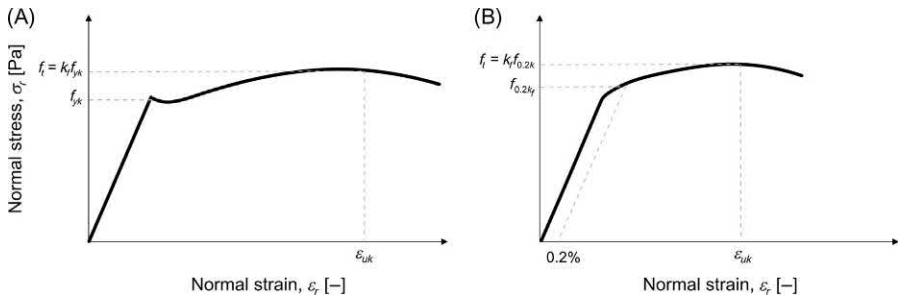

Figure 13.10 Stress–strain relationship for the analysis of reinforcing steel: (A) hot rolled steel and (B) cold worked steel. *Redrawn after EN 1992, 2004. Design of Concrete Structures – Part 1-1: General Rules and Rules for Buildings. British Standards Institution, London, p. 225.*

Table 13.12 Reinforcing steel classes.

Property	Ductility class A	Ductility class B	Ductility class C
Maximum to yield strength ratio, $k_f = f_t/f_{yk}$ [−]	≥ 1.05	≥ 1.08	≥ 1.15 but < 1.35
Characteristic strain at maximum load, ε_{uk} [%]	≥ 2.5	≥ 5.0	≥ 7.5

Source: Modified after EN 1992, 2004. Design of Concrete Structures – Part 1-1: General Rules and Rules for Buildings. British Standards Institution, London, p. 225.

Table 13.13 Some relevant properties of reinforcing steel.

Product form	Bars and decoiled rods			Wire fabrics		
Class	A	B	C	A	B	C
Characteristic yield strength, f_{yk} [MPa]	400 to 600					
Characteristic strain at maximum force, ε_{uk} [%]	≥ 2.5	≥ 5.0	≥ 7.5	≥ 2.5	≥ 5.0	≥ 7.5

Source: Modified after EN 1992, 2004. Design of Concrete Structures – Part 1-1: General Rules and Rules for Buildings. British Standards Institution, London, p. 225.

Based on the values of ε_{uk} and f_t/f_{yk}, ductility classes for reinforcing steel can be defined. Table 13.12 presents a summary of these classes according to the EN 1992 (2004). Properties of reinforcing steel that are valid for a temperature level in the finished structure between $T = -40$ and $+100°C$ are reported in Table 13.13. According to the EN 1992 (2004), the mean modulus of elasticity of reinforcing steel may be taken as equal to $E_r = 200$ GPa, whereas the linear thermal expansion coefficient of steel may be taken as $\alpha_r = 12\ \mu\varepsilon/°C$ in the absence of more accurate information. The difference between the values of thermal expansion coefficient of concrete and steel may normally be ignored in design.

In addition to the idealised stress–strain relationship for the analysis of steel, two different idealised *stress–strain relationships for the design of steel* are available and may be used for such purpose. In both cases, these relationships are bilinear (cf. Fig. 13.11). However, while one relationship assumes a constant *plateau* for the second branch, another assumes a linearly increasing function for the second branch.

When referring to the stress–strain relationship based on the horizontal top branch, no limit on the tensile strain should be imposed. In contrast, when referring to the stress–strain relationship based on the inclined top branch, reference should be

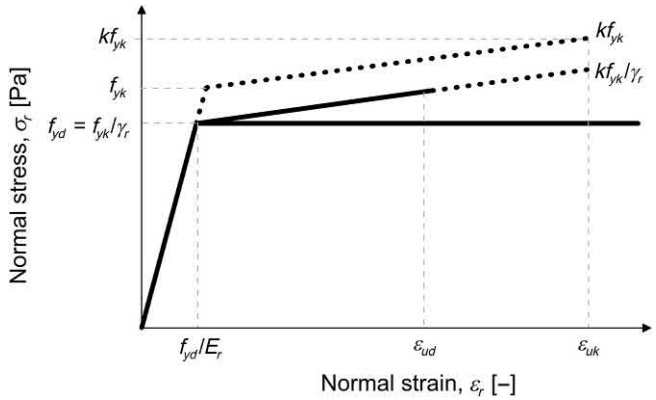

Figure 13.11 Stress–strain relationship for the design of reinforcing steel: bilinear models. *Redrawn after EN 1992, 2004. Design of Concrete Structures – Part 1-1: General Rules and Rules for Buildings. British Standards Institution, London, p. 225.*

made to the ductility class of the reinforcing steel to define its characteristics and the ultimate strain of $\varepsilon_{ud} = 0.9\varepsilon_{uk}$. Referring to a stress–strain relationship that assumes a linear function for the second branch yields economic advantages over the assumption of a constant *plateau* for the second branch. According to Narayanan and Beeby (2005), a potential 8% saving in reinforcement may be achieved by using the latter approach compared to the former, although this value is only rarely achievable and resorts to the expense of considerably more complex calculations. For this reason, reference is made in the following to the former stress–strain relationship for the reinforcing steel assuming a horizontal *plateau* for the second branch.

Similar to the approach employed for concrete, design parameters may be defined for steel. The value of design yield stress of reinforcing steel is defined according to the EN 1992 (2004) as

$$f_{yd} = \frac{f_{yk}}{\gamma_r} \tag{13.32}$$

where γ_r is the partial factor for steel. Values of γ_r are summarised in Table 13.14 according to the EN 1992 (2004).

13.13 Structural and geotechnical analysis

In many practical situations, the structural and geotechnical analyses of structures are characterised by one key difference: while the structural analysis popularly assumes a linear elastic behaviour for the material characterising the structure (e.g. reinforced concrete), the geotechnical analysis often assumes a more complex constitutive behaviour for the soil or the rock surrounding the structure. Linear elastic analyses are

Table 13.14 Value of the partial factor γ_r for reinforcing steel.

Design situations	Value of γ_r [−]
Persistent and transient	1.15
Accidental	1.0

Source: Modified after EN 1992, 2004. Design of Concrete Structures − Part 1-1: General Rules and Rules for Buildings. British Standards Institution, London, p. 225.

usually employed in the course of the structural design of even large constructions and represent the basic approach detailed for this purpose in standards such as the EN 1992 (2004). In contrast to the previous approach, linear or nonlinear elastic analyses typically accounting for plastic phenomena are employed in the course of the geotechnical design (after linear elastic analyses are often initially carried out) and are considered a particularly suitable approach for this purpose in standards such as the EN 1997 (2004).

The aim of a structural analysis is to establish a wise distribution of internal forces, moments, stresses, strains and displacements over the whole or part of a structure. In the context of the design of geostructures, a geotechnical analysis complements the previous information by accounting for the interaction of the structure with the surrounding ground. According to the EN 1992 (2004):

- A linear analysis of structural elements based on the theory of elasticity may be used for both the serviceability and ultimate limit states;
- For the determination of the action effects on the structure, the linear analysis may be carried out assuming:
  - Uncracked cross sections;
  - Linear stress−strain relationships;
  - Mean value of the modulus of elasticity.
- When computing the effects of deformation, shrinkage and settlement, a reduced stiffness corresponding to the cracked cross section should be used.

13.14 Design for ultimate limit states

13.14.1 General

Among the different design problems that can characterise structures at ultimate limit states, bending, axial loading, shearing and punching shearing are those that most commonly characterise energy geostructures. In the following, the theoretical essentials and the approaches included in the EN 1992 (2004) to design at ultimate limit states reinforced concrete structures against the effects of bending (with or without axial force), shear and punching shear are proposed.

When addressing the following design problems at ultimate limit states, thermal actions associated with the geothermal operation of energy geostructures can be neglected. The reason for this is because, provided that a ductility-oriented design approach is ensured, the influence of thermal actions associated with geothermal operations is not considered relevant for structures at ultimate limit states.

13.14.2 Bending and axial force

13.14.2.1 Problem statement

The design problem of simple bending (i.e. flexure) or combined bending and normal (i.e. axial) load of reinforced concrete cross sections belonging to undisturbed regions of beams, slabs or similar types of members, involves the simultaneous consideration of different aspects. These aspects are (1) the compatibility between the concrete and the reinforcing steel, (2) the constitutive relations of the concrete and the reinforcing steel, and (3) the equilibrium at the section level.

With reference to the compatibility considerations, the following assumptions are typically made (EN 1992, 2004):

- Plane sections remain plane before and after loading.
- The strain in bonded reinforcement tendons, whether in tension or in compression, is the same as that in the surrounding concrete. In other words, no slip between the reinforcement and the concrete occurs.

The previous assumptions are associated with the Bernoulli's idealisation and allow the distribution of strain over the cross section to be defined by just two variables: (1) the strain at the centre of gravity ε_G of the cross section and (2) the curvature of the cross section χ_ε. According to Narayanan and Beeby (2005), the previous assumptions are not strictly true, as the deformations within a section are very complex. Locally, plane sections do not remain plane and the strains in the concrete are not exactly the same as those in the steel because of local bond slip. Nevertheless, on average, the previous assumptions are correct and are sufficiently accurate for practical purposes when dealing with the design of reinforced concrete.

With reference to the constitutive relations of the concrete and steel, the following assumptions are typically made (EN 1992, 2004):

- The tensile strength of the concrete is ignored;
- The compressive stresses in the concrete are derived from the design stress–strain relationships shown in Fig. 13.7,13.8 and 13.9, which are schematised in the form of stress–strain distributions in Fig. 13.12;
- The stresses in the reinforcing steel are derived from the design curves shown in Fig. 13.11;
- Strains (e.g. compressive) are limited. The compressive strain in the concrete shall be limited to ε_{cu2} or ε_{cu3} depending on the stress–strain diagram used, whereas the

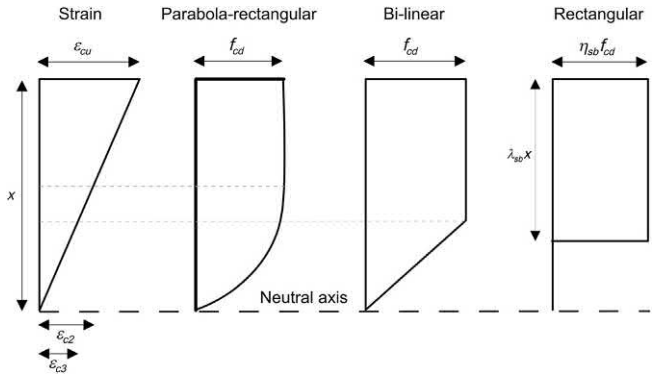

Figure 13.12 Stress–strain distributions for the design of concrete cross sections. *Redrawn after Narayanan, R., Beeby, A., 2005. Designers' Guide to EN 1992-1-1 and EN 1992-1-2. Eurocode 2: Design of Concrete Structures: General Rules and Rules for Buildings and Structural Fire Design. Thomas Telford, London.*

strains in the reinforcing steel shall be limited to ε_{ud}. For concrete strengths not exceeding 50 MPa that are modelled according to a parabola–rectangle stress–strain relationship, the previous statement involves adopting, for example the following limits. For simple bending and for combined bending and axial load where the neutral axis remains within the section, a limit of $\varepsilon_{cu2} = 0.0035$ should be considered. For sections loaded so that the whole section is in compression, a limit of between $\varepsilon_{cu2} = 0.0035$ and $\varepsilon_{c2} = 0.002$ should be considered. For reinforcing steel, the previous statement involves adopting $\varepsilon_{ud} = 0.01$. The possible range of strain distributions is shown in Fig. 13.13.

With reference to the equilibrium of the cross section, the following should be verified for the governing combination of acting bending moment, M_{Ed}, and acting normal force, N_{Ed} (cf. Fig. 13.14)

$$N_{Ed} \leq N_{Rd} = \int_A \sigma dA = \int_{A_c} \sigma_c dA_c + \int_{A_r'} \sigma_r' dA_r' + \int_{A_r} \sigma_r dA_r \tag{13.33}$$

$$M_{Ed} \leq M_{Rd} = \int_A \sigma y dA = \int_{A_c} \sigma_c y dA_c + \int_{A_r'} \sigma_r' y dA_r' + \int_{A_r} \sigma_r y dA_r \tag{13.34}$$

where M_{Rd} is computed relative to the location where N_{Rd} is applied, with y being the distance of each differential area dA_c, dA_r' or dA_r from the location of the point about which the stress resultants act. Without loss of generality, the normal force load N_{Rd} and moment M_{Rd} that equilibrate the internal stress resultants are assumed to act

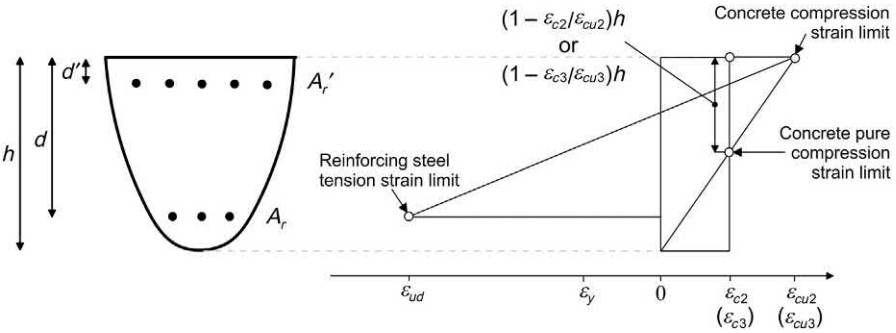

Figure 13.13 Possible range of strain distributions for a general doubly reinforced concrete cross section. *Modified after EN 1992, 2004. Design of Concrete Structures – Part 1-1: General Rules and Rules for Buildings. British Standards Institution, London, p. 225.*

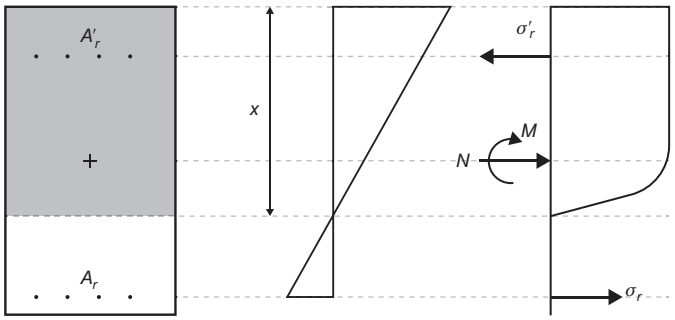

Figure 13.14 Equilibrium of a reinforced concrete cross section.

about the centre of gravity of the cross section. The moment M_{Rd} is considered positive if it produces tensile strain on the bottom fibre. For consistency, in the case that the applied loads cause compression over the depth of the section, the moment is considered positive if the compressive strain at the bottom fibre is smaller than the compressive strain at the top fibre.

13.14.2.2 Strain and strength domains

Based on the previous considerations, an analysis of the strain configurations [also termed strain domains by the EN 1992 (2004)] associated with an ultimate limit state that characterise any reinforced concrete cross section allows determining the so-called *strength domain*, *normal force-moment diagram* or $N-M$ *interaction diagram* (Whitney and Cohen, 1956) for the considered section at ultimate limit states. Strength domains can be determined for all cross sections and represent the domain of the infinite pairs of design values of resisting normal force-moment for (1) a given shape of the section (2) specific material properties and (3) a given reinforcing steel positioning in the section.

An example of design strength domain for a reinforced concrete cross section is shown in Fig. 13.15. Action effects associated with the pair of design values of acting normal force-moment on the section (N_{Ed}; M_{Ed}) that are enclosed within or lie on the boundary of the strength domain represent an admissible state for the cross section. Action effects associated with the pair (N_{Ed}; M_{Ed}) that lie outside the boundary of the strength domain represent an inadmissible state for the cross section. In other words, a strength domain represents the infinite pairs of design normal load and moment values that can be applied to the section without exceeding an ultimate limit state.

For the case of a rectangular cross section made of reinforced concrete such as that represented in Fig. 13.16, the following six strain domains can be highlighted and correspond to the achievement of an ultimate limit state:

- *Strain domain 1*: The cross section is entirely subjected to tensile stress. The neutral axis is external to the section (for example as a consequence of the influence of a

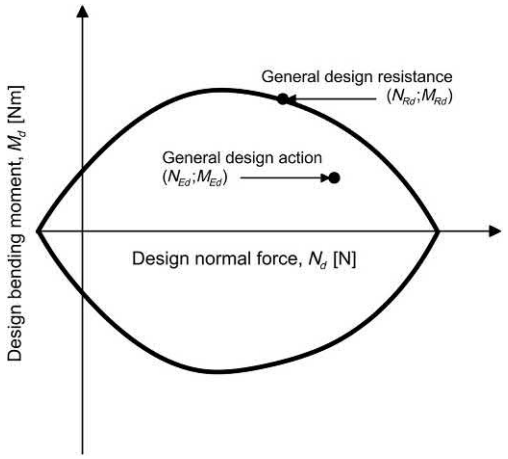

Figure 13.15 Example of strength domain for a reinforced concrete cross section.

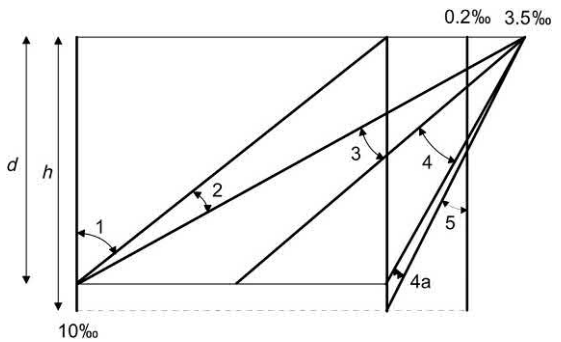

Figure 13.16 Strain domains characterising reinforced concrete cross sections.

traction load with low eccentricity). An ultimate limit state is reached for the reinforcing steel. No contribution to the (tensile) strength is assumed to be provided by the concrete.

- *Strain domain 2*: The cross section is partly subjected to a compressive stress and partly to a tensile stress. The neutral axis is internal to the section (for example as a consequence of the influence of a traction load with remarkable eccentricity or pure bending with extremely high percentages of reinforcing steel under tension). An ultimate limit state is reached for the concrete. The strain capacity of the reinforcing steel as well as of the concrete for $\varepsilon_c \leq \varepsilon_{c2}$ is exploited at maximum.
- *Strain domain 3*: The cross section is partly subjected to a compressive stress and partly to a tensile stress. The neutral axis is internal to the section (for example as a consequence of the influence of a compression load with remarkable eccentricity or pure bending with extremely low percentages of reinforcing steel under tension). An ultimate limit state is reached for the concrete. The strain capacity of the reinforcing steel as well as of the concrete is exploited at maximum. The neutral axis position $x_{lim} = \varepsilon_{cu2} d/(\varepsilon_{cu2} + \varepsilon_{yd})$ is associated with the so-called *balanced condition*.
- *Strain domain 4*: The cross section is partly subjected to a compressive stress and partly to a tensile stress. The neutral axis is internal to the section (for example as a consequence of the influence of a compression load with remarkable eccentricity or pure bending with extremely high percentages of reinforcing steel under tension). An ultimate limit state is reached for the concrete. The reinforcing steel is no more yielded and the strain capacity of the concrete is exploited at maximum. Beyond this strain domain, attention needs to be devoted to the ductility of the section.
- *Strain domain 4a*: The cross section is subjected to a compressive stress. The neutral axis is internal to the section (for example as a consequence of the influence of a compression load with low eccentricity). An ultimate limit state is reached for the concrete. The reinforcing steel is under compression and the strain capacity of the concrete is exploited at maximum. Beyond this strain domain, attention needs to be devoted to the ductility of the section.
- *Strain domain 5*: The cross section is completely subjected to a compressive stress. The neutral axis is external to the section (for example as a consequence of the influence of a compression load with low eccentricity). An ultimate limit state is reached for the concrete.

Strength domains are typically used for design situations involving prevalent tension (i.e. strain domain 1) or prevalent compression (i.e. strain domains 4, 4a and 5) of the cross sections. In situations of simple or prevalent bending (i.e. strain domains 2, 3 and 4), other more expedient design approaches that the definition of the entire strength domain for a given cross section may be employed. These approaches are detailed in the following for singly or doubly reinforced concrete cross sections.

13.14.2.3 Design of singly reinforced cross sections

The equilibrium of normal forces and moments for a singly reinforced cross section of concrete such as that represented in Fig. 13.14 leads to the following equations:

$$\overline{f}bx = f_{yd}A_r \quad \text{or} \quad \frac{x}{d} = \rho_r \frac{f_{yd}}{\overline{f}} \tag{13.35}$$

$$M = f_{yd}A_r \quad \text{or} \quad \frac{M}{bd^2} = \overline{f}\left(1 - \frac{\tilde{\beta}x}{d}\right)\frac{x}{d} \tag{13.36}$$

where A_r is the area of steel under tension, $\overline{f}$ is the average stress acting on the compression zone, f_{yd} is the design yield strength of the steel, $\tilde{\beta}$ is the ratio of the distance of the centre of compression from the compression face to the neutral axis depth, and $\rho_r = A_r/A_c$ is the reinforcement ratio.

Working with Eq. (13.35) and (13.36) allows performing different design calculations:

- Knowing (1) the acting design moment on a simply reinforced concrete cross section, (2) the geometry of the section and (3) the material properties of the concrete and the reinforcing steel, the needed reinforcing steel area A_r ensuring $M_{Ed} \leq M_{Rd}$ can be determined.
- Knowing (1) the acting design moment on a simply reinforced concrete cross section, (2) the geometry of the section, (3) the material properties of the concrete and the reinforcing steel and (4) the reinforcing steel area characterising the cross section, the design resisting moment M_{Rd} can be determined to verify the inequality $M_{Ed} \leq M_{Rd}$.

However, the main limitation with the previous design approach for the determination of A_r is that it does not always ensure appropriate ductility of the cross section. To this aim, it is typically imposed that $\varepsilon_r \geq \varepsilon_{yd} = f_{yd}/E_r$ and the neutral axis depth is limited to $x/d \leq 0.45$ and 0.35 for concretes characterised by a characteristic compressive cylinder strength of $f_{ck} \leq 50$ and 55, respectively.

13.14.2.4 Design of doubly reinforced cross sections

Associated with the previous limitations of neutral axis depth for singly reinforced concrete cross sections, there exist a limiting design moment value M_{lim}. If $M_{Ed} > M_{lim}$, the geometry of the cross section must be modified or reinforcing steel in the compression zone of the section must be added. The situation in which compression reinforcement is added to a singly reinforced concrete cross section to maintain the neutral axis depth at the relevant limiting value when $M_{Ed} > M_{lim}$ is considered

hereafter. The following equations satisfy the above and can be used for the design of doubly reinforced concrete cross sections

$$A_r^{'} = \frac{M - M_{lim}}{f_{yd}(d - d^{'})} \tag{13.37}$$

$$A_r = A_r^{'} + A_{r,lim} \tag{13.38}$$

where $A_r^{'}$ is the area of reinforcing steel in the compression zone, $d^{'}$ is the depth at which the compression reinforcement is placed from the most compressed fibre of the cross section and $A_{r,lim}$ is the value of A_r when $M = M_{lim}$. To obtain the previous equations, it is assumed that (1) the area displaced by the compression reinforcement is ignored and (2) the compression reinforcement is working at its design yield strength. Assumption (2) is only true if the following holds

$$\frac{f_{yd}}{E_r} < \frac{\varepsilon_{cu}\left(x - d^{'}\right)}{x} \tag{13.39}$$

When interest may lie in determining the design resisting moment for any possible cross section, the following iterative procedure can be applied:

1. Guess a value for the depth of the neutral axis, x.
2. Calculate the compressive force in the compression zone using the relevant chosen stress–strain relationship. For simple calculations, the rectangular idealisation of the stress–strain distribution is the easiest to apply.
3. From the neutral axis depth and the ultimate strain, calculate the strain in each layer of reinforcement and hence the stress and the force in each layer.
4. Check whether the total compressive force is equal to the total tension force. If this verification is successful, then the assumed neutral axis depth is correct and the moments of the internal forces may be taken to obtain the design resisting moment for the cross section. If the tension and compression forces are not equal, adjust the value of the neutral axis depth and repeat the calculation from step 2.

13.14.3 Shear

13.14.3.1 Problem statement

The design problem of shear is more complex than that of bending and presents one crucial difference: while the analysis of the effects of bending can be carried out with reference to a cross section of any considered structure, the analysis of the effects of shear must be carried out with reference to a finite portion of the structure. Various theories are available to interpret and account for the shear phenomenon in design and considerable areas of uncertainty and disagreement exist. Among the various

aspects that characterise the shear behaviour of reinforced concrete members (1) the presence, significance and orientation of the reinforcement, (2) the shape of the cross section, (3) the type and position of the loads and (4) the adherence between concrete and reinforcing steel are of crucial importance.

The approach included in the EN 1992 (2004) to deal with the shear behaviour of reinforced concrete member will change in the new version of the Eurocodes. Therefore the current approach to deal with the design against shear of reinforced concrete members is only summarised in the following, with a focus on (1) the strength of members not requiring design shear reinforcement and (2) the strength of members requiring design shear reinforcement.

13.14.3.2 Design of members not requiring design shear reinforcement

The design of members not requiring design shear reinforcement is particularly relevant to slabs, whereas it is usually of limited importance for beams. In fact, design shear reinforcement may be omitted in the former cases, while it is generally of crucial importance in the latter situations.

The condition allowing to avoid the need of providing design shear reinforcement to reinforced concrete members is that the design value of acting shear action does not exceed the design shear resisting force of the member without shear reinforcement, that is $V_{Ed} \leq V_{Rd} \equiv V_{Rd,c}$ (where V_{Rd} is the design shear resisting force and $V_{Rd,c}$ is the design shear resisting force of the member without shear reinforcement). In those situations, although there would be no need to provide design shear reinforcement to the considered member, minimum shear reinforcement should in any case be provided.

The condition requesting the need of providing design shear reinforcement to reinforced concrete members is that the design value of shearing action exceeds the design shear resisting force of the member without shear reinforcement, that is $V_{Ed} > V_{Rd,c}$. In those situations, sufficient design shear reinforcement should be provided to verify that $V_{Ed} \leq V_{Rd} \equiv V_{Rd,c}$.

According to Narayanan and Beeby (2005), the shear strength of any reinforced concrete member without shear reinforcement primarily depends on (1) the concrete tensile strength, (2) the reinforcement ratio (e.g. against bending) and (3) the depth of the member. The design value for the shear resisting force of members without shear reinforcement can be determined according to the EN 1992 (2004) as

$$V_{Rd,c} = \left[C_{Rd,c} k_d \left(100 \rho_l f_{ck}\right)^{\frac{1}{3}} + k_1 \sigma_{cp}\right] b_w d \tag{13.40}$$

where $C_{Rd,c}$ is a nationally determined parameter with a recommended expression of $\frac{0.18}{\gamma_c}$, $k_d = 1 + \sqrt{\frac{200}{d}} \leq 2.0$ (with d expressed in [mm]), $\rho_l = \frac{A_{sl}}{b_w d} \leq 0.02$ (with A_{sl} the area of tensile reinforcement and b_w the smallest width of the cross section in the tensile area), k_1 is a nationally determined parameter with a recommended value of 0.15 and $\sigma_{cp} = N_{Ed}/A_c < 0,2 f_{cd}$ (with f_{cd} expressed in [MPa]).

In all cases, expression (13.40) should verify the following (EN 1992, 2004)

$$V_{Rd,c} \leq V_{rd,c,min} = (v_{min} + k_1 \sigma_{cp}) b_w d \tag{13.41}$$

where v_{min} is a nationally determined parameter with a recommended expression of $0.035 k_d^{3/2} f_{ck}^{1/2}$.

13.14.3.3 Design of members requiring design shear reinforcement

The design of members requiring design shear reinforcement is particularly relevant to beams and retaining walls, for example. A typical analysis approach to address the shear phenomenon is the 'truss model'. The idealisation characterising the considered modelling approach is presented in Fig. 13.17, with the assumption that the compressive and tensile cord governing the diffusion of the shear are represented by the concrete in the compressed zone of the member and by the tension reinforcing steel, whereas the connecting paths are represented by steel tension members providing shear reinforcement and virtual concrete struts.

For members with general inclined shear reinforcement (where the inclination is represented by the angle between shear reinforcement and the beam axis perpendicular to the shear force, $\tilde{\alpha}$), it should be verified that $V_{Ed} \leq \min\{V_{Rd,r}; V_{Rd,max}\}$, where $V_{Rd,r}$ is the design shear force that can be sustained by the yielding shear reinforcement and $V_{Rd,max}$ is the design value of the maximum shear force that can be sustained by the member, limited by crushing of the compression struts.

Both definitions of $V_{Rd,r}$ and $V_{Rd,max}$ can be derived from equilibrium considerations referring to the truss model. The definition of $V_{Rd,r}$ follows considerations of vertical equilibrium across a section parallel to the virtual compression strut. The definition of $V_{Rd,max}$ follows considerations of vertical equilibrium across a section perpendicular to the virtual compression strut.

According to the EN 1992 (2004), the design value of the shear force which can be sustained by the yielding shear reinforcement reads

$$V_{Rd,r} = \frac{A_{rw}}{s} \tilde{z} f_{ywd} \left(\cot\tilde{\theta} + \cot\tilde{\alpha}\right) \sin\tilde{\alpha} \tag{13.42}$$

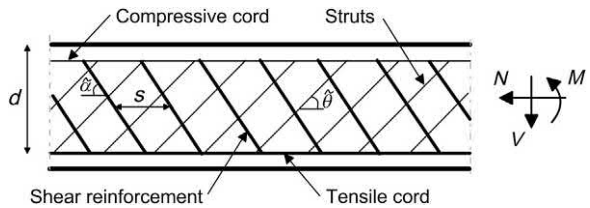

Figure 13.17 Truss model for describing shear phenomenon.

where A_{nw} is the sectional area of the shear reinforcement, s is the spacing of the stirrups, $\tilde{z}$ is the inner lever arm (for a member with constant depth corresponding to the bending moment in the element under consideration) that in the shear analysis of reinforced concrete without axial force may be considered equal to $\tilde{z} = 0.9d$, f_{ywd} is the design yield strength of the shear reinforcement and $\tilde{\theta}$ is the angle between the concrete compression strut and the beam axis perpendicular to the shear force that should verify $1 \leq \cot\tilde{\theta} \leq 2.5$ according to the EN 1992 (2004). The definition of this resisting force can be simplified for usual applications in which vertical reinforcement is employed by considering the smaller value of

$$V_{Rd,r} = \frac{A_{nw}}{s}\tilde{z}f_{ywd}\cot\tilde{\theta} \tag{13.43}$$

According to the EN 1992 (2004), the design value of the maximum shear force that can be sustained by the member reads

$$V_{Rd,max} = \alpha_{cw}b_w\tilde{z}\nu_1 f_{cd}\frac{\left(\cot\tilde{\theta} + \tan\tilde{\theta}\right)}{\left(1 + \cot^2\tilde{\theta}\right)} \tag{13.44}$$

where α_{cw} is a nationally determined parameter accounting for the state of stress in the compression chord with a recommended value of 1 for nonprestressed structures and ν_1 is another nationally determined parameter with a recommended value of $\nu_1 = 0.6\left(1 - \frac{f_{ck}}{250}\right)$ (with f_{ck} is expressed in [MPa]). The definition of this resisting force can be simplified for usual applications in which vertical reinforcement is employed by considering the value of

$$V_{Rd,max} = \frac{\alpha_{cw}b_w\tilde{z}\nu_1 f_{cd}}{\cot\tilde{\theta} + \tan\tilde{\theta}} \tag{13.45}$$

To ensure ductility, the maximum shear reinforcement $A_{nw,max}$ should verify

$$\frac{A_{nw,max}f_{ywd}}{b_w s} \leq \frac{\alpha_{cw}\nu_1 f_{cd}}{2\sin\tilde{\alpha}} \tag{13.46}$$

with the following simplification for vertical shear reinforcement

$$\frac{A_{nw,max}f_{ywd}}{b_w s} \leq \frac{\alpha_{cw}\nu_1 f_{cd}}{2} \tag{13.47}$$

The influence of the design shear force causes the insurgence of an additional tensile force that is applied to the longitudinal reinforcement (i.e. the tensile axial force in the longitudinal reinforcement is not only a function of bending, but also of shear).

For a general section along a member, this additional force may be calculated as (EN 1992, 2004)

$$\Delta F_{td} = \frac{M_{Ed}}{\tilde{z}} + \frac{V_{Ed}}{2}\left(\cot\tilde{\theta} - \cot\tilde{\alpha}\right) \tag{13.48}$$

with $\Delta F_{td} \leq M_{Ed,max}/\tilde{z}$, with $M_{Ed,max}$ being the maximum design bending moment acting along the member.

13.14.4 Punching shear

13.14.4.1 Problem statement

The design problem of punching shear results from the influence of a concentrated load or a reaction acting on a relatively small area and involves local shear failures rotated around the loaded area. The punching shear problem is typically relevant for slabs. According to Narayanan and Beeby (2005), while the design problem of shear is addressed by considering the equilibrium of cross sections, the design problem of punching shear involves the transformation of sections into a 'basic control perimeter' resorting to a similar approach.

In the following, the design problem of punching shear is summarised, with a focus on (1) the definition of the basic control perimeter, (2) the definition of the design shear force, (3) the design of members not requiring design shear reinforcement and (4) the design of members requiring design shear reinforcement.

13.14.4.2 Basic control perimeter

The definition of the basic control perimeter is of great significance for the design of reinforced concrete members against punching shear because it represents the basis for the verification of the member to be performed as well as for the area of influence of the punching shear phenomenon to be determined.

According to the EN 1992 (2004), the basic control perimeter u_1 may be taken at a distance of $2d$ from the loaded area and should be constructed as to minimise its length. Typical shapes that may be considered for the basic control perimeter around loaded areas are reported in Fig. 13.18. According to the EN 1992 (2004), the basic control perimeters at a distance less than $2d$ should be considered for situations in which a concentrated force is opposed by a high pressure (e.g. soil pressure on a base).

The basic control perimeter encloses a control surface A_{cont} that surrounds a surface where the load is applied A_{load} as shown in Fig. 13.19 for solid slabs, waffle slabs with solid areas over columns and foundations. If on the basis of the verification design shear reinforcement would be needed, the basic control perimeters must be extended to a wider perimeter $u_{out,ef}$ outside of which shear reinforcement is no longer required. The reinforcement for punching shear may generally be considered an additional reinforcement to that potentially needed for shear.

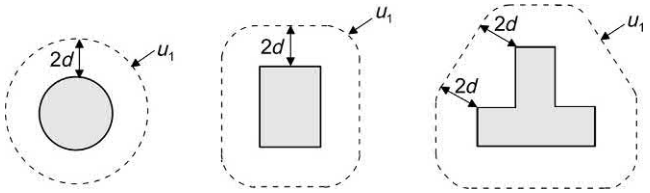

Figure 13.18 Typical basic control perimeters around simple loaded areas. *Modified after EN 1992, 2004. Design of Concrete Structures – Part 1-1: General Rules and Rules for Buildings. British Standards Institution, London, p. 225.*

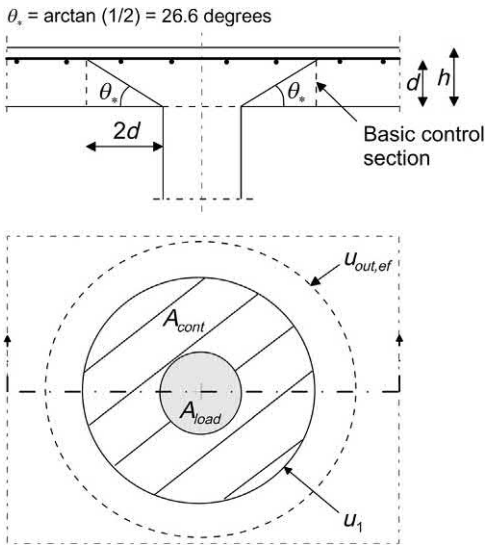

Figure 13.19 The design problem of punching shear. *Modified after EN 1992, 2004. Design of Concrete Structures – Part 1-1: General Rules and Rules for Buildings. British Standards Institution, London, p. 225.*

13.14.4.3 Definition of design shear force

The design procedure for punching shear is based on checks at the face of the column and at the basic control perimeter. According to the EN 1992 (2004), at the column perimeter or at the perimeter of the loaded area, the design value of maximum acting punching shear stress should not exceed the design value of maximum punching shear resistance along the control section considered

$$v_{Ed} \leq v_{Rd,max} = 0.5\nu_1 f_{cd} \tag{13.49}$$

The design value of maximum acting punching shear stress can be determined as (EN 1992, 2004)

$$v_{Ed} = \tilde{\tilde{\beta}} \frac{V_{Ed}}{u_i d} \tag{13.50}$$

where V_{Ed} is the design value of acting shear force (which may be reduced in a foundation slab due to the favourable action of soil pressure), u_i is the length of the control perimeter considered and $\tilde{\tilde{\beta}}$ is a factor depending on the geometry of the considered perimeter and the significance of the moment transferred from a column to a slab member. The factor $\tilde{\tilde{\beta}}$ aims at increasing the design value of acting punching shear. The rationale for this increase results from the assumption of a uniform distribution of forces along the perimeter that is made to address the design problem of punching shear, which is actually an approximation of reality and causes lower values of the actual punching shear resistance. According to Narayanan and Beeby (2005), the multiplier $\tilde{\tilde{\beta}}$ is defined to model the effect of transferring a moment between a slab and a column by considering the distribution of shear around the control perimeter considered, such that it provides a moment equal to the moment transferred. The shear multiplier $\tilde{\tilde{\beta}}$ can be defined as (EN 1992, 2004)

$$\tilde{\tilde{\beta}} = 1 + k_{AR} \frac{\Delta M_{Ed}}{V_{Ed}} \frac{u_1}{W_1} \tag{13.51}$$

where k_{AR} is a coefficient depending on the dimensions (e.g. aspect ratio) of the considered column (cf. Table 13.15), ΔM_{Ed} is the difference in moment from one side of a column to the other and W_1 is the corresponding distribution of shear, such as that illustrated in Fig. 13.20, which is given by

$$W_1 = \int_0^{u_i} \frac{\Delta M_{Ed}}{V_{Ed}} dl \tag{13.52}$$

Table 13.15 Value of the aspect ratio coefficient k_{AR} for rectangular loaded areas.

Ratio between the dimensions of the cross sections perpendicular and parallel to the axis of bending, c_1/c_2 [−]	Aspect ratio coefficient, k_{AR} [−]
≤ 0.5	0.45
1.0	0.60
2.0	0.70
≥ 3.0	0.80

Source: Data from EN 1992, 2004. Design of Concrete Structures – Part 1-1: General Rules and Rules for Buildings. British Standards Institution, London, p. 225.

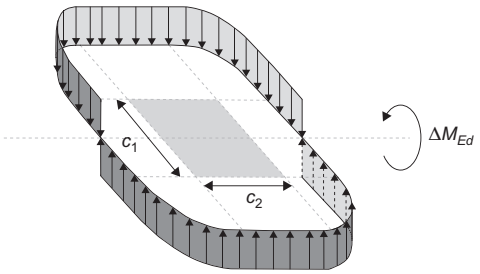

Figure 13.20 Shear distribution due to an unbalanced moment at a slab-internal column intersection. *Modified after EN 1992, 2004. Design of Concrete Structures – Part 1-1: General Rules and Rules for Buildings. British Standards Institution, London, p. 225.*

where $\Delta M_{Ed}/V_{Ed}$ is the eccentricity of the concentrated load relative to the centroid of the loaded area, dl is a length increment of the perimeter considered.

Table 13.16 presents formulations summarised by Narayanan and Beeby (2005) to determine the coefficient $\tilde{\tilde{\beta}}$, drawing from the EN 1992 (2004). Approximate values of $\tilde{\tilde{\beta}}$ that may be employed as nationally determined parameters in situations where the lateral stability of structures does not depend on frame action between the slab and the columns are as follows (EN 1992, 2004): $\tilde{\tilde{\beta}} = 1.15$ for internal columns, $\tilde{\tilde{\beta}} = 1.4$ for edge columns and $\tilde{\tilde{\beta}} = 1.5$ for corner columns.

13.14.4.4 Design of members not requiring design shear reinforcement

Design punching shear reinforcement is not necessary if $v_{Ed} \leq v_{Rd,c}$, where $v_{Rd,c}$ is the design punching shear resistance of a slab without punching shear reinforcement along the control section considered. Design punching shear reinforcement is needed if $v_{Ed} > v_{Rd,c}$.

The design punching shear resistance of a slab without punching shear reinforcement along the control section considered can be determined according to the EN 1992 (2004) as

$$v_{Rd,c} = C_{Rd,C} k_d \left(100 \rho_l f_{ck}\right)^{1/3} + k_1 \sigma_{cp} \geq \left(v_{min} + k_1 \sigma_{cp}\right) \tag{13.53}$$

where $\rho_l = \sqrt{\rho_{ly} \rho_{lz}} \leq 0.02$ (with ρ_{ly} and ρ_{lz} being the reinforcement ratios in the y and z directions, respectively, calculated for the reinforcement within a width equal to the column dimension plus $3d$ on each side), k_1 is a nationally determined parameter with a recommended value of 0.1 (in contrast with the value of 0.15 for the coefficient k_1 associated with the design problem of shear) and $\sigma_{cp} = (\sigma_{cy} + \sigma_{cz})/2$ is the *average* longitudinal stress (with σ_{cy} and σ_{cz} the normal concrete stresses in the considered section in the y and z directions, respectively).

Table 13.16 Values of the punching shear enhancement factor for various types of columns (Narayanan and Beeby, 2005).

Case	Value for $\tilde{\tilde{\beta}}$
Internal rectangular column, uniaxial bending	$\tilde{\tilde{\beta}} = 1 + k_{AR}\left(\Delta M_{Ed}/V_{Ed}\right)\left(u_1/W_1\right)$ $W_1 = {c_1}^2/2 + c_1 c_2 + 4c_2 d + 16d^2 + 2\pi d c_1$ Values of k_{AR} from Table 13.15
Internal rectangular column, biaxial bending	$1 + 1.8\sqrt{\left[\Delta M_{Edy}/(c_z + 4d)\right]^2 + \left[\Delta M_{Edz}/\left(c_y + 4d\right)\right]^2}$ ΔM_{Edy} and ΔM_{Edz} are respectively the moments transferred in the y and z directions while c_y and c_z are respectively the section dimensions in the y and z directions.
Rectangular edge column; axis of bending parallel to the slab edge, eccentricity is towards the interior	$\tilde{\tilde{\beta}} = u_1/u_1^*$ (i.e. shear is assumed uniformly distributed over perimeter u_1^* as defined in Fig. 13.21A)
Rectangular edge column; bending abut both axes. Eccentricity perpendicular to the slab edge is towards the exterior	$\tilde{\tilde{\beta}} = 1 + k_{AR}\left(\Delta M_{Ed}/V_{Ed}\right)\left(u_1/W_1\right)$ W_1 calculated by taking moments about the centroid of the control perimeter, u_1 Values of k_{AR} from Table 13.15
Rectangular edge column; bending about both axes. Eccentricity perpendicular to the slab edge is towards the interior	$\tilde{\tilde{\beta}} = u_1/u_1^* + k_{AR}\left(\Delta M_{Ed,par}/V_{Ed}\right)\left(u_1/W_1\right)$ $W_1 = {c_2}^2/4 + c_1 c_2 + 4c_1 d + 8d^2 + \pi d c_2$ $\Delta M_{Ed,par}$ is the moment transfer about an axis perpendicular to the slab edge. The value of k_{AR} is determined from Table 13.15 with c_1/c_2 put equal to $0.5\left(c_1/c_2\right)$ c_1 is the section dimension perpendicular to the slab edge; c_2 is the dimension parallel to the slab edge
Rectangular corner column, eccentricity is towards the interior	$\tilde{\tilde{\beta}} = u_1/u_1^*$ (i.e. punching force is considered uniformly distributed along perimeter u_1^* in Fig. 13.21B)
Rectangular corner column, eccentricity is towards the exterior	$\tilde{\tilde{\beta}} = 1 + k_{AR}\left(\Delta M_{Ed}/V_{Ed}\right)\left(u_1/W_1\right)$ $W_1 = {c_1}^2/2 + c_1 c_2 + 4c_2 d + 16d^2 + 2\pi d c_1$ Values of k_{AR} from Table 13.15
Interior circular column	$\tilde{\tilde{\beta}} = 1 + 0.6\pi\left(\Delta M_{Ed}/V_{Ed}\right)/(D + 4d)$ D is the diameter of the column
Circular edge or corner columns	No information given

13.14.4.5 Design of members requiring design shear reinforcement

When $v_{Ed} > v_{Rd,c}$, it must be verified that $v_{Ed} \leq v_{Rd,cr}$, where $v_{Rd,cr}$ is design punching shear resistance of a slab with punching shear reinforcement along the control section considered. According to the EN 1992 (2004), the design punching shear

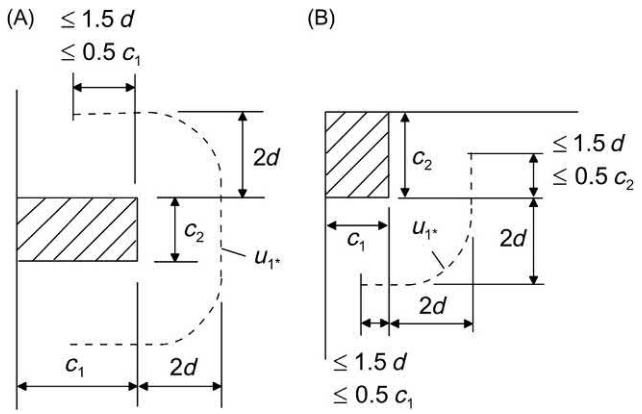

Figure 13.21 Reduced basic control perimeter, u_1^*. *Redrawn after EN 1992, 2004. Design of Concrete Structures – Part 1-1: General Rules and Rules for Buildings. British Standards Institution, London, p. 225.*

resistance of a slab with punching shear reinforcement along the control section considered reads

$$v_{Rd,cr} = 0,75v_{Rd,c} + 1,5\left(\frac{d}{s_r}\right)A_{nw}f_{ywd,ef}\left[\frac{1}{(u_1 d)}\right]\sin\tilde{\alpha} \tag{13.54}$$

where s_r is the radial spacing of perimeters of shear reinforcement, A_{nw} is the area of one perimeter of shear reinforcement around a considered column, $f_{ywd,ef}$ is the effective design strength of the punching shear reinforcement expressed as $f_{ywd,ef} = 250 + 0,25d \leq f_{ywd}$ (f_{ywd} is expressed in [MPa]) and $\tilde{\alpha}$ is the angle between the shear reinforcement and the plane of the slab.

The control perimeter beyond which shear design shear reinforcement is no longer required reads (EN 1992, 2004)

$$u_{out,ef} = \tilde{\tilde{\beta}}\frac{v_{Ed}}{v_{Rd,c}d} \tag{13.55}$$

Punching shear failure is unlikely to take place along the control perimeter, $u_{out,ef}$, which represents the outer boundary of the potential failure zone. However, punching shear failure may occur at any perimeter within $u_{out,ef}$. The inner boundary for the basic control perimeter, u_1, may be considered of $0.3d$ from the loaded area (EN 1992, 2004). Given that the maximum spacing of shear reinforcement is $0.75d$ and that at least two sets of reinforcement are required, shear reinforcement could be provided at distances of $0.5d$ and $1.25d$ from the loaded area (e.g. column face) leaving a gap of $0.75d$ between the outermost reinforcement and the basic control perimeter u_1 (Narayanan and Beeby, 2005).

13.15 Design for serviceability limit states

13.15.1 General

Among the different design problems that can characterise structures at serviceability limit states, the limitation of stresses, the control of cracking and the control of deflections are those that most commonly characterise energy geostructures. In the following, the theoretical essentials and the approaches included in the EN 1992 (2004) to design at serviceability limit states reinforced concrete structures with reference to the limitation of stresses, the control of cracking and the control of deflections are discussed.

When addressing the following design problems at serviceability limit states, thermal actions associated with the geothermal operation of energy geostructures should be considered. The reason for this is because the influence of thermal actions associated with geothermal operations is extremely relevant for structures at serviceability limit states. This approach agrees with the provisions of the EN 1992 (2004), which state that temperature effects should be considered where they are likely to be significant.

13.15.2 Stress limitation

13.15.2.1 Problem statement

The stress limitation is a core point of serviceability limit state verifications. The rationale for limiting compressive stresses in concrete is twofold: (1) to avoid the formation of microcracks in the concrete that may reduce durability and (2) to avoid excessive creep. The rationale for limiting tensile stresses in the reinforcement is also twofold: (1) to ensure that inelastic deformations of the reinforcing steel are encountered under service loads (thus preserving the hypothesis of an elastic behaviour of the reinforcing steel that is made for cracking or deflection control calculations) and (2) to avoid the formation of excessively large cracks in the concrete. Cracking may decrease durability.

13.15.2.2 Compressive stress limitation

According to the EN 1992 (2004), longitudinal cracks may occur if the stress level under the characteristic combination of loads exceeds a critical value. In areas exposed to environments of exposure classes XD, XF and XS (i.e. environmental conditions associated with corrosion induced by chlorides, freeze-thaw attack and corrosion induced by chlorides from sea water, respectively), it may be appropriate to limit the compressive stress to a value (EN 1992, 2004)

$$\sigma_c \leq \tilde{k}_1 f_{ck} \tag{13.56}$$

where $\tilde{k}_1$ is a nationally determined parameter with a value of 0.6. In the serviceability analysis of energy geostructures, the value of σ_c included in the previous inequality (13.56) should include the effects of both mechanical and thermal actions.

According to the EN 1992 (2004), linear creep may be assumed if the stress in the concrete, under the quasipermanent combination of loads, reads

$$\sigma_c \leq \tilde{k}_2 f_{ck} \tag{13.57}$$

where $\tilde{k}_2$ is a nationally determined parameter with a recommended value of 0.45. Otherwise, nonlinear creep should be considered. In the serviceability analysis of energy geostructures, the value of σ_c included in the previous inequality (13.57) should include the effects of both mechanical and thermal actions.

13.15.2.3 Tensile stress limitation

Unacceptable cracking or deformation caused by tensile stresses may be assumed to be avoided if, under the characteristic combination of loads, the tensile stress caused by a load in the reinforcement does not exceed

$$\sigma_r \leq \tilde{k}_3 f_{yk} \tag{13.58}$$

where $\tilde{k}_3$ is a nationally determined parameter with a recommended value of 0.8.

Where the stress is caused by an imposed deformation, such as in situations involving thermal actions applied to energy geostructures due to their geothermal operation, the tensile stress in the reinforcement should not exceed

$$\sigma_r \leq \tilde{k}_4 f_{yk} \tag{13.59}$$

where $\tilde{k}_4$ is a nationally determined parameter with a recommended value of 1. In the serviceability analysis of energy geostructures, the value of σ_r included in the previous inequality (13.59) should include the effects of both mechanical and thermal actions.

13.15.2.4 Procedure for stress check at serviceability limit states

The determination of the stress for the related verifications at serviceability limit states is based on the following assumptions: (1) plane sections remain plane; (2) concrete and reinforcing steel under tension are assumed to follow an elastic behaviour; (3) when the tensile strength of concrete f_{ctm} is reached, the cross section is considered to be cracked and the concrete tension is ignored.

For uncracked cross sections subjected to moments and axial loads, the stress in the concrete may be estimated following the Navier's formula

$$\sigma_n = \frac{My}{J} + \frac{N}{A_c} \tag{13.60}$$

where M is the applied moment, y is the distance from the neutral axis to the point considered, J is the second moment of area of the section, N is the applied normal force and A_c is the concrete area.

For cracked cross sections, the stresses in the concrete are more challenging to estimate because the second moment of area of the section is a function of the normal force. In those situations, a suitable procedure consists in writing the equations of equilibrium for the sections and solving them iteratively.

13.15.3 Crack control

13.15.3.1 Problem statement

The rationale for limiting cracks in the concrete is threefold: (1) to avoid possible corrosion damage to the reinforcement due to deleterious substances (e.g. fluids) penetrating to the reinforcement through the cracks; (2) to avoid or limit leakage through cracks (e.g. for water retaining structures); and (3) to avoid an unsightly appearance. The various phenomena that may cause crack insurgence include, without being limited to: (1) plastic shrinkage or plastic settlement; (2) corrosion; (3) expansive chemical reactions with the concrete; (4) restrained deformations; and (5) loading.

Cracking shall be limited to an extent that will not impair the proper functioning or durability of the structure (EN 1992, 2004). To limit the significance of cracking in reinforced concrete members with unbonded tendons, for example the EN 1992 (2004) establishes the values reported in Table 13.17 with reference to the quasipermanent load combination.

Particular risks of large cracks characterise sections where there are sudden variations of stress. These variations may typically arise (1) due to changes of section, (2) near concentrated loads, (3) where bars are curtailed, or (4) in areas of high bond stress, particularly at the ends of laps. In the context of energy geostructures, regions close to the null point of the vertical displacement may be particularly sensitive to cracking because of the noteworthy potential changes of stress sign.

Table 13.17 Recommended values of maximum crack opening.

Exposure class	Maximum value of crack opening, w_{max} [mm]
X0, XC1	0.40[a]
XC2, XC3, XC4	0.30
XD1, XD2, XS1, XS2, XS3	

[a]For X0 and XC1 exposure classes, crack width has no influence on durability and this limit is set to guarantee acceptable appearance. In the absence of appearance conditions this limit may be relaxed.
Source: Data from the EN 1992, 2004. Design of Concrete Structures – Part 1-1: General Rules and Rules for Buildings. British Standards Institution, London, p. 225.

13.15.3.2 Principles of cracking phenomena

For sections subjected to pure tension, the development of cracks corresponds to the transition from a composite cross section to a section where only the longitudinal reinforcement contributes to the resistance (cf. Fig. 13.22).

The behaviour of single mean reinforced concrete cross sections, before reaching the tensile strength of concrete, is linear elastic and characteristic of a composite cross section. In this context, the steel to concrete stiffness ratio is defined as

$$n_{rc} = \frac{E_r}{E_c} \tag{13.61}$$

where E_r and E_c are the Young's moduli of the reinforcement steel and concrete, respectively. The reinforcement ratio of the cross section is

$$\rho_r = \frac{A_r}{A} \tag{13.62}$$

where A_r is the sectional area of the longitudinal reinforcement present in the considered total cross section A. In this case, the product of the Young's modulus and cross section of the energy pile is approximately

$$EA = E_c A_c + E_r A_r = E_c A\left(1 - \rho_r\right) + n_{rc} E_c \rho_r A = E_c A\left[1 + \rho_r (n_{rc} - 1)\right] \approx E_c A \tag{13.63}$$

Given a sectional axial force, N, the proportions of the axial force received by the concrete, N_c, and by the reinforcement, N_r, are, respectively,

$$N_c = N\frac{E_c A_c}{EA} = N\frac{E_c A(1 - \rho_r)}{E_c A[1 + \rho_r (n_{rc} - 1)]} = N\frac{1 - \rho_r}{1 + \rho_r (n_{rc} - 1)} \tag{13.64}$$

$$N_r = N\frac{E_r A_r}{EA} = N\frac{n_{rc} E_c \rho_r A}{E_c A[1 + \rho_r (n_{rc} - 1)]} = N\frac{n_{rc}\rho_r}{1 + \rho_r (n_{rc} - 1)} \tag{13.65}$$

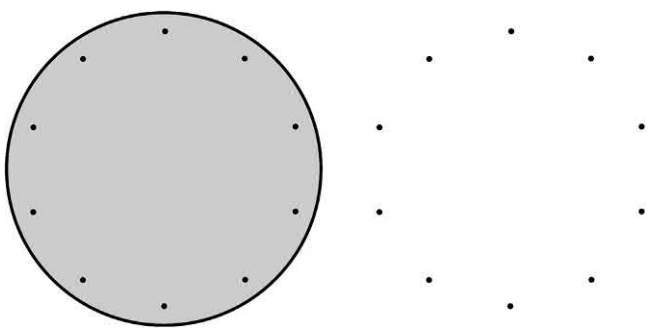

Figure 13.22 Transition from a composite reinforced concrete cross section to a section in which only the longitudinal reinforcement contributes to the resistance.

When concrete cracks, a sudden decrease in the stiffness of the section takes place, and stress redistribution occurs from concrete to steel. In this case, the axial strain is

$$\varepsilon_c = \frac{f_{ct}}{E_c} \tag{13.66}$$

where f_{ct} is the tensile strength of concrete. The axial force needed to crack the reinforced concrete cross section is

$$N_{cr} = EA\varepsilon_c = E_c A\left[1 + \rho_r(n_{rc} - 1)\right]\frac{f_{ct}}{E_c} = f_{ct}A\left[1 + \rho_r(n_{rc} - 1)\right] \approx f_{ct}A \tag{13.67}$$

The axial force mobilised by concrete and steel upon cracking can be determined, respectively, as

$$N_{cr,c} = A_c f_{ct} = f_{ct}A\left(1 - \rho_r\right) \approx f_{ct}A \tag{13.68}$$

$$N_{cr,r} = N_{cr}\frac{n_{rc}\rho_r}{1 + \rho_r(n_{rc} - 1)} = f_{ct}An_{rc}\rho_r \tag{13.69}$$

After concrete cracks in the reinforced concrete cross section, only the steel contributes to the resistance against the action effects. In this case,

$$EA = E_r A_r \tag{13.70}$$

$$N = N_r \tag{13.71}$$

$$N_R = f_y A_r = f_y \rho_r A \tag{13.72}$$

where N_R is the resisting axial force and f_y is the steel yield strength.

The actual response of *whole reinforced concrete members* differs from that of *single mean cross sections* described above (the latter actually coinciding with the response of reinforced concrete members characterised by the simultaneous occurrence of cracks). The reason for this is because, in reality, cracking will always occur progressively along reinforced concrete members. Furthermore, the response of any reinforced concrete members differs from that of the reinforcement steel alone because the concrete cannot crack everywhere along the member and the concrete between two cracks contributes to its stiffness (so-called 'tension-stiffening' phenomenon).

To ensure adequate ductility capacity of reinforced concrete members, (1) the resisting axial force of the reinforced concrete cross sections needs to be greater than or equal to the axial force needed to crack them in view of potential strain localisation effects, (2) the reinforcement has to be characterised by a large deformation capacity and (3) the ratio f_t/f_y has to respect a lower bound.

In general, condition (1) implies that

$$N_R \geq N_{cr} \tag{13.73}$$

Equivalently,

$$f_y \rho_r A \geq f_{ct} A \left[1 + \rho_r (n_r - 1)\right] \approx f_{ct} A \tag{13.74}$$

By simplifying Eq. (13.74), a minimum reinforcement ratio can be expressed as (Rotta Loria et al., 2019)

$$\rho_r = \rho_{r,min} \geq \frac{f_{ct}}{f_y} \tag{13.75}$$

where f_{ct} and f_y are, in this case, appropriate values of the tensile strength of concrete and steel yield strength, respectively. A conservative value of f_{ct} that can be considered for condition (1) is the mean value of axial tensile strength of concrete, f_{ctm}. This value can be calculated according to the EN 1992 (2004) (for relevant concrete classes used in energy geostructure applications lower than or equal to C50/60) as $f_{ctm} = 0.3 f_{ck}^{2/3}$. An appropriate value for f_y is the characteristic yield strength of reinforcing steel, f_{yk}.

Condition (2) is related to the magnitude of the action effects. Condition (3) is generally met because standards prescribe minimum values of the ratio f_t/f_y.

13.15.3.3 Minimum areas of reinforcement

Eq. (13.75) is proposed in EN 1992 (2004) in a different fashion, which accounts for the different stress redistribution occurring in cross sections characterised by a different shape through a factor k_{sr} and the phenomenon of internal nonuniform self-equilibrating stresses through a factor k_ε. The minimum reinforcement of cross sections (e.g. not involving any prestressing tendons) accordingly reads

$$A_{r,min} \sigma_r = k_{sr} k_\varepsilon f_{ct,eff} A_{ct} \tag{13.76}$$

where $A_{r,min}$ is the minimum area of reinforcing steel within the tensile zone, σ_r is the value of the maximum stress permitted in the reinforcement immediately after formation of the crack (e.g. $\sigma_r \equiv f_{yk}$), $f_{ct,eff}$ is the mean value of the tensile strength of the concrete effective at the time when the cracks may first be expected to occur (e.g. $f_{ct,eff} \equiv f_{ctm}$ or a lower value of $f_{ctm}(t)$ where t is the time) and A_{ct} is the area of concrete within the tensile zone.

For pure tension, k_{sr} may be taken as equal to 1. For rectangular cross sections or the webs of box or flanged sections subjected to pure bending, k_{sr} may be taken as equal to 0.4. According to Narayanan and Beeby (2005), in situations where, under the characteristic combination of loads, the stress in the cross section remains more

compressive than f_{ctm}, k_{sr} may be considered equal to zero. Otherwise, it should be calculated. Approaches for this purpose are presented, for example in the EN 1992 (2004).

For cross sections subjected to imposed deformations caused by external loads, such as those caused by the settlement for foundations, k_{ε} may be taken as equal to 1.0. The reason for this is that, in the previous situations, the question of the nonlinear distribution of strains across a section does not arise (Narayanan and Beeby, 2005). In contrast, for cross sections subjected to imposed deformations arising from internal loads, such as those caused by shrinkage or temperature variations, values of k_{ε} lower than 1.0 should be considered. In those situations, the question of the nonlinear distribution of strains across a section does arise and may be implicitly considered in the analyses through a value of $k_{\varepsilon} = 1$ for cross sections with a height lower than 300 m whereas through a value of $k_{\varepsilon} = 0.65$ for cross sections with a height greater than 800 m (Narayanan and Beeby, 2005). Intermediate values should be interpolated.

13.15.3.4 Control of cracking without direct calculation

Bending or tension cracking can be normally controlled by application of detailing rules. In the EN 1992 (2004) detailing rules are summarised in tabular form. Table 13.18 and Table 13.19 report values of maximum bar diameters and values of maximum bar spacing for crack control, respectively, which constitute the considered detailing rules. According to Narayanan and Beeby (2005), for controlling cracking caused by loads, either Table 13.18 or Table 13.19 should be considered, whereas for controlling cracking caused by imposed deformation only Table 13.18 should be considered. Furthermore, for cracking caused by loads, the relevant reinforcing steel stress is that resulting from the quasipermanent combination of loading.

According to EN 1992 (2004), for reinforced slabs subjected to bending without significant axial tension, no specific measures to control cracking are necessary when

Table 13.18 Maximum bar diameter for crack control, to be modified according to EN 1992 (2004).

Steel stress [MPa]	Maximum bar size [mm]		
	$w_k = 0.4$ mm	$w_k = 0.3$ mm	$w_k = 0.2$ mm
160	40	32	25
200	32	25	16
240	20	16	12
280	16	12	8
320	12	10	6
360	10	8	5
400	8	6	4
450	6	5	–

Table 13.19 Maximum bar diameter for crack control, to be modified according to EN 1992 (2004).

Steel stress [MPa]	Maximum bar spacing [mm]		
	$w_k = 0.4$ mm	$w_k = 0.3$ mm	$w_k = 0.2$ mm
160	300	300	200
200	300	250	150
240	250	200	100
280	200	150	50
320	150	100	–
360	100	50	–

the overall depth of the slab does not exceed 200 m and the mentioned detailing rules are applied.

13.15.3.5 Control of cracking with direct calculation

In some situations, interest may lie in estimating the crack width to verify the control of cracking. The crack width w_k may be calculated according to the EN 1992 (2004) as

$$w_k = s_{r,max}(\varepsilon_{rm} - \varepsilon_{cm}) \tag{13.77}$$

where $s_{r,max}$ is the maximum crack spacing, ε_{rm} is the mean strain in the reinforcement under the relevant combination of loads, including the effect of imposed deformations and considering the effects of tension stiffening, and ε_{cm} is the mean strain in the concrete between cracks.

The maximum cracking spacing (for members without pretensioned or posttensioned tendons) can be determined as (EN 1992, 2004)

$$s_{r,max} = \tilde{\tilde{k}}_3 c_c + \tilde{\tilde{k}}_1 \tilde{\tilde{k}}_2 \tilde{\tilde{k}}_4 \frac{\varnothing}{\rho_{p,eff}} \tag{13.78}$$

where $\tilde{\tilde{k}}_3$ is a nationally determined parameter with a recommended value of 3.4, c_c is the concrete cover to the longitudinal reinforcement, $\tilde{\tilde{k}}_1$ is a coefficient that considers the bond properties of the bonded reinforcement with a value of 0.8 for high bond bars whereas with a value of 1.6 for smooth bars, $\tilde{\tilde{k}}_2$ is a coefficient that considers the distribution of strain with values of 0.5 for bending and 1.0 for pure tension, $\tilde{\tilde{k}}_4$ is a nationally determined parameter with a recommended value of 0.425, $\varnothing$ is the average diameter of the reinforcing bars and $\rho_{p,eff} = A_r/A_{c,eff}$ (with $A_{c,eff}$ being the effective area of concrete in tension surrounding the reinforcement of depth $h_{c,ef}$, as shown in Fig. 13.23).

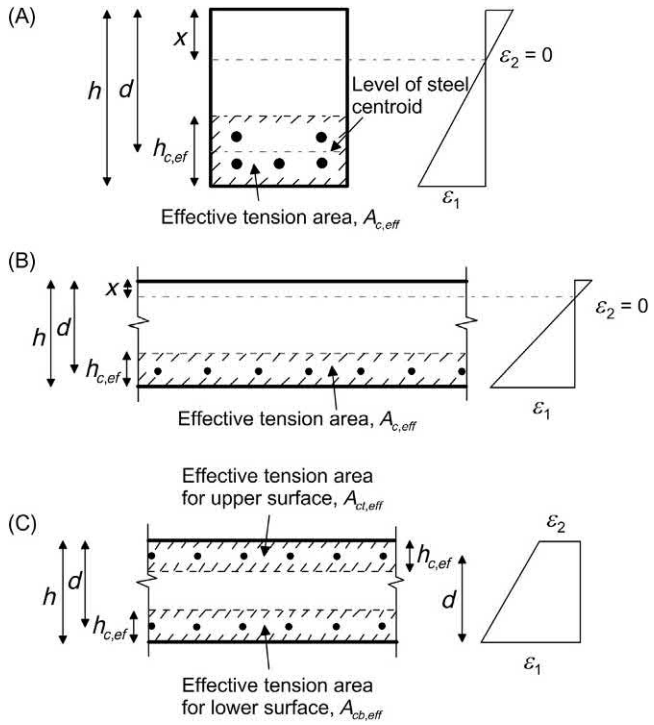

Figure 13.23 Effective tension area for (A) a beam, (B) a slab and (C) a member in tension. *Modified after EN 1992, 2004. Design of Concrete Structures – Part 1-1: General Rules and Rules for Buildings. British Standards Institution, London, p. 225.*

The difference between the mean strain in the reinforcement and in the cracks (for members without pretensioned or posttensioned tendons) can be determined as (EN 1992, 2004)

$$\varepsilon_{rm} - \varepsilon_{cm} = \frac{\sigma_r - k_t \frac{f_{ct,eff}}{\rho_{p,eff}}\left(1 + \alpha_E \rho_{p,eff}\right)}{E_r} \geq 0.6\frac{\sigma_r}{E_r} \tag{13.79}$$

where σ_r is the stress in the tension reinforcement assuming cracked section, k_t is a factor that dependent on the duration of the load with recommended values of 0.6 for short-term loading while of 0.4 for long-term loading, and $\alpha_E = E_r/E_{cm}$ is a modular ratio.

13.15.4 Deflection control

13.15.4.1 Problem statement

The rationale for limiting deflections is to avoid adverse effects on the proper functioning or appearance of a structure. Limiting values of deflection may be considered

depending on the nature of the structure, the finishes, partitions and fixings, and upon the function of the structure (EN 1992, 2004).

Deflection control belongs to a wider series of checks related to the deformation of structures that should be performed at serviceability limit states. These checks usually involve (1) vertical displacements, (2) lateral movements and (3) rotations. In the serviceability analysis of energy geostructures, all of the previous aspects should be verified considering the influence of both mechanical and thermal actions. Different combinations for heating and cooling thermal loads considered as variable actions should be made as appropriate.

When focusing on problems related to vertical displacements, the following aspects should be considered drawing from the considerations of Poulos et al. (2002):

1. Overall vertical displacement (e.g. settlement or heave);
2. Tilt, both local and overall;
3. Angular distortion (or relative rotation) between two points, which is the ratio of the difference in settlement divided by the distance between the two points;
4. Relative deflection (for walls and panels).

Graphical representation of the previous aspects is reported in Fig. 13.24.

13.15.4.2 Control of deflections

As highlighted by Poulos et al. (2002), data on allowable values of settlement, tilt, angular distortion and relative deflection have been collected by a number of sources, including Meyerhof (1947), Skempton and MacDonald (1956), Polshin and Tokar (1957), Bjerrum (1963), Grant et al. (1974), Wroth and Burland (1974), Burland et al. (1977), Wahls (1994), Boscardin and Cording (1989), Barker et al. (1991) and Boone (1996). Some of the recommendations drawn from the previous studies by Poulos et al. (2002) are summarised in Table 13.20. When associated with settlements, the previous recommendations may also be considered with respect to heave phenomena, for example caused by heating thermal actions applied to energy geostructures.

Depending on the features of the structure considered, the previous recommendations may refer either to the total settlements since the beginning of the construction or to only the settlement arose after the construction. Typically, reference to the quasipermanent combination of loads should be made to verify the requirements of structures according to the criteria proposed in Table 13.20. The values of angular distortion ranging from 1/250 to 1/500 reported in Table 13.20 for framed buildings and reinforced load-bearing walls are also proposed as reference in the EN 1992 (2004) for acceptable values of deflection within which the structure may not be impaired. Additional approaches through which calculations of deflections may be carried out are reported in the EN 1992 (2004).

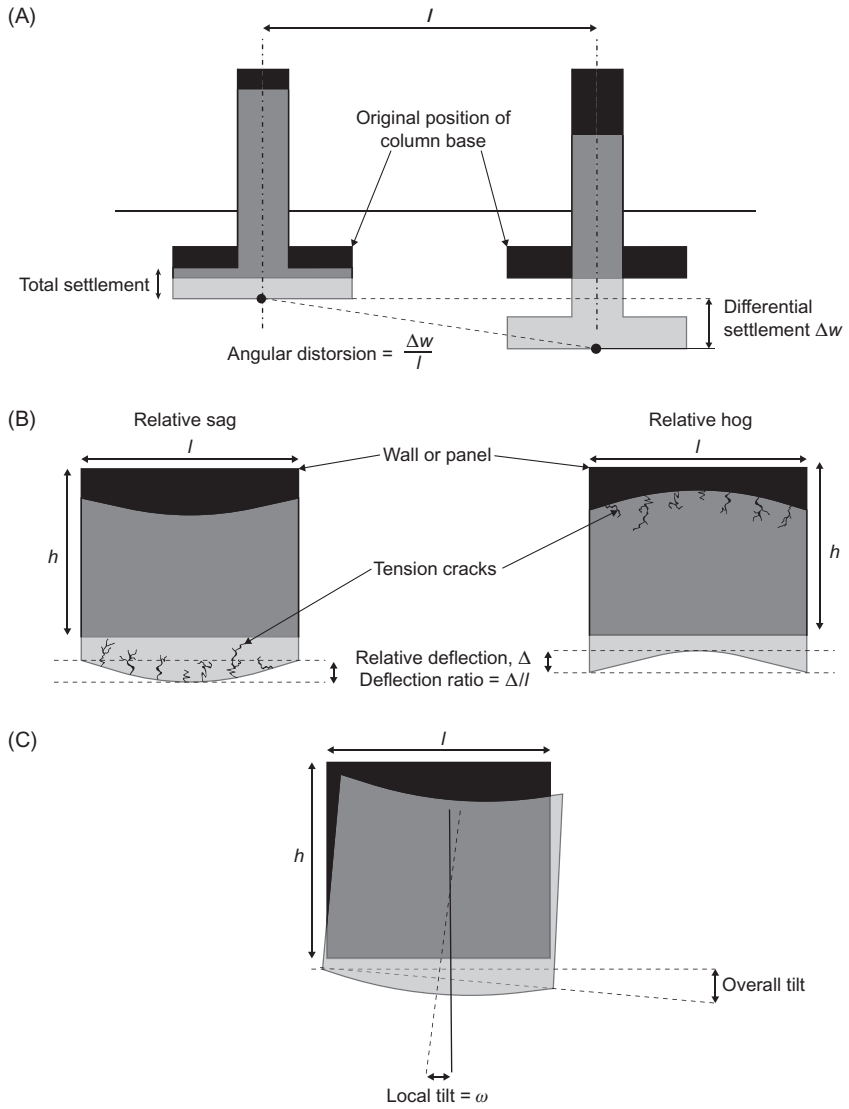

Figure 13.24 Definitions of (A) angular distortion, (B) deflection and (C) tilt for framed and wall structures. *Modified after Wroth, C., Burland, J., 1974. Settlement of buildings and associated damage. In: SOA Review, Conf. Settlement of Structures, Cambridge, pp. 651–654 and Poulos, H.G., Carter, J.P., Small, J.C., 2002. Foundations and retaining structures – research and practice. In: International Conference on Soil Mechanics and Geotechnical Engineering, vol. 4, Balkema, pp. 2527–2606.*

According to Boone (1996), when addressing the serviceability of structures, the use of a single criterion, such as angular distortion, may not be comprehensive. Other factors, such as (1) flexural and shear stiffness of building sections, (2) nature of the ground movement profile, (3) location of the structure within the settlement profile,

Table 13.20 Summary of criteria for settlement and differential settlement of structures (Poulos et al., 2002).

Type of structure	Type of damage/ concern	Criterion	Limiting value(s)
Framed building and reinforced load-bearing walls	Structural damage	Angular distortion	1/150−1/250
	Cracking in walls and partitions	Angular distortion	1/500
	Visual appearance	Tilt	1/300
	Connection to services	Total settlement	50−75 mm (sand)
Tall buildings	Operation of lifts and elevators	Tilt after lift installation	1/1200−1/2000
Structures with unreinforced load-bearing walls	Cracking by sagging	Deflection ratio	1/2500 ($l/h = 1$) 1/1250 ($l/h = 5$)
	Cracking by hogging	Deflection ratio	1/5000 ($l/h = 1$) 1/2500 ($l/h = 5$)
Bridges − general	Ride quality	Total settlement	100 mm
	Structural distress	Total settlement	63 mm
	Function	Horizontal movement	38 mm
Bridges − multiple span	Structural damage	Angular distortion	1/250
Bridges − single span	Structural damage	Angular distortion	1/200

(4) degree of slip between the foundation and the ground, and (5) building configuration, should be considered.

Information on the severity of cracking damage for buildings is given by Day (2000), who also concluded that the following relationship, first suggested by Skempton and MacDonald (1956), is reasonable for estimating the relationship between the absolute value of differential settlement Δ_{max} and the angular distortion $\Delta w/l$ to cause cracking:

$$\Delta_{max} \approx 8900 \frac{\Delta w}{l} [\text{mm}] \tag{13.80}$$

References

Abdelaziz, S.L., Ozudogru, T.Y., 2016. Selection of the design temperature change for energy piles. Appl. Therm. Eng. 107, 1036−1045.

Barker, R.M., Duncan, J., Rojiani, K., Ooi, P., Tan, C., Kim, S., 1991. Manuals for the Design of Bridge Foundations: Shallow Foundations, Driven Piles, Retaining Walls and Abutments, Drilled Shafts, Estimating Tolerable Movements, and Load Factor Design Specifications and Commentary. Transportation Research Board.

Bauduin, C., 2002. Design of axially loaded compression piles according to Eurocode 7. In: Proceedings of Ninth International Conference on Piling and Deep Foundations.

Bjerrum, L., 1963. Discussion on compressibility of soils. In: European Conference of Soil Mechanics and Foundation Engineering, vol. 2, pp. 16–17.

Bond, A.J., Schuppener, B., Scarpelli, G., Orr, T.L., Dimova, S., Nikolova, B., et al., 2013. Eurocode 7: Geotechnical Design Worked examples. In: Worked Examples Presented at the Workshop "Eurocode 7: Geotechnical Design", Dublin, Ireland.

Boone, S.J., 1996. Ground-movement-related building damage. J. Geotech. Eng. 122 (11), 886–896.

Boscardin, M.D., Cording, E.J., 1989. Building response to excavation-induced settlement. J. Geotech. Eng. 115 (1), 1–21.

Burland, J.B., Broms, B.B., de Mello, V.F., 1977. Behaviour of foundations and structures. In: 9th International Conference on Soil Mechanics and Foundation Engineering, vol. 2, Tokyo.

Burlon, S., Habert, J., Szymkievicz, F., Suryatriyastuti, M., Mroueh, H., 2013. Towards a design approach of bearing capacity of thermo-active piles. In: European Geothermal Congress, pp. 1–6.

CFMS-SYNTEC-SOFFONS-FNTP, 2017. Recommandations pour la conception, le dimensionnement et la mise en úuvre des géostructures thermiques. Rev. Franç. Géotech. 149, 120.

Day, R.W., 2000. Geotechnical Engineer's Portable Handbook. McGraw Hill, Columbus.

EN 1990, 2002. Eurocode: Basis of Structural Design. British Standards Institution, London, p. 112.

EN 1991, 2003. Eurocode 1: Actions on Structures – Part 1-5: General Actions – Thermal Actions. British Standards Institution, London, p. 46.

EN 1992, 2004. Design of Concrete Structures – Part 1-1: General Rules and Rules for Buildings. British Standards Institution, London, p. 225.

EN 1997, 2004. Eurocode 7: Geotechnical Design. British Standards Institution, London, p. 171.

Grant, R., Christian, J.T., Vanmarcke, E.H., 1974. Differential settlement of buildings. J. Geotech. Eng. Div. 100 (9), 973–991.

Ground Source Heat Pump Association, N. E. C., 2012. Thermal Pile Design, Installation & Materials Standards. National Energy Center, Milton Keyenes, p. 86.

Gulvanessian, H., Calgaro, J.-A., Holický, M., 2002. Designer's Guide to EN 1990: Eurocode: Basis of Structural Design. Thomas Telford.

Jelušič, P., Žlender, B., 2018. Determining optimal designs for conventional and geothermal energy piles. Renew. Energy . Available from: https://doi.org/10.1016/j.renene.2018.08.016.

Jirásek, M., Bažant, Z.P., 2001. Inelastic analysis of structures. John Wiley & Sons.

Loveridge, F.A., Powrie, W., 2016. The average temperature of energy piles. In: Geo-Chicago 2016, pp. 166–175.

MacGregor, J.G., Wight, J.K., Teng, S., Irawan, P., 1997. Reinforced Concrete: Mechanics and Design. Prentice Hall, Upper Saddle River, NJ.

McCormac, J.C., Brown, R.H., 2015. Design of Reinforced Concrete. John Wiley & Sons.

Meyerhof, G., 1947. The settlement analysis of building frames. Struct. Eng. 25 (9), 369–409.

Narayanan, R., Beeby, A., 2005. Designers' Guide to EN 1992-1-1 and EN 1992-1-2. Eurocode 2: Design of Concrete Structures: General Rules and Rules for Buildings and Structural Fire Design. Thomas Telford, London.

Nilson, A.H., Darwin, D., Dolan, C.W., 2004. Design of Concrete Structures, thirteenth ed. McGraw-Hill.

Polshin, D., Tokar, R., 1957. Maximum allowable non-uniform settlement of structures. In: Proc., 4th Int. Conf. on Soil Mechanics and Foundation Engineering, vol. 1. Butterworth's London, pp. 402–405.

Poulos, H.G., Carter, J.P., Small, J.C., 2002. Foundations and retaining structures—research and practice, International Conference on Soil Mechanics and Geotechnical Engineering, vol. 4. Balkema, pp. 2527–2606.

Rammal, D., Mroueh, H., Burlon, S., 2018. Impact of thermal solicitations on the design of energy piles. Renew. Sustain. Energy Rev. 92, 111–120.

Rotta Loria, A.F., Bocco, M., Garbellini, C., Muttoni, A., Laloui, L., 2019. The role of thermal loads in the performance-based design of energy piles, Geomech. Energy Environ. Available from: https://doi.org/10.1016/j.gete.2019.100153.

SIA-D0190, 2005. Utilisation de la Chaleur du Sol par des Ouvrages de Fondation et de Soutènement en Béton. Guide pour la Conception, la Realisation et la Maintenance, Zurich, Switzerland.

Skempton, A.W., MacDonald, D.H., 1956. The allowable settlements of buildings. Proc. Inst. Civil Eng. 5 (6), 727–768.

VDI 4640, 2009. Thermal use of the underground. Ground Source Heat Pump Systems. Association of German Engineers, Dusseldorf.

Wahls, H.E., 1994. Tolerable deformations. Vertical and Horizontal Deformations of Foundations and Embankments. ASCE, pp. 1611–1628.

Whitney, C.S., Cohen, E., 1956. Guide for ultimate strength design of reinforced concrete. J. Proc. 53, 455–490.

Wroth, C., Burland, J., 1974. Settlement of buildings and associated damage. In: SOA Review, Conf. Settlement of Structures, Cambridge, pp. 651–654.

Xiao, J., Luo, Z., Martin, J.R., Gong, W., Wang, L., 2016. Probabilistic geotechnical analysis of energy piles in granular soils. Eng. Geol. 209, 119–127.

Questions and problems

Statements

a. Highlight the fundamental difference between a performance-based and a prescriptive design approach.
b. Specify three design recommendations that address the geotechnical and structural design of energy geostructures.
c. Define ultimate limit states and serviceability limit states.
d. What are persistent design situation?
e. Define variable actions and propose two examples of such actions.
f. Classify thermal actions considering their variation in time, origin, spatial variation and nature.
g. Thermal actions applied to energy geostructures should be considered as:
  i. Permanent actions
  ii. Variable actions
  iii. None of the above
h. Define the characteristic value of an action as well as the possible accompanying values of an action.
i. What are the relevant limit states for most energy geostructure applications?
j. Write the fundamental inequality governing the verification of the performance of structures considering a limit state of rupture or failure of a section, member, connection or medium.
k. Describe the essentials governing the performance-based design approach of energy geostructures. Should the effects of thermal actions associated with the geothermal operation of energy geostructures be considered in their design at ultimate limit states?
l. Write the *fundamental combination* of design effects of actions for persistent and transient design situations at ultimate limit states and define all of the involved terms.
m. Write the *characteristic, frequent and quasipermanent combinations* for serviceability limit states.
n. In the *characteristic, frequent and quasipermanent combinations* at serviceability limit states, the value of the characteristic temperature variation ΔT_k, rather than the value of the effect of this temperature variation $Q_k(\Delta T_k)$, must be used:
  i. True
  ii. False
o. Describe the idealised stress–strain relationships for the design of concrete and reinforcing steel reported in the EN 1992 (2004).
p. Describe the three essential features of the linear structural analysis highlighted in the EN 1992 (2004).

q. What is the strength domain of a cross section?
r. State the crucial difference characterising the object of study associated with the design problem of bending and shear.
s. What are three fundamental design problems characterising the design of structures, such as energy geostructures, at serviceability limit states?

Solutions

a. Performance-based design approaches resort to statistical concepts and provide verifications of broad applicability to ensure an optimal performance. Prescriptive design approaches resort to deterministic specifications and are consequently of limited applicability, with the marked limitation of being uneconomical.
b. The Swiss (SIA-D0190, 2005), United Kingdom (Ground Source Heat Pump Association, 2012) and French (CFMS-SYNTEC-SOFFONS-FNTP, 2017) recommendations address the geotechnical and structural design of energy geostructures.
c. In structural design, limit states are the states whose achievement involves the loss of functioning or required performance for which the structure is designed. According to the EN 1990 (2002), distinction shall be made between ultimate limit states, associated with the collapse or failure of the structure or components, and the serviceability limit states, associated with the loss of functionality of a structure with reference to the requirements of its normal use, comfort, appearance and durability. The former therefore involves the safety of people while the latter does not.
d. According to the EN 1990 (2002), persistent design situations are relevant for conditions of normal use, that is for periods of the same order as the design working life of the structure.
e. Variable actions are characterised by a variation in magnitude with time that is neither negligible nor monotonic. These actions can have either a long or short duration with reference to the design working life and typically include wind actions and snow loads.
f. Thermal actions are variable, indirect, free and static actions. They are variable actions because related to the aleatory and varied nature of the conditions and factors that characterise the outer environment (e.g. for bridges), and/or the interaction between the outer environment and the inner environment (e.g. for buildings). They are indirect actions because resulting from imposed loads that cause a temperature variation. They are free actions because characterised by an intrinsic variable distribution

in space. They are static actions because not associated with accelerations.

g. Thermal actions applied to energy geostructures should be considered as:
  i. Permanent actions
  ii. Variable actions
  iii. None of the above

h. The characteristic value of an action is its main representative value and shall be specified as a mean value, as an upper or lower value, as a nominal value (which does not refer to a known statistical distribution), or in the project documentation. The possible accompanying values of an action, usually considered for variable actions, account for the probability of a simultaneous occurrence of these actions in specific design situations referred to the design working life of the structure and are related to the intensity of the variable action within the reference period.

i. The relevant ultimate limit states for most energy geostructure applications may generally be considered to be equilibrium (EQU) ultimate limit states, related to the loss of static equilibrium of the structure or any part of it considered as a rigid body, structural (STR) ultimate limit states, related to internal failure or excessive deformation of the structure or structural members, and geotechnical (GEO) ultimate limit states, related to failure or excessive deformation of the ground.

j. The prescription (e.g. *inequality*) that shall be verified when considering a limit state of rupture or failure of a section, member, connection or medium, that is a structural and/or geotechnical ultimate limit state(s), is

$$E_d \leq R_d$$

where E_d represents the design effects of actions and R_d represents the design resistances of the relevant ultimate criterion.

The prescription (e.g. *inequality*) that shall be verified when considering a limit state of loss of functionality of a section, member, connection or medium, that is a serviceability limit state, is

$$E_d \leq C_d$$

where E_d and C_d are the design value of the effects of actions and the limiting design value for the serviceability criterion, respectively.

k. The most appropriate and effective design approach for energy geostructures appears as follows: verify the performance of the energy geostructure against the action of only mechanical loads at ultimate limit states and verify the performance of the energy geostructure against the combined action of mechanical and thermal loads at serviceability limit states.

l. The fundamental combination of design effects of actions for persistent and transient design situations at ultimate limit states can be written as

$$\sum_{j\geq 1}\gamma_{G,j}G_{k,j}+\gamma_P P_c+\gamma_{Q,1}Q_{k,1}+\sum_{i\geq 1}\gamma_{Q,i}\psi_{0,i}Q_{k,i}$$

where the symbol '+' may be read as 'combined with' and the symbol '$\sum$' implies 'the combined effect of'. In the previous expression, $\gamma_{G,j}$ are partial factors to be applied to the j-th characteristic permanent loads $G_{k,j}$, γ_P are partial factors to be applied to the j-th precompression loads P_c, $\gamma_{Q,1}$ is the partial factors to be applied to the dominant characteristic variable loads $Q_{k,1}$, and $\gamma_{Q,i}$ and $\psi_{0,i}$ are partial factors to be applied to the i-th characteristic variable loads $Q_{k,i}$.

m. The *characteristic combination* is normally used to refer to irreversible limit states and can be expressed as

$$\sum_{j\geq 1}G_{k,j}+P_c+Q_{k,1}+\sum_{i\geq 1}\psi_{0,i}Q_{k,i}$$

The *frequent combination* is normally used to refer to reversible limit states and can be expressed as

$$\sum_{j\geq 1}G_{k,j}+P_c+\psi_{1,1}Q_{k,1}+\sum_{i\geq 1}\psi_{2,i}Q_{k,i}$$

The *quasipermanent combination* is normally used to refer to conditions involving long-term effects and the appearance of the structure, and can be expressed as

$$\sum_{j\geq 1}G_{k,j}+P_c+\sum_{i\geq 1}\psi_{2,i}Q_{k,i}$$

n. In the *characteristic, frequent and quasipermanent combinations* at serviceability limit states, the value of the characteristic temperature variation ΔT_k, rather than the value of the effect of this temperature variation $Q_k(\Delta T_k)$, must be used:

a. True

b. False

o. Two different idealised stress–strain relationships for the design of concrete cross sections are reported in the EN 1992 (2004) and may be used for such purpose: the parabola–rectangle relationship and the bilinear relationship. In both cases, these relationships assume a perfectly plastic behaviour after the yield stress is reached. However, while the former relationship assumes an initial nonlinear elastic behaviour, the latter assumes an initial linear elastic behaviour.

Two different idealised stress–strain relationships for the design of steel are also reported in the EN 1992 (2004) and may be used for such purpose: both of these relationships are bilinear. However, while one relationship assumes a perfectly plastic behaviour after the yield stress is reached, another assumes a linearly increasing plastic behaviour after the yield stress is reached.

p. According to the EN 1992 (2004):

- **A linear analysis of structural elements based on the theory of elasticity may be used for both the serviceability and ultimate limit states;**
- **For the determination of the action effects on the structure, the linear analysis may be carried out assuming:**
  - **Uncracked cross sections**
  - **Linear stress–strain relationships**
  - **Mean value of the modulus of elasticity**
- **When computing the effects of deformation, shrinkage and settlement reduced stiffness corresponding to cracked cross section should be used.**

q. The strength domain of a cross section represents the domain of the infinite pairs of (e.g. design) values of resisting normal force-moment for (i) a given shape of the section (ii) specific material properties and (iii) a given reinforcing steel positioning in the section.

r. The design problem of shear is more complex than that of bending and presents the crucial difference that while the analysis of the effects of bending can be carried out with reference to a cross section of any considered structure, the analysis of the effects of shear must be carried out with reference to a finite portion of the structure.

s. Among the different design problems that can characterise structures at serviceability limit states, the limitation of stresses, the control of cracking and the control of deflections are those that most commonly characterise energy geostructures.

CHAPTER 14

Determination of design parameters for energy geostructures

14.1 Introduction

Various input data are required to carry out the analysis and design of energy geostructures. These data allow developing qualitative and quantitative characterisations of any planned energy geostructure application and include, without being limited to, material properties and material parameters. In principle, a clear distinction between the terms *parameters* and *properties* exists. Material properties are quantities that are independent of the state conditions. Material parameters are quantities that change with the state conditions. In practice, as is often made in the scope of energy geostructures, the two aforementioned terms are used as synonyms. The same approach is considered here.

Investigations must be performed to determine parameters serving analysis and design processes. These investigations are carried out considering the features and goals of the analysis or design to be performed, and can be empirical or theoretical. Empirical approaches include experimental full-scale in situ tests, laboratory tests and centrifuge tests. Theoretical approaches include literature surveys and analytical calculations. In principle, theoretical or experimental investigations can be employed for analysis and design purposes. In practice, no analysis or design can be considered comprehensive without resorting to parameters defined through detailed experimental tests.

Experimental in situ tests have the advantage to allow the ground or the geostructure to be tested under full-scale conditions and thus to inherently include the peculiarities of any site (e.g. stress state, groundwater flow, undisturbed ground temperature). Laboratory tests and centrifuge tests have the advantage to allow comprehensive experimental campaigns to be carried out and to be quicker and cheaper compared to in situ tests. With particular reference to the stress state, centrifuge tests have the advantage of allowing for a replication of the in situ conditions through the use of appropriate scaling factors and experimental methodologies. No preferable experimental approach should be stipulated. The choice of the experimental approach may often be driven by temporal and economic availabilities as well as by the targeted comprehensiveness of the analysis or design to be performed. Determining the parameters required for the analysis and design of energy geostructures and understanding the features of the experimental tests that can address the previous purpose is paramount for successful applications of this technology.

Analysis and Design of Energy Geostructures
DOI: https://doi.org/10.1016/B978-0-12-816223-1.00014-X

This chapter addresses the parameters required for the design of energy geostructures, with a focus on their determination through experimental approaches. In this context, specific reference is made to parameters required for design purposes, but the same parameters may be considered for analysis activities. Yet, while a focus is given to full-scale in situ tests and laboratory tests, centrifuge tests are disregarded.

With this aim, the *characterisation of sites* is discussed first: the objective of this part is to summarise key features of energy geostructure applications and to link these features to the behaviour (e.g. thermal, hydraulic and mechanical) and performance (e.g. energy, geotechnical and structural) of the considered structures. Second, *design parameters* are summarised: in this context the goal is to propose categories of parameters allowing the previous types of behaviour and performance of energy geostructures to be addressed. Next, *testing methods* are presented: the aim of this digression is to summarise experimental approaches for determining the highlighted parameters. Then, *guarded hot plate testing* as well as *oedometer, triaxial* and *direct shear testing under nonisothermal conditions* are addressed: the aim of this part is to expand on the considered experimental laboratory tests. Afterwards, *thermal response testing* and *load testing under nonisothermal conditions* are described: the purpose of this part is to discuss key features of the addressed in situ tests. Finally, *questions and problems* are proposed: the purpose of this part is to fix and test the understanding of the subjects covered in this chapter by addressing a number of exercises.

14.2 Characterisation of sites

Any energy geostructure project presents specific features that characterise the multiphysical behaviour and performance of such structures. Addressing these features is paramount for analysis and design purposes. Several features characterising energy geostructure applications have been summarised by Brandl (2006). A modified and expanded list of these features is as follows:

1. Geothermal features of site:
   - **a.** Thermal properties;
   - **b.** In situ temperature field,
2. Aerothermal features of site (where applicable):
   - **a.** Significance of airflow in underground built environment (e.g. flow condition);
   - **b.** Features of velocity and thermal boundary layers;
   - **c.** Presence and significance of heat sources.
3. Hydrogeological features of site:
   - **a.** Depth of groundwater table;
   - **b.** Presence and significance of seasonal fluctuation of groundwater table;
   - **c.** Presence and significance of groundwater flow (e.g. flow velocity, flow direction).

4. Geotechnical features of site:
   a. Ground layering;
   b. Intrinsic soil properties;
   c. Ground permeability and water saturation;
   d. Ground strength and deformation;
   e. Swelling–shrinking sensitivity (e.g. if intensive heat extraction is required);
   f. Freezing–thawing sensitivity (e.g. if intensive heat extraction is required);
   g. Viscous effects (e.g. if sensitive soils are encountered).
5. Structural features of energy geostructure and superstructure:
   a. Type and size of the energy geostructure (e.g. length, width, thickness, diameter where applicable);
   b. Position, arrangement and spacing of the energy geostructure or geostructure element;
   c. Strength of the material(s) constituting the energy geostructure;
   d. Deformation of the material(s) constituting the energy geostructure;
   e. Stiffness of the superstructure supported (where applicable);
   f. Method of installation of the geostructure and construction sequence;
   g. Details of reinforcement (where applicable);
   h. Properties of reinforced concrete (where applicable).
6. Details of geothermal heating–cooling system:
   a. Pipes configuration;
   b. Pipes location (e.g. on built environment side or ground side for energy walls and tunnels, for example);
   c. Heat carrier fluid flow rate;
   d. Heat carrier fluid composition;
   e. Thermal insulation length of pipes;
   f. Available space for connecting lines;
   g. Position of header block (distributor/collector);
   h. Position of heat pump machine(s) and technical service centre;
   i. Features of heat pump machine(s);
   j. Runout length of pipes.
7. Building physics features:
   a. Insulation thickness of roof and walls floors (where applicable);
   b. Size and quality of windows (where applicable);
   c. Location and design of staircase (closed/open);
   d. Presence of heat bridges;
   e. Temperature conditions in energy circuits.
   f. Monthly heating/cooling demand and peak demands;
   g. Type of heating/cooling system;
   h. Type/mixture and velocity of circulating heat carrier fluid within energy system;

i. Heating/cooling intervals;
j. Operation plan.

The geothermal, aerothermal and hydrogeological features of sites (1)−(3), together with the details of the geothermal system and the building physics related-aspects (6)−(7), primarily govern the thermohydraulic behaviour as well as the energy performance of energy geostructures. In contrast, the geotechnical features of sites and the structural features of superstructures and geostructures (4)−(5) primarily govern the thermomechanical behaviour as well as the geotechnical and structural performance of energy geostructures. However, because of the coupling between the phenomena involved with the operation of energy geostructures, a variation of the previous features can globally affect the thermohydromechanical behaviour and the related performance of energy geostructures. This variation can require a change in one or all of the relevant analysis and design types of energy structures (e.g. energy, geotechnical and structural).

Usually, features (1)−(4) are fixed for any given project, whereas features (5)−(7) can be tailored. Knowledge of the previous features may become available at different stages of the design. Nevertheless, successful energy geostructure applications are often associated with a remarkable amount of the previous information available since early stages of the analysis and design process.

14.3 Design parameters

Design parameters can be employed to quantitatively characterise the features of sites and distinguished in categories depending on whether they are needed for the energy, geotechnical or structural design (or analysis) of energy geostructures. Nevertheless, as the multiphysical behaviour and phenomena governing energy geostructures are coupled, the previous parameters may enter in one or more designs and have a comparable influence on the associated results.

Table 14.1 summarises key parameters required for the design of energy geostructures, based on the work of Loveridge et al. (2017). Thermal and hydraulic parameters are crucial for addressing the energy design of energy geostructures. Mechanical parameters are key for addressing the geotechnical and structural design of energy geostructures.

14.4 Testing methods

Different methods can be required to determine input parameters depending on the stage of the design process as well as on the complexity of the geostructure. The former aspect is often related to the increasing complexity, comprehensiveness and amount of input data characterising modelling tools employed at successive stages of

Table 14.1 Design parameters in the context of energy geostructures.

Design type	Design variable and associated parameter	Comment
Energy design	Soil/rock thermal properties (e.g. thermal conductivity, specific heat)	An average value of thermal conductivity is used in most design approaches, although real conditions are likely to be anisotropic and heterogeneous
	Reinforced concrete thermal properties (e.g. thermal conductivity, specific heat)	
	Undisturbed soil/rock and geostructure temperature (e.g. initial temperature)	Average value, or preferably a profile with depth
	Groundwater flow rate (e.g. Darcy's velocity)	An indication is required of whether significant groundwater flow is to be expected
	Thermal resistance of heat exchanger (e.g. conductive thermal resistance)	
Geotechnical design	Soil/rock strength (e.g. angle of shear strength, unconfined compressive strength)	In total or effective stress terms as appropriate
	Soil/rock stiffness (e.g. Young's or shear moduli, Poisson's ratio)	Should include an estimate of whether likely to be significantly temperature dependent
	In situ stresses and pore water pressure field (e.g. unit weight)	
	Stress history (e.g. overconsolidation ratio)	Should include an estimate of whether likely to be significantly temperature dependent
	Soil/rock thermal expansion potential (e.g. linear or volumetric thermal expansion coefficient)	
	Soil permeability (e.g. intrinsic permeability)	
Structural design	Reinforced concrete strength (e.g. compressive and tensile strengths, ultimate strain levels)	
	Reinforced concrete stiffness (e.g. Young's modulus, Poisson's ratio)	
	Concrete thermal expansion potential (e.g. linear or volumetric thermal expansion coefficient)	

Source: Modified after Loveridge, F., Low, J., Powrie, W., 2017. Site investigation for energy geostructures. Q. J. Eng. Geol. Hydrogeol. 50, 158–168.

Table 14.2 Approaches to determine input parameters for the design of energy geostructures depending on the advancement stage.

Design stage	Level of detail
Planning stages	'Rules of thumb'
Schematic design	Literature
Detailed design	Site-specific testing

Source: Modified after Loveridge, F., Low, J., Powrie, W., 2017. Site investigation for energy geostructures. Q. J. Eng. Geol. Hydrogeol. 50, 158–168.

the design. The latter aspect can be requested by norms with the aim of ensuring reliable designs and verifications.

Different methods suggested to determine input parameters depending on the design stage of energy geostructures are reported in Table 14.2 with reference to the work of Loveridge et al. (2017). Parameters defined through (1) 'rules of thumb' values (2) the literature or (3) site-specific testing may be needed depending on the design stage.

A further example of methods that should be employed for determining parameters depending on the design (or analysis) stage are reported in Table 14.3 with reference to the classification of Poulos et al. (2002). In principle, this classification has been proposed with reference to the geotechnical and structural design of conventional geostructures. In practice, the same classification can be considered for the geotechnical and structural design of energy geostructures and extended to the energy design of such structures according to the following considerations:

- Preliminary investigations involving simple in situ or laboratory tests, with correlations, should be performed for Category 1 analysis and design procedures, which are characterised by a purely empirical nature. Since recent years, these procedures have accounted for a large proportion of the design of conventional geostructures. However, these procedures may currently be considered of limited applicability to the design of both conventional and energy geostructures for the scarce accuracy and information provided.
- Laboratory or in situ tests, with the potential to require some correlations, should be performed for Category 2 analysis and design procedures, which have a proper theoretical basis, often resort to the use of design charts and generally involve significant simplifications. In the context of the geotechnical and structural design, the simplifications involved by these procedures are primarily associated with the behaviour of the ground. Simplified linear elastic or rigid plastic models characterise Category 2A procedures. Nonlinear elastic or linear or nonlinear elastoplastic models (to address the deformation and stability of the geostructures, respectively) characterise Category 2B procedures. In the context of the energy design, the referenced simplifications are primarily associated with the behaviour of the

Table 14.3 Categories of analysis and design procedures, and related features.

Category	Subdivision	Features	Testing method for parameters determination
1	–	Empirical – not based on theoretical principles	Simple laboratory or in situ tests, with correlations
2	2A	Based on simplified theory or charts – amenable to hand calculation	Relevant laboratory or in situ tests – may require some correlations
	2B	As for 2A, but theory is more advanced	
3	3A	Based on theory – require the use of a computer	Careful laboratory and/or in situ tests which follow the appropriate stress and/or temperature paths
	3B	As for 3A, but accounting for more complex features of the problems involved in a simplified manner	
	3C	As for 3A, but accounting for more complex features of the problems involved in a rigorous manner	

Source: Modified after Poulos, H.G., Carter, J.P., Small, J.C., 2002. Foundations and retaining structures—research and practice. In: International Conference on Soil Mechanics and Geotechnical Engineering, vol. 4, Balkema, pp. 2527–2606.

modelled heat exchanger(s). Simplified one-dimensional heat transfer models characterise Category 2A procedures. Two-dimensional heat transfer models typically characterise Category 2B procedures.

- Site-specific laboratory or in situ testing should be carried out for Category 3 analysis and design procedures, which have a proper theoretical nature, require the use of a computer and generally employ relatively advanced numerical or analytical techniques. In the context of the geotechnical and structural design, linear elastic models accounting for nonisothermal conditions address the behaviour of the ground and may also be employed to account for nonlinear deformation phenomena through simplified approaches still resorting to linear elastic theory. More advanced elastoplastic models accounting for nonisothermal conditions are often considered to address the latter referenced phenomena in a more rigorous way. In the context of the energy design, the seasonal, monthly and daily energy operation of energy geostructures are typically addressed by the considered procedures. According to Poulos et al. (2002), many of the design charts employed in Category 2 procedures are developed from Category 3 analyses. Thermohydraulic,

Table 14.4 Geotechnical categories.

Geotechnical category	Description	Design requirements	Design and testing procedures
1	Small and relatively simple structures with negligible risk	Negligible risk of instability or ground movements Ground conditions known to be straightforward No excavation below water table (or such excavation is straightforward)	Routine design and construction methods
2	Structures and foundations with no exceptional risk or difficult soil or loading conditions	Quantitative geotechnical data and analysis to ensure fundamental requirements are satisfied	Routine testing, design and execution
3	Structures or parts of structures not covered above	Include alternative provisions and rules to those in EN 1997 (2004)	

Source: Modified after Bond, A.J., Schuppener, B., Scarpelli, G., Orr, T.L., Dimova, S., Nikolova, B., Pinto, A.V., 2013. Eurocode 7: geotechnical design worked examples. In: Worked Examples Presented at the Workshop "Eurocode 7: Geotechnical Design", Dublin, Ireland.

thermomechanical or thermohydromechanical numerical simulations are typically performed for the considered purpose. The proposition of multiphysical mathematical formulations (e.g. thermohydromechanical) is a scope under continuous development (see, e.g. Noorishad et al., 1984; Lewis et al., 1986; Zienkiewicz and Chan, 1989; Olivella et al., 1996; Gatmiri and Delage, 1997; Lewis and Schrefler, 1998; Collin, 2003; Cui et al., 2018).

An example of the required methods to determine design parameters based on the complexity of the considered structure is reported in Table 14.4 with reference to the EN 1997 (2004). Specific geotechnical categories are highlighted to assist in the establishment of minimum requirements for the extent and content of geotechnical investigations, calculations and construction control checks to be employed in design, and should be defined with the associated risks. A distinction shall be made between simple structures with negligible risks, structures with no exceptional risk and structures with noteworthy risk. In the first category, routine design and construction methods based on empiricism may be employed. In the second category, routine in situ and laboratory testing as well as design and execution resorting to theory and empiricism should be employed. In the third category, alternative provisions than those covered in the EN 1997 (2004) should be considered. Energy geostructures belong to geotechnical category 2.

Among the previous testing methods that allow determining input parameters for the design (and analysis) of energy geostructures, various types of experimental tests can be considered. These tests include, for example so-called (1) guarded hot plate tests, (2) oedometer tests (3) triaxial tests, (4) direct shear tests, (5) thermal response tests (i.e. TRTs) and (6) load tests. Tests (1)−(4) are laboratory tests, while tests (5) and (6) are full-scale in situ tests.

All of the previous tests have long historical developments. Guarded hot plate tests have been extensively used to characterise the thermal behaviour of insulating materials (see, e.g. Poensgen, 1912; Dickinson and Van Dusen, 1916). Oedometer and triaxial tests have been largely employed to investigate the hydromechanical behaviour of geomaterials (e.g. soils) (see, e.g. Terzaghi, 1943; Bishop and Henkel, 1957; Head and Epps, 1980). Direct shear tests have been widely used to address the mechanical behaviour of interfaces (e.g. soil−concrete interfaces) (see, e.g. Coulomb, 1773; Collin, 1846). TRTs have been developed to address the thermohydraulic behaviour of the ground surrounding vertical borehole heat exchangers (see, e.g. Austin, 1998; Gehlin, 2002). Load tests have been commonly used to analyse the mechanical behaviour of conventional geostructures (see, e.g. Poulos and Davis, 1980; Fleming et al., 2008).

All of the previous tests have undergone modifications to provide information for the analysis and design of energy geostructures. The different structure and physical features of geomaterials compared to insulating materials have requested to develop specific testing procedures for guarded hot plate tests. The different geometry and time required to reach steady thermal conditions for energy geostructures compared to borehole heat exchangers have required to carry out TRTs on the considered structures under revised time-scales. The unprecedented geothermal operation of energy geostructures and the associated application of thermal loads have required to carry out oedometer, triaxial and direct shear tests as well as load tests under nonisothermal conditions, with the possibility to apply thermal loads in addition to the conventionally applied mechanical loads in such tests. In this context, three different types of loading paths can be considered (Laloui, 2001): thermal (Path 1), isothermal-mechanical (Path 2) and thermomechanical (Path 3). Path 1 involves the application of temperature variations under constant stress conditions (cf. Fig. 14.1). Path 2 involves the application of mechanical loads at a given constant temperature (cf. Fig. 14.2). Path 3 involves the application of both thermal and mechanical loads at different stages to allow for the differentiation of the effects of these loads (cf. Fig. 14.3).

Based on the previous modifications, guarded hot plate tests can currently address the thermal behaviour of geomaterials (see, e.g. Tarnawski et al., 2009; Nikolaev et al., 2013; Venuleo et al., 2016). Oedometer and triaxial tests can characterise the thermohydromechanical behaviour of geomaterials (see, e.g. Finn, 1951; Paaswell, 1967; Plum and Esrig, 1969; Campanella and Mitchell, 1968; Cekerevac and Laloui, 2004). Direct shear tests can provide information about the thermomechanical

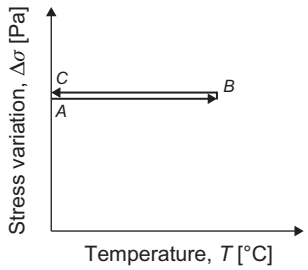

Figure 14.1 Thermal loading, that is Path 1. *Redrawn after Laloui, L., 2001. Thermo-mechanical behaviour of soils. Rev. Franç. Gén. Civ. 5 (6), 809–843.*

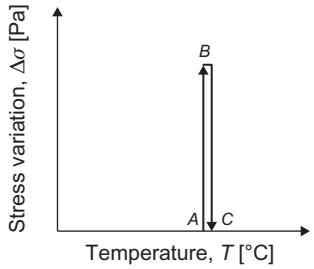

Figure 14.2 Isothermal-mechanical loading, that is Path 2. *Redrawn after Laloui, L., 2001. Thermo-mechanical behaviour of soils. Rev. Franç. Gén. Civ. 5 (6), 809–843.*

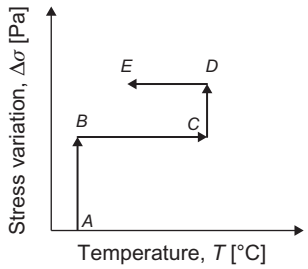

Figure 14.3 Thermomechanical loading, that is Path 3. *Redrawn after Laloui, L., 2001. Thermo-mechanical behaviour of soils. Rev. Franç. Gén. Civ. 5 (6), 809–843.*

behaviour of interfaces (see, e.g. Di Donna et al., 2015; Yavari et al., 2016; Yazdani et al., 2018). TRTs can address the thermohydraulic behaviour of the ground surrounding energy geostructures (see, e.g. Loveridge et al., 2014a). Load tests can characterise the thermomechanical behaviour of such structures (see, e.g. Laloui et al., 2003; Bourne-Webb et al., 2009).

Table 14.5 Test result and design parameters associated with guarded hot plate tests.

Testing technique	Test results	Design parameter
Guarded hot plate testing	Temperature trends, T	Effective thermal conductivity, λ

In the following sections, critical features of the aforementioned testing approaches are proposed. Further information is reported, for example by Vieira et al. (2017). The adopted sign convention assumes compressive stresses, contractive strains and downward displacements as positive.

14.5 Guarded hot plate testing

14.5.1 General

Guarded hot plate testing is an experimental laboratory method for the thermal characterisation of materials that can serve the energy design of energy geostructures. This test involves imposing a heat flow through any tested soil, rock or concrete specimen and interpreting with reference to one-dimensional steady-state conditions the measured temperature evolution across the specimen over time. The results and thermal parameter that can be determined through guarded hot plate testing are presented in Table 14.5.

14.5.2 Testing equipment

A guarded hot plate apparatus has been employed, for example by Venuleo et al. (2016). The considered apparatus (cf. Fig. 14.4) includes a cylindrical specimen, a thermally insulated support embedding vertically the specimen, two plates made of a highly conductive material that maintain the temperature constant on the top and bottom of the specimen, an electrical circuit, measuring sensors (e.g. temperature and voltage-reading sensors) and a data acquisition system. The lower plate is characterised by a heat flux sensor connected to a voltage-reading instrument. Two thermocouples are placed at the top and bottom of the specimen and allow measuring the temperature trend within this medium. A sketch of the considered apparatus is reported in Fig. 14.5.

14.5.3 Testing procedure

Different types of guarded hot plate tests exist and can be classified depending on the following factors: (1) the geometry of the tested specimen (e.g. cylindrical or cubic) and (2) the materials characterising the plates of the apparatus (e.g. aluminium or copper). In any case, the following main testing phases can be summarised for guarded hot plate tests:

1. *Specimen preparation*: the specimen is prepared for the test over the bottom plate of the apparatus that typically represents a heat sink. A thermally insulated support

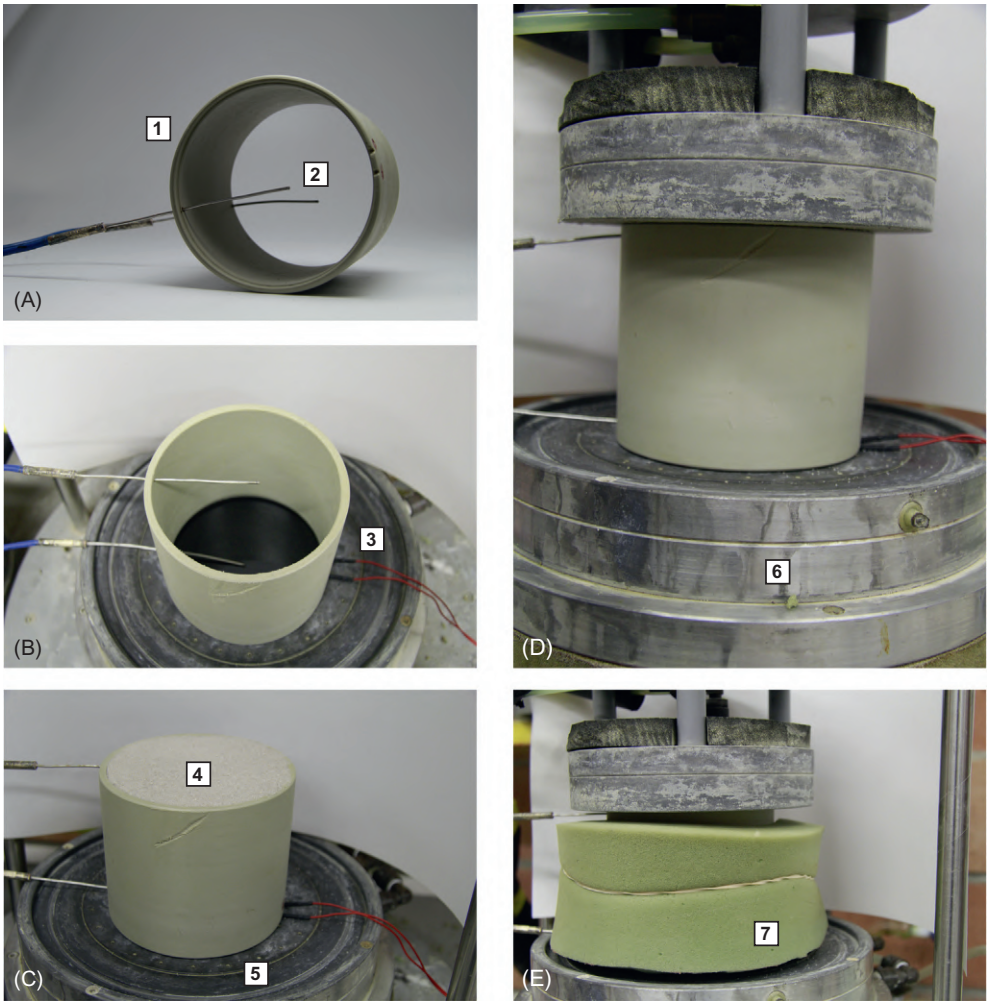

Figure 14.4 Example of guarded hot plate apparatus, employed by Venuleo et al. (2016) (1: specimen vertical support, 2: thermocouples, 3: electrical circuit, 4: specimen, 5: guarded plate, 6: support, 7: thermal insulation).

surrounds vertically the specimen, and provides one-dimensional heat transfer conditions. The top plate of the specimen that typically represents a heat source closes the system.

2. *Thermal loading*: an electrical current flow is imposed between the two plates of the guarded hot plate apparatus to establish a heat flow across the tested specimen. Meanwhile, sensors allow to independently measure the temperature trend at the top and bottom edges of the specimen together with the applied electrical current flow. The former data serve to assess when steady-state conditions are achieved

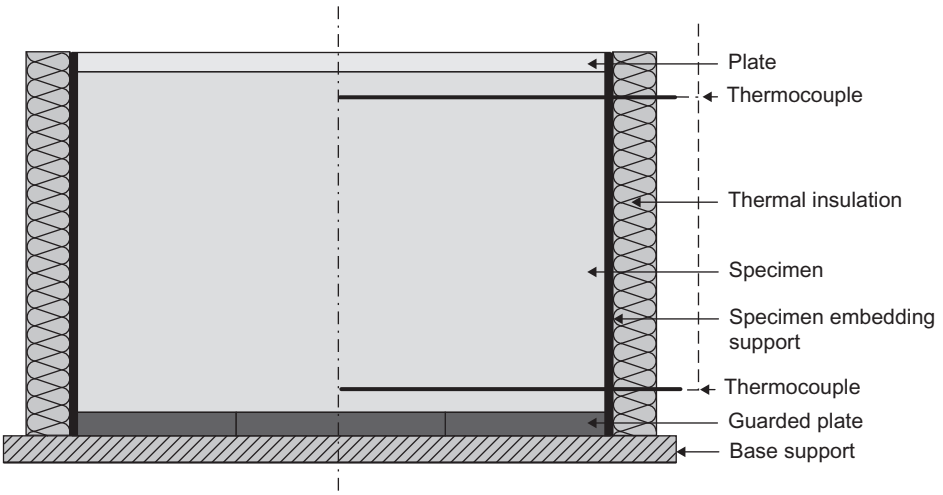

Figure 14.5 Sketch of a guarded hot plate apparatus employed by Venuleo et al. (2016).

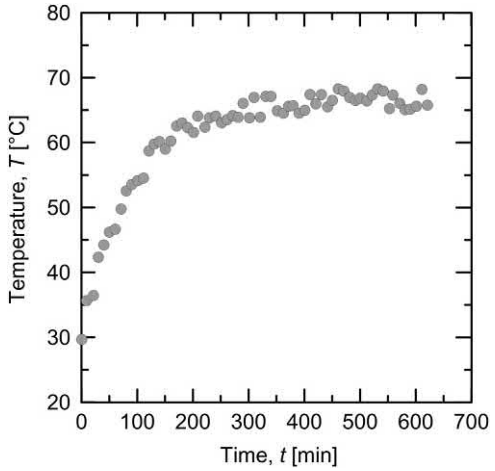

Figure 14.6 Evolution of temperature recorded throughout a guarded hot plate test. *Redrawn after Xamán, J., Lira, L., Arce, J., 2009. Analysis of the temperature distribution in a guarded hot plate apparatus for measuring thermal conductivity. Appl. Therm. Eng. 29 (4), 617–623.*

while the latter data to determine the heat flow resulting from the imposed electrical current.

3. *Test completion and dismounting*: once steady-state conditions are achieved, final readings are taken to determine the effective thermal conductivity of the specimen, the test can end and the apparatus is retired.

An example of measured data during the phase (2) of a guarded hot plate test is presented in Fig. 14.6 with reference to the results of Xamán et al. (2009). A clear

distinction between the transient and steady thermal state characterising the specimen can be observed. This distinction is associated with an initial period of the test characterised by markedly increasing temperature values with time and a following period characterised by approximately constant values of temperature with time.

The execution of guarded hot plate tests is recommended for providing an estimate of the thermal conductivity of soil layers composing stratified deposits, as well as for corroborating the results of in situ tests that are capable of providing similar information (e.g. TRTs). Examples of guarded hot plate tests of soils have been reported by Xamán et al. (2009), Alrtimi et al. (2014) and Venuleo et al. (2016).

14.5.4 Testing recommendations

Recommendations for guarded hot plate testing of geomaterials such as soils and rocks can be highlighted considering the guidance developed for insulating materials (see, e.g. EN 12667, 2001; ISO 8302, 1991; ASTM C177, 2010) and the investigations addressing the considered materials. In the following, noteworthy aspects for guarded hot plate tests of soils and rocks are expanded.

14.5.4.1 Heat transfer and contact thermal resistance

Ensuring a one-dimensional heat flow is paramount in guarded hot plate tests. In practice, some heat losses can occur in the horizontal direction of the specimen and can affect the measurements with an impact on the estimate of the thermal conductivity. The common method that should be employed to minimise horizontal heat losses consists in surrounding the specimen by an insulating material (Alrtimi et al., 2014). Heat losses can also occur in correspondence with the plates. The contact thermal resistance between the plates and the specimen should be estimated and minimised through a suitable specimen preparation (Jensen et al., 2012). The plates of the guarded apparatus should be as thin and flat as possible and highly conductive to ensure a uniform temperature over the plate (Alrtimi et al., 2014). The plates should also have high emissivity surfaces, particularly when materials characterised by a low thermal conductivity are tested (Vieira et al., 2017). Yet, the plates should remain planar during the test, with a maximum departure from a plane that shall not exceed 0.025% of the linear dimension of the metred section during the test (ASTM C177, 2010).

Using thin and highly conductive plates also helps achieving a uniform heat flux across the specimen. For medium temperature applications, aluminium and copper plates are suitable; for high temperature applications, nickel, high-purity alumina or aluminium nitride plates are preferable (ASTM C177, 2010). The temperature balance between the guard(s) and the metring area should be maintained within restrained limits (of approximately 0.01°C) (Vieira et al., 2017). The materials selected for the heaters and the plates (hot and cold plates) should be chemically and physically stable to withstand any disturbance during the test operation (ASTM C177, 2010).

14.5.4.2 Specimen dimensions and preparation

Short specimens (with a height of a few centimetres) should be preferably tested because they minimise the horizontal heat losses (Alrtimi et al., 2014). Testing relatively high specimens may involve moisture migration and desaturation after long testing periods (Venuleo et al., 2016).

The water content and mass of the specimen should be determined prior to the test as these parameters markedly influence the thermal conductivity. Other physical properties can be derived from volume-mass relationships (Alrtimi et al., 2014).

If the specimen is obtained from routine soil investigations using sampling tubes, it can be directly pushed out of the tube provided that it has adequate stiffness. After this procedure, the specimen can be cut at the desired height. When it is not possible to push the sample without any disturbance from a sampling tube, the tube must be directly cut and inserted in the guarded apparatus (Alrtimi et al., 2014). If the specimen is prepared in the laboratory, the following should be considered: fine-grained soil specimens should be prepared by mixing dry soil and water, with a high moisture content, and consolidated in a cell characterised by the same diameter of the guarded apparatus, if possible; coarse-grained soil specimens should be prepared by mixing dry soil and water, at the desired moisture content, and compacted in a cell. Volume and density should be controlled before testing (Alrtimi et al., 2014).

14.5.5 Effective thermal conductivity determination

The effective thermal conductivity of geomaterials such as soils, rocks or concrete is a key parameter to characterise the geothermal potential of sites for energy geostructure applications. According to Vieira et al. (2017), higher values of ground thermal conductivity involve larger heat transfer rates and allow the ground to recuperate more rapidly from thermal depletions and thermal build-ups. Meanwhile, higher values of thermal conductivity for the grouting material characterising energy geostructures involve lower temperature variations within these structures for the same applied thermal load, geometry and initial and boundary conditions.

The thermal conductivity governs the heat transfer phenomenon under steady-state conditions. In the context of guarded hot plate tests, this parameter can be defined via the interpretation of the measured data and the direct application of Fourier's law with reference to one-dimensional conditions.

The voltage-reading sensor that is typically placed on the bottom plate of guarded hot plate apparatuses allows determining the heat flux across the specimen through the relation

$$\dot{q}_i = \frac{\dot{Q}}{A} = C_E \cdot \text{measured voltage } [\text{mV}] \tag{14.1}$$

where $\dot{Q}$ is the thermal power, A is the cross-sectional area of the specimen and C_E is a constant provided by the manufacturer. This heat flux is continuously measured throughout guarded hot plate tests. The two thermocouples that are placed on the top and bottom extremities of the specimen at a distance z_{tc} also allow measuring the temperature trend at the top, T_{top}, and bottom, T_{bottom}, of the specimen. Based on the previous information, once steady-state thermal conditions are reached, the thermal conductivity of the specimen can be calculated from Fourier's law as

$$\lambda = \dot{q}_i \frac{z_{tc}}{\left(T_{bottom} - T_{top}\right)} = \frac{\dot{Q}}{A} \frac{z_{tc}}{\left(T_{bottom} - T_{top}\right)} \tag{14.2}$$

Based on the considerations highlighted in Chapter 3, Heat and mass transfers in the context of energy geostructures, from a practical perspective the thermal conductivity of geomaterials can be considered *independent* of temperature with reference to the temperature variations associated with the geothermal operation of energy geostructures.

14.5.6 Comparison with other methods

Guarded hot plate tests are so-called absolute experimental techniques that belong to *steady-state methods* for the determination of the effective thermal conductivity of materials. These techniques differ from so-called comparative experimental techniques because they do not employ any reference material of known physical properties to estimate λ. The main rationale for employing comparative instead of absolute techniques is that ensuring a one-dimensional heat flow can be difficult and the use of reference materials allows improving the accuracy of the measurements (Vieira et al., 2017). An example of a comparative experimental technique to estimate the thermal conductivity of materials is the comparative cut-bar technique (ASTM E1225, 2013). Such a technique has been applied to determine the thermal conductivity of rocks, for example by Midttømme and Roaldset (1999) and Barry-Macaulay et al. (2013).

In addition to steady-state methods, *transient methods* are also available to determine the effective thermal conductivity of materials. Four main differences characterise steady-state compared to transient methods (Vieira et al., 2017): (1) while the former methods can provide an estimate of only the effective thermal conductivity, the latter methods can often estimate the specific heat as well; (2) while the former methods establish a temperature difference across the specimen that does not change with time, the latter methods monitor the time-dependent heat transfer within a specimen; (3) while difficulties associated with the need to ensure a one-dimensional heat flow can be encountered through the former methods, these difficulties may be less burdensome through the latter methods; (4) while noteworthy waiting times (hours to days for single data points) are required to achieve steady-state conditions through the

former methods, these times are usually less notable through the latter methods because they do not require to achieve steady-state thermal conditions for determining the parameters of interest.

In transient methods, measurements are usually performed during a modulated heating process that is achieved by an either electrical or optical heat source, and temperature is measured by instruments that may resort to contact (e.g. thermocouples) or not (e.g. infrared sensors) (Vieira et al., 2017). These methods include the needle probe method (Van der Held and Van Drunen, 1949; Blackwell, 1954), the transient plane source method (ISO 22007−2, 2015; Gustafsson, 1991) and the optical laser scanning technique (Popov et al., 1999).

Thermal needle probe tests or derivatives [such as tests resorting to the twin heat probe method (Kasubuchi, 1992) or the dual thermal needle probe method (Campbell et al., 1991)] have been applied to measure the thermal conductivity of soils, for example by Midttømme and Roaldset (1999), Hiraiwa and Kasubuchi (2000), Lockmuller et al. (2004), Valente et al. (2006) and Merckx et al. (2012). Transient plane source tests should be preferably applied to stiff geomaterials such as rocks (Vieira et al., 2017). Tests resorting to the optical laser scanning technique on rocks have been presented, for example by Popov et al. (1999), Haffen et al. (2013) and Liu et al. (2011).

A comparison of the estimate of the thermal conductivity by steady-state and transient methods for soil specimens at different degrees of saturation, S_r, porosity, n, and temperature, T, is presented in Fig. 14.7 with reference to the data reported by Vieira

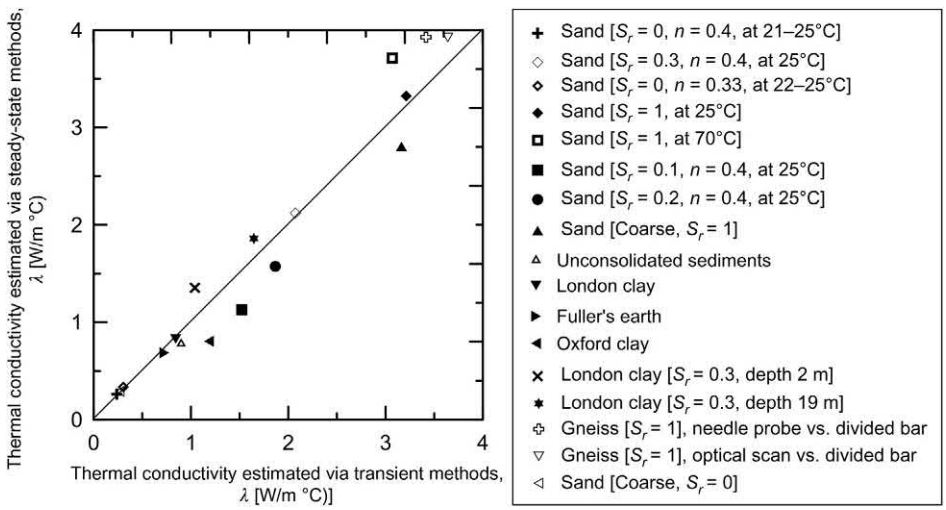

Figure 14.7 Comparison of transient and steady-state derived thermal conductivity. *Redrawn after Vieira, A., Maranha, J., Christodoulides, P., Alberdi-Pagola, M., Loveridge, F., Nguyen, F., et al., 2017. Characterisation of ground thermal and thermo-mechanical behaviour for shallow geothermal energy applications. Energies 10 (12), 2044.*

et al. (2017). While close agreement can be highlighted with reference to the results of steady-state and transient methods for dry soils (or for soil with low moisture content), this agreement markedly decreases for soils with high moisture content and temperature above 50°C (Vieira et al., 2017). Alrtimi et al. (2014) affirm that steady-state methods are more accurate than transient approaches. However, the previous consideration appears reasonable only if heat losses can be truly controlled (Low et al., 2015). Discrepancies between steady-state and transient test methods can be highlighted and the reasons are not always clear (Loveridge et al., 2017).

A summary of the advantages and limitations of the various laboratory methods that can be used for measuring soil and rock thermal properties is provided in Table 14.6 drawing from the work of Vieira et al. (2017).

14.6 Oedometer testing under nonisothermal conditions

14.6.1 General

Oedometer testing under nonisothermal conditions is an experimental laboratory method for the characterisation of the deformation of soils that can serve the geotechnical and structural design of energy geostructures. This test involves applying combinations of mechanical and thermal loads to soil specimens under one-dimensional deformation conditions and measuring the resulting variations of axial (i.e. vertical) displacement. The results and key thermohydromechanical parameters that can be determined through oedometer testing under nonisothermal conditions are reported in Table 14.7.

14.6.2 Testing equipment

A series of oedometer apparatuses allowing for soil testing under nonisothermal conditions has been developed, for example by Di Donna and Laloui (2015). These devices are four oedometer cells (cf. Fig. 14.8) that have been adapted to include temperature control. Key constituents of these apparatuses include a cylindrical specimen, one porous stone placed on the bottom surface of the specimen, one porous stone connected to a cap and an axial mechanical loading apparatus on top of the specimen, a highly-rigid ring surrounding laterally the specimen, the oedometer cell, a highly-rigid frame supporting the axial mechanical loading apparatus, a bath, a heating–cooling system connected to a closed thermal circuit, measuring sensors (e.g. linear variable differential transformers, i.e. LVDTs, and temperature sensors) and a data acquisition system.

In these apparatuses, the vertical stress is imposed through calibrated dead weights and the vertical displacements are measured by LVDT, with operating scale of OS $\pm$ 2.5 mm, sensitivity of 0.099 mm/mV and accuracy of $\pm$ 0.21% OS. The

Table 14.6 Summary of the advantages and disadvantages of experimental laboratory tests for measuring soil and rock thermal properties.

Method	Limitations	Advantages
Guarded hot plate	Large specimen required; presence of contact resistance between the specimen and the plates that is difficult to evaluate and eliminate; overestimates the thermal conductivity of saturated coarse-grained soils because of buoyancy driven flows; potentially characterised by moisture migration when dealing with partially saturate soils; does not allow to easily control the degree of saturation across the specimen; characterised by long test duration.	Standardised method for rocks; most suited to dry specimens; allows measuring thermal conductivity at different temperature levels.
Divided bar	Similar limitations characterising the guarded hot plate method.	Larger thermally activated zone than transient methods; well suited for rock testing.
Thermal needle probe	Need stable applied current; small specimen volume is thermally activated; specimens need to be large enough to avoid the effect of boundaries. contact resistance errors created when hole is drilled into rock specimens or hard soils.	Standardised method; very rapid test; minimises moisture migration and is thus effective for partially saturate soils; portable version for in situ measurements; different needle sizes available to test specimens depending on their size.
Transient plane source	Requires complex decision-making to select adequate sensors, power and measuring times; not standardised for soil and rock specimens.	Applicable to all types of soils and rocks; fast measurements.
Optical scanning technique	Not a standardised method for soils and rocks; not well suited to soils given the requirement for smooth polished surfaces.	Well suited for use with rocks; allows measuring the variations of the thermal conductivity along a scanning line on the specimen; gives indications of the heterogeneity of the material.

Source: Modified after Vieira, A., Maranha, J., Christodoulides, P., Alberdi-Pagola, M., Loveridge, F., Nguyen, F., et al., 2017. Characterisation of ground thermal and thermo-mechanical behaviour for shallow geothermal energy applications. Energies 10 (12), 2044.

Table 14.7 Test results and key design parameters associated with oedometer tests under nonisothermal conditions.

Testing technique	Test results	Design parameters
Oedometer testing under nonisothermal conditions	Consolidation curves Oedometer curves Secondary compression curve (creep curve)	Oedometric modulus, E_{oed}, Preconsolidation pressure, σ_p Recompression index, C_r Compression index, C_c Swelling index, C_s Hydraulic conductivity, k Volumetric thermal expansion coefficient, β Primary consolidation coefficient, c_v Secondary compression index, C_α

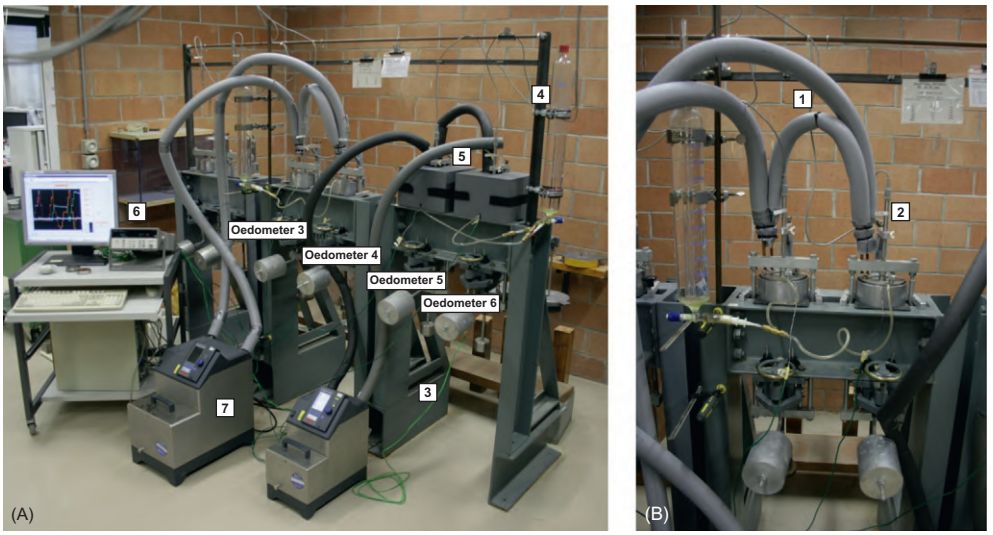

Figure 14.8 Example of an oedometer apparatus with temperature control, employed by Di Donna and Laloui (2015): (A) global view and (B) detail (1: tubes with circulating water at the desired temperature, 2: LVDTs, 3: thermocouples, 4: water supplier, 5: insulation, 6: acquisition system, 7: heaters).

thermal load is provided by a spiral tube that is positioned around the oedometer ring and is connected to a heater. The heater consists of a thermostat through which the temperature of a bath is imposed. A pump circulates the water at the desired temperature inside the spiral tube, from the thermocontrolled bath to the cells. Both heating

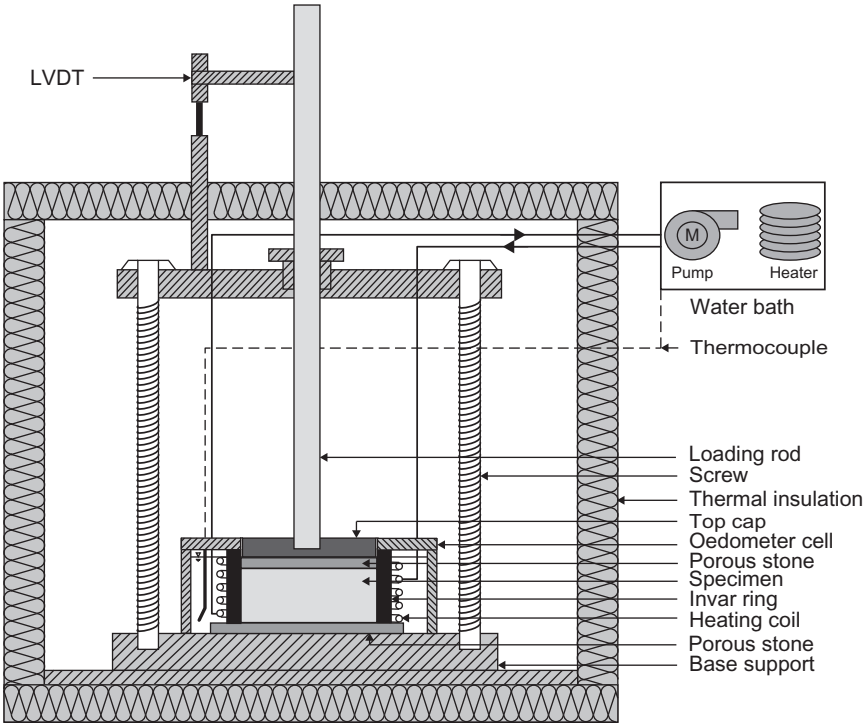

Figure 14.9 Sketch of an oedometer apparatus with temperature control employed by Di Donna and Laloui (2015).

and cooling are possible. During the tests, the temperature is constantly monitored inside each cell through four thermocouples (type-K, accuracy of 0.1°C). The cells are insulated with a polystyrene box to minimise thermal losses. Oedometer rings made of invar (coefficient of linear thermal expansion of $5.5 \times 10^{-7}°C^{-1}$) are used to minimise the thermally induced radial deformation and guarantee the oedometric conditions during temperature variations. A system for water supply is installed to face the water evaporation during heating and maintain constantly saturated conditions. A sketch of the considered apparatuses is reported in Fig. 14.9.

14.6.3 Testing procedure

Different types of oedometer tests under nonisothermal conditions exist and can be classified depending on the following factors: (1) the type of mechanical loading system (e.g. employing an hydraulic piston or a level arm loading apparatus), (2) the type of thermal loading system (e.g. imposing temperature variations from the inside of the apparatus through a thermal circuit or from the outside of the apparatus through the control of the surrounding ambient temperature) and (3) the type of loading path

(e.g. isothermal-mechanical or thermomechanical). In any case, the following main testing phases can be summarised for oedometer tests under nonisothermal conditions:

1. *Specimen preparation*: the specimen is prepared for the test in a rigid ring that does not allow any radial pore fluid flow and radial displacement during loading (under isothermal conditions) and is placed in the oedometer cell.
2. *Saturation*: distilled water (or any other relevant fluid) is potentially employed to saturate the specimen, while the porous stones located on its top and bottom prevent via filter paper discs any particle flow but allow drainage. Meanwhile, sensors allow measuring the vertical displacement of the top of the specimen over time together with the relevant temperature(s) (e.g. inside or outside the oedometer cell upon interest). Measuring vertical displacements allows assessing the saturation effect on the volume change of the material and monitoring the variations in specimen height throughout the test. If swelling of the material under saturation is observed and may affect the structure of the specimen, increments of mechanical load are imposed on the cap that is placed above the top porous stone to maintain the initial height of the specimen constant.
3. *Isothermal-mechanical and possible thermal loading*: isothermal-mechanical loading of the specimen is performed by employing the axial mechanical loading apparatus; thermal loading can be potentially imposed through the heating–cooling system once a stress at least equal to the preconsolidation pressure (the maximum stress that the specimen has ever underwent) is applied. Adequate time for the specimen to dissipate the excess pore water pressures is provided after either mechanical or thermal loading is applied; increments of mechanical loads, each of which is double the previous value, are typically applied.
4. *Isothermal-mechanical and possible thermal unloading:* isothermal-mechanical or thermal unloading of the specimen is carried out. A new loading phase (step (3)) can be imposed after adequate time has allowed the specimen to equilibrate; double increments of mechanical or thermal unloading compared to those employed during loading are typically considered.
5. *Test completion and dismounting*: the test is typically completed by removing any load from the specimen. The apparatus is dismounted and the specimen may be used for subsequent experimental tests.

An example of measured data during the phase (4) of an oedometer test is presented in Fig. 14.10 with reference to the result reported by Rotta Loria et al. (2014). The data show a typical *consolidation curve* caused by the influence of a given increment of mechanical load on a tested soil specimen. Although loading steps are typically maintained for approximately 24 hours, in most cases the consolidation process associated with the dissipation of pore water pressures occurs within a few ours (Lancellotta, 1995). Beyond this time interval, which is generally associated with the primary consolidation phenomenon, the secondary compression phenomenon associated with

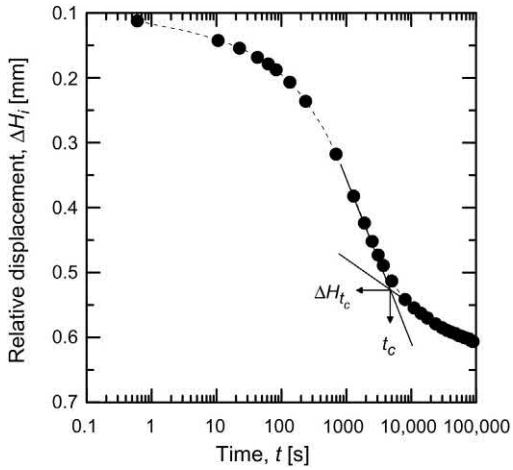

Figure 14.10 Consolidation curve for an undisturbed soil specimen of lean clay with sand. *Redrawn after Rotta Loria, A.F., Ferrari, A., Laloui, L., 2014. Thermo-mechanical analysis of soil characteristics from energy piles tests in Richmond, TX by Virginia Tech University, Lausanne, Switzerland, p. 51.*

viscous effects (i.e. creep) develops. To highlight the end of the so-called primary consolidation phenomenon and the onset of the secondary compression phenomenon, the time t_c and the associated variation of specimen height ΔH_{t_c} corresponding to the intersection of the two lines tangent to the linear portions of the consolidation curve are considered to build oedometer curves (Casagrande, 1936; Terzaghi, 1943).

14.6.4 Testing recommendations

Recommendations for oedometer testing of soils under nonisothermal conditions can be highlighted considering the guidance developed for isothermal oedometer tests (see, e.g. ISO 17892-5, 2017; ASTM D2435, 2004) and accounting for specific aspects related to the temperature variations involved with thermal loading. In the following, noteworthy aspects for oedometer tests under nonisothermal conditions are expanded.

14.6.4.1 General considerations

Thermomechanical testing of soils through oedometer and other experimental tests is much more complex than conventional isothermal testing. An additional field variable, that is temperature, must be controlled. Therefore an additional thermal loading system with the following requirements is needed (Cekerevac et al., 2005): (1) the system should work independently of the other parts of the apparatus (mechanical loading system, measuring and acquisition systems); (2) the system should impose a uniform temperature field to the specimen; and (3) the thermal loading circuit should be as close as possible to the specimen (e.g. inside the cell) to improve temperature control.

14.6.4.2 Specimen features and preparation

The specimen should be cylindrical, with a diameter and a height not exceeding 35 and 12 mm, respectively. A ratio between the diameter and the height of the specimen at least greater than 2.5 should be ensured (ISO 17892-5, 2017). Undisturbed, recompacted, remoulded or reconstituted soil may constitute the specimen. The specimen may be extruded from an undisturbed soil sample directly into the oedometer ring (if dimensions allow it) or may be reconstituted in the laboratory. The soil weight should be measured right after preparation. The test should start right after the specimen preparation. Otherwise, the specimen should be wrapped to prevent air-drying.

14.6.4.3 Oedometer ring

The internal surface of the ring should be smooth to avoid surface friction. Expansion under load should be restricted, attention should be paid to the lateral confinement of the ring and the sample should have a sufficient stiffness so that the internal diameter does not expand more than 0.05% when subjected to the maximum horizontal stress (ISO 17892-5, 2017).

The oedometer rings used for nonisothermal tests should be preferably made of a material characterised by the lowest possible thermal expansion coefficient to limit the radial deformations caused by thermal loading that may affect the oedometric conditions. Invar appears to be a particularly effective material for addressing this aspect (Di Donna and Laloui, 2015; Ng et al., 2017). For each imposed temperature, the deformation of the ring may typically be computed by subtracting the deformation of a dummy sample from the measured deformation. In any case, a thorough understanding of the deformation of the ring under temperature variations is needed. Calibration should be made by reproducing the exact loading paths (e.g., rate and duration) that are going to characterise the actual experimental tests.

14.6.4.4 Porous discs

The material constituting porous discs should be resistant to corrosion and should allow water drainage while preventing intrusion of soil particles into its pores (ISO 17892-5, 2017). A calibration for temperature effects should be carried out for porous disks. Filter paper may be used to prevent intrusion of soil into the porous disks, without disturbing the drainage of the specimen (ISO 17892-5, 2017). The material of porous disks should also have a compressibility preventing any breakage during the sample loading. The porous discs should be cleaned and clogged prior to the test, and they should be immersed in water (or the relevant fluid) until required for use. If soils that quickly absorb water are tested, the porous disks should be air-dried prior to testing. If new porous disks are used, they should be saturated with distilled water and cooled before use (ISO 17892-5, 2017). The dimensions of the porous disks should be sufficient to prevent any extrusion of the sample and risk of binding.

14.6.4.5 Loading frame

The loading cap and oedometer cell should be rigid enough to prevent deformation under load. The loading cap should present perforations or grooves to allow drainage of the pore water (ISO 17892-5, 2017). The material of the oedometer cell (similar to that of the ring) should be resistant to corrosion. The loading frame should apply vertical stress centrally on the loading cap only.

14.6.4.6 Water

If the tested soil is chemically active, water with a similar chemistry should be used (ISO 17892-5, 2017). If the chemistry of the pore water is unknown, tap water should be used (ISO 17892-5, 2017).

14.6.4.7 Heating and cooling rates

Drained conditions upon thermal (and mechanical) loading are essential to suitably interpret the results of oedometer tests. Heating thermal loads resulting in temperature variations of the order of 2°C per hour may be considered to ensure drained conditions (Di Donna and Laloui, 2015). Cooling thermal loads may be imposed by applying temperature variations of the order of −5°C per hour (Di Donna and Laloui, 2015).

14.6.4.8 Sensors

All sensors employed for oedometer tests under nonisothermal conditions should be tested and calibrated against temperature effects (Cekerevac and Laloui, 2004; Di Donna and Laloui, 2015). Calibration should also be applied to correlate the temperature inside the cell with the one externally imposed. This procedure allows quantifying the thermal losses and knowing the needed imposed temperature to have the desired one inside the specimen. Insulation of the oedometer cells should be considered to ensure an approximately constant thermal field in the vicinity of the tested specimens.

14.6.4.9 Dismantling

Water should be drained from the cell and the porous disks prior to dismantling. Dry mass of the specimen should be determined (ISO 17892-5, 2017). The specimen may be cut and checked to record any inhomogeneity.

14.6.5 Compressibility parameters determination

The compressibility parameters of soils are key to characterise the significance of volume changes caused by loading and are thus essential to predict the deformation and stability of energy geostructure applications. According to Mitchell and Soga (2005), different compressibility parameters are associated with varying settlements due to

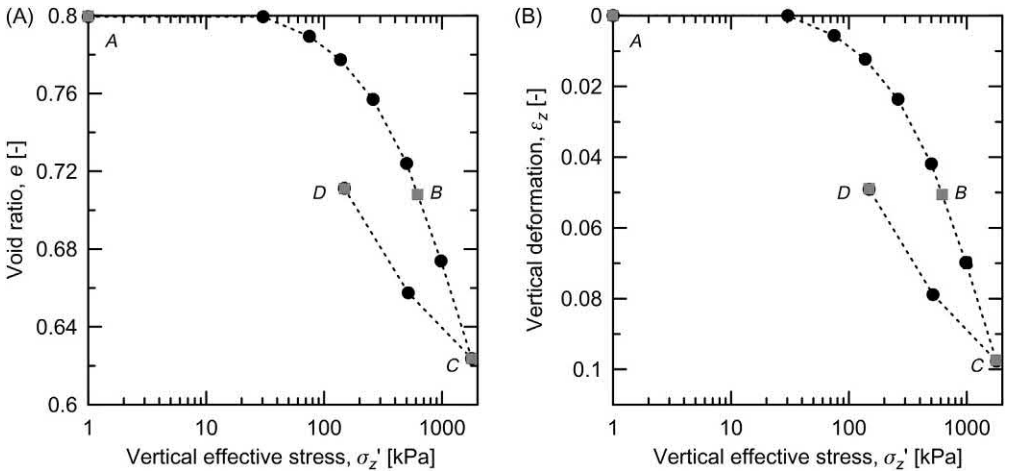

Figure 14.11 Oedometric curves expressed in terms of the relationship between the vertical effective stress and (A) the void ratio or (B) vertical deformation. *Redrawn after Rotta Loria, A.F., Ferrari, A., Laloui, L., 2014. Thermo-mechanical analysis of soil characteristics from energy piles tests in Richmond, TX by Virginia Tech University, Lausanne, Switzerland, p. 51.*

compression and heaves due to expansion, and contribute with the shear strength parameters to the characterisation of the deformation of materials.

Compressibility parameters can be defined from the results of oedometer tests by referring to the relationship between the vertical effective stress, σ'_z (expressed in natural or logarithmic scale) and the void ratio, e, or the vertical strain, ε_z. The graphical representation of the previous relationship is generally termed *oedometric curve*. To draw an oedometric curve, the vertical effective stress can be determined with reference to the load applied to the rigid cap of the oedometer apparatus at any given step of the test, while the void ratio can be determined from the vertical strain associated with the considered loading increment, $\varepsilon_{z,i} = \Delta H_i / H_{0,i}$, (where ΔH_i is the variation of the specimen height corresponding to the considered loading step i and $H_{0,i}$ is the specimen height at the beginning of the considered step) as $e_i = e_{0,i} - \left(1 + e_{0,i}\right)\Delta H_i / H_{0,i}$ (where $e_{0,i}$ is the void ratio at the beginning of the step). An example of oedometric curves is presented in Fig. 14.11 for an undisturbed soil specimen of lean clay with sand tested by Rotta Loria et al. (2014) at the ambient temperature of $T = 20°C$.

With reference to the approximately linear portions that describe the material response in an oedometer test, which correspond to the so-called recompression curve (portion from A to B in Fig. 14.11), the compression curve (portion from B to C in Fig. 14.11) and the swelling curve (portion from C to D in Fig. 14.11), the following compressibility characteristics can be defined (Casagrande, 1936; Terzaghi, 1943):

1. Compressibility index, a_v, defined as

$$a_v = -\frac{\Delta e_i}{\Delta \sigma'_{z,i}} \tag{14.3}$$

2. Compressibility coefficient, m_v, or oedometric modulus, E_{oed}, defined respectively as

$$m_v = \frac{\Delta \varepsilon_{z,i}}{\Delta \sigma'_{z,i}} \tag{14.4}$$

$$E_{oed} = \frac{1}{m_v} = \frac{\Delta \sigma'_{z,i}}{\Delta \varepsilon_{z,i}} = -\frac{\Delta \sigma'_{z,i}}{\Delta e_i}\left(1 + e_{0,i}\right) \tag{14.5}$$

3. Compression index, C_c, (i.e. the slope of the compression curve in the semilogarithmic $\sigma'_z - e$ plot), defined as (similar to the recompression index, C_r, and the swelling index, C_s, for the recompression and unloading curves in the semilogarithmic plot)

$$C_c = -\frac{\Delta e_i}{\Delta \log \sigma'_{z,i}} \tag{14.6}$$

4. Compression ratio, CR, (i.e. the slope of the compression curve in the semilogarithmic $\sigma'_z - \varepsilon_z$ plot), defined as (similar to the recompression ratio, RR, and the swelling ratio, SR, for the recompression and unloading curves in the semilogarithmic plot)

$$CR = \frac{\Delta \varepsilon_{z,i}}{\Delta \log \sigma'_{z,i}} \tag{14.7}$$

From the knowledge of the normal compression line (NCL), that is the tangent to the compression curve in the semilogarithmic $\sigma'_z - e$ plot [also representing the setting of the maximum void ratio at a given reference temperature for a normally consolidated (NC) soil], and the unloading-reloading line (URL), that is the tangent to the swelling curve, it is possible to compute the plastic rigidity index β_p and the bulk modulus of the specimen K_{ref} at a reference mean effective stress p'_{ref} as:

$$\beta_p = \frac{1 + e_0}{\tilde{\lambda} - \tilde{\kappa}} \tag{14.8}$$

$$K_{ref} = \frac{1 + e_0}{\tilde{\kappa}} p'_{ref} \tag{14.9}$$

where $\tilde{\lambda}$ and $\tilde{\kappa}$ are the compression and swelling indexes, that is the slopes of the NCL and URL, respectively, in the semilogarithmic $\sigma'_z - e$ plot. These parameters can be calculated as

$$\tilde{\lambda} = \frac{C_c}{\ln 10} = \frac{C_c}{2.303} \tag{14.10}$$

$$\tilde{\kappa} = \frac{C_s}{\ln 10} = \frac{C_s}{2.303} \tag{14.11}$$

From a practical perspective the compressibility parameters of soils can be considered *independent* of temperature with reference to the temperature variations associated with the geothermal operation of energy geostructures.

14.6.6 Preconsolidation pressure and overconsolidation ratio determination

The preconsolidation pressure is a key variable for determining the vertical effective stress level corresponding to the onset of an irreversible mechanical behaviour of any considered soil, and is thus crucial to characterise the response of the energy geostructures embedded within this medium. The preconsolidation pressure allows determining the value of the overconsolidation ratio, *OCR*. According to Lancellotta (1995), this latter parameter, together with the coefficient of Earth pressure at rest, K_0, gives a quantitative description of the stress history of any considered soil deposit and represents a key point of any geotechnical design.

The preconsolidation pressure can be defined from the analysis of oedometric curves in the semilogarithmic $\sigma'_z - e$ plot, with reference to various methods (Casagrande, 1936; Burmister, 1951; Janbu, 1969; Schmertmann, 1955). The Casagrande method (1936) is widely used for the considered purpose and involves the following steps:

- Consider the point of maximum curvature of an oedometric curve in the semilogarithmic plane (the setting delimiting, at least theoretically, the recompression and compression curves). Draw a horizontal line passing through this point as well as a tangent line to the oedometric curve passing through this point;
- Draw the bisector line between the previous horizontal and tangent lines, and draw the NCL;
- The vertical stress corresponding to the point of intersection between the bisector line and the NCL represents the preconsolidation pressure, σ'_p.

From the preconsolidation pressure, the isotropic preconsolidation pressure can be computed as

$$p'_c = \frac{(1 + 2K_0)\sigma'_p}{3} \tag{14.12}$$

The preconsolidation pressure of soils is markedly *dependent* of temperature with reference to the temperature variations associated with the geothermal operation of energy geostructures (it decreases for the same initial void ratio with an increase in temperature). However, from a practical perspective, only through advanced constitutive models that may be used at advanced stages of design the temperature dependence of this parameter can be considered and is justified.

Knowledge of the *OCR* allows determining if the tested soil is for example normally consolidated ($OCR = 1$) or overconsolidated ($OCR > 1$). Such a consideration plays a critical role in the understanding and prediction of the mechanical behaviour of soils under nonisothermal conditions.

14.6.7 Volumetric thermal expansion coefficient determination

The thermal expansion coefficient provides information on the thermal expansion potential of any material and is essential to characterise the mechanical response of energy geostructures. According to Rotta Loria and Laloui (2017), being able to characterise this parameter for the ground and the material constituting energy geostructures provides information on which among the considered subjects governs the deformation phenomenon at successive stages of the geothermal operation.

The volumetric thermal expansion coefficient of soils can be determined through an oedometer test from the relationship between the volumetric deformation and the applied temperature variation associated with a heating–cooling cycle, with reference to the thermal unloading branch. An example of this relationship is proposed in Fig. 14.12 with reference to the results of Di Donna and Laloui (2015) for a soil specimen under normally consolidated (NC) and overconsolidated (OC) conditions. An example of the material response that can be expected in terms of its oedometric curve during thermal cycling is reported in Fig. 14.13 with reference to the results of Rotta Loria et al. (2014).

From the slope of the thermal unloading curves it is possible to evaluate the volumetric thermal expansion coefficient of the solid skeleton, keeping in mind that the test is run in oedometric conditions (Di Donna and Laloui, 2015). Applying the theory

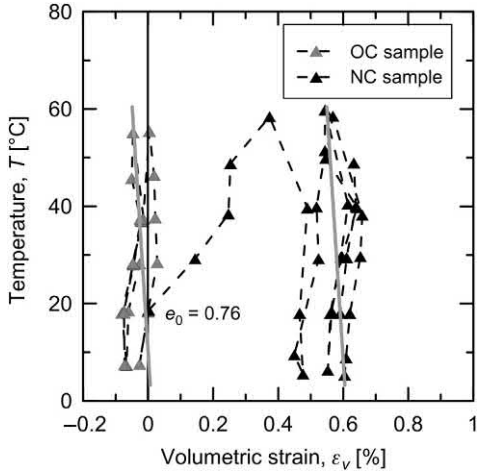

Figure 14.12 Relationship between volumetric strain and temperature applied to overconsolidated (OC) and normally consolidated (NC) specimens in oedometric conditions. *Redrawn after Di Donna, A., Laloui, L., 2015. Response of soil subjected to thermal cyclic loading: experimental and constitutive study. Eng. Geol. 190 (1), 65–76.*

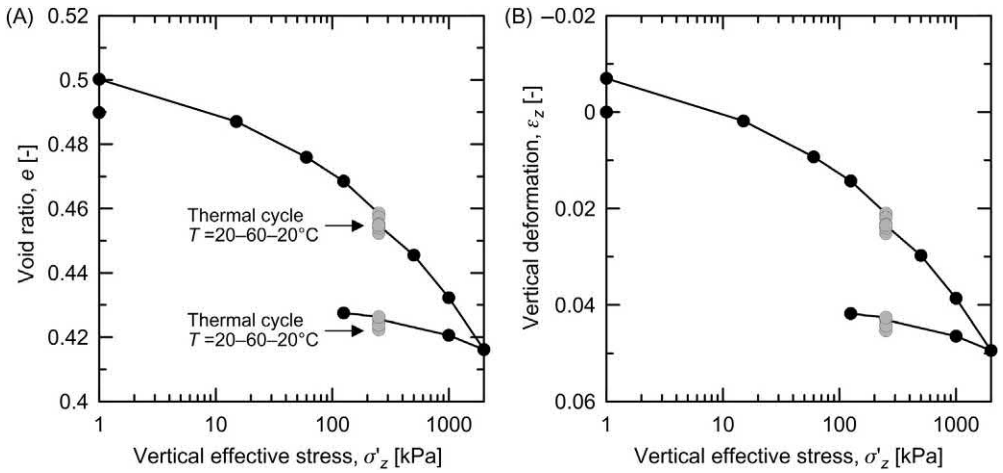

Figure 14.13 Influence of heating–cooling cycle on oedometric curves expressed in terms of the relationship between the vertical effective stress and (A) the void ratio or (B) vertical deformation. *Redrawn after Rotta Loria, A.F., Ferrari, A., Laloui, L., 2014. Thermo-mechanical analysis of soil characteristics from energy piles tests in Richmond, TX by Virginia Tech University, Lausanne, Switzerland, p. 51.*

of thermoelasticity and assuming an isotropic thermal response (volumetric thermal expansion coefficient β equal to three times the linear one α) the following relationships hold:

$$\Delta\varepsilon_x = \Delta\varepsilon_y = 0; \quad \Delta\sigma'_x = \Delta\sigma'_y; \quad \Delta\sigma'_z = 0$$
$$\Delta\varepsilon_x - \frac{1}{3}\beta\Delta T = \frac{1-\nu}{E}\Delta\sigma'_x$$
$$\Delta\sigma'_x = \frac{E}{1-\nu}\frac{1}{3}\beta\Delta T \tag{14.13}$$
$$\Delta\varepsilon_z = -\frac{1+\nu}{1-\nu}\frac{1}{3}\beta\Delta T$$

where $\Delta\varepsilon_z$ is the increment of vertical deformation measured during the test, $\Delta\varepsilon_x$ and $\Delta\varepsilon_y$ are the increments of horizontal deformation prevented in oedometric conditions, $\Delta\sigma'_z$ is the increment of vertical effective stress, $\Delta\sigma'_x$ and $\Delta\sigma'_y$ are the increments of horizontal effective stress (not zero due to the prevented thermoelastic deformation), ν is the Poisson's ratio of the soil and E is the Young's modulus of the soil.

14.6.8 Consolidation parameters determination

Consolidation parameters provide information about the consolidation phenomenon characterising any soil subjected to a change in effective stress and can thus be relevant to characterise the response of energy geostructures with time. These parameters include the primary consolidation coefficient c_v and the secondary compression index C_α, and are a measure of the rate at which the primary consolidation and secondary compression phenomena occur, respectively.

The primary consolidation coefficient can be determined from the analysis of consolidation curves through various fitting methods that include the square root method (Taylor, 1942) and the log method (Casagrande, 1936). With the square root method, the coefficient c_v is determined with reference to the relationship between the square root of the time and the variation in specimen height due to an increment of loading. With the log method, the coefficient c_v is determined with reference to the relationship between the time expressed in logarithmic scale and the variation in specimen height.

The secondary compression index can also be derived referring to the semilogarithmic $\sigma'_z - e$ plot as

$$C_\alpha = -\frac{\Delta e_i}{\Delta \log t} \quad \text{for} \quad t \geq t_{95} \tag{14.14}$$

where t_{95} is the time at which the 95% of the primary consolidation has taken place. Alternatively, the secondary compression ratio can be determined referring to the semilogarithmic $\sigma'_z - \varepsilon$ plot as

$$C_{\alpha\varepsilon} = -\frac{\Delta\varepsilon_{z,i}}{\Delta \log t} = \frac{C_\alpha}{1 + e_{0,1}} \quad \text{for } t \geq t_{95} \tag{14.15}$$

Knowing the primary consolidation coefficient and the oedometric modulus, E_{oed}, it is also possible to estimate the hydraulic conductivity k of the material (Terzaghi, 1923) as:

$$k = \frac{\gamma_w c_v}{E_{oed}} \tag{14.16}$$

where γ_w is the water unit weight.

The primary consolidation coefficient and the hydraulic conductivity of most soils are markedly *dependent* of temperature with reference to the temperature variations associated with the geothermal operation of energy geostructures. However, from a practical perspective, only through advanced mathematical formulations that may be used at advanced stages of design the temperature dependence of the primary consolidation coefficient and the hydraulic conductivity of soils can be considered and is justified.

14.7 Triaxial testing under nonisothermal conditions

14.7.1 General

Triaxial testing under nonisothermal conditions is an experimental laboratory method for the characterisation of the deformation and failure of soils that can serve the geotechnical and structural design of energy geostructures. This test involves applying mechanical loads representative of a bidimensional stress state in combination with thermal loads to soil specimens and measuring the associated variations of axial or confinement stress, vertical displacement, variation of water volume (or pore water pressure, depending on whether drainage is allowed or prevented during testing), and temperature. The results and key thermomechanical parameters that can be determined through triaxial testing under nonisothermal conditions are reported in Table 14.8.

14.7.2 Testing equipment

A triaxial apparatus allowing for soil testing under nonisothermal conditions has been developed, for example by Cekerevac et al. (2005). The considered apparatus (cf. Fig. 14.14) includes a cylindrical specimen, one porous stone placed on the bottom surface of the specimen and connected to an axial mechanical loading apparatus, an impermeable membrane surrounding laterally the specimen, one porous stone to a cap, the triaxial cell, a highly-rigid frame supporting the axial mechanical loading

Table 14.8 Test results and key design parameters associated with triaxial tests under nonisothermal conditions.

Testing technique	Test results	Design parameters
Triaxial testing under nonisothermal conditions	Stress–strain curve and pore water pressure curve Stress paths Mohr circles	Cohesion, c' Angle of shear strength, φ' Angle of shear strength under constant volume conditions, φ'_{cv} Young's modulus, E Poisson's ratio, ν Other pairs of deformation parameters Volumetric thermal expansion coefficient, β

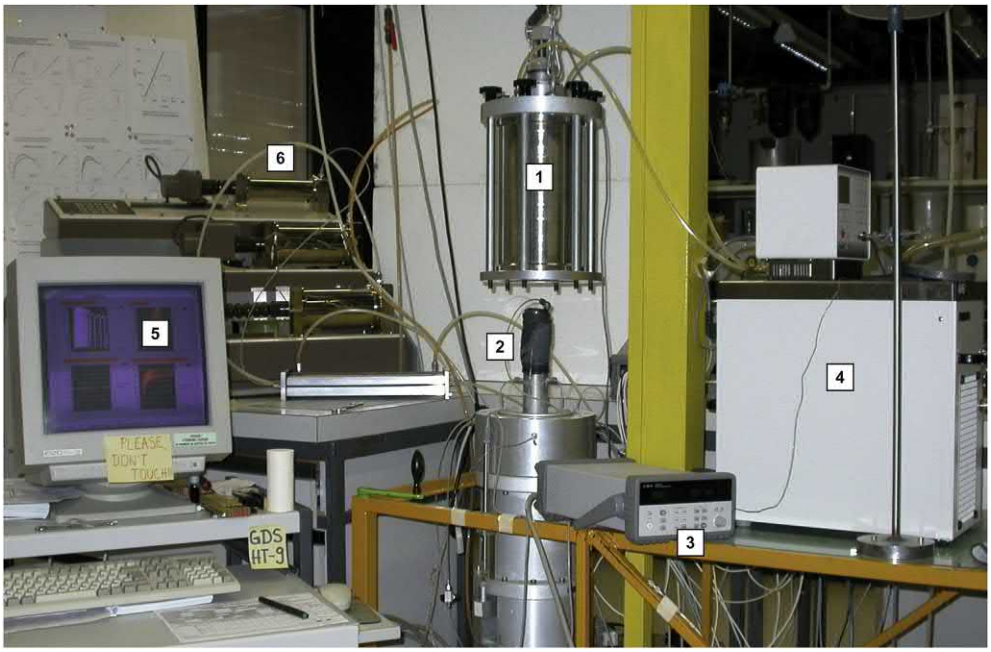

Figure 14.14 Example of a triaxial apparatus with temperature control, employed by Cekerevac et al. (2005) (1: triaxial cell, 2: sample, 3: multiplexer, 4: thermal loading bath, 5: acquisition system, 6: pressure-volume controllers).

apparatus, a bath connected to a confinement pressuring system, a heating–cooling system connected to a closed thermal circuit located in the bath, a drainage or back pressure system, a pore water pressure system, measuring sensors (e.g. LVDTs and temperature sensors) and a data acquisition system.

The triaxial cell is based on an isothermal Wykeham Farrance triaxial cell modified to suitably deal with temperature effects. To this aim, a stainless steel cylinder replaces the original standard Perspex cell of the original equipment and accommodates specimens of 55 mm in diameter and of 110 mm in height. Three advanced pressure/volume controllers are connected to the considered cell. These controllers are used to control the state of stress and are microprocessor-controlled screw pumps designed for a precise regulation and measurement of fluid pressure and volume changes. Additional instrumentation consists of a load cell to measure axial force, two LVDTs to measure axial displacement externally and a pressure transducer to measure pore water pressure at the top and bottom of the specimen. The LVTDs (maximum operating range of 50 mm) are diametrically placed around the cell. The equipment allows triaxial tests to be carried out under a constant rate of strain or constant rate of stress. The maximum cell pressure is 2 MPa and the maximum axial force is 4 kN, corresponding to a maximum deviator stress of 1.7 MPa. The three principal stresses $(\sigma_1, \sigma_2 = \sigma_3)$ and the pore water (back) pressure can be imposed independently: hence, the triaxial cell can be used for any stress path defined in the triaxial plane (σ_1 vs $\sqrt{2}\sigma_2 = \sqrt{2}\sigma_3$). The modified cell employs thermally resistant Viton O-rings instead of the standard O-rings provided by the supplier. These rings are resistant to temperatures ranging from $-20°C$ to $+200°C$ for 1000 hours.

An internal load cell is used for measuring the axial (deviator) force. The load cell is fixed to the top of the triaxial cell, touching the specimen through the top cap. During loading, a moving pedestal pushes the specimen against the fixed load cell. The use of an internal measurement of axial force is much more appropriate than an external one, because internal measurements are not influenced by the friction between the pedestal and the base of the cell. Yet, as friction is a function of the testing temperature and the confining pressure, calibration against this variable is performed in the range $5°C-90°C$.

A thermal loading system characterised by a maximum testing temperature of $90°C$ is employed. This system consists of a heater (placed in the heating bath with water serving as the circulating fluid), a circulating pump, insulation and a temperature-controlling unit. Heating of the specimen is obtained indirectly by circulating water inside a spiral metal tube placed around the specimen. The hot water comes from the heating bath, situated outside the triaxial cell, flows through the tube around the specimen and finally returns to the heating bath. A centrifugal pump installed inside the bath imposes water circulation. The temperature of the circulating water is applied by means of an electric heater (2000 W at 220 V) submerged into the heating bath. Electrical power is automatically regulated by means of a programmable thermostat measuring and controlling temperature inside the triaxial cell near the specimen with one of the K-type thermocouples. The temperature is maintained at a required level

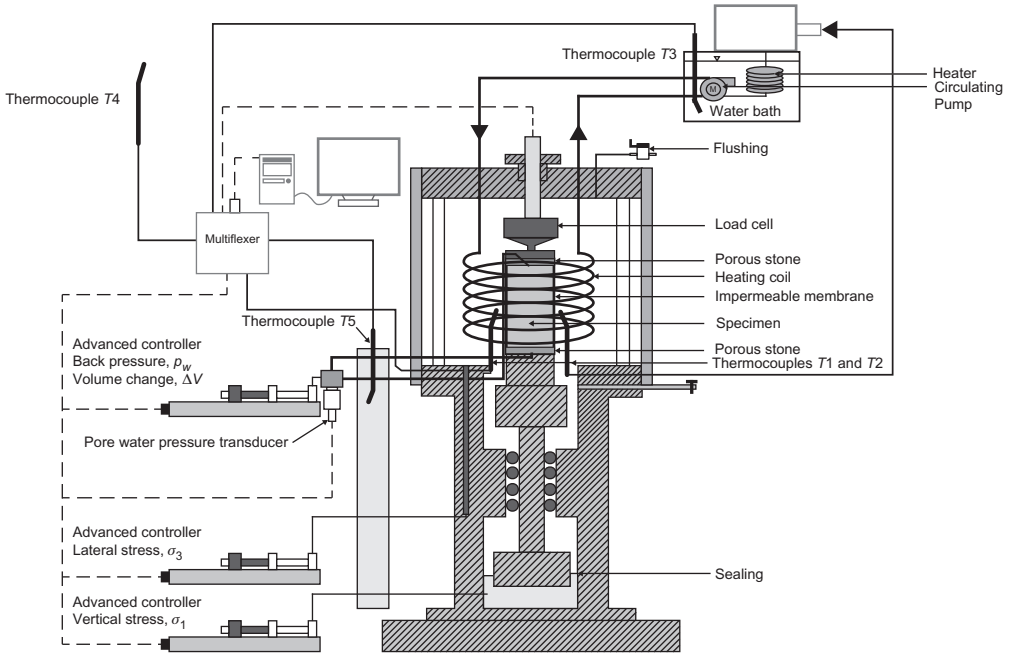

Figure 14.15 Sketch of a triaxial apparatus with temperature control. *Redrawn after Cekerevac, C., Laloui, L., Vulliet, L., 2005. A novel triaxial apparatus for thermo-mechanical testing of soils. Geotech. Test. J. 28 (2), 161–170.*

by balancing dissipating energy by input energy. Five K-type thermocouples are used to measure the temperature. These thermocouples are a combination of Nickel-Chromium and Nickel Aluminium ('Ni' −10% CR (+) vs 'Ni' 5% 'Al' and 'Si' (−)) and are suitable for temperature ranges from −200°C to +1370°C. Two thermocouples are diametrically situated inside the cell, at a distance of about 0.5 cm from the specimen ($T1$ and $T2$ in Fig. 14.15). One thermocouple measures the temperature inside the heating bath ($T3$), one the room temperature ($T4$ in Fig. 14.15) and one the temperature inside the cooling container ($T5$ in Fig. 14.15). One of the thermocouples located inside the cell gives the feedback signal to the heater and the second one is used for data acquisition. Since temperature is measured near the specimen (and not directly inside the specimen to avoid disturbances), preliminary calibration tests allow obtaining the correlation between the measured temperature and the temperature inside the specimen. The employed heating system allows imposing temperatures from 5°C to 150°C with an accuracy of ±0.25°C.

All units of the equipment are controlled by a personal computer and data acquisition is carried out continuously using a dedicated programme. Experimental data are stored in their original forms, that is output voltage for transducers and pressure/volume change for controllers. A software converts the output voltage of the different

transducers, at certain intervals, into the desired engineering units. The converted data is used for graphical interpretation of the running tests by using different plots: $\log t - \varepsilon_v$, $p' - q$, $\varepsilon_z - q$, $\varepsilon_z - \varepsilon_v$ etc. (depending on the test type). A sketch of the considered apparatus is reported in Fig. 14.15.

14.7.3 Testing procedure

Different types of triaxial tests under nonisothermal conditions exist and can be classified depending on the following factors: (1) the type of axial mechanical loading system (e.g. hydraulic or pneumatic); (2) the type of confinement pressuring system (e.g. exploiting water, oil or air); (3) the type of thermal loading system (e.g. imposing temperature variations from the inside of the apparatus through a thermal circuit or from the outside of the apparatus through an external thermal loading machine); (4) the type of loading path (e.g. isothermal-mechanical or thermomechanical); and (5) the type of drainage conditions characterising the loading (e.g. involving or preventing the dissipation of pore water pressure). In any case, the following main testing phases can be summarised for triaxial tests under nonisothermal conditions:

1. *Specimen preparation*: the soil specimen prepared for the test is laterally embedded by an impermeable membrane and is placed in the triaxial cell. O-rings are used to hold the impermeable membrane. Two filter paper discs are placed between the top and bottom surfaces of the specimen and the porous stones to ensure full contact during testing.
2. *Saturation*: distilled water (or any other relevant fluid) is potentially employed to saturate the specimen. The porous stones located on the top and bottom surfaces of the specimen allow achieving a uniform pressure distribution across the specimen while allowing drainage. The filter paper discs prevent any particle flow. The membrane isolates the specimen from the surrounding bath. Whenever pore water pressure is applied to saturate the specimen, a confining pressure at least equal to the pore water pressure is imposed.
3. *Consolidation*: consolidation of the specimen achieved via isothermal-mechanical loading can be applied to reproduce an isotropic, anisotropic or K_o stress state (isotropic consolidation is generally employed). In this case, the triaxial test is termed 'consolidated' and adequate time for the specimen to dissipate the excess pore water pressures is provided during loading. Isothermal-mechanical unloading of the specimen, succeeded by thermal loading or unloading, may follow consolidation. Otherwise, thermal loading or unloading of the specimen, without a previous isothermal-mechanical unloading, may directly follow consolidation. Meanwhile, sensors allow measuring the vertical displacement of the top of the specimen over time, together with the relevant temperature(s) (e.g. inside the triaxial cell upon interest), applied axial stress, confinement pressure and radial strain. These data

allow monitoring the variations in specimen height, axial and radial stress, radial strain and temperature throughout the test. When consolidation is prevented, the triaxial test is termed 'unconsolidated'.

4. *Shearing*: shearing of the specimen is performed via isothermal-mechanical loading. Various stress states can be imposed for such purpose (e.g. by increasing the axial load and maintaining constant the confining pressure as in conventional triaxial compression tests). Shearing may be imposed at the same initial temperature characterising the specimen or at a different temperature. Shearing may also occur under drained or undrained conditions, leading to three types of triaxial tests: 'consolidated-drained', 'consolidated undrained' or 'unconsolidated-undrained'. While shearing is imposed, sensors are employed to monitor relevant variables.
5. *Test completion and dismounting*: the test is typically completed by removing any load from the specimen. The apparatus is dismounted and the specimen may be used for subsequent experimental tests.

The geothermal operation of energy geostructures is associated in most cases with drained loading conditions. Therefore consolidated-drained triaxial tests may in most cases represent an appropriate and relevant approach to characterise the behaviour of soils. An example of loading paths followed in a series of conventional triaxial compression tests performed by Cekerevac et al. (2005) is reported in Fig. 14.16. The considered paths are represented in the three-dimensional space of coordinate axes represented by the mean effective stress, p', the deviatoric stress, q, and the temperature, T, and are as follows:

1. Isotropic consolidation (Path $0 \rightarrow 1$), followed by mechanical unloading in some cases (Path $1 \rightarrow 1'$);
2. Drained heating (Path 1 or $1' \rightarrow 2$);
3. Drained shearing by applying a conventional triaxial shearing path ($\delta q/\delta p' = 3$, Path $2 \rightarrow 4$);
4. Drained consolidation at high temperature (Path $2 \rightarrow 3$).

14.7.4 Testing recommendations

Recommendations for triaxial testing of soils under nonisothermal conditions can be highlighted considering the guidance developed for isothermal triaxial tests (see, e.g. ASTM D2850-03a, 2007; ASTM D7181, 2011; ASTM D4767, 2011; BS 1377-1, 1990; ISO 17892-8, 2018; ISO 17892-9, 2018) and accounting for specific aspects related to the temperature variations involved with thermal loading. In the following, noteworthy aspects characterising conventional triaxial compression tests under nonisothermal conditions are reported.

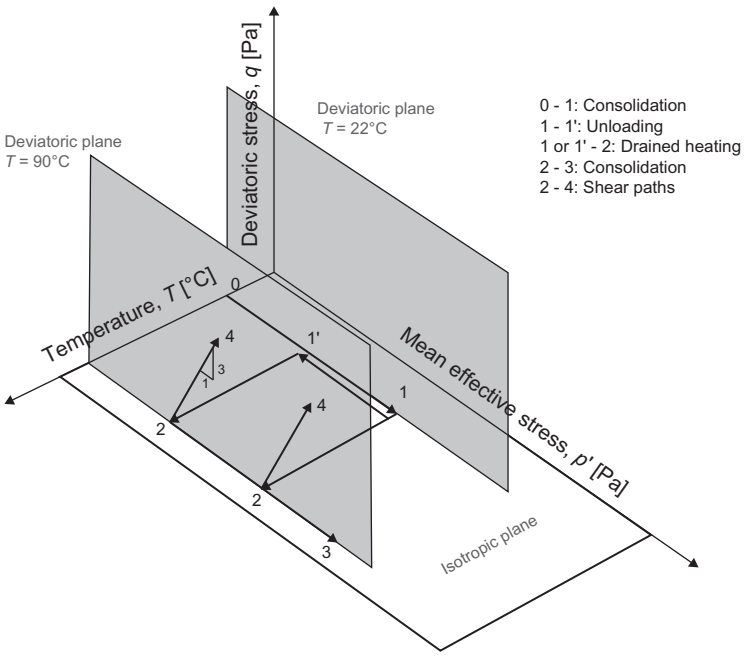

Figure 14.16 Example of loading paths followed in a triaxial testing campaign under nonisothermal conditions. *Redrawn after Cekerevac, C., Laloui, L., Vulliet, L., 2005. A novel triaxial apparatus for thermo-mechanical testing of soils. Geotech. Test. J. 28 (2), 161–170.*

14.7.4.1 Specimen features and preparation

The specimen should be cylindrical, with a diameter at least greater than 34 mm and a height comprised between 1.8 and 2.5 times the diameter. Undisturbed, recompacted, remoulded or reconstituted soil may constitute the specimen (ISO 17892-9, 2018). The largest particle size of the specimen should not exceed 1/6 of its diameter. Specimen height, mass and volume should be measured before the testing procedure (ISO 17892-9, 2018).

Deformation or disturbance of the specimen should be avoided when the sample is cut from a sampling tube and trimmed during the preparation process. The end surfaces of the specimen should be plane and perpendicular to the longitudinal axis. If some holes or grooves at the surface not exceeding 1/6 of the specimen diameter are identified, they need to be filled with remoulded specimen material. If some holes or grooves at the surface exceeding 1/6 of the specimen are identified, the specimen must be further cut and trimmed or a new sample must be selected for testing (ISO 17892-9, 2018).

Water content of the specimen should be maintained during the preparation process. If preparation is interrupted, attention should be paid to preserve the aimed water content, that is the specimen should be protected from air (ISO 17892-9, 2018).

The specimen (and the membrane) should be well positioned, centred with the top and bottom caps of the apparatus. Attention should be paid not to deform the specimen during the mounting process (ISO 17892-9, 2018).

If specimens are reconstituted in the laboratory, they should be compacted in layers to split the mould. If water is used in the mixture, at least 16 hours before compaction should be consider to let the water equalise in the soil (ISO 17892-9, 2018). Reconstituted coarse-grained soil specimens can be prepared by pluvial compaction in air or under water (ISO 17892-9, 2018).

14.7.4.2 Confining membrane

A so-called confining membrane consisting of an elastic material should be placed around the specimen to prevent the cell fluid from penetrating into the soil. Elastic or rubber membranes can be used. The confining membrane should be sealed to the top cap and to the pedestal of the cell with O-ring or similar equipment (ISO 17892-9, 2018).

Confining membranes should be immersed in water for at least 24 hours before use. Attention should be paid to the potential excess of surface water on the inside of the membrane before placing it in contact with the soil specimen (ISO 17892-9, 2018). To prevent any leakage during the test, the membrane should be checked prior testing to not present any damage. If leakage of water happens during the test or if any water line is observed, the effect of leak on the results should be evaluated and the test may be invalidated (ISO 17892-9, 2018).

14.7.4.3 Physical contact and porous disks

Contact between the load cell and the specimen should be ensured with a setting load that should be kept as small as possible. The porous discs placed at the end of the specimen should be constituted by a rigid, noncorrodible material and shall have a larger compressive strength than the soil tested (ISO 17892-9, 2018). These disks should be cleaned prior testing and not clogged (ISO 17892-9, 2018). The diameter of the porous discs should be equal to the specimen diameter. Planeness of the surface between the specimen and the disks should be ensured (ISO 17892-9, 2018).

Attention should be paid to soils that swell in contact with water (e.g. fine-grained soil specimens). Swelling should be prevented from the specimen sucking water from the porous discs. To this aim, it is recommended to mount the specimen with dry porous discs and to subsequently flush water while applying a vertical and horizontal stress high enough to eliminate the potential swelling (ISO 17892-9, 2018). De-aired fluid should be used for the saturation or the flush of porous discs and filter papers. Tap water is often used for this purpose, but when results may be affected water with a similar chemistry to the specimen pore water may be used (ISO 17892-9, 2018).

14.7.4.4 Filter papers

To prevent fine material to be washed into the porous discs, a filter paper or other similar material should be placed between the specimen and the porous discs (ISO 17892-9, 2018). The filter paper should be composed of a material that does not react with the specimen (ISO 17892-9, 2018). New filter papers should be used for each test, similar to new filter paper strips used as side drains. The side drains are used to enhance the drainage of the radial edge when low permeability specimens are tested. The side drains should be positioned vertically or spirally around the specimen. Vertically oriented filter paper strips should be evenly spaced. Spirally oriented strips are oriented at 30−45 degrees to the vertical. Vertically and spirally paper strips should not cover more than 50% of the radial specimen surface (ISO 17892-9, 2018).

14.7.4.5 Loading frame

The load frame should be chosen to provide a range of vertical strain rates as required for the test. The rate should not change more than 10% of the intended value (ISO 17892-8, 2018). Movement of the plate should be smooth, with no vibrations to prevent fluctuations in the tests results. A value of 30% of the specimen height is recommended for the stroke of the load frame (ISO 17892-8, 2018). The device should not be influence by any changes in horizontal forces or bending moments, neither by any unwanted change of temperature and cell pressure during the test (ISO 17892-8, 2018).

14.7.4.6 Cell pressure fluid

Cell pressure fluid should not penetrate in the specimen, neither extract pore water from the specimen. In general, de-aired water is suitable as a cell pressure fluid. The cell fluid should be stabilised at the same temperature as the test location (ISO 17892-8, 2018).

14.7.4.7 Saturation

Coarse-grained soil specimens may be flushed with carbon dioxide before flushing them with water to speed up the saturation process. In general, a volume of carbon dioxide equal to three specimen volumes is suitable for the previous purpose. If the specimen is likely to be chemically affected by the carbon dioxide dissolved, the previous method should not be used (ISO 17892-9, 2018).

Saturation should be checked prior to the consolidation or immediately prior to shearing (ISO 17892-9, 2018). Saturation should be checked with reference to the value of the Skempton coefficient, B (Skempton, 1954). Saturation is achieved if a B-value of 0.95 is at least obtained and if the value of B does not increase over subsequent B-checks, that is B is constant. The volume change should be measured during drained shearing (ISO 17892-9, 2018).

14.7.4.8 Temperature effects

Temperature variations cause significant variations in dimensions of the apparatus components and the specimen. Because of the previous reason, calibrations are required prior to each test (Mitchell and Campanella, 1963). The components of the triaxial test should be corrected in length for each temperature variation. Pipettes should be calibrated to indicate true volume.

The cell, lines and membrane materials should be chosen so that their characteristics are suitable for thermal loading. Cell and line materials should resist to corrosion and high pressure (Baldi et al., 1988).

During thermal loading, temperature variations deform the triaxial cell and the specimen, and lead to volume and pressure changes. This phenomenon is due to the thermal deformation that occurs in the porous disks, the drainage lines and the water filling them. Attention should be paid to these spurious changes of volumes and pressures. Thermal expansion of pressure tubing, porous disks and the water filling them should be determined at different temperature and pressure when processing the drained test results. Water volume and transmissions lines can be determined as a function of temperature (Baldi et al., 1988). During thermal loading, it is recommended to measure periodically volume and height of the specimen, as well as the volume of water expelled or absorbed by the specimen.

Thermocouples should be evenly placed to verify the achievement of a uniform temperature profile (Mitchell and Campanella, 1963; Baldi et al., 1988). Thermocouples placed into the specimen might disturb the consolidation process. To avoid this issue, thermocouples may be placed on the surfaces of the specimen during the test or in the bath containing the confinement pressuring fluid (Cekerevac et al., 2005). Because in these situations temperature is measured near the specimen, preliminary calibration tests should be performed to obtain the correlation between the measured temperature and the temperature inside the specimen. From these calibration tests, a relationship between imposed temperature to the heater and temperature in the middle of the specimen (after stabilisation of temperature) should be obtained for different confining pressures (Cekerevac et al., 2005).

14.7.5 Pair of elastic parameters determination

Pairs of elastic parameters are essential to characterise the deformation behaviour of materials. The pair constituted by bulk modulus, K, and shear modulus, G, for example can be respectively determined in any triaxial test through the following plots: volumetric strain, ε_v, against deviatoric stress, q, and differential axial to radial strain, $\varepsilon_z - \varepsilon_r$, against deviatoric stress, q. The slope of an appropriate loading-unloading branch depicted in the former plot represents K while that depicted in the latter represents $2G$ (Vulliet et al., 2016). Determining q, ε_z and ε_v is essential to construct the previous plots.

In conventional triaxial compression tests, the deviatoric stress can be computed from the knowledge of the radial stress, σ_r, and the axial stress, σ_z, that is $q = \sigma_z - \sigma_r$, while the volumetric strain can be computed from the knowledge of the radial strain, ε_r, and the axial strain, ε_z, that is $\varepsilon_v = \varepsilon_z + 2\varepsilon_r$. The axial stress can be calculated assuming that the imposed axial force leads to a uniform stress state as:

$$\sigma_z = \frac{P}{A} + \sigma_r \tag{14.17}$$

where P is the axial force and A is the corrected area (due to radial strain) of the specimen. According to Head (1986), the corrected area A is given by:

$$A = \frac{1 - \varepsilon_v}{1 - \varepsilon_z} A_0 = \frac{1 + \Delta V_i / V_0}{1 + \Delta H_i / H_0} A_0 \tag{14.18}$$

where A_0 is the area of the specimen after consolidation, $\varepsilon_v = -\Delta V / V_0$ is the volumetric strain associated with the drainage of the specimen (with ΔV_i and V_0 being the change in volume during the loading stage i and the initial volume of the specimen, respectively) and $\varepsilon_z = -\Delta H_i / H_0$ is the axial deformation (with ΔH_i and H_0 being the measured change in the value of axial displacement during the loading stage i and the initial specimen height, respectively).

From a practical perspective the deformation parameters of soils (e.g. Young's modulus) can be considered in most cases *independent* of temperature with reference to the temperature variations associated with the geothermal operation of energy geostructures. Adequate care should however be devoted to this aspect when dealing with high-plasticity fine-grained soils or general sensitive soils.

Further representations of interests for the determination of design parameters and the characterisation of the material behaviour are, for example in the $p'-q$ plane (instructing about the stress paths and the Critical State Line), as well as in the $\varepsilon_a - q$ plane (instructing about the Young's modulus as well as about the strength behaviour of the material – peak/postpeak behaviour).

14.7.6 Volumetric thermal expansion coefficient determination

The volumetric thermal expansion coefficient of soils can be also determined through triaxial tests by plotting the volumetric strain against the temperature variation applied to the specimen under constant stress conditions and by considering the slope of the tangent to the thermal unloading portion of the curve, similar to the procedure highlighted for oedometer tests.

During thermal loading, the volume change of the specimen can be separated in different components as (Campanella and Mitchell, 1968; Cekerevac et al., 2005)

$$\Delta V_i = \Delta V_{dr} - \Delta V_{de} - \Delta V_w - \Delta V_s \tag{14.19}$$

where ΔV_{dr} is the volume of water flowing out of or into the specimen (measured using a backpressure volume controller), ΔV_{de} is the thermal expansion of the drainage system (the irreversible component of deformation during a calibration test), ΔV_w is the thermal expansion of the pore water and ΔV_s is the thermal expansion of the solid skeleton characterising the specimen.

Accordingly:

$$\varepsilon_v = -\frac{\Delta V_{dr} - (\Delta V_{de} + \Delta V_w + \Delta V_s)}{V_0} \tag{14.20}$$

To calculate the thermal expansion of the pore water, Campanella and Mitchell (1968) consider the thermal properties of the so-called free water, that is regular water present in the pore of soils that is characterised by no particularly recognisable structure of cations and anions:

$$\Delta V_w = \beta_w V_w \Delta T \tag{14.21}$$

where β_w is the volumetric thermal expansion coefficient of the water, V_w is the volume of pore water in the specimen after mechanical consolidation and ΔT is the applied temperature variation. According to Baldi et al. (1988), the volumetric thermal expansion coefficient of the free pore water is a function of temperature, T, and pore water pressure, p_w, and can be determined as

$$\beta_w(T, p_w) = \alpha_0 + (\alpha_1 + \beta_1 T)\ln\ m_t \cdot p_w + (\alpha_2 + \beta_2 T)(\ln\ m_t \cdot p_w)^2 \tag{14.22}$$

where $\alpha_0 = 4.50 \times 10^{-4\circ}\mathrm{C}^{-1}$, $\alpha_1 = 9.15 \times 10^{-5\circ}\mathrm{C}^{-1}$, $\alpha_2 = 6.38 \times 10^{-6\circ}\mathrm{C}^{-1}$, $\beta_1 = -1.2 \times 10^{-6\circ}\mathrm{C}^{-1}$, $\beta_2 = -5.76 \times 10^{-8\circ}\mathrm{C}^{-1}$ and $m_t = 1\ \mathrm{MPa}^{-1}$.

To calculate the thermal expansion of the solid skeleton, the following expression can be considered

$$\Delta V_s = \beta_s V_s \Delta T \tag{14.23}$$

where β_s is the volumetric thermal expansion of the solid particles and V_s is the volume of the solid skeleton characterising the specimen after mechanical consolidation.

14.7.7 Shear strength parameters determination

Shear strength parameters, including the cohesion and the angle of shear strength, are key parameters to characterise the failure of materials. These parameters can be determined through at least two triaxial tests by plotting the Mohr circles associated with the imposed shearing stress path (e.g. conventional triaxial compression) and by

referring to the slope (i.e. the angle of shear strength) and the intercept with the ordinate axis of the tangent line to the circles.

From a practical perspective the shear strength parameters of soils (e.g. under constant volume conditions) can be considered *independent* of temperature with reference to the temperature variations associated with the geothermal operation of energy geostructures.

14.8 Direct shear testing under nonisothermal conditions

14.8.1 General

Direct shear testing under nonisothermal conditions is an experimental laboratory method for the characterisation of the failure of soils or interfaces with soils that can serve the geotechnical and structural design of energy geostructures. This test involves deforming a specimen at a controlled strain rate on or near a single shear plane determined by the configuration of the apparatus and measuring the resulting variations of displacement and stress. The results and key mechanical parameters that can be determined through direct shear testing under nonisothermal conditions are reported in Table 14.9. The parameters that can be determined via direct shear tests under nonisothermal conditions are the same ones that can be determined via direct shear tests under isothermal conditions, with the unique difference that the potential significance of temperature on the referenced parameters can be assessed in the former tests while not in the latter.

14.8.2 Testing equipment

A direct shear apparatus allowing for the control of temperature and the testing of interfaces has been developed, for example by Di Donna et al. (2015). This device represents an automated direct shear box (cf. Fig. 14.17) that has been modified to test both soil–soil interfaces by shearing uniform soil specimens and soil–concrete interfaces by shearing composite soil–concrete specimens. The device enables imposing constant normal stiffness (CNS) conditions and constant normal load (CNL) conditions, as well as applying thermal loads, in addition to mechanical loads, through a

Table 14.9 Test results and key design parameters associated with direct shear tests under nonisothermal conditions.

Testing technique	Test results	Design parameters
Direct shear testing under nonisothermal conditions	Stress–displacement curve Failure envelope	Cohesion, c' Angle of shear strength, φ' Angle of shear strength under constant volume conditions, φ'_{cv}

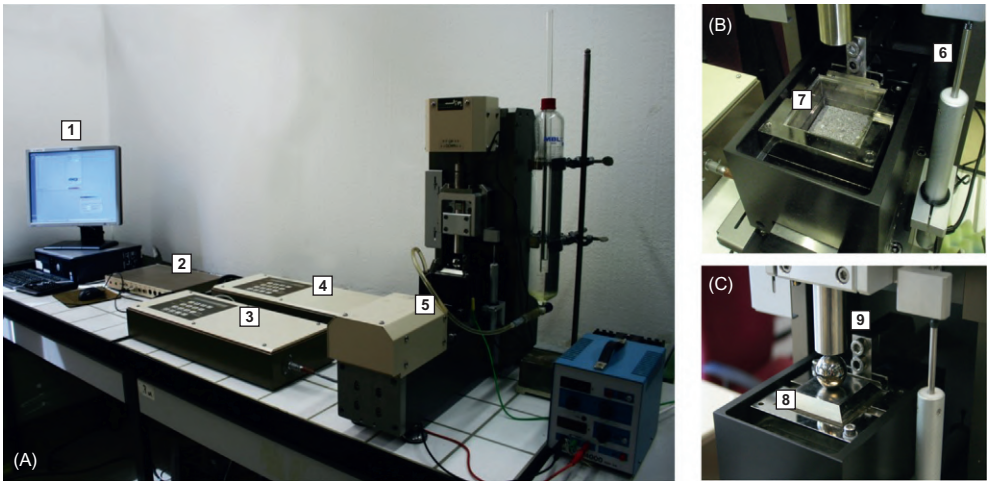

Figure 14.17 Original version of the direct shear device, modified by Di Donna et al. (2015): (A) global view, (B) detail of the open shear box, (C) detail of the closed shear box (1: software control, 2: LVDTs acquisition pad, 3: normal actuator, 4: horizontal actuator, 5: Load cells, 6: LVDTs, 7: specimen placement, 8: top cap, 9: axial piston).

heating system. Key constituents of this apparatus include a parallelepiped soil specimen, a concrete specimen (when soil–concrete interfaces are tested), a heating tissue, one porous stone connected to a cap and an axial mechanical loading apparatus on top of the soil specimen, a lateral mechanical loading apparatus, the direct shear box constituted by two portions that can be characterised by a relative displacement in one horizontal direction, measuring sensors (e.g. LVDTs and temperature sensors) and a data acquisition system. A sketch of the considered apparatus is reported in Fig. 14.18.

In this device, the normal and shear forces are controlled by two electromechanical force actuators, which can be used to pilot the tests in terms of both displacement and force. Two load cells are installed to measure the vertical and horizontal loads that are applied to the specimen. Two LVDTs are used to measure the horizontal and vertical displacements. A dedicated software is used to control the system and for the data acquisition. From this programme it is possible to control both the horizontal and the vertical directions. For each of them, the load, the stress, the displacement or the strain can be imposed. All of them can be applied instantaneously as a constant value, imposing a temporal ramp or a cyclic path. The software reads the load (or displacement) measured by the load cells (or the LVDT), communicates to the actuators the subsequent step to be applied and iterates to guarantee the higher accuracy provided by the sensors with respect to the actuator measurements. The shear box is designed to accommodate a soil specimen with a horizontal surface area of 60 mm × 60 mm and a

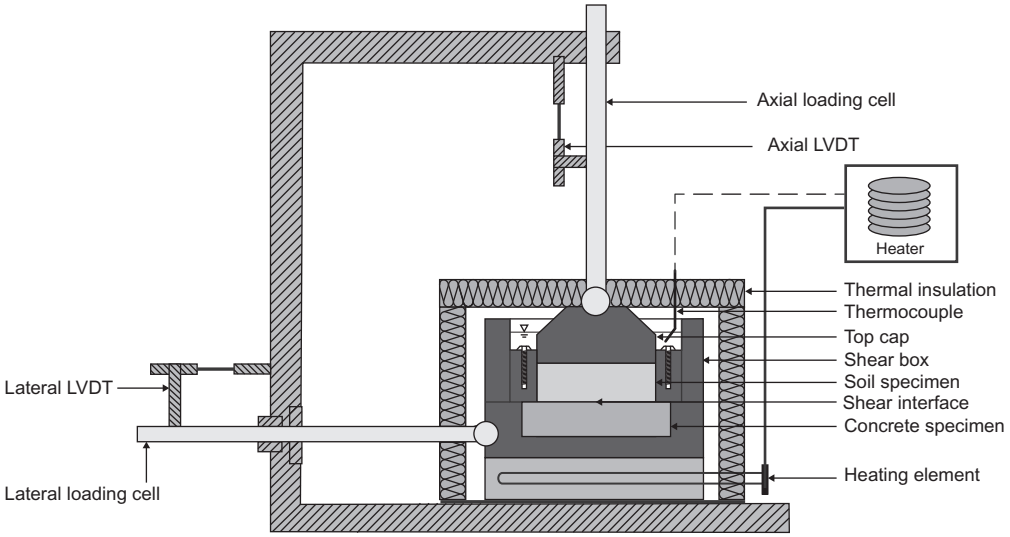

Figure 14.18 Sketch of a direct shear apparatus with temperature control employed by Di Donna et al. (2015).

height of 20 mm. The box is divided into an upper and a lower part that are separated during shearing.

The lower part of the shear box includes the heating system allowing for the control of temperature. When tests on interfaces are to be performed, a 60 mm × 105 mm lower part of the shear box is used, with a height of 16 mm. This part of the box accommodates a concrete sample, while ensuring a constant contact surface during shearing. When tests on soil samples are to be performed, a 60 mm × 60 mm lower part of the shear box is used, with a height of 10 mm. The upper part of the box accommodates soil specimens characterised by a 60 mm × 60 mm surface and a height of 10 mm.

The normal stiffness during the test can be controlled through a dedicated software (1) in terms of stress [kPa/mm] or (2) in terms of force [kN/mm]. The difference between the two possibilities is that the former considers the contact area variation during shearing while the latter assumes a constant contact area between the concrete and the soil. For the first control mode, the implemented algorithm at each increment of applied solicitation is (Di Donna, 2014):

- Read the increment of normal and horizontal displacement $\Delta\delta_n$ and $\Delta\delta_h$;
- Multiply the increment of normal displacement by the value of stiffness K_s [kPa/mm] imposed by the user to compute the increment of normal stress as $\Delta\sigma_n = -K_s\Delta\delta_n$;

- Compute the increment of force to be transmitted to the specimen considering the actual contact area $\tilde{A}$ (computed based on $\Delta\delta_h$) as $\Delta F_n = \tilde{A}\Delta\sigma_n$;
- Change the applied force to the specimen as $F_n = F_n + \Delta F_n$.

For the second control mode, the following algorithm is employed (Di Donna, 2014):

- Read the increment of normal displacement $\Delta\delta_n$;
- Multiply it by the value of stiffness K_s [kN/mm] imposed by the user to compute the increment of vertical force ΔF_n to be transmitted to the specimen as $\Delta F_n = -K\delta_n$;
- Change the applied force to the specimen as $F_n = F_n + \Delta F_n$.

In summary, if the test is performed with the 60 mm × 60 mm shear box (changing contact area) the first option must be used, while if the test is performed with the 60 mm × 105 mm shear box (constant contact area) the second option must be chosen.

To control temperature during testing, a heating system composed of an electrical resistance, electrical power supplier, insulation system and a thermocouple is introduced. The heating element of the electrical resistance is made up of a nickel–chrome alloy heating wire wound in a spiral around a slender fibreglass core. The heating element is placed between two layers of woven glass fibre impregnated with silicon elastomer, resulting in a heating tissue with a thickness of 5 mm. This material is an excellent electrical insulator (dielectric strength of 12 kV/mm) and has good thermal conductivity [0.07 W/(m °C)]. The electrical tissue is waterproof and is installed in the lower part of the box (cf. Fig. 14.19A). The tissue is protected by a metal plate to minimise its compression and, consequently, any spurious normal movements occurring when the normal load is applied (cf. Fig. 14.19B). The concrete sample is placed on the metal plate (cf. Fig. 14.19C). The upper part of the shear box can consequently be mounted over the bottom part with the inclusion of the soil specimen (cf. Fig. 14.19D). Calibration tests were carried out to assess the shear strength offered by the apparatus in the two directions of motion. The shear box is insulated by polystyrene to minimise heat loss and temperature variations of the sensors.

Besides the standard isothermal calibration of the displacement sensors and load cells, the effects of temperature on all components of the apparatus are quantified, with a focus on (Di Donna, 2014): (1) the temperature effects on the sensors, (2) the relationship between the temperature at the concrete–soil interface and the voltage imposed on the heating tissue and (3) the device thermal deformation.

14.8.3 Testing procedure

Different types of direct shear tests under nonisothermal conditions exist and can be classified depending on the following factors: (1) the type of subject being tested (e.g.

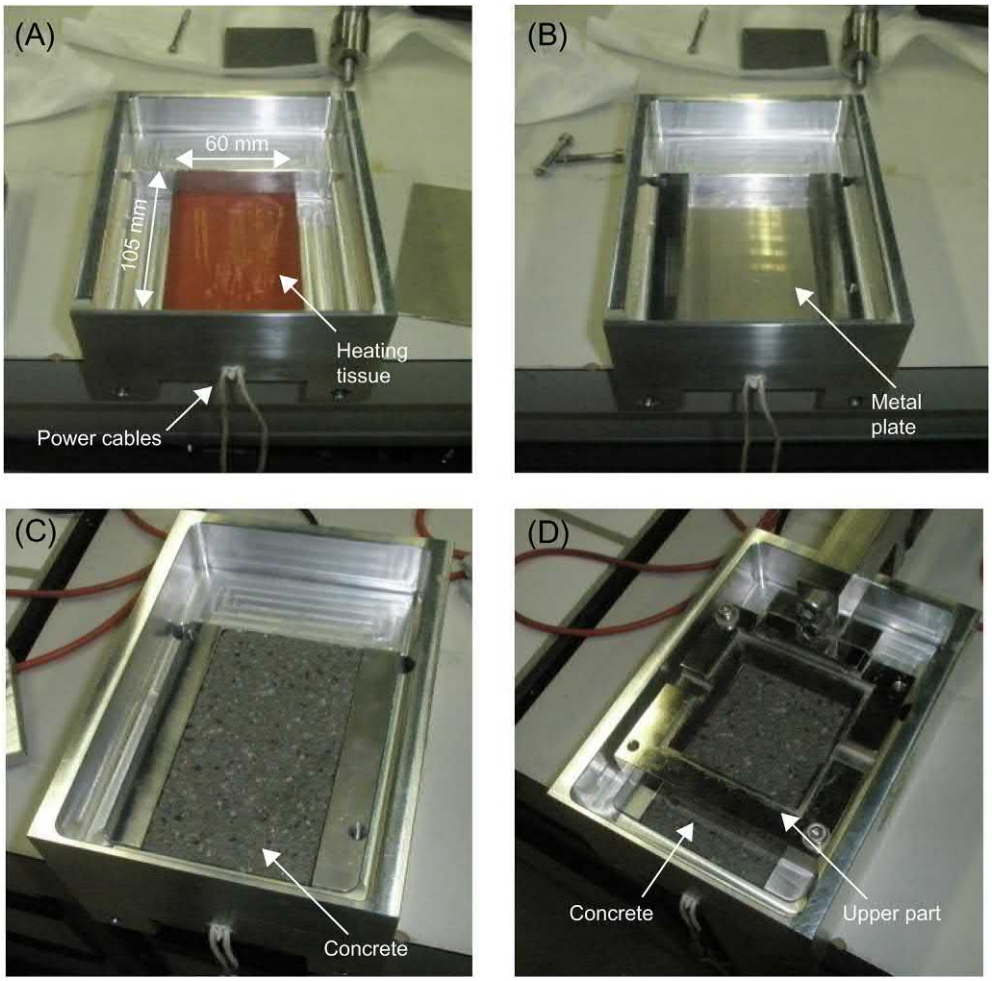

Figure 14.19 Development of the shear box for soil–concrete interface shear tests at different temperatures: (A) installation of tissue in lower part of the shear box, (B) support for concrete specimen, (C) position of concrete specimen and (D) initial position of upper part of the box containing the soil. *Redrawn after Di Donna, A., Ferrari, A., Laloui, L., 2015. Experimental investigations of the soil–concrete interface: physical mechanisms, cyclic mobilisation and behaviour at different temperatures. Can. Geotech. J. 53 (4), 659–672.*

a soil specimen or a soil–concrete specimen, (2) the type of loading conditions (e.g. CNL or CNS), (3) the type of thermal loading system (e.g. based on electrical resistances or exploiting a closed circuit in which a heat carrier fluid circulates to impose the temperature variations to the specimen) and (4) the type of loading path (e.g. isothermal-mechanical or thermomechanical). In any case, the following main testing phases can be summarised for direct shear tests under nonisothermal conditions:

1. *Specimen preparation*: the soil specimen prepared for the test is placed in the shear box. When a uniform soil specimen is tested, porous stones at the top and bottom of the specimen are employed. When an interface between a soil specimen and a different material is tested, a unique porous stone is typically employed and is located at the top of the shear box.
2. *Saturation*: distilled water (or any other relevant fluid) is potentially employed to saturate the specimen, while the porous stone located on its top (and potentially on its bottom) allows drainage. Meanwhile, sensors allow measuring the vertical displacement of the top of the specimen over time together with the relevant temperature(s) (e.g. inside or outside the shear box upon interest). Measuring vertical displacements serve assessing the saturation effect on the volume change of the material and allow monitoring the variations in specimen height throughout the test. If swelling of the material under saturation is observed and may affect the structure of the specimen, increments of mechanical load are imposed on the cap that is placed above the top porous stone to maintain the initial height of the specimen constant.
3. *Consolidation*: consolidation of the specimen achieved via isothermal-mechanical loading is applied to the sample. Adequate time for the specimen to dissipate the excess pore water pressures must be provided after the loading is applied, the considerations proposed for oedometer tests being valid also for this phase of shear tests. Isothermal-mechanical unloading of the specimen, succeeded by thermal loading or unloading, may follow consolidation. Otherwise, thermal loading or unloading of the specimen, without a previous isothermal-mechanical unloading, may directly follow consolidation. Meanwhile, sensors allow measuring the vertical displacement of the top of the specimen over time, together with the relevant temperature(s) (e.g. inside or outside the shear box upon interest) and applied vertical stress. These data allow monitoring the variations in specimen height, vertical stress and temperature throughout the test.
4. *Shearing*: shearing of the specimen is performed under isothermal conditions by applying a mechanical shearing force. Shearing may be imposed at the same initial temperature characterising the specimen or at a different temperature. Shearing should occur under drained conditions and may be monotonic or cyclic. While shearing is imposed, sensors are employed to monitor the vertical and shear stress, vertical and horizontal displacement and temperature.
5. *Test completion and dismounting*: the test is typically completed by removing any load from the specimen. The apparatus is dismounted and the specimen may be used for subsequent experimental tests.

An example of loading paths followed in a series of direct shear tests at ambient or elevated temperature under CNS or CNL conditions performed by Di Donna et al. (2015) is reported in Fig. 14.20. The considered paths are represented in the

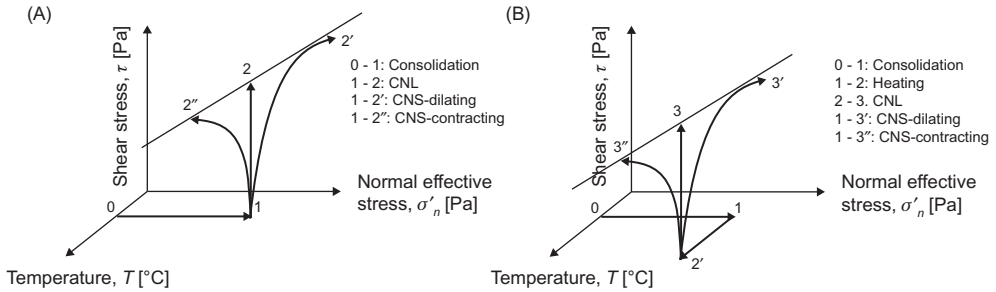

Figure 14.20 Stress–temperature paths followed during the concrete–soil interface tests: (A) at ambient temperature and (B) at high temperature.

three-dimensional space of coordinate axes represented by the normal effective stress, σ'_n, the shear stress, τ, and the temperature, T, and are as follows:

i. Consolidation (Path $0 \rightarrow 1$), followed by mechanical unloading in some cases;

ii. a. Shearing at constant initial temperature (Path $1 \rightarrow 2$, $1 \rightarrow 2'$ or $1 \rightarrow 2''$), for the isothermal tests;

ii. b. Heating thermal loading (Path $1 \rightarrow 2^*$) and shearing (Path $2^* \rightarrow 3$, $2^* \rightarrow 3'$ or $2^* \rightarrow 3''$), for the nonisothermal tests.

14.8.4 Testing recommendations

Recommendations for direct shear testing of soils under nonisothermal conditions can be highlighted considering the guidance developed for isothermal direct shear tests (see, e.g. ASTM D3080/D3080M, 2011; ISO 17892-7, 2018) and accounting for specific aspects related to the temperature variations involved with thermal loading. In the following, noteworthy aspects for direct shear tests under nonisothermal conditions are expanded.

14.8.4.1 General considerations

In direct shear tests, an appropriate specimen height cannot be defined to calculate shear strain and the only known stress components are the normal and shear stress acting on the horizontal plane. As the previous information does not allow to fully determine the stress state, stress–strain relationships or deformation parameters cannot be addressed from such tests.

14.8.4.2 Specimen size

Square specimens characterised by a minimum width 60 mm or cylindrical specimens characterised by a minimum diameter of 70 mm should be used (ISO 17892-7, 2018). The height of the specimens should not be less than 10 mm and chosen so that the height-to-width or height-to-diameter ratio does not exceed 1/3. The larger grain size should not exceed 1/5 of the specimen height (ISO 17892-7, 2018).

14.8.4.3 Specimen preparation

For tests under isothermal conditions, the minimum number of specimens to be tested varies depending on the granulometry of the tested samples. For fine-grained soils, it is recommended to prepare and test at least three similar specimens from undisturbed or reconstituted samples (ISO 17892-7, 2018). For coarse-grained soils, it is recommended to prepare and test a minimum of five specimens (ISO 17892-7, 2018). The specimens should be as homogeneous as possible, cut directly from undisturbed samples or reconstituted in the laboratory. In any case, they should reproduce as closely as possible the in situ conditions. The specimens should be cut and trimmed to prevent disturbance or any loss/gain of moisture.

14.8.4.4 Mounting

During the mounting of the two halves of the direct shear box, care should be given in such a way that no relative displacement between the two parts is observed. A thin coating of silicone grease or petroleum jelly may be applied to the inside faces and the caps of the box to prevent friction and the development of unwanted shear stresses on the inside faces (ISO 17892-7, 2018). A clearance between the shear box halves should be maintained to avoid friction during the test. However, the clearance should not permit extrusion of the soil between them. A clearance is obtained with the disconnection of the frame/halves before the shearing.

14.8.4.5 Consolidation

The vertical stress applied to consolidate the specimen should be applied as smoothly and rapidly as possible while preserving the aimed drainage conditions. The end of the primary consolidation should be determined with the definition of the time t_c according to the procedures developed for oedometer tests. This characteristic time allows determining the minimum time required to reach failure upon drained shearing (Gibson and Henkel, 1954).

14.8.4.6 Shearing

In direct shear tests, the pore water pressure cannot be monitored. Accordingly, appropriate shearing rates must be considered. Among the various reference values for the shearing rate that may preferably employed in direct shear tests to ensure drained conditions, the rates of 0.001 mm/min for clays, 0.01 mm/min for silts and 1 mm/min for sands may be employed (Lambe, 1951; Bolton, 2003).

A maximum shearing velocity should be considered for the test. This velocity can be determined as $v_s = \delta_f / t_f$, where δ_f is the horizontal displacement corresponding to the sample failure and $t_f \approx 10t_c$ is the minimum time required to reach failure upon drained shearing (Gibson and Henkel, 1954). According to Head and Epps (1980), δ_f

ranges between 5 and 8 mm for NC fine-grained soils while it ranges between 1 and 5 mm for OC fine-grained soils.

The normal load or normal stiffness may be maintained constant during shearing. During testing, shear stresses and displacements are nonuniformly distributed within the specimen.

14.8.4.7 Temperature effects

In addition to the standard isothermal calibration of the load cells and strain sensor, attention should be paid to the temperature effects on all components of the apparatus, in particular the temperature effect on the apparatus sensors and the thermal deformation of the device (Di Donna et al., 2015). Thermocouples should be employed to monitor the temperature in the apparatus. To avoid any disturbance of the mechanical behaviour of the specimen during the test, all thermocouples placed into the specimen before the beginning of the test to control the temperature and the homogeneity of the temperature gradient in the specimen should be retrieved prior to the test (Yavari et al., 2016). Heating thermal loads resulting in temperature variations of the order of 2°C per hour may be considered to ensure drained conditions (Di Donna et al., 2015).

14.8.5 Determination of shear strength parameters

Shear strength parameters such as cohesion, peak angle of shear strength and angle of shear strength under constant volume conditions can be effectively determined for both soil and interfaces with soil specimens by plotting in the Mohr plane the points of coordinates $(\sigma_n'; \tau)$ corresponding to the relevant stage of the shear test (e.g. when the peak strength of the material is reached and identified in the plane δ_h - τ or in the plane δ_h–δ_n). Interpolation of more than two points of coordinates $(\sigma_n'; \tau)$ in the Mohr plane allows highlighting the failure envelope of the material and the relevant values of intercept cohesion (where applicable) and angle of shear strength (at peak or under constant volume conditions).

From a practical perspective the shear strength parameters of concrete–soil interfaces can be considered *independent* of temperature with reference to the temperature variations associated with the geothermal operation of energy geostructures. The angle of shear strength under constant volume conditions of soils, which should be employed in capacity formulations, shows a negligible sensitivity (if observed) to temperature variations. An increase in the intercept cohesion may be observed for soils characterised by the thermal collapse phenomenon (caused, e.g. by drained heating under NC conditions). However, while this effect is beneficial for the design and may be considered through advanced constitutive models in numerical analyses, the contribution of cohesion (similar to the contribution of adhesion) is typically neglected in

analytical formulations employed for the definition of the capacity of geostructures and thus represents an approach on the safety side.

From the previous considerations, performing direct shear tests under nonisothermal conditions can be considered relevant from a design perspective only when sensitive soils are encountered, whereas not essential otherwise. Similar to direct shear tests under isothermal conditions, direct shear tests under nonisothermal can be of primary interest to address the influence of cyclic loading conditions on the (mechanical) degradation of the properties of the tested material or interface. Cyclic thermal loads, similar to cyclic mechanical loads, can cause a variation of the material properties via degradation effects. However, this degradation can again be considered independent of temperature and only a result of a mechanical solicitation (which can be mechanically or thermally induced).

An example of the plots that can be achieved via monotonic direct shear tests is presented in Figs 14.21 and 14.22 with reference to the results reported by Di Donna et al. (2015) for sand-sand (Quartz sand) and clay−clay (Illite clay) specimens.

For the sand-sand specimen (cf. Fig. 14.21), the evolution of the mobilised shear stress with the imposed horizontal displacement shows that the material undergoes a peak phase before reaching constant volume conditions (critical state) for the chosen initial density. According to theoretical soil mechanics, the peak shear strength, τ, of any geomaterial under a given normal load includes two components (Rowe, 1962): the shear strength due to the soil dilatancy, τ_D, and the shear strength at constant volume, τ_{cv} (critical state). Mathematically, the above can be expressed as

$$\tau = \tau_D + \tau_{cv} \tag{14.24}$$

The first component of shear strength depends on the material density (void ratio). The second component of shear strength includes sliding resistance at the particles contacts and particles rearrangement (Rowe, 1962), and is unique at a given normal effective stress independent of the initial conditions. Consequently, during a shear test under a given CNL, the second component is constant and the maximum shear stress is reached when the dilatancy contribution reaches its maximum. To study this latter component, the volumetric deformation of the material must be considered (cf. Fig. 14.21C). The considered material contracts slightly at the beginning and dilates subsequently. The derivative of this curve, that is the variation of the vertical displacement, with respect to the horizontal displacement represents the contribution of the dilatancy during the test (cf. Fig. 14.21D). The maximum of this curve corresponds to the dilatancy angle, ψ, which is defined as

$$\psi = \max\left[\tan^{-1}\left(\frac{\Delta\delta_n}{\Delta\delta_h}\right)\right] \tag{14.25}$$

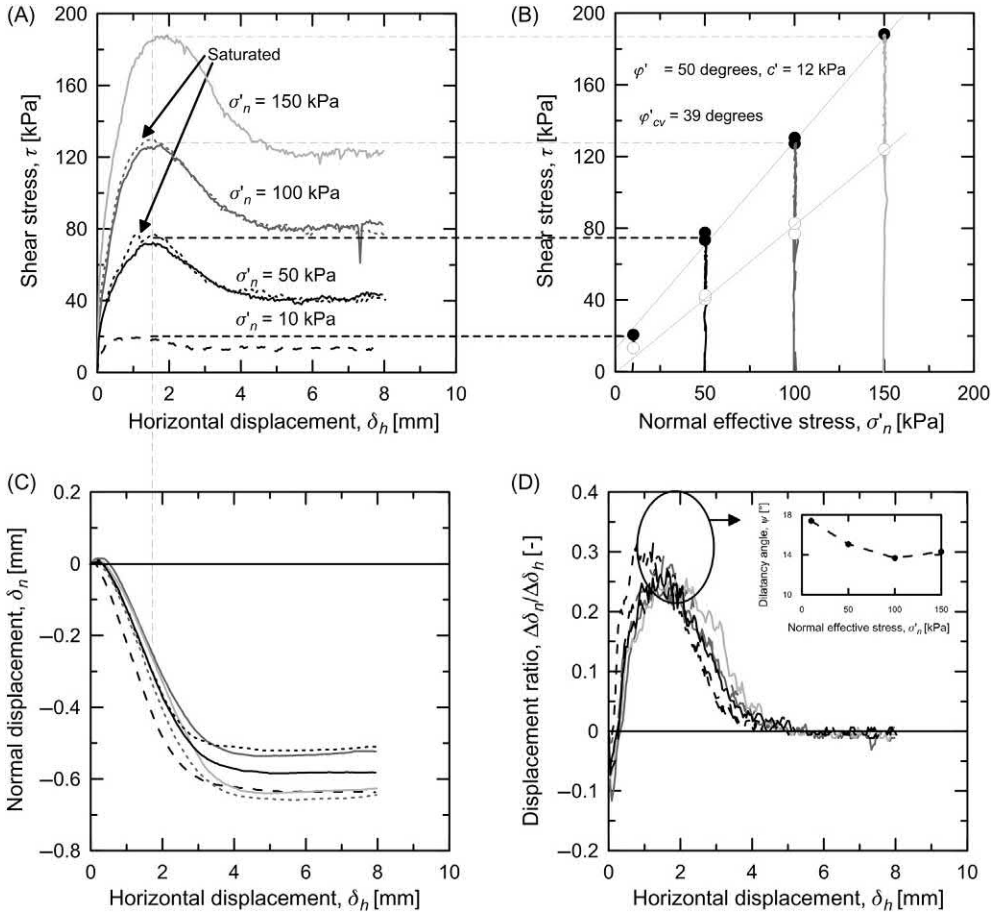

Figure 14.21 Quartz sand response during direct shear testing: (A) shear stress – horizontal displacement plane; (B) Mohr plane; (C) volumetric behaviour; (D) dilatancy angle. *Redrawn after Di Donna, A., Ferrari, A., Laloui, L., 2015. Experimental investigations of the soil–concrete interface: physical mechanisms, cyclic mobilisation and behaviour at different temperatures. Can. Geotech. J. 53 (4), 659–672.*

In the considered test, dilatancy is observed between 1 and 2 mm of horizontal displacement (depending on the test). This condition corresponds with the peak condition (cf. Fig. 14.21A). As expected, the dilatancy angle decreases as the normal effective stress increases (cf. Fig. 14.21D inset). The failure envelope determines the peak angle of shear strength, φ' (cf. Fig. 14.21B). For a generic stress path, the peak envelope is reached when the ratio between the shear stress and normal effective stress is maximised. Because the normal effective stress is constant in this case, it is reached at the maximum shear stress (cf. Fig. 14.21A). The critical state strength is reached when the variation of the dilatancy component is zero. In the considered case, critical state

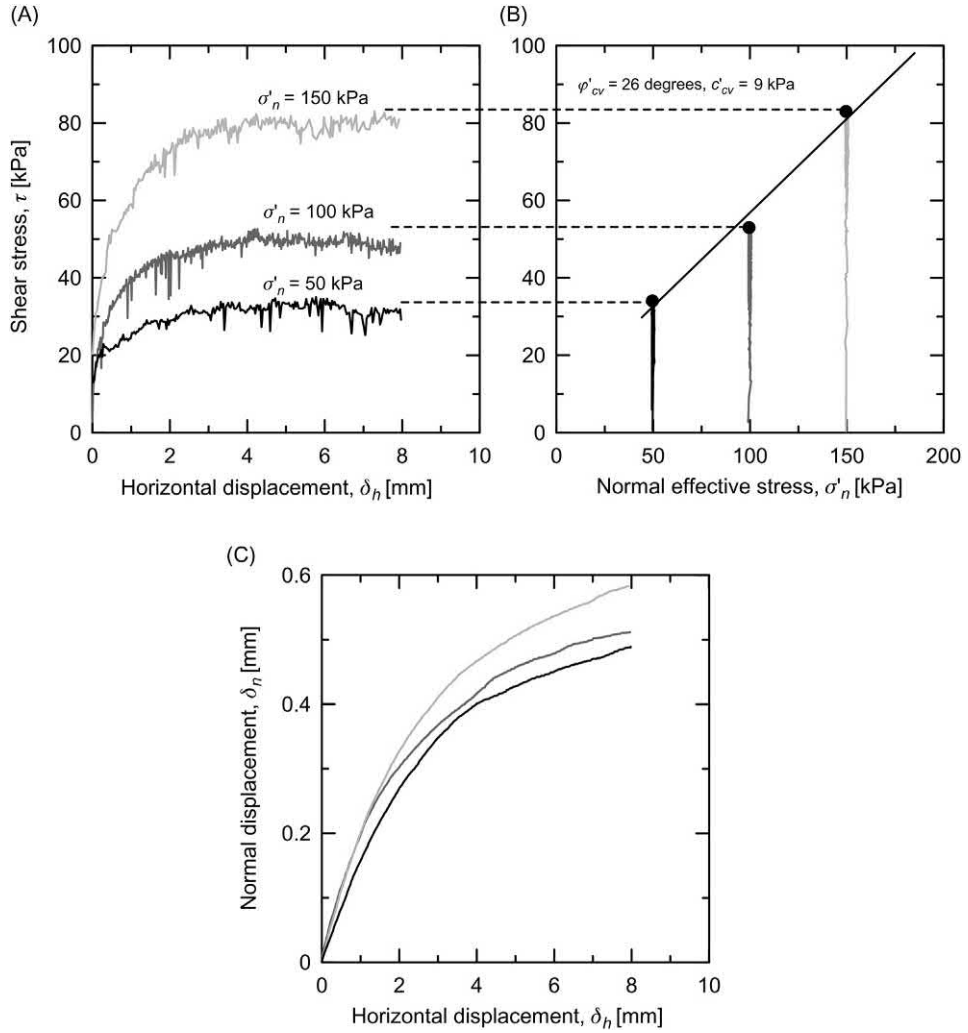

Figure 14.22 Illite clay response during direct shear testing: (A) shear stress – horizontal displacement plane; (B) Mohr plane; (C) volumetric behaviour. *Redrawn after Di Donna, A., Ferrari, A., Laloui, L., 2015. Experimental investigations of the soil–concrete interface: physical mechanisms, cyclic mobilisation and behaviour at different temperatures. Can. Geotech. J. 53 (4), 659–672.*

corresponds to a horizontal displacement of approximately 4 mm. The envelope described by the pair of normal and shear stress corresponding to critical state conditions determines the angle of shear strength under constant volume conditions, φ'_{cv} (cf. Fig. 14.21B). Associated with the previous values of angle of shear strength at the peak and under constant volume conditions are values of cohesion at the peak, c', and under constant volume conditions, c'_{cv}.

Table 14.10 Test results and design parameters achievable through thermal response tests (TRTs).

Testing technique	Test results/design parameters
Thermal response testing	Undisturbed ground temperature, T_0 Effective ground thermal conductivity, λ_{soil} Time-independent thermal resistance of heat exchanger, R'_{ghe}

For the clay−clay specimen (cf. Fig. 14.22), NC conditions are achieved after the consolidation phase and hence the results do not show any peak. Accordingly, the material contracts throughout the shear test and the failure envelope corresponds to critical state conditions.

14.9 Thermal response testing

14.9.1 General

Thermal response testing (often referred to as 'TRT') is an experimental in situ method for the characterisation of the geothermal potential of sites that can serve the energy design of energy geostructures. This test involves applying a prescribed thermal load to a geothermal heat exchanger and interpreting through a suitable heat transfer model the measured temperature evolution of the heat exchanger over time. The results and key thermal parameters that can be determined through a TRT are reported in Table 14.10.

14.9.2 Testing equipment

A module belonging to the family of TRT machines has been developed, for example by Mattsson et al. (2008). The module fits in a flight-case (cf. Fig. 14.23) and can be used to inject a heat rate of up to 9 kW at three different flow rates of up to 21 L/min. This minimodule is equipped with two heaters and one expansive vessel. The heater has a flow-regulating valve to maintain constant flow. A security system disrupts the heater in case of shortage of water where the pressure falls below 1 bar, caused by for example a breach in the tubes. High fluid pressures (e.g. greater than 3 bar) are released by a regulating valve. To protect the piping, a thermostat regulates the temperature by temporarily cutting the electrical power supply if the temperature exceeds 80°C. The heater has also a second thermal security system with an emergency switch-off at 95°C. After a switch-off, the system needs to be restarted manually. A pump is dedicated to the filling of the absorber pipes and pressurisation of the circuit. Another pump is used to circulate the heat carrier fluid (Mattsson et al., 2008). The module requires a 380 V power source with 16 or 32 A, depending on the power level reached during the tests. A modem and a data logger, connected with thermometers, pressuremeters and flowmeters, allow the temperatures inside and outside of

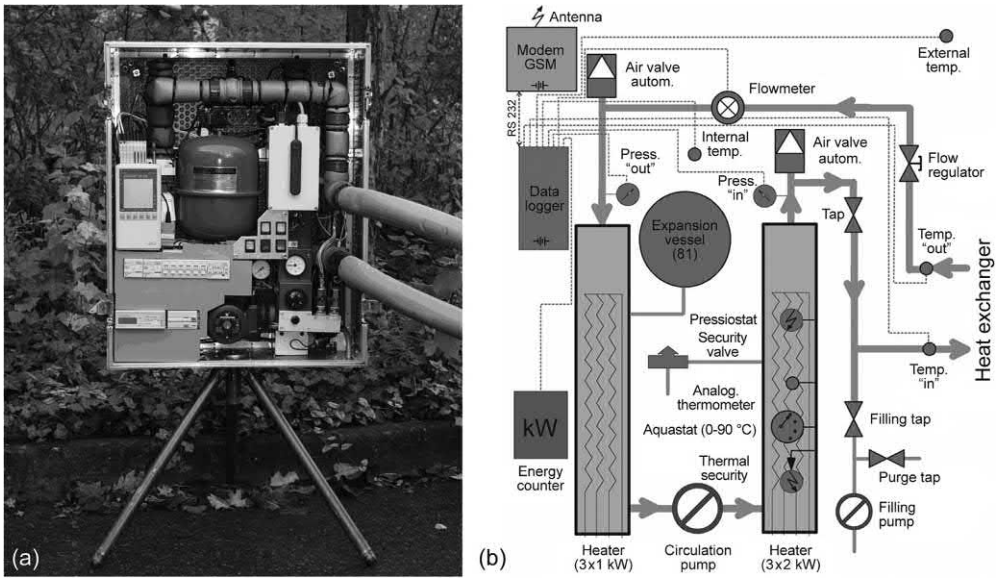

Figure 14.23 (A) Photograph and (B) schematic of the heating module. *Modified after Mattsson, N., Steinmann, G., Laloui, L., 2008. Advanced compact device for the in-situ determination of geothermal characteristics of soils. Energy Build. 40 (7), 1344–1352.*

the suitcase in which the module is placed, the inlet and outlet fluid temperatures in the pipes, the inlet and outlet fluid pressures, the flow rate, and the electrical consumption of the module to be recorded during the test. An electrical transformer installed within the module provides 220 V and 10 A of electricity to the sensors and data logger. Electrical outlets are also powered by the electrical transformer, allowing to connect a computer or other appliances. A sketch of a TRT setup is reported in Fig. 14.24. Key constituents of this setup include the TRT machine, a geothermal heat exchanger and a system of pipes allowing to connect the previous subjects, in addition to pumps, heaters and data loggers equipping the TRT.

14.9.3 Testing procedure

Different types of TRTs exist and can be classified depending on the following factors: (1) the operation mode of the TRT machine (i.e. heating or cooling), (2) the applied boundary conditions to the geothermal heat exchanger (i.e. constant heat flux or constant inflow temperature), (3) the considered analysis period (i.e. active phase or recovery phase) and (4) the employed measurement system (i.e. standard, distributed, or enhanced sensing). In any case, the following main testing phases can be summarised for TRTs:

1. *Formation of a closed system and pressurisation*: a closed circuit is formed between the TRT device and the pipes of the heat exchanger to be tested, and water (or any

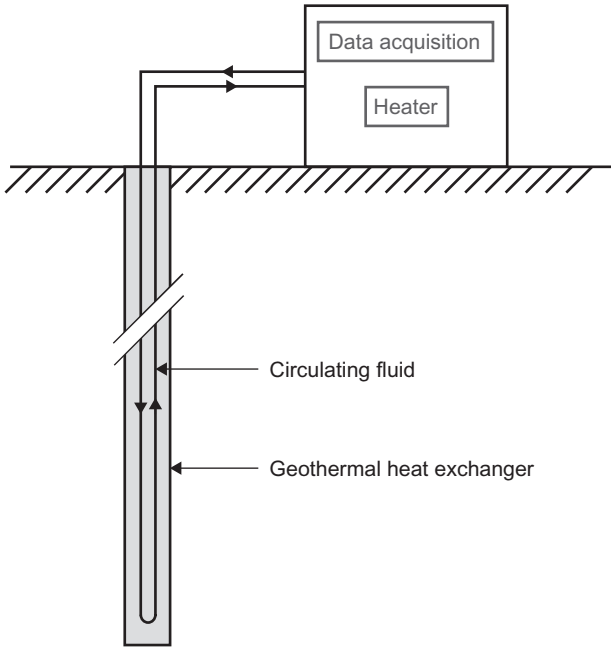

Figure 14.24 Sketch of a thermal response test (TRT) setup.

other heat carrier fluid envisaged to be used in the actual operation of the energy system) is pressurised in the circuit.

2. *Isothermal fluid circulation*: water (or the relevant heat carrier fluid) is pumped in the pipes without applying any thermal solicitation to the heat carrier fluid. Meanwhile, sensors allow measuring the inlet and outlet fluid temperatures. These measurements serve to estimate the initial undisturbed ground temperature.
3. *Thermal loading*: heating or cooling is applied through the TRT machine to impose either a fixed thermal power or a fixed inlet temperature over time to the heat carrier fluid circulating in the pipes of the geothermal heat exchanger. Meanwhile, sensors allow measuring the inlet and outlet fluid temperatures and pressures, electrical consumption of the heater and circulation pump, and air temperature close to the test location. These data serve to estimate the effective thermal conductivity of the ground and the thermal resistance of the heat exchanger.
4. *Thermal recovery*: once steady thermal conditions are achieved in the previous phase, the heating or cooling of the fluid is stopped and a natural recovering period for the temperature in the heat exchanger and the surrounding ground is achieved by pumping the heat carrier fluid in the pipes.
5. *Test completion and dismounting*: the closed system is opened, the pipes of the device are emptied and the device is stored.

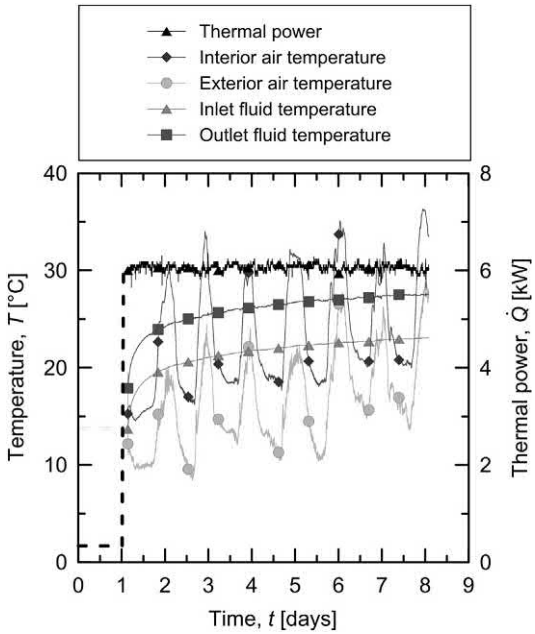

Figure 14.25 Evolution of variables recorded throughout a thermal response test. *Redrawn after Mattsson, N., Steinmann, G., Laloui, L., 2008. Advanced compact device for the in-situ determination of geothermal characteristics of soils. Energy Build. 40 (7), 1344–1352.*

An example of measured data during the phases (2–4) of a TRT is presented in Fig. 14.25 with reference to the result presented by Mattsson et al. (2008). The difference between the inlet and outlet fluid temperature is approximately constant over time due to the constant thermal power applied through the TRT machine. Comparison with the air temperature shows a negligible influence of the ambient conditions on the test results.

The execution of TRTs is recommended for installation capacities larger than 30 kW (VDI 4640, 2009). For smaller projects, laboratory testing is suggested. Examples of TRTs on energy geostructures have been reported by Hemmingway and Long (2013), Murphy et al. (2014), Loveridge et al. (2014b, c), Low et al. (2015), Park et al. (2015) and Alberdi and Poulsen (2015).

14.9.4 Testing recommendations

Recommendations for TRT of energy geostructures can be highlighted considering the guidance developed for borehole heat exchangers (ASHRAE, 2002; Ground Source Heat Pump Association, 2011; ISO 17628, 2015), the knowledge proposed with particular reference to energy piles (SIA-D0190, 2005; Ground Source Heat Pump Association, 2012; CFMS-SYNTEC-SOFFONS-FNTP, 2017) and the related

scientific investigations. In the following, recommendations for TRTs of energy piles characterised by a diameter lower than or equal to 300 mm are proposed, while TRTs of energy piles characterised by a greater diameter than 300 mm are disregarded. The reason for the previous approach is that the duration of TRTs required for steady conditions to be achieved within energy piles characterised by a diameter greater than 300 mm is significant and rapidly escalates beyond what is both economical and practical. For this reason, TRT is generally suggested for energy piles characterised by a diameter lower than or equal to 300 mm and at maximum of 450 mm (Loveridge et al., 2017). The development of TRTs on energy piles characterised by diameters exceeding the previous values could anyhow be performed by considering the following recommendations, while devoting great care to the selection of the interpretation method of the experimental results with reference to the geometry of the tested heat exchanger. A detailed laboratory characterisation of the site using core samples collected near the location of the TRT should be conducted to confirm the obtained results.

14.9.4.1 Test location

TRT must be carried out in the vicinity of the future construction and always in a location characterised by representative hydrogeological conditions (Poppei et al., 2008). The distance between the tested geothermal heat exchanger and the TRT machine should generally be smaller than 1.5 m. A heavy insulation of the pipes and the testing machine should be applied to ensure no influence of the ambient conditions on the test results (Ground Source Heat Pump Association, 2012).

14.9.4.2 Sensors

All sensors employed for the TRT should be tested and calibrated (Poppei et al., 2008). The ambient air temperature shall be monitored during the TRT to detect interference effects (Ground Source Heat Pump Association, 2012). The heat carrier fluid temperature should be measured in correspondence with the location where the pipes enter and exit the ground, respectively, unless thermal insulation of the runout length of the pipes is employed (Sanner et al., 2005). The TRT machine should allow to apply several thermal load steps and the flow rate of the circulation pump should be adjustable. Safety devices, for example against loss of flow or overheating, should be installed. Variables should be measured during the test at time intervals of 1–10 minutes (Vieira et al., 2017).

14.9.4.3 Geothermal heat exchanger features

The features of the tested geothermal heat exchanger should be as similar as possible to those of the heat exchanger to be constructed (Ground Source Heat Pump Association, 2012). The thermal conductivity of the grouting material should be greater than 1.30 W/(m °C) to overcome a significant thermal resistance at early stages

of the test. The use of a grouting material with a lower thermal conductivity influences the minimum test duration.

When grouting materials involving exothermic reactions (cementitious grouts) are employed in situ, a waiting period should be considered to ensure thermal equilibrium between the geothermal heat exchanger and the surrounding ground. Thermal equilibrium can be assumed if three sequential daily temperature measurements below the influence zone of daily temperature fluctuations (approximately of 5 m depth) show a maximum difference of 0.5°C (Ground Source Heat Pump Association, 2012). Normally, the test should not start until 21 days after the concrete has been poured (Ground Source Heat Pump Association, 2012). Shorter waiting periods may be considered if the temperature within the geothermal heat exchanger can be measured and thermal equilibrium is reached. Potentially, waiting periods ranging from 8 to 10 days could be considered.

14.9.4.4 Imposed physical variables

The pipe(s) may be filled with drinking water and in case of doubts regarding the quality of the water a biocide cleaning shall be used prior to testing (Ground Source Heat Pump Association, 2012). If the heat carrier fluid may possibly freeze, an antifreeze mixture of known volumetric heat capacity should be used. An air purging device should be installed to ensure that all air trapped in the pipes is removed (Sanner et al., 2005). The flow regime should be chosen as a function of the desired temperature difference of the fluid between the entrance and exit of the system (Poppei et al., 2008). The thermal load should be chosen in such a way that the temperature change in the system is as close as possible to the temperature variation expected from the future operating system, which can be calculated with an estimated thermal conductivity. For energy piles and other slender geothermal heat exchangers, these values normally range from 30 to 80 W/m (Sanner et al., 2005) or from 30 to 50 W/m (Poppei et al., 2008) for soil deposits characterised by low to high thermal conductivity, respectively. When a TRT machine involving the application of a fixed thermal power is employed, the delivered power should be defined in such a way that the expected temperature difference of the fluid between the inlet and outlet of the system is no less than 3°C for turbulent flow (Poppei et al., 2008), with an optimal interval of 3.7°C–7°C (Ground Source Heat Pump Association, 2012). If laminar flow is of interest, a maximum heating power has to be respected to avoid overheating. To avoid perturbations of the tests results because of free convection effects when a heating TRT is applied, the increase in temperature should not be greater than 30°C (Poppei et al., 2008).

14.9.4.5 Thermal loading duration

The required test duration to achieve steady conditions in energy piles is certainly longer compared to the duration characterising vertical borehole heat exchangers because

of geometrical considerations. While a test duration lasting more than 7 days is typically needed for TRTs on energy piles, 2–3 days represent the minimum test duration for TRTs on borehole heat exchangers (Vieira et al., 2017). The inferior time limit should be considered as $t = 5R^2/\alpha_{ghe}$ (Ground Source Heat Pump Association, 2012), where R is the heat exchanger radius and α_{ghe} is the thermal diffusivity of the filling material constituting the heat exchanger. Longer tests yield more accurate and reliable evaluation of the effective thermal conductivity and thermal resistance, not only because steady conditions are more likely to occur within the tested heat exchanger but also because the influence power and thermal fluctuations is reduced (Vieira et al., 2017).

14.9.4.6 Test repetition

In the case of a retest or of an interruption and restart of the test, a waiting period to allow the water in the pipes to naturally come back to the undisturbed ground temperature in a range of $\pm 0.3°C$ is needed (Ground Source Heat Pump Association, 2012).

14.9.5 Initial ground temperature determination

The undisturbed ground temperature is a key parameter for assessing the geothermal potential of sites. According to Vieira et al. (2017), the difference between the undisturbed ground temperature and the mean temperature of the heat carrier fluid circulating in the pipes of the geothermal heat exchanger leads to the heat transfer between the heat exchanger and the ground. Therefore the undisturbed ground temperature crucially characterises the sizing of geothermal heat exchangers, the extracted or injected thermal power and the performance of heat pumps, among other factors (MCS, 2013; Kavanaugh and Rafferty, 1997; Kurevija et al., 2014; Dehkordi and Schincariol, 2014; Radioti et al., 2017).

To estimate the undisturbed ground temperature via TRTs, two approaches may be considered: (1) the so-called fluid circulation method and (2) the downhole temperature logging method. While both of the previous approaches are effective, the downhole temperature logging method is not detailed in the following because it requires additional instrumentation in the TRT machine compared to the fluid circulation method (Spitler and Gehlin, 2015).

The fluid circulation method consists in circulating the heat carrier fluid in the pipes of the geothermal heat exchanger without imposing any thermal load; meanwhile, the fluid temperature is recorded through thermistors installed at the inlet and outlet of the TRT machine. In this context, three approaches can estimate the undisturbed ground temperature (Vieira et al., 2017):

1. Once the heat carrier fluid circulating in the pipes reaches thermal equilibrium with the surroundings (i.e. it reaches an approximately constant value representative of steady conditions), the outlet value of the stabilised fluid temperature is taken as an approximation of the undisturbed ground temperature;

2. Once the first circulation cycle of the heat carrier fluid is completed, the *minimum* value of the fluid temperature is selected and considered as an approximation of the undisturbed ground temperature;
3. Once the first circulation cycle of the heat carrier fluid is completed, the *average* value of the fluid temperature is selected and considered as an approximation of the undisturbed ground temperature;

According to Javed and Fahlén (2011) and Gehlin and Nordell (2003), the best way to estimate the undisturbed ground temperature is through approach (3), while approaches (1) and (2) are characterised by shortcomings. According to Vieira et al. (2017): when referring to approach (1), the undisturbed ground temperature value could be greatly influenced by ambient coupling and heat gains from the circulation pump; when referring to approach (2), the undisturbed ground temperature value could be strongly underestimated, especially with low ambient temperatures during the measurement.

14.9.6 Effective thermal conductivity and time-independent thermal resistance determination

The effective thermal conductivity of the ground and the time-independent thermal resistance are key parameters to assess the geothermal potential of sites and the thermohydraulic behaviour of geothermal heat exchangers, respectively. According to Vieira et al. (2017), lower values of thermal resistance lead to higher system performance, smaller ground heat exchanger size and lower installation costs.

To estimate the effective thermal conductivity of the ground and the time-independent thermal resistance of geothermal heat exchangers, two approaches may be considered: (1) direct evaluation methods and (2) parameter estimation methods. Direct evaluation methods are suggested for situations in which the extracted or injected thermal power from or in the geothermal heat exchanger is approximately constant throughout the test, with a standard deviation of the input power lower than $\pm 1.5\%$ of the mean input power and the maximum variation smaller than $\pm 10\%$ (Ashrae, 2007). Parameter estimation methods are suggested for situations in which the extracted or injected thermal power from or in the geothermal heat exchanger is considered inacceptable with direct evaluation methods. These approaches initially use estimated values of ground thermal conductivity and thermal resistance to simulate the heat carrier fluid temperature by accounting for variations in input power through stepwise-constant heat pulses rather than an overall constant input power.

Both direct evaluation and parameter estimation methods resort to analytical or semianalytical models and numerical models. The most common approach used to serve these methods for TRTs of vertical borehole heat exchangers or energy piles is the infinite line source model (Ingersoll et al., 1954; Carslaw and Jaeger, 1959). Applying the infinite line source model is recommended for times $t \geq 20R^2/\alpha_{d,ghe}$ that

is when steady conditions can be assumed to occur with a high accuracy *within* the geothermal heat exchanger. When the time $t = 5R^2/\alpha_{d,ghe}$ is considered as the lower limit for the interpretation of experimental results, a visual check of the obtained data should be carried out to ensure the appropriateness of the considered approach (Sanner et al., 2005).

The direct estimation of the thermal conductivity via the infinite line source model can be achieved by plotting the experimental measures of mean temperature of the heat carrier fluid circulating in the pipes of the geothermal heat exchanger against the logarithmic time. After the chosen reference time, the relationship between heat carrier fluid temperature and the logarithmic time is typically linear and can be fitted by a straight line. This relationship can be expressed as

$$\overline{T}_f = k_{sl} \ln t + m_{sl} \tag{14.26}$$

where $\overline{T}_f$ is the mean fluid temperature, k_{sl} is the slope of the straight line and m_{sl} is the intercept with the vertical axis. The slope of the considered straight line, k_{sl}, can be employed through the infinite line source model to determine the effective thermal conductivity of the ground as follows (Carslaw and Jaeger, 1959; Mogensen, 1983)

$$\lambda_{soil} = \frac{\dot{q}_l}{4\pi k_{sl}} \tag{14.27}$$

where $\dot{q}_l$ is the linear thermal power applied to the tested geothermal heat exchanger.

The determined value of λ_{soil} includes the influence of groundwater flow as well as of grouting, pipe and ground properties. Yet, this value represents an average of the thermal conductivity of any soil deposit over the entire length of the heat exchanger. The previous feature of λ_{soil} specifically applies to standard TRTs but it can be overcome through distributed and enhanced TRTs (i.e. these latter tests allow to measure variations of ground thermal conductivity along the entire length of the heat exchangers). In the presence of significant groundwater flow, attention must be made to the reliability of the estimated value of effective thermal conductivity. Due to the enhanced heat transfer between the heat carrier fluid and the ground, the evolution of heat carrier fluid temperature over time is inhibited by the presence of groundwater and results into a higher but inaccurate estimation of ground thermal conductivity that continuously increases with time (Vieira et al., 2017). The results of TRTs in these conditions can be analysed through the infinite moving line source model (see, e.g. Ingersoll et al., 1954) or other analytical or numerical models accounting for convection heat transfer (see, e.g. Diao et al., 2004; Raymond et al., 2011; Wagner et al., 2013).

Once the effective thermal conductivity of the ground is determined and the volumetric heat capacity of this medium is available, the variation in ground temperature for the relatively large reference times commented above can be calculated as follows (Carslaw and Jaeger, 1959)

$$\Delta T \approx \frac{\dot{q_l}}{4\pi\lambda_{soil}}\left[\ln\left(\frac{4\alpha_{d,soil}t}{R^2}\right) - \gamma_E\right] \tag{14.28}$$

where $\alpha_{d,soil}$ is the thermal diffusivity of the ground and γ_E is the Euler's constant.

Finally, the relationship between the temperature variation and the linear thermal power characterising the geothermal heat exchanger allows defining its time-independent thermal resistance. The thermal resistance can be calculated as follows (Beier and Smith, 2003)

$$R'_{ghe} = \frac{\Delta T}{\dot{q}_l} = \frac{1}{4\pi\lambda_{soil}}\left[\ln\left(\frac{4\alpha_{d,soil}t}{R^2}\right) - \gamma_E\right] \tag{14.29}$$

An example of the use of data measured during a TRTs to estimate the effective thermal conductivity of the ground and the thermal resistance of a geothermal heat exchanger is presented in Fig. 14.26 with reference to the results presented by Mattsson et al. (2008). The time-independent character of the thermal resistance can be appreciated considering its approximately constant value over the considered time.

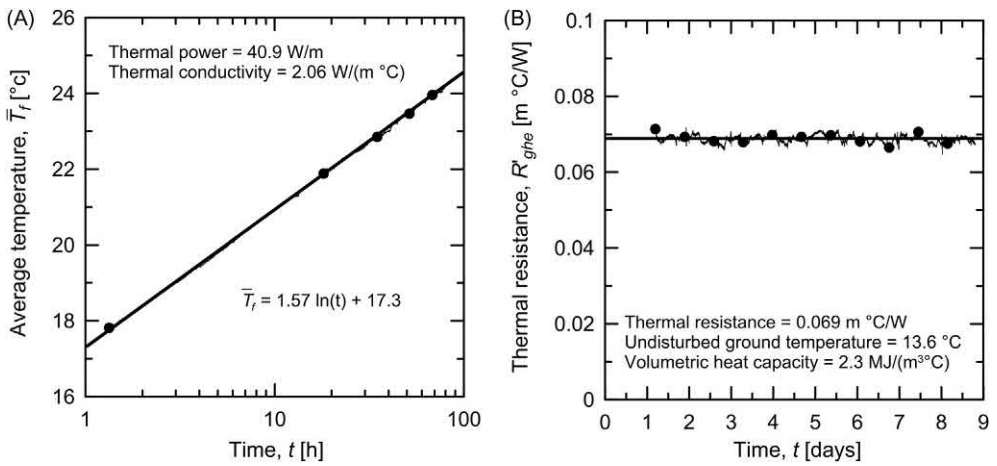

Figure 14.26 Evolution with time of (A) the mean heat carrier fluid temperature and (B) the thermal resistance of a geothermal heat exchanger. *Redrawn after Mattsson, N., Steinmann, G., Laloui, L., 2008. Advanced compact device for the in-situ determination of geothermal characteristics of soils. Energy Build. 40 (7), 1344–1352.*

Despite the infinite line source model represents the most widely used tool to interpret the results of TRTs, the accuracy of the interpretation of test results deriving from the application of this model decreases with the slenderness ratio of the tested geothermal heat exchanger. In fact, while the infinite line source assumption generally describes with accuracy the thermal response of geothermal heat exchangers such as vertical boreholes, it may be characterised by shortcomings to describe the thermal response of energy piles. The reason for the previous remark is associated with the different bluffness characterising vertical borehole heat exchangers and energy piles. According to Vieira et al. (2017), vertical borehole heat exchangers are characterised by slenderness ratios from 100 to 1500, whereas energy piles are characterised by slenderness rations typically smaller than 50. Therefore besides the longer time required to achieve steady conditions within energy piles compared to boreholes for the same thermal solicitation applied, the hypothesis of a log-linear thermal response of the heat exchanger with time that is assumed by the line source model may no more hold. For energy piles characterised by low slenderness ratios, the commented thermal response never truly occurs (Vieira et al., 2017). The reason for the previous result is because three-dimensional effects caused by variations of the thermal conditions at the surface and at the edges of the heat exchanger cause the actual thermal response of energy piles to diverge from that described by the infinite line source model (Loveridge and Powrie, 2013). According to Vieira et al. (2017), these effects imply that the measured temperatures always fall below the line source modelled temperatures, such an aspect further leading to a systematic overestimate of the thermal conductivity by analyses resorting to the infinite line source model.

To overcome the previous limitations, other more appropriate models and methods can be used. These include (1) analytical models, such as the line and cylindrical source finite models proposed by Ingersoll et al. (1954), Carslaw and Jaeger (1959) and Claesson and Hellström (2011), the composite cylindrical models presented by Bandos et al. (2009) and Hu et al. (2014) and the infinite solid cylindrical models developed by Li and Lai (2015) and Man et al. (2010); (2) semianalytical models, such as those described by Maragna and Rachez (2015); (3) semiempirical functions (i.e. G-functions), such as those proposed by Loveridge and Powrie (2013) and (4) two- or three-dimensional numerical models, such as those employed by Franco et al. (2016), Park et al. (2013), Cecinato et al. (2015) and Cecinato and Loveridge (2015).

14.9.7 Analysis of paired values of λ_{soil} and R'_{ghe}

According to Marcotte and Pasquier (2008), more than one combination of the values of ground thermal conductivity and time-independent thermal resistance can match the experimental results of TRTs. Because the influence of these parameters on the actual thermal response of geothermal heat exchangers is counterbalanced

(Javed et al., 2011), it is always preferable to use in analysis and design the pairs of λ_{soil} and R'_{ghe} estimated by the results of the TRT, and not only one of the two parameters. This approach allows mitigating the effect of a poor estimation of the values of λ_{soil} and R'_{ghe}. Analytical, semianalytical and numerical approaches are available to estimate the thermal resistance of geothermal heat exchangers and may be considered to check the validity of the value of this parameter estimated through the results of TRTs (Vieira et al., 2017).

14.9.8 From geothermal potential of sites to actual energy performance

The estimation of the effective thermal conductivity of the ground through TRTs (or other complementary approaches such as experimental laboratory tests), together with the hydraulic conductivity and the Darcy's velocity characterising any given site, allows making considerations about the attractiveness of a geothermal application. According to the SIA-D0190 (2005), values of $\lambda_{soil} \leq 1.5$ W/(m °C) may result in economically ineffective applications of geothermal heat exchangers. Greater values of λ_{soil} should generally provide particularly adequate conditions to apply the considered energy systems.

Depending on the value of effective thermal conductivity of the ground and the Darcy's velocity, preliminary considerations about the thermal power that can be harvested from energy geostructures can also be performed. A chart for performing the previous considerations, initially developed by Fromentin et al. (1999) and subsequently reported in the SIA-D0190 (2005), is reproduced in Fig. 14.27. While providing relevant information, the considered chart should only be used to address energy piles and no other energy geostructures. Furthermore, while being useful to develop preliminary considerations about the geothermal potential associated with energy pile applications, such a chart fails in considering the actual performance of energy piles, which must be specifically addressed on a case-by-case basis. In fact, the same site can result in markedly different energy performances of the same energy geostructure, simply because of different design solutions adopted for these heat exchangers (e.g. pipe layout, flow rate of the heat carrier fluid circulating in the pipes, etc.) (see, e.g. Batini et al., 2015). In other words, although charts of the previous type provide relevant information to carry out preliminary designs, they should not be considered representative of the actual energy performance of energy geostructure applications.

14.10 Load testing under nonisothermal conditions

14.10.1 General

Load testing under nonisothermal conditions is an experimental in situ method for the characterisation of the load–displacement relationship of geostructures that can serve

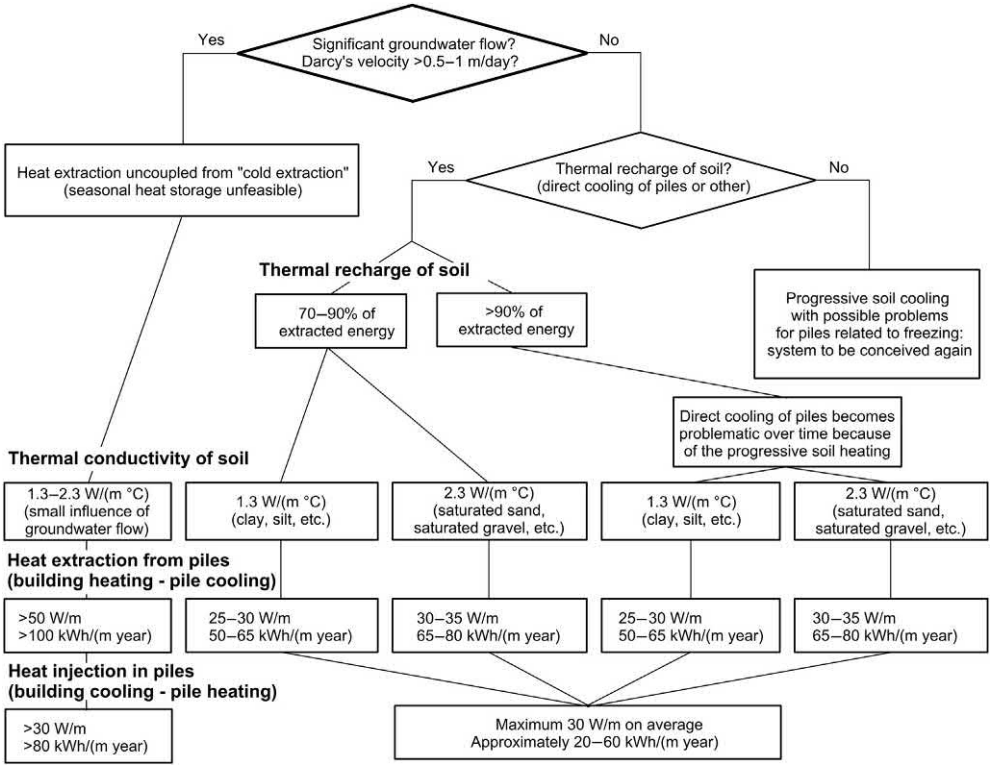

Figure 14.27 Chart addressing the geothermal potential of energy pile applications depending on the site conditions. *Redrawn after Fromentin, A., Pahud, D., Laloui, L., Moreni, M., 1999. Pieux échangeurs: conception et règles de pré—dimensionnement. Rev. Franç. Gén. Civ. 3 (6), 387–421.*

the geotechnical and structural design as well as the monitoring of energy geostructures. This test involves applying combinations of mechanical and thermal loads to energy geostructures and measuring the resulting variations of temperature, strain, stress, displacement in such structures and the surrounding ground. Measurements of pore water pressure in the ground can also be achieved. The results and key mechanical parameter that can be determined through full-scale load tests are reported in Table 14.11.

Different types of thermomechanical load tests exist and can be classified depending on whether these tests address (1) the deformation of energy geostructures under the combined influence of mechanical and thermal loading or (2) the failure of such structures caused by the influence of mechanical loading, applied alone or in conjunction with thermal loading. Examples of load tests performed on energy geostructures have been reported, for instance, by Laloui et al. (2003), Bourne-Webb et al. (2009), McCartney and Murphy (2012), Wang et al. (2014), Akrouch et al. (2014), Murphy

Table 14.11 Test results and key design parameters achievable through load tests under nonisothermal conditions.

Testing technique	Test results	Design parameters
Load testing under nonisothermal conditions	Load–settlement curve Strain variations, $\Delta\varepsilon$ Temperature variations, ΔT Stress variations, $\Delta\sigma$ Pore water pressure variations, Δp_w Displacement variations, Δw	Load capacity, Q_u

and McCartney (2015), Murphy et al. (2015), Sutman et al. (2015, 2017), You et al. (2016), Luo et al. (2017), Chen et al. (2017), Allani et al. (2017) and McCartney and Murphy (2017).

14.10.2 Testing equipment

A dedicated equipment and instrumentation for the load testing of energy geostructures have been employed, for example by Laloui et al. (2003) and by Mimouni and Laloui (2015). The considered testing equipment and instrumentation have been used in the context of load tests on energy piles but they may also be used to address the response of other energy geostructures.

In the experimental campaign by Laloui et al. (2003), the response of a single energy pile located on the edge of a pile foundation supporting a four-storey building under construction at the Swiss Federal Institute of Technology in Lausanne (EPFL) has been investigated (cf. Fig. 14.28A). The building of the test site has a length of 100 m and a width of 30 m and was constructed on 97 piles of approximately 25 m in length. The tested energy pile is a predominantly end-bearing, nondisplacement pile made of reinforced concrete with a diameter of $D = 0.88$ m and a length of $L = 25.8$ m, which is equipped with a U-shaped configuration of polyethylene pipes along its reinforcing cage (cf. Fig. 14.28B). The soil stratigraphy at the considered site consists in a layered deposit made of two alluvial layers (from a depth of $z = 0–5.5$ m and from $z = 5.5–12$ m), two moraine layers (from $z = 12–22$ m and from $z = 22–25$ m) and a sandstone bedrock (from $z = 2$ m on below the pile toe) (cf. Fig. 14.28C). The groundwater table in this zone is located at the surface. Relevant materials properties reported by Laloui et al. (2003, 2006) for this site are summarised in Tables 14.12 and 14.13 [with updated values than those suggested by Laloui et al. (2006)].

In the experimental campaign by Mimouni and Laloui (2015), the response of a group of energy piles located on the edge of a pile foundation supporting a 9×25 m^2 water retention tank under the Swiss Tech Convention Centre of the EPFL has been

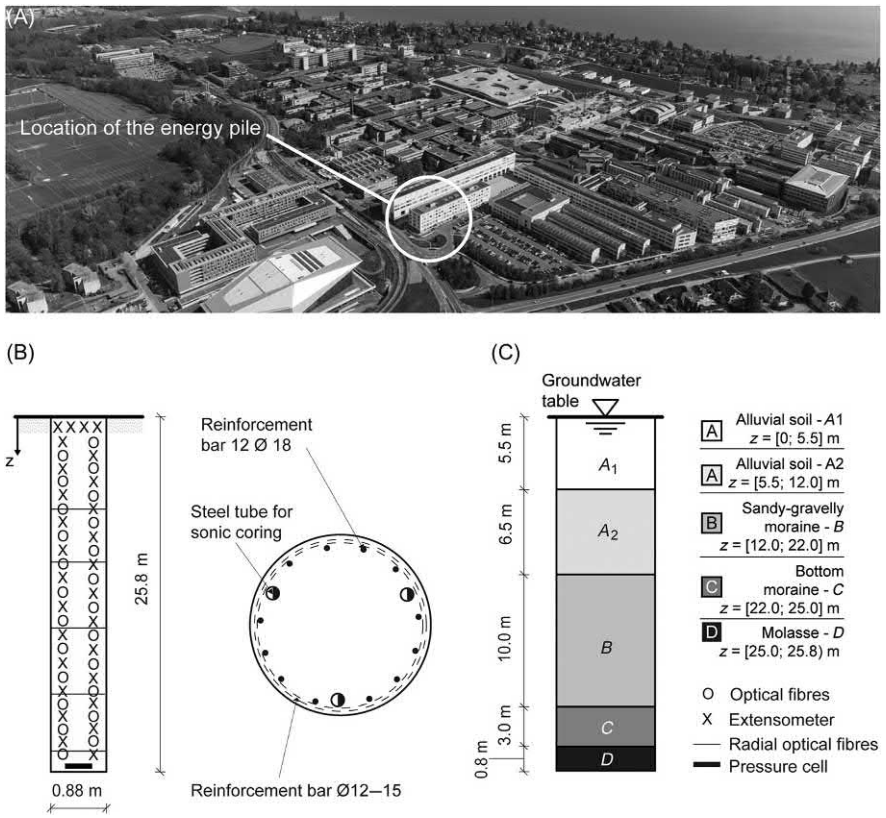

Figure 14.28 (A) View of the Lausanne single energy pile test site; (B) vertical cross-sections depicting the monitoring instrumentation that was installed in the energy pile; (C) schematic diagram of the soil stratigraphy. Views not to scale. *Redrawn after Laloui, L., Moreni, M., Vulliet, L., 2003. Comportement d'un pieu bi-fonction, fondation et échangeur de chaleur. Can. Geotech. J. 40 (2), 388-402.*

Table 14.12 Material properties of the energy pile tested by Laloui et al. (2003).

	Energy pile
Young's modulus, E [GPa]	29.2
Poisson's ratio, ν [−]	0.16
Bulk density, ρ [kg/m^3]	2500
Linear thermal expansion coefficient, α [1/°C]	1.0×10^{-5}
Thermal conductivity, λ [W/(m °C)]	2.1
Volumetric heat capacity, ρc_p [J/(m^3 °C)]	2.0×10^6

investigated (cf. Fig. 14.29A). The foundation comprises a group of four predominantly end-bearing energy piles (labelled EP1, EP2, EP3 and EP4 in Fig. 14.29B) and sixteen predominantly floating conventional piles (labelled P1-16 in Fig. 14.29B) below a heavily reinforced 0.9 m-thick slab. The energy piles are 28 m long and

Table 14.13 Material properties of the soil layers embedding the energy pile tested by Laloui et al. (2003).

	Soil layers				
	A1	**A2**	**B**	**C**	**D**
Young's modulus, E [MPa]	190	190	84	90	3000
Poisson's ratio, ν [−]	0.22	0.22	0.4	0.4	0.3
Bulk density, ρ [kg/m^3]	2769	2769	2735	2740	2556
Porosity, n [−]	0.1	0.1	0.35	0.3	0.1
Peak angle of shear strength, φ' [degrees]	30	27	23	27	–
Cohesion, c' [kPa]	5	3	6	20	–
Linear thermal expansion coefficient, α [1/°C]	3.3×10^{-6}	3.3×10^{-6}	3.3×10^{-5}	3.3×10^{-5}	3.3×10^{-7}
Thermal conductivity, λ [W/(m °C)]	1.8	1.8	1.8	1.8	1.1
Volumetric heat capacity, ρc_p [J/(m^3 °C)]	2.4×10^6	2.4×10^6	2.4×10^6	2.4×10^6	2.0×10^6
Hydraulic conductivity, k [m/s]	2×10^{-6}	7×10^{-7}	1×10^{-6}	1×10^{-6}	–

0.9 m in diameter, and the conventional piles are 16 m long and 0.6 m in diameter (cf. Fig. 14.29C). All of the piles are nondisplacement piles (bored and cast onsite) made of reinforced concrete. The energy piles were equipped with four 24-m-long high-density polyethylene U-loops that are connected in series. The inlets and outlets of the absorber pipes were thermally insulated to a depth of 4 m below the pile heads to limit the influence of the climatic conditions on the heat exchange process. The soil stratigraphy of the site (cf. Fig. 14.29D) consists of an upper soil profile of the alluvial soil reaching a depth from the uppermost surface of the successively built slab of $z = 8.6$ m., a lower sandy-gravelly moraine layer located between depths of $z = 8.6$ and 16.6 m (Laloui et al., 2003, 2006), a thin layer of bottom moraine between depths of $z = 16.6$ and 20.1 m and a bottom molasse layer. Relevant material properties reported by Rotta Loria and Laloui (2017) and Rotta Loria and Laloui (2018) for this site are summarised in Table 14.14.

In both of the previous tests, the heating module developed by Mattsson et al. (2008) was employed to apply thermal loading, while mechanical loading resulted

Table 14.14 Material properties of the energy pile foundation tested by Rotta Loria and Laloui (2017, 2018).

Material	Young's modulus, E [MPa]	Poisson's ratio, ν [–]	Volumetric heat capacity, ρc_p [kJ/(m^3 °C)]	Thermal conductivity, λ [W/(m °C)]	Linear thermal expansion coefficient, α [1/°C]
Soil layer A – alluvial soil	190	0.22	2612	1.40	3.3×10^{-6}
Soil layer B – sandy-gravelly moraine	84	0.4	3047	2.60	3.3×10^{-6}
Soil layer C – bottom moraine	90	0.4	2963	2.60	3.3×10^{-6}
Soil layer D – molasse (i.e. sandstone)	3000	0.3	2219	3.50	2.3×10^{-5}
Piles	28,000	0.25	2050	1.47	1×10^{-5}
Slab	35,000	0.25	2050	1.47	1×10^{-5}
Pipes	–	–	–	0.42	–

from the weight of the structure present above the foundation. In the test of Laloui et al. (2003), the energy pile was instrumented with the following instrumentation: vibrating wire strain gauges and thermocouples, optical fibres, and extensometers located along the pile length; and pressure cells located at the pile toe. In the test of Mimouni and Laloui (2015), the energy piles were instrumented with the following instrumentation: vibrating wire strain gauges and thermocouples, and optical fibres located along the pile length; pressure cells located at the pile toe; and piezometers, thermistors and borehole extensometers located in the soil. The previous instruments are examples of sensors that allow the thermomechanical response of energy geostructures to be monitored when addressing simulated or actual geothermal and structural support operations.

14.10.3 Strain and temperature determination along energy geostructures

Determining strains and temperature variations in energy geostructures is paramount to develop considerations related to both the mechanical and thermal behaviour of such structures, respectively. From the knowledge of the strains caused by the mechanical and thermal loads applied to energy geostructures, mathematical developments can provide estimations of the stresses characterising such structures that in turn lead further insights in their thermomechanical behaviour.

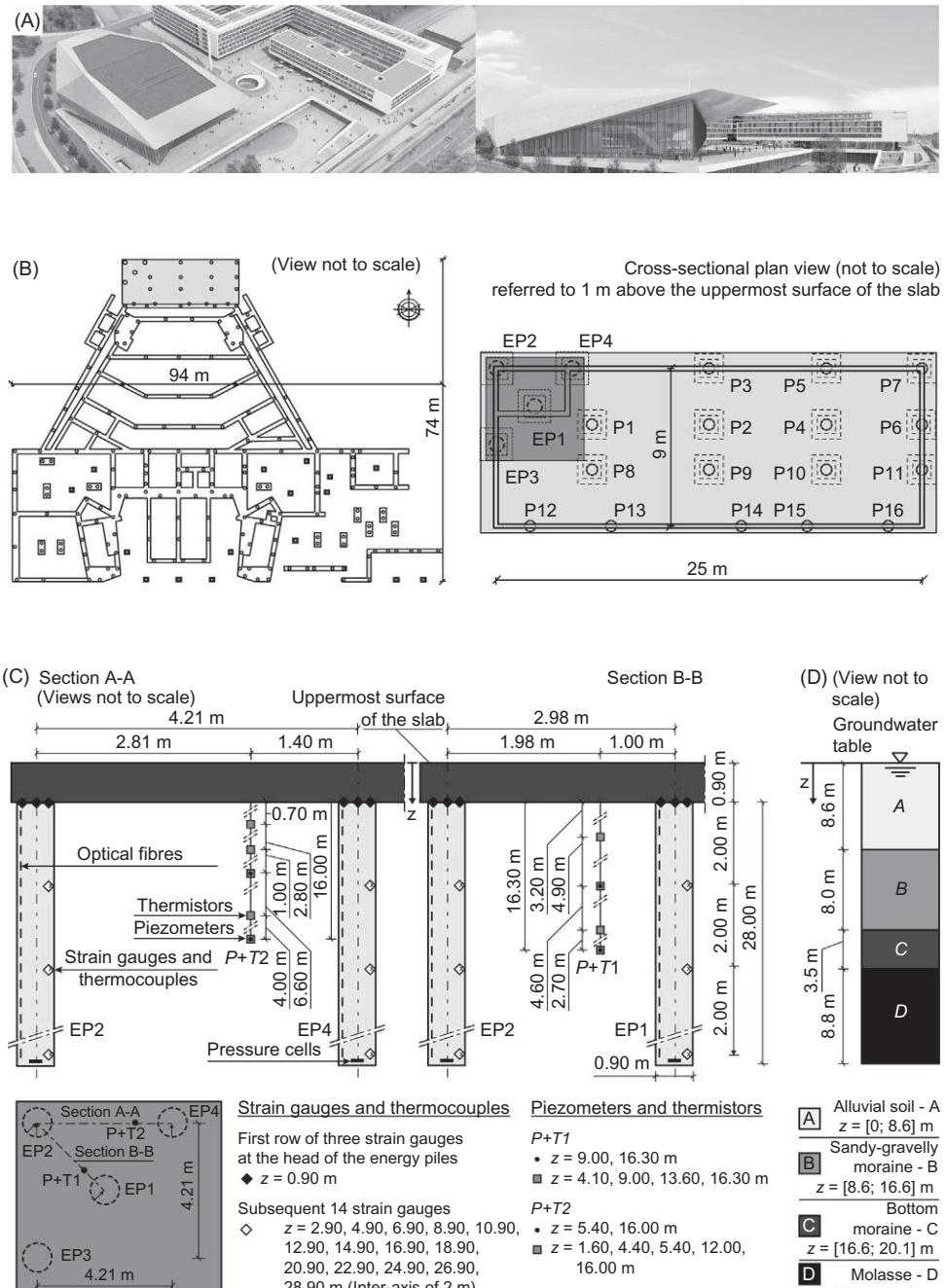

Figure 14.29 (A) The EPFL Swiss Tech Convention Centre foundation (modified from the original image, courtesy of Richter Dahl Rocha & Associés architects SA); (B) plan view of the foundation; (C) vertical cross-sections depicting the monitoring instrumentation that was installed in the energy piles and soil; (D) schematic diagram of the soil stratigraphy. Views not to scale. *Modified after Rotta Loria, A.F., Laloui, L., 2017. Thermally induced group effects among energy piles. Geotechnique 67 (5), 374–393.*

Measuring strains can be achieved with two types of sensors: optical fibres and strain gauges. Measuring temperature can be achieved with thermistors. Both optical fibres and strain gauges can be considered to provide reliable measurements of strain (Mimouni and Laloui, 2013). However, strain measurements through optical fibres typically require more logistics (i.e. a relatively large dedicated reading unit plus a computer to operate it) than those via vibrating wire strain gauges (i.e. a small and relatively simple reading unit). The SOFO system of optical fibres from SMARTEC/Roctest and the vibrating wire strain gauges C 110 from TELEMAC are two types of the aforementioned sensors.

Optical fibres systems of the SOFO type are based on the comparison of a signal travelling along a reference fibre and a measuring fibre (Mimouni and Laloui, 2013). These fibres can be fixed along the reinforcing cage of energy geostructure to measure relevant strains. When applied to energy piles, for example these sensors allow measuring both vertical and radial strains. As optical fibres are delivered with anchors already mounted on the sensor body, tie wires or plastic ties need to be used to attach them along the rebar of the reinforcing cages (cf. Fig. 14.30). The fibres must be attached with an initial tension to avoid their loosening after the mechanical compression of

Figure 14.30 Attachment of optical fibres to the reinforcing cage of an energy pile to measure its radial strains.

the geostructure (Mimouni and Laloui, 2013). The reference fibre is long enough so that it never undergoes to tension. Therefore strains of the reference fibre are only caused by temperature variations and the system is autocorrected in temperature because the reference fibre is under the same conditions as the measuring fibre (Glišić and Simon, 2000; Lloret et al., 2000; Inaudi et al., 2000). A dedicated reading unit with a pilot computer allows the lengthening of the optical fibre, Δl_{OF}, to be measured during the test without any further data treatment. The vertical strain variations, $\Delta\varepsilon_z$, are determined as

$$\Delta\varepsilon_z = -\frac{\Delta l_{OF}}{l_{OF}} \tag{14.30}$$

where l_{OF} is the initial length of the fibre. Assuming a homogeneous radial deformation field in a circular cross-section, radial strain variations, $\Delta\varepsilon_r$, are similarly determined as

$$\Delta\varepsilon_r = -\frac{\Delta l_{OF}}{l_{OF}} \tag{14.31}$$

Vibrating wire strain gauges of the type TELEMAC are based on the concept of measuring the resonant frequency and temperature of a vibrating tensioned wire to determine its strain (an increase in the tension of the wire increases the resonant frequency). In the TELEMAC system, a 3 kΩ thermistor is included in each strain gauge to correct for the effect of temperature variations. Similar to the optical fibres, vibrating wire strain gauges can also be fixed to the reinforcing cage of energy geostructures. The wire needs to be attached perpendicular to the gauge axes to avoid measuring the axial strain of the frame (Mimouni and Laloui, 2013). The frames need to be designed to fit exactly in between the rebar of the reinforcing cages and can subsequently attached to the reinforcing cages with wire ties (cf. Fig. 14.31). This approach allows saving a substantial amount of time on site and provides a reliable attachment of the sensors (Mimouni and Laloui, 2013). The gauge outputs are the resonant frequency of the vibrating wire and its temperature. Therefore data processing is required. The vertical strain variations, $\Delta\varepsilon_z$, can be calculated based on the recorded values of the wire frequency and temperature as

$$\Delta\varepsilon_z = \frac{K_g}{1000}\left(F^2 - F_0^2\right) + \alpha_{wire}(T - T_0) \tag{14.32}$$

where K_g is a gauge factor that is provided by the sensor supplier that depends on the wire characteristics, F and F_0 are the wire resonant frequencies at the actual (t) and reference (t_0) times, respectively, α_{wire} is the linear thermal expansion coefficient of the wire (11.5 με/°C) and T and T_0 are the actual and reference wire temperatures, respectively.

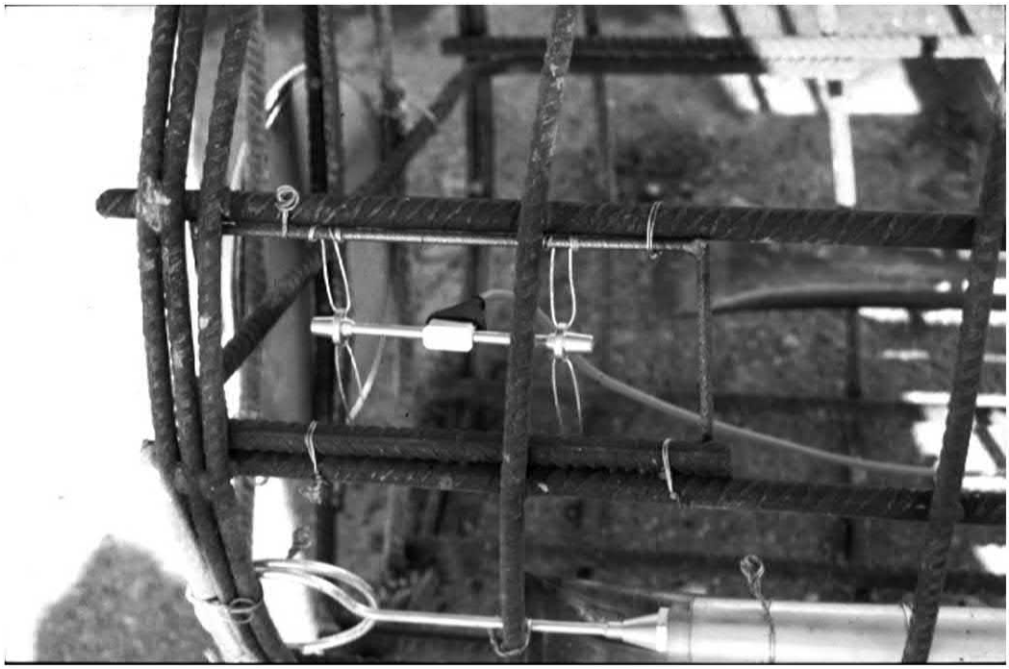

Figure 14.31 Attachment of vibrating wire strain gauges to the reinforcing cage of an energy pile to measure its vertical strains.

14.10.4 Stress determination in energy geostructures

Determining stresses caused by mechanical and thermal loads in energy geostructures is key to develop considerations related to the thermomechanical behaviour of such structures. When dealing with three-dimensional problems whose geometry can be appropriately simplified through one- or two-dimensional geometries, stresses may in principle be calculated through the theory of thermoelasticity starting from the strains. Otherwise, stresses may also be determined through specific instrumentation.

Pressure cells with vibrating wire transducers allow variations in the vertical stress to be monitored at targeted locations. The HVC pressure cells from SMARTEC are one type of these systems. The installation of this type of cells is challenging because shrinkage of the concrete might degrade the contact between the cell and the surroundings even if the cell may be attached to a welded cross-section (Mimouni and Laloui, 2013). An application example of pressure cells to energy piles is reported in Fig. 14.32. Pressurisation tubes are available to inflate the cell when concrete shrinkage is deemed to be important but having such a tube along the whole length of the geostructure can present several additional challenges. Precasting the cells within a mass of concrete and then inflating them before installing the block at the toe of the

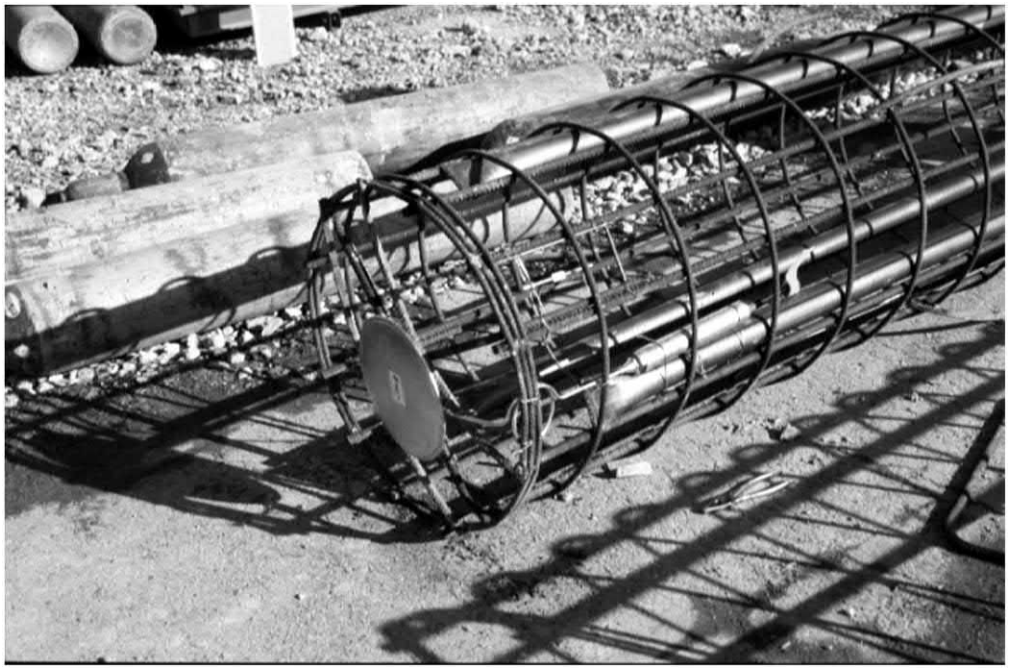

Figure 14.32 Pressure cell installed at the toe of an energy pile to measure vertical stress variations.

reinforcing cages can be markedly time consuming (Mimouni and Laloui, 2013). One solution adopted to overcome these difficulties can be to pour some concrete into the bottom of the boreholes using a pit tube and to push the reinforcing cages, with the cells attached at their base, into the fresh concrete. The vertical stress variations can be determined as

$$\Delta\sigma_z = A^* \frac{K_g^2}{1000^2}\left(F^4 - F_0^4\right) + B^* \frac{K_g}{1000}\left(F^2 - F_0^2\right) - C^*(T - T_0) \tag{14.33}$$

where A^*, B^* and C^* are calibration factors that are provided by the sensor supplier.

14.10.5 Pore water pressure and temperature determination in the ground

Determining pore water pressures in the ground may be particularly relevant to address the hydromechanical behaviour of the ground surrounding energy geostructures (concept of effective stress) when encountering stiff soil deposits in which the influence of the applied loads may affect the pore water pressure field. Determining temperature variations in the ground is particularly relevant to address the thermal behaviour of energy

geostructures as well as to address the mechanical response of such structures through the understanding of the sensitivity to loading (e.g. thermal) of the deposit.

Piezometers and thermistors allow temperature and pore water pressure variations in the ground to be measured. The piezometers PWS with stainless steel filters from Roctest and thermistors TH-T from Roctest are two types of these sensors. Both the piezometers and thermistors can be deployed in boreholes filled with a mixture of coarse- and fine-grained soil. Thermistors must be used with the piezometers because the latter employ vibrating wire transducers that require temperature corrections due to the nonisothermal conditions involved with the geothermal operation of energy geostructures. The pore water pressure variations can be calculated as

$$\Delta p_w = A^* \frac{K_g^2}{1000^2}\left(F^4 - F_0^4\right) + B^* \frac{K_g}{1000}\left(F^2 - F_0^2\right) - C^*(T - T_0) \tag{14.34}$$

where A^*, B^* and C^* are calibration factors that are provided by the sensor supplier.

14.10.6 Displacement determination in the soil

Assessing the magnitude of displacements caused by the loading of the energy geostructures is another key point for addressing the thermohydromechanical behaviour of such structures. Displacements of primary interest are usually those of the geostructure itself. However, ground displacements can also be of interest.

LVDTs can be employed to measure the displacement of energy geostructures. Extensometers allow ground displacements to be measured. The borehole extensometers BOR-EX from Roctest are one type of these latter sensors. Extensometers can be put in place via boreholes to be filled with adequate material. Rebar anchors located at different depths and linked to a reference plate (e.g. made of stainless steel rods) may be used to measure the displacements (Mimouni and Laloui, 2013).

References

Akrouch, G.A., Sánchez, M., Briaud, J.-L., 2014. Thermo-mechanical behavior of energy piles in high plasticity clays. Acta Geotech. 9 (3), 399–412.

Alberdi, M., Poulsen, S.E., 2015. Thermal response testing and performance of quadratic cross section energy piles (Vejle, Denmark).

Allani, M., Van Lysebetten, G., Huybrechts, N., 2017. Experimental and numerical study of the thermo-mechanical behaviour of energy piles for Belgian practice, Advances in Laboratory Testing and Modelling of Soils and Shales, vol. 1. Springer, pp. 405–412.

Alrtimi, A., Rouainia, M., Manning, D., 2014. An improved steady-state apparatus for measuring thermal conductivity of soils. Int. J. Heat Mass Transf. 72, 630–636.

ASHRAE, 2002. Methods for Determining soil and Rock Formation Thermal Properties from Field Tests. American Society of Heating, Refrigerating and Air-Conditioning Engineers, p. 6.

Ashrae, A.H., 2007. HVAC Applications. Inch-Pound Edition.

ASTM C177, 2010. Standard Test Method for Steady State Heat Flux Measurements and Thermal Transmission Properties by Means of the Guarded Hot Plate Apparatus. ASTM, West Conshohocken.
ASTM D2435, 2004. Test Methods for One-Dimensional Consolidation Properties of Soils Using Incremental Loading. ASTM International, West Conshohocken.
ASTM D2850-03a, 2850. Standard Test Method for Unconsolidated-Undrained Triaxial Compression Test for Cohesive Soils. ASTM International, West Conshohocken.
ASTM D3080/D3080M, 2011. Standard Test Method for Direct Shear Test of Soils Under Consolidated Drained Conditions. ASTM International, West Conshohocken, United States of America.
ASTM D4767, 2011. Standard Test Method for Consolidated Undrained Triaxial Compression Test for Cohesive Soils. ASTM International, West Conshohocken.
ASTM D7181, 2011. Standard Test Method for Consolidated Drained Triaxial Compression Test for Soils. ASTM International, West Conshohocken.
ASTM E1225, 2013. Standard Test Method for Thermal Conductivity of Solids Using the Guarded-Comparative-Longitudinal Heat Flow Technique. ASTM International, West Conshohocken.
Austin, W.A., 1998. Development of an In Situ System for Measuring Ground Thermal Properties (Ph. D. thesis), Oklahoma State University, Stillwater.
Baldi, G., Hueckel, T., Pellegrini, R., 1988. Thermal volume changes of the mineral water-system in low-porosity clay soils. Can. Geotech. J. 25 (4), 807–825.
Bandos, T.V., Montero, Á., Fernández, E., Santander, J.L.G., Isidro, J.M., Pérez, J., et al., 2009. Finite line-source model for borehole heat exchangers: effect of vertical temperature variations. Geothermics 38 (2), 263–270.
Barry-Macaulay, D., Bouazza, A., Singh, R., Wang, B., Ranjith, P., 2013. Thermal conductivity of soils and rocks from the Melbourne (Australia) region. Eng. Geol. 164, 131–138.
Batini, N., Rotta Loria, A.F., Conti, P., Testi, D., Grassi, W., Laloui, L., 2015. Energy and geotechnical behaviour of energy piles for different design solutions. Appl. Therm. Eng. 86 (1), 199–213.
Beier, R.A., Smith, M.D., 2003. Minimum duration of in-situ tests on vertical boreholes. ASHRAE Transactions 109, 475.
Bishop, M.A., Henkel, D.J., 1957. The Measurement of Soil Properties in the Triaxial Test. Edward Arnold Ltd.
Blackwell, J., 1954. A transient-flow method for determination of thermal constants of insulating materials in bulk part I—theory. J. Appl. Phys. 25 (2), 137–144.
Bolton, M.D., 2003. A Guide to Soil Mechanics. MacMillan Press.
Bond, A.J., Schuppener, B., Scarpelli, G., Orr, T.L., Dimova, S., Nikolova, B., Pinto, A.V., 2013. Eurocode 7: geotechnical design worked examples. In: Worked Examples Presented at the Workshop "Eurocode 7: Geotechnical Design", Dublin, Ireland.
Bourne-Webb, P.J., Amatya, B.L., Soga, K., Amis, T., Davidson, C., Payne, P., 2009. Energy pile test at Lambeth College, London: geotechnical and thermodynamic aspects of pile response to heat cycles. Geotechnique 59 (3), 237–248.
Brandl, H., 2006. Energy foundations and other thermo-active ground structures. Geotechnique 56 (2), 81–122.
BS 1377-1, 1990. Methods of Test for Soils for civil engineering purposes. General Requirements and Sample Preparation. British Standards Institution (BSI).
Burmister, D.M., 1951. Soil Mechanics. Columbia University, Department of Civil Engineering.
Campanella, R.G., Mitchell, J.K., 1968. Influence of the temperature variations on soil behaviour. J. Soil Mech. Found. Eng. Div. ASCE 94 (SM3), 709–734.
Campbell, G., Calissendorff, C., Williams, J., 1991. Probe for measuring soil specific heat using a heat-pulse method. Soil Sci. Soc. Am. J. 55 (1), 291–293.
Carslaw, H., Jaeger, J., 1959. Conduction of Heat in Solids. Oxford University Press, Oxford.
Casagrande, A., 1936. The determination of preconsolidation load and its practical significance. In: Proceedings of Conference on Soil Mechanics Foundation Engineering, vol. 3, pp. 60–66.
Cecinato, F., Loveridge, F.A., 2015. Influences on the thermal efficiency of energy piles. Energy 82, 1021–1033.
Cecinato, F., Loveridge, F., Gajo, A., Powrie, W., 2015. A new modelling approach for piled and other ground heat exchanger applications. In: Proceedings of XVI European Conference for Soil Mechanics and Geotechnical Engineering, pp. 13–17.

Cekerevac, C., Laloui, L., 2004. Experimental study of thermal effects on the mechanical behaviour of a clay. Int. J. Numer. Anal. Methods Geomech. 28 (3), 209–228.
Cekerevac, C., Laloui, L., Vulliet, L., 2005. A novel triaxial apparatus for thermo-mechanical testing of soils. Geotech. Test. J. 28 (2), 161–170.
CFMS-SYNTEC-SOFFONS-FNTP, 2017. Recommandations pour la conception, le dimensionnement et la mise en úuvre des géostructures thermiques. Rev. Fr. Geotech. 149, 1–120.
Chen, Y., Xu, J., Li, H., Chen, L., Ng, C.W., Liu, H., 2017. Performance of a prestressed concrete pipe energy pile during heating and cooling. J. Perform. Constr. Facil. 31 (3), 06017001.
Claesson, J., Hellström, G., 2011. Multipole method to calculate borehole thermal resistances in a borehole heat exchanger. HVAC&R Res. 17 (6), 895–911.
Collin, A., 1846. Recherches experimentales sur les glissements spontanes des terrains argileux, accompagnees de considerations sur quelques principes de la mecanique terrestre. Carilian-Goeury, Paris.
Collin, F., 2003. Couplages thermo-hydro-mécaniques dans les sols et les roches tendres partiellement saturés. Faculté des Sciences Appliquées, Université de Liège, Liège, Belgium, p. 300.
Coulomb, C., 1773. Essai sur une application des règles de maximis et minimis à quelques problèmes de statique, relatifs à l'architecture. Memoires de Mathematique de l'Academie Royale de Science 7, Paris.
Cui, W., Potts, D.M., Zdravković, L., Gawecka, K.A., Taborda, D.M., 2018. An alternative coupled thermo-hydro-mechanical finite element formulation for fully saturated soils. Comput. Geotech. 94, 22–30.
Dehkordi, S.E., Schincariol, R.A., 2014. Effect of thermal-hydrogeological and borehole heat exchanger properties on performance and impact of vertical closed-loop geothermal heat pump systems. Hydrogeol. J. 22 (1), 189–203.
Diao, N., Li, Q., Fang, Z., 2004. Heat transfer in ground heat exchangers with groundwater advection. Int. J. Therm. Sci. 43 (12), 1203–1211.
Dickinson, H., Van Dusen, M., 1916. The testing of thermal insulators. ASRE J. 3 (2), 5–25.
Di Donna, A., 2014. Thermo-mechanical aspects of energy piles. Laboratory of Soil Mechanics. Swiss Federal Institute of Technology in Lausanne (EPFL), Lausanne.
Di Donna, A., Laloui, L., 2015. Response of soil subjected to thermal cyclic loading: experimental and constitutive study. Eng. Geol. 190 (1), 65–76.
Di Donna, A., Ferrari, A., Laloui, L., 2015. Experimental investigations of the soil-concrete interface: physical mechanisms, cyclic mobilisation and behaviour at different temperatures. Can. Geotech. J. 53 (4), 659–672.
EN 12667, 2001. Thermal Performance of Building Materials and Products. Determination of Thermal Resistance by Means of Guarded Hot Plate and Heat Flow Meter Methods. Products of High and Medium Thermal Resistance. BS EN, London.
EN 1997, 2004. Eurocode 7: Geotechnical Design. BS EN, London, p. 171.
Finn, F.N., 1951. The Effects of Temperature on the Consolidation Characteristics of Remoulded Clay. Report No. 126, pp. 65–71.
Fleming, K., Weltman, A., Randolph, M., Elson, K., 2008. Piling Engineering. CRC Press.
Franco, A., Moffat, R., Toledo, M., Herrera, P., 2016. Numerical sensitivity analysis of thermal response tests (TRT) in energy piles. Renew. Energy 86, 985–992.
Fromentin, A., Pahud, D., Laloui, L., Moreni, M., 1999. Pieux échangeurs: conception et règles de pré—dimensionnement. Rev. Franç. Gén. Civ. 3 (6), 387–421.
Gatmiri, B., Delage, P., 1997. A formulation of fully coupled thermal–hydraulic–mechanical behaviour of saturated porous media—numerical approach. Int. J. Numer. Anal. Methods Geomech. 21 (3), 199–225.
Gehlin, S., 2002. Thermal Response Test: Method Development and Evaluation. Luleå tekniska universitet, Luleå.
Gehlin, S., Nordell, B., 2003. Determining undisturbed ground temperature for thermal response test. ASHRAE Trans. 109, 151–156.
Gibson, R., Henkel, D., 1954. Influence of duration of tests at constant rate of strain on measured "drained" strength. Geotechnique 4 (1), 6–15.
Glišić, B., Simon, N., 2000. Monitoring of concrete at very early age using stiff SOFO sensor. Cem. Concr. Compos. 22 (2), 115–119.

Ground Source Heat Pump Association, N. E. C., 2011. Closed-Loop Vertical Borehole Design Installation and Material Standards. National Energy Center, Milton Keyenes, p. 86.
Ground Source Heat Pump Association, N. E. C., 2012. Thermal Pile Design, Installation & Materials Standards. National Energy Center, Milton Keyenes, p. 86.
Gustafsson, S.E., 1991. Transient plane source techniques for thermal conductivity and thermal diffusivity measurements of solid materials. Rev. Sci. Instrum. 62 (3), 797–804.
Haffen, S., Géraud, Y., Diraison, M., Dezayes, C., 2013. Determination of fluid-flow zones in a geothermal sandstone reservoir using thermal conductivity and temperature logs. Geothermics 46, 32–41.
Head, K.H., 1986. Manual of Soil Laboratory Testing. Pentech Press, London.
Head, K.H., Epps, R., 1980. Manual of Soil Laboratory Testing. Pentech Press, London.
Hemmingway, P., Long, M., 2013. Energy piles: site investigation and analysis. Proc. ICE Geotech. Eng. 166, 1–15.
Hiraiwa, Y., Kasubuchi, T., 2000. Temperature dependence of thermal conductivity of soil over a wide range of temperature (5–75 C). Eur. J. Soil Sci. 51 (2), 211–218.
Hu, P., Zha, J., Lei, F., Zhu, N., Wu, T., 2014. A composite cylindrical model and its application in analysis of thermal response and performance for energy pile. Energy Build. 84, 324–332.
Inaudi, D., Laloui, L., Steinmann, G., 2000. Looking below the surface. Concr. Eng. Int. 4 (3).
Ingersoll, L.R., Zabel, O.J., Ingersoll, A.C., 1954. Heat Conduction with Engineering, Geological, and Other Applications. Mc-Graw Hill, New York.
ISO 17628, 2015. Geotechnical Investigation and Testing: Geothermal Testing – Determination of Thermal Conductivity of Soil and Rock Using Borehole Heat Exchanger. ISO – International Organization of Standards, Geneva.
ISO 17892-5, 2017. Geotechnical Investigation and Testing – Laboratory Testing of Soil – Part 5: Incremental Loading Oedometer Test. ISO – International Organization of Standards, Geneva.
ISO 17892-7, 2018. Geotechnical Investigation and Testing – Laboratory Testing of Soil – Part 7: Unconfined Compression Test. ISO – International Organization of Standards, Geneva.
ISO 17892-8, 2018. Geotechnical Investigation and Testing – Laboratory Testing of Soil – Part 8: Unconsolidated Undrained Triaxial Test. ISO – International Organization of Standards, Geneva.
ISO 17892-9, (2018. Geotechnical Investigation and Testing – Laboratory Testing of Soil – Part 9: Consolidated Triaxial Compression Tests on Water Saturated Soils. ISO – International Organization of Standards, Geneva.
ISO 22007–2, 2015. International Organization for Standardization. Plastics – Determination of Thermal Conductivity and Thermal Diffusivity – Part 2: Transient Plane Heat Source (Hot Disc) Method. ISO – International Organization of Standards, Geneva.
ISO 8302, 1991. Thermal Insulation-Determination of Steady-State Thermal Resistance and Related Properties-Guarded Hot Plate Apparatus. ISO – International Organization of Standards, Geneva.
Janbu, N., 1969. The resistance concept applied to deformations of soils. In: Proceedings of the 7th International Conference on Soil Mechanics and Foundation Engineering, Mexico City, vol. 2529, pp. 191–196.
Javed, S., Fahlén, P., 2011. Thermal response testing of a multiple borehole ground heat exchanger. Int. J. Low Carbon Technol. 6 (2), 141–148.
Javed, S., Spitler, J.D., Fahlén, P., 2011. An experimental investigation of the accuracy of thermal response tests used to measure ground thermal properties. ASHRAE Trans. 117 (1), 13–21.
Jensen, C., Xing, C., Folsom, C., Ban, H., Phillips, J., 2012. Design and validation of a high-temperature comparative thermal-conductivity measurement system. Int. J. Thermophys. 33 (2), 311–329.
Kasubuchi, T., 1992. Development of In-Situ Soil Water Measurement by Heat-Probe Method. JARQ, Tsukuba.
Kavanaugh, S.P., Rafferty, K., 1997. Ground-Source Heat Pumps: Design of Geothermal Systems for Commercial and Institutional Buildings. American Society of Heating, Refrigerating and Air-Conditioning Engineers.
Kurevija, T., Vulin, D., Macenic, M., 2014. Impact of geothermal gradient on ground source heat pump system modeling. Rud. Geol. Naft. Zb. 28 (1), 39.
Laloui, L., 2001. Thermo-mechanical behaviour of soils. Rev. Franç. Gén. Civ. 5 (6), 809–843.
Laloui, L., Moreni, M., Vulliet, L., 2003. Comportement d'un pieu bi-fonction, fondation et échangeur de chaleur. Can. Geotech. J. 40 (2), 388–402.

Laloui, L., Nuth, M., Vulliet, L., 2006. Experimental and numerical investigations of the behaviour of a heat exchanger pile. Int. J. Numer. Anal. Methods Geomech. 30 (8), 763–781.
Lambe, T.W., 1951. Soil Testing for Engineers. Wiley.
Lancellotta, R., 1995. Geotechnical Engineering. Balkema, Rotterdam.
Lewis, R.W., Schrefler, B.A., 1998. The Finite Element Method in the Static and Dynamic Deformation and Consolidation of Porous Media. Wiley, Chichester.
Lewis, R., Majorana, C., Schrefler, B., 1986. A coupled finite element model for the consolidation of nonisothermal elastoplastic porous media. Transp. Porous Media 1 (2), 155–178.
Li, M., Lai, A.C., 2015. Review of analytical models for heat transfer by vertical ground heat exchangers (GHEs): a perspective of time and space scales. Appl. Energy 151, 178–191.
Liu, S., Feng, C., Wang, L., Li, C., 2011. Measurement and analysis of thermal conductivity of rocks in the Tarim Basin, Northwest China. Acta Geol. Sin. Engl. Ed. 85 (3), 598–609.
Lloret, S., Inaudi, D., Glisic, B., Kronenberg, P., Vurpillot, S., 2000). Optical set-up development for the monitoring of structural dynamic behaviour. In: 7th Annual International Symposium on Smart Structures and Materials, vol. 3986, p. 27.
Lockmuller, N., Redgrove, J., Kubicar, L., 2004. Measurement of thermal conductivity with the needle probe. High Temp. -High Press. 36 (2), 127–138.
Loveridge, F., Powrie, W., 2013. Temperature response functions (G-functions) for single pile heat exchangers. Energy 57, 554–564.
Loveridge, F., Brettmann, T., Olgun, C., Powrie, W., 2014a. Assessing the applicability of thermal response testing to energy piles. In: Proceedings of DFI-EFFC International Conference on Piling and Deep Foundations.
Loveridge, F., Olgun, C.G., Brettmann, T., Powrie, W., 2014b. The thermal behaviour of three different auger pressure grouted piles used as heat exchangers. Geotech. Geol. Eng. 33 (2), 273–289.
Loveridge, F., Powrie, W., Nicholson, D., 2014c. Comparison of two different models for pile thermal response test interpretation. Acta Geotech. 9 (3), 367–384.
Loveridge, F., Low, J., Powrie, W., 2017. Site investigation for energy geostructures. Q. J. Eng. Geol. Hydrogeol. 50, 158–168.
Low, J.E., Loveridge, F.A., Powrie, W., Nicholson, D., 2015. A comparison of laboratory and in situ methods to determine soil thermal conductivity for energy foundations and other ground heat exchanger applications. Acta Geotech. 10 (2), 209–218.
Luo, J., Zhao, H., Gui, S., Xiang, W., Rohn, J., 2017. Study of thermal migration and induced mechanical effects in double U-tube energy piles. Comput. Geotech. 91, 1–11.
Man, Y., Yang, H., Diao, N., Liu, J., Fang, Z., 2010. A new model and analytical solutions for borehole and pile ground heat exchangers. Int. J. Heat Mass Transf. 53 (13), 2593–2601.
Maragna, C., Rachez, X., 2015. Innovative Methodology to Compute the Temperature Evolution of Pile Heat Exchangers. In: Proceedings of the World Geothermal Congress, Melbourne, Australia, pp. 19–25.
Marcotte, D., Pasquier, P., 2008. On the estimation of thermal resistance in borehole thermal conductivity test. Renew. Energy 33 (11), 2407–2415.
Mattsson, N., Steinmann, G., Laloui, L., 2008. Advanced compact device for the in-situ determination of geothermal characteristics of soils. Energy Build. 40 (7), 1344–1352.
McCartney, J.S., Murphy, K.D., 2012. Strain distributions in full-scale energy foundations. DFI J. 6 (2), 26–38.
McCartney, J.S., Murphy, K.D., 2017. Investigation of potential dragdown/uplift effects on energy piles. Geomech. Energy Environ. 10, 21–28.
MCS, 2013. Microgeneration Installation Standard, MIS 3005: Requirements for Contractors Undertaking the Supply, Design, Installation, Set to Work, Commissioning and Handover of Microgeneration Heat Pump Systems, Issue 4. 1. MIS.
Merckx, B., Dudoignon, P., Garnier, J., Marchand, D., 2012. Simplified transient hot-wire method for effective thermal conductivity measurement in geo materials: microstructure and saturation effect. Adv. Civil Eng. 2012.
Midttømme, K., Roaldset, E., 1999. Thermal conductivity of sedimentary rocks: uncertainties in measurement and modelling. Geol. Soc., Lond. Spec. Publ. 158 (1), 45–60.

Mimouni, T., Laloui, L., 2013. Full-scale in situ testing of energy piles. In: Laloui, L., Di Donna, A. (Eds.), Energy Geostructures: Innovation in Underground Engineering. Wiley-ISTE, pp. 23–43.
Mimouni, T., Laloui, L., 2015. Behaviour of a group of energy piles. Can. Geotech. J. 52 (12), 1913–1929.
Mitchell, J.K., Campanella, R.G., 1963. Creep studies on saturated clays. In: Symposium on Laboratory Shear Testing of Soils. ASTM-NRC, Ottawa.
Mitchell, J.K., Soga, K., 2005. Fundamentals of Soil Behavior. Wiley, New York.
Mogensen, P., 1983. Fluid to duct wall heat transfer in duct system heat storages. Doc. -Swedish Counc. Build. Res. 16, 652–657.
Murphy, K., McCartney, J.S., 2015. Seasonal response of energy foundations during building operation. Geotech. Geol. Eng. 33 (2), 343–356.
Murphy, K.D., McCartney, J.S., Henry, K.S., 2014. Impact of horizontal run-out length on the thermal response of full-scale energy foundations. In: Geo-Congress 2014: Geo-Characterization and Modeling for Sustainability, pp. 2715–2724.
Murphy, K.D., McCartney, J.S., Henry, K.S., 2015. Evaluation of thermo-mechanical and thermal behavior of full-scale energy foundations. Acta Geotech. 10 (2), 1–17.
Ng, C.W.W., Mu, Q., Zhou, C., 2017. Effects of boundary conditions on cyclic thermal strains of clay and sand. Géotech. Lett. 7 (1), 73–78.
Nikolaev, I.V., Leong, W.H., Rosen, M.A., 2013. Experimental investigation of soil thermal conductivity over a wide temperature range. Int. J. Thermophys. 34 (6), 1110–1129.
Noorishad, J., Tsang, C., Witherspoon, P., 1984. Coupled thermal-hydraulic-mechanical phenomena in saturated fractured porous rocks: numerical approach. J. Geophys. Res.: Solid Earth 89 (B12), 10365–10373.
Olivella, S., Gens, A., Carrera, J., Alonso, E., 1996. Numerical formulation for a simulator (CODE_BRIGHT) for the coupled analysis of saline media. Eng. Comput. 13 (7), 87–112.
Paaswell, R.E., 1967. Temperature effects on clay soil consolidation. J. Soil Mech. Found. Div. 93 (SM3), 9–22.
Park, H., Lee, S.-R., Yoon, S., Choi, J.-C., 2013. Evaluation of thermal response and performance of PHC energy pile: field experiments and numerical simulation. Appl. Energy 103, 12–24.
Park, S., Sung, C., Jung, K., Sohn, B., Chauchois, A., Choi, H., 2015. Constructability and heat exchange efficiency of large diameter cast-in-place energy piles with various configurations of heat exchange pipe. Appl. Therm. Eng. 90, 1061–1071.
Plum, L., Esrig, M.I., 1969. Some temperature effects on soil compressibility and pore water pressure. Report No. 103, Washington, pp. 231–242.
Poensgen, R., 1912. Ein technisches Verfahren zur Ermittlung der Wärmeleitfähigkeit plattenförmiger Stoffe. Mitteilungen über Forschungsarbeiten auf dem Gebiete des Ingenieurwesens. Springer, pp. 25–40.
Popov, Y.A., Pribnow, D.F., Sass, J.H., Williams, C.F., Burkhardt, H., 1999. Characterization of rock thermal conductivity by high-resolution optical scanning. Geothermics 28 (2), 253–276.
Poppei, J., Péron, H., Silvani, C., Steinmann, G., Laloui, L., Wagner, R., Lochbühler, T., Rohner, E., 2008. Innovative Improvements of Thermal Response Tests. Final Report. Swiss Federal Office of Energy, pp. 1–34.
Poulos, H.G., Davis, E.H., 1980. Pile Foundation Analysis and Design. Wiley, New York.
Poulos, H.G., Carter, J.P., Small, J.C., 2002. Foundations and retaining structures—research and practice, International Conference on Soil Mechanics and Geotechnical Engineering, vol. 4. Balkema, pp. 2527–2606.
Radioti, G., Sartor, K., Charlier, R., Dewallef, P., Nguyen, F., 2017. Effect of undisturbed ground temperature on the design of closed-loop geothermal systems: a case study in a semi-urban environment. Appl. Energy 200, 89–105.
Raymond, J., Therrien, R., Gosselin, L., Lefebvre, R., 2011. Numerical analysis of thermal response tests with a groundwater flow and heat transfer model. Renew. Energy 36 (1), 315–324.
Rotta Loria, A.F., Laloui, L., 2017. Thermally induced group effects among energy piles. Geotechnique 67 (5), 374–393.
Rotta Loria, A.F., Laloui, L., 2018. Group action effects caused by various operating energy piles. Geotechnique 68 (9), 834–841.

Rotta Loria, A.F., Ferrari, A., Laloui, L., 2014. Thermo-Mechanical Analysis of Soil Characteristics from Energy Piles Tests in Richmond, TX by Virginia Tech University, Lausanne, Switzerland, p. 51.
Rowe, P.W., 1962. The stress–dilatancy relation for static equilibrium of an assembly of particles in contact. Report No. 1364-5021, pp. 500–527.
Sanner, B., Hellström, G., Spitler, J., Gehlin, S., 2005. Thermal response test–current status and worldwide application. Proceedings World Geothermal Congress. International Geothermal Association, pp. 24–29.
Schmertmann, J.H., 1955. The undisturbed consolidation behavior of clay. Trans. ASCE 120, 1201–1233.
SIA-D0190, 2005). Utilisation de la Chaleur du Sol par des Ouvrages de Fondation et de Soutènement en Béton. Guide pour la Conception, la Realisation et la Maintenance, Zurich, Switzerland.
Skempton, A.W., 1954. The pore-pressure coefficients A and B. Geotechnique, 4(4), pp. 143–147.
Spitler, J.D., Gehlin, S.E., 2015. Thermal response testing for ground source heat pump systems—an historical review. Renew. Sustain. Energy Rev. 50, 1125–1137.
Sutman, M., Olgun, C., Brettmann, T., 2015. Full-scale field testing of energy piles, Proceedings of IFCEE 2015, vol. 1. ASCE, pp. 1638–1647.
Sutman, M., Olgun, G., Laloui, L., Brettmann, T., 2017. Effect of end-restraint conditions on energy pile behavior. In: Geotechnical Frontiers 2017, pp. 165–174.
Tarnawski, V.R., Momose, T., Leong, W., Bovesecchi, G., Coppa, P., 2009. Thermal conductivity of standard sands. Part I. Dry-state conditions. Int. J. Thermophys. 30 (3), 949–968.
Taylor, D.W., 1942. Research on Consolidation of Clays. Massachusetts Institute of Technology.
Terzaghi, K., 1923. Die Berechnung des Durchlassigkeitszifferdes Tones aus dem Verlauf der hydrodynamischen Spannungserscheinungen. Sitz. Akad. Wissen, Wien MAth-naturw KI. Abt IIa 132, 125–138.
Terzaghi, K., 1943. Theoretical Soil Mechanics. John Wiley & Sons, New York.
Valente, A., Morais, R., Tuli, A., Hopmans, J., Kluitenberg, G., 2006. Multi-functional probe for small-scale simultaneous measurements of soil thermal properties, water content, and electrical conductivity. Sens. Actuators A Phys. 132 (1), 70–77.
Van der Held, E., Van Drunen, F., 1949. A method of measuring the thermal conductivity of liquids. Physica 15 (10), 865–881.
VDI 4640, 2009. Thermal Use of the Underground. Ground Source Heat Pump Systems. Association of German Engineers, Dusseldorf.
Venuleo, S., Laloui, L., Terzis, D., Hueckel, T., Hassan, M., 2016. Microbially induced calcite precipitation effect on soil thermal conductivity. Géotech. Lett. 6 (1), 39–44.
Vieira, A., Maranha, J., Christodoulides, P., Alberdi-Pagola, M., Loveridge, F., Nguyen, F., et al., 2017. Characterisation of ground thermal and thermo-mechanical behaviour for shallow geothermal energy applications. Energies 10 (12), 2044.
Vulliet, L., Laloui, L., Zhao, J., 2016. Mécanique des sols et des roches (TGC volume 18): avec écoulements souterrains et transferts de chaleur. PPUR Presses polytechniques.
Wagner, V., Blum, P., Kübert, M., Bayer, P., 2013. Analytical approach to groundwater-influenced thermal response tests of grouted borehole heat exchangers. Geothermics 46, 22–31.
Wang, B., Bouazza, A., Singh, R.M., Haberfield, C., Barry-Macaulay, D., Baycan, S., 2014. Posttemperature effects on shaft capacity of a full-scale geothermal energy pile. J. Geotech. Geoenviron. Eng. 141 (4), 04014125.
Xamán, J., Lira, L., Arce, J., 2009. Analysis of the temperature distribution in a guarded hot plate apparatus for measuring thermal conductivity. Appl. Therm. Eng. 29 (4), 617–623.
Yavari, N., Tang, A.M., Pereira, J.-M., Hassen, G., 2016. Effect of temperature on the shear strength of soils and the soil–structure interface. Can. Geotech. J. 53 (999), 1–9.
Yazdani, S., Helwany, S., Olgun, G., 2018. Influence of temperature on soil–pile interface shear strength. Geomech. Energy Environ. 18, 69.
You, S., Cheng, X., Guo, H., Yao, Z., 2016. Experimental study on structural response of CFG energy piles. Appl. Therm. Eng. 96 (1), 640–651.
Zienkiewicz, O., Chan, A., 1989. Coupled problems and their numerical solution. Advances in Computational Nonlinear Mechanics. Springer, pp. 139–176.

Questions and problems

Statements

a. List at least three features that can have a marked effect on the results of the analysis and design of energy geostructures, with at least two variables per feature.

b. The aerothermal features of sites primarily govern the thermohydraulic behaviour as well as the energy performance of energy geostructures:
- **i.** True
- **ii.** False

c. The geothermal features of any specific project are typically:
- **i.** Fixed
- **ii.** Variable

d. A variation of one parameter characterising the energy performance of energy geostructures does not typically influence the geotechnical or structural performance:
- **i.** True
- **ii.** False

e. Define the design variables and associated parameters characterising the energy design of energy geostructures

f. The strength, stiffness and thermal expansion potential of the considered geomaterial (e.g. soil or concrete) can be broadly considered to be three design variables that majorly affect the geotechnical and structural design of energy geostructures:
- **i.** True
- **ii.** False

g. Different approaches are typically required to determine input parameters depending on the stage of the design process as well as on the complexity of the geostructure:
- **i.** True
- **ii.** False

h. Define the level of detail characterising the approaches usually available to determine input parameters depending on the design stage of energy geostructures.

i. How many categories distinguish analysis and design procedures? Briefly discuss salient features of these categories and their relationship with testing approached to determine input parameters.

j. With reference to the geotechnical categories highlighted in the EN 1997 (2004) to assist in the establishment of minimum requirements for the extent and content of geotechnical investigations, energy geostructures typically belong to:
- **i.** Category 1
- **ii.** Category 2
- **iii.** Category 3

k. Guarded hot plate testing provides a mechanical parameter that can serve the geotechnical design of energy geostructures:
  i. True
  ii. False

l. List the three phases of a guarded hot plate test.

m. Guarded hot plate testing allows defining the thermal conductivity of soil specimens during the transient phase of a one-dimensional heat transfer imposed on the specimen:
  i. True
  ii. False

n. What are the four main differences characterising so-called transient methods compared to steady-state methods in the context of the determination of the thermal properties of materials?

o. The effective thermal conductivity of geomaterials should be considered temperature dependent for the analysis and design of energy geostructures:
  i. True
  ii. False

p. What type(s) of design can the parameters defined through oedometer testing under nonisothermal conditions serve?

q. List the five phases of an oedometer test under nonisothermal conditions.

r. What is the rationale of applying increments of mechanical load on the cap that is placed above the top porous stone to maintain the initial height of the specimen constant during its saturation phase in an oedometer test?

s. What is the definition of the oedometric modulus, E_{oed}? What does this parameter represent from a graphical perspective when considering an oedometer curve?

t. What is the definition of the compression index, C_c? What does this parameter represent from a graphical perspective when considering an oedometer curve? In what the definition of the compression index differs from that of the recompression index, C_r, and the swelling index, C_s?

u. From a practical perspective, the compressibility parameters of soils can be considered *independent* of temperature with reference to the temperature variations associated with the geothermal operation of energy geostructures:
  i. True
  ii. False

v. Define the preconsolidation pressure, σ'_p, and the isotropic preconsolidation pressure, p'_c.

w. The preconsolidation pressure should be considered temperature dependent for the analysis and design of energy geostructures:
  i. True
  ii. False

x. Define the overconsolidation ratio, *OCR*, and describe the physical phenomena that can lead to underconsolidation, normal consolidation and overconsolidation.

y. Describe the procedure to determine the volumetric thermal expansion coefficient of a soil specimen, β, from the results of an oedometer test under nonisothermal conditions.

z. In an oedometer tests, the application of a symmetrical heating–cooling cycle to a specimen in an overconsolidated state produces, at least theoretically, zero residual deformations at the end of thermal loading:
- **i.** True
- **ii.** False

aa. The consolidation parameters of most fine-grained soils are markedly *dependent* of temperature with reference to the temperature variations associated with the geothermal operation of energy geostructures:
- **i.** True
- **ii.** False

bb. Consider an oedometer test where the specimen is subjected to a vertical stress of 50 kPa. Given the properties of the tested material (Young's modulus $E =$ MPa; Poisson's ratio $\nu = 0.2$), calculate the different stress components of the stress tensor. Use the elastic relationship between the stress and strain components.

cc. What type(s) of design can the parameters defined through triaxial testing under nonisothermal conditions serve?

dd. List the five phases of a triaxial test under nonisothermal conditions.

ee. What are the three types of stress state that can be achieved during the consolidation phase of a triaxial test via isothermal-mechanical loading? Express these stress states mathematically.

ff. From a practical perspective, the deformation parameters of soils (e.g. Young's modulus) can be considered in most cases *dependent* of temperature with reference to the temperature variations associated with the geothermal operation of energy geostructures:
- **i.** True
- **ii.** False

gg. Define the different components of volume change of a specimen caused by thermal loading in a triaxial test under nonisothermal conditions.

hh. The thermal expansion coefficient of geomaterials should be considered temperature dependent for the analysis and design of energy geostructures:
- **i.** True
- **ii.** False

ii. Consider a specimen prepared in a triaxial cell in the following initial conditions:
- Initial isotropic loading up to a cell pressure $\sigma_c = 300$ kPa,
- Initial pore water pressure $p_w = 100$ kPa,
- Initial specimen diameter $D_0 = 38$ mm and height $H_0 = 78$ mm.

The sample undergoes a conventional drained triaxial compression test with cell pressure and pore water pressure held constant.

The following results are obtained, where during each loading stage, P is the applied force, ΔH is the measured change in the value of axial displacement and ΔV_w is the volume variation of pore water in the specimen after mechanical consolidation.

Sample		
P [N]	ΔH [mm]	ΔV_w [mm^3·]
0	0	0
115	− 1.95	880
235	− 5.85	3720
325	− 11.7	7070
394	− 19.11	8400
458	− 27.3	8400

Calculate deviatoric stress, mean effective stress axial strain, and volumetric strain for each step of the test. Then, plot the experimental results in the following planes:

$$(q - \varepsilon_z); (\varepsilon_v - \varepsilon_z); (q - p')$$

jj. What type(s) of design can the parameters defined through direct shear testing under nonisothermal conditions serve?

kk. List the five phases of a direct shear test under nonisothermal conditions.

ll. State how shear strength parameters such as cohesion, peak angle of shear strength and angle of shear strength under constant volume conditions can be defined through direct shear tests.

mm. From a practical perspective the shear strength parameters of concrete−soil interfaces can be considered *independent* of temperature with reference to the temperature variations associated with the geothermal operation of energy geostructures:

i. True

ii. False

nn. Can stress−strain relationships be defined through direct shear tests? Justify your answer.

oo. What are the key thermal parameters that can be defined through thermal response tests?

pp. List the five phases of a thermal response test.

qq. Describe the three approaches that can be employed to estimate the undisturbed ground temperature in a thermal response test. What is the best approach?

rr. Describe the direct estimation approach of the thermal conductivity via the infinite line source model via the results of a thermal response test.

ss. Thermal response tests provide pairs of effective thermal conductivity of the ground and time-independent thermal resistance? Is the independent use of these parameters suggested for the analysis or design of energy geostructures? Justify your answer.

tt. What is the lower bound of effective thermal conductivity that allow considering an energy geostructure application effective from the energy exploitation perspective?

uu. The theory available to interpret the result of thermal response test on energy piles can be directly applied to the result of tests on energy tunnels or walls:

i. True

ii. False

vv. Consider a 23 m long and 0.6 m in diameter energy pile made of reinforced concrete that is embedded in a stratified soil deposit. The pile is equipped with a polyethylene pipe of 32 mm in diameter that is attached to its reinforcement cage with a double U-shaped layout. During a thermal response test (TRT), a heat carrier fluid (water) is circulated for 19 hours without turning on the heating. After the first stage, heat is injected for 5 days into the energy pile. The data measured during the TRT are presented in the following figure. With reference to this problem, determine (1) the undisturbed temperature and (2) the effective thermal conductivity of the ground.

Assuming that the results of a TRT performed on a neighbouring energy pile led to a lower thermal conductivity value, which value would you recommend using for the design of a system markedly resorting to heat extraction? Justify your answer.

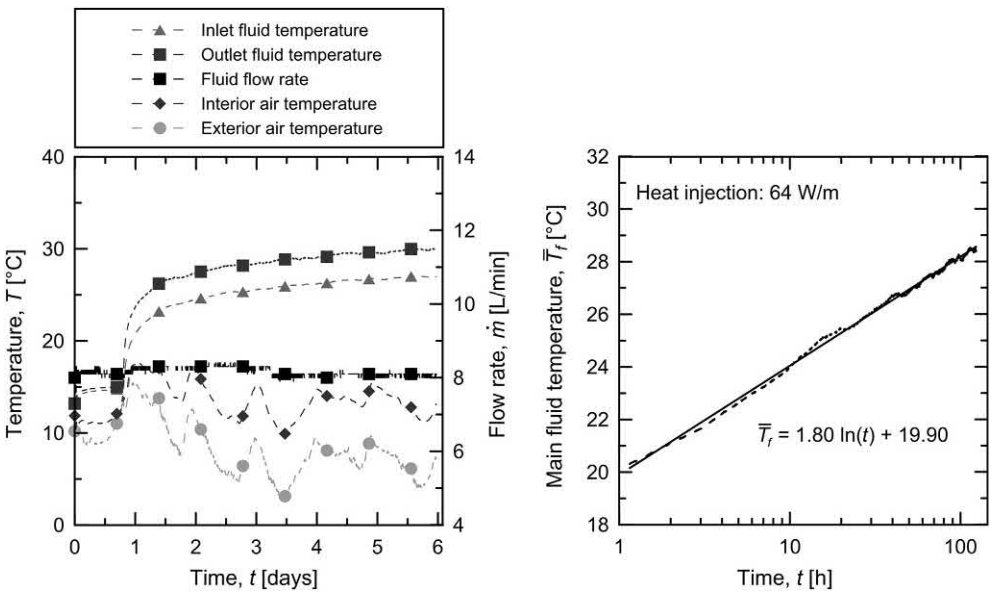

ww. Consider a 35 m long and 0.8 m in diameter energy pile made of reinforced concrete that is embedded in a stratified soil deposit. The pile is equipped with a polyethylene pipe of 32 mm in diameter that is attached to its reinforcement cage with a double U-shaped layout. During a TRT, a heat carrier fluid (water) is circulated for 20 hours without turning on the heating. After the first stage, heat is injected for 7 days into the energy pile. The data measured during the TRT are presented in the following figure. With reference to this problem, determine (1) the undisturbed temperature and (2) the effective thermal conductivity of the ground.

Assuming that the results of a TRT performed on a neighbouring energy pile led to a lower thermal conductivity value, which value would you recommend using for the design of a system markedly resorting to heat extraction? Justify your answer.

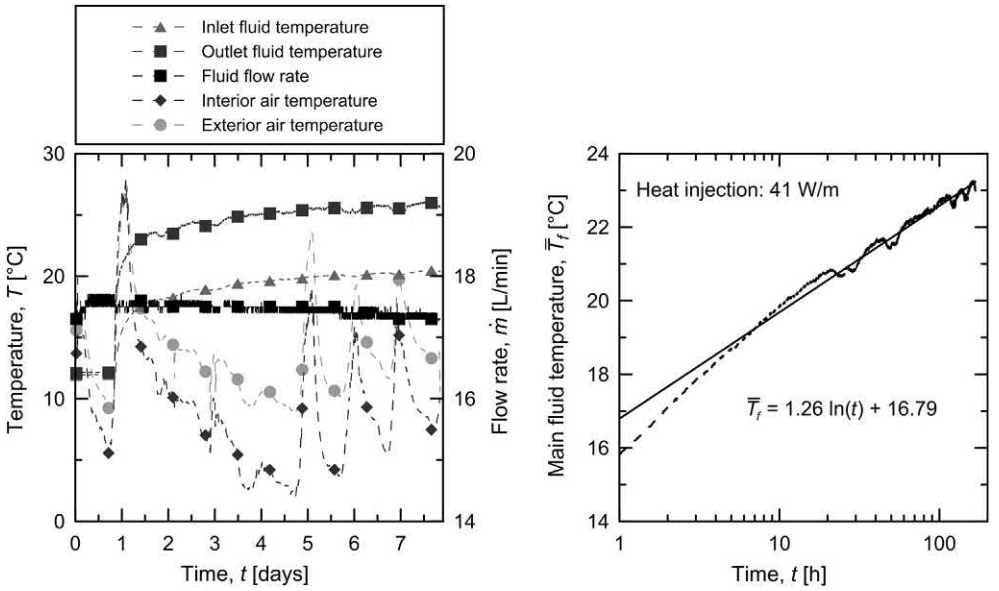

xx. The goal of this exercise is to perform the preliminary energy design of a group of energy piles. With reference to the features of a building founded on a piled foundation, the purpose is to define: (1) the number of piles that need to be equipped as geothermal heat exchangers and will operate as energy piles, (2) the thermal powers applied to each energy pile and (3) the associated temperature variations for given operational periods. Typical data that in practical applications are provided by the various practitioners involved are assumed to be available. The design follows recommendations for energy piles (SIA-D0190, 2005). A final analysis of the features of some of the analytical models that are used to solve this exercise will be requested.

The building is to be founded on 162 piles that are 0.8 m in diameter and whose average length is 19.2 m. The piles penetrate in three layers. The first layer is 2 m-thick and made of backfill material. The second layer is made of moraine and extends from 2 to 18 m below the pile head. The third layer upon which the piles rest is made of molasse. A groundwater survey identifies a water table almost at the soil surface, whose flow velocity is estimated to $\overline{v}_{nv} = 0.2$ m/day. A thermal response test carried out at the site indicates a natural temperature of the ground of 11°C and an effective thermal conductivity of $\lambda_{soil} = 1.5$ W/(m °C). The ground thermal diffusivity is approximately of $\alpha_{d,soil} = 6.4 \times 10^{-7}$ m^2/s.

The needs for the heating and cooling of the building are as follows:

- The heating of the building requires a peak power of 340 kW and a quantity of heat of $E_{H,tot} = 738$ MWh/year. The heating period lasts from October to May (i.e. 8 months).
- The cooling of the building requires a quantity of heat of $E_{C,tot} = 105$ MWh/year homogeneously distributed over the warm period. The cooling period lasts from June to September (i.e. 4 months).
- The heat pump to be installed has a nominal heating power of $\dot{Q}_S = 6$ kW and a coefficient of performance of $COP = 3.5$.
- The cooling during warm periods is to be achieved using direct cooling (i.e. bypassing the heat pump).

The relation that links the amount of energy supplied by the heat pump, Q_S, to the energy required from the piles, Q_R, is:

$$Q_S = \frac{COP}{COP - 1} Q_R \tag{1}$$

In the analyses, consider on average 29.5 days per month and assume negative thermal powers for extraction while positive thermal powers for injection.

Aspects to address:

a. Maximum thermal powers involved. Considering the reported in the SIA-D0190 (2005), depicting typical values of thermal resistance for energy piles for usual values of groundwater flow velocity and effective thermal conductivity, and using the soil data available, estimate the linear thermal powers applicable to the piles for heating (i.e. heat extraction) and cooling (i.e. heat injection). Consider that a thermal recharge of the ground is achieved by injecting 70%–90% of thermal energy in this medium.

b. Heating supply. From the heating needs and the heat pump features, estimate the minimum number of piles that are to be equipped with absorber pipes as energy piles. Estimate the total amount of heat that can be obtained through this design with the minimum number possible of equipped piles.

c. Estimation of the temperature variation in the piles due to heating. Based on the highest linear thermal power involved with heat extraction (in

absolute value), estimate the temperature variation at the end of the heating period (i.e. $t = 8$ months) through the simplified infinite cylindrical-surface source model (Carslaw and Jaeger, 1959) and the simplified infinite line source model (Carslaw and Jaeger, 1959; Ingersoll et al., 1954)

$$T(t,R) - T_0 = \dot{q}_l \, G_f'(t,R) = \dot{q}_l \frac{1}{4\pi\lambda_{soil}} \left[\ln \frac{4\alpha_{d,soil} t}{R^2} - \gamma_E + \frac{R^2}{2\alpha_{d,soil} t} \left(\ln \frac{4\alpha_{d,soil} t}{R^2} - \gamma_E + 1 \right) \right] \tag{2}$$

$$T(t,R) - T_0 = \dot{q}_l \, G_f'(t,R) = \dot{q}_l \frac{1}{4\pi\lambda_{soil}} \left(\ln \frac{4\alpha_{d,soil} t}{R^2} - \gamma_E \right) \tag{3}$$

where R [m] is the energy pile radius, T_0 [°C] is the initial ground temperature, $G_f'(t,R)$ [(m °C)/W] is the G-function and $\gamma_E = 0.5772$ [−] is the Euler constant. Note that these analyses do not account for any pile thermal resistance.

After having developed the previous analyses, based on the assumption of a 2-U pipe equipment per energy pile, estimate the appropriate value of thermal resistance R'_{ghe} [(m °C)/W] for the considered case study through the following graph reported in the SIA-D0190 (2005) depicting typical values of thermal resistance for energy piles different diameters and pipe configurations. Next, perform two different analyses with the infinite cylindrical-surface source model and the infinite line source model to estimate the temperature variation in the energy piles according to the following more rigorous approach

$$\Delta T = \dot{q}_l \left[R'_{ghe} + G_f'(t,R) \right] \tag{4}$$

The minimum temperature value in the soil of 1°C may be prescribed to prevent freezing and the heat pump performance to drop. Is this margin respected considering the worst-case prediction of the models? If no, define the maximum linear power for which, in the worst-case scenario among those considered above, the considered requirement is respected. Modify the number of piles to are to be equipped accordingly.

d. Cooling supply. Assuming that the cooling power is constant during the period of interest, estimate the linear thermal power that is applied to the energy piles.

Based on the flow chart proposed by the SIA-D0190 (2005), is the long-term temperature evolution of the ground a concern for this design? If yes, please define the range in which the amount of heat injected should remain while using direct cooling. Does this range provide acceptable linear heat injection levels? If no, how many piles would you need to equip? How does the linear power evolve during heat extraction?

How much heat is needed to guarantee the feasibility of this solution in addition to the 105 MWh? From which source this heat could be obtained to ensure the sustainability of the system?

e. Estimation of the temperature variation in the piles due to cooling. Based on the linear thermal power involved with heat injection, estimate the temperature variation at the end of the cooling period (i.e. $t = 4$ months) through the four methods considered thus far.

f. Conclude on the present design. Based on the obtained results presented in this study, specify the number of piles that are to be equipped with energy piles, the maximum linear thermal powers involved for heating and cooling as well as the resulting temperature variations in the piles.

g. Comments on the simplified infinite cylindrical-surface and line source models. Assuming a linear thermal power of 1 W/m and considering the material properties employed this far, estimate with the simplified infinite cylindrical-surface and line source models (i.e. do not consider the pile thermal resistance) the evolution of the temperature variation from the energy pile wall with radial distance from the pile axis up to the value of $r = 10D$. Plot the evolution of the temperature variation from the pile wall with radial distance obtained with the two approaches for time steps of $t = 1$, 5, 10, 20, 40, 80, 160 and 182.5 days. With reference to the pile wall and for the considered time steps, estimate the error between the two solutions.

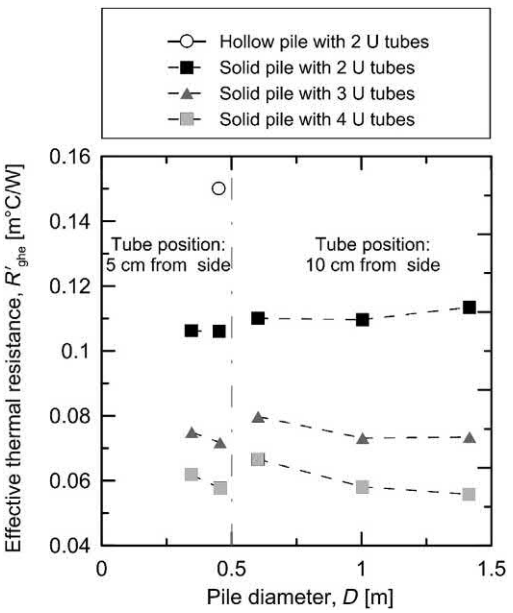

yy. Define two instruments that can be used to measure strains in full-scale energy geostructures. Briefly describe the principle upon which such technologies are based.

Solutions

a. The following features can be considered to markedly characterise the analysis and design of energy geostructures:
- **i. Hydrogeological properties of site:**
  - **Depth and seasonal fluctuation of the groundwater table;**
  - **Flow direction and velocity of groundwater.**
- **ii. Geotechnical properties of site:**
  - **Shear strength parameters;**
  - **Elastic parameters.**
- **iii. Geothermal properties of site:**
  - **Thermal conductivity and specific heat;**
  - **In situ temperature field.**

b. The aerothermal features of sites primarily govern the thermohydraulic behaviour as well as the energy performance of energy geostructures:
- **i. True**
- **ii.** False

c. The geothermal features of any specific project are typically:
- **i. Fixed**
- **ii.** Variable

d. A variation of one parameter characterising the energy performance of energy geostructures does not typically influence the geotechnical or structural performance:
- **i.** True
- **ii. False**

e. The design variables and associated parameters characterising the energy design of energy geostructures comprise the soil/rock and reinforced concrete thermal properties (e.g. thermal conductivity, specific heat), the undisturbed soil/rock and geostructure temperature (e.g. initial temperature) and the groundwater flow rate (e.g. Darcy's velocity).

f. The strength, stiffness and thermal expansion potential of the considered geomaterial (e.g. soil or concrete) can be broadly considered to be three design variables that majorly affect the geotechnical and structural design of energy geostructures:
- **i. True**
- **ii.** False

g. Different approaches are typically required to determine input parameters depending on the stage of the design process as well as on the complexity of the geostructure:
  i. True
  ii. False

h. Different methods should be used to determine input parameters depending on the design stage of energy geostructures. In the context of planning stages, parameters may be defined through 'rules of thumb' values. In the context of the schematic design, they should resort to the literature. For detailed design stages, input parameters require site-specific testing.

i. Three categories distinguish analysis and design procedures. Preliminary investigations involving simple in situ or laboratory tests, with correlations, should be performed for Category 1 analysis and design procedures, which are characterised by a purely empirical nature. Laboratory or in situ tests, with the potential to require some correlations, should be performed for Category 2 analysis and design procedures, which have a proper theoretical basis, often resort to the use of design charts and generally involve significant simplifications. Site-specific laboratory or in situ testing should be carried out for Category 3 analysis and design procedures, which have a proper theoretical nature, require the use of a computer and generally employ relatively advanced numerical or analytical techniques.

j. With reference to the geotechnical categories highlighted in the EN 1997 (2004) to assist in the establishment of minimum requirements for the extent and content of geotechnical investigations, energy geostructures typically belong to:
  i. Category 1
  ii. Category 2
  iii. Category 3

k. Guarded hot plate testing provides a mechanical parameter that can serve the geotechnical design of energy geostructures:
  i. True
  ii. False

l. The following main testing phases can be identified for guarded hot plate tests:
  1. Specimen preparation.
  2. Thermal loading.
  3. Test completion and dismounting.

m. Guarded hot plate testing allows defining the thermal conductivity of soil specimens during the transient phase of a one-dimensional heat transfer imposed on the specimen:
  i. True
  ii. False

n. Four main differences characterise steady-state compared to transient methods: (i) while the former methods can provide an estimate of only the effective thermal conductivity, the latter methods can often estimate the specific heat as well; (ii) while the former methods establish a temperature difference across the specimen that does not change with time, the latter methods monitor the time-dependent heat transfer within a specimen; (iii) while difficulties associated with the need to ensure a one-dimensional heat flow can be encountered through the former methods, these difficulties may be less burdensome through the latter methods; (iv) while noteworthy waiting times (hours to days for single data points) are required to achieve steady-state conditions through the former methods, these times are usually less notable through the latter methods because they do not require to achieve steady-state thermal conditions for determining the parameters of interest.

o. The effective thermal conductivity of geomaterials should be considered temperature dependent for the analysis and design of energy geostructures:
  i. True
  ii. False

p. Oedometer testing under nonisothermal conditions can serve the geotechnical and structural designs of energy geostructures.

q. The following main testing phases can be identified for oedometer tests under nonisothermal conditions:
  1. Specimen preparation.
  2. Saturation.
  3. Isothermal-mechanical and possible thermal loading.
  4. Isothermal-mechanical and possible thermal unloading.
  5. Test completion and dismounting.

r. The rationale for applying increments of mechanical load on the cap that is placed above the top porous stone in an oedometer apparatus is to maintain the initial height of the specimen constant when swelling of the material under saturation is observed and may affect the structure of the specimen.

s. The oedometric modulus E_{oed} is a key compressibility parameter of soils characterising the significance of volume changes caused by loading. It is defined as

$$E_{oed} = \frac{\Delta\sigma'_{z,i}}{\Delta\varepsilon_{z,i}}$$

From a graphical perspective, it is the inverse of the compressibility coefficient, which is the slope of the semi logarithmic $\sigma'_z - \varepsilon_z$ plot.

t. The compression index, C_c, is defined as:

$$C_c = -\frac{\Delta e_i}{\Delta \log \sigma'_{z,i}}$$

From a graphical perspective, it is the slope of the compression curve in the semilogarithmic $\sigma'_z - e$ plot. It is similar to the recompression index, C_r, and the swelling index, C_s, derived from the recompression and unloading curves in the semilogarithmic plot.

u. From a practical perspective, the compressibility parameters of soils can be considered *independent* of temperature with reference to the temperature variations associated with the geothermal operation of energy geostructures:

i. True

ii. False

v. The preconsolidation pressure is the maximum stress that a specimen has ever underwent. From the preconsolidation pressure, the isotropic preconsolidation pressure can be computed as

$$p'_c = \frac{(1 + 2K_0)\sigma'_p}{3}$$

w. The preconsolidation pressure should be considered temperature dependent for the analysis and design of energy geostructures:

i. True

ii. False

x. From the preconsolidation pressure, the *OCR* can also be computed as

$$OCR = \frac{\sigma'_p}{\sigma'_{z,0}}$$

where $\sigma'_{z,0}$ is the overburden vertical effective stress at a given depth where the soil specimen has been sampled or refers to. Values of $OCR < 1$ are associated with a underconsolidated state for the soil. A value of $OCR = 1$ is associated with a normally consolidated state for the soil. Values of $OCR > 1$ are associated with an overconsolidated state for the soil. Underconsolidation can result from processes including, for example deposition at a faster rate than consolidation. Normal consolidation, although extremely rare in the field, can result from significant loading processes leading to effective stress equilibrium with the overburden effective stress. Overconsolidation can result from unloading phenomena caused, for example by the movement of the groundwater table.

y. The volumetric thermal expansion coefficient of soils can be determined through an oedometer test from the relationship between the volumetric deformation and the applied temperature variation associated with a heating–cooling cycle, with reference to the thermal unloading branch. From the slope of the thermal unloading curves it is possible to evaluate the volumetric thermal expansion coefficient of the solid skeleton. Applying the theory of thermoelasticity and assuming an isotropic thermal response (volumetric thermal expansion coefficient β equal to three times the linear one α) the following relationships hold:

$$\Delta\varepsilon_x = \Delta\varepsilon_y = 0; \quad \Delta\sigma'_x = \Delta\sigma'_y; \quad \Delta\sigma'_z = 0$$

$$\Delta\varepsilon_x - \frac{1}{3}\beta\Delta T = \frac{1-\nu}{E}\Delta\sigma'_x$$

$$\Delta\sigma'_x = \frac{E}{1-\nu}\frac{1}{3}\beta\Delta T$$

$$\Delta\varepsilon_z = -\frac{1+\nu}{1-\nu}\frac{1}{3}\beta\Delta T$$

where $\Delta\varepsilon_z$ is the increment of vertical deformation measured during the test, $\Delta\varepsilon_x$ and $\Delta\varepsilon_y$ are the increments of horizontal deformation prevented in oedometric conditions, $\Delta\sigma'_z$ is the increment of vertical effective stress, $\Delta\sigma'_x$ and $\Delta\sigma'_y$ are the increments of horizontal effective stress (not zero due to the prevented thermoelastic deformation), ν is the Poisson's ratio of the soil and E is the Young's modulus of the soil.

z. In an oedometer tests, the application of a symmetrical heating–cooling cycle to a specimen in an overconsolidated state produces, at least theoretically, zero residual deformations at the end of thermal loading:
i. True
ii. False

aa. The consolidation parameters of most fine-grained soils are markedly *dependent* of temperature with reference to the temperature variations associated with the geothermal operation of energy geostructures:
i. True
ii. False

bb. The general elastic relationship for normal strain-normal stress relationship reads:

$$\varepsilon_x = \frac{1}{E}[\sigma_x - \nu(\sigma_y + \sigma_z)]$$

$$\varepsilon_y = \frac{1}{E}[\sigma_y - \nu(\sigma_x + \sigma_z)]$$

$$\varepsilon_z = \frac{1}{E}[\sigma_z - \nu(\sigma_x + \sigma_y)]$$

In oedometric conditions $\varepsilon_x = \varepsilon_y = \varepsilon_r = 0$, $\sigma_x = \sigma_y = \sigma_r$ and $\sigma_z = \sigma_v$
Substituting these conditions in the three equations above, we can obtain:

$$\varepsilon_r = \frac{1}{E}[\sigma_r - \nu(\sigma_r + \sigma_v)] = 0$$

The above gives:

$$\sigma_r = \frac{\nu}{1-\nu}\sigma_v = 12.5 \text{ kPa}$$

and the following stress tensor:

$$\sigma_{ij} = \begin{bmatrix} 12.5 & 0 & 0 \\ 0 & 12.5 & 0 \\ 0 & 0 & 12.5 \end{bmatrix}$$

cc. Triaxial testing under nonisothermal conditions is an experimental laboratory method for the characterisation of the deformation and failure of soils that can serve the geotechnical and structural design of energy geostructures.

dd. The following main testing phases can be identified for triaxial tests under nonisothermal conditions:

1. **Specimen preparation.**
2. **Saturation.**
3. **Consolidation.**
4. **Shearing.**
5. **Test completion and dismounting.**

ee. Consolidation of the specimen achieved via isothermal-mechanical loading can be applied to reproduce an isotropic, anisotropic or K_o stress state. Those states are expressed mathematically as:

$$\textbf{Isotropic: } \sigma'_x = \sigma'_y = \sigma'_z$$

$$\textbf{Anisotropic: } \sigma'_x \neq \sigma'_y \neq \sigma'_z$$

$$K_o\textbf{: } \sigma'_x = \sigma'_y = K_o \sigma'_z$$

ff. From a practical perspective, the deformation parameters of soils (e.g. Young's modulus) can be considered in most cases *dependent* of temperature with reference to the temperature variations associated with the geothermal operation of energy geostructures:

i. True

ii. **False**

gg. During thermal loading, the volume change of the specimen can be separated in different components as

$$\Delta V_i = \Delta V_{dr} - \Delta V_{de} - \Delta V_w - \Delta V_s$$

where ΔV_{dr} is the volume of water flowing out of or into the specimen (measured using a backpressure volume controller), ΔV_{de} is the thermal expansion of the drainage system (the irreversible component of deformation during a calibration test), ΔV_w is the thermal expansion of the pore water and ΔV_s is the thermal expansion of the solid skeleton characterising the specimen.

hh. The thermal expansion coefficient of geomaterials should be considered temperature dependent for the analysis and design of energy geostructures:

i. True
ii. **False**

ii. **The following formulae are used to determine the axial and volumetric strain, the deviatoric stress and the mean effective stress:**

$$\varepsilon_v = -\frac{\Delta V}{V_0}$$

with $\Delta V = -\Delta V_w$
and $V_0 = H_0 \pi \left(\frac{D_0}{2}\right)^2 = 88{,}460\ \text{mm}^3$

$$\varepsilon_z = -\frac{\Delta H}{H_0}$$

$$A = \frac{V}{H} = \frac{V_0 + \Delta V}{H_0 + \Delta H} = A_0 \frac{1 - \varepsilon_v}{1 - \varepsilon_z}$$

with $A_0 = 1134\ \text{mm}^2$

$$q = \sigma_1 - \sigma_3 = \frac{P}{A}$$

with

$$\sigma_1 = \sigma_c + \frac{P}{A}$$

and

$$\sigma_3 = \sigma_c$$

$$p' = p - p_w = \frac{\sigma_1 + 2\sigma_3}{3} - p_w = \frac{\frac{P}{A} + 3\sigma_c}{3} - p_w$$

The results are presented in the following table for each loading stage.

P[N]	ΔH[mm]	$\Delta V_w\,[\text{mm}^3]$	$\varepsilon_v[-]$	$\varepsilon_z[-]$	$A\,[\text{mm}^2]$	q[kPa]	p'[kPa]
0	0	0	0	0	1134	0	200
115	−1.95	880	0.0099	0.025	1151	99.86	233.28
235	−5.85	3720	0.042	0.075	1174	200.09	266.69
325	−11.7	7070	0.0799	0.15	1227	264.76	288.25
394	−19.11	8400	0.095	0.245	1359	289.85	296.61
458	−27.3	8400	0.095	0.35	1578	290.07	296.69

The results are plotted in the following graphs.

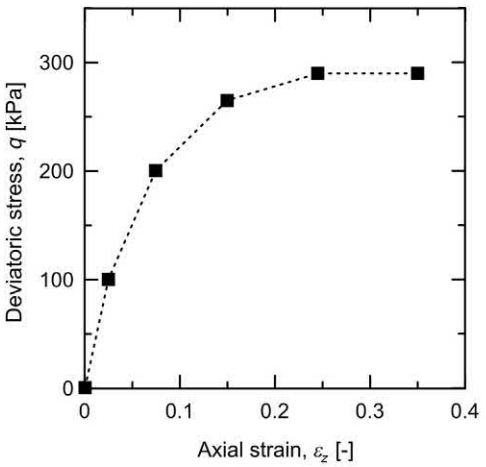

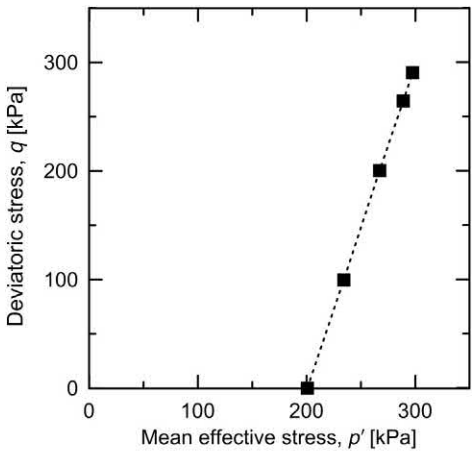

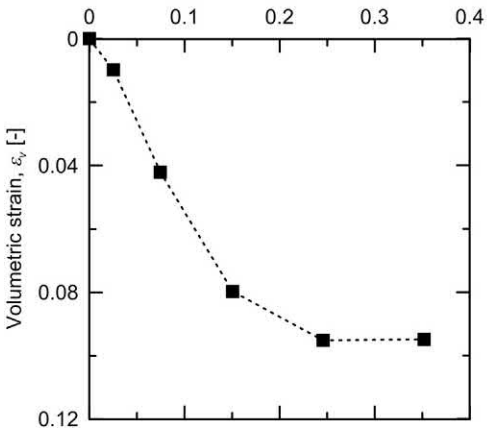

jj. Direct shear testing under nonisothermal conditions is an experimental laboratory method for the characterisation of the failure of soils or interfaces with soils that can serve the geotechnical and structural design of energy geostructures.

kk. The following main testing phases can be identified for the direct shear test under nonisothermal conditions:

1. **Specimen preparation.**
2. **Saturation.**
3. **Consolidation.**
4. **Shearing.**
5. **Test completion and dismounting.**

ll. Shear strength parameters such as cohesion, peak angle of shear strength and angle of shear strength under constant volume conditions can be effectively determined for both soil and interfaces with soil specimens by plotting in the Mohr plane the points of coordinates $(\sigma'_n;\tau)$ corresponding to the relevant stage of the shear test (e.g. when the peak strength of the material is reached and identified in the plane $\delta_h - \tau$ or in the plane $\delta_h - \delta_n$). Interpolation of more than two points of coordinates $(\sigma'_n;\tau)$ in the Mohr plane allows highlighting the failure envelope of the material and the relevant values of intercept cohesion (where applicable) and angle of shear strength (at peak or under constant volume conditions).

mm. From a practical perspective the shear strength parameters of concrete–soil interfaces can be considered *independent* of temperature with reference to the temperature variations associated with the geothermal operation of energy geostructures:

i. True

ii. False

nn. In direct shear tests, an appropriate specimen height cannot be defined to calculate shear strain and the only known stress components are the normal and shear stress acting on the horizontal plane. As the previous information does not allow to fully determine the stress state, stress–strain relationships or deformation parameters cannot be addressed from such tests.

oo. The key thermal parameters that can be defined through thermal response tests are the undisturbed ground temperature, T_0, the effective ground thermal conductivity λ_{soil} and the time-independent thermal resistance of heat exchanger R'_{ghe}.

pp. The following main testing phases can be identified for the thermal response test:

1. **Formation of a closed system and pressurisation.**
2. **Isothermal fluid circulation.**
3. **Thermal loading.**
4. **Thermal recovery.**
5. **Test completion and dismounting.**

qq. Three approaches can estimate the undisturbed ground temperature:

1. **Once the heat carrier fluid circulating in the pipes reaches thermal equilibrium with the surroundings (i.e. it reaches an approximately constant value representative of steady conditions), the outlet value of the stabilised fluid temperature is taken as an approximation of the undisturbed ground temperature;**

2. **Once the first circulation cycle of the heat carrier fluid is completed, the *minimum* value of the fluid temperature is selected and considered as an approximation of the undisturbed ground temperature;**
3. **Once the first circulation cycle of the heat carrier fluid is completed, the *average* value of the fluid temperature is selected and considered as an approximation of the undisturbed ground temperature;**

The best way to estimate the undisturbed ground temperature is through approach (3), while approaches (1) and (2) are characterised by shortcomings.

rr. The direct estimation of the thermal conductivity via the infinite line source model can be achieved by plotting the experimental measures of mean temperature of heat carrier fluid circulating in the pipes of the geothermal heat exchanger against the logarithmic time. After the chosen reference time, the relationship between heat carrier fluid temperature and the logarithmic time is typically linear and can be fitted by a straight line. This relationship can be expressed as

$$\overline{T}_f = k_{sl} \ln t + m_{sl}$$

where $\overline{T}_f$ [°C] is the mean fluid temperature, k_{sl} [°C] is the slope of the straight line and m_{sl} [°C] is the intercept with the vertical axis. The slope of the considered straight line, k_{sl}, can be employed through the infinite line source model to determine the effective thermal conductivity as follows

$$\lambda_{soil} = \frac{\dot{q}_l}{4\pi k_{sl}}$$

where $\dot{q}_l$ [W/m] is the linear thermal power applied to the geothermal heat exchanger.

ss. Because the influence of the ground thermal conductivity and time-independent thermal resistance on the actual thermal response of geothermal heat exchangers is counterbalanced, it is always preferable to use in analysis and design the pairs of λ_{soil} and R'_{ghe} estimated by the results of the thermal response test, and not only one of the two parameters. This approach allows mitigating the effect of a poor estimation of the values of λ_{soil} and R'_{ghe}.

tt. Values of $\lambda_{soil} \leq 1.5$ W/(m °C) may result in economically ineffective applications of geothermal heat exchangers.

uu. The theory available to interpret the result of thermal response test on energy piles can be directly applied to the result of tests on energy tunnels or walls:
   i. True
   ii. **False**

vv. **The undisturbed ground temperature can be determined as the average value of the inlet and outlet temperatures during the first phase of a TRT (when no thermal load is applied). The undisturbed ground temperature determined from the considered TRT is of 14.9°C. The undisturbed ground temperature determined via this approach may slightly differ from the actual one, because the considered approach suffers from the influence of the heating effect of the circulation pump of the TRT.**

The effective thermal conductivity of the ground can be estimated from the plot of the mean fluid temperature against time (in logarithmic scale). Graphically, the mean temperature is expressed as:

$$T_f(t) = k_{sl} \ln t + m = 1.80 \ \ln t + 19.90$$

where $\overline{T}_f$ [°C] is the mean fluid temperature, k_{sl} [°C] is the slope of the straight line and m [°C] is the intercept with the vertical axis. Knowing the applied thermal power per metre length of pile, $\dot{q}_l$, the effective thermal conductivity can be obtained as

$$\lambda_{soil} = \frac{\dot{q}_l}{4\pi k_{sl}} = \frac{64}{4\pi \cdot 1.80} = 2.83 \ \mathrm{W/(m\,^{\circ}C)}$$

Concerning the design of a system markedly resorting to heat extraction via energy geostructures and the development of more than one TRT leading to different values of effective thermal conductivity, a safety side approach would always consist in relying on the lower value of thermal conductivity. The reason for this is that the heat extraction potential decreases with the thermal conductivity. Therefore the use of lower values of the considered parameter will always lead to results that represent a lower bound compared to what may be foreseen to be achieved in practice.

ww. **The undisturbed ground temperature can be determined as the average value of the inlet and outlet temperatures during the first phase of a TRT (when no thermal load is applied). The undisturbed ground temperature determined from the considered TRT is of 12.0°C. The undisturbed ground temperature determined via this approach may slightly differ from the actual one, because the**

considered approach suffers from the influence of the heating effect of the circulation pump of the TRT.

The effective thermal conductivity of the ground can be estimated from the plot of the mean fluid temperature against time (in logarithmic scale). Graphically, the mean temperature is expressed as:

$$T_f(t) = k_{sl}\ln\ t + m = 1.26\ \ln t + 16.79$$

where $\overline{T}_f$ [°C] is the mean fluid temperature, k_{sl} [°C] is the slope of the straight line and m [°C] is the intercept with the vertical axis. Knowing the applied thermal power per metre length of pile, $\dot{q}_l$, the effective thermal conductivity can be obtained as

$$\lambda_{soil} = \frac{\dot{q}_l}{4\pi k_{sl}} = \frac{41}{4\pi \cdot 1.26} = 2.59\ \text{W/(m °C)}$$

Concerning the design of a system markedly resorting to heat extraction via energy geostructures and the development of more than one TRT leading to different values of effective thermal conductivity, a safety side approach would always consist in relying on the lower value of thermal conductivity. The reason for this is that the heat extraction potential decreases with the thermal conductivity. Therefore the use of lower values of the considered parameter will always lead to results that represent a lower bound compared to what may be foreseen to be achieved in practice.

xx. Answers:

a. With the ground conditions of interest, the SIA D0 190 prescribes a linear thermal power of −25 to −30 W/m for heat extraction and a maximum linear thermal power of 30 W/m for heat injection.

b. The most important demand is related to the heating of the building. The nominal power of the heat pump has to be distributed over the equipped piles. With the given *COP* [-], the extracted power from the piles can be calculated as:

$$\dot{Q}_R = \frac{COP - 1}{COP}\dot{Q}_S \tag{1}$$

where $\dot{Q}_R$ is the required thermal power from the ground and $\dot{Q}_S$ is the supplied thermal power to the building, comprising the power given by the work of the heat pump.

Thus

$$\dot{Q}_R = \frac{3.5 - 1}{3.5} \cdot (-60) = -42.9\ \text{kW}$$

The above thermal power corresponds to a heat energy extracted from the ground that is associated with the $\dot{Q}_S = 6$ kW of thermal power supplied by the heat pump for the heating of the building per unit time t. The associated energy to this power reads

$$Q_{R,H} = \dot{Q}_R t \tag{2}$$

With the available data, the aforementioned heat energy reads

$$Q_{R,H} = \dot{Q}_R t = -42.9(8 \cdot 29.5 \cdot 24) \times 10^{-3} = -243 \text{ MWh}$$

According to the SIA-D0190 (2005), the maximum linear thermal power that can be extracted from the piles is of −30 W/m. Considering that the total linear thermal power that can be extracted from a group of n_{EP} piles with a given thermally active length L is

$$\dot{q}_l = \frac{\dot{Q}_R}{n_{EP} L} \tag{3}$$

This leads to the following inequality

$$n_{EP} \geq \frac{\dot{Q}_R}{\dot{q}_l L} \Rightarrow n_{EP} \geq \frac{42.9 \times 10^3}{30 \cdot 19.2} = 74.4 \approx 75$$

Therefore at least 75 piles must be equipped with absorber pipes. The amount of heat that can be supplied after the heat pump operation for heating can be calculated according to the following relation

$$Q_{S,H} = \dot{Q}_S t \tag{4}$$

Otherwise, once $Q_{R,H}$ is calculated through Eq. (2), $Q_{S,H}$ can be directly determined from Eq. (1). Based on Eq. (4), the supplied heat energy to the building reads

$$Q_{S,H} = \dot{Q}_S t = -60(8 \cdot 29.5 \cdot 24) \times 10^{-3} = -340 \text{ MWh}$$

Because $Q_{S,H} < E_{H,tot}$, another technology (conventional heating systems) needs to be used to provide the remaining amount of heat of −738-(−340) = −398 MWh.

If all the heating is targeted from the energy piles, the peak power of −340 kW must be respected. With heat pumps with a *COP* of 3.5, a peak power of

$$\dot{Q}_R = \frac{COP - 1}{COP}\dot{Q}_S = \frac{3.5 - 1}{3.5}\cdot(-340) = -243 \text{ kW}$$

should be extracted from the piles. This corresponds to a maximum linear thermal power of

$$\dot{q}_l = \frac{\dot{Q}_R}{n_{EP}L} = \frac{-243\cdot10^3}{162\cdot19.2} = -78 \text{ W/m}$$

The aforementioned linear thermal power is higher than that proposed by the SIA-D0190 (2005) and therefore is considered unachievable.

c. The following temperature variations are estimated to occur in the energy piles due to heat extraction. The thermal resistance R'_{ghe} value used is 0.11 m °C/W.

Modelling approach		Modelled temperature variation, ΔT [°C]
Infinite cylindrical-surface source model	Simplified approach	−8.4
	Rigorous approach	−11.8
Infinite line source model	Simplified approach	−8.3
	Rigorous approach	−11.6

The prescribed margin is not respected considering the worst-case prediction of the models. The maximum linear thermal power for which an absolute temperature of 1°C is observed (i.e. associated to a temperature variation of $\Delta T = -10$°C from the natural temperature of the ground of 11°C) is −25.3 W/m. To guarantee the supplied thermal power for the heating of the building, the number of piles to be equipped as energy piles needs to increase up to

$$n_{EP} \geq \frac{-42.9 \times 10^3}{-25.3\cdot19.2} = 88.3 \approx 89$$

By lowering the applied thermal power to satisfy the aforementioned prescription, the temperature variation characterising the energy piles varies according to the different methods. The updated following temperature variations are estimated to occur in the energy piles for a thermal power of −25.3 W/m.

Modelling approach		Modelled temperature variation, ΔT [°C]
Infinite cylindrical-surface source model	Simplified approach	−7.0
	Rigorous approach	−10.0
Infinite line source model	Simplified approach	−7.0
	Rigorous approach	−9.8

d. The continuous power associated with the amount of energy that need to be supplied for cooling over four months can be estimated as

$$\dot{Q}_S = \dot{Q}_R = \frac{E_{C,tot}}{t} = \frac{Q_{R,C}}{t} = \frac{105 \times 10^6}{(4 \cdot 29.5 \cdot 24)} = 37 \text{ kW}$$

As a result, the linear thermal power applied to the piles is

$$\dot{q}_l = \frac{\dot{Q}_S}{n_{EP} L} = \frac{37 \times 10^3}{89 \cdot 19.2} = 21.65 \text{ W/m}$$

Yes, the long-term temperature is a concern. This fact can be appreciated by comparing the amount of injected and extracted heat through the piles. During warm periods, $Q_{R,C} = 105$ MWh are injected in the soil. During cold periods, $Q_{R,H} = -243$ MWh are extracted. The above corresponds to a ratio $|Q_{R,C}/Q_{R,H}| = 43\%$. The SIA-D0190 (2005) prescribes to inject at least 70% of the extracted energy and at maximum 90% to maintain the long-term efficiency of the system. As a result, a long-term drop in ground temperature is to be expected, with a consequent reduction in heating efficiency.

The range between 70% and 90% proposed by the SIA-D0190 (2005) corresponds to 170−219 MWh/year. To reach this level, one solution may be to increase the amount of injected heat to each pile that is foreseen to be equipped as geothermal heat exchanger. The corresponding range of linear thermal power would be

$$\dot{Q}_R = \frac{Q_{R,C}}{t} = \frac{170 \times 10^6}{(4 \cdot 29.5 \cdot 24)} = 60 \text{ kW}$$

(with a percentage of 70% of the extracted heat)

$$\dot{Q}_R = \frac{Q_{R,C}}{t} = \frac{219 \times 10^6}{(4 \cdot 29.5 \cdot 24)} = 77.3 \text{ kW}$$

(with a percentage of 90% of the extracted heat)

$$\dot{q}_l = \frac{\dot{Q}_R}{n_{EP} L} = \frac{60 \times 10^3}{89 \cdot 19.2} = 35.1 \text{ W/m}$$

(with a percentage of 70% of the extracted heat)

$$\dot{q}_l = \frac{\dot{Q}_R}{n_{EP} L} = \frac{77.3 \times 10^3}{89 \cdot 19.2} = 45.2 \text{ W/m}$$

(with a percentage of 90% of the extracted heat)

The aforementioned solution cannot be considered because it exceeds the limit of 30 W/m prescribed by the SIA-D0190 (2005). To overcome this issue, another solution may be to consider only the minimum amount of heat to inject (i.e. 70% of the extracted) to minimise the number of piles to be equipped and to vary the number of piles. This approach yields to a total number of piles of

$$n_{EP} = \frac{\dot{Q}_R}{\dot{q}_l L} = \frac{60 \times 10^3}{30 \cdot 19.2} = 104.2 \approx 105$$

The extraction rate decreases therefore from −25.3 W/m to

$$\dot{q}_l = \frac{\dot{Q}_R}{n_{EP} L} = -\frac{42.9 \times 10^3}{105 \cdot 19.2} = -21.3 \text{ W/m}$$

The aforementioned solution can be considered because it does not exceed the lower limit of −25 W/m prescribed by the SIA-D0190 (2005). Furthermore, it is associated to the following temperature variations.

Modelling approach		Modelled temperature variation, ΔT [°C]
Infinite cylindrical-surface source model	Simplified approach	−5.9
	Rigorous approach	−8.4
Infinite line source model	Simplified approach	−5.9
	Rigorous approach	−8.4

An additional amount of 170−105 MWh = 65 MWh of heat is needed. This amount of heat could be obtained from alternative heat sources such as solar thermal panels.

e. The following temperature variations are estimated to occur in the energy piles due to heat injection.

Modelling approach		Modelled temperature variation, ΔT [°C]
Infinite cylindrical-surface source model	Simplified approach	7.3
	Rigorous approach	10.8
Infinite line source model	Simplified approach	7.2
	Rigorous approach	10.5

f. The final energy design, which neglects any geotechnical or structural consideration about the performance of the piles, involves the equipment as geothermal heat exchanger of 105 energy piles over the 162 piles that are required for structural support. The features corresponding to this design are listed in the following table.

	Injection	Extraction
Heat transfer rate [W/m]	30	−21.3
Temperature variation [°C]	10.8	−8.4

g. The temperature variation modelled by the considered approaches is reported in the following table. The comparison between the (1) infinite cylindrical-source and (2) line source analytical solutions is reported in the following figure, while the error between the analytical solutions and the Fourier number with time are reported in the figure proposed thereafter.

Modelling approach		Modelled temperature variation, ΔT [°C]
Infinite cylindrical-surface source model	Simplified approach	−0.2
	Rigorous approach	−0.4
Infinite line source model	Simplified approach	−0.2
	Rigorous approach	−0.3

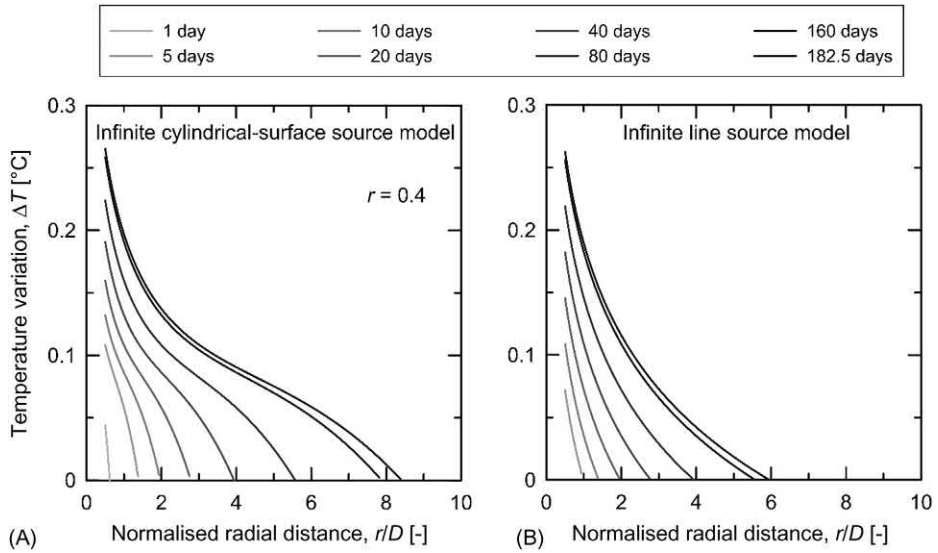

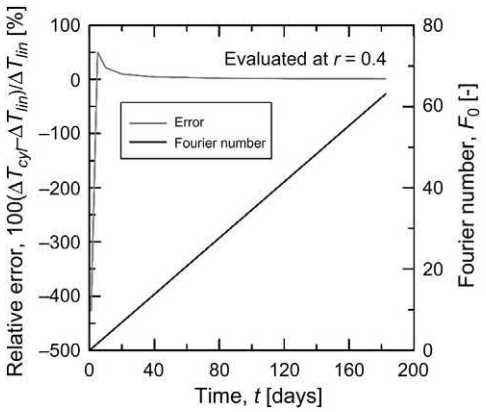

yy. Optical fibres systems are based on the comparison of a signal travelling along a reference fibre and a measuring fibre. The fibres are then fixed to the reinforcing cage of energy piles to measure vertical or radial strains.

Vibrating wire strain gauges measure the resonant frequency and temperature of a vibrating tensioned wire to determine its strain (an increase of the wire increases the resonant frequency). These vibrating wire strain gauges are fixed on the reinforcing cage of the pile.

CHAPTER 15

Performance-based design of energy piles

15.1 Introduction

The coupled application of thermal and mechanical loads to energy piles due to their multifunctional operation represents a challenge. From a design perspective, such a challenge is primarily related to the fundamentally different nature of thermal and mechanical loads, which yields to diverse effects on the mechanical (stress and deformation) response of energy piles. These effects must be considered in the geotechnical and structural design of energy piles via performance-based design approaches.

Thermal loads can be idealised as imposed deformations. These loads cause expansion and contraction of the energy piles and the surrounding ground. While energy piles expand upon heating and contract upon cooling, soils can expand or contract upon heating, and contract upon cooling. In most cases, a portion of the thermally induced deformation of energy piles is restrained by the surroundings and causes thermally induced stress in such foundations. The significance of the observed thermally induced strains and stresses depends on the end-restraint conditions and the ratio between the thermal expansion coefficient of the ground and that of the energy piles. Both of these aspects also characterise the vertical displacement and shear stress variations within energy piles. Energy piles subjected to thermal loads generally displace in opposite directions from the so-called null point of the vertical displacement and mobilise shear stress at the pile shaft to ensure equilibrium from the so-called null point of the shear stress. The locations of the referenced null points are generally different and can vary throughout loading. The stress, strain and displacement variations characterising energy piles can critically vary because of the influence of group effects associated with thermal loads. These effects are responsible for a greater group deformation than that of a single isolated pile under the same average load.

Mechanical loads can be idealised as prescribed forces. These loads typically cause stress and strain variations that decrease along the depth of the energy piles and the surrounding ground. In most cases, the evolutions with depth of the variations caused by mechanical loads are more uniform than those caused by thermal loads and are associated with displacement variations in a unique direction. The end-restraint conditions also govern, in this context, the significance of the

Analysis and Design of Energy Geostructures
DOI: https://doi.org/10.1016/B978-0-12-816223-1.00015-1

stress, strain and displacement variations, together with group effects caused by mechanical loads.

Much theoretical and empirical knowledge and many analysis tools have been made available to characterise the response of energy piles subjected to thermal and mechanical loads as well as to address the geotechnical and structural performance of such geostructures. In relatively recent years, design recommendations have been proposed and studies addressing performance-based design approaches have been carried out. Along with the previous developments, a performance-based design methodology for the considered geostructures is essential.

This chapter focuses on the performance-based design of energy piles subjected to axial mechanical loads and thermal loads. The considered subject is addressed via the proposition of a dedicated framework with particular reference to the Eurocodes. Nonetheless, the proposed developments may be extended to other performance-based standards and frameworks via potential modifications. Particular attention is given to energy piles made of reinforced concrete, as well as to the influence of compressive mechanical loads applied in conjunction with thermal loads to such foundations.

To address the aforementioned aspects, *performance-based design principles for general pile foundations* are presented first: in this context the objective is to highlight norms and relevant limit states that may be considered for the design of pile foundations. Second, a *performance-based design methodology for energy pile foundations* is proposed: the objective of this part is to define design criteria, problems and verification approaches to address the performance-based design of such foundations. Then, the *design for ultimate and serviceability limit states* is addressed: in this context the purpose is to expand on key steps characterising the design of energy piles at the considered limit states. Finally, *questions and problems* are proposed: the purpose of this part is to fix and test the understanding of the subjects covered in this chapter by addressing a number of exercises.

15.2 Performance-based design principles for general pile foundations

15.2.1 General

Principles and provisions for the performance-based design of pile foundations can be found in the EN 1997 (2004). Particular attention to the action of axial loads on pile foundations is given in the EN 1997-1 (2004). The considered provisions apply to piles installed by driving, boring, jacking and screwing, with or without grouting, and characterised by either a predominantly friction or end-bearing character. These provisions should not be applied to the design of piles that are intended as settlement reducers (e.g. applications of piles in some piled raft foundations).

According to Frank (2004), the reason for this is because the bearing function provided by the spread or raft foundation rather than from the piles in those cases involves overconservative partial factors for the piles. Complementary information that may be useful for the design or the execution of pile foundations is included in the EN 1992 (2004) for reinforced concrete piles, in EN 1993–5 (2007) for steel piles, in the EN 1536 (1999) for bored piles, in the EN 12063 (1999) for sheet pile walls, in the EN 12699 (2000) for displacement piles, in the EN 14199 (2005) for micropiles and in the EN 12794 (2005) for piles characterised by precast concrete products. The information contained in the previously listed documents should be considered as a basis for the design of the energy piles and the connected structural members or systems.

15.2.2 Relevant limit states

The most common limit states that need to be considered for the design of piles involve (EN 1997-1, 2004) (1) the loss of overall stability of the pile foundation, (2) the bearing resistance failure of the pile foundation, (3) the uplift or insufficient tensile resistance of the pile foundation, (4) the failure in the ground due to transverse loading of the pile foundation, (5) the structural failure of the pile in compression, tension, bending, buckling or shear, (6) the combined failure in the ground and the pile, (7) the combined failure in the ground and the structure, (8) excessive settlement, (9) excessive heave, (10) excessive lateral movement, or (11) vibrations. The considered limit states may affect the geotechnical and/or the structural performance of the referenced structures. Phenomena (1–7) generally involve ultimate limit states. Phenomena (8–10) generally involve serviceability limit states for the geostructure or ultimate limit states for the superstructure supported. The phenomenon (11) generally represents a serviceability limit state.

In the case of axially loaded piles, the design shall demonstrate that exceeding the following limit states is sufficiently improbable (EN 1997-1, 2004):

1. Ultimate limit states of compressive or tensile resistance failure of a single pile.
2. Ultimate limit states of compressive or tensile resistance failure of the pile foundation as a whole.
3. Ultimate limit states of collapse or severe damage to a supported structure caused by excessive displacement or differential displacements of the pile foundation.
4. Serviceability limit states in the supported structure caused by displacement of the piles.

Critical approaches and aspects to verify the performance of energy piles with reference to the considered limit states are provided in the following.

15.3 Performance-based design methodology for energy pile foundations

15.3.1 General

In principle, the geotechnical and structural performance of energy piles should be verified against the influence of thermal loads, applied in conjunction with mechanical loads, at both ultimate and serviceability limit states. In practice, according to Rotta Loria et al. (2019), the effects of thermal loads should only be considered for serviceability limit state verifications because they are unlikely to exceed ultimate limit states. In other words, thermal loads involve effects that can be neglected in the performance-based design of energy piles at ultimate limit states, while they should only be considered at serviceability limit states. Therefore the design and verification of energy piles at ultimate limit states can be considered as a conventional process against the action of mechanical loads only. In contrast, the design and verification of energy piles at serviceability limit states is a modified process that must account for the action of mechanical and thermal loads. The previous approach agrees with the Eurocodes (EN 1992, 2004), in which it is specified that 'thermal effects should be considered for ultimate limit states only where they are significant (e.g., fatigue conditions, [...] second order effects [...]). In other cases, they need not be considered, provided that the ductility and rotation capacity of the elements are sufficient'.

Typical characteristic values of temperature variation associated with cooling thermal loads applied to energy piles can be considered to range between $\Delta T_k = -5°C$ and $-10°C$. At worst, a value of $\Delta T_k = -15°C$ may be considered in warm climates. Typical characteristic values of the temperature variation associated with the heating thermal loads applied to energy piles range between $\Delta T_k = 10°C$ and $20°C$. At worst, a value of $\Delta T_k = 30°C$ may occur in cool climates.

15.3.2 Design criteria

The previous methodology for which the performance of energy piles against thermal loads is verified only at serviceability limit states (while not at ultimate limit states) can be considered appropriate as long as the following two design criteria are employed, and is corroborated by the arguments subsequently proposed (Rotta Loria et al., 2019):

1. A design compressive strength of the reinforced concrete section (e.g. for no moments applied) at least equal to the design bearing capacity of the pile must be ensured (increasing the compressive strength of reinforced concrete sections can be achieved, e.g. through an increase of the concrete class or reinforcement. Attention must be given to the technical feasibility of using higher concrete classes with reference to the quality of the concrete, especially when dealing with bored piles). When this approach is not employed, the design loads sustained from a

geotechnical perspective may induce or exceed an ultimate limit state from a structural perspective. In contrast, the proposed approach guarantees a potential ductile collapse mechanism related to the excess of ultimate limit states from a geotechnical perspective first.

2. A minimum steel reinforcement area of the reinforced concrete section must be chosen. When this approach is not employed, the requirements of durability and deformation (e.g. cracking) of the materials constituting the designed structures may not be satisfied. In contrast, this approach guarantees durability and ductility.

15.3.3 Geotechnical arguments

From a geotechnical perspective, displacement and equilibrium considerations allow verifying that ultimate limit states are not exceeded. Displacement considerations involve limiting differential displacements occurring among the piles in the ground to ensure that superstructures (e.g. hyperstatic) are not affected by unacceptable stress variations that may be associated with failure or collapse mechanisms. Equilibrium considerations involve comparing the design values of the load acting on the pile and the load supported by the pile (i.e. load capacity) to ensure that no failure or collapse mechanisms in the ground are achieved.

In this context, with regards to both displacement and equilibrium considerations, the worst foreseeable condition for the geotechnical performance of energy piles involves foundations with fully mobilised shaft and base capacities caused by a cooling thermal load and a (compressive) mechanical load (Rotta Loria et al., 2019). In this theoretical condition where the shaft and base capacities are fully mobilised and soil behaviour can be assumed as perfectly plastic, the null point of an energy pile subjected to cooling thermal loading is located at or towards the toe depending on whether a slab is present at the head. Therefore the maximum possible head settlements of energy piles caused by thermal loading, in addition to those caused by mechanical loading, occur. This phenomenon has the potential to exceed a geotechnical ultimate limit state. Piles with fully mobilised capacities subjected to a heating thermal load are of no concern because such a load causes no head settlement. In this theoretical condition where the shaft and base capacities are fully mobilised and soil behaviour can be assumed as perfectly plastic, the null point of an energy pile subjected to heating thermal loading is necessarily located at the head irrespective of whether a slab is present or not at the head. This is the only way to ensure equilibrium. Otherwise, any other location of the null point would cause an increase of the compression force within the pile in the zone above the null point (upward movement), which could not be balanced because a downward movement of the part below the null point would be produced freely (perfect plasticity). The application of a heating thermal load in all other cases in which full mobilisation of the shaft and

base capacities is not achieved induces an upward head displacement of the energy piles. However, the considered phenomenon represents a serviceability limit state problem and is thus not relevant for considerations related to ultimate limit states.

From the perspective of displacement considerations, cooling thermal loads are unlikely to involve energy pile settlements (e.g. differential) capable of generating a collapse mechanism (Rotta Loria et al., 2019). Typical orders of magnitude of energy pile settlements caused by a cooling thermal load applied after mechanical loading are of $0.10\%D$–$0.70\%D$ for pile slenderness rations ranging from $L/D = 20 - 50$ (where L and D are the pile length and diameter, respectively) (Rotta Loria et al., 2019). Therefore from the perspective of displacement considerations, the effects of thermal loads can be considered negligible for the sake of geotechnical verifications at the ultimate limit states. Group effects caused by the interactions among piles may increase these displacements. However, these effects should only be considered at serviceability limit states due to the magnitude of the phenomena involved.

From the perspective of equilibrium considerations, even though in principle full mobilisation of the capacity of energy piles may be caused by the combined application of thermal loads and mechanical loads, in practice the null points always ensure equilibrium with respect to the influence of thermal loads (Rotta Loria et al., 2019). In fact, for any magnitude of thermal load applied to energy piles, the reactions provided by the soil below and above the null point of the shear stress compensate for each other and prevent the formation of a collapse mechanism (cf. Fig. 15.1). Energy pile equilibrium will thus always be ensured, with zero thermally induced displacements occurring in correspondence with the null point of the vertical displacement that will prevent the formation of a collapse mechanism. Based on the above, thermal loads cannot cause a geotechnical collapse mechanism for energy piles from an equilibrium perspective, that is they cannot involve geotechnical ultimate limit states.

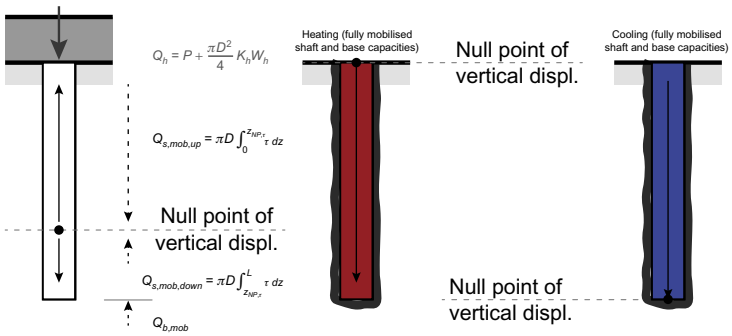

Figure 15.1 Vertical equilibrium of energy piles provided in any case by the presence of the null point.

15.3.4 Structural arguments

From a structural perspective, equilibrium considerations allow verifying that ultimate limit states are not exceeded. Equilibrium considerations involve comparing the design values of the acting load on the pile and the load supported by the considered pile cross section (or portion) to ensure that no failure mechanisms in the structure are achieved.

In this context, the worst foreseeable conditions for the structural performance of energy piles involves foundations with partially mobilised shaft and base capacities caused by either a significant cooling thermal load and a low (compressive) mechanical load or by a significant heating thermal load and a high (compressive) mechanical load (Rotta Loria et al., 2019). In these conditions, stresses are generated by the applied loads, with the potential to exceed a structural ultimate limit state.

From the perspective of equilibrium considerations, heating thermal loads applied in conjunction with mechanical loads are unlikely to overcome the design compressive strength characterising the cross sections of energy piles, that is they are unlikely to exceed the structural ultimate limit states (Rotta Loria et al., 2019). This result is ensured by the design criterion related to the design compressive strength characterising the cross sections of energy piles proposed by Rotta Loria et al. (2019) and has been highlighted in the same study. In contrast, at least in principle, cooling thermal loads applied in conjunction with mechanical loads may overcome the design tensile strength characterising the cross sections of energy piles, that is they may exceed the structural ultimate limit states. This result is corroborated data presented by Rotta Loria et al. (2019), although it has been highlighted to unlikely occur in practice in the same referenced study because of the following considerations.

The actual behaviour of reinforced concrete is nonlinear and characterised by the appearance of cracks beyond specific strain levels. If the minimum reinforcement is able to sustain the cracking force, the member does not fail upon the formation of the first crack (brittle behaviour) and the appearance of cracks leads to stress redistribution and a decrease in the stiffness of the structure. The considered stiffness involves lower values of stress compared to those associated with a stiffness related to uncracked cross sections and linear stress–strain relationships. Therefore although the Eurocodes (EN 1992, 2004) state to consider linear stress–strain relationships and uncracked cross sections in performance-based design, lower stresses can be expected after the strain levels associated with cracking are achieved.

As soon as a due account of the nonlinear stress–strain relationship characterising reinforced concrete is made, a ductility-oriented design approach becomes essential. The reason for this is that, when a displacement is imposed to a redundant structural member, equilibrium is ensured as far as ductility capacity is sufficient. Therefore thermally imposed tensile strains can be accommodated by the structure and the induced stress is simply derived from the constitutive model. To ensure an adequate ductility

capacity of the reinforced concrete members, (1) the resisting axial force of the cross sections needs to be greater than the axial force needed to crack them due to potential strain localisation effects, (2) the reinforcement has to be characterised by a large deformation capacity and (3) the ratio f_t/f_y has to respect a lower bound (where f_t and f_y are the tensile strength and yield strength of the reinforcement steel). Condition (1) is achieved by ensuring the minimum reinforcement ratio reported by Rotta Loria et al. (2019). Condition (2) is related to the magnitude of the action effects. Condition (3) is generally met because standards prescribe minimum values of the ratio f_t/f_y.

Once a ductility-oriented design approach is ensured, the key aspect eventually relies on understanding the level of deformation associated with a given load. This final consideration allows considering unsatisfactory verifications, such as those previously encountered, to be *satisfactory* (Rotta Loria et al., 2019).

Based on the above, the following aspects can be highlighted for energy piles:

1. The choice of a suitable minimum reinforcement area, such as that proposed by Rotta Loria et al., (2019), ensures ductility. Although concrete cracking causes a variation of axial stiffness along the piles that might involve phenomena of strain localisation, the strain caused by thermal loads remains within the cracked development stage for practical temperature variations. This result is qualitatively shown in Fig. 15.2 with reference to the relationship between the design traction axial load N_d and the normalised axial displacement $\Delta w/L$ characterising a reinforced concrete energy pile member that has minimum reinforcement. This relationship is compared with that of the same member characterised by the simultaneous occurrence of cracks (i.e. coinciding with the response of a single mean cross section), as well as with the relationship of the reinforcement steel alone.
2. By comparing the imposed strain levels caused by thermal loads with the deformation capacity of an appropriately designed cross-section, it can be realised that the structural ultimate limit states will never be exceeded by the influence of these loads, irrespective of whether strain localisation is developed or not. Cracking may occur in concrete because of the action of cooling thermal loads. However, a sufficient ductility capacity is ensured by the proposed design approach, and structural ultimate limit states cannot occur. Concrete cracking is an ordinary phenomenon that needs to be controlled.

Based on the above, thermal loads cannot involve the structural failure of energy piles, that is they cannot exceed the structural ultimate limit states.

15.3.5 Typical design problems

Two typical design problems exist for piles and may arise in design (Rotta Loria et al., 2019):

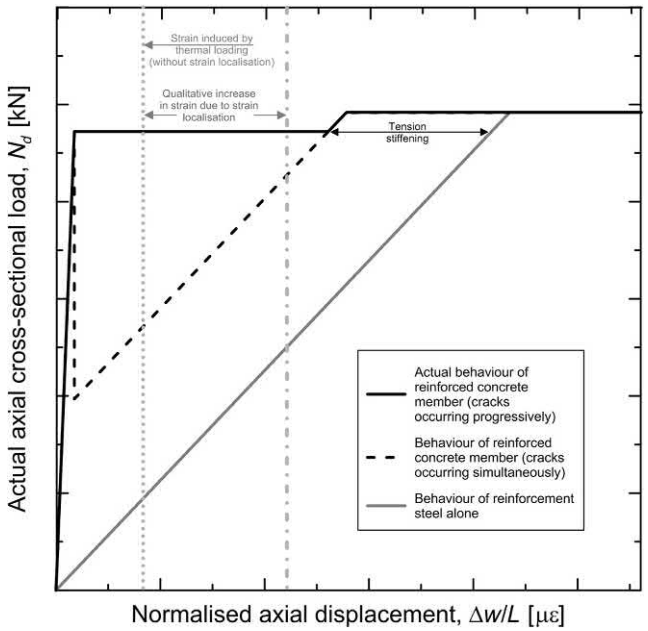

Figure 15.2 Relationships between axial cross sectional load and normalised axial displacement for energy piles made of reinforced concrete. *Redrawn after Rotta Loria, A.F., Bocco, M., Garbellini, C., Muttoni, A., Laloui, L., 2019. The role of thermal loads in the performance-based design of energy piles. Geomech. Energy Environ. Available from: https://doi.org/10.1016/j.gete.2019.100153.*

1. *Constant applied mechanical load and varying pile length* – A pile length may be defined for each pile of a foundation to sustain an applied design mechanical load. However, the considered length may be increased to a more meaningful length. As a result, the actual pile design load capacity will be higher than the needed value.
2. *Varying applied mechanical load and constant pile length* – A design mechanical load may be considered for all piles of a foundation based on the maximum load applied to one or more piles. However, not all the piles of the foundation need to effectively sustain this load. As a result, the actual length of the pile will be increased compared to the necessary value.

As soon as a length greater than needed characterises energy piles subjected to a given mechanical load, the axial load capacity of such foundations increases and thermally induced effects become more burdensome for the same applied temperature variation. From a geotechnical perspective, the previous aspect is related to the fact that, for the same applied temperature variation ΔT and linear thermal expansion coefficient α_{EP}, longer piles involve proportionally greater variations in length $\Delta L = \alpha_{EP}\Delta TL$ despite the thermally induced strain under free expansion conditions is independent of their length, that is $\varepsilon_f^{th} = -\alpha_{EP}\Delta T$. From a structural perspective,

the previous aspect can be highlighted considering that longer energy piles subjected to the same value of mechanical load are characterised by greater thermally induced stresses. Based on the previous considerations, oversizing energy piles should be avoided while an adequate sizing of these foundations should be considered. In particular, if the aim is to limit the vertical displacement of energy piles caused by thermal loads, greater pile diameters should be employed while longer pile lengths should be avoided (Rotta Loria et al., 2019). The previous result is in contrast with the belief that longer piles ensure greater safety against the action of thermal loads. It should also be distinguished by the justified consideration that designs considering longer piles ensure greater safety against the actions of mechanical loads.

15.3.6 Verification method

Two aspects must be considered to verify the structural and geotechnical performance of energy piles (Rotta Loria et al., 2019):

1. The vertical stress variations caused by mechanical and thermal loads must be considered with respect to the entire length of the energy piles, and the most stressed section must be verified.
2. The vertical displacement variations caused by mechanical and thermal loads must be considered with respect to the head of the energy piles.

Both the vertical stress and displacement variations caused by mechanical and thermal loads vary along energy piles. However, while the most stressed section must be verified along energy piles to ensure adequate performance that would be potentially unsatisfied otherwise (e.g. locally), only the displacements at the head of such foundations should be considered because their performance (together with that of the connected structure(s)) is primarily related to the displacements of the considered setting.

15.3.7 Partial factors for thermal loads acting on energy piles

To consider in the combinations of actions at serviceability limit states the influence of thermal loads, the following factors for the combination, frequent and quasipermanent values of such variable actions should be employed, respectively (Rotta Loria et al., 2019): $\psi_0 = 0.60$, $\psi_1 = 0.50$ and $\psi_2 = 0.50$.

15.4 Design for ultimate limit states

15.4.1 General

The fundamental inequality that must be verified for all load combinations at ultimate limit states when dealing with single and groups of piles subjected to axial mechanical loading reads

$$F_{c;d} \leq R_{c;d} \tag{15.1}$$

where $F_{c;d}$ is the design axial load (e.g. compression) acting on a single pile or a group of piles and $R_{c;d}$ is the design value of the ground resisting load (e.g. compression) associated with a single pile or a group of piles. The design acting load is typically determined from the combinations of actions that follow the general format of the partial factor method. The design ground resisting load is typically determined through either among three approaches: (1) the results of load tests (e.g. static or dynamic), (2) calculations from profiles of ground tests and (3) calculations from soil shear strength parameters.

For the sake of verifications against ultimate limit states, the following considerations should be borne in mind:

- A settlement of the pile head equal to 10% of the pile base diameter should be adopted as the 'failure' criterion (EN 1997, 2004).
- When pile foundations significantly displace downwards or upwards with negligible increase or decrease of resistance, the design should consider the margin of safety with respect to compressive or tensile resistance failure.
- Ultimate limit states of pile foundations are only reached when a significant number of piles fail simultaneously or when the structure connected to the piles fails. As long as pile foundations are not subjected to one of these mechanisms, an ultimate limit state is not reached (EN 1997, 2004).
- Two failure mechanisms may be considered for pile groups (EN 1997, 2004): (1) compressive or pull-out resistance failure of the piles individually and (2) compressive or pull-out resistance failure of the piles and the ground contained between them acting as a block. The design resisting load should be taken as the lower value associated with the previous failure mechanisms.
- To define the strength design of individual piles, the actions should be determined considering (EN 1992, 2004) (1) the interaction between the piles, (2) the pile cap and (3) the supporting ground.
- Where the piles are located in several rows, the action on each pile should be evaluated by considering the interaction between the piles (EN 1992, 2004). This interaction may be ignored when the clear distance between the piles is greater than two times the pile diameter (EN 1992, 2004).
- The pull-out resistance of individual piles should be checked through the Eurocodes using the geotechnical (GEO) set of partial factors and the relevant inequality (EN 1997, 2004). Uplift failure of group of piles in tension may be considered through the resistance of the block of ground containing the piles and checked through the Eurocodes using the uplift (UPL) set of partial factors and the relevant inequality (EN 1997, 2004).

- The main difference between the methods for determining the ground resistance of piles in tension and those for piles in compression is that the base resistance is always neglected in the former case in contrast to the latter case.

15.4.2 Calculation of the design acting load

The design value of a mechanical load acting on a single pile or a group of piles, F_d, may either be assessed directly through the combination of the relevant loads or derived from representative values of actions as follows

$$F_d = \gamma_F F_{rep} \tag{15.2}$$

with

$$F_{rep} = \psi F_k \tag{15.3}$$

where γ_F and ψ are partial factors, and F_{rep} and F_k are the representative and characteristic values of the considered action(s), respectively.

In situations where a single permanent load G_{rep} and a single variable mechanical load Q_{rep} are present, for example the combination of actions allows defining the design axial compressive load $F_{c;d}$ by multiplying the representative permanent and variable loads by the corresponding partial factors γ_G and γ_Q in a relatively straightforward way as follows

$$F_{c;d} = \gamma_G G_{rep} + \gamma_Q Q_{rep} \tag{15.4}$$

Two sets of recommended partial factors for actions and effects of actions are provided in Table 15.1 with reference to the EN 1997 (2004). The self-weight of the pile should be included when calculating the design axial compressive load $F_{c;d}$ along

Table 15.1 Recommended partial factors for actions and effects of actions.

Action	Symbol	Set	
		A1	A2
Permanent			
Unfavourable Favourable	γ_G	1.35 1.0	1.0 1.0
Variable			
Unfavourable Favourable	γ_Q	1.5 0	1.3 0

Source: Data from the EN 1997, 2004. Eurocode 7: Geotechnical Design. London, United Kingdom, p. 171.

with any downdrag, heave or transverse loading. However, the common practice of assuming that the weight of the pile is balanced by the overburden allows excluding this contribution from $F_{c;d}$ and $R_{c;d}$. The pile weight may not cancel the weight of the overburden if the downdrag is significant, the ground is light or the pile extends above the ground surface (EN 1997, 2004).

15.4.3 Calculation of the design ground resisting load

The design value of the compressive ground resisting load may be obtained in two ways: by treating the resisting load as a total load or by separating it into the shaft and base components developed along the pile(s). In the former case, the design value of such load is obtained by dividing the total characteristic resisting load, $R_{c;k}$, by the relevant partial factor, γ_t, as

$$R_{c;d} = \frac{R_{c;k}}{\gamma_t} \tag{15.5}$$

In the latter case, the design value of the compressive ground resisting load is obtained by dividing the characteristic shaft and base loads, $R_{s;k}$ and $R_{b;k}$, respectively, by the relevant partial factors γ_s and γ_b, as

$$R_{c;d} = \frac{R_{s;k}}{\gamma_s} + \frac{R_{b;k}}{\gamma_b} \tag{15.6}$$

Different sets of partial factors should be considered for driven, bored and continuous flight auger (CFA) piles EN 1997-1 (2004). Four sets of recommended values of these factors are reported in Table 15.2 with reference to the EN 1997 (2004). The following aspects should be considered when employing the previous partial factors:

- The R1 partial factor values are greater than 1.0 for bored and CFA piles in compression, but are equal to 1.0 for driven piles;
- The R2 partial factors are the same for all three different types of pile;
- The R3 partial factors are all equal to 1.0 for all three different types of pile;
- The R4 partial factors are all greater than 1.0 and greater than the R2 partial factor values;
- For piles in tension, only the shaft resistance factor is relevant and this has the same value for all three types of pile.

In the following, noteworthy aspects for the definition of the design value of the compressive ground resisting load are highlighted. To this aim, the three typical approaches resorting to static load tests, ground profile results and shear strength parameters that can be used to determine this design quantity are considered.

Table 15.2 Recommended partial resistance factors for driven, bored and continuous flight auger piles.

Resistance	Symbol	Set			
		R1	R2	R3	R4
Pile resistance factors for driven piles					
Base	γ_b	1.0	1.1	1.0	1.3
Shaft (compression)	γ_s	1.0	1.1	1.0	1.3
Total/combined (compression)	γ_t	1.0	1.1	1.0	1.3
Shaft in tension	$\gamma_{s,t}$	1.25	1.15	1.1	1.6
Partial resistance factors for bored piles					
Base	γ_b	1.25	1.1	1.0	1.6
Shaft (compression)	γ_s	1.0	1.1	1.0	1.3
Total/combined (compression)	γ_t	1.15	1.1	1.0	1.5
Shaft in tension	$\gamma_{s,t}$	1.25	1.15	1.1	1.6
Partial resistance factors for CFA piles					
Base	γ_b	1.1	1.1	1.0	1.45
Shaft (compression)	γ_s	1.0	1.1	1.0	1.3
Total/combined (compression)	γ_t	1.1	1.1	1.0	1.4
Shaft in tension	$\gamma_{s,t}$	1.25	1.15	1.1	1.6

Source: Data from the EN 1997, 2004. Eurocode 7: Geotechnical Design. London, United Kingdom, p. 171.

15.4.3.1 Calculation from static load test

Load tests directly allow determining the characteristic ground resisting load $R_{c;k}$ from measured resisting load values $R_{c;m}$ associated with an ultimate limit state, by applying correlation factors ξ_1 and ξ_2 to the mean and minimum values of measured loads as follows

$$R_{c;k} = \min\left\{\frac{\left(R_{c;m}\right)_{mean}}{\xi_1}; \frac{\left(R_{c;m}\right)_{min}}{\xi_2}\right\} \tag{15.7}$$

Recommended values for ξ_1 and ξ_2 depending on the number of pile load tests are given in Table 15.3 with reference to the EN 1997 (2004). The discussed values for ξ_1 and ξ_2 show the advantage of carrying out more load tests, because the correlation values reduce as the number of load tests increases, so that higher $R_{c;k}$ values are determined. For structures that have sufficient stiffness to transfer loads from weak to strong piles, the ξ_i values may be divided by 1.1 (EN 1997, 2004).

For piles in compression, it is often difficult to identify the value of load associated with the likely achievement of an ultimate limit state from static load test results because the pile load-settlement curve shows a continuous curvature. Especially in

Table 15.3 Recommended correlation factors ξ_1 and ξ_2 to determine characteristic pile resistance from pile load results.

Number of tests	1	2	3	4	≥ 5
ξ_1	1.4	1.3	1.2	1.1	1.0
ξ_2	1.4	1.2	1.05	1.0	1.0

Source: Data from the EN 1997, 2004. Eurocode 7: Geotechnical Design. London, United Kingdom, p. 171.

Table 15.4 Recommended correlation factors ξ_3 and ξ_4 to determine characteristic pile resistance from ground test results.

Number of tests	1	2	3	4	5	7	10
ξ_3	1.4	1.35	1.33	1.31	1.29	1.27	1.25
ξ_4	1.4	1.27	1.23	1.20	1.15	1.12	1.08

Source: Data from the EN 1997, 2004. Eurocode 7: Geotechnical Design. London, United Kingdom, p. 171.

these cases, a value of settlement of the pile head equal to 10% of the pile base diameter should be adopted as the 'failure' criterion to get the associated value of load (EN 1997, 2004).

15.4.3.2 Calculation from ground test profiles

Ground test profiles obtained from in situ tests, such as cone or standard penetration tests, directly allow determining the characteristic ground resisting load $R_{c;k}$ from measured resisting load values $R_{c;m}$ associated with an ultimate limit state, by applying correlation factors ξ_3 and ξ_4 to the mean and minimum values of measured loads as follows

$$R_{c;k} = \min\left\{\frac{\left(R_{c;m}\right)_{mean}}{\xi_3}; \frac{\left(R_{c;m}\right)_{min}}{\xi_4}\right\} \tag{15.8}$$

Recommended values for ξ_3 and ξ_4 depending on the pile load tests are given in Table 15.4 with reference to the EN 1997 (2004).

15.4.3.3 Calculation from soil shear strength parameters

Shear strength parameters indirectly allow determining the shaft and base contributions of characteristic ground resisting load, $R_{s;k}$ and $R_{b;k}$, through appropriate capacity formulations. Because the ground is the material that absorbs all the actions through the pile, the selection of characteristic values for geotechnical parameters shall take account of the following (EN 1997, 2004):

- Geological and other background information, such as data from previous projects;

Table 15.5 Partial factors for ground parameters.

Ground parameter	Symbol	Set	
		M1	M2
Angle of shear strength[a]	$\gamma_{\varphi'}$	1.0	1.25
Cohesion	$\gamma_{c'}$	1.0	1.25
Undrained shear strength	γ_{c_u}	1.0	1.4
Unconfined strength	γ_{UCS}	1.0	1.4
Weight density	γ_{γ}	1.0	1.0

[a]This factor is applied to $\tan\varphi'$.
Source: Data from the EN 1997, 2004. Eurocode 7: Geotechnical Design. London, United Kingdom, p. 171.

- Variability of the measured property values and other relevant information, for example from existing knowledge;
- Extent of the field and laboratory investigation;
- Type and number of samples;
- Extent of the zone of ground governing the behaviour of the geotechnical structure;
- Limit state being considered;
- Ability of the geotechnical structure to transfer loads from weak to strong zones in the ground.

To obtain the design value of ground resisting load via the present approach, partial factors γ_M may be applied either to the characteristic ground properties X_k, to the characteristic resisting loads R_k or to both. Two sets of recommended partial factors for ground parameters γ_M are reported in Table 15.5 with reference to the EN 1997 (2004).

15.5 Design for serviceability limit states

15.5.1 General

The geotechnical and structural performance of the energy piles as well as the structural performance of the connected superstructure at serviceability limit states must be verified against the effects of thermal loads, applied alone or in conjunction with mechanical loads (Rotta Loria et al., 2019). The following aspects should be addressed for the considered purpose:

1. Single and group vertical displacement (e.g. differential and average) limitation, considering group effects;
2. Deflection and angular distortion control;
3. Compressive stress limitation;
4. Tensile stress limitation;
5. Crack control.

15.5.2 Vertical displacement, deflection and angular distortion control

Limiting the vertical displacements of energy piles [i.e. aspect (1) highlighted in Section 15.5.1] is strictly related to the control of deflection and angular distortion characterising such foundations [i.e. aspect (2) highlighted in Section 15.5.1], and represents a key step for ensuring the required geotechnical serviceability performance of such foundations. The previous result can typically be achieved by ensuring that a sufficient low fraction of the ground strength is mobilised to keep deformations within the required limits.

Limiting movements of foundations is crucial and any differential movements leading to deformation in the supported structure shall be limited to ensure that they do not lead to a limit state in the structure (EN 1997, 2004). The selection of design values for limiting movements and deformations depends on a vast list of parameters and the calculation of differential displacements shall take into account (1) the occurrence and rate of vertical displacements and ground movements; (2) random and systematic variations in ground properties; and (3) the stiffness of the structure during and after construction, among others. The previous aspects shall be considered as guidance criteria to evaluate vertical displacements of energy piles caused by mechanical and thermal loads. Limits shall be fixed and justified by the designer. In fact, defining general recommendations valid for all possible design situations is probably undoable: vertical displacements acceptable in some design situations may be unacceptable in others as a result of the conception and details of the structure, the related function of the structure and the reaction of users.

The critical situation related to the head settlement of energy piles can be associated with the combined action of a downward mechanical load and a negative temperature variation applied to the piles. Head heave can also occur due to a positive temperature variation applied to the piles against the settlement induced by the downward mechanical load. Irrespective of the loading considered, assuming energy piles to be free of any head restraint provides conservative estimates of the vertical head displacement that is likely to be encountered in practice (Rotta Loria et al., 2019).

Assuming a balanced thermal field of the subsurface over time, an increase of the head settlement of individual energy piles can occur mainly because of the following aspects:

1. Group effects;
2. Irreversible phenomena;
3. Variations of ground properties;
4. Negative skin friction or downgrad phenomena;
5. Time-dependent effects.

In principle, consideration of all of the previous aspects requires the development of comprehensive analyses (e.g. numerical) employing appropriate mathematical

formulations. In practice, comprehensive analyses are often impractical, simplified calculations are performed and the following aspects are employed to corroborate the obtained results or conclusions drawn for the verifications (Rotta Loria, 2018):

1. Group effects and interactions occur among energy piles located sufficiently close to each other because of the presence of and loadings (e.g. mechanical and thermal) on the neighbouring piles (Jeong et al., 2014; Mimouni and Laloui, 2015; Salciarini et al., 2015; Saggu and Chakraborty, 2016; Salciarini et al., 2017; Rotta Loria and Laloui, 2017, 2018; Ng and Ma, 2019). These phenomena involve a different response of the piles in the group than that of an isolated pile. Analyses of the deformation of single energy piles are not exhaustive and cannot represent the actual behaviour of energy piles operating in a closely spaced group (Rotta Loria and Laloui, 2018). In contrast, analyses of the stress development in single energy piles are considered useful because conservative also for piles located in a closely spaced group (Rotta Loria and Laloui, 2018).
2. Irreversible phenomena in the ground surrounding energy piles can be caused by the cyclic influence of thermal loads, applied alone or in conjunction with mechanical loads (Dupray et al., 2014; Rotta Loria et al., 2015; Saggu and Chakraborty, 2015; Ozudogru et al., 2015; Salciarini et al., 2015, 2017; Suryatriyastuti et al., 2015; Gawecka et al., 2016; Ng at al., 2016; Adinolfi et al., 2018). The significance of these phenomena primarily depends on (1) the level of mechanical loading applied prior to thermal loading, (2) the amplitude of the thermal loading cycle, (3) the number of thermal cycles and (4) the ground properties. Limiting the magnitude of the applied mechanical loads to approximately 30% of the value associated with 'failure' often represents the most effective approach to avoid the insurgence of irreversible phenomena in the ground and may be considered to neglect this phenomenon when more exhaustive information is not available.
3. Variations of ground properties can be caused, for example by mechanical degradation phenomena and thermally induced effects (Cekerevac and Laloui, 2004, McCartney and Rosenberg, 2011; Vieira and Maranha, 2016; Eslami et al., 2017). The considered variations may result in irreversible phenomena, although the physical processes causing these variations differ compared to those governing the aforementioned set of phenomena highlighted in item (2).

   A mechanical degradation of pile–soil interfaces due to repeated shearing caused by mechanical or thermal loading and unloading may be observed especially when dealing with two loading situations: (1) significant magnitudes of mechanical loads applied prior to thermal cyclic loading or (2) significant thermal cyclic loads subsequently applied to limited mechanical loading. However, this phenomenon is considered independent of temperature and negligible for most restraint conditions characterising energy piles, especially when the significance of thermal and

mechanical loads may have been previously limited to avoid the insurgence of irreversible phenomena in the ground. Neglecting the degradation of pile–soil interface shear strength properties due to cyclic loading of energy piles is in accordance with the French recommendations (CFMS-SYNTEC-SOFFONS-FNTP, 2017).

Thermally induced effects may be considered, at least in principle, to induce a variation of both strength and deformation properties of soils. In practice: (1) the effect of temperature on the shear strength parameters of soils and soil–concrete interfaces, such as the angle of shear strength under constant volume conditions, can be considered negligible in the typical temperature range of 2°C–60°C of current energy pile applications; and (2) the effect of temperature on the deformation properties of soils, such as the Young's modulus, appears negligible for coarse-grained soils appears negligible, whereas potentially relevant for fine-grained soils in the typical range of 2°C–60°C of current energy pile applications. However, this sensitivity is limited in magnitude if not absent in many situations, and thus negligible for design unless particularly sensitive soils are encountered.

4. Negative skin friction or downgrad phenomena can be caused by the influence of thermal loads, applied alone or in conjunction with mechanical loads, especially when dealing with energy piles embedded in lightly overconsolidated to normally consolidated soil deposits. Negative skin friction and downgrad phenomena caused by body forces can be highlighted in the previous situations and are typically tackled by assuming the null point to be at the interface between the consistent and the soft layer and then computing the negative friction as a fraction (dependent on the soil type) of the effective vertical stress. Negative skin friction and downgrad phenomena can also arise as a consequence of thermal loads and the influence of the thermal collapse of soils under positive temperature variations (Bourne-Webb et al., 2016). Actions arising from the ground should be considered in design using their maximum values (i.e. conservatively defined by upper values of the ground stiffness and strength) (EN 1997-1, 2004). In this context, one of the following two approaches shall be adopted: (1) the ground displacement is taken as the action in the design calculations and an interaction analysis is carried out, or (2) the load on the pile caused by the ground movement is taken as the action.
5. Time-dependent effects, such as consolidation or creep, may characterise energy piles subjected to mechanical or thermal loads. For piles subjected to mechanical loading only, no appreciable settlements caused by creep may be generated as far as the loading level is approximately 30% of the one associated with 'failure', while a further increase of approximately 10% of the performed estimation may be considered to occur due to consolidation for piles in fine-grained soil (Poulos and Davis, 1980). Creep may be accelerated by temperature increases (Leroueil and Soares Marques, 1996; Mitchell and Soga, 2005; Laloui et al., 2008) and result in greater long-term settlement. While no evidences of unacceptable displacements caused by

thermally accelerated creep are available at the present time, limiting the mechanical loading level of energy piles may help to ensure adequate performance similar to what currently foreseen for piles subjected to mechanical loading only.

In the assessment of the vertical deformation of energy piles, considering the temperature sensitivity of the volumetric behaviour of soils may also be relevant when the thermal expansion coefficient of the ground exceeds that of the pile. The reason for the previous aspect is that at successive stages of the geothermal operation of the energy piles the respective deformation would be governed by that of the soil and such a phenomenon would be unpredicted otherwise.

15.5.3 Stress limitations and crack control

Limiting the compressive and tensile stresses developed in energy piles as a consequence of the application of thermal and mechanical loads (i.e. aspects (3) and (4) highlighted in Section 15.5.1) is strictly related to the control of cracks in such foundations (i.e. aspect (4) highlighted in Section 15.5.1), and represents a key step for ensuring the required structural serviceability performance of such foundations. The previous results can typically be resolved by considering the verifications highlighted in the framework of the Eurocodes (EN 1992, 2004) as well as by ensuring a minimum area of longitudinal reinforcement with reference to the same norms.

Care must be given to the stress development within energy piles when such foundations are embedded in soils characterised by a greater thermal expansion coefficient. The reason for this is because tensile stress can be caused by energy pile heating and compressive stress can be caused by energy pile cooling. Irrespective of the ratio between the thermal expansion coefficient of the soil to that of the energy piles, assuming energy piles to be restrained at their head by an infinitely rigid structural member (e.g. a slab) provides conservative estimates of the thermally induced stress variations that are likely to be encountered in practice (Rotta Loria et al., 2019).

15.5.4 Concrete cover and reinforcement areas

To calculate the minimum concrete cover and the minimum area of reinforcement steel that needs to be provided to energy piles, the provisions proposed in the EN 1992 (2004) may be considered. Additional provisions are provided, for example for bored piles in the EN 1536 (1999). Adequate concrete cover, that is the distance between the surface of the reinforcement closest and the nearest concrete surface, is required to assure durability.

Bored piles characterised by diameters of up to 600 mm should be characterised by a concrete cover of 50 mm, while for greater diameters they should be characterised by a concrete cover of 60 mm (EN 1992, 2004). The concrete cover may be reduced to 40 mm when on the external face a permanent casing or lining is used

Table 15.6 Recommended minimum longitudinal reinforcement area in bored piles.

Pile concrete cross section, A_c	Minimum area of longitudinal reinforcement: $A_{r,min}$
$A_c \leq 0.5\ m^2$	$A_r \geq 0.005\ A_c$
$0.5\ m^2 < A_c < 1.0\ m^2$	$A_r \geq 25\ cm^2$
$A_c > 1.0\ m^2$	$A_r \geq 0.0025\ A_c$

Source: Values from the EN 1992, 2004. Design of Concrete Structures – Part 1-1: General Rules and Rules for Buildings. London, United Kingdom, p. 225.

(EN 1992, 2004). The minimum cover should be increased to 75 mm where (1) piles penetrate soft soil and are constructed without a casing; (2) an exposure class associated with attack of freeze/thaw cycles with or without de-icing agents is encountered [class 5 in accordance with the DD ENV 206 (1992)]; (3) submerged placement of concrete when a dimension of maximum aggregate is out-dated; and (4) reinforcement is installed subsequent to concrete placement or the borehole walls have even surface (EN 1992, 2004). A minimum cover of 80 mm for dense concrete is essential, but greater cover is advisable (BS 8004, 2015).

Bored piles may typically be equipped with recommended values of minimum longitudinal reinforcement $A_{r,min}$ depending on the concrete cross sectional area A_c. Recommended values of minimum reinforcement drawing from the previous considerations are reported in Table 15.6 with reference to the EN 1992 (2004). It should always be ensured that the previous (or other) provisions ensure ductility (Rotta Loria et al., 2019). The minimum diameter for the longitudinal bars should not be less than 16 mm and at least six longitudinal bars should be considered (EN 1992, 2004). The clear distance between bars should not exceed 200 mm measured along the periphery of the pile (EN 1992, 2004). Spacing of longitudinal bars should always be maximised in order to allow proper flow of concrete but should not exceed 400 mm (EN 1992, 2004).

The minimum diameter of 6 mm should be considered for transverse reinforcement represented by links, hoops or helical reinforcement, while the diameter of 5 mm should be considered for wires of welded mesh (EN 1992, 2004).

References

Adinolfi, M., Maiorano, R.M.S., Mauro, A., Massarotti, N., Aversa, S., 2018. On the influence of thermal cycles on the yearly performance of an energy pile. Geomech. Energy Environ. 16, 32–44.

Bourne-Webb, P., Burlon, S., Javed, S., Kürten, S., Loveridge, F., 2016. Analysis and design methods for energy geostructures. Renew. Sustain. Energy Rev. 65, 402–419.

BS 8004, 2015. Code of practice for foundations. London, United Kingdom, p. 112.

Cekerevac, C., Laloui, L., 2004. Experimental study of thermal effects on the mechanical behaviour of a clay. Int. J. Numer. Anal. Methods Geomech. 28 (3), 209–228.

Dupray, F., Li, C., Laloui, L., 2014. Heat-exchanger piles for the de-icing of bridges. Acta Geotech. 9 (3), 413–423.

CFMS-SYNTEC-SOFFONS-FNTP, 2017. Recommandations pour la conception, le dimensionnement et la mise en úuvre des géostructures thermiques. Rev. Fr. Geotech. 149 (1), 120.
DD ENV 206, 1992. Concrete. Performance, Production, Placing and Compliance Criteria. London, United Kingdom, p. 44.
EN 1536, 1999. Execution of Special Geotechnical Work. Bored Piles. London, United Kingdom, p. 83.
EN 1992, 2004. Design of Concrete Structures – Part 1-1: General Rules and Rules for Buildings. London, United Kingdom, p. 225.
EN 1993–5, 2007. Eurocode 3: Design of Steel Structures – Part 5: Piling. London, United Kingdom.
EN 1997, 2004. Eurocode 7: Geotechnical Design. London, United Kingdom, p. 171.
EN 1997-1, 2004. Eurocode 7: Geotechnical Design – Part 1: General Rules. London, United Kingdom, p. 171.
EN 12063, (1999. Execution of Special Geotechnical Work. Sheet Pile Walls. London, United Kingdom, p. 77.
EN 12699, 2000. Execution of Special Geotechnical Work. Displacement Piles. London, United Kingdom, p. 50.
EN 12794, 2005. Precast Concrete Products. Foundation Piles. London, United Kingdom, p. 48.
EN 14199, 2005. Execution of Special Geotechnical Works. Micropiles. London, United Kingdom, p. 52.
Eslami, H., Rosin-Paumier, S., Abdallah, A., Masrouri, F., 2017. Pressuremeter test parameters of a compacted illitic soil under thermal cycling. Acta Geotech. 1–14.
Gawecka, K.A., Taborda, D.M., Potts, D.M., Cui, W., Zdravkovic, L., Haji Kasri, M.S., 2016. Numerical modelling of thermo-active piles in London Clay. Proc. Inst. Civ. Eng. Geotech. Eng. 170 (3), 1353–12618.
Frank, R., 2004. Designers' Guide to EN 1997-1 Eurocode 7: Geotechnical Design – General rules. Thomas Telford.
Hansen, J.B., 1970. A revised and extended formula for bearing capacity. Dan. Geotech. Inst. Bull. 28, 5–11.
Jeong, S., Min, H., Lee, J.K., 2014. Thermally induced mechanical response of energy piles in axially loaded pile groups. Appl. Therm. Eng. 71 (1), 608–615.
Laloui, L., Leroueil, S., Chalindar, S., 2008. Modelling of the combined effect of strain rate and temperature on one-dimensional compression of soils. Can. Geotech. J. 45 (12), 1765–1777.
Leroueil, S., Soares Marques, M.E., 1996. Importance of strain rate and temperature effects in geotechnical engineering. Measuring and Modeling Time Dependent Soil Behavior. ASCE, pp. 1–60.
Mitchell, J.K., Soga, K., 2005. Fundamentals of Soil Behavior. Wiley, New York.
McCartney, J.S., Rosenberg, J.E., 2011. Impact of heat exchange on side shear in thermo-active foundations. Proceedings of Geo-Frontiers: Advances in Geotechnical Engineering. ASCE, pp. 488–498.
Mimouni, T., Laloui, L., 2015. Behaviour of a group of energy piles. Can. Geotech. J. 52 (12), 1913–1929.
Ng, C.W.W., Ma, Q.J., 2019. Energy pile group subjected to non-symmetrical cyclic thermal loading in centrifuge. Géotech. Lett. 1–5.
Ng, C.W.W., Ma, Q.J., Gunawan, A., 2016. Horizontal stress change of energy piles subjected to thermal cycles in sand. Comput. Geotech. 78, 54–61.
Ozudogru, T.Y., Ghasemi-Fare, O., Olgun, C.G., Basu, P., 2015. Numerical modeling of vertical geothermal heat exchangers using finite difference and finite element techniques. Geotech. Geol. Eng. 33 (2), 291–306.
Poulos, H.G., Davis, E.H., 1980. Pile Foundation Analysis and Design. Wiley, New York.
Rotta Loria, A.F., 2018. Performance-based design of energy pile foundations. DFI J.: J. Deep Found. Inst. 12 (2), 94–107.
Rotta Loria, A.F., Laloui, L., 2017. Thermally induced group effects among energy piles. Geotechnique 67 (5), 374–393.
Rotta Loria, A.F., Laloui, L., 2018. Group action effects caused by various operating energy piles. Geotechnique 68 (9), 834–841.

Rotta Loria, A.F., Bocco, M., Garbellini, C., Muttoni, A., Laloui, L., 2019. The role of thermal loads in the performance-based design of energy piles. Geomech. Energy Environ. Available from: https://doi.org/10.1016/j.gete.2019.100153.

Rotta Loria, A.F., Gunawan, A., Shi, C., Laloui, L., Ng, C.W., 2015. Numerical modelling of energy piles in saturated sand subjected to thermo-mechanical loads. Geomech. Energy Environ. 1 (1), 1–15.

Saggu, R., Chakraborty, T., 2015. Cyclic thermo-mechanical analysis of energy piles in sand. Geotech. Geol. Eng. 33 (1), 1–22.

Saggu, R., Chakraborty, T., 2016. Thermomechanical response of geothermal energy pile groups in sand. Int. J. Geomech. 16 (4), 04015100.

Salciarini, D., Ronchi, F., Cattoni, E., Tamagnini, C., 2015. Thermomechanical effects induced by energy piles operation in a small piled raft. Int. J. Geomech. 15 (2), 04014042.

Salciarini, D., Ronchi, F., Tamagnini, C., 2017. Thermo-hydro-mechanical response of a large piled raft equipped with energy piles: a parametric study. Acta Geotech. 12 (4), 703–728.

Suryatriyastuti, M., Burlon, S., Mroueh, H., 2015. On the understanding of cyclic interaction mechanisms in an energy pile group. Int. J. Numer. Anal. Methods Geomech. Available from: https://doi.org/10.1002/nag.2382.

Vieira, A., Maranha, J.R., 2016. Thermoplastic analysis of a thermoactive pile in a normally consolidated clay. Int. J. Geomech. 17 (1), 04016030.

Zhang, L., Einstein, H.H., 1998. End bearing capacity of drilled shafts in rock. J. Geotech. Geoenviron. Eng. 124 (7), 574–584.

Questions and problems

Statements

a. List the most common limit states that need to be considered for the design of piles in the framework of the Eurocodes. Distinguish ultimate and serviceability limit states.

b. List the limit states that shall be considered for the design of axially loaded piles.

c. The effects of thermal loads should only be considered for serviceability limit state verifications because they are unlikely to exceed ultimate limit states:

i. True

ii. False

d. The design and verification of energy piles at serviceability limit states can be considered as a conventional process against the action of mechanical loads only:

i. True

ii. False

e. What are the two design criteria that allow considering the methodology for which the performance of energy piles against thermal loads can be verified only at serviceability limit states, while not at ultimate limit states?

f. What types of considerations allow verifying in the design of structures that ultimate limit states are not exceeded?

g. The worst foreseeable condition for the geotechnical performance of energy piles involves foundations with fully mobilised shaft and base capacities caused by a heating thermal load and a (compressive) mechanical load:

i. True

ii. False

h. From the perspective of displacement considerations, cooling thermal loads are unlikely to involve energy pile settlements (e.g. differential) capable of generating a collapse mechanism:

i. True

ii. False

i. What are the typical orders of magnitude of energy pile settlements caused by a cooling thermal load applied after mechanical loading for pile slenderness ratios ranging from $\frac{L}{D} = 20-50$?

j. Explain why, from the perspective of equilibrium considerations, thermal loads cannot cause a geotechnical collapse mechanism for energy piles, that is they cannot involve geotechnical ultimate limit states.

k. The appearance of cracks leads to stress redistribution and an increase in the stiffness of structures:

i. True

ii. False

l. Once a ductility-oriented design approach is employed, thermal loads associated with the geothermal operation of energy piles cannot involve the structural failure of the piles, that is they cannot exceed the structural ultimate limit states:
  i. True
  ii. False

m. List the two typical design problems for energy piles. Explain the consequences involved with a design oriented to oversize energy piles from the perspective of the influence of thermal loads.

n. The vertical stress variations caused by mechanical and thermal loads must be considered only at the head of energy piles for the sake of verifications.
  i. True
  ii. False

o. List five aspects that must be considered to address the geotechnical and structural performance of the energy piles as well as the structural performance of the connected superstructure at serviceability limit states against the effects of thermal loads, applied alone or in conjunction with mechanical loads.

p. What are five phenomena that can lead to an increase of the head settlement of individual energy piles, assuming a balanced thermal field of the subsurface over time?

q. What is the typical range of concrete cover that should be considered for the reinforcement steel of energy piles made of concrete?

r. Consider a displacement pile made of reinforced concrete and embedded in a uniform normally consolidated soil deposit, with reference to the material properties reported in the following figure. Assume that the applied axial load to the pile head is known. With reference to this problem:
  i. Perform the geotechnical design of the pile at ultimate limit states to evaluate the minimum length of the pile required to sustain the applied load through an analysis in terms of effective stresses. Develop this design considering the different approaches proposed by the Eurocode (DA1-C1, DA1-C2 and DA2) and compare the obtained results. In this context, estimate the base capacity by applying the approach proposed by Hansen (1970). Estimate the shaft capacity by considering that no pile load tests have been performed and that the factor $\xi_1 = 1.4$.
  ii. Perform the structural design of the pile at ultimate limit states to verify that the design resisting load for no moments applied of the most solicited cross section of the pile is greater than or equal to the applied design load. In this context, consider a concrete class C25/30 and a reinforcing steel B500B.

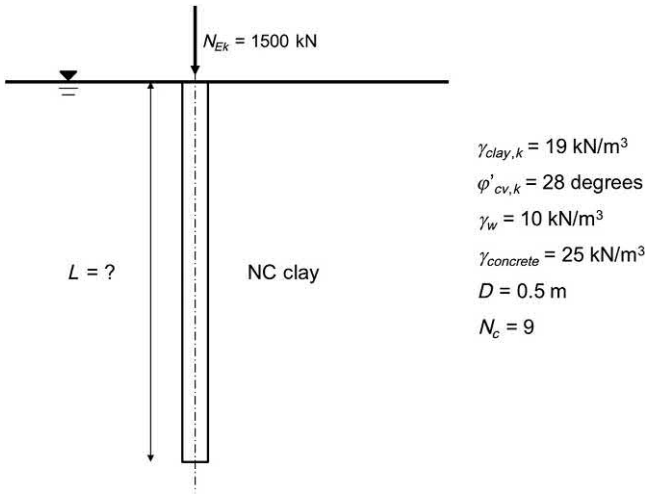

s. Consider a displacement pile made of reinforced concrete and resting on a rock stratum, with reference to the material properties reported in the following figure. Assume that the applied axial load to the pile head is known. With reference to this problem:

i. Perform the geotechnical design of the pile at ultimate limit states to evaluate the minimum length of the pile required to sustain the applied load through an analysis in terms of effective stresses. Develop this design considering the different approaches proposed by the Eurocode (DA1-C1, DA1-C2 and DA2) and compare the obtained results. In this context, estimate the pile base capacity by applying the approach proposed by Hansen (1970) or by Zhang and Einstein (1998) where appropriate. Estimate the shaft capacity by considering that no pile load tests have been performed and that the factor $\xi_1 = 1.4$. Neglect the pile weight.

ii. Perform the structural design of the pile at ultimate limit states to verify that the design resisting load for no moments applied of the most solicited cross section of the pile is greater than or equal to the applied design load. In this context, consider a concrete class C32/40 and a reinforcing steel B500B.

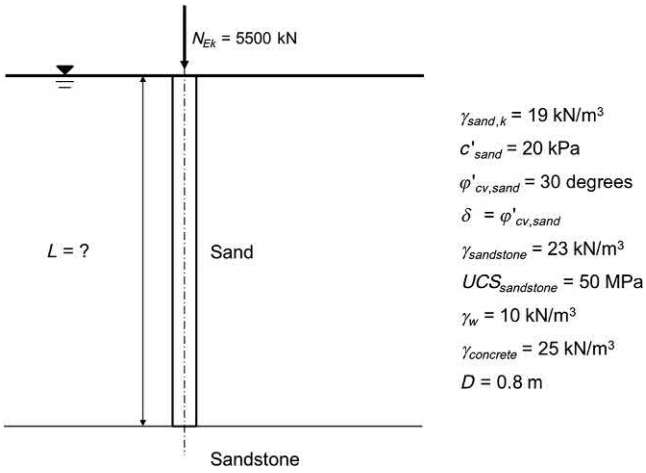

t. Consider a displacement pile made of reinforced concrete and embedded in a uniform soil deposit, with reference to the material properties reported in the following figure. Assume that the applied axial load to the pile head is known. With reference to this problem:

i. Perform the geotechnical design of the pile at ultimate limit states to evaluate the minimum length of the pile required to sustain the applied load through an analysis in terms of effective stresses. Develop this design considering the different approaches proposed by the Eurocode (DA1-C1, DA1-C2 and DA2) and compare the obtained results. In this context, estimate the pile base capacity by applying the approach proposed by Hansen (1970). Estimate the shaft capacity by considering that no pile load tests have been performed and that the factor $\xi_1 = 1.4$. Neglect the pile weight.

ii. Perform the structural design of the pile at ultimate limit states to verify that the design resisting load for no moments applied of the most solicited cross section of the pile is greater than or equal to the applied design load. In this context, consider a concrete class C25/30 and a reinforcing steel B500B.

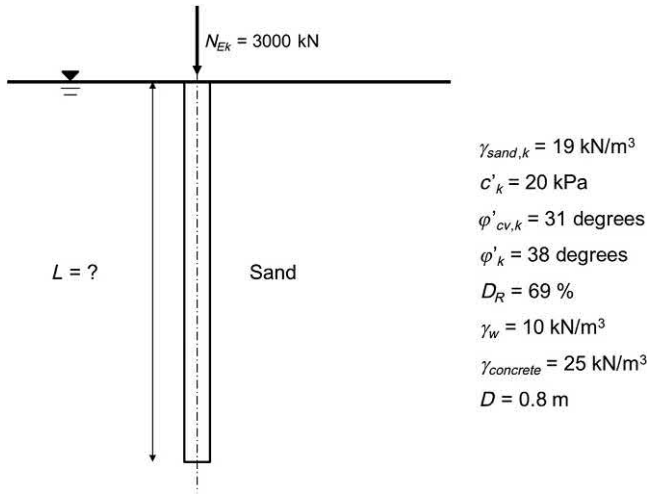

u. Consider a displacement pile made of reinforced concrete and embedded in a stratified soil deposit composed of two layers of overconsolidated clay, with reference to the material properties reported in the following figure. Assume that the applied axial load to the pile head is known. With reference to this problem:

i. Perform the geotechnical design of the pile at ultimate limit states to evaluate the minimum length of the pile required to sustain the applied load through an analysis in terms of effective stresses. Develop this design considering the different approaches proposed by the Eurocode (DA1-C1, DA1-C2 and DA2) and compare the obtained results. In this context, estimate the pile base capacity by applying the approach proposed by Hansen (1970). Estimate the shaft capacity by considering that no pile load tests have been performed and that the factor $\xi_1 = 1.4$. Neglect the pile weight.

ii. Perform the structural design of the pile at ultimate limit states to verify that the design resisting load for no moments applied of the most solicited cross section of the pile is greater than or equal to the applied design load. In this context, consider a concrete class C25/30 and a reinforcing steel B500B.

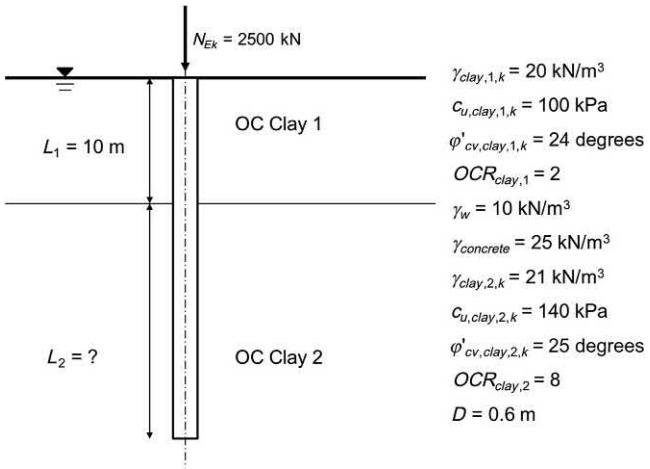

Solutions

a. The most common limit states that need to be considered for the design of piles involve (EN 1997-1, 2004) (1) the loss of overall stability of the pile foundation, (2) the bearing resistance failure of the pile foundation, (3) the uplift or insufficient tensile resistance of the pile foundation, (4) the failure in the ground due to transverse loading of the pile foundation, (5) the structural failure of the pile in compression, tension, bending, buckling or shear, (6) the combined failure in the ground and the pile, (7) the combined failure in the ground and the structure, (8) excessive settlement, (9) excessive heave, (10) excessive lateral movement, or (11) vibrations. Phenomena (1—7) generally involve ultimate limit states. Phenomena (8−10) generally involve serviceability limit states for the geostructure or ultimate limit states for the superstructure supported. The phenomenon (11) generally represents a serviceability limit state.

b. In the case of axially loaded piles, the design shall demonstrate that exceeding the following limit states is sufficiently improbable (EN 1997-1, 2004):

i. Ultimate limit states of compressive or tensile resistance failure of a single pile.

ii. Ultimate limit states of compressive or tensile resistance failure of the pile foundation as a whole.

iii. Ultimate limit states of collapse or severe damage to a supported structure caused by excessive displacement or differential displacements of the pile foundation.

iv. Serviceability limit states in the supported structure caused by displacement of the piles.

c. The effects of thermal loads should only be considered for serviceability limit state verifications because they are unlikely to exceed ultimate limit states:

i. True

ii. False

d. The design and verification of energy piles at serviceability limit states can be considered as a conventional process against the action of mechanical loads only:

i. True

ii. False

e. The two design criteria that allow considering in design the influence of thermal loads on the geotechnical and structural performance of only at serviceability limit states, while not at ultimate limit states, are as follows:

1. A design compressive strength of the reinforced concrete section (e.g. for no moments applied) at least equal to the design bearing capacity of the pile must be ensured. When this approach is not employed, the design loads sustained from a geotechnical perspective may induce or exceed an ultimate limit state from a structural perspective. In contrast, the proposed approach guarantees a potential ductile collapse mechanism related to the excess of ultimate limit states from a geotechnical perspective first.

2. A minimum steel reinforcement area of the reinforced concrete section must be chosen. When this approach is not employed, the requirements of durability and deformation (e.g. cracking) of the materials constituting the designed structures may not be satisfied. In contrast, this approach guarantees durability and ductility.

f. Displacement and equilibrium considerations allow verifying that ultimate limit states are not exceeded.

g. The worst foreseeable condition for the geotechnical performance of energy piles involves foundations with fully mobilised shaft and base capacities caused by a heating thermal load and a (compressive) mechanical load:

i. True

ii. False

h. With regards to displacement considerations, cooling thermal loads are unlikely to involve energy pile settlements (e.g. differential) capable of generating a collapse mechanism:

i. **True**
ii. False

i. **Typical orders of magnitude of energy pile settlements caused by a cooling thermal load applied after mechanical loading are of $0.10\%D$—$0.70\%D$ for pile slenderness rations ranging from $L/D = 20$ to 50 (where L [m] and D [m] are the pile length and diameter, respectively)**.

j. **For any magnitude of thermal load applied to energy piles, the reactions provided by the soil below and above the null point of the shear stress compensate for each other and prevent the formation of a collapse mechanism. Energy pile equilibrium will thus always be ensured, with zero thermally induced displacements occurring in correspondence with the null point of the vertical displacement that will prevent the formation of a collapse mechanism. Based on the above, thermal loads cannot cause a geotechnical collapse mechanism for energy piles from an equilibrium perspective, that is they cannot involve geotechnical ultimate limit states**.

k. The appearance of cracks leads to stress redistribution and an increase in the stiffness of structures:
i. True
ii. **False**

l. Once a ductility-oriented design approach is employed, thermal loads associated with the geothermal operation of energy piles cannot involve the structural failure of the piles, that is they cannot exceed the structural ultimate limit states:
i. **True**
ii. False

m. **Two typical design problems exist for piles and may arise in design**:
1. ***Constant applied mechanical load and varying pile length***.
2. ***Varying applied mechanical load and constant pile length***.

As soon as a length greater than needed characterises energy piles subjected to a given mechanical load, the axial load capacity of such foundations increases and thermally induced effects become more burdensome for the same applied temperature variation. From a geotechnical perspective, the previous aspect is related to the fact that, for the same applied temperature variation ΔT [°C] and linear thermal expansion coefficient α_{EP} [1/°C], longer piles involve proportionally greater variations in length $\Delta L = \alpha_{EP}\Delta TL$ [m] despite the thermally induced strain under free expansion conditions is independent of their length, that is $\varepsilon_f^{th} = -\alpha_{EP}\Delta T$ [−]. From a structural perspective, the previous aspect can be highlighted considering that longer energy piles subjected to the same value of mechanical load are characterised by greater thermally induced stresses.

n. The vertical stress variations caused by mechanical and thermal loads must be considered only at the head of energy piles for the sake of verifications.
  i. True
  ii. False

o. The following aspects should be addressed to verify the geotechnical and structural performance of the energy piles as well as the structural performance of the connected superstructure at serviceability limit states against the effects of thermal loads, applied alone or in conjunction with mechanical loads:
  i. Single and group vertical displacement (e.g. differential and average) limitation, considering group effects;
  ii. Deflection and angular distortion control;
  iii. Compressive stress limitation;
  iv. Tensile stress limitation;
  v. Crack control.

p. Assuming a balanced thermal field of the subsurface over time, an increase of the head settlement of individual energy piles can occur mainly because of the following aspects:
  i. Group effects;
  ii. Irreversible phenomena;
  iii. Variations of ground properties;
  iv. Negative skin friction or downgrad phenomena;
  v. Time-dependent effects.

q. The typical concrete cover that should be considered for the reinforcement steel of energy piles made of concrete ranges between 40 and 80 mm depending on the pile characteristics.

r.
  i. Geotechnical design

  Approach DA1-C1 (A1 + M1 + R1)

  According to this approach, the design values of actions, the design material properties and the design resistances are derived from their characteristic values considering the partial factors of the group A1, M1 and R1, respectively.

  It is supposed that the acting characteristic load N_{Ek} [N] is characterised for 70% by a permanent contribution, N_{Gk}, and for 30% by a variable contribution, N_{Qk}:

$$N_{Gk} = 0.7N_{Ek} = 0.7 \cdot 1500 = 1050\,\text{kN}$$

$$N_{Qk} = 0.3N_{Ek} = 0.3 \cdot 1500 = 450\,\text{kN}$$

The permanent and variable design loads are computed by multiplying their characteristic values by the partial factors A1:

$$N_{Gd} = \gamma_G N_{Gk} = 1.35 \cdot 1050 = 1417.5\,\text{kN}$$

$$N_{Qd} = \gamma_Q N_{Qk} = 1.5 \cdot 450 = 675\,\text{kN}$$

Hence, the total design acting load N_{Ed} [N] reads:

$$N_{Ed} = N_{Gd} + N_{Qd} = 1417.5 + 675 = 2092.5\,\text{kN}$$

The design material properties are computed by dividing their characteristic values by the partial factors M1:

$$\gamma_{clay,d} = \frac{\gamma_{clay,k}}{\gamma_\gamma} = \frac{19}{1} = 19\,\text{kN/m}^3$$

$$\varphi'_{cv,d} = \tan^{-1}\left(\frac{\tan\varphi'_{cv,k}}{\gamma_{\varphi'}}\right) = \tan^{-1}\left(\frac{\tan 28}{1}\right) = 28\ \text{degrees}$$

Based on the above, the shaft capacity reads:

$$Q_{s,d} = \frac{q_{s,k}A_s}{\gamma_s\xi_1} = \frac{\overline{K}\overline{\sigma'_z}\tan\delta_d A_s}{\gamma_s\xi_1} = \frac{\left(1-\sin\varphi'_{cv,d}\right)\overline{\sigma'_z}\tan\varphi'_{cv,d}A_s}{\gamma_s\xi_1}$$
$$= \frac{(1-\sin 28)9\frac{L}{2}\tan 28 \cdot \pi 0.5L}{1 \cdot 1.4} = 1.42L^2$$

The base capacity reads:

$$Q_{b,d} = \frac{q_{b,k}A_b}{\gamma_b\xi_1} = \frac{N_q d_q \sigma'_{zb}A_b}{\gamma_b\xi_1} = \frac{K_p e^{\pi\tan\varphi'_{cv,d}} d_q \sigma'_{zb}\pi\left(\frac{D}{2}\right)^2}{\gamma_b\xi_1}$$

$$= \frac{\left(K_p e^{\pi\tan\varphi'_{cv,d}}\right)\left(1+2\tan\varphi'_{cv,d}\left(1-\sin\varphi'_{cv,d}\right)^2 k_H\right)\sigma'_{zb}\pi\left(\frac{D}{2}\right)^2}{\gamma_b\xi_1}$$

$$= \frac{\left(\frac{1+\sin\varphi'_{cv,d}}{1-\sin\varphi'_{cv,d}} e^{\pi\tan\varphi'_{cv,d}}\right)\left(1+2\tan\varphi'_{cv,d}\left(1-\sin\varphi'_{cv,d}\right)^2\tan^{-1}\left(\frac{L}{D}\right)\right)\sigma'_{zb}\pi\left(\frac{D}{2}\right)^2}{\gamma_b\xi_1}$$

$$= \frac{\left(\frac{1+\sin 28}{1-\sin 28} e^{\pi \tan 28}\right)\left(1 + 2\tan 28(1-\sin 28)^2 \tan^{-1}\left(\frac{L}{0.5}\right)\right)(19-10)L\pi\left(\frac{0.5}{2}\right)^2}{1.25 \cdot 1.4}$$

$$= \frac{14.72\left(1 + 0.3\tan^{-1}\left(\frac{L}{0.5}\right)\right)9L\pi 0.0625}{1.25 \cdot 1.4}$$

$$= \frac{26.01L\left(1 + 0.3\tan^{-1}\left(\frac{L}{0.5}\right)\right)}{1.75}$$

$$= 14.86L\left(1 + 0.3\tan^{-1}\left(\frac{L}{0.5}\right)\right)$$

By substituting the aforementioned formulations in the equation of vertical pile equilibrium, an equation in the unknown L is obtained:

$$Q_{u,d} = Q_{s,d}(L) + Q_{b,d}(L)$$

$$2092.5 = 1.42L^2 + 14.86L\left(1 + 0.3\tan^{-1}\left(\frac{L}{0.5}\right)\right)$$

$$1.42L^2 + 14.86L\left(1 + 0.3\tan^{-1}\left(\frac{L}{0.5}\right)\right) - 2092.5 = 0$$

By solving the aforementioned equation, a design pile length of $L = 31.5$ m is obtained.

Approach DA1-C2 (A2 + M1 + R4)

According to this approach, the design values of actions, the design material properties and the design resistances are derived from their characteristic values considering the partial factors of the group A2, M1 and R4, respectively.

The permanent and variable design loads are computed by multiplying their characteristic values by the partial factors A1:

$$N_{Gd} = \gamma_G N_{Gk} = 1 \cdot 1050 = 1050\,\text{kN}$$

$$N_{Qd} = \gamma_Q N_{Qk} = 1.3 \cdot 450 = 585\,\text{kN}$$

Hence, the total design load N_{Ed} reads:

$$N_{Ed} = N_{Gd} + N_{Qd} = 1050 + 585 = 1635\,\text{kN}$$

The design material properties are computed by dividing their characteristic values by the partial factors M1:

$$\gamma_{clay,d} = \frac{\gamma_{clay,k}}{\gamma_\gamma} = \frac{19}{1} = 19\,\text{kN/m}^3$$

$$\varphi'_{cv,d} = \tan^{-1}\left(\frac{\tan\varphi'_{cv,k}}{\gamma_{\varphi'}}\right) = \tan^{-1}\left(\frac{\tan 28}{1}\right) = 28\ \text{degrees}$$

Based on the above, the shaft capacity reads:

$$Q_{s,d} = \frac{q_{s,k}A_s}{\gamma_s\xi_1} = \frac{\overline{K}\overline{\sigma'_z}\tan\delta_d A_s}{\gamma_s\xi_1} = \frac{\left(1-\sin\varphi'_{cv,d}\right)\overline{\sigma'_z}\tan\varphi'_{cv,d}A_s}{\gamma_s\xi_1}$$
$$= \frac{(1-\sin 28)9\frac{L}{2}\tan 28\cdot\pi 0.5L}{1.3\cdot 1.4} = 1.1L^2$$

The base capacity reads:

$$Q_{b,d} = \frac{q_{b,k}A_b}{\gamma_b\xi_1} = \frac{N_q d_q \sigma'_{zb}A_b}{\gamma_b\xi_1} = \frac{K_p e^{\pi\tan\varphi'_{cv,d}} d_q \sigma'_{zb}\pi\left(\frac{D}{2}\right)^2}{\gamma_b\xi_1}$$
$$= \frac{\left(K_p e^{\pi\tan\varphi'_{cv,d}}\right)\left(1+2\tan\varphi'_{cv,d}\left(1-\sin\varphi'_{cv,d}\right)^2 k_H\right)\sigma'_{zb}\pi\left(\frac{D}{2}\right)^2}{\gamma_b\xi_1}$$
$$= \frac{\left(\frac{1+\sin\varphi'_{cv,d}}{1-\sin\varphi'_{cv,d}} e^{\pi\tan\varphi'_{cv,d}}\right)\left(1+2\tan\varphi'_{cv,d}\left(1-\sin\varphi'_{cv,d}\right)^2\tan^{-1}\left(\frac{L}{D}\right)\right)\sigma'_{zb}\pi\left(\frac{D}{2}\right)^2}{\gamma_b\xi_1}$$
$$= \frac{\left(\frac{1+\sin 28}{1-\sin 28} e^{\pi\tan 28}\right)\left(1+2\tan 28(1-\sin 28)^2\tan^{-1}\left(\frac{L}{0.5}\right)\right)(19-10)L\pi\left(\frac{0.5}{2}\right)^2}{1.6\cdot 1.4}$$
$$= \frac{14.72\left(1+0.3\tan^{-1}\left(\frac{L}{0.5}\right)\right)9L\pi 0.0625}{1.6\cdot 1.4}$$

$$= \frac{26.01L\left(1 + 0.3\tan^{-1}\left(\frac{L}{0.5}\right)\right)}{2.24}$$

$$= 11.61L\left(1 + 0.3\tan^{-1}\left(\frac{L}{0.5}\right)\right)$$

By substituting the aforementioned formulations in the equation of vertical pile equilibrium, an equation in the unknown L is obtained:

$$N_{Ed} \equiv Q_{u,d} = Q_{s,d}(L) + Q_{b,d}(L)$$

$$1635 = 1.1L^2 + 11.61L\left(1 + 0.3\tan^{-1}\left(\frac{L}{0.5}\right)\right)$$

$$1.1L^2 + 11.61L\left(1 + 0.3\tan^{-1}\left(\frac{L}{0.5}\right)\right) - 1635 = 0$$

By solving the aforementioned equation, a design pile length of $L = 31.7$ m is obtained.

Approach DA2 (A1 + M1 + R2)

According to this approach, the design values of actions, the design material properties and the design resistances are derived from their characteristic values considering the partial factors of the group A1, M1 and R2, respectively.

The permanent and variable design loads are computed by multiplying their characteristic values by the partial factors A1:

$$N_{Gd} = \gamma_G N_{Gk} = 1.35 \cdot 1050 = 1417.5\ \text{kN}$$

$$N_{Qd} = \gamma_Q N_{Qk} = 1.5 \cdot 450 = 675\ \text{kN}$$

Hence, the total design load N_{Ed} reads:

$$N_{Ed} = N_{Gd} + N_{Qd} = 1417.5 + 675 = 2092.5\ \text{kN}$$

The design material properties are computed by dividing their characteristic values by the partial factors M1:

$$\gamma_{clay,d} = \frac{\gamma_{clay,k}}{\gamma_\gamma} = \frac{19}{1} = 19\ \text{kN/m}^3$$

$$\varphi'_{cv,d} = \tan^{-1}\left(\frac{\tan\varphi'_{cv,k}}{\gamma_{\varphi'}}\right) = \tan^{-1}\left(\frac{\tan 28}{1}\right) = 28 \text{ degrees}$$

Based on the above, the shaft capacity reads:

$$Q_{s,d} = \frac{q_{s,k}A_s}{\gamma_s\xi_1} = \frac{\overline{K}\overline{\sigma'_z}\tan\delta_d A_s}{\gamma_s\xi_1} = \frac{\left(1-\sin\varphi'_{cv,d}\right)\overline{\sigma'_z}\tan\varphi'_{cv,d}A_s}{\gamma_s\xi_1}$$
$$= \frac{(1-\sin 28)9\frac{L}{2}\tan 28\cdot\pi 0.5L}{1.1\cdot 1.4} = 1.29L^2$$

The base capacity reads:

$$Q_{b,d} = \frac{q_{b,k}A_b}{\gamma_b\xi_1} = \frac{N_q d_q \sigma'_{zb}A_b}{\gamma_b\xi_1} = \frac{K_p e^{\pi\tan\varphi'_{cv,d}} d_q \sigma'_{zb}\pi\left(\frac{D}{2}\right)^2}{\gamma_b\xi_1}$$
$$= \frac{\left(K_p e^{\pi\tan\varphi'_{cv,d}}\right)\left(1+2\tan\varphi'_{cv,d}\left(1-\sin\varphi'_{cv,d}\right)^2 k_H\right)\sigma'_{zb}\pi\left(\frac{D}{2}\right)^2}{\gamma_b\xi_1}$$
$$= \frac{\left(\frac{1+\sin\varphi'_{cv,d}}{1-\sin\varphi'_{cv,d}}e^{\pi\tan\varphi'_{cv,d}}\right)\left(1+2\tan\varphi'_{cv,d}\left(1-\sin\varphi'_{cv,d}\right)^2\tan^{-1}\left(\frac{L}{D}\right)\right)\sigma'_{zb}\pi\left(\frac{D}{2}\right)^2}{\gamma_b\xi_1}$$
$$= \frac{\left(\frac{1+\sin 28}{1-\sin 28}e^{\pi\tan 28}\right)\left(1+2\tan 28(1-\sin 28)^2\tan^{-1}\left(\frac{L}{0.5}\right)\right)(19-10)L\pi\left(\frac{0.5}{2}\right)^2}{1.1\cdot 1.4}$$
$$= \frac{14.72\left(1+0.3\tan^{-1}\left(\frac{L}{0.5}\right)\right)9L\pi 0.0625}{1.1\cdot 1.4} =$$
$$= \frac{26.01L\left(1+0.3\tan^{-1}\left(\frac{L}{0.5}\right)\right)}{1.54} =$$
$$= 16.89L\left(1+0.3\tan^{-1}\left(\frac{L}{0.5}\right)\right)$$

By substituting the aforementioned formulations in the equation of vertical pile equilibrium, an equation in the unknown L is obtained:

$$N_{Ed} \equiv Q_{u,d} = Q_{s,d}(L) + Q_{b,d}(L)$$

$$2092.5 = 1.29L^2 + 16.89L\left(1 + 0.3\tan^{-1}\left(\frac{L}{0.5}\right)\right)$$

$$1.29L^2 + 16.89L\left(1 + 0.3\tan^{-1}\left(\frac{L}{0.5}\right)\right) - 2092.5 = 0$$

By solving the aforementioned equation, a design pile length of $L = 31.8$ m is obtained.

The parameters related to the geotechnical design at ultimate limit states according to the different approaches proposed by the Eurocodes are reported in the following table, together with the effective length assigned to the pile, L_{eff} [m].

	N_{Ed} [kN]	$Q_{s,d}$ [kN]	$Q_{b,d}$ [kN]	$Q_{u,d}$ [kN]	L [m]	L_{eff} [m]
DA1-C1	2092.5	1413.2	686.1	2099.3	31.5	32
DA1-C2	1635	1100.9	539.5	1640.4	31.7	32
DA2	2092.5	1334.2	759.1	2093.2	31.8	32

ii. Structural design

The structural design at ultimate limit states of the cross section of the considered axially loaded pile requires defining the design acting load N_{Ed} and comparing it with the design resisting load N_{Rd} for no moment applied. Alternatively, the design can be performed by verifying the position of the design action effects (N_{Ed}; M_{Ed}) in the strength domain of the cross section. This latter approach is considered here.

As for the geotechnical design, it is supposed that the acting characteristic load N_{Ek} is characterised for 70% by a permanent contribution, N_{Gk}, and for 30% by a variable contribution, N_{Qk}:

$$N_{Gk} = 0.7N_k = 0.7 \cdot 1500 = 1050\,\text{kN}$$

$$N_{Qk} = 0.3N_k = 0.3 \cdot 1500 = 450\,\text{kN}$$

The permanent and variable design loads are computed by multiplying their characteristic values by the partial factors A1:

$$N_{Gd} = \gamma_G N_{Gk} = 1.35 \cdot 1050 = 1417.5\,\text{kN}$$

$$N_{Qd} = \gamma_Q N_{Qk} = 1.5 \cdot 450 = 675\ \text{kN}$$

Hence, the total design load N_{Ed} reads:

$$N_{Ed} = N_{Gd} + N_{Qd} = 1417.5 + 675 = 2092.5\ \text{kN}$$

The following material properties and features are considered to obtain the strength domain for the designed section. The concrete class C25/30, chosen to satisfy the condition of durability (XC2), is characterised by the following properties:

$$f_{ck} = 25\ \text{MPa}$$

$$f_{ck,cube} = 30\ \text{MPa}$$

$$E_{cm} = 31\ \text{GPa}$$

$$f_{cd} = \frac{\alpha_{cc} f_{ck}}{\gamma_c} = \frac{0.85 \cdot 25}{1.5} = 14.2\ \text{MPa}$$

$$\varepsilon_{uc} = 0.0035 = 3500\ \mu\varepsilon/^{\circ}\text{C}$$

The steel reinforcement B500B is characterised by the following properties:

$$f_{yk} = 500\ \text{MPa}$$

$$E_r = 200\ \text{GPa}$$

$$f_{yd} = \frac{f_{yk}}{\gamma_r} = \frac{500}{1.15} = 434.8\ \text{MPa}$$

$$\varepsilon_{yd} = \frac{f_{yd}}{E_r} = \frac{434.8}{200000} = 0.00217 = 2170\ \mu\varepsilon/^{\circ}\text{C}$$

The minimum longitudinal reinforcement employed to ensure ductility reads:

$$\rho = \rho_{r,min} \geq \frac{f_{ct}}{f_y}$$

with $f_{ct} = f_{ctm} = 0.3 f_{ck}^{\frac{2}{3}}$ (for $f_{ck} < 50$ MPa)

For this case, considering the concrete properties detailed before:

$$f_{ct} = 0.3 f_{ck}^{\frac{2}{3}} = 0.3 \cdot 25^{2/3} = 2.6 \text{ MPa}$$

Thus

$$\rho_{r,min} \geq 0.006$$

The effective longitudinal reinforcement is computed as

$$\rho_{eff} = \frac{A_r}{A_{EP}}$$

with $A_{EP}[\text{mm}^2]$ the surface of the pile cross section and $A_r[\text{mm}^2]$ is the total surface of the steel cross sections that can be calculated as

$$A_r = n_\phi \frac{\pi \phi^2}{4}$$

where n_ϕ [−] is the number of reinforcement bars and ϕ[mm] is their diameter. According to the EN 1992 (2004), the minimum diameter for the longitudinal bars should not be less than 16 mm and piles should at least have six longitudinal bars.

Installing $n_\phi = 6$ reinforcement bars of diameter $\phi = 16$ mm, the effective longitudinal reinforcement reads:

$$\rho_{eff} = 0.006 \geq \rho_{r,min}$$

In this case, a nominal concrete cover of 50 mm is considered as a design value. As no shear forces are applied to the considered pile, the minimum transverse reinforcement is placed. This reinforcement represents one bar of 6 mm diameter every 400 mm.

Based on the previous features, the strength domain depicted in the following figure is obtained. As the design effects of actions are included within the strength domain, no structural ultimate limit states are exceeded with the regards to the most solicited reinforced concrete cross section.

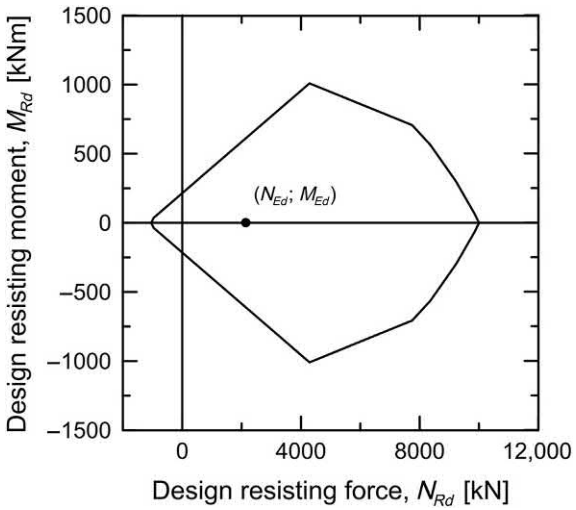

s.

i. Geotechnical design

Approach DA1-C1 (A1 + M1 + R1)

According to this approach, the design values of actions, the design material properties and the design resistances are derived from their characteristic values considering the partial factors of the group A1, M1 and R1, respectively.

It is supposed that the characteristic load N_{Ek} [N] is composed for 70% of a permanent load, N_{Gk}, and for 30% of a variable load, N_{Qk}:

$$N_{Gk} = 0.7N_k = 0.7 \cdot 5500 = 3850\,\text{kN}$$

$$N_{Qk} = 0.3N_k = 0.3 \cdot 5500 = 1650\,\text{kN}$$

The permanent and variable design loads are computed by multiplying their characteristic values by the partial factors A1:

$$N_{Gd} = \gamma_G N_{Gk} = 1.35 \cdot 3850 = 5197.5\,\text{kN}$$

$$N_{Qd} = \gamma_Q N_{Qk} = 1.5 \cdot 1650 = 2475\,\text{kN}$$

Hence, the total design acting load N_{Ed} [N] reads:

$$N_{Ed} = N_{Gd} + N_{Qd} = 5197.5 + 2475 = 7672.5\,\text{kN}$$

The design material properties are computed by dividing their characteristic values by the partial factors M1:

$$\gamma_{sand,d} = \frac{\gamma_{sand,k}}{\gamma_\gamma} = \frac{19}{1} = 19\,\text{kN/m}^3$$

$$\varphi'_{cv,sand,d} = \tan^{-1}\left(\frac{\tan\varphi'_{cv,sand,k}}{\gamma_{\varphi'}}\right) = \tan^{-1}\left(\frac{\tan 30}{1}\right) = 30\ \text{degrees}$$

$$UCS_{sandstone,d} = \frac{UCS_{sandstone,k}}{\gamma_{UCS}} = \frac{50000}{1} = 50000\,\text{kPa}$$

By assumption, the minimum length needed to sustain the design acting load is calculated with reference to the only sand deposit. If a pile length of at least 20 m will be found, the formulation for the shaft capacity will be considered still valid for the sand deposit, while another appropriate formulation will be employed for the calculation of the base capacity. Based on the above, the shaft capacity reads:

$$Q_{s,d} = \frac{q_{s,k}A_s}{\gamma_s\xi_1} = \frac{\overline{K}\overline{\sigma'_z}\tan\delta_d A_s}{\gamma_s\xi_1} = \frac{0.7\left(1-\sin\varphi'_{cv,sand,d}\right)\overline{\sigma'_z}\tan\varphi'_{cv,sand,d}A_s}{\gamma_s\xi_1}$$
$$= \frac{0.7(1-\sin 30)9\frac{L}{2}\tan 30\cdot\pi 0.8L}{1\cdot 1.4} = 1.63L^2$$

The base capacity reads:

$$Q_{b,d} = \frac{q_{b,k}A_b}{\gamma_b\xi_1} = \frac{N_q d_q \sigma'_{zb}A_b}{\gamma_b\xi_1} = \frac{K_p e^{\pi\tan\varphi'_{cv,sand,d}} d_q \sigma'_{zb}\pi\left(\frac{D}{2}\right)^2}{\gamma_b\xi_1} =$$

$$= \frac{\left(K_p e^{\pi\tan\varphi'_{cv,sand,d}}\right)\left(1+2\tan\varphi'_{cv,sand,d}\left(1-\sin\varphi'_{cv,sand,d}\right)^2 k_H\right)\sigma'_{zb}\pi\left(\frac{D}{2}\right)^2}{\gamma_b\xi_1}$$

$$= \frac{\left(\frac{1+\sin\varphi'_{cv,sand,d}}{1-\sin\varphi'_{cv,sand,d}} e^{\pi\tan\varphi'_{cv,sand,d}}\right)\left(1+2\tan\varphi'_{cv,sand,d}\left(1-\sin\varphi'_{cv,sand,d}\right)^2\tan^{-1}\left(\frac{L}{D}\right)\right)\sigma'_{zb}\pi\left(\frac{D}{2}\right)^2}{\gamma_b\xi_1}$$

$$= \frac{\left(\frac{1+\sin 30}{1-\sin 30} e^{\pi\tan 30}\right)\left(1+2\tan 30(1-\sin 30)^2\tan^{-1}\left(\frac{L}{0.8}\right)\right)(19-10)L\pi\left(\frac{0.8}{2}\right)^2}{1.25\cdot 1.4}$$

$$= \frac{18.40\left(1 + 0.289\tan^{-1}\left(\frac{L}{0.8}\right)\right)9L\pi 0.16}{1.25 \cdot 1.4} =$$

$$= \frac{83.24L\left(1 + 0.289\tan^{-1}\left(\frac{L}{0.8}\right)\right)}{1.75} =$$

$$= 47.57L\left(1 + 0.289\tan^{-1}\left(\frac{L}{0.8}\right)\right)$$

By substituting the aforementioned formulations in the equation of vertical pile equilibrium, an equation in the unknown L is obtained:

$$N_{Ed} \equiv Q_{u,d} = Q_{s,d}(L) + Q_{b,d}(L)$$

$$7672.5 = 1.63L^2 + 47.57L\left(1 + 0.289\tan^{-1}\left(\frac{L}{0.8}\right)\right)$$

$$1.63L^2 + 47.57L\left(1 + 0.289\tan^{-1}\left(\frac{L}{0.8}\right)\right) - 7672.5 = 0$$

By solving the aforementioned equation, a pile length of $L = 50.7$ m is obtained.

Once the length of the pile reaches the depth of the rock formation, that is 20 m, the base capacity should be evaluated using the approach proposed by Zhang and Einstein (1998):

$$Q_{b,d} = \frac{q_{b,k}A_b}{\gamma_b\xi_1} = \frac{15p_a\sqrt{\frac{UCS_{sandstone,d}}{p_a}}A_b}{\gamma_b\xi_1} = \frac{15 \cdot 101.325 \cdot \sqrt{\frac{50{,}000}{101.325}} \cdot \pi \cdot 0.4^2}{1.25 \cdot 1.4}$$

$$= \frac{33762 \cdot \pi \cdot 0.4^2}{1.75} = 9698\,\text{kN}$$

Therefore the pile length of $L = 20$ m is sufficient to provide sufficient capacity (through the only base contribution) and is associated with a shaft capacity of

$$Q_{s,d} = \frac{q_{s,k}A_s}{\gamma_s\xi_1} = 1.63L^2 = 1.63 \cdot 20^2 = 652\,\text{kN}$$

Approach DA1-C2 (A2 + M1 + R4)

According to this approach, the design values of actions, the design material properties and the design resistances are derived from their characteristic values considering the partial factors of the group A2, M1 and R4, respectively.

The design loads are the characteristic ones multiplied by the partial factors A1:

$$N_{Gd} = \gamma_G N_{Gk} = 1 \cdot 3850 = 3850\,\text{kN}$$

$$N_{Qd} = \gamma_Q N_{Qk} = 1.3 \cdot 1650 = 2145\,\text{kN}$$

Hence, the total design load N_{Ed} reads:

$$N_{Ed} = N_{Gd} + N_{Qd} = 3850 + 2145 = 5995\,\text{kN}$$

The design material properties are computed by dividing their characteristic values by the partial factors M1:

$$\gamma_{sand,d} = \frac{\gamma_{sand,k}}{\gamma_\gamma} = \frac{19}{1} = 19\,\text{kN/m}^3$$

$$\varphi'_{cv,sand,d} = \tan^{-1}\left(\frac{\tan\varphi'_{cv,sand,k}}{\gamma_{\varphi'}}\right) = \tan^{-1}\left(\frac{\tan 30}{1}\right) = 30 \text{ degrees}$$

$$UCS_{sandstone,d} = \frac{UCS_{sandstone,k}}{\gamma_{UCS}} = \frac{50{,}000}{1} = 50{,}000\,\text{kPa}$$

Based on the above, the shaft capacity reads:

$$Q_{s,d} = \frac{q_{s,k}A_s}{\gamma_s\xi_1} = \frac{K\overline{\sigma'_z}\tan\delta_d A_s}{\gamma_s\xi_1} = \frac{0.7\left(1-\sin\varphi'_{cv,sand,d}\right)\overline{\sigma'_z}\tan\varphi'_{cv,sand,d}A_s}{\gamma_s\xi_1}$$
$$= \frac{0.7(1-\sin 30)9\frac{L}{2}\tan 30 \cdot \pi 0.8L}{1.3 \cdot 1.4} = 1.26L^2$$

The base capacity reads:

$$Q_{b,d} = \frac{q_{b,k}A_b}{\gamma_b\xi_1} = \frac{N_q d_q \sigma'_{zb}A_b}{\gamma_b\xi_1} = \frac{K_p e^{\pi\tan\varphi'_{cv,sand,d}} d_q \sigma'_{zb}\pi\left(\frac{D}{2}\right)^2}{\gamma_b\xi_1} =$$

$$= \frac{\left(K_p e^{\pi\tan\varphi'_{cv,sand,d}}\right)\left(1+2\tan\varphi'_{cv,sand,d}\left(1-\sin\varphi'_{cv,sand,d}\right)^2 k_H\right)\sigma'_{zb}\pi\left(\frac{D}{2}\right)^2}{\gamma_b\xi_1}$$

$$= \frac{\left(\frac{1+\sin\varphi'_{cv,sand,d}}{1-\sin\varphi'_{cv,sand,d}} e^{\pi\tan\varphi'_{cv,sand,d}}\right)\left(1+2\tan\varphi'_{cv,sand,d}\left(1-\sin\varphi'_{cv,sand,d}\right)^2\tan^{-1}\left(\frac{L}{D}\right)\right)\sigma'_{zb}\pi\left(\frac{D}{2}\right)^2}{\gamma_b\xi_1}$$

$$= \frac{\left(\frac{1+\sin 30}{1-\sin 30} e^{\pi \tan 30}\right)\left(1 + 2\tan 30(1-\sin 30)^2 \tan^{-1}\left(\frac{L}{0.8}\right)\right)(19-10)L\pi\left(\frac{0.8}{2}\right)^2}{1.6 \cdot 1.4}$$

$$= \frac{18.40\left(1 + 0.289\tan^{-1}\left(\frac{L}{0.8}\right)\right)9L\pi 0.16}{1.6 \cdot 1.4} =$$

$$= \frac{83.24L\left(1 + 0.289\tan^{-1}\left(\frac{L}{0.8}\right)\right)}{2.24} =$$

$$= 37.16L\left(1 + 0.289\tan^{-1}\left(\frac{L}{0.8}\right)\right)$$

By substituting the aforementioned formulations in the equation of vertical pile equilibrium, an equation in the unknown L is obtained:

$$N_{Ed} \equiv Q_{u,d} = Q_{s,d}(L) + Q_{b,d}(L)$$

$$5995 = 1.26L^2 + 37.1L\left(1 + 0.289\tan^{-1}\left(\frac{L}{0.8}\right)\right)$$

$$1.26L^2 + 37.16L\left(1 + 0.289\tan^{-1}\left(\frac{L}{0.8}\right)\right) - 5995 = 0$$

By solving the aforementioned equation, a pile length of $L = 50.8$ m is obtained.

Once the length of the pile reaches the depth of the rock formation, that is 20 m, the base capacity should be evaluated using the approach proposed by Zhang and Einstein (1998):

$$Q_{b,d} = \frac{q_{b,k}A_b}{\gamma_b \xi_1} = \frac{15 p_a \sqrt{\frac{UCS_{sandstone,d}}{p_a}} A_b}{\gamma_b \xi_1} = \frac{15 \cdot 101.325 \cdot \sqrt{\frac{50{,}000}{101.325}} \cdot \pi \cdot 0.4^2}{1.6 \cdot 1.4}$$

$$= \frac{33{,}762 \cdot \pi \cdot 0.4^2}{2.24} = 7576\,\text{kN}$$

Therefore the pile length of $L = 20$ m is sufficient to provide sufficient capacity (through the only base contribution) and is associated with a shaft capacity of

$$Q_{s,d} = \frac{q_{s,k}A_s}{\gamma_s \xi_1} = 1.26L^2 = 1.26 \cdot 20^2 = 504\,\text{kN}$$

Approach DA2 (A1 + M1 + R2)

According to this approach, the design values of actions, the design material properties and the design resistances are derived from their characteristic values considering the partial factors of the group A1, M1 and R2, respectively.

The permanent and variable design loads are computed by multiplying their characteristic values by the partial factors A1:

$$N_{Gd} = \gamma_G N_{Gk} = 1.35 \cdot 3850 = 5197.5\,\text{kN}$$

$$N_{Qd} = \gamma_Q N_{Qk} = 1.5 \cdot 1650 = 2475\,\text{kN}$$

Hence, the total design load N_{Ed} reads:

$$N_{Ed} = N_{Gd} + N_{Qd} = 5197.5 + 2475 = 7672.5\,\text{kN}$$

The design material properties are computed by dividing their characteristic values by the partial factors M1:

$$\gamma_{sand,d} = \frac{\gamma_{sand,k}}{\gamma_\gamma} = \frac{19}{1} = 19\,\text{kN/m}^3$$

$$\varphi'_{cv,sand,d} = \tan^{-1}\left(\frac{\tan\varphi'_{cv,sand,k}}{\gamma_{\varphi'}}\right) = \tan^{-1}\left(\frac{\tan 30}{1}\right) = 30\ \text{degrees}$$

$$UCS_{sandstone,d} = \frac{UCS_{sandstone,k}}{\gamma_{UCS}} = \frac{50000}{1} = 50{,}000\,\text{kPa}$$

Based on the above, the shaft capacity reads:

$$Q_{s,d} = \frac{q_{s,k}A_s}{\gamma_s \xi_1} = \frac{\overline{K}\overline{\sigma'_z}\tan\delta_d A_s}{\gamma_s \xi_1} = \frac{0.7\left(1 - \sin\varphi'_{cv,sand,d}\right)\overline{\sigma'_z}\tan\varphi'_{cv,sand,d}A_s}{\gamma_s \xi_1}$$
$$= \frac{0.7(1 - \sin 30)9\frac{L}{2}\tan 30 \cdot \pi 0.8L}{1.1 \cdot 1.4} = 1.48L^2$$

The base capacity reads:

$$Q_{b,d} = \frac{q_{b,k}A_b}{\gamma_b\xi_1} = \frac{N_q d_q \sigma'_{zb} A_b}{\gamma_b\xi_1} = \frac{K_p e^{\pi\tan\varphi'_{cv,sand,d}} d_q \sigma'_{zb}\pi\left(\frac{D}{2}\right)^2}{\gamma_b\xi_1} =$$

$$= \frac{\left(K_p e^{\pi\tan\varphi'_{cv,sand,d}}\right)\left(1+2\tan\varphi'_{cv,sand,d}\left(1-\sin\varphi'_{cv,sand,d}\right)^2 k_H\right)\sigma'_{zb}\pi\left(\frac{D}{2}\right)^2}{\gamma_b\xi_1}$$

$$= \frac{\left(\frac{1+\sin\varphi'_{cv,sand,d}}{1-\sin\varphi'_{cv,sand,d}} e^{\pi\tan\varphi'_{cv,sand,d}}\right)\left(1+2\tan\varphi'_{cv,sand,d}\left(1-\sin\varphi'_{cv,sand,d}\right)^2\tan^{-1}\left(\frac{L}{D}\right)\right)\sigma'_{zb}\pi\left(\frac{D}{2}\right)^2}{\gamma_b\xi_1}$$

$$= \frac{\left(\frac{1+\sin 30}{1-\sin 30} e^{\pi\tan 30}\right)\left(1+2\tan 30(1-\sin 30)^2\tan^{-1}\left(\frac{L}{0.8}\right)\right)(19-10)L\pi\left(\frac{0.8}{2}\right)^2}{1.1\cdot 1.4}$$

$$= \frac{18.40\left(1+0.289\tan^{-1}\left(\frac{L}{0.8}\right)\right)9L\pi 0.16}{1.1\cdot 1.4}$$

$$= \frac{83.24L\left(1+0.289\tan^{-1}\left(\frac{L}{0.8}\right)\right)}{1.54}$$

$$= 54.04L\left(1+0.289\tan^{-1}\left(\frac{L}{0.8}\right)\right)$$

By substituting the aforementioned formulations in the equation of vertical pile equilibrium, an equation in the unknown L is obtained:

$$N_{Ed} \equiv Q_{u,d} = Q_{s,d}(L) + Q_{b,d}(L)$$

$$7672.5 = 1.48L^2 + 54.04L\left(1 + 0.289\tan^{-1}\left(\frac{L}{0.5}\right)\right)$$

$$1.48L^2 + 54.04L\left(1 + 0.289\tan^{-1}\left(\frac{L}{0.5}\right)\right) - 7672.5 = 0$$

By solving the aforementioned equation, a pile length of $L = 50.3$ m is obtained.

Once the length of the pile reaches the depth of the rock formation, that is 20 m, the base capacity should be evaluated using the approach proposed by Zhang and Einstein (1998):

$$Q_{b,d} = \frac{q_{b,k}A_b}{\gamma_b \xi_1} = \frac{15 p_a \sqrt{\frac{UCS_{sandstone,d}}{p_a}} A_b}{\gamma_b \xi_1} = \frac{15 \cdot 101.325 \cdot \sqrt{\frac{50{,}000}{101.325}} \cdot \pi \cdot 0.8^2}{1.1 \cdot 1.4}$$
$$= \frac{33762 \cdot \pi \cdot 0.8^2}{1.54} = 11{,}020\,\text{kN}$$

Therefore the pile length of $L = 20$ m is sufficient to provide sufficient capacity (through the only base contribution) and is associated with a shaft capacity of

$$Q_{s,d} = \frac{q_{s,k}A_s}{\gamma_s \xi_1} = 1.48L^2 = 1.48 \cdot 20^2 = 592\,\text{kN}$$

The quantities related to the geotechnical design at ultimate limit states according to the different approaches proposed by the Eurocodes are reported in the following table, together with the effective length assigned to the pile, L_{eff} [m].

	N_{Ed} [kN]	$Q_{s,d}$ [kN]	$Q_{b,d}$ [kN]	$Q_{u,d}$ [kN]	L [m]	L_{eff} [m]
DA1-C1	7672.5	652	9698	10,350	20	20
DA1-C2	5995	504	7576	8080	20	20
DA2	7672.5	592	11,020	11,612	20	20

ii. Structural design

The structural design at ultimate limit states of the cross section of the considered axially loaded pile requires to define the design acting load N_{Ed} and comparing it with the design resisting load N_{Rd} for no moment applied. Alternatively, the design can be performed by verifying the position of the design action effects (N_{Ed}; M_{Ed}) in the strength domain of the cross section. This latter approach is considered here.

As for the geotechnical design, it is supposed that the acting characteristic load N_{Ek} is characterised for 70% by a permanent contribution, N_{Gk}, and for 30% by a variable contribution, N_{Qk}:

$$N_{Gk} = 0.7N_k = 0.7 \cdot 5500 = 3850\,\text{kN}$$

$$N_{Qk} = 0.3N_k = 0.3 \cdot 5500 = 1650\,\text{kN}$$

The permanent and variable design loads are computed by multiplying their characteristic values by the partial factors A1:

$$N_{Gd} = \gamma_G N_{Gk} = 1.35 \cdot 3850 = 5197.5\,\text{kN}$$

$$N_{Qd} = \gamma_Q N_{Qk} = 1.5 \cdot 1650 = 2475\,\text{kN}$$

Hence, the total design load N_{Ed} reads:

$$N_{Ed} = N_{Gd} + N_{Qd} = 5197.5 + 2475 = 7672.5\,\text{kN}$$

The following material properties and features are considered to obtain the strength domain for the designed section. The concrete class C32/40 is characterised by the following properties:

$$f_{ck} = 32\,\text{MPa}$$

$$f_{ck,cube} = 40\,\text{MPa}$$

$$E_{cm} = 35\,\text{GPa}$$

$$f_{cd} = \frac{\alpha_{cc} f_{ck}}{\gamma_c} = \frac{0.85 \cdot 32}{1.5} = 18.1\,\text{MPa}$$

$$\varepsilon_{uc} = 0.0035 = 3500\,\mu\varepsilon/^{\circ}\text{C}$$

The steel reinforcement B500B is characterised by the following properties:

$$f_{yk} = 500\,\text{MPa}$$

$$E_r = 200\,\text{GPa}$$

$$f_{yd} = \frac{f_{yk}}{\gamma_r} = \frac{500}{1.15} = 434.8\,\text{MPa}$$

$$\varepsilon_{yd} = \frac{f_{yd}}{E_r} = \frac{434.8}{200{,}000} = 0.00217 = 2170\,\mu\varepsilon/^{\circ}\text{C}$$

The minimum longitudinal reinforcement employed to ensure ductility reads:

$$\rho = \rho_{r,min} \geq \frac{f_{ct}}{f_y}$$

with $f_{ct} = f_{ctm} = 0.3 f_{ck}^{\frac{2}{3}}$ (for $f_{ck} < 50$ MPa)

For this case, considering the concrete properties detailed before:

$$f_{ct} = 0.3 f_{ck}^{\frac{2}{3}} = 0.3 \cdot 32^{\frac{2}{3}} = 3.0 \text{ MPa}$$

Thus

$$\rho_{r,min} \geq 0.007$$

The effective longitudinal reinforcement is computed as

$$\rho_{eff} = \frac{A_r}{A_{EP}}$$

with $A_{EP}[\text{mm}^2]$ the surface of the pile cross section and $A_r[\text{mm}^2]$ is the total surface of the steel cross sections that can be calculated as

$$A_r = n_\phi \frac{\pi \phi^2}{4}$$

where n_ϕ [−] is the number of reinforcement bars and ϕ[mm] is their diameter. According to the EN 1992 (2004), the minimum diameter for the longitudinal bars should not be less than 16 mm and piles should at least have six longitudinal bars.

Installing $n_\phi = 10$ reinforcement bars of diameter $\phi = 22$ mm, the effective longitudinal reinforcement reads:

$$\rho_{eff} = 0.008 \geq \rho_{r,min}$$

In this case, a nominal concrete cover of 60 mm is considered as a design value. As no shear forces are applied to the considered pile, the minimum transverse reinforcement is placed. This reinforcement represents one bar of 6 mm diameter every 400 mm.

Based on the previous features, the strength domain depicted in the following figure is obtained. As the design effects of actions are included within the strength domain, no structural ultimate limit states are

exceeded with the regards to the most solicited reinforced concrete cross section.

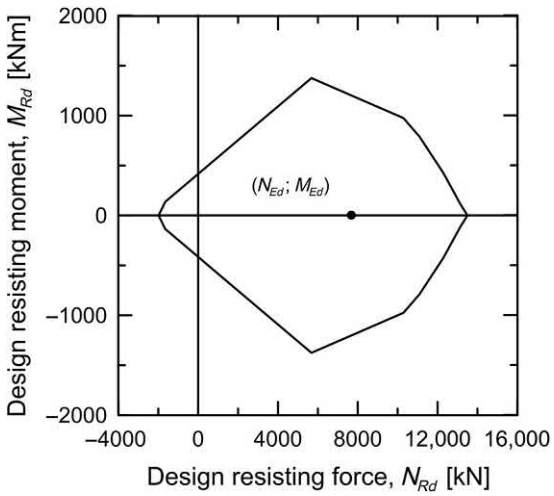

t.

i. Geotechnical design

Approach DA1-C1 (A1 + M1 + R1)

According to this approach, the design values of actions, the design material properties and the design resistances are derived from their characteristic values considering the partial factors of the group A1, M1 and R1, respectively.

It is supposed that the acting characteristic load N_{Ek} [N] is characterised for 70% by a permanent contribution, N_{Gk}, and for 30% by a variable contribution, N_{Qk}:

$$N_{Gk} = 0.7N_k = 0.7 \cdot 3000 = 2100\,\text{kN}$$

$$N_{Qk} = 0.3N_k = 0.3 \cdot 3000 = 900\,\text{kN}$$

The permanent and variable design loads are computed by multiplying their characteristic values by the partial factors A1:

$$N_{Gd} = \gamma_G N_{Gk} = 1.35 \cdot 2100 = 2835\,\text{kN}$$

$$N_{Qd} = \gamma_Q N_{Qk} = 1.5 \cdot 900 = 1350\,\text{kN}$$

Hence, the total design acting load N_{Ed} [N] reads:

$$N_{Ed} = N_{Gd} + N_{Qd} = 2835 + 1350 = 4185\,\text{kN}$$

The design material properties are computed by dividing their characteristic values by the partial factors M1:

$$\gamma_{sand,d} = \frac{\gamma_{sand,k}}{\gamma_\gamma} = \frac{19}{1} = 19\,\text{kN/m}^3$$

$$c_d^{'} = \frac{c_k^{'}}{\gamma_{c'}} = \frac{20}{1} = 20\,\text{kPa}$$

$$\varphi_{cv,d}^{'} = \tan^{-1}\left(\frac{\tan\varphi_{cv,k}^{'}}{\gamma_{\varphi'}}\right) = \tan^{-1}\left(\frac{\tan 31}{1}\right) = 31\ \text{degrees}$$

Based on the above, the shaft capacity reads:

$$Q_{s,d} = \frac{q_{s,k}A_s}{\gamma_s\xi_1} = \frac{\overline{K}\overline{\sigma_z^{'}}\tan\delta_d A_s}{\gamma_s\xi_1} = \frac{0.7\left(1-\sin\varphi_{cv,d}^{'}\right)\overline{\sigma_z^{'}}\tan\varphi_{cv,d}^{'}A_s}{\gamma_s\xi_1}$$
$$= \frac{0.7(1-\sin 31)9\frac{L}{2}\tan 31\cdot\pi 0.8L}{1\cdot 1.4} = 1.65L^2$$

The base capacity reads:

$$Q_{b,d} = \frac{q_{b,k}A_b}{\gamma_b\xi_1} = \frac{N_q d_q \sigma_{zb}^{'}A_b}{\gamma_b\xi_1} = \frac{K_p e^{\pi\tan\varphi_{cv,d}^{'}} d_q \sigma_{zb}^{'}\pi\left(\frac{D}{2}\right)^2}{\gamma_b\xi_1} =$$

$$= \frac{\left(K_p e^{\pi\tan\varphi_{cv,d}^{'}}\right)\left(1+2\tan\varphi_{cv,d}^{'}\left(1-\sin\varphi_{cv,d}^{'}\right)^2 k_H\right)\sigma_{zb}^{'}\pi\left(\frac{D}{2}\right)^2}{\gamma_b\xi_1}$$

$$= \frac{\left(\frac{1+\sin\varphi_{cv,d}^{'}}{1-\sin\varphi_{cv,d}^{'}} e^{\pi\tan\varphi_{cv,d}^{'}}\right)\left(1+2\tan\varphi_{cv,d}^{'}\left(1-\sin\varphi_{cv,d}^{'}\right)^2\tan^{-1}\left(\frac{L}{D}\right)\right)\sigma_{zb}^{'}\pi\left(\frac{D}{2}\right)^2}{\gamma_b\xi_1}$$

$$= \frac{\left(\frac{1+\sin 31}{1-\sin 31} e^{\pi\tan 31}\right)\left(1+2\tan 31(1-\sin 31)^2\tan^{-1}\left(\frac{L}{0.8}\right)\right)(19-10)L\pi\left(\frac{0.8}{2}\right)^2}{1.25\cdot 1.4}$$

$$= \frac{20.6\left(1+0.283\tan^{-1}\left(\frac{L}{0.8}\right)\right)9L\pi 0.16}{1.25\cdot 1.4} =$$

$$= \frac{93.19L\left(1 + 0.283\tan^{-1}\left(\frac{L}{0.8}\right)\right)}{1.75} =$$

$$= 53.25L\left(1 + 0.283\tan^{-1}\left(\frac{L}{0.8}\right)\right)$$

By substituting the aforementioned formulations in the equation of vertical pile equilibrium, an equation in the unknown L is obtained:

$$N_{Ed} \equiv Q_{u,d} = Q_{s,d}(L) + Q_{b,d}(L)$$

$$4185 = 1.65L^2 + 53.25L\left(1 + 0.283\tan^{-1}\left(\frac{L}{0.8}\right)\right)$$

$$1.65L^2 + 53.25L\left(1 + 0.283\tan^{-1}\left(\frac{L}{0.8}\right)\right) - 4185 = 0$$

By solving the aforementioned equation, a pile length of $L = 32.3$ m is obtained.

Approach DA1-C2 (A2 + M1 + R4)

According to this approach, the design values of actions, the design material properties and the design resistances are derived from their characteristic values considering the partial factors of the group A2, M1 and R4, respectively.

The permanent and variable design loads are computed by multiplying their characteristic values by the partial factors A1:

$$N_{Gd} = \gamma_G N_{Gk} = 1 \cdot 2100 = 2100\,\text{kN}$$

$$N_{Qd} = \gamma_Q N_{Qk} = 1.3 \cdot 900 = 1170\,\text{kN}$$

Hence, the total design load N_{Ed} reads:

$$N_{Ed} = N_{Gd} + N_{Qd} = 2100 + 1170 = 3270\,\text{kN}$$

The design material properties are computed by dividing their characteristic values by the partial factors M1:

$$\gamma_{sand,d} = \frac{\gamma_{sand,k}}{\gamma_\gamma} = \frac{19}{1} = 19\,\mathrm{kN/m^3}$$

$$c_d^{'} = \frac{c_k^{'}}{\gamma_{c'}} = \frac{20}{1} = 20\,\mathrm{kPa}$$

$$\varphi_{cv,d}^{'} = \tan^{-1}\left(\frac{\tan\varphi_{cv,k}^{'}}{\gamma_{\varphi'}}\right) = \tan^{-1}\left(\frac{\tan 31}{1}\right) = 31 \text{ degrees}$$

Based on the above, the shaft capacity reads:

$$Q_{s,d} = \frac{q_{s,k}A_s}{\gamma_s\xi_1} = \frac{\overline{K}\overline{\sigma_z^{'}}\tan\delta_d A_s}{\gamma_s\xi_1} = \frac{0.7\left(1-\sin\varphi_{cv,d}^{'}\right)\overline{\sigma_z^{'}}\tan\varphi_{cv,d}^{'}A_s}{\gamma_s\xi_1}$$
$$= \frac{0.7(1-\sin 31)9\frac{L}{2}\tan 31\cdot\pi 0.8L}{1.3\cdot 1.4} = 1.27L^2$$

The base capacity reads:

$$Q_{b,d} = \frac{q_{b,k}A_b}{\gamma_b\xi_1} = \frac{N_q d_q \sigma_{zb}^{'}A_b}{\gamma_b\xi_1} = \frac{K_p e^{\pi\tan\varphi_{cv,d}^{'}}d_q\sigma_{zb}^{'}\pi\left(\frac{D}{2}\right)^2}{\gamma_b\xi_1}$$

$$= \frac{\left(K_p e^{\pi\tan\varphi_{cv,d}^{'}}\right)\left(1+2\tan\varphi_{cv,d}^{'}\left(1-\sin\varphi_{cv,d}^{'}\right)^2 k_H\right)\sigma_{zb}^{'}\pi\left(\frac{D}{2}\right)^2}{\gamma_b\xi_1}$$

$$= \frac{\left(\frac{1+\sin\varphi_{cv,d}^{'}}{1-\sin\varphi_{cv,d}^{'}}e^{\pi\tan\varphi_{cv,d}^{'}}\right)\left(1+2\tan\varphi_{cv,d}^{'}\left(1-\sin\varphi_{cv,d}^{'}\right)^2\tan^{-1}\left(\frac{L}{D}\right)\right)\sigma_{zb}^{'}\pi\left(\frac{D}{2}\right)^2}{\gamma_b\xi_1}$$

$$= \frac{\left(\frac{1+\sin 31}{1-\sin 31}e^{\pi\tan 31}\right)\left(1+2\tan 31(1-\sin 31)^2\tan^{-1}\left(\frac{L}{0.8}\right)\right)(19-10)L\pi\left(\frac{0.8}{2}\right)^2}{1.6\cdot 1.4}$$

$$= \frac{20.6\left(1+0.283\tan^{-1}\left(\frac{L}{0.8}\right)\right)9L\pi 0.16}{1.6\cdot 1.4}$$

$$= \frac{93.19L\left(1+0.283\tan^{-1}\left(\frac{L}{0.8}\right)\right)}{2.24}$$

$$= 41.6L\left(1+0.283\tan^{-1}\left(\frac{L}{0.8}\right)\right)$$

By substituting the aforementioned formulations in the equation of vertical pile equilibrium, an equation in the unknown L is obtained:

$$N_{Ed} \equiv Q_{u,d} = Q_{s,d}(L) + Q_{b,d}(L)$$

$$3270 = 1.27L^2 + 41.6L\left(1 + 0.283\tan^{-1}\left(\frac{L}{0.8}\right)\right)$$

$$1.27L^2 + 41.6L\left(1 + 0.283\tan^{-1}\left(\frac{L}{0.8}\right)\right) - 3270 = 0$$

By solving the aforementioned equation, a pile length of $L = 32.4$ m is obtained.

Approach DA2 (A1 + M1 + R2)

According to this approach, the design values of actions, the design material properties and the design resistances are derived from their characteristic values considering the partial factors of the group A1, M1 and R2, respectively.

The permanent and variable design loads are computed by multiplying their characteristic values by the partial factors A1

$$N_{Gd} = \gamma_G N_{Gk} = 1.35 \cdot 2100 = 2835\,\text{kN}$$

$$N_{Qd} = \gamma_Q N_{Qk} = 1.5 \cdot 900 = 1350\,\text{kN}$$

Hence, the total design load N_{Ed} reads:

$$N_{Ed} = N_{Gd} + N_{Qd} = 2835 + 1350 = 4185\,\text{kN}$$

The design material properties are computed by dividing their characteristic values by the partial factors M1:

$$\gamma_{sand,d} = \frac{\gamma_{sand,k}}{\gamma_\gamma} = \frac{19}{1} = 19\,\text{kN/m}^3$$

$$c'_d = \frac{c'_k}{\gamma_{c'}} = \frac{20}{1} = 20\,\text{kPa}$$

$$\varphi'_{cv,d} = \tan^{-1}\left(\frac{\tan\varphi'_{cv,k}}{\gamma_{\varphi'}}\right) = \tan^{-1}\left(\frac{\tan 31}{1}\right) = 31 \text{ degrees}$$

Based on the above, the shaft capacity reads:

$$Q_{s,d} = \frac{q_{s,k}A_s}{\gamma_s\xi_1} = \frac{\overline{K}\overline{\sigma'_z}\tan\delta_d A_s}{\gamma_s\xi_1} = \frac{0.7\left(1-\sin\varphi'_{cv,d}\right)\overline{\sigma'_z}\tan\varphi'_{cv,d}A_s}{\gamma_s\xi_1}$$
$$= \frac{0.7(1-\sin 31)9\frac{L}{2}\tan 31\cdot\pi 0.8L}{1.1\cdot 1.4} = 1.50L^2$$

The base capacity reads:

$$Q_{b,d} = \frac{q_{b,k}A_b}{\gamma_b\xi_1} = \frac{N_q d_q \sigma'_{zb}A_b}{\gamma_b\xi_1} = \frac{K_p e^{\pi\tan\varphi'_{cv,d}} d_q \sigma'_{zb}\pi\left(\frac{D}{2}\right)^2}{\gamma_b\xi_1}$$

$$= \frac{\left(K_p e^{\pi\tan\varphi'_{cv,d}}\right)\left(1+2\tan\varphi'_{cv,d}\left(1-\sin\varphi'_{cv,d}\right)^2 k_H\right)\sigma'_{zb}\pi\left(\frac{D}{2}\right)^2}{\gamma_b\xi_1}$$

$$= \frac{\left(\frac{1+\sin\varphi'_{cv,d}}{1-\sin\varphi'_{cv,d}} e^{\pi\tan\varphi'_{cv,d}}\right)\left(1+2\tan\varphi'_{cv,d}\left(1-\sin\varphi'_{cv,d}\right)^2\tan^{-1}\left(\frac{L}{D}\right)\right)\sigma'_{zb}\pi\left(\frac{D}{2}\right)^2}{\gamma_b\xi_1}$$

$$= \frac{\left(\frac{1+\sin 31}{1-\sin 31} e^{\pi\tan 31}\right)\left(1+2\tan 31(1-\sin 31)^2\tan^{-1}\left(\frac{L}{0.8}\right)\right)(19-10)L\pi\left(\frac{0.8}{2}\right)^2}{1.1\cdot 1.4}$$

$$= \frac{20.6\left(1+0.283\tan^{-1}\left(\frac{L}{0.8}\right)\right)9L\pi 0.16}{1.1\cdot 1.4}$$

$$= \frac{93.19L\left(1+0.283\tan^{-1}\left(\frac{L}{0.8}\right)\right)}{1.54}$$

$$= 60.51L\left(1+0.283\tan^{-1}\left(\frac{L}{0.8}\right)\right)$$

By substituting the aforementioned formulations in the equation of vertical pile equilibrium, an equation in the unknown L is obtained:

$$N_{Ed} \equiv Q_{u,d} = Q_{s,d}(L) + Q_{b,d}(L)$$

$$4185 = 1.50L^2 + 60.51L\left(1 + 0.283\tan^{-1}\left(\frac{L}{0.8}\right)\right)$$

$$1.50L^2 + 60.51L\left(1 + 0.283\tan^{-1}\left(\frac{L}{0.8}\right)\right) - 4185 = 0$$

By solving the aforementioned equation, a pile length of $L = 31.3$ m is obtained.

The quantities related to the geotechnical design at ultimate limit states according to the different approaches proposed by the Eurocodes are reported in the following table, together with the effective length assigned to the pile, L_{eff} [m].

	N_{Ed} [kN]	$Q_{s,d}$ [kN]	$Q_{b,d}$ [kN]	$Q_{u,d}$ [kN]	L [m]	L_{eff} [m]
DA1-C1	4185	1719.1	2475.3	4194.5	32.3	33
DA1-C2	3270	1330.6	1939.9	3270.5	32.4	33
DA2	4185	1505.3	2689.6	4195.0	31.3	32

ii. Structural design

The structural design at ultimate limit states of the cross section of the considered axially loaded pile requires defining the design acting load N_{Ed} and comparing it with the design resisting load N_{Rd} for no moment applied. Alternatively, the design can be performed by verifying the position of the design action effects (N_{Ed}; M_{Ed}) in the strength domain of the cross section. This latter approach is considered here.

As for the geotechnical design, it is supposed that the acting characteristic load N_{Ek} is characterised for 70% by a permanent contribution, N_{Gk}, and for 30% by a variable contribution, N_{Qk}:

$$N_{Gk} = 0.7N_k = 0.7 \cdot 3000 = 2100\,\text{kN}$$

$$N_{Qk} = 0.3N_k = 0.3 \cdot 3000 = 900\,\text{kN}$$

The permanent and variable design loads are computed by multiplying their characteristic values by the partial factors A1:

$$N_{Gd} = \gamma_G N_{Gk} = 1.35 \cdot 2100 = 2835\,\text{kN}$$

$$N_{Qd} = \gamma_Q N_{Qk} = 1.5 \cdot 900 = 1350\,\text{kN}$$

Hence, the total design load N_{Ed} reads:

$$N_{Ed} = N_{Gd} + N_{Qd} = 2835 + 1350 = 4185\,\text{kN}$$

The following material properties and features are considered to obtain the strength domain for the designed section. The concrete class C25/30, chosen to satisfy the condition of durability (XC2), is characterised by the following properties:

$$f_{ck} = 25\,\text{MPa}$$

$$f_{ck,cube} = 30\,\text{MPa}$$

$$E_{cm} = 31\,\text{GPa}$$

$$f_{cd} = \frac{\alpha_{cc} f_{ck}}{\gamma_c} = \frac{0.85 \cdot 25}{1.5} = 14.2\,\text{MPa}$$

$$\varepsilon_{uc} = 0.0035 = 3500\,\mu\varepsilon/^{\circ}\text{C}$$

The steel reinforcement B500B is characterised by the following properties:

$$f_{yk} = 500\,\text{MPa}$$

$$E_r = 200\,\text{GPa}$$

$$f_{yd} = \frac{f_{yk}}{\gamma_r} = \frac{500}{1.15} = 434.8\,\text{MPa}$$

$$\varepsilon_{yd} = \frac{f_{yd}}{E_r} = \frac{434.8}{200000} = 0.00217 = 2170\,\mu\varepsilon/^{\circ}\text{C}$$

The minimum longitudinal reinforcement employed to ensure ductility reads:

$$\rho = \rho_{r,min} \geq \frac{f_{ct}}{f_y}$$

with $f_{ct} = f_{ctm} = 0.3 f_{ck}^{\frac{2}{3}}$ **(for** $f_{ck} < 50\,\text{MPa}$**)**

For this case, considering the concrete properties detailed before:

$$f_{ct} = 0.3 f_{ck}^{\frac{2}{3}} = 0.3 \cdot 25^{2/3} = 2.6\,\text{MPa}$$

Thus

$$\rho_{r,min} \geq 0.006$$

The effective longitudinal reinforcement is computed as

$$\rho_{eff} = \frac{A_r}{A_{EP}}$$

with A_{EP}[mm^2] the surface of the pile cross section and A_r[mm^2] is the total surface of the steel cross sections that can be calculated as

$$A_r = n_\phi \frac{\pi \phi^2}{4}$$

where n_ϕ [−] is the number of reinforcement bars and ϕ[mm] is their diameter. According to the EN 1992 (2004), the minimum diameter for the longitudinal bars should not be less than 16 mm and piles should at least have six longitudinal bars.

Installing $n_\phi = 8$ reinforcement bars of diameter $\phi = 22$ mm, the effective longitudinal reinforcement reads:

$$\rho_{eff} = 0.006 \geq \rho_{r,min}$$

In this case, a nominal concrete cover of 60 mm is considered as a design value. As no shear forces are applied to the considered pile, the minimum transverse reinforcement is placed. This reinforcement represents one bar of 6 mm diameter every 400 mm.

Based on the previous features, the strength domain depicted in the following figure is obtained. As the design effects of actions are included within the strength domain, no structural ultimate limit states are exceeded with the regards to the most solicited reinforced concrete cross section.

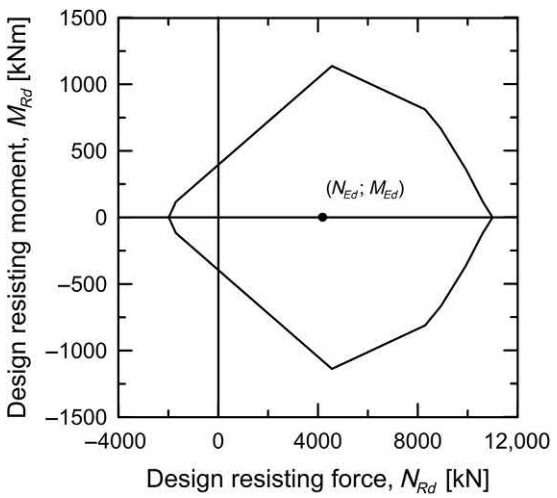

u.

i. Geotechnical design

Approach DA1-C1 (A1 + M1 + R1)

According to this approach, the design values of actions, the design material properties and the design resistances are derived from their characteristic values considering the partial factors of the group A1, M1 and R1, respectively.

It is supposed that the acting characteristic load N_{Ek} [N] is characterised for 70% by a permanent contribution, N_{Gk}, and for 30% by a variable contribution, N_{Qk}:

$$N_{Gk} = 0.7N_k = 0.7 \cdot 2500 = 1750\,\text{kN}$$

$$N_{Qk} = 0.3N_k = 0.3 \cdot 2500 = 750\,\text{kN}$$

The permanent and variable design loads are computed by multiplying their characteristic values by the partial factors A1:

$$N_{Gd} = \gamma_G N_{Gk} = 1.35 \cdot 1750 = 2362.5\,\text{kN}$$

$$N_{Qd} = \gamma_Q N_{Qk} = 1.5 \cdot 750 = 1125\,\text{kN}$$

Hence, the total design acting load N_{Ed} [N] reads:

$$N_{Ed} = N_{Gd} + N_{Qd} = 2362.5 + 1125 = 3487.5\,\text{kN}$$

The design material properties are computed by dividing their characteristic values by the partial factors M1:

$$\gamma_{clay,1,d} = \frac{\gamma_{clay,1,k}}{\gamma_\gamma} = \frac{20}{1} = 20\,\text{kN/m}^3$$

$$\varphi'_{cv,clay,1,d} = \tan^{-1}\left(\frac{\tan\varphi'_{cv,clay,1,k}}{\gamma_{\varphi'}}\right) = \tan^{-1}\left(\frac{\tan 24}{1}\right) = 24\ \text{degrees}$$

$$\gamma_{clay,2,d} = \frac{\gamma_{clay,2,k}}{\gamma_\gamma} = \frac{21}{1} = 21\,\text{kN/m}^3$$

$$\varphi'_{cv,clay,2,d} = \tan^{-1}\left(\frac{\tan\varphi'_{cv,clay,2,k}}{\gamma_{\varphi'}}\right) = \tan^{-1}\left(\frac{\tan 25}{1}\right) = 25\ \text{degrees}$$

Based on the above, the shaft capacity reads:

$$Q_{s,d} = \frac{q_{s,k}A_s}{\gamma_s\xi_1} = \frac{\overline{K}\,\overline{\sigma'_z}\tan\delta_d A_s}{\gamma_s\xi_1} = \frac{\overline{K_1}\,\overline{\sigma'_{z,1}}\tan\delta_d A_{s,1} + \overline{K_2}\,\overline{\sigma'_{z,2}}\tan\delta_d A_{s,2}}{\gamma_s\xi_1}$$

$$= \frac{\begin{aligned}&\left(1-\sin\varphi'_{cv,clay,1,d}\right)OCR^{0.5}\gamma_{clay,1,d}\frac{L_1}{2}\tan\delta_d A_{s,1}\\&+\left(1-\sin\varphi'_{cv,clay,2,d}\right)OCR^{0.5}\left(\gamma_{clay,1,d}L_1+\frac{\gamma_{clay,2,d}L_2}{2}\right)\tan\delta_d A_{s,2}\end{aligned}}{\gamma_s\xi_1}$$

$$= \frac{(1-\sin 24)\cdot 2^{0.5}\cdot 10\cdot\frac{10}{2}\cdot\tan 24\cdot\pi\cdot 0.6\cdot 10}{1\cdot 1.4}$$

$$+\frac{(1-\sin 25)\cdot 8^{0.5}\cdot\left(10\cdot 10+\frac{11L_2}{2}\right)\tan 25\cdot\pi\cdot 0.6L_2}{1\cdot 1.4} = \frac{352+143.5L_2+7.89L_2^2}{1.4}$$

$$= 251.5+102.5L_2+5.64L_2^2$$

The base capacity reads:

$$Q_{b,d} = \frac{q_{b,k}A_b}{\gamma_b\xi_1} = \frac{N_q d_q \sigma'_{zb}A_b}{\gamma_b\xi_1} = \frac{K_p e^{\pi\tan\varphi'_{cv,clay,2,d}} d_q\sigma'_{zb}\pi\left(\frac{D}{2}\right)^2}{\gamma_b\xi_1}$$

$$= \frac{\left(K_p e^{\pi\tan\varphi'_{cv,clay,2,d}}\right)\left(1+2\tan\varphi'_{cv,clay,2,d}\left(1-\sin\varphi'_{cv,clay,2,d}\right)^2 k_H\right)\sigma'_{zb}\pi\left(\frac{D}{2}\right)^2}{\gamma_b\xi_1}$$

$$= \frac{\left(\frac{1+\sin\varphi'_{cv,clay,2,d}}{1-\sin\varphi'_{cv,clay,2,d}}e^{\pi\tan\varphi'_{cv,clay,2,d}}\right)\left(1+2\tan\varphi'_{cv,clay,2,d}\left(1-\sin\varphi'_{cv,clay,2,d}\right)^2\tan^{-1}\left(\frac{L}{D}\right)\right)\sigma'_{zb}\pi\left(\frac{D}{2}\right)^2}{\gamma_b\xi_1}$$

$$= \frac{\begin{aligned}&\left(\frac{1+\sin 25}{1-\sin 25}e^{\pi\tan 25}\right)\left(1+2\tan 25(1-\sin 25)^2\tan^{-1}\left(\frac{10+L_2}{0.6}\right)\right)\\&\times\left(\gamma_{clay,1,d}L_1+\gamma_{clay,2,d}L_2\right)\pi\left(\frac{0.6}{2}\right)^2\end{aligned}}{1.25\cdot 1.4}$$

$$= \frac{10.66\left(1+0.31\tan^{-1}\left(\frac{10+L_2}{0.6}\right)\right)(10\cdot 10+11L_2)0.283}{1.25\cdot 1.4}$$

$$= \frac{3.02\left(1 + 0.31\tan^{-1}\left(\frac{10+L_2}{0.6}\right)\right)(10 \cdot 10 + 11L_2)}{1.75}$$

$$= 172.57\left(1 + 0.31\tan^{-1}\left(\frac{10+L_2}{0.6}\right)\right) + 18.97L_2\left(1 + 0.31\tan^{-1}\left(\frac{10+L_2}{0.6}\right)\right)$$

By substituting the aforementioned formulations in the equation of vertical pile equilibrium, an equation in the unknown L is obtained:

$$N_{Ed} \equiv Q_{u,d} = Q_{s,d}(L) + Q_{b,d}(L)$$

$$= 251.5 + 102.5L_2 + 5.64L_2^2 + 172.57\left(1 + 0.31\tan^{-1}\left(\frac{10+L_2}{0.6}\right)\right)$$
$$+ 18.97L_2\left(1 + 0.31\tan^{-1}\left(\frac{10+L_2}{0.6}\right)\right) - 3487.5$$

By solving the aforementioned equation, a length L_2 of 14.2 m is obtained, so the total length of the pile is equal to $L = 24.2$ m

Approach DA1-C2 (A2 + M1 + R4)

According to this approach, the design values of actions, the design material properties and the design resistances are derived from their characteristic values considering the partial factors of the group A2, M1 and R4, respectively.

The permanent and variable design loads are computed by multiplying their characteristic values by the partial factors A1:

$$N_{Gd} = \gamma_G N_{Gk} = 1 \cdot 1750 = 1750\,\text{kN}$$

$$N_{Qd} = \gamma_Q N_{Qk} = 1.3 \cdot 750 = 975\,\text{kN}$$

Hence, the total design load N_{Ed} reads:

$$N_{Ed} = N_{Gd} + N_{Qd} = 1750 + 975 = 2725\,\text{kN}$$

The design material properties are computed by dividing their characteristic values by the partial factors M1:

$$\gamma_{clay,1,d} = \frac{\gamma_{clay,1,k}}{\gamma_\gamma} = \frac{20}{1} = 20\,\text{kN/m}^3$$

$$\varphi'_{cv,clay,1,d} = \tan^{-1}\left(\frac{\tan\varphi'_{cv,clay,1,k}}{\gamma_{\varphi'}}\right) = \tan^{-1}\left(\frac{\tan 24}{1}\right) = 24 \text{ degrees}$$

$$\gamma_{clay,2,d} = \frac{\gamma_{clay,2,k}}{\gamma_\gamma} = \frac{21}{1} = 21\,\mathrm{kN/m^3}$$

$$\varphi'_{cv,clay,2,d} = \tan^{-1}\left(\frac{\tan\varphi'_{cv,clay,2,k}}{\gamma_{\varphi'}}\right) = \tan^{-1}\left(\frac{\tan 25}{1}\right) = 25 \text{ degrees}$$

Based on the above, the shaft capacity reads:

$$Q_{s,d} = \frac{q_{s,k}A_s}{\gamma_s\xi_1} = \frac{\overline{K}\overline{\sigma'_z}\tan\delta_d A_s}{\gamma_s\xi_1} = \frac{\overline{K_1}\overline{\sigma'_{z,1}}\tan\delta_d A_{s,1} + \overline{K_2}\overline{\sigma'_{z,2}}\tan\delta_d A_{s,2}}{\gamma_s\xi_1}$$

$$= \frac{\begin{array}{l}\left(1-\sin\varphi'_{cv,clay,1,d}\right)OCR^{0.5}\gamma_{clay,1,d}\dfrac{L_1}{2}\tan\delta_d A_{s,1} + \left(1-\sin\varphi'_{cv,clay,2,d}\right)OCR^{0.5} \\ \times\left(\gamma_{clay,1,d}L_1 + \dfrac{\gamma_{clay,2,d}L_2}{2}\right)\tan\delta_d A_{s,2}\end{array}}{\gamma_s\xi_1}$$

$$= \frac{(1-\sin 24)\cdot 2^{0.5}\cdot 10\cdot\frac{10}{2}\cdot\tan 24\cdot\pi\cdot 0.6\cdot 10}{1.3\cdot 1.4}$$

$$+\frac{(1-\sin 25)\cdot 8^{0.5}\cdot\left(10\cdot 10+\frac{11L_2}{2}\right)\cdot\tan 25\cdot\pi\cdot 0.6\cdot L_2}{1.3\cdot 1.4} = \frac{352+143.5L_2+7.89L_2^2}{1.82}$$

$$= 193.4 + 78.87L_2 + 4.34L_2^2$$

The base capacity reads:

$$Q_{b,d} = \frac{q_{b,k}A_b}{\gamma_b\xi_1} = \frac{N_q d_q \sigma'_{zb}A_b}{\gamma_b\xi_1} = \frac{K_p e^{\pi\tan\varphi'_{cv}} d_q \sigma'_{zb}\pi\left(\frac{D}{2}\right)^2}{\gamma_b\xi_1}$$

$$= \frac{\left(K_p e^{\pi\tan\varphi'_{cv,clay,2,d}}\right)\left(1+2\tan\varphi'_{cv,clay,2,d}\left(1-\sin\varphi'_{cv,clay,2,d}\right)^2 k_H\right)\sigma'_{zb}\pi\left(\frac{D}{2}\right)^2}{\gamma_b\xi_1}$$

$$= \frac{\left(\frac{1+\sin\varphi'_{cv,clay,2,d}}{1-\sin\varphi'_{cv,clay,2,d}} e^{\pi\tan\varphi'_{cv,clay,2,d}}\right)\left(1+2\tan\varphi'_{cv,clay,2,d}\left(1-\sin\varphi'_{cv,clay,2,d}\right)^2\tan^{-1}\left(\frac{L}{D}\right)\right)\sigma'_{zb}\pi\left(\frac{D}{2}\right)^2}{\gamma_b\xi_1}$$

$$\left(\frac{1+\sin 25}{1-\sin 25}e^{\pi\tan 25}\right)\left(1+2\tan 25(1-\sin 25)^2\tan^{-1}\left(\frac{10+L_2}{0.6}\right)\right)$$
$$=\frac{\times\left(\gamma_{clay,1,d}L_1+\gamma_{clay,2,d}L_2\right)\pi\left(\frac{0.6}{2}\right)^2}{1.6\cdot 1.4}$$

$$=\frac{10.66\left(1+0.31\tan^{-1}\left(\frac{10+L_2}{0.6}\right)\right)(10\cdot 10+11L_2)0.283}{1.6\cdot 1.4}$$

$$=\frac{3.02\left(1+0.31\tan^{-1}\left(\frac{10+L_2}{0.6}\right)\right)(10\cdot 10+11L_2)}{2.24}$$

$$=\frac{302\left(1+0.31\tan^{-1}\left(\frac{10+L_2}{0.6}\right)\right)+33.2L_2\left(1+0.31\tan^{-1}\left(\frac{10+L_2}{0.6}\right)\right)}{2.24}$$
$$=134.82\left(1+0.31\tan^{-1}\left(\frac{10+L_2}{0.6}\right)\right)+14.82L_2\left(1+0.31\tan^{-1}\left(\frac{10+L_2}{0.6}\right)\right)$$

By substituting the aforementioned formulations in the equation of vertical pile equilibrium, an equation in the unknown L is obtained:

$$N_{Ed}\equiv Q_u=Q_s(L)+Q_b(L)$$

$$=193.4+78.87L_2+4.34L_2^2+134.82\left(1+0.31\tan^{-1}\left(\frac{10+L_2}{0.6}\right)\right)$$
$$+14.82L_2\left(1+0.31\tan^{-1}\left(\frac{10+L_2}{0.6}\right)\right)-2725$$

By solving the aforementioned equation, a length L_2 of 14.3 m is obtained, so the total length of the pile is of $L=24.4$ m.

Approach DA2 (A1 + M1 + R2)

According to this approach, the design values of actions, the design material properties and the design resistances are derived from their characteristic values considering the partial factors of the group A1, M1 and R2, respectively.

The permanent and variable design loads are computed by multiplying their characteristic values by the partial factors A1:

$$N_{Gd} = \gamma_G N_{Gk} = 1.35 \cdot 1750 = 2362.5\,\text{kN}$$

$$N_{Qd} = \gamma_Q N_{Qk} = 1.5 \cdot 750 = 1125\,\text{kN}$$

Hence, the total design load N_{Ed} reads:

$$N_{Ed} = N_{Gd} + N_{Qd} = 2362.5 + 1125 = 3487.5\,\text{kN}$$

The design material properties are computed by dividing their characteristic values by the partial factors M1:

$$\gamma_{clay,1,d} = \frac{\gamma_{clay,1,k}}{\gamma_\gamma} = \frac{20}{1} = 20\,\text{kN/m}^3$$

$$\varphi'_{cv,clay,1,d} = \tan^{-1}\left(\frac{\tan\varphi'_{cv,clay,1,k}}{\gamma_{\varphi'}}\right) = \tan^{-1}\left(\frac{\tan 24}{1}\right) = 24 \text{ degrees}$$

$$\gamma_{clay,2,d} = \frac{\gamma_{clay,2,k}}{\gamma_\gamma} = \frac{21}{1} = 21\,\text{kN/m}^3$$

$$\varphi'_{cv,clay,2,d} = \tan^{-1}\left(\frac{\tan\varphi'_{cv,clay,2,k}}{\gamma_{\varphi'}}\right) = \tan^{-1}\left(\frac{\tan 25}{1}\right) = 25 \text{ degrees}$$

Based on the above, the shaft capacity reads:

$$Q_{s,d} = \frac{q_{s,k}A_s}{\gamma_s\xi_1} = \frac{\overline{K}\overline{\sigma'_z}\tan\delta_d A_s}{\gamma_s\xi_1} = \frac{\overline{K_1}\ \overline{\sigma'_{z,1}}\tan\delta_d A_{s,1} + \overline{K_2}\ \overline{\sigma'_{z,2}}\tan\delta_d A_{s,2}}{\gamma_s\xi_1}$$

$$= \frac{\begin{array}{l}\left(1 - \sin\varphi'_{cv,clay,1,d}\right) OCR^{0.5}\gamma_{clay,1,d}\dfrac{L_1}{2}\tan\delta_d A_{s,1} \\ + \left(1 - \sin\varphi'_{cv,clay,2,d}\right) OCR^{0.5}\left(\gamma_{clay,1,d}L_1 + \dfrac{\gamma_{clay,2,d}L_2}{2}\right)\tan\delta_d A_{s,2}\end{array}}{\gamma_s\xi_1}$$

$$= \frac{(1 - \sin 24)\cdot 2^{0.5}\cdot 10\cdot\frac{10}{2}\cdot\tan 24\cdot\pi\cdot 0.6\cdot 10}{1.1\cdot 1.4}$$

$$+\frac{(1-\sin 25)\cdot 8^{0.5}\cdot\left(10\cdot 10+\frac{11L_2}{2}\right)\cdot\tan 25\cdot\pi\cdot 0.6L_2}{1.1\cdot 1.4}$$
$$=\frac{352+143.5L_2+7.89L_2^2}{1.54}$$

$$=228.61+93.2L_2+5.13L_2^2$$

The base capacity reads:

$$Q_{b,d}=\frac{q_{b,k}A_b}{\gamma_b\xi_1}=\frac{N_q d_q \sigma'_{zb}A_b}{\gamma_b\xi_1}=\frac{K_p e^{\pi\tan\varphi'_{cv,clay,2,d}}d_q\sigma'_{zb}\pi\left(\frac{D}{2}\right)^2}{\gamma_b\xi_1}$$

$$=\frac{\left(K_p e^{\pi\tan\varphi'_{cv,clay,2,d}}\right)\left(1+2\tan\varphi'_{cv,clay,2,d}\left(1-\sin\varphi'_{cv,clay,2,d}\right)^2 k_H\right)\sigma'_{zb}\pi\left(\frac{D}{2}\right)^2}{\gamma_b\xi_1}$$

$$=\frac{\left(\frac{1+\sin\varphi'_{cv,clay,2,d}}{1-\sin\varphi'_{cv,clay,2,d}}e^{\pi\tan\varphi'_{cv,clay,2,d}}\right)\left(1+2\tan\varphi'_{cv,clay,2,d}\left(1-\sin\varphi'_{cv,clay,2,d,}\right)^2\tan^{-1}\left(\frac{L}{D}\right)\right)\sigma'_{zb}\pi\left(\frac{D}{2}\right)^2}{\gamma_b\xi_1}$$

$$=\frac{\left(\frac{1+\sin 25}{1-\sin 25}e^{\pi\tan 25}\right)\left(1+2\tan 25(1-\sin 25)^2\tan^{-1}\left(\frac{10+L_2}{0.6}\right)\right)\times\left(\gamma_{clay,1,d}L_1+\gamma_{clay,2,d}L_2\right)\pi\left(\frac{0.6}{2}\right)^2}{1.1\cdot 1.4}$$

$$=\frac{10.66\left(1+0.31\tan^{-1}\left(\frac{10+L_2}{0.6}\right)\right)(10\cdot 10+11L_2)0.283}{1.1\cdot 1.4}$$

$$=\frac{3.02\left(1+0.31\tan^{-1}\left(\frac{10+L_2}{0.6}\right)\right)(10\cdot 10+11L_2)}{1.54}$$

$$= \frac{302\left(1 + 0.31\tan^{-1}\left(\frac{10+L_2}{0.6}\right)\right) + 33.2L_2\left(1 + 0.31\tan^{-1}\left(\frac{10+L_2}{0.6}\right)\right)}{1.54}$$

$$= 196.1\left(1 + 0.31\tan^{-1}\left(\frac{10+L_2}{0.6}\right)\right) + 22.56L_2\left(1 + 0.31\tan^{-1}\left(\frac{10+L_2}{0.6}\right)\right)$$

By substituting the aforementioned formulations in the equation of vertical pile equilibrium, an equation in the unknown L is obtained:

$$N_{Ed} \equiv Q_u = Q_s(L) + Q_b(L)$$
$$= 228.61 + 93.2L_2 + 5.13L_2^2 + 196.1\left(1 + 0.31\tan^{-1}\left(\frac{10+L_2}{0.6}\right)\right)$$
$$+ 22.56L_2\left(1 + 0.31\tan^{-1}(10 + L_20.6)\right) - 3487.5$$

By solving the aforementioned equation, a length L_2 of 14.7 m is obtained, so the total length of the pile is equal to $L = 24.8$ m.

The quantities related to the geotechnical design at ultimate limit states according to the different approaches proposed by the Eurocodes are reported in the following table, together with the effective length assigned to the pile, L_{eff} [m].

	N_{Ed} [kN]	$Q_{s,d}$ [kN]	$Q_{b,d}$ [kN]	$Q_{u,d}$ [kN]	L [m]	L_{eff} [m]
DA1-C1	3487.5	2844.5	653.5	3498.0	24.2	25
DA1-C2	2725	2228.7	515.7	2744.4	24.4	25
DA2	3487.5	2731.0	762.9	3494.0	24.8	25

ii. Structural design

The structural design at ultimate limit states of the cross section of the considered axially loaded pile requires defining the design acting load N_{Ed} and comparing it with the design resisting load N_{Rd} for no moment applied. Alternatively, the design can be performed by verifying the position of the design action effects (N_{Ed}; M_{Ed}) in the strength domain of the cross section. This latter approach is considered here.

As for the geotechnical design, it is supposed that the acting characteristic load N_{Ek} is characterised for 70% by a permanent contribution, N_{Gk}, and for 30% by a variable contribution, N_{Qk}:

$$N_{Gk} = 0.7N_k = 0.7 \cdot 2500 = 1750\,\text{kN}$$

$$N_{Qk} = 0.3N_k = 0.3 \cdot 2500 = 750\,\text{kN}$$

The permanent and variable design loads are computed by multiplying their characteristic values by the partial factors A1:

$$N_{Gd} = \gamma_G N_{Gk} = 1.35 \cdot 1750 = 2362.5\,\text{kN}$$

$$N_{Qd} = \gamma_Q N_{Qk} = 1.5 \cdot 750 = 1125\,\text{kN}$$

Hence, the total design load N_{Ed} reads:

$$N_{Ed} = N_{Gd} + N_{Qd} = 2362.5 + 1125 = 3487.5\,\text{kN}$$

The following material properties and features are considered to obtain the strength domain for the designed section. The concrete class C25/30, chosen to satisfy the condition of durability (XC2), is characterised by the following properties:

$$f_{ck} = 25\,\text{MPa}$$

$$f_{ck,cube} = 30\,\text{MPa}$$

$$E_{cm} = 31\,\text{GPa}$$

$$f_{cd} = \frac{\alpha_{cc} f_{ck}}{\gamma_c} = \frac{0.85 \cdot 25}{1.5} = 14.2\,\text{MPa}$$

$$\varepsilon_{uc} = 0.0035 = 3500\,\mu\varepsilon/^{\circ}\text{C}$$

The steel reinforcement B500B is characterised by the following properties:

$$f_{yk} = 500\,\text{MPa}$$

$$E_r = 200\,\text{GPa}$$

$$f_{yd} = \frac{f_{yk}}{\gamma_r} = \frac{500}{1.15} = 434.8\,\text{MPa}$$

$$\varepsilon_{yd} = \frac{f_{yd}}{E_r} = \frac{434.8}{200{,}000} = 0.00217 = 2170\,\mu\varepsilon/^{\circ}\mathrm{C}$$

The minimum longitudinal reinforcement employed to ensure ductility reads:

$$\rho = \rho_{r,min} \geq \frac{f_{ct}}{f_y}$$

with $f_{ct} = f_{ctm} = 0.3 f_{ck}^{\frac{2}{3}}$ (for $f_{ck} < 50$ MPa)

For this case, considering the concrete properties detailed before:

$$f_{ct} = 0.3 f_{ck}^{\frac{2}{3}} = 0.3 \cdot 25^{2/3} = 2.6\,\mathrm{MPa}$$

Thus

$$\rho_{r,min} \geq 0.006$$

The effective longitudinal reinforcement is computed as

$$\rho_{eff} = \frac{A_r}{A_{EP}}$$

with $A_{EP}[\mathrm{mm}^2]$ the surface of the pile cross section and $A_r[\mathrm{mm}^2]$ is the total surface of the steel cross sections that can be calculated as

$$A_r = n_\phi \frac{\pi \phi^2}{4}$$

where n_ϕ [−] is the number of reinforcement bars and ϕ[mm] is their diameter. According to the EN 1992 (2004), the minimum diameter for the longitudinal bars should not be less than 16 mm and piles should at least have six longitudinal bars.

Installing $n_\phi = 6$ reinforcement bars of diameter $\phi = 20$ mm, the effective longitudinal reinforcement reads:

$$\rho_{eff} = 0.007 \geq \rho_{r,min}$$

In this case, a nominal concrete cover of 60 mm is considered as a design value. As no shear forces are applied to the considered pile, the minimum transverse reinforcement is placed. This reinforcement represents one bar of 6 mm diameter every 400 mm.

Based on the previous features, the strength domain depicted in the following figure is obtained. As the design effects of actions are included within the strength domain, no structural ultimate limit states are exceeded with the regards to the most solicited reinforced concrete cross section.

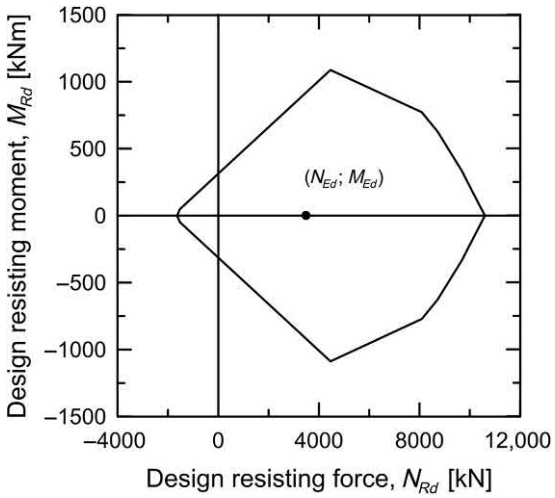

CHAPTER 16

Design of details for construction of energy geostructures

16.1 Introduction

One practical basic feature distinguishing energy geostructures from conventional geostructures is the presence of noteworthy amounts of pipes that need to be installed for the sake of the energy harvesting of such technology. In relatively small energy geostructure projects, kilometres of pipes may have to be installed.

While precise specifications and plans are needed during the construction of energy geostructures about supply, potential stock, installation, verification and testing, quality control and maintenance of materials, products and components, various details must be defined from the analysis and design phases of any project. These details typically involve determining the configuration of the pipes to be installed in an energy geostructure, in what manner and quantity these pipes should be installed, how the piping network may be connected and tested, and what materials or components would need a quality control following specific verifications. All of these aspects play a crucial role for the expedient yet effective application of energy geostructures as well as for their optimal operation and performance. In this context, designing the details characterising the construction of energy geostructures appears of comparable importance to the aspects characterising the energy, geotechnical and structural designs of such geostructures.

This chapter focuses on the design of details for the expedient yet effective construction of energy geostructures. The analysis is based on the available recommendations at the national level in Switzerland, United Kingdom and France as well as on practical experience in this scope, and focuses on the features characterising the piping network installed within and between energy geostructures.

To address the aforementioned aspects, the *pipe features and bending* are presented first: in this context the objective is to highlight possible materials that may be employed for the pipes characterising energy geostructure applications as well as the details that should be accounted for bending the pipes within energy geostructures. Second, the *pipe fixing to the reinforcing cage* of general energy geostructures is treated: the objective of this part is to define the methods through which pipes may preferably be installed within energy geostructures. Next, the *energy geostructure installation* is analysed: in this context the purpose is to expand on approaches for the effective

Analysis and Design of Energy Geostructures
DOI: https://doi.org/10.1016/B978-0-12-816223-1.00016-3

construction of energy geostructures. Afterward, the *piping network and connections* are treated: in this framework the purpose is to comment on the features that should be considered to connect the pipes installed between energy geostructures. Then, aspects related to *quality control* are described: the purpose of this part is to expand on verifications aimed at ensuring durability and performance of a number of components constituting energy geostructures. Finally, *questions and problems* are proposed: the purpose of this part is to fix and test the understanding of the subjects covered in this chapter by addressing a number of exercises.

16.2 Pipe features and bending

Restrictions for the minimum and maximum depth that should be considered for equipping energy geostructures with pipes are mostly driven by the aim of limiting the influence of the surface conditions on the thermohydraulic behaviour and energy performance of the geostructures, and by practical construction considerations linked to the installation of both the pipes and the geostructures, respectively. According to the SIA-D0190 (2005), a minimum depth of $z = 10$ m in order for an energy geostructure project to be economically sustainable as well as a maximum depth of $z = 60$ m for a relatively straightforward installation of the energy geostructure may be considered. While the former specification may be considered in many situations for all types of energy geostructures, the latter specification should be considered for general energy geostructures except energy tunnels, which can be constructed relatively easily also at greater depths.

In the horizontal direction, the number of pipes that can be installed in an energy geostructure typically depends on its geometry. For energy piles, Tomlinson and Woodward (1993) suggest a typical value of four loops to be installed within piles with a diameter of $D = 60$ cm, whereas the CFMS-SYNTEC-SOFFONS-FNTP (2017) prescribe the number of pipes to be chosen as a function of the pile diameter: for $D \leq 40$ cm, one loop should be considered; for $D > 40$ cm, one additional loop may be considered for a successive increase of 20 cm in the pile diameter. For a 60 cm diameter energy pile, this latter approach would yield a maximum of three loops, which approximately agrees with the value given by Tomlinson and Woodward (1993). For other energy geostructures, such as energy walls, slabs and tunnels, similar recommendations are currently unavailable. However, the CFMS-SYNTEC-SOFFONS-FNTP (2017) suggest that an energy wall may contain several cages with pipes. Therefore looking at each cage individually, similar considerations may be made as for energy piles, with reference to a rectangular section. A minimum spacing of 15 cm between the pipes may generally be considered (SIA-D0190, 2005; CFMS-SYNTEC-SOFFONS-FNTP, 2017).

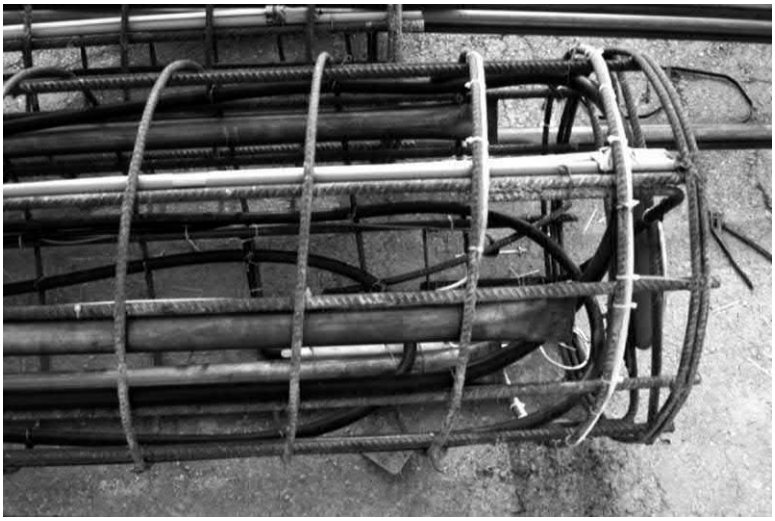

Figure 16.1 Example of pipe bending at the edge of an energy pile.

As for the material constituting the pipes, there is consensus on the use of polyethylene pipes. According to the SIA-D0190 (2005), the use of PE100 pipes is preferable over PE80 pipes. According to the Ground Source Heat Pump Association (2012), scratch-resistant PE-X pipes should be employed. In general, a pipe wall thickness of 2−3 mm and a pipe diameter of 25−32 mm may be considered.

A limiting factor for the installation and the operation of the pipes is represented by the bending radius at the bottom or top of the loop (i.e. the loop edges). As a general approach, the material specifications given by the pipe manufacturer should be respected. When bending of the pipe is considered, a curvature radius of $r_\chi > 20d_p$ should be respected, where d_p is the pipe diameter (SIA-D0190, 2005; CFMS-SYNTEC-SOFFONS-FNTP, 2017). An unusually low temperature at the time of installation may require a greater bending radius, with $r_\chi = 35d_p$ for a temperature of $T = 10°C$ and $r_\chi = 50d_p$ for a temperature of $T = 0°C$ (Ground Source Heat Pump Association, 2012). When the pipes are not bent but are placed approximately straight along the energy geostructure, cut and thermally welded through U-bends at their extremes, a smaller bending radius than those specified above may be considered. The typical bending radius characterising the edges of pipes installed in an energy pile through direct pipe bending is shown in Fig. 16.1. Key steps involved with the connection of pipes at their edge through thermally welded U-bends are shown for an energy pile in Fig. 16.2.

16.3 Pipe fixing to reinforcing cages

Fixing the pipes to supports within energy geostructures is common in most applications. These supports may or may not have a structural support function. In some

Figure 16.2 Example of the connection of pipes at their edge through thermally welded U-bends in an energy pile.

cases, these supports may also be absent and the pipes could be buried in reinforced concrete or other filling materials (e.g. hollow precast reinforced concrete energy piles filled with a mix of concrete and bentonite).

When energy geostructures do not resort to prefabricated elements, such as in the case of bored energy piles or energy walls, pipe fixing typically takes place on site, prior to the placement of the reinforcing cage in an appropriate excavation and the successive concreting. When energy geostructures resort to prefabricated elements, such as in the case of precast energy piles or energy segmental tunnel linings, pipe fixing typically takes place on factory and is followed by concreting prior to the successive placement on site of the prefabricated element. To date, the majority of energy geostructure applications involve the former pipe installation procedure.

When the frame that holds the pipes plays a structural role, such as in the case of reinforcement cages, the pipes may be placed on the inside of the cage to avoid any damage to the loops (SIA-D0190, 2005; Ground Source Heat Pump Association, 2012; CFMS-SYNTEC-SOFFONS-FNTP, 2017). While the previous consideration may be generally borne in mind, specific recommendations are available for energy walls, slabs and tunnels. According to the CFMS-SYNTEC-SOFFONS-FNTP (2017), the pipes should not be fixed to the intrados (e.g. close to the airside) of energy walls because damage to the pipes may be caused by anchors or cut-outs. This feature may also be considered for energy tunnels. In any case, the minimum distance of 20 cm from the wall intrados should be considered for the location of the pipes due to fire-related considerations. According to the CFMS-SYNTEC-SOFFONS-FNTP (2017), the pipes may be placed just above the bottom reinforcement of energy slabs. Although Park et al. (2015) fixed pipes on the outside of the reinforcing cage of energy piles, this approach should be considered rare and preferably avoided in practice due to the risk of pipe damage upon construction. An example of pipes embedded on the inside of the reinforcing cage of an energy pile is shown in Fig. 16.3.

When the frame that holds the pipes does not play a structural function, the pipes and their support should be placed to simplify the concreting (CFMS-SYNTEC-SOFFONS-FNTP, 2017). This approach also applies to situations in which no rigid elements that hold the pipes are employed.

With respect to the pipe fixing to the reinforcement, according to the CFMS-SYNTEC-SOFFONS-FNTP (2017), the pipes should be fixed to the horizontal

Figure 16.3 Pipe fixing on the inside of the reinforcing cage of an energy pile.

reinforcement with a minimum distance of $4D_{max}$ (where D_{max} is diameter of the biggest aggregate characterising the mix design of the filling material) between the pipes and the longitudinal reinforcements. At the same time, the pipes may be fixed to the longitudinal bars if this does not interfere with their structural function. In either case, the pipes should be fixed in the horizontal direction to avoid excessive deformations during construction (CFMS-SYNTEC-SOFFONS-FNTP, 2017). A minimum longitudinal spacing of 1 m for wire ties and of 50 cm for plastic ties should be consider to fix the pipes along the reinforcing cage, with special care for the pipe regions near the top and bottom of the loop where a spacing of 25 cm should be respected (CFMS-SYNTEC-SOFFONS-FNTP, 2017). The previous recommendations are consistent with those proposed by the Ground Source Heat Pump Association (2012), which advises to fix the pipes to helical reinforcements placed between and not adjacent to the longitudinal bars. The Ground Source Heat Pump Association (2012) does not give any quantitative criteria for the minimum values of spacing at which ties should be placed to fix the pipes along the longitudinal direction of the reinforcement, but in contrast to the CFMS-SYNTEC-SOFFONS-FNTP (2017) suggests avoiding the use of wire ties that can cause point load damage to the loops but to use only plastic ties. The SIA-D0190 (2005) only provides minimum values of spacing for wire ties that should be placed every 1−2 m. An example of the use of wire ties to fix pipes to an energy pile is shown in Fig. 16.4.

Besides the previous approach that involves fixing the pipes to the reinforcing cage prior to its installation on site, it is also possible to fix the pipes to the cage while it is installed. The same recommendations should be followed as when pipework is placed

Figure 16.4 Use of wire ties to fix the pipes to an energy pile.

Figure 16.5 Protection of the inlet and outlet of pipes at the head of energy piles by a plastic connection (characterised by a *black colour* in the figure) to avoid any damage during concreting.

on a cage lying on the ground. Fixing the pipes to the reinforcing cage while it is installed is less common than fixing the pipes prior to the cage installation because it leaves less flexibility to the project schedule and yields to lower working speed.

Due to the trimming of the uppermost portion of vertical energy geostructures such as energy piles and walls after concreting, special care needs to be devoted to the integrity of the pipes in correspondence with the interested portion of the energy geostructure. This may be achieved through the application of a protective coating surrounding the pipes, to be removed after the installation of the energy geostructure. An example of this protection approach of the inlet and outlet of pipes at the head of energy piles by a plastic connection is shown in Fig. 16.5. While both the Ground Source Heat Pump Association (2012) and CFMS-SYNTEC-SOFFONS-FNTP (2017) specify that any parts of the pipes should be appropriately protected up to 10 cm below the cut-off level of vertical energy geostructures, the CFMS-SYNTEC-SOFFONS-FNTP (2017) also specify a minimum distance of 20 cm under the cutoff level for the potential bending of the pipes in the top portion of such geostructures. In general, the inlet and outlet of the pipes must be at a sufficient vertical distance from the cut-off to guarantee both loop integrity and ease for pressure tests and connections (CFMS-SYNTEC-SOFFONS-FNTP, 2017).

16.4 Energy geostructure installation

Besides the aforementioned recommendations referring to the pipe fixing, the following considerations for the installation on site of the reinforcing cages characterising

energy geostructures prior to their filling should be borne in mind. With reference to bored energy piles, the Ground Source Heat Pump Association (2012) prescribes the use of rings and weights to maintain the shape of pipes hanging below the reinforcing cage. This procedure may also be employed for other vertical energy geostructures, such as energy walls. The use of dip tubes for concreting is also discussed by the CFMS-SYNTEC-SOFFONS-FNTP (2017) and the minimum vertical distance of 25 cm from the base of the reinforcement cage to the bottom of the pipe loop may be considered when such a device is used.

After installing the reinforcing cage of a vertical energy geostructure equipped with pipes, dip pipes placed at the base of the excavation for concreting should be employed. During the concreting phase, the pipes should be subjected to nominal pressure to avoid kinking (SIA-D0190, 2005; Ground Source Heat Pump Association, 2012; CFMS-SYNTEC-SOFFONS-FNTP, 2017). While the Ground Source Heat Pump Association (2012) emphasises that special protection should be provided to the pipework in case of relevant risk of abrasion, the CFMS-SYNTEC-SOFFONS-FNTP (2017) raise concern about removing the dip tube slowly enough to avoid damage to the pipework and further emphasise risks of movement of the cage while the concrete is still fresh. The level of the cage head should always be monitored and blocked if necessary to avoid the cage sinking or floating out of its position (CFMS-SYNTEC-SOFFONS-FNTP, 2017). In case of upward concreting, additional support should be provided to the loops to prevent damaging (Ground Source Heat Pump Association, 2012).

Along with the previous aspects, additional relevant information concerns the construction of energy piles and is summarised by the SIA-D0190 (2005), the Ground Source Heat Pump Association (2012) the CFMS-SYNTEC-SOFFONS-FNTP (2017) as well as by Tomlinson and Woodward (1993). When dealing with precast energy piles, full and hollow precast piles can be distinguished. In contrast to bored energy piles or other piles that require concreting on site, both full and hollow precast energy piles are driven into the ground. However, the following key aspects differentiate full and hollow precast energy piles:

- Full precast energy piles are constructed on factory and are successively brought on site where they only need to be driven in the ground and connected between them. Their main advantage is that pipe fixing can be tailored and optimised at will, and on-site climatic conditions do not affect the end result because concreting takes place on factory. An issue potentially arising during the installation of those energy piles is that some piles might need to be shortened if they cannot reach their planned depth, which implies special care for the pipework during head cut-off. Also, if a full precast energy pile gets damaged during the driving process, no replacement of the piping is possible and the energy pile cannot be used for heat exchange purposes anymore.

Figure 16.6 Example of hollow precast reinforced concrete energy piles prior to their installation on site, piping equipment and filling with appropriate material. *Image courtesy: SACAC.*

- Hollow precast energy piles are also constructed on factory but are not equipped with the piping and do not involve any filling material prior to their installation on site (cf. Fig. 16.6). Hollow precast energy piles are first driven in the ground and trimmed without the pipes. Only afterward the pipes are placed in the hollow pile core, which is eventually filled by the designed material. Filling hollow precast energy piles can be quite difficult due to the lack of space in between the pipework. As a consequence, a mix of cement and bentonite is usually used instead of regular concrete. Besides the previous considerations, with hollow precast energy piles it is also important to put enough weight at the bottom of the pipe loops since they are not fixed and would float during concreting. The advantage of hollow precast energy piles is that the driving of the pile and the installation of the pipes are independent from each other, leaving more flexibility to the project schedule. Unlike full precast energy piles, damage during pile driving does not have any impact on the pipework.

Recommendations referring to the piling method and the pile installation provided by the SIA-D0190 (2005), the Ground Source Heat Pump Association (2012) the CFMS-SYNTEC-SOFFONS-FNTP (2017) as well as by Tomlinson and Woodward (1993) are summarised in Table 16.1. Tomlinson and Woodward (1993) comment on the piling method that should yield a stable borehole needed for a safe cage insertion. Depending on the soil stability, casing, supporting fluid (bentonite) or a withdrawal tube method should be used to avoid the collapse of the borehole. Following Tomlinson and Woodward's (1993) suggestion to pour concrete before the reinforcement cage is placed when the stability of the soil is too low, the Ground Source Heat Pump Association (2012) and CFMS-SYNTEC-SOFFONS-FNTP (2017) include a few remarks on the concrete mix that should be used in such situations. With regards

Table 16.1 Recommendations referring to the piling method and the pile installation.

Reference	Piling method and pile installation
SIA-D0190 (2005)	Focus on full and hollow precast energy piles, no indication about concreting of piles
Ground Source Heat Pump Association (2012)	Only on-site concreting considered, include remarks about pipe protection and concrete mix
CFMS-SYNTEC-SOFFONS-FNTP (2017)	Precast energy piles mentioned but not considered, include remarks about how to avoid cage movement and specify a concrete mix class of S4
Tomlinson and Woodward (1993)	Casing, supporting fluid or withdrawable tube method should be used

Figure 16.7 Stock of pipes in a dedicated portion of a construction site.

to this issue, the Ground Source Heat Pump Association (2012) only emphasises that the concrete mix should be adjusted, while a minimal consistency class S4 (slump test) should be assured according to the CFMS-SYNTEC-SOFFONS-FNTP (2017).

Concerning the site organisation during installation of energy geostructures, it is of utmost importance to store the pipes in a safe place when already on site but not yet in use. According to the Ground Source Heat Pump Association (2012), the pipes should always be placed on a reeler instead of being precut and simply placed on the ground in order to avoid any damage. Meanwhile, the SIA-D0190 (2005) prescribes the use of sealing caps to avoid material entering the pipes during any of the construction phases. Practical experience suggests that the best way to avoid any damage or contamination of the pipes is to dedicate a space on the project site that is only used for storage and assembly of the loops. An example of this approach is shown in Fig. 16.7.

16.5 Piping network and connections

Horizontal pipework connecting the individual energy geostructures to a central collector and/or a heat pump is a key element in any energy geostructures project. As the pipes are to be placed on the ground surface during construction, good planning is essential in order not to interfere with other construction phases as well as not to damage the pipework.

Recommendations related to the horizontal pipework positioning provided by the SIA-D0190 (2005), the CFMS-SYNTEC-SOFFONS-FNTP (2017) and the Ground Source Heat Pump Association (2012) are summarised in Table 16.2. In general, the piping network may be placed through the use of trenches underneath the slab that are to be backfilled once the pipework is in place. In addition to the previous approach, the SIA-D0190 (2005) also mentions the possibility of placing the horizontal pipework in a layer of lean concrete that forms a part of the slab, suggesting to fix the pipework to the slab via a metal truss in the case of an important settlement risk, as well as between layers of reinforcement within the slab. However, experience has shown that in this case coordination during construction becomes increasingly difficult. If trenches are used for the horizontal pipework, the bed surface material should be selected carefully. While the CFMS-SYNTEC-SOFFONS-FNTP (2017) specify the use of materials without sharp edges, the Ground Source Heat Pump Association (2012) considers hard materials as being generally inappropriate for trench beds. The SIA-D0190 (2005) suggests using sand beds for horizontal pipework. Concerning the backfill material, while the SIA-D0190 (2005) does not provide any specification, the Ground Source Heat Pump Association (2012) suggests using the excavation material as long as it is considered appropriate, with sand being the alternative in case it is not.

With respect to piping connections, series connections may be employed to reduce the number of horizontal feeder and return pipes. At the same time, according to the CFMS-SYNTEC-SOFFONS-FNTP (2017) no more than five energy piles (or other relevant energy geostructures) should be connected in series to be able to isolate potential issues affecting the pipework. No information on this aspect is provided by the SIA-

Table 16.2 Recommendations referring to the positioning of horizontal pipework.

Reference	Positioning of horizontal pipework
SIA-D0190 (2005)	Under slab in trenches, in layer of clean concrete in slab or between layers of reinforcement in slab
CFMS-SYNTEC-SOFFONS-FNTP (2017)	Under slab in trenches
Ground Source Heat Pump Association (2012)	Under slab in trenches, with a minimum depth of 1 m to avoid services and frost damage

D0190 (2005), whereas the Ground Source Heat Pump Association (2012) only mentions that energy piles in series can be isolated at a manifold in case of loop failure.

According to the Ground Source Heat Pump Association (2012), a minimum distance of 50 cm between feeder and return pipes should be employed, or else insulation is necessary. In contrast with this approach, the SIA-D0190 (2005) simply suggests to separate feeder pipes from return pipes without giving values for the minimum distance between pipes and recommends considering a thermal insulation from the slab depending on space use at the ground surface and the pipe characteristics. The Ground Source Heat Pump Association (2012) only mentions the need of insulating pipes passing within 1.5 m from walls, structures, drainage pipes, etc.

Marking pipes is also essential. The pipes have to be easily identifiable for their peculiar heat exchanger role by the construction personnel in order to prevent damage from other construction activity. The CFMS-SYNTEC-SOFFONS-FNTP (2017) suggest using warning mesh above the pipework for this purpose, while warning tape is suitable according to the Ground Source Heat Pump Association (2012). A clear numbering or marking scheme of individual energy geostructures such as energy piles and the corresponding pipework is also essential when it comes to connecting the loops to the plant and/or the heat pump. As shown in Figs 16.8 and 16.9, relatively small energy geostructure projects lead to complicated pipe network. Proper identification of each loop element is a must, especially to adequately cope with potential pipe failure.

Figure 16.8 Pipe network between the groups of energy geostructures and the manifolds. *Image courtesy: Marti Construction.*

Figure 16.9 Technical room where all manifolds arrive when the system is ready for connection to the heat pump. *Image courtesy: Marti Construction.*

16.6 Quality control

Quality control is key to ensure the serviceability and durability of any type of energy geostructure. Quality checks should be performed with particular attention to the pipe network, with the aim of identifying defects prior to concreting so that components can be easily repaired or replaced. A spray on the pipe surface may be used to detect defects (CFMS-SYNTEC-SOFFONS-FNTP, 2017). Quality checks made after concreting only permit the identification of defective pipes that will in most cases not be connected to the manifold, because it is usually not possible to conduct any repair once concreting is finished or because the project would be delayed.

The CFMS-SYNTEC-SOFFONS-FNTP (2017) provide a very detailed procedure of quality control for the different phases of the construction of energy geostructures, strongly recommending the constant use of manometers for pressure tests of the piping elements (cf. Fig. 16.10):

1. *Pipe arrival*: Visual inspection.
2. *After fixation to the cage*: Pressure test with minimum pressure of 4 bars. No information about the use of air or water is specified for the pressure test. If the test fails, pipework needs to be reinstalled. The pressure is maintained while transferring the pipes to the installation site.
3. *Installation*: During the installation, a continuous visual inspection is needed that focuses on scratches and deformations. Pipework needs to be under nominal pressure during this stage.

Figure 16.10 Manometer placed at the end of pipe loops to control the pressure at any time during the construction.

4. *After installation*: A pressure test needs to be done after concreting with the same pressure as after the fixing to the cage. If a pressure drop greater than 0.1 bar is measured, the loop should be repaired. If not possible, the loop must be noted as lost and the horizontal connections need to be adapted accordingly.
5. *After cut-off*: A pressure test is performed that needs to fulfil the same requirements than the one after installation, that is a drop of pressure greater than 0.1 bar means that the loop is lost.
6. *After tube networking*: All the pipes are under pressure and any element showing a pressure drop needs to be repaired if possible or noted as lost. Both flush and pressure test need to be performed before handing the system over to the client.

The Ground Source Heat Pump Association (2012) recommends a set of normalised tests that may be performed at any relevant phase of the construction:

1. *Observation test*: visual inspection of the pipework to ensure its conformity to the installation scheme and to identify potential defects. This test has to be performed when the loops are ready on the construction site and during the installation of the cage.
2. *Bidirectional flow test*: the loop is filled with water and it has to be ensured that water can flow in both directions of the loop. No visual loss of flow is needed for acceptance of the test. This test has to be performed before concreting as well as before and after trimming of the heads.
3. *Type A water pressure test*: water pressure is raised to 150% of the pipes working pressure. The criteria for acceptance does not allow any loss of pressure during this test. It has to be performed once the loops are assembled. This test is usually made

off site when the loops are assembled before their delivery to the construction site but may also be performed on site if the assembly is made on-site. In factory conditions, air pressure may be appropriate instead of water pressure.

4. *Type B water pressure test*: water pressure is maintained at 8 bars for 10 minutes (water is added if necessary). The pressure is then reduced to 4 bars and held for another 30 minutes. The test is accepted if no pressure loss is measured over the last 30 minutes. This test has to be performed before concreting as well as before trimming. Nominal water pressure should remain in the pipes after the test when performed before concreting to avoid the crushing of pipes.
5. *Type C water pressure test*: same as type B except that after 10 minutes at 8 bars, the loops remain pressurised at 4 bars during 24 hours instead of 30 minutes. The acceptance criteria allow no pressure loss during 24 hours. This test has to be performed immediately after concreting as well as after trimming (before connections with header are realised). When performed during concreting, an increase of pressure is expected during the hydration of concrete.
6. *Dip Test*: use of a probe to measure the depth of the installed thermal loops and to ensure it is in accordance with the planning scheme. This test has to be performed after the trimming of the pile heads and prior to adding header connections.

While the Ground Source Heat Pump Association (2012) states that water shall to be used for the pressure tests and not air, the same considerations are not proposed by the CFMS-SYNTEC-SOFFONS-FNTP (2017). In either case, the general handling of tests that do not reach the acceptance criteria is the same: replace the defective elements if possible or note the loop as lost.

In addition to the previous recommendations, the Ground Source Heat Pump Association (2012) advises to keep the piping system under pressure all the time until it is connected to the heat pump, with the aim of logging any relevant pressure drop. In addition to this recommendation, a final check before the handover should be made to make sure that the whole system is functioning correctly. The system has to be flow tested in its entirety or in sections depending on its size. Pressure drops need to be compared to design values and a minimum of 3 flow rates and head loss measurements have to be performed.

In contrast with the pressure testing procedures detailed by the CFMS-SYNTEC-SOFFONS-FNTP (2017) and Ground Source Heat Pump Association (2012), the SIA-D0190 (2005) prescribes pressure tests before and during concreting only, with pipes maintained under pressure during concreting to avoid damage to pipework. The same approach is detailed by Tomlinson and Woodward (1993).

According to the SIA-D0190 (2005), a nominal pressure of 6 bars before concreting should be employed for pressure testing. This value of fluid pressure is slightly lower than the value of 8 bars specified for the same purpose by Tomlinson and Woodward (1993).

The duration of the pressure tests detailed by the SIA-D0190 (2005) should be of at least 4 hours and a pressure drop of up to 0.5 bar may be allowed. This pressure drop is noticeably higher than the pressure drop of 0.1 bar allowed, for example by the CFMS-SYNTEC-SOFFONS-FNTP (2017). According to the SIA-D0190 (2005), all pressure tests should also be registered in a logbook that must be handed over to the client once the system is completed. Because the height of junctions and valves can vary up to 1 m from the designed position, the displacement of the cage during and after concreting should be carefully overseen to avoid having to rebuild the connections after trimming.

Experience gives some critical steps at which pressure tests as described in the SIA-D0190 (2005) should be performed:

1. after mounting of pipework in the reinforcement cage;
2. after concreting;
3. after trimming of pile heads;
4. after installation of horizontal networking;
5. after final coating of pipes in the sand (pipes under the invert) or before concreting of the invert (pipes inside the invert);
6. before installation of the manifolds.

References

CFMS-SYNTEC-SOFFONS-FNTP, 2017. Recommandations pour la conception, le dimensionnement et la mise en úuvre des géostructures thermiques. Rev. Fr. Geotech. 149, 1–120.

Ground Source Heat Pump Association, 2012. Thermal Pile Design, Installation & Materials Standards. National Energy Center, Milton Keyenes, p. 86.

Park, S., Sung, C., Jung, K., Sohn, B., Chauchois, A., Choi, H., 2015. Constructability and heat exchange efficiency of large diameter cast-in-place energy piles with various configurations of heat exchange pipe. Appl. Therm. Eng. 90, 1061–1071.

SIA-D0190, 0190. Utilisation de la Chaleur du Sol par des Ouvrages de Fondation et de Soutènement en Béton. Guide pour la Conception, la Realisation et la Maintenance, Zurich, Switzerland.

Tomlinson, M., Woodward, J., 1993. Pile Design and Construction Practice. CRC Press.

Questions and problems

Statements

a. According to SIA-D0190 (2005), what is the minimum and maximum depth that should be considered for equipping energy geostructures with pipes to ensure the project to be economically sustainable and to have a relative straightforward installation?
  i. $z_{min} = 5$ m and $z_{max} = 65$ m
  ii. $z_{min} = 10$ m and $z_{max} = 60$ m
  iii. $z_{min} = 15$ m and $z_{max} = 55$ m

b. According to the available norms and recommendations for energy geostructures, what is the minimum spacing to be considered between the pipes?
  i. 5 cm
  ii. 10 cm
  iii. 15 cm

c. What are the orders of magnitude of pipe wall thickness and pipe diameter?
  i. Pipe thickness of 1–2 mm and pipe diameter of 18–25 mm
  ii. Pipe thickness of 2–3 mm and pipe diameter of 25–32 mm
  iii. Pipe thickness of 3–4 mm and pipe diameter of 32–39 mm

d. What is the main limiting factor for the installation and operation of the pipes? Provide its related criterion as a function of the pipe geometry. Provide two strategies for dealing with this problem.

e. In general, when the pipes are fixed to a reinforcing cage, they should be placed on the inside of the cage to avoid any damage to the loops:
  i. True
  ii. False

f. Describe two recommendations to follow for the installation of the pipes within energy walls

g. The minimum distance to consider for fixing the pipes to the horizontal reinforcements is a function of the biggest aggregate characterising the concrete mix:
  i. True
  ii. False

h. The minimum distance to consider for fixing the pipes along the longitudinal reinforcement of energy geostructures should be increased close to pipe edges because these regions are less critical than the middle portion of the pipes:
  i. True
  ii. False

i. Full and hollow precast energy piles can be distinguished. Describe both types of energy piles and give their pros and cons in terms of pipe installation.

j. If trenches are used for the horizontal pipework network, the available norms and recommendations advise the use of sand beds:
  i. True
  ii. False

k. Pipe connections in series are good practice because they reduce the number of horizontal feeder and return pipes, and should not suffer any limitation:
  i. True
  ii. False

l. Quality checks done after concreting the energy geostructures are sufficient to control the piping network and to repair and replace easily its components:
  i. True
  ii. False

m. Describe critical steps at which pressure tests of the piping network should be performed.

Solutions

a. According to SIA-D0190 (2005), what is the minimum and maximum depth that should be considered for equipping energy geostructures with pipes to ensure the project to be economically sustainable and to have a relative straightforward installation?
  i. $z_{min} = 5$ m and $z_{max} = 65$ m
  ii. $\boldsymbol{z_{min} = 10}$ **m and** $\boldsymbol{z_{max} = 60}$ **m**
  iii. $z_{min} = 15$ m and $z_{max} = 55$ m

b. According to the available norms and recommendations for energy geostructures, what is the minimum spacing to be considered between the pipes?
  i. 5 cm
  ii. 10 cm
  iii. 15 cm

c. What are the orders of magnitude of pipe wall thickness and pipe diameter?
  i. Pipe thickness of 1–2 mm and pipe diameter of 18–25 mm
  ii. Pipe thickness of 2–3 mm and pipe diameter of 25–32 mm
  iii. Pipe thickness of 3–4 mm and pipe diameter of 32–39 mm

d. The main limiting factor for the installation and operation of the pipes is represented by the bending radius at the bottom or the top of the loop. A general criterion to consider when bending pipes is a curvature radius of

$$\boldsymbol{r_\chi > 20 d_p}$$

where $\boldsymbol{d_p}$ **[m] is the pipe diameter**.

Too large values of bending radius for pipes may be problematic for the installation of energy geostructures in narrow environments. One strategy to avoid remarkable values of pipe radii is to install the pipes at sufficiently high ambient temperatures levels. One additional strategy is to use U-bends where pipes can be thermally welded, reducing the bending radius.

e. In general, when the pipes are fixed to a reinforcing cage, they should be placed on the inside of the cage to avoid any damage to the loops:
   i. True
   ii. False

f. The pipes should not be fixed to the intrados of energy walls because damage to the pipes may be caused by anchors or cut-outs. At the same time, a minimum distance of 20 cm from the wall intrados should be considered for fire-related considerations.

g. The minimum distance to consider for fixing the pipes to the horizontal reinforcements is a function of the biggest aggregate characterising the concrete mix:
   i. True
   ii. False

h. The minimum distance to consider for fixing the pipes along the longitudinal reinforcement of energy geostructures should be increased close to pipe edges because these regions are less critical than the middle portion of the pipes:
   i. True
   ii. False

i. Full precast energy piles are constructed on factory and are successively brought on site where they only need to be driven in the ground and connected between them. Pipe fixing can be tailored and optimised easily in the factory and on-site climatic conditions have no effect. A possible issue concerning the pipes may arise during the pile installation. Some piles may need to be shortened, which implies special care for the pipework during head cut-off. Moreover, if a full precast energy pile gets damaged during the driving process, no replacement of the pipes is possible.

Hollow precast energy piles are also constructed on factory but are not equipped with the pipes and do not involve any filling material prior to their installation on site. Hollow precast energy piles are first driven in the ground and trimmed without the pipes. The pipes are placed afterward in the hollow pile core, which may be eventually filled with a given material. An issue may arise during the filling of the cavity, with a risk of pipes damage in a narrow space. The advantage of hollow precast energy piles is that pile driving and pipes installation are independent, giving

more flexibility to the project schedule. Unlike full precast energy piles, damage during pile driving does not have any impact on the pipes.

j. If trenches are used for the horizontal pipework network, the available norms and recommendations advise the use of sand beds:
  i. True
  ii. False

k. Pipe connections in series are good practice because they reduce the number of horizontal feeder and return pipes, and should not suffer any limitation:
  i. True
  ii. False

l. Quality checks done after concreting the energy geostructures are sufficient to control the piping network and to repair and replace easily its components:
  i. True
  ii. False

m. Critical steps at which pressure tests of the piping network should be performed are as follows: (1) After mounting of pipework in the reinforcement cage. (2) After concreting. (3) After trimming of pile heads. (4) After installation of horizontal networking. (5) After final coating of pipes in the sand (pipes under the invert) or before concreting of the invert (pipes inside the invert). (6) Before installation of the manifolds.

Appendix A: Survey about energy geostructure projects worldwide

A.1 Summary

This appendix presents the questionnaire that was submitted as a part of the international survey reported in Chapter 2, Energy geostructures, with the aim of estimating the number of applications and the features of energy geostructures worldwide, as well as the best practice methods employed to design and construct such structures by practitioner companies.

A.2 Questionnaire

The following questions concern information that we would need about the projects involving energy geostructures that were designed/built by your company. These questions are grouped into two sets: a general part and a more specific part. We would be grateful if you could answer to as many questions as possible and send this survey back to us. The addition of any material that you could share with us would be greatly appreciated.

I. *General part*

1. *How many projects involving energy geostructures were realised by your company (please specify the name and the location of such project(s))?*
2. *For these projects, how many elements/surfaces of these geostructures were equipped as a geothermal heat exchanger (e.g. number of energy piles, surfaces of energy walls)?*
3. *In general, in which type of soil do you realise energy geostructures (e.g. coarse-grained soil, fine-grained soil or rock)?*
4. *Based on your experience, in which type of soil do you observe the greatest energy performances?*
5. *In general, what is the operation of the realised energy geostructures (e.g. heat exchange operation for cooling and/or heating, or heat storage operation with solar thermal panels)?*
6. *What were the types of constructed energy piles (e.g. floating piles, end-bearing piles) and the employed construction method?*
7. *What were the types of constructed energy walls (e.g. diaphragm wall, sheet pile wall and slurry wall) and the employed construction method?*
8. *What were the types of constructed energy tunnels (e.g. cut and cover, segmental lining) and the employed construction method?*

9. *In general, do you use a specific method to design energy geostructures from a geotechnical and structural point of view, with reference to the influence of the thermal loads applied to such structures?*

II. *Specific part*

For this part, we would be grateful if you could describe in detail at least one project that you consider representative for the work of your company in this field.

1. *Geotechnical study of the soil deposit involved (e.g. geological and/or geotechnical analysis, including soil stratigraphy, material properties and depth of the groundwater table).*
2. *Description of the project (e.g. type of geostructure, construction method employed).*
3. *Method(s) used for the geotechnical and structural designs of the thermo-active elements/parts of the foundation, highlighting possible differences with the approach used to design the conventional foundations in the same project.*
4. *Method of estimation of the future energy performance of the thermo-active foundations and results, before their realisation (e.g. energy consumption, energy supply and energy efficiency).*
5. *Potential verification or monitoring of the energy performance by in situ measurements (amounts of energy supplied and efficiency).*

Appendix B: Thermohydromechanical modelling in the context of energy geostructures

B.1 Summary

This appendix proposes a coupled mathematical formulation addressing the thermohydromechanical behaviour of materials to characterise the influences between heat transfer, mass transfer and deformation, which occur, for example in the context of energy geostructures. The considered developments resort to an analysis of the influences between mass transfer and deformation, and the proposition of a coupled mathematical formulation addressing the hydromechanical behaviour of geomaterials under isothermal conditions. This latter formulation completes the paired analysis of heat transfer, mass transfer and deformation phenomena with the theory treated in Chapters 3, Heat and mass transfers in the context of energy geostructures, and Chapter 4, Deformation in the context of energy geostructures, and serves as a basis for the understanding of the core subject of this appendix.

B.2 Hydromechanical modelling

B.2.1 General

The analysis of the interactions between mass transfer and deformation through mathematical formulations that link the key variables governing the considered phenomena represents a typical example of hydromechanical modelling. Hydromechanical modelling is particularly relevant to address the behaviour of geomaterials such as soils and rocks as a consequence of the interactions between the solid matrix and the fluid(s) contained in the material pores. These interactions are related to the fact that the deformation of porous materials affects the flow of the fluid(s) contained in the pores of their structure, and the fluid pressure influences the mechanical behaviour of these structures. In fact, both the solid matrix and the fluid(s) in the pores support the load acting on porous materials. This hydromechanical coupling influences the expansion or contraction of the deforming matrix, and the pressure gradient of the diffusing pore fluid(s). A thorough understanding of hydromechanical interactions is key to model problems involving consolidation as well as the general (isothermal) loading of geomaterials, and is relevant for the analysis and design of geostructures, for example.

The foundations of the hydromechanical modelling of geomaterials can be addressed to the works of Biot (1941, 1956). The theory of consolidation proposed by Terzaghi (1923) represents a particular case of the general framework characterising the problem addressed (Vulliet et al., 2016). Detailed information on the

hydromechanical modelling of geomaterials has been reported, for example by Lewis and Schrefler (1987).

The key variables that govern the hydromechanical behaviour of geomaterials are the displacement field of the solid skeleton and the pressure field of the pore fluid(s). Hereafter, reference is made to porous materials fully saturated with water, so that the variables into play are the displacement field of the solid matrix and the pore water pressure field.

The mathematical description of the hydromechanical behaviour of materials can be addressed referring to the concept of Representative Elementary Volume (REV) (cf. Chapter 3, Heat and mass transfers in the context of energy geostructures), which allows considering the material as homogeneous at the scale of the REV. In this context, the Biot's theory (Biot, 1941, 1956) or the theory of porous media (Bedford and Drumheller, 1983; De Boer and Ehlers, 1988) (which includes the averaging theory and the theory of mixtures) can be employed. Developments of the Biot's theory have been proposed, for example by Coussy (1995). Developments of the averaging theory have been proposed, for example by Marle (1982) and Kalaydjian (1987). Developments of the theory of mixtures have been presented, for example by Hutter et al. (1999) and Laloui et al. (2003).

The analysis of the hydromechanical behaviour of geomaterials proposed in the following resorts to the *averaging theory*. In this context, two scales are defined: one scale, referring to the pore size, while another scale, referring to the whole domain of the porous medium. At the level of the former scale, it is assumed that each constituent of the system (e.g. soil particles and water, for a soil fully saturated with the considered fluid) occupies a specific domain. At the level of the latter scale, it is assumed that each phase is a continuum medium that fills up the entire domain, average variables are assigned to the respective phase independent from the other(s), and the interaction between the solid and fluid phase(s) takes place through volume fraction variations.

The solution of the considered problems starts from the formulation of the relevant governing equations (e.g. mass and momentum conservation equations) for each phase of the material (e.g. solid and liquid) that constitutes the pore space and the definition of the constitutive laws (see, e.g., Whitaker and Cooke, 1966). The modelled materials are characterised by pores that are fully saturated with a fluid that in the considered case is water. The fluid embedded in the pores characterising the solid skeleton of the material is under compression. The solid matrix is compressible, similar to the fluid embedded in the pores. Darcy's law (Darcy, 1856) is valid, while no mass transfer occurs at the interfaces of the system constituents. Quasistatic conditions are ensured and small deformations take place. The resulting field equations are valid at the scale referring to the pore size. A REV that contains both solid particles and pores is

considered to obtain the average values of variables. The size of the REV should be such that the parameters representing distributions of solids and pores within it are statistically meaningful. Through averaging techniques (see, e.g., Bachmat and Bear, 1986), these equations are then averaged over suitable time and space scales to derive averaged (or macroscopic) sets of coupled field equations.

B.2.2 Mass conservation equation

Considering a constituent with density $\overline{\rho}$ (i.e. amount of mass m per unit volume), the total amount of mass m in the volume V at the relevant scale (where $V = V_s + V_f$, with V_s the volume of solid and V_f the volume of fluid) reads

$$m = \int^{V} \overline{\rho}(x_i, t) dV \tag{B.1}$$

where x_i is the general coordinate vector and t is the time. The mass conservation equation for the solid, s, and the fluid, f, requires

$$\frac{d}{dt} \int^{V} \overline{\rho}_i dV = 0 \quad \text{with} \quad i = s \text{ or } f \tag{B.2}$$

By using the divergence theorem

$$\frac{d}{dt} \int^{V} \overline{\rho}_i dV = \int^{V} \frac{\partial}{\partial t} \overline{\rho}_i dV + \int^{V} \nabla \cdot \left(\overline{\rho}_i \overline{v}_{i,i} \right) dV \tag{B.3}$$

and considering that expression (B.2) is valid for any considered volume, the integrand must vanish so that the Eulerian or local expression of mass conservation equation is obtained

$$\frac{\partial \overline{\rho}_i}{\partial t} + \nabla \cdot \left(\overline{\rho}_i \overline{v}_{i,i} \right) = 0 \tag{B.4}$$

where $\nabla \cdot$ represents the divergence, $\overline{v}_{i,i} = \partial u_{i,i} / \partial t$ is the velocity vector for the considered phase associated with the displacement field u_i of the same phase. By introducing the volume fraction $\tilde{n}_i$ associated with each phase i in the REV, the following holds true

$$\overline{\rho}_i = \tilde{n}_i \rho_i \tag{B.5}$$

where ρ_i is the density of phase i.

Based on the above, the mass conservation equation for the fluid phase reads

$$\frac{\partial n\rho_f}{\partial t} + \rho_f \nabla \cdot \left(n \frac{\partial u_{f,i}}{\partial t} \right) = 0 \tag{B.6}$$

while the mass conservation equation for the solid phase reads

$$\frac{\partial \left[(1-n)\rho_s \right]}{\partial t} + \rho_s \nabla \cdot \left[(1-n) \frac{\partial u_{s,i}}{\partial t} \right] = 0 \tag{B.7}$$

where n is the material porosity, ρ_f is the density of the fluid, $u_{f,i}$ is the displacement vector of the fluid, ρ_s is the density of the solid particles and $u_{s,i}$ is the displacement vector of the solid matrix.

By summing Eqs (B.6) and (B.7), the following equation is obtained

$$n \frac{\partial \rho_f}{\partial t} \frac{1}{\rho_f} + (1-n) \frac{\partial \rho_s}{\partial t} \frac{1}{\rho_s} + \nabla \cdot \left(n \frac{\partial u_{f,i}}{\partial t} \right) + \nabla \cdot \left[(1-n) \frac{\partial u_{s,i}}{\partial t} \right] = 0 \tag{B.8}$$

Considering that

$$\frac{\partial \rho_f}{\partial t} \frac{1}{\rho_f} = \frac{1}{K_f} \frac{\partial p_f}{\partial t} \tag{B.9}$$

where ρ_f is the fluid pressure and

$$\frac{1}{K_f} = \frac{\partial \rho_f}{\partial p_f} \frac{1}{\rho_f} \tag{B.10}$$

where $1/K_f$ is the compressibility of the fluid, and that

$$\frac{\partial \rho_s}{\partial t} \frac{1}{\rho_s} = \frac{1}{K_s} \frac{\partial p_f}{\partial t} \tag{B.11}$$

where $1/K_s$ is the compressibility of the solid matrix, and that

$$\overline{v}_{rf,i} = \frac{\partial u_{rf,i}}{\partial t} = n \left(\frac{\partial u_{f,i}}{\partial t} - \frac{\partial u_{s,i}}{\partial t} \right) \tag{B.12}$$

$$\overline{v}_{s,i} = \frac{\partial u_{s,i}}{\partial t} \tag{B.13}$$

where $\overline{v}_{rf,i}$ is the relative velocity of the fluid with respect to the solid matrix and $\overline{v}_{s,i}$ is the velocity of the solid matrix, the mass conservation equation for the considered two-phase system reads

$$\frac{\partial p_f}{\partial t}\left[n\frac{1}{K_f}+(1-n)\frac{1}{K_s}\right]+\nabla\cdot\overline{v}_{rf,i}+\nabla\cdot\overline{v}_{s,i}=0 \tag{B.14}$$

Equivalently, Eq. (B.14) can be expressed as

$$\frac{\partial p_f}{\partial t}\left[n\frac{1}{K_f}+(1-n)\frac{1}{K_s}\right]+\nabla\cdot\left(\frac{\partial u_{rf,i}}{\partial t}\right)+\nabla\cdot\left(\frac{\partial u_{s,i}}{\partial t}\right)=0 \tag{B.15}$$

The mass conservation equation for a porous material fully saturated with water under isothermal conditions reads

$$\frac{\partial p_w}{\partial t}\left[n\frac{1}{K_f}+(1-n)\frac{1}{K_s}\right]+\nabla\cdot\overline{v}_{rw,i}+\nabla\cdot\overline{v}_{s,i}=0 \tag{B.16}$$

where p_w is the pore water pressure and $\overline{v}_{rw,i}$ is the relative velocity of water with respect to the solid matrix. The variable $\overline{v}_{rw,i}$ appearing in Eq. (B.16) can be further expanded through Darcy's law (Darcy, 1856).

Eq. (B.16) presents two unknowns: the pore water pressure, p_w (also included in the term $\overline{v}_{rw,i}$), and the displacement field of the solid matrix, $u_{s,i}$ (included in the term $\overline{v}_{s,i}$). It expresses that pore water pressure variations (first term in the equation) are associated with mass transfer (second term) as well as with the deformation of the considered system (last term).

B.2.3 Equilibrium equation

The equilibrium equation for a porous material fully saturated with water under isothermal conditions can be obtained by the indefinite equilibrium equations and the Terzaghi's formulation for the effective stress (hydromechanical coupling). For a porous material fully saturated with water, the equilibrium equation reads

$$\nabla\cdot\sigma'_{ij}+\nabla p_w+\rho g_i=0 \tag{B.17}$$

where σ'_{ij} is the effective stress tensor, ∇ represent the gradient, $\rho=n\rho_w+(1-n)\rho_s$ is the bulk density of the porous material, which includes the densities of water ρ_w and of solid particles ρ_s through the porosity n, and g_i is the gravity vector.

The effective stress tensor is expressed by introducing the relevant constitutive model through the stress–strain relation. Accordingly, Eq. (B.17) can be rewritten as

$$\nabla\cdot\left(M_{ijkl}{:}\varepsilon_{kl}\right)+\nabla p_w+\rho g_i=0 \tag{B.18}$$

or, equivalently, as

$$\nabla\cdot\left[M_{ijkl}{:}\varepsilon_{kl}\left(u_{s,i}\right)\right]+\nabla p_w+\rho g_i=0 \tag{B.19}$$

where M_{ijkl} is the general constitutive tensor of the material and ε_{kl} is the strain tensor.

Eq. (B.19) represents a second expression that is a function of the two unknowns previously highlighted. This equation can be coupled with Eq. (B.16) to address the hydromechanical behaviour of any considered material under isothermal conditions.

B.3 Thermohydromechanical modelling

B.3.1 General

The analysis of the interactions between heat transfer, mass transfer and deformation through mathematical formulations that link the key variables governing the considered phenomena represents a typical example of thermohydromechanical modelling. Thermohydromechanical modelling is particularly relevant to address the behaviour of geomaterials such as soils and rocks as a consequence of the interactions between the solid matrix and the fluid(s) contained in the pores of the material under nonisothermal conditions. These interactions are related to the fact that temperature variations cause expansion or contraction of the system constituents: these phenomena contribute to the relative influence between the displacement field of the solid matrix as well as the pore fluid(s) pressure, and induce a variation of the overall system response. A thorough understanding of thermohydromechanical interactions is key to model problems involving the general (nonisothermal) loading of geomaterials, and is relevant for the analysis and design of energy geostructures, for example.

Detailed information on the thermohydromechanical modelling of geomaterials has been reported, for example by Lewis and Schrefler (1987). In the following, the referenced problem is addressed considering the averaging theory expanded for the hydromechanical modelling of geomaterials, with the particularity that nonisothermal conditions are accounted for the key variables that govern the thermohydromechanical behaviour of geomaterials are the temperature field, the displacement field of the solid skeleton and the pressure field of the pore fluid(s). In this context, the energy, mass and momentum conservation equations need to be appropriately formulated and solved simultaneously. Hereafter, reference is made to porous materials fully saturated with water, so that the variables into play are the displacement field of the solid matrix, the pore water pressure field and the temperature field. This problem has been considered, for example by Charlier (1987), Collin (2003) and Charlier et al. (2006).

B.3.2 Mass conservation equation

The mass conservation equation for a porous material fully saturated with water under nonisothermal conditions reads

$$\frac{\partial p_w}{\partial t}\left[n\frac{1}{K_w}+(1-n)\frac{1}{K_s}\right]+\frac{\partial T}{\partial t}\left[n\beta_w+(1-n)\beta_s\right]+\nabla\cdot\overline{v}_{rw,i}+\nabla\cdot\overline{v}_{s,i}=0 \qquad \text{(B.20)}$$

where T is the temperature and β_w and β_s are the volumetric thermal expansion coefficients of water and the solid skeleton, respectively. As previously highlighted with reference to Eq. (B.16), the term $\overline{v}_{rw,i}$ can be expressed through Darcy's law (Darcy, 1856) as a function of the hydraulic conductivity k, which can be further expressed as a function of the density and the dynamic viscosity of water. The thermal dependence of hydraulic conductivity (thermohydraulic coupling) can be achieved by considering a dependency of μ_w on temperature that has been formulated, for example by Thomas and King (1994). A further expression between ρ_w and temperature may be considered and reads, for example (Thomas and King, 1994)

$$\rho_w = \rho_{w0}\left(1 + \frac{1}{K_w}\frac{\partial p_w}{\partial t} - \beta_w \frac{\partial T}{\partial t}\right) \tag{B.21}$$

where ρ_{w0} is the density of water at the reference temperature and pressure.

B.3.3 Equilibrium equation

The equilibrium equation for a porous material fully saturated with water under nonisothermal conditions coincides with Eq. (B.17), with the only difference that an appropriate stress–strain relation accounting for the influence of temperature (i.e. through a thermoelastic or a thermoelastic, thermoplastic mathematical formulation) is employed. This approach involves

$$\nabla \cdot \left[M_{ijkl} : \varepsilon_{kl}\left(u_{s,i}, T\right)\right] + \nabla p_w + \rho g_i = 0 \tag{B.22}$$

In Eq. (B.22), similar to Eq. (B.20), but in contrast to Eqs (B.19) and (B.16), respectively, temperature arises as an additional variable. To solve the considered problem, one additional equation (represented by the energy conservation equation discussed hereafter) is needed in addition to Eqs (B.20) and (B.22).

B.3.4 Energy conservation equation

The energy conservation equation for a porous material fully saturated with water reads

$$\nabla \cdot (\lambda \nabla T) = \rho c_p \frac{\partial T}{\partial t} + \rho_w c_{p,w} \overline{v}_{rw,i} \cdot \nabla T \tag{B.23}$$

where $\rho c_p = n\rho_w c_{p,w} + (1-n)\rho_s c_{p,s}$ is the specific heat of the soil (including the water and solid components $c_{p,w}$ and $c_{p,s}$), and $\lambda = n\lambda_w + (1-n)\lambda_s$ is the thermal conductivity of the soil (including the water and solid components λ_w and λ_s). In Eq. (B.23), any internal volumetric heat generation has been neglected.

References

Bachmat, Y., Bear, J., 1986. Macroscopic modelling of transport phenomena in porous media. 1: The continuum approach. Transp. Porous Media 1 (3), 213–240.
Bedford, A., Drumheller, D.S., 1983. Theories of immiscible and structured mixtures. Int. J. Eng. Sci. 21 (8), 863–960.
Biot, M.A., 1941. General theory of three-dimensional consolidation. J. Appl. Phys. 12 (2), 155–164.
Biot, M.A., 1956. General solutions of the equations of elasticity and consolidation for a porous material. J. Appl. Mech. 23 (1), 91–96.
Charlier, R., 1987. Approche unifiée de quelques problèmes non linéaires de mécanique des milieux continus par la méthode des éléments finis: grandes déformations des métaux et des sols, contact unilatéral de solides, conduction thermique et écoulements en milieu poreux. Faculté des Sciences Appliquées, Université de Liége, Liège.
Charlier, R., Laloui, L., Collin, F., 2006. Numerical modelling of coupled poromechanics processes. Rev. Eur. Gén. Civ. 10 (6–7), 669–701.
Collin, F., 2003. Couplages thermo-hydro-mécaniques dans les sols et les roches tendres partiellement saturés. Faculté des Sciences Appliquées, Université de Liège, Liège, p. 300.
Coussy, O., 1995. Mechanics of Porous Continua. Wiley.
Darcy, H., 1856. Les fontaines publiques de la ville de Dijon: exposition et application. Victor Dalmont.
De Boer, R., Ehlers, W., 1988. A historical review of the formulation of porous media theories. Acta Mech. 74 (1–4), 1–8.
Hutter, K., Laloui, L., Vulliet, L., 1999. Thermodynamically based mixture models of saturated and unsaturated soils. Mech. Cohes. Frict. Mater. Int. J. Exp.Model. Comput. Mater. Struct. 4 (4), 295–338.
Kalaydjian, F., 1987. A macroscopic description of multiphase flow in porous media involving spacetime evolution of fluid/fluid interface. Transp. Porous Media 2 (6), 537–552.
Laloui, L., Klubertanz, G., Vulliet, L., 2003. Solid–liquid–air coupling in multiphase porous media. Int. J. Numer. Anal. Methods Geomech. 27 (3), 183–206.
Lewis, R., Schrefler, B., 1987. The Finite Element Method in the Deformation and Consolidation of Porous Media. John Wiley & Sons.
Marle, C., 1982. On macroscopic equations governing multiphase flow with diffusion and chemical reactions in porous media. Int. J. Eng. Sci. 20 (5), 643–662.
Terzaghi, K., 1923. Die Berechnung des Durchlassigkeitszifferdes Tones aus dem Verlauf der hydrodynamischen Spannungserscheinungen. In: Wissen, S.A. (Ed.), Wien MAth-naturw KI. Abt IIa, vol. 132. Akademie der Wissenschaften, Wien, pp. 125–138.
Thomas, H., King, S., 1994. A non-linear, two-dimensional, potential-based analysis of coupled heat and mass transfer in a porous medium. Int. J. Numer. Methods Eng. 37 (21), 3707–3722.
Vulliet, L., Laloui, L., Zhao, J., 2016. Mécanique des sols et des roches (TGC volume 18): avec écoulements souterrains et transferts de chaleur. PPUR Presses Polytechniques.
Whitaker, T., Cooke, R.W., 1966. An investigation of the shaft and base resistance of large bored piles in London clay. Symposium on Large Bored Piles. Thomas Teldford Publishing, London, pp. 7–49.

Appendix C: Advanced Constitutive Model for Environmental Geomechanics-Temperature effects

C.1 Summary

A framework allowing for the modelling of the reversible and irreversible mechanical behaviour of materials has been presented in Chapter 4, Deformation in the context of energy geostructures. However, no specific reference to mathematical formulations for modelling the elastoplastic behaviour of any particular material and account for the influence of nonisothermal conditions on this behaviour has been reported. Various mathematical formulations can be employed for the considered purpose. The features of these formulations depend on the mechanical behaviour of the modelled material because they are generally tailored to capture key aspects of such behaviour depending on the purpose and the aimed accuracy of the investigation.

In the following, the *Advanced Constitutive Model for Environmental Geomechanics, with Temperature effects included* (ACMEG-T) is presented to capture advanced aspects of the behaviour of geomaterials such as soils. The model can characterise the thermoelastic, thermoplastic behaviour of soils in the framework of the critical state theory (Schofield and Wroth, 1968) and may be used in the analysis and design of energy geostructures to capture the mechanical response of soils under nonisothermal conditions through an advanced approach. The isothermal part of the model is based on the work of Hujeux (1979). The nonisothermal part of the model has been developed to address monotonic and cyclic loading conditions through successive studies by Laloui (1993), Modaressi and Laloui (1997), Laloui and Cekerevac (2008), Laloui and Francois (2009) and Di Donna and Laloui (2015). Further improvements have been presented by Vilarrasa et al. (2016).

C.2 Stress–strain behaviour and elastic relations

The increment of total strain reads

$$d\varepsilon_{ij} = \frac{1}{3} d\varepsilon_v \delta_{ij} + de_{ij} \tag{C.1}$$

with

$$d\varepsilon_v = \mathrm{tr}\left(d\varepsilon_{ij}\right) \tag{C.2}$$

and

$$d\varepsilon_q = \frac{\sqrt{6}}{3}\sqrt{\mathrm{tr}(de_{ij})^2} \tag{C.3}$$

where $d\varepsilon_v$ is the volumetric strain increment, $d\varepsilon_q$ is the deviatoric strain increment and e_{ij} is the deviatoric strain tensor. In the elastic nonisothermal domain, the increment of volumetric strain reads

$$d\varepsilon_v^e = \frac{dp'}{K} - \beta dT \tag{C.4}$$

where p' is the mean effective stress, K is the bulk modulus of the material, β is the volumetric thermal expansion coefficient of the material and dT the temperature increment. The deviatoric component of the elastic strain is not affected by temperature and reads

$$d\varepsilon_q^e = \frac{dq}{3G} \tag{C.5}$$

where q is the deviatoric stress and G is the shear modulus of the material.

The reversible response of the material is considered to follow a nonlinear thermoelastic behaviour through the following expressions

$$K = K_{ref}\left(\frac{p'}{p'_{ref}}\right)^{n_e} \quad \text{and} \quad G = G_{ref}\left(\frac{p'}{p'_{ref}}\right)^{n_e} \tag{C.6}$$

where K_{ref} and G_{ref} are the two moduli at the reference mean effective stress p'_{ref}, and n_e is a material parameter controlling the nonlinearity of the elastic law (Vilarrasa et al., 2016).

C.3 Yield surface and potential function – monotonic loading

The yield surface is the combination of two surfaces, accounting respectively for two plastic mechanisms: one isotropic and one deviatoric. These mechanisms are coupled through the concept of preconsolidation pressure (cf. Fig. C.1). The isotropic yield limit reads

$$f_{iso} = p' - p'_c r_{iso} = 0 \quad \text{with} \quad r_{iso} = r_{iso}^e + \frac{\varepsilon_v^{p,iso}}{c_r + \varepsilon_v^{p,iso}} \tag{C.7}$$

where p'_c is the preconsolidation pressure, r_{iso} is the degree of mobilisation of plasticity of the isotropic mechanism, r_{iso}^e its initial value, $\varepsilon_v^{p,iso}$ is the volumetric plastic strain

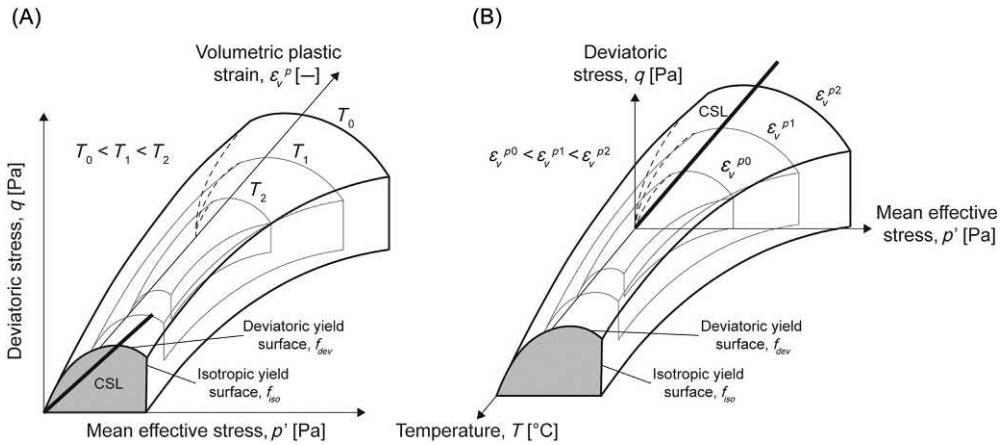

Figure C.1 Combined effect of strain hardening and thermal softening on the size of the elastic domain at (A) different temperatures and (B) different amount of developed plastic volumetric strain. *Redrawn after Di Donna, A., Laloui, L., 2015. Response of soil subjected to thermal cyclic loading: experimental and constitutive study. Eng. Geol. 190 (1), 65–76.*

developed by the activation of the isotropic mechanism and c_r is a material parameter. The deviatoric yield limit reads

$$f_{dev} = q - M_c p' \left[1 - b_r \ln\left(\frac{d_r p'}{p'_c}\right)\right] r_{dev} = 0 \quad \text{with} \quad r_{dev} = r_{dev}^e + \frac{\varepsilon_q^p}{a_r + \varepsilon_q^p} \tag{C.8}$$

where M_c is the slope of the critical state line in the $p'-q$ plane, b_r and d_r are two material parameters, r_{dev} is the degree of mobilisation of plasticity for the deviatoric mechanism, r_{dev}^e its initial value, a_r is a material parameter and ε_q^p is the deviatoric plastic strain. The parameter b_r defines the shape of the deviatoric yield limit in the $p'-q$ plane and can be assumed equal to 0 for sand and 1 for clay (Di Donna and Laloui, 2015). The parameter d_r reads

$$d_r = \frac{p'_{c0}}{p'_{cr0}} \tag{C.9}$$

The deviatoric yield limit formulated in Eq. (C.8) has been initially considered a function of two invariants of the effective stress tensor, that is q and p'. According to Di Donna and Laloui (2015) and Vilarrasa et al. (2016), this implies assuming that the projection of the yield surface on the octahedral plane is circular. Such a circular yield surface in the octahedral plane involves that yielding conditions are reached at the same deviatoric stress regardless of the direction of the stress path (Lode's angle). However, according to Vilarrasa et al. (2016), plasticity is stress path dependent for

both coarse-grained (see, e.g., Lade and Duncan, 1973) and fine-grained soils (see, e.g., Lade and Musante, 1978) as well as for rocks (see, e.g., Colmenares and Zoback, 2002; Makhnenko et al., 2015).

To overcome the previous limitations, the yield surface has been formulated in terms of three stress invariants (Di Donna and Laloui, 2015), with the new invariant being the Lode's angle, which varies from −30 to 30 degrees. The Lode's angle equals 30 degrees if the stress path is triaxial in compression, −30 degrees if the stress path is triaxial in extension and an intermediate value for plane strain and plane stress conditions (Vilarrasa et al., 2016). Although a circular yield surface can capture with accuracy triaxial stress paths in compression, it generally overestimates the strength for other stress paths. Therefore a different shape than the circular one may be desirable. The Mohr−Coulomb yield surface is more accurate than the circular surface, but the corners of its irregular hexagonal shape are difficult to handle numerically if an associated flow rule is employed (Potts and Gens, 1984). According to Vilarrasa et al. (2016), the direction of the plastic strain is non defined in the corners and proper techniques must be employed to overcome this issue. To overcome the previous limitations via the employment of a smooth yield surface in the principal stress space, the coefficient M_c has been chosen to depend on the Lode's angle according to the formulation proposed by Van Eekelen (1980):

$$M_c = 3\sqrt{3}a_L(1+b_L\sin 3\vartheta_l)^{n_L} \tag{C.10}$$

where a_L, b_L and n_L are material parameters.

The expressions proposed by Barnichon (1998) can be employed to determine a_L and b_L based on knowledge of the values of angle of shear strength in triaxial compression and extension φ'_c and φ'_e, respectively, as

$$a_L = \frac{r_c}{(1+b_L)^{n_L}} \quad \text{with} \quad a_L > 0 \tag{C.11}$$

and

$$b_L = \frac{\left(\frac{r_c}{r_e}\right)^{1/n_L} - 1}{\left(\frac{r_c}{r_e}\right)^{1/n_L} + 1} \quad \text{with} \quad b_L n_L > 0; -1 < b_L < 1 \tag{C.12}$$

where

$$r_c = \frac{1}{\sqrt{3}}\left(\frac{2\sin\varphi'_c}{3-\sin\varphi'_c}\right) \quad \text{and} \quad r_e = \frac{1}{\sqrt{3}}\left(\frac{2\sin\varphi'_e}{3+\sin\varphi'_e}\right) \tag{C.13}$$

If the angles of shear strength of the material are equal in compression and extension, the formulation proposed by Van Eekelen (1980) coincides with the Mohr–Coulomb one for $\vartheta_l = \pm 30$ degrees, with

$$M_c = \frac{6\sin\varphi'_{cv}}{3 - \sin\varphi'_{cv}} \quad \text{for compression} \tag{C.14}$$

and

$$M_c = \frac{6\sin\varphi'_{cv}}{3 + \sin\varphi'_{cv}} \quad \text{for extension} \tag{C.15}$$

When experimental data in extension are not available, assuming the corresponding angle of shear strength equal to the one in compression leads often to negligible errors both in extension and plane strain conditions, or, at least, to errors smaller than the ones induced by assuming a circular surface (Di Donna, 2014).

The value of n_L has to be assumed in order to ensure the convexity condition (Barnichon, 1998). In this sense Van Eekelen (1980) showed that the optimised value is -0.229. Other models, such as the ones proposed by Lade and Duncan (1975), Zienkiewicz and Pande (1977) and Gudehus (1973) are specific cases of the one proposed by Van Eekelen for values of n_L equal to -0.25, -1 and 0.5, respectively.

C.4 Hardening rule

The dependency of the preconsolidation pressure p'_c on the volumetric plastic strain (strain hardening, horizontal plane in Fig. C.1A) is described according to the critical state theory and its evolution with temperature (thermal softening, horizontal plane in Fig. C.1B) is introduced according to the equation proposed by Laloui and Cekerevac (2003) as

$$p'_c = p'_{c0}\exp\left(\beta_p \varepsilon_v^p\right)\left[1 - \gamma_T \ln\left(\frac{T}{T_0}\right)\right] \tag{C.16}$$

where β_p is the plastic rigidity index and γ_T is a material parameter that defines the shape of the isotropic yield function with respect to temperature. The coupling between thermal softening and strain hardening is represented in Fig. C.1: for a certain amount of developed volumetric plastic deformation, the size of the elastic domain decreases with increasing temperature (thermal softening), while for a constant temperature, the size of the elastic domain increases for increasing volumetric plastic strain (strain hardening). The global response of the soil under thermomechanical loading is

a combination of the two effects. The flow rule is associated for the isotropic mechanism, but not associated for the deviatoric one. Accordingly, purely isotropic loading causes only volumetric plastic deformation, while purely deviatoric loading causes both deviatoric and volumetric plastic deformation. Calling the isotropic and deviatoric plastic potentials g_{iso} and g_{dev} respectively, $g_{iso} = f_{iso}$ but $g_{dev} \neq f_{dev}$ and (Nova and Wood, 1979):

$$g_{dev} = q - \frac{\alpha_h}{\alpha_h - 1} M_c p' \left[1 - \frac{1}{\alpha_h} \left(\frac{d_r p'}{p'_c} \right)^{\alpha_h - 1} \right] = 0 \tag{C.17}$$

where α_h is a nonassociativity material parameter that expresses the dilatancy rule as

$$\frac{d\varepsilon_v^p}{d\varepsilon_q^p} = \alpha_h \left(M_c - \frac{q}{p'} \right) \tag{C.18}$$

The flow rules for the volumetric and the deviatoric plastic strains are:

$$d\varepsilon_v^p = \lambda_{iso}^p \frac{\partial g_{iso}}{\partial p'} + \lambda_{dev}^p \frac{\partial g_{dev}}{\partial p'} \tag{C.19}$$

$$d\varepsilon_q^p = \lambda_{dev}^p \frac{\partial g_{dev}}{\partial q} \tag{C.20}$$

where λ_{iso}^p and λ_{dev}^p are the plastic multipliers for the isotropic and the deviatoric mechanisms, respectively.

C.5 Generalised stress–strain relation

The definition of the generalised stress–strain relation resorts to the knowledge of the plastic multipliers. These terms can be determined by solving the consistency condition via the substitution of the appropriate flow rules. Considering the two plastic mechanisms, the consistency equation for this model is:

$$\frac{\partial f_l}{\partial \sigma'_i} D_{ij} \left(d\varepsilon_j - \lambda_l^p \frac{\partial g_l}{\partial \sigma'_j} + \beta_j dT \right) + \frac{\partial f_l}{\partial T} dT + \frac{\partial f_l}{\partial \tilde{h}} \frac{\partial \tilde{h}}{\partial \varepsilon_i^p} \lambda_l^p \frac{\partial g_l}{\partial \sigma'_i} = 0 \tag{C.21}$$

where f_l represents the vector containing the two yield surfaces f_{iso} and f_{dev}, D_{ij} is the elastic stiffness tensor, λ_l^p the vector containing the two plastic multipliers λ_{iso}^p and λ_{dev}^p, g_l the vector containing the two plastic potentials g_{iso} and g_{dev}, and $\tilde{h}$ the hardening variable.

C.6 Yield surface – cyclic loading

The possibility of reproducing the mechanical behaviour of soils under thermal cyclic loading has been introduced by Di Donna and Laloui (2015) via the bounding surface theory. The model has been modified to show (beyond the thermoelastic, thermoplastic behaviour depending on the stress state) the accumulation of plastic deformation during a certain number of thermal cycles, followed by stabilisation. Such a behaviour typically characterises fine-grained soils under normally consolidated conditions under the application of heating–cooling thermal cycles (Di Donna and Laloui, 2015). According to experimental evidence presented by Di Donna and Laloui (2015), after the insurgence of plastic strains during the initial heating thermal loading of a normally consolidated soil, soil response is thermoelastic during cooling and the first phase of reheating, but an increment of plastic strain must then be produced. The magnitude of this plastic strain is smaller cycle after cycle, tending to zero after a certain number of cycles. These features have been introduced by allowing the degree of mobilisation of plasticity of the isotropic yield mechanism, r_{iso}, evolving during cooling. The above can be seen as a reinitialisation of the locus of points at which plasticity starts during the next heating phase. From a mathematical point of view, r_{iso} is reinitialised at each temperature reduction as (Di Donna and Laloui, 2015):

$$r_{iso} = r_{iso}^{cyc} + \frac{p'}{p'_c} \tag{C.22}$$

where r_{iso}^{cyc} is a material parameter that depends on the tendency of the material to accumulate plastic deformation during thermal cycles. When heating restarts, r_{iso} remains constant as long as the reinitialised yield surface is reached. Therefore during reheating, plasticity starts again at the temperature $\tilde{T}$ that verifies the following equation:

$$f_{iso} = p' - p'_{c0}\exp\left(\beta_p \varepsilon_v^p\right)\left[1 - \gamma_T \ln\left(\frac{\tilde{T}}{T_0}\right)\right]\left(r_{iso}^{cyc} + \frac{p'}{p'_{c0}e^{\beta\varepsilon_v^p}}\right) = 0 \tag{C.23}$$

Once that this temperature is reached, if heating continues the degree of mobilisation of plasticity for the isotropic mechanism evolves according to

$$r_{iso} = r_{iso}^{cyc} + \frac{p'}{p'_{c,cool}} + \frac{\varepsilon_v^{p,iso,cyc}}{c_r + \varepsilon_v^{p,iso,cyc}} \tag{C.24}$$

where $p'_{c,cool}$ is the preconsolidation pressure at the end of the previous cooling phase and $\varepsilon_v^{p,iso,cyc}$ the volumetric plastic strain induced by the isotropic mechanism starting from the last reheating. The temperature $\tilde{T}$, at which plasticity occurs,

increases at each cycle. Consequently, after a certain number of cycles it coincides with the maximum temperature imposed and no more thermal plastic strain is developed starting from the next cycle. The schematic model response during a heating–cooling–reheating path under a constant mean effective stress $\overline{p'}$ is presented in Fig. C.2. Referring to Fig. C.2A, during the first heating from T_0 to T_1, the response is thermoelastic, as the stress point is inside the elastic domain ($p' < p'_{c0} r^e_{iso}$).

The corresponding thermoelastic dilatant strain is represented by the segment 0–1. Plasticity starts at the temperature T_1 when Eq. (C.7) for the yield surface is satisfied, considering Eq. (C.16) and that $\varepsilon^p_v = 0$ (first cycle):

$$T_1 = T_0 \exp\left(\frac{r^e_{iso} p'_{c0} - \overline{p'}}{p'_{c0} \gamma_T r^e_{iso}}\right) \tag{C.25}$$

Heating further from T_1 to T_2 (cf. Fig. C.2B), plastic deformation is developed. In this phase, r_{iso} evolves according to Eq. (C.7) up to the value of $r^1_{iso} \leq 1$ and the preconsolidation pressure at the initial temperature T_0 increases to $p'_{c1} = p'_{c0} \exp(\beta_p \varepsilon^p_v)$. The corresponding plastic strain is represented by the segment 1–2 in Fig. C.2B. If the temperature is then decreased from T_2 to $T_3 = T_0$ (cf. Fig. C.2C), the stress point enters inside the elastic domain and consequently the response is thermoelastic contraction (segment 2–3). Nevertheless, during this phase r_{iso} is reinitialised accordingly to Eq. (C.22) and at $T_3 = T_0$ its value is:

$$r_{iso} = r^{cyc}_{iso} + \frac{\overline{p'}}{p'_{c1}} \tag{C.26}$$

If the material is heated again it shows a thermoelastic response from T_3 to T_4 (cf. Fig. C.2D, segment 3–4), where T_4 verifies the Eq. (C.23), being:

$$T_4 = T_0 \exp\left(\frac{p'_{c1} r^{cyc}_{iso}}{\gamma_T p'_{c1} r^{cyc}_{iso} + \gamma_T \overline{p'}}\right) \tag{C.27}$$

Heating further, from point 4 to point 5, plasticity occurs according to the same concept illustrated for the heating phase from point 1 to point 2 (cf. Fig. C.2B, segment 4–5). Comparing Eqs (C.25) and (C.27), it is possible to verify that at each cycle the thermal plasticity occurs at a higher temperature than the one at which it occurs at the previous cycle. As a consequence, after a certain number of cycles, it reaches the value of the maximum temperature imposed (T_2) and, if the temperature continues to vary cyclically among T_0 and T_2, no more plastic deformation is developed (phenomenon of accommodation).

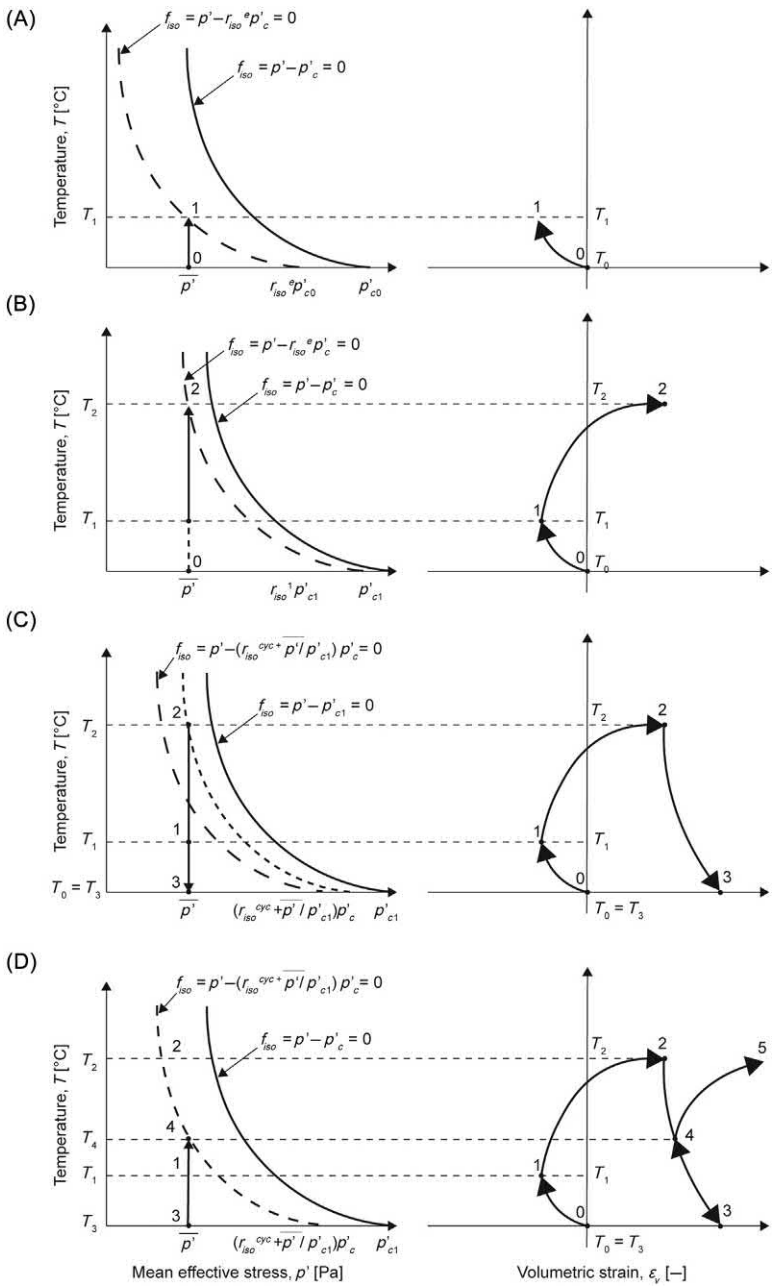

Figure C.2 ACMEG-T response during a heating−cooling−reheating path under constant mean effective stress. *Redrawn after Di Donna, A., Laloui, L., 2015. Response of soil subjected to thermal cyclic loading: experimental and constitutive study. Eng. Geol. 190 (1), 65−76.*

References

Barnichon, J.D., 1998. Finite Element Modelling in Structural and Petroleum Geology. Universite de Liege, Faculte des Sciences appliquees, Liege.

Colmenares, L., Zoback, M., 2002. A statistical evaluation of intact rock failure criteria constrained by polyaxial test data for five different rocks. Int. J. Rock Mech. Min. Sci. 39 (6), 695–729.

Di Donna, A., 2014. Thermo-mechanical aspects of energy piles. Laboratory of Soil Mechanics. Swiss Federal Institute of Technology in Lausanne (EPFL), Lausanne.

Di Donna, A., Laloui, L., 2015. Response of soil subjected to thermal cyclic loading: experimental and constitutive study. Eng. Geol. 190 (1), 65–76.

Gudehus, G., 1973. Elastoplastische Stoffgleichungen fur sand. Ing. Arch. 42, 151–169.

Hujeux, J.C., 1979. Calcul numérique de problèmes de consolidation elastoplastique (Ph.D. thesis). Ecole Centrale, Paris.

Lade, P.V., Duncan, J.M., 1973. Cubical triaxial tests on cohesionless soil. J. Soil Mech. Found. Eng. Div. 99 (SM10), 793–812.

Lade, P.V., Duncan, J.M., 1975. Elastoplastic stress–strain theory for cohesionless soil. J. Geotech. Eng. Div. 101 (10), 1037–1053.

Lade, P.V., Musante, M., 1978. Three-dimensional behavior of remolded clay. J. Geotech. Eng. Div. 104 (2), 193–209.

Laloui, L., 1993. Modélisation du comportement thermo-hydro-mécanique des milieux poreux anélastique (Ph.D. thesis). Ecole Centrale de Paris.

Laloui, L., Cekerevac, C., 2003. Thermo-plasticity of clays: an isotropic yield mechanism. Comput. Geotech. 30 (8), 649–660.

Laloui, L., Cekerevac, C., 2008. Non-isothermal plasticity model for cyclic behaviour of soils. Int. J. Numer. Anal. Methods Geomech. 32 (5), 437–460.

Laloui, L., Francois, B., 2009. ACMEG-T: Soil thermoplasticity model. J. Eng. Mech. ASCE 135 (9), 932–944.

Makhnenko, R.Y., Harvieux, J., Labuz, J.F., 2015. Paul–Mohr–Coulomb failure surface of rock in the brittle regime. Geophys. Res. Lett. 42 (17), 6975–6981.

Modaressi, H., Laloui, L., 1997. A thermo-viscoplastic constitutive model for clays. Int. J. Numer. Anal. Methods Geomech. 21 (5), 313–335.

Nova, R., Wood, D.M., 1979. Constitutive model for sand in triaxial compression. Int. J. Numer. Anal. Methods Geomech. 3 (3), 255–278.

Potts, D.M., Gens, A., 1984. Formulation of quasi-axisymmetric boundary value problems for finite element analysis. Eng. Comput. 1 (2), 144–150.

Schofield, A.N., Wroth, C.P., 1968. Critical State Soil Mechanics. McGraw-Hill.

Van Eekelen, H.A.M., 1980. Isotropic yield surfaces in three dimensions for use in soil mechanics. Int. J. Numer. Anal. Methods Geomech. 4 (1), 89–101.

Vilarrasa, V., Parisio, F., Laloui, L., 2016. Strength evolution of geomaterials in the octahedral plane under nonisothermal and unsaturated conditions. Int. J. Geomech. 17 (7), 04016152.

Zienkiewicz, O.C., Pande, G.N., 1977. Some useful forms of isotropic yield surfaces for soil and rock mechanics. In: Gudehus, G. (Ed.), Finite Element in Geomechanics. ISTE Ltd and John Wiley & Sons Inc, Chichester.

Further reading

Dafalias, Y.F., 1980. Materials with vanishing elastic region. Int. J. Numer. Anal. Methods Geomech. 4 (4), 389.

Index

Note: Page numbers followed by '*f*' and '*t*' refer to figures and tables, respectively.

C

E

F

G

H

N

O

P

Q

R

S

T

U

V

W

Y

Analysis and Design of Energy Geostructures

Theoretical Essentials and Practical Application

Analysis and Design of Energy Geostructures: Theoretical Essentials and Practical Application gathers a unified framework of the theoretical and experimental competence available on energy geostructures: innovative multifunctional earth-contact structures that can provide renewable energy supply and structural support to any built environment. The book covers the broad, interdisciplinary and integrated knowledge required to address the analysis and design of energy geostructures from energy, geotechnical and structural perspectives. This knowledge includes (Part A) an introduction to the technology; (Part B) the fundamentals of heat and mass transfers as well as of the mechanics of geomaterials and structures required to address the unprecedented behaviour of energy geostructures; (Part C) the experimental evidence characterising the considered geostructures; (Part D) various analytical and numerical modelling approaches to analyse the response of energy geostructures and (Part E) the performance-based design and detailing essentials of energy geostructures. Designed with civil engineers in mind, this book targets energy engineers, environmental engineers, geologists, architects and urban project managers as well.

Key Features

- Proposes the theoretical and practical application essentials required to address the analysis and design of energy geostructures from energy, geotechnical, and structural perspectives
- Presents a substantial amount of resolved exercises on key aspects governing the behaviour and performance of energy geostructures to be considered in analysis and design
- Summarises and discusses the most recent scientific and technical knowledge about energy geostructures, including energy piles, energy tunnels and energy walls

About the Authors

Lyesse Laloui

Lyesse Laloui, PhD, is a chaired professor at the Swiss Federal Institute of Technology in Lausanne, EPFL, Switzerland. He is also an adjunct professor at Duke University, United States, and an advisory professor at Hohai University, China. His main research interests are in Geomechanics as well as Environmental and Energy Sustainability. He has written and edited 12 books, authored over 300 refereed scientific papers and is the editor-in-chief of the international journal *Geomechanics for Energy and the Environment*. He has served as a keynote speaker and honourary lecturer at more than 40 leading international scientific events and he has also delivered training courses for practitioners and scientists on various topics including the analysis and design of energy geostructures. He has cofounded the GEOEG engineering company, providing integrated solutions for energy geostructures for prominent architectural and engineering projects around the world.

Alessandro F. Rotta Loria

Alessandro F. Rotta Loria, PhD, is an assistant professor at Northwestern University, United States, and a qualified professional civil and environmental engineer of the Italian Order of Engineers. His main research interests are at the interface of Geomechanics, Structural Mechanics and Energy. He is an editorial associate of the international journal *Geomechanics for Energy and the Environment* and is actively involved in many international scientific events as invited lecturer and presenter. Over the past 5 years, he has received various prizes and honours for excellence in scientific research, among which the 2019 Zeno Karl Schindler Prize for key contributions in the field of environmental sustainability, and he has also delivered training courses for practitioners and scientists on the analysis and design of energy geostructures. He has cofounded the GEOEG engineering company, providing integrated solutions for energy geostructures for prominent architectural and engineering projects around the world.

ELSEVIER

ACADEMIC PRESS

An imprint of Elsevier

elsevier.com/books-and-journals

ISBN 978-0-12-820623-2